ICNBME-2011

INTERNATIONAL CONFERENCE

on Nanotechnologies and Biomedical Engineering

German-Moldovan Workshop on

Novel Nanomaterials for Electronic, Photonic and Biomedical Applications

Chisinau, Moldova, July 7-8, 2011

PROCEEDINGS

Organized by

- *Academy of Sciences of Moldova*
- *Technical University of Moldova*
- *State Medical and Pharmaceutical University "Nicolae Testemitanu" of the Republic of Moldova*
- *Moldavian Society of Biomedical Engineering*

In cooperation with

- *Medical Imagistic Society of Moldova*
- *Moldavian Association of Medical Informatics*

Under the auspices

- *of the German Ambassador to Moldova*

Supported by

- *European Federation for Medical Informatics*
- *GE Healthcare*
- *Alexander von Humboldt Foundation (Workshop)*
- *Global Biomarketing Group-Moldova*
- *NITECH S.R.L.*
- *Intermed Company*
- *XEROX Moldova*

CZU ??????????????????????????????
T ???

Published by: Technical University of Moldova

Editors: Corr. member Ion Tiginyanu and Prof. Dr. Victor Sontea

Responsibil for edition: Dr. Serghei Railean

Cover designer: Dmitri Anghiloglu

??????????????????????????????
??????????????????????????????
??????????????????????????????
??????????????????????????????
??????????????????????????????
??????????????????????????????
??????????????????????????????
??????????????????????????????
??????????????????????????????

Elan Poligraf ??????????????????????????????

ISBN ??????????????????????????????

Honorary Chairmans oh the ICNBME - 2011

- ***Academician Ion Ababii*, Rector of the State Medical and Pharmaceutical University "Nicolae Testemitanu" of the Republic of Moldova**
- ***Academician Ion Bostan*, Rector of the Technical University of Moldova**
- ***Academician Gheorghe Duca*, President of the Academy of Sciences of Moldova**

International Advisory Committee

R. Adelung	*Germany*	O. Maiorov	*Ukraine*
A. Andriesh	*Moldova*	F. J. Manjón Herrera	*Spain*
E. Arushanov	*Moldova*	H. Mimura	*Japan*
R. Boyd	*Canada*	R. Negoescu	*Romania*
J.-C. Buisson	*France*	T. Pauporte	*France*
L. Chow	*USA*	D. Pavlidis	*Germany*
P. Cristea	*Romania*	V. Pershenkov	*Russia*
D. Dascalu	*Romania*	P. Schmuki	*Germany*
D. Dimova-Malinovska	*Bulgaria*	A. Schulte	*USA*
R. Engelbrecht	*Germany*	C. Schwab	*France*
H. Föll	*Germany*	A. Simashkevich	*Moldova*
V. Fomin	*Germany*	B. Simionescu	*Romania*
Gh.Gheorghe	*Romania*	R. Singh	*USA*
Gh.Ghidirim	*Moldova*	T. Sisianu	*Moldova*
S. Groppa	*Moldova*	V. Socolov	*Ukraine*
H. Hartnagel	*Germany*	M. Stevens-Kalceff	*Australia*
N. Jula	*Romania*	R. Strungaru	*Romania*
V. Kantser	*Moldova*	H. Teodorescu	*Romania*
D. Lincot	*France*	V. Ushenco	*Ukraine*
V. Litovchenko	*Ukraine*	D. Zaharia	*Romania*

Program Committee

I. Tiginyanu	*Moldova Chairman*	S. Langa	*Germany*
V. Prisacari	*Moldova Co-Chairman*	J. Lloyd-Hughes	*UK*
V. Dorogan	*Moldova Co-Chairman*	A. Rotaru	*Moldova*
S. Andronic	*Moldova*	E.Rusu	*Moldova*
G. Arzumanyan	*Russia*	A. Salam Hamdy	*Germany*
E. Badinter	*Moldova*	A. Sarua	*UK*
I. Balmus	*Moldova*	A. Saulea	*Moldova*
A. Casian	*Moldova*	A. Sidorenco	*Moldova*
R. Ciorap	*Romania*	V. Skuratov	*Russia*
S. Ciubotaru	*Germany*	M. Sleahtitchi	*Moldova*
A. Cojocaru	*Germany*	P. Stratulat	*Moldova*
Gh.Curocichin	*Moldova*	N. Syrbu	*Moldova*
M. Dragoman	*Romania*	V. Trofim	*Moldova*
P. Filip	*Moldova*	D. Tsiulyanu	*Moldova*
C. Gaindric	*Moldova*	V. Ursaki	*Moldova*
P. Gashin	*Moldova*	A. Usatîi	*Moldova*
V. Harabagiu	*Romania*	R. Werlein	*Swiss*
V. Iakovlev	*Swiss*	I. Zatusevski	*Moldova*
L. Kulyuk	*Moldova*		

Organizing Committee

V. Sontea	*Moldova Chairman*	Iu. Nica	*Moldova*
V. Vovc	*Moldova Co - Chairman*	Pocaznoi	*Moldova*
S. Railean	*Moldova Secretary*	V. Popa	*Moldova*
T. Ciaicovschii	*Moldova*	A. Rosca	*Moldova*
V. Captari	*Moldova*	A. Rosioru	*Moldova*
L. Ghimpu	*Moldova*	V. Scripnic	*Moldova*
O. Lupan	*Moldova*	S. Sisianu	*Moldova*

CONTENTS

German-Moldovan Workshop on Novel Nanomaterials for Electronic,Photonic and Biomedical Applications

Section 1: Nanotechnologies and Nanomaterials

Section 2: Micro- and Nano-objects, Nanostrucured and higly integrated systems, Biophysics

Section 3: Biomedical Instrumentation and Devices

Section 4: Biomaterials

Section 5: Medical Imaging, Image and Signal Processing

Section 6: Information Technologies for Health Care, Telemedicine and E-Health

Monte-Carlo-Simulation of Crystallographical Pore Growth in III-V-Semiconductors

Malte LEISNER, Jürgen CARSTENSEN, and Helmut FÖLL
Institute for Materials Science, Christian-Albrechts-University of Kiel, Kaiserstrasse 2, 24143 Kiel, Germany
ml@tf.uni-kiel.de

***Abstract* – The growth of crystallographical pores in III-V-semiconductors can be understood in the framework of a simple model, which is based on the assumption that the branching of pores is proportional to the current density at the pore tips. The stochastic nature of this model allows its implementation into a three-dimensional Monte-Carlo-simulation of pore growth. The simulation is able to reproduce the experimentally observed crysto pore structures in III-V-semiconductors in full quantitative detail. The different branching probabilities for different semiconductors, as well as doping levels, can be deduced from the specific passivation behavior of the semiconductor-electrolyte-interface at the pore tips.**

***Index Terms* – III-V, crystallographical pores, electrochemical etching, Monte-Carlo-Simulation, InP.**

I. INTRODUCTION

Crystallographical pores (crysto pores) owe their name to their crystallographic growth direction, e.g. the <111>B-direction in III-V-semiconductors, which are the most prominent semiconductor family to feature crysto pores. They have been successfully etched into n-type InP, GaAs, and GaP [1, 2] and show crystallographically defined tetrahedron-shaped pore tips and crystallographical pore walls. Due to the appearance of crystos in several other semiconductors [3, 4], as well as in different electrolytes, the mode of crystallographical pore growth can be seen as a meta feature of pore growth [5]. Therefore crysto pore growth can serve as a model system for the development of a meta model of pore growth. As a starting point, the pore growth in III-V-semiconductors, especially InP, will be considered.

II. EXPERIMENTAL

Samples consisted of (100)-oriented n-type InP and GaAs with different doping levels. All experiments have been carried out in the electrochemical double cell described in [6] at T = 20 °C. As electrolyte, 5 wt.% HCl has been used. Experiments have been performed in constant-current-mode with a short 1 s high voltage pulse in the beginning to enable a homogeneous nucleation of pore growth.

III. RESULTS

An example of the resulting crysto pore structures is presented in Fig. 1 for three different etching times in InP with the doping level of $N_D = 8 \cdot 10^{17}$ cm^{-3} and for a constant current density of j = 0.4 mA/cm^2. The left hand side shows SEM images of the (1$\bar{1}$0)-plane of the pore structures, the right hand side the corresponding simulation details, as will be discussed in the subsequential part of this manuscript. Crysto pores growing into the two downward pointing <111>B-directions can be identified as lengthy tunnels, whereas pores growing into the two upward pointing <111>B-directions are intersecting the plane of view and are therefore visible as triangular intersection points.

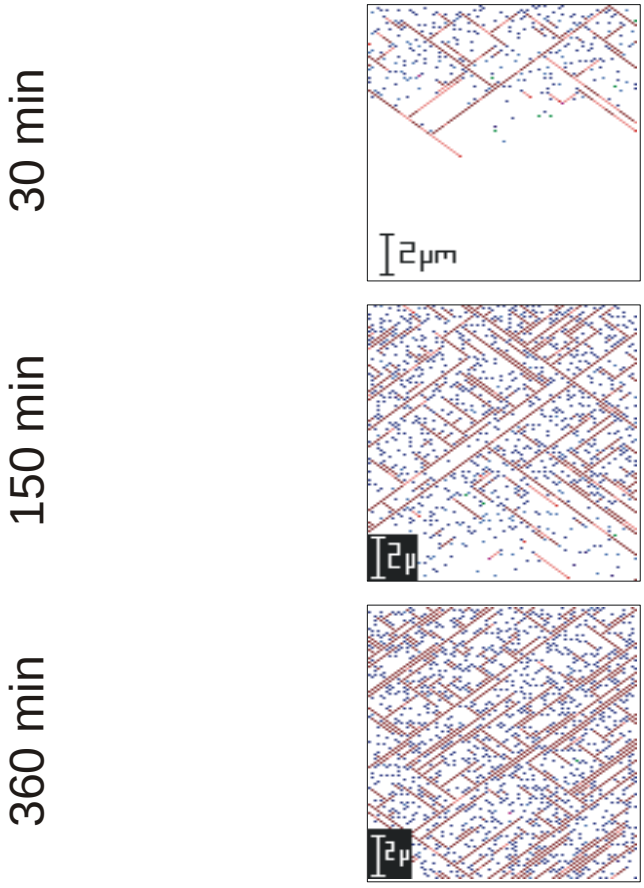

Fig. 1. Resulting crysto pore structures in a constant current experiment, j = 0.4 mA/cm2, on InP with the doping level ND = 8 · 1017 cm-3, (1$\bar{1}$0)-plane. Different etching times are indicated. The left hand side shows SEM images of the pore structure, the right hand side the corresponding simulation result.

Further data has been obtained in these experiments: the pore density of upward and downward growing pores as function of depth, the pore depth as function of time, as well as the number of active pores are all facts which the simulation aims to reproduce. But first a short description of the model which is implemented in the simulation follows.

IV. MODEL

The model basically consists of two assumptions:

i) The branching probability per area and time at the pore tips p_{tips}, resp. pore walls p_{walls}, is proportional to the current density at the pore tips j_{tips}. Since current density is just charge per time and area, within the current burst model this assumtion can easily be understood as an increased branching probability for short times of interface passivation.
ii) The valence of dissolution is constant, i.e. a constant amount of semiconductor material is etched per unit time.

V. MONTE-CARLO-SIMULATION

The stochastic nature of the above described model allows for its implementation into a three-dimensional Monte-Carlo-Simulation, which has been carried out in a three-dimensional simulation-array, which is schematically illustrated in Fig. 2.

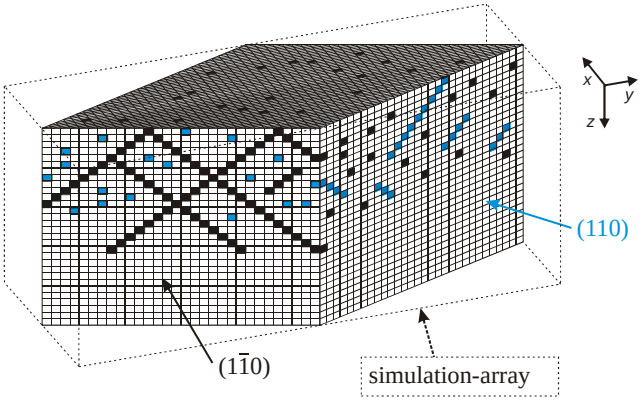

Fig. 2. Schematic illustration of the three-dimensional simulation-array used in the Monte-Carlo-Simulation. The black chains of voxels represent the crysto pores growing into the two upward pointing <111>B-directions respective to the (100)-oriented surface, the blue chains of voxels the crysto pores growing into the two downward pointing <111>B-directions.

The array usually consists of $(1024)^3$ voxels, which can be allocated with different numbers that represent pore walls or tips, which can be active or inactive, and be growing in upward or downward direction. In an initial nucleation routine, pores are randomly distributed in the topmost layers of the nucleation area. The simulation array will then be transformed into a new state in each iteration step according to fixed rules:
1) Each pore grows one more voxel into its growth direction.
2) Branching and growth can only occur into free space, i.e. no other pores are in the trajectory of the growing pore in an adjustable distance called l_{free}.
3) Pores can branch at pore tips, the resulting pore will grow into the same direction (upward resp. downward) as the initial pore. The branching probability per iteration k_{tips} is proportional to the current density at the pore tips j_{tips} and the branching probability per area and time p_{tips}.
4) Pores can branch out of pore walls, the resulting pore will grow into the opposite direction (upward resp. downward) as the initial pore. The branching probability per iteration k_{walls} is proportional to the current density at the pore tips j_{tips} and the branching probability per area and time p_{walls}.
5) If two pore tips meet in one voxel, one tip will continue to grow, whereas the other one will stop to grow.

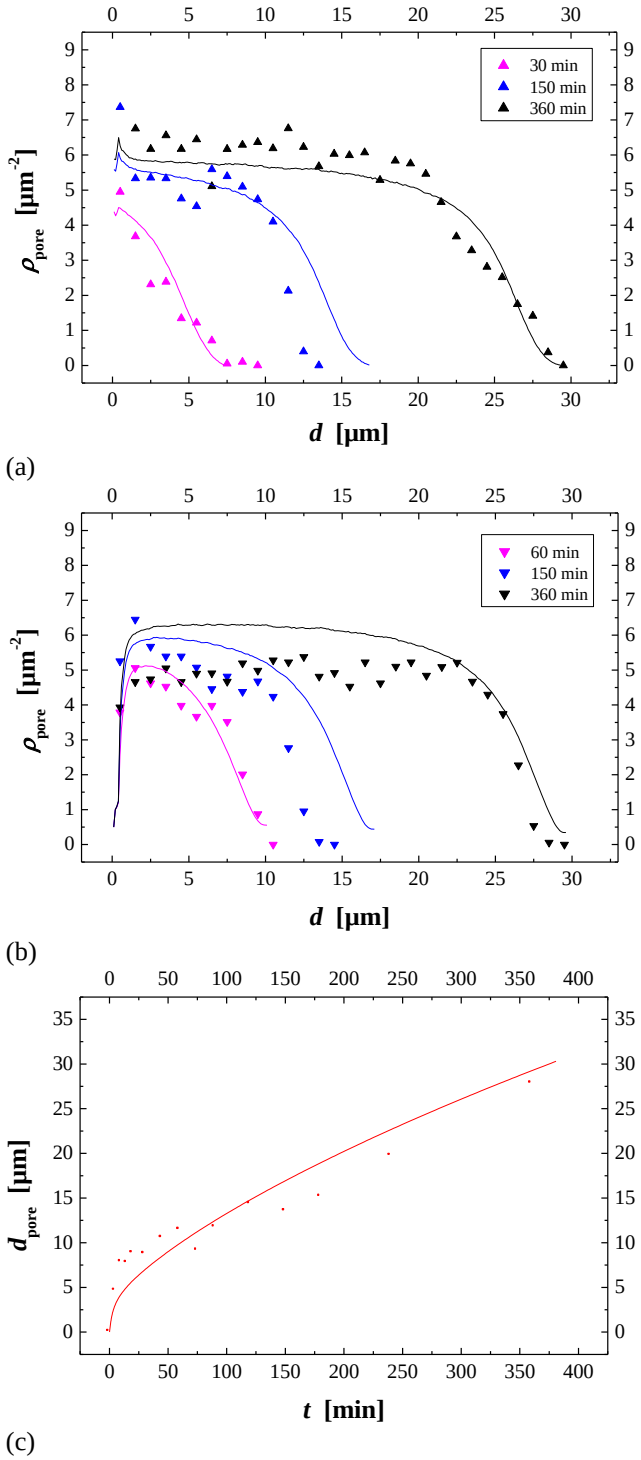

Fig. 3. Comparison of experiment (dots) and simulation (lines). Pore density ρpore as function of pore depth of a) upward growing pores and b) downward growing pores for three etching times. c) Pore depth dpore as function of etching time.

6) If branching has occurred at one voxel, no branching can occur out of the neighboring voxels, which will be set to an "inactive" pore wall state. The number of affected neighbor voxels can be adjusted by the parameter l_{pass}.

As already mentioned, Fig. 1 shows the crysto pore structures resulting from the Monte-Carlo-Simulation of crysto pore growth on (100) n-type InP with a doping level of level of $N_D = 8 \cdot 10^{17}$ cm^{-3} and for a constant current density of $j = 0.4$ mA/cm^2. The (1$\bar{1}$0)-plane is shown for

three different etching times besides the respective SEM image of the electrochemically etched pore structure. The similarity between experimental and simulation results is already striking on first view for all shown examples. Similar results have been obtained for the (110)- plane (not shown here). A more quantitative comparison is given in Fig. 3. In Fig. 3a) the pore density ρ_{pore} of upward growing pores is shown as function of depth for three etching times, as evaluated from SEM images (triangles). The lines show the corresponding simulation results. Fig. 3b) shows the respective result for downward growing pores. Fig. 3c) shows a comparison of the pore depth as function of etching time. All simulation results show a very good agreement with the experimental results.

VI. DISCUSSION

In the preceding part of this manuscript it has been demonstrated, that crysto pore growth can be very well modeled by a simple stochastic model which assigns specific probabilities to the branching of pores at pore tips, resp. out of pore walls. For different materials and different doping levels, the branching probabilities per area (W_{tips}, resp. W_{walls}) given in Table 1 have been obtained.

Parameter	InP $8 \cdot 10^{17}$ cm^{-3}	InP $1 \cdot 10^{17}$ cm^{-3}	GaAs $2.5 \cdot 10^{17}$ cm^{-3}
W_{tips} / mm^{-2}	19	59	30
W_{walls} / mm^{-2}	190	22	30

The physico-chemical nature of the branching probabilities can be understood in a simple meta model, which links the branching probability to the passivation behavior of the semiconductor-electrolyte-interface at the pore tips, resp. pore walls. Passivation in this context means the coverage of the surface by chemical species, which impedes current flow and thus electrochemical dissolution. The rather similar values of the normalized branching probabilities for the pore tips can be understood by the fact, that the passivation at the pore tips is rather similar because it is nearly not present, i.e. the pore tips are not passivated. On the contrary, the increasing normalized branching probability at the pore walls with increasing doping level can be understood by the fact that pore walls are well passivated, which results in the formation of a space-charge-region (SCR) in the semiconductor. A part of the available etching potential can thus drop in the SCR, leaving a decreased etching potential which drops in the electrolyte and is thus available for the electrochemical reaction. Since the potential drop in the SCR decreases with increasing doping level, the potential left in the electrolyte increases with increasing doping level, leading to increasing branching probabilities with increasing doping level.

ACKNOWLEDGMENTS

This work was funded by the collaborative research center 855 “Magnetoelectric Composites – Future Biomagnetic Interfaces” by the DFG.

REFERENCES

[1] T. Takizawa, S. Arai, and M. Nakahara, "Fabrication of vertical and uniform-size porous InP structure by electrochemical anodization", Japan J. Appl. Phys. **137(2, 5A)**, L643 (1994).

[2] H. Föll, S. Langa, J. Carstensen, S. Lölkes, M. Christophersen, and I.M. Tiginyanu, "Review: Pores in III-V Semiconductors", Adv. Mater. **15(3)**, 183 (2003).

[3] V. Lehmann, Electrochemistry of Silicon, Wiley-VCH, Weinheim (2002).

[4] C. Fang, H. Föll, and J. Carstensen, "Electrochemical pore etching in germanium", J. Electroanal. Chem. **589**, 259 (2006).

[5] M. Leisner, H. Föll, and J. Carstensen, "A meta model for electrochemical pore growth in semiconductors", in Nanostructured semiconductors: from basic research to applications, ed. P. Granitzer, Springer (2011).

[6] S. Langa, I.M. Tiginyanu, J. Carstensen, M. Christophersen, and H. Föll, "Formation of porous layers with different morphologies during anodic etching of n-InP", Electrochem. Solid-State Lett. **3(11)**, 514 (2000).

Porous InP as Piezoelectric Matrix Material in 1-3 Magnetoelectric Composite Sensors

M.-D. GERNGROSS*, M. LEISNER, J. CARSTENSEN and H. FÖLL
Institute for Materials Science, Christian-Albrechts-University of Kiel,
Kaiserstrasse 2, 24143 Kiel, Germany
* *mdg@tf.uni-kiel.de*

***Abstract* – This work shows the results of the fabrication of semi-insulating piezoelectric porous InP structures by electrochemical etching and subsequent purely chemical post–etching in an isotropic HF, HNO_3, EtOH and HAc containing electrolyte. The piezoelectric modulus d_{14} of porous InP is measured to around |60| pm / V, which larger by a factor of 30 compared to bulk InP.**

***Index Terms* – indium phosphide, porous, piezoelectricity, magnetoelectric sensor.**

I. INTRODUCTION

This paper focuses on the production of an effective and cheap piezoelectric material for the application in magnetoelectric 1-3 composite sensors. The concept is to apply porous and piezoelectric InP as the matrix material. In the second step a multilayer stack consisting of NiFe / FeGa showing giant magnetostrictive behavior will be used as magnetostrictive filler.

The 1-3 composite arrangement of piezoelectric and magnetostrictive materials is chosen, because it allows for very large contact areas, providing excellent mechanical coupling between both components, and thus high sensitivity to magnetic fields.

The main characteristic of piezoelectric materials is the lack of an inversion center. InP as a III-V compound semiconductor belongs to the $4,\bar{3}3m$ cubic crystal system. This crystal class is non centro-symmetric and non-polar. Thus InP is piezoelectric, but not pyroelectric. Looking at the piezoelectric modulus tensor of InP reveals that the d_{14} component is the only remaining component of the piezoelectric modulus tensor [1]. The maximum piezoelectric effect is calculated to be in the <100> direction.

The piezoelectric properties of bulk InP have only been measured very rarely [2, 3]. Up to now InP has not been used as piezoelectric material, because it is not possible to produce intrinsic InP. Even highly pure InP contains a lot of impurities, which serve as doping centers, so that a large number of free charge carriers exist short-circuiting the charges induced by the piezoelectric effect.

To overcome this problem, our approach is to produce a self-organized, hexagonally closed packed array of so-called current-line pores with completely overlapping space charge regions (SCR). Inside the space charge regions hardly any free charge carriers are present, so that the induced polarization by the piezoelectric effect will not be shortened anymore.

II. EXPERIMENTAL

For the experiments only single crystalline, double-side polished (100) InP wafers are used. The wafers are doped with S with a carrier concentration of $N_D = 1.1 \cdot 10^{17}$ cm^{-3}. The resistivity is 0.019 Ωcm. The wafer thickness is 500 µm ± 10 µm. The sample size is $A = 0.25$ cm^2.

All electrochemical etching experiments have been performed in the electrochemical double-cell as described elsewhere [4]. The electrochemical etching has been performed under potentiostatic conditions at a constant temperature of 20 °C. For the first second a voltage pulse of 15 V is applied to the sample in order to obtain a homogenous pore nucleation. It is followed by a constant etching potential of 7 V for 70 min. Afterwards the samples are carefully rinsed in deionized water and blown dry in nitrogen.

The purely chemical post-etching is carried out in a plastic beaker at room temperature. The post-etching electrolyte consist of HF : HNO_3 : EtOH : HAc (3 : 8 : 15 : 24). In this etching solution, the hydrofluoric acid serves as an etching agent, nitric acid as an oxidizing agent, and ethanol and acetic acid as wetting agents. The ethanol also serves as a passivating agent in order to decrease the etching speed.

The samples are purely chemical post-etched for various times from 8 h to 48 h to investigate the etching properties of the etchant. After the post-etching process the samples are carefully rinsed in deionized water and blown dry in nitrogen.

The etched porous InP nanostructures have been investigated with a HELIOS D477 SEM. The piezoelectric response to an applied voltage has been measured with a double beam laser interferometer (DBLI) from aixACCT.

III. RESULTS & DISCUSSION

Figure 1 (a) presents the InP current-line pore structure after anodic electrochemical etching ($U > 0$ V) with adjacent mechanical polishing to remove the nucleation layer, which was performed for imaging and comparing the resulting pore structures after different chemical treatments. This structure is the result of the anodic electrochemical etching process optimized to produce hexagonally closed packed pore arrays in a self-organized manner.

During the anodic electrochemical etching process the minimum distance between pore walls is assumed to be twice the width of the space charge region. At the end of the electrochemical etching process, the externally applied voltage by the potentiostat is to a value determined by the surface charges. Hence the width of the space charge region shrinks and thus the remaining conductive areas, where no space charge region is present, increase. These conductive

areas can only be reduced if the pore wall width is reduced to twice the length of the SCR at cell off conditions. This can be achieved by performing a post-etching step. The post-etching electrolyte has to be isotropic over the complete pore length and should be self-limiting as soon as the space charge regions of neighboring pores overlap again. As post-etching electrolyte an HF : HNO_3 : EtOH : HAc (3 : 8 : 15 : 24) containing electrolyte has been developed. The pore structure resulting from post-etching in this electrolyte is shown in Fig. 1 (b).

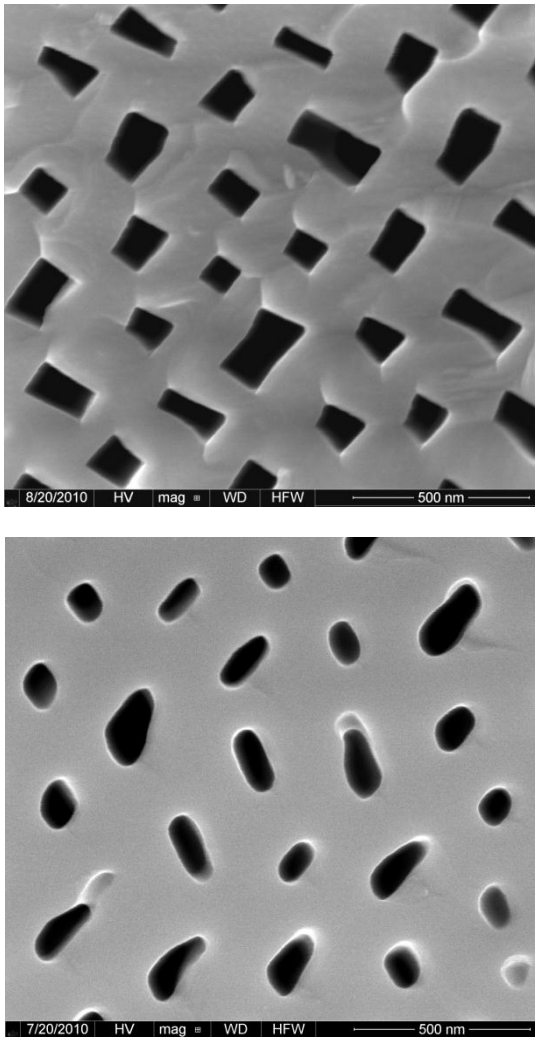

(a)

(b)

Fig. 1 Top view of porous InP (a) after anodic electrochemical etching (U > 0 V) and (b) after subsequent purely chemical post-etching (U = 0 V) after 48 h.

Comparing both pore structures, one observes that the pores change their shape from rectangular / square-like after the anodic electrochemical etching to elliptic /circular after subsequent post-etching for 48 h. This etching behavior is only possible for isotropic etchants.

Looking at the distances between the pores, one recognizes that the pore wall width of two neighboring square-like resp. circular pores is mostly the smallest measured in the SEM images shown, while for two neighboring rectangular like resp. elliptical pores oriented parallel to each other is the largest found in the majority of the cases.

Figure 2 (a) shows the pore-ratio as a function of the etching time in the post-etching electrolyte. The pore ratio is the ratio of the longitudinal and the transverse side of the rectangular resp. elliptical pores. It is a quantitative measure for the change in the shape of the rectangular pores as a result of the post-etching. Fig. 2 (a) shows an increasing pore-ratio in the range from 0 h to 28 h of post-etching from around 1.7 for the not post-etched sample to a level in the range of 2.35, reached after approximately 28 h of post-etching. The pore-ratio of the samples, being etched for 8 h and 16 h in the post-etchant respectively, deviates from the red line. A possible explanation for this could be that the etch rate is higher for the surface near part of the pores in the beginning of the post-etching process, but drops to zero after twice the width of the SCR is reached.

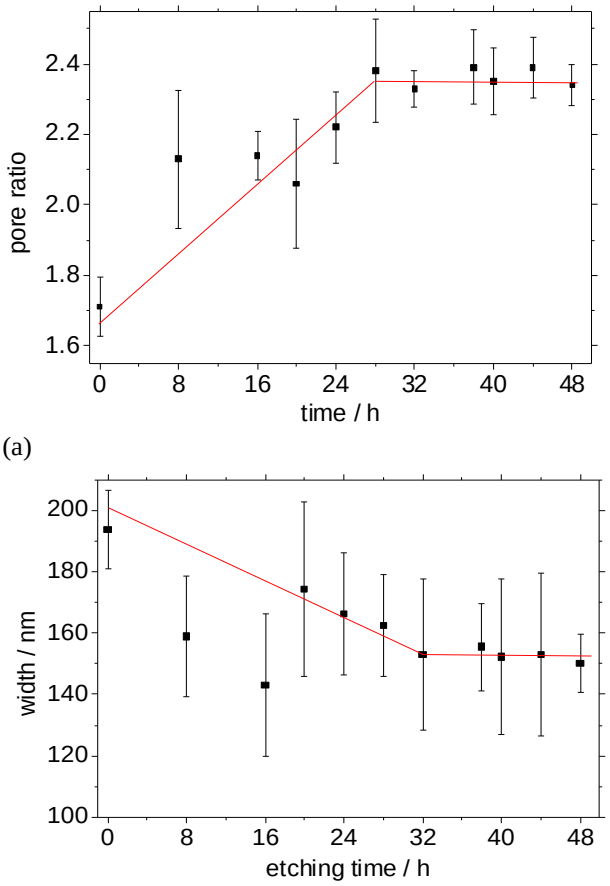

(a)

(b)

Fig. 2 (a) pore ratio as a function of the etching time in the post-etching electrolyte and (b) mean width of the pore walls as a function of the post-etching time in the post-etching electrolyte.

Fig. 2 (b) shows the average pore wall width as a function of the etching time in the post-etching electrolyte.

The mean pore wall width is decreasing from around 190 nm of the not post-etched sample to a level in the range of 150 nm. Again the mean pore wall width for the samples being post-etched for 8 h and 16 h deviate from the red line, possibly due to the same reason as given for the pore ratio, because the mean pore wall width of these two samples fits to the mean pore wall width of samples being post-etched for a much longer time.

The level of 150 nm is reached after approximately 32 h of post-etching and does not change with increasing post-

etching time. This indicates the self-limiting behavior of the post-etching electrolyte.

This result is consistent with the result obtained in the analysis of the pore-ratio of these samples, because an increased pore-ratio goes along with a smaller mean pore wall width. The saturation value of both quantities is reached approximately at the same time, as one can see from the diagrams shown in Figure 2 (a) and 2 (b).

The characteristic change in the pore geometry can be understood by considering the space charge region surrounding each pore, the resulting voltage drop across the SCR and the crystal-orientation dependence of the electrochemical and chemical etching in InP. The pores are expanding in all directions, until an overlap of SCR of neighboring pores occurs, which allows no further dissolution of the InP by the post-etchant.

Figure 3 (a) and (b) show the result of the DBLI measurement of the only electrochemically etched and the electrochemically etched sample with additional post-etching. The DBLI measures the displacement of the InP sample due to the piezoelectric effect as a function of the voltage, which is externally applied in <100> direction of the sample via two micromanipulators.

As InP is not a ferroelectric material, one expects a linear dependence of the applied voltage on the measured displacement. The chemical post-etching of the electrochemically etched samples reduces the leakage currents to a level low enough to use the piezoelectric properties. In general, the expected piezoelectric performance of the sample is better, the lower the leakage currents are.

For the only electrochemically etched sample the voltage is linearly increased from 0 V to 3 V, then linearly decreased to –3 V and finally increased to 0 V again. For the electrochemically etched and additionally post-etched sample the voltage is linearly increased from 0 V to 0.5 V, then linearly decreased to –0.5 V and finally increased to 0 V again. The resulting displacement of the InP sample is measured.

Figure 3 (a) shows the piezoelectric performance of the only electrochemically etched sample. In the voltage range, where the applied voltage increases from 0 V to 3 V, one observes a linear behavior of the resulting displacement until a voltage of 2.5 V is reached. At this position the displacement strongly increases, although the applied voltage remains constant. Decreasing the applied voltage to 1.65 V also causes an increase in the displacement, though the displacement is expected to decline for a decreasing voltage. In the voltage range from 1.65 V to -3 V the expected linear behavior is observed and again in the range from -3 V to 0 V. That the ending displacement of the displacement/voltage curve is not equal to the starting displacement of 0 nm is most probably due to dielectric losses, which increase with the frequency of the applied voltage. The slope d_{av} of the linear fit of the displacement / voltage curve is 0.078 nm / V. From the slope of the linear displacement vs. applied voltage curve, the d_{14} component of the porous InP sample can be derived, resulting in a value of |19| pm / V.

As shown in figure 3 (a) it is now possible to fabricate nanostructures in InP by electrochemical etching, where the leakage currents do not completely short the induced polarization by the piezoelectric effect. Although the displacement/voltage curve is not completely linear over the entire voltage range, the d_{14} component of the only electrochemically etched sample is already larger by a factor of about 10 compared to the d_{14} component of bulk InP [5].

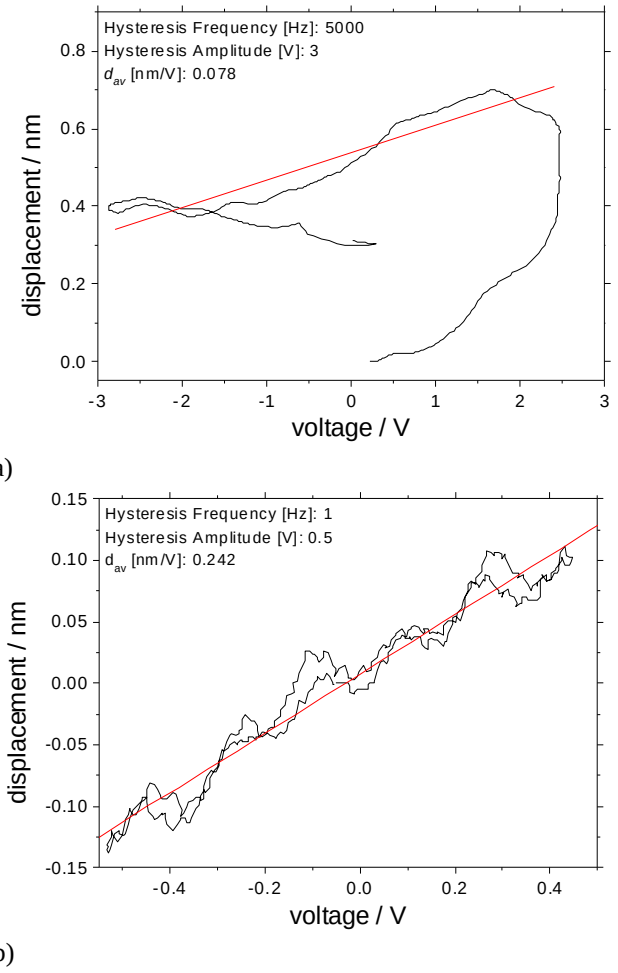

Fig. 3 DBLI measurement of porous InP (a) after anodic electrochemical etching ($U > 0$ V) and (b) after subsequent purely chemical post-etching ($U = 0$ V) after 48 h. The slope of the linear fit is denoted as d_{av}.

Figure 3 (b) shows the piezoelectric performance of the electrochemically etched and subsequently post-etched sample. One obtains a linear dependence of the applied voltage on the measured displacement. In contrast to the purely electrochemically etched sample the positive limit of the applied voltage is reached completely. But more eye-catching is the wavy shape of the displacement/voltage curve of the sample. The waviness of the curve is an artifact of specimen mounting.

The sample exhibits a significantly higher slope with d_{av} = 0.242 nm / V compared to the only electrochemical etched sample. The linear dependence of the applied voltage on the displacement has been measured severeal times with a variation in d_{av} by a factor of 2 in maximum.

It is found to be around |60| pm/V, about a factor of 30 larger than the values measured on bulk InP [5].

IV. CONCLUSION

The first steps on the way to a magnetoelectric 1-3 composite sensor consisting of a piezoelectric matrix and a magnetostrictive filler have been made.

It has been demonstrated that it is possible to produce semi-insulating piezoelectric InP by anodic electrochemical etching and subsequent purely chemical post-etching in an HF, HNO3, EtOH, HAc containing electrolyte. This electrolyte has been optimized to show an isotropic and self-limiting etching behavior over the complete pore length.

The d_{14} component of post-etched macroporous InP is found to be around |60| pm/V, which is about a factor of 30 larger than the values reported for bulk InP [5].

Though InP is the most suitable candidate for this approach, in principle a new class of semi-insulating porous single-crystalline piezoelectric materials can be fabricated from III-V semiconductors by this concept of electrochemical and pure chemical post-etching.

ACKNOWLEDGMENTS

This work was funded by the collaborative research center 855 “Magnetoelectric Composites – Future Biomagnetic Interfaces” by the DFG.

REFERENCES

[1] J.F. Nye, Physical properties of crystals: their representation by tensors and matrices, Oxford University Press, Oxford (1985).

[2] K. Rottner, R. Helbig, and G. Müller, Appl. Phys. Lett. 62(4), 352 (1993).

[3] G. Arlt and P. Quadflieg, Phys. Stat. Sol. 25, 323-330 (1968).

[4] S. Langa, I.M. Tiginyanu, J. Carstensen, M. Christophersen, and H. Föll, Electrochem. Solid-State Lett. 3(11), 514 (2000).

[5] T.P. Pearsall, Properties, processing and applications of indium phosphide, IEEE, London (2000).

The Collaborative Research Center "Magnetoelectric Composites - Future Biomagnetic Interfaces" at the Christian-Albrechts-University in Kiel

H. FÖLL
Institute for Materials Science, Christian-Albrechts-University of Kiel
hf@tf.uni-kiel.de

I. ABSTRACT

In Jan. 2010 the "Deutsche Forschungsgemeinschaft" (DFG) established a so-called "Sonderforschungsbereich" (Collaborative Research Center) for Research into magnetoelectric composites for future biomagnetic interfaces at the Christian-Albrechts-University (CAU) in Kiel / Germany; the project is funded with more than then 10 Mio €. The Institute of Materials Science with it's background in functional materials and nanotechnology background was instrumental in writing the proposal and in getting together ... primary researchers from Electrical Engineering, Physics, and Medicine besides almost all groups of Materials Science and Engineering. The speaker is Prof. E. Quandt from Materials Science.

The project is scheduled for 4 (+ another 4) years. Its primary goal is the development of extremely sensitive (vector) sensor for magnetic fields. These sensors are to be used in dense arrays (about 1 sensor /cm^2) primarily for medical purposes. A sensor-studded "cap", for example, put around the head of patients suffering from various neural disorder syndromes, should be able to pick up the magnetic fields from neuronal firing deep in the brain and tallow to localize malfunctioning brain areas with far higher precision than present techniques; similar potential uses are seen in cardiography. The necessary sensitivity for magnetic field must rival those of SQUIDs; the project thus is fairly ambitious because present technology is many orders of magnitude less sensitive than SQUIDs.

The project has 4 major partial projects an a central project: Partial Project A develops the magnetoelectric composites and is thus the core project for the undertaking; it will be discussed in some detail in the presentation. Partial Project B investigates the detailed structural. magnetic and electric properties of the interfaces between the magnetostrictive and piezoelectric materials used. Partial Project C develops the sensor systems including theory and simulation tools, and partial project D introduces the medical component. The central Project provides analytical services like electron microscopy or a room heavily shielded against magnetic fields for sensitive measurement (including patients).

The project depends on the exploitation of magnetoelectric composites, meaning mechanically coupled structures of magnetostrictive and piezoelectric materials. The working principle is very simple. A magnetic field causes dimensional changes of a magnetostrictive material. The mechanical coupling to a piezoelectric material then puts elastic stress on the piezoelectric material, resulting in a voltage that is a measure of the magnetic field strength. In reality, magnetoelectric composites are rather complex systems. An input vector (magnetic field) produces an output scalar (voltage), and the coupling between the input and the output relies on several vector / tensor relations (stress / strain induced in the magnetostrictive material, transfer to the (tensor) piezomaterial, position of contacts). In addition, noise and time constants (e.g. for mechanical resonance and damping) need to be considered since the sensors are to be used for low-frequency (< 100 Hz) signals.

Advanced technologies, usually derived from micro- or nanotechnology including MEMS and implemented in the "Kiel Nanolab", are used to make magnetoelectric composites. In addition, some novel concepts are pursued. For example, layered structures of alternating piezo- and magnetostrictive materials clamped a only on end (and thus able to oscillate in one direction) have already proved sensitivities able to measure magnetic fields smaller 1 nT. A novel approach that will be presented elsewhere in the workshop intend to use porous III-V semiconductors, in particular InP, as the piezoelectric component. The piezoelectric properties of III-V semiconductors are well known but useless so far since the charges produced by mechanical stress are quickly short-circuited by the conductivity of the material. Porous membranes, however, can be made to be semi-insulating and thus can be used as a new single-crystalline piezoelectric materials, as will be shown. Filling the pores with a magnetostrictive material then will produce a sensor with properties that could be advantageous for certain applications.

The presentation will give a general overview of the project but then will focus on the material aspects.

Investigation of Mesoporous Structures for Thermoelectric Applications

A. COJOCARU[1*], J. CARSTENSEN[1], J. BOOR[2], V. SCHMIDT[2] and H. FÖLL[1]
[1]*Institute for Materials Science, Christian-Albrechts-University of Kiel. Kaiserstr. 2, D-24143 Kiel, Germany.*
[2] *Max-Planck-Institute of Microstructure Physics Weinberg 2, D-06120 Halle, Germany*
[*]*ac@tf.uni-kiel.de*

***Abstract* — Mesoporous silicon is an attractive material for thermoelectric application. For pore wall thicknesses around <100nm, phonons can not penetrate the porous layer while electrons still can, due to there smaller mean free path length. The resulting good electrical and bad thermal conductivity is a premise for efficient thermoelectric devices. This paper presents results regarding homogeneity, high porosity, and optimal pore wall thicknesses for porous silicon based thermoelectric devices.**

***Index Terms* — electrochemical etching, mesoporous silicon, thermoelectric**

I. INTRODUCTION

Porous silicon (PSi) has found various applications, e.g. in photonic devices [1], sensor systems [2] or drug-delivery devices [3]. In this paper electrochemically etched porous Si layers suitable for thermoelectric devices are discussed. Thermoelectric devices need a high electrical conductivity and low thermal conductivity. While in most materials electrical and thermal conductivity are coupled by the Wiedemann-Franz law, in porous material the big difference in mean free path lengths between electrons (≈110nm) and phonons (≈300nm) [4] allows for a decoupling of both conductivities.

In contrast to bulk silicon mesoporous silicon is well known to show a very low thermal conductivity as soon as the distance between pores becomes smaller than the mean free path length of the phonons, while the electrical conductivity stays high. Several papers describe efforts to enlarge the figure of merit *ZT* for thermoelectric application by optimizing porous materials [5 - 7]. This paper focuses on producing porous Si layers [8, 9] with pore walls sizes in the range of 20 - 100 nm.

II. EXPERIMENTAL DATA

Low doped silicon allows for larger mobilities of the electrons, which would be beneficial for the thermoelectric effect. Thus various electrolytes and etching conditions had been tested on low-doped material without getting reasonable porous layers. Thus in this paper we will only focus on mesopores etched on (100)-oriented highly doped n-type Si with resistivity of (0.02 – 0.05) Ωcm. Etching has been carried out in the electrochemical cell described in detail in [10] without illumination. As electrolyte of 48 wt. % HF dissolved in acetonitrile in a volume ratio of 1:2 has been used.

All experiments have been performed at a constant temperature of T = 20 °C.

III. RESULTS UND DISCUSSION

Just by etching pore walls less than 100 nm the thermal conductivity is drastically reduced. In order to get a good electrical conductivity the pore walls should fulfill several properties:

- The porous layer should be uniform with a small spread of pore dimensions.
- The pore walls should be structurally as perfect as possible (not containing side pores, for example) to minimize scattering of carriers and thus the resistivity.

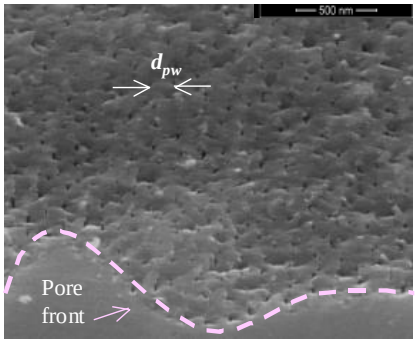

Fig. 1. SEM pictures of a cross section for pores. Electrochemically etched, 5 s, into n-type Si at 2 V for (0.02 –0.05) Ωcm resistivity.

Since galvanostatically etched mesopores tend to show diameter oscillation (cf., e.g., [11, 12]) all mesoporous layers presented here have been etched under potentiostatic condition.

A typical result of mesopores with an average pore wall thickness of $d_{pw} \approx 100$ nm when etching 5 sec and 15 sec, i.e. just after finishing the pore nucleation, is shown respectively in Fig. 1 and Fig. 2a). The length of the pores is quite inhomogeneous, probably due to a small variation in the speed of pore nucleation at different position on the sample surface.

Etching for a longer time, e.g. for 30 min, the pore front becomes straight as shown in Fig. 2b). This is a general aspect of mesopore growth. Probably due to diffusion limitation increasing with pore length, the dissolution at the pore tips slows down, leading to a self-stabilizing adjustment of pore lengths.

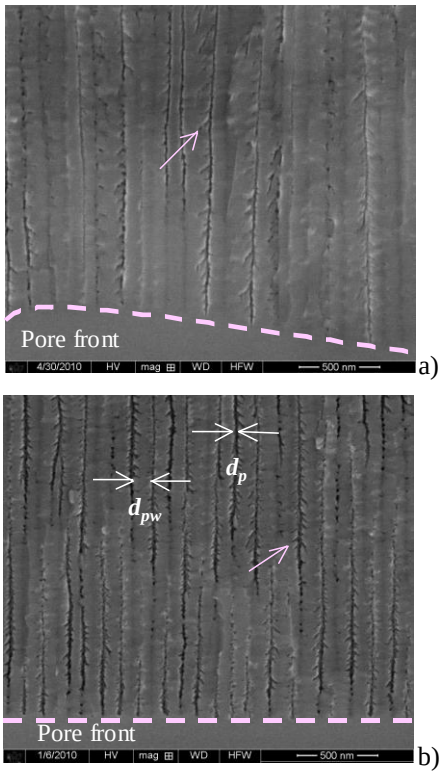

Fig. 2. SEM pictures of a cross section for pores in nucleation stage electrochemically etched a) 15 s, 2V; b) 30 min, 2V into n-type Si for (0.02 –0.05) Ω·cm resistivity.

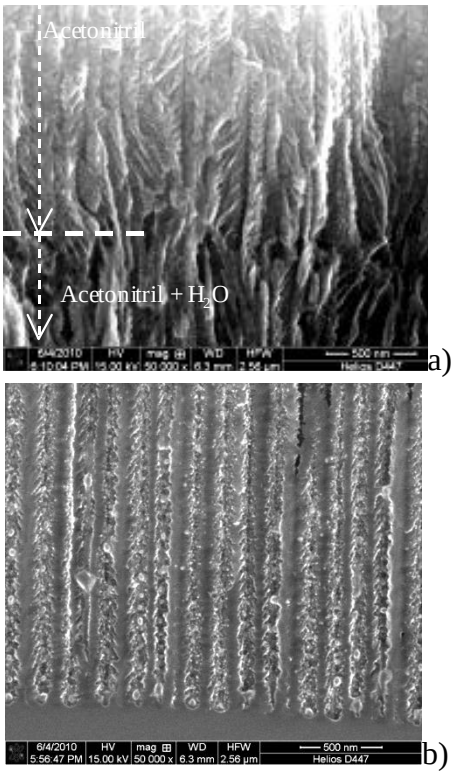

Fig. 4. SEM pictures of pores obtained with a "differential" electrolyte. Start with acetonitril containing 48 wt.% HF in a ratio of (2:1), growth with addition of water; a) overview (top region); b) pore tips.

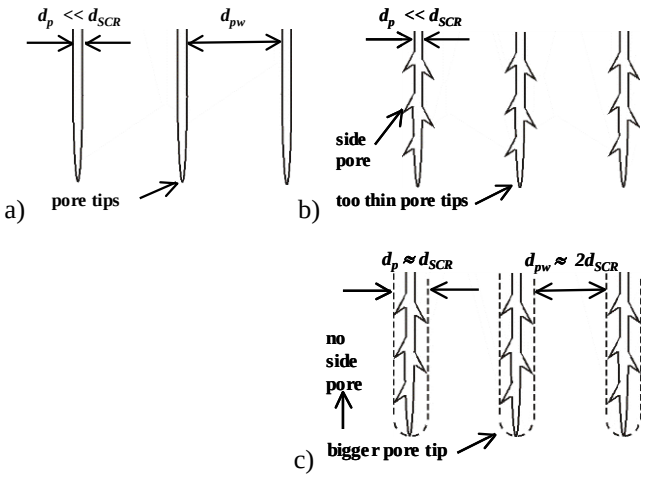

Fig. 3. Schematic illustrations for a model of the pore nucleation phase.

Since a straight pore front is essential for producing a thermoelectric device, the mesoporous layers have typically been etched to a length of 100µm, which is a thicker layer than necessary for the device. As visible in Fig. 2 for longer pores, the morphology changes from top to tip. Since a top layer can be polished off, the relevant pore morphologies are near the pore tips.

The main problem when increasing the etch time is the formation of side pores. These side pores do not form instantly near the pore tips but their density and length increases with etching time; e.g. at the beginning of all experiments the pores have no side pores near the top, but after further etching many side pores are found near the top. This feature does not become perfectly clear from Fig. 2a) and Fig. 2b) but at least the trend becomes visible.

The nucleation phase has a substantial influence on the pore morphology. In the nucleation phase the pores are very thin and have a rather homogeneous pore density (Fig. 1). The pore wall thickness d_{pw} is around 100 µm, which corresponds to $2d_{SCR}$ for the used resistivity, (d_{SCR} – thickness of the space charge region). As visible in Fig. 1 and Fig. 2, the pore diameter d_p is much smaller then the pore wall thickness d_{pw}. This geometry is illustrated in Fig. 3 a). It is well known that optimal pore growth needs $d_p \approx d_{pw} \approx 2d_{SCR}$ (e.g. see [8]). For $d_p << 2d_{SCR}$ the electrical field around the pore tips will be drastically increased. Since the side pores have roughly the same diameter as the main pores, the strong increase of the electrical field around any small "bump" in a pore wall may trigger the formation of side pores, leading to pore morphologies as schematically shown in Fig. 3b), which correspond to the SEM images in Fig. 2b). So, to avoid side pore formation, a larger pore diameter could be helpful, as illustrated in Fig. 3c).

As e.g. discussed in [8] diameters of mesopores etched with aqueous electrolytes are larger in comparison to pores etched with organic electrolytes. Therefore H_2O was added to the electrolyte in a ratio acetonitril : H_2O : HF = 2 : 1 : 1. Indeed, larger pore diameters d_p are found but the distance between the pores d_{pw} was larger as well, leading to the same morphologies as shown schematically in Fig. 3, just on a larger scale. Consequently side pores still occur.

Fig. 4 shows the resulting pores when starting the etching with pure organic electrolyte and adding water after roughly

5 seconds. As expected, a significant increase in pore diameter was found as shown in Fig. 4a). Subsequently a number of pores died out, leading finally to a pore morphology as shown in Fig. 4b) where again the pore walls are quite rough.

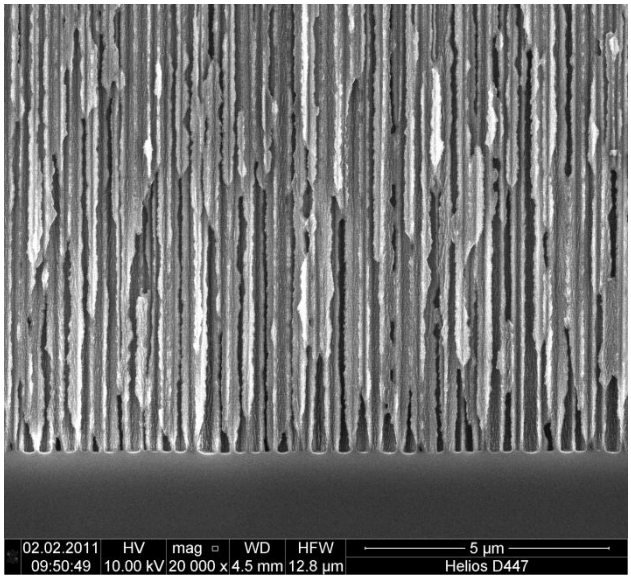

Fig. 5. SEM pictures of a cross section of pores etched with electrolytes acetonitril:HF in ratio (4:1) under galvanostatic condition for constant applied etching current 50mA for 30 min.

The water-free (as far as possible) electrolytes are the best ones. While many other electrolytes have been tried too, further improvements are still possible. Lowering the temperature a few degrees or increasing the viscosity of the electrolyte has been shown to improve pore morphologies in other cases, for example [13, 14] and need yet to be tried. Fig. 5 shows the best pore structures produced so far. The high growth rates of 3.3 µm/min for 100 µm could be obtained. While not all goals are achieved yet, these pores already show promising results.

IV. CONCLUSION

The experimental results obtained permit to claim that silicon with low resistivity is an attractive material for thermoelectric application.

The "water-free" electrolytes are the best ones for mesopore structure formation. Much work remains to be done and further optimization of the etching process is necessary.

ACKNOWLEDGMENTS

Dr. N. Abrosimov and Dr. H. Riemann from the IKZ Berlin grew and wafered the Si-Ge crystals; their help is greatly appreciated. This work has been supported by the BMBF (Project PoSiTeM – 03X3539B).

REFERENCES

[1] F. Müller, A. Birner, U. Gösele, V. Lehmann, S. Ottow, and H. Föll, J. Por. Mat. 2000, 7, 201.
[2] K.A. Kilian, T. Böcking, and J.J. Gooding, Chem. Commun. 2009, Feature Article, 630.
[3] E.J. Anglin, L. Cheng, W.R. Freeman, and M.J. Sailor, Adv. Drug Delivery Rev. 2008, 60(11), 1266.
[4] A.I. Hochbaum, R. Chen, R.D. Delgado, W. Liang, E.C. Garnett, M. Najarian, A. Majumdar, and P. Yang, Nature 2008, 451, 163.
[5] G. Joshi, H. Lee, Y. Lan, X. Wang, G. Zhu, D. Wang, R.W. Gould, D.C. Cuff, M.Y. Tang, M.S. Dresselhaus, G. Chen, and Z. Ren, Nano Letters 2008, 8(12), 4670.
[6] J. Lee, G.A. Galli, and J.C. Grossman, Nano Letters 2008, 8(11), 3750.
[7] H.J. Goldsmid, Materials 2009, 2, 903.
[8] V. Lehmann, Electrochemistry of Silicon, Wiley-VCH, Weinheim (2002).
[9] V. Kochergin and H. Föll, Porous semiconductors: Optical properties and applications, Springer, London (2009).
[10] H. Föll, M. Christophersen, J. Carstensen, and G. Hasse, Mat. Sci. Eng. R 2002, 39(4), 93.
[11] S. Langa, J. Carstensen, I.M. Tiginyanu, M. Christophersen, and H. Föll, Electrochem. Solid-State Lett. 2001, 4(6), G50.
[12] A. Cojocaru, J. Carstensen, J. Boor, D.S. Kim, V. Schmidt, and H. Föll, ECS Trans. 2011, 33(16), 193.
[13] E.K. Ossei-Wusu, A. Cojocaru, J. Carstensen, M. Leisner, and H. Föll, ECS Trans. 2008, 16(3), 109.
[14] A. Cojocaru, J. Carstensen, E.K. Ossei-Wusu, M. Leisner, O. Riemenschneider, and H. Föll, Phys. Stat. Sol. (c) 2009, 206(7), 1571.

Ballistic Charge Carrier Devices for Terahertz Signal Generation.

H.L. HARTNAGEL
Technical University Darmstadt
Fachgruppe Mikrowellenelektronik
Darmstadt, Germany
www.mwe.tu-darmstadt.de
hartnagel@hf.tu-darmstadt.de

It is of great interest, to produce light-weight Terahertz sources for the many appl ications such as security testing. By reducing the transit distance suitably, the charge carrier can be approximately ballistic, that is without any collision damping. Such structures have been fabricated by epitaxial technology. Another feature can be employed there, namely the loss-free reflection of carriers at a heterojunction barrier. Therefore the charge carriers can be made to resonate between two such barriers at a Terahertz frequency.

Optimum conditions for this to occur are to be presented. Some time back, one of the doctoral candidates of the speaker manufactured and measured the first experimental structure, thus verifying the initial theoretical results of Monte Carlo simulation by this author and his partner. This presentation describes a more detailed understanding of the charge bunching effects. An outlook is presented of further possible concepts such as structures made with graphene.

Two Simple Examples for the Micro-nano Integration of Nanowires as Electronic Device Elements

Rainer ADELUNG
Functional Nanomaterials, Institute for Materials Science, University of Kiel, Kaiserstr.2, 24143, Kiel, Germany
ra@tf.uni-kiel.de

***Abstract* – As a part of the conference talk about the mass fabrication and applications of nanostructures, the aim of this paper is to review and compare two approaches for the simple fabrication and integration and of nanostructures into Si-based microchips. The purpose of the integration is the utilization of the different and advanced electronic properties of nanowires. The first method is based on a fracture approach, that integrates nanowires bound to a Si substrate between micro electrodes. These are arrange in a horizontal manner, the second approach allows to integrate free standing nanowires and even 3 dimensional nanowire networks in the chip. As an example for the electronic properties of the nano-micro integrated structures the UV light sensitivity is sown here.**

***Index Terms* – nanowires, nanostructures, Si-based nanochips**

I. INTRODUCTION

One dimensional (1D) metal and semiconductor structures have gained significant research interest due to their different, partially advanced properties originating from effects like a high surface to volume ratio or quantum mechanical influenced properties dominating low dimensional materials, become the important components of micro and nanoelectronic devices [1]. In the past 15 years, significant progress in synthesis and characterization of nanostructures is done, applicability was typically demonstrated by connecting nanowires with techniques like EBL, FIB or direct connections with scanning probe tips revealing suitability of nanostructures in electronic and optoelectronic devices [2].Various methods such as templates [3,4,5], solution growths [6], vapor-liquid-solid (VLS) and its modified versions [7,8,9] as well as several others have been used to synthesize 1D structures. However, easy fabrication routes allowing the integration of nanowires into standard lithography are not yet well established. An optimal integration route should add minimal additional fabrication steps and be compatible with the standard micro processing.

II. NANOWIRE FORMATION AND INTEGRATION APPROACHES

One approach called "fracture approach" is based on a thin film fracture approach [10,11,12], the other one is based on a modified VLS process allowing a bridging of the contacts through interpenetrating junctions [13], will be called here "penetration approach".

In general, the fabrication of the nanowire within the fracture approach microchips contains 5 steps, compare [14] and see figure 1. As first step, Shipley 1813 photoresist is spin coated in a thickness of ~560 nm thickness on silicon substrates of 76 mm-diameter with <100> orientation and a p-doping resulting in a resistivity of 1-10 Ωcm. Please note that the 380 μm thick wafers are top terminated with a 100 nm thick thermally grown insulating SiO2. In a second step, a mould for micro contact lines and the nanowires will be formed. Conventional photolithography is used to microstructure the photoresist. The main step for the nanowire template formation is the exposure of the samples to thermal cycling down to cryogenic temperatures in order to induce the stress in the photoresist thin film resulting in thin film cracks in the photoresist with nanoscopic openings (~100 nm). By using the described pattern with parts of the photoresist that are 200 μm long and 10 μm wide, the fracture pattern forms a highly reproducible well defined 'zig zag' pattern of cracks. The third step contains the deposition of metals or semiconductors by sputter deposition or another a PVD-process in high or ultra high vacuum. This deposition covers the whole wafer surface including the cracks. A deposition of material in the dimensions of about 50-100 nm nominal thickness with an adhesion promoter underneath (thin layer of Ti or Cr) forms nanowires in a reliable manner in the crack. Too high amounts will lead to an overfilling, too small amounts in a dissentious chain of clusters. Please note that the cracks have a relatively high aspect ration of 5-7 which reduces the amount that will be deposited into the crack up to a factor of 10. In contrast, the nominal thickness will be reached in the lithographically formed openings that form the connectors to the nanowires. The fifth final step is the lift off to separate the superfluous metal on top of the photoresist from the microstructured contacts grown in the openings formed by lithography and the nanosized wires formed within the thin film cracks. This photoresist mask lift off was performed by first soaking the sample in acetone for about 1 minute and then keeping it in an ultrasonic bath for roughly 2 seconds. Keeping the sample for long time in an ultrasonic bath may destroy the nanowires.

Vapor-liquid-solid (VLS) or Vapor-Solid (VS) methods are typically utilized to grow free standing nanostructures in a large variety like nano -rods, -wires, -sails, -etc. Usually VLS growth processes can be performed in a horizontal tube furnace equipped with a controlled gas flow control. The needed recipes are the precursor material (typically metalls), catalytic nanoparticles (e.g. gold) and the substrate on which structures will be grown. Experimental variants are

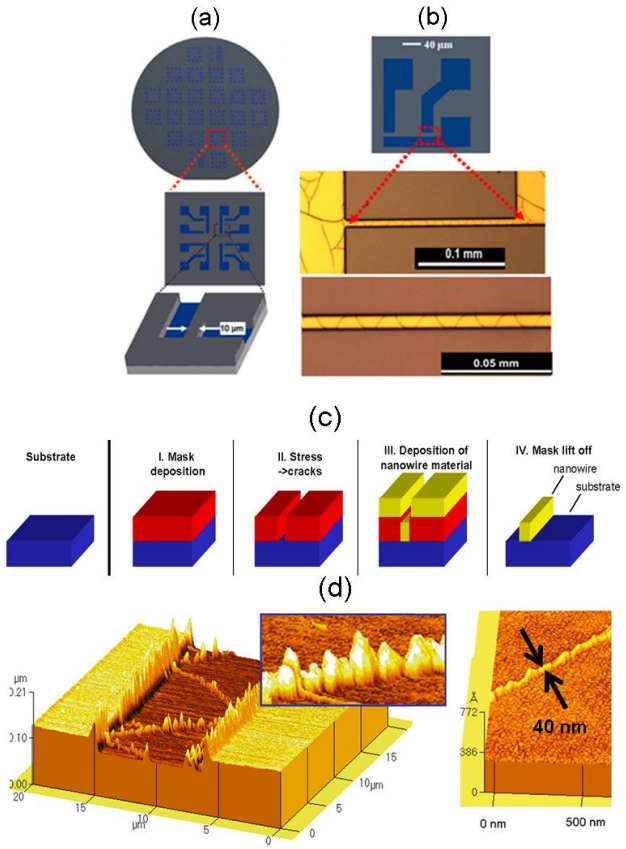

Fig.1. Fracture approach for the fabrication of nanowires with contacts on a Si-chip. a) Photoresist on a Si-wafer is microstructured to form a mold for the later contact lines and a prerequisit for the nanowire formation at the 10 µm wide bridge (magnified). b) The image shows a different view of the bridge used for the nanowire formation. The magnification shows an optical microscopy image of the photoresist in the bridge area after exposing it to thermal cycling that effects the fracture of the thin film. The higer magnification shows the regularity of the crack pattern. c) Schematic overview over the process that is described in the text, resulting in nanowires, represented in d) AFM image of nanowires formed in the 10 µm wide area between the micro contacts. The magnification shows that the wires consist of a chain of clusters.

temperature, gas flow rate and relative source and substrate distances. The growth contains the following 3 steps: (i) During heating in the furnace above the melting temperature of the eutectic, the precursor mixture (ZnO + graphite) transforms into vapor phase and is transported to substrates by carrier gas. (ii) The deposited precursor atoms or molecules form liquid-droplet eutectic alloy with catalytic particles. (iii) Caused by supersaturation, the precursor material is deposited at the interface between the catalyst droplet and its surface. This enables to lift the droplet due to capillary forces and continue to grow nanowires. During cooling the phase separation occurs resulting in formation of 1D rods with catalytic particle on the top [15,16,17]. In typical VLS process, temperature, amount of precursor material, size of catalytic particles and the gas flow rate are the main controlling parameters for growth of 1type of the 1D structure. The nanostructures grow in preferential crystal directions faster than in others, causing the material to shape in a crystalline manner. For the VLS process exists, the here used process doesn't need a catalyst and a tube furnace. A prime example for the nanostructure growth is ZnO. By using the ability of ZnO to interpenetrate during crystal growth, gaps between current lines can be bridged above chips, see Figure 2.

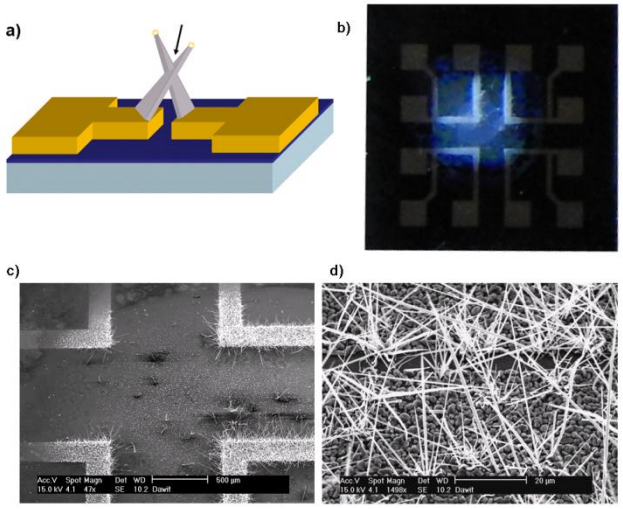

Fig. 2. Growth of three dimensional nanostructures on the current lines of a Si-chip. a) shows the principle, a gap between two current lines can be bridges by growing free standing but interpenetrating nanostructures (arrow point to the interpenetration area). b) Photograph of a 1 cm2 Si chip that is exposed on the area occurring bright with the nanostructure growth conditions. c) This are is shown under the electron microscope where free standing ZnO structures are growing. d) The magnification from c shows the gap between the current lines (darker contrast in the middle) which is bridged by interpenetrating and free standing ZnO structures.

This allows to shape individual nanoscale connectors at specific places on a circuit. A precondition for the integration is the possibility to keep the synthesis temperate on a level that will not destroy already structured electronics. This can be achieved by an active cooling of the silicon substrate or as in our case to lower the process temperature on the chip by shielding all areas where no deposition will take place.

III. EXAMPLES FOR THE ELECTRONIC PROPERTIES:

The above described Nanostructures are already used as gas sensors or field effect transistors, depending on the used metals or semiconductors. It turns out that the nanostructure sensors are advanced in terms of responding pressure and time. A remarkable feature was shown by Penner et al. [18] that is a change in mechanism of a hydrogen sensor. While usually the conductivity decreases with increased hydrogen concentration, the conductivity increases in a Pd-nanowire if they are exposed to hydrogen. This phenomenon could be observed also for gold nanowires integrated by the above described approach [14]. Figure 3 shows the respones of ZnO nanowires formed by the above described methods on chips. In Figure 3a, the fracture approach was utilized and nanowires were formed from sputter deposited ZnO. For comparison, the response shown in 3b originates from free standing interpenetrating ZnO structures. The viewgraph shows a fast response in both cases, however, differences are characteristic for both fabrication procedures. As a general tendency, polycrystalline wires are faster and more sensitive. The grain boundaries between the particles are important sensitive elements that enlarge the effective surface of a nanowire.

IV. CONCLUSION

The two briefly shown examples for micro nano integration demonstrate a feasibility of nanowire based electronics, especially for sensor applications. In the presentation, further examples for the application of nanostructures will be given based on the large scale

synthesis of nanoscale building blocks into macroscopically expanded 3 D networks.

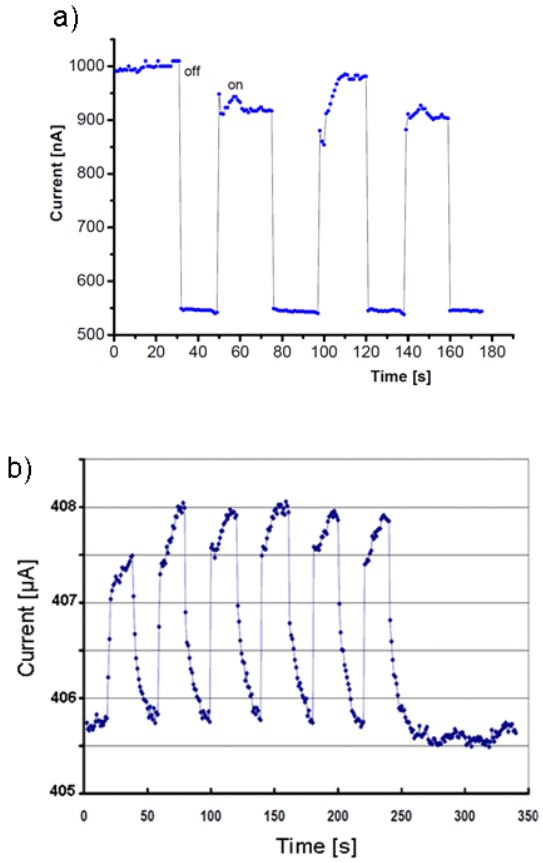

Fig. 3. Response to UV-light of integrated nanowires a) nanowires made by the fracture approach, b) free standing nanostructures formed by interpenetration during growth.

Applications include flexible semiconductors and ceramics as well as applications of superhydrophilicity and superhydrophobicity.

REFERENCES

[1] C. M. Lieber, and Z. L. Wang, "Functional Nanowires," MRS Bulletin, vol. 32, pp. 99-108, 2007.

[2] J. T. Hu, T. W. Odom, and C. M. Lieber, "Chemistry and Physics in One Dimension: Synthesis and Properties of Nanowires and Nanotubes," *Acc. Chem. Res.* vol. 32, pp. 435-445, 1999.

[3] F. Schlottig, M. Textor, N. D. Spencer, K. Sekinger, and F. Ochanda, "Characterization of nanoscale metal structures obtained by template synthesis", *Fresenius J. Anal. Chem.* vol. 361, pp. 684–686, 1998.

[4] O. Rabin, P. R: Herz, Y. M. Lin, A. I. Akinwande, S. B. Cronin, and M. S. Dresselhaus, "Formation of thick porous anodic alumina films and nanowire arrays on silicon wafers and glass," *Adv. Funct. Mater.* vol. 13, pp. 631-638, 2003.

[5] L. Shi, C. Pei, and Q. Li, "Fabrication of ordered single crystalline CuInSe2 nanowires arrays," *Cryst. Eng. Comm.* vol. 12, pp. 3882-3885, 2010.

[6] J. D. Holmes, K. P. Johnston, R. C. Doty, and B. A. Korgel, " Control of Thickness and Orientation of Solution-Grown Silicon Nanowires," *Science*, vol. 287, pp. 1471, 2000.

[7] C. Y. Lee, T. Y. Tseng, S.Y Li and P. Lin, "Growth of zinc oxide nanowires on silicon (100)," *Tamkang J. Sci. Eng.*, 6, no.2, pp. 127-132, 2003.

[8] H. J. Fan, P. Werner, and M. Zacharias, "Semiconductor nanowires: from self-organization to patterned growth,", *Small* 2, pp.700-717, no. 6, 2006.

[9] S. Jebril, H. Kuhlmann, S. Müller, C. Ronning, L. Kienle, V. Duppel, Y. K. Mishra, and R. Adelung, "Epitactically interpenetrated high quality ZnO nanostructured junctions on microchips grown by the vapor-liquid-solid method," *Crystal Growth & Design*, vol. 10, pp.2842-2846, 2010.

[10] R. Adelung , O. C Aktas, J. Franc, A. Biswas, R. Kunz, M. Elbahri, J. Kanzow, U. Schürmann, and F. Faupel. "Strain-controlled growth of nanowires within thin-film cracks,", *Nat. Mater.*, vol. 3, pp. 375-379, 2004.

[11] M. Elbahri, S. K. Rudra, S. Wille, S. Jebril, M. Scharnberg, D. Paretkar, R. Kunz, H. Rui, A. Biswas, and R. Adelung, "Employing thin-film delamination for the formation of shadow masks for nanostructure Fabrication,", *Adv. Mater.*, vol. 18, pp.1059–1062, 2006.

[12] B. E. Alaca, H. Sehitoglu, and T. Saif, "Guided self-assembly of metallic nanowires and channels," *Appl. Phys. Lett.*, vol. 84, pp.4669-4671, 2004.

[13] S. Jebril, H. Kuhlmann, S. Müller, C. Ronning, L. Kienle, V. Duppel, Y.K. Mishra, R. Adelung: Epitactically Interpenetrated High Quality ZnO Nanostructured Junctions on Microchips Grown by the Vapor-Liquid-Solid Method, *J. Cryst. Growth Des.* 10(7), pp. 2842-2846, 2010.

[14] S. Jebril, M. Elbahri, G. Titazu, K. Subbannajui, S. Essa, F. Niebelschutz, C.C. Rohling, V. Cimalla, O. Ambacher, B. Schmidt, D. Kabiraj, D. Avasti, and R. Adelung " Integration of thin film fracture based nanowires into microchip fabrication", *Small 4(12)* pp. 2214-2221, 2008.

[15] R. S. Wagner and W. C. Ellis, "Vapor liquid solid growth of mechanism of single crystal growth" *Appl. Phys. Lett*, vol. 4, pp. 89, 1964.

[16] H. Huang, "Fabrication and mechanics of nanorods," *Rev. Adv. Mater. Sci*., vol. 13, pp. 41, 2006.

[17] D. S. Kim, R. Scholz, U. Gösele, M. Zacharias, "Gold at the root or at the tip of ZnO nanowires: A model," *Small*, vol. 4, pp.1615-1659, 2008.

[18] F. Favier, E. C. Walter, M. P. Zach, T. Benter, R. M. Penner, Science, vol. 293, pp. 2227-2231, 2001.

Strain-Tunable Quantum Dot Devices

A. RASTELLI, R. TROTTA, E. ZALLO, P. ATKINSON, E. MAGERL, F. DING, J. D. PLUMHOF, S. KUMAR, K. DÖRR, O.G. SCHMIDT
Institute for Integrative Nanosciences, IFW Dresden, Helmholtzstr. 20, 01069 Dresden, Germany
a.rastelli@ifw-dresden.de

***Abstract* – We introduce a new class of quantum dot-based devices, in which the semiconductor structures are integrated on top of piezoelectric actuators. This combination allows on one hand to study in detail the effects produced by variable strains (up to about 0.2%) on the excitonic emission of single quantum dots and on the other to manipulate their electronic- and optical properties to achieve specific requirements. In fact, by combining strain with electric fields we are able to obtain (i) independent control of emission energy and charge-state of a QD, (ii) wavelength-tunable single-QD light-emitting diodes and (iii) frequency-stabilized sources of single photons at predefined wavelengths. Possible future extensions and applications of this technology will be discussed.**

***Index Terms* – Epitaxial Quantum Dots, Single photon sources, Strained semiconductors, Tunable sources of single photons.**

I. INTRODUCTION

Optically active semiconductor quantum dots (QDs) can be made as nanoinclusions of a low energy bandgap material in a matrix with larger energy bandgap. One of the simplest ways to obtain QDs with excellent structural, electronic, and optical properties is represented by self-assembly of 3D nanoislands during lattice-mismatched heteroepitaxial growth. In this, so-called Stranski-Krastanow (SK) growth mode, elastic stress is one of the main driving forces leading to the formation and evolution of QDs. The most prominent example is represented by InGaAs QDs in GaAs matrix. A large number of experiments have demonstrated that these QDs are excellent quantum emitters which can be used as sources of triggered single photons, indistinguishable photons and polarization entangled photon pairs. On the other hand virtually strain-free GaAs/AlGaAs QDs can be made by using templates of self-assembled nanoholes on an AlGaAs surface.

Whatever approach is used, QDs are affected by dot-to-dot fluctuations. This makes it difficult to obtain QDs with electronic and optical properties which meet (sometimes very stringent) requirements for their use in advanced quantum optics experiments, especially involving independent sources. Post-growth techniques are therefore required to fine-tune the optical properties of QDs. Vertical electric fields (applied along the growth direction) represent the most powerful "tuning knob" to date. By using the so called "giant Stark effect" (GSE) both the emission energy and the excitonic fine-structure splitting can be widely tuned [1, 2]. The latter is important for generation of entangled photon pairs. Electric fields can also be used to electrically pump single QDs. This feature, which takes profit of mature semiconductor technology, is one of the major advantages of epitaxial QDs compared to other solid state emitters. On the other hand the structure designs for electrical pumping and for exploiting the GSE are not compatible, making additional "tuning knobs" indispensible.

II. RESULTS

In this contribution we introduce a new class of QD-based devices, in which the semiconductor structures are integrated on top of piezoelectric actuators. This combination allows us on one hand to study in detail the effects produced by variable strains (up to about 0.2%) on the excitonic emission of single QDs and on the other to add a powerful "tuning knob" to QDs.

We first discuss the effects of biaxial strain on the emission of single QDs embedded in optical microcavities [3]. Afterwards we show that strain does not only affect the emission energy of QDs but also the relative binding energies of excitonic species confined in QDs [4] and the fine structure splitting of neutral excitons[5].

We then discuss a technological approach to combine strain with electric fields on the same device.

REFERENCES

[1] R.B. Patel et al. Nature Photon. 4, 632 (2010)
[2] A.J. Bennet et al Nature Phys. Nature Physics 6, 947 (2010)
[3] T. Zander, A. Herklotz, S. Kiravittaya, M. Benyoucef, F. Ding, P. Atkinson, S. Kumar, J. D. Plumhof, K. Dörr, AR, O. G. Schmidt, Optics Express 17, 22452 (2009)
[4] F. Ding et al PRL 104, 067405 (2010). D. Knuth, The Art of Programming. Addison-Wesley, 1973
[5] J. D. Plumhof, V. Krapek, F. Ding, K. D. Jöns, R. Hafenbrak, P. Klenovsky, A. Herklotz, K. Dörr, P. Michler, AR, O. G. Schmidt, Phys. Rev. B (R) **83**, 121302 (2011)

Zinc Oxide Nanostructures:New Properties for Advanced Applications

Oleg LUPAN, Lee CHOW, Thierry PAUPORTÉ
Technical University of Moldova
University of Central Florida, USA
Chimie-Paristech, LECIME, UMR7575, CNRS, France
lupan@mail.utm.md

***Abstract* – Zinc oxide is a material which exhibits a variety of new properties at nanometer dimensions. Various synthesis techniques have been carried out to provide growth of nanowires, nanorods, nanorings, nanosprings, and nanobelts of ZnO under various conditions. These nanostructures show that ZnO possesses probably the richest family of nanoarchitectures among all materials, including their structures and properties. Such nanoarchitectures are potential building blocks for novel applications in optoelectronics, sensors, photovoltaic and nano-biomedical sciences. This work presents a review of various nano architectures of ZnO grown by the electrochemical, hydrothermal and solid–vapor phase techniques and their properties. The possible applications of ZnO nanowires as sensors, nano-DSSC, photodetectors and nano-LEDs will be presented.**

***Index Terms* – ZnO, nanowire, nanorod, nanosensor, nano-LED, nanophotodetector.**

I. INTRODUCTION

Low-dimensional ZnO materials have become the focus of a lot of researches due to their performances in electronics, optoelectronics, photonics and biomedical applications. In the last decade, the growth of ZnO has been an active research field due to their applications as sensors and catalysts. However, since the nanotechnology initiative led by the USA, investigations of one-dimensional (1D) materials, like nanowires and nanorods has become a leading edge for the nanotechnologies and for nanoscience. The reduction of material size induces new electrical, chemical, optical and mechanical performances, which are believed to be the results of aspect-ratio impact, size and quantum confinement effects. 1D nanorods are ideal for investigating the transport process in confined spaces. This can result in future understanding of new phenomena in low-dimensional structures. It could be a forward step for developing new generation of nanodevices with better performance [1-8].

In this context zinc oxide is one of the key materials. It combines strong piezoelectric and pyroelectric properties. Also, ZnO posses a wide direct band-gap (3.36 eV), which is good for optoelectronic applications. The exciton binding energy (60 meV) in ZnO crystal is higher that in GaN, which can give excitonic emission at room temperature more efficient than other materials. At the same time, ZnO is a transparent material to visible light and could be doped easily to obtain lower resistivity and/or bandgap for specific applications. It is a strong candidate for high temperature electronic devices that can reliably operate in space and other harsh environments [3].

The topic of our presentation here is to review the low-dimensional structures that have been grown for ZnO by electrochemical or hydrothermal deposition and corresponding mechanisms. The potential applications of ZnO low-dimensional structures in novel nanodevices will be discussed.

II. EXPERIMENTAL

The fabrication method of nanosensors by using individual ZnO nanowire or nanorod released from an agglomeration of nanowires as-grown on initial substrate has been described in our previous works [5,6] and reviewed in [3,4]. Nanowires can be released from the initial substrate by sonication in ethanol or it can be used a direct contact technique can be used to transfer nanowires to a SiO_2-coated Si substrate. These procedures can be found in our previous works [4,5]. Rigid contacts were fabricated with a single ZnO nanowire on the sensor substrate template (glass with Cr/Au as electrodes) by using FIB metal deposition. For the sensor characterization, the measuring apparatus consists of a closed quartz chamber connected to a gas flow system [4-6]. The concentration of gases for test was measured using a pre-calibrated mass flow controller. Gases and air were introduced to a gas mixer via a two-way valve using separate mass flow controllers. By monitoring the output voltage across the nanorod based sensor, the resistance was measured in dry air and in a test gas. A computer with suitable LabView interface allows all controls and acquisition of data. A linear behavior of the current-voltage curves was recorded, which is important for the sensing. ZnO nanowires have also been synthesized by electrodeposition, a soft deposition technique that is suitable with plastic lightweight substrates [7].

III. RESULTS

A scanning electron microscope image of the connected ZnO nanowire is presented in Figure 1. Focused ion beam (FIB) instrument was used to pattern metal electrodes contacting both ends of a single ZnO nanowire. The separation of the electrodes was about 5 μm. The fabricated

device based on a single wire of 100 nm in diameter shown in Figure 1a, was used in our studies.

Figure 1b shows the transient response of the 100 nm ZnO-nanowire gas sensor under exposure to 100 ppm of H_2 gas at room temperature.

Ultraviolet (UV) photoconductive nanosensors based on an individual ZnO nanowire (100 nm in diameter) are important for nanoscience. This nano-detector is prepared in a FIB set-up by using nanodeposition for metal electrodes and studied as was reported before [8,9]. The photoresponse of the ultraviolet sensor demonstrated that the output signal of the sensors is reproducible under UV irradiation. The photoresponse and characteristics of the ZnO nanowire device demonstrates that focused ion beam process offers a way to fabricate novel nanodevices on a single ZnO nanowire with diameters as small as 100 nm [6]. The response and recovery times to UV light exposure are relatively fast for a single ZnO nanowire photodetector compared to an individual zinc oxide nanorod grown by aqueous chemical deposition [9].

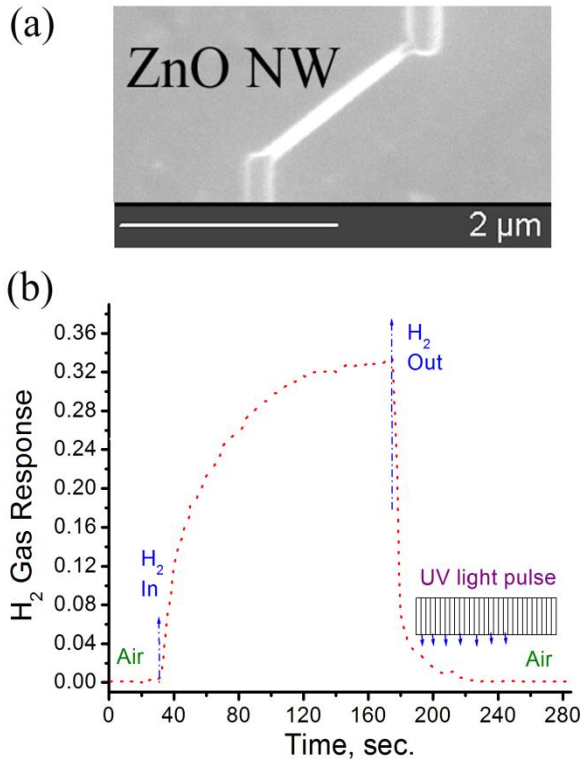

Fig. 1. (a) FESEM image of a single ZnO nanowire (NW) connected in a nanosensor structure by FIB technique. (b) Gas response curves of the 100 nm zinc oxide nanowire–based gas sensor under exposure to 100 ppm of H_2 gas at room temperature.

The epitaxial synthesis of ZnO nanowire arrays on a *p*-type GaN (0001) single crystalline thin film on sapphire by an electrochemical technique was demonstrated for the first time in our works [10,11]. The nanowires were directly epitaxially grown onto the *p*-GaN films with an in-plane relationship of ZnO[10-10] parallel to GaN[10-10]. By GA-XRD experiments, the ZnO mosaicity was shown to be as low as 1.18°. The n-ZnO NWs/*p*-GaN heterostructure was integrated in a light emitting diode structure device [10,11]. The rectifying behavior was shown with a forward current onset at 3V. The LEDs emitted a unique UV-light centered at ~393 nm for either as-prepared or annealed samples. The light emission turn-on voltage was ~4.4 V and the UV-emission was very bright even at low applied forward bias ~6.4 V. Our data clearly state the remarkable quality of the electrochemical ZnO material and ZnO-NWs/*p*-GaN interface as well as effectiveness of electrodeposited epitaxial ZnO as an active layer in UV-LED structure [10,11]. By copper-doping the ZnO NWs, we have shown that the emission wavelength of the LED structure could be shifted towards the visible wavelength region [12]. ZnO NWs were also grown by electrodeposition on *p*-Si and LED structures, were made and discussed in Ref. [13]. Other applications of electrodeposited zinc oxide low-dimensional structures also include dye-sensitized solar cells which were reported in Ref.[14]. The ZnO wires ensure a fast electron transfer from the excited dye to the back contact of the photoanode [14]. Photodetectors and other devices structures were reported in other papers [15-17]. In Appendixes A-E, some morphological and structural properties of the ZnO nanostructures and applications have been shown. More detailed description for these low-dimensional structures and their characteristics have been reported in our works [2-20].

IV. CONCLUSION

We report on zinc oxide nanostructures – properties and possible applications in future devices. It has been shown a single nanowire nanosensors made from ZnO nanowire can be produced. Fabricated nanodevices showed a promising sensitivity to H_2 gas, which makes possible its further applications in sensors. The presented single ZnO nanowire sensor proves to be promising for application in various processes [3,4]. Also, ZnO nanowires grown by electrodeposition or hydrothermal techniques have been integrated in LEDs and DSSC structures and have been discussed here.

APPENDIX A

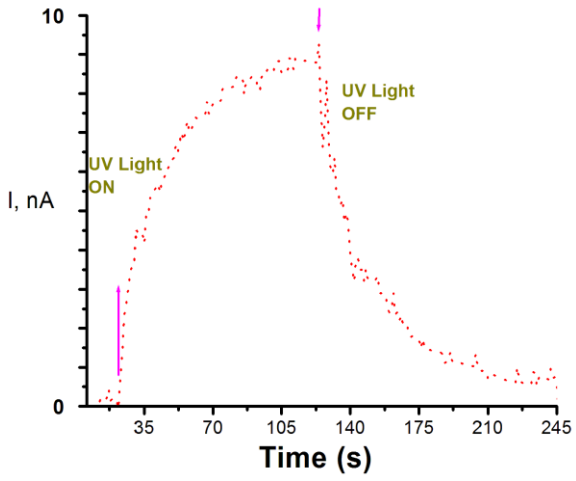

Fig. A. The UV response for a single ZnO nanowire-based UV photoconductive detector.

APPENDIX B

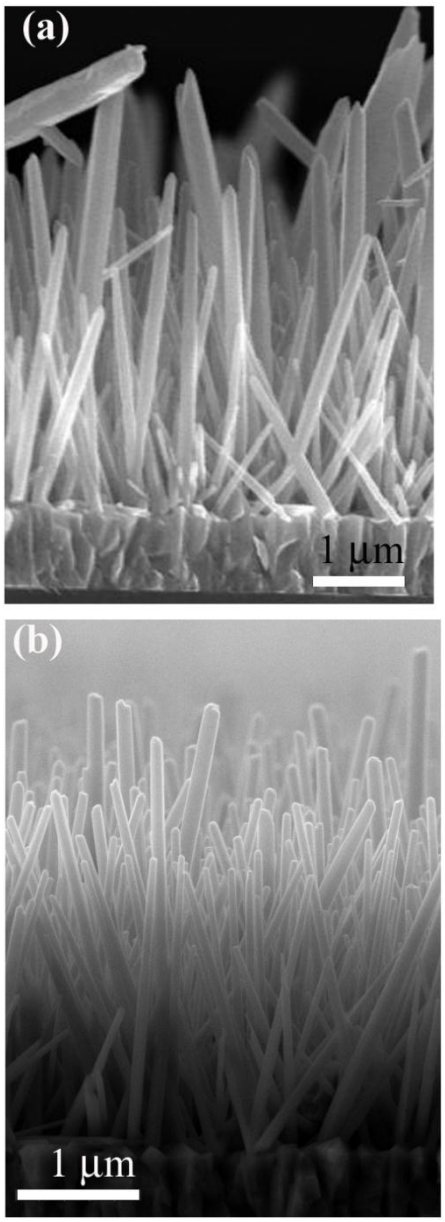

Fig. B. SEM image of the ZnO nanowires grown by an electrochemical technique at 90 °C from $ZnCl_2$ and KCl solution. (a) pure ZnO grown for 9000s; (b) Cd-ZnO grown on FTO substrate for 7200 s. These nanowires were used as building nanoblocks for LED, DSSC solar cells and for nanosensors structures.

APPENDIX C

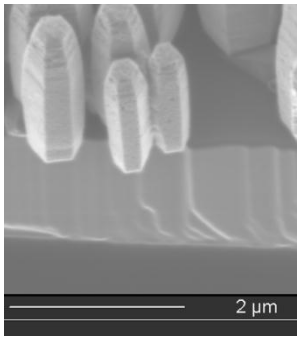

Fig. C. SEM image (tilted 65 °) of epitaxial ZnO Nanorods grown on *p*-GaN by hydrothermal technique. It is forming a heterostructure (*n*-ZnO/*p*-GaN) used for low-dimensional-LED applications.

APPENDIX D

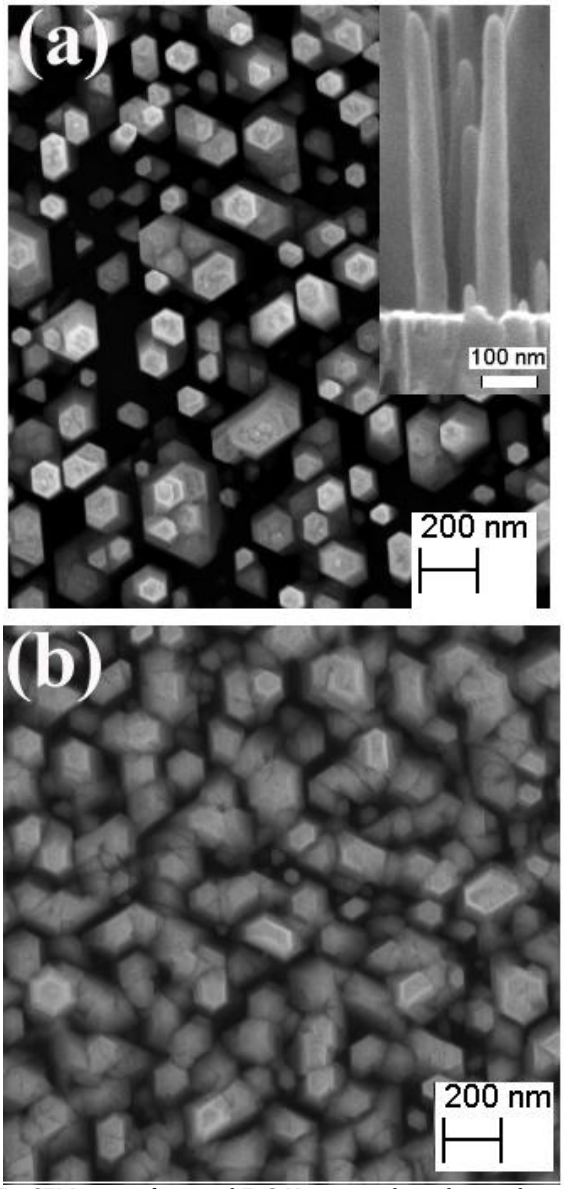

Fig. D. SEM image of epitaxial ZnO Nanowires electrodeposited on p-GaN (0.10 mM $ZnCl_2$) and (b) (0.25 mM $ZnCl_2$). Inset shows cross-sectional view of the ZnO nanowires on p-GaN single crystal forming a heterostructure used for nano-LED applications.

APPENDIX E

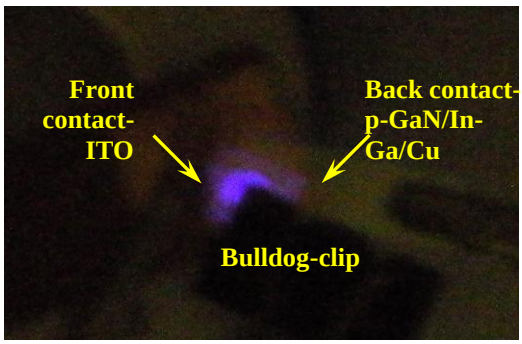

Fig. E. The inset shows an image of the blue- light emission spot under a dc bias of 8.5 V at room temperature from zinc oxide nanowires grown on *p*-GaN substrate.

ACKNOWLEDGMENTS

This research was performed with the financial support of the C-nano Ile-de-France program (nanoZnO-LED Project).

Dr. O. Lupan acknowledges the CNRS for support as an invited scientist at the LECIME-ENSCP, France. Dr.L. Chow acknowledges partial financial support from US Department of Agriculture, award #58-3148-8-175. Financial support by Supreme Council for Science and Technological Development of the Academy of Sciences of Moldova are acknowledged.

REFERENCES

[1] Z. L. Wang, "Zinc oxide nanostructures: growth, properties and applications," J. Phys.: Condens. Matter., vol. 16, pp. R829–R858, 2004.

[2] T. Pauporté, Design of solution-grown ZnO nanostructures. In: Z.M. Wang, Editor, Lecture Notes on Nanoscale Science and Technology. Volume 5. Toward Functional Nanomaterials, Springer Books, New York, pp. 77–125, 2009.

[3] I. M. Tiginyanu, O. Lupan, V. V. Ursaki, L. Chow, M. Enachi, "Nanostructures of Metal Oxides." Comprehensive Semiconductor Science & Technology, Chapter 3.11, pp. 396-479, 2011.

[4] G. Chai, O. Lupan, L. Chow, "Focused ion beam fabrication of carbon nanotube and ZnO nanodevices" in Nanofabrication Using Focused Ion and Electron Beams Principles and Applications, Edited by Ivo Utke, Stanislav Moshkalev and Phillip Russell ISBN13: 9780199734214 ISBN10: 0199734216 752 pages, Nov 2011.

[5] O. Lupan, G. Chai, L. Chow, "Novel hydrogen gas sensor based on single ZnO nanorod," Microelectronics Eng., vol. 85, pp. 2220-2226, 2008.

[6] O. Lupan, V.V. Ursaki, G. Chai, L. Chow, G.A. Emelchenko, I.M. Tiginyanu, A.N. Gruzintsev, A.N. Redkin, "Selective hydrogen gas nanosensor using individual ZnO nanowire with fast response at room temperature," Sensors and Actuators B: Chemical, vol. 144(1), pp. 56-66, January 2010.

[7] Lupan O., Pauporté T., "Hydrothermal treatment for the marked structural and optical quality improvement of ZnO nanowire arrays deposited on lightweight flexible substrates.," J. Cryst. Growth, vol. 312, pp. 2454-2458, 2010.

[8] O. Lupan, G. Chai, L. Chow, "Fabrication of ZnO nanorod-based hydrogen gas nanosensor," Microelectronics Journal, vol. 38, pp. 1211-1216, December 2007.

[9] O. Lupan, L. Chow, G. Chai, L. Chernyak, O. Lopatiuk-Tirpak, H. Heinrich, "Focused-ion-beam fabrication of ZnO nanorod-based UV photodetector using the in-situ lift-out technique," Physica Status Solidi (a), vol. 205(11), pp. 2673–2678, Nov. 2008.

[10] O. Lupan, Th. Pauporté, B. Viana, Low-Voltage UV-Electroluminescence from ZnO-Nanowire Array/p-GaN Light-Emitting Diodes, Advanced Materials, vol. 22(30), pp. 3298–3302, August 2010.

[11] O. Lupan, Th. Pauporté, B. Viana, I. M. Tiginyanu, V. V. Ursaki and R. Cortés, "Epitaxial Electrodeposition of ZnO Nanowire Arrays on *p*-GaN for Efficient UV-Light-Emitting Diode Fabrication," ACS Appl. Mater. Interfaces, 2010, 2 (7), pp 2083–2090, July 2010.

[12] O. Lupan, T. Pauporté, B. Viana, P. Aschehoug, "Electrodeposition of Cu-doped ZnO nanowire arrays and heterojunction formation with *p*-GaN for color tunable light emitting diode applications, Electrochimica Acta, In Press, doi:10.1016/j.electacta.2011.02.004 online Feb. 2011.

[13] O. Lupan, T. Pauporté and B. Viana, "Low-Temperature Growth of ZnO Nanowire Arrays on p-Silicon (111) for Visible-Light-Emitting Diode Fabrication," J. Phys. Chem. C, 2010, 114 (35), pp 14781–14785, August 2010.

[14] O. Lupan, V.M. Guérin, I.M. Tiginyanu, V.V. Ursaki, L. Chow, H. Heinrich, T. Pauporté, "Well-aligned arrays of vertically oriented ZnO nanowires electrodeposited on ITO-coated glass and their integration in dye sensitized solar cells", Journal of Photochemistry and Photobiology A: Chemistry, vol. 211(1), pp. 65-73, March 2010.

[15] L. Chow, O. Lupan, Guangyu Chai, "FIB fabrication of ZnO nanotetrapod and cross-sensor," Physica Status Solidi (b), vol. 247(7), pp. 1628–1632, July 2010.

[16] O. Lupan, L. Chow, S. Shishiyanu, E. Monaico, T. Shishiyanu, V. Şontea, B. Roldan Cuenya, A. Naitabdi, S. Park, and A. Schulte, "Nanostructured zinc oxide films synthesized by successive chemical solution deposition for gas sensor applications," Materials Research Bulletin, vol. 44, pp. 63-69, 2009.

[17] O. Lupan, G. Chai, L. Chow, G. A. Emelchenko, H. Heinrich, V. V. Ursaki, A. N. Gruzintsev, I. M. Tiginyanu and A. N. Redkin, "Ultraviolet photoconductive sensor based on single ZnO nanowire," Physica Status Solidi (a), vol. 207(7), July 2010, Pages: 1735–1740.

[18] O. Lupan, G. Chai, L. Chow, "Fabrication of ZnO nanorod-based hydrogen gas nanosensor," Microelectronics Journal, vol. 38, pp. 1211-1216, December 2007.

[19] V.V. Ursaki, O.I. Lupan, L. Chow, I.M. Tiginyanu, V.V. Zalamai, "Rapid thermal annealing induced change of the mechanism of multiphonon resonant Raman scattering from ZnO nanorods," Solid State Communications, vol. 143, pp. 437-441, 2007.

[20] O. Lupan, G.A. Emelchenko, V.V. Ursaki, G. Chai, A.N. Redkin, A.N. Gruzintsev, I.M. Tiginyanu, L. Chow, L.K. Ono, B. Roldan Cuenya, H. Heinrich, E.E. Yakimov, "Synthesis and characterization of ZnO nanowires for nanosensor applications," Materials Research Bulletin, vol 45(8), pp. 1026-1032, August 2010.

Surface Plasmon Enhanced Luminescence from Ag covered Anatase Titania Nanotubes

Mihai ENACHI[1], Veaceslav URSAKI[2], Vladimir SERGENTU[2]

[1]*National Center for Materials Study and Testing, Technical University of Moldova, Stefan cel Mare av. 168, Chisinau MD-2004, Republic of Moldova, e-mail: enachim2002@yahoo.com*

[2]*Institute of Applied Physics of the Academy of Sciences of Moldova, Academy str. 5, Chisinau MD-2028, Moldova*

enachim2002@yahoo.com

***Abstract* – We show that coating of titania nanotubes by Ag layers with thickness of 5 – 20 nm leads to the increase of the near-bandgap photoluminescence intensity by one order of magnitude, while the effect of Au coatings is insignificant. Titania nanotibes with average outer diameter of 250 nm and wall thickness of 70 nm with anatase structure were produced by anodization of Ti foils in an ethylene glycol based electrolyte containing a mixture of HF and H_3PO_4 followed by annealing at 300 ^oC. The enhancement of the band-edge emission is believed to be due to the effect of surface plasmons in Ag coatings. This suggestion is supported by calculations of dispersion relations of surface plasmons at the Ag/TiO_2 interface and by the measurement of the transmission spectra of uncoated and metal coated titania nanotubes.**

***Index Terms* – luminescence, optical absorption, surface plasmons, titania nanotuves, dispersion relations.**

I. INTRODUCTION

Titania (TiO_2) is widely used as a pigment, in sensors, electrocatalysis, and Graetzel-type solar cells (e.g. [1] and references therein). Among titatia nanostructures, titania nanotubes (TiO_2 NTs) have improved properties for application in photocatalysis, sensing, photoelectrolysis, photovoltaics, lithium ion batteries, and biomedical applications [2]. Recently, titania also gained interest as a material used in photonic band gap crystals for the visible spectrum of light due to its high index of refraction and low absorption [3].

Titania nanotubes have been produced by a variety of methods including deposition into a nanoporous alumina template, sol–gel transcription using organo-gelators as templates, seeded growth, and hydrothermal processes [1,2]. However, among all methods, electrochemical anodization of titanium is a cost-effective approach for the growth of highly ordered TiO_2 NTs [4].

Optical properties of TiO_2 NTs, particularly luminescence, are very important for photonic applications. In a recent work, the spectral distribution of cathodoluminescence from a cluster of nanotubes clearly demonstrated the formation of resonator modes [5]. Taking into account the possibility of doping porous titania templates with rare earth and transition metal ions and the morphology controlled light scattering properties, one can expect that luminescent materials prepared on porous TiO_2 templates are prospective for random laser applications [6]. The development of methods for enhancing the luminescence efficiency from titania nanotubes is an important task. Enhancement of the emission due to surface plasmons was observed in some metal-semiconductor systems such as Ag/ZnO films [7], Ag (or Al)/InGaN quantum wells [8].

In this work, we demonstrate that the band-edge emission from titania nanotubes produced by electrochemical anodization of titanium can be enhanced by the deposition of Ag films. This enhancement is due to the excitation of surface plasmons in Ag.

II. SAMPLE PREPARATION AND EXPERIMENTAL DETAILS

Technological conditions for the preparation of porous TiO_2 layers with controlled morphology and porosity on the basis of Ti foils (Aldrich) include rinsing and sonicating in isopropyl alcohol, drying and anodizing. The investigated samples were anodized in a mixture of HF (1 ml) and H_3PO_4 (11 ml) in ethylene glycol (120 ml) under 120 V during 2 hours. This treatment results in the fabrication of TiO_2 nanotubes with outer diameters around 250 nm and the wall thickness of 70 nm, as illustrated in Fig. 1. The samples were annealed at 300 ^oC during one hour after anodization. Ag and Au coatings were deposited onto titania nanotubes by means of a Cressington magnetron sputtering coater.

A VEGA TESCAN TS 5130 MM scanning electron microscope (SEM) was used for morphological characterization of the samples.

Photoluminescence (PL) was excited by 351 nm line of an Ar^+ SpectraPhysics laser and analyzed through a double spectrometer at low temperature (10 K). The resolution was better than 0.5 meV. The samples were mounted on the cold station of a LTS-22-C-330 cryostat.

Raman spectra were measured at room temperature with a Confocal MonoVista CRS spectrometer.

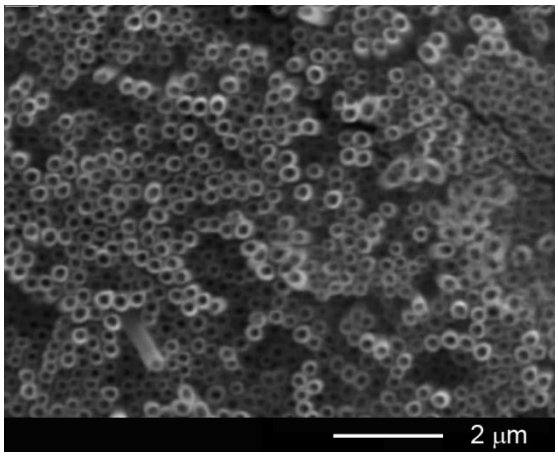

Fig. 1. SEM image of TiO_2 nanotubes produced by etching Ti foils in a mixture of HF and H_3PO_4 in ethylene glycol.

III. RESULTS AND DISCUTIONS

Figure 2 presents the PL spectra of TiO_2 nanotubes (with the morphology illustrated in Fig.1) subjected to annealing at 300 °C and covered with Ag films of different thicknesses. The luminescence measured in the spectral range from 370 to 500 nm is dominated by the near bandgap emission which includes two narrow lines at 371 nm (3.34 eV) and 372 nm (3.33 eV) followed by several phonon replica with phonon energy equal to 50 meV.

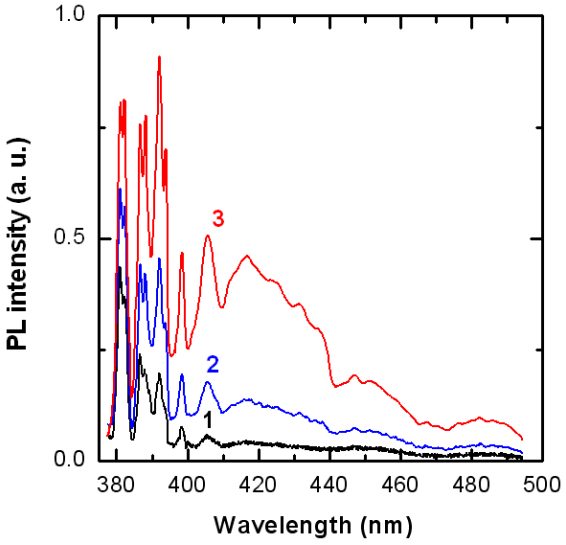

Fig. 2. PL spectra of TiO_2 NTs covered with Ag films with thickness of 5 nm (1), 10 nm (2) and 20 nm (3) measured at 10 K.

The luminescence comes from the anatase phase of titania as demonstrated by the Raman spectrum presented in Fig. 3. Anatase is tetragonal, with two TiO_2 formula units (six atoms) per primitive cell. The space group is D_{4h}^{19} (I4/amd). The 18-dimensional reducible representation generated by the atomic displacements contains the zone-center (*k=0)* modes: 3 acoustic modes and 15 optical modes. The irreducible representations corresponding to the 15 optical modes are $1A_{1g} + 1A_{2u} + 2B_{1g} + 1B_{2u} + 3E_g + 2E_u$. Three modes are infrared active, the A_{2u} mode and the two E_u modes. The B_{2u} mode is silent. The remaining six modes corresponding to symmetries $A_{1g} + 2B_{1g} + 3E_g$ are Raman active. The Raman shift for these phonons is 514 cm^{-1} for the A_{1g} mode, 399 cm^{-1} and 514 cm^{-1} for the B_{1g} modes, and 144 cm^{-1}, 197 cm^{-1} and 639 cm^{-1} for the E_g modes [9]. Therefore, the A_{1g} and one of the B_{1g} modes overlap. The two E_g modes at 144 cm^{-1}, 197 cm^{-1} are outside of the range of measured Raman shifts.

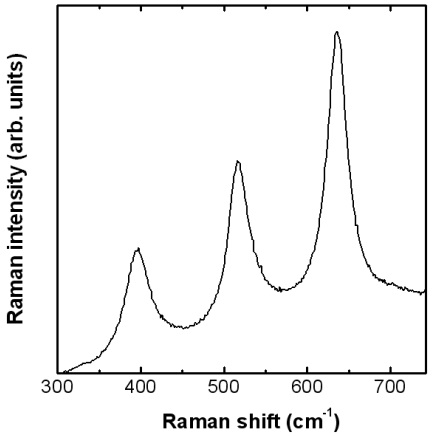

Fig. 3. Raman spectrum of TiO_2 NTs measured at room temperature.

As concerns the nature of the observed PL bands, previously two sharp lines peaking at 3.31 and 3.37 eV have been observed in the near bandgap PL spectra of anatase titania [10]. These lines were interpreted as defect-trapped-exciton related although the free-exciton origin of the 3.31 eV peak was also argued. Apart from this possible nature of the PL lines at 3.34 eV and 3.33 eV observed in our samples, their relation to free-to-bound transitions can not be excluded [11].

The data presented in Fig. 2 demonstrate that covering of TiO_2 NTs with Ag films with thickness of 5 to 20 nm leads to increased near-bandgap luminescence intensity. The thicker is the Ag film the stronger is luminescence. However, the increase of the film thickness beyond 20 nm results in a decrease of the luminescence intensity (not shown in this graph). We believe that this decrease is due to increased absorption in the metal film of both excitation and emission light. As concerns the increase of the luminescence intensity with Ag films up to 20 nm, it is suggested to be due to the enhancement of both the excitation field and the bandedge emission via surface plasmons in the Ag film, the second effect being stronger, since the excitation wavelength (351 nm) does not match very well the surface plasmon (SP) resonance. Fig. 4 shows the dispersion relations of surface plasmon polaritons (SPP) on Ag/TiO_2 and Au/TiO_2 surfaces calculated by the dielectric functions. For a single interface between a metal and a dielectric the dispersion relation can be derived from Maxwell's equations and boundary conditions [12]:

$$k_{SPP}(\omega) = \frac{\omega}{c}\sqrt{\frac{\varepsilon_d(\omega)\cdot\varepsilon_m(\omega)}{\varepsilon_d(\omega)+\varepsilon_m(\omega)}}, \qquad (1)$$

with $\varepsilon_m(\omega)$ and $\varepsilon_d(\omega)$ being the permittivity of the metal and the dielectric, respectively (*c* is the speed of light).
Therefore, the SP frequencies of Ag/TiO_2 and Au/TiO_2 are calculated as ~3 eV and ~2.3 eV, respectively, and the density states of the SP mode become dramatically larger with approaching these frequencies.

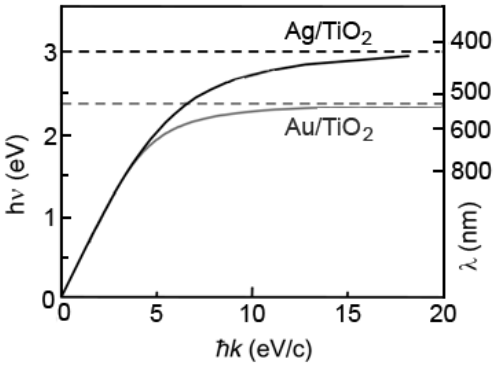

Fig. 4. Dispersion relations of the SPP at Ag/TiO_2, and Au/TiO_2 interfaces.

One can see from Fig. 2 that the emission around 380 nm is enhanced by a factor of 2 with Ag coating, while the emission around 400 – 440 nm is enhanced by an order of magnitude, since the energy of this emission corresponds to the resonance energy of the surface plasmons. At the same time, one should note that the emission intensity from samples coated with Au films is not influenced with film thicknesses up to 20 nm, it being decreased by thicker films. These data are corroborated by measurements of the optical transmission in Ag and Au coated TiO_2 NTs (Fig. 5). Absorption bands are observed around 420 nm and 630 nm in Ag and Au coated samples, respectively. One can expect that the luminescence intensity in the range of 600 nm would be increased by Au coating. However, our samples do not exhibit any emission at these wavelengths.

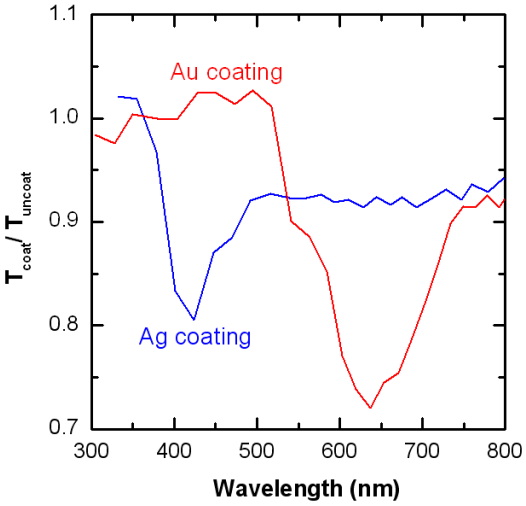

Fig. 5. Transmission curves of Ag (20 nm) and Au (20 nm) coated TiO_2 NTs. The transmission of coated samples (T_{coat}) is divided by the transmission of uncoated ones (T_{uncoat}).

IV. CONCLUSION

The results of this study demonstrate possibilities to enhance the luminescence from titania nanotubes via coating with metal films. The near-bandgap photoluminescence intensity from anatase titania nanotubes with average diameter of 250 nm and wall thickness of 70 nm is increased by an order of magnitude by coating with an Ag film with the thickness of 20 nm. The enhancement is due to the effect of surface plasmons in Ag coatings.

ACKNOWLEDGMENTS

This work was supported by the Academy of Sciences of Moldova under Contract No. 10.820.05.01/BF.

REFERENCES

[1] I. M. Tiginyanu, O. Lupan, V. V Ursaki, L. Chow, M. Enachi, Nanostructures of Metal Oxides. Comprehensive Semiconductor Science and Technology, Chapter 3.11, pp. 396-479, 2011.

[2] C. Grimes and G. K. Mor, TiO_2 Nanotube Arrays: Synthesis, Properties, and Applications. Springer, Berlin, 2009.

[3] V. V. Sergentu, I. M. Tiginyanu, V. V. Ursaki, M. Enachi, S. P. Albu, and P. Schmuki, "Prediction of negative index material lenses based on metallo-dielectric nanotubes", Phys. Status Solidi (RRL), vol. 2, pp. 242-244, 2008.

[4] M. Enachi, I. Tiginyanu, V. Sprincean, V. Ursaki, "Self-organized nucleation layer for the formation of ordered arrays of double-walled TiO_2 nanotubes with temperature controlled inner diameter", Phys. Status Solidi (RRL), vol. 4, pp. 100–102, 2010.

[5] M. Enachi, M. Stevens-Kalceff, I. Tiginyanu, V.V. Ursaki, "Cathodoluminescence of TiO_2 nanotubes prepared by low-temperature anodization of Ti foils", Materials Letters, vol. 64, pp. 2155–2158, 2010.

[6] V. V. Ursaki, I. M. Tiginyanu, L. Sirbu, and M. Enachi, "Luminescent materials based on semiconductor compound templates for random laser applications", Phys. Status Solidi C, Vol. 6, No. 5, 1097–1104, 2009.

[7] M. Liu, S. W. Qu, W. W. Yu, S. Y. Bao, C. Y. Ma, Q. Y. Zhang, J. He, J. C. Jiang, E. I. Meletis, C. L. Chen, "Photoluminescence and extinction enhancement from ZnO films embedded with Ag nanoparticles", Appl. Phys. Lett., vol. 97, pp. 231906, 2010.

[8] K. Okamoto, I. Niki, A. Shvartser, Y. Narukawa, T. Mukai, and A. Scherer, "Surface-plasmon-enhanced light emitters based on InGaN quantum wells", Nature Mater., vol. 3, 601-605, 2004.

[9] T. Ohsaka, F. Izumi, Y. Fujiki, "Raman spectrum of anatase TiO_2", J. Raman Spectrosc, vol. 7, pp. 321-324 (1978).

[10] A. Suisalu, J. Aarik, H. Mändar, I. Sildos, "Spectroscopic study of nanocrystalline TiO_2 thin films grown by atomic layer deposition", Thin Solid Films, vol. 336, pp. 295-298, 1998.

[11] M. Enachi, V. Trofim, V. Coseac, I. M. Tiginyanu, V. V. Ursaki, "Structure and luminescence properties of titania nanotubes", Mold. J. Phys. Sci., vol. 8, pp. 2014-220, 2009.

[12] H. Raether, Surface Plasmons on Smooth and Rough Surfaces and on Gratings. Springer, Berlin, 1988.

Development of GaN-based Nanosensors using Surface Charge Lithography

Veaceslav POPA,[1] Tudor BRANISTE,[1] Olesea VOLCIUC,[1] Dimitris PAVLIDIS,[2] Andrei SARUA,[3] Peter HEARD,[4] Martin KUBALL[3]

[1] *National Center for Materials Study and Testing, Technical University of Moldova, Stefan cel Mare av. 168, Chisinau MD-2004, Republic of Moldova*

[2] *Technical University Darmstadt, Darmstadt 23584, Germany*

[3] *H.H. Wills Physics Laboratory, University of Bristol, Tyndall Avenue, Bristol BS81TL, United Kingdom*

[4]*Interface Analysis Centre, Oldbury House, 121 St. Michael's Hill, Bristol BS28BS, United Kingdom*

popa_sl@yahoo.com

***Abstract* – Semiconductor nanotechnology is a fast developing branch of modern engineering that offers perspectives for the development of electronic devices with superior parameters. A special and important niche in nanotechnology is allocated to the fabrication of nanosensors which are expected to exhibit higher sensitivity in comparison with classical microelectronic sensors. Various aspects of fabrication of GaN based nanosensors using Surface Charge Lithography are discussed and preliminary tests for gas sensors applications are presented.**

***Index Terms* – GaN, nanostructuring, surface charge lithography, sensors.**

I. INTRODUCTION

GaN and related ternary alloys became important materials for UV light emitting devices and for high-temperature high-power electronics. MBE, MOCVD and HVPE have been developed for the epitaxial growth of these materials. A strong impetus to the development of device structures based on GaN was given by the implementation of AlGaN/GaN interface, leading to the fabrication of 2DEG FETs capable to operate at GHz frequencies with low noise and high gain parameters [1]. The development of GaN-based bipolar transistors is unfortunately limited by poor p-type doping, that is why Schottky and field effect devices became the most intensive developed electronic elements on this material [2].

An important and challenging property specific to III-group nitrides is their chemical stability. In this connection processing of the materials involved require usually high energy particles, e.g. reactive ion etching techniques instead of wet chemical treatment. This leads to the creation of surface defects which diminish the performance of the fabricated devices. An alternative technique, called Surface Charge Lithography, for meso- and nanostructuring of GaN was developed by our group over the last years [3-5]. This is a maskless technique that offers the possibility to fabricate GaN-based structures with dimensions less than 100 nm by direct 'writing' in a controlled fashion by the focused ion beam with subsequent photoelectrochemical etching of the sample. The role of ion beam treatment is to induce surface negative charge that shields the material against photoelectrochemical etching. The potential application of the fabricated structures by this method is demonstrated for FETs and gas sensors.

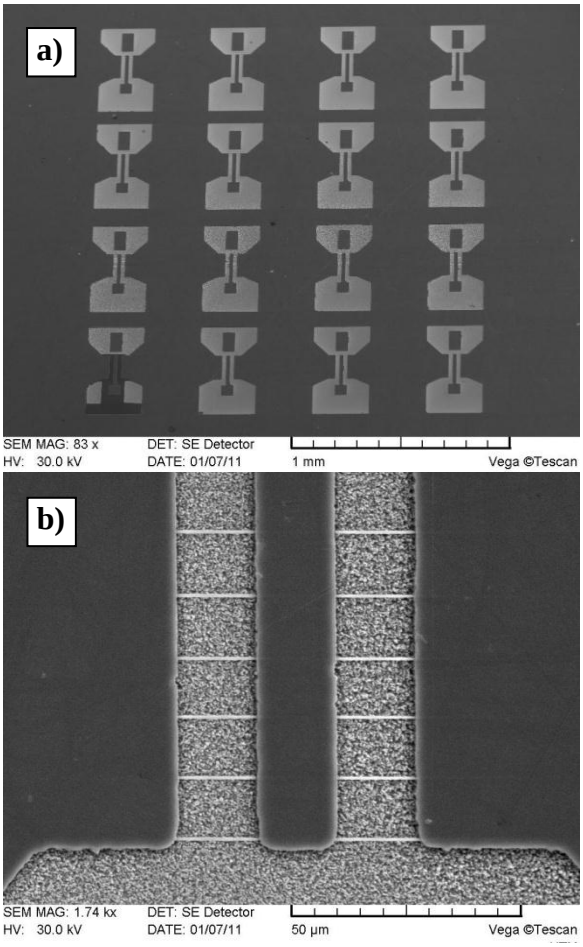

Fig.1 The general view of FETs (a) and GaN nanowalls connecting source and drain (b).

II. TECHNOLOGICAL PART

GaN epilayers used in our experiments were grown by MOCVD on c-plane sapphire substrates. The free carrier concentration was about 10^{17} cm^{-3} whereas the dislocations density was about 10^{9} cm^{-2}. Ohmic contacts were formed by evaporation of Ti/Au metals (50nm/150nm). Rapid thermal annealing necessary to improve the quality of ohmic contacts was excluded in order to avoid modifications of surface

properties. For the focused ion beam treatment the FEI Strata FIB 201 was used at the energy of 30 keV and dose of $6.6*10^{12}$ cm^{-2} of Ga ions. The photoelectrochemical etching was performed in 0.1 M of KOH solution under focused UV illumination provided by a 350 W Hg lamp. Figure 1 presents the design of the future transistors after mesa-structuring with surface charge lithography method.

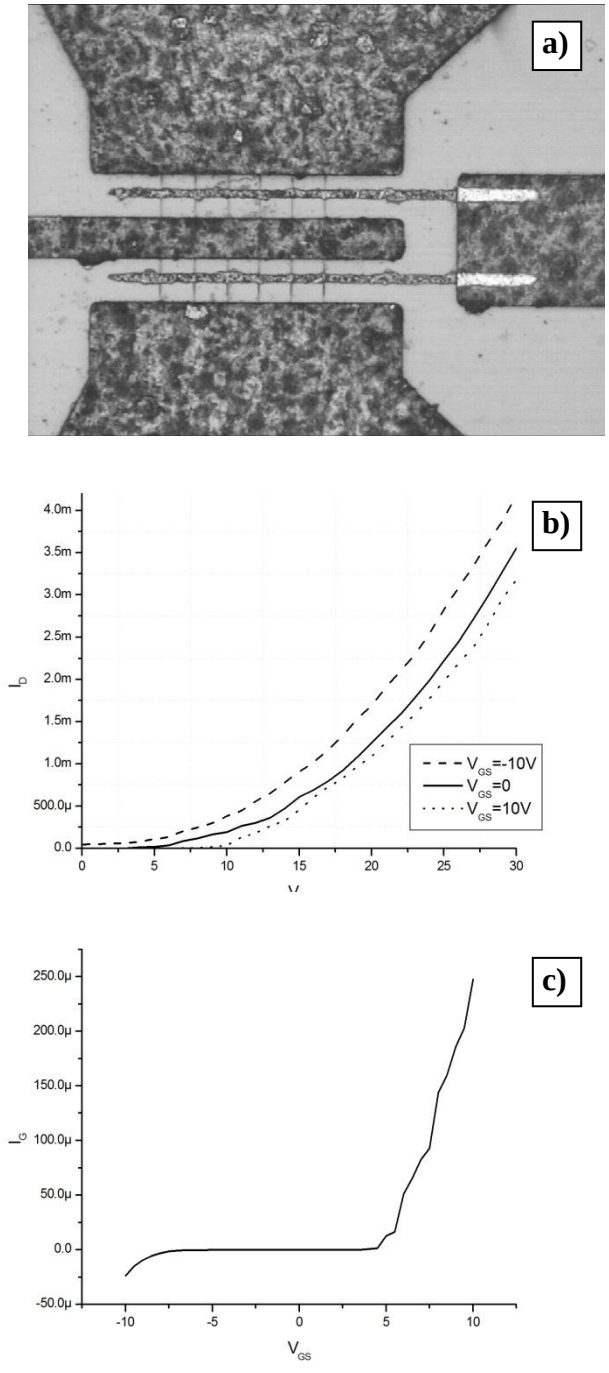

Fig.2. Ni gate on top of GaN nanowalls (a), drain current variation by gate potential (b) and gate-source I-V characteristics (c).

In order to achieve modulation of the drain-source current, we deposited Ni gate using RF-magnetron sputtering with the thickness of 500 nm after rapid thermal annealing (RTA) process at 800°C during 30 sec in nitrogen atmosphere. Thick layers are necessary in order to exclude discontinuity of the gates after lift-off process. An optical image of the final structure is presented in Figure 2a, whereas its I-V characteristics are presented in Figures 2b and 2c.

It is important to note that the gate-source characterization shows high leakage related to the highly defective gallium nitride nucleation layer which is also resistant to photoelectrochemical etching. This problem was partially solved using RIE process during 2 minutes in Ar atmosphere resulting in gate-source current decrease by almost 2 times.

As one can see from I-V characteristics illustrated in Figure 2b, there is a high leakage between Ni gate and source-drain channel related to poor Schottky contact quality resulting from the high density of surface defects caused by FIB treatment. Also the weak modulation of drain current by gate-source potential is the result of highly shunting effect of the thick channel in comparison with thin modulated space charge region.

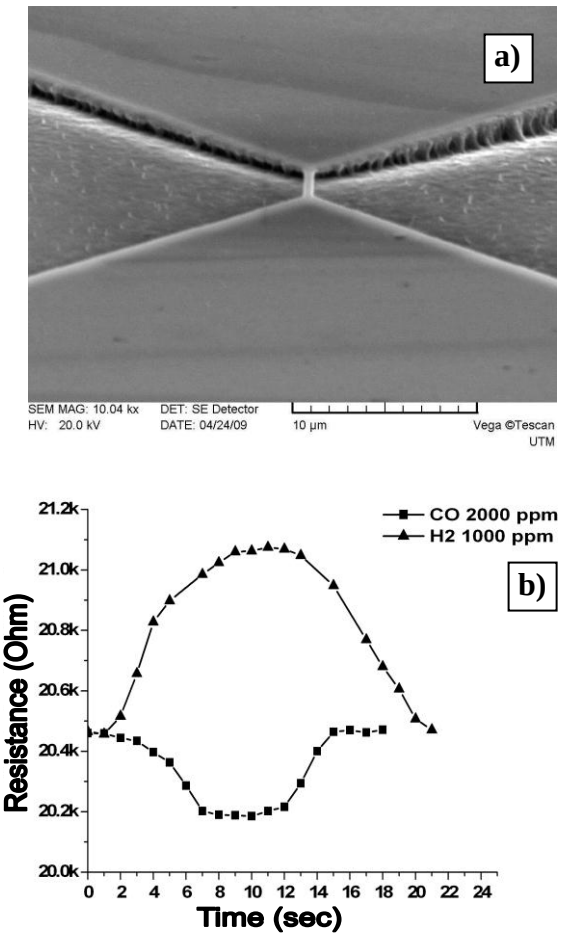

Fig.3. SEM image of the fabricated GaN-based nanowall (a) and its gas response characteristics (b)

GaN material has the potential for applications in gas sensors, especially in harsh environments where other materials exhibit fast degradation. The SCL technique was used for the fabrication of individual nanowires of GaN for the gas sensor applications. The design of the GaN nanowire-based gas sensors is presented in Figure 3, along with the gas response characteristics towards H_2 and CO gases at the temperature of 280°C.

From the characteristics involved we found a linear dependence between the sensitivity and operation

temperature for both investigated gaseous species. In addition, there are different threshold temperatures: 215°C in case of 1000 ppm H_2 and 110°C for 2000 ppm of CO. The transient characteristics are promising, in particular they reveal 5 sec response and recovery times for the case of CO, and 10 seconds response time and 15 sec recovery time for H_2. The possible gas response mechanism is discussed in one of our previous paper [4].

In order to improve the sensitivity parameter of our sensors we made use of cathalythic properties of Pt nano-dots deposited by the DC-plasma sputtering method. The effect can be easily seen from the dependences presented in Figure 4 where the sensitivity towards H_2 increased 6 times after 20 sec deposition and 3 times for the case of CO.

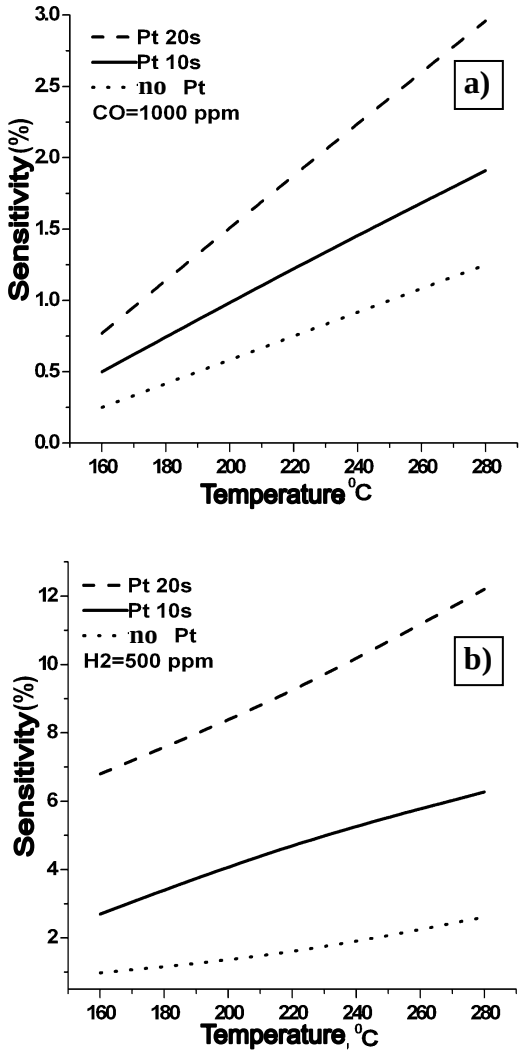

Fig.4. Improvement of sensitivity parameter towards CO (a) and H_2 (b) after Pt sputtering.

III. . CONCLUSION

We demonstrated the possibility of the Surface Charge Lithography for the fabrication of electronic devices based on GaN nanowalls and nanowires. There are still open questions regarding buffer layer shortcutting effect and quality of interface between metal contacts and FIB treated GaN surface.

ACKNOWLEDGMENTS

This work was supported by the Academy of Sciences of Moldova under the State Programme on Nanotechnologies and Nanomaterials. VP would like to thank the Alexander von Humboldt Foundation for the financial support. AS would like to thank Great Western Research for funding.

REFERENCES

[1] S. Strite, "GaN, AlN and InN: A Review" J. Vac. Sci. Technol. B 10, pp.1237 (1992).

[2] X.J.Wang, "Electrical characteristics of high performance Au/n-GaN Schottky diodes" Journal of Electronic Materials V. 27, Number 11, pp.1272-1276 (1998).

[3] I. M. Tiginyanu, V. Popa, and O. Volciuc, "Surface-charge lithography for GaN microstructuring based on photoelectrochemical etching techniques" Applied Physics Letters, Vol. 86, pp. 174102 (2005).

[4] Veaceslav Popa, Ion Tiginyanu, Olesea Volciuc, Andrei Sarua, Peter Heard, Martin Kuball, "Fabrication of GaN nanowalls and nanowires using surface charge lithography" Materials Letters, V. 62, Issue 30, pp. 4576-4578 (2008).

[5] I. M. Tiginyanu, V. Popa, and M. A. Stevens-Kalceff, "Membrane-assisted revelation of the spatial nanoarchitecture of dislocation networks", Materials Letters, Vol. 65, pp. 360-362 (2011).

Development of Conductive Nanotemplates on ZnSe

Eduard MONAICO[1], Ion TIGINYANU[1,2], Gleb COLIBABA[3], D. D. NEDEOGLO[3], Ala COJOCARU[4], Helmut FÖLL[4]

[1] *National Center for Materials Study and Testing, Technical University of Moldova, m_eduard_y@yahoo.com*

[2] *Laboratory of Nanotechnology, Institute of Electronic Engineering and Nanotechnology, Academy of Sciences of Moldova, Chisinau 2028, Moldova tiginyanu@yahoo.com*

[3] *State University of Moldova, Chisinau 2009, Moldova GKolibaba@yandex.ru, nedeoglo@usm.md*

[4] *Chair for General Materials Science and Microwave Laboratory, Christian-Albrechts-University of Kiel, Kaiserstr. 2, Kiel 24143, Germany alasprin@yahoo.com, kb@tf.uni-kiel.de*

***Abstract* – We demonstrate the possibility to fabricate arrays of pores oriented perpendicular and parallel to the top surface of the ZnSe nanotemplate. The control of material conductivity allows one to produce porous ZnSe samples with the mean pore diameter and characteristic skeleton wall thickness from several hundreds of nanometers to about 15 nm. In addition, electrochemical treatment of ZnSe single crystals using photoresist masks allows one to prepare buried porous structures with pores directed parallel to the top template surface, which is especially important for photonic applications.**

***Index Terms* – electrochemical etching, porous ZnSe, in-plane approaches, wide-band-gap semiconductor nanotemplates, morphology characterization.**

I. INTRODUCTION

Nanotemplates are widely used in nanofabrication, particularly in the production of large assembles of nanowires and nanotubes of various materials with defined diameters and lengths. For many concrete applications it is necessary to integrate a large amount of nanowires in one bundle or array to achieve required functionalities. Over the last decade, different template-based nanofabrication approaches have been developed which offer the possibility to produce large assembles of nanowires and nanotubes of various materials with defined diameters and lengths. Two types of templates are widely used for nanofabrication purposes, namely porous Al_2O_3 [1-4] and etched ion track membranes based either on inorganic materials or on organic polymers [5,6]. Both, porous Al_2O_3 and etched ion track membranes, however, exhibit high resistivity and therefore they often play a passive role in nanofabrication processes. In particular, templated growth of nanowires via electroplating is provided usually by the metal contact deposited on the back side of the high-resistivity membranes, while electroplating of metal nanotubes requires additional technological steps e.g. chemical modification of the inner surface of the pores prior to electrodeposition which leads to the incorporation of spurious phases in the nanotube walls. In this connection an important technological task is the development of cost-effective semiconductor nanotemplates which properties could be easily controlled by external illumination, applied electric fields etc. We have proposed a cost-effective technology for controlled fabrication of semiconductor nanotemplates with self-organized quasi-ordered distribution of nanochannels using anodic etching of III-V (GaAs, InP) and II-VI (CdSe) crystalline substrates in a neutral electrolyte [7-9]. Besides, the feasibility of indium phosphide nanotemplates for electrochemical deposition of arrays of platinum nanotubes with diameters both larger and smaller than 100 nm was demonstrated [7].

The electronic band gaps of InP, GaAs and CdSe are 1.3; 1.4 and 1.7 eV at 300 K respectively, which means that the nanotemplates based on these materials are opaque in the visible region of the spectrum. Among III–V and II–VI semiconductors one may consider the wide band gap compounds GaN (Eg = 3.3 eV), ZnO (3.3 eV) and ZnSe (2.7 eV) as good candidates for the fabrication of conductive nanotemplates transparent in the visible region. We were forced to exclude the first two materials from consideration since GaN crystalline substrates are not yet commercially available, while ZnO, according to our preliminary studies, seems to be inappropriate for electrochemical pore growth. It is difficult to obtain wide bandgap semiconductors, like ZnSe, with high electrical conductivity due to self-compensation phenomena inherent to these materials [10].

In connection with this, over the last years special efforts have been undertaken at the State University of Moldova which resulted in the development of an approach of co-doping ZnSe by Al and Zn impurities for the purpose of controlling the material electrical conductivity necessary for the application of the technology of electrochemical porosification [11].

II. PREPARATION OF ZNSE NANOTEMPLATES

We used 1 mm thick n-ZnSe substrates with free electron concentrations from 7×10^{16} cm^{-3} to 2×10^{18} cm^{-3}. A method based on doping the samples with Al from a Zn+Al melt was used for controlling the conductivity of ZnSe

crystals [11]. This doping procedure allows one to produce suitable conductive samples for controlled nanostructuring using electrochemical etching techniques.

Anodic etching of ZnSe was carried out in dark at room temperature in $K_2Cr_2O_7$:H_2SO_4:H_2O electrolyte with the ratio 5:100:10. Anodization was performed in potentiostatic regime in an electrochemical double cell as described elsewhere [12], the sample being mounted between the cells. The area of the sample exposed to the electrolyte was 0.25 cm^2. The electrolyte was pumped through both cells in a continuous mode. A four-electrode configuration was used [12]: a Pt reference electrode in the electrolyte, a Pt sense electrode on the sample, a Pt counter electrode, and a Pt working electrode. The electrodes were connected to a specially designed potentiostat. The applied voltage was varied from +5 V to +30 V for ZnSe samples, depending on the substrate conductivity. After growth of pores, the top nucleation layer of samples was removed by isotropic wet etching.

A TESCAN Scanning Electron Microscope (SEM) equipped with an Oxford Instruments INCA Energy Dispersive X-ray (EDX) system was used to study the morphology and chemical composition of the samples.

III. MORPHOLOGY CHARACTERIZATION OF ZNSE NANOTEMPLATES

The anodization of ZnSe substrates with electron concentration of 7 x 10^{16} cm^{-3} at the applied voltage of 25 V results in the formation of pores with the mean diameter of around 400 nm (Fig. 1a), while pores with the mean diameter of around 40 nm are produced in ZnSe substrates with the electron concentration of 2 x 10^{18} cm^{-3} anodized at 8 V (Fig. 1b). The width of the porous skeleton walls correlates with the diameter of pores, i.e. in all porous samples the width of the skeleton walls proves to be nearly equal to the pore diameter. Note, that the minimum pore diameter obtained by electrochemical etching of ZnSe until now is 40 nm [13]. According to our explorations, the higher is the electron concentration, the lower should be the applied voltage during anodization, and the smaller is the diameter of the pores produced. We succeeded to reduce de pore diameter down to 15 nm by anodization of ZnSe substrates with the electron concentration of 2 x 10^{18} cm^{-3} at 5 V, but the porous skeleton walls thickness in this case remain around 40 nm. This can be explained by overlapping in the pore wall of two regions representing depletion layers. Thus, to reduce the wall thickness is necessary to further increase the electron concentration in ZnSe substrates, which unfortunately cannot be easily realized. But, for some applications of nanotemplates it is not strictly necessary to have small pore wall thickness. Due to reduction of pore wall thickness the number of free electron concentration is also reduced. At the same time it is clear that for uniform electrochemical deposition of metal species on the inner surface of pores along the whole length, the semiconductor nanotemplates have to possess high skeleton conductivity.

We explained for the first time the dynamics of pore growth in n-ZnSe by analyzing the development of the pore morphology as a function of depth and demonstrated the possibility to use a porous ZnSe matrix for the purpose of electroplating arrays of metal nanotubes [14].

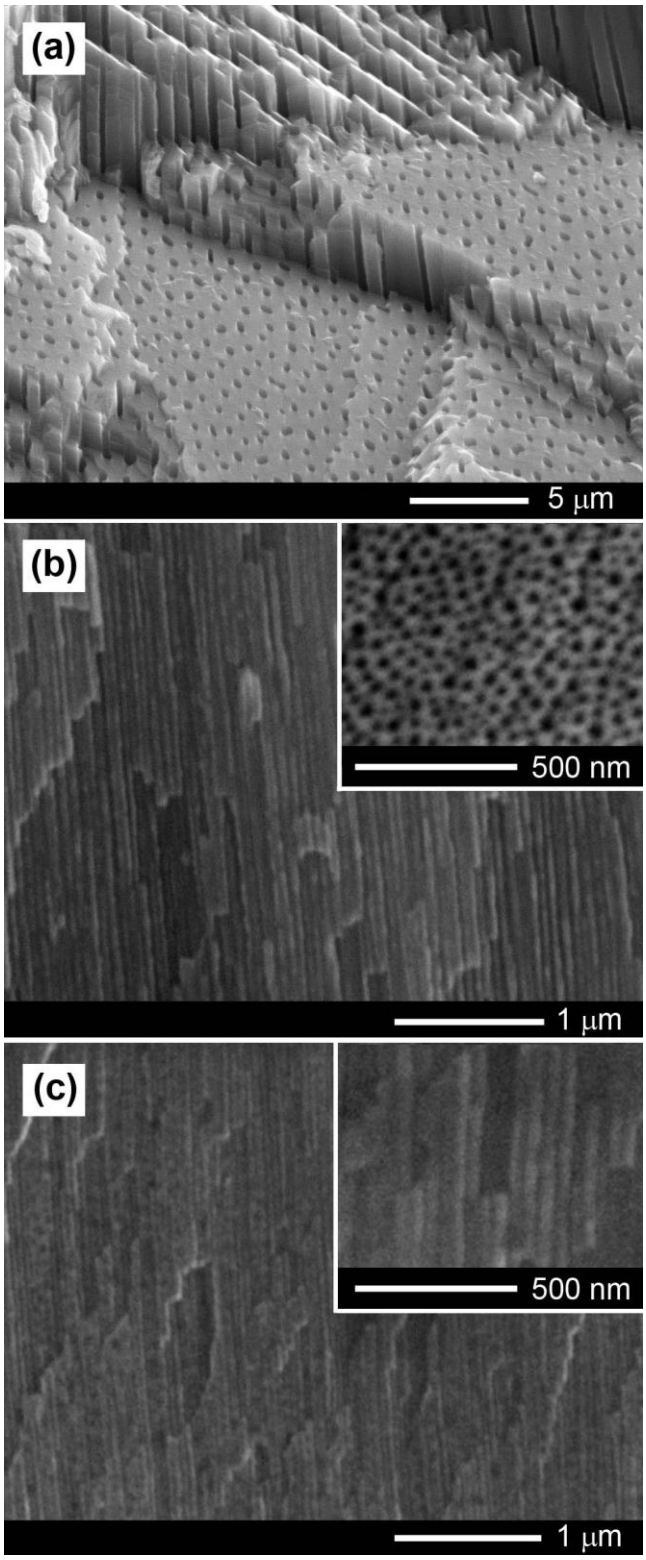

Fig. 1. SEM images taken from ZnSe nanotemplate prepared on crystalline substrates with free electron concentration of 8 x 10^{16} cm^{-3} (a) and 2 x 10^{18} cm^{-3} (b,c) by anodization in a $K_2Cr_2O_7$:H_2SO_4:H_2O electrolyte with the ratio of 5:100:10.

The possibility to control the diameter of pores just by changing the applied potential during anodic etching enables one to prepare multilayer porous structures in one technological process. Thus, successive anodization of ZnSe

substrates at varied applied voltage results in layer porosification at different length scales [14].

IV. IN-PLANE TECHNOLOGICAL APPROACHES OF ZNSE NANOTEMPLATE FABRICATION

Porous ZnSe structures with pores propagating in the direction parallel to the sample surface (Fig. 2a) are of especial interest for the fabrication of two-dimensional photonic crystals, including metallo-dielectric ones, since this geometry allows a wide implementation of structures which can be easily explored under different polarizations of the incident electromagnetic radiation.

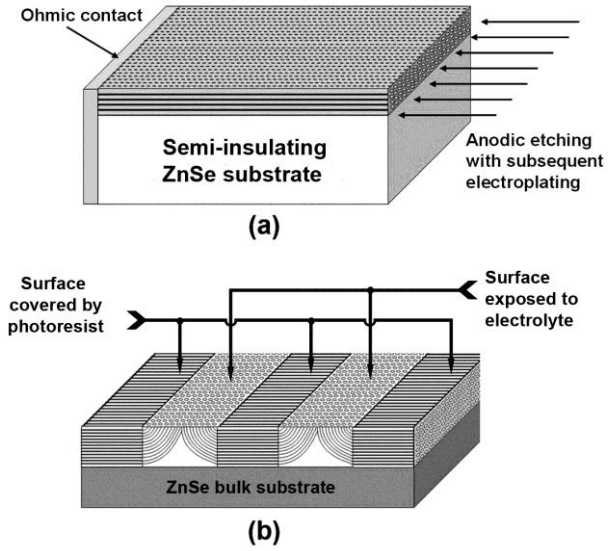

Fig. 2. (a) Schematic representation of the technology for the preparation of nanotemplates with pores propagating in the direction parallel to the sample surface (in-plane approach) and (b) after optimization of the etching conditions.

Nanowires and nanotubes are generally grown in the perpendicular direction to the substrate surface. Nanowires grown in-plane with the substrate surface are more suitable for conventional planar processing techniques. The first approach was initially demonstrated using GaAs [15], but in-plane growth from etched facets (such as sidewalls and V-grooves) on the substrate surface has been more widely used for Si [16-18]. On the Si (110) substrate, deep trenches with (111) side walls can be easily formed by anisotropic etching.

While the design shown in Fig. 2a is more suitable for in-plane porosification of epilayers, the approach shown in Fig. 2b proves to be efficient for in-plane pore growth in bulk substrates. In the latter case the ohmic contact is deposited onto the opposite surface of the sample, and electrochemical etching is performed through windows in the photoresist. The experiments demonstrated that the electrochemical etching starts at the interface between the open surface and the electrolyte. Consequently, due to the high conductivity of the sample, the pores propagate along the current lines in all directions, inclusively underneath the photoresist in a direction parallel to the sample surface, as illustrated in Fig. 3. Moreover, the photoresist can be easily dissolved in base solution.

An interesting feature of porous structures obtained by this method is the fabrication of buried porous layers, as illustrated in Fig. 3. The pores grow under a thin surface layer which remains intact during the electrochemical treatment. The thickness of this surface layer is of the order of the surface depletion region, i. e. from several tens to several hundreds of nanometers, depending on the conductivity of the anodized substrate. A three layer structure is shown in Fig. 8a for a ZnSe sample, where a resist layer is reminiscent on a part of the sample. A surface layer of the virgin ZnSe is seen under the resist layer, and the porous structure is buried under this surface layer.

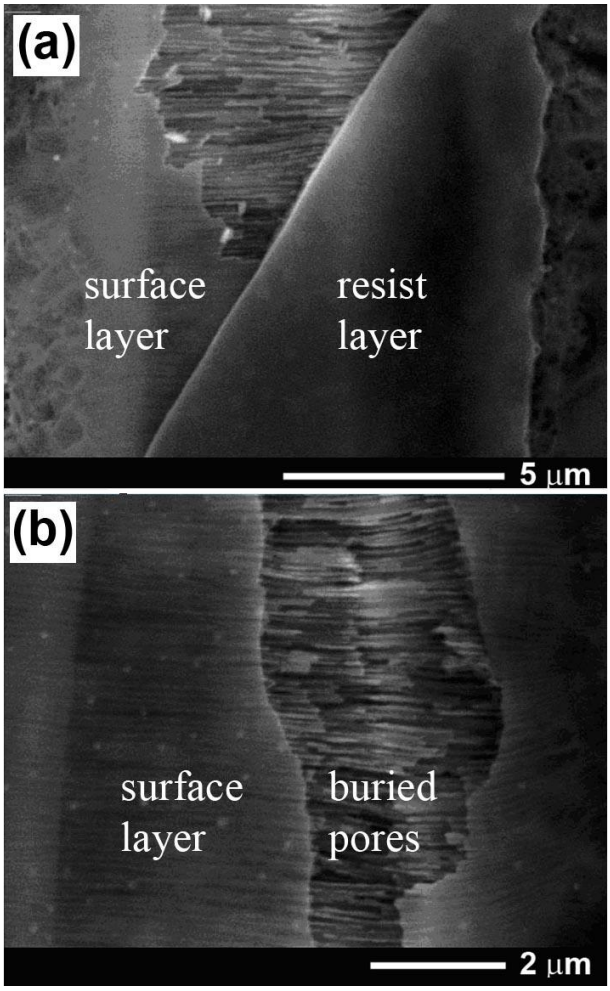

Fig. 3. Porous structures buried in ZnSe substrates.

The developed ZnSe nanotemplates with pores parallel to the crystal surface are suitable for the electrochemical deposition of metals inside pores, similar to the nanotemplates with pores perpendicular to the surface of the sample.

V. CONCLUSION

The results of this study demonstrate the possibility to fabricate porous ZnSe nanotemplates with uniform distribution of pores and geometrical parameters controlled by the conductivity of the substrate and the technological conditions applied by etching in a $K_2Cr_2O_7$:H_2SO_4:H_2O electrolyte. Electrochemical treatment in these electrolytes using photoresist masks allows one to prepare buried porous structures with pores directed parallel to the template top surface, which is especially important for photonic applications.

The high conductivity of the semiconductor nanotemplate skeleton provides conditions for uniform electrochemical deposition of metal species on the inner surface of pores. Moreover, the high value of the refractive index of ZnSe and its transparency in the visible region suggest that metallo–semiconductor structures are promising for the elaboration of negative refractive index metamaterials, in particular of novel focusing elements and beam splitters for applications in the visible region of the spectrum.

ACKNOWLEDGMENTS

This work was supported by the Supreme Council for Research and Technological Development of the Academy of Sciences of Moldova under grant no 11.819.05.12A and by Alexander von Humboldt Foundation.

REFERENCES

[1] M. V. Kamalakar and A. Raychaudhuri, A Novel Method of Synthesis of Dense Arrays of Aligned Single Crystalline Copper Nanotubes Using Electrodeposition in the Presence of a Rotating Electric Field. Advanced Materials, vol. 20, pp. 149–154, 2008.

[2] Y. Piao, H. Kim, Fabrication of nanostructured materials using porous alumina template and their applications for sensing and electrocatalysis. J. Nanosci. Nanotechnol., vol. 9, pp. 2215-2233, 2009.

[3] S. Gaurav, M. V. Pishko and G. A. Craig, Fabrication of metallic nanowire arrays by electrodeposition into nanoporous alumina membranes: effect of barrier layer. Journal of Materials Science, vol. 42, pp. 4738-4744, 2007.

[4] A. Ghahremaninezhad and A. Dolati, A study on electrochemical growth behavior of the Co–Ni alloy nanowires in anodic aluminum oxide template. Journal of Alloys and Compounds, vol. 480, pp. 275-278, 2009.

[5] T.W. Cornelius, B. Schiedt, D. Severin, G. Pépy, M. Toulemonde, P.Y. Apel, P. Boesecke and C. Trautmann. Nanopore4s in track-etched polymer membranes characterized by small-angle x-ray scattering. Nanotechnology, vol. 21, 155702, 2010.

[6] J. Duan, J. Liu, D. Mo, H. Yao, K. Maaz, Y. Chen, Y. Sun et al., Controlled crystallinity and crystallographic orientation of Cu nanowires fabricated in ion-track templates. Nanotechnology, vol. 21, 365605, 2010.

[7] Ion Tiginyanu, Elena Monaico, Eduard Monaico, Ordered arrays of metal nanotubes in semiconductor envelope. Electrochem. Commun., vol. 10, pp. 731–734, 2008.

[8] I.M. Tiginyanu, V.V. Ursaki, E. Monaico, E. Foca, H. Föll, Pore Etching in III-V and II-VI Semiconductor Compounds in Neutral Electrolyte. Electrochemical and Solid-State Letters, vol. 10, D127, 2007.

[9] I.M. Tiginyanu, E. Monaico, S. Albu and V.V. Ursaki, Environmentally friendly approach for nonlithographyc nanostructuring of materials. Physica Status Solidi (RRL), vol. 1, pp. 98-100, 2007.

[10] Y. Marfaing, Self-Compensation in II-VI Compounds. Prog. Cryst. Growth Charact., vol. 4, pp. 317-343, 1981.

[11] G. N. Ivanova, D. D. Nedeoglo, N. D. Negeoglo, V. P. Sirkeli, I. M. Tiginyanu and V. V. Ursaki, Interaction of intrinsic defects with impurities in Al doped ZnSe single crystals. J. Appl. Phys., vol. 101, 063543, 2007.

[12] S. Langa, J. Carstensen, M. Christophersen, H. Foll and I. M. Tiginyanu, Observation of crossing pores in anodically-etched n-GaAs. J Appl. Phys. Lett., vol. 78 pp. 1074–1076, 2001.

[13] E. Monaico, I. M. Tiginyanu, V.V. Ursaki, A. Sarua, M. Kuball, D.D. Nedeoglo and V.P. Sirkeli, Photoluminescence and vibrational properties of nanostructured ZnSe templates. Semicond. Sci. Technol., vol. 22, pp. 1115–1121, 2007.

[14] E. Monaico, P. Tighineanu, S. Langa, H. L. Hartnagel and I. M. Tiginyanu ZnSe-based conductive nanotemplates for nanofabrication. Phys. Stat. Sol. (RRL), vol. 3, pp. 97-99, 2009.

[15] K. Haraguchi, K. Hiruma, K. Hosomi, M. Shirai and T. Katsuyama, Growth mechanism of planar-type GaAs nanowhiskers. J. Vac. Sci. Technol. B, vol. 15, pp. 1685-1687, 1997.

[16] R. He, D. Gao, R. Fan, A. I. Hochbaum, C. Carraro, R. Maboudian and P. Yang, Si nanowires bridges in microtrenches: integration of growth into device fabrication. Adv. Mater., vol. 17, pp. 2098-2102, 2005.

[17] M. S. Islam, S. Sharma, T. I. Kamins and R. S. Williams, A novel interconnection technique for manufacturing nanowires devices. Appl. Phys. A, vol. 80, pp. 1133-1140, 2005.

[18] M. S. Islam, S. Sharma, T. I. Kamins and R. S. Williams, Ultrahigh-density silicon nanobridges formed between two vertical silicon surfaces. Nanotechnology, vol. 15, L5-L8, 2004.

Perspectives of Single Cast Nanowires Technology

Anatolii IOISHER[1], Efim BADINTER[1], Nicolae LEPORDA[2] ,
Vitalie POSTOLACHE[1], Eduard MONAICO[3], Ion TIGHINYANU[2]
[1] *Institite "ELIRI"(Chisinau), ioisher@eliri.md, bad@eliri.md,*
[2] *Institute of Electronic Engineering and Nanotechnologies, Academy of Sciences of Moldova*
nicul@lises.asm.md, tiginyanu@asm.md
[3] *National Center for Materials Study and Testing, Technical University of Moldova,*
m_eduard_y@yahoo.com

***Abstract* – The paper is dedicated to production potential of glass-coated cast nanowire with metal-, semimetal- and semiconductor-based cores by means of Taylor-Ulitovsky method. Criteria of melted core-formative material penetration into a drawing capillary were analyzed. Theoretical preconditions of the reduction of cast microwire diameter up to nano-dimensions of core are reviewed and an improved method of cast nanowire manufacturing is proposed. Correctness of conclusions was experimentally proved and laboratory samples of micro- and nano-wires with core diameter of about 200-300 nanometers were produced, even in case of materials with poor adhesion.**

***Index Terms* – nanowire, cast microwire, glass insulation, electromagnetic field.**

I. INTRODUCTION

Rapid development of nanotechnology, including various aspects of application, has led to an increased interest in production of glass-coated micro- and nanowires with core diameter less than 300 nanometers [1]. Such micro- and nanowires can find application in the field of medicine and biology, e.g. for the development of miniature sensors and probes, including thermoelectric ones, ecological small power engineering and electronics for binding nano- and micro-objects and other branches of science and engineering.

The process of cast micro- and nanowire production is known to include the following:

- melting of a definite amount of conductive material (metal, semimetal, semiconductor) placed into a glass tube in a suspended state at electromagnetic (EM) field of a high-frequency inductor;
- heating and softening of the glass pipe end owing to thermal contact with a molten drop of conductive material and forming a microbath in the form of softened glass which is flowing round this levitating drop;
- pulling down of the lower end of that coating (for instance by means of coiling onto a spool) into a capillary, which is later on filled in with the said conductive material from the microbath that is a core-formative material;
- cooling of the pulled down filament, which after crystallization of core and glass forms the said glass-coated cast micro- or nanowire.

Attempts of production of super-thin glass-coated cast microwires (by means of Taylor-Ulitovsky method [2]) with core diameter less than 1 micron have been undertaken since early 70 of the past century, when nano-technology was not so advanced [3]. Such microwires, especially semimetal- and semiconductor-based ones, were of interest from the view of solid-state physics, as a sample of quasi-one-dimensional crystalline object. Quantum dimensional effects have been investigated on the basis of microwires with small core diameter and a number of interesting results have been obtained [4, 5]. However, such microwires have not found practical application. Some components and devices made on the basis of super-thin metal- and metal alloy-based microwires confined themselves to laboratory samples such as, for instance, radiation electrometer involving conductive and mechanical properties of such microwires.

Due to the abrupt reduction of production and application of cast microwires in nineties, investigations on manufacturing methods of such microwires have been stopped. Though nowadays there is a revival of interest in some types of such microwires, especially magnetic ones [6], casting technology still remain insufficiently investigated. Potential of further reduction of microwire diameter and estimation of prospects of cast nanowire production are reviewed in the present report.

II. RESULTS AND DISCUSIONS

Theoretical and experimental studies of glass-coated cast microwire production have demonstrated that core diameter as well as overall diameter significantly depend on such physical parameters of applied materials, as dynamic viscosity η and surface tension σ_g of glass within the temperature range investigated, interfacial tension on glass-coreformative material border σ_{mg} within the area of microwire formation, density of materials used for microwire casting, as well as on rate of microwire drawing v_s and some other technological parameters. Many of the abovementioned parameters depend on temperature T of casting process and in a complicated way on main technological parameters [2].

The mass of the drop of core-formative material M forming (along with covering softened glass-coating) the so-called micro-bath is of great importance too. This drop is at a suspended state because of ponderomotive forces of high-

frequency electromagnetic field (EF) of inductor and pressure difference Δp under and over the micro-bath (owing to glass-tube rarefaction). The weight of the drop M_k, suspended only by EF, is called critical one. If $M > M_k$, the microwire core diameter is to a greater extent defined by thermophysical parameters of glass and rate of microwire drawing [3, 7]. At that glass tube feeding rate v_g, geometry and rarefaction, density of core-formative material γm and configuration of intensity of electromagnetic field over and below inductor is of a great importance for microwire geometry formation.

Over the time of broad application and research of cast microwires with resistive core, diminution of the core diameter as much as possible has been considered mainly in order to increase microwire linear resistance. In the framework of Zotov's theoretical model [7], the dependence of microwire radius r (which is considered as a homogenous filament) on a number of physical parameters of glass and microwire drawing rate (in case of not so great rates) has been deduced:

$$r = D/2 = 0{,}9\eta^{2/3} / (\sigma_g^{2/3} \cdot v_{dr}^{1/3} \gamma_g), \quad (1)$$

where γ_g – glass density. Here D should be considered as an overall microwire diameter, though the authors regard it as the core diameter.

If the weight of drop of melted core-formative material in the micro-bath is less than the critical value, then the authors of the present work define semiempirical dependence of core diameter d on a number of technological parameters, which have a direct impact on the geometry of forming micro- and nanowires and which may be regarded as governing parameters of casting process [8]:

$$d = k_T \eta_g^{4/3} / (\gamma_g \sigma_g^{1/3} v_{dr}^{2/3}), \quad (2)$$

where v_{dr} is capillary drawing rate; k_T – nondimensional empirical coefficient dependent on a number of additional technological parameters (in case of our experiments $k_T \sim 1 \cdot 10^{-6}$, all the values of physical parameters are expressed in SI units). The empirical formula (2) is close to theoretical formula (1) in terms of structure, though its distinguishing feature is stronger power dependence of diameter on glass viscosity.

As evident from both mentioned formulas, the lesser glass viscosity and greater casting rate the lesser microwire diameter becomes without limitations. Having ensured a great rate of microwire coiling onto a spool and decreasing glass viscosity, for instance by means of increase of operating temperature of the micro-bath, cast nanowires with core diameter less than 100 nanometers might be produced. As long ago as in eighties of the past century the authors of the present report have managed to produce microwires with ultra-thin bismuth-based core with core diameter within the range from 80 up to 300 nanometers by means of the said method. But at that time the overall diameter of the produced microwire was over 30 - 40 microns. Its casting method was unstable, the core diameter fluctuating within a broad range (up to 300 %), and such a super-thin microwire was able to be made of two core-formative materials with perfect adhesion to glass only. Having selected samples with required diameter, such microwires (with core made of Bi and Bi-based alloys with ***Sb, Pb*** and ***Sn***) were used for research of their physical properties (as quasi-one-dimensional objects) [4, 5].

It must be however emphasized that the mentioned formulas (1) and (2) are correct only for a definite range of casting rate and some other technological parameters, such as glass tube feeding rate, its overall dimensions, microbath temperature range and others. Thus, in the case of increase of rate v_{dr} , starting from 1,5 m/s, at other fixed parameters, some increase of core diameter with further stabilization at higher rates has been observed instead of decrease of the said parameter. (Especially when weight of drop is over the critical value). This is indicative of the need in further investigation of Taylor-Ulitovsky process in order to define potential and requirements of production of long single cast microwires on the basis of various materials.

Currently there is no comprehensive theory unambiguously describing interconnection and interdependency of different technological and physical parameters affecting the process of microwire casting and final properties of microwire (and, perhaps, there will be no ever owing to its extremely complexity of the process). Accordingly, there is an unsolved problem regarding ultimate potential of this manufacturing method and minimal achievable core diameter. Thus, it would be expedient to divide description of microwire casting process by means of Ulitovsky method into separate partial problems which can be solved easier regarding tasks put by later on.

In order realize this let us formulate two main sub-tasks:

1) determination of the criteria of initial penetration of melted core-formative material into forming capillary and extreme allowable diameters of such a capillary;

2) revealing of input values physicotechnological parameters of casting process ensuring combined drawing of glass capillary with minimal diameter and melted core-formative material filling in this capillary with further crystallization.

When melted core-formative material (let call it metal) penetrates into capillary the main role is played by the following: 1) capillary effect due to the surface tension of metal; 2) inter-phase tension on a border glass-metal; 3) pressure over a melted metal inside of a glass-tube of a micro-bath; 4) dimensions of drop of melted metal (to be more exact, height of drop of melted metal in a micro-bath H_m over the point of penetration point into a capillary), forces which carry metal, induced by downward movement of walls of primary stretching cone and metal adhesion to glass. It is worth to be pointed out that in the upper part of the primary stretching cone the speed of wall movement is slow enough and it does not exceed $(2\ldots5) \cdot v_g$, where v_g – the rate of glass tube feeding into inductor area. Correspondingly, carrying force F is also weak; it rises in its bottom part and in the beginning of the secondary stretching cone.

It is especially worth to emphasize that the internal diameter of forming capillary $d = 2r$ is mostly defined by variable radius $r_c(x)$ of primary stretching cone, giving onion-like shape to drop of metal and microbath in a whole (x – is vertical axe). In the report of Yu. Chugaevsky [9] it was obtained the theoretical relation describing the shape of

the mentioned primary cone:

$$r_c^2 = R_0^2 + \left[x - \frac{2H}{1 + 2\ln(r_c / \xi)} \ln(R_0 / r_c) \right]^2, \quad (3)$$

where R_0, H – radius and height of molten drop, ξ - radius of a conditional column of melt on which ponderomotive force of electromagnetic field does not operate,.

Derivation of the obtained formula assumes by default that the weight of the drop is completely counterbalanced by ponderomotive forces of electromagnetic field of inductor excluding a thin cylindrical "rod" with radius ξ along axis of the drop. The weight of this rod $P = \pi\gamma_m g H \xi^2$ generates vertical pressure along axis of area of capillary formation and it is along with pressure difference over the drop of melted metal both inside of capillary and under it $(p_0 - \Delta p)$ one of the component forces, promoting penetration of metal into the capillary. Here γ_m – density of core-formative material, g – acceleration of gravity, p_a – atmosphere pressure, Δp – rarefaction inside a glass tube over a microbath.

The said model does not take into account horizontal component of metal pressure on glass coating of a primary stretching cone, which significantly impacts on the diameter of the said cone and, in the end, on the diameter d of stretching capillary in comparison with expected one in accordance with calculation.

As is well known, the high-frequency field of inductor (both cup-like and multi-coil one) has a singularity along the vertical axis where expulsive force equals to zero. Correspondingly, in case of suspended melt of metal within the bottom part of incipient drop a special area is formed (a "black spot" in a way), where ponderomotive forces do not impact on that drop and the weight of this part of the drop can be counterbalanced by cohesion and surface tension of metal σ_m only, while during microwire casting it can be counterbalanced by surface tension of glass σ_g, as well. A definite impact on balance of forces influencing on metal inside of the microbath is contributed by the abovementioned pressure difference $(p_0 - \Delta p)$, if pressure inside of an empty capillary is close to vacuum gage pressure.

Experiments carried out during microwire casting show that in the case of metals with low capillary constant $a = 2\sigma_m / (g\,\gamma_m)$ (e.g., ***Pb*** and ***Bi***), the metal drop is likely to leak out of a microbath. This takes place, e.g. during Bi-based microwire casting at every slightest vertical oscillation or insufficient glass viscosity close to the bottom of a microbath. We suppose that it takes place when the diameter of a primary stretching cone in the bottom part is greater than some critical value, which exceeds 2ξ, i.e. dimensions of a "black spot" of expulsive forces of electromagnetic field of inductor. Usually, it lays within the range from 0.05 up to 0.2 mm.

As a first approximation balance of forces at entrance to a stretching cone impacting on penetration of metal into a capillary can be presented in the following way:

$$F_1 + F_2 + F_3 = F_4, \quad (4)$$

where forces promoting penetration of metal into a capillary are listed on the left, while forces preventing from that are listed on the right. Here:

$F_1 = (p_0 - \Delta p)\cdot\pi r^2$ – force, caused by pressure difference over and below drop of melted metal in a microbath;

$F_2 = \pi\,\gamma_m\, g\, H\, r^2$ – force of pressure of column of melted metal with height H on its surface at entrance to a capillary (this height depends on diameter and shape of drop of melted metal in a microbath);

F_3 – carrying force related to movement of walls of the primary stretching cone and adhesion of metal to glass. Taking into account that this force must ensure acceleration of column of melted metal from close to zero speed up to speed v_s of capillary pulling drawing, it is easy to show that

$$F_3 = (\pi/2)\gamma_m v_s^2 r^2;$$

$F_4 = 2\sigma_m r$ – forces of surface tension of metal on a border metal-vacuum inside of glass capillary.

With the help of the abovementioned formulas it can be shown that the radius of capillary a core-formative material can penetrate in is defined by the following equation:

$$r = 4\sigma_m / \{\pi [(p_0 - \Delta p) + \gamma_m g H + \gamma_m v_s^2]\}. \quad (5)$$

As it can be seen from (5) in case of reduction of surface tension of metal σ_m and increase of capillary drawing rate v_s reduction of diameter of microwire to be obtained $d = 2r$ can be achieved without any limitations, that does not contradict to equations (1) and (2). It is worth to emphasize that we discuss conditions of metal penetration into glass capillary, in case of poor degree of moistening and adhesion between them. Increase of casting rate of micro- and nanowires is limited by viscosity of glass η_g and metal η_m, and microwire diameter itself. In case of too poor viscosity of any of components, slippage of metal or glass layers on a border between them may takes place.

Fig.1 shows dependencies of minimal diameter $d=2r$ on a number of parameters of core-formative material and rate of capillary drawing v_s. Hands-on experience shows, that minimal diameters of obtained micro- and nanowires are easily achieved in case of metals with greater adhesive to glass, since in that case metal penetration into a capillary is facilitated as well as its acceleration up to required speed v_s, which can be even greater.

Thus, in order to produce cast nanowires with minimal cross-section, both core and coating thickness, proper selection of glass-metal couple is required, which ensure minimal inter-phase tension between glass and melted metal in a microbath.

Usually such a selection allows to achieve inter-phase tension (at temperature of casting) about 0.5…0.7 of surface tension σ_m of such a melted metal in vacuum. Quantitative assessment of typical casting process (and microbath dimensions) provides r about a couple of microns for many materials at casting rate up to 5 m/sec. E.g., in case of ***Bi***

estimated value of initial minimal microwire core diameter $d_i = 2r = 3.5$ μm.

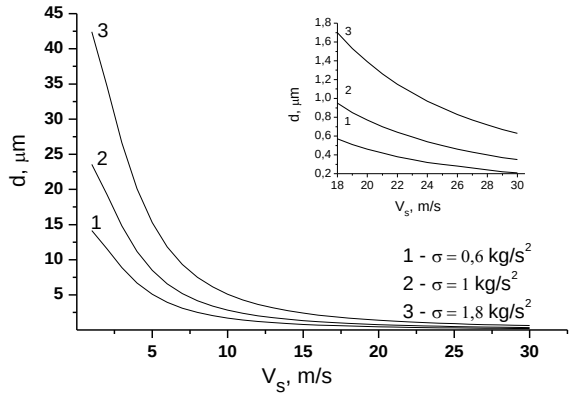

Fig 1. Dependence of minimum of core diameter on stretching speed for different surface tension values.

However, after the melt entered the capillary and during the continuation of the process of nanowire drawing, the condition of further joint flow of the glass capillary with the melt inside changes, and the reduction of the thread diameter becomes possible. If the melt mass in the microbath does not exceed the critical mass, the geometric parameters of the drawn micro- and nanowires depend mainly on properties of the glass tube (its geometry, viscosity, and surface tension) and main parameters of the technological process (speed of capillary drawing, strength of an electromagnetic field of the inductor, micro-bath temperature, and speed of the tube feeding). In that case, in accordance with formula (2), reduction of core diameter of micro- and nanowire is possible, e.g. at increase of speed and tempearture of microbath. It is worth to mention that such a reduction starts from some initial diameter of stretching cone, a core-formative material has already penetrated in.

Therefore, the geometry of the primary and secondary stretching cones has priority for nanowire formation. According to the formula (5) increasing the height of melt drops in microbath (usually H is comparable to the drop diameter $2R_0$) capillary diameter, suitable for entry the metal into it must also decrease. But in case if magnitude of γmgH is much less that $\gamma m v_s^2$ its impact is small in this process. The value of H is critical to the shape of the drop and the diameter of the secondary stretching cone, which in turn determine the diameter of the drawn out glass capillary and the microwire thread after entering of metal in the capillary.

The calculations executed in [9] according to formula (3) have been carried out at a relation of parameters, specific for typical casting process of a resistive microwire. For example, it was assumed that the length of the primary stretching cone L is comparable with the dimensions of metal drop ($L \sim H$). The new calculations made for the conditions of small values of $L < 2H$, showed that in this case the radius of the stretching cone significantly decrease (see fig.2) which should ensure ceteris paribus decrease in diameter of microwire thread cast to nanometric dimensions.

To reduce the length of L, it is proposed to reduce the height of the melt drop. In this case, the pressures of the melt on the critical zone of inflection glass surface microbath also sharply decrease (fig. 3).

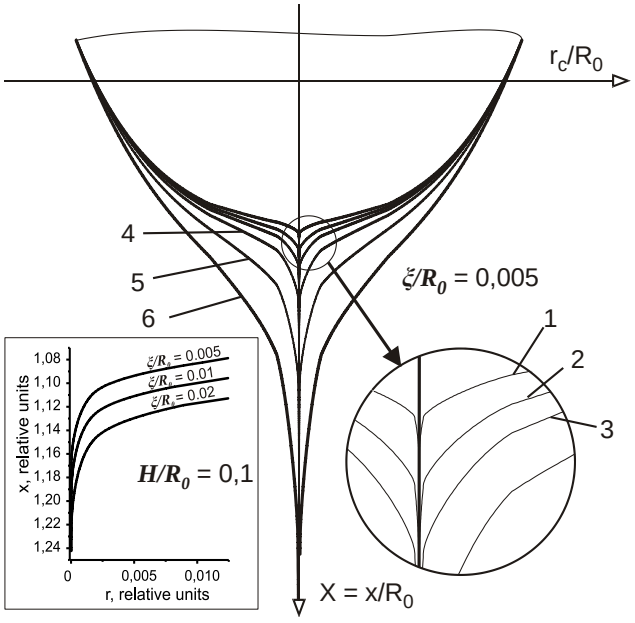

Fig 2. Influence parameters H and ξ on drop shape.

Values of H/R_0: 1 – 0,1; 2 – 0,2; 3 – 0,03; 4 – 0,5; 5 – 1; 6 – 2.

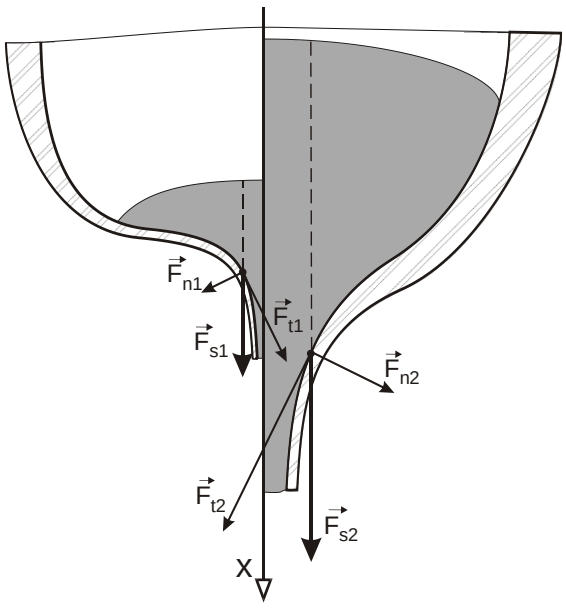

Fig.3. Influence of a melt pressure force on the shape of a primary stretching cone (for the small drop – on the left, for the big drop – on the right).

Correspondingly, the normal component of this force to the surface of the glass envelope of the primary stretching cone is reduced, the diameter throughout its length decreases. This provides a reduction of the inner diameter of the drawn out of the capillary and the received microwire thread.

The obtained conclusions were experimentally checked on the existing equipment for casting microwire with a core from pure (the anode) copper. To do this, after the formation of microbath, the metal drop was decreased by so-called

"Reset" 2/3 of its mass to achieve a more flat (i.e., flattened in the vertical direction) of the form microbath.

Then, the capillary extraction process is continued until filling it with metal. The obtained microwire had a diameter of about 200 ... 300 nm (fig. 4) at the drawing rate 4 m/s.

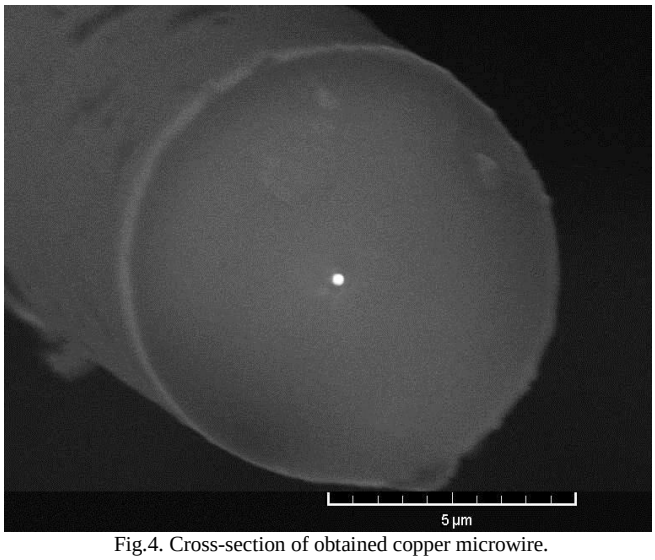

Fig.4. Cross-section of obtained copper microwire.

For further reducing these dimensions and obtaining of nanowires with diameters around 100 nm or less it is necessary to undertake further experiments with other high-frequency inductors: with the larger cone angle, larger diameter and a smaller lower opening.

This is required to form a shallow drop with a sufficiently large amount of metal (not less than 140 mm^3). It is necessary to use also glass pipes with smaller viscosity.

III. CONCLUSION

The carried out analysis and preliminary experiments demonstrated principal potential of production of cast nanowire with nano-core diameter up to 100 nanometers by means of Taylor-Ulitovsky manufacturing method. Improvement of the described technology in combination with selection of compatible materials can ensure further reduction in both core diameter and overall diameter of nanowire.

REFERENCES

[1] Nanotechnologies market: state and prospects. Under general edition ESNL-2008 UMNITS "Sokolinaia Gora". M.MIREA-IKAR, (2008), 100.

[2] E.Badinter, N.Berman, I.Drabenko and others. Cast microwire and its properties, Shtiintsa, Kishinev (1973).

[3] A.Ioisher, I.Nesterovsky. Microwire and devices of resistance, Ed. IX (1972), 25-33.

[4] N.B. Brandt, D.V. Gitsu, A.M. Ioisher, B.P. Kotrubenko, A.A. Nikolaeva. Prib. Tekn. Exp.,3, (1976), 2561.

[5] K..Yu. Arutunov, N.P.Danilova, A.A. Nikolaeva, J.Appl.Phys., p.2, v.76, No 10 (1994), 7139-7141.

[6] R.Zuberek, H.Szymezak, A.Zhukov, M. Vazques and others. J. Magn. Mater. (2007), Vol.316, 890-894.

[7] S.Zotov, K.Kabisov, I.Silkis. Microwire in instrument-making, Ed. IX "Cartea moldoveneasca", Kishinev (1974), 3-17.

[8] E.Badinter, T.Huber, A.Ioisher, A.Nikolaeva, I.Starush. Proceedings of SPIE - Volume 5401. Micro- and Nanoelectronics 2003, K.Valiev, A.Orlikovsky, Editors, May 2004, 257-268.

[9] Yu.Chugaevsky. Microwire and devices of resistance, v. III "Cartea moldoveneasca", Kishinev (1965), 16-26.

Smart Self-healing Eco-friendly Nano and Nano-composite Protective Coatings

Abdel Salam Hamdy MAKHLOUF
Center of Research Excellence in Corrosion, King Fahd University of Petroleum & Minerals
Dhahran 31261, Saudi Arabia
asalam85@yahoo.com

***Abstract* – This paper reports our achievements in designing high performance eco-friendly coatings technologies for light-weight materials through international collaborations with USA, Italy, France, Romania, UK and Germany**

Aluminum and its alloys are used widely in aerospace, automotive and packaging applications. The demand for weight savings for automotive and aerospace materials has focused attention on magnesium alloys.

Several automobile manufacturers (Ford, GM, Chrysler, Volkswagen, Opel, FIAT) have co-operated to develop new magnesium alloys for manufacturing less energy-consuming and hence, less polluted automobiles. Because of its growing use in the transportation industry, the world demand and production of magnesium have been growing steadily. Magnesium alloys have a variety of excellent properties. However, Mg alloys remain very susceptible to corrosion despite their superior mechanical properties.

Chromate has been reported as the most efficient widespread conversion coatings for many metallic substrates. However, the waste containing hexavalent chromate has many limitations due to the environmental consideration and health hazards.

The aim of this article is to deepen the current understanding of corrosion and protection of aluminum and magnesium and their alloys and to provide a base for future research work in this field. It will also report the recent development in designing eco-friendly conversion coatings based on cerate, stannate, zirconate, vanadate or molybdate conversion coatings as alternatives to the process involving toxic chromate.

***Index Terms* – Aerospace and automotive industry, chrome-free coatings, corrosion protection, surface treatments.**

Nanowires of Silicon Carbide and 3D SiC/C Nanocomposites With Inverse Opal Structure

G.A. EMELCHENKO, A.A. ZHOKHOV, V.M. MASALOV, E.A. KUDRENKO, A.N. TERESHENKO, E.A. STEINMAN, I.I. KHODOS[1], V.I. ZINENKO[1], Yu.A. AGAFONOV[1]

Institute of Solid State Physics, Russian Academy of Sciences 142432 Chernogolovka, Moscow District, Russia

[1]Institut of Microelectronics Technology and High Purity Materials,Russian Academy of Science, 142432, Chernogolovka, Moscow District, Russia

E-mail: emelch@issp.ac.ru

***Abstract* – Synthesis, morphology, structural and optical characteristics of SiC NWs and SiC/C nanocomposites with an inverse opal lattice have been investigated. The samples were prepared by carbothermal reduction of silica (SiC NWs) and by thermo-chemical treatment of opal matrices (SiC/C) filled with carbon compounds which was followed by silicon dioxide dissolution. It was shown that the nucleation of SiC NWs occurs at the surface of carbon fibers felt. It was observed three preferred growth direction of the NWs: [111], [110] and [112]. HRTEM studies revealed the mechanism of the wires growth direction change. SiC/C- HRTEM revealed in the structure of the composites, except for silicon carbide, graphite and amorphous carbon, spherical carbon particles containing concentric graphite shells (onion-like particles).**

I. INTRODUCTION

Studies on the synthesis of nanostructures with new functional properties expand the area of their potential use and, therefore, highly desirable. We have studied synthesis, morphology, structural and optical characteristics of SiC nanowires and SiC/C nanocomposites with an inverse opal lattice.

II. EXPERIMENTAL

Carbothermal reduction of silica is most useful method for the synthesis of SiC NWs. In this work we used both silica and colloidal carbon in carbothermal reduction method as a Si and C sources, respectively.

SiC/C composites in silicon dioxide were obtained using an opal matrix which was a three-dimensional close-packed system of monodisperse sphere-shaped (globules) silicon dioxide particles (240 - 280 nm in diameter). The samples were prepared by thermo-chemical treatment of opal matrices filled with carbon compounds which was followed by silicon dioxide dissolution [1]. The samples were studied by electron microscopy, x-ray diffraction, photoluminescence, IR and Raman scattering spectroscopy. The samples implantation has been carried out by He^+ ions with energy 40 keV and doses of 10^{13}-10^{15} ions/cm^2.

III. SIC NANOWIRES

Fig. 1(a) shows FESEM images of the synthesized product general view on the carbonic felt surface. From the image, the product consists of the wires with a

diameter of 20-200 nm and a length of tens to hundreds of micrometers. Figures 1(c-g) further reveals, that the nanowires have different types of the morphology. From the TEM images (d-g), all the wires have a well-pronounced striped structure, which indicates the presence of twins and stacking faults (SFs) in the wires. Mainly, the three types of the wires morphologies were assigned: «smooth» (fig.1e,f), «bamboo-like» (fig.1d, c) and "Y-types" (fig.1 g) wires. In turn, «smooth» wires have SFs, which placed either perpendicular (fig.1e) or at an angle to the growth axis of the SiC wires (fig.1f). In general case, the "smooth" wires growth in a hexagonal-prism shape as shown in fig. 1(b).

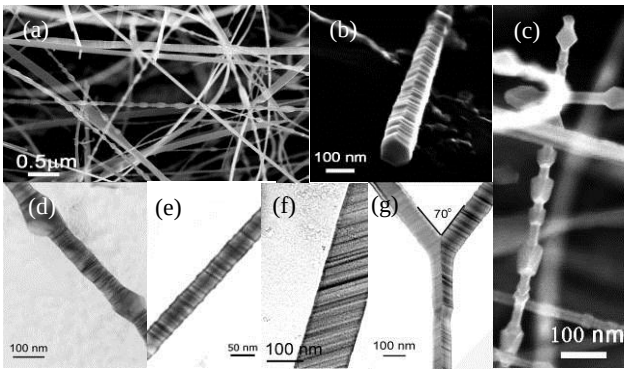

Fig. 1. (a)- FESEM image of the NWs general view; (b,c) – FESEM images of the single hexagonal prism-shaped wire and bamboo-like wire, respectively; (d-g) – TEM bright-field images of the NWs types.

Electron microscopy studies have shown that "smooth" wires could have different growth axes depending on the wire's diameter. The NWs with diameter size < 100 nm ("thin" wires) have high-density of SFs. The growth axis of the wire coincide with normal to the close-packed planes and so with [111] crystallographic direction of 3C – structure. The NWs with diameter size >100 nm ("thick" wires) can have either the [110] or the [112] growth axis.

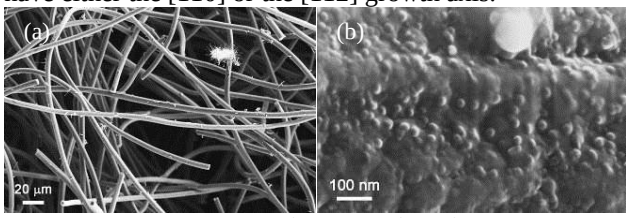

Fig. 2. (a) - FESEM image of the carbon felt before synthesis; (b) – magnified view of the carbon fiber surface.

The carbon substrate consists of carbon fibers with a diameter of 5 – 8 μm (fig.2 a). Figure 2b shows a magnified FESEM image of the fiber surface before the SiC wires synthesis. From the image, the fiber surface is

covered by a randomly distributed ball-shaped "hillocks"

with a size of 20 – 50 nm (however the hillocks with a size of 300 nm are observed at scanning of the fiber surface). The EDX analysis reveals a low concentration (~0.08 atomic %) of Si of the initial carbon fiber. The silicon is uniformly distributed over the fiber surface and Si content varies within the range 0.05 – 0.1 at. %. Taking

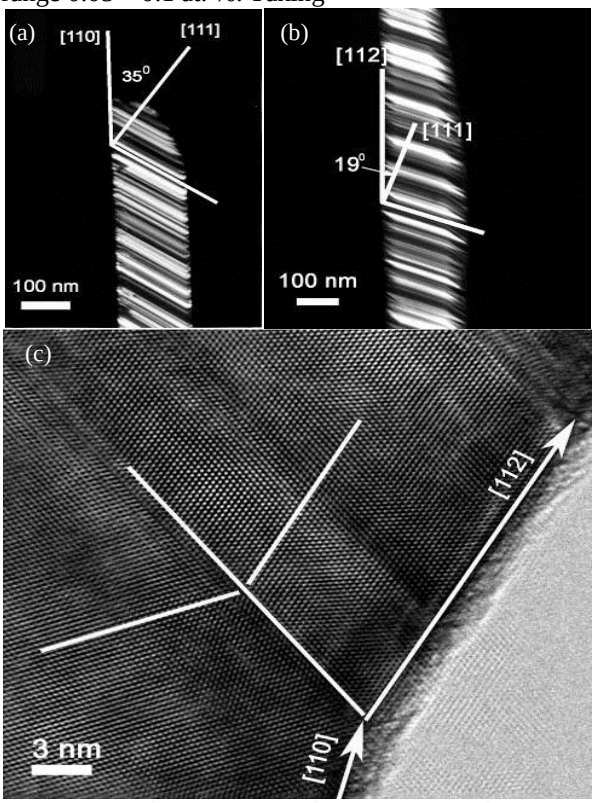

Fig.3. (a) –dark field TEM image of [110] orientation of the wire;

(b)-dark field TEM image of [112] orientation of the wire;

(c)-HREM image of the twin part showing change the growth direction depending on the direction of the lateral boundaries of twin domains.

into account un-uniform distribution of the SiC crystallites over carbon fibers we assume that some hillocks" can be places of silicon agglomerations and the templates for further SiC NWs nucleation.

Figure 3 (a, b) shows TEM dark-field images of the "thick smooth" wires. From figure 3a, the boundaries of SFs ({111} close-packed planes in cubic structures) are inclined at the angle of 55^0 (125^0) with respect to the wire growth axis and so the boundaries normal makes the angle 35^0 with the growth axis. This angle is close to the crystallographic angle between the [111] and the [110] directions of a cubic structure. Hence, the growth axis of the wire is the [110]. In the case of the wire (fig. 3b), the boundaries normal of the close-packed planes is inclined at the angle 19^0 with respect to the wire growth axis, which corresponds to the angle between the [111] and the [112] directions of a cubic structure. Therefore, the wire growth axis is [112].

Figure 3c shows HRTEM image of the region of the wire with [112] growth direction. From image, there is defect-free section with the twin 3C-structure in the wire. The bottom domain has the side boundary with the [110] direction, while the upper domain has the side boundary with the [112] direction (white lines show the traces of the {111} planes). Though the average growth axis of the wire is [112], because of such type domains are predominant in the wire.

Thus, the certain type of 3C-structure twin domains in the "thick smooth" wires generates the crystallographic orientations of the SiC close-packed planes and the wire's growth direction, respectively.

The SiC NWs with core (SiC) – shell (SiO_2) structure were reported in many works. The physical properties of such wires very differ from the "bare" ones. In this report, the core-shell wires were produced via annealing of the initial "bare" SiC wires at the temperature of 850^0C for 4 h in air.

IV. SIC/C NANOCOMPOSITES WITH INVERSE OPAL STRUCTURE

The electron microscopy data revealed a highly porous periodic structure which was a three-dimensional replica of the voids of the initial opal lattice (Fig. 4, 5).

High temperature treatment (1770 – 1870K) causes sintering of the composite with 15% shrinkage calculated by the change of the diameter of the silicon dioxide sphere. Etching-out of silicon dioxide results in formation of highly porous structure (figure 4), whose density is

estimated as 0.03 g/cm^3 (~1.3% of graphite density). The specific surface measured by the BET method was 275 -430 m^2/g in dependence of silica globule size. All the inside cuts demonstrate a three-dimensional replica of the voids of the initial opal lattice (figure 4, 5). The pictures show distinct void semispheres with oval-shaped holes pointing to the sites of the silicon dioxide sphere contact in the initial opal structure. Three holes in each semisphere can be seen in figure 4 and in figure 5 there are four holes which corresponds to the structure of the opal (111) and (100) faces. Beside such windows smaller random holes (defects) occur in the sphere shells (figure 2). The shell thickness estimated by SEM pictures varies from 4 nm до 10 nm.

The hexagonal silicon carbide was found to be non-uniformly distributed throughout the volume, its greater part located in the surface layer up to 50 micron deep. Correlation of the data of element and diffraction analysis yields the following data on the phase composition of the sample after etching in HF solution: The SiC content in the sub-surface layer is ~55% wt., inside the sample 1% wt., the carbon content on the sample surface was ~32% wt., in the bulk ~90% wt. ; the silicon dioxide content on the sample surface and in the bulk varies about 10% wt. There is a natural explanation of the large amount of silicon carbide in the surface layer compared to that in the bulk. The reaction of carbothermal reduction of SiO_2 with SiC formation requires removal of gaseous carbon oxide which is realized in subsurface layers and hindered in the sample bulk on closure of nanopores in the course of sintering.

As to the SiO_2 phase state, it is worth mentioning the absence of narrow diffraction peaks is indicative of the amorphous state of silicon dioxide in our samples.

The data of x-ray diffraction, IR and Raman scattering spectroscopy enabled us to assume that the composite had hexagonal diamond fragments. The assumption of the presence of the diamond phase in the composite based on the x-ray data was confirmed by RS and IR spectroscopy. The RS spectrum of the sample under study consists of two 1318 cm^{-1} (halfwidth 75 cm^{-1}) and 1258 cm^{-1} (halfwidth 40 cm^{-1})

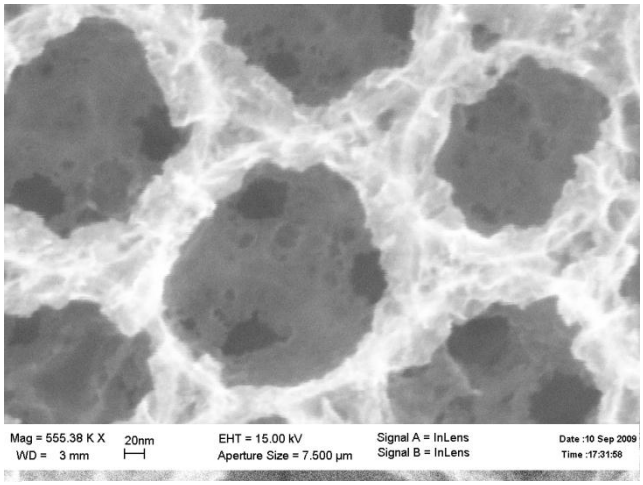

Fig. 4 (111) side cut of SiC/C inverse opal upon etching in HF solution

lines. The intensity of the second line is by an order of magnitude less than that of the first. The IR transmission spectrum of the composite shows a 2000 cm^{-1} band which is in the region of intrinsic absorption of the diamond crystal lattice. No such absorption line is observed in the spectra of

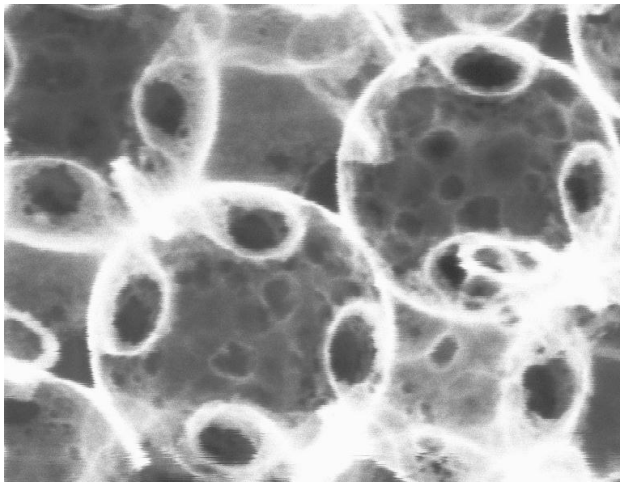

Fig. 5. (100) side cut of SiC/C inverse opal upon etching in HF solution.

different graphite types. The weak intensity and large halfwidth indicate that the phase is strongly disordered and the crystalline sizes do not exceed several nanometers.

Implanted samples show weak photoluminescence in the blue - green region of about 3.1 - 2.5 eV (400 - 500 nm). Annealing after implantation at temperature of 800° C in an inert atmosphere leads to the emergence of local dots in the sample, glowing orange-red (ORD). PL spectra of two typical points are given in Fig. 6 (curves 1 and 2). Curve 3 (Fig. 6) measured with the sample area, where there were no glowing orange-red. Its intensity in the blue spectral region is almost two orders of magnitude below the intensity of ORD (Fig. 6, curves 1 and 2). It should be noted that the orange-red dots (ORD), were detected in only one of the 4 samples of the series.

Band with maximum of about 2.16 eV (574 nm) (Fig. 6, curve 2), 0.40 eV FWHM, similar to the band, as observed in [1]. Radiation of ORD (curve 1) represents a broader band with a maximum of about 2.12 eV (585 nm), which admits the expansion (see inset in Fig. 6) into two bands with maxima at about 2.17 eV (571 nm) and 2.0 eV (620 nm), which are characteristic for two types of N - V centers in diamond: the neutral $(NV)^0$ center (575 nm) and negatively charged $(NV)^-$ center (638 nm) [2,3].

Peaks shift and the large width of the lines indicate the small size of the radiation centers, comparable with 5-nm nanodiamonds [4]. While studies temporal instability of the PL centers have been found. About a few months of ORD disappeared in the samples. It should be noted that the comparison samples used in the irradiation with helium ions, did not show an orange-red luminescence.

In order to identify structural fragments of the diamond samples were investigated by transmission electron microscopy, high resolution (HRTEM). At the structure of the composites, except for silicon carbide, graphite and amorphous carbon, spherical carbon particles containing concentric graphite shells (onion-like particles) were found.

In [5] have shown that when such particles are heated to 700°C and irradiated with electrons so their nuclei can transform into a diamond. The distance between carbon planes in onions decreases as we move from the outer to inner shells in the range of 0.34 nm - 0.22 nm. This decrease in the interplanar distance is the result of compression of the

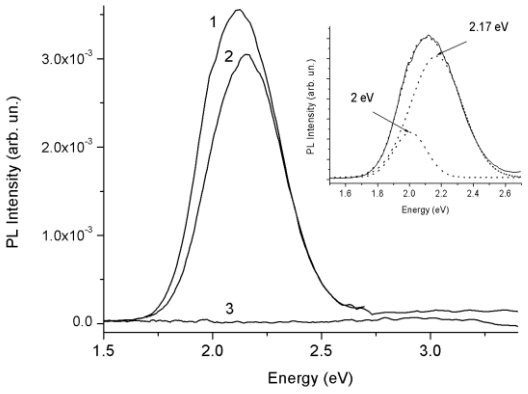

Fig. 6. PL spectra of two typical orange-red dots (curves 1 and 2) and site without ORD.

irradiated particles, which leads to the formation of diamond particles in the nucleus. In [5] the pressure inside the particle was estimated, which can exceed the equilibrium pressure of the transition of graphite - diamond. The formation of diamond nuclei was observed for many onions -like particles, with the number of shells of more than 15. The size of crystalline diamond in the nucleus varies from 2 nm to 50 nm. At room temperature, however, the lattice of the irradiated onions -like particles broken because of the many defects such as boundaries, which reduce the stability of onions [5].

Fig. 7 shows a composite image of SiC / C, containing onion-like particles. Interplanar distance in the nucleus corresponds to the graphite phase of carbon. On one of

twenty different parts of the sample giant onion-like particle with diameter of 100 nm was observed. Fig. 8 shows images of the upper half of the particle. Apparently, a giant onion-like particle formed at the site of the octahedral voids in the opal lattice, completely filled with carbon, since the size of the octahedral cavities is $0.42D_{SiO2}$, where D_{SiO2} is ball diameter.

We used in this study silica spheres about 260 nm in size. Dimensions of oktaporous in this matrix corresponds to the inscribed sphere of diameter about 100 nm. As seen from the images (Fig. 8), the continuity of the graphite layers disrupted in many places. There are areas of disorientation

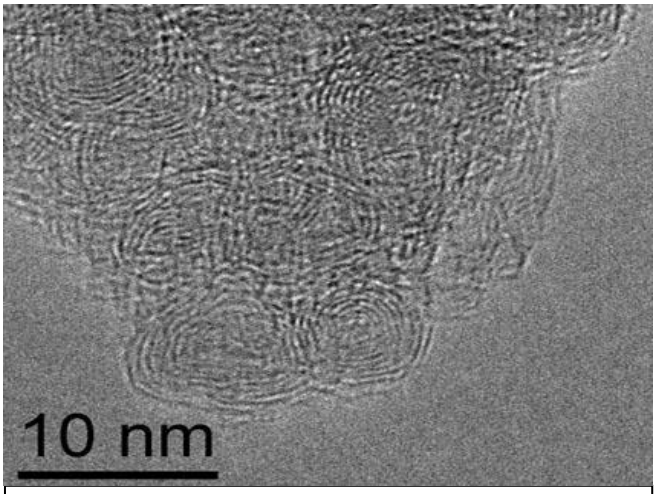

Fig. 7 Spherical carbon particles, consisting of concentric graphite shells (onion-like particles), HRTEM.

and disordering the graphite layers at the atomic level, which is consistent with observations in [5].

Analyzing results of measurements of set of parts of a composite, it is possible to note, that the typical size of

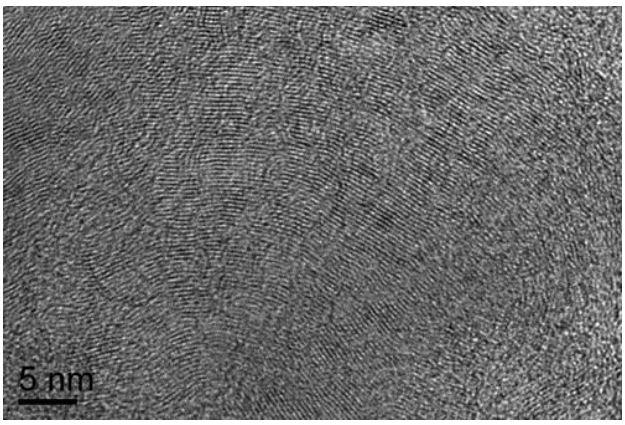

Fig. 8. SEM image of giant onion-like particle with diameter of 100 nm (upper half of the particle)

onion-like particles makes about 10 nanometers. The kernel in such particle has the size about 2 nanometers according to data [5]. Such small size of particles logically explains their temporary instability. It is possible to assume, that the kernel is formed in the form of a diamond phase as a result of high-temperature processing a composite opal - carbon. In due course the thermodynamic instable phase of diamond is transformed to graphite at room temperature. Implantation of a composite by ions of helium initiates N – V centers formation in a diamond phase that ORD luminescence confirms. After transformation of diamond in graphite ORDs also disappear.

In the investigated samples we could not to detect fragments of a diamond phase, including and in kernels of onion-like-particles. It is no wonder if to consider the lowest concentration ORDs in samples (1 ORD per cm^2), high localness of HRTEM method and thermodynamic instability small (2-3 nanometers) diamond clusters.

V. CONCLUSION

The SiC NWs were synthesized via carbothermal reduction method using both the colloidal graphite and the colloidal SiO_2 as carbon and silicon sources, respectively. It was detected the SiC NWs of the two types: “smooth” and “bamboo-like” wires. The “smooth” wires with the diameter < 100 nm have the [111] growth direction, while the wire with diameter > 100 nm can have either the [110] or the [112] growth direction. SiC/C-HRTEM revealed in the structure of the composites, except for silicon carbide, graphite and amorphous carbon, spherical carbon particles containing concentric graphite shells (onion-like particles). It was established that the onion-like particles formed during the manufacture of SiC / C nanocomposite at high temperature treatment. It is shown that after implantation followed by heat treatment samples exhibit of the luminescence characteristic for the N - V centers in diamond. It is suggested that the diamond crystallites formed in the center of the onion-like particles during high temperature treatment of the composite.

This work was supported by RFBR grant № 10-02-00460.

REFERENCES

[1] G.A. Emelchenko, A A Zhokhov, V M Masalov et al, SiC/C nanocomposites with inverse opal structure, Nanotechnology 2010, 21, №47, p. 475604

[2] Davies, G. & Hamer, M. F. Optical studies of 1.945 eV vibronic band in diamond. Proc. R. Soc. Lond. A 348, 285–298 (1976).

[3] YI-R. Chang, H.-Y. Lee, K. Chen et al., Nature nanotechnology, 2008, v. 3, p. 284-287

[4] C. Bradac, T. Gaebel, N. Naidoo, M. J. Sellars, J. Twamley, L. J. Brown, A. S. Barnard,T. Plakhotnik, A. V. Zvyagin and J. R. Rabeau Nature Nanotechnology v. 5 (2010) 345-349

[5] F. Banhart and P.M. Ajayan, Nature **382** (1996) 433

ZnO Growth Technologies:Current Status and Perspectives

Oleg LUPAN
Technical University of Moldova
lupan@mail.utm.md

***Abstract* – Development of new technologies for ZnO nanomaterials and thin films is of critical importance for further fundamental investigations and practical applications. We discuss on the main technical control of the synthesis of zinc oxide and its properties, which are of significance in understanding the growth mechanism and further developing ZnO-based devices. Next, we present a brief summary of recent research activities, current status and progress in developing improved control of technological processes for zinc oxide as advanced material.**

***Index Terms* – ZnO, nanostructures, thin films, synthesis.**

I. INTRODUCTION

Semiconducting metal oxide functional nanomaterials are of potentially broad fundamental and technological interests in science ranging from the quantum physics to optoelectronics [1,2]. Bulk crystals are of importance for making substrates of high quality and for enhanced devices with extended lifetime. However, size reduction to the nanometer range causes quantization of density of states, which alters the intrinsic properties of crystalline materials. Scientific interest for studying the behavior of low-dimensional matter (micro-nano-scale) has accelerated the elaboration of a number of new advanced multifunctional materials with well defined structures, sizes and properties. These novel electronic, magnetic or optical performances of the materials ranging from micro to nano-scale, along with multifunctionality derived from small size effect, have contributed extensively to different fields of device applications, especially for optoelectronics, medical diagnostics, and chemical sensing. Zinc oxide is one of technologically important materials, which presents significant practical and scientific importance for different areas [1-4]. For example, ZnO exhibits various applications in gas sensors, electrodes for dye-sensitized solar cells DSSCs, light-emitting devices, luminescent materials, and thin-film transistors [1-12]. To show potential utilities of zinc oxide material, we noted some typical applications of ZnO low-dimensional structures in Table I (here we present our results only).

TABLE I. OUR RECENT REPORTED APPLICATIONS ON ZNO LOW-DIMENSIONAL STRUCTURES (OUR RESULTS ONLY).

Authors	Year	Application	Refs
Lupan *et al.*	2007	Single Tripod-Nanosensor	[5]
Lupan *et al.*	2008	Nano-photodetector	[6]
Lupan *et al.*	2008	Single Nanorod-sensor	[7]
Lupan *et al.*	2009	Single tetrapod - microsensor	[8]
Lupan *et al.*	2010	Individual Nanowire-nanosensor	[9]
Lupan *et al.*	2010	Nanowire-DSSC	[10]
Lupan *et al.*	2010	Nanowire-LED	[11]
Lupan *et al.*	2011	Tunable-LED	[12]

Thus, understanding its technological aspects is of importance for solving great difficulties in achieving stable doped ZnO due to low-doping efficiency and others.

II. PROBLEMS AND SOLUTIONS

For reliable device applications, a major problem is the lack of reproducible and reliable *n*- and *p*-type conductivity with shallow donor or acceptor states in ZnO, respectively. It is expected that doping low-dimensional crystals will lead to new physics and chemistry as these complex assemblies are investigated [13]. Just like their bulk counterpart, doping of semiconductor nanocrystals by impurity atoms permits tailoring their behavior, which can enable their new application in nano-electronics and nano-optoelectronics [14]. However, multiple previous reports indicated dopant could be difficult for nanocrystals [14]. It has to be mentioned that by a simple addition of a transition metal compounds to the growth solution does not result in incorporation of dopants. These difficulties could be due to the fact that the surface-bound dopants may have different geometries, and exchange coupling interactions with the semiconductor band electrons than substitutionally incorporated dopants have, and the target physical properties of the material may therefore be compromised. Enormous efforts have been directed to this area of research by different research groups worldwide.

Currently several dopants are considered as the most promising dopant for *p*-type ZnO, like Sb, Ag, P, Li, Cu. Another approach is co-doping of elements, which can enhance the solubility of the doping atoms and produce shallower defect levels. At the same time it is still controversial about co-doping, since it requires a complex decision on multiple aspects related to the impurity impact on the crystal structure or the formation of possible secondary phase in the doped region, and the uniformity in distribution for the dopant. Extensive research efforts have been made for the design and control of ZnO crystals with low-dimensions via innovative strategies. Zinc oxide one-dimensional (1D) nano-structures are important due to their conduction behavior of quantum particles and large aspect ratio which permits for distinct structural performance as well as greater chemical reactivity. It is reported that different ZnO nanowires/nanorods can be synthesized easily

by using a pattern on any kind of substrate. However, for the monocrystalline-based optoelectronic device fabrications, it is important to control the growth of ZnO single crystalline nanowires directly on film in order to eliminate the strain effect derived from lattice mismatch between mono-crystalline substrates and ZnO single crystalline low-dimensional structures. In this way, the film may serve as a convenient pathway for the transport of electrons, phonons, and photons. Another significant problem is defect chemistry or possibility to control defects in ZnO material. By solving it, it will be possible to tune the functional properties. The most abundant point defects in ZnO are interstitial zinc atom (Zn_i) or oxygen vacancy (V_O). Therefore, it is of importance to carry out more comprehensive study of the technically control over the synthesis technique in order to allow exact control over the defects, the type conduction and the emission properties with the possibility to elaborate and fabricate nano-ZnO -based electrical, magnetic and optical nanodevices.

III. GROWTH OF ZNO

Zinc oxide material posses several types of fastest growth directions [1]. The preferred crystallization could be understood by considering that ZnO wurtzite crystals have different growth rates for different planes too: $V_{(0001)} > V_{(10\bar{1}1)} > V_{(10\bar{1}0)}$ [1,15]. Due to different growth rates, the controlled synthesis of preferred nanoarchitecture for specific applications can be realized by a well control of the synthesis process [15]. The crystal synthesis on a specific surface in the aqueous solution is based on heterogeneous nucleation and subsequent growth. Considering these directions and the polar surfaces due to atomic terminations, zinc oxide exhibits a variety of nanostructures that can be synthesized by controlling the growth rates along these directions. It is well known that a crystal posses different kinetic parameters for different crystal planes, which are emphasized under controlled growth conditions. Thus, synthesis techniques and regimes are very important for synthesis of a specific structure.

The growth techniques for zinc oxide nanostructures can broadly be classified as:

1. solution phase synthesis and
2. gas phase synthesis.

In the solution growth procedures, the synthesis of the material is carried out in a liquid. In most of reports they are in aqueous solutions and the process is referred to as hydrothermal synthesis. Due to the fact that the heterogeneous nucleation takes place at a low level of supersaturation of the complex solution, we can grow different ZnO nanoarchitectures by controlling the reactant concentration, process temperature, and pH value [15]. This technique can be represented by: template assisted growth; spray pyrolysis for growth of thin films; electrophoresis; electrodeposition; sol-gel route; hydrothermal [1,15].

In the gas phase growth procedures: gas phase synthesis is realized in the gaseous environment in a closed chamber. In most of the reports such kind of growth is carried out at elevated temperatures from 450 °C to 1450 °C. The following gas phase methods has been reported: physical vapor deposition; vapor phase transport, which includes vapor solid (VS) and vapor liquid solid (VLS) growth; metal organic chemical vapor deposition (MOCVD); chemical vapor deposition; thermal oxidation of pure Zn and condensation; field assisted thermal decomposition [1]. In Appendixes A-M - some morphological and structural properties of the ZnO low-dimensional structures have been shown. Detailed technological description for these low-dimensional structures and their characteristics has been reported in our works [15-30].

These new developments of the technological methods are believed to offer new perspectives for zinc oxide crystal and nanostructures growth by well established techniques.

IV. CONCLUSION

ZnO low-dimensional structures are attractive building-blocks for applications in a micro-nano- devices like sensors, photodetectors, energy generators, solar cells, light-emitting devices as well as artificial structures for tissue engineering. Within the next decade, zinc oxide nanostructures will move into industrial applications, if its growth and performances can be well controlled. Also, if synthesized low-dimensional structures will be integrated in devices by using different approaches, e.g. focused ion beam nanoliphography [29], self-assembly, electric-field assisted assembly, etc.

Aligning of the grown nanorods and nanowires can be realized using a specific template. Simplest way used to make ordered nanowire arrays during of growth is ZnO film grown on substrate is to create on the surface equal conditions to form seeds and grow to form uniformly distributed nucleus and finally nanorods [15]. It is anticipated that the ZnO branched rods will find many applications in novel nanodevices and are expected to promote synthesis of nanorod *p-n* junctions.

Future work: Our future research efforts will be directed towards synthesizing oriented one – dimensional nanorods, which will facilitate construction of semiconductor oxide-based nanodevices with well-ordered alignment, which are extremely important for scientific, technological and industrial application. Development of single doped ZnO nanorod LED for light emission sources. Also, high sensitivity and selective nanosensors as well.

APPENDIX A

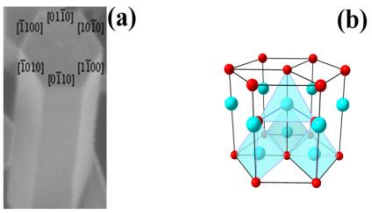

Fig. A. (a) SEM image of the single ZnO Nanorod grown by an aqueous technique at 97 °C from $ZnSO_4$ and NaOH solution. Also directions are indicated on SEM image. (b) Stick-and-ball representation of zinc oxide crystal structures.

APPENDIX B

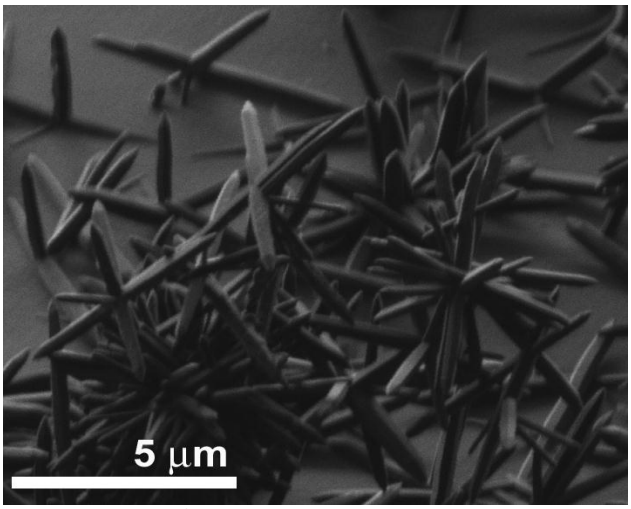

Fig. B. SEM image of the ZnO Nanowires branched in complex structures grown by an aqueous technique at 97 °C from $ZnSO_4$ and NaOH solution.

APPENDIX C

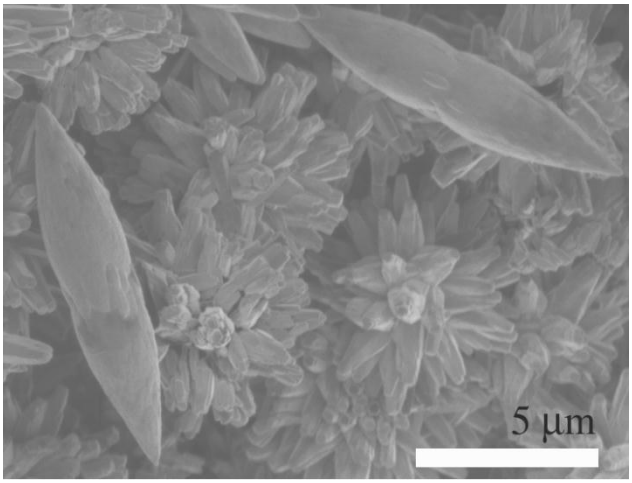

Fig. C. SEM image of the ZnO branched needles synthesized in a hydrothermal process at 77 °C from $ZnSO_4$ and NH_4OH solution.

APPENDIX D

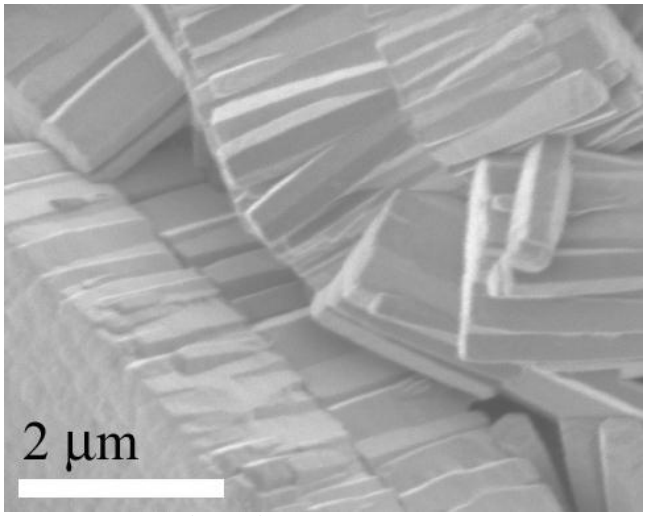

Fig. D. SEM image of the self-assembled nanorods grown by hydrothermal technique.

APPENDIX E

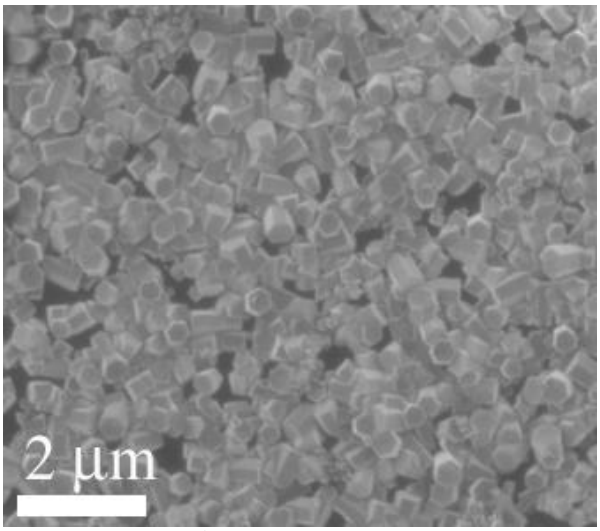

Fig. E. SEM image of the Mn-doped ZnO nanorods synthesized in a hydrothermal process at 97 °C aqueous solutions.

APPENDIX F

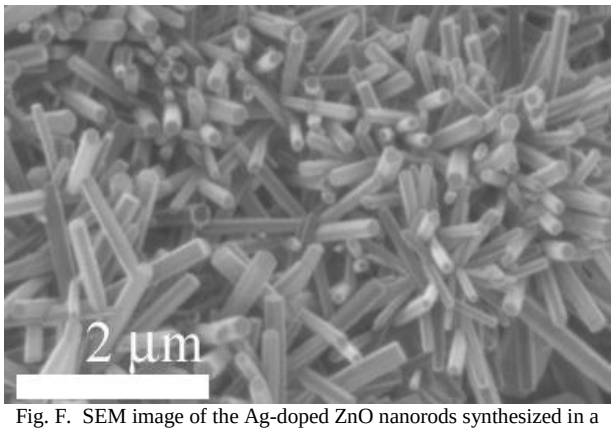

Fig. F. SEM image of the Ag-doped ZnO nanorods synthesized in a hydrothermal process at 95 °C from $ZnSO_4$, $AgNO_3$ and NH_4OH solution.

APPENDIX G

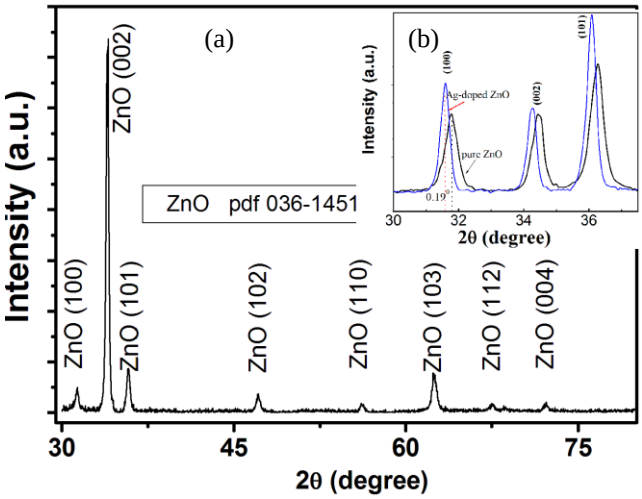

Fig. G. (a) XRD pattern of ZnO nanorod arrays as-prepared on glass synthesized by the aqueous-solution method. (b) XRD pattern of doped ZnO nanorod arrays on glass synthesized by the aqueous-solution method showing shift of the peaks due to lattice parameters changes.

APPENDIX h

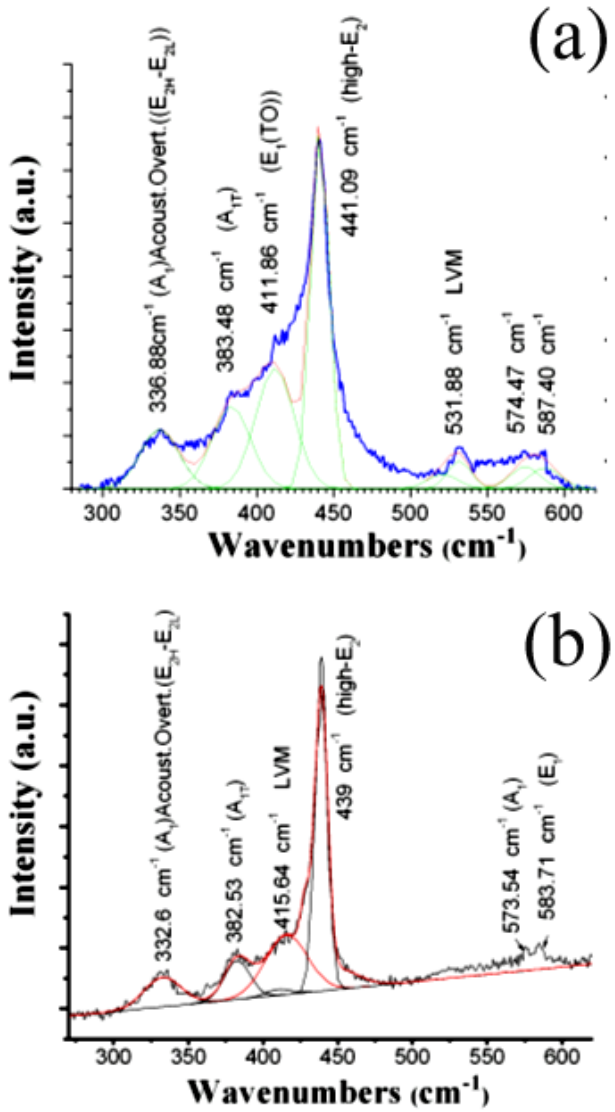

Fig. H. Deconvolution of the 300-600 cm-1 region with Raman peaks using Gaussian fit of Micro-Raman scattering spectra of: (a) Sb-doped ZnO nanorods and (b) Ag-doped ZnO nanorods.

APPENDIX I

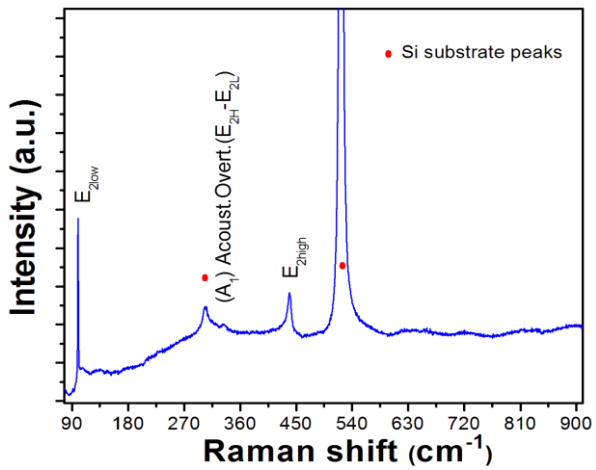

Fig. I. Raman shift of ZnO nanorod arrays on Si substrate synthesized by the hydrothermal method showing the good crystalline quality of the material to be used in a nano *p-n* junction applications.

APPENDIX J

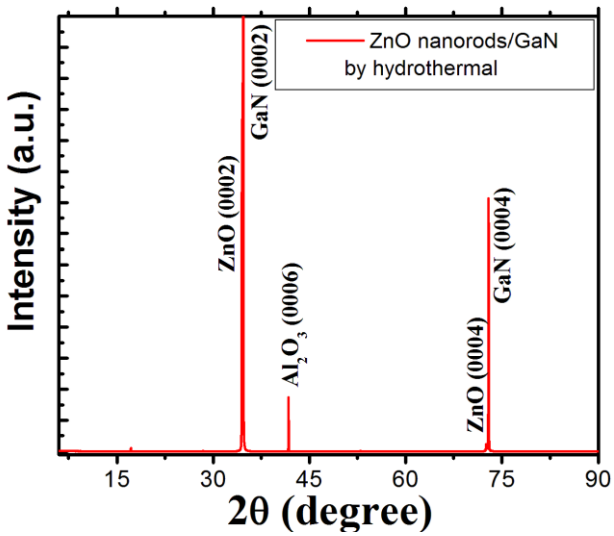

Fig. J. X-ray diffraction θ-2θ scan of the ZnO nanorods grown on GaN/sapphire (0001) substrate by hydrothermal technique.

APPENDIX K

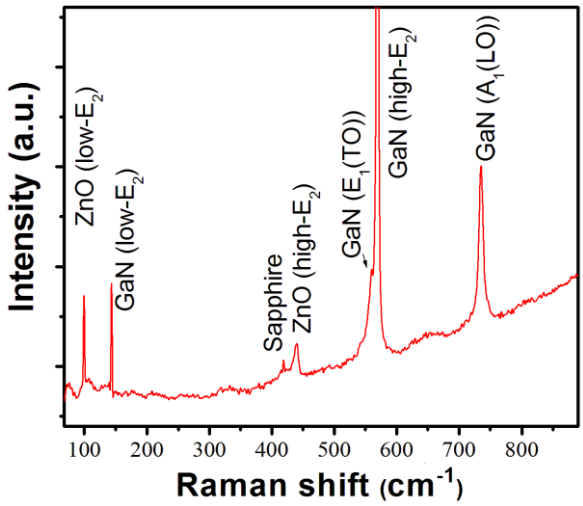

Fig. K. Room-temperature Raman spectra of ZnO nanorods hydrothermally grown on GaN substrate.

APPENDIX L

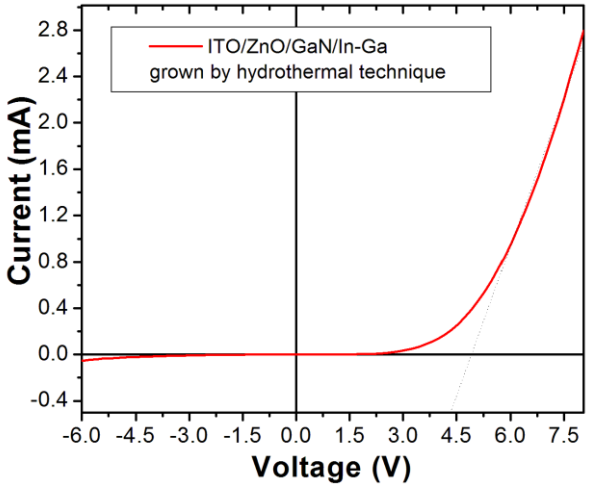

Fig. L. *I-V* characteristics of the ZnO nanorods/*p*-GaN heterojunction in the dark measured at 300 K.

APPENDIX M

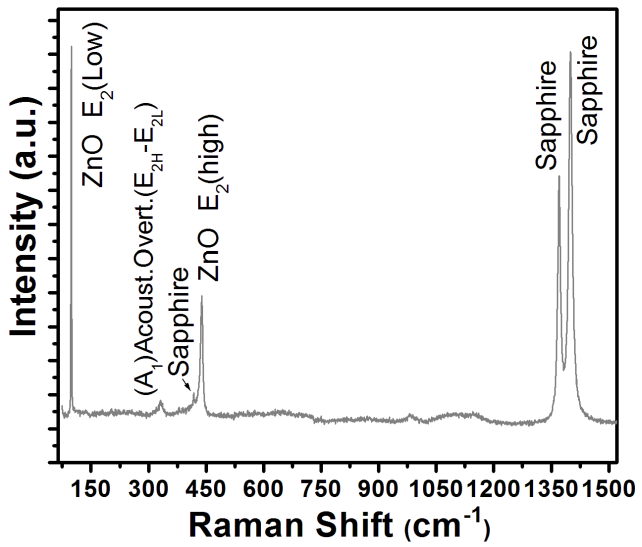

Fig. M. Room-temperature Micro-Raman scattering spectrum of the zinc oxide nanorods grown by hydrothermal technique on sapphire substrate with single crystal structure.

ACKNOWLEDGMENTS

Dr. Lupan would like to acknowledge Professors I.Tighineanu, Th.Pauporté and L.Chow for their guidance of my post-doctorate research in their laboratories in Moldova, France and U.S.A., respectively. Also, their enormous support of all performed scientific research and detailed discussions of our experimental data are gratefully acknowledged.

REFERENCES

[1] I. M. Tiginyanu, O. Lupan, V. V. Ursaki, L. Chow, M. Enachi, "Nanostructures of Metal Oxides." Comprehensive Semiconductor Science & Technology, Chapter 3.11, pp. 396-479, 2011.

[2] C. Burda, X. Chen, R. Narayanan, M. A. El-Sayed, "The chemistry and properties of nanocrystals of different shapes," Chem. Rev., vol. 105(4), pp. 1025-1102, 2005.

[3] Z. L. Wang, "Zinc oxide nanostructures: growth, properties and applications," J. Phys.: Condens. Matter., vol. 16, pp. R829–R858, 2004.

[4] U. Ozgur, D. Hofstetter, H. Morkoc, "ZnO Devices and Applications: A Review of Current Status and Future Prospects," Proceedings of the IEEE, vol. 98(7), pp. 1255-1268, July 2010.

[5] O. Lupan, G. Chai, L. Chow, "Fabrication of ZnO nanorod-based hydrogen gas nanosensor," Microelectronics Journal, vol. 38, pp. 1211-1216, December 2007.

[6] O. Lupan, L. Chow, G. Chai, L. Chernyak, O. Lopatiuk-Tirpak, H. Heinrich, "Focused-ion-beam fabrication of ZnO nanorod-based UV photodetector using the in-situ lift-out technique," Physica Status Solidi (a), vol. 205(11), pp. 2673–2678, Nov. 2008.

[7] O. Lupan, G. Chai, L. Chow, "Novel hydrogen gas sensor based on single ZnO nanorod," Microelectronics Eng., vol. 85, pp. 2220-2226, 2008.

[8] O. Lupan, L. Chow, G. Chai, "A single ZnO tetrapod-based sensor," Sensors and Actuators B: Chemical, vol. 141(2), pp. 511-517, September 2009.

[9] O. Lupan, V.V. Ursaki, G. Chai, L. Chow, G.A. Emelchenko, I.M. Tiginyanu, A.N. Gruzintsev, A.N. Redkin, "Selective hydrogen gas nanosensor using individual ZnO nanowire with fast response at room temperature," Sensors and Actuators B: Chemical, vol. 144(1), pp. 56-66, January 2010.

[10] O. Lupan, V.M. Guérin, I.M. Tiginyanu, V.V. Ursaki, L. Chow, H. Heinrich, T. Pauporté, "Well-aligned arrays of vertically oriented ZnO nanowires electrodeposited on ITO-coated glass and their integration in dye sensitized solar cells", Journal of Photochemistry and Photobiology A: Chemistry, vol. 211(1), pp. 65-73, March 2010.

[11] O. Lupan, Th. Pauporté, B. Viana, Low-Voltage UV-Electroluminescence from ZnO-Nanowire Array/p-GaN Light-Emitting Diodes, Advanced Materials, vol. 22(30), pp. 3298–3302, August 2010.

[12] O. Lupan, T. Pauporté, B. Viana, P. Aschehoug, "Electrodeposition of Cu-doped ZnO nanowire arrays and heterojunction formation with *p*-GaN for color tunable light emitting diode applications, Electrochimica Acta, In Press, doi:10.1016/j.electacta.2011.02.004 online Feb. 2011.

[13] A. P. Alivisatos, "Semiconductor Clusters, Nanocrystals, and Quantum Dots," Science, vol. 16, pp. 933-937, February 1996.

[14] D. J. Norris, A. L. Efros, S. C. Erwin, "Doped Nanocrystals," Science, vol. 319(5871), pp. 1776-1779, 28 March 2008.

[15] O. Lupan, L. Chow, G. Chai, B. Roldan, A. Naitabdi, A. Schulte, H. Heinrich, "Nanofabrication and characterization of ZnO nanorod arrays and branched microrods by aqueous solution route and rapid thermal processing," Materials Science and Engineering: B, vol. 145(1-3), pp. 57-66, December 2007.

[16] L. Chow, O. Lupan, Guangyu Chai, "FIB fabrication of ZnO nanotetrapod and cross-sensor," Physica Status Solidi (b), vol. 247(7), pp. 1628–1632, July 2010.

[17] O. Lupan, L. Chow, S. Shishiyanu, E. Monaico, T. Shishiyanu, V. Şontea, B. Roldan Cuenya, A. Naitabdi, S. Park, and A. Schulte, "Nanostructured zinc oxide films synthesized by successive chemical solution deposition for gas sensor applications," Materials Research Bulletin, vol. 44, pp. 63-69, 2009.

[18] V.V. Ursaki, O.I. Lupan, L. Chow, I.M. Tiginyanu, V.V. Zalamai, "Rapid thermal annealing induced change of the mechanism of multiphonon resonant Raman scattering from ZnO nanorods," Solid State Communications, vol. 143, pp. 437-441, 2007.

[19] L. Chow, O. Lupan, H. Heinrich, G. Chai, "Self-assembly of densely packed and aligned bilayer ZnO nanorod arrays," Appl. Phys. Lett. vol. 94, pp. 163105, April 2009.

[20] O. Lupan, L. Chow, G. Chai, H. Heinrich, "Fabrication and characterization of Zn–ZnO core–shell microspheres from nanorods," Chemical Physics Letters, vol. 465(4-6), pp. 249-253, November 2008.

[21] O. Lupan, G.A. Emelchenko, V.V. Ursaki, G. Chai, A.N. Redkin, A.N. Gruzintsev, I.M. Tiginyanu, L. Chow, L.K. Ono, B. Roldan Cuenya, H. Heinrich, E.E. Yakimov, "Synthesis and characterization of ZnO nanowires for nanosensor applications," Materials Research Bulletin, vol 45(8), pp. 1026-1032, August 2010.

[22] O. Lupan, L. Chow, G. Chai, A. Schulte, S. Park, O. Lopatiuk-Tirpak, L. Chernyak, H. Heinrich,

"Biopolymer-assisted self-assembly of ZnO nanoarchitectures from nanorods," Superlattices and Microstructures, vol. 43(4), pp. 292-302, April 2008.

[23] O. Lupan, Th. Pauporté, "Hydrothermal treatment for the marked structural and optical quality improvement of ZnO nanowire arrays deposited on lightweight flexible substrates," Journal of Crystal Growth, vol. 312(16-17), pp. 2454-2458, August 2010.

[24] O. Lupan, T. Pauporté, L. Chow, B. Viana, F. Pellé, L.K. Ono, B. Roldan Cuenya, H. Heinrich, "Effects of annealing on properties of ZnO thin films prepared by electrochemical deposition in chloride medium," Applied Surface Science, vol. 256(6), pp. 1895-1907, January 2010.

[25] O. Lupan, L. Chow, L. K. Ono, B. Roldan Cuenya, G. Chai, H. Khallaf, S. Park, A. Schulte, "Synthesis and Characterization of Ag- or Sb-Doped ZnO Nanorods by a Facile Hydrothermal Route," J. Phys. Chem. C, vol. 114 (29), pp 12401–12408, July, 2010.

[26] O. Lupan, Th. Pauporté, B. Viana, I. M. Tiginyanu, V. V. Ursaki and R. Cortés, "Epitaxial Electrodeposition of ZnO Nanowire Arrays on p-GaN for Efficient UV-Light-Emitting Diode Fabrication," ACS Appl. Mater. Interfaces, 2010, 2 (7), pp 2083–2090, July, 2010.

[27] O. Lupan, T. Pauporté, L. Chow, B. Viana, F. Pellé, L.K. Ono, B. Roldan Cuenya, H. Heinrich, "Effects of annealing on properties of ZnO thin films prepared by electrochemical deposition in chloride medium," Applied Surface Science, vol. 256(6), pp. 1895-1907, January 2010.

[28] O. Lupan, T. Pauporté and B. Viana, "Low-Temperature Growth of ZnO Nanowire Arrays on p-Silicon (111) for Visible-Light-Emitting Diode Fabrication," J. Phys. Chem. C, 2010, 114 (35), pp 14781–14785, August 2010.

[29] G. Chai, O. Lupan, L. Chow, "Focused ion beam fabrication of carbon nanotube and ZnO nanodevices" in Nanofabrication Using Focused Ion and Electron Beams Principles and Applications, Edited by Ivo Utke, Stanislav Moshkalev and Phillip Russell ISBN13: 9780199734214 ISBN10: 0199734216 752 pages, Nov 2011.

High-Pressure Study of YVO_4 Nanoboxes

F.J. MANJÓN[1], O. GOMIS[2], S. RAY[1], S. F. LEÓN-LUIS[3], U.R. RODRÍGUEZ-MENDOZA[3], V. LAVÍN[3], A. SEGURA[4], D. MARTÍNEZ-GARCÍA[4], and Ch. FERRER-ROCA[4]

[1]*Instituto de Diseño para la Fabricación y Producción Automatizada, MALTA Consolider Team, Universitat Politècnica de València, Camí de Vera s/n, 46022 València (Spain*), *e-mail*: *fjmanjon@fis.upv.es*[1]

[2]Instituto 2Instituto de Centro de Tecnologías Físicas, MALTA Consolider Team, Universitat Politècnica de València, Camí de Vera s/n, 46022 València (Spain)

[3]Instituto de MALTA Consolider Team and Departamento de Física Fundamental y Experimental, Electrónica y Sistemas, Universidad de La Laguna, E-38200 San Cristóbal de La Laguna, Santa Cruz de Tenerife (Spain)

[4] Instituto de Ciencia de Materiales de la Universidad de Valencia, MALTA Consolider Team, Universitat de València, C/. Dr. Moliner 50, 46100 Burjassot, València (Spain)

***Abstract* – YVO_4 nanoboxes doped with Eu ions (4 at%) have been studied by means of X-ray diffraction, Raman and photoluminescence measurements under high pressure. Photoluminescence measurements in nanoboxes provide evidence that Eu ions locate at different symmetry sites in the nanoenvironment than in bulk crystal. On the other hand, Raman scattering measurements under pressure provide evidence that YVO_4 nanoboxes undergo a monoclinic distortion of the zircon structure prior to their phase transition towards the scheelite structure at high pressure.**

***Index Terms* – high pressure, vanadates, X-ray diffraction, Raman scattering, photoluminescence.**

YVO_4 is a very interesting material which finds an extensive use in material science and technology due to its outstanding optical properties. YVO_4:Nd^{3+} is used in industrial diode pumped solid state lasers [1]. The improvement of luminescence properties in nanosized and pressure-treated materials has opened an enormous working field in phosphors [2] and the study of rare-earth ions in the nano-environment of ABO_4 compounds is important for the development of phosphors with enhanced luminescence efficiency by combining the promising optical properties of rare-earth ions and nanoparticles [3,4].

Bulk YVO_4 crystallizes in the zircon structure (space group S.G. #141) and it undergoes two pressure-induced phase transitions: a first one towards the scheelite structure (S.G. #81) above 7.5 GPa [5,6] and a second one towards the fergusonite structure (S.G. #15) above 23 GPa [7]. Knowing the phase transitions in nanocrystals could give a better insight into the relation between compositional, structural and optical properties in order to design better phosphors or even provide novel nanocrystal phases which could be retained in metastable way, like diamond, at ambient conditions with enhanced optical properties with respect to parent materials.

We have synthesized Eu-doped YVO_4 nanoboxes with zircon structure and 25 ± 5 nm lateral size. Nanoboxes have been characterized by X-ray diffraction, Raman scattering, and photoluminescence under pressure up to 18 GPa. The pressure behaviour of nanocrystals has been compared to that of bulk material [2,5-7]. We have found that the zircon-to-scheelite phase transition occurs at a much higher pressure in nanocrystals as compared to the bulk and that Eu ions show a different photoluminescence spectrum in nanocrystals than in the bulk likely due to the occupation of different symmetry sites by Eu ions in nanocrystals. Additionally, a possible intermediate monoclinic phase resulting from the distortion of the zircon phase and occurring between the zircon and scheelite phases could be present in nanocrystals unlike in the bulk as recently suggested to occur in zircon-type chromates [8].

REFERENCES

[1] W. Koechner, Solid-state Laser Engineering, Springer, New York, 2006.

[2] G. Chen, N.A. Stump, R.G. Haire, J.R. Peterson, M.M. Abraham, J. Phys. Chem. Solids 53 (1992) 1253.

[3] A.J. Silversmith, W. Lenth, R.M. Macfarlane, Appl. Phys. Lett. 51 (1987) 1977.

[4] A. Patra, C.S. Friend, R. Kapoor, P.N. Prasad, Appl. Phys. Lett. 83 (2003) 284.

[5] A. Jayaraman, G. A. Kourouklis, G. P. Espinosa, A. S. Cooper, and L. G. Van Uitert, J. Phys. Chem. Solids 48 (1987) 755.

[6] X. Wang, I. Loa, K. Syassen, M. Hanfland, and B. Ferrand, Phys. Rev. B 70 (2004) 064109.

[7] F.J. Manjón, P. Rodríguez-Hernández, A. Muñoz, A. H. Romero, D. Errandonea, and K. Syassen, Phys. Rev. B 81 (2010) 075205.

[8] A.K. Mishra, N.Garg, K.K. Pandey, K.V. Shanavas, A.K. Tyagi, and S.M. Sharma, Phys. Rev. B 81 (2010) 104109.

Collective Elementary Excitations of 2D Magnetoexcitons Taking Into Account Excited Landau levels.

S.A.MOSKALENKO[1], M.A.LIBERMAN[2], E.V.DUMANOV[1], S.RUSU[1], F.CERBU[1]
[1]*Institute of Applied Physics of the Academy of Sciences of Moldova, Academic Str. 5, Chisinau, MD2028, Republic of Moldova*
[2]*Departmant of Physics, Uppsala University, Box 530, SE-751 21, Uppsala, Sweden*
exciton@phys.asm.md

***Abstract* – The collective elementary excitations of the two-dimensional magnetoexcitons in a state of Bose-Einstein condensation (BEC) with wave vector $\vec{k}=0$ were investigated in the frame of the Bogoliubov theory of quasiaverages. The starting Hamiltonian of the electrons and holes lying on the lowest Landau levels (LLLs) contains the supplementary interactions due to the virtual quantum transitions of the particles to the excited Landau levels (ELLs) and return back. As a result the interaction between the magnetoexcitons with $\vec{k}=0$ does not vanish and their BEC becomes stable as regards the collapse. The energy spectrum of the collective elementary excitations consists from two exciton-type branches (energy and quasienergy branches) each of them with energy gap and roton-type section, from the gapless optical plasmon branch and from the acoustical plasmon branch, which reveals the absolute instability in the range of small wave vectors.**

***Index Terms* – Bose-Einstein Condensation, elementary excitations, magnetoexciton, plasmon**

I. INTRODUCTION

Properties of atoms and excitons are dramatically changed in strong magnetic fields, such that the distance between Landau levels $\hbar\omega_c$, exceeds the corresponding Rydberg energies R_y and the magnetic length $l=\sqrt{\hbar c/eH}$ is small compared to their Bohr radii [1,2]. Even more interesting phenomena are exhibited in the case of two-dimensional (2D) electron systems due to the quenching of the kinetic energy at high magnetic fields, with the representative example being integer and fractional Quantum Hall effects [3-5]. The discovery of the FQHE [6-8] changed fundamentally the established concepts about charged elementary excitations in solids [5]. The notion of the incompressible quantum liquid (IQL) was introduced in Ref.[7] as a homogeneous phase with the quantized densities $\nu=p/q$, where p is an integer and $q\neq 1$ is odd having charged elementary excitations with a fractional charge $e^*=\pm e/q$. These quasiparticles were named as anyons. A classification for free anyons and their hierarchy were studied in [9,10]. An alternative concept to hierarchical scheme was proposed in [11], where the notion of composite fermions (CF) was introduced. The CF consists from the electron bound to an even number of flux quanta. In the frame of this concept the FQHE of electrons can be physically understood as a manifestation of the IQHE of CFs [11]. The statistics of anyons was determined in [10,12]. It was established that the wave function of the system changes by a complex phase factor $\exp[i\pi\alpha]$, when the quasiparticles are interchanged. For bosons $\alpha=0$, for fermions $\alpha=1$ and for anyons with $e^*=-e/3$ their statistical charge is $\alpha=-1/3$. As was shown in Ref.[13], there were no soft branches of neutral excitations in IQL. The energy gap Δ for formation of a quasielectron-quasihole pair has the scale of Coulomb energy $E_Q=e^2/\varepsilon l$, where ε is the dielectric constant of the background. However delta was found to be small $\Delta \approx 0.1E_Q$. The lowest branch was called as magnetoroton [13] and can be modelled as a quasiexciton [5]. As was mentioned in [5] the traditional methods and concepts based either on the neglecting of the electron-electron interaction or on self-consistent approximation are inapplicable to IQL. In a strong magnetic field the binding energy of an exciton increases from R_y to I_l.

There are two small parameters of the theory. One of them determines how strong the magnetic field strength H is, and it verifies whether the starting supposition of a strong magnetic field is fulfilled. This parameter is expressed by the ratio $I_l/\hbar\omega_c<1$. Here I_l is the magnetoexciton ionization potential, ω_c is the cyclotron frequency $eH/\mu c$ calculated with the reduced mass μ and the magnetic length l. Another small parameter has a completely different origin and is related with the concentration of the electron-holes(e-h) pairs. In our case it can be expressed as a product of the filling factor $\nu=\mathrm{v}^2$ and of another factor $(1-\mathrm{v}^2)$ which reflects the Pauli exclusion principle and the phase-space filing(PSF) effect. This compound parameter $\mathrm{v}^2(1-\mathrm{v}^2)$ in the case of Bose-Einstein condensed excitons can take the form $u^2\mathrm{v}^2$, where u, v are Bogoliubov transformation coefficients and $u^2=(1-\mathrm{v}^2)$. The both small parameters will be used below. But in the case of FQHE the filling factor $\nu=\mathrm{v}^2$ basically determines the underlying physics and it can not be changed arbitrarily. Instead of the

perturbation theory on the filling factor ν the exact numerical diagonalization for a few number of particles $N \le 10$ proved to be the most powerful tool in studies of such systems [5]. The spherical geometry for these calculations was proposed [10, 14], considering a few number of particles on the surface of a sphere with the radius $R = \sqrt{S}l$, so as the density of the particles on the sphere to be equal with the filling factor of 2DEG. The magnetic monopole in the center of the sphere creates a magnetic flux through the sphere $2S\phi_0$, which is multiple to the flux quantum $\phi_0 = 2\pi\hbar c/e$. The angular momentum L of a quantum state on the sphere and the quasimomentum k of the FQHE state on the plane obey the relation $L = Rk$. Spherical model is characterized by continuous rotational group, which is analogous with the continuous translational symmetry in the plane.

Properties of the symmetric 2D electron-hole (e-h) system (i.e. $h = 0$), with equal concentrations for both components, with coincident matrix elements of Coulomb electron-electron, hole-hole and electron-hole interactions in a strong perpendicular magnetic field also attracted a great attention during last two decades [15-22]. A hidden symmetry and the multiplicative states were discussed in many papers [19, 23, 24]. The collective states such as the Bose-Einstein condensation (BEC) of two-dimensional magnetoexcitons and the formation of metallic-type electron-hole liquid (EHL) were investigated in [15-22]. The search for Bose-Einstein condensates has became a milestone in the condensed matter physics [25]. The remarkable properties of super fluids and superconductors are intimately related to the existence of a bosonic condensate of composite particles consisting of an even number of fermions. In highly excited semiconductors the role of such composite bosons is taken on by excitons, which are bound states of electrons and holes. Furthermore, the excitonic system has been viewed as a keystone system for exploration of the BEC phenomena, since it allows to control particle densities and interactions *in situ*. Promising candidates for experimental realization of such system are semiconductor quantum wells (QWs) [26], which have a number of advantages compared to the bulk systems. The coherent pairing of electrons and holes occupying only the lowest Landau levels (LLLs) was studied using the Keldysh-Kozlov-Kopaev method and the generalized random-phase approximation [20, 27]. The importance of the excited Landau levels (ELLs) and their influence on the ground states of the systems was first noticed by the authors of the papers [16-19]. The influence of the excited Landau levels (ELLs) of electrons and holes was discussed in details in paper [21, 22]. The indirect attraction between electrons (e-e), between holes (h-h) and between electrons and holes (e-h) due to the virtual simultaneous quantum transitions of the interacting charges from LLLs to the ELLs is a result of their Coulomb scattering. The first step of the scattering and the return back to the initial states were described in the second order of the perturbation theory.

II. HAMILTONIAN OF THE SUPPLEMENTARY INTERACTION

The Hamiltonian of the Coulomb interaction of the electrons and holes in the frame of lowest Landau levels(LLLs) has the form:

$$\hat{H} = \frac{1}{2}\sum_{\vec{Q}} W_{\vec{Q}}\left[\hat{\rho}(\vec{Q})\hat{\rho}(-\vec{Q}) - \hat{N}_e - \hat{N}_h\right] - \mu_e\hat{N}_e - \mu_h\hat{N}_h + \hat{H}_{\text{suppl}} \quad (1)$$

where $W_{\vec{Q}}$ is the Fourier transform of the Coulomb interaction in the frame of LLLs, $\hat{N}_e$ and $\hat{N}_h$ are the operators of the numbers of electrons and holes on the LLLs. They are determined below. $\hat{H}_{\text{suppl}}$ is the supplementary indirect attractive interaction between the particle lying on the lowest Landau levels(LLLs) in view of their virtual transitions on the excited Landau levels(ELLs) and their return back [22]:

$$H_{\text{suppl}} = -\frac{1}{2}\sum_{p,q,s}\phi_{e-e}(p,q;s)a_p^\dagger a_q^\dagger a_{q+s}a_{p-s} - \frac{1}{2}\sum_{p,q,s}\phi_{h-h}(p,q;s)b_p^\dagger b_q^\dagger b_{q+s}b_{p-s} - \sum_{p,q,s}\phi_{e-h}(p,q;s)a_p^\dagger b_q^\dagger b_{q+s}a_{p-s} \quad (2)$$

Here the creation and annihilation operators $a_p^\dagger, a_p$ for electrons and $b_q^\dagger, b_q$ for holes were introduced. The matrix elements of indirect interaction $\phi_{i-j}(p,q,z)$ are described by the common expressions [22]

$$\phi_{i-j}(p,q,s) = \sum_{n,m}\frac{\phi_{i-j}(p,q,z;n,m)}{n\hbar\omega_{ci} + m\hbar\omega_{cj}} \quad (3)$$

In the case of electron-electron and hole-hole interaction the expression (3) has the form[22]:

$$\phi_{i-i}(p,q,z;n,m) \cong \sum_{t,\kappa,\sigma} W_{t,k}W_{z-t,\sigma}\exp\left(i\kappa(p-q-t)l^2\right)\times \exp\left(i\sigma(p-q-t-z)l^2\right)(t+i\kappa)^{n+m}(t-z+i\sigma)^{n+m} \quad (4)$$

but in the case of electron-hole interaction is:

$$\phi_{e-h}(p,q,z;n,m) \cong \sum_{t,\kappa,\sigma} W_{t,k}W_{z-t,\sigma}\exp\left(i(\kappa+\sigma)(p+q)l^2\right)\times (t+i\kappa)^n(t-i\kappa)^m(t-z+i\sigma)^n(t-z-i\sigma)^m, \quad (5)$$

where

$$W_{s,\kappa} = \frac{2\pi e^2}{\varepsilon_0 S\sqrt{s^2+k^2}}e^{-\frac{(s^2+k^2)l^2}{2}}, \quad (6)$$

$$W_{s,k} = W_{-s,-k} = W_{-s,k} = W_{s,-k}$$

The Hamiltonian of supplementary indirect attractive interaction (2) has the form:

$$H_{\text{suppl}} = \frac{1}{2}B_{i-i}N - \frac{1}{2N}\sum_{s,\sigma}\psi_{i-i}(s,\sigma)\times \left[\rho_e(-s,-\sigma)\rho_e(s,\sigma) + \rho_h(-s,-\sigma)\rho_h(s,\sigma)\right] - \frac{1}{N}\sum_{s,\sigma}\psi_{e-h}(s,\sigma)\rho_e(-s,-\sigma)\rho_h(-s,-\sigma) \quad (7)$$

Instead of density operators for electrons and holes we can introduce their in-phase and in opposite-phase linear combinations

$$\hat{\rho}(\vec{Q}) = \hat{\rho}_e(\vec{Q}) - \hat{\rho}_h(-\vec{Q});$$
$$\hat{D}(\vec{Q}) = \hat{\rho}_e(\vec{Q}) + \hat{\rho}_h(-\vec{Q});$$
$$\hat{\rho}_e(\vec{Q}) = \frac{1}{2}\Big[\hat{\rho}(\vec{Q}) + \hat{D}(\vec{Q})\Big]; \qquad (8)$$
$$\hat{\rho}_h(\vec{Q}) = \frac{1}{2}\Big[\hat{D}(-\vec{Q}) - \hat{\rho}(-\vec{Q})\Big]$$

They lead to the following relations

$$\hat{\rho}_e(-\vec{Q})\hat{\rho}_e(\vec{Q}) + \hat{\rho}_h(-\vec{Q})\hat{\rho}_h(\vec{Q}) =$$
$$= \frac{1}{2}\Big[\hat{\rho}(-\vec{Q})\hat{\rho}(\vec{Q}) + \hat{D}(-\vec{Q})\hat{D}(\vec{Q})\Big];$$
$$\sum_Q \psi_{e-h}(Q)\Big[\hat{\rho}(-\vec{Q})\hat{D}(\vec{Q}) - \hat{D}(-\vec{Q})\hat{\rho}(\vec{Q})\Big] =$$
$$= \sum_Q \psi_{e-h}(Q)\Big[\hat{\rho}(-\vec{Q})\hat{D}(\vec{Q}) - \hat{D}(\vec{Q})\hat{\rho}(-\vec{Q})\Big] = 0;$$

and to the final expression

$$H_{\text{suppl}} = \frac{1}{2}B_{i-i}N - \frac{1}{4N}\sum_Q V(Q)\hat{\rho}(\vec{Q})\hat{\rho}(-\vec{Q})$$
$$-\frac{1}{4N}\sum_Q U(Q)\hat{D}(\vec{Q})\hat{D}(-\vec{Q}) \qquad (9)$$

where

$$U(Q) = \psi_{i-i}(Q) + \psi_{e-h}(Q);$$
$$V(Q) = \psi_{i-i}(Q) - \psi_{e-h}(Q); \qquad (10)$$
$$\psi_{i-j}(s,\sigma) = \sum_\kappa \phi_{i-j}(s,\kappa)\exp(i\kappa\sigma l^2)$$

The estimations show that

$$U(0) = 2A_{i-i}; \quad V(0) = 0;$$
$$\frac{1}{N}\sum_{\vec{Q}} U(\vec{Q}) = B_{i-i} + \Delta(0)$$

It means that one can suppose the dependences

$$U(\vec{Q}) \cong U(0)e^{-\frac{Q^2l^2}{2}}; \quad V(\vec{Q}) \cong V(0) = 0 \qquad (11)$$

III. BOSE-EINSTEIN CONDENSATION OF MAGNETOEXCITONS IN TWO ALTERNATIVE DESCRIPTIONS

Bose-Einstein condensation(BEC) of 2D magnetoexcitons was considered in Ref.[20, 21] in the frame of Keldysh-Kozlov-Kopaev method [27], when the influence of the ELLs was neglected. The main results of this description will be remembered below.

The creation $d^\dagger(\vec{P})$ and annihilation $d(\vec{P})$ operators of the 2D magnetoexciton have the form:

$$d^\dagger(\vec{P}) = \frac{1}{\sqrt{N}}\sum_t e^{-iP_y tl^2} a^\dagger_{t+\frac{P_x}{2}} b^\dagger_{-t+\frac{P_x}{2}};$$
$$d(\vec{P}) = \frac{1}{\sqrt{N}}\sum_t e^{iP_y tl^2} b_{-t+\frac{P_x}{2}} a_{t+\frac{P_x}{2}}; \qquad (12)$$

The energy of the two-dimensional magnetoexciton $E_{ex}(P)$ depends on the two-dimensional wave vector $\vec{P}$ and forms a band with the dependence

$$E_{ex}(\vec{P}) = -I_{ex}(\vec{P}) = -I_l + E(\vec{P});$$
$$I_{ex}(\vec{P}) = I_l e^{-\frac{P^2l^2}{4}} I_0\left(\frac{P^2l^2}{4}\right); \qquad I_l = \frac{e^2}{\varepsilon_0 l}\sqrt{\frac{\pi}{2}}; \quad \sum_{\vec{Q}} W_{\vec{Q}} = I_l \qquad (13)$$

To introduce the phenomenon of Bose-Einstein condensation (BEC) of excitons the gauge symmetry of the initial Hamiltonian was broken by the help of the unitary transformation $\hat{D}(\sqrt{N_{ex}})$ following the Keldysh-Kozlov-Kopaev method [27]. We can shortly remember the main outlines of the Keldysh-Kozlov-Kopaev method [27], [33] as it was realized in the papers [20, 21]. The unitary transformation $\hat{D}(\sqrt{N_{ex}})$ was determined by the formula (8) [20]. Here N_{ex} is the number of condensed excitons. It transforms the operators a_p, b_p to another ones α_p, β_p, as is shown in the formulas (13), (14) [20], and gives rise to the BCS-type wave function $\left|\psi_g(\bar{k})\right\rangle$ of the new coherent macroscopic state represented by the expression (10) [20]. These results are summarized below

$$\hat{D}(\sqrt{N_{ex}}) = \exp[\sqrt{N_{ex}}(d^\dagger(\bar{k}) - d(\bar{k}))]$$
$$\left|\psi_g(\bar{k})\right\rangle = \hat{D}(\sqrt{N_{ex}})\left|0\right\rangle$$
$$\alpha_p = \hat{D}a_p\hat{D}^\dagger = ua_p - \mathrm{v}(p - \frac{k_x}{2})b^\dagger_{k_x-p}$$
$$\beta_p = \hat{D}b_p\hat{D}^\dagger = ub_p + \mathrm{v}(\frac{k_x}{2} - p)a^\dagger_{k_x-p} \qquad (14)$$
$$a_p = u\alpha_p + \mathrm{v}(p - \frac{k_x}{2})\beta^\dagger_{k_x-p}$$
$$b_p = u\beta_p - \mathrm{v}(\frac{k_x}{2} - p)\alpha^\dagger_{k_x-p}$$

$$a_p\left|0\right\rangle = b_p\left|0\right\rangle = 0;$$
$$\alpha_p\left|\psi_g(\bar{k})\right\rangle = \beta_p\left|\psi_g(\bar{k})\right\rangle = 0$$
$$u = \cos g; \quad \mathrm{v} = \sin g; \qquad \mathrm{v}(t) = \mathrm{v}e^{-ik_y tl^2} \qquad (15)$$
$$g = \sqrt{2\pi l^2 n_{ex}}; \quad n_{ex} = \frac{N_{ex}}{S} = \frac{\mathrm{v}^2}{2\pi l^2} \quad g = \mathrm{v}; \quad \mathrm{v}=\mathrm{Sin}\mathrm{v};$$

The developed theory [20, 21] is true in the limit $\mathrm{v}^2 \approx Sin^2\mathrm{v}$, what means the restriction $\mathrm{v}^2 < 1$. In the frame of this approach the collective elementary excitations can be studied constructing the Green's functions on the base of operators α_p, β_p and having deal with the transformed cumbersome Hamiltonian $\hat{\tilde{H}} = D(\sqrt{N_{ex}})\hat{H}D^\dagger(\sqrt{N_{ex}})$.

IV. EQUATIONS OF MOTION FOR THE TWO-PARTICLE OPERATORS AND FOR THE CORRESPONDING GREEN'S FUCTIONS

The starting Hamiltonian in the quasiaverages theory approximation has the form

$$\hat{H} = \frac{1}{2}\sum_{\vec{Q}} W_{\vec{Q}}\Big[\rho(\vec{Q})\rho(-\vec{Q}) - \hat{N}_e - \hat{N}_h\Big] - \mu_e\hat{N}_e - \mu_h\hat{N}_h -$$
$$-\tilde{\eta}\sqrt{N}\left(e^{i\varphi}d^\dagger(k) + e^{-i\varphi}d(k)\right) + \frac{1}{2}B_{i-i}N - \qquad (16)$$
$$-\frac{1}{4N}\sum_Q V(Q)\hat{\rho}(\vec{Q})\hat{\rho}(-\vec{Q}) - \frac{1}{4N}\sum_Q U(Q)\hat{D}(\vec{Q})\hat{D}(-\vec{Q})$$

The density fluctuation operators (24) with different wave vectors P and Q do not commute, which is related with the helicity or spirality accompanying the presence of the strong magnetic field [18]. They are expressed by the phase factors in the structure of operators (6) and by the vector-product of two 2D wave vectors P and Q and its projection on the direction of the magnetic field. These properties

considerably influence structure of the equations of motion for the operators and determine new aspects of the 2D electron-hole (e-h) physics.

The equation of motion for the creation and annihilation operators $d^{+}(\vec{P})$, $d(\vec{P})$ (12) and for the density fluctuation operators (8) will be deduced, when the BEC takes place on the state $k=0$. They are:

$$
\begin{aligned}
&i\hbar\frac{d}{dt}d(\vec{P})=[d(\vec{P}),\hat{H}]=(-\bar{\mu}+E(\vec{P})-\Delta(\vec{P}))d(\vec{P})-\\
&2i\sum_{\vec{Q}}\tilde{W}(\vec{Q})Sin\left(\frac{[\vec{P}\times\vec{Q}]_z l^2}{2}\right)\hat{\rho}(\vec{Q})d(\vec{P}-\vec{Q})-\\
&-\frac{1}{N}\sum_{\vec{Q}}U(\vec{Q})Cos\left(\frac{[\vec{P}\times\vec{Q}]_z l^2}{2}\right)D(\vec{Q})d(\vec{P}-\vec{Q})\\
&-\tilde{\eta}\sqrt{N}e^{i\varphi}\delta_{kr}(\vec{P},0)+\tilde{\eta}e^{i\varphi}\frac{D(\vec{P})}{\sqrt{N}};
\end{aligned}
\qquad (17)
$$

$$
\begin{aligned}
&i\hbar\frac{d}{dt}d^{\dagger}(-\vec{P})=[d^{\dagger}(-\vec{P}),\hat{H}]=(\bar{\mu}-E(-\vec{P})+\Delta(-\vec{P}))d^{\dagger}(-\vec{P})+\\
&+2i\sum_{\vec{Q}}\tilde{W}(\vec{Q})Sin\left(\frac{[\vec{P}\times\vec{Q}]_z l^2}{2}\right)d^{\dagger}(-\vec{P}-\vec{Q})\hat{\rho}(-\vec{Q})+\\
&+\frac{1}{N}\sum_{\vec{Q}}U(\vec{Q})Cos\left(\frac{[\vec{P}\times\vec{Q}]_z l^2}{2}\right)d^{\dagger}(-\vec{P}-\vec{Q})D(-\vec{Q})\\
&+\tilde{\eta}\sqrt{N}e^{-i\varphi}\delta_{kr}(\vec{P},0)-\tilde{\eta}e^{-i\varphi}\frac{D(\vec{P})}{\sqrt{N}};
\end{aligned}
$$

$$
\begin{aligned}
&i\hbar\frac{d}{dt}\hat{\rho}(\vec{P})=[\hat{\rho}(\vec{P}),\hat{H}]=\\
&=-i\sum_{\vec{Q}}\tilde{W}(\vec{Q})Sin\left(\frac{[\vec{P}\times\vec{Q}]_z l^2}{2}\right)[\hat{\rho}(\vec{P}-\vec{Q})\hat{\rho}(\vec{Q})+\hat{\rho}(\vec{Q})\hat{\rho}(\vec{P}-\vec{Q})]+\\
&+\frac{i}{2N}\sum_{\vec{Q}}U(\vec{Q})Sin\left(\frac{[\vec{P}\times\vec{Q}]_z l^2}{2}\right)\left[D(\vec{P}-\vec{Q})D(\vec{Q})+D(\vec{Q})D(\vec{P}-\vec{Q})\right];
\end{aligned}
$$

$$
\begin{aligned}
&i\hbar\frac{d}{dt}\hat{D}(\vec{P})=[\hat{D}(\vec{P}),\hat{H}]=\\
&-i\sum_{\vec{Q}}\tilde{W}(\vec{Q})Sin\left(\frac{[\vec{P}\times\vec{Q}]_z l^2}{2}\right)[\hat{\rho}(\vec{Q})\hat{D}(\vec{P}-\vec{Q})+\hat{D}(\vec{P}-\vec{Q})\hat{\rho}(\vec{Q})]+\\
&+\frac{i}{2N}\sum_{\vec{Q}}U(\vec{Q})Sin\left(\frac{[\vec{P}\times\vec{Q}]_z l^2}{2}\right)[\hat{D}(\vec{Q})\hat{\rho}(\vec{P}-\vec{Q})+\hat{\rho}(\vec{P}-\vec{Q})\hat{D}(\vec{Q})]\\
&+2\tilde{\eta}\sqrt{N}\left[e^{-i\varphi}d(\vec{P})-e^{i\varphi}d^{\dagger}(-\vec{P})\right];
\end{aligned}
$$

Following the equations of motion (49) we will introduce four interconnected retarded Green's functions at $T=0$ [28, 29]

$$
\begin{aligned}
&G_{11}(\vec{P},t)=\left\langle\left\langle d(\vec{P},t);\hat{X}^{\dagger}(\vec{P},0)\right\rangle\right\rangle;\\
&G_{12}(\vec{P},t)=\left\langle\left\langle d^{\dagger}(-\vec{P},t);\hat{X}^{\dagger}(\vec{P},0)\right\rangle\right\rangle;\\
&G_{13}(\vec{P},t)=\left\langle\left\langle \frac{\hat{\rho}(\vec{P},t)}{\sqrt{N}};\hat{X}^{\dagger}(\vec{P},0)\right\rangle\right\rangle;\\
&G_{14}(\vec{P},t)=\left\langle\left\langle \frac{\hat{D}(\vec{P},t)}{\sqrt{N}};\hat{X}^{\dagger}(\vec{P},0)\right\rangle\right\rangle;
\end{aligned}
\qquad (18)
$$

The average $\langle\ \rangle$ will be calculated at $T=0$ in HFB approximation using the ground state wave function $|\psi_g(k)\rangle$ (14).

The Green's functions (18) will be named as one-operator Green's functions because they contain in the left hand side of the vertical line only one summary operator of the types $d(P)$, $d^{\dagger}(P)$, $\hat{\rho}(P)$ and $\hat{D}(P)$. At the same time these Green's functions are two-particle Green's functions, because the summary operators are expressed through the products of two Fermi operators. In this sense the Green's functions (18) are equivalent with the two-particle Green's functions introduced by Keldysh and Kozlov in their fundamental paper [27], forming the base of the theory of high density excitons in the electron-hole description. But in difference on [27] we are using the summary operators, which represent integrals on the wave vectors of relative motions.

The equations of motion for the Green's functions in a special case, when the BEC of magnetoexcitons takes place on the state with $k=0$, are:

$$
\begin{aligned}
&(\hbar\omega+i\delta+\bar{\mu}-E(P)+\Delta(P))G_1(P,\omega)=C\\
&-2i\sum_{Q}\tilde{W}(Q)Sin\left(\frac{[P\times Q]_z l^2}{2}\right)\left\langle\left\langle\rho(Q)d(P-Q)|X\right\rangle\right\rangle_{\omega}-\\
&-\frac{1}{N}\sum_{Q}U(Q)Cos\left(\frac{[P\times Q]_z l^2}{2}\right)\left\langle\left\langle D(Q)d(P-Q)|X\right\rangle\right\rangle_{\omega}+\tilde{\eta}G_4(P,\omega)e^{i\varphi};\\
&(\hbar\omega+i\delta-\bar{\mu}+E(-P)-\Delta(-P))G_2(P,\omega)=C\\
&+2i\sum_{Q}\tilde{W}(Q)Sin\left(\frac{[P\times Q]_z l^2}{2}\right)\left\langle\left\langle d^{\dagger}(-P-Q)\rho(-Q)|X\right\rangle\right\rangle_{\omega}+\\
&+\frac{1}{N}\left\langle\left\langle d^{\dagger}(-P-Q)D(-Q)|X\right\rangle\right\rangle_{\omega}-\tilde{\eta}G_4(P,\omega)e^{-i\varphi};\\
&(\hbar\omega+i\delta)G_3(P,\omega)=C-i\sum_{Q}\tilde{W}(Q)Sin\left(\frac{[P\times Q]_z l^2}{2}\right)\\
&\times\left\langle\left\langle\frac{\rho(P-Q)\rho(Q)}{\sqrt{N}}+\frac{\rho(Q)\rho(P-Q)}{\sqrt{N}}|X\right\rangle\right\rangle_{\omega}+\\
&+\frac{i}{2N}\sum_{Q}U(Q)Sin\left(\frac{[P\times Q]_z l^2}{2}\right)\left\langle\left\langle\frac{D(P-Q)D(Q)}{\sqrt{N}}+\frac{D(Q)D(P-Q)}{\sqrt{N}}|X\right\rangle\right\rangle_{\omega};\\
&(\hbar\omega+i\delta)G_4(P,\omega)=C-i\sum_{Q}\tilde{W}(Q)Sin\left(\frac{[P\times Q]_z l^2}{2}\right)\\
&\times\left\langle\left\langle\frac{D(Q)\rho(P-Q)}{\sqrt{N}}+\frac{D(P-Q)\rho(Q)}{\sqrt{N}}|X\right\rangle\right\rangle_{\omega}+\\
&+\frac{i}{2N}\sum_{Q}U(Q)Sin\left(\frac{[P\times Q]_z l^2}{2}\right)\left\langle\left\langle\frac{D(Q)\rho(P-Q)}{\sqrt{N}}+\frac{\rho(P-Q)D(Q)}{\sqrt{N}}|X\right\rangle\right\rangle_{\omega}\\
&+2\tilde{\eta}\left[e^{-i\varphi}G_1(P,\omega)-e^{i\varphi}G_2(P,\omega)\right];
\end{aligned}
$$

V. DYSON EQUATION AND SELF-ENERGY PARTS

Using Zubarev's procedure [29] for the Green's function we obtain a closed system of Dyson equation for the Green's functions in the forms:

$$
\sum_{j=1}^{4}G_{1j}(\vec{P},\omega)\Sigma_{jk}(\vec{P},\omega)=C_{1k};\qquad k=1,2,3,4 \qquad (20)
$$

The self-energy parts $\Sigma_{jk}(\vec{P},\omega)$ contain the different average values of the two-operator products. They were calculated using the ground state wave function $|\psi_g(0)\rangle$ taken with $k=0$ and have the expressions:

$$
\begin{aligned}
&\left\langle D(\vec{Q})D(-\vec{Q})\right\rangle=4u^2v^2N;\\
&\bar{\mu}=-\Delta(0)+2v^2(B_{i-i}-2A_{i-i}+\Delta(0));\\
&\left\langle D(\vec{Q})d(-\vec{Q})\sqrt{N}\right\rangle=\left\langle d^{\dagger}(\vec{Q})D(-\vec{Q})\sqrt{N}\right\rangle=-2uv^3N;\\
&\left\langle d(0)\right\rangle=\left\langle d^{\dagger}(0)\right\rangle=uv\sqrt{N};\qquad \tilde{\eta}=-(\Delta(0)+\bar{\mu})v
\end{aligned}
\qquad (21)
$$

All these averages are extensive values proportional to N or $\sqrt{N}$, they essentially depend on the small parameters of the types u^2v^2 or uv^3, or uv.
The cumbersome dispersion equation is expressed in general form by the determinant equation:

$$\det\left|\Sigma_{ij}(\vec{P},\omega)\right| = 0; \qquad (22)$$

We introduced some simple approximations which allow calculating our complicate equation (22). They are $\Delta(\vec{P}) \approx \Delta(0);\ U(\vec{P}) \cong U(0)e^{-\frac{P^2l^2}{2}},\ U(0) = 2A_{i-i}$. Following these transformations we obtained results that are shown in the Figures 1, 2, 3. It is spectrum of collective elementary excitations. Three of them are energy branches, whereas another three are quasienergy branches representing the mirror reflection of the energy branches. Between three energy branches two of them are excitonic branches and one of them is the acoustic plasmon branch. One-exciton energy branch has an energy gap due to the attractive Hartree-type interaction terms, which it is needed to be got over during the excitation as well as a roton-type section in the range of the intermediary values of the wave vectors. At higher values of the wave vector its dispersion law tends to saturation. Another two-exciton energy branch is interpreted by us as being the previous one-exciton energy branch accompanied by the excitation of an condensate exciton with wave vector k=0, the extraction of which from the Hartree-type attractive environment needs also energy.

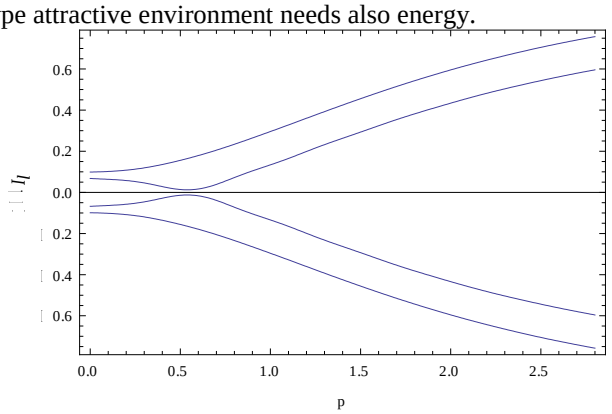

Fig. 1 The exciton branches of the energy spectrum of collective elementary excitations of the Bose-Einstein condensed magnetoexcitons on the wave vector $\vec{k} = 0$, calculated in HFBA, the filling factor $\nu^2 = 0{,}1$.

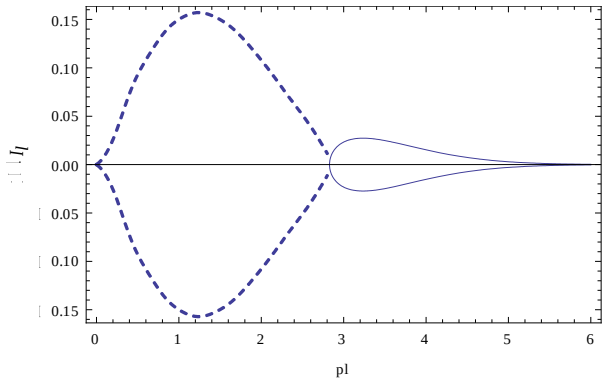

Fig. 2. The dispersion law of acoustical plasmon branch in the presence of the BEC of magnetoexcitons on the wave vector $\vec{k} = 0$, calculated in HFBA, filling factor $\nu^2 = 0{,}1$.

The third energy branch taking part in this set is the acoustical plasmon branch. It reveals the absolute instability of the spectrum in the range of small and intermediary values of the wave vector k and has a very small real values tending to zero in the limiting case k→∞. The optical plasmon dispersion law is gapless with quadratic dependence in the range of small wave vectors and with saturation-type dependence in the remaining part of the spectrum.

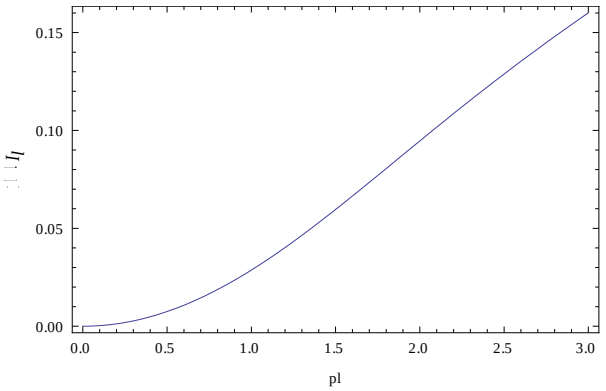

Fig. 3. The dispersion law of optical plasmon branch in the presence of the BEC of magnetoexcitons on the wave vector $\vec{k} = 0$, calculated in HFBA, the filling factor $\nu^2 = 0{,}1$.

VI. CONCLUSION

The energy spectrum of the collective elementary excitations of a 2D electrom-hole (e-h) system situated in a strong perpendicular magnetic field in a state of Bose-Einstein condensation (BEC) with wave vector $\vec{k} = 0$ was investigated in the frame of Bogoliubov theory of quasiaveraes. The starting Hamiltonian describing the e-h system contains not only the Coulomb interaction between the particles lying on the lowest Landau levels, but also the supplementary interaction due to their virtual quantum transitions from the LLLs to the excited Landau levels and return back. This supplementary interaction generates after the averaging on the ground state BCS-type wave function the direct Hartree-type terms with attractive character, the exchange Fock-type terms giving rise to repulsion as well as the similar terms arising after the Bogoliubov $u-v$ transformation. The interplay of these three parameters gives rise to the resulting different from zero interaction between the magnetoexcitons with wave vector $\vec{k} = 0$ and to stability of their BEC as regards the collapse. It influences also on the energy spectrum as well as on the collective elementary excitations. It consists from four branches. Two of them are excitonic-type branches, one of them being the usual energy branch whereas the second one is the quasienergy branch representing the mirror reflection of the energy branch, which will be described below. Another two branches are the optical and acoustical plasmon branches. The exciton energy branch has an energy gap due to the attractive interaction terms, which is needed to be got over during the excitation as well as a roton-type section in the range of intermediary values of the wave vectors. At higher values of wave vector its dispersion law tends to saturation. The optical plasmon dispersion law is gapless with quadratic dependence in the range of small wave vectors and with saturation-type dependence in the remaining part of the spectrum. The

acoustical plasmon branch reveals the absolute instability of the spectrum in the range of small and intermediary values of the wave vectors. In the remaining range of the wave vectors the acoustical plasmon branch has a very small real value of the energy spectrum tending to zero in the limiting case of great wave vectors.

REFERENCES

[1] M.A.Liberman and B.Johanson, Uspekhi Fiz. Nauk **165**, 121 (1995).
[2] Dong Lai, Rev. Mod. Phys. **73**, 629 (2001).
[3] H.L.Stormer, Rev. Mod. Phys. **71**, 875-889 (1999).
[4] Perspectives in Quantum Hall Effects, edited by S. Das Sarma, and A. Pinczuk (John Wiley & Sons, Inc., New York, 1997).
[5] E.I.Rashba, Pure and Applied Chem. **67**, 409, (1995).
[6] D.C.Tsui, H.L.Stormer, and A.C.Gossard, Phys. Rev. Lett. **48**, 1559, (1982).
[7] R.B.Laughlin, Phys. Rev. Lett. **50**, 13, (1983).
[8] A.H.MacDonald, E.H.Rezayi, and D.Keller, Phys. Rev. Lett. **68**, 1939, (1992).
[9] F.D.M.Haldane, Phys. Rev. Lett. **51**, 605, (1983).
[10] B.I. Halperin, Phys. Rev Lett **52**, 1583, (1984).
[11] J.K.Jain, Phys. Rev. Lett. **63**, 199, (1989).
[12] D.Arovas, J.R.Schriffer, and F.Wilczek, Phys. Rev. Lett. **53**, 722, (1984).
[13] S.M.Girvin, A.H.MacDonald and P.M.Platzman, Phys. Rev. B **33**, 2481, (1986).
[14] F.G.H.Haldane and E.H.Rezayi, Phys. Rev. Lett. **54**, 359, (1985).
[15] I.V.Lerner and Yu.E.Lozovik, Zh. Eksp. Teor. Fiz. **78**, 1167, (1980).
[16] I.V.Lerner and Yn.E.Lozovik, J. Low Temper. Phys. **38**, 333, (1980).
[17] I.V.Lerner and Yn.E.Lozovik, Zh. Eksp. Teor. Fiz. **80**, 1488, (1981) [Sov.Phys.-JETP **53**, 763, (1981)].
[18] A.B.Dzyubenko and Yn.E.Lozovik, Fiz. Tverd. Tela (Leningrad) **25**, 1519, (1983); **26**, 1540, (1984) [Sov. Phys. Solid State **25**, 874, (1983); **26**, 938, (1984)]; J.Phys. A, **24**, 415, (1991).
[19] D.Paquet, T.M.Rice, and K.Ueda, Phys. Rev. B **32**, 5208, (1985); T.M.Rice, D.Paquet and K.Ueda, Helv. Phys. Acta **58**, 410, (1985).
[20] S.A.Moskalenko, M.A.Liberman, D.W.Snoke, and V.Botan, Phys. Rev. B, **66**, 245316, (2002);
[21] S.A.Moskalenko, M.A.Liberman, D.W.Snoke, V.Botan and B. Johansson, Physica E **19**, 278, (2003); V.Botan, M.A.Liberman, S.A.Moskalenko, D.W.Snoke and B.Johansson, Physica B **346-347 C**, 460, (2004).
[22] S.A.Moskalenko, M.A.Liberman, P.I.Khadzhi, E.V.Dumanov, Ig.V.Podlesny and V.Botan, Sol. State Comm. **140/5**, 236, (2006); S.A.Moskalenko, M.A.Liberman, P.I.Khadzhi, E.V.Dumanov, Ig.V.Podlesny and V.Botan, Physica E, **39/1**, 137-149, (2007)
[23] V.M.Apalkov and E.I.Rashba, Phys. Rev. B **46**, 1628, (1992); ibid. **48**, 18312, (1993); idem., Pisma Zh. Eksp. Teor. Fiz. **54**, 160, (1991); ibid. **55**, 38, (1992).
[24] X.M.Chen and J.J.Quinn, Phys. Rev. Lett. **70**, 2130, (1993).
[25] Bose-Einstein Condensation, edited by A.Griffin, D.W.Snoke, and S.Stringari (Cambridge University Press, Cambridge, 1995).
[26] L.V.Butov, A.L.Ivanov, A.Imamoglu, P.B.Littlewood, A.A.Shashkin, V.T.Dolgopolov, K.L.Campman, and A.C.Gossard, Phys. Rev. Lett. **86**, 5608, (2001).
[27] L.V.Keldysh, and A.N.Kozlov, Zh. Eksp. Teor. Fiz. **54**, 978, (1968) [Sov.Phys.- JETP **27**, 52, (1968)].
[28] A.A.Abrikosov, L.P.Gor`kov and I.E. Dzyaloshinskii Methods of quantum field theory in statistical physics (Dover, New York, 1975).
[29] D.N.Zubarev Sov.Phys.Uspekhi Fiz.Nauk **71**, 71(1960)

Influence of Adsorption of Organic Molecules on the PL Spectra of Porous Nanostructure and Carbon Nanotubes, Covering the Surface of Silicon.

V.G. LITOVCHENKO, T.I. GORBANYUK

V. Lashkaryov Institute of Semiconductor Physics of NAS Ukraine
Prospect Nauki, 41, 03028 Kiev, Ukraine; e-mail: lvg@isp.kiev.ua

Surface layers can be very sensitive to adsorption of organic molecules, introduced from liquid solution. So, it will be play the role of the detector for different, sometime ecological dangerous, molecules included organic.

Our research has been focused on the preparation and characterization of layered semiconductor structures based on porous silicon (Si_{por}) with embedded nanoclusters of catalytic (Pd, W, Ni), noncatalytic (Cu) and metal-oxide (CuO_x, NiO, WO_x) by means of I(V) characteristics and PL spectra undo organic molecule adsorption and H_2S gas adsorption. The distribution of catalytically active metal on the thickness of porous silicon studied by secondary ion mass spectroscopy (SIMS). The thin metal films were deposited by dc magnetron sputtering from Pd, W, Ni, Cu target in Ar on unheated $Si_{por}/_cSi$ substrate. The morphology of catalytic active composite has been characterized by AFM and SEM.

The adsorption of the donor (glycine, H_2S) and acceptor (methionine) types of molecules was investigated in concentration range of 6,7– 67 μmol/l and 1-100 ppm for . H_2S. Methionine is essential amino acids, belongs to a class of non-polar amino acids with hydrophobic radical. Glycine is a class of polar amino acids with hydrophilic radical. As a result of our experimental studies it was showed that the photoluminescense intensity decreases during methionine adsorption on $Si_{por}/Me(MeO_x)$ composite, while the adsorbed molecules of glycine leads to an increase in intensity photoluminescense, i.e. the signal is changing in two opposite directions.

It was aslo found that the sensor structures with porous silicon filled by palladium, is more sensitive to glycine, while the filling of the pores by copper leads to increased sensitivity to methionine. The structures with W and WO_3 clusters in Si_{por} are more sensitive to adsorption of hydrogen sulfide. Selectivity fo these structures in relation to different types of adsorption of organic compounds makes them promising for producing multi sensor.

A possible mechanism of adsorption sensitivity and selectivity of layered semiconductor structures based on porous silicon filled by different metal clusters to adsorbed amino acids and H_2S gas was proposed.

Photoelectric Converters: Current State Analysis and Prospects of Evolution

Y.I. YAKIMENKO[1], G.M. MLADENOV[2], V.M. SPIVAK[1], A.V. BOGDAN[1], V.M.KOVAL[1]
[1]*National Technical University of Ukraine "Kiev Polytechnic Institute", Kiev, Ukraine*
[2]*Institute of Electronics, Bulgarian Academy of Sciences, Sofia, Bulgaria*
viktor_m53@mail.ru

***Abstract* – This review provides the analysis of current state and prospects of evolution of photoelectric converters (PEC). There are shown the directions, ways and means of PEC research and development. It is discussed the state of research in Ukraine and industrialized countries, given the forecast of changes in the efficiency of converting solar energy into electricity as well as the cost of industrial production of solar cells. It is shown the comparative characteristic properties of amorphous and nanocrystalline silicon solar cells. The recommendations about promising areas of research and development to improve the efficiency of solar cells are included.**

***Index Terms* – nanocrystalline silicon, nanomaterials, photoelectric converters, photovoltaics, solar power.**

I. INTRODUCTION

In recent years, the subjects of nanotechnology and nanomaterials are the scientific priorities of industrialized countries. The development of nanotechnology and nanomaterials is considered as a new industrial revolution. In the coming decades, the efficiency of nanotechnology will determine the status of every developed nation in the world.

Ukrainian government does not stand apart from these trends. In a joint order of Ministry of Education and Science of Ukraine and National Academy of Sciences of the November 26, 2009 №1066/609 "The approval of the main research directions and the most important issues of fundamental research in 2009-2013 in Ukraine" the sections 1.4.5. "Nanophysics and nanotechnology", and 1.6.5. "Nanostructured (nanodisperse, nanocrystalline) materials" are specially underlined.

The silicon photoelectric converters (PEC) efficiency at level 25-28% and a unit cost 2,0-2,5$/W of generated electric power, impacted on the development of photovoltaic systems. The main directions in this area include photoelectric converters based on monocrystalline, multicrystalline, amorphous silicon, triple-A^3B^5 semiconductor compounds, systems Cu-In-Se [1-5].

II. THE ANALYSIS OF PROBLEMS AND THE FORECAST OF PHOTOVOLTAICS DEVELOPMENT IN UKRAINE.

The overcoming of major obstacles to the development of solar energy - the high cost of electricity and thermal energy, which is generated by solar plants, will be implemented due to a gradual increase in the cost of fossil fuels and the introduction of the environmental component in rates for electricity and heating.

The key factors that have influenced on promoting of the use of solar energy in the world till year 2030:

- the compliance with the Kyoto protocol on greenhouse gas emissions;
- Government support of scientific and technical organizations specializing in the development of highly efficient solar-energy equipment. Creating the necessary legal and economic conditions and mechanisms to stimulate development of solar energy;
- the existence of a scientific and technical human resources, which can ensure development and establish mass production of highly competitive solar energy equipment, as well as construction and operation of solar power plants.

Photoelectric converter production grows 25-30% per year. It is forecasted that their production reaches a value 16 GW in 2012.

The forecast of photovoltaics development is shown in Fig.I.

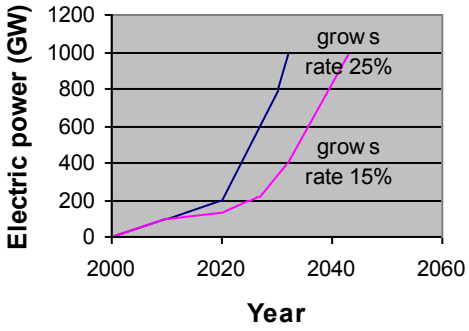

Fig I. The prospect of photovoltaic systems

Table I shows the forecasted volumes and the dynamics of photovoltaics development in Ukraine for the period up to 2030.

Taking into account the current level of technology of converting solar energy into electricity and heating as well as the possible progress in this area over the period up to 2030, we can conclude that a significant contribution to the overall energy balance of the country can be made at the expense of large-scale introduction of two key technologies:

- first phase 2011-2015 – solar photoelectric power plants electricity production distant from the power network. The second phase 2015-2030 – operation in the united energy system of Ukraine.
- the production of low-grade energy by solar installations for partial or full supply of hot water

in the warm season (April-October) for industrial and agricultural enterprises, households, fitness and spa facilities, schools, etc.

-

TABLE I. KEY PARAMETERS OF PHOTOVOLTAICS IN UKRAINE FOR THE PERIOD UP TO 2030

Year	Capacity (MW)	Electricity production thousand kWh
2010	60	102000
2015	120	204000
2020	200	340000
2025	300	510000
2030	400	680000

Moreover, we assume the use of solar energy in industrial processes: for the production of fresh water, in water-pumps, in high-temperature metallurgy, in solar refrigeration and domestic refrigeration, in solar dryers and in air-conditioning. Nevertheless, for the period until 2012 the use of solar energy in these technologies will not make a significant contribution to the overall energy balance of the country.

It should be noticed that the development strategy of photovoltaics in the world's leading countries (USA, Japan, Germany, Australia, India, China, etc.) has a goal to cover consumption up to 30%. The concept of global energetic (Fig.II) clearly shows the future grows of solar energy.

Leading Japan companies (Sharp, Kyocera, Mitsubishi) produce photoelectric modules on the basis of multicrystalline, monocrystalline, amorphous silicon, and cover 45% of world production of photoelectric systems (Fig.III) [6].

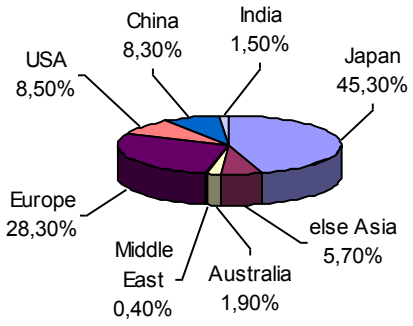

Fig. III. The distribution of world production of photoelectric systems based on multicrystlline, monocrystalline silicon. [6]

According to the USA program SAI (“Solar America Initiative”) [7], it is provided a strong support for U.S. companies and universities (more than 10 billion $), engaged in the development and large-scale production of photoelectric modules and systems

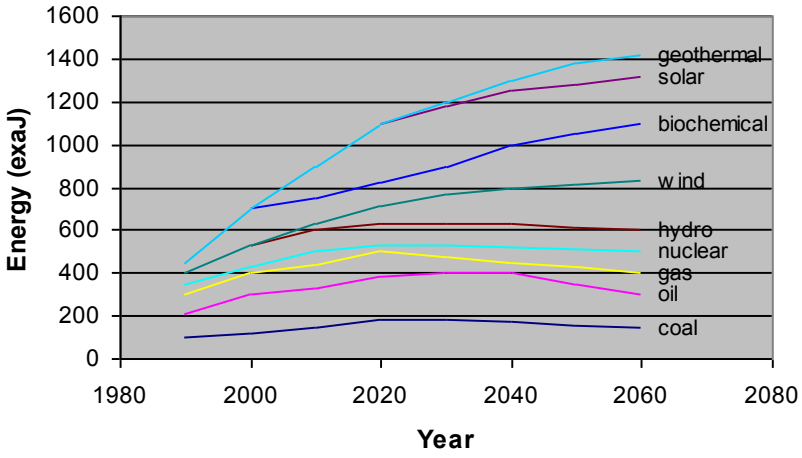

Fig II. The concept of global energetic evolution

TABLE II. FORECAST OF CHANGES IN CONVERSION EFFICIENCY AND THE COST OF PEC.

PEC type	Modern level	Efficiency, % 2010.	Efficiency, % 2020.	Efficiency, % 2030.
PEC based on monocrystalline silicon	13-16 (19)	16 (20)	19 (25)	22 (25)
Thin-film silicon solar cells	10 (14,7)	12 (15)	14 (18)	18 (20)
CIS (Cu-In-Se) – PEC	10–12 (18,9)	13 (19)	18 (25)	22 (25)
PEC based on A^3B^5 compounds	38,9 (40,2)	28 (40)	35 (45)	40 (50)
Electrochemical PEC	(10,5)	6 (10)	10 (15)	15 (18)

. In the scientific aspect it is defined the development of: new low-cost materials with high efficient capacity, chemical stability, efficiency of industrial processes; thin films of semiconductor and organic semiconductors; silicon wafers thinner than 100 mcm; silicon solar cells with conversion efficiency 25%; nanostructured materials; multitransition PES; thermphotoelectric converters; new types of concentrating systems, etc.

To ensure the competitiveness of photoelectric systems (PES) with other sources of energy (fossil fuels, nuclear power, other renewable energy) it is necessary to reduce the cost of a watt peak power of at least 2 times (less than

2,8$/W) and increased to year 2030 the production volume in 1000 times [8-9]. Also, it must be taken into consideration the prevalence of the basic material in the nature, environmental cleanliness, not only finished PES, but their production processes, energy costs of production and a payback period.

Nowadays, more than 90% of the total production of the PES is flat-panel modules made of crystalline and multicrystalline silicon. At this stage of development of photovoltaics in the light of the above, silicon has a leading position. In this direction, it is planned to increase the conversion efficiency from 12-16% to 20-22% due to improved design and technological parameters and to reduce the consumption of silicon by more than 2 times, since 50% of the module is the initial price of silicon wafers. It should be noted that, the use of concentrator and bilateral PEC can be an effective way to reduce the cost [10]. Table II shows the forecast of increasing the conversion efficiency of the basic types of PEC [11].

According to expert estimates in the coming decades it is expected a real "boom" in the industry. It should be noted that the main objectives of this production – improving conversion efficiency and reducing the cost of generated electricity – are impossible without providing cheap raw materials in sufficient quantity and of reducing energy consumption in the manufacture process. Highly efficient photoelectric converters based on gallium arsenide and related materials because of the high cost should be used to power spacecrafts.

The main raw materials for photovoltaic production are polycrystalline, multicrystalline and monocrystalline silicon, which cost has increased recently. Also there are problems with the shortage of raw materials. The cost of the silicon in the price of photoelectric converters (PEC) is at least 50%. It is necessary to develop new technological approaches for reducing the amount of materials used in production combined with flexible adjustment of production to manufacture ultra-thin wafers of "solar" and nanocrystalline silicon. In this case, the risk of production of basic products is dramatically decreasing.

Modern production of photoelectric converters is based on the use of energy-intensive processes, such as thermal diffusion processes, screen printing, in which the operating temperatures reach 1070-1300K. There is a need of creating new heterostructure converters using cheap materials, low-labor and low-energy processes.

The decision of increasing the conversion efficiency of PEC for well-known technologies is usually associated with an increasing of the complexity of production, costs of energy and materials, which leads to an inevitable increase in price. It is usually used the silicon with a high carrier lifetime, which is typical for higher quality, and hence, more expensive silicon. In this aspect it is necessary to develop low-cost technological process that would ensure the improvement of this parameter.

The conversion efficiency of today's photoelectric converters on silicon is relatively low, because of conversion losses of short and infrared solar radiation, losses as a result of surface and bulk recombination, as well as optical reflectivity. It highlights the need for new methods of converting short-wave radiation, technological methods of passivation, gettering and nanostructuring of surfaces.

The solution of these problems will give the opportunity to organize highly profitable production of photoelectric converters and modules; stand-alone energy sources for different purposes; combined photothermogenetarors, that produce both electricity and heating; irrigation systems; drinking water production; photoelectric electrolyzers, portable photoelectric devices for disinfection, etc.

One of the way to reduce the cost of photoelectric modules is to create on their basis the architectural blocks. Energy architectural glass blocks are manufactured for different purposes (for example, ASI Glass, Austria):

- shading to reflect light;
- lighting, light transmission;
- heat;
- solar panels to produce electricity.

TABLE III. PARAMETERS OF THIN-FILM SILICON PEC.

Parameters	Crystalline Si (thin films)	Amorphous silicon	Nanocrystalline silicon	Organic Semiconductors
Unit cost, $/W	2,4-2,7	2,0-2,4	1,7-1,8	1,5
The prospects of reducing the costs, $/W	1,75	1,25	0,9-1	0,5
Conversion efficiency, %	15-20	10–13,6	14-16	5-7

All this can be accomplished with the use of optical coatings and thin-film solar cells. For example, by changing the conditions of film deposition ITO (transparent conductive coatings based on oxides of indium and tin), we can control the opacity of different regions of the spectrum [12]. ITO film can serve as an excellent reflector of infrared (heat) radiation, ie, implement cooling. By changing the conditions of its deposition, we can ensure the transmission of infrared radiation, ie provide heating. The closest prototype unit to produce electrical energy is a solar cell based on amorphous silicon – ASI Thin Film Solar Cells.

III. THE USE OF NANOSTRUCTURED CRYSTALLINE SILICON TO CREATE THIN-FILM PEC

The construction in which a film battery is placed between the glasses remains, but solar battery runs on nanocrystalline silicon with improved technical performance. Foe example, the U.S. company UNI-Solar manufactures thin-film modules on the basis of amorphous silicon (the nearest prototype of the proposed production). In 2006 their solar battery's capacity was 25 MW. In 2010 - the planned production capacity was 300 MW, ie increased by 12 times.

Table III shows the comparative characteristics of the parameters of thin-film silicon PEC.In nanocrystalline films by changing the size of the nanocrystallites and the band gap can be optimized the layer structure of the PEC for the conversion of various ranges of the spectrum, and thus, theoretically increase the conversion efficiency of 50-60%. These achievements become possible when the technology of thin-film solar cells based on nanocrystalline semiconductors, in particular, nanocrystalline silicon is developed.

Table IV shows the comparative analysis of properties of nanocrystalline silicon and amorphous silicon (on the basis of which, a large-scale production lines are opened in Japan and USA).

Thin-film photovoltaic modules can significantly improve the specific energy characteristics: the conversion efficiency at 8% - 600W/kg, 9% - 1250 W/kg, 10% - 2000 W/kg. That is why they are seen as a close future of photovoltaic systems, including space purposes.

IV. CONCLUSIONS AND CHALLENGING AREAS OF RESEARCH AND DEVELOPMENT

The results of our studies led to creating the photoelectric converters with an efficiency of more than 21% (monocrystalline silicon wafers with size of 100x100 mm).

The main directions of improving the parameters of photoelectric converters are:

- optimization of the parameters of existing converters;
- improving the manufacturing technology of PEC in order to reduce material and energy costs of its production;
- the appliance of new materials in PEC technology.

From the authors point o view, the following ways to improve the efficiency of PEC are possible:

1. Development of technological methods of producing photoelectric structures that preserve the quality of the original semiconductor. The solution of this problem gives a rise of carrier lifetime, which accordingly increases the rate of collection of photogenerated charge carriers.
2. Creating a specially located doped regions in the semiconductor material that create the so-called pulling electric field in three-dimensional space, which increases the mobility of charge carriers in the direction of current collectors.
3. The extension of the PEC absorption spectrum in the direction of the ultraviolet and infrared spectral regions.
4. Decrease the series resistance of the contact transition zones and contacts.
5. The use of new, more efficient optical and protective coatings.
6. Creation of new types of heterojunctions using alloys of amorphous and nanocrystalline silicon.

TABLE IV. COMPARATIVE CHARACTERISTICS OF THE PROPERTIES OF AMORPHOUS AND NANOCRYSTALLINE SILICON [12-16]

Parameters	Amorphous silicon	Nanocrystalline silicon	Nanocrystalline silicon (Section III of this paper)
1. Band gap, eV	1,75	1,96–2,2	1,85–2,25 (depending on the size of crystallites and the properties of the interface)
2. Electron mobility, $cm^2/V \cdot s$	0,1	40	42-45
3. Hole mobility, $cm^2/V \cdot s$	0,001	0,2	0,22-0,25
4. Photosensitivity (the ratio of photoconductivity to dark conductivity)	$7 \cdot 10^3$	$5 \cdot 10^5$	$(5,6–6,4) \cdot 10^5$
5. Photosensitivity heterostructures in the visible range, mA/lm	12	45	79-135
6. Photosensitivity of the heterostructures at a wavelength of 350 nm, A/W	0,3-0,35	0,4-1,1	6,95
7. Degradation level, %	30-35	10-15	8-10
8. Manifestation of the degradation effect Staebler–Wronski	yes	no	no
9. Toxicity of the process	yes	yes	no

REFERENCES

[1] *Наноэлектроника: монография в двух книгах. Кн. 1. Введение в наноэлектронные технологии* / Г. М. Младенов, В. М. Спивак, Е. Г. Колева, А. В. Богдан.– Киев-София: Аверс, 2010. – 334 с.

[2] *Наноэлектроника: монография в 2 кн. Кн. 2. Наноструктурированные материалы и функциональные устройства* /Ю.И. Якименко, А. Н. Шмырева, Г. М. Младенов, В. М. Спивак, Е. Г. Колева, А. В. Богдан; под общей редакцией действительного члена Национальной академии наук Украины Ю.И. Якименко. – Киев-София: Аверс, 2011. – 394 с

[3] Green M.A. *Third generation photovoltaic – theoretical and experimental progress* // Proc. of the 19 th European Photovoltaic Solar Energy Conf. and Exhibition. – 2004. - Paris (France). - P. 12 - 19.

[4] Roca F., Carabe J. *Silicon heterojunction cells* // Proc. of the 19 th European Photovoltaic Solar Energy Conf. and Exhibition. - Paris (France). - 2004. - P. 1321 - 1328.

[5] Longo C., De Paoli M. Dye – *Sensitized Solar Cells: A Successful Combination of Materials* // J.

Braz. Chem. Soc. - 2003. - Vol. 14, № 6. - P. 889 – 901.

[6] Aratani F., Goto S. *The Present status and future direction of technology development for photovoltaic power generation in Japan* // Proc. of the 20 th European Photovoltaic Solar Energy Conf. - Barcelona (Spain). - 2005. - P. 2846 - 2849.

[7] Barnett A., Honsberg C., Kirkpatrick D. *New US Ultra High Efficiency R&D Programme* // Proc. of the 21 th European Photovoltaic Solar Energy Conf. - Dresden (Germany). - 2006. - P. 124 - 128.

[8] Swanson R.M. *A Vision for crystalline silicon solar cells* // Proc. 19 th European Photovoltaic Solar Energy Conf. - Paris (France). - 2004. - P. 968 - 974.

[9] Унтила Г.Г., Кост Т.Н., Чеботарева А.Б., Закс М.Б., Ситников А.М., Солодуха О.И. *Новый тип высокоэффективных двусторонних кремниевых солнечных элементов с внешними шинами и проволочной контатной сеткой* // Физика и техника полупроводников. - 2005. - Т.39, Вып.11. - С. 1393 - 1398.

[10] Gasman L. *Thin film and organic PV: New Applications for solar energy* // Nanomarkets. - 2006. - P. 1- 61.

[11] Arya R.R. *Technology and market challenges to mainstream thin – film photovoltaic modules and applications* // Proc. of the 19 th European Photovoltaic Solar Energy Conf. - Paris (France). - 2004. - P. 2024 – 2029.

[12] Repmann T., Appenzeller W. *Advanced PECVD processes for thin film silicon solar cells on glass* // Proc. of the 19 th European Photovoltaic Solar Energy Conf. - Paris (France). - 2004. - P. 1334 - 1339.

[13] Jun K.N., Stiebig H. *Amorphous silicon multilayer solar cell deposited by PECVD method* // Proc. of the 14 th European Photovoltaic Solar Energy Conf. - Paris (France). - 2004. - P. 1387 - 1390.

[14] Hofmann M., Glunz S., Preu R., Willeke G. *21% - efficient silicon solar cells using amorphous silicon rear side passivation* // Proc. of the 21 th European Photovoltaic Solar Energy Conf. - Dresden (Germany). - 2006. - P. 124 - 128.

Synthesis and Characterization of Colloidal PbS Quantum Dots in Gelatin

Anatolie MITIOGLU, Cornel GHERMAN, Renata LASCOVA,
Anatolii CUHARUC, Anatolie GAVRILUŢA, Leonid CULIUC
Institute of Applied Physics of the Academy of Sciences of Moldova
anatol.mitioglu@phys.asm.md

***Abstract* – Colloidal solutions of lead sulphide (PbS) quantum dots (QDs) stabilized in gelatine were obtained using a novel simple method. Nanoparticle sizes were tuned during the synthesis by means of reaction temperature. In addition, the effect of acidity of solution, of reagents concentrations and of S to Pb molar ratio was investigated. Transmission electron microscopy (TEM) and energy-dispersive X-ray spectroscopy (EDX) was used to characterize the size and composition of PbS nanoparticles. Also, the peculiarities of photoluminescence (PL) spectra of PbS QDs in gelatine were studied. It was observed that PL spectrum consists of a relatively narrow excitonic band with the maximum located at 0.95– 1.3 eV depending on the QDs size.**

***Index Terms* – colloidal solution, gelatin, lead sulfide (*PbS*), photoluminescence, quantum dots.**

I. INTRODUCTION

Specific properties of nano-sized materials and the progress of the last two decades in nanotechnology necessitates to face the task of finding methods of commercial production of different nanomaterials with controllable properties for various applications, including those based on nanocrystals.

Among important group IV–VI semiconductors, *PbS* QDs have attracted considerable attention owing to their especially small direct band gap (0.41eV) and larger excitation Bohr radius (18 nm) [1] and have been widely used in many applications such as photography, Pb^{2+} ion-selective sensors, IR detectors and solar absorbers [2–4].

Recently, these nanomaterials have received great attention for their promising use in medicine. A key issue in evaluating the utility of these materials is assessing their potential toxicity - due to their inherent chemical composition [1]. In addition, *PbS* QDs are an example of nanomaterials that have been shown to be useful as an alternative to luminescent dyes for biological imaging, due to their bright luminescence, narrow emission, broad UV excitation and high photostability.

So far various methods for the preparation of semiconductor QDs in liquid media have been proposed [3, 5, 6]. Most of them use different surfactants as stabilizers for QDs, thus determining their chemical and physical properties, such as solubility, aggregative and kinetic stability, as well as stability against photocorrosion; they can change the position of the optical absorption edge or activate/suppress luminescence.

In this work, we propose a novel easy method of the synthesis of *PbS* QDs in aqueous solutions of a natural polymer, gelatin, and present the results of our investigation of their optical properties affected by synthesis conditions such as concentration of reagents, germination and growth temperature, molar ratio *S/Pb* and *pH* of the solution.

The modification of the reaction of formation *PbS* QDs offers a possibility to obtain the QDs sized in the range of 2-20 nm; the size can be estimated from the excitonic bands in photoluminescence/optical absorption spectra within the range of 800-1500 nm.

II. MATERIALS AND METHODS

Materials. The materials used in this work such as sodium sulfide $Na_2S{\cdot}9H_2O$ (ACS reagent), gelatin powdered (Ph. Eur.) and lead (II) nitrate (ACS reagent) were purchased from Aldrich and used without further purification.

Synthesis of colloidal solution of PbS QDs.

In a typical experiment, preparation of colloidal solutions of *PbS* QDs stabilized with gelatin consists of three steps:

I) producing an aqueous solution of gelatin (0.1-20 % by mass) and lead (II) nitrate (10^{-4}-0.1 M): 1 *gr* of gelatin was dissolved in 10 mL of 0.1 M $Pb(NO_3)_2$ upon slight heating in a conical flask;

II) heating the solution up to the required temperature (in the range 20 ÷ 90 °C) while stirring;

III) adding to the solution obtained 1 mL of the aqueous solution of 10^{-3}-1 M Na_2S dropwise, keeping stirring at the temperature indicated. This step lasts about 5 min.

Optical characterization.

The photoluminescence (PL) emission spectra were investigated using a grating monochromator and a photodetectors (IR photomultiplier ФЭУ-62, for wavelengths λ<1.1μm and/or InGaAs photodiode – 1μm <λ < 1.6μm).

Taking into account the fact that the emission spectrum of *PbS* QDs is located in the near IR region [7], He-Ne laser (λ_{L1} = 633nm) and the second harmonic of YAG:Nd laser (λ_{L2} = 532 nm) were used as excitation sources.

The absorption spectra in the same region were recorded by means of Shimadzu UV-3600 spectrophotometer. In order to ensure that the PL emission corresponds to the radiative recombination of excitons, the comparison between the emission and absorption spectra was carried out [8].

III. RESULTS AND DISCUSSION

Photoluminescence properties of gelatin stabilized PbS nanoparticles.

The PL properties of gelatin stabilized *PbS* nanoparticles in different applications are investigated and described in several papers and books [9-11].

In this work the PL spectra of the colloids prepared have been recorded and the QDs sizes correlated to the position of

the spectral maxima.

The solutions of *PbS* nanoparticles exhibit clear exciton peaks and bright band-edge exitonic luminescence at room temperature located in the near-IR spectral range (Fig. 1). The PL broad bands are mostly attributed to the recombination of the carriers trapped in surface states of bare *PbS* QDs. These surface defects are associated with Pb^{2+} and S^{2-} vacancies (such as nonstoichiometric defects and dangling bonds), that can induce nonradiative transitions or radiative emission [12], resulting in the degrading of luminescence properties.

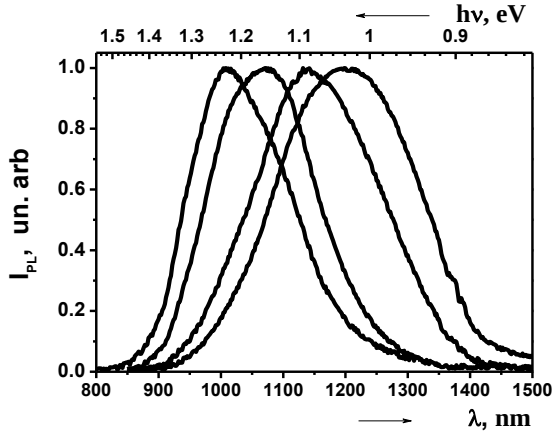

Fig. 1. Photoluminescence of PbS QDs synthesized in gelatin.

Generally, the PL of these QDs is intricate because it is sensitive to the synthesis conditions, crystalline sizes and shapes.

TEM analysis.

The particles sizes of the synthesized colloids were determined by TEM. The typical micrograph in Fig. 2 shows *PbS* QDs of about 4 nm in diameter coated with gelatin chains. This suggests that the core-shell products exhibit uniform sphere-shaped particles.

Fig. 3 shows the EDX spectrum of the synthesized *PbS* QDs in gelatin. The strong peaks for *Pb* and *S* in the spectrum confirmed the main components of the *PbS* QDs. EDX analysis also indicated the presence of copper (*Cu*) on the surface of *PbS* QDs, which was due to the copper substrate used.

Desirable changes in size of QDs in a broad range (2-20 nm) can be achieved by modifying the acidity of the solution, reagents concentrations, *S* to *Pb* molar ratio or the synthesis temperature. The changes in particle sizes were proved by the shift of the position of the maxima of excitonic luminescence spectra in the range 800-2000 nm.

Influence of gelatin concentration on PL properties.

The concentration of gelatin was varied in order to study its effect on the *PbS* QDs formed and on their optical properties.

In Fig. 4 the PL peak dependence on gelatin concentrations for the samples at ambient temperature are presented. The PL emission peaks are seen to shift to shorter wavelengths.

In our experiments, when the gelatin concentration was raised up to 12 – 20% a slight displacement of the maximum position of the band of excitonic PL towards the shorter wavelength was noticed, signifying a decrease of the average diameter of QDs.

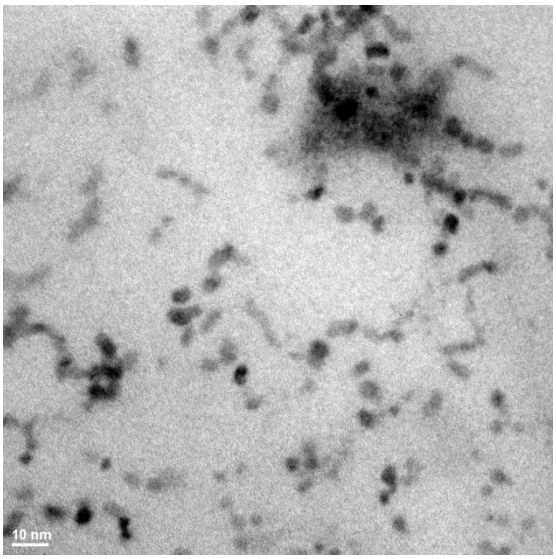

Fig. 2. TEM micrographs of *PbS* nanoparticles in gelatin.

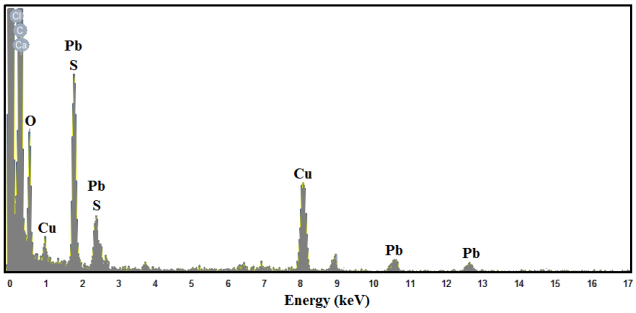

Fig. 3. EDX spectrum of the PbS nanoparticles in gelatin.

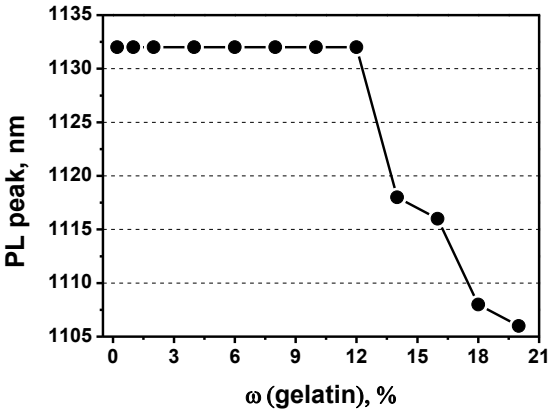

Fig. 4. PL emission peak dependence on gelatin concentration.

When the gelatin concentration was set in the range 0.5 - 12%, the maximum of the excitonic PL remained practically unchanged, which means that the final diameter of the particles was unaffected.

The results obtained might be interpreted by the increased efficiency of the passivation of surface states of the nanoparticles: greater concentrations of gelatine result in a larger number of chemical bonds between gelatine molecules and the surface atoms having dangling bonds. Besides, according to [13], gelatine immobilizes QDs, increasing their dipole interactions because of lower mobility.

Influence of the synthesis temperature on PL properties.

As can be seen in Fig. 5, with the raise of the synthesis

temperature from 20 to 90 °C, the maximum of the photoluminescence spectrum was found to become monotonously displaced from the lowest wavelength value of 900 nm to the highest of 1300 nm, by means of increasing the crystals diameter.

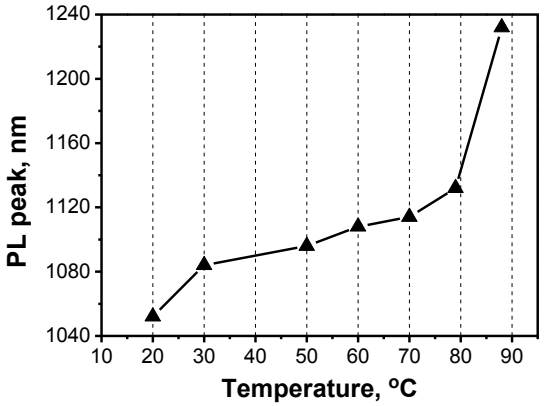

Fig. 5. PL emission peak dependence on reaction temperature.

Influence of *S* to *Pb* molar ratio on PL properties.

The growth of the ratio of *S:Pb* from 1:4 up to 4:1 leads, first, to the increase of the luminescence wavelength (crystal diameter), reaching the max. at the ratio 2:1, after which it starts to decrease (Fig. 6).

It is worthwhile mentioning that "better" synthesis conditions, in terms of narrower QDs' size distribution due to the improved separation of nucleation and growth stages, were found to lie in the region of smaller *S:Pb* ratios [14].

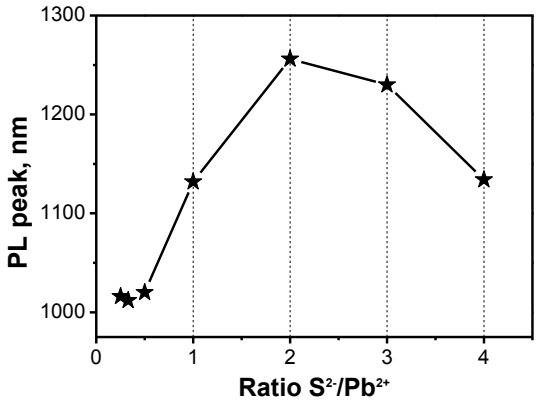

Fig. 6. PL emission peak dependence on S:Pb ratio.

Influence of pH solution on PL properties.

The experimental data presented in Fig. 7 show that the decrease of the solution *pH* from 13 to 4 did not result in a significant change in the dimensions of the produced QDs.

However, an increase of the crystals dimensions was observed at lower *pH*.

The method presented here has some advantages over other known synthetic procedures, namely:

- it is simple and fast;
- the final size of the QDs can be easily controlled;
- there is no need in complex and expensive equipment;
- it uses non-toxic and non expensive reagents;
- no harmful residues are formed and, last, but not least,
- the obtained nanocrystals are soluble in polar environments, such as water.

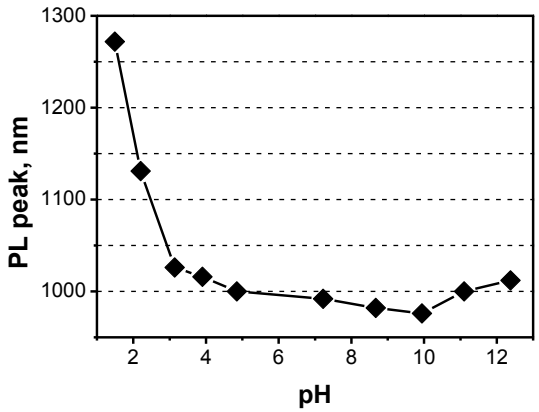

Fig. 7. PL emission peak dependence on solution pH.

IV. CONCLUSIONS

A novel easy method for the synthesis of colloidal lead sulphide nanocrystals in gelatin is presented. TEM studies showed that the sizes of QDs obtained were within 2 – 20 nm and EDX spectroscopy confirmed the elemental composition of nanoparticles. The sizes were tuned during the synthesis by modifying the acidity of the solution, reagents concentrations, *S* to *Pb* molar ratio and the synthesis temperature.

V. ACKNOWLEDGMENTS

This research was supported by SCSTD within the frame of the state program "Nanotechnologies and nanomaterials".

REFERENCES

[1] A.M. Derfus, W.C.W. Chan, S.N. Bhatia, Nano Lett. 4, 11 (2004).
[2] Wang A., Pan A., Yin H., He Y., Xu Z., Zou B., Mater. Lett. 60, 1242 (2006).
[3] Patel A.A., Wu F., Zhang J.Z., Torres-Martines C.L., Mehra R.K., Yang Yi, Risbud S.H., J. Phys. Chem. B 104, 11598 (2000).
[4] Ji Y., Ma X., Zhang H., Xu J., Yang D., J. Phys.: Condens. Matter 15, 7611 (2003).
[5] Bakueva L.; Gorelikov I.; Musikhin S.; Zhao X.; Sargent E. H.; Kumacheva E., Adv. Mater 16, 926 (2004).
[6] X. Zhao, I. Gorelikov, S. Musikhin, S. Cauchi, V. Sukhovatkin, E. H. Sargent, and E. Kumacheva, Langmuir 21, 1086 (2005).
[7] Zhang, S.; Cyr, P. W.; McDonald, S. A.; Konstantatos, G.; Sargent, E. H., Applied Physics Letters 2005, 87.
[8] Gaponenko S. V., Optical properties of semiconductor nanocrystals – Cambridge University Press, 1998.
[9] Gau H., Herminghaus S., Lenz P., Lipowski R., Science 283, 46, 1999.
[10] Zhao M.Q., Sun L., Crooks R.M., J. Am. Chem. Soc. 120, 4877, 1998.
[11] Beecroft L. L., Ober C.K., Chem. Mater. 9, 1302, 1997.
[12] Chestnoy N., Harris T.D., Hull R., Brus L.E., J. Phys.Chem. 90, 3393, 1986.
[13] Wang Y., Chen H., Ye C., Hu Y., Mater. Lett. 62, 3382 (2008).
[14] Abel K.A., Shan J., Boyer J-C, Harris F., Veggel F. Chem. Matter 20, 3794-3796 (2008).

Synthesis of AAO Nanotemplate and Its Properties

Natalia TSYNTARU*, Berkay KAVAS**, Jean-Pierre CELIS*
* *Katholieke Universiteit Leuven, Leuven, Belgium*
***Istanbul Technical University, Istanbul, Turkey*
Natalia.Tintaru@mtm.kuleuven.be

***Abstract* – The objective of this study is to synthesize and to characterize anodized aluminium oxide (AAO) nano-templates suited for large area device applications. The wear performance and the mechanical properties of well-ordered nanoporous AAO obtained after a two step anodizing process in sulphuric acid were investigated. Pores with different aspect ratios were obtained at cell voltages of 15 V and 21V. Ppore diameters of ~16 nm and ~ 27 nm were noticed. The mechanical behaviour of such anodized aluminium oxides (AAO) was determined by nanoindentation at 2 -200mN normal loads. The tribological behaviour of these nano-templates was studied under reciprocating (ball on flat) sliding against alumina counter-balls. The dependence of the properties of AAO-templates on the small pore diameter is discussed**

***Index Terms* – anodized aluminium oxide; friction and wear; hardness; pore diameter.**

I. INTRODUCTION

Due to the rapid development in nanotechnologies, a lot of attention is given to the preparation and characterization of anodic aluminium oxide (AAO) membranes. AAO is a nanostructured material which can be of interest in many fields like catalysis, chemical sensors, biosensors, filters, templates for self-assembly, and humidity sensors [1, 2]. The AAO film can also be used as a support for measuring mechanical properties of nanocarbon tube ropes [3]. AAO films are potentially advantageous for tribological applications since the nanoporous structure can be used as a reservoir or a template for solid lubricants and nano-tubes or nano-fibers to form self lubricating structures [4]. AAO microstructures can be classified into two types: a relatively pure alumina type (inner layer) consisting entirely of Al_2O_3, and an acid anion-contaminated type (outer layer) resulting from the incorporation of anions into the alumina structure during anodizing [5]. These phases present in the AAO structures are important when using AAO membranes in applications requiring a high mechanical strength. Friction and wear performance of filled-in AAO films were previously studied [6].

However, a better understanding of wear and friction properties of AAO and how the behaviour of AAO changes with further processing, are still needed. In this investigation, AAO films have been synthesized with narrow pores, and tribological and mechanical studies of these AAO films supported by an aluminium substrate have been performed.

II. EXPERIMENTAL

2.1 Sample preparation

Prior to anodizing, commercial pure Al sheet (% 99.99, Alfa Aesar Johnson Matthey GmbH) was cut into round pieces with a diameter of 9 mm that perfectly match in a sample holder. Samples were ultrasonically degreased in acetone and ethanol followed by a rinsing with deionised water. Anodizing was done on a surface with low roughness. Hereto aluminium samples were electropolished at a constant current density of 500 $mA.cm^{-1}$ for 1 min in an electrolyte consisting of perchloric acid (60 wt %) and ethanol (abs.) in a volumetric ratio of 1:4. Temperature was kept at ~10 ^oC [7, 8]. [9]. Perchloric acid was used to achieve the proper low pH and to ensure that Al ionizes into Al^{3+} and does not form oxides [10]. It must be noted that the edges of the sample were electrically isolated.

2.2. Anodizing

Two step anodizing was performed in a 20 wt % sulphuric acid electrolyte using a two electrode electrochemical cell set up with a magnetic stirrer rotating at 500 rpm. The temperature was kept at ~ 1 ^oC during anodizing. Electropolished samples were cleaned in de-ionized water and anodised at a potential of either 15 or 21V for 10 min. After a first anodizing step, samples were rinsed with de-ionized water and immersed in a solution of chromic acid (1.8 wt%) and phosphoric acid (6 wt %) for 10 and 15 min respectively, at ~60 $^{\circ}C$ to achieve a removal of the oxide layer. In this way, we achieved a prepatterning of the aluminium surface for pores to grow inwards during the second anodizing step at a constant potential of either 15 or 21 V for 97 and 20 min respectively at ~ 1 $^{\circ}C$. The AAO thickness was ~17 μm (Fig.1.). Pore sizes 16 and 27 nm.

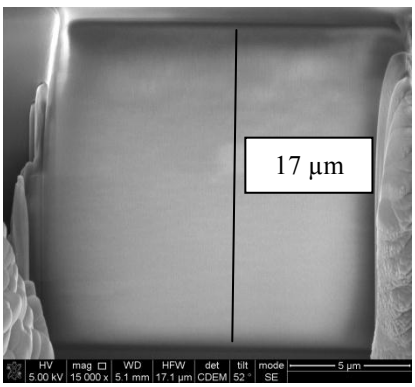

Fig.**1.** Cross section on AAO with a thickness of 17 μm (light grey area: AAO, dark grey area Al).

2.3. Tribological and mechanical characterisation

For the investigation of tribological properties at meso- and macro-loads, we used Falex Modular Universal Surface Tester (MUST) and a KUL-MTM fretting mode I apparatus [11]. The counterbody was a 5 mm corundum ball reciprocating on AAO samples at a frequency of 1 Hz. The stroke length was 100 µm. Tests were repeated at least three times at normal loads between 40 mN and 1,000 mN to reveal the tribological behaviour at low and rather high loads. Test temperature was kept constant at 23°C. Humidity was 50% RH. Samples were cleaned before fretting tests for degreasing them, and after fretting tests ultrasonically in ethanol for 7-10 min to remove the debris. Samples were examined using scanning electron microscopy (SEM, Philips XL-30), Field Ion Beam SEM (FIB-SEM) and white light interferometer (VeeCo) before and after wear tests. Chemical composition was identified by energy-dispersive spectroscopy (EDS).

Nanoindentation was performed at six different loads as 2, 5, 20, 50, 100 and 200 mN using Berkovich nanoindenters (CSM Instruments). Loading and unloading rates were as twice as the maximum load applied. Indentation marks were examined by optical microscopy and SEM.

III. RESULTS AND DISCUSSION

3.1. Influence of sample preparation procedure

The anodizing of aluminium was done on samples with a low surface roughness. Indeed, anodising reactions take place at the surface of the anode, and a low surface roughness is a must to get a uniform anodizing rate at each spot. SEM and white light interferometer investigation performed before and after electropolishing, revealed how this pre-treatment influences the surface roughness. Roughness values, Ra and Rz were ~740 nm and ~7 µm prior to electropolishing. After electropolishing Ra and Rz were ~140 nm and ~1.5 µm respectively. SEM images of the two types of surfaces are given in Fig.2.

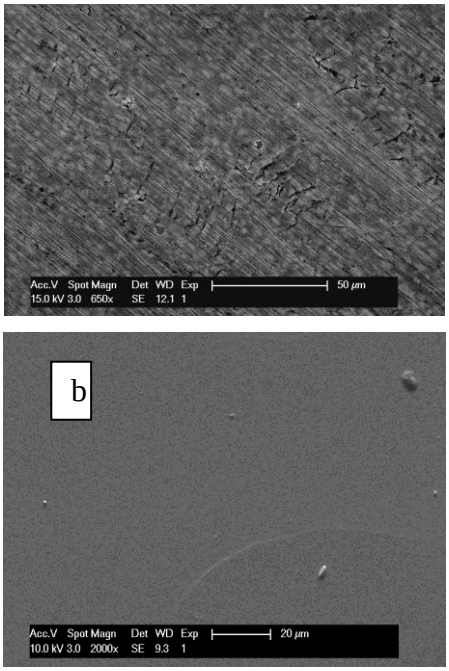

Fig. 2. SEM images of the aluminium surface before (a) and after electropolishing (b).

3.2. Tribological performance of as-received AAO films

In order to determine the tribological behaviour of amorphous [5] as-produced AAO films supported on aluminium substrate, fretting test were carried out. The evolution of the coefficient of friction with fretting cycles is given in Fig. 3. It shows the dependence of the coefficient of friction on the pore diameter and normal load applied. The coefficient of friction increases steeply at the beginning of the sliding tests. After around 80-100 cycles at meso-loads, a steady state is reached during which the coefficient of friction is approximately the same for both pore sizes. The coefficient of friction for AAOs with the same pore diameter, remained practically the same independently the load applied. At high loads of 1,000 mN, the coefficient of friction is higher probably due to of debris formed during the fretting tests. At a smaller AAO pore diameter namely 16 nm, this effect is more obvious (Fig. 3a). Since we used a counterbody also made of alumina, the coefficient of friction can reach high values, but it also assures that no chemical reaction will occur in the sliding contact. However, after reaching a peak value, the coefficient of friction decreases slightly especially at a normal load of 1,000 mN (Fig. 3).

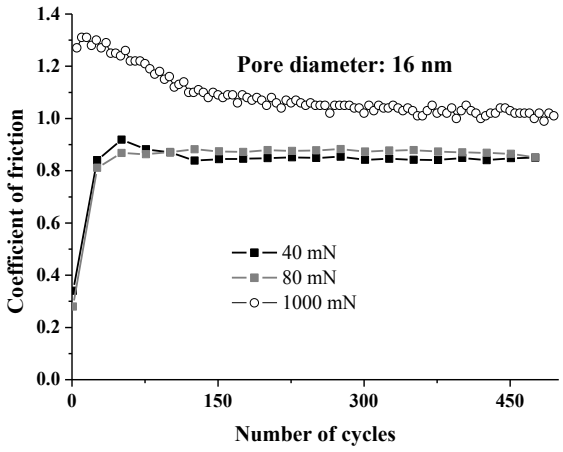

Fig. 3. Evolution of AAO coefficient of friction at meso- and macroscale loads.

To reveal the wear mechanism during the running-in period, short sliding tests of 50 cycles were done. Wear tracks observed using SEM (Fig.4) revealed that the pores were filled up with very fine debris formed in the sliding contact. Some pores could still partially be seen underneath a very thin debris layer covering the surface. It can be noticed that the pores were obtained without any serious damage to the tubes.

To study the propagation of wear, wear tracks after 500 fretting cycles (steady state part) were analyzed (Fig 5). These experiments show that a tribolayer is formed by a progressive degradation of the AAO top layer and by filling up the pores with nanosized debris. This tribolayer consists of a compacted bed of wear particles and has a partially layered structure which we observed after 500 fretting cycles. That tribolayer is not equally spread over the whole wear track area (Figures 4 and 5).

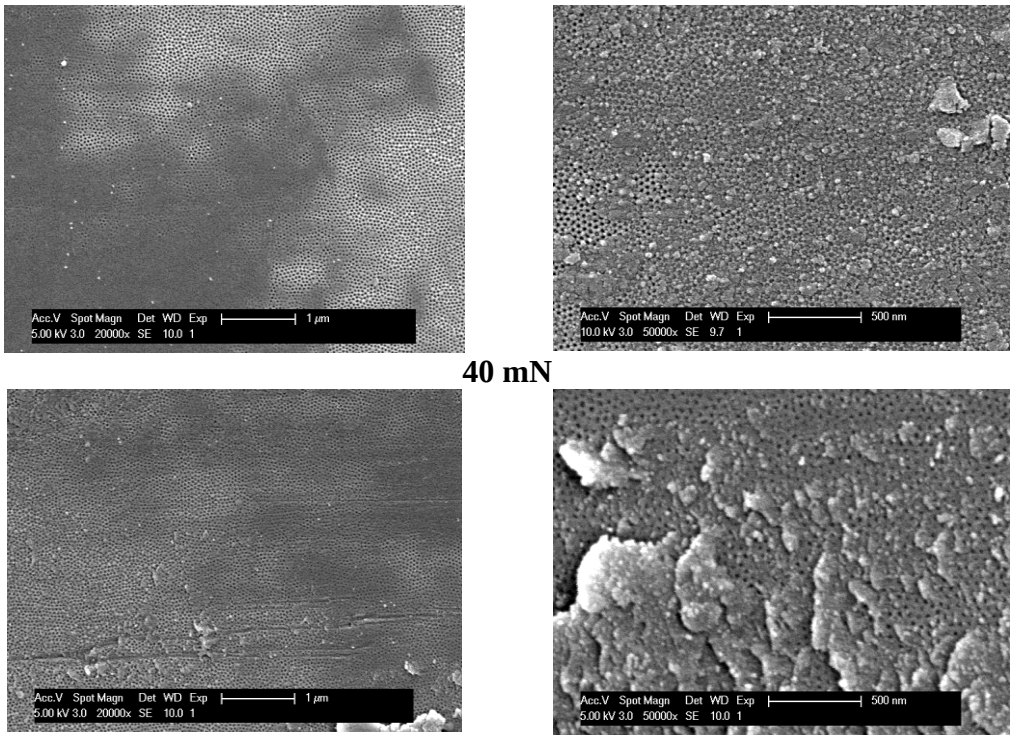

Fig. 4. SEM images of AAO (pore diameter 27 nm) after 50 fretting cycles.

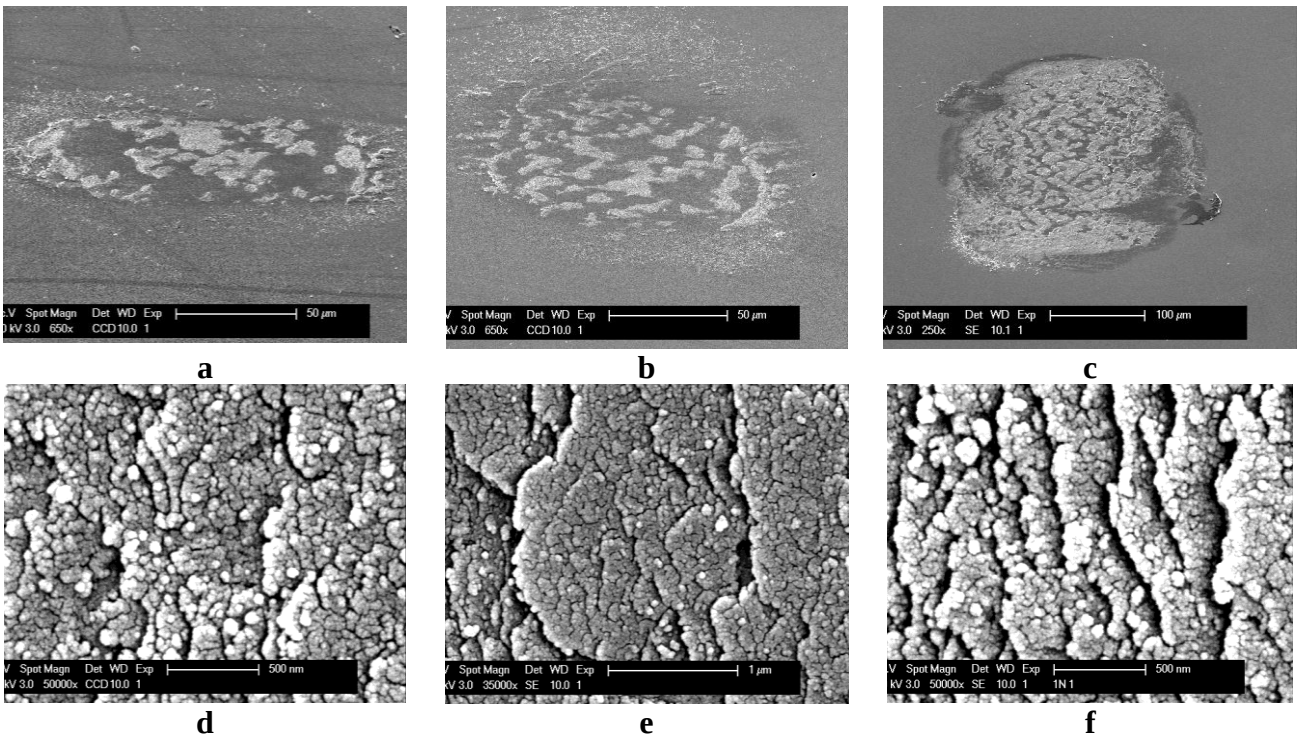

Fig. 5. SEM images of wear tracks on AAO membrane (pore diameter 27nm) after 500 sliding cycles at normal loads of 40, 80 and 1000 mN at low magnification (a, b and c) and high magnification (d, e and f) respectively

Ultrasonic cleaning of the tested samples in ethanol after the wear tests, did not allow to remove the bed of debris from the surface. This reveals that the debris iss sticky, adhering locally on some parts of the wear track and on the counterbody (not shown here), resulting in a complex wear mechanism being a combination of abrasive and adhesive wear, and in a high coefficient of friction. The increasing coefficient of friction at the start of the sliding tests can be linked to the formation of this tribolayer. On further sliding, compacted small worn debris may cause abrasion wear and a high coefficient of friction.

3.2. Nanoindentation

Nanoindentation tests were performed over a wide range

of normal loads (2-200 mN) to study the mechanical behaviour of anodized aluminium oxides. The investigation of nanoindentation imprints and surrounding areas was done by using SEM. The study did not reveal major cracks inside and outside the indentation imprints (Fig. 6). Considering that alumina is a ceramic material, the actual mechanism of deformation within the material during indentation comes into question. A high magnification SEM image of an indentation in an AAO film is shown in Fig. 6, in which a pore crushing is evident as the mechanism caused permanent deformation in the material. The corner of the imprint seen in Fig. 6, is surrounded by a regular pore structure, while the pores appear to be deformed within the imprint due to an overall collapse of the porous structure. Rather than through pure material plasticity, the overall structure of the AAO membranes is progressively deformed on indenter loading.

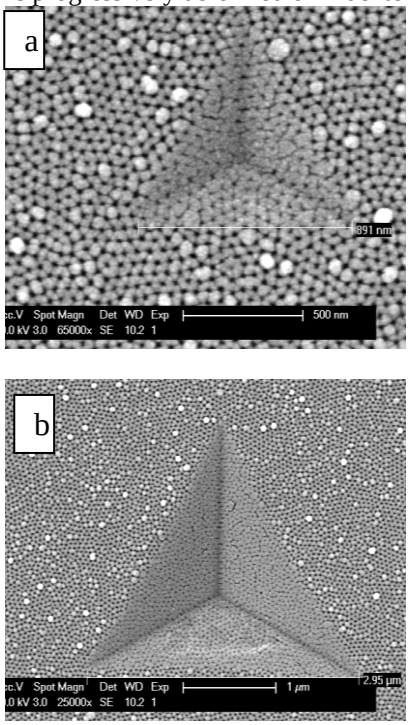

Fig. 6. Nanoindentation imprints at 2, 20 mN (a and b) respectively and surrounding area on AAO templates at pore diameter 27 nm.

Data on hardness and elastic modulus are plotted in Fig.8 versus indentation depth. At low indentation depth, a large scatter in hardness (e.g. 9.5±0.8 GPa and 5.4±0.5 GPa for 2mN, Fig.7 a) and elastic modulus (97±5 GPa for 2mN Fig.7 b) are observed. It is noticed that at on AAO with a 16 nm pore diameter, the scatter is large. This scatter may be due to the high surface roughness and the presence of different structures (such as remains of electrolytes) inside the pores. At large indentation depth, hardness and elastic modulus exhibit a lower scatter. The hardness varies between 3 and 6 GPa and the elastic modulus between 30 and 65 GPa. The hardness and Youngs' modulus of AAO nanotemplate are in good agreement with values reported by other researchers [12]. However, the values are significantly lower than the values found in literature for pure, well crystalline corundum or sapphire, which are usually in the range between 20 and 25 GPa [13]. This difference is mainly attributed to the porous structure, which is responsible for the unique mechanical response of the membranes.

It is noticed that with increasing pore diameter, the hardness at low loads are smaller which can be linked to the 'hole effect' described in [14]. This research shows that the elastic modulus and hardness vary when the normal load is increased. The difference is thought to be due to the anisotropy which is not accounted for in the indentation method and also due to the influence of the aluminium substrate underneath the AAO film.

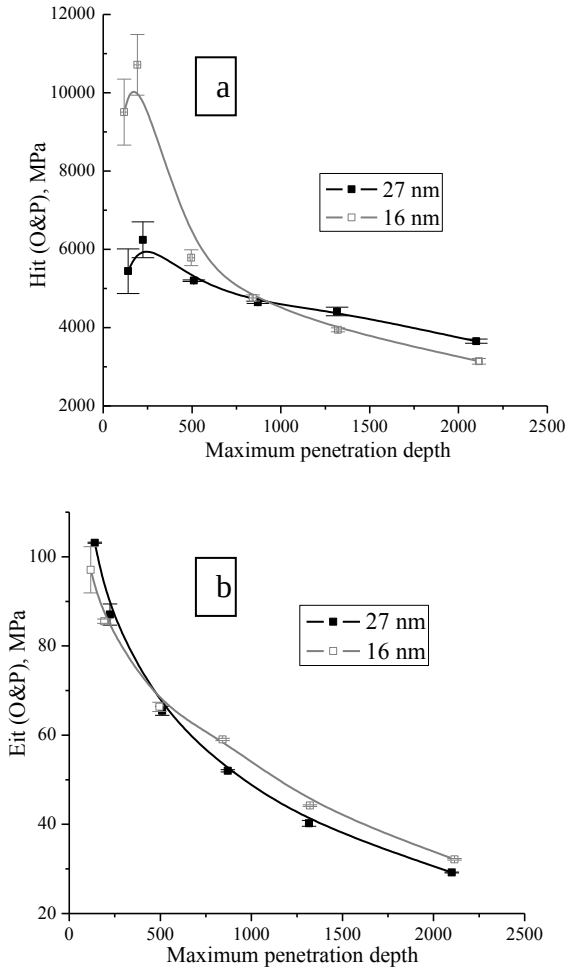

Fig. 7. Hardness (a) and elastic modulus (b) as a function of indentation depth recorded on 17 µm thick AAO membrane produced at 15 and 21 V.

IV. CONCLUSION

Well-ordered nanoporous AAO film was obtained with relative small pore diameters of 16 and 27 nm. It was been shown that AAO films subjected to meso- and macro-load fretting tests form very fine debris on their surface. Debris produced during sliding on the surface fill up the pores in a first stage, followed by the formation of a tribolayer.

Major cracks were not observed inside or along the edges of the wear tracks. Cracks which formed during fretting at 1000 mN don't propagate and are only located at the edges of the wear track. This effect can be linked to the aluminium supporting the AAO template and which is a softer material than the AAO film. The variation in the coefficient of friction with pore size and normal load was not considerably high. The wear mechanism did not change with increasing applied loads due to a similarity in the tribofilm formed under meso- and macro-load sliding testing.

Hardness and Young's modulus of highly ordered alumina were measured by nanoindentation. The hardness and elastic modulus values depend on the load applied. Hardness can reach up to 10 GPa at 2 mN on AAO films

with a 16 nm pore diameter. At increasing loads the nanopores collapse in 'shear bands', rather than being cracked as observed around the indent, suggesting that the pores in the alumina lead to a higher toughness in the transverse direction.

ACKNOWLEDGMENTS

This research was funded by a FP7 grants: "NANOALLOY" (Marie Curie IIF contract n° 252407), "NANOCOAT" (FP7-SME-2010 contract n°262078), and "TEMADEP" (IRSES contract n° 05-104-7540).

REFERENCES

[1] M. Almasi Kashi, A. Ramazani, M. Raoufi, A. Karimzadeh, Thin Solid Films 518, 6767-6772, 2010

[2] Te-Hua Fang, Tong Hong Wang, Chien-Hung Liu, Liang-Wen Ji, Shao-Hui Kang, Nanoscale Res Lett 2, 410-415, 2007

[3] J.-P. Salvetat, G. Andrew, D. Briggs, J.-M. Bonard, R.R. Bacsa, A.J. Kulik, T. Stöckli, N.A. Burnham and L. Forró, Phys. Rev. Lett. 82, 944. 1999

[4] H. Kim, D. Kim, W. Lee, S. Jai Cho, J.-H. Hahn, and H.-S. Ahn, Surf. Coatings Techn., doi:10.1016/j. surfcoat.2010.07.056, in Press.

[5] M. Kylan McQuaig Jr., Alejandro Toro, William Van Geertruyden, Wojciech Z. MisiolekJ, Mater Sci 46, 243–253, 2011

[6] J.P. Tua, C.X. Jiang, S.Y. Guoc, X.B. Zhaoa, M.F. Fu, Wear 259, 759–764, 2005

[7] G.D. Sulka, S. Stroobants, V. Moschalkov, G. Borghs, and J.-P. Celis, J. Electrochem. Soc., 149 (7), D97-D103, 2002

[8] G.D. Sulka, K. G. Parkola, Thin Solid films, 515, 338–345, 2006

[9] H. Adelkhani, S. Nasoodi, A.H. Jafari, Int. J. Electrochem. Sci., 4, 238 – 246, 2009

[10] Di Ma, Shuying Li, Chenghao Liang, Corrosion Science 51, 713-718, 2009

[11] H. Mohrbacher, J.-P. Celis and J.R. Roos, Tribo. Int., 28 (5), 296-278, 1995

[12] Z. Xia, L. Riester, B. W. Sheldon, W. A. Curtin, J. Liang, A. Yin and J. M. Xu, Rev.Adv.Mater.Sci., 6, 131-139, 2044

[13] AB Sinani, NK Dynkin, LA Lytvinov, PV Konevsky, EP Andreev, Bull Russ Acad Sci Phys, 73, 1380, 2009

[14] S. Ko et al., Thin Solid Films 515, 1932–1937, 2006

Analysis of the Behavior of PVDF Layers Deposited under Various Conditions

Victor COJOCARU[1], Alexei KATASHEV[2], Horia-Nicolai TEODORESCU [1, 3]
[1] 'Gheorghe Asachi' Technical University of Iasi, Faculty of Electronics, Communications and I.T., Romania
[2] Riga Technical University, Biomedical Engineering and Nanotechnologies Institute, Riga, Latvia
[3] Institute of Computer Science of the Romanian Academy, Iasi, Romania
vcojocaru@etti.tuiasi.ro, katashev@latnet.lv, hteodor@etc.tuiasi.ro

***Abstract*–We analyze the surface and piezoelectric properties of PVDF films deposited on the surface of Si wafer by solution casting under various conditions of temperature and electric field.**
***Index Terms* – PVDF, Kelvin Probe, AFM**

I. INTRODUCTION

In this paper we present a preliminary study of the piezoelectric properties of polyvinylidene fluoride (PVDF) film materials grown on Si substrate under various conditions. Our targets for this research are to test the possibility to elaborate new ultrasound and piezoelectric sensors, based on PVDF materials.

In 1969, Kawai, [1] have discovered that, applying a strong electrical field on PVDF, the piezoelectric effect can be observed. This was an important step for the development of electro-active polymer sensors. PVDF is a ferroelectric polymer; its dipoles can be „aligned" by an external electrical field, thus polarization is being kept [2].

Such films are intended to be used as pyroelectric and electro-acoustic transducers. Piezoelectric films of this polymer are flexible and have high mechanical strength. Moreover, they have low acoustic impedance that is comparable with one of the biological tissues, a low acoustic resistance and a high elastic constant. Besides, sensors made of PVDF are good for wet environment [3].

This research is relevant to the need for new ultrasonic and pyroelectric sensors for bioengineering applications and other domains where small dimensions sensors are need.

II. METHOD

A)PVDF film

PVDF is a polymer with the degree of crystallization being around 50%. As other poly-crystals, PVDF polymer is a structure with amorphous areas. Addition of copolymer, such as TrFE, highly increases the degree of crystallinity [7]. PVDF film strongly absorbs infrared radiation in the range of 7 - 0.20 microns, corresponding to the wavelength spectrum emitted by the human body. PVDF is mechanically strong and flexible material with a density of approximately 1780 kg/m^3.

To increase piezoelectric response, PVDF film is stretched in one or both directions, so its size increases several times. Elastic coefficients (such as Young's modulus) are determined by the strain. For example, if the film was stretched at 140° C to a 4:1 ratio, Young's modulus is 2.1 GPa, and if the ratio is 6.8:1, the modulus is 4.1 GPa [4]. Another way to achieve high polarization is poling in a strong electric field (over 300 kV/cm), thick films have to be heated in this process up to 100^{o}C.

B)Probe *microscopy*

In scanning probe microscopy, the surface micro-relief and its local properties are explored by scanning with a needle-shaped probe. The tip of the probe has tens nanometers in diameter. The distance between the tip and the scanned area is 0.1-10 nm.

To verify the piezoelectric properties of PVDF material we used a scanning probe microscope Solver P47H-PRO that provides spatial resolution of 0.1nm (as evaluated by minimal scanning step). In comparison with scanning electron microscopy (SEM), atomic force microscope has several advantages. The electronic microscope (SEM) gives a pseudo three-dimensional image for the test area, while AFM give a really three-dimensional topography.

Furthermore, the non-conducting areas viewed by AFM don't need to have a conductive metal layer, which often lead to deformation of the surface. For normal operation in SEM, it is necessary that the sample is placed in a vacuum, while most microscope AFM modes can be implemented in air or even in the liquid. One of the drawbacks is that AFM can scan a small area of the sample [5].

C)Kelvin probe method (MKS)

The Kelvin probe method is used to visualize distribution of the electric potential over the surface of specimen. The Kelvin probe method works in two steps. In the first step the topography is determined. For the second pass, the probe is moved over the sample at certain distance from its surface to determine the surface electrical potential $\Phi(x)$. For this, the console is put into vibrations by applying to the probe a voltage V that contains static and dynamic components.

$$V_{varf} = V_{dc} + V_{ac}\sin(wt) \quad (1)$$

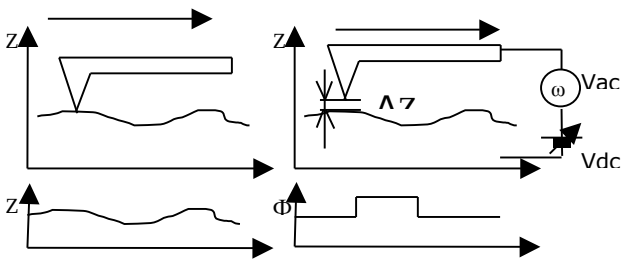

Fig.1.Kelvin probe method (MKS)

The capacitive force, that forces console to vibrate, is given [6] by:

$$F_{cap} = (1/2)*(V_{tip} - \Phi(x))^2 * (dC/dz), \quad (2)$$

where Cz is the capacitance between the sample and console. The force

$$F_{capw} = (dC/dz*(V_{dc} - \Phi(x)*V_{ac})\sin(wt) \quad (3)$$

which comprises the first harmonic, leads to console oscillations with the same frequency w [5].

For every surface point, the feedback system change DC component of the probe voltage (V_{dc}) until the w component of console oscillation (and w force component) disappears and $V_{dc}(x)$ becomes equal with F(x). Thus the $V_{dc}(x)$ distribution will reflect the surface potential distribution over the sample area.

III. EXPERIMENTS

For our experiments, aimed to obtain cheap and easy-manufactured ultrasonic sensors, the PVDF – TrFE copolymer films (molar ratio 70:30) were deposited on the surface of commercial Si wafer by solution casting. The 1 μl drop of PVDF-TrFE solution in dimethylformamide was placed over the SI substrate and dried in air either at room temperature or at 135°C. Some samples were dried in a weak electric field (600 V/cm).

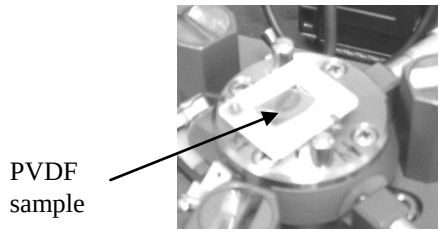

Fig.2. PVDF sample.

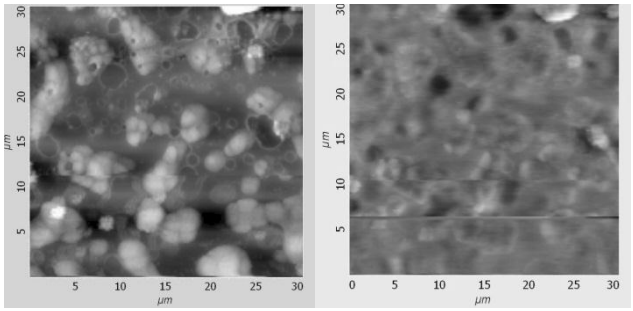

Fig.3. Surface of the sample, crystallised in electric field (E = 600 V/cm,) at the temperature 20^0 C, Scan size 30x30 μm, surface topography (left) range 0÷250nm, surface potential (right) range –60 ÷ +90 mV

The topography of the obtained films as well as distribution of the surface potential can be seen at Fig. 3-5. We used the method of piezoelectric response force microscopy to evaluate piezoelectric response of the film. It is widely applied to study ferroelectric materials and allows exploration of its domain structure. The method is based on the evaluation of the impact of the local electric field under the tip.

The tip is brought in contact with the specimen surface and alternating voltage is applied to the tip. The voltage produces local electric field under the tip, which in turn cause piezoelectric specimen to shrink and expand periodically hereby moving the tip itself.

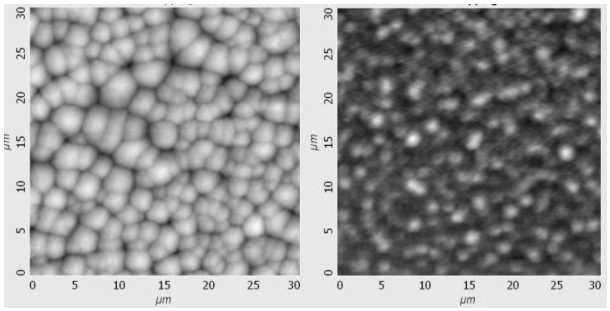

Fig.4. Surface of the sample, crystallised at the temperature 20^0 C, without electric field. Scan size 30x30 μm, surface topography (left) range 0÷150 nm, surface potential (right) range –50 ÷ +180 mV

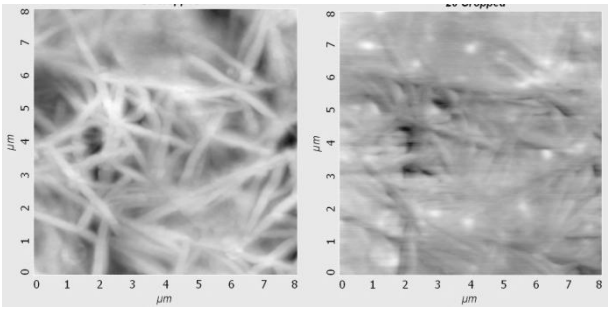

Fig. 5. Surface of the sample, crystallised in electric field (E = 600 V/cm) at a temperature of 135^0 C. Scan size 30x30 μm, surface topography (left) range 0÷300 nm, surface potential (right) range –700 ÷ - 300 mV

Thus the tip will move with the frequency, equal to one of the alternating voltage, while the amplitude of movement depends on the magnitude of electric field, piezoelectric properties of the material and mutual orientation of the electric field and polarization vector of the measured object [6]. The images of piezoelectric response (figs. 6, 7) are obtained by depicting the amplitude of the tip oscillations in arbitrary units.

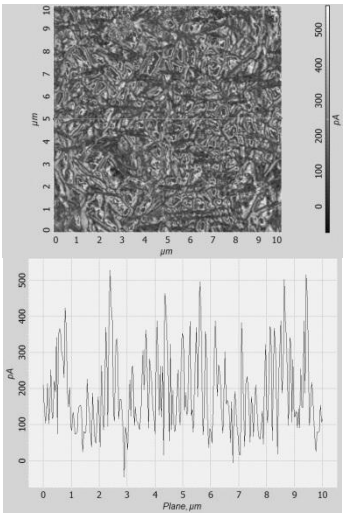

Fig.6. Piezoelectric response (relative units) of the sample, crystallised in electric field (E = 600 V/cm) at a temperature of 135^0 C (left), profile of the sample (right).

Fig. 6 demonstrates piezoelectric response of the obtained PVDF film. Non-uniformity of image implies different piezoelectric properties of small (0.1-0.5 μm) film areas that, probably, may be interpreted as PVDF domains. The different response over the film may be explained by different orientation of the domains. To validate this

supposition, additional DC electric potential was applied between the tip and sample. Figure 7 demonstrates increment in magnitude of piezoelectric response due to introduction of both negative and positive voltage. From this, one may suggest, for instance, that PVDF domains are initially poorly oriented. Application of electric field causes them to become more aligned more, thus the specimen under the tip becomes more polarized and its piezo-response increases.

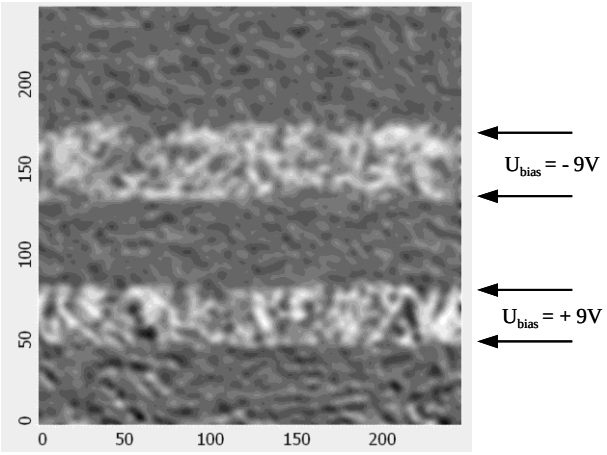

Fig.7. Change of the piezoelectric response of PVDF film (relative units) due to bias voltage applied to the probe (areas indicated with arrows)

IV. CONCLUSIONS

The experimental analysis demonstrated that the piezoelectric properties of PVDF films, grown on Si substrate by solution casting depend strongly on the film growth conditions. Under proper growth conditions, the ferroelectric properties may be suitable for the use in micro-sensors.

V. ACKNOWLEDGMENT

The first author thanks for being granted with a BRAIN scholarship that contributed to financing some of these studies and to Riga Technical University, Biomedical Engineering and Nanotechnologies Institute, for allowing him to follow a doctoral study stage at this university.

AUTHORS' CONTRIBUTIONS

The first author (VC) conducted experiments, collected the data under the supervision of the second author and wrote a major part of the paper. The second author (AK) conducted some AFM experiments, provided the whole guidance and planning for the experiments, interpreted results and contributed writing the paper. The third author originated the idea of the study, helped interpreting some of the results and contributed to writing the paper.

REFERENCES

[1] J. Tribol, Effects of Applied Potential on Friction of a Piezoelectric Material, Oct. 2007, Vol. 129, Issue 4, 836 (5 pages)

[2] Ye.Bormashenko, R. Pogreb, O. Stanevsky, and Ed. Bormashenko, Vibrational spectrum of PVDF and its interpretation, Polymer Testing, Vol. 23, Issue 7, October 2004, pp. 791-796

[3] A. Batagiannis, M. Wübbenhorst, J. Hulliger, "Piezo- and pyroelectric microscopy", Current Opinion in Solid State and Materials Science, Vol. 14, Issue 5, October 2010, pp 107-115

[4] D. Saikia, and A. Kumar, "Ionic conduction in P(VDF-HFP) / PVDF–(PC+DEC)–LiClO4 polymer gel electrolytes", Electrochimica Acta, Vol. 49, Issue 16, 15 July 2004, pp. 2581-2589

[5] A.V. Shirinov, and W.K. Schomburg, "Pressure sensor from a PVDF film", Sensors and Actuators A: Physical, Vol. 142, Issue 1, 10 March 2008, pp. 48-55

[6] http://www.ntmdt.ru/spm-principles/view/kelvin-probe-microscopy, accessed 02.2011

[7] Q. M. Zhang, V. Bharti, G. Kavarnos, M. Schwartz. (Ed.), "Poly (Vinylidene Fluoride) (PVDF) and its Copolymers", *Encyclopedia of Smart Materials, Volumes 1-2*, John Wiley & Sons, 2002. 807-825.

Exciton Luminescence in $In_{0.3}Ga_{0.7}As/GaAs$ Quantum Well Heterostructures

Eli KAPON[1], Alexandru MEREUŢA[1], Andrei DOROGAN[2], Nicolae DRAGUTAN[2],Tatiana VIERU[2], Nicolae SYRBU[2]
[1]*Swiss Federal Institute of Technology in Lausanne, Lausanne, Switzerland*
[2]*Technical University of Moldova, Kishinev, Moldova*
syrbunn@yahoo.com

***Abstract* – Radiation maxima were observed in photoluminescence spectra of GaAs/ $In_{0.3}$ $Ga_{0.7}As$/ GaAs in case of 632.8nm and 532nm He-Ne laser excitation conditioned by the recombination from ground (e1-hh1, e1-lh1) and excited (e2-hh2, e2-lh2) states of polarionic excitons in quantum wells. The doublet character of e1-hh1, e1-lh1 transitions can be explained by the interaction of excitons in quantum wells. Radiation maxima are revealed in the region of 1.5eV energy conditioned by recombination transitions E^b-hh1, E^b-lh1of the GaAs buffer layer.**

***Index Terms* – quantum wells, heterostructure, exciton, luminescence.**

I. INTRODUCTION

In quantum wells intersubband and intrasubband optical transitions are possible, as well as processes of quantum wells "photoionization", accompanied by a transition from size-quantized discrete states in overbarrier states of the continuous spectrum.

II. EXPERIMENTAL METHOD

The luminescence spectra were measured at 10 and 300K temperature with excitation lines of 632.8nm He-Ne and 532nm laser at high-aperture (1:2) МДР-2 and double diffraction spectrometer СДЛ-1.

III. EXPERIMENTAL DATA AND DISCUSSIONS

The transitions between different subbands of size quantization of the V-zone into C-zone, caused by light with $\hbar\omega > E_a$, can generate a whole family of electronic transitions and hence the bands of interband absorption and luminescence [1 – 3]. Figure 1 shows the luminescence spectra of $In_{0,3}Ga_{0,7}As/GaAs$ structure excited with a He-Ne laser line 632.8nm. At room temperature and low level of excitation the luminescence is practically absent. The luminescence is detected at 200K temperature and with further temperature decreasing the luminescence intensity increases. The emission maximum 1.163eV (200K) while the temperature is shifted to the energy of 1.2032eV (30K), has a FWHM equal to 10meV and is conditioned by the transitions *e1-hh1* (*e1-lh1*) from the quantum well layers A and B of $In_{0.3}Ga_{0.7}As/GaAs$ structure. In the high-energy region of $In_{0.3}Ga_{0.7}As/GaAs$ structures with quantum wells it is observed an emission band at 1.342eV (300K), which is shifted to higher energies with temperature decreasing (fig. 2). At 30K temperature it was revealed a narrow peak at 1.4131eV due to radiative recombination of electrons with heavy holes E^b-*hh1* and the maximum E^{x1} at 1.5433 eV, which, we believe, is due to radiative recombination from a discrete level of E^{x1} excitons located in the continuum region at the level of heavy and light holes.In order to increase the intensity the light was focused on the surface area. Radiation maxima at 1.2071 eV and 1.2201 eV, which are due to exciton recombination in quantum

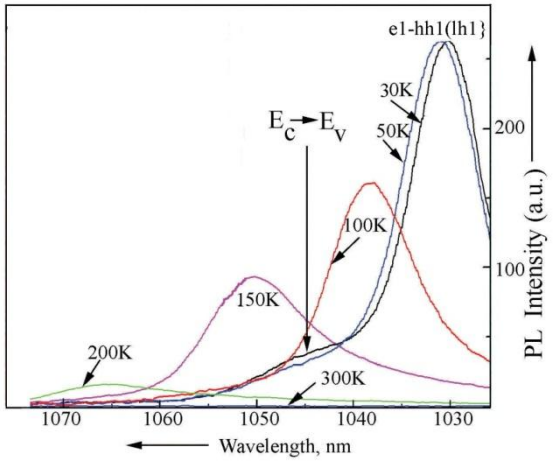

a)

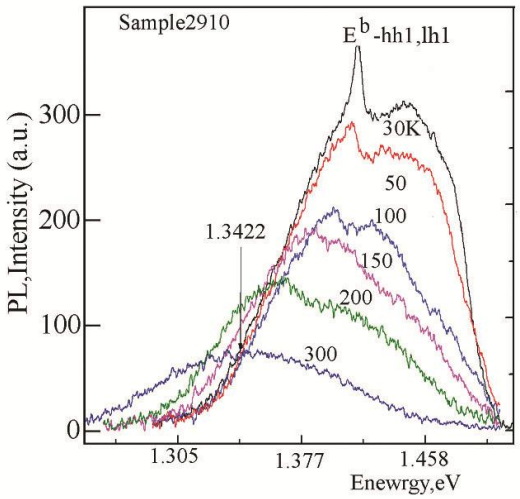

b)

Fig.1 a) - The luminescence spectra of $In_{0.3}Ga_{0.7}As/GaAs$ structure with quantum wells at different temperatures (30-200K) and 632.8 nm He-Ne laser excitation line; b) - Temperature dependence of the energy maxima of radiation for $In_{0.3}Ga_{0.7}As/GaAs$ structure with quantum wells excited with 632.8nm He-Ne laser line.

wells from the *e1-hh1* and *e1-lh1* states are detected at high intensities and 10K temperature in the long wave region. In this case, the splitting of the heavy (hh1) and light (lh1)

holes in the quantum well is equal to 13.0 meV and the value of FWHM is 5 meV.

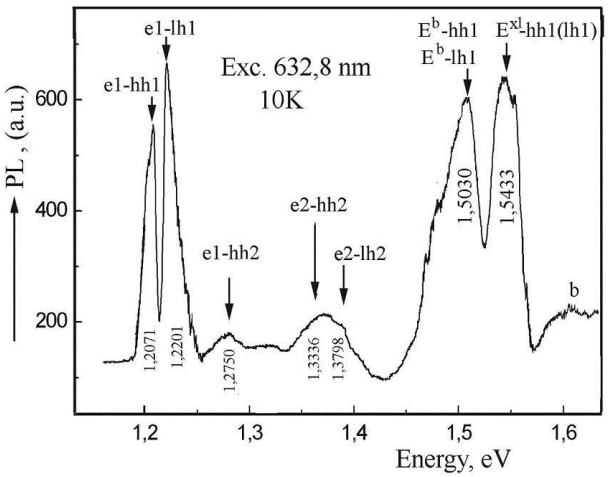

Fig.2 The luminescence spectra of $In_{0.3}Ga_{0.7}As/GaAs$ structure with quantum wells at 10K excited with a 632.8 nm He-Ne laser line (curve b is shown not to scale).

Radiation maxima at the energies 1.2750, 1.3336 and 1.3798 eV, which are due to transitions *e1-hh1*, *e2-hh2* and *e3-lh2*, respectively, are also found at 10K temperature. Intense emission lines at 1.5030eV energies and a weak shoulder at 1.4899eV energy and an intense maximum at 1.5433eV are found at these temperatures in a higher-energy region. The first two peaks are conditioned by bulk excitons in GaAs buffer layer, i.e. *Eb-hh1* and *Eb-lh1* transitions. In the related articles [1-3] the luminescence energy of the exciton transitions from the GaAs buffer layer at 8K temperature is detected at the energy 1.500-1.505 eV, which agrees with our determined value of 1.5030eV. The zones' splitting value of the heavy and light holes defined by the location of high-energy transitions is 13.1eV, which, practically, agrees with the splitting value (13.0 meV) determined from the maxima conditioned by the *e1-hh1* and *e1-lh1* transitions. The most short-wave radiation maximum at 1.5433eV we believe is due to recombination transitions from discrete energy states of the quantum well located in the E^{k1} continuum to the heavy holes zone *hh1*.

Temperature dependences of the detected transitions *e1-hh1* (*e1-lh1*) and E^{k1}*-hh1*, E^{k1}*-lh1* are presented in figure 3. Transition energies are shifted to higher energy almost linearly with temperature decreasing in the range 100-200K. The transitions energy *e1-hh1* (*e1-lh1*) and E^{b1}*-hh1* (*lh1*) vary linearly in the temperature range 100-10K, and the transitions energy E^{x1}*-hh1* (*lh1*) remains linear. The different temperature coefficient of the transitions' shift is linked with the difference of the coefficients of linear displacement of the heavy and light hole's zones, effective mass of heavy and light hole levels and exciton polariton levels in quantum wells [1 - 3].

Peaks at 1.2003 and 1.2138 eV are detected in the luminescence spectra at 10K and 532nm laser line excitation in unpolarized light, which are due to the transitions *e1-hh1* and *e1-lh*1 (fig. 4). It is evident that the luminescence maxima at 1.2003 and 1.2138 eV have the doublet character with a splitting of a several meV order In the luminescence spectra excited by unpolarized light and recorded in case of E_P and E_S polarization there are detected, as low-energy (1.2003eV) as high-energy (1.2138eV) peaks.

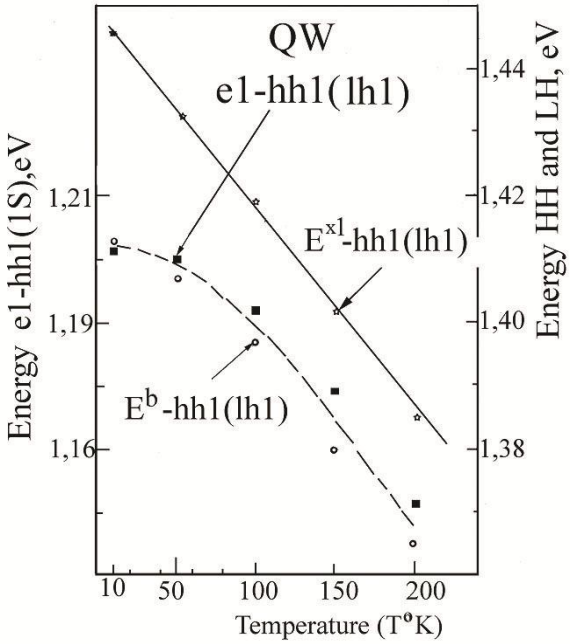

Fig.3 Temperature dependence of the levels of exciton polaritons in a quantum well

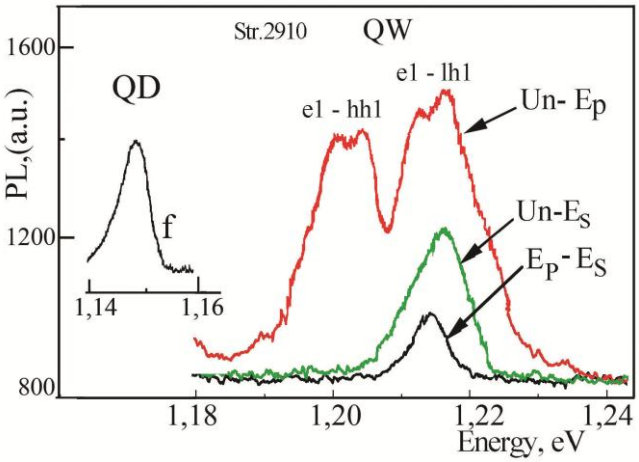

Fig.4 Luminescence spectra of $In_{0.3}Ga_{0.7}As/GaAs$ structure with quantum wells at 10K and excitation with 532 nm laser line, U_n-E_p curve corresponds to the excitation of unpolarized light and radiation in the P-polarization; curve U_n-E_S is unpolarized radiation excitation in the S-polarization; E_p-E_S corresponds to the excitation of P-polarized radiation in the S-polarization; f - the curve measured in unpolarized light and with the intensity increased up to 10 times.

When excited with E_P polarized light and a recorded luminescence at E_S and E_P there can be found also high-energy radiation maximum, but the emission intensity decreases because of reducing the intensity of the exciting light. In the study of photoluminescence spectra of localized excitons in GaAs/AlGaAs (001) quantum wells in the optical near-field regime it was observed the exchange splitting of the doublet *el-hh1* (*Is*) into two components polarized along the [100] and [110], i.e. the phase of these waves varies by ± 90 °. The emission maxima *e1-hh1* and *e1-lh1* (fig. 4) have a doublet character in the luminescence spectra considered by us at 10K temperature. The luminescence maximum (1.2133 eV) is observed at lower energies in the E_S polarization than in the E_P polarization (1,2166 eV).

IV. CONCLUSIONS

Photoluminescence spectra of GaAs/$In_{0.3}Ga_{0.7}As$/GaAs nanostructures are formed by the recombination of exciton polaritons in quantum wells from the main (*e1-hh1*, *e1-lh1*) and excited (*e2-hh2*, *e2-lh2*) states.

Recombination transitions E^b*-hh1*, E^b*-lh1* of the GaAs buffer layer and the transitions from the quantum level located in the continuum of barrier layer E^{k1}-hh1 contribute to the luminescence from the short-wave part of the spectrum. The doublet nature of the transitions e1-hh1, e1-lh1 is explained by the exchange interaction of excitons in quantum wells.

REFERENCES

[1] N. N. Ledentsov, M. Grundmann, N. Kirstaedter, O. Schmidt, R. Heitz, J. Bohrer, D. Bimberg, V. M. Ustinov, V. A. Shchukin, P. S. Kopiev, Zh. I. Alferov, S. S. Ruvimov, A. O. Kosogov, P. Werner, U. Richter, U. Gosele, J. Heydenreich. Sol. St. Electron., 40, 785 (1996).

[2] E. L. Ivchenko. Optical spectroscopy of semiconductor nanostructures (Alpha Science International, Harrow, UK, 2005).

[3] Mark Fox, Optical Properties of Solids, Oxford University Press, 2001.

Effect of Harmful Gases on the A.C. Conductivity of Tellurium Thin Films

D.TSIULYANU, O.MOCREAC

Technical University, Department of Physics
tsiu@molddata.md, doleaster@gmail.com

***Abstract* – Impedance spectra of tellurium films with interdigital platinum electrodes have been investigated in NO_2 and H_2S gaseous media at room temperature. Analyses of Nyquist complex diagrams allowed evaluating the characteristic frequency, time constant, resistance and capacity of the film in different target gases. It is shown that the spectra of both real and imaginary parts of impedance are strongly influenced by gaseous environment. The**
gas sensitivity for impedance or its imaginary part depends on frequency, being ~50 % / ppm for nitrogen dioxide and ~ 8 % / ppm for hydrogen sulfide respectively.
It is suggested that effect of NO_2 and H_2S results respectively from "strong" and "weak" chemisorptions of these molecules on the surface and intra grain regions.

***Keywords*–- *Impedance,* A.C.; *Tellurium,* NO_2, H_2S**

I. INTRODUCTION

Tellurium evaporated thin films show p- type conductivity, which depends [1-3] on thickness, rate of deposition and annealing process. Interesting semiconducting properties of Te films have stimulated their wide investigation and propositions for applications as thin films infrared detectors [4], strain - sensitive [5] and writing memory [6] devices.

Recently, tellurium thin films have been found to be sensitive to toxic and harmful gases [7-9], which allowed proposing them for the development of gas sensors [10]. Different gases may be easily detected at room temperature using these films. Although the cross sensitivity to mentioned gases is essential different, the distinguishing between them becomes important.

One of possibilities to obtain a selective detection of gases has been mentioned by Sbeveglieri [11] and consists in a fast sweeping of sensitivity of a single sensor at different frequencies. The sensitivity of sensor to different gases at different frequencies can be rather different. That is, by monitoring a.c. conductance at specific frequencies, the sensitivity to different gas components can be enhanced [12]. Moreover, a.c. measurements allow obtaining impedance or admittance spectra of a sensor, to calculate equivalent circuit and to distinguish between contributions from the surface, bulk or contacts to film conductivity [13].

In the present paper the a.c. conductivity of microcrystalline tellurium thin films with platinum interdigital electrodes have been investigated in dry synthetic air, nitrogen dioxide and hydrogen sulfide gaseous media at room temperature. An analysis of impedance spectra in a complex interpretation has allowed to represent the equivalent circuit, as well as to point out the effect of harmful gases on frequency dependences of real and imaginary parts of impedance of the films.

II. EXPERIMENTAL

Tellurium thin films of $\approx 100nm$ thickness, were prepared by thermal vacuum evaporation of pure tellurium from tantalum boat onto ceramic substrates with a priory deposited platinum interdigital electrodes (Fig. 1a). The electrode structure was structured at SIEMENS AG with electrode width of $15\mu m$ and interelectrode distances of $45\mu m$. The evaporation of tellurium was performed at the working pressure of $10^{-4} Pa$. The growing velocity of the film was in the order of 10 nm/s and the area of deposition around 10 mm^2.

The surface morphology of the films was controlled with a SEM TELSA BS 340 and was pointed out to be the same as in previous paper [3]. The film was encapsulated in a standard TO – 8 sockets and then the contacts were thermally bounded to socket pins, using the copper wires.

The sockets with thin film sensing devices were put into a test cell (of $10ml$ volume) in which the gases were injected with a flow rate of $100ml/\min$, parallel to the film surface.

Different gaseous media were obtained by using the experimental set up described in [14]. NO_2 and H_2S vapors with concentrations of $15ppm$ and $50ppm$ respectively were obtained by using calibrated permeation tubes (Vici Metronics, USA), which were incorporated subsequent into the experimental set – up. Dry synthetic air was used as the carrier and reference gas.

A.c. measurements were carried out in frequency range of $5Hz$ to $13MHz$ using a HP4192A impedance analyzer.

III. RESULTS AND DISCUSSION

3.1 Impedance behavior under dry air

Before checking the effect of different harmful gases on a.c. conductivity the tellurium films were aged by 12 months in normal conditions and the measurements have been performed under synthetic dry air. Figure 1b shows the typical complex impedance diagram in Nyquist plot obtained in pure synthetic dry air from a thin film device at room ($22^\circ C$) temperature.

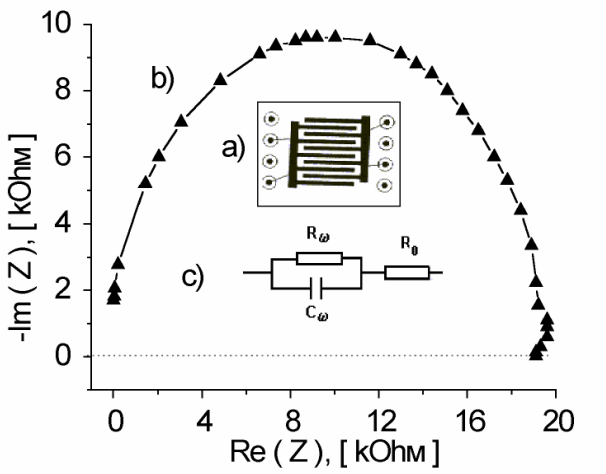

Fig.1. a) Interdigital electrode structure used to measure the a.c. conductivity;

b) Nyquist diagram of an aged at $22^\circ C$ tellurium thin film in pure synthetic dry air;

c) Suggested equivalent circuit.

The diagram shows a slightly depressed semi – circular arc with a center displaced below the real axis, owing to presence of distributed elements in tellurium-based device [13]. These elements can be related to grain boundary heterogeneity of polycrystalline material [15], more exactly to grain boundary and intra – grained regions [3, 9]. A simplified equivalent circuit inserted in Fig. 1 (c) can interpret the Nyquist plot. The frequency independent serial resistance R_0 is assigned to a sum of Ohmic resistance due to electric connection, but resistance R_ω and capacity C_ω are distributed to others contributors, the grain boundary resistance and capacity being the main.

The circle of Nyquist – diagram shown in fig. 1b is depressed owing to the dependence of both C_ω and R_ω on frequency. From the left and right intercepts of semi – circle with the $\mathrm{Re}(Z)$ axis the values of R_0 and $R_r = R_\omega + R_0$ can be estimated. Thus, R_0 was found to be very small, only about 5 Ohm. That is the arc practically passes through the origin and the right intercept gives the value of $R_r \approx 20 kOhm$.

For a parallel R_ω C_ω circuit the impedance is given as:

$$Z(\omega) = \frac{1}{Y(\omega)} = \frac{1}{\frac{1}{R_\omega} + i \cdot \omega \cdot C_\omega} = \frac{R_\omega}{1 + i \cdot \omega \cdot C_\omega \cdot R_\omega} = \frac{R_\omega (1 - i \cdot \omega \cdot C_\omega \cdot R_\omega)}{1 + (\omega \cdot C_\omega \cdot R_\omega)^2} \quad (1)$$

where $Y(\omega)$ is the admittance, $i = \sqrt{-1}$ is the imaginary number , $\omega = 2\pi f$, f -the frequency.

Thus, the real and imaginary parts of the impedance are:

$$\mathrm{Re}(Z) = \frac{R_\omega}{1 + \omega^2 R_\omega^2 C_\omega^2} \quad (2)$$

and

$$\mathrm{Im}(Z) = \frac{\omega \cdot C_\omega R_\omega}{1 + \omega^2 R_\omega^2 C_\omega^2} \quad (3)$$

From these system of equations the values of R_ω and C_ω of the film can be evaluated as:

$$R_\omega = \frac{\mathrm{Im}^2(Z) + \mathrm{Re}^2(Z)}{\mathrm{Re}(Z)} \quad (4)$$

and

$$C_\omega = \frac{\mathrm{Im}(Z)}{\omega \left[\mathrm{Im}^2(Z) + \mathrm{Re}^2(Z) \right]} \quad (5)$$

From equations (4) and (5) the resistance R_m , capacitance C_m and time constant $\tau_m = (2\pi f_m)^{-1}$ of the film can be estimated at characteristic frequency f_m ,wich is the frequency at which the imaginary part - $I_m(Z)$ reaches its maximum value:

$$\tau_m = \omega_m^{-1} = \frac{1}{2\pi f_m} = R_m C_m \quad (6)$$

Because of heterogeneity of the material-electrode system the relaxation time (time constant) τ_m , estimated from the complex impedance represents a mean value for the complete thin film device.

The characteristic frequency (f_m), impedance (Z) and estimated from equation (6) the time constant (τ_m) of the sample in dry synthetic air, are listed in table 1.

3.2 Impedance behavior in gaseous media of NO_2 and H_2S .

Fig. 2 reports the spectra of the real part of impedance of tellurium films upon exposure to different test gases.

TABLE1. CHARACTERISTIC FREQUENCY, IMPEDANCE AND R-C VALUES AT DIFFERENT ENVIRONMENTS

Environment	f_m kHz	Z $kOhm$	τ_m $10^{-7} s$	R_m $kOhm$	C_m pF
Dry air	900	13,3	1,8	19,2	9,6
1,5 ppm NO_2	1500	7,5	1,1	11,8	9,3
50ppm H_2S	400	29	4	44,5	9

It is seen that addition of 1,5 ppm of NO_2 to dry synthetic air diminishes the real part of impedance by ~ 10 kOhm in the frequency range 1,0 - 10^3 kHz. On the contrary, the addition of 50 ppm of H_2S to dry synthetic air enhances the real part of impedance by ~30 kOhm in the much shorter frequency range: 1,0 – 100 kHz. This behavior is compatible with spectra of imaginary part of impedance (Fig. 3). They exhibit the maximums strongly influenced by

harmful gases species. The NO_2 vapors diminish the peak of imaginary part of impedance shifting it to higher frequencies but the addition of H_2S vapors results in a vice-versa behavior. Analysis of these spectra allowed determining the influence of tested harmful gases on all elements of the equivalent circuit of the sample.

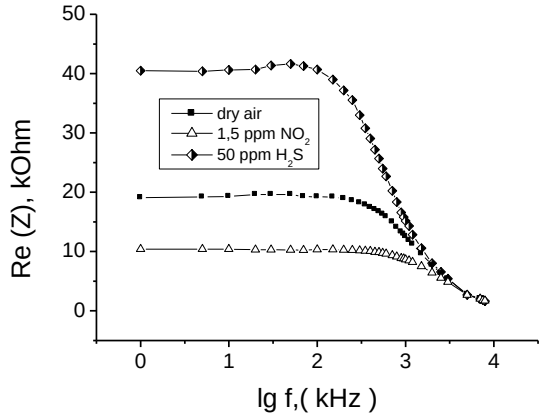

Fig. 2. Effect of target gas on the real part of impedance.

The values of characteristic frequency, impedance and time constant τ_m of the film at this frequency, by indicated concentrations of NO_2 and H_2S at room temperature, are summarized in table 1.

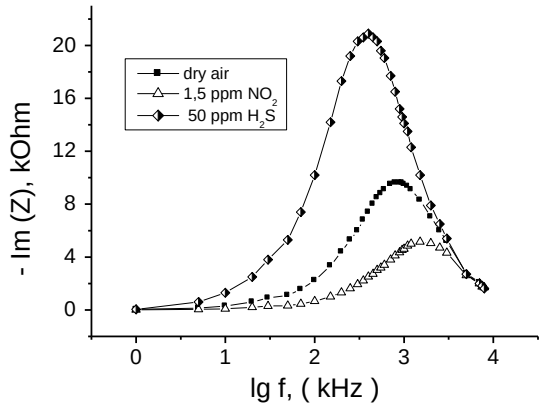

Fig. 3. Spectra of imaginary part of impedance upon exposure to different test gases.

Listed in this table values of R_m and C_m (thé résistance and capacitance at characteristic frequency) have been obtained from Eq. (4) and (5) applied to the data of Fig.2 and Fig.3.

From this table, it is seen that as the environment is changed from dry air to its mixture with gases in question, the resistance R_m is mainly influenced and capacitance C_m does not very essentially. And what is more, the addition of NO_2 decreases both impedance and R_m (at characteristic frequency, which also is gas influenced) but addition of H_2S increases these parameters. In this context it becomes interesting to analyze the frequency dependences of sensitivity to different target gases.

3.2.1 Nitrogen dioxide

D. c. resistance of tellurium films is known to decrease reversibly in presence of NO_2 due to interaction of adsorbed species with lone – pair electrons, which from the upper part of the valence band [14]. Apparently by changing from d.c. to a.c. technique the mechanism of interaction can not be modified but the sensitivity (or selectivity) can be increased.

Fig. 4 shows the sensor sensitivity as a function of the measurement frequency during the exposure to 1,5 ppm NO_2. The sensitivity (here and further) is defined as absolute variation of measured value (impedance or imaginary part of impedance) for a selected frequency in mixture of carrier gas with NO_2 divided by the measured value in the carrier gas at the same frequency, in percents per ppm.

The response curves for either impedance or imaginary part are nearly independent on frequency until approximately 300 kHz, then go down, but sensitivity to NO_2 is maintained until 10 MHz.

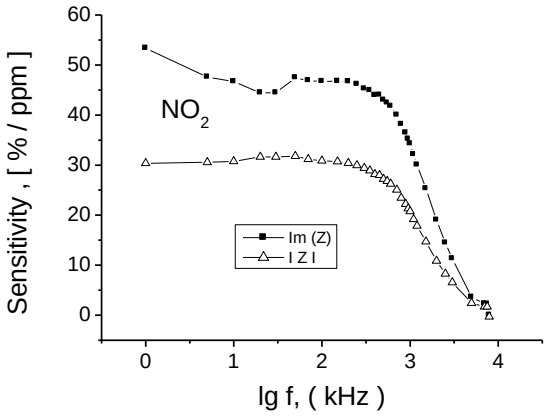

Fig.4. Sensitivity to NO_2 for impedance and its imaginary part as a function of frequency.

The sensitivity in d.c. and impedance measurements amounts to approximately 30 % /ppm, but evaluating the imaginary part as the sensor response results in an increasing of sensitivity until ~50 % /ppm. The high sensitivity, as well as the large frequency range of response to NO_2 supports the early-proposed mechanism of nitrogen dioxide interaction with chalcogenides [14], which involves ″strong″ chemisorption due to interaction between odd electrons of NO_2 molecules and lone – pair electrons of tellurium based chalcogenides.

3.2.2. Hydrogen sulfide

As sensing of hydrogen sulfide by tellurium films has been investigated early [9], here we show only some peculiarities related to sensitivity of such films to H_2S at a.c. measurements, as well as make some comments related to mechanism of interaction between this gas and chalcogenide tellurium thin film.

As have been pointed out (Fig. 2 and 3) hydrogen sulfide leads to increasing of both real and imaginary parts of impedance of the film. Fig. 5 shows the results from a.c. impedance measurements, in which the sensor sensitivity for

impedance and its imaginary part are, plotted as a function of the measured frequency during exposure to 50 ppm H_2S. First it is observed that sensitivity of tellurium films to H_2S is by ten times smaller then sensitivity to NO_2. Further, the sensor sensitivity evaluated from imaginary part exhibits a maximum at frequency of around 100 kHz. Evaluation of sensor response by this maximum results in an evident increase of sensitivity. Being of about 8 % / ppm it is four times higher than the sensitivity evaluated either from impedance or d.c. measurements.

Taking into consideration that the electron configurations of water and hydrogen sulfide are similar the interaction of tellurium film with H_2S is likely, to take place similar as proposed early [14] mechanism of interaction of water vapor with these films.

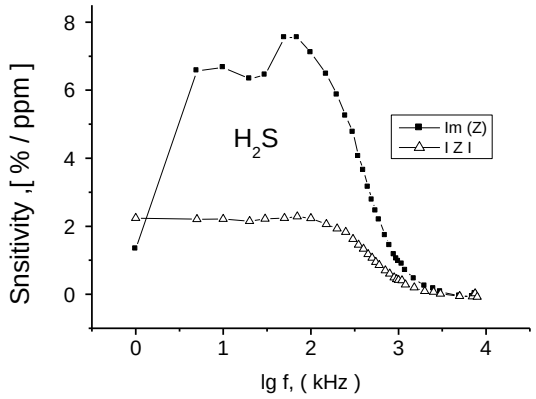

Fig.5. Sensitivity to H_2S for impedance and its imaginary part versus frequency.

That is, as the molecule of H_2S approaches the surface of positive charged tellurium film, it rotates and orientates its dipole moment perpendicular to this surface with negative pole inward. Simultaneously the free hole becomes more and more localized at the point of the surface that H_2S molecule approaches and a very week bond due to forces of electrostatic polarization is formed. And what is more, the orientation polarization of same H_2S molecules on the surface is accompanied by their stretching along the dipole, which can result in a "weak" form of chemisorbtion.

IV. CONCLUSIONS

A.c. conductivity of tellurium thin films is strongly influenced by composition of gaseous environment. The effect of harmful gases is mainly due to variation of both real and imaginary parts of film's impedance. Addition of NO_2 decreases, whereas addition of H_2S increases them in a large range of frequencies.

The sensitivity for either impedance or its imaginary part strongly depend on harmful gas species (NO_2 or H_2S) and applied frequency, because of different mechanisms of interaction between these gases with tellurium based films, which involves ″strong″ or "weak" forms of chemisorbtion respectively.

ACKNOWLEDGEMENT

Authors express their gratitude to colleagues from Institute of Physics, Munich University of Armed Forces for interests and help in carrying out this work.

REFERENCES

[1] M. A. Dinno , M. Schwartz, Structural dependence of electrical conductivity of thin tellurium films, J. Appl. Phys, 45, 1974, pp. 3328 – 3331.

[2] B. Chakrabarti, A.K.Pal, Electrical and Galvanomagnetic properties of Te films, Jap. J. Appl. Phys, vol. 19, no. 4, 1980, pp. 591 – 596.

[3] D. Tsiulyanu, S. Marian, H - D. Liess, I. Eisele,Effect of annealing and temperature on the NO_2 sensing properties of tellurium based films, Sens. Actuators B 100, 2004, pp. 380-386.

[4] N.G. Shyampasad, C.H. Champness, I. Shih, Thickness dependence of photoconductivity in tellurium, Infrared Phys. vol. 21, 1981, pp.45 -52 .

[5] M. Granveaud, Y. Petroff, On the electroresistance effect in evaporated tellurium films, Phys. Stat. Sol. (a), vol. 3, 1970, pp. 629 – 638.

[6] A. Milch, P. Tasaico, The stability of tellurium films in moist air, Journ. Electrochemical Soc., vol.127, no. 4,1980,pp. 884 – 891.
"Electrochemical Soc", 127 pp. 884, 1980

[7] D. Tsiulyanu, S. Marian, V. Miron, H - D. Liess, High sensitive tellurium based NO_2 gas sensor ,Sens. Actuators B 73, 2001 pp.35 - 39.

[8] D. Tsiulyanu, S. Marian, H - D. Liess, Sensing properties of tellurium based thin films to propylamine and carbon oxide, Sens. Actuators, B 85, 2002,pp.232-238.

[9] S. Sen, V. Bhandarkar, K.P. Muthe, J. M. Roy, S.K. Deshpande, R.C. Aiyer, S.K.Gupta, J. V. Yakmi, V. C. Sahni, Highly sensitive hydrogen sulphide sensors operable at room temperature, Sens. Actuators B 115 ,2006, pp 270-275.

[10] D. Tsiulyanu, Chalcogenide Semiconductor Based Gas Sensors, in Encyclopedia of Sensors edited by C. Grimes, E.C. Dickey and M. Pishko, American Scientific Publishers, vol. 2, 2006, pp.113 -123.

[11] G. Sberveglieri, Recent developments in semiconducting thin films gas sensors, Sens. Actuators, B 23, 1995, pp. 103 -109.

[12] U. Weimar, W. Gopel, AC measurements of thin oxide sensors to improve selectivities and sensitivities", Sens. Actuators, B 26 / 27, 1995, pp.13-18.

[13] J.R. Macdonald, Impedance spectroscopy, Wiley, New York, 1987.

[14] D.Tsiulyanu, I.Stratan, A. Tsiulyanu, H.-D. Liess , I. Eisele, Investigation of the oxygen, nitrogen and water vapour cross - sensitivity to NO_2 of tellurium based thin films, Sens. Actuators B 121, 2007 pp. 406 –413.

[15] C.J.F. Bottcher, S. Havrilak, S.Negami, Theory of electronic Polarization, Elsevier, Amsterdam, 1982.

Optical Properties of Phase Change Memory $Ge_1Sb_2Te_4$ Glasses

M.S.IOVU, E.P.COLOMEICO, V.G.BENEA, A.M.ANDRIESH
Institute of Applied Physics, ASM, Str. Academiei 5, MD-2028 Chisinau, R. Moldova
Mihail.iovu@phys.asm.md

Abstract – **Phase change memory materials are promising for the next-generation of non-volatile flash memory that will serve in new mobile computing, entertainment and other handheld electronics. Among them are chalcogenide glasses Ge-Sb-Te (GST) which can exist in two separates structural states – amorphous and cristalline. Switching of the material from one to another state can be done by heating applying an electrical pulse or by exposure to intense laser beam. We report the changes of optical parameters of amorphous $Ge_1Sb_2Te_4$ films under heat treatment and light exposure.**

Index Terms – **Phase change memory materials, optical properties, refractive index**

I. INTRODUCTION

The discovery of chalcogenide glasses in 1955 year as non-crystalline semiconductors and the first systematical investigation of this class of materials belong to Prof. N.A.Goriunova and B.T.Kololmiets [1,2]. The new class of non-crystalline semiconductors is the chalcogenide glasses containing elements of the VI group such as S, Se, Te. The typical representatives of chalcogenide glasses are the arsenic sulfide (As_2S_3) and arsenic selenide (As_2Se_3). The chalcogenide glasses exhibit excellent electrical properties and are suitable optical materials for IR region [3]. In 1968 S.R.Ovshinsky discovered the electrical switching and memory (OVONIC) effects in amorphous semiconductors [4]. These effects stays on the bases to use the amorphous materials as new phase change materials for optical storage media such as CD and DVD recordable and rewritable discs. The concept of phase change memories consists in the use of such semiconductor materials which can exist in two separate structural stable states (for example, amorphous and crystalline). Switching of the material from one to another state can be done by applying an electrical pulse or by exposure to intense laser beam. Using of semiconductor materials with the same composition in amorphous and crystalline phases provides long life, and as such materials were chosen the ternary alloys of the Ge-Sb-Te (GST with the ratio 2:2:5) system and other more complicated chalcogenide glass [5]. Now we briefly will listed the two modern electronic devices: random access memory (RAM) and read only memory (ROM), because they provide high-speed storage [6].

I. ***Random Access Memory (RAM).*** RAM is used in the computer systems for main memory or primary storage. RAM can be divided in volatile and non-volatile type of memories. Volatile memory (temporary memory), also known as volatile storage, is computer memory that requires power to maintain the stored information. Most forms of modern RAM are volatile storage, including dynamic random access memory (DRAM) and static random access memory (SRAM).

II. ***Non-volatile memory (NVM)*** is computer memory that can retain the stored information even when not powered. Examples of non-volatile memory include read-only memory (ROM), flash memory, most types of magnetic computer storage devices (e.g. hard disks, floppy disks), and optical disks. ROM is memory that users cannot write to – traditionally it has been used to store BIOS code in computers.

III. ***Phase Change Random Access Memory (PRAM)*** is also a type of non-volatile computer memory which uses the unique behavior of chalcogenide glass - the "switching" between two states, crystalline and amorphous with the application of heat. PRAM is one of a number of new memory technologies that are attempting to compete in the non-volatile role with the almost universal Flash memory. PRAM is viewed as a next-generation version of non-volatile flash memory that will serve in new mobile computing, entertainment and other handheld electronics.

***Some historical aspects of development of Phase Change Memory Technology*: [7]**

- **September 1966**: Stanford Ovshinsky files first patent on phase change technology;
- **January 1969**: Charles H. Sie published a dissertation at Iowa State University on chalcogenide phase change memory device;
- **June 1969**: US Patent 3,448,302 licensed to Ovshinsky claims first reliable operation of phase change memory;
- **September 1970**: Gordon Moore publishes research in Electronics Magazine;
- **June 1999**: Ovonyx joint venture is formed to commercialize PRAM technology;
- **November 1999**: Lockheed Martin works with Ovonyx on PRAM for space applications;
- **February 2000**: Intel invests in Ovonyx, licenses technology;
- **December 2000**: ST Microelectronics licenses PRAM technology from Ovonyx;
- **March 2002**: Macronix files a patent application for transistor-less PRAM;

- **July 2003**: Samsung begins work on PRAM technology;
- **2003 through 2005**: PRAM-related patent applications filed by Toshiba, Hitachi, Macronix, Renesas, Elpida, Sony, Matsushita, Mitsubishi, Infineon and more;
- **August 2004**: Nanochip licenses PRAM technology from Ovonyx for use in MEMS probe storage;
- **August 2004**: Samsung announces successful 64 Mbit PRAM array;
- **February 2005**: Elpida licenses PRAM technology from Ovonyx;
- **September 2005**: Samsung announces successful 256 Mbit PRAM array, touts 400 μA programming current;
- **October 2005**: Intel increases investment in Ovonyx;
- **December 2005**; Hitachi and Renesas announce 1.5 V PRAM with 100 μA programming current;
- **December 2005**: Samsung licenses PRAM technology from Ovonyx;
- **July 2006**: BAE Systems begins selling the first commercial PRAM, a Radiation Hardened C-RAM 512Kx8 chip;
- **September 2006**: Samsung announces 512 Mbit PRAM device;
- **October 2006**: Intel and STMicroelectronics show a 128 Mbit PRAM chip;
- **December 2006**: IBM Research Labs demonstrate a prototype 3 by 20 nanometers;
- **January 2007**: Qimonda licenses PRAM technology from Ovonyx;
- **April 2007**: Intel's chief technology officer Justin Rattner is set to give the first public demonstration of the company's PRAM (phase-change RAM) technology;
- **October 2007**: Hynix begins pursuing PRAM by licensing Ovonyx technology;
- **February 2008**: Intel and STMicroelectronics announce four-state MLC PRAM and begin shipping samples to customers;
- **December 2008**: Numonyx announces mass production 128 Mbit PCM device to selected customer;
- **June 2009**: Samsung's phase change RAM will go into mass production starting in June;
- **September 2009**: Samsung announces mass production start of 512 Mbit PRAM device;
- **October 2009**: Intel and Numonyx announce they have found a way to stack phase change memory arrays on one die;
- **December 2009**: Numonyx announces 1 Gb 45 nm product;
- **April 2010**: Numonyx releases Omneo PCM Series (P8P and P5Q), both in 90 nm;
- **April 2010**: Samsung releases 512 Mbit PCM with 65 nm process, in Multi-Chip-Package.

During this period and at the present in many research centers in the world, the chalcogenide glasses with phase change properties are studied faceted. Special interests represent the phase change chalcogenides from the cut-of Sb_2Te_3-GeTe (Fig.1a [8]). The investigated glass composition in the present work $Ge_1Sb_2Te_4$ is one of the most stable materials for switching and memory applications.

II. EXPERIMENTAL RESULTS AND DISCUSSION

The chalcogenide $Ge_1Sb_2Te_4$ phase change material was synthesized from high purity initial components Ge, Sb, Te (99.999 %) by conventional melt quenching method. The mixture of high-purity precursors was melted in sealed evacuated quartz ampoules (p=5·10^{-6} Torr) placed in a rocking furnace. The total weight of the synthesized sample was 10 grams. The temperature of the quartz ampoule was slowly increased to 550 ^{o}C at the rate of 50 ^{o}C/hour and kept at this temperature during 24 hours for homogenization. Than the temperature was increased up to 980 ^{o}C at the rate 50 ^{o}C/hour and homogenized at this temperature during 72 hours, and then quenched in the regime of the disconnected furnace. Fig.2 shows the fragment of the crystal structure of the $Ge_1Sb_2Te_4$ [9]. Thin film samples of thickness d~1÷2 μm were prepared by flash thermal evaporation in vacuum of the synthesized initial glasses onto glass substrates.

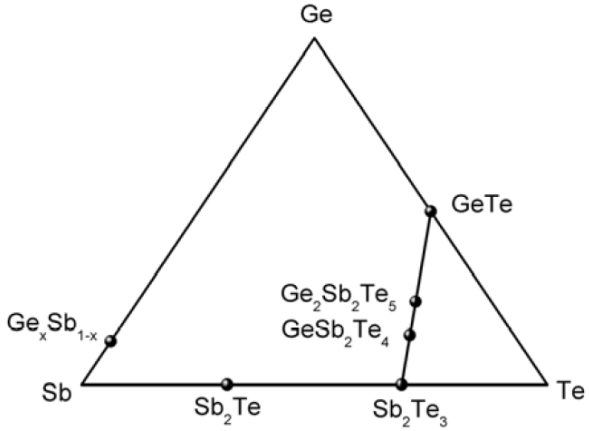

Fig.1. Ternary diagram of the Ge-Sb-Te with phase change materials [8].

For optical transmission spectra measurements a UV/VIS (λ=300÷800 nm) and 61 NIR (λ=800÷3500 nm) Specord's CARLZEISS Jena production were used. For calculation of the optical constants from the transmission spectra, the computer program *PARAV-V1.0* (*www.chalcogenide.eu.org*) was used [10].

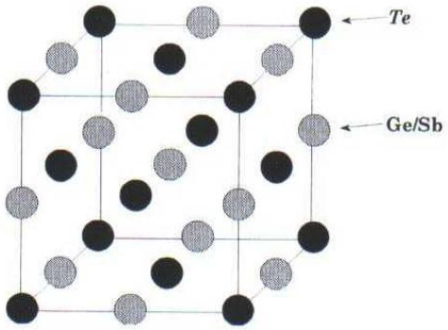

Fig.2. Crystal structure of metastable $Ge_1Sb_2Te_4$ [9].

Fig.3 shows the transmission spectra of as-deposited amorphous $Ge_1Sb_2Te_4$ thin films (1) and annealed at T=150 ^{o}C during 2 minutes. After annealing at high temperature T=150 ^{o}C, due to the crystallization process of the

amorphous film the transmission decrease, and the Urbach tail is shifted in the long wave region of spectrum. The illumination with white during 1 hour does not change the transmission spectra of the as-deposited amorphous film. The spot of phase change transformation of the amorphous material was observed when the film was illuminated with UV laser pulses. According to [9], the samples $Ge_1Sb_2Te_4$ with small addition of oxygen the crystallization phase appear in the temperature range T=130-145 °C, and at higher temperature (around T=275 °C) this phase is transformed into the $Ge_1Sb_2Te_4$ hexagonal phase.

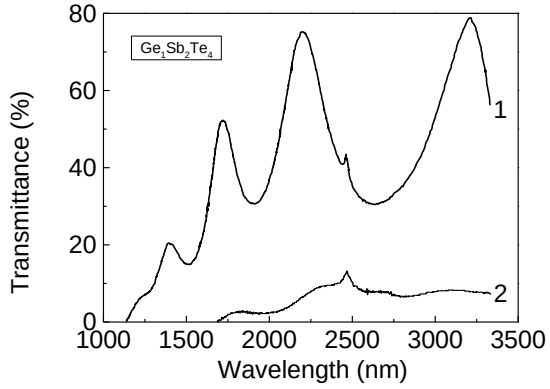

Fig.3. The transmission spectra of as-deposited amorphous $Ge_1Sb_2Te_4$ thin films (1) and annealed at T=150 °C during 2 minutes (2). d=1.57 μm.

Fig.4 shows the dependences of the absorption coefficient α versus photon energy $h\nu$ $(\alpha=f(h\nu)$ (curve 1) and $(\alpha \cdot h\nu)^{1/2}=f(h\nu)$ (curve 2) for as-deposited amorphous $Ge_1Sb_2Te_4$ thin films derivates from the transmission spectra using the computer program *PARAV-V1.0* [8]. The optical transmission $T(\lambda)$ for thin semiconductor films is determined by the expression:

$$T = \frac{(1-R)^2 \exp(-\alpha d)}{1-R^2 \exp(-2\alpha d)}, \qquad (1)$$

where R - is the optical reflection, α - the absorption coefficient, and d - the thickness of the amorphous film. In the consideration that the member $R^2 e^{-2\alpha d} << 1$ from the equation (1) we can obtain the expression for calculation of the absorption coefficient

$$\alpha = \frac{1}{d} \ln \frac{(1-R)^2}{T} \qquad (2)$$

The optical band gap E_g for as-deposited amorphous films was calculated from the relation:

$$(\alpha\, h\nu)^{1/2} = A(h\nu - E_g), \qquad (3)$$

where A – is a constant. A plot $(\alpha \cdot h\nu)^{1/2} \sim h\nu$ (Tauc plot) yields a straight line and the extrapolation of the photon energy axis $(\alpha \cdot h\nu)^{1/2} \to 0$ give the values of the optical band gap E_g. The estimated value of the optical band gap of the as-deposited amorphous $Ge_1Sb_2Te_4$ film is E_g=1.08 eV. For $Ge_1Sb_2Te_4$ it was demonstrated that the measured indirect band gap energies are compared to those of the electronic band-structure calculations [12].

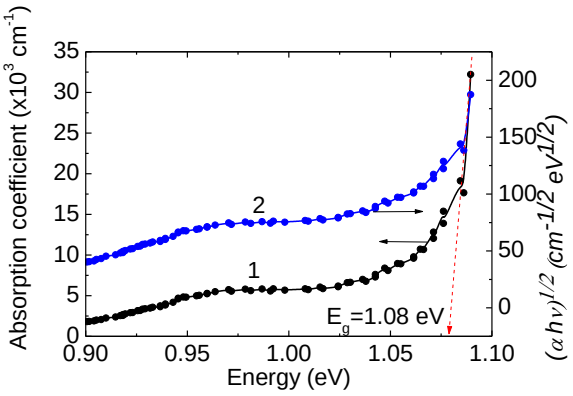

Fig.4. The dependences of the absorption coefficient α versus photon energy $h\nu$ $(\alpha=f(h\nu)$ (1) and $(\alpha \cdot h\nu)^{1/2}=f(h\nu)$ (2) for as-deposited amorphous $Ge_1Sb_2Te_4$ thin films (d=1.57 μm).

Fig.5 represents the dispersion curve of the refractive index $n=f(\lambda)$ for as-deposited amorphous $Ge_1Sb_2Te_4$ thin films. The points are the experimental data, and the continuum line is the computer fitting curve. The plot $(n^2-1)^{-1}$ *vs.* $(h\nu)^2$ (Fig.6) allow to determine the oscillator parameters by fitting a straight line to the experimental points. By extrapolating the fitting line towards $h\nu=0$, one can obtain the static refractive index n_0=3.0 and the static dielectric constant $\varepsilon_s = n^2(0)$ = 9.0.

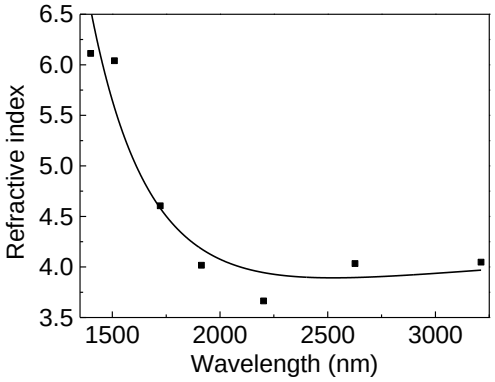

Fig.3a. The dispersion curve of the refractive index $n=f(\lambda)$ for as-deposited amorphous $Ge_1Sb_2Te_4$ thin films (d=1.57 μm).

The dispersion of the refractive index is related to the electronic absorption spectrum through the Wemple equation based on the single electronic oscillator model [13]

$$(n^2-1) = \frac{E_d E_0}{E_0} - (h\nu)^2 \qquad (4)$$

where E_0 is the average electronic energy gap, and E_d is the dielectric oscillator strength.

Large values of the refractive index n are obtained for smaller E_0 and for large E_d and leads to a large dispersion throughout the chalcogenide glass material. From equation (4) we obtain

$$(n^2-1)^{-1} = \frac{E_0}{E_d} - \left(\frac{1}{E_0 E_d}\right)(h\nu)^2 \qquad (5)$$

Using the plot from Fig.3b, the E_0 and E_d were calculated with the values E_0=0.931 eV and E_d=7.448 eV, respectively.

The value of E_0 is smaller than optical band gap E_g=1.08 eV obtained from the Tauc plot (Fig.4).

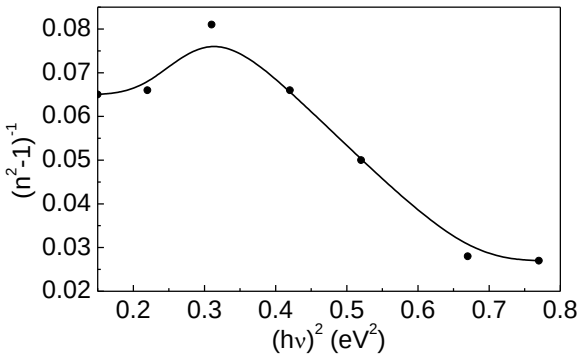

Fig.6. The dependence $(n^2-1)^{-1} = f(h\nu)^2$ for as-deposited amorphous $Ge_1Sb_2Te_4$ thin films (d=1.57 μm).

III. CONCLUSIONS

The X-ray diffraction patterns and optical properties of phase change materials $Ge_1Sb_2Te_4$ were studied. It was established that after annealing of the amorphous films a high temperature (T=150 ^oC) take place the crystallization and the Urbach tail is affected. Grom the transmission spectra the optical constants absorption coefficient α, optical band gap E_g, and the refractive index n) of the amorphous $Ge_1Sb_2Te_4$ were determined.

The static refractive index n_0=3.0, static dielectric constant $\varepsilon_s = n^2(0)$ = 9.0, average electronic energy gap E_0=0.931 eV, and the dielectric oscillator strength E_d=7.448 eV were estimated from the optical measurements.

REFERENCES

[1] N.A.Goriunova, B.T.Kolomiets, Structure and properties of ternary semiconducting systems, *Journal of Technical Physics* **25,** 984-994 (1955) (in Russian).

[2] N.A.Goriunova, B.T.Kolomiets, New vitreous semiconductors, *USSR Academy of Sciences Letters, Physical Series* **20**, 1496-1500 (1956) (in Russian).

[3] N.F.Mott, E.A.Davis, *Electron processes in non-crystalline materials*, Clarendon Press, Oxford (1979).

[4] S.R.Ovshinsky, Reversible electrical switching phenomena in disordered structures, *Physical Review Letters* **21**, 1450-1453 (1968).

[5] Mihai A.Popescu, Ovonic materials, *J. of Ovonic Research* **1**, 69-76 (2005).

[6] http://www.giac.org/resources/whitepaper/architecture/102.php

[7] http://en.wikipedia.org/wiki/Phase-change_memory

[8] A.Velea. Tellurium based phase change materials. Journal of Optoelectronics and Advanced Materials **11**(12), 1983-1987 (2009).

[9] Mihai Popescu. Structural modeling of ovonic materials. *J. of Ovonic Research* **2**(4), 45-52 (2006).

[10] Ganjoo A., Golovchak R. *Journal of Optoelectronics and Advanced Materials*, **10**(6), 1328 (2008).

[11] M.Frumar, T.Kohoutek, J.Prikryl, J.Orava, T.Wagner. On the atomic structure of thin amorphous Ge-Sb-Te films. *Physica Status Solidi* (b) **246**(8), 1871-1874 (2009).

[12] Jun-Woo Park, S.E.Eom, H.Lee et al. Optical properties of pseudobinary GeTe, $Ge_2Sb_2Te_5$, $GeSb_2Te_4$, $GeSb_4Te_7$, and Sb_2Te_3 from ellipsometry and density functional theory. *Phys. Rev*. **B 80**, 115209 (2009) [14 pages].

[13] Y.Ruan, R.A.Jarvis, A.V.Rode et al. Wavelength dispersion of Verdet constants in chalcogenide glasses for magneto-optical waveguide devices. *Optics Communications* **252**, 39-45 (2005).

Exchange Electron-Hole Interaction of Two-Dimensional Magnetoexcitons under the Influence of the Rashba Spin-Orbit Coupling

S.A. MOSKALENKO[1,*], I.V. PODLESNY[1], B.V. NOVIKOV[2], E.S. KISELYOVA[3], I.A. LELYAKOV[1], and L. GHERCIU[1,3]

[1]*Institute of Applied Physics, Academy of Sciences of Moldova, 5, Academiei str., MD-2028, Chisinau, Republic of Moldova*

[2]*Department of Solid State Physics, Institute of Physics, St.Petersburg State University, 1, Ulyanovskaya str., Petrodvorets, 198504, St.Petersburg, Russia*

[3]*Moldova State University, 60, A. Mateevici str., MD-2009, Chisinau, Republic of Moldova*

[*]*exciton@phys.asm.md*

***Abstract* – The Rashba spin-orbit coupling (RSOC) in the case of two-dimensional (2D) electrons and holes in a strong perpendicular magnetic field was studied. The spinor-type wave functions are characterized by different numbers of Landau levels in different spin projections. For electrons they differ by 1 as was established earlier by Rashba [1], whereas for holes they differ by 3. Two lowest electron states and four lowest hole states of Landau quantization give rise to eight 2D magnetoexciton states. The exchange electron-hole interaction in the frame of these states is investigated.**

***Index Terms* – quantum transitions, Rashba spin-orbit coupling, Landau quantization, magnetoexcitons.**

I. INTRODUCTION[**]

Since the mid 1980s, there has been an extensive interest in the effects of an applied electric field normal to the layers on the optical properties of semiconductor quantum wells (QWs) and superlattices (SLs) [2]. The electric field strength perpendicular to the layer surface gives rise to Rashba spin-orbit coupling (RSOC). The spin-orbit effects are discussed in a special monograph [3] and papers [2, 4-9]. In the Ref. [10-12] the energy spectrum of 2D magnetoexcitons were studied supposing that the spin polarizations of electrons and holes take place and the spin-orbit coupling was neglected. In reality, as was shown in Ref. [13], the RSOC leads to breaking of the pure spin polarizations and the new spinor-type states are characterized by different numbers of Landau levels for different spin projections. These numbers for electrons differ by 1, whereas for holes differ by 3. Spin polarized states under the influence of the RSOC are transformed into mixed spinor components. The two lowest electron states and four lowest hole states were used to construct eight lowest 2D magnetoexciton states [13]. The direct Coulomb electron-hole interaction gives rise to the binding energies and ionization potentials of the magnetoexciton states. They were calculated in Ref. [10-12]. Below we will use these results to determine the exchange electron-hole interaction.

II. EXCHANGE ELECTRON-HOLE INTERACTION

The electron-hole Coulomb interaction is calculated below taking into account the influence of the RSOC in the frame of conduction and valence bands. The corresponding Bloch wave functions including their periodic parts are

$$\left|\Psi_c(R_1,p;x,y)\right\rangle = \frac{e^{ipx}}{\sqrt{L_x}}U_{c,s,p}(\vec{r})\begin{vmatrix} a_0\varphi_{c,0}(y,p) \\ b_1\varphi_{c,1}(y,p)\end{vmatrix};$$

$$\left|\Psi_c(R_2,p;x,y)\right\rangle = \frac{e^{ipx}}{\sqrt{L_x}}U_{c,s,p}(\vec{r})\begin{vmatrix} 0 \\ \varphi_{c,0}(y,p)\end{vmatrix};$$

$$\left|\Psi_v(R_1,q;x,y)\right\rangle = \frac{e^{iqx}}{\sqrt{L_x}}\frac{1}{\sqrt{2}}(U_{v,P,X,q}(\vec{r})-iU_{v,P,Y,q}(\vec{r}))\begin{vmatrix} c_3\varphi_{v,3}(y,q) \\ d_0\varphi_{v,0}(y,q)\end{vmatrix};$$

$$\left|\Psi_v(R_2,q;x,y)\right\rangle = \frac{e^{iqx}}{\sqrt{L_x}}\frac{1}{\sqrt{2}}(U_{v,P,X,q}(\vec{r})+iU_{v,P,Y,q}(\vec{r}))\begin{vmatrix} \varphi_{v,0}(y,q) \\ 0\end{vmatrix};$$

$$\left|\Psi_v(R_3,q;x,y)\right\rangle = \frac{e^{iqx}}{\sqrt{L_x}}\frac{1}{\sqrt{2}}(U_{v,P,X,q}(\vec{r})-iU_{v,P,Y,q}(\vec{r}))\begin{vmatrix} c_4\varphi_{v,4}(y,q) \\ d_1\varphi_{v,1}(y,q)\end{vmatrix};$$

$$\left|\Psi_v(R_4,q;x,y)\right\rangle = \frac{e^{iqx}}{\sqrt{L_x}}\frac{1}{\sqrt{2}}(U_{v,P,X,q}(\vec{r})+iU_{v,P,Y,q}(\vec{r}))\begin{vmatrix} \varphi_{v,1}(y,q) \\ 0\end{vmatrix}. \quad (1)$$

The orthogonality each other of the conduction and valence electron Bloch wave functions is attained due to their orthogonal periodic parts, whereas the orthogonality of the wave functions belonging to the same bands and having the same periodic parts is reached due to different numbers of the Landau quantization wave functions $\varphi_{c,n}(y,p)$ and $\varphi_{v,m}(y,p)$. The conduction and valence electrons have the same electric charge — $|e|$ and their dimensionless variables have the same structure $\frac{y}{l}-pl$ and $\frac{y}{l}-ql$. The last variable looks as $\frac{y}{l}+ql$ in the case of the hole wave function $\varphi_{h,n}(y,q)$ due to the positive value of the hole charge $|e|$.

We will consider eight combinations of the electron-hole pairs taking into account two spin-splitted electron Landau levels $\left|e,R_1\right\rangle$ and $\left|e,R_2\right\rangle$ and four spin-splitted hole Landau levels $\left|h,R_j\right\rangle$ with $j=1,2,3,4$. These combinations will be denoted by

[**] I.V.P. thanks the Foundation for young scientists of the Academy of Sciences of Moldova for financial support (11.819.05.13F).

$$f_s = (e, R_i; h, R_j);\ s = 1,\ldots,8;\ i = 1,2;\ j = 1,2,3,4. \quad (2)$$

The wave functions of eight magnetoexciton states with electron states R_1 and R_2 and with four hole states R_1, R_2, R_3 and R_4 can be expressed through the corresponding creation and annihilation operators. For example, in the compositions f_s represented by the formulas (2), we have

$$\Psi_{ex}(\vec{k}, f_s) = \frac{1}{\sqrt{N}}\sum_t e^{-ik_y tl^2} a^{\dagger}_{R_i, \frac{k_x}{2}+t} b^{\dagger}_{R_j, \frac{k_x}{2}-t};$$
$$s = 1,2,\ldots,8;\ i = 1,2;\ j = 1,2,3,4. \quad (3)$$

Side by side with the direct Coulomb interaction it is necessary to study the exchange Coulomb e-h interaction. In the case of Wannier-Mott excitons in the absence of external magnetic field and RSOC it gives rise to the singlet-triplet splitting of the exciton levels. It is due to the contact or short-range part of the exchange e-h interaction and is revealed very well experimentally in the case of ortho- and para-excitons in Cu_2O crystal. The long-range part of this interaction determines the longitudinal-transverse splitting of the three-fold degenerated dipole-active exciton levels in cubic crystals as well as the polariton gap [14]. These questions were not studied at all in the case of 2D magnetoexcitons and more so in the presence of the RSOC. They will be discussed below. The exchange e-h interaction has its origin in the exchange Coulomb interaction between the conduction electron and valence electron. At first we will consider the conduction electron in the state R_1 and the valence electron in the state R_1 in the frame of Landau quantization and RSOC.

The corresponding Hamiltonian is

$$H^{c-v}_{exch} = \sum_{p,q,s} F_{c-v}(c, R_1, p; v, R_1, q; v, R_1, p-s; c, R_1, q+s) \times a^{\dagger}_{c,R_1,p} a^{\dagger}_{v,R_1,q} a_{c,R_1,q+s} a_{v,R_1,p-s}, \quad (4)$$

where

$$F_{c-v}(c, R_1, p; v, R_1, q; v, R_1, p-s; c, R_1, q+s) = \int d\bar{1}\int d\bar{2}\left\langle c, R_1, p, (\bar{1})\middle|\left\langle v, R_1, q, (\bar{2})\middle|V(\bar{1}-\bar{2})\right\rangle\middle|v, R_1, p-s, (\bar{1})\right\rangle\middle|c, R_1, q+s, (\bar{2})\right\rangle \quad (5)$$
$$= \int d\bar{1}\int d\bar{2}\frac{e^{is(x_2-x_1)}}{L_x^2} W\ (\bar{1}; c, p; v, p-s)$$
$$\times\left[a_0^* c_3 \varphi^*_{c,0}(y_1, p)\varphi_{v,3}(y_1, p-s) + b_1^* d_0 \varphi^*_{c,1}(y_1, p)\varphi_{v,0}(y_1, p-s)\right] V(\bar{1}-\bar{2})$$
$$\times W^*(\bar{2}; c, q+s; v, q)\left[c_3^* a_0 \varphi^*_{v,3}(y_2, q)\varphi_{c,0}(y_2, q+s) + d_0^* b_1 \varphi^*_{v,0}(y_2, q)\varphi_{c,1}(y_2, q+s)\right]$$

and

$$b_1 = \frac{-i\alpha\sqrt{2}a_0}{\frac{1}{2}+\sqrt{\frac{1}{4}+2\alpha^2}};\ |a_0|^2 + |b_1|^2 = 1;$$
$$c_3 = \frac{-i\beta 4\sqrt{3}d_0}{\frac{3}{2}+\sqrt{\frac{9}{4}+48\beta^2}};\ |d_0|^2 + |c_3|^2 = 1. \quad (6)$$

with electron and hole SOC parameters $\alpha = \alpha_e E_z / l\hbar\omega_{ce}$, $\beta = \beta_h E_z / l^3\hbar\omega_{ch}$ correspondingly.

Here the exchange charge density of electron was introduced

$$W\ (\vec{r}; c, p; v, p-s) = U^*_{c,S,p}(\vec{r})\frac{1}{\sqrt{2}}\left(U_{v,P,X,p-s}(\vec{r}) - iU_{v,P,Y,p-s}(\vec{r})\right). \quad (7)$$

It depends on the product of two periodic parts of the Bloch functions of electron in conduction and valence bands. We have introduced the variables $\vec{\rho}_1$ and $\vec{\rho}_2$, changing inside the lattice cell with the volume $v_0 = a_l^3$, where a_l is the lattice period, as well as two continuous variables $\vec{R}_1$ and $\vec{R}_2 = \vec{R}_1 + \vec{R}$ enumerating the lattice nodes. Four integrations are effectuated separately, two on the volume v_0 of the lattice cell and two integrations on $\vec{R}_1$ and $\vec{R}$ on the surface of the 2D layer. In difference on the case of the direct Coulomb interaction, the integration on the lattice cell volume v_0 of the exchange charge densities without participation of the functions describing the Coulomb interaction vanish due to the orthogonality of the periodic parts of the Bloch functions belonging to different bands

$$\frac{1}{v_0}\int_{v_0} d\vec{\rho}_1 W\ (\vec{\rho}_1; c, p; v, p-s) = 0;\ \frac{1}{v_0}\int_{v_0} d\vec{\rho}_2 W^*(\vec{\rho}_2; c, q+s; v, q) = 0. \quad (8)$$

It means that in the frame of the exchange Coulomb interaction two electrons do not behave as a point charges, but rather as two inter-band dipoles situated on different nodes $(R \neq 0)$ of the lattice. To demonstrate this picture the Coulomb interaction potential will be represented in the form

$$\frac{1}{|\vec{r}_2 - \vec{r}_1|} = \frac{1}{|\vec{R} + \vec{\rho}_2 - \vec{\rho}_1|} = \begin{cases} \dfrac{1}{|\vec{\rho}_2 - \vec{\rho}_1|}, & R = 0 \\ \dfrac{1}{R} + \dfrac{(\vec{\rho}_1 \cdot \vec{\rho}_2)}{R^3} - \dfrac{3(\vec{\rho}_1 \cdot \vec{R})(\vec{\rho}_2 \cdot \vec{R})}{R^5}, & R \neq 0. \end{cases} \quad (9)$$

This representation permits to separate the contact or short-range interaction, when both electrons are in the same unit lattice cell $(R = 0)$, and the long-range part, where $\vec{R}$ differs from zero $(\vec{R} \neq 0)$.

The inter-band dipole moments appear as follows

$$\vec{d}_{cv}(p, p-s) = \frac{e}{v_0}\int_{v_0} d\vec{\rho}_1 W\ (\vec{\rho}_1; c, p; v, p-s)\vec{\rho}_1 e^{-is\rho_{1x}},$$
$$\vec{d}^*_{cv}(q+s, q) = \frac{e}{v_0}\int_{v_0} d\vec{\rho}_2 W^*(\vec{\rho}_2; c, q+s; v, q)\vec{\rho}_2 e^{-is\rho_{2x}}. \quad (10)$$

The integrations on the large-scale variable $\vec{R}_1$ involve different combinations of the Landau quantization functions $\varphi_n(R_{1y}, p)$ and $\varphi_n(R_{1y}+R_y, p)$ in the following combinations

$$G_{0,0;3,3}(R_y) = G(0, p; 0, q+s; 3, p-s; 3, q \mid R_y)$$
$$= \int dR_{1y}\varphi^*_{c,0}(R_{1y}, p)\varphi_{c,0}(R_{1y}+R_y, q+s)\varphi_{v,3}(R_{1y}, p-s)\varphi^*_{v,3}(R_{1y}+R_y, q);$$
$$G_{1,1;0,0}(R_y) = G(1, p; 1, q+s; 0, p-s; 0, q \mid R_y)$$
$$= \int dR_{1y}\varphi^*_{c,1}(R_{1y}, p)\varphi_{c,1}(R_{1y}+R_y, q+s)\varphi_{v,0}(R_{1y}, p-s)\varphi^*_{v,0}(R_{1y}+R_y, q);$$
$$G_{0,1;3,0}(R_y) = G(0, p; 1, q+s; 3, p-s; 0, q \mid R_y)$$
$$= \int dR_{1y}\varphi^*_{c,0}(R_{1y}, p)\varphi_{c,1}(R_{1y}+R_y, q+s)\varphi_{v,3}(R_{1y}, p-s)\varphi^*_{v,0}(R_{1y}+R_y, q);$$
$$G_{1,0;0,3}(R_y) = G(1, p; 0, q+s; 0, p-s; 3, q \mid R_y)$$
$$= \int dR_{1y}\varphi^*_{c,1}(R_{1y}, p)\varphi_{c,0}(R_{1y}+R_y, q+s)\varphi_{v,0}(R_{1y}, p-s)\varphi^*_{v,3}(R_{1y}+R_y, q). \quad (11)$$

The exchange e-h interaction is represented below as a sum of contact and long-range parts

$$F_{c-v}(c, R_1, p; v, R_1, q; v, R_1, p-s; c, R_1, q+s) = A_{cont}(R_1, R_1; p, q, s) + V_{l-r}(R_1, R_1; p, q, s). \quad (12)$$

The contact part equals to

$$A_{cont}(R_1, R_1; p, q, s) = \frac{a_l^2}{L_x}\frac{1}{v_0}\int_{v_0} d\vec{\rho}_1 \frac{1}{v_0}\int_{v_0} d\vec{\rho}_1 W\ (\vec{\rho}_1; c, p; v, p-s) W^*(\vec{\rho}_2; c, q+s; v, q)\frac{e^2}{\varepsilon_0|\vec{\rho}_2 - \vec{\rho}_1|}e^{-s(\rho_{2x}-\rho_{1x})}$$
$$\times\left[|a_0|^2|c_3|^2 G_{0,0;3,3}(0) + |d_0|^2|b_1|^2 G_{1,1;0,0}(0) + a_0^* d_0^* c_3 b_1 G_{0,1;3,0}(0) + b_1^* c_3^* d_0 a_0 G_{1,0;0,3}(0)\right], \quad (13)$$

whereas the long-range part contains a supplementary

summation on the large scale variable $\vec{R}$

$$V_{l-r}(R_1,R_1;p,q,s)=\frac{a_l^2}{L_x}\sum_{\vec{R}\neq 0}e^{isR_x}$$
$$\times\left[\frac{\left(\vec{d}_{cv}(p,p-s)\cdot\vec{d}^{\,*}_{cv}(q+s,q)\right)}{R^3}-\frac{3\left(\vec{d}_{cv}(p,p-s)\cdot\vec{R}\right)\left(\vec{d}^{\,*}_{cv}(q+s,q)\cdot\vec{R}\right)}{R^5}\right] \quad (14)$$
$$\times\Big[|a_0|^2|c_3|^2\,G_{0,0;3,3}(R_y)+|d_0|^2|b_1|^2\,G_{1,1;0,0}(R_y)$$
$$+a_0^*d_0^*c_3b_1G_{0,1;3,0}(R_y)+b_1^*c_3^*d_0a_0G_{1,0;0,3}(R_y)\Big].$$

Here the summation on the variable $\vec{R}$ can be substituted by integration as follows $a_l^2\sum_{\vec{R}\neq 0}=\int dR_x\int dR_y$.

The Hamiltonian (4) with the operators

$$b^\dagger_{R_j,q}=a_{v,R_j,-q};\ b_{R_j,q}=a^\dagger_{v,R_j,-q};\ a_{c,R_i,p}=a_{R_i,p};$$
$$a^\dagger_{v,R_j,q}a_{v,R_j,q+s}=b_{R_j,-q}b^\dagger_{R_j,-q-s}=-b^\dagger_{R_j,-q-s}b_{R_j,-q}+\delta_{kr}(s,0). \quad (15)$$

after the normal ordering of the hole operators will give rise to the Hamiltonian of the exchange e-h interaction concerning the states c,R_1 and v,R_1. It is

$$H^{e-h}_{exch}=\sum_{p,q,s}\left[A_{cont}(R_1,R_1;p,q,s)+V_{l-r}(R_1,R_1;p,q,s)\right]$$
$$\times a^\dagger_{R_1,p}b^\dagger_{R_1,-p+s}b_{R_1,-q}a_{R_1,q+s}. \quad (16)$$

On the ways from the initial expression (4) to the final form (16) correspondingly we have separated the quadratic free electron Hamiltonian

$$\sum_p\left[F_{c-v}(c,R_1,p;v,R_1,q;c,R_1,p-s;v,R_1,q+s)\right.$$
$$\left.-F_{c-v}(c,R_1,p;v,R_1,q;v,R_1,p-s;c,R_1,q+s)\right]a^\dagger_{R_1,p}a_{R_1,p}. \quad (17)$$

It describes the influence on the conduction electron of the valence electrons, which together with the electrons of the inner atomic shells create the effective periodic potential of the lattice. The terms (17) compensate the difference between the periodic potential created by the inner atomic shells and the real effective periodic potential created by all electrons including the valence electrons [14]. The effective periodic potential determines the electron wave functions (1) used in our calculations and at the same time depends in a self-conjugated way on their forms, it means on the presence of a strong perpendicular magnetic field as well as on the RSOC. Above we have calculated the exchange interaction matrix element for the first combination f_1 of the electron wave functions $|c,R_i,p\rangle$ and $|v,R_j,q\rangle$ with $i=1,2$ and $j=1,2$. For another three combinations we have obtained the formulas similar to the expressions (13) and (14). The only differences concern the square brackets, where must be written correspondingly

$$\begin{aligned}&|a_0|^2\,G_{0,0;0,0}(R_y)\ \text{ for }\ f_2=(c,R_1;v,R_2),\\ &|d_0|^2\,G_{1,1;0,0}(R_y)\ \text{ for }\ f_3=(c,R_2;v,R_1),\\ &0\ \text{ for }\ f_4=(c,R_2;v,R_2).\end{aligned} \quad (18)$$

The Hamiltonian describing the exchange electron-hole interaction has the form

$$H^{e-h}_{exch}=\sum_{p,q,s}\sum_{i=1,2}\sum_{j=1,2,3,4}F_{c-v}(c,R_i,p;v,R_j,q;v,R_j,p-s;c,R_i,q+s)$$
$$\times a^\dagger_{R_i,p}b^\dagger_{R_j,-p+s}b_{R_j,-q}a_{R_i,q+s}. \quad (19)$$

The average values of this Hamiltonian were calculated with the exciton wave functions (3). They determine the shifts of the magnetoexciton energy levels due to the exchange e-h interactions. They are equal to

$$\frac{1}{N}\sum_{p,q}F_{c-v}(c,R_i,p;v,R_j,q;v,R_j,p-k_x;c,R_i,q+k_x)e^{ik_y(p-q-k_x)l^2}, \quad (20)$$
$$i=1,2;\ \ j=1,2,3,4.$$

III. CONCLUSION

The spinor-type wave functions of the 2D electrons and holes in the presence of the RSOC were used to calculate the exchange electron-hole interaction in the frame of 2D magnetoexcitons. Two lowest Landau levels for electrons $|e,R_1\rangle$, $|e,R_2\rangle$ and four lowest Landau levels for holes $|h,R_1\rangle$, $|h,R_2\rangle$, $|h,R_3\rangle$, and $|h,R_4\rangle$ were combined in such a way so as to form eight electron-hole states corresponding to the combinations: $f_1=(e,R_1;h,R_1)$; $f_2=(e,R_1;h,R_2)$; $f_3=(e,R_2;h,R_1)$; $f_4=(e,R_2;h,R_2)$; $f_5=(e,R_1;h,R_3)$; $f_6=(e,R_1;h,R_4)$; $f_7=(e,R_2;h,R_3)$; $f_8=(e,R_2;h,R_4)$. The exchange e-h interaction consists from the contact and long-range terms. The contact interaction depends only on the integration on the elementary lattice cell, whereas the long-range part contains a supplementary summation on the large scale variable representing the distance between two lattice nodes in the neighborhood of which the electron and hole are localized. In the frame of exchange Coulomb interaction conduction electron and valence electron do not behave as a point charges, but rather as two inter-band dipoles situated on different nodes of the lattice.

REFERENCES

[1] E.I. Rashba, Sov. Phys. Fiz. Tverd. Tela (Leningrad), vol. 2, p. 1224, 1960.

[2] Bang-fen Zhu and Yia-Chung Chang, Phys. Rev. B, vol. 50, p. 11932, 1994.

[3] Roland Winkler, Spin-Orbit Coupling Effects in Two-Dimensional Electron and Hole Systems, Springer Tracts in Modern Physiscs: Springer, Berlin, Heidelberg, vol. 191, 228 pages, 2003.

[4] Ralph van Gelderen and C. Morais Smith, Phys. Rev. B, vol. 81, p. 125435, 1994.

[5] S.A. Brazovskii, Zh. Eksp. Teor. Fiz., vol. 68, p. 175, 1975; Sov. Phys. JETP, vol. 41, p. 85, 1975.

[6] R. Winkler, M. Merkler, T. Darnhofer, and U. Rossler, Phys. Rev. B, vol. 53, p. 10858, 1996.

[7] U. Ekenberg and M. Altarelli, Phys. Rev. B, vol. 32, p. 3712, 1985.

[8] R. Winkler, Phys. Rev. B, vol. 62, p. 4245, 2000.

[9] R. Winkler, H. Noh, E. Tutuc, and M. Shayegan, Phys. Rev. B, vol. 65, p. 155303, 2002.

[10] S.A. Moskalenko, M.A. Liberman, P.I. Khadzhi, E.V. Dumanov, Ig.V. Podlesny, and V.V. Botan, Solid State Commun., vol. 140, p. 236, 2006.

[11] S.A. Moskalenko, M.A. Liberman, P.I. Khadzhi, E.V. Dumanov, Ig.V. Podlesny, and V.V. Boţan, Physica E, vol. 39, p. 137, 2007.

[12] S.A. Moskalenko, M.A. Liberman, and I.V. Podlesny, Phys. Rev. B, vol. 79, p. 125425, 2009.

[13] T. Hakioglu, M.A. Liberman, S.A. Moskalenko, and I.V. Podlesny, Phys. Rev. B, (submitted).

[14] S.A. Moskalenko, Introduction in the theory of high density excitons, Chisinau, Shtiintsa, 304 pages, 1983.

Magnetotransport Properties of Ultrathin $LaMnO_3$ Layers

Oleg SHAPOVAL, Alexander BELENCHUK, Efim ZASAVITSKY, Valeriu KANTSER,
IIEN, AS RM, str. Academiei 3/3, MD 2028, Chisinau, Republica Moldova
shapoval@lises.asm.md
Vasily MOSHNYAGA
Erstes Physikalisches Institut, Universität Göttingen, Friedrich-Hund-Platz 1, 37077 Göttingen, Germany

***Abstract* – We report the transport and magnetic properties of La-deficient ultrathin films of $La_{1-\delta}MnO_3$ (LMO) grown on $SrTiO_3$ (STO) and engineered by using different interfacial layers. LMO layer and adjusting interface oxide (LaO-STO and SMO) layers were grown by a metalorganic aerosol deposition technique with monolayer accuracy. The role of LaO-TiO_2 interface in the formation of ferromagnetic metallic state in very thin LMO films was demonstrated. Ferromagnetic metallic ground state in LMO films with the thickness down to 6 monolayers is stabilized by a combination of a La-deficiency and the interface-induced doping.**

***Index Terms* – magnetotransport, metal-insulator transition, metalorganic aerosol deposition, oxide interfaces, thin film.**

I. INTRODUCTION

To enhance the functionality of all-oxide based devices the idea of the interface engineering of multilayered oxide heterostructures was put forward in the last few years. $LaMnO_3$ (LMO) is one of the promising materials used for the interfacial design of different multilayer systems. The stoichiometric LMO with the nominal $t^3_{2g}e^1_g$ occupancy of Mn^{3+} ions is an insulator with strong Mott-Hubbard correlations in a half-filled e_g band [1]. An *A*-type antiferromagnetic (AFM) ground state originates due to the orbital ordering of e_g-orbitals with ferromagnetic (FM) in-plane and AFM out-of-plane exchange interactions. Nevertheless, LMO can be easily transformed into an FM metal, particularly in thin films [2] and superlattices of LMO/SMO [3] and LMO/STO [4]. The ferromagnetism was shown to be due to the change of: a) stoichiometric cationic composition; b) optimal oxygen content as well as c) due to epitaxial stabilization of a nonstoichiometric state in the layers grown on $SrTiO_3$ (STO) (100) substrates [2, 5]. The "electron leakage" phenomenon, caused by the polar discontinuity at the interfaces, was shown to control the magnetotransport in superlattices [4, 6]. The main parameter, influencing the direction of charge leakage and, therefore, the magnetic properties, is the substrate-induced epitaxial strain. The interest to LMO as a functional material was recently stirred up by the demonstration of a metal-insulator transition at T_{MI} >400 K in a heavy La-deficient films [7].

An important question, concerning to electronic and structural reconstruction at the interfaces, is the atomic structure of stacking planes. The LMO/SMO system demonstrates exclusively the LaO-MnO_2-SrO sequence of atomic planes at the interface [8]. In contrast, the LMO/STO system reveals two types of interfaces due to different A- and B-site occupancies in the perovskite lattices. Namely, 1) (LaO-MnO_2)-(SrO-TiO_2) (compactly MnO_2-SrO)) and 2) (MnO_2-LaO)-(TiO_2-SrO) (or LaO-TiO_2) [9] interfaces were observed. In this case one should expect different interface-induced properties [10]. An example of such different properties attributed to A^1O-B^2O_2 and A^2O-B^1O_2 interfaces for the $A^1B^1O_3$-$A^2B^2O_3$ stacked perovskites was demonstrated for the well-known $LaAlO_3/SrTiO_3$ system [11], where AlO_2-LaO-TiO_2 stacked planes are electronically reconstructed and show a metallic behavior, whereas the AlO_2-SrO-TiO_2 interface is insulating due to atomic reconstruction.

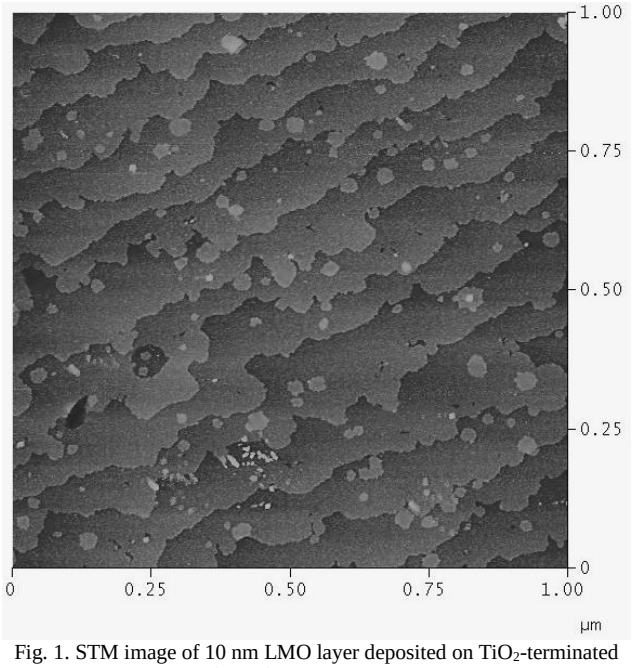

Fig. 1. STM image of 10 nm LMO layer deposited on TiO_2-terminated surface of STO(100) substrate.

A single heterojunction for an $A^1B^1O_3$ layer, grown on the STO(100) substrate, can be modified by TiO_2- or SrO-termination of the substrate surface. In the case of multilayered $A^1B^1O_3$-$A^2B^2O_3$ structures a conventional growth techniques produce two types of interfaces [9]. The first layer starts from A^1O-plane on TiO_2-terminated surface STO(100) substrate and terminates by B^1O_2-plane; the next layer repeats the alternation of AO- and BO_2-planes. A possibility to tailor the superlattices with single type of interface by introducing an extra-plane was recently demonstrated for LMO/STO system [4]. The presence of

extra LaO-planes in manganite layers and TiO_2-planes in titanate layers was confirmed by STEM combined with EELS analysis.

The aim of the presented work was to study magnetotransport properties of ultrathin LMO films with thicknesses comparable to the thickness of single layers in SL's. To design the LMO-based layered structures with optimized FM metallic behavior two approaches were applied: 1) the La-deficiency was intentionally generated in the LMO layer and 2) ultrathin LMO films were engineered by different interfaces.

II. EXPERIMENT AND RESULTES

The samples were prepared by a metalorganic aerosol deposition (MAD) technique, elaborated earlier for the preparation of complex oxide thin films and further developed for the deposition of ultrathin films and superlattices [12]. Aerosols of organic solutions, containing metal β- diketonates (e.g. La-, Sr-, Mn-acetylacetonates), were sprayed onto a heated substrate. A film grows on the substrate as a result of a heterogeneous pyrolysis reaction of the metalorganic component. Within the MAD technique one can easily manipulate the precursor solutions, which contain either a single precursor for mono-oxide layers or a mixture of two and more precursors to produce layers of complex oxides. The monolayer accuracy was achieved by accurate calibration of dosing units. Vacuum-free MAD technique allowed us to interrupt deposition process and to continue the preparation of the layered structure after intermediate express measurements.

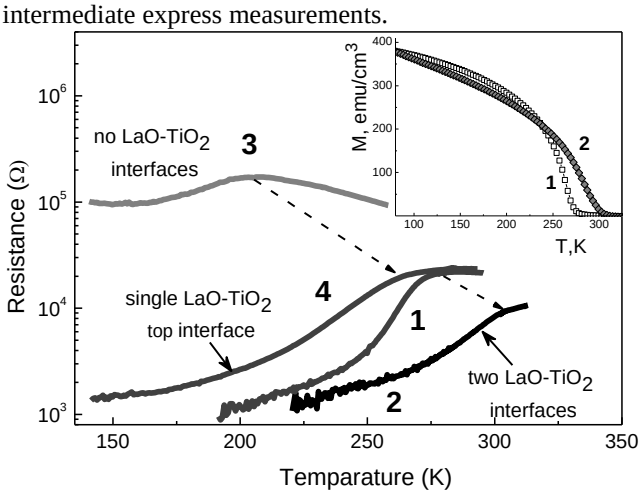

Fig. 2. Evolution of transport properties of 10 nm LMO layers deposited on STO(100) substrates and equipped with: (1) bottom LaO-TiO2 interface; (2) top and bottom LaO-TiO2 interfaces; (3) no LaO-TiO2 interface; (4) top LaO-TiO2 interface. Insert: Magnetization as function of temperature.

STO(100) substrate was chosen due to the possibility to study the influence of both surface terminations. The atomically smooth TiO_2-terminated STO(100) with terrace steps of one unit cell in height was obtained by treating the crystal surface with a pH-controlled NH_4F-HF solution [13]. SrO-terminated surface was produced by deposition of SrO monolaeyer (ML) on TiO_2- terminated surface. The exact oxygen stoichiometry in the prepared $LaMnO_3$ layers was assumed due to a high (atmosphere) gas pressure conditions [12].As the criteria of a stoichiometric La/Mn=1:1 relation we used the insulating behavior of the film, unique for a stoichiometric LMO, as well as smooth and flat surface morphology (Fig. 1) with terraces inherited from STO. The deviation of La molar content from the "right" La/Mn-ratio in the solution was used in the sequel as a measure of the La-deficiency. The La-deficiency of LMO layers was varied in the range 0-12%. The thickness of LMO films was d=6-30 unit cells (u.c.) or d=2.5-12 nm.

LMO layers were deposited directly onto both TiO_2- and SrO-terminated substrates or onto the STO surface, buffered by 2 u.c. of SMO. The top surface of LMO films have been remained free or covered by 2 u.c. of the cap layer, e.g. STO or SMO. Electron transport measurements were performed by standard 4-probe technique using commercial PPMS from "Quantum Design". Magnetization was measured by means of commercial SQUID (MPMS, "Quantum Design").

The role of LaO-TiO_2 interface was examined on series of samples with the same La-deficiency, δ=6 %, and thickness of LMO layer. The influence of LaO-TiO_2 interfaces on the electron transport as a function of temperature is shown in Fig. 2. We suppose that the growth of LMO on the TiO_2-terminated STO(100) from a solution, containing both La and Mn precursors, occurs in the following way. It starts from LaO-plane, forming the LaO-TiO_2 interface, and terminates with MnO_2 plane completing perovskite monolayer [9]. Thus, the LMO film with one (bottom) LaO-TiO_2 interface and free surface (top) was prepared after deposition of 26 perovskite unit cells of LMO. Such film demonstrates a metal-insulator (MI) transition at T_{MI}=285K and metallic behavior at low temperatures (curve 1 Fig. 2). A deposition of one monolayer of LaO, followed by 2 u.c. of STO on the top surface of the LMO film has resulted in the enhancement of T_{MI} by 45 K and in the decrease of the resistance at T_{MI} by 2 times (curve 2 Fig. 2). An LMO film without LaO-TiO_2 interfaces was prepared by the deposition of one monolayer of SrO onto the TiO_2-terminated STO(100) prior to the deposition of LMO. In this case the manganite had to start the growth from the MnO_2 plane. LMO film with bottom SrO-MnO_2 interface and free top surface shows a decreased T_{MI}=210K and an insulating behavior at low temperatures (curve 3 Fig. 2). Deposition of 2 u.c. of STO on the top of LaO-terminated manganite film results in the formation of an LaO-TiO_2 top interface, thus, recovering the transport (curve 4 Fig. 2) to that described above for the film with one LaO-TiO_2 bottom interface.

We assume that optimized metallic behavior in LMO engineered films is because each LaO-TiO_2 interface creates effective conductive channels close to (or inside) the LMO layer. Magnetization as a function of temperature (see inset to Fig. 2) reveals, however, an unexpected behavior: after adding the second LaO-TiO_2 interface the Curie temperature (T_C) was increased up to 305 K (the film with one interface shows T_C=275 K). The increase of T_C correlates with increase of T_{MI}, but T_C is consistently lower than T_{MI}. Surprisingly, the saturation magnetization and magnetic hysteresis did not change after adding the second interface, M_s~400 emu/cm^3~2.5 μ_B/Mn. This value is larger than that for undoped LMO [14] but it is significantly lower than magnetization for optimal doped manganites, M_s~3.7 μ_B/Mn [15]. Relatively high residual resistivity, $\rho_{10K}=1.6\cdot10^{-4}$ Ωcm, also indicates insufficient doping level.

Magnetic and transport properties of the samples with different thickness and the same La deficiency of LMO layers (see Fig. 3) stay in line with the probably lowered doping level. The highest temperature of the metal-insulator transition T_{MI}≈330 K was achieved in LMO with the

thickness 26 uc and La-deficiency, δ=6-8 %. The resistance shows metallic behavior down to the lowest temperature. By decreasing the thicknesses of LMO layer a decrease of T_{MI} and an increase of the resistance was observed. The thickness dependence of the transport properties can be rationalized within the "electron leakage" from the interface into the LMO layer. The reduced oxidation state in the sample is consistent with some degree of electron doping, coming from the electron from the extra (LaO) plane. The depth of charge spreading is larger than 2 uc as calculated for the insulating LMO [6]; it looks like charge is evenly distributed among the tens of LMO unit cells [4]. By reducing the thickness of LMO, one extra-electron distributed among smaller amount of LMO unit cells would give a stronger reduction of the averaged oxidation state. Such scenario suggests that LMO layers become progressively less hole-doped as the thickness is reduced, i.e. it is consistent with an increased electron leakage into LMO. Finally, for samples thinner than as 3 nm (6-7 uc) no metallic behavior was more observed regardless to the La deficiency; note that 2.5 nm thick film still remains ferromagnetic.

A further support for the above model comes from magnetization measurements. We observed a gradual decrease of M_S with decreasing of the LMO thickness (see Fig. 4a), that correlates both with the decrease of T_C and T_{MI}. Magnetic hysteresis behavior also comes to agreement with this model. The value of coercive field H_c ~30 Oe indicates magnetic homogeneity of the 26 uc thick film. Apparently (see Fig. 4b)), magnetic inhomogeneity increases and the saturation magnetization decreases dramatically with decreasing of the thickness, i.e. M_S<1 μ_B/Mn for the 6 uc thick film, that is typical for an undoped LMO [14]. From a magnetic point of view only, the system looks like a weak ferromagnet. However, the e_g-hole is localized within a certain regions with very few Mn-ions. The ground state is a mixed state, composed from a disordered nm-size "double-exchange" metallic clusters and coexisting insulating domains. Even for high magnetic fields the system with magnetically aligned FM clusters do not reach the percolation limit [16] even if they grow in size.

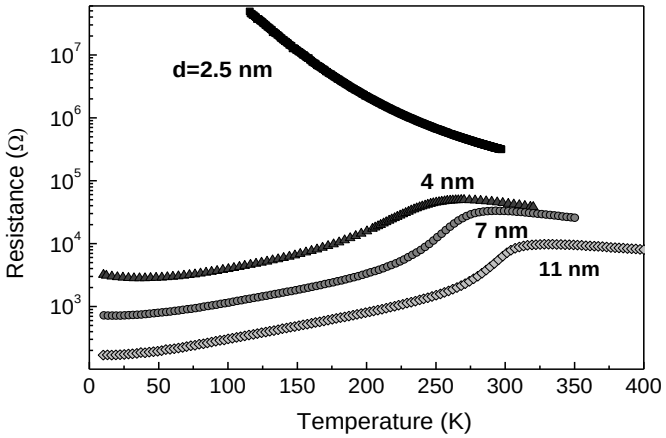

Fig. 3. Dependence of transport properties on temperature for STO-LMO-STO structures with different LMO layer thickness.

Inversion of the LaO-TiO_2 interface to SrO-MnO_2 by introducing SrO extra-layer (see Fig. 2) leads to the degradation of transport properties. A new design of SrO-

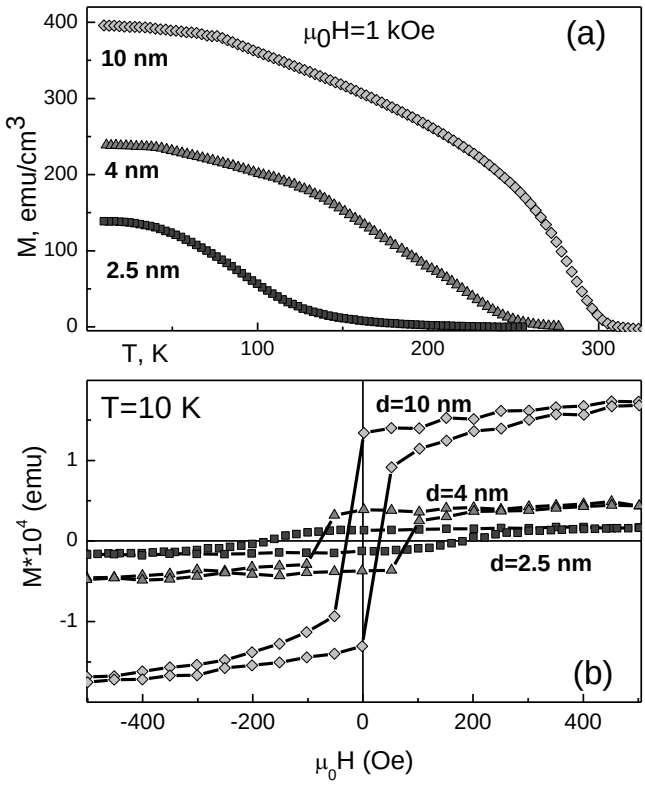

Fig. 4. Magnetization as a function of temperature (a) and magnetic histeresis (b) for the STO-LMO-STO structures with different thickness of LMO layers.

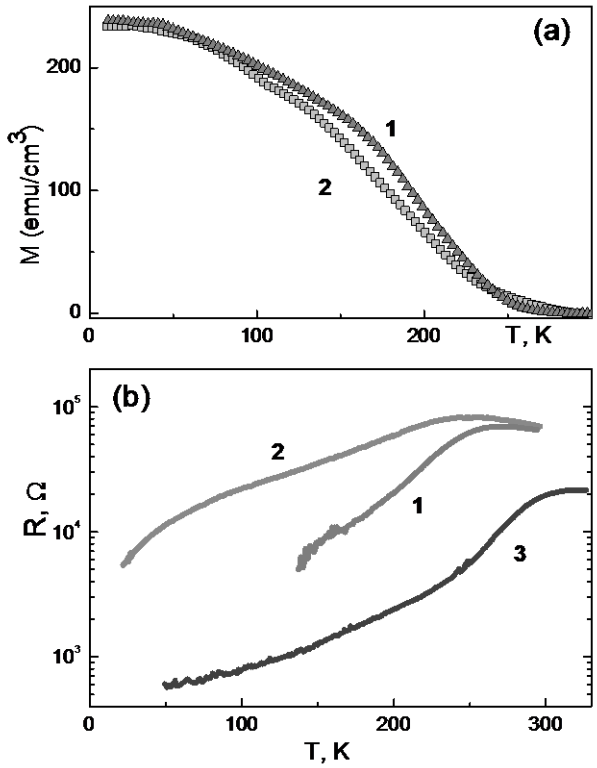

Fig. 5. Magnetization as a function of temperature (a) and resistance as function of temperature (b) for: (1) STO-LMO(10 ML)-STO; (2) SMO-LMO(6 ML)-SMO; (3) SMO-LMO(10 ML)-SMO structures.

MnO_2 could improve the magnetotransport in LMO layer. According to the calculations [6] the Mn e_g electrons leak out from the LMO layer to the SMO one and change the magnetism at the interface, while away from the interface,

the magnetism of the respective bulk materials is preserved. Introduction of the 2 u.c. of SMO as the buffer and the cape layers allowed us to change the direction of the charge leakage and as a consequence to restore metallic behavior in very thin LMO films.

The resistance of SMO-LMO-SMO structure was found to be about 5 times lower than the resistance for STO-LMO-STO sample with the same thickness (10 u.c.) and La-deficiency (see Fig. 5(b)). LMO film confined by 2 SMO u.c. demonstrates metallic behavior down to the thickness of 6 u.c. The saturation magnetization and T_C of SMO-LMO(6 u.c.)-SMO and STO-LMO(10 u.c.)-STO are very similar (Fig. 5(a)), but the thinning of LMO layer in any way leads to rising of inhomogeneity that reflects in increased resistance (curve 2 in Fig. 5(b)). It is worth to note that the upper limit of the layer thickness is absent in the case of La-deficient LMO with ferromagnetic metallic behavior.

CONCLUSIONS

We have shown that tailoring of the interfaces can be very effective in modifying the magnetotransport properties of ultrathin LMO films. Combination of the doping effects due to the La-deficiency with the interface-induced doping allowed us to preserve ferromagnetic metallic behavior in STO-LMO-STO structures with the thickness down to 10 u.c. of LMO. Interface modification of LMO layers by the 2 u.c. thick SMO bottom and top interfaces has led to a further shrinkage of the metallic LMO layer thickness down to 6 u.c. Engineering of the single type LaO-TiO_2 interface in the STO/LMO stacked perovskites can be performed within the MAD technique by deposition of an extra LaO plane. Thus, we show the possibility to change the natural growth sequence, i.e. AO-BO_2, along the <100> direction of the perovskite structure.

REFERENCES

[1] A. Yamasaki, *et al.*, "Pressure-Induced Metal-Insulator Transition in $LaMnO_3$ Is Not of Mott-Hubbard Type," *Physical Review Letters,* vol. 96, p. 166401, 2006.

[2] A. Gupta, *et al.*, "Growth and giant magnetoresistance properties of La-deficient $La_xMnO_{3-\delta}$($0.67< x <1$) films," *Applied Physics Letters,* vol. 67, pp. 3494-3496, 1995.

[3] A. Bhattacharya, *et al.*, "Metal-Insulator Transition and Its Relation to Magnetic Structure in $(LaMnO_3)_{2n}/(SrMnO_3)_n$ Superlattices," *Physical Review Letters,* vol. 100, p. 257203, 2008.

[4] J. Garcia-Barriocanal, *et al.*, "“Charge Leakage” at $LaMnO_3/SrTiO_3$ Interfaces," *Advanced Materials,* vol. 22, pp. 627-632, 2010.

[5] P. Orgiani, *et al.*, "Enhanced transport properties in $La_xMnO_{3-\delta}$ thin films epitaxially grown on $SrTiO_3$ substrates: The profound impact of the oxygen content," *Applied Physics Letters,* vol. 95, pp. 013510-3, 2009.

[6] B. R. K. Nanda and S. Satpathy, "Polar catastrophe, electron leakage, and magnetic ordering at the $LaMnO_3/SrMnO_3$ interface," *Physical Review B,* vol. 81, p. 224408, 2010.

[7] P. Orgiani, *et al.*, "Multiple double-exchange mechanism by Mn^{2+} doping in manganite compounds," *Physical Review B,* vol. 82, p. 205122, 2010.

[8] J. Verbeeck, *et al.*, "$SrTiO_3(100)/(LaMnO_3)_m(SrMnO_3)_n$ layered heterostructures: A combined EELS and TEM study," *Physical Review B,* vol. 66, p. 184426, 2002.

[9] M. Varela, *et al.*, "Oxide Interfaces Under the Electron Microscope," *Microscopy and Microanalysis,* vol. 14, pp. 1346-1347, 2008.

[10] H. Zenia, *et al.*, "Electronic and magnetic properties of the (001) surface of hole-doped manganites," *Physical Review B,* vol. 71, p. 024416, 2005.

[11] D. H. A. B. J. Mannhart, H.Y. Hwang, A.J. Millis and J.-M. Triscone, "Two-Dimensional Electron Gases at Oxide Interfaces," *MRS Bulletin,* vol. 33, pp. 1027-1034, 2008.

[12] K. Gehrke, *et al.*, "Interface controlled electronic variations in correlated heterostructures," *Physical Review B,* vol. 82, p. 113101, 2010.

[13] M. Kawasaki, *et al.*, "Atomic Control of the $SrTiO_3$ Crystal Surface," *Science,* vol. 266, pp. 1540-1542, December 2, 1994 1994.

[14] C. Adamo, *et al.*, "Electrical and magnetic properties of $(SrMnO_3)_n/(LaMnO_3)_{2n}$ superlattices," *Applied Physics Letters,* vol. 92, pp. 112508-3, 2008.

[15] J. M. D. Coey, *et al.*, "Mixed-valence manganites," *Advances in Physics,* vol. 48, pp. 167 - 293, 1999.

[16] P. A. Algarabel, *et al.*, "Peculiar ferromagnetic insulator state in the low-hole-doped manganites," *Physical Review B,* vol. 67, p. 134402, 2003.

Nonlinear Transmission of Two Successive Ultrashort Laser Pulses by a Thin Semiconductor Film under Two-Photon Generation of Biexcitons. Giant Oscillator Strength Model

Igor BELOUSSOV[1], Peter KHSDZHI[1,2], Tatiana SHEMYAKOVA[1], and Spiridon RUSU[3]
[1] *Institute of Applied Physics, Academy of Sciences of Moldova, Kishinev, Moldova*
[2] *Dniester State University, Tiraspol, Moldova*
[3] *Technical University of Moldova, Kishinev, Moldova*
igor.beloussov@phys.asm.md

***Abstract* – The possibility was investigated to compress and to split laser pulses at their nonlinear optical transmission through semiconductor films.**

***Index Terms* – biexciton, exciton, thin semiconductor film, ultrashort laser pulse.**

I. INTRODUCTION†

In recent years the processes of interaction of resonance laser radiation with excitons and biexcitons in thin semiconductor films were studied in several works.

The thin-film approximation allows one to reduce the set of nonlinear partial differential equations for the electromagnetic field and the medium to a relatively simple set of ordinary differential equations, which in some cases admits exact analytical solutions.

Recent considerable advances in manufacturing of dimensionally confined semiconductor structures stimulate the investigations of nonlinear optical properties of semiconductor thin films. This research is of an obvious practical interest owing to the promising applications of thin semiconductor films for the development of the systems of ultrafast optical processing of information.

In this work the results are presented of theoretical investigations of the effects of nonstationary nonlinear transmission of two successive ultrashort pulses of resonance laser radiation, received from the same source, through a thin semiconductor film under conditions when each of the pulses can induce a two-photon generation of biexcitons from the crystal ground state. A similar problem for the case of one pulse was considered in [1, 2].

Let ultrashort pulses of laser radiation with the envelopes of the electric field strength $E_{in}(t)$ and the photon carrier frequency ω are normally incident on a thin semiconductor films with the thickness *L* in vacuum. It is assumed that the duration of each pulse t_p considerably exceeds the photon time of flight through the film t_f ($t_p >> t_f$), and the sum energy of two photons is in resonance with the generation energy of a biexciton from the crystal ground state. A part of radiation is reflected by the front end of the film, another part enters the film and generates biexcitons from the crystal ground state due to the process of two-photon absorption. The film thickness is of the order of the wavelength of propagating radiation or greater. Therefore, owing to the multiple re-reflections from the front and rear crystal ends a forward and a backward electromagnetic waves with the amplitudes $E_f(z,t)$ and $E_b(z,t)$, respectively, appear in the film. The amplitude of the forward wave on the rear end $E_f(L,t)$ defines the amplitude of the wave transmitted through the film; the amplitude of the backward wave on the front end $E_b(0,t)$ defines the amplitude of the reflected wave. The problem is to find the amplitudes of the transmitted and reflected waves. Such condition of the problem can be realized, for example, in CuCl or CuBr crystals, where the biexciton binding energy amounts to ~30–40 meV, and the oscillator strength of two-photon generation of biexcitons is gigantic.

II. MAIN RESULTS

We consider the case of ultrashort laser pulses such that $t_p << \gamma_{biex}^{-1}$ and assume $t_p = 1\,ps$. For this case, the condition $t_p >> t_f$ is satisfied for the film thickness $L < 10^{-3}\,cm$. The results of numerical calculation of the set of equations describing the transmission of ultrashort pulses through a semiconductor film are shown in Figs. 1-4.

For large delay times between the incident pulses t_d, the first pulse induces the polarization of media, which completely disappears by the moment of incidence of the second pulse. Therefore, we can consider that there exist envelopes of each of two independent transmitted (reflected) pulses generated by two incident pulses. A considerable variation of the envelope of transmitted (reflected) radiation

† This work is supported by the joint grant of the Academy of Sciences of Moldova (project 10.820.05.18/UF) and the Ministry of Education and Science of Ukraine.

occurs for $0 \le t_d \le t_p$ when the envelopes of incident pulses partially overlap. For this case, the polarization of media induced by the first pulse has not enough time to disappear by the moment when the second pulse falls. In this case a nonlinear interaction of polarizations from the both pulses occurs; owing to this, the shape of the transmitted (reflected) pulse becomes more complicated.

It can be also seen in Figs. 1-4 that the amplitude of transmitted (reflected) pulse decreases fast with the increasing of the delay time between the incident pulses in the range of small delay times ($t_d \ll t_p$); the pulse further splits into two pulses, which propagate independently.

It follows from Fig. 1 that for low intensities of incident radiation $S \ll 10 MW/cm^2$ the envelope of the transmitted (reflected) pulse even for zero delay between the incident pulses practically repeats their shape.

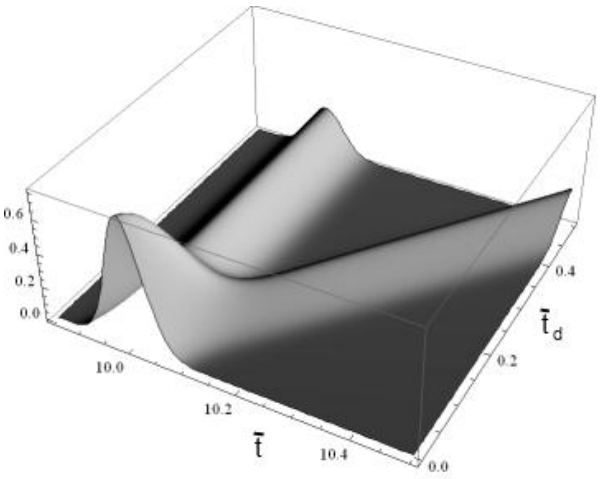

Fig. 1. Dependence of the normalized intensity of transmitted radiation versus the dimensionless time $\bar{t}$ and delay time between the pulses $\bar{t}_d$ for the film thickness $L = 10^{-3}\ cm$ and intensity of the incident radiation $S = 10\ MW/cm^2$ in the conditions of exact resonance ($2\omega = \omega_m$, where $\hbar\omega_m$ is the exciton formation energy).

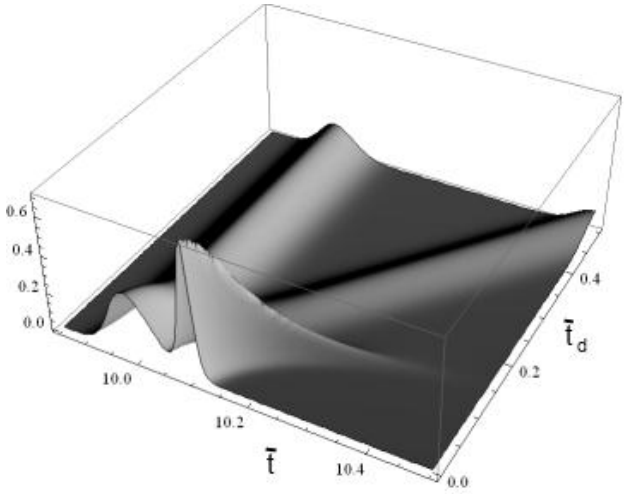

Fig. 2. Same as in Fig. 1 for $S = 60 MW/cm^2$.

The transmission of incident pulses through a semiconductor film acquires additional peculiarities when the intensity of the pulses increases. For the intensity $S = 60 MW/cm^2$ the transmission and reflection exhibit two or several peaks (see Fig. 2). It is interesting that the amplitude of the additional peak of transmission increases with the increasing of the excitation level and for $S = 60 MW/cm^2$ it can already exceed the amplitude of the main peak. But for the case of reflection the amplitude of the additional peak is always smaller than the amplitude of the main peak.

For intensity $S = 100 MW/cm^2$ the second transmission peak considerably exceeds the first (main) peak by its amplitude, and the third peak arise (Fig. 3).

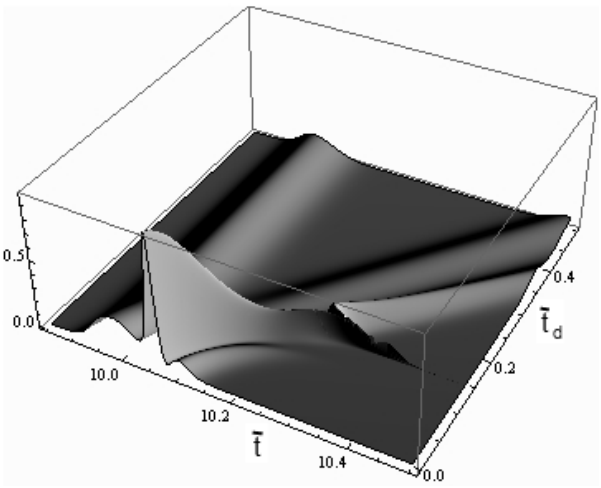

Fig. 3. Same as in Fig.1 for $S = 100 MW/cm^2$.

For intensity $S = 200 MW/cm^2$ and relatively large t_d the second subpulse of transmission arise.

When S further increases the number of additional transmission (reflection) peaks increases; their width becomes considerably less than the width of the incident pulses. The envelope of subpulses for transmission has the shape of the incident pulse.

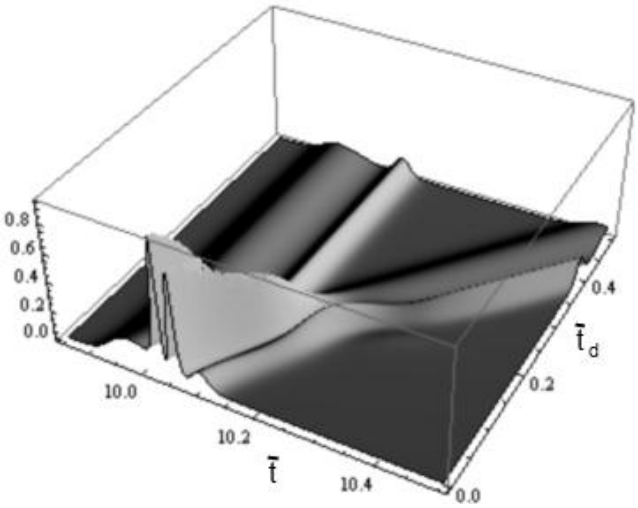

Fig. 4. Same as in Fig.1 for $S = 200 MW/cm^2$.

III. CONCLUSION

Consequently, the thin semiconductor film substantially transforms successive ultrashort pulses passed through it and changes both their intensity and shape. While using films with various thickness, changing the intensity of incident pulses and the delay time between them one can obtain the compression of the initial pulse or to split it into a sequence of two or several pulses with considerably less duration.

REFERENCES

[1] I. Beloussov, P. Khadzhi, A. Corovai, and D. Markov, *Abstracts of International Conferences on Coherent and Nonlinear Optics/Lasers, Applications and Technologies* (Russia, Kazan, August 23-27, 2010).

[2] I. Beloussov, P. Khadzhi, A. Corovai, and D. Markov, *Abstracts of 5th International Conference on Materials Science and Condensed Matter Physics* (Moldova, Chisinau, September 13-17, 2010), p. 57.

Quantum Oscillations of Conductivity in Bismuth Wires

Elena CONDREA
Institute of Electronic Engineering and Nanotechnologies, Academy of Science of Moldova, Chisinau, condrea@lises.asm.md

***Abstrect* – Measurements of the resistance of bismuth nanowires with several diameters and different quality reveal oscillations on the dependence of resistance under uniaxial strain at T = 4.2 K. Amplitude of oscillations is significant (38 %) at helium temperature and becomes smearing at T = 77 K. Observed oscillations originate from quantum size effect.**
A simple evaluation of period of oscillations allows us to identify the groups of carriers involved in transport. Calculated periods of 42.2 and 25.9 nm satisfy approximatively the ratio 2:1 for two experimentally observed sets of oscillations from light and heavy electrons.
***Index Terms* – nanowires, quantum size effect.**

I. INTRODUCTION

The emergence of the investigations concerned with various nanostructures is motivated partially by the very interesting thermoelectric and magnetotransport properties of bismuth nanowires (NWs) that make them potentially useful for device applications. Theoretical calculations [1-3] predicted that Bi nanowires should have an enlarged thermoelectric figure of merit, which results from the quantum size effect, have induced extensive studies of Bi NWs. Under the quantum size effect (QSE), several fundamental macroscopic characteristic of solids exhibit an anomalous dependence on reduced size. Therefore, for subsequent applications, a precise determination of the size-dependent parameters of investigated nanostructures is required. If the decreased size of wires or films becomes comparable with the electron wavelength $(d \sim \lambda)$, the transverse motion of carriers is quantized. Thus, the energy spectrum splits into subbands. When the discreteness of the energy subbands becomes significant, an oscillatory behavior of electron and hole density of states (DOS) as a function of thickness is expected for metal films [3,4]. Oscillations of DOS are due to variation in number of the subbands with diameter. According to the theoretical considerations of the QSE [3,4,9] all the transport coefficients which depend on the DOS should oscillate as a function of sample thickness with the period:

$$\Delta d = h/2(2m_t^*E_F)^{1/2}, \quad (1),$$

where m_t^* is the transverse effective masses, and E_F is Fermi level.

The main experimental results in the investigations of the QSE have been obtained for thin semimetal films. The first quantum size oscillations in the resistivity, Hall coefficient, and magnetoresistance with a period of 400 Å were observed in thin bismuth films [5]. Investigations [6] of bismuth films in large range of thickness (200 - 3000 Å) revealed that the period of the resistance oscillations varied from 40 to 250 Å with sample thickness. The difference in the period was attributed to the differences in the carrier concentrations due to growth conditions.

Quantum oscillations in the resistance of bismuth-antimony alloy films were registered under variation in both thickness and Sb concentration at a fixed thickness [7]. The concentration oscillations in a sample with constant thickness are explained by the change of the transverse quasi-momentum caused by composition variation in the Bi-Sb alloy. An other manifestation of the QSE [8] was observed while studying the thickness dependence of the ratio of the electron and hole density of states measured under electric field effect (EFE). The method allows a rather precise determination of the film thickness period of the oscillations, which is about 370 Å.

In most of the above-mentioned cases, QSE was shown as an oscillatory behavior of the resistance dependence on film thickness. As is pointed out in [9], a variation in the value of the band overlap should also produce an oscillatory behavior of the kinetic coefficients. The changes in band overlap in a bulk Bi samples under deformation was described by Brandt [15]. The influence of the deformation on the band overlap changes was tested for bismuth films condensed on mica substrates [10]. Observed non-monotonous behavior of the resistance in bismuth films under sagging deformation is in a good agreement with the concept of QSE.

To our knowledge, up to now, most of the studies on quantum oscillations in transport properties of Bi nanostructures are concerned with thin films. The conditions of observation of the QSE on thickness dependences of the kinetic coefficients of thin wires are complicated by difficulties in the preparation of a series of samples with a small increment in thickness and identical characteristics of the bulk. Despite a lot of recently developed techniques for preparation of nanowires [1, 2, 16] the bulk characteristic data from different experiments depend not only on sample cross-sectional dimensions and crystallographic orientation, but also on sample quality and
purity, shell/matrix material and annealing treatment. It is possible to observe the oscillations of kinetic parameters, due to size-quantized energy spectrum on the individual cylindrical nanowire under certain external influence, for example, by impurity doping or deformation.

The aim of this study was to study transport coefficients of individual bismuth nanowires under condition of QSE by applying uniaxial stress for tuning the electronic structure and inducing band overlap changes. According to the condition of QSE realization ($d \sim \lambda$), an oscillating behavior in transport coefficient of Bi samples is expected at diameters below 100 nm. One should note that uniaxial strain in Bi NWs promotes the increases of band overlap

between L-electron pockets and T-holes pocket at constant band gap, in contrast to its decrease under QSE.

II. EXPERIMENTAL METHODS AND SAMPLES

Long Pyrex-coated Bi wires were fabricated using the same improved variant of the Taylor method. This method, which is presently known as the glass-coated melt spinning method, consists in the melting of a metal in a glass tube by rf induction heating and drawing a glass capillary in which the molten metal is entrapped.

The wire axis is at an angle of about 19° with the bisector axis C_1 in the bisector-trigonal plane C_1C_3. This orientation is the same as that observed in Bi nanowire arrays by Z. Zhang et al. [1]. Due to high elasticity of Pyrex capillaries, the limit of elastic stretching of the glass-coated Bi wires attains $\varepsilon = 3.5$ % (in comparison for Bi whiskers $\varepsilon = 2.0$ % [11] and for bulk Bi samples $\varepsilon = 0.4$ % [12]. Due to small dimensions of glass-coated NWs, it was not possible to apply mechanical loading directly to them. For the measurements under uniaxial strain, the glass-coated wires with $d = 70 – 150$ nm and the length $L_0 = 2.0 – 3.0$ mm were mounted on an elastic bronze ring in a special insert with stretching device similar to the method, used for whiskers [11]. The stretching was directed along the wire axis, i.e., close to the bisector axis C_1. The measurements of resistance were performed using two-probe method. Resistance variation was noted as $\Delta R/R = (R - R_0)/R_0$ where R_0 is the value of resistance in non-deformed state. Strain variation was noted as $\varepsilon = (L - L_0)/L_0$ where L_0 is the length of the wire in non-deformed state. Electrical contacts to the wire ends were made by Wood's alloy. Low dc currents ($0.1\ \mu A \leq I \leq 1\ \mu A$) were used to make sure that the voltage of the sample was a linear function of the applied current.

III. RESULTS AND DISCUSSION

The studies of the strain dependences of the resistance $R(\varepsilon)$ at 4.2 K for wires

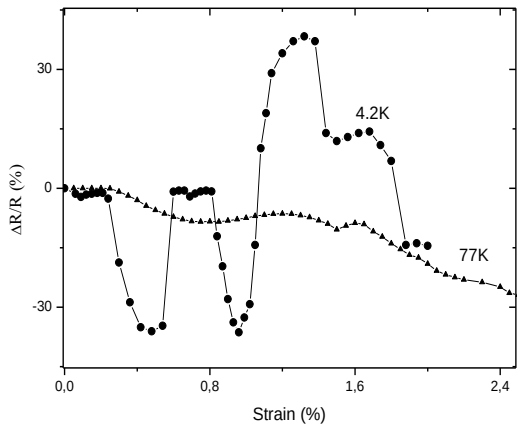

Fig. 1. Relative variation of the resistance as a function of applied strain for 90 nm Bi nanowire measured at 4.2 K and 77 K.

with various diameters revealed the oscillating dependence of the resistance on applied deformation in wires with a diameter of 90 nm subjected to thermal annealing (Fig.1). Since an oscillating behavior in transport coefficient of Bi wires is expected at diameters below 100 nm, we can suppose that observed oscillations are due to QSE. To our surprise, non-discernable and non-reproducible quantum oscillations on $R(\varepsilon)$ were observed in the thinner NWs with a diameter of 70 nm. The dependences of resistance versus uniaxial strain R(ε) for Bi wires with the diameters $d \geq 100$ nm do not exhibits any oscillations and is similar to the one observed by us for thicker wires [13] and whiskers [11].

Fig. 2 shows the temperature dependences of the electrical resistance $R(T)$ for Bi NWs with various diameters. Observed $R(T)$ dependences are consistent with previous results for Bi wires [14] and Bi nanowire arrays [1]. Curve 2 in Fig. 2 presents $R(T)$ dependence for a 90 nm NW after thermal treatment. History of the thermal treatment was not simple. Various variants of thermal treatment were tested and the optimal one was chosen. The NWs were annealed at 180° C for 10 h under vacuum with slow cooling back to room temperature. An evident increase of value of a residual resistance ratio (RRR) for the 90 nm wire after thermal treatment testified to an improved quality of annealed NWs. This supports the idea that a semiconducting behavior of R(T) does not imply that a band gap opens even in the thin wires, a negative TCR may be rather an evidence of large defect density inside the as-prepared wires.

If we attribute the presence of oscillations on $R(\varepsilon)$ in Fig. 1 to the manifestation of QSE, in addition to the main condition $d \sim \lambda$ for QSE occurrence [4], we should consider some important requirements such as a small washing out of the discrete energy spectrum:

$$h/\tau << \Delta E, \qquad (2)$$

and a small temperature smearing:

$$kT << \Delta E, \qquad (3)$$

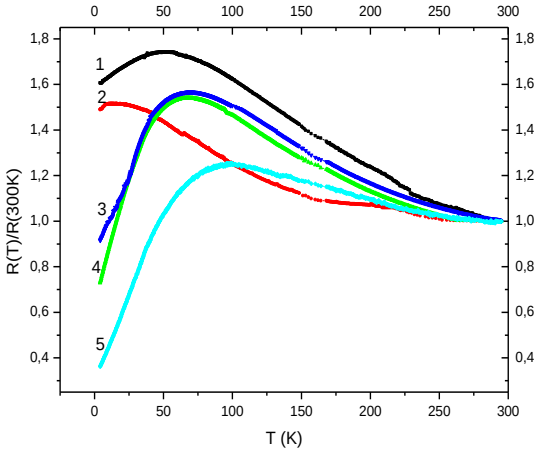

Fig. 2. Temperature dependence of resistance normalized to the resistance at 300 K for as-prepared Bi NWs: (1) d = 90 nm, (3) d = 120 nm and thermal annealed: (2) d = 90 nm, (4) d = 120 nm, (5) d = 150 nm.

where τ is the relaxation time, taking into account scattering both in volume and on the surface; ΔE is the distance between discrete energy subbands. Inequality (2) means a high mobility and/or large free path length for carriers involved in transport. It seems that all the requirements for QSE are satisfied for annealed 90 nm wire at T = 4.2 K.

The observed resistance oscillations were reproduced on all the wires with a diameter of 90 nm from the series of samples subjected to thermal annealing. As one can see from Fig. 1, the $R(\varepsilon)$ dependence at 4.2 K exhibits a modulating profile consisting of two sets of oscillations with different periods determined by different groups of carriers. First, we

supposed that two different periods of oscillations are due to contribution of electrons and holes to electrical conductivity. It is known that difference in the periods of electron and hole quantum oscillations results from the anisotropic properties of Bi.

A rough evaluation of possible periods of quantum oscillations in 90 nm bismuth wire was made by formula (1). The value of effective transverse mass of heavy and light electrons was used from the model of the subband structure calculated in [1] for the Bi nanowire arrays with the same crystal orientation, corresponding to [1011]. This is our case where three groups of carriers operate: heavy electrons from two equivalent pockets A and B, light electrons from pockets C, and heavy T-holes. According to [1], as the diameter of Bi nanowire arrays decreases below 100 nm, the band overlap between light and heavy electron pockets and T-hole pocket decreases in the different ways, thus resulting in the splitting of the L-point band edge. In this model, the band edge energy of each subband is determined by the average transverse effective mass, approximated by the appropriate effective cyclotron mass. The values of effective masses calculated by authors of [1] are: $m^* = 0.00212m_0$ and $m^* = 0.00372m_0$ for light and heavy electrons, respectively. Estimated periods for our 90 nm NW are: $\Delta d_1 = 42.2$ nm; $\Delta d_2 = 25.9$ nm and $\Delta d_3 = 16.0$ nm for light and heavy electrons and holes, respectively.

Coming back to measured quantum oscillations of resistance (Fig.1) we note the period ratio of 2 : 1 for two set of observed oscillations. Two of calculated periods 42.2 nm and 25.9 nm satisfy approximatively the ratio 2 : 1. The calculated value of 16.6 nm for hole period is overestimated as a result of using the value for hole transverse mass $m^* = 0.21m_0$ available for bulk Bi. The absence of quantum oscillations from holes can be caused by its small period and non-detectable amplitude versus background. Thus, we can suppose that quantum oscillations with large amplitude and period of 42.2 nm occur from the light electrons with smallest effective mass, and quantum oscillations with weak amplitude and period of 25.9 nm occur from heavy electrons from pockets A and B. A significant amplitude (38%) of resistance quantum oscillations with $\Delta d_1 = 42.2$ nm is due to the low quantum numbers of the subbands located below Fermi energy level in the pocket C with light electrons. The vanishing of these oscillations at the deformation higher than 1% is suggestive of a change in the Fermi surface topology, known as an electronic topological transition (ETT) or Lifshitz transition. As a result of our previous investigations [13] of the changes in the Fermi surface topology under stress by means of Shubnikov-de Haas oscillation measurements, we have found the upward shift of the light electron pocket C relative to the other two pockets A and B up to its complete vanish at a high strain. Due to the continuing increase in the band overlap between L-electron pockets (A and B) and T-hole pocket, quantum oscillations with a period of 25.9 nm are detected at a strain higher than 1 %.

If we attribute the presence of the oscillations on $R(\varepsilon)$ to the QSE manifestation, it is natural to make a brief analysis of correlation between the value of uniaxial strain and the period of observed oscillations Δd in 90 nm wires. Though the precise interrelation between applied uniaxial strain and Δd is not known, we try to follow the influence of strain on the Fermi level shifting through quantized subbands in electron pockets. In terms of previous results on ETT with the vanishing of one electron pocket, the work of extension of $\varepsilon = 0.96$ % should be on the order of the energy shift of electron pocket C with strain. Since the measurements were made in the elastic deformation range, we may use the value of the elastic modulus for bulk Bi crystal along the bisector direction; thus, it is possible to determine the tensile load dependence P on the value of extension $\varepsilon = \Delta L / L_0$ which is approximatively $P = 0.38$ GPa at $\varepsilon = 0.96$ %.

A rough estimation of value of the energy shift was made by using the values of shifting rate dE/dF of electron pockets under anisotropic deformation along the bisector direction for bulk Bi crystals calculated by authors in [17], which are: $dE/dF = 0.5$ meV/kg for pocket C and $dE/dF = -0.6$ meV/kg for pockets A and B. In our case, the value of energy shift was determined at a strain of 0.96 %, where quantum oscillations with large period disappear. Calculated value is $dE \approx 19$ meV. Because of some involved calculational uncertainties, the value of $dE \approx 19$ meV is rather appreciative; nevertheless, it is reasonable of the same order with value of Fermi energy level and of the band overlap (16 meV) for light electron pocket from the model of electronic band structure for 90 nm Bi NWs, advanced by authors of [1].

IV. CONCLUSIONS

Systematic measurements of the resistance of bismuth nanowires with several diameters and different quality reveal oscillations on the dependence of resistance under uniaxial strain at T = 4.2 K. Amplitude of oscillations is significant (38 %) at helium temperature and becomes smearing at T = 77 K. Observed oscillations originate from quantum size effect.

The absence of quantum size oscillations in resistance dependence for 70 nm wires can be explained partially by scarce number of light electrons responsible for oscillations with decreasing diameter [1] and partially by imperfection of the nanowires.

A simple evaluation of period of oscillations allows us to identify the groups of carriers involved in transport. Calculated periods of 42.2 and 25.9 nm satisfy approximatively the ratio 2:1 for two experimentally observed sets of oscillations from light and heavy electrons.

The importance of the quantum size effect manifestation in the resistance dependence on strain goes beyond studying the structure of electron spectrum, it can also be applied to investigate the spectrum of phonons. With a view to elucidate some aspects of the practical use of nanowires, we plan the further investigations under strain of the thermopower, which at low temperature may be due to the diffusive or phonon drag mode of carrier interaction.

ACKNOWLEDGEMENTS

This work was made possible by National Project no. 210 PF under funding from CSSDT.

REFERENCES

[1] Z. Zhang, X. Sun, M. S. Dresselhaus, J. Y. Ying and J. Heremans Phys. Rev. B **61** 4850 (2000)

[2] Y-M. Lin, X. Sun, and M. S. Dresselhaus Prys. Rev B **62** 4680 (2000)

[3] V. B. Sandomirskii Zh. Eksp. Teor. Fiz. **52** 158 (1967) [Sov. Phys. JETP 25 101(1967)]

[4] B. A. Tavger, V. Ya. Demikhovskii Uspekhi Fiz. Nauk **96** 61 (1968)
[Sov. Phys. Usp. (1969) 11 644]
[5] Yu. F. Ogrin, V. N. Lutskii, and M. I. Elinson Zh. Eksp. i Teor. Fiz. Pis'ma v Redaktsyu **3** 114 (1966)
[Sov. Phys. JETP Letters 3 71 (1966)]
[6] E. P. Fesenko Fiz. Tverd. Tela **11** 2647 (1969)
[Sov.Phys. Solid State 11 2135 (1970)]
[7] E. I. Bukhshtab, Yu. V. Nikitin and Yu. F. Komnik Fiz. Nizk. Temp. **3** 755 (1977)
[8] A. V. Butenko, Dm. Shvarts, V. B. Sandomirskii and Y. Schlesinger Physica B **284-288** 1942 (2000)
[9] E. F. Schulte Surf. Sci. **55** 427(1976)
[10] N. B. Brandt, E. S. Itskevich and N. Ya. Minina Zh.Eksp. Teor. Fiz. **47** 455 (1964)
[11] V. N. Lutskii Phys. Stat. Sol. A **1** 199 (1970)
[12] T. W. Cornelius, M.E. Toinil Molares, R. Neumann,and S. Karin J. Appl. Phys. **100** 114307 (2006)
[13] Yu. P. Gaidukov, N. P. Danilova and M. V. Shcherbina-Samoilova Zh. Eksp. Teor. Fiz. **77** 2125 (1979) [Sov. Phys. JETP 50 1018 (1979)]
[14] O. P. Hansen, I. F. Mikhail, M. Yu. Lavrenyuk and N. Ya. Minina J. Low Temp. Phys. **95** 481 (1994)
[15] M. Gurvitch J. Low. Temp. Phys. **38** 777 (1980)
[16] P. P. Bodiul, V. F. Garabazhiu, E. P. Condrea and A. A. Nikolaeva Czech J. Phys. **46** 2417 (1996)
[17] E. V. Bogdanov, M. Yu. Lavrenyuk and N. Ya. Minina Fiz. Tehn. Pol. **22** 1348 (1988).

Superposition of the luminescence spectra of free and bound excitons in ZnP_2-D_4^8

Ion STAMOV, Lucretia NEMERENCO, Iurii IVANENCO, Nicolae SYRBU
Technical University of Moldova
lnemerenco@yahoo.com

***Abstract* – The luminescence spectra of ZnP_2 tetragonal crystals doped Mn, Sn, Cd, Sb at 10 K emission lines of bound excitons is detected. In the spectra non-phonon emission lines of bound and free excitons and their phonon replicas is isolated. The emission lines by the levels of the axial center are described. The composition of the luminescence of free and bound excitons at the axial center is investigated. In the region of phonon replicas of free excitons observed enhancement of lines due to forbidden transitions involving the recombination of excitons. A model of optic recombination transitions of the axial centre is proposed.**

***Index Terms* – luminescence spectra, free and bound exciton, optical phonon, electron transitions, axial center**

I. INTRODUCTION

Compound ZnP_2-D_4^8 indirect-gap semiconductors with band gap 2.21 eV at 10K. ZnP_2-D_4^8 crystals have a pronounced birefringence, bright luminescence and a high photosensitivity [1-3]. On the basis of these crystals active elements p-n structures, Schottky diodes, switches, optical pulses are created and are promising materials for optoelectronic devices polarization.

II. RESULTS AND DISCUSSION.

Optic spectra of absorption and luminescence are measured in cryostat LTS-32C330 Workhorse-type Optical with the help of double Raman spectrometer with the light force 1:5 and dispersion of 5 A/mm. The crystals

ZnP_2 - D_4^8 have the structure described by the space group D_4^8 (D_4^4).The band gap (E_g) is determined by indirect transitions is equal to 2.21 eV. Fig.1 shows photoluminescence spectra of specially nondoped and doped with Mn crystals ZnP_2 at 10 K in the short-wave region, i.e. in the region adjoining the free exciton level. At the energy 2,2085 eV a weak peak of luminescence is found E_{ext}^L, according to the edge absorption data it coincides with the radiation energy from the free exciton level. We explain peculiarity x_1 - x_{10} in the luminescence spectra by phonon replicas of the free exciton recombination. The band x_i is behind the free exciton energy E_{gx}^{lib} = 2.2085 by the value of optic phonons. In the luminescence spectra various optic phonons can take part [1]. The luminescence spectra with many narrow lines bound excitons, in which different optical phonons were observed in the crystals ZnP_2 - D_4^8 [1-3] and CdP2 - D_4^8 [4].

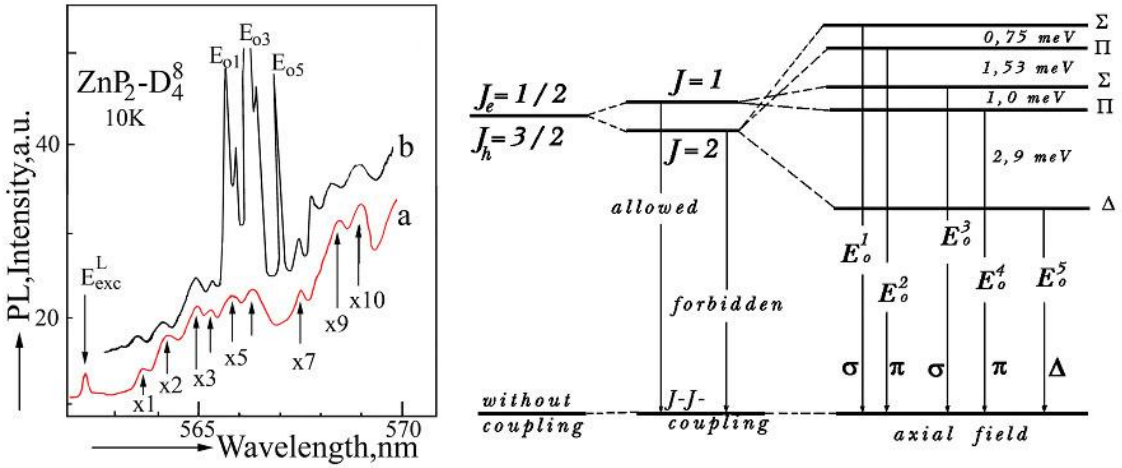

Fig.1. Luminescence spectra of undoped (a) and doped with Mn (b) crystals ZnP_2- D_4^8 at 10K and the energy levels of the electron transitions of bound excitons on axial center of Mn in the crystals ZnP_2- D_4^8.

In the unit cell stacked 8 formula units, i.e. 24 atoms will go into unit cell, in the general case the number of phonon branches is equal to 72. Availability of this quantity of oscillation modes makes it possible to observe radiation of free excitons with emission of many phonons. The luminescence spectra doped with Mn of crystals ZnP2- D_4^8 discovered narrow lines E_{01}-E_{05} and weaker lines x_1-x_{10} (fig.1, curve a). Emission bands of x_i are phonon replicas of free-exciton emission. These bands are observed simultaneously with the narrow emission lines E_{01}-E_{05} bound excitons at the center of the impurity atoms Mn. Non-phonon lines of radiation of bound exciton E_{01}(2,1951 eV),

E_{02} (2,19440 eV), E_{03} (2,1928), E_{04} (2,19277) and E_{05} (2,18987) are seen as narrows lines. The bands x_i are weaker by hundreds times and they have halfwidth being practically by an order larger than the lines. These E_{01}-E_{05} two types of lines x_i and E_{01}-E_{05} of the radiative recombination are observed simultaneously practically in one and the same energy interval (fig.1). As it is known, in the unit cell of the crystal ZnP_2 - D_4^8 there are many atoms (N=24), this determining big quantity of oscillation modes of different symmetry [1-3] in the wide energy range. At the temperature 10 K in the crystals ZnP_2 - D_4^8 the energy distance between the level of free (G_{ext1}) and bound E_0^1 (G_{ext2}) excitons is equal to 13,3 meV, and optic phonons achieve the energy value of 59.5 meV. Hence, exciton levels of bound (E_0) and free exciton (E_{gx}) satisfy the condition $E_{p1}=G_{ext1}-G_{ext2}+E_{p2}$. Thus, the process of recombination radiation may occur simultaneously from two centres. The radiation caused by annihilation of free excitons leads to appearance of a row of bands (x_i) in the longwave region from E_{ext}^{lib} (2,2085 eV) at the energy distance being equal to the energy of optic phonons.

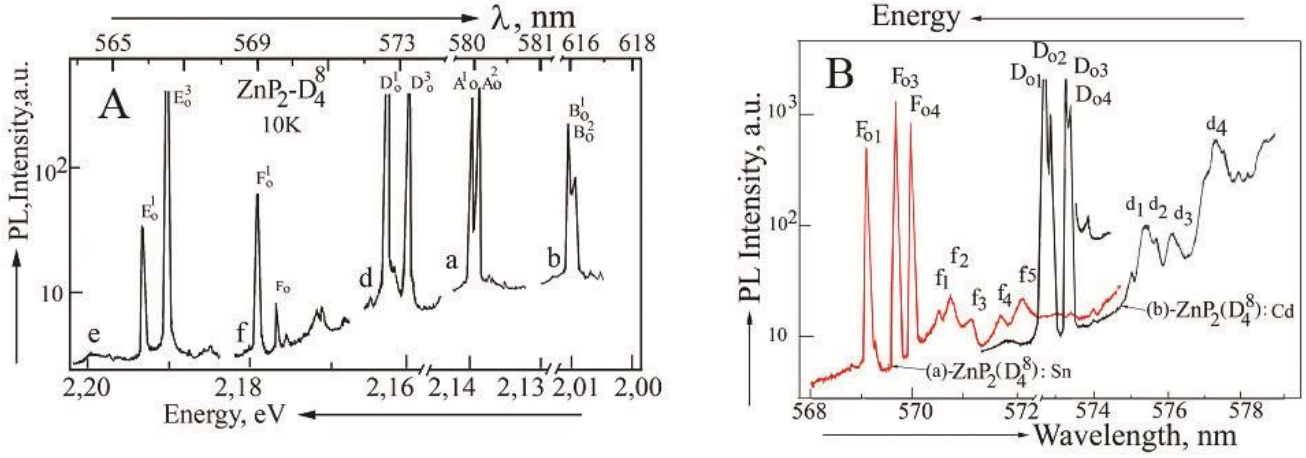

Fig.2. Fragments of the most intense luminescence lines ZnP_2 - D_4^8 crystals at 10 K, doped Mn (curve-e), Sn (curve-f), Cd (curve-a), Sb (curve a and b) and luminescence spectra ZnP_2 - D_4^8 crystals at 10 K doped tin (Sn) and cadmium(Cd).

Electron transitions of the exciton bound on axial centre in the ZnP_2 are shows in the fig.1. We consider that narrow lines $E_0^1 - E_0^5$ are due to phononless lines of exciton bound on axial centre [1-4]. The exciton consisting of the electron with spin 1/2 and hole with spin 3/2 bound on the centre with the axial symmetry forms (from the level J = 1) two levels (Σ and Π). Optic radiative transitions from the levels Σ and Π (J = 1) are allowed and they determine phononless lines E_0^3 and E_0^4. These lines are the most intense and they disappear with the temperature growth (≈40 K). These lines are split by small value (~0,1 meV). The state with J = 2 under the action of the axial field is split into three levels Σ, Π and Δ. Transitions from these levels are forbidden by the selection rules. The phonon energy radiated by the crystal in the result of the free exciton annihilation in the luminescence spectra corresponds to the energy of radiation of the bound exciton forbidden transition. This leads to the resonance excitation of the bound exciton forbidden states and to the removal of the ban and intensification of luminescence from the forbidden levels. The radiation lines E_0^3 and E_0^4 are determined by allowed transitions from the zones of symmetry Σ and Π correspondingly. These levels are split by the crystal axial field of the centre whereon the exciton is bound. The radiation lines E_0^1 and E_0^2 are split by 0,75 meV and they are due to the levels Σ and Π of the forbidden state of the bound exciton. Spin-orbit interaction also leads to the state splitting and appearance of the level Δ. The energy distance between Σ(Π)-Δ determines the value of the level splitting due to spin-orbit interaction (Δ_{SO}). In this model the value of splitting due to the spin-orbit interaction is larger than the value of splitting due to the crystal field. The energy interval between Σ-Σ levels is equal to 2,2 meV. The resulting intensity of the luminescence lines and their energy position shows that the spin-orbit splitting is greater than the splitting due to crystal field (fig. 2). In the transition levels of bound excitons at the axial center should be observed two intense emission lines as a permitted. These lines should be detected in the short wave region. Luminescence lines due to transitions from the levels from which transitions are forbidden by selection rules may occur as weak intensity lines. The situation may change if the phonon energy emitted by the crystal as a result of annihilation of free excitons in the luminescence corresponds to the radiation energy of the forbidden transition of a bound exciton. This can lead to resonant excitation of forbidden states of the bound exciton and to the lifting of the ban and increase the luminescence of prohibited levels. The radiated energy of the phonon may coincide with the energy position of the level of forbidden states of bound exciton. At the free exciton annihilation (E_{gx}^{lib} = 2,2085 eV) the phonon radiative band different from E_{gx}^{lib} at the energy distance 13,3 meV is observed. There is such a phonon of the symmetry E, it is radiated at the energy 2,1951 eV. This radiative band coincides with the energy position of the level of bound exciton E_{0x}^1 (2,19515 eV)

and is close to E_{0x}^{2} (2,19440 eV). E_{gx}^{lib} (2,2085 eV) - E_{gx} (13,3 meV) = E_i (2,1952 eV). Such a coincidence of energies of phonon radiation resulting from the free exciton annihilation with the energy levels of bound excitons may remove a ban of optic transitions from the levels of bound exciton, which is put by rules of the bound exciton selection. The ZnP_2 crystals doped with tin (Sn), cadmium (Cd) and antimony (Sb) also exhibit intense luminescence. In these crystals narrow lines of radiation and more gentle luminescence lines are observed. Figure 2A shows fragments of the narrow luminescence lines, which are due non-phonons excitons lines of emission bound these impurities. The luminescence spectra were measured on crystals doped with these impurities under the same experimental conditions. In addition to these luminescence lines are observed their phonon replicas. The luminescence spectra ZnP_2 - D_4^8 crystals at 10K doped with tin (Sn) and cadmium (Cd) are shows in the fig.2B. In these spectra revealed non-phonon excitons lines bound to the tin (Sn) atoms (F_{o1}, F_{o2}, F_{o3}) and their phonon replicas f_1, f_2, f_3, f_4, f_5. In these spectra in the longwave region of the band f_5 has a large number of peaks, which in this figure are not shown. In crystals doped with cadmium discovered a group of intense narrow lines D_{o1}, D_{o2}, D_{o3}, D_{o4} and weaker lines d_1-d_n (fig.2 shows only the four lines).

Narrow and intense luminescence lines D_{o1}, D_{o2}, D_{o3}, D_{o4} crystals ZnP_2 - D_4^8 doped cadmium also caused by excitons bound to the cadmium atom, which, as in previous cases, an axial center. Line D_{o1}, D_{o2}, D_{o3}, D_{o4} are non-phonon luminescence lines and the lines d_1-d_n - their phonon replicas. The experimental results indicate that the considered centers have identical parameters. Energy interval $\Sigma - \Sigma$ of the crystals doped with Mn ($E_0^{\,1} - E_0^{\,3}$) equals 2.28 meV, Sn-doped (F_{o1} - F_{o3}) is 2.0 eV and Cd-doped interval $D_{o1} - D_{o3}$ is 2.3 meV. As can be seen, the splitting due to crystal field of the states of electron with spin J_e = 1 / 2 and a hole with spin J_h = 3 / 2 for the three considered centers (impurity atoms) is almost identical.

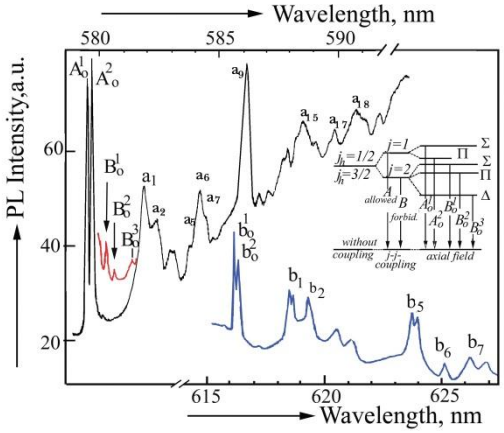

Fig.3. The luminescence spectra ZnP_2 - D_4^8 crystals at 10K doped with tin (Sn)

In the long wave region in the ZnP_2 - D_4^8 crystals Sb-doped there are two groups of lines that were previously found in [1-3]. Narrow intense luminescence line A_0^1 (2.1444 eV) and A_0^2 (2.1442 eV) are non-phonon emission lines of bound excitons to the axial center and are due to transitions from levels Σ, Π (J = 1) in the ground state. These lines are split into 0.22 meV. Weak luminescence line B_0^1 (2.1422 eV), B_0^2 (2.1417 eV) and B_0^3 (2.1400 eV) are due to forbidden transitions from levels Σ, Π and Δ (J = 3 / 2) in the ground state (fig.3). Emission bands a_1, a_2, ..., a_{18} are lines phonon replicas of the non-phonon emission lines A_0^1 and A_0^2. In these spectra, there is no lifting of the ban because of the involvement of phonons, so the luminescence line B_0^1, B_0^2 and B_0^3 are weak. In addition, the luminescence line B_0^1, B_0^2 and B_0^3 located in the long wave region of A_0^1 and A_0^2. Thus, in the band model of the center spin-orbit splitting is less than the splitting due to crystal field. Splitting of the states J = 1 and J = 3 / 2 defined by the energy spacing between levels A_0^1 and B_0^1 is equal to 2.2 meV. Scheme of electronic transitions responsible for the luminescence line (spectra) is shown in fig. 3. In the long wave region observed by us previously in [2, 3] lines B_0^1 (2,0212 eV) and B_0^2 (2,0210 eV) are non-pho luminescence lines of bound excitons to different axial center.

III. CONCLUSION

The luminescence spectra of crystals diphosphide zinc doped tetragonal Mn, Sn, Cd, Sb describes allowed and forbidden recombination transitions in the model levels of the axial center. Superposition of the luminescence of free and bound exciton increase emission lines due to forbidden recombination transitions involving of excitons on the axial center. Amplification with the levels of forbidden transitions of bound excitons occurs at the coincidence of the phonon energy with the energy of the forbidden transition of a bound exciton.

REFERENCES

[1] N.N. Syrbu, Optoelectronic properties compounds A_2B_5, td.Stiinca, Kishinev, 1983

[2] N.N.Syrbu, V.I.Morozova, G.I.Stratan, Phys. and Technics of Semicond., vol. 23 (10), 1771 – 1777, 1989.

[3] N.N.Syrbu, V.I.Morozova, G.I. Stratan, Sov.Phys.Semicond, vol 26 (1), pp. 42-46, Jan 1992, Translated from Phys. and Technics of Semiconductors, vol. 26 (1), pp. 74 – 82, 1992.

[4] R. Bindemann, H.Fisher, K.Kreher, N. N.Syrbu, Phys. St. Sol. (b), vol. 69 (2), pp. K79 – K84, 1975,

Exciton Spectra of $AgAsS_2$ Crystals

Lucretsia NEMERENCO, Iurie IVANENCO
Technical University of Moldova
lnemerenco@yahoo.com

***Abstract* – Reflectivity and wavelength modulated reflectivity spectra of $AgAsS_2$ crystals are investigated in the region of exciton resonances. The exciton and energy band structure parameters were determined.**

***Index Terms* – Reflectivity, modulated reflectivity spectra, energy band structure, exciton spectra**

I. INTRIDUCTION

$AgAsS_2$ crystals belong to layered materials with different anisotropy degree of interatomic interaction forces. $AgAsS_2$ compound crystallizes in a monoclinic lattice with $C_{2/c} - C_{2h}^6$ spatial group. The lattice parameters are as following: a - 17.23, b = 7.78, c= 15.19Å, β- 101°12'. Unit cell contains 24 formula units (Z=24), while the primitive Bravias lattice contains 12 units (Z=12). Smithite crystal structure belongs to the C_c — C_s^4 spatial group. In $AgAsS_2$ crystals interatomic interaction forces are divided into strong intramolecular (intralayer) forces and weak intermolecular (interlayer) forces. In these crystals, it was possible to distinguish the splitting of vibrational modes caused by intralayer and interlayer interaction and to define the splitting of vibrational modes by the double Davydov resonance. Effective Szigeti charge, dynamic effective Born charge, cation and anion relative ionic charges were defined. $AgAsS_2$ crystals grown in ampoules by chemical vapor transport method represent plates with mirror surface 2.5x1.0 cm^2 with thickness of 300-400 μm. The surfaces of some plates were parallel to the C axis. Reflection spectra and wavelength modulated reflection spectra were measured by the MDP-2 spectrometer. For low-temperature measurements the samples were mounted on the cold station of a LTS-22 C 330 optical cryogenic system.

II. EXPERIMENTAL TECHNIQUE AND RESULTS

The edge absorption edge of $AgAsS_2$ crystals at room temperature for E||c and E⊥c polarization is different. The absorption edge for E||c and E⊥c polarization at photon energies energy E ≥ 2,3eV increases rapidly and crystals with thickness of few microns become opaque (fig. 1). $AgAsS_2$ absorption edges are shifted to higher energies with decreasing temperature. The temperature shift coefficient $\beta=\Delta E/\Delta T$ for E||c and E⊥c polarization is equal to $3{,}1\times10^{-4}$ eV/K. The E_g^A and E_g^B absorption bands are observed at energies of 2,358eV and 2,402eV in the transmittance spectra of crystals with thickness d = 5,7 μm measured in E||c polarization (fig. 1). For E⊥c polarization, the E_g^C and E_g^D absorption bands are observed at energies of 2,445eV and 2,510eV, respectively. The character of changes in the spectra of edge transmittance (absorption) gives evidence that the absorption edge is formed by direct allowed transitions. The anisotropy of edge absorption is due to direct polarized electronic transitions which take place in accordance with the selection rules for electronic transitions of C_{2h}^6 symmetry group crystals. The four observed maximums of transmittance (absorption) spectra in the region of the intrinsic absorption for E||c and E⊥c polarization are due to electronic transitions from the V1 and V2 valence bands to the C1 and C2 conduction bands in the center of the Brillouin zone. The energy values of 2,358 eV, 2,402 eV, 2,358 eV and 2,402 eV define the minimal energy intervals between V1-C1, V2-C1, V1-C2 and V2-C2 bands, respectively.

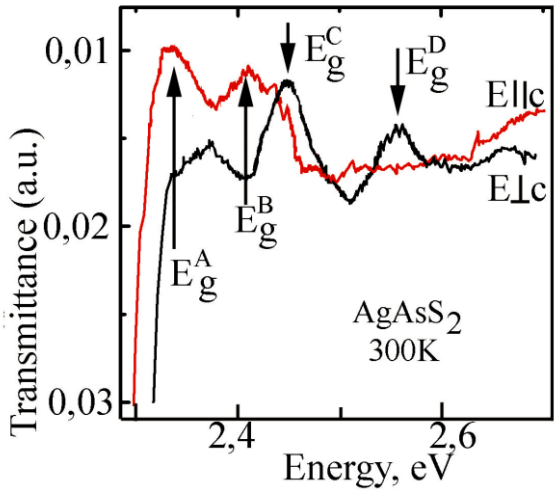

Fig.1. Transmittance spectra of $AgAsS_2$ crystals at 300K with E||c and E⊥c polarization (crystal thickness of 78μm - curves p1,p2,p3; crystal thickness of 54μm -curve p4; crystal thickness of 4,5μm - curve p5).

Absorption spectra at 300K and 10K (spectra are discussed below) give evidence that the fundamental bandgap is formed by direct allowed transitions. The exciton binding energy is small (12,3meV) and the excitons are dissociated at room temperature. The anisotropy of the absorption edge at 2.3 eV is due to the presence of polarized electronic transitions which take place in accordance with the selection rules for electronic transitions of C_{2h}^5 symmetry group crystals [1-2]. The transitions are split due to crystal field. At the same time, there is a splitting due to the spin-orbit interaction.

Low-temperature measurements showed that the fundamental bandgap is formed by direct allowed transitions. The fine structure of the wavelength modulated optical reflection spectra was investigated in the fundamental absorption edge region at the temperature of 10K. For the first time, the ground and excited states of four exciton series A, B, C and D were observed. Series A were observed for E||c polarization with the ground state n=1 at 10K at the energy of 2,3975eV and with the excited state n=2 at the energy of 2,4075eV. The Rydberg constant is equal to 13,3meV and the minimum bandgap is equal to

2,4108eV. Exciton series B, C and D are situated in the short-wavelength interval. For exciton series D the minimum bandgap is equal to 2,5792eV. The Rydberg constant is equal to 24,4meV. Therefore, the exciton binding energy is small (13,3meV and 24,4meV), and they are dissociated at room temperature. Consequently, the structure of the polarized electronic transitions can be discussed within the framework of the selection rules for electronic transitions without taking into account the symmetry of exciton states.

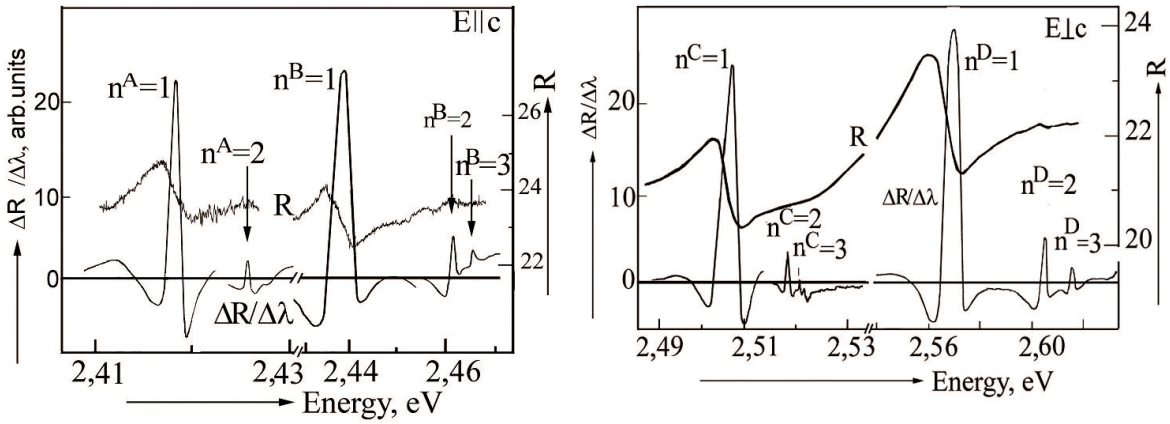

Fig.2 Reflection spectra and wavelength modulated reflection spectra of $AgAsS_2$ crystals in E||c and E⊥c polarization at 10K.

The lines n=1 were observed in the reflection spectra of $AgAsS_2$ crystals at the temperature of 10K and E||c polarization (ω_t = 2.417eV, ω_L = 2.418eV, see Fig.1). For this polarization type, the excitons of $\Gamma_2^-(z)$ symmetry are active for crystals of C_{2h} symmetry. The reflection spectra in the region of the line n=1 has a usual exciton form with a maximum and a minimum. These features are due to the presence of transverse and longitudinal excitons. Based on these data the energy of longitudinal-transverse splitting of $\Gamma_2^-(z)$ excitons was estimated to be equal to 1meV. In the spectral dependence of the wavelength modulated reflection (fig.2), the intensive lines were defined at the energy levels of 2,4175eV and 2,4275eV which are due to the states n=1 and n=2 of the hydrogen-like $\Gamma_2^-(z)$ exciton series. The Rydberg constant determined from the energy position of the lines n=1 and n=2 (fig.1) for these exciton series is equal to 13,3meV. The energy continuum (E_g, $n = \infty$) is equal to 2.4108 eV. A maximum and minimum of reflection with a weak change in the intensity of the reflection (2%) are detected for E⊥c polarization in the reflection spectra at the energies 2,439 – 2,440eV. Intensive features are revealed in the wavelength modulated reflection spectra at the energies 2,4396eV, 2,4642eV and 2,4682eV which are due to the states n=1, n=2 and n=3 of excitons with $\Gamma_2^-(z)$ symmetry. The Rydberg constant for these exciton series obtained from the calculation according to the energy position of the ground and excited states is equal to 32,8meV. The energy continuum (E_g, $n = \infty$) is equal to 2.4724 eV (fig.2).

TABLE 1. EXCITON PARAMETERS OF $AGASS_2$ CRYSTALS

		A(eV)	B(eV)	C(eV)	D(eV)	Δ_{cf}(meV)	Δ_{so}(meV)
Exciton	n=1	2.418	2.440	2.509	2,575	-0.002	151
state	n=2	2.428	2.464	2.520	2,593		
	n=3		2,468	2,522	2,597		
	R	0.013	0.032	0.015	0,024		
E_g 10K	(n=∞)	2.431	2.472	2.450	2,529	-49.6	149
E(min.T) 300K		2,358	2,402	2,445	2,510		

A maximum at 2,505eV (transverse exciton) and a minimum at 2,508eV (longitudinal exciton, fig.3) are observed in E⊥c polarization. Longitudinal-transverse splitting of Γ_5 exciton is equal to 2,0meV. This hydrogen-like series detected in the E⊥c polarization (conventionally named C- Series), in accordance with the selection rules [1-3], can be formed by the states of orthoexciton with $2\Gamma_1^- + \Gamma_2^-$ symmetry. These states are forbidden in the electric quadrupole approximation. The lines n=1, n=2 and n=3 at the energies 2,5089eV, 2,5199eV, 2,5201eV, respectively, are observed in the wavelength modulated reflection spectra. Taking into account the energy position of the ground state n=1 and excited state n=2, the exciton series C binding energy is equal to 14,6meV and the continuum (E_g, $n = \infty$) is equal to 2,5235eV. A maximum and a minimum of the reflection spectra are found at the energies of 2,566eV and 2,572eV in the short-wavelength region of the C-series for E⊥c polarization. In the wavelength modulated reflection spectra, the features are observed at the energies of 2,5752eV, 2,5932eV and 2,5970eV, which are due to the states n=1, n=2 and n=3 of excitons series D with $2\Gamma_1^- + \Gamma_2^-$ symmetry, respectively. The Rydberg constant of these exciton series is equal to 24,4meV from the calculation of the lines n=1 and n=2 energy position. The continuum (E_g, $n = \infty$) of these series is equal to 2,5992eV.

TABLE 2. EXCITON PARAMETERS AND ENERGY BAND PARAMETERS OBTAINED FROM THE CALCULATIONS OF THE OPTICAL REFLECTION SPECTRA AND WAVELENGTH MODULATED REFLECTION SPECTRA OF $AGASS_2$ CRYSTALS

E‖c, 10K, $\varepsilon_\infty = 7.4$			E⊥c, 10K, $\varepsilon_\infty = 7.26$	
Parameters	A	B	C	D
ω_0, eV	2.411	2.439	2.506	2.566
ω_{LT}, meV	1	1	2	4
γ, meV	0.2	0,2	0.16	0,5
M, m_0				1,5
R, eV	0.013	0.032	0.015	0.024
μ, m_0	0.054	0,129	0.06	0,093
m_C^*, m_0	0.1	0.1	0.1	0,1
m_V^*, m_0	0,12	0.44	0.14	1,4

In the region of exciton resonance, the reflection coefficient is equal to 0,22-0,23 and ε_d changes in the interval 7,26-7,4. The value of the background dielectric constant near the exciton resonance was used in calculations. With ε_d = 7.4, the effective mass $\mu = \varepsilon_b^2 R/R_H$ equal to $0.054m_0$ was obtained for the most long-wavelength exciton, where R (0,013eV) is the Rydberg constant for Γ_2^-(z)-exciton and R_{H_2} is the Rydberg energy of hydrogen atom (13,6eV). The Bohr radius (a_B) of the S-State for Γ_2^-(z)-exciton is equal to 0.3×10^{-6} cm^{-1}. With ε_d = 7.4, the effective mass $\mu = \varepsilon_b^2 R/R_H$ of B-excitons with Γ_2^-(z)-symmetry is equal to $0.129m_0$, the exciton binding energy being equal to R =0.032eV. The Bohr radius (a_B) of the S-State for Γ_4-exciton is equal to $0,21\times10^{-6}$ cm^{-1} (table 2).

REFERENCES

[1] E.P.Zaretskaya, V.F.Gremenok, Yu.Rud, V.Yu.Rud,S.Schorr, Book of Abstrakts, 16th International Conf.on Ternary and Multinary Compounds, Sept. 15-19, 2008, Berlin

[2] Chichibu S, Mizutani T, Murakami K, Shioda T, Kurafuji T, Nakanishi H, Niki S, Fons P J, and Yamada A J. 1998 Appl. Phys. **83**, 3678

[3] Schuler S, Siebentritt S, Nishiwaki S, Rega N, Beckmann J, Brehme S, and Lux-Steiner M Ch 2004 *Phys. Rev. B* **69** 045210

Large Oscillator Strength Excitons in $PbGa_2S_4$ Crystals

PARVAN V., MIROVSCII V., MASNIC A.
Technical University of Moldova
parvan_vladimir_ion@rambler.ru

***Abstract* – In $PbGa_2S_4$ crystals the exciton states with the energy of about 290 meV and high oscillator strength (longitudinal – transversal dissipation of 75 meV) were observed. The ground states of the excitons are not dissociated at the room temperature. At the temperature of 77 K and 8.6 K the ground (n=1) and excited (n=2,3) states of two excitons series A and B are observed. The Bor radius for A excitons is about 70 Å and for B excitons is about 10Å.**

***Index Terms* – $PbGa_2S_4$, excitons series, Bor radius for excitons, excitons with large binding energy and oscillator strength, parameters of excitons**

I. INTRODUCTION

Usually, the excitons are not observed in semiconductors at room temperature due to low value of their exciton binding energy. The efficiency of absorption and refraction at the exciton resonance frequency is low due to the week exciton strength and the high values of the exciton radius. According to the literature data [1,2], two factors restrain the implementation of semiconductors in optoelectronic devices: (i) the low value of exciton binding energy and the dissociation of excitons at room temperature, and (ii) the low contribution of exciton states to the optical constants of crystals (the low value of the exciton oscillator strength) due to the high values of the exciton radius.

In this paper we present results of investigation of exciton states in $PbGa_2S_4$ crystals with the ground state Bohr radius of 70 Å and 10 Å. The excitons with the Bohr radius of 10 Å are observed at both low and room temperatures. Apart from that, excited n = 2 and n = 3 states are observed al low temperature. The reflectivity spectra contours are calculated and the main exciton parameters are determined. A model of bands responsible for exciton transitions at K=0 is proposed.

II. EXPERIMENTAL DETAILS

$PbGa_2S_4$ crystals are promising materials for photo-detectors sensitive in the UV region. These crystals has wide ban, with a band gap > 3 eV. Exciton transition are detected at room temperature. Reflection and transmission spectra were measured on JASCO-870 spectrometer, spectra at 10K were measured on СДЛ-1 spectrometer in cryostat LTS-22 C330 Workhorse type Optikal. The comaund $PbGa_2S_4$ crystallizes in rombic lattice with space group D_{2h}^{24} with parameters a=20.706 Å, b=20.380Å, c=12.156 Å [7, 8]. Edge absorption is due to direct allowed transition. For the polarization E||c and E⊥c the edge absorption split to 20-25 meV.Line spacing: single. Text organization: two columns. Column width: 8.3. Space between columns: 0.9 cm. Last page columns must be equal in length. Header and footer: different for odd and even pages. In the reflection spectra of $PbGa_2S_4$ crystals at the minimum of interband interval at 10K in the polarization E‖c and E⊥c were detected lines at 3,042eV ones and weaker line at 3,094eV.

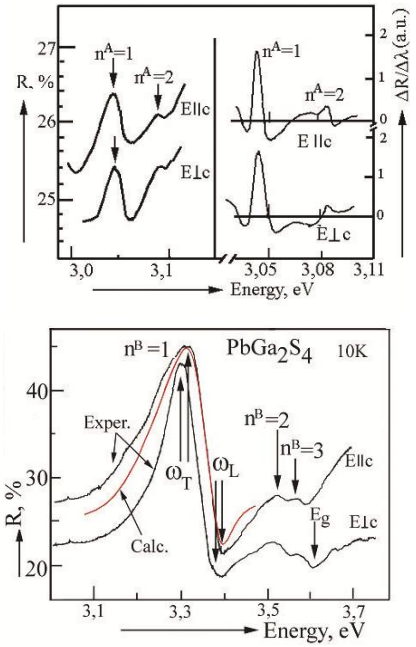

Fig.1 Reflection spectra and wavelength-modulated reflection spectra of crystal $PbGa_2S_4$ in the polarization E‖c and E⊥c measured at 10K and calculated by the dispersion relation contour of reflection spectra for polarization E‖c

The reflection spectra in the vicinity of these lines has traditionally form characteristic excitons with maximum and minimum. Maximum of reflection spectra at 3,042eV is the basic state n=1 and maximum at 3,094eV is the excited state n=2 of longwave exciton series A (series conventionally designated A). In the spectra form Fig.1 clearly stand out the minima of reflection spectra at 3,053eV. These features are due to the presence of transversal (maximum) and longitudinal (minimum) of excitons. Based on these data were estimated the energy of transverse-longitudinal splitting of the basic state of A-exciton $\Delta\omega_{LT,}$ which is equal ~11meV. In the right side of Fig.1 is presents the reflection spectra modulated by the wavelength at 10K of $PbGa_2S_4$ crystals.In the polarizations E‖c and E⊥c in a modulated reflectance spectra revealed the line n = 1 (ω_t = 3,043eV) and n = 2 (3.096eV). In the region of exciton resonance reflection coefficient is 0.24-0.25, and ε_d varies in the range 7.4-8.2. The calculations used the value of the background

dielectric constant near the exciton resonance. When ε_d = 7.6 and 7.0 reduced effective mass of the A-exciton $\mu = \varepsilon_b^2 R/R_H = 0.352 m_0$, where - R_{H_2} the energy of the Rydberg hydrogen atom (13.6 eV). Rydberg constant R, obtained from the calculations on lines n = 1 and n = 2 is equal to 0.070 eV. The minimum gap width at 10 K is 3.112 eV. In the short-wavelength region of the exciton A series of reflection spectra revealed intense peaks at an energy of 3.326 eV for polarization E‖c and at an energy of 3.317 eV for polarization E⊥c. These lines are due to the base state n = 1 exciton of B series. In the short-wave region were detected maxima at energies 3.544 eV and 3.584 eV, which are the excited states n = 2 and n = 3 in the exciton series. In the spectra clearly stand out a minimum of reflection at 3.382 eV and 3.408 eV. These minima are caused by the energy of the longitudinal exciton of B series.

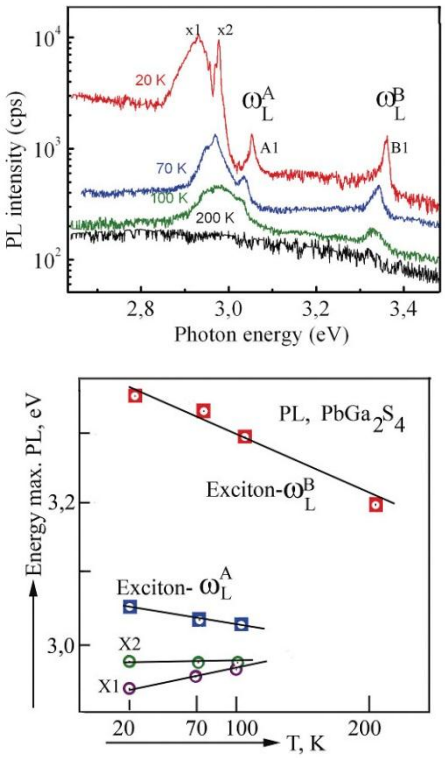

Fig.2 The luminescence spectra of $PbGa_2S_4$ crystals at temperature 20K, 70K, 100K and 200K and changes of the energy maxima of the luminescence with temperature change in the crystal.

In the photoluminescence spectra of the crystals *$PbGa_2S_4$* excited by argon laser line observed narrow emission lines x1, x2, A1 and B1 at the energies 2.9312, 2.9771, 3.0534 and 3.3613 eV, respectively. The nature of the lines x1 and x2 has the impurity character, with the temperature increases, their intensity decreases (especially peak-x2). Increase in temperature leads to a shift in luminescence peaks in energy position (Fig. 2). Temperature gradient changes of emission maxima position for ω_L^B and ω_L^A within the limits of experimental error coincide. Temperature gradient changes of the maxima energy position for x1 and x2 differ (Fig. 2), which indicates extrinsic nature of these peaks. Most likely, these peaks are due to bound excitons. The energy position of lines A1 and B1 correspond to the energy of longitudinal excitons A and B. The estimated value of the transverse-longitudinal splitting $\Delta\omega_{LT}$ (were taken the difference between the energy minimum and maximum of reflection spectra) of B-excitons for the polarizations E‖c and E⊥c is equal with 50 and 52 meV. Considering the energy position of the base and excited states of B-excitons was defined Rydberg constant which is equal with 291 meV in the polarization E‖c and 292meV in the polarization E⊥c. Taking into account magnitude of background dielectric constant (7,6-7,0) was calculated the B-exciton reduced mass μ , which is equal with 1,126 m_0. Energy of continuum for B exciton series is equal with 3.617 eV (E‖c) and 3.610 eV (E⊥c). The values obtained for the binding energy 291-292 meV for B-excitons in crystals $PbGa_2S_4$ are near a record for the crystals with a bandgap of 3 eV. Exciton energy exceeds 290 meV are observed in crystals [1]. In NaI crystals the Rydberg constant is equal with 300 meV in the KI crystal binding energy is equal with 400 meV. In other alkali-halide crystals the binding energy is more. Excitons with the same binding energy is related to the Frenkel exciton. [1].

Thus, the observed exciton states in a series of crystals $PbGa_2S_4$ can be attributed to the Frenkel exciton, and it should be noted that the crystals are $PbGa_2S_4$ narrower gap than the crystals of KI and NaI. The difference in bandgap crystals $PbGa_2S_4$ and KI (NaI) is equal to 2.3 eV.

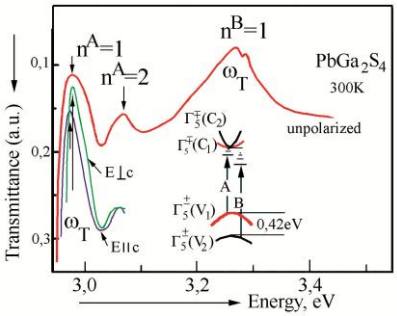

Fig.3 The transmission spectra of $PbGa_2S_4$ crystals measured at 300K in the polarizations E‖c (curve shifted vertically downwards by 0,5, E⊥c and in unpolarized light (the thickness of the crystals 17 microns).

In Figure 3 shows the transmission spectra of $PbGa_2S_4$ crystals at 300K in a polarized and not polarized light. In the transmission spectra revealed state n = 1 and n = 2 for A-excitons, respectively, at energies 2.990 eV and 3.044 eV.

TABLE 1. *PARAMETERS OF EXCITONS AND BANDS OBTAINED FROM THE CALCULATIONS OF THE OPTICAL REFLECTION SPECTRA AND WAVELENGTH-MODULATED REFLECTION SPECTRA OF $PBGA_2S_4$ CRYSTALS*

Parameters	E‖c, 10K, ε_∞ = 7.6		E⊥c, 10K, ε_∞ = 7.0	
	A	B	A	B
ω_0, eV	3.042	3.326	3.042	3.317
ω_{LT}, meV	11	50	11	52
γ, meV	0.19	60	0.16	60
t, Å	25	20	25	20
M, m_0	3	5	3	5
R, eV	0.070	0.291	0.070	0.292
μ, m_0	0.352	1.134	0.352	1.134
m_C^*, m_0	0.17	1.71	0.17	1.71
m_V^*, m_0	2.83	3.29	2.83	3.29

The difference in energy for base state n = 1 in the polarization E‖c and E⊥c does not exceed 20 meV. At the energy of 3.257 eV observed maximum of absorption due to

transitions to the base state of transversal B-excitons. Taking into account the energy position of n = 1 and n = 2, Rydberg constant is equal to 90 meV. This value coincides with the binding energy determined at 10K. Using the conditions $M = m_V^* + m_C^*$ and $\frac{1}{\mu} = \frac{1}{m_V^*} + \frac{1}{m_C^*}$ were calculated the effective mass of electrons and holes which are responsible for A and B series of excitons (Table 1).

As seen from the table, the effective mass of electrons and holes are responsible for A and B exciton series are different. These data indicate that the exciton series A is formed by a pair of zones $V_1 - C_1$ and Series B is formed by a pair of zones $V_2 - C_2$. Effective Bohr radius a_{ex} are defined by formulas of Bohr for hydrogen atom

$$a_{ex} = a_B \varepsilon m_0 / \mu$$

where a_B the Bohr radius of hydrogen atom, ε and μ-dielectric constant and the reduced effective exciton mass. In discussed crystal $PbGa_2S_4$ exciton base state (n = 1) have different radii of Bohr. For A-excitons a_B is 70 Å, and for B-excitons in aB is 10 Å. Thus, we see two different exciton with different Bohr radius. A series of excitons refer to Wannier-Mott excitons and B series can be considered the Frenkel exciton. Exciton parameters are given in Table 1.

We will analyze the energy band structure of PbGa2S4 crystals taking into account the exciton transitions discussed above. The wave functions of the valence and conduction bans of PbGa2S4 crystals are transformed according to the irreducible representations Γ_5^+ or Γ_5^- of the point symmetry group D_{2h} [23]. Therefore, one needs to consider the selection rules of transitions from the ground crystal state |0> to the exciton K, Γex, j> state, i. e. the conditions of difference from zero of the matrix element of the transition <0|Hint|K, Γex, j>, where K is the exciton wave vector, Γex is the irreducible representation according to which the wave function of the exciton is transformed, j is the row, Γex is the direct product of the irreducible representations $\Gamma_l \times \Gamma_h \times D_l$ (i = 0,1…) according to which the wave functions of electrons, holes and their relative motion are transformed. The transitions occur under the action of the light. In the $PbGa_2S_4$ crystals Γ_2^- excitons are dipole-active in the E||b, (k||a, k||c) polarization, while the Γ_3^- excitons are active in the E||c, (k||a, k||b) polarization, and the Γ_4^- excitons are dipole-active in the E||a, (k|b, k|c) polarization.If one compares the obtained experimental results with the exciton symmetries, one can note that the long-wavelength A-excitons with Γ_3^- and Γ_4^- (or Γ_2^-) symmetry have similar parameters. The splitting of the ground exciton states does not exceed 20 meV. The symmetry of the B-excitons is the same as that of A-excitons. The energy position of the n = 1 state of B-excitons in the E||c and E⊥c polarizations also does not exceed 20 meV. On the basis of the selection rules and the obtained values of electron and hole effective masses, one can propose a following model of energy bands explaining the exciton spectra: the A-exciton series is formed by the (V1-C1) bands with $\Gamma_5^{\pm} - \Gamma_5^{\mp}$ symmetry, while the B-exciton series is produced by the V2-C2) bands with $\Gamma_5^{\pm} - \Gamma_5^{\mp}$ symmetry. According to this model, the both exciton series are produced in the center of the Brillouin zone as shown in Fig. 7. The C1 and C2 bands are probably degenerated in the center of the Brillouin zone, since the bandgaps for the E⊥c and E||c polarizations obtained from exciton spectra coincide in the limits of experimental errors.

III. CONCLUSION

In conclusion, we note that the crystals were first discovered $PbGa_2S_4$ excitons with large binding energy and oscillator strength. These excitons contribute significantly to the optical constants even at room temperature. On the basis of such materials, you can create optoelectronic devices operating at room temperature, which action is based on physical principles of light interaction with excitons [2,3].

REFERENCES

[1] R. Knox, Theory of excitons, (Mir, Moscow, 1966), 1 st ed., p. 219.,Song,K.S.and Williams R.T.)1993).Self-trapped excitons.Springer-Verlag,Berlin

[2] L.V.Keldish Excitons in Semiconductor-Dielectric anostructures/Phys.St.Sol.1997,Vol.164,N3

[3] V.S.Dneprovskii, E.A.Jucov, E.A.Malearov, S.G.Tihodeev, JETF,1998

Effect of Time on the Properties of Crystallization Agents: Ice-forming Aerosols

Efim ZASAVITSKY[1], Valerii KANTSER[1], Anatolii SIDORENKO[1],
Ion GARABA[2], Evghenii POTAPOV[2], Nicolai KIM[3]
[1]*Institute of Electronic Engineering and Nanotechnologies "D.Ghitu" of the Academy of Sciences of Moldova, efim@lises.asm.md*
[2]*Special Service for Active Influences on Hydrometeorological Processes of Republic of Moldova,*
[3]*Scientific Production Center "Meteoteh", Russia*

***Abstract* — The results of studies of the efficiency (yield) of pyrotechnic compositions used for the prevention of hail in the Republic of Moldova as a function of storage time are described. The studies are performed using an ingenious installation based on a small aerodynamic stand, which makes it possible to control the efficiency of ice-formation of full-size generators in the on-line mode and to study the nucleation activity of new reagents under dynamic conditions. It is shown that the efficiency of the pyrotechnic compositions based on silver iodide (AgI) decreases depending on storage time. At the same time, the decrease in yield for given standard storage conditions is on the order of 10% per year.**

***Index Terms* — Ice-forming aerosol, silver iodide, AgI, aerodynamic stand**

I. INTRODUCTION

The relevance of work on active impacts for the prevention of hail, the redistribution of precipitation, and the thinning of fog and clouds does not give rise to doubts. These works are carried out in many states. In the RM, large-scale works on the protection of agricultural crops from hail damage are carried out on a regular basis (in 2010 the area of territories under protection was 1.4 mln ha); thousands of antihail rockets are utilized for these purposes every year.

Along with cooling agents, ice-forming aerosols are widely used as artificial means of crystallization in the practice of active influences on supercooled cloud environments. Ice-forming aerosols are fine particles of a substance that, under given thermodynamic conditions in a cloud, can act as nuclei (seed) for the formation and growth of ice crystals.

Ice-forming reagents are most commonly used owning to a number of technical advantages, which result from the conditions of storage, delivery and dispersion in the zone of cloud seeding, etc. In the case of using these substances, the method of active impacts is based on the formation of a necessary concentration of artificial ice crystals in the seeded part of the cloud environment; that is, in a potentially hail-hazardous cloud environment, it is necessary to form a certain number of active ice-forming nuclei under given conditions in the cloud and known conditions of introduction of reagents into the atmosphere.

Ice-forming reagents are effective means of artificial crystallization of supercooled clouds and fog, which determines their extensive use in the practice of active influences (AIs) in many countries, including the Republic of Moldova (RM). The ice-forming aerosol based on applied reagents is dispersed into cloudy atmosphere by means of special generators (rockets, pyrocartridges, ground-based and airborne devices); their application is determined by techniques and objectives of AIs [1].

To date, we know a wide class of materials whose fine aerosols can initiate the formation of ice crystals with a high probability. One of the most widely used reagents are those based on silver iodide (AgI). Ice-forming pyrotechnical compositions based on silver iodide (AgI), which are used in antihail rockets for impacts on hail-hazardous clouds in the RM, yield more than 10^{13} g^{-1} of active ice-forming particles at a temperature of the cloud (simulated) environment of -10°C.

The theoretical foundation for describing the effects of fine aerosols of ice-forming reagents based on the theory of nucleation of ice on the surface of aerosol particles developed by H. Fletcher [2, 3].

The use of pyrotechnic generators in different exposure techniques requires reliable knowledge of their efficiency. Therefore, before using these tools in the active intervention, it is necessary to experimentally prove their efficiency.

We can state that the result of this impact on a potentially hail-hazardous cloud with ice-forming reagents depends on many factors and, not least of all, on the yield of a particular generator, which depends on many factors: storage conditions, temperature, storage duration, etc. Thereby, the efficiency of pyrotechnic generators depends on observance of technological conditions of their manufacture as well as on the period and conditions of storage. Herein, a tendency of efficiency decreasing, sometimes by orders of magnitude, can be observed [4].

In this regard, laboratory technologies aimed at studying the yield of generators are particularly relevant. To implement an ideal case in which a technique for determining the efficiency of means of crystallization most fully takes into account different situations of impact on supercooled clouds and various characteristics of generators of ice-forming nuclei or crystals, we must provide the following conditions:

• The efficiency of a generator should be studied using direct simulation over the entire set of parameters, both parameters of the motion of the generator and the parameters of the environment in which the generator operates;
• Any dilution and transfer of selected aerosol samples must not be accompanied by changes in temperature and humidity;
• The nucleation and growth of ice crystals must occur under the direct simulation of the basic parameters of the seeding zone: temperature, humidity, and the spectrum of droplet size distribution.

The preference is given to aerodynamic tubes. Studies of generators in aerodynamic tubes make it possible to acquire reliable information on the efficiency of a particular generator in strictly controlled measurement conditions.

II. THE TECHNIQUE FOR THE DETERMINATION OF EFFICIENCY OF ICE-FORMING AEROSOL GENERATORS AND EXPERIMENTAL DATA

The aerodynamic stand for the testing of full-size generators of ice-forming aerosols is designed in the Institute of Electronic Engineering and Nanotechnologies of the Academy of Sciences of the RM with the participation of the Special Service for Active Influences on Hydrometeorological Processes of the RM.

This aerodynamic stand allows testing any type of pyrotechnical generators of ice-forming aerosols, which are used at present both in operations on protection of agricultural crops from hail damage and in operations (experiments) on modification of precipitation.

It should be noted that the simulation of conditions of the flight of a rocket using an aerodynamic stand is also caused by the fact that the ice-forming activity of aerosols is affected, to different extents, by many factors. One of them is the ratio of the velocity of the generator to the velocity of discharge of a gas-vapor stream from the nozzle of the generator. In addition, the yield of active ice-forming particles of AgI heavily and monotonically depends on this parameter.

The main difficulty in these experiments is to form particles, which are adequate to really used particles by their physicochemical and, accordingly, ice-forming characteristics. A practically significant parameter of artificial crystallization, which is necessary to characterize their performance under real conditions of impact, is the yield of ice-forming particles in a temperature range of $(-5 \div -15)^{o}$C.

It should be noted that, despite the considerable number of countries implementing projects on AIs, laboratories of this level are scarce in Europe (Russia, Bulgaria).

The aim of this work is to experimentally reveal the dependence of the main parameter of rocket generators, i.e., yield, on external factors, i.e., temperature, time, storage conditions, etc., under laboratory conditions with a maximal consistence of model conditions to real conditions of the flight of a rocket in a potentially hazardous cloud upon seeding with an ice-forming reagent.

To simulate real conditions of the operation of generators, the technique was based on the use of a stand prepared of a small horizontal aerodynamic tube (HAT) designed and constructed at the Institute of Electronic Engineering and Nanotechnologies, Academy of Science of Moldova.

The diameter of the HAT d = 330 mm; the length L = 9 m. In the Eiffel chamber (d = 500 mm, L = 3 m), a device for taking samples of ice-forming aerosol from the air flow is placed. The general arrangement of the aerodynamic tube in two project views is shown in Figs. 1 and 2. In the front part of the aerodynamic tube, in front of the Eiffel chamber, an access panel is arranged for the installation of full-size generators of ice-forming aerosols and large fragments of samples of pyrotechnical compositions with reagents. The flow velocity (m/s) in the HAT is determined by the method of measurement of gas dynamic pressure using a "Pitot tube."

Fig. 1. A fragment of the HAT.

Fig. 2. A fragment of the HAT with a system for sampling and dilution of aerosol.

To ensure a correct representativeness of the aerosol sample in the aerodynamic tube, we carried out special experiments to study the distribution of air velocity in the tube. Figure 3 shows the results of the air velocity distribution over cross section in the zone of the aerosol generator at a flow rate in the working part of 30 m/s.

It is evident that, for the used installation, the axis of symmetry in the horizontal direction almost coincides with the cross-section center.

For better homogenization and mixing of the aerosol and the air, at a certain distance behind the generator, we installed a special unit, i.e., turbulator intended for the intensive stirring of the aerosol plume in order to obtain a uniform aerosol concentration over the cross section at the sampling point. The estimation of the uniformity of the distribution of aerosol concentration over the cross section

showed that the ratio of the concentration at the center to the concentration at any point of the cross section varies within 10%.

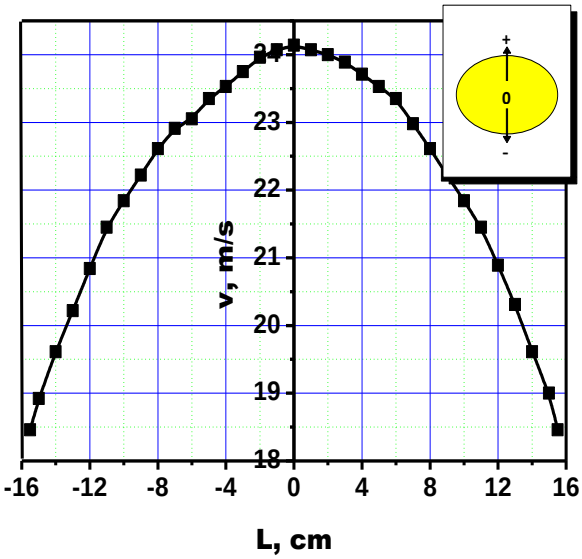

Fig. 3. Distribution of air velocity in the cross section of the aerodynamic tube

The system of sampling and dilution allows representative sampling of the aerosol generated by a generator in the air flow of the HAT. The intake is placed in the Eiffel chamber. The intake consists of a stainless pipe exposed at the center of the tube with holes directed toward the flow, a piping system, and a syringe. Since the difference between atmospheric pressure and dynamic pressure is usually no more than 1%, the transfer of the sample from the tract of the aerodynamic tube into a mixing chamber is carried out isothermally and with a constant humidity.

To prevent the suppression of the activity of ice-forming particles due to the effect of "re-seeding", it is necessary to obtain an optimum concentration of crystals in the mixing chamber, which would provide a statistically significant result of the experiment. In order to reduce the aerosol concentration, the sample had previously been dissolved in a cube with a volume of 1000 and 125 l, respectively (Figs. 1, 2).

The nucleation and growth of ice crystals occurs in a supercooled fog produced in the working volume of the mixing chamber. In the capacity of a mixing chamber in the stand under discussion, we used an ILKA KTLK-1250 climate chamber with a working volume of 1200 l manufactured in the German Democratic Republic. In accordance with the objectives of the experiments, the camera was modified as follows.

- Access holes were made in the door for the placing and removal of microthermostats.
- A system for introducing a measured sample of the active aerosol into the working volume was prepared.
- A fan to mix the air to reduce temperature gradients was installed in the working volume.
- A temperature and humidity sensor was installed.
- In the upper part of the cloud chamber, a lighting unit was installed; it generated a beam of light for the visual observation of the process of formation of fog, variation in its density, and formation of ice crystals.

Supercooled fog in the chamber is created by the injection of hot vapor, which condenses to form water aerosol with a modal diameter of droplets of about 4 μm.

Given the linear dimensions of the chamber, the vertical temperature gradient in the chamber does not exceed 0.02 deg/cm; the horizontal gradient, 0.005 deg/cm.

The initial water content of fog depends on the duration of the introduction of vapor; it was 0.4-3.0 g/m^3.

The accuracy of temperature measurement in the chamber working volume is ±0.1^{o}C.

For the experiment (measurement) temperature, we take the temperature settled in the chamber working volume after the formation of fog in it, before the introduction of the aerosol sample.

The lifetime of vapor fog in the chamber for an initial water content of 1÷2 g/m^3 is 2÷3 min.

Fog in the cloud chamber is generated by the condensation of a hot water vapor being introduced into a cooled volume.

The activation of samples of ice-forming aerosol is carried out in the chamber at specified temperature levels up to T = -20^{o}C.

Ice crystals that are formed on introduced nuclei grow to sedimentation sizes and are recorded at the bottom of the chamber using a thermostat. The quantity of the microthermostats is determined by objectives of the specific experiment. According to the number of crystals formed, knowing the characteristics of the equipment and consumption data for the generator, we can calculate the yield of nuclei. It should be noted that the time of the manifestation of ice-forming nuclei depends on temperature; in addition, the kinetic constant decreases with decreasing temperature, and the time of the manifestation of a given fraction of nuclei increases and is about 3 min at -5^{o}C.

The duration of one measurement (experiment) using the aerodynamic stand, which consists in the measurement of the yield of active ice-forming particles, is 30-40 min at a given temperature.

For the determination of the yield of active ice-forming particles according to this technique, it is necessary to take into account a number of factors, the disregard of which can significantly distort results:

- presence of significant temperature gradients in the chamber working volume;
- inhomogeneity of water content of supercooled fog;
- run-to-run reproducibility of fog parameters;
- local supersaturation of water vapor upon the introduction of aerosol in the chamber;
- coagulation of aerosol particles in the process of formation and introduction into the chamber, their precipitation on chamber walls, injector, and feeding hoses.

The estimation of accidental errors of measurements showed that the error of a single measurement is ±15% in a temperature range of -10 to 20^{o}C and ±30% at the fog temperature of -5^{o}C. As the temperature decreases, the error is reduced. The total systematic error is ± 3% and can be ignored in the calculations.

Based on the designed aerodynamic stand and developed procedure of testing of ice-forming pyrotechnic

compositions, we carried out experiments on the determination of the practical yield of active particles of a pyrotechnic composition for different series of antihail rockets, which were produced in different years and used for active impacts on hail-forming processes by the Special Service for Active Influences on Hydrometeorological Processes of the Republic of Moldova in the respective years (Fig. 4).

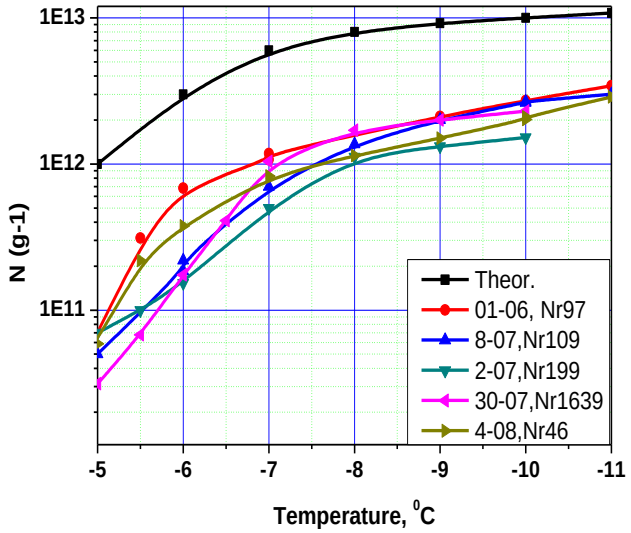

Fig. 4. Temperature dependence of the yield of active particles of a pyrotechnic composition of antihail rockets.

Analysis of Fig. 4 shows that, in general, the behavior of temperature dependence remains the same. However, depending on the year of manufacture of the rocket (the rocket's storage time at deposit), an interesting relationship is observed: the "older" the pyrotechnic composition, the lower its yield. On the basis of general considerations, this dependence of the generator yield is clear. Under the influence of external factors (temperature, time, storage conditions, etc.), irreversible changes take place in a pyrotechnic composition and lead to the experimentally observed decrease in yield of the generator of antihail rockets.

III. CONCLUSION

Based on the technique and devices that were developed and introduced into practice for studying the efficiency of crystallization means on the basis of silver iodide AgI, we analyzed the yield of really used generators of rockets of the "Alazan" type as a functions of external factors. This technique makes it possible to perform a direct simulation of the formation of aerosols and their interaction with the supercooled cloud environment, which gives the possibility to obtain adequate information about the efficiency of the generator in a real process of exposure. The technique is based on a direct aerodynamic modeling of the motion of a real generator in the air in an aerodynamic tube. It is shown that the efficiency of the pyrotechnic compositions based on silver iodide (AgI) decreases depending on storage time. The decrease in yield for given standard storage conditions is on the order of 10% per year.

The technique is protected by an author's certificate. To date, it has been used for the practical testing of generators of ice-forming aerosols based on Alazan' and Loza rockets used in our country. The developed technique and devices make it possible to systematically study the yield of mass-produced generators of rockets that are used in the practice of active influences (Alazan', Loza).

Thus, the totality of the studies is a solution to the important scientific and technical problem, i.e., the rapid determination of the yield of real generators used in Moldova in the practice of active influences on supercooled cloud environments to prevent hail. The results of these studies based on the experimentally measured value of yield give the possibility to correctly calculate the minimum number of rockets required for the processing of a potentially hail-hazardous cloud.

REFERENCES

[1] A. S. Dennis Weather Modification by Cloud Seeding. Academic Press, 1980.

[2] N. H. Fletcher “Size effect in heterogeneous nucleation” J.Chem.Phys., vol.29, pp. 572-576, 1958.

[3] N. H. Fletcher The physics of rainclouds. Cambrige, University Press, 1962.

[4] E. I. Zotov, N. I. Zotova, T. D. Nikorich, and E. I. Potapov, “The influence of gas impurities on ice-forming activity of pyrotechnic compositions with 2% content of AgI (in Russian)” – Chisinau, Collection «Active influence on atmospheric processes in Moldova”, issue 3, pp. 86-90, 1992.

[5] E. A. Zasavitsky “The aerodynamic stand for research of ice-forming characteristics of reagents” Moldavian Journal of the Physical Sciences, vol 9(2), pp.237-242, 2010.

Detection in the Contacts With Bismuth-Antimony Alloy: Numerical Modeling of the Contact Area Role

Iacov KERNER
Institute of Electronic Engineering and Nanotechnologies "D. Gitsu"
Academy of Sciences of Moldova
iacov@lises.asm.md

***Abstract*: Diode detectors (DD) are widely used in electronic information and communication systems. The use of diodes with Schottky barrier gave a possibility to master radiowaves of high frequencies (above 1 GHz). These diodes use the quick-acting metal-semiconductor contacts.**

The further improvement of their parameters was achieved due to fall of the working temperature (T). This direction was named cryogenic electronics or briefly cryoelectronics, it allows to raise the nonlinearity of the current-voltage dependences (CVD) and current responsivity (CR).

In this paper the numerical modeling of the electrical potential distribution and current passing in the contacts of normal metal with semiconductor alloy bismuth-antimony (Bi-Sb) with different contact area was made. There were analyzed possibilities to create the diode detectors based on these contacts and working at liquid helium temperature 4.2 K. The dependences of the current responsivity, the voltage responsivity (VR) and the noise equivalent power (NEP) on the signal frequency (f) were analyzed. The obtained results were compared with literature data. Both DD working at temperature of liquid nitrogen (T = 77.4 K) and liquid helium (T= 4.2 K) were considered.

The comparison with existent literature data shows the proposed DD can be 10÷100 times better. The physical reasons of these advantages were discussed too. It is shown that unique properties of Bi-Sb alloys and especially of $Bi_{0.88}Sb_{0.12}$ alloy make these alloys to be the very perspective materials for cryoelectronics.

Therefore these DD are perspective for cryogenic electronics and there is an actual problem to elaborate them.

***Key words*- detection, Schottky diodes.**

I. INTRODUCTION

The diode detectors play an important role in radio technics and electronics. The use of high frequencies (above 1 GHz) stimulated the careful study of diodes with Schottky barrier. These diodes use the quick-acting metal-semiconductor contacts [1].

The further improvement of their parameters was achieved due to fall of the working temperature. This direction was named cryoelectronics [2], it allows to raise the nonlinearity of the current-voltage dependences and current responsivity. The thermal noise power decreases too. For example there were elaborated DD based on the contacts Pb-pGaAs [3, 4]. At the signal frequency f = 9 GHz and T= 4.2 K these diodes had CR ≈ 500 A/W and noise equivalent power 5×10^{-15} W/$\sqrt{Hz}$. Also the deep cooling allows using the materials with little energy gap width but high mobility of electrons, such as solid solutions Bi-Sb [2, 5].

After the discovery of the high temperature superconductors (HTSC) the possibilities to use HTSC in cryoelectronics were studied too. At the liquid nitrogen temperature T = 77 K and signal frequency f = 37.5 GHz the corresponding structures revealed the voltage responsivity 3000 V/W [6]. The further studies [7] allowed to create the structures with VR=5000 V/W and noise equivalent power NEP = 2×10^{-12} W/$\sqrt{Hz}$ at the signal frequency f=31 GHz and temperature T = 77 K. According to our publication [8] the diode detectors based on the contacts HTSC-InSb may have CR ≈ 40 A/W, VR ≈ 10^6 V/W and NEP ≈ 8×10^{-15} W/$\sqrt{Hz}$ at T = 77.4 K and f = 10 GHz. At the same temperature and f = 30 GHz these DD may have CR ≈ 15 A/W, VR ≈ 3.5×10^5 V/W and NEP ≈ 2×10^{-14} W/$\sqrt{Hz}$.

On the other hand often there is an oxidation of semiconductor in HTSC-semiconductor contacts, because oxygen is an integral part of HTSC. Also cooling to the liquid nitrogen temperature 77.4 K may be insufficient to obtain the good DD parameters. In this situation, taking into account the rapid development of cryogenics, the study of DD based on the contacts traditional superconductor – semiconductor seems to be actual problem. Usually these DD work at liquid helium temperatures (T ≤ 4.2 K). In this article there are discussed DD based on the contacts of normal metal with semiconductor solid solution Bi-Sb. We tried to analyze the contact area role in this DD.

II. RESULTS AND DISCUSSION

The contacts of semiconductor solid solution $Bi_{0.88}Sb_{0.12}$ with normal metal were considered. The normal metal may be aluminum at T ≥ 1.2 K and silver or gold at lower temperatures. Materials properties were taken from [9-11]. Results of calculations are shown in figures (figs.) 1-3. In all figures the logarithmic scale for X-axes is used. An exponential form is often used for numbers of axes.

Figs. 1 - 3 show that current and voltage responsivities decrease and NEP increases at the frequencies more 3 GHz.

At these frequencies the negative role of the barrier capacity is revealed and it begins to shunt the nonlinear contact resistance. On the other hand at high frequencies the contact capacity resistance becomes compared with ohm spreading resistance. The current redistribution occurs, it leads to reduction of the rectified current and DD parameters become worse.

The round flat contacts with contact area 100, 10 and 1 μ^2 were studied. Taking into account the little surface area these contacts may be considered as point contacts [1].In this case the barrier capacity is proportional to *S*, where *S* is the contact area, and ohm spreading resistance is proportional to $S^{-1/2}$ [1]. In this situation, when the contact area decreases, the capacity resistance rises faster then the ohm spreading resistance. Therefore the redistribution of applied variable voltage occurs, the contact voltage grows and DD parameters become well (see curves 1, 2, 3 in fig. 1). When the contact area reduces the contact differential resistance rises and voltage responsivity rises too. On the other hand noise current falls and noise equivalent power falls too (see figs. 2 and 3).

For comparison our results [12] for contacts HTSC-semiconductor with contact area 100 μ^2 are presented in figs. 4, 5.

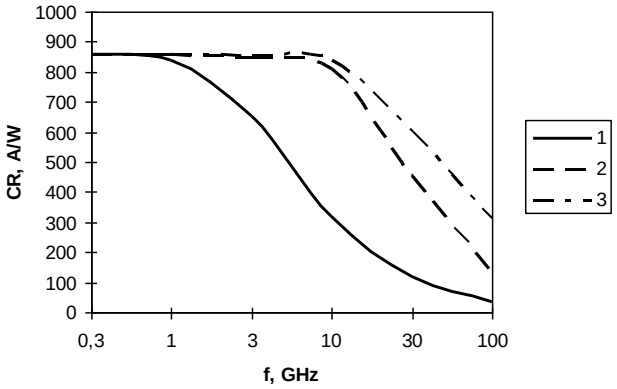

Fig. 1. The calculated current responsivity dependence on the signal frequency in the contacts with $Bi_{0.88}Sb_{0.12}$. The legend inscriptions 1, 2 and 3 correspond to the contact area 100, 10 and 1 μ^2. T = 4.2 K.

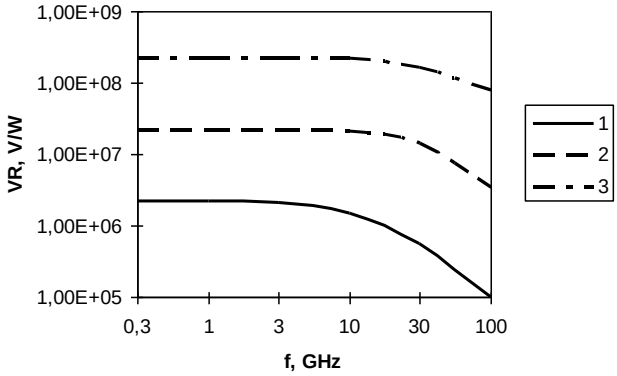

Fig. 2. The calculated voltage responsivity dependence on the signal frequency. The legend inscriptions and other data are similar to those in fig. 1. T = 4.2 K.

The main advantages of Bi-Sb are next:

(i) Little barriers heights due to narrow energy gap. This fact provides a big CVD nonlinearity and big current responsivity.

(ii) High mobility of electrons, which reduces ohm resistance and improves frequencies properties.

(iii) Little barrier capacity, due to little barriers heights and small effective masses of electrons, which also improves frequencies properties.

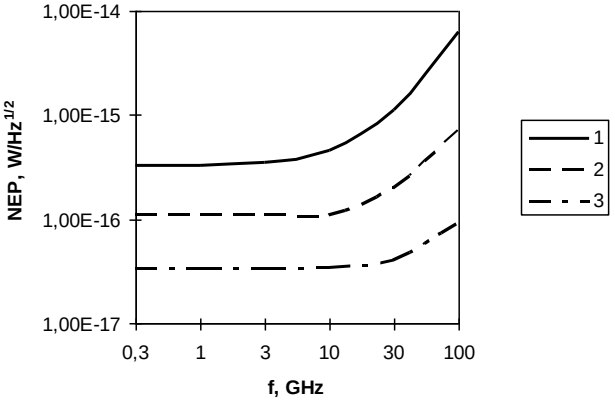

Fig. 3. The calculated noise equivalent power dependence on the signal frequency. The legend inscriptions and other data are similar to those in fig. 1. T = 4.2 K.

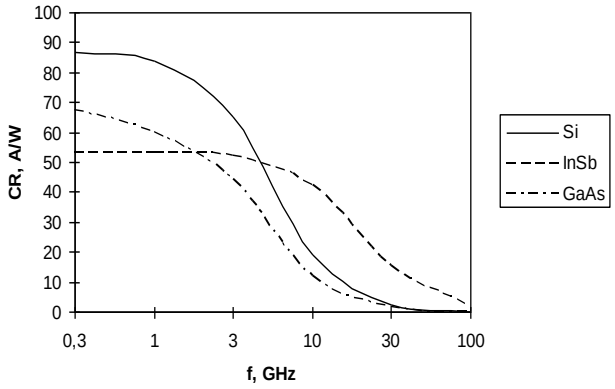

Fig. 4. The calculated current responsivity dependence on the signal frequency for contacts HTSC-semiconductor (the semiconductor substance is shown in legend inscriptions). T = 77.4 K.

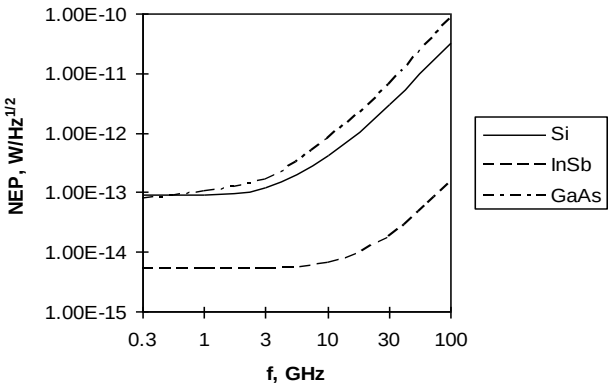

Fig. 5. The calculated noise equivalent power dependence on the signal frequency for contacts HTSC-semiconductor. The legend inscriptions and other data are similar to those in fig. 4. T = 77.4 K.

These unique properties of Bi-Sb alloys and especially of $Bi_{0.88}Sb_{0.12}$ alloy make these alloys to be the very perspective materials for cryoelectronics.

Taking into account results [3, 4, 6-8] we may conclude that contacts with Bi-Sb allow improving considerably DD parameters. On one hand they are much more effective than contacts HTSC-superconductor [6-8]. On the other hand they are better than contacts with GaAs [3, 4] working at liquid helium temperature.

III. CONCLUSION

The comparison with [3, 4] data shows that in the proposed DD current responsivity can be 2 times more and noise equivalent power can be 100 times less than the ones in existing DD (at the same temperature and signal frequency). Also they may have very high voltage responsivity.

The contact area reduction may sufficiently improve the frequencies properties, noise equivalent power and especially voltage responsivity.

This fact draws the conclusion the contacts with Bi-Sb are perspective to elaborate them.

REFERENCES

[1] V.I. Striha, E.V. Buzaneva, I.A. Radzievsky, Semiconductor devices with Schotttky barrier. Physics, technology, application (in Russian). M., Sov. Radio, 1974.

[2] V.N. Alfeev Superconductors, semiconductors and paraelectrics in cryoelectronics (in Russian), M., Sov. Radio, 1979.

[3] M. Mc Call, M.F. Millea, A.H. Silver, The superconductor-semiconductor Schottky barrier diode detecto, Applied Physics Letters, vol. 23, no. 5, 1973, pp. 263-264.

[4] M. Mc Call, M.F. Millea, A.H. Silver et al., The super Schottky microwave mixer, IEEE Transactions on Magnetics, vol. MAG-13, no. 1, 1977, pp.221-227.

[5] V.G. Alekseeva, T.M. Lifshits, E.G. Chirkova, A.Ia. Shul'man, $Bi_{1-x}Sb_x$ is a new semiconductor material, Radio technics and Electronics (in Russian), vol. 23, no. 9, 1978, pp.1926-1938.

[6] V.A. Kulikov, L.V. Matveets, A.Iu. Serebryakov et al,. The detecting properties of the superconducting thin film micro bridges from $YBa_2Cu_3O_{7-x}$, Pis'ma v JTF (Letters in Journal of Technical Physics – in Russian), vol. 15, no. 20, 1989, pp. 74-77.

[7] L.S. Kuz`min, V. N. Ohrimenko, E. S. Soldatov, A. N. Tavhelidze, The detecting properties of the YBaCuO films micro bridges. (1990) Sverhprovodimost` (Superconductivity– in Russian), vol. 3, no.11, 1990, pp. 2650-2660.

[8] Ia.I. Kerner, HTSC-Si and HTSC-InSb contacts for diode detectors: comparison of characteristics. Moldavian Journal of the Physical Sciences, vol. 5, no. 3-4, 2006, pp. 360-365.

[9] D.V. Gitsu, I.M. Holban, V.G. Kantser, F.M. Munteanu, Transport phenomena in bismuth and its alloys (in Russian), Kishinev, Stiinta,1983.

[10] Ch. Kittel, Introduction to Solid State Physics (in Russian), M., Nauka, 1978.

[11] Tables of the physical values. Reference book (in Russian), Edited by academician I.K. Kikoin, M., Atomizdat,1976.

[12] Ia.I. Kerner, Contacts of HTSC with different semiconductors for diode detectors: comparison of characteristics, Proceeding of the 3-rd Internatinal Conference "Telecommunications,Electronics and Informatics", Chişinău, Moldova, May 20-23, 2010, vol. 1, Chişinău, UTM, 2010, pp. 268-273.

Optical Properties of Amorphous As-Se Thin Films

D.V.HAREA, M.S.IOVU, V.G.BENEA, E.P.COLOMEICO, I.A.COJOCARU
Institute of Applied Physics, Academy of Sciences of Moldova,
dyanaharea@yahoo.com

***Abstract* – Photostructural transformations in amorphous films of chalcogenide glasses (ChG) under light irradiation present scientific and practical interests. From scientific point of view, because the composition of ChG determine the kind of structural units and the mean coordination number, in the present work the amorphous films of the chalcogenide systems $As_{100-x}Se_x$ (x=40÷98) and $As_{40}Se_{60}$:Sn_y (y=0÷10.0 at.% Sn) were studied. The experimental investigation of the transmission spectra, photodarkening relaxation and holographic characteristics of the amorphous films under study, including the thickness dependence are presented. The dependences of the refractive index under light irradiation and heat treatment were revealed. It was established that the more sensitive to light irradiation are the amorphous films of $As_{60}Se_{40}$ and $As_{50}Se_{50}$, which exhibit big modifications of the refractive index (** $(\Delta n/n) = 0.394$ **)**

Keywords –: **Amorphous chalcogenide films, optical absorbtion, refractive index, photoinduced phenomena**

I. INTRODUCTION

Optical properties and photoinduced phenomena in chalcogenide glasses are very attractive for many applications in photonics and optoelectronics (inorganic photoresists, registration media for optical and holographic information, passive and active elements for integrated optics, all-optical switching, imaging devices, vapor sensors, etc.) [1-3]. The arsenic selenide amorphous films usually became darkened under action of light from the region of fundamental optical absorption $h\nu \geq E_g$ and so-called photodarkening effect takes place. Increasing of the optical absorption is accompanied by the red shift of the absorption edge and increasing of the refractive index. In this paper the effect of the composition in the glassy systems $As_{100-x}Se_x$ (x=40÷98) and $As_{40}Se_{60}$:Sn_y (y=0÷10.0 at.% Sn) on the optical properties and on the degree of photostructural transformations are presented. The kinetics of photodarkening and the dynamics of optical registration process of micro-holograms in α-$As_{100-x}Se_x$ thin films also were investigated. On the base of the observed changes of the refractive index in both $As_{100-x}Se_x$ and $As_{40}Se_{60}$:Sn glassy systems was established the higher sensitive to light exposure compounds. It was shown that the more sensitive to photostructural transformations under light exposure are the non-stoichiometric $As_{50}Se_{50}$ and $As_{60}Se_{40}$ amorphous films, and decrease with increasing of Se content in the $As_{100-x}Se_x$ glasses.

II. EXPERIMENTAL

The glasses $As_{100-x}Se_x$ (x=40÷98) and $As_{40}Se_{60}$:Sn_y (y=0÷10.0 at.% Sn) were synthesized from the elements of 6N (As, Se, Sn) purity by conventional melting technique. The amorphous $As_{100-x}Se_x$ and $As_{40}Se_{60}$:Sn_y thin films of different thickness (L=0.2÷5.0 μm) were prepared by "flash" thermal evaporation in vacuum onto the glass substrates kept at T_{subs}=100 °C.

To initiate photostructural transformations in thin film samples a continuous He-Ne lasers (λ=630 nm, P=0.6 mW and λ=*540* nm, P=0.75 mW) were used as a source of light exposure. The experimental set-up included a laser, a digital build-in *PC*-card *PCI-1713A* for data acquisition connected with the *Si*-photodetector. Special software was elaborated for automatic measurements.

III. RESULTS AND DISCUSSION

The optical transmission spectra for amorphous As_xSe_{100-x} (L~1,3 μm) was investigated at room temperature (as-deposited, heat treated in vacuum at T_{treat}=120 °C during 1 hour and exposed with light E=50000 Lx during 1 hour). Increasing of the As content $As_{100-x}Se_x$ system shift the absorption edge in the red region of the spectra. The band gap value for amorphous $As_{40}Se_{60}$ thin films, determined from the absorption spectra is E_g=1.82 eV. This is in good agreement with the experimental data presented in [4], according which the optical band-gap values decrease from E_g=1,95 eV for As_8Se_{92} up to E_g=1,83 eV for $As_{36}Se_{64}$.

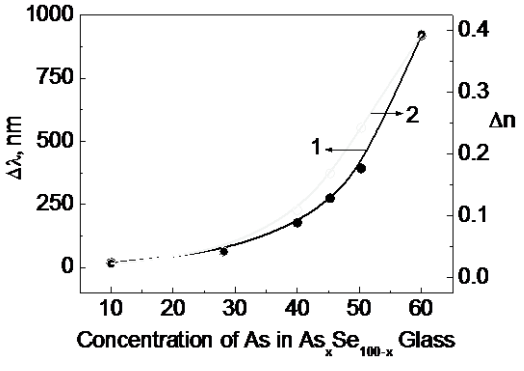

Fig.1. The shift of the absorption edge ($\Delta\lambda$, curve 1) and the degree of modification of the refractive index (Δn, curve 2) under the light irradiation for different film composition of the glassy system $As_{100-x}Se_x$.

The displacement of the absorption edge under light exposure and heat treatment for all amorphous $As_{100-x}Se_x$ films is accompanied by the respective modifications of the refractive index n. For calculation of the optical constants

the Programme ***PARAV-V1.0*** was used [5]. The degree of the displacement of the absorption edge in the red region depends on the composition of the amorphous film, intensity and time of exposure, and heat treatment. Influence of the light exposure at the level of transmission T=20 % is manifested by the shift of the absorption edge $\Delta\lambda$=920 nm which correspond to the amorphous $As_{60}Se_{40}$, and decrease with increasing of Se content up to $\Delta\lambda$=2÷5 nm for As_5Se_{95} and $As_{10}Se_{90}$ (Fig.1).

Increasing of Sn concentration in amorphous $As_{40}Se_{60}$ thin films shifts the absorption edge in the red region of the spectra. Concentration of Sn in amorphous $As_{40}Se_{60}$ thin films increases the refractive index n (Fig.2).

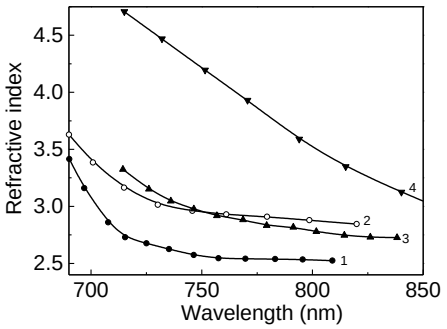

Fig.2. Dispersive curves of the refractive index n for amorphous $As_{40}Se_{60}$ (1), $As_{40}Se_{60}$:$Sn_{0.5}$ (2), $As_{40}Se_{60}$:$Sn_{1.0}$ (3), and $As_{40}Se_{60}$:$Sn_{2.0}$ (4) thin films.

For x=2.0 at. % of Sn the refractive index n=3.5 at λ=800 nm. Fig.3 represents the influence the light exposure and heat treatment on the degree of modification of the refractive index n for amorphous $As_{40}Se_{60}$:$Sn_{1.0}$ thin films. In these cases, the light exposure as well as the heat treatment increases the refractive index n.

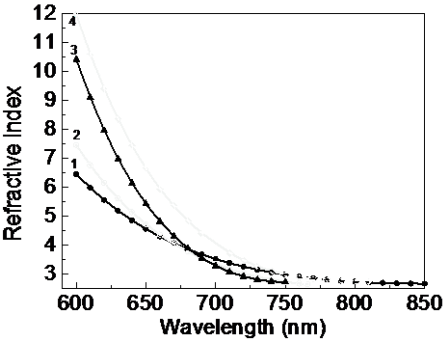

Fig.3. Dispersive curves of the refractive index n for amorphous $As_{40}Se_{60}$:$Sn_{1.0}$ thin films: 1 – as-deposited, 2 – as-deposited and light exposed, 3 – heat treated, 4 – heat treated and exposed.

Fig.4 shows the dependence of the refractive index n on Sn concentration in as-deposited amorphous $As_{40}Se_{60}$:Sn_x thin films calculated at different wavelengths λ.

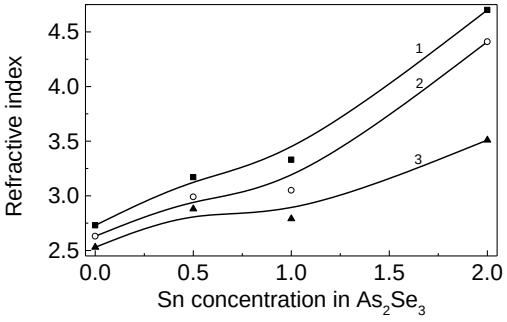

Fig.4. Dependence of the refractive index n vs. Sn concentration in as-deposited amorphous $As_{40}Se_{60}$:Sn_y thin films calculated at different wavelengths λ, nm:

1 – 715, 2 – 735, 3 – 800.

Photodarkening relaxation was measured during illumination for as-deposited amorphous $As_{100-x}Se_x$ (x=40÷98). The relaxation of the relative optical transmission $T(t)/T(0)$ of the amorphous $As_{100-x}Se_x$ films is shown in Fig.5. Increasing of Se in the $As_{100-x}Se_x$ system suppressed the photodarkening effect and x=72÷98 is absent or is very small. The relaxation of photodarckening is described by the stretched exponential function $T(t)/T(0)=A_0+Aexp[-(t-t_0)/\tau]^{(1-\alpha)}$. Here t is the exposure time, τ is the apparent time constant, A characterizes the exponent amplitude, t_0 and A_0 are the initial co-ordinates, and α is the dispersion parameter ($0<\alpha<1$).

The dependence of the relaxation time τ and of the dispersion parameter α for as-deposited (UN) and annealed (AN) films is shown in Fig.6. The dispersion parameter α is close to α =0.3 for almost all UN $As_{100-x}Se_x$ (x=40÷60), and non-monotonously is changed with composition.

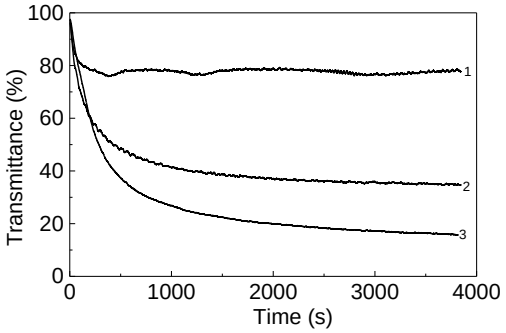

Fig.5. Photodarkening kinetics (T/T_0) of as-deposited amorphous $As_{28}Se_{72}$ (1), $As_{40}Se_{60}$ (2), and $As_{50}Se_{50}$ (3) films vs. exposure time t. Excitation wavelength λ_{exc}=0.63 μm.

In our experimental conditions, for the AN films the lower value of the dispersion parameter $\alpha\approx0.3$ is for the $As_{45}Se_{55}$ composition and increase up to $\alpha\approx0.6\div0.65$ for the $As_{40}Se_{60}$ and $As_{60}Se_{40}$. Such behaviour of the dispersion parameter α with composition may be associated with the structure of the investigated glasses. According to [6], for the glassy system $As_{100-x}Se_x$ the composition x=0.45 took the maximum value of the glass transition temperature T_g.

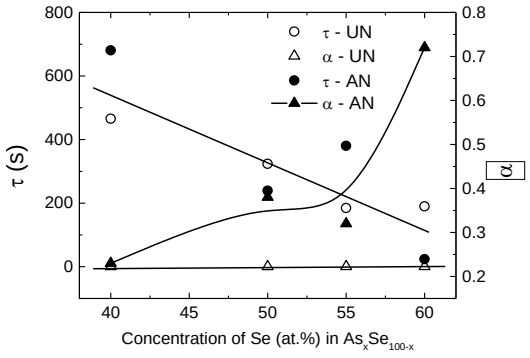

Fig.6. The dependence of the parameters τ and α of the stretched exponential for the as-deposited (UN) and annealed (AN) amorphous $As_{100-x}Se_x$ thin films.

The relaxation of the relative optical transmission *T(t)/T(0)* of the amorphous $As_{60}Se_{40}$ films of different thickness is shown in Fig.7. The experimental data show that for the thicker films the photodarkening is stronger, and almost is absent for the films with thickness about $L \leq 0.2$-0.3 μm. The influence of the thickness on the photodarkening effect also was demonstrated for the amorphous As_2S_3 and As_2Se_3 films [7], and for As_2Se_3 pure and doped with Dy and Pr films [8]. Fig.9 shows the kinetics of growth of the diffraction efficiency for amorphous $As_{100-x}Se_x$ thin films during exposure as result of interference of two He-Ne laser beams (λ=0.63 μm) with a power of W=30 mW. The intensity of the first interference maximum was recorded in the transmittance mode.

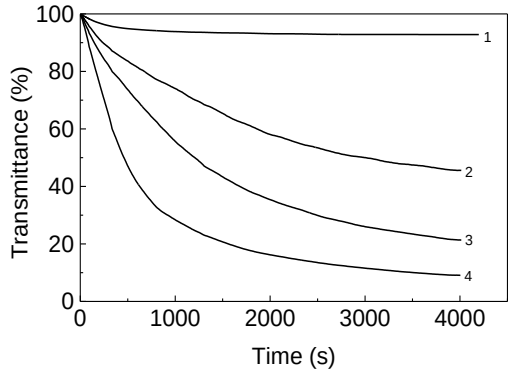

Fig.8. The dependence of transmission versus exposure time for amorphous $As_{60}Se_{40}$ films of different thickness L, μm 1-0.27; 2-0.69, 3-2.04, 4-4.07.

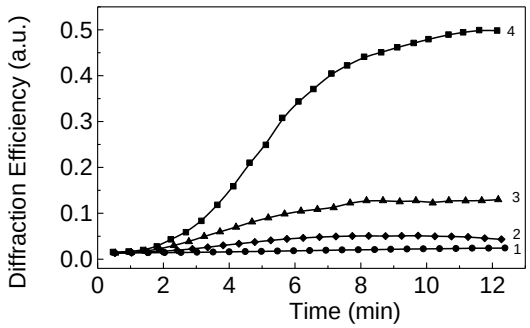

Fig.9. The kinetics of growth of the diffraction efficiency vs. exposure time for amorphous $As_{40}Se_{60}$ (curve 1), $As_{45}Se_{55}$ (curve 2), $As_{50}Se_{50}$ (curve 3), and $As_{60}Se_{40}$ (curve 4) thin films.

The maximum of the diffraction efficiency is reached at 10-15 min of the exposure and after that for the compositions richer in Se the saturation take place. For the compositions richer in As atoms the kinetics of the diffraction efficiency represents a curve with maximum or a sinusoidal (not shown in the Fig.9).

Prolonged time exposure decreases the diffraction efficiency after the maximum. At the same time we have demonstrated that doping of amorphous $As_{40}Se_{60}$ doped with Sn allow to rich saturation on the curve of growth of the diffraction efficiency in dependence with the exposure dose [9]. This effect we have explained by the specific of structure of the tin doped films.

The holographic sensitivity of the amorphous films and the diffraction efficiency of the hologram have decreases with increasing of the selenium content in $As_{100-x}Se_x$ glassy system (Fig.10, curve 1).

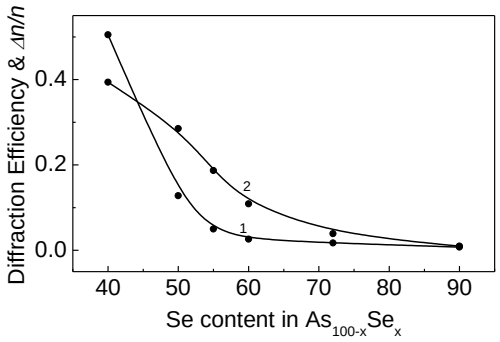

Fig.10. The dependence of the diffraction efficiency (curve 1) and the degree of modification of the refractive index $\Delta n/n$ (curve 2) vs. Se concentration in the $As_{100-x}Se_x$ glassy system.

The measured value of the diffraction efficiency for different amorphous films of the $As_{100-x}Se_x$ glassy system are in good correlation with the degree of modifications of the refractive index $\Delta n/n$ under the light exposure (Fig.10, curve 2).

The thickness dependence of the diffraction efficiency for amorphous $As_{60}Se_{40}$ films also was investigated. Increasing of thickness from L=0.27 μm up to L=4.07 μm also lead to rising of diffraction efficiency with decreasing of the recording time.

IV. CONCLUSION

Photostructural transformations in amorphous $As_{100-x}Se_x$ (x=40÷98) and $As_{40}Se_{60}$:Sn_y (y=0÷5.0 at.% Sn) films were investigated. The changes of the refractive index under light irradiation and heat treatment calculated from the transmission spectra exhibits composition dependence due to the difference of the existing structural units. The more sensitive to light irradiation are the amorphous films of $As_{60}Se_{40}$ and $As_{50}Se_{50}$, which exhibit big modifications of the refractive index ($(\Delta n/n) = 0.394$) and high holographic parameters. Metal impurities effectively reduce the photodarkening, and the degree of reduction becomes stronger as the impurity concentration is increased. Changes in the optical transmission of the investigated amorphous films under illumination may be described by a stretched exponential with the dispersive parameter $0.4 \leq \alpha \leq 1.0$.

The composition dependence of the transmission spectra, photodarkening characteristics, and kinetics of recording

process of holographic information in the films of the glassy system $As_{100-x}Se_x$ (x=40÷98) was investigated. It was established, that the higher sensitivity to light exposure exhibit the non-stoichiometric $As_{50}Se_{50,}$ $As_{55}Se_{45}$, and $As_{60}Se_{40}$ amorphous films, and decrease with increasing of Se content in the $As_{100-x}Se_x$ glass. The experimental results are interpreted in terms of structural optical polymerization process, which includes the transformation of As_4Se_4 and Se_2 structural units in homogenius $AsSe_{3/2}$ network.

The photodarkening phenomenon in chalcogenide glass films under illumination has no plain explanation up to now in spite of detailed investigation and a series of models advanced for interpretation of it. The red shift of the absorption edge indicating the narrowing of the optical gap of the film at photodarkening, is believed to be due to broadening of the valence band, the top of which is formed mainly by states of lone-pare electrons of the chalcogen atom. According to the model for photodarkening in a-$As_2Se(S)_3$ [10], the photoexcited charge carriers in extended states are considered as responsible for photodarkening. Unlike to the previous conceptions this takes into account the layered cluster structure of a chalcogenide glass. During exposure the layer is negatively charged due to capture of photoexcited electrons, and repulsive forces are built between the layers. These forces cause enlargement of the interlayer distance (leading to photoexpansion) and slip motion along the layers. This latter process alters interaction of lone-pair electrons between the layers leading to photodarkening effect.

AKNOWLEDGEMENTS

For calculation of the optical constants the Programme ***PARAV-V1.0*** was used (www.chalcogenide.eu.org).

REFERENCES

[1] M.Popescu, A.Andriesh, V.Chiumach, M.Iovu, S.Shutov, and D.Tsiuleanu. The Physics of Chalcogenide Glasses, Ed. Stiintifica Bucharest - I.E.P.Stiinta, Chisinau, 1996 (In Romanian).

[2] A.Kovalskiy. M.Vlcek, H.Jain, A.Fiserova, C.M.Waits, J. of Non-Cryst. Solids **352**, 589 (2006).

[3] Mihail Iovu & Maria Iovu, Chalcogenide glass photonic devices, In: Proceedings of 33 American Romanian Academy of Sciences and Arts, 02-07 June 2009, Sibiu, Romania.

[4] P.Nagels, Romanian Reports in Physics **51**, 209 (1999).

[5] A.Ganjoo, R.Golovchak, J. of Optoelectronics and Advanced Materials **10**, 1328 (2008).

[6] S.Mamedov, D.G.Georgiev, Tao Qu, P.Boolchand, J. of Phys.: Condens. Matter **15**, 2397 (2003).

[7] K.Hayashi, N.J.Mitsuishi, J. of Non-Cryst. Solids **299&302**, 949 (2002).

[8] M.S.Iovu, S.D.Shutov, P.Boolchand, E.P.Colomeico, V.G.Ciorba, S.M.Iovu, M.Popescu, J. of Optoel. and Adv. Materials **4**, 857 (2002).

[9] A.I.Buzdugan, M.S.Iovu, A.A.Popescu, P.G.Cherbari, Balkan Phys. Letters **1**, 7 (1993).

[10] A. Ganjoo, N. Yoshida and K.Shimakawa. Recent Research Developments in Applied Physics, ed. M.Kawasaki, N. Ashgritz and R. Anthony (Research Signpost, Trivandrum, **2**, 129 (1999).

Morphology and Luminescence Properties of ZnO layers produced by Magnetron Spattering

Emil RUSU[1], Irina GHIŢU[1], Vladimir PRILEPOV[2], Victor ZALAMAI[3], Veaceslav URSAKI[3]
[1]*Institute of Electronic Engineering and Nanotechnologies, Academy of Sciences of Moldova, Academy str. 3/3, Chisinau MD-2028, Republic of Moldova, e-mail: rusue@lises.asm.md*
[2]*State University of Moldova, Mateevici str. 60, Chisinau MD-2009, Moldova*
[3]*Institute of Applied Physics of the Academy of Sciences of Moldova, Academy str. 5, Chisinau MD-2028, Moldova*

***Abstract* – We show that the morphology and the luminescence properties of ZnO layers produced by magnetron sputtering can be controlled by technological parameters of sputtering, particularly by the ratio of argon to oxygen gases in the gas flow during the growth process. Smooth and flat layers were produced with a high Ar/O ratio, while porous layers with various morphologies were obtained with a low Ar/O ratio. The layers produced with O/Ar ration equal to 10 exhibit extremely high near-bandgap luminescence intensity even higher in comparison with bulk ZnO single crystals. The free carrier density estimated from the analysis of photoluminescence spectra is also very high in these samples suggesting that these technological conditions promote both optical and electrical activation of the doping Al impurity. The samples grown with high Ar/O ratios exhibit strong visible emission which is controlled by the technological conditions.**

***Index Terms* – ZnO, magnetron sputtering, morphology, luminescence, excitonic emission, deep centers.**

I. INTRODUCTION

ZnO demonstrates increasing fundamental interest and technological applications due to its wide and direct band gap (3.37 eV at room temperature), large exciton binding energy (60 meV), large bond strength (with a cohesive energy of 1.89 eV), and large mechanical stability (with a melting point of about 2200 K) [1], it being of a particular interest for optoelectronic and photonic devices [2-4].

In recent years, with the development of different growth techniques, gallium nitride (GaN) has become the most important building block for LEDs operating in the green to ultraviolet light range [5-7]. ZnO and GaN are analogous materials with many similar properties. ZnO has an advantage over GaN, due to the availability of high quality ZnO substrates, while there is a lack of GaN substrates. This makes possible the preparation of ZnO based homojunction in addition to heterojunctions.

A multitude of synthesis methods, such as various wet chemical methods [8-12], sol-gel methods [13,14], metal organic chemical vapour deposition (MOCVD) [15-17], molecular beam epitaxy (MBE) [18,19], electrochemical deposition [20-22], metal-catalyzed vapour-liquid-solid (VLS) growth [3,23], and thermal chemical vapour transport and condensation method without metal catalysts [24-28] have been employed for the fabrication of ZnO layers.

Such methods as chemical, electrochemical, sol-gel, VLS, and chemical vapour transport and condensation growth are cost effective. However, they basically lead to the production of nanostructured layers, such as wires, rods, ribbons, belts, tubes, discs, tetrapods, combs, rings, springs, propeller arrays, etc, it being hard to produce smooth and flat layers with these techniques. Smooth and flat films are highly desired in homojunction and heterojunctions. Smooth surfaces can be obtained with MOCVD and MBE methods. However, these technologies are quite expensive. Magnetron sputtering is a technique which allows one to produce both nanostructured and flat layers, in being at the same time less expensive than MOCVD and MBE technologies.

In this work, we investigate the morphology and the photoluminescence (PL) properties of ZnO layers produced by magnetron stuttering in order to establish their dependence upon the technological conditions of growth.

II. SAMPLE PREPARATION AND EXPERIMENTAL DETAILS

Magnetron sputtering of ZnO films was performed in an installation assembled on the basis of a VUP-5 instrument. A control sample was placed in the stuttering chamber near the Si, SiO_2/Si, or ITO-on-glass basic support for monitoring the deposition process via measuring the resistivity of the layer deposited on the control sample. A 99,99 % purity Zn plate with a diameter of 40 mm and thickness of 5 mm doped with 2% wt of Al was used as target. The temperature of both the control and the basic supports was maintained at a temperature from the interval 200 – 220 ^{o}C, while the magnetron power was W=360 V x 100 mA. The Si support was treated in a 30% $Na_2S_2O_3x5H_2O$ solution before the sputtering process for improving the adhesion of the deposited ZnO layer.

A mixture of Ar+O was used as working gas. The ratio of Ar/O in the gas flow was changed and air was introduced in the grouth chamber for a certain period of time during the sputtering process in order to controll morphology and the raditive properties of the deposted ZnO film. The samples were annealed in air during 30 min at 450 ^{o}C after the deposition process.

A VEGA TESCAN TS 5130 MM scanning electron microscope (SEM) was used for morphological characterization of the samples.

Photoluminescence was excited by 325 nm line of a He-Cd Melles Griot laser and was analyzed through a double

spectrometer at low temperature (10 K). The resolution was better than 0.5 meV. The samples were mounted on the cold station of a LTS-22-C-330 cryostat.

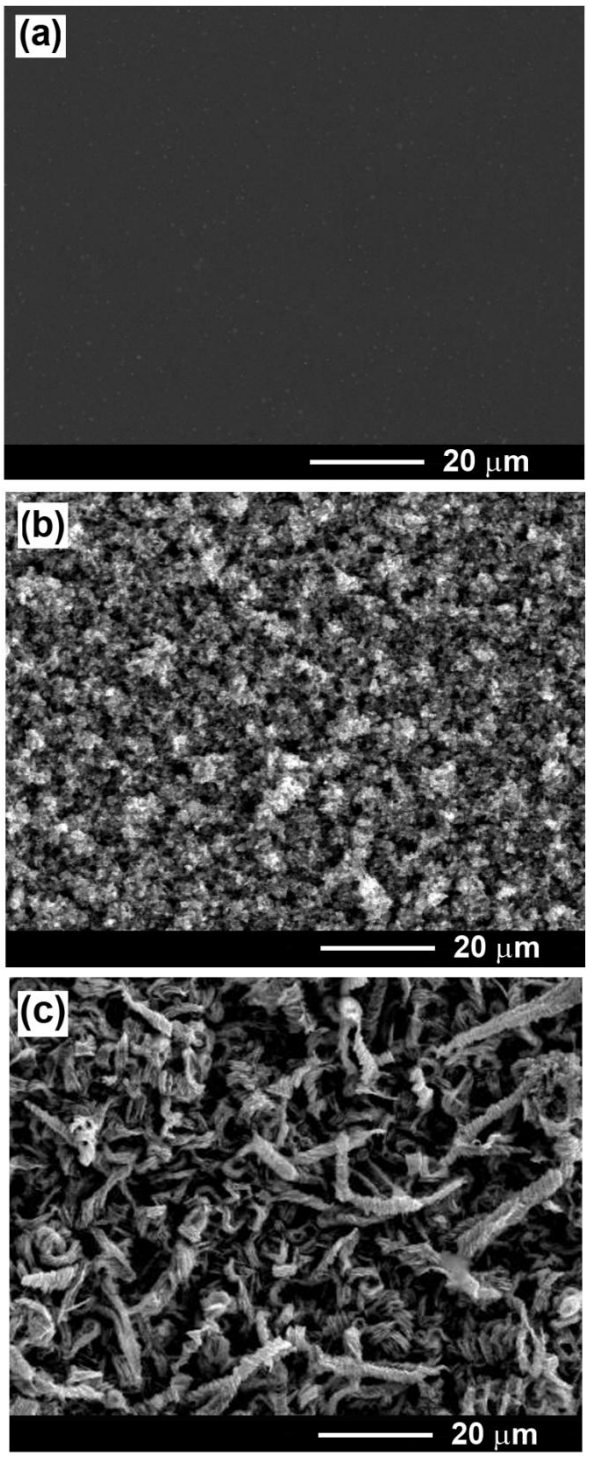

Fig. 1. SEM image of ZnO layers produced by magnetron sputtering in processes with different ratio of argon to oxygen gases in the gas flow during the growth process as follows: Ar:O = 10:1 (a); Ar:O = 1:1 (b); Ar:O = 1:10 (c).

III. RESULTS AND DISCUTIONS

Wide-gap oxide semiconductors are attractive materials as phosphors if they exhibit visible emissions arising from defect levels in the bandgap. Apart from the near-band-edge ultraviolet emission at approximately 380 nm, ZnO is also known to exhibit a complex luminescence behavior in the visible wavelength region [29,30]. Visible deep-level emissions can be observed with a peak position varying in a wide wavelength range from 450 to 830 nm.

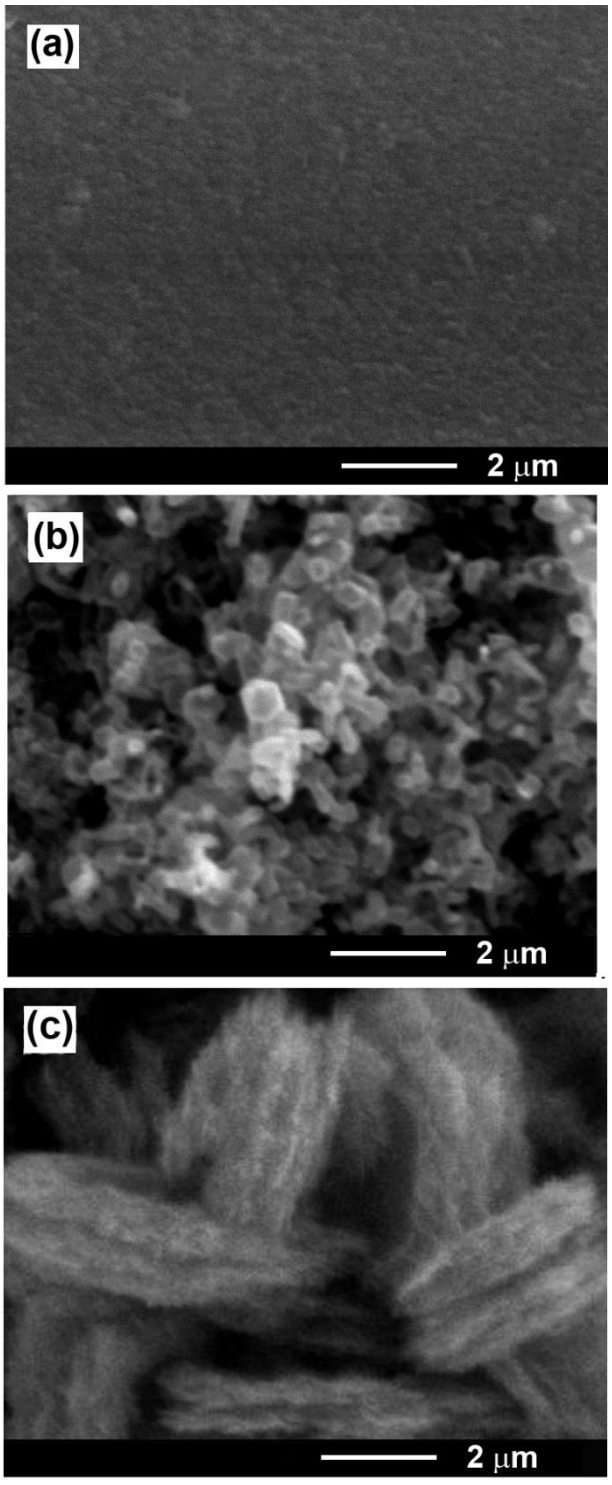

Fig. 2. Enlarged SEM view of ZnO layers produced by magnetron sputtering in processes with different ratio of argon to oxygen gases in the gas flow during the growth process as follows: Ar:O = 10:1 (a); Ar:O = 1:1 (b); Ar:O = 1:10 (c).

Since the defect-related emissions are known to be sensitive to technological conditions of sample preparation, one can expect that the luminescence spectrum from ZnO samples in the visible range as well as the morphology of layers can be controlled by the technological parameters of magnetron sputtering.

The investigation of the morphology as well as the radiative properties of ZnO layers grown by magnetron

sputtering demonstrated that they are determined by the technological conditions such as the pressure of gases in the growth chamber, the concentration of oxygen, as well as by the substrate used. It was found that the introduction of air in the grouth chamber for a period of time longer than 30 min during the sputtering process leads to the oxidation of the target. This oxidation, in turn, affects the magnetron power and creates instabilities in plasma maitaining. The velosity of gas flows into the chamber is set to a value assuring the maintainance of a constant pressure, and therefore a stability of the created plasma.

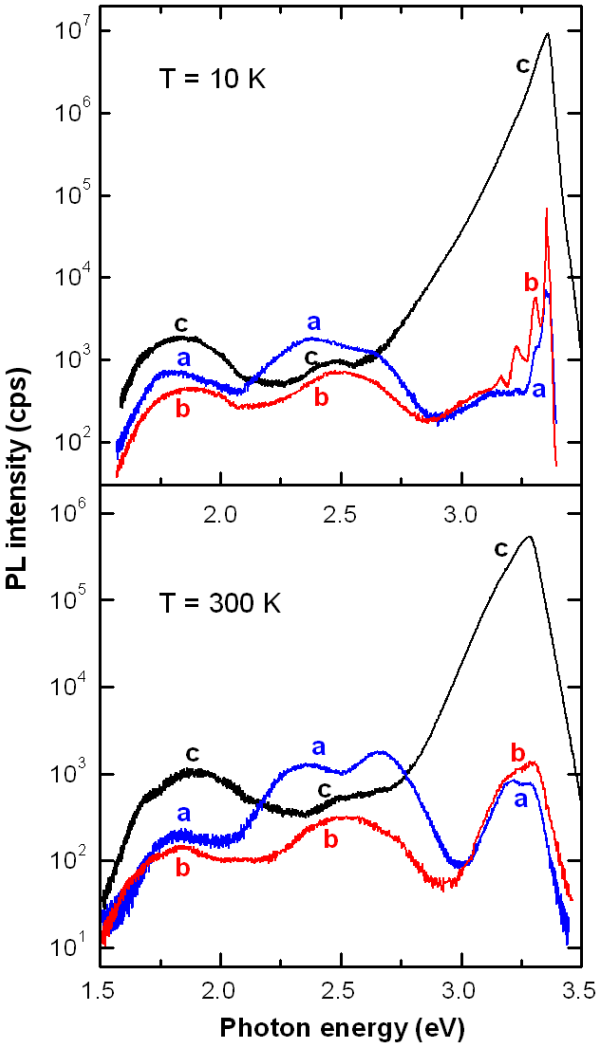

Fig. 3. PL spectra of ZnO layers produced by magnetron sputtering in processes with different ratio of argon to oxygen gases in the gas flow during the growth process as follows: Ar:O = 10:1 (a); Ar:O = 1:1 (b); Ar:O = 1:10 (c). The samples were annealed in air during 30 min at 450 °C after the deposition process

The morphology of the produced ZnO layers was found to be determined first of all by the ratio of argon to oxygen gases in the gas flow during the growth process. High values of the Ar/O ratio result in the production of smooth and flat ZnO films with the morphology illustrated in Fig. 1a for a film produced with the Ar/O ratio equal to 10. The increase of the oxygen content into the gas flow leads to the production of porous layers as shown in Fig. 1b and 1c. When the Ar:O ratio is 1:1, the obtained ZnO layer consists of microcrystallites as shown in Fig. 1b. The size of these crystallites determined from the enlarged view presented in Fig. 2b is around 200 – 500 nm. Further increase of the oxygen content leads to the creation of spectacularly twisted microstructures (Fig. 1c) which prove to be porous at a more accurate analysis (Fig. 2c). The length of the microstructures produced with an Ar:O ratio of 1:10 on an ITO-on-glass substrate vary in the range of 4 to 20 μm with a diameter of 1 – 4 μm.

Apart from morphology, the ratio of argon to oxygen gases in the gas flow during the growth process strongly influences the radiative properties of the produced ZnO layers. The smooth films produced with a high Ar/O ratio exhibit weak luminescence suggesting an amorphous nature of the film. Annealing of samples in air during 30 min at 450 °C after the deposition process leads to increasing luminescene intensity due to the crystalization [curve (a) in Fig. 3].

Several visible PL bands are observed in the luminescence spectrum in addition to the near band-edge emission. The visible emission from the sample produced with the Ar/O ratio equal to 10 (Fig. 3) consists of three bands located around 1.85 eV, 2.37 eV, and 2.67 eV at both 10 K and room temperature. The near-band-edge luminescence at 10 K is dominated by two bands at 3.61 and 3.71 eV related to the recombination of donor bound excitons (D^0X) (Fig. 4).

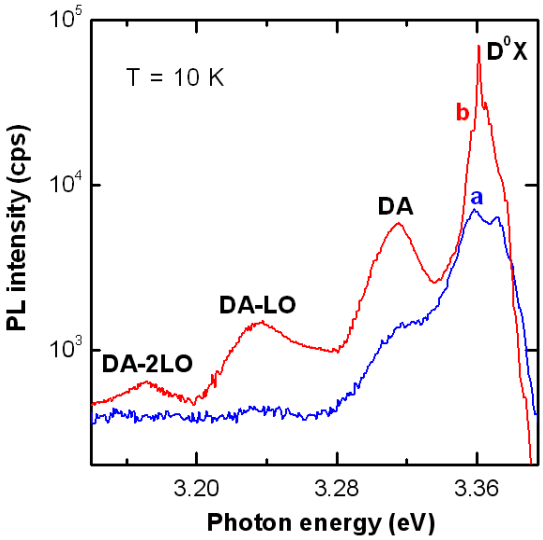

Fig. 4. Near band-edge PL spectra of the samples (a) and (b).

The D^0X bands at 3.61 eV and 3.71 eV correspond to the previously observed I_1 and I_6 bands, the I_6 band being associated with the Al impurity [31]. Apart from the D^0X bands, a PL band is observed at 3.314 eV accompanied by LO phonon replicas, it being previously attributed to the donor-acceptor pair recombination (DA) [32]. At room temperature, the near-band-edge luminescence represents a band due to the recombination of free excitons at 3.30 eV with a LO phonon replica.

As concerns the visible luminescence, taking into account the n-type of the produced material, one can suggest that assignment of these PL bands to the electron transitions from a deep donor level to the valence band (*D-h*-type recombination) is very improbable [33]. Most probably, these PL bands are due to electronic transitions from the conduction band to acceptor levels (*e-A*-type recombination). The red band at 1.85 eV is supposed to be associated with a deep unidentified acceptor with the energy level situated close to the middle of the bandgap [34]. The PL bands in the spectral interval of 2.3 – 2.7 eV are most

probably due to different defect complexes involving the V_{Zn} acceptor center. The isolated zinc vacancy is expected to have charge −2 in *n*-type ZnO where its formation is more favorable. The transition level between the −1 and −2 charge states of V_{Zn} occurs at ~0.8 eV above the valence band [34]. Thus, one may expect transitions from the conduction band to the V_{Zn} acceptor at around 2.6 eV in *n*-type ZnO. Other PL bands observe in this spectral range can be attributed to complex defects involving the V_{Zn} center such as zinc vacancies and zinc antisites (V_{Zn}–Zn_O) [35], zinc vacancies and oxygen vacancies [36,37], or more complex defect clusters [38].

The increase of the oxygen content in the Ar/O ratio to 1:1 leads to the emergence of a PL band centered at 2.50 eV instead of bands at 2.37 eV and 2.67 eV which suggest the reconfiguration of the defect complexes (Fig. 3). Apart from that, the near-band-edge luminescence is intensified by an order of magnitude, the D^0X band related to the Al impurity becoming highly predominant (Fig. 4) suggesting an efficient optical activation of this impurity.

Further increase of the oxygen content leads to a spectacular increase of the near-band-edge luminescence intensity by additional several orders of magnitude with a concomitant broadening of the near-band-edge luminescence band. A characteristic feature of this PL band is the broadening toward the Stokes part of the emission. The width of this PL band is 58 meV at 10 K and 115 meV at room temperature. It was previously shown that most probably this PL band is due to direct transitions of electrons from the conduction band tails to valence band tails [39]. The broadening of the PL band involved can be accounted for by the broadening of the band edges due to potential fluctuations induced by the high concentration of intrinsic defects or impurities. This model has been applied to correlate the width of the PL band to the free carrier concentration in highly doped ZnO samples [39]. By using the established dependence, one can estimate that the electron concentration in the sample produced with the Ar:O ratio of 1:10 is 4.0×10^{19} cm^{-3} at T = 10 K, and 1.5×10^{20} cm^{-3} at room temperature. These data suggest that increasing the oxygen content in the Ar/O ratio during the magnetron sputtering promotes the optical and electrical activation of the doping Al impurity.

IV. CONCLUSION

The results of this study demonstrate that the morphology and the luminescence properties of ZnO layers can be controlled by technological parameters of magnetron sputtering. High values of the ratio of argon to oxygen gases in the gas flow during the growth process lead to the production of smooth and flat layers with nearly identical intensity of the near-band-edge and visible luminescence, while the layers obtained with low values of this ratio are porous and exhibit extremely high near-bandgap luminescence intensity.

ACKNOWLEDGMENTS

This work was supported by the Academy of Sciences of Moldova under Contract No. 10.820.05.20/RoF.

REFERENCES

[1] S. Tuzemen, E. Gur, "Principal issues in producing new ultraviolet light emitters based on transparent semiconductor zinc oxide", Opt. Mater., vol. 30, pp. 292-310, 2007.

[2] S. Choopun, H, Tabata, K. Kawai, "Self-assembly ZnO nanorods by pulsed laser deposition under argon atmosphere", J. Cryst. Growth, vol. 274, pp. 167-172, 2005.

[3] M. Huang, S. Mao, H. Feick, H. Yan, Y. Wu, H. Kind, E. Weber, R. Russo, P. Yang, "Room-Temperature Ultraviolet Nanowire Nanolasers", Science, vol. 292, pp. 1897-1899, 2001.

[4] R. Hauschild, H. Kalt, "Guided modes in ZnO nanorods", Appl. Phys. Lett. 89, pp. 123107, 2006.

[5] Y. Y. Naoi, K. Ikeda, T. Hama, K. Ono, R. Choi, T. Fukumoto, K. Nishino, S. Sakai, S. M. Lee, M. Koike, "Blue light emitting diode fabricated on a-plane GaN film over r-sapphire substrate and on a-plane bulk GaN substrate", Phys. Status Solidi c, vol. 4, pp. 2810–2813, 2007.

[6] Z. Zhong, F. Qian , D. Wang, C. M. Lieber, "Synthesis of p-Type Gallium Nitride Nanowires for Electronic and Photonic Nanodevices", Nano Lett., vol. 3, pp. 343-346, 2003.

[7] F. A. Ponce, D. P. Bour, "Nitride-based semiconductors for blue and green light-emitting devices", Nature, vol. 386, pp. 351-359, 1997.

[8] J. Zhang, L. D. Sun, J. L. Yin, H. L. Su, C. S. Liao, C. H. Yan, "Control of ZnO Morphology via a Simple Solution Route", Chem. Mater., vol. 14, pp. 4172-4177, 2002.

[9] B. Liu B. H. C. Zeng, „Hydrothermal Synthesis of ZnO Nanorods in the Diameter Regime of 50 nm", J. Am. Chem. Soc., vol. 125, pp. 4430-4431, 2003.

[10] H. L. Cao, X. F. Qian, Q. Gong, W. M. Du, X. D. Ma, Z. K. Zhu, "Shape- and size-controlled synthesis of nanometre ZnO from a simple solution route at room temperature", Nanotechnology, vol. 17, pp. 3632-2636, 2006.

[11] S. T. Shishiyanu, O. I. Lupan, E. V. Monaico, V. V. Ursaki, T. S. Shishiyanu, I. M. Tiginyanu, "Photoluminescence of chemical bath deposited ZnO:Al films treated by rapid thermal annealing", Thin Solid Films, vol. 488, pp. 15-19, 2005.

[12] V.V. Ursaki, O.I. Lupan, L. Chow, I.M. Tiginyanu, V.V. Zalamai, "Rapid thermal annealing induced change of the mechanism of multiphonon resonant Raman scattering from ZnO nanorods", Solid State Communications, vol. 143, pp. 437-441, 2007.

[13] G. Westin, A. Ekstrand, M. Nygren, R. Österlund, P. Merkelbach, "Preparation of ZnO-based varistors by the sol–gel technique", J. Mater. Chem., vol. 4, pp. 615-621, 1994.

[14] S.-Y. Chu, T.-M. Yan, S.-L. Chen, "Characteristics of sol-gel synthesis of ZnO-based powders", J. Mater. Sci. Lett., vol. 19, pp. 349-352, 2000.

[15] W. I. Park, D. H. Kim, S. W. Jung, G. C. Yi, "Metalorganic vapor-phase epitaxial growth of vertically well-aligned ZnO nanorods", Appl. Phys. Lett., vol. 80, pp. 4232-4235, 2002.

[16] Y. J. Zeng, Z. Z. Z. Ye, W. Z. Xu, L. P. Zhu, B. H. Zhao, "Well-aligned ZnO nanowires grown on Si substrate via metal–organic chemical vapor deposition", Appl. Surf. Sci., vol. 250**,** pp. 280-283, 2005.

[17] A. Burlacu, V. V. Ursaki, V. A. Skuratov, D. Lincot, T. Pauporte, E. V. Rusu, I. M. Tiginyanu, "The impact of morphology upon the radiation hardness of ZnO layers", Nanotechnology, vol. 19, 215714, 2008.

[18] El-Shaer, A. Che Mofor, A. Bakin, M. Kreye, A. Waag, "High-quality ZnO layers grown by MBE on sapphire", Superlattices and Microstructures, pp. 265-271, 2005.

[19] H. Kato, M. Sano, K. Miyamoto, T. Yao, B.-P. Zhang, K. Wakatsuki, Y. Segawa, "MBE growth of Zn-polar ZnO on MOCVD-ZnO templates", Phys. Status Solidi (b), vol. 241, pp. 2825–2829, 2004.

[20] T. Pauporté, D. Lincot, "Heteroepitaxial electrodeposition of zinc oxide films on gallium nitride", Appl. Phys. Lett., vol. 75, pp. 3817-3820, 1999.

[21] M. J. Zheng, L. D. Zhang, G. H. Li, W. Z. Shen, "Fabrication and optical properties of large-scale uniform zinc oxide nanowire arrays by one-step electrochemical deposition technique", Chem. Phys. Lett., vol. 363, pp. 123-128, 2002.

[22] O. Lupan, T. Pauporte, B. Viana, I. M. Tiginyanu, V. V. Ursaki, and R. Cortes, Epitaxial Electrodeposition of ZnO Nanowire Arrays on p-GaN for Efficient UV-Light-Emitting Diode Fabrication, ACS J. Appl. Materilas and Interfaces, 2, No. 7, 2083–2090 (2010).

[23] S. Y. Li, C. Y. Lee, T. Y. Tseng, "Copper-catalyzed ZnO nanowires on silicon (1 0 0) grown by vapor–liquid–solid process", J. Cryst. Growth., vol. 247, pp. 357-362, 2003.

[24] P. X. Gao, Z. L. Wang, "Nanoarchitectures of semiconducting and piezoelectric zinc oxide", J. Appl. Phys. 97, 044304, 2005.

[25] F. Xu, K. Yu, G. Li, Q. Li, Z. Zhu, "Synthesis and field emission of four kinds of ZnO nanostructures: nanosleeve-fishes, radial nanowire arrays, nanocombs and nanoflowers", Nanotechnology, vol. 17, 2855-2859, 2006.

[26] C. Li, G. Fang, F. Su, G. Li, X. Wu, X. Zhao, "Synthesis and photoluminescence properties of vertically aligned ZnO nanorod–nanowall junction arrays on a ZnO-coated silicon substrate", Nanotechnology, vol. 17, 3740-3744, 2006.

[27] Y. H. Yang, B Wang, G. W. Yang, "Growth mechanisms of one-dimensional zinc oxide hierarchical structures", Nanotechnology, vol. 17, 5556-5560, 2006.

[28] V. V. Ursaki, E. V. Rusu, A. Sarua, M. Kuball, G. I. Stratan, A. Burlacu, I. M. Tiginyanu, "Optical characterization of hierachical ZnO structures grown with a simplified vapour transport method", Nanotechnology, vol. 18, 215705 (2007).

[30] K. Vanheusden, C. H. Seager, W. L. Warren, D. R. Tallant, J. A. Voigt, "Correlation between photoluminescence and oxygen vacancies in ZnO phosphors "Appl. Phys. Lett., vol. 68, pp. 403-405, 1996.

[31] R. M. Nyffenegger, B. Craft, M. Shaaban, S. Gorer, G. Erley, R. M. Penner, "A Hybrid Electrochemical/ Chemical Synthesis of Zinc Oxide Nanoparticles and Optically Intrinsic Thin Films", *Chem. Mater.*, vol. 10, pp. 1120-1129,1998.

[32] Meyer B K et al., "Bound exciton and donor–acceptor pair recombinations in ZnO", Phys. Stat. Sol. (b), vol. 241, pp. 231-260, 2004.

[33] V.V. Ursaki, I.M. Tiginyanu, V.V. Zalamai, V.M. Masalov, E.N. Samarov, G.A. Emelcenko, F. Briones, "Photoluminescence of ZnO layers grown on opals by chemical deposition from zinc nitrate solution", Semiconductor Science and Technology, vol. 19, pp. 851-854, 2004.

[34] M. A. Reshchikov, R. Y. Korotkov, "Analysis of the temperature and excitation intensity dependencies of photoluminescence in undoped GaN films", Phys. Rev. B, vol. 64, 115205, 2001.

[35] U. Ozgur, Ya. I. Alivov, C. Liu, A. Teke, M. A. Reshchikov, S. Doğan, V. Avrutin, S.-J. Cho, H. Morkoç, "A comprehensive review of ZnO materials and devices", J. Appl. Phys., vol. 98, 041301, 2005.

[36] Z. Q. Chen, K. Betsuyaku, A. Kawasuso, "Vacancy defects in electron-irradiated ZnO studied by Doppler broadening of annihilation radiation", Phys. Rev., vol. B 77, 113204, 2008.

[37] S. A. Studenikin, M. Cocivera, "Time-resolved luminescence and photoconductivity of polycrystalline ZnO films, J. Appl. Phys., vol. 91, pp. 5060-5064, 2002.

[38] J. Zhong, A. H. Kitai, P. Mascher, W. Puff, "The influence of processing conditions on point defects and luminescence centers in ZnO", J. Electrochem. Soc., vol. 140, pp. 3644-3649, 1993.

[39] Y. Dong, F. Tuomisto, B. G. Svensson, A. Yu. Kuznetsov, L. J. Brillson,"Vacancy defect and defect cluster energetics in ion-implanted ZnO", Phys. Rev. B, vol. 81, 081201(R), 2010.

[40] V.V. Zalamai, V.V. Ursaki, E. Rusu, P. Arabadji, I.M. Tiginyanu, L. Sirbu, "Photoluminescence and resonant Raman scattering in highly conductive ZnO layers", Appl. Phys. Lett., vol. 84, pp. 5168-5170, 2004.

Effective Laser Luminescence of Nanocomposites $Eu(TTA)_2(Ph_3PO)_2NO_3$-Polyvinylpyrrolidone

V.I. VERLAN[A], M.S. IOVU[A], S.A. BUZURNIUC[A], Yu.H. NISTOR[A], I. CULEAC[A], C.I. TURTA[B], V.E. ZUBAREVA[B], L.A. MALAHOV[C]

[a] *Institute of Applied Physics, Academy of Sciences of Moldova.*
[b] *Institute of Chemistry of the Academy of Sciences of Moldova*
[c] *Institute of Mathematics of Academy of Sciences of Moldova. vverlan@gmail.com*

***Abstract* –Thin films (1-10 μm thickness) of nanocomposites (NC) based on organic coordinated compound (OCC) $Eu(TTA)_2(Ph_3PO)_2NO_3$ (where *TTA* is thenoyltrifluoroacetonate ($C_8H_5F_3O_2S$), Ph_3PO - triphenylphosphine (C_6H_5PO) and polymer – polyvinylpyrrolidone ($(C_6H_9NO)_n$) (*PVP*)) were obtained by chemical methods and with different molar ratios into organic polymer matrix. NC have been characterized by measurements of optical transmission, excitation spectra of photoluminescence (PL) and photoluminescence of NC at different concentrations of $Eu(TTA)_2(Ph_3PO)_2NO_3$ in NC. In the optical transmission of NC, the characteristic parameters of NC such as threshold absorbance, dependence on the concentration of the organic coordinated compound in NC, etc., have been determined The displacement of threshold absorption to infrared is observed with increasing of the concentration of the coordination material in NC. The excitation spectrum of photoluminescence of NC led the range from 200 to 400 nm energy at which takes place the photoluminescence in NC. The PL of nanocomposites was detected as specific for internal transitions $4f \rightarrow 4f$ of the Eu^{3+} ion $^5D_0 \rightarrow {}^7F_i$ (i = 0,1,2,3 and 4) centred at 537, 578, 615, 632,649, 690 and 705 nm, respectively at T=300 K. The dominant PL is in the position to 615 nm and the halfwidth is less than 10 nm and it is attributed to the transition $^5D_0 \rightarrow {}^7F_2$. The comparison of PL of NC with organic coordinated compounds at equal ultraviolet exciting show the increasing of the external efficiency of NC luminescence. In nanocomposites, the effect of energy transfer from polymer matrix to coordinated molecule with subsequent transfer of them to Eu^{+3} ion have been identified. It was proposed some applications of given nanocomposites in optoelectronics and medicine.**

***Key words* – nanocomposites, rare earth ion, photoluminescence, polymer, energy transfer, laser emission**

I. INTRODUCTION

Nanocomposites (NC) based on polymers and coordinate complex organic compounds of rare earth metals are excellent materials for a new generation of light emitting devices with high efficiency due to strong luminescence, easy colour tuneable, temperature insensitivity, and high stability. Luminous properties of the complex coordinated compounds and nanocomposites on their basis can be a subject of different applications in medicine, solar cells devices on the flexible substrates, optical signal amplification, etc. For the visible spectrum, more frequently are used the compounds with Europium (Eu^{3+}) and Terbium (Tb^{3+}) ions. Improving of their luminescence properties depends on the type of ligands using for surrounding of the rare earth ions. Photoactive complexes of organic compounds of lanthanides may be used, as an example, like the trivalent ion of Europium chelated with β-diketonates, or the cyclic ligands of carboxylate when the coordination number of Eu^{3+} varies in the range from 6 to 9. Future researches should be oriented towards achieving coordinated surrounding of the ion of Eu^{3+} in order to improve luminescence efficiency, and to obtain a final stable compound for various practical applications. The fundamental studies of the spectroscopy photophysic of rare earth metals and applications of the technology connected with effective luminescence with the halfwidth of the luminescence bands less than 10 nm in the visible and near-infrared regions of spectrum at different excitations are of special interest.

Advantage of application of coordinated compounds of rare earth ions with β-diketonates and ligands in nanocomposites is based on the so-called "antenna" effect, or the transfer of excitation energy from outside of the system of Eu^{3+} ion towards their energy levels. The population of upper energy levels with subsequent transition to ground states is increased in this case. The intermolecular energy transfer to the Eu^{3+} ion takes place via the levels of ligands and their surroundings.

In prevous paper we report the investigations of the NC from copolymer butylmetacrylate and styrene in ratio of 1:1 in whose matrix $Eu(TTA)_3H_2O$, $Eu(TTA)_3Phen$ and $Eu(DBM)$3Phen were introduced [1-4]. For all investigated materials with NC, photoluminescence levels caused by $4f \rightarrow 4f$ transitions of *Eu* were identified. The most intensive luminescence band was centered at 615 nm and halfwidth ca 10 nm in all studied cases.

II. METHODOLOGY

The synthesis of organic coordinated compound of bis(thenoyltrifluoroacetonato) bis(triphenyl-phosphine oxide)(mononitrate) europium (III) ($Eu(TTA)_2(Ph_3PO)_2NO_3$) was carried out after the scheme described in [5,6] for analogue compounds. An amount of 4 mmol (0.44 g) of β-diketone and 2 mmol (0.56 g) of neutral ligand were dissolved in 10 ml. of hot 96% ethanol, and 2 ml. of 1N

sodium hydroxide were added. The mixture was stirred, while 1 mmol of Europium nitrate in 5 ml. of water was added dropwise. A type of light cream precipitate formed immediately. The precipitate was filtered off, washed with ethanol, dried thoroughly in air, and the solid of the complex was obtained. Yield was (0.85 g) :

For $C_{52}H_{38}F_6EuNO_9P_2S_2$ calcd, %: C = 51.49; H = 3.16; N = 1.15; S = 5.28.

Found, %: C = 51.49; H = 3.48; N = 0.95; S = 5.14.

The formula of the structure of OCC bis(thenoyltrifluoroacetonato)bis(triphenylphosphine oxide) (mononitrate)Europium(III) $C_{52}H_{38}F_6EuNO_9P_2S_2$ is shown on Fig.1.

Nanocomposites $PVP/Eu(TTA)_2(Ph_3PO)_2NO_3$ were prepared from chemical solutions of separate components by detailed method of preparation which will be described separately later [7]. Polyvinylpyrrolidone $((C_6H_9NO)_n$ was used as the polymer with an average molecular weight 1 300 000 $g \cdot mol^{-1}$, white to light yellow, hygroscopic, amorphous powder (purchased from Aldrich Chemical Company). The Europium complex $Eu(TTA)_2(Ph_3PO)_2NO_3$ was successfully incorporated with different molar ratios into organic polymer matrix of *PVP* via sol–gel process. Drop- and spin-coated thin films on optical glass and quartz substrates were obtained. The dried layers with thickness around 1-10 μm turn out to be transparent in visible range of spectrum.

The microscopic investigations of the morphology of the NC surface on a microscope MII-4 show that the dimensions of $Eu(TTA)_2(Ph_3PO)_2NO_3$ particles, incorporated in the polymer matrix are invisible and hence are less than 100 nm. Photoluminescence spectra have been measured using a set-up based on MDR-23 monochromator connected to PC. NC excited with N_2-laser (λ = 0.337 μm) or Deuterium lamp have generated some sharp emission bands in the spectral range of 300 – 800 nm. For optical transmission investigations a Specord UV/VIS (300÷800 nm) CARL ZEISS Jena unit was used. Absorption and luminescence properties of powder of Europium complex and NC were measured on each step of technology.

III. EXPERIMENTAL RESULTS

Fig.2a,b shows the surface images of the NC films at different concentration of $Eu(TTA)_2(Ph_3PO)_2NO_3$ in the nanocomposites under white (Fig. 2a) and UV illumination (Fig. 2b). The photos also reveal that $Eu(TTA)_2(Ph_3PO)_2NO_3$ complex are dispersed in *PVP* homogenously without any phase separation.

Transmission spectra $T(\lambda)$ of thin layers of NC on quartz substrates in the ultraviolet (UV) show clearly 3 absorption bands with maximums at 3.8, 4.5 and 4.8 eV, and with increasing of the OCC concentration in NC they grow until complete darkening in UV range. The sharp absorption threshold (Fig.3,4) is presented for all concentrations of coordinated compounds of OCC in NC in the range of 370 - 380 nm of spectrum. The absorption spectra ($\alpha(\lambda)$) are calculated from the transmission spectra $T(\lambda)$ by the formula $\alpha(\lambda) = - lnT/d$ (where d is the thickness of NC, α – absorption coefficient). The energies of forbidden bands of NC (ΔE_{NL}= *LUMO – HOMO,* were *HOMO* is energy of high occupied molecular orbital and *LUMO* – low unoccupied molecular orbital) obtained from 80 % of absorption threshold of $T(\lambda)$ are in the range 3.14 - 3.16 eV. Forbidden band ΔE_{NL} = *LUMO – HOMO= 3.15 eV* are referred to coordinated compounds of $Eu(TTA)_2(Ph_3PO)_2NO_3$.

On Fig.5a,5b,5c the spectra of photoluminescence of NC $Eu(TTA)_2(Ph_3PO)_2NO_3$-PVP under excitation by N_2 laser are presented. The detected fluorescence bands correspond to the radiative transitions between the energy levels of the Europium ions centred at 537, 578, 615 (611, 613, 617, 620), 650 and 702 nm, and can be attributed to the spin forbidden *4f → 4f* transitions $^5D_0 \rightarrow {}^7F_i$ (i = 0,1,2,3 and 4), respectively. The most effective luminescence has the maximum at 615 nm at temperature 293 K which is about 20 times higher than others, and its halfwidth is less than 10 nm.

The optimal concentrations of $Eu(TTA)_2(Ph_3PO)_2NO_3$ in nanocomposite were found in the range of 6 – 11% (Fig.6). There is an almost monotonous increase of intensity of photoluminescence up to some 6 % of the OCC concentration in NC, and this feature is characteristic for all thin film samples at room temperature. The main feature of these characteristics is a quite low signal of photoluminescence in liquid solution samples, while thin film samples exhibits a significant grow of the intensity of photoluminescence.

IV. DISCUSSION

The measuring of PL spectra determine the effective transfer of energy from polymer matrix *PVP* to energy levels LUMO chelates of the complex $Eu(TTA)_2(Ph_3PO)_2NO_3$ and subsequent energy transfer to the energetic levels of Eu^{3+} ion. HOMO and LUMO of complex $Eu(TTA)_2(Ph_3PO)_2NO_3$ are found to be situated between levels *S* and *T* of polymer, and this case is similar to the doping case of semiconductor into its forbidden band with particularities of they dimensions.

By comparing the PL of $Eu(TTA)_2(Ph_3PO)_2NO_3$ complex with PL of NC, the enhancing of the efficiency for photoemission in NC was observed. The enhancing can be explained by the coordination ability of the organic counterpart of the host structure of polymer, which is strong enough to stabilise the position of chelates in $Eu(TTA)_2(Ph_3PO)_2NO_3$ neighborhood after incorporation process.

The emission spectra of $PVP/Eu(TTA)_2(Ph_3PO)_2NO_3$ NC and $Eu(TTA)_2(Ph_3PO)_2NO_3$ powder was studied and analyzed. The emission spectra of NC were similar to that of corresponding $Eu(TTA)_3Phen$ complex [2], and the halfwidths of the strongest bands of PL were found to be less than 10 nm, but in this case the $PVP/Eu(TTA)_2(Ph_3PO)_2NO_3$ have most high fluorescence intensity and color purity. Nanocomposites display a bright and narrow Eu^{3+} ion emission, which is due to the so-called "antenna" effect, defined as a light conversion process via an absorption energy transfer-emission sequence involving distinct absorption by a polymer and ligand and their energy transfer to Eu^{3+} ions and later their emission.

The experimental data of photoluminescence can be explained from the viewpoint of the surrounding environment where the Eu^{3+} ion resides. *PVP* and OCC significantly affected the strength of the hypersensitive transitions ($^5D_0 \rightarrow {}^7F_i$ (i = 0,1,2,3 and 4) for Eu^{3+}) of the complexes and the maximum of PL intensity at 613 nm.

For the Europium complex, the intensity of the transitions of $^5D_0 \rightarrow {}^7F_i$ (i = 0,1,2,3 and 4) increases in the nanocomposite with grows the concentration of OCC in NC. When $Eu(TTA)_2(Ph_3PO)_2NO_3$ complexes were incorporated

into *PVP*, the complexes exhibited disorder. Under the influence of the electric field of the surrounding ligands, the distortion of the symmetry around the lanthanide ion by the capping *PVP* due to the polarization of Eu^{3+}, which increases the probability for electric dipole allowed transitions. The influence of *PVP* on the coordinated environment of Europium ions changes the energy-transfer probabilities of electric-dipole transitions, accounting for the increase in luminescent intensity of 615 nm peak of NC.

The difference of the photoluminescence of *Eu* complex in different nanocomposites can be interpreted as follows: when *Eu* complexes are introduced into the *PVP*, the molecular motion is restricted and the stretching and bond vibration are weakened by the *PVP*, both of which decrease the non-radiative transition. These results show that the nanocomposites could provide a relatively stable environment for lanthanide complexes and improve their luminescence properties.

We suppose that the interaction of macromolecular ligands at high concentrations of Eu^{3+} ion leads to partial formation of coordinated unsaturated complexes and ionic aggregates, leading to the quenching of luminescence. From these positions, the resulting polymer composites open the most promising way to neutralize the coordinated complexes and to obtain structurally homogeneous materials with desired properties. From the spectra of NC (Fig. 5a,b), we can also suppose a low local symmetry of ligand field of ion Eu^{3+} observed line transition $^5D_0 \rightarrow {}^7F_0$, which is interdicted under the high symmetry of the luminescence centre. The intensity of the transition $^5D_0 \rightarrow {}^7F_0$ is comparable with intensities of $^5D_0 \rightarrow {}^7F_1$, indicating also a significant asymmetry around of rare-earth ions. The presence of splitting of the transition line $^5D_0 \rightarrow {}^7F_1$ on three components and of the transition line $^5D_0 \rightarrow {}^7F_2$ on five components indicates the absence of axial symmetry of the inner coordination sphere of central ion Eu^{3+}.

V. CONCLUSION

The nanocomposites $PVP/Eu(TTA)_2(Ph_3PO)_2NO_3$ were obtained by the method of chemical solutions.

From transmission spectra of NC measured in range 200 to 800 nm we have identified the absorption bands with maximums centred at 3.8, 4.5 and 4.8 eV in the UV, and the threshold of absorption forbidden band ΔE_{NL} = 3.15 eV was estimated. It is shifted slightly in the IR direction of the spectrum with increasing the percentage of $Eu(TTA)_2(Ph_3PO)_2NO_3$ concentration in NC.

The photoluminescence spectra of NC was attributed to the internal of transition of Eu^{3+} ion $^5D_0 \rightarrow {}^7F_i$ (i = 0,1,2,3 and 4) centred at 537, 578, 615 (611, 613, 617, 620), 650 and 702 nm. The halfwidth of PL band at 615 nm is less than 10 nm, which indicates that the nanocomposite exhibits high fluorescence intensity and colour purity.

The positive influence of *PVP* matrix on the coordinative environment of Eu^{3+} ions was determined. A possible method of raising the fluorescence of NC $PVP/Eu(TTA)_2(Ph_3PO)_2NO_3$ is energy transfer from polymer *PVP* levels and from levels of ligand to internal levels of Eu^{3+} ion. It was demonstrated the amplification of PL in the NC compared with organic complex compound special.

ACKNOWLEDGMENTS

This work was supported by the Supreme Council for Science and Technological Development of the Academy of Sciences of Moldova (Project 06.408.012F**).**

REFERENCES

[1] M. S. Iovu, A. M. Andriesh, S. A. Buzurniuc, V. I. Verlan, M. I. Caraman, V. E. Zubarev. Luminescence properties of Eu3+/thenoyltrifluoroacetonate composites. J. of Optoel. and Advan. Mater, 10, iss.4, 841(2008).

[2] A. Andriesh, S. Buzurniuc, V. Verlan, M.I. Caraman, S. Robu, N. Barbă. Fluorescent properties of nanocomposite organic luminophore compound – polymer. J. of Optoel. and Advan. Mater., 10, 353(2008).

[3] M.S. Iovu, A.M. Andriesh, S.A. Buzurniuc, V.I. Verlan, C.I. Turta, V.E. Zubareva, M.I. Caraman. New photoluminophore nanocomposite based on organic compound with Eu3+ ions and copolymer styrene-butylmethacrilate. J. of Non-Crystalline Solids, v.355, p.1890(2009).

[4] M. S. Iovu, S. A. Buzurniuc, V. I. Verlan, I. P. Culeac, and Yu. H. Nistor. New composite materials for optoelectronic applications. Advan. Topics in Optoel, Microel. and Nanotechn. IV. Ed. by Paul Schiopu, Cornel Panait, George Caruntu, Andrian Manea Proc. SPIE, 7297, (2009) 729703.

[5] Melby L.R., Rose N.J., Abramson E., Caris J.C. Synthesis and Fluorescence of Some Trivalent Lanthanide Complexes. J. Am. Chem. Soc. 86, 5117(1964).

[6] Batyreva V.A., German A.I. Serebrenicov V.V. Synthesis of rare earth compounds, Part 2, Tomsk (Russia), ed. by university of Tomsk, 121(1986).

[7] Iovu Mihail, Verlan Victor, Buzurniuc Svetlana, Zubareva Vera, Turtă Constantin. Process for obtaining of luminophore composite based on polymer and organic coordinated compound. Patent filed with the Agency AGPI of Moldova Republic. Number and date of deposit: S 2010 0087 at 2010-05-11.

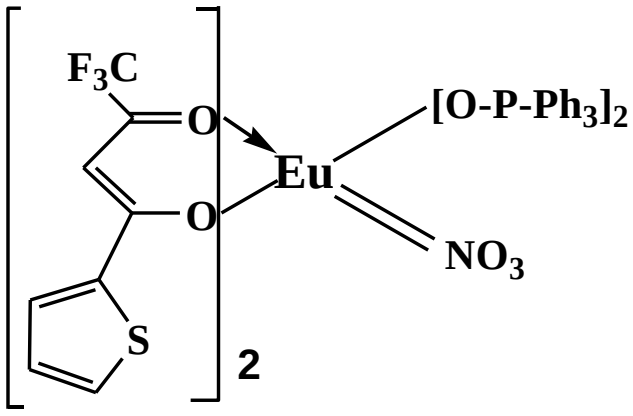

Fig.1. Formula of the structure of bis(thenoyltrifluoroacetonato)bis(triphenylphosphine oxide)(mononitrate)Europium(III) $C_{52}H_{38}F_6EuNO_9P_2S_2$.

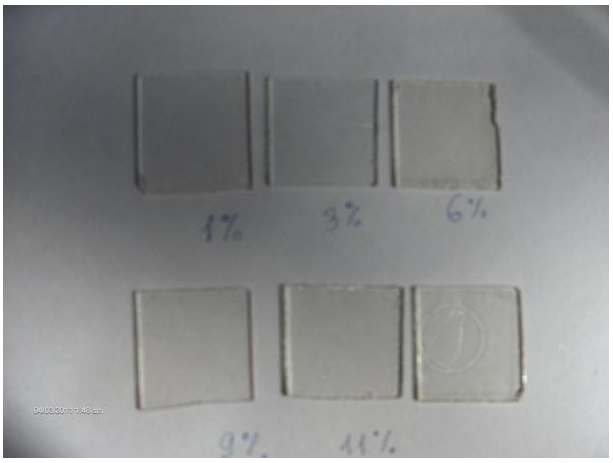

a

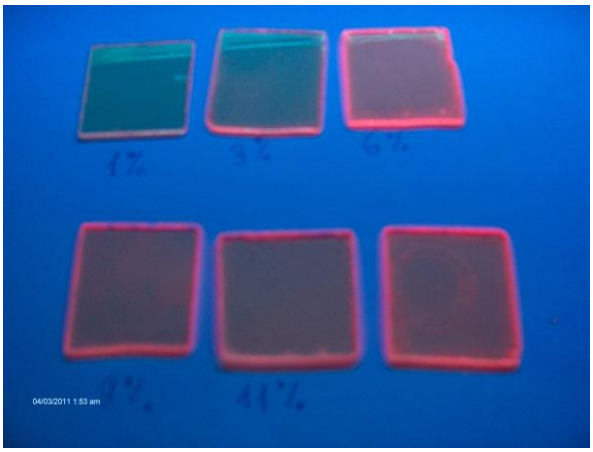

b

Fig.2. Samples of thin layers of NC illuminated with visible (a) and UV light (b).

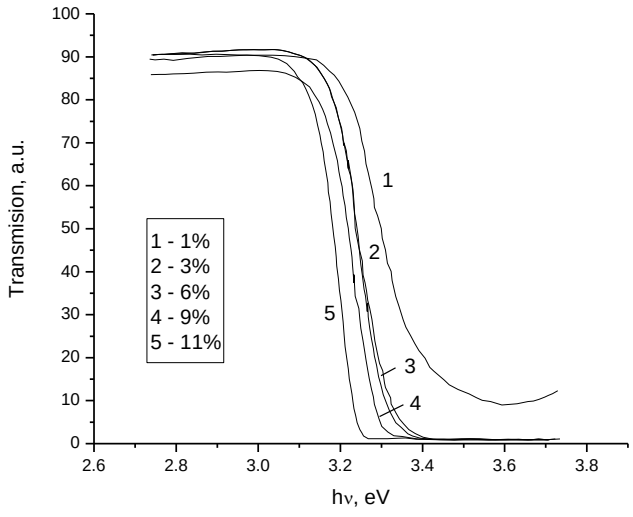

Fig.3. The transmission spectra of samples of thin layers of NC on glass substrates for different concentration of *Eu(TTA)$_2$(Ph$_3$PO)$_2$NO$_3$* in PVP at room temperature (T=293 K).

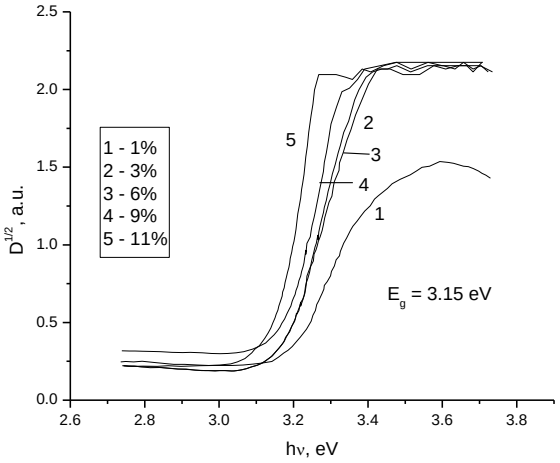

Fig.4. The optical density transmission spectra of samples of thin layers of NC on glass substrates for different concentration of *Eu(TTA)$_2$(Ph$_3$PO)$_2$NO$_3$* in PVP at room temperature (T=293 K).

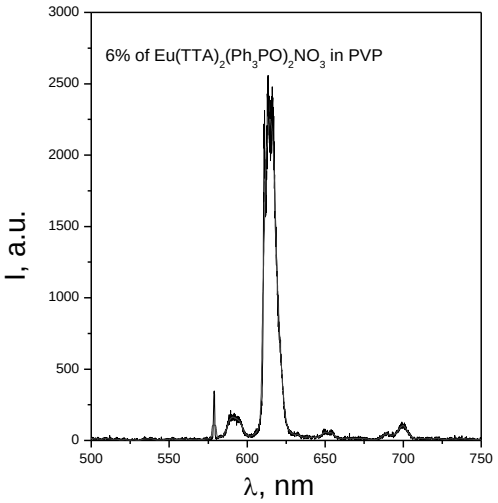

Fig.5a

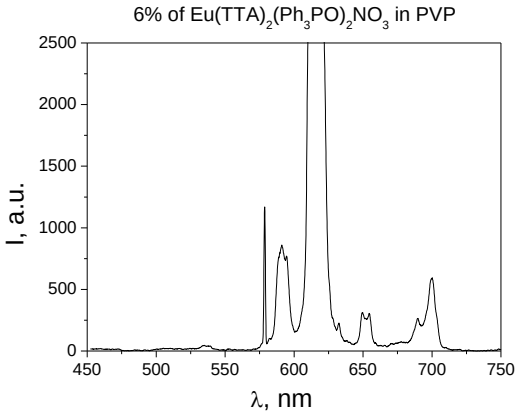

Fig.5b

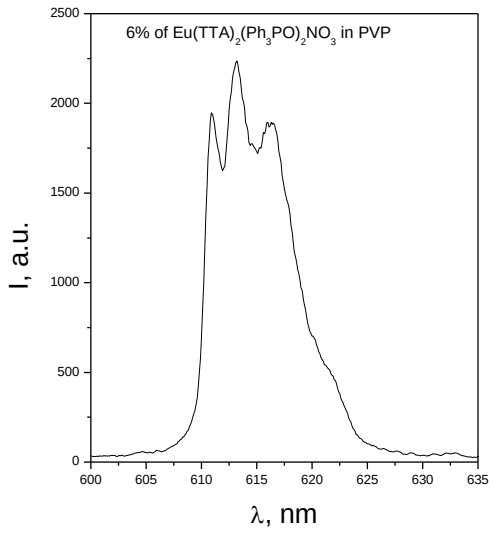

Fig.5c

Fig.5. The photoluminescence spectrum of thin layer of NC *PVP/Eu(TTA)₂(Ph₃PO)₂NO₃* 10 wt.% of concentration of complex *Eu(TTA)₂(Ph₃PO)₂NO₃* in NC: a,b – whole spectrum, c – detailed spectrum of main maximum at room temperature (T=293 K).

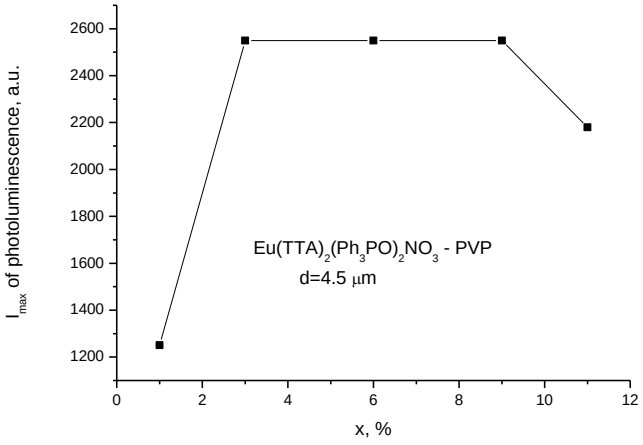

Fig.6. The maximum of intensity of photoluminescence at 615 nm of thin layers of NC versus of concentration *x* of *Eu(TTA)₂(Ph₃PO)₂NO₃* in NC.

Nanoporous Zinc Oxide Films Prepared by Magnetron Sputtering

L. GHIMPU, O. LUPAN, L. POPESCU, I.M. TIGINYANU
Laboratory of Nanotechnology, IEEIT, Academy of Sciences of Moldova
National Center for Materials Study and Testing, T.U.M.
Technical University of Moldova
ghimpu@iieti.asm.md

***Abstract* – In this paper we demonstrate an inexpensive approach for the fabrication of nanoporous zinc oxide films by using magnetron sputtering. Study of the structural properties proves the crystallographic perfection of porous nanostructures and the possibility of its controlling by adjusting the technological parameters in the growth process. The XRD pattern of nanoporous ZnO films exhibits high intensity of the peaks relative to the background signal which is indicative of the ZnO hexagonal phase and a good crystallinity of the samples grown by magnetron sputtering.**

***Index Terms* – ZnO, nanoporous, films, magnetron sputtering.**

I. INTRODUCTION

Over the last decade, nanostructured materials have received much greater attention because of their new properties promising for various applications [1-6]. Control of size and morphology of materials is of interest to researchers dealing with the design of functional devices; especially taking into account that optical and electronic properties of nanometer sized materials depends upon the dimensions and shape [1,7].

Exploration of zinc oxide has proven its piezoelectric properties, which led to its application in electronics, in particular in thin layers for devices with surface acoustic waves [8]. Currently the research of zinc oxide as a semiconductor material exhibits a new period of intense development. Over the last years, remarkable results have been published in the most prestigious international journals. Increased interest in ZnO as an optical material has been unleashed on *p*-type conductivity with ferromagnetic properties, and manufacture of field effect transistors in thin layers. A major driving force for research of zinc oxide as a semiconductor material is its prospective use as a wide-band semiconductor for light emitting devices and solar cells [4-6]. Note that the exciton binding energy of 60 meV is bigger than the effective thermal energy at 300 K (26 meV).

These characteristics make ZnO promising in a variety of fields, along with electronics and optoelectronics. Further development of efficient systems for drug delivery for health care needs new sensible and selective biosensors [9-10]. ZnO nanoparticles have been used in many applications in our daily life, such as drug carriers and cosmetics [11]. However, although inhalation of ultrafine ZnO particles at relatively high dose (500 mg/m^3) for 2 hours did not induce acute systemic effects in humans, inhalation of ZnO fumes in an occupational setting can cause metal fume fever (fatigue, chills, fever, myalgias, cough, dyspnea, leukocytosis, metallic taste, and salivation) [12]. Generally, nanostructures with high surface to volume ratio exhibit high sensitivity to adsorbed molecules and therefore are suitable for implementation in sensors. There are many types of biosensors for use in physiological environments. Of these, those based on potentiometric measurement technique (there, where current flow is not necessary during the measurement) using zinc oxide, are interesting and necessary, because current flow could damage biological systems and environments. Zinc oxide is biocompatible, biosafe and, moreover, it is a semiconductor with photonic properties potentially usable for biophotonics. It is important to note that, along with UV, it emits in the visible region [13-15]. In addition, ZnO has an excellent electrochemical activity and good properties of electron transport. Nanowire arrays or nanoporous films found application dye-solar cells as well [13-15]. Most importantly, in the nanostructured form zinc oxide can be grown on any substrates, either crystalline or amorphous, and at various temperatures, including the possibility to grow it at relatively low temperatures, even at the temperature as low as 300 K. In this work, we will present the magnetron sputtering of zinc oxide nanoporous films. Its structural, morphological and vibrational properties are shown and discussed in details.

II. EXPERIMENTAL PART AND DISCUSSIONS

Basic parameters of the magnetron sputtering method are the voltage and discharge current power, specific power on the cathode, the gas pressure in the working chamber and magnetic induction. The main advantages of this method consist in high speed of layers deposition and reproducibility accuracy of the composition of the deposited layers. The condensation rate of the magnetron sputtering depends on the power of the discharge current and gas pressure in the working chamber. Thus, using this method we succeeded to grow ZnO layers in the atmosphere of argon by applying a constant current (DC) and radio-frequency (RF) AC. A disc of 99.99 % pure zinc served as target.

Pure porous-Zn was deposited over SnO_2 thin films of size 1.5 cm^2 on glass substrates by direct current (DC) magnetron sputtering. Preliminary, the substrates were cleaned for 2-3 hours in the mixed solution of chromium ($7g K_2Cr_2O_7$-10ml

H_2O-100ml H_2SO_4) at room temperature. The argon (Ar) working gas pressure was regulated in such a way to maintain a constant vacuum pressure of 5×10^{-3} Torr. The DC current used was 0.12-0.15 A, and the deposition time was 9-22 min. The substrate was kept at a constant temperature around 210°C. Several sets of samples have been prepared in this way. Afterwards, these nanolayers grown on tin oxide/glass substrate were introduced into a reactor and annealed at a temperature of 481°C for 45 minutes in an oxygen atmosphere; gas flow was approximately -100 ml/min.

The phase structure of the deposited films was studied using Rigaku X-ray diffractometer (XRD) (CuK_α radiation (λ=1.54178 Å)) and optimized operating conditions of 30 mA and 40 kV at a scanning rate of 0.04°/s in the 2θ range of 24-90°. The XRD pattern of doped nanoporous ZnO films is shown in Figure 1. All tin oxide substrate peaks are marked and are assigned to SnO_2 according to PDF 00-041-1445 card.

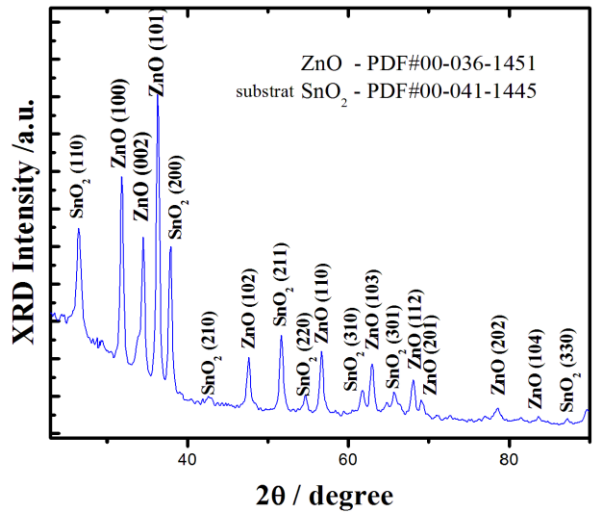

Fig. 1. XRD pattern of nanoporous ZnO grown by magnetron at 5°C on tin oxide/glass substrate. Substrate peaks are marked as SnO_2.

The diffraction peaks in the pattern can be indexed to hexagonal wurtzite structured ZnO [space group: $P6_3mc$(186); a=0.3249 nm, c=0.5206nm] and diffraction results are in agreement with JCPDS 036-1451 card for ZnO [16]. The intensity of the peaks relative to the background signal demonstrates high purity of the ZnO hexagonal phase of the products and a very good crystallinity of the samples [17-19] grown by magnetron sputtering. The characteristic peaks of impurities was not observed, which is indicative of a single phase hexagonal ZnO. The nanocrystallites are oriented along the (101) indicated by the highest intensity peak [16].

The morphology and chemical composition of the nanostructured films of ZnO were studied using a TESCAN Scanning Electron Microscope (SEM) equipped with an Oxford Instruments INCA Energy Dispersive X-ray (EDX) system. The EDX analysis of the produced structures demonstrates a relative stoichiometric ZnO composition (within a precision of 1 at.%). The composition was characterized by Energy Dispersion X-ray Spectrometer (EDX).

In the Figure 2a the results of EDX analysis of the nanostrucured films are represented. As one can see from the table, the chemical compozition shows 41.44 % of zinc and 57.27 % of oxygen.

A section of ZnO structure morphology is represented in Figure 2. It is clearly seen that the zinc oxide layer is porous and is quite homogenous over the whole surface of the samples.

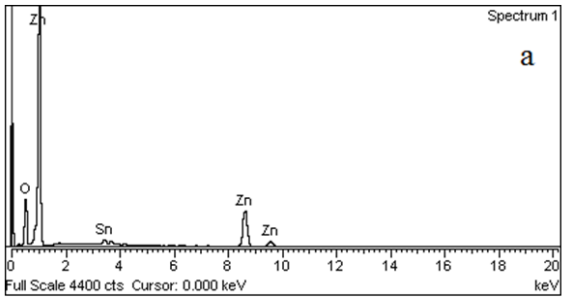

Element	Weight%	Atomic%	
O K	24.25	57.27	
Zn K	71.70	41.44	
Sn L	4.05	1.29	
Totals	100.00		

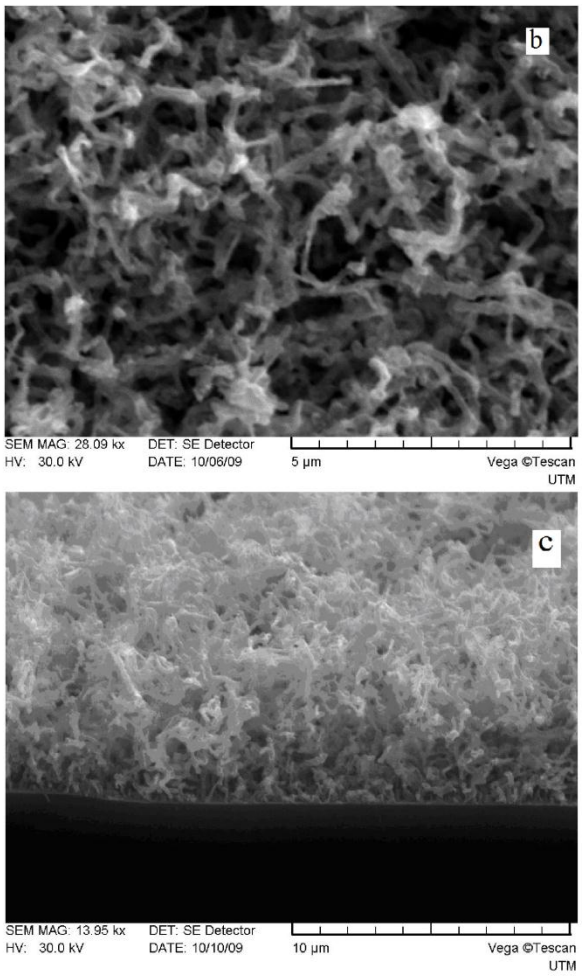

Fig. 2. a) EDX images of nanoporous ZnO; b,c) SEM images of nanoporous zinc oxide films grown by magnetron sputtering on tin oxide/glass substrate: top and cross-sectional views, respectively. Scale bars are 5 µm and 10 µm, respectively.

The room temperature Raman scattering was studied with

a Confocal Laser Raman System in the backscattering geometry under the excitation by a laser. Raman investigations (see Fig. 3) provide information about the material quality, the phase and purity, allowing one to understand vibrational properties and phonon interaction with the free carriers [15,17]. The group for ZnO is C_{6v}, and 12 degrees of freedom exist since there are four atoms per primitive cell. There are nine optical phonon modes and three acoustic phonon modes. Phonon modes E_2 (low and high frequency), A_1 [(TO)-transverse optical and (LO)-longitudinal optical] and E_1 (TO and LO) are expected, all being Raman and infrared active [17,20]. According to group theory, the optical modes at the Γ point of the Brillouin zone can be expressed by [20]:

$$\Gamma_{opt} = 1A_1 + 2B_1 + 1E_1 + 2E_2$$

A_1(z), E_1(x), E_1(y) and E_2 are Raman active modes, except the silent mode B_1. Figure 3 shows the Raman spectrum measured in backscattering geometry in the nanoporous ZnO grown by magnetron sputtering on TO substrate. The E_2 optical mode corresponds to dominant peaks at 100 cm^{-1} and 438 cm^{-1}, which are commonly detected in the wurtzite structure of ZnO [20]. The Raman spectrum of the ZnO films demonstrates a high quality of the wurtzite crystal structure in the produced material.

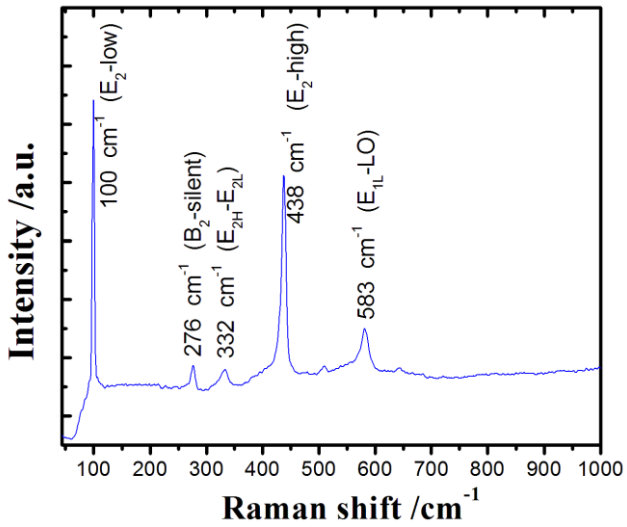

Fig. 3. Raman spectrum for nanoporous zinc oxide films grown on tin oxide/glass substrate.

III. CONCLUSION

Novel nanoporous ZnO films were synthesized by magnetron sputtering. The obtained results of the ZnO structure morphology and the XRD data prove the possibility to control the properties in a controlled fashion. Wurtzite crystal structure corresponds to a single hexagonal phase of ZnO, where the nanocrystallites are oriented along the (101) axis. This study allows one to conclude that these layers are useful for DSSC solar cells and light emitting devices.

ACKNOWLEDGMENTS

Financial support by Supreme Council for Science and Technological Development of the Academy of Sciences of Moldova are acknowledged.

REFERENCES

[1] Z. L. Wang, "Zinc oxide nanostructures: growth, properties and applications," J. Phys.: Condens. Matter., vol. 16, pp. R829–R858, 2004.

[2] R. Baron, F. W. Campbell, I. Streeter, L. Xiao, R. G. Compton, Int. J. Electrochem. Sci. 3, pp. 556, 2008.

[3] O. Lupan, G.A. Emelchenko, V.V. Ursaki, G. Chai, A.N. Redkin, A.N. Gruzintsev, I.M. Tiginyanu, L. Chow, L.K. Ono, B. Roldan Cuenya, H. Heinrich, E.E. Yakimov, "Synthesis and characterization of ZnO nanowires for nanosensor applications," Materials Research Bulletin, vol 45(8), pp. 1026-1032, August 2010.

[4] O. Lupan, L. Chow, G. Chai, A. Schulte, S. Park, O. Lopatiuk-Tirpak, L. Chernyak, H. Heinrich, "Biopolymer-assisted self-assembly of ZnO nanoarchitectures from nanorods," Superlattices and Microstructures, vol. 43(4), pp. 292-302, April 2008.

[5] O. Lupan, Th. Pauporté, B. Viana, I. M. Tiginyanu, V. V. Ursaki and R. Cortés, "Epitaxial Electrodeposition of ZnO Nanowire Arrays on p-GaN for Efficient UV-Light-Emitting Diode Fabrication," ACS Appl. Mater. Interfaces, 2010, 2 (7), pp 2083–2090, July, 2010.

[6] O. Lupan, T. Pauporté and B. Viana, "Low-Temperature Growth of ZnO Nanowire Arrays on p-Silicon (111) for Visible-Light-Emitting Diode Fabrication," J. Phys. Chem. C, 2010, 114 (35), pp 14781–14785, August 2010.

[7] A. Bayandori Moghaddam, M. Kazemzad, M. R. Nabid, H. H. Dabaghi, Int. J. Electrochem. Sci. 3, pp. 291, 2008.

[8] D. J. Milliron, S. M. Hughes, Y. Cui, L. Manna, J. Li, L.-W. Wang, A. P. Alivisatos, Nature 430, pp. 190, 2004.

[9] D. C. Look, Mater. Sci. Eng. B 80, pp. 383, 2001.

[10] Vavrinsky E., Flyckyngerova, S.Gaspierik, P.Skriniarova, J.Novotny, et all. Micro-nano-structuralized interfaces of conductive and transparent thin film microelectrodes for biomedical application. App.Scien. in Biomedical and Communication Technologies, 2009, ISABEL, 2009, 2nd International Sympozium.

[11] Haijun Zhanga, Baoan Chena, Hui Jiang, Cailan Wang, Huangpin Wang and Xuemei Wang. A strategy for ZnO nanorod mediater multi-mode cancer treatment. Biomaterials Volume 32, Issue 7, pp.1906-1914, 2011.

[12] W. S. Beckett, D. F. Chalupa, A. Pauly-Brown, D. M. Speers, J. C. Stewart, M. W. Frampton, M. J. Utell, Li-Shan Huang, C. Cox, W. Zareba and G. Oberdörster, American Journal of Respiratory and Critical Care Medicine 171, pp. 1129, 2005.

[13] J. Zhou, N. S. Xu, Z. L. Wang, Adv. Mater. 18, pp. 2432, 2006.

[14] O. Lupan, V.M. Guérin, I.M. Tiginyanu, V.V. Ursaki, L. Chow, H. Heinrich, T. Pauporté, "Well-aligned arrays of vertically oriented ZnO nanowires electrodeposited on ITO-coated glass and their integration in dye sensitized solar cells", Journal of Photochemistry and Photobiology A: Chemistry, vol. 211(1), pp. 65-73, March 2010.

[15] I. M. Tiginyanu, O. Lupan, V. V. Ursaki, L. Chow, M. Enachi, "Nanostructures of Metal Oxides."

Comprehensive Semiconductor Science & Technology, Chapter 3.11, pp. 396-479, 2011.

[16] XRD. American Society for Testing and Material. Powder Diffraction Files; Joint Committee on Powder Diffraction Standards: Swarthmore, PA, pp.3-888. Joint Committee on Powder Diffraction Standards, Powder Diffraction File PDF# 021-1250.

[17] O. Lupan, L. Chow, G. Chai, B. Roldan, A. Naitabdi, A. Schulte, H. Heinrich, "Nanofabrication and characterization of ZnO nanorod arrays and branched microrods by aqueous solution route and rapid thermal processing," Materials Science and Engineering: B, vol. 145(1-3), pp. 57-66, December 2007.

[18] L. Chow, O. Lupan, Guangyu Chai, "FIB fabrication of ZnO nanotetrapod and cross-sensor," Physica Status Solidi (b), vol. 247(7), pp. 1628–1632, July 2010.

[19] O. Lupan, L. Chow, G. Chai, H. Heinrich, "Fabrication and characterization of Zn–ZnO core–shell microspheres from nanorods," Chemical Physics Letters, vol. 465(4-6), pp. 249-253, November 2008.

[20] O. Lupan, V.V. Ursaki, G. Chai, L. Chow, G.A. Emelchenko, I.M. Tiginyanu, A.N. Gruzintsev, A.N. Redkin, "Selective hydrogen gas nanosensor using individual ZnO nanowire with fast response at room temperature," Sensors and Actuators B: Chemical, vol. 144(1), pp. 56-66, January 2010.

Interband Optical Transitions in the Region of Excitonic Resonance in $In_{0.3}Ga_{0.7}As/GaAs$ Quantum Wells

Eli KAPON[1], Alexandru MEREUŢA[1], Andrei DOROGAN[2], Nicolae DRAGUTAN[2],Tatiana VIERU[2], Nicolae SYRBU[2], Victor ZALAMAI[3]
[1]*Swiss Federal Institute of Technology in Lausanne, Lausanne, Switzerland*
[2]*Technical University of Moldova, Kishinev, Moldova*
[3] *Institute of Applied Physics, Kishinev, Republic of Moldova*
syrbunn@yahoo.com

***Abstract* – Reflection spectra of *$In_{0.3}Ga_{0.7}As$* layers with 8nm thickness with quantum wells limited by *GaAs* barrier layer with *100nm* thickness (bottom) and *9nm* (upper) had been measured at *S* and *P* polarizations in the interval of photon energies *0.6 – 1.6eV* at an incident angle near the normal one (*4.5°*) and Brewster angle (*76 °*). Thin absorption lines *0.9021eV, 1.0161eV, 1.1302eV, 1.1973eV, 1.2766eV* conditioned by the transitions *hh1-e1(1s), lh1-e1(1s), hh2-e2(1s), lh2e-2(1s), hh3-3(1s)* and *lh3-3e(1s)* had been revealed. The intensity of absorption lines changes in the limits *10 – 70%*.**

***Index Terms* – quantum wells, optical properties, exciton, resonance.**

I. INTRODUCTION

The study of semiconductor heterostructures with quantum points and wells are of big interest if talking about revealing fundamental electronic states of excitonic polaritons in quantum points and wells. At the same time, it has to be highlighted, that basing on quantum well structures are developed opto- and micro-electronic devices of new generation [1-3]. Injection lasers based on quantum points that prove a high temperature stability of threshold current density J_{th}, low value of J_{th} and continuous generation at room temperature with 3W output power are created at the moment.

II. EXPERIMENTAL DATA AND DISCUSSIONS

The optical reflection has been measured on JASCO-680 spectrometer at 300K and s and p polarizations, at different light angles incident on the surface of the heterojunction with quantum wells.

The reflection spectra $R(\omega)=|r(\omega)|^2$, among the photoluminescence analysis, is the simplest method of characterization of heterostructures with quantum wells.

The inferior surface of the structure was polished till a mirror state in order to study transparency spectra $T(\omega)=|t(\omega)|^2$. It is necessary to measure R and T to determine the absorption of structures with quantum wells, and to determine the $A(\omega)$ values.

$$A(\omega)=1-R(\omega)-R(T). \qquad (1)$$

It is known, that not the idealness of the structure influences the optical reflection and absorption spectra, broadening the exciton resonance frequency in heterostructures. The inhomogeneity can lead to a smooth coordinate dependence of ω_0 in the quantum well plane or in the volume of the supperlattice, which leads to a broadening of the absorption and reflection lines. The simplest and most effective method of accounting the inhomogeneous broadening while calculating the reflection coefficient is the change of the nonradiative decay Γ with the effective nonradiative decay in the respective expression $\Gamma_{eff}=\Gamma+\Gamma_{inh}$, where Γ_{inh} is the broadening parameter. Figure 1 shows the reflection spectra of $In_{0.3}Ga_{0.7}As/GaAs$ with quantum wells at *300K* and incident angles *7°* and 76° (Brewster angle) for *S-S (A)* and *P-P (B)* lightwaves' polarization. The experimental rays' path is presented in the insertions *a* and *b*. The reflection minimums *b1- b6*, which have and increasing half with in case of Brewster angle, are present at *S-S* polarization at a *7°* incident angle. The same minimums are present in reflection spectra at *P-P* polarization at a *7°* incident angle.

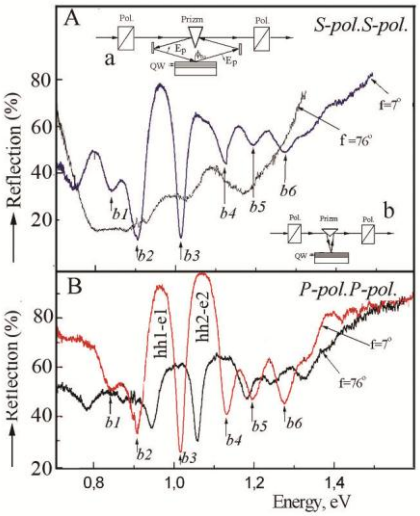

Fig. 1 Reflection spectra of GaAs /$In_{0.3}Ga_{0.7}As$/GaAs structure with quantum wells at 300K and incident light angle 7° and 76° (Brewster angle) for S-S (A) and P-P (Bpolarizations of lightwaves. The experimental rays' path is presented in the insertions *a* and *b*.

The minimums *a1- a6* are revealed in the reflection spectra at an incident angle equal to the Brewster one (*76°*), i.e. they are shifted. The shifting value for all reflection minima is approx equal. The measurement amplitude of reflection spectra (max – min) is also twice decreased for

this polarization.

Figure 2 shows the scheme of the periodical structure, consisted of *$In_{0.3}Ga_{0.7}As$* layers with *8nm* thickness with quantum wells divided by *GaAs* barrier layers with *9nm* thickness and the electronic transitions from the ground excitonic states in quantum wells. The reflection spectra presented in figure 3 are measured at an incident angle of *7°* and the transparency spectra at a normal light angle incident to the *$GaAs/In_{0.3}Ga_{0.7}As/GaAs$* heterostructure surface with quantum wells.

As the measurements were done at a spectrometer with high resolution, it can be noted that the minimums' energy of reflection spectra completely coincide with the energetic position of the maxima in the absorption spectra. The reflection geometry is presented in figure 1, *b*. The plane monochromatic wave $E(r,t)=E_0\exp(-i\omega t+ikr)$ falls on the *$In_{0.3}Ga_{0.7}As$* quantum well, positioned between two identical *GaAs* barriers, which are characterized by real permittivity ε_b. The lightwave vector is linked with the frequency correlation ω $k=(\omega/c)\sqrt{\varepsilon_b}$, where *c* – light speed in vacuum.

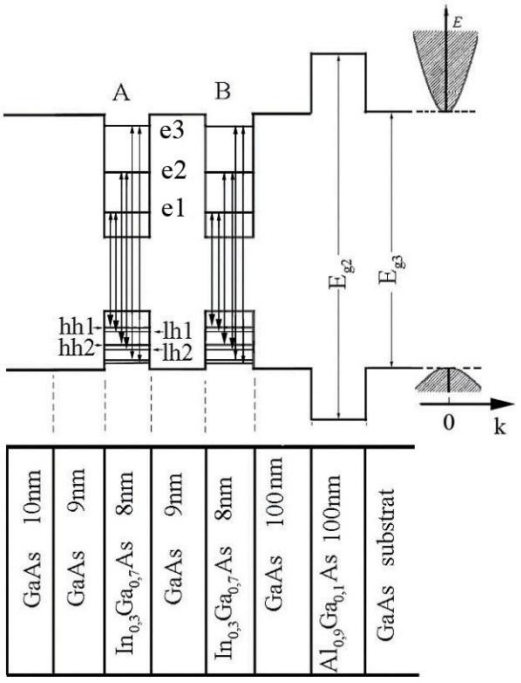

Fig. 2 Periodical structure consisted of two $In_{0.3}Ga_{0.7}As$ layers with 8nm thickness with quantum wells, divided by GaAs barrier layers with 9nm thickness and the electronic transitions from the excitonic states in quantum wells.

In case of normal incident light, when the lightwave vector *k* is parallel to the main structure axis *z*, the lightwave amplitude E_0 lays in the interface plane (x,y). As the system possesses axial symmetry in reference of *k* to *z* axis, the electrical vectors of the incident, reflected and passed lightwaves are parallel to each other and scalar amplitudes E_0, E_r and E_t can be used instead of vector amplitudes. The amplitude reflection and absorption coefficients are:

$$r=E_r/E_0, \qquad t=E_t/E_0 \tag{2}$$

In case of energy dissipation absence inside the quantum well the law of energy conservation lays on these coefficients:

$$|r|^2+|t|^2=1 \tag{3}$$

In case of normal incident light the exciton with a null bidimensional wave vector is excited, i.e. with $K_x=K_y=0$. A detailed analysis of the reflection and transparency coefficients of quantum well heterostructures is presented in the work [1], where the reflection r_{QW} has the expression:

$$r_{QW}=\frac{i\Gamma_0}{\omega_0-\omega-i(\Gamma+\Gamma_0)} \tag{4}$$

$$\omega_0^*=\omega_0+r_{10}\Gamma_0\sin 2\varphi \qquad \Gamma_0=\Gamma_0(1+r_{10}\cos 2\varphi) \tag{5}$$

ω_0^* and Γ_0 are the resonance frequency and the radiative decay of the exciton, renormalized taking into account the exciton interaction with the lightwave, induced by this exciton and reflected from the external surface.

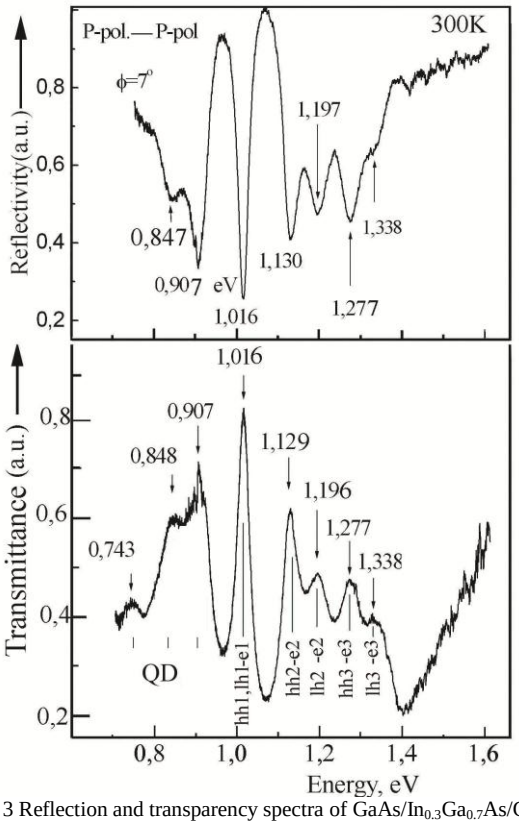

Fig. 3 Reflection and transparency spectra of $GaAs/In_{0.3}Ga_{0.7}As/GaAs$ heterojunctions with quantum wells.

The dependence of the reflection coefficient was established after some transformations [1] on the reflection and absorption coefficients:

$$R(\omega)=|r(\omega)|^2=R_0+\frac{A+Bx}{1+x^2} \tag{6}$$

$$X=\frac{\omega-\omega_0^*}{\Gamma}, \quad R_0=r_{01}^2 \tag{7}$$

where

$$A=t_{01}t_{10}S[t_{01}t_{10}S-2r_{01}(1+S^*)cos2\varphi] \tag{8}$$

$$B=2r_{01}t_{01}t_{10}Ssin2\varphi, \ S=\frac{\Gamma_0}{\Gamma}, \ S^*=\frac{\Gamma_0^*}{\Gamma} \tag{9}$$

According to the Fresnel formulas, in case of normal incident light:

$$r_{10}=-r_{01}=\frac{n_b-1}{n_b+1}, \quad t_{01}t_{10}=\frac{4n_b}{(n_b+1)^2} \tag{10}$$

The *A* and *B* coefficients can obtain different sign values, and, separately, become null, depending on the distance between the well center and the external surface. If $A=0$, $B<0$ the resonance contour is consisted of a maximum

$\omega < \omega_0^*$ and minimum at $\omega > \omega_0^*$. If $B = 0$, the spectra has one maximum ($A > 0$) or one minimum ($A < 0$) [1, 2].

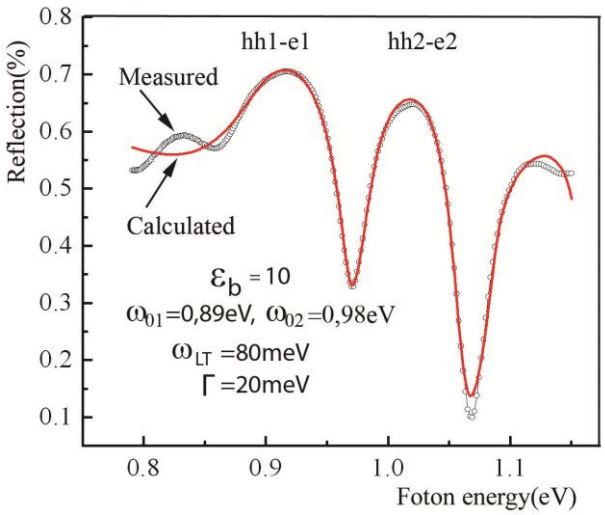

Fig.4 Experimental reflection spectra and the ground excitonic state contours in quantum wells of GaAs /$In_{0,3}Ga_{0,7}As$/GaAs heterojunctions calculated by the dispersion correlations.

The calculations of the reflection spectra of the ground excitonic states in quantum wells are made basing on the dispersion correlations which is based on multi oscillatory model [3].

The best correlation between calculated and experimental spectra was obtained at a decay factor $\Gamma \approx \Gamma_0$, $\Gamma_0 = (20 \pm 2) meV$, and background dielectric permittivity $\varepsilon_b = 10$ and the longitudinal-transversal permeability $\omega_{LT} = 80 meV$. The exciton lifetime is $\tau_0 = (2\Gamma_0)^{-1} \approx 2 \cdot 10^{-11} s = 10 ps$. The thin absorption and reflection lines and the theoretically obtained parameters can prove the quality of the structure with quantum wells.

REFERENCES

[1] E. L. Ivchenko, Optical spectroscopy of semiconductor nanostructures (Alpha Science International, Harrow, UK, 2005).

[2] L. E. Vorobjev, E. L. Ivchenko, D. A. Firsov, V. A. Shalygin, Optical nanostructures properties., Edited by V. I. Iljina and A. Ja. Shika, Edition "Science", Sankt-Petersburg, 2001.

[3] N. N. Syrbu and V. V. Ursaki, Book, Exciton Quasiparticles: Theory, Dynamics and Applications, Editors: Randy M. Bergin, (Nova Science Publisher. Inc., USA, 2010).

Multi-gated Field Emitters for a Micro-column

Hidenori MIMURA[1], Akifumi KOIKE[1], Toru AOKI[1], Yoichiro NEO[1], Tomoya YOSHIDA[2], and Masayoshi NAGAO[2]
[1]*Research Institute of Electronics, Shizuoka University, Hamamatsu, 432-8011, Japan*
[2]*National Institute of Advanced Industrial Science and Technology, Tsukuba, 305-8568, Japan*
mimura@rie.shizuoka.ac.jp

***Abstract* – We have developed a multi-gated field emitter (FE) such as a quadruple-gated FE with a three-stacked electrode lens and a quintuple-gated FE with a four-stacked electrode lens. Both the FEs can focus the electron beam. However, the quintuple-gated FE has a stronger electron convergence than the quadruple-gated FE, and a beam crossover is clearly observed for the quintuple-gated FE.**

***Index Terms* – beam crossover, electron beam, focusing, micro-column, multi-gated field emitter**

I. INTRODUCTION

A field emitter array (FEA) with a focusing electrode is an attractive device for applications, such as a scanning electron microscope and electron beam lithography and so on. As the FEAs with a focusing electrode, double-gated FEAs have been proposed. However, the double-gated FEA has a problem that the emission current decreases under the strong focusing conditions. This is due to the lowered field enhancement at the emitter tip caused by the low potential of a vicinal focusing electrode. [1] To solve such the problem, we have reported the other approach that uses the focusing electrode located below the extraction gate electrode in a volcano structure. [2, 3] However, we observed that some electrons cannot penetrate the potential barrier formed by the focusing electrode potential under strong focusing conditions. These electrons go back to the extraction gate electrode. To overcome these problems simultaneously (field enhancement and potential barrier), an electrostatic lens using a multistacked-electrode should be integrated at the emitter tip, and at least three additional electrodes are necessary. The first electrode (near the emitter tip) is used to maintain the potential at the emitter tip; therefore, a voltage higher than the extraction gate voltage is applied. The second electrode is used to focus the electron beam; therefore, a voltage lower than the extraction gate voltage is applied. The third electrode is used to inhibit the generation of a potential barrier on the electron trajectory; therefore, a voltage higher than the second electrode voltage is applied.

In this paper, we have developed a multi-gated field emitter (FE) with a four-stacked gate electrode, and a FE with a five-stacked gate electrode, that is, quadruple-gated FE with a three-stacked electrode lens and quintuple-gated FE with a four-stacked electrode lens.

II. FABRICTION OF THE MULTI-GATED FIELD EMITTERS

The fabrication process for the multi-gated FEs is schematically shown in Fig. 1. (a) An emitter cone is formed from single crystalline Si by reactive ion etching (RIE) using a SiO_2 dot as an etching mask. The apex radius of the tip is 5-10 nm. (b) A SiO_2 insulating layer is deposited by plasma-enhanced chemical vapor deposition (PE-CVD) using tetraethoxysilane (TEOS) gas followed by Nb deposition. (c) After the deposition of SiO_2 and Nb films, a photoresist is spin coated on the Nb film. The thickness of the photoresist on top of the mountain structure becomes thinner than that on the flat surface. (d) Therefore, the Nb electrode at the tip is selectively etched by the following RIE step without precise lithography. The electrode height can be controlled by the etching time and is adjusted to be the same as that of the emitter tip. The first Nb electrode acts as an extraction gate electrode. (e) In the quadruple-gated FE, three additional electrodes, which form an electrostatic lens, are stacked by repeating the steps from (b) to (d) three times. In the quintuple-gated FE, four additional electrodes, which form an electrostatic lens, are stacked in the similar way. (f) Finally, the emitter tip is opened by the buffered hydrofluoric acid (BHF).

Figures 2 (a) and (b) show cross sectional SEM images of the quadruple-gated FE and quintuple-gated FE, respectively. In the both FEs, the first Nb electrode acts as an extraction gate electrode. In the quadruple-gated FE, the G1 and G2 among the three-stacked electrostatic lens are set at the same voltage. In the quintuple-gated FE, G1 and G4 among the four-stacked electrostatic lens are set at the same voltage. G2 and G3 (G2,3) are connected through a contact hole, and are set at the same voltage. Therefore, both the three-stacked and four-stacked electrostatic lenses form an eizel lens.

Figure 3 shows the top-view micrograph of the quadruple-gated FE. The dotted line in the micrograph shows that the electrode holes from accurate concentric circles with the emitter tip as a center pole. This is due to the full self-aligned process. The alignment of electrode holes is very important for the electrostatic lens to avoid an aberration.

III. ELECTRON EMISSION CHARACTERISTICS

The electron emission from both the quadruple-gated FE and quintuple-gated FE were measured in a high-vacuum chamber at a pressure of 1×10^{-7} Pa. Figures 4 (a) and (b) show extraction-gate-voltage (Gex) versus anode-current characteristics of the quadruple-gated FE and quintuple-gated FE, respectively. An anode phosphor screen biased at 1 kV was located 1 mm above the FE substrate. For the simple anode-current characteristics, the all potentials of the electrostatic lens were set equal to that of the extraction gate electrode, as schematically shown in the insert of Figs. 4 (a)

and (b). In the quadruple-gated FE, emission started at 20 V and reached 3 μA at an extraction voltage of 60 V, while in the quintuple-gated FE, emission started at 30 V and reached 100 nA at an extraction voltage of 60 V. In the quintuple-gated FE, more electrons entered the gate electrodes in nonfocusing condition, because the lens size is larger than that of the quadruple -gated FE.

Figure 5 shows the beam spots measured from the anode phosphor screen images for the quadruple-gated FE and quintuple-gated FE. In the quadruple-gated FE, the voltages of Gex, G1 and G3 were fixed at 50, 100, and 100 V, respectively. The voltage of G2 was changed from 100 V (nonfocusing condition) to -20 V (focusing condition). In the quintuple-gated FE, the voltages of Gex, G1, and G4 were fixed at 50, 100, and 100 V, respectively. The voltage of G2,3 was changed from 100 V (nonfocusing condition) to -10 (focusing condition). Figure 5 also shows the phosphor images at G2,3 = 100, 10, and -10 V for the quintuple-gated FE. For the quadruple-gated FE, the beam spot monotonously decreases as the G2 voltage decreases from 100 to -30 V. On the other hand, for the quintuple-gated FE, the beam spot decreases as the G2,3 voltage decreases from 100 to 10 V, but then the beam spot increases as the G2,3 voltage go from 10 to -10 V. This indicates that a beam crossover (a beam focal point) is formed between the anode and the field emitter. Since the field emitter and anode are 1 mm apart and the crossover is formed immediately in front of the field emitter, the beam spot size shown in Fig. 5 are not exact size, and real beam size of the crossover is expected less than 50 nm. The results in Fig. 5 also show that the lens function for the quintuple-gated FE is stronger than that of the quadruple-gated FE.

IV. CONCLUSION

We have successfully fabricated a multi-gated FE such as quadruple-gated FE with a three-stacked electrode lens and a quintuple-gated FE with a four-stacked electrode lens. The fabrication process uses an etch-back technique. In our method, gate hole opening is a self-aligned process; therefore, the axes of electrode holes are well aligned without precise lithography. Both the quadruple-gated FE and quintuple-gated FE can focus the electron beam. However, lens function for the quintuple-gated FE is stronger than that of the quadruple-gated FE, and a beam crossover is formed for the quintuple-gated FE. The multi-gated FE is a promising device for a micro-column for a scanning electron microscope and electron beam lithography.

REFERENCES

[1] Y. Yamaoka, S. Kanemaru, and J. Itoh, Jpn. J. Appl. Phys. 35, pp.6626, 1996.

[2] Y. Neo, T. Soda, M. Takeda, M. Nagao, T. Yoshida, C. Yasumuro, S. Kanemaru, T. Sakai, K. Hagiwara, N. Saito, T. Aoki, and H. Mimura, Appl. Phys. Express 1, pp.053001, 2008.

[3] T. Soda, M. Nagao, C. Yasumuro, S. Kanemaru, T. Sakai, N. Saito, Y. Neo, T. Aoki, and H. Mimura, Jpn. J. Appl. Phys. 47, pp.5252, 2008.

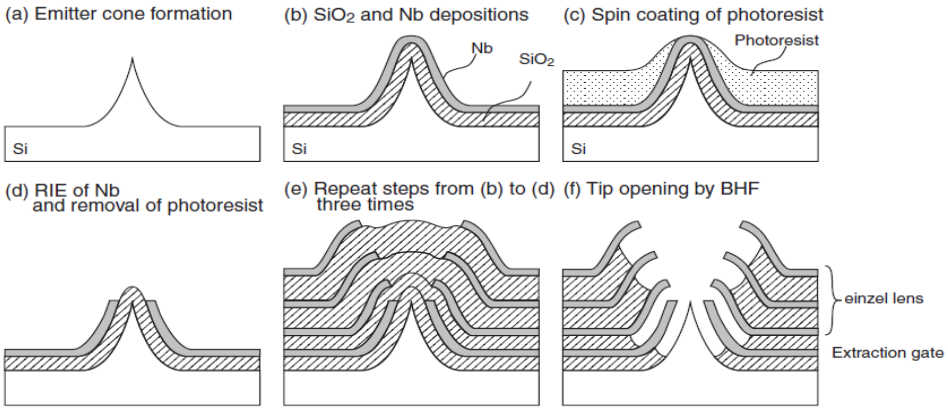

Fig. 1 Fabrication process for the quadruple-gated FE with a three-

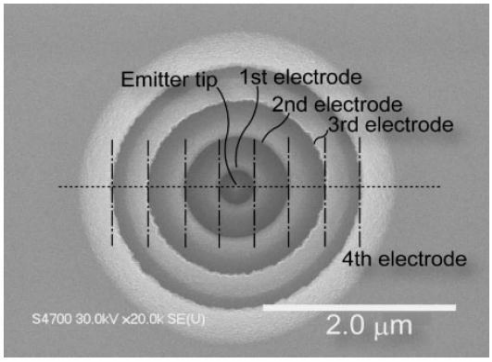

Fig. 2. Top-view SEM image of the quadruple-gated FE.

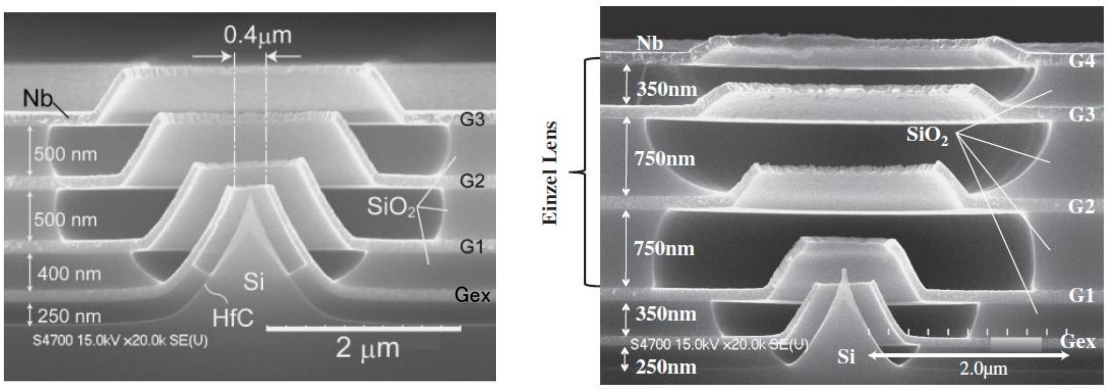

(a) (b)

Fig. 3 Cross-sectional SEM images of the quadruple-gated FE (a) and the quintuple-gated FE.

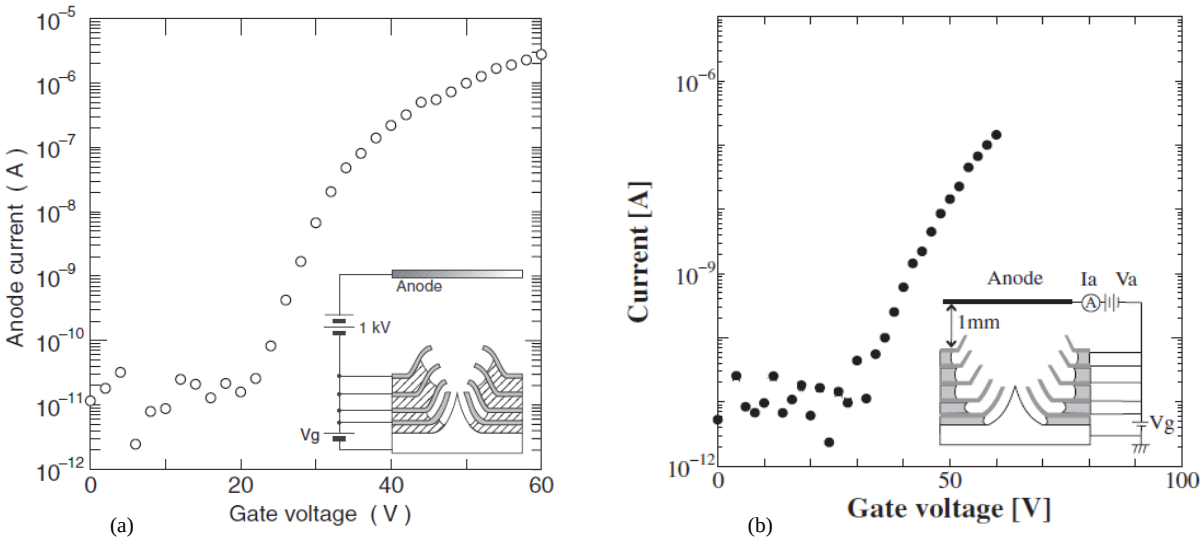

(a) (b)

Fig. 4 Emission characteristics of the quadruple-gated FE (a) and the quintuple-gated FE (b).

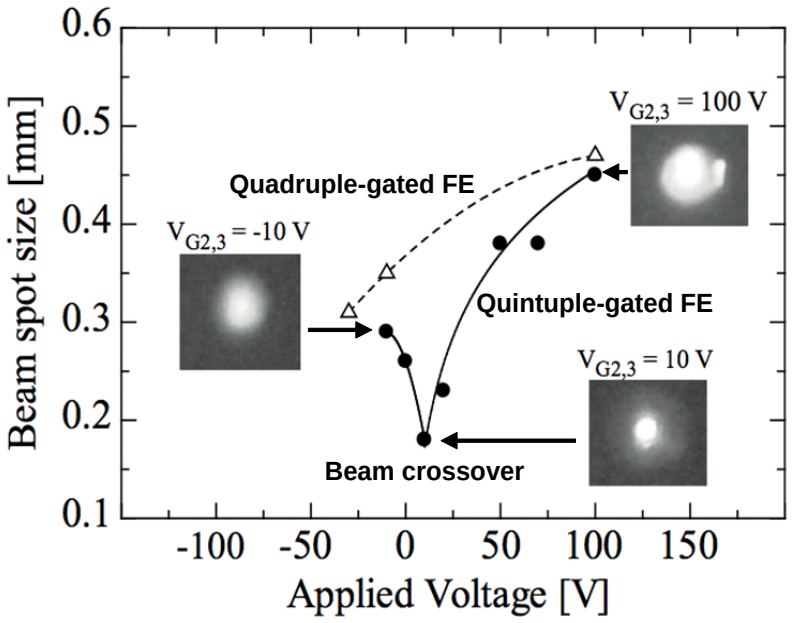

Fig. 5 Beam spots measured from phosphor screen images for the quadruple-gated FE (a) and the quintuple-gated FE (b). Solid and dashed lines are the least-square estimations for the quadruple-gated FE and the quintuple-gated FE, respectively.

Nano Metrology Aspects of Design, Simulation, Fabrication, Testing , Reliability and Failure Analysis of Wafer Fused VCSEL

Vladimir IAKOVLEV, *LPN EPFL*

***Abstract* – In this paper are presented several application aspects of nano metrology tools in characterization and fabrication of high performance long wavelength wafer fused VCSELs as well as for failure analysis. As long wavelength VCSELs are emerging as attractive light-sources for replacing DFB lasers in power consumption sensitive applications, the main challenges in developing the cost and time efficient nano metrology tools for supporting processing and characterization are discussed.**

***Index Terms* – Long-wavelength, VCSELs, wafer fusion, VCSEL technology, failure analysis, nanometrology**

I. INTRODUCTION

Long wavelength (LW) vertical cavity surface emitting lasers (VCSELs) emitting in the 1300 and 1550 nm band with single mode (SM) output power in excess of 1mW in a wide temperature range up to 85°C, high speed modulation capabilities and accurate emission wavelength setting present interest in broad band optical communications, and sensing . Compared with standard distributed feedback (DFB) edge-emitting lasers, VCSELs offer advantages of

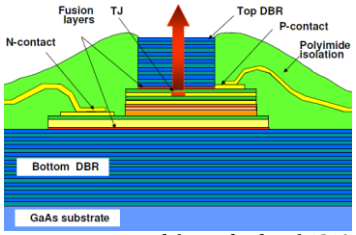

Fig. 1. Schematic cross section of the wafer fused 1310 nm VCSEL

symmetric far-field emission pattern, low power consumption and continuous wavelength tuning with current. State of the art longwavelength VCSELs with increased single mode output power have a hybrid structure combining GaAs/AlGaAs or dielectric distributed Bragg reflectors (DBRs) for high reflectivity with InP/InAlGaAs quantum well (QW) active regions for high optical gain at elevated temperatures. In addition, employing tunnel junctions has allowed intra-cavity contacting with low-absorption DBRs, a crucial ingredient for reaching high single mode power and high modulation speed. Among all leading LW-VCSEL technologies, localized wafer fusion offers the greatest flexibility in selecting the emission wavelength while the utilized GaAs/AlGaAs DBRs provide the best thermal conductivity . Consequently, the wafer fusion approach yielded 1300 and 1500 nm VCSELs with state of the art performances [1,2]. In this paper we describe the design, fabrication process and characterization results of wafer fused 1310 and 1550 nm single-mode VCSELs with lower power consumption as compared with corresponding DFB edge-emitting lasers at the same output power level of 1mW and operation speed above 5 Gb/s . The capability of cavity adjustment for setting the emission wavelength in a specified position of the CWDM grid, on the full wafer-scale industrial fabrication process demonstrates the possibility of wavelength inventory selection in the range 40 nm on the same 2-inch VCSEL wafer. The first documented reliability data obtained on wafer-fused VCSELs processed in the industrial wafer fab of a leading optical component manufacturer in Europe. Results show that VCSELs fabricated with the wafer-fusion technique and displaying high performance level, meet Telcordia generic requirement standards. Finally, the first results of implementing state of the art nanometrology tools for failure analysis as well as the main challenges in decreasing the cost and duration of full range on ongoing failure analysis are briefly discussed.

II. VCSEL DESIGN AND SIMULATIONS

The VCSEL device structure comprises an InP-based 5/2 λ-active cavity that is fused on both sides to undoped AlGaAs/GaAs DBRs, as schematically depicted on Figure 1. The active cavity includes an InAlGaAs/InP multi-QW region with 4-6 compressively strained quantum wells and a p++/n++ InAlGaAs tunnel junction."

Figure 2 presents transverse gain and mode profiles of this design at different temperatures that were obtained by numerical solving of a fully coupled 2-dimentionsional set of elctro-opto-thermal equations [4].

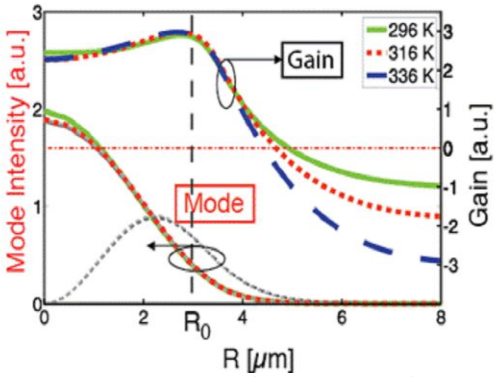

Fig. 2. Lateral gain and optical field distributions from the center of the tunnel junction . Ro represent the edge of a TJ mesa with diameter of 6 um

As one can observe the fundamental mode is predominant and the gain and mode profiles spread by about 1-1.5 μm outside the active region defined by the tunnel junction mesa. The optical confinement is due to a lateral refractive index variation that corresponds to a difference in the optical

paths of about 7 nm for the light propagating through the tunnel junction mesa and adjacent re-grown InP.

III. FABRICATION AND TESTING

The InP-based active cavity and GaAs-based DBRs are grown by low pressure metal-organic vapor phase deposition (LP-MOVPE) on 2 (100) wafers [3] . A mesa-structure of 6-7 µm in diameter formed in the tunnel junction that is regrown with n-type InP serves for carrier and photon confinement.

Electrical contacting is performed by top and bottom intra-cavity n-InP layers. This contacting scheme allows using un-doped top and bottom DBR mirrors. InGaAsP cavity adjustment layers that are located on both sides of the active cavity serve for precise adjustment of the emission wavelength.

Figure 4 depicts images of tunnel junction mesas at different stages of the fabrication process: a- initial mesas etched in the tunnel junction, b,c after regrowth, before first fusion step, d, e-after the first fusion step. As one can observe from Figure 4, after re-growth mesas have elliptical shape and a size that is 2-2.5 times larger compared with initial mesas that have a round shape (please note that the image size and picture resolution are not enough to give all the details, Figure 4 should be considered only for concept description). This occurs due to predominant lateral overgrowth with a tendency to planarization occurring during regrowth by MOVPE. Consequently, the optical mode, that extends by about 1.5 µm outside the active region defined by the mesa etched in the tunnel junction (Figure 4) is well within the edges of the re-grown region that will help in selection of the fundamental mode. The elliptical shape of the regrown mesa provides a way for discrimination of polarization modes. Before the first fusion process, the top InGaAsP cavity-adjustment layer is selectively etched on one half of the wafer. The oblique line on Figure.2,c represents the border between two regions on the wafer with different cavity lengths.

During the fusion process, InP-based and GaAs-based 2-inch wafers are brought into contact at 600°C in vacuum, and by applying a pressure of 7000 N for 30 min in an industrial custom-built wafer bonding machine. At these values of temperature and pressure, both wafers undergo a slight plastic deformation resulting in a uniform contacting on a nanometer scale. As a result, covalent bonds are formed between InP-based and GaAs-based wafers. After cooling down the stack that includes InAlGaAs/InP-AlGaAs/GaAs half-cavity with InP and GaAs substrates on respective sides is bowed. This bowing with a radius of curvature of about 1 m occurs because of different values of thermal expansion coefficients of GaAs-based wafers with lattice parameter of 5.6535Å and InP-based wafers with lattice parameter of 5.86875Å, (5.8x10-6 /K for GaAs and 4.8x10-6 /K for InP). After selectively etching the InP substrate the remaining GaAs substrate containing the fused stack re-gains its planarity.

In the second fusion step a second DBR is fused to the InP-based active cavity in the same conditions as during the first fusion. The difference is that the fused stack is not bowed any more. SEM and TEM images (that will be presented elsewhere) shows that the misfit dislocations resulting from the lattice mismatch of GaAs and InP are confined at the fused interface and do not propagate inside the VCSELs structure. Double fused VCSEL wafers are produced systematically without any voids at both fused

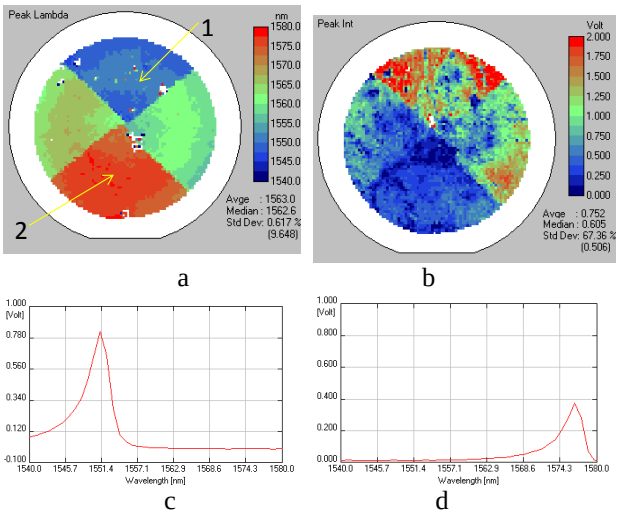

Fig. 3. (a) Peak lambda map, (b) peak intensity map (c) spectrum in point 1 and (d) spectrum in point 2.

interfaces, with a high surface quality over the full 2-inch wafer.One of the big advantage of vertical cavity surface emitting laser technology is the possibility to perform full wafer test without cutting the wafer is parts. In Figure 3 it is presented the pictures of wafer map performed immediately after removing substrate form top DBR side. One can clearly see 4 different wavelength regions, the shortest wavelength is in region denoted by 1 in Figure 3a and the longest is in region denoted by 2. The PL spectra are presented in Figure 3c and d respectively: In Figure 3b it is presented the map of peak intensity. As one can see, the highest intensity it is observed in region 1, the lowest it is observed in region 2. One of the challenges in the future work in developing nano metrology tools for

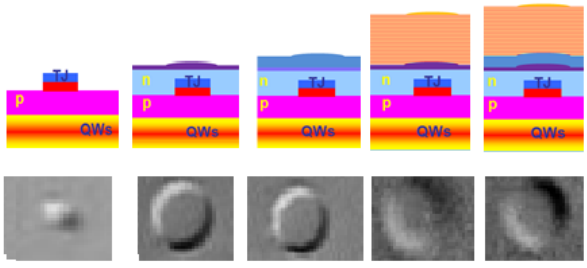

Fig. 4. Images of TJ mesas: a - initially etched 7 µm mesas, b,c-regrown mesas before fusion, d, e - after fusion.

supporting
fabrication technology of longwavelength VCSELs is to find the necessary vertical design and processing flow that will allow correlation between PL map data and device performance.

The processing of the double-fused VCSEL wafer is performed in a standard way. It includes reactive ion etching of the top DBR, selective chemical etching steps in the InAlGaAs/InP active cavity region, dielectric deposition, dry etching steps and e-beam deposition of metals for contacts and electroplating for bond-pads (Figure 5). After wafer qualification by performing on-wafer continuous work (CW) and high frequency (HF) tests, the wafer is thinned and scribed into individual chips. Figure 6 depicts a typical VCSEL chip that is mounted on a sub-mount and electrically

contacted with Au wires by ball-bonding

The 1310 nm range VCSELs fabricated by wafer fusion technique exhibit excellent performance in terms of spectral and power emission in the temperature range up to 100°C as well as modulation response up to 10Gb/s [5,6] .

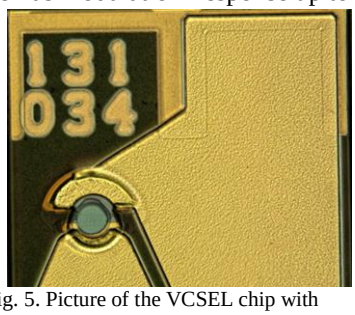

Fig. 5. Picture of the VCSEL chip with electroplated contact pads

Fig. 6. VCSEL chip mounted on a TO header

The devices from this group showed stable operation with no failures during 5000h, as it is shown in Figure 8. [1].VCSEL mean time to failure (MTTF) value at 25°C and 10 mA bias current was estimated to be in the range of 32 million hours and about 2 million hours at 70 °C [7].

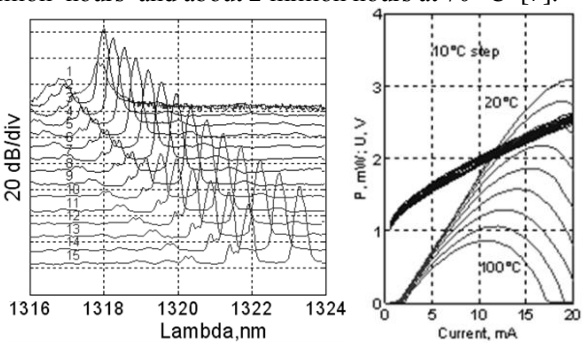

Fig.7. . (a) -Spectral emission at 20°C (the numbers near curves indicate the operation current, curves are shifted down for clarity), (b)- Light-Current-Voltage characteristics up to 100°C

An example of performance versus test time plots, used

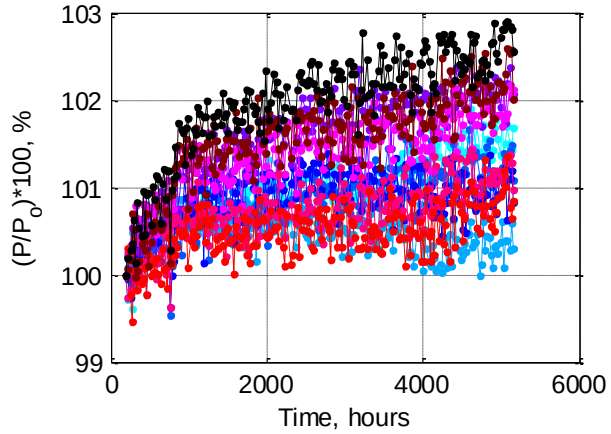

Fig. 8. Power change for 11 devices from qual group showed stable operation with no failures during 5000h

in evaluation MTTF values (as will be presented in [7]) .are depicted in Figure 9-11. The test conditions used for acquisition these plots will be described elsewhere [7].

As one can see from these plots there are more or less steady decreasing of the emission power for all tested devices, and in a few of them the rate of degradation is quite fast (devices under numbers 236, 250 252 and 256).

In this paper we will not try to give a rigorous explanation of the root causes of the device failures, this will be the goal of a long lasting project and will be described in a dedicated publications. The reason to present the experimental results depicted in Figure 8-11 is to describe the initial phase of work in selecting the minimum necessary tools and characterization algorithms for time and cost effective failure analysis.

As one can see from comparison of Figure 8 and Figure 9, under relatively low current and temperature stress there are no devices failures and more than that, there is a small increase in emission power versus test time, while under increased temperature and current stress the threshold current is increasing and emission power is decreasing with time. Without going into more complex analysis, one can conclude that power decrease with time under high temperature and current stress has a component related to increase of threshold current (see Figure 10) as

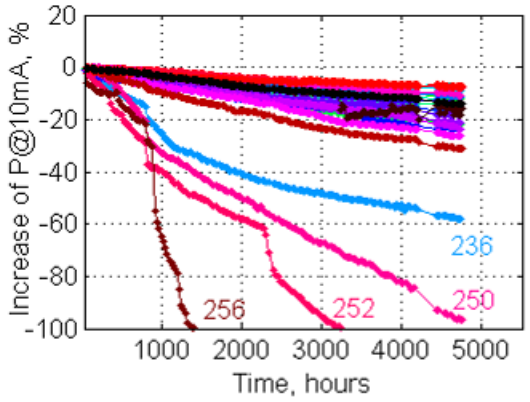

Fig. 9. Plots of changes in power at 10 mA driving current versus time for a set of 24 devices under current and temperature stress

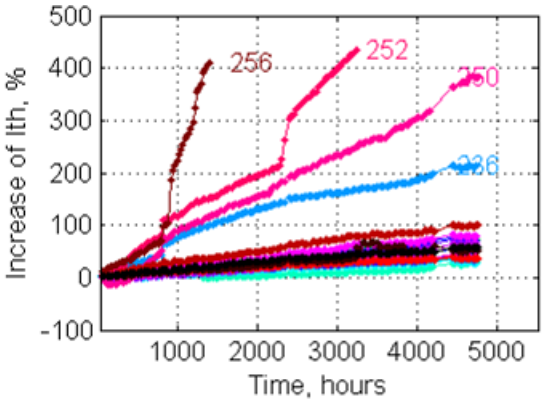

Fig. 10. Plots of changes in threshold current versus time for a set of 24 devices under current and temperature stress

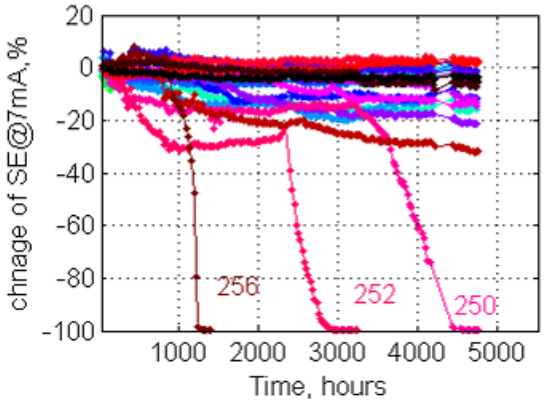

Fig.11. Plots of changes in slope efficiency near threshold current versus time for a set of 24 devices under current and temperature stress

well as related to decrease of slope efficiency (see Figure 11).

IV. ANALYSIS OF THE DEVICE STRUCTURE USING STATE OF THE ART NANO RESOLUTION TOOLS

As one can conclude from the results of the tests of the devices under current and temperature tests, there are device failures during accelerated life tests. Failure analysis is a very challenging, time consuming and costly investigation . One of scientific objectives of the ongoing projects on wafer fused longwavelength VCSELS is to establish the relationship between degradation in VCSEL device performance(e.g., reduction in output power, increase in threshold current, reduction in slope efficiency, electrical short circuits, etc.)

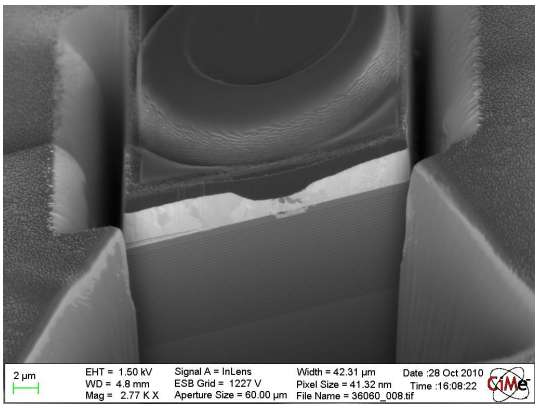

Fig.12. FIB milling around the sample to avoid deposition of the material from milled section

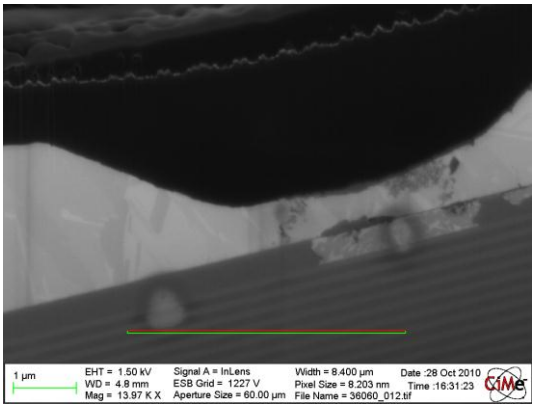

Fig. 13. SEM picture of the identified local diffusion of the gold in InP layer

and devices structure. Understanding this relationship will lead to the identification of specific failure modes and corrective actions for avoiding them, demonstrated using modified fabrication approaches. Achieving this scientific goal will entail the development and perfection of novel analytic tools, such as position-defined transmission electron microscopy (TEM), scanning electron microscopy (SEM) and cathodoluminescence (CL), which will also be useful in a broader area of nano-characterization of complex nano-devices and nano-systems. It should be emphasized that usually such characterization is implemented on micro-structured and nano-structured materials rather than devices, let alone devices fabricated in an industrial environment. The application of such characterization tools is, however, much more difficult and the linkage of the observations to failure modes is extremely complicated for the case of devices (e.g., accurate positioning of the observation area is essential) and needs to be advanced also as a technique by itself.

A feasibility study of the fabrication of focused ion beam (FIB) cross sections was already successfully performed in cooperation with CIME-EPFL. The results of the feasibility study are presented in Figure 12 and Figure 13. A functional VCSEL was wax-mounted on a standard aluminum holder and coated with a very thin gold layer to release the electrostatic charges. The milling around the sample was performed before the tomography was started in order to avoid the deposition of the material from the milled section. This gave an already important result, showing that some of the Au-coating was able to penetrate through the Pt barrier, as evidenced in Figure 14. Device tomography was performed by cutting through the sample every 0.5 um in an automatic mode. In this feasibility study, we were using the automatic mode, but the manual

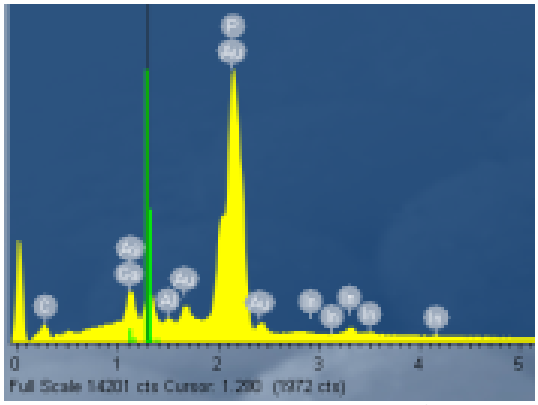

Fig.14. Energy Data Dispersive Scans (EDS) confirming the presence of gold that escaped the Pt barrier

mode in the vicinity of the tunnel-junction allow for getting enough resolution to identify the current confinement aperture , see Figure 16a . In Figure 15 we can notice the appearance of a gap in the structure.The gap could have occurred through the penetration of the etching agents during processing steps. The excess etching time of some layers in the VCSEL structure during processing may have unwanted results such as the GaAs under-etching along fused interfaces. Under-etching of GaAs may cause

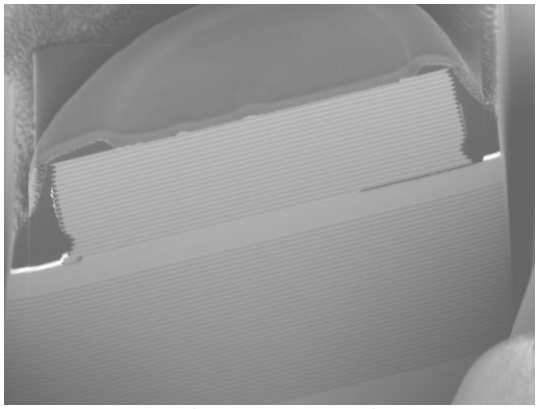

Fig.15. Detailed views of selected elements of the VCSEL structure

the partial delamination of the top DBR from the active structure. Figure 16b depicts the schematic of the top view of the structure, where the dashed line represents the top DBR mesa edge, the irregular shape is constructed from

the successive SEM/FIB images and the full gray line represents the image position depicted in Figure 15. If such a feature will be discovered to be common for wafer fused devices processed in this particular way, this may have a certain impact on VCSEL device reliability.

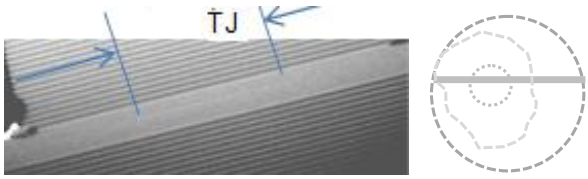

a b

Fig. 16a-detailed views of selected elements of the VCSEL structure. b-Schematic of the top views of the structure, where the dashed line represents the top DBR mesa edge, the irregular shape is constructed from the successive SEM/FIB images and the full gray line represents the image position depicted in Figure 15 b

A time and cost effective way of detecting hidden features at the fused interface is infrared images taken in sub threshold operation mode, as it is presented in Figure 17. A challenging task is to establish correlations between the contrast observed in infrared near field pictures like presented in Figure 17.Fig. and features observed during FIB tomography (Figure 18). Please note that in this paper the pictures in Figure 15, Figure 17 and Figure 18are not from the same devices.

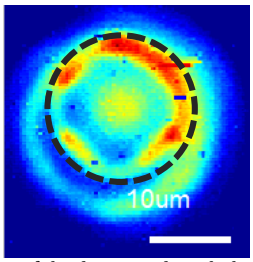

Fig.17. Near field picture of the device under sub threshold current pumping

Another power full tool for characterization of the device structure is cathodoluminescence (CL) [7]. Figure 18. and Figure 19 are presenting the type of images that one can acquire during failure analysis work using CL in long wavelength spectral region.

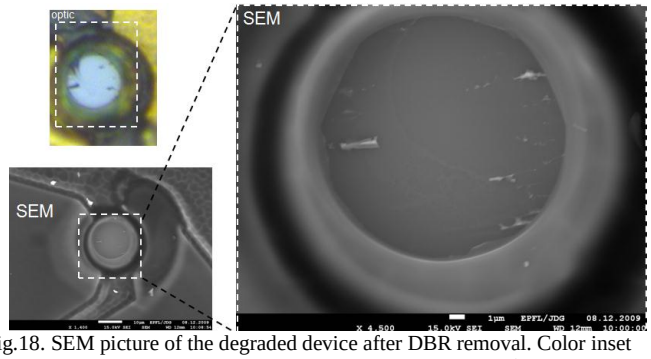

Fig.18. SEM picture of the degraded device after DBR removal. Color inset is the optical microscope picture. There are some residuals after top DBR removal

As one can see, the contrast of the image taken on the same sample in spectral rage of 1220 nm is different form the contrast taken in the range of 1330 nm. Please note the images in Figure 18 and Figure 19 are taken on a device from which top DBR was selectively removed, that is such a failure analysis tool is destructive, as well as cross section image acquisition using FIB.

V. DISCUSSION

As long wavelength VCSELs are emerging as attractive light-sources for replacing DFB lasers for a number of applications, and so far their reliability has always been questioned by the industry as no solid data supporting their reliability was demonstrated, the documented reliability and failure analysis data obtained on wafer-fused VCSELs are of big interest.

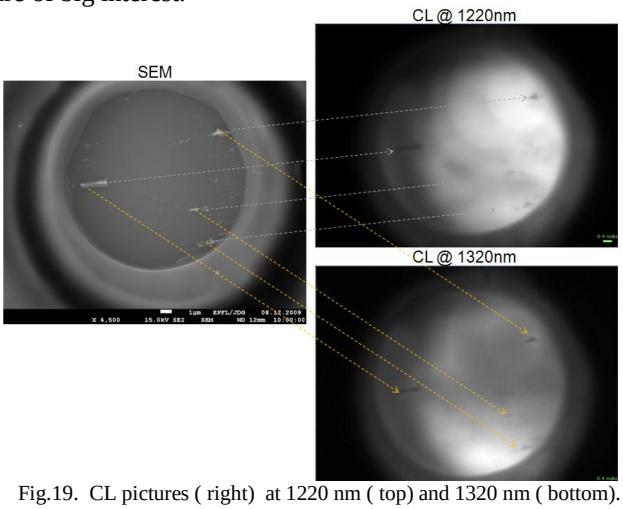

Fig.19. CL pictures (right) at 1220 nm (top) and 1320 nm (bottom).

Results show that VCSELs fabricated with the wafer-fusion technique and displaying high performance level, meet Telcordia generic requirement standards [7], thus making more actual the development of appropriate metrology tools for supporting the fabrication technology and further failure analysis .

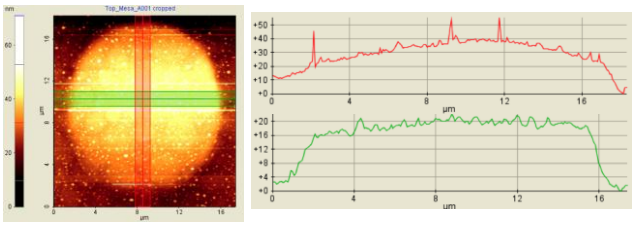

Fig.20. AFM picture at the fabrication step depicted in Figure 4b

Simulations [4] indicates that a very important operation parameter of side mode suppression ratio (SMSR) is sensitive to geometrical dimension of the structured tunnel junction layer. As one can see on Fig. 4 and Figure 20, the vertical and lateral configuration of the epitaxial layer in the vicinity of TJ aperture presents a complex surface with features at nano metric scale. One can demonstrate (it will be presented elsewhere) that a more detailed information on the 3 dimensional shape can be acquired using atomic force microscope(Figure 20) and state of the art optical confocal microscope (Figure 21)

The similar images can be acquired at all processing steps of structuring of the wafer in double fused fabrication process. It is possible even to take pictures of 100 % of the mesas, thus acquiring the necessary information for making statistical correlation between structuring and device performance.

It is very interesting to develop a confocal microscopy tool that will work at wavelengths at which VCSEL materials is transparent. This will allow to detect in the

structures the possible voids as depicted in Figure 15. The work now is in progress to establish correlation between the contrast seen in near field images as depicted in Figure 17 and contrast of the CL pictures (see Figure 19) from one hand, and the voids and trenches that was several times detected by FIB in the double fused VCSEL structures, as in Figure 15. As FIB investigation is destructive , lengthy and costly, a relative simple optical non destructive observation have the potential to become a powerful tool for detection nanometric size defects in a device structure at very early stage of characterization on wafer, thus decreasing the cost of final systems based on VCSELs.

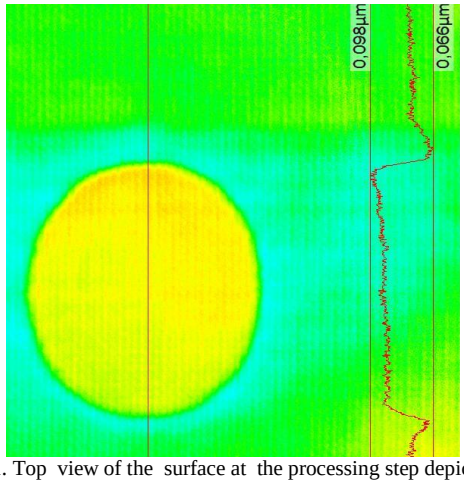

Fig.21. Top view of the surface at the processing step depicted in Figure 4b, taken using confocal optical microscope

Finally, even in the case there will be no structural defects detected in the VCSEL structure by any state of the art nano metrology tools, fabrication of the lamelas (see for TEM CL study presents an ultimate nanocharacterisation tool for revealing the changes in the QWs as a result of accelerated life tests.

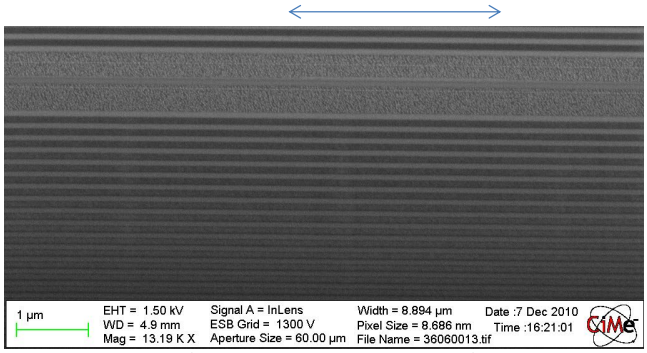

Fig.22. Example of high resolution SEM picture of the TEM lamella fabricated using FIB. Double arrow lined indicated the position of the current aperture defined by buried TJ. CL Figure 22 and TEM study of such a lamella is the subject of ongoing work and it will be presented elsewhere

VI. CONCLUSION

As the work on failure analysis is on its starting stage, the continuous open discussion on implementation of advance nano tools for characterization of the device structure within LPN, BX and international partnership will be crucial for success of this challenging task

ACKNOWLEDGMENTS

The author acknowledge the extremely productive working environment in EPFL, especially in LPN group and BeamExpress, that made possible to initiate and maintain research and development of the wafer fused long wavelength VCSELs.

REFERENCES

[1] Sirbu A, Iakovelv V, Mereuta A, et al. Wafer-fused heterostructures: application to vertical cavity surface-emitting lasers emitting in the 1310 nm band. Semiconductor Science and Technology. 2011;26(1):

[2] Kapon E, Sirbu A. Power-efficient answer. *Nature Photonics,VOL 3 JANUARY 2009; www.nature.com/naturephotonics*. pp.27-29..,

[3] Iakovlev V, Suruceanu G, Caliman a, et al. High-performance single-mode VCSELs in the 1310-nm waveband. *IEEE Photonics Technology Letters*. 2005;17(5):947-949

[4] Backer A, Odermatt S, Santschi R, et al. Transverse optical mode analysis of long-wavelength VCSELs for high single-mode power operation. *2008 International Conference on Numerical Simulation of Optoelectronic Devices (NUSOD)*

[5] Kapon E, Sirbu a, Iakovlev V, et al. Recent developments in long wavelength VCSELs based on localized wafer fusion. 2009 11th International Conference on Transparent Optical Networks. 2009:1-4

[6] Mereuta A, Suruceanu G, Caliman A, et al. 10-Gb / s and 10-km error-free transmission up to VCSELs. Optics Express. 2009;17(15):12981-12986.

[7] G. Suruceanu, A. Mereuta, J-C. Charlier , A. Sirbu, V. Iakovlev, A. Caliman, E. Kapon; Reliable Performance of 1.3µm Waveband VCSELs made by Localized Wafer Fusion; to be presented at ECOC2011, Geneve

[8] M. Merino, S. Sonderegger, A. Crottini, S. Collin, E. Pelucchi, P. Renucci, A. Malko, M.H. Baier, E.Kapon, J.D. Ganiere, B. Deveaud, Time-resolved cathodoluminescence of InGaAs/AlGaAs tetrahedral pyramidal quantum structures, Appl. Phys. B 84, 343–350 (2006),pp. 333-350.

Fundamental Issues in the Manufacturing of Nanoelectromechanical (NEMS) and Related Nanosystems

R. SINGH, G.F. ALAPATT, N. GUPTA, K.F. POOLE
Holcombe Department of Electrical & Computer Engineering and Center for Silicon Nanoelectronics Clemson University, Clemson, SC 29634, USA
srajend@clemson.edu

***Abstract* – Nanostructures in dimension below about 10 nm show interesting properties because of the effect of low-dimension physics. However, to utilize these properties in practice to commercialize NEMS and related nano-systems require an extremely precise manufacturing process. This paper briefly evaluates the fundamental issues involved in manufacturing the nano-scale systems.**

***Index Terms* – NEMS, manufacturing nanoelectronics.**

I. INTRODUCTION

A Nanoelectromechanical System (NEMS) may include electronic, optical, magnetic, mechanical, chemical, biological, energy sources, and sensing components. To qualify as a nano-scale system, at least one of these functional components should have a dimension in the range of 1 - 100 nm and a property arising due to the extremely small size should be used by the system [1]. However, significant advantages are seen only at dimensions below about 10 nm, where quantum confinement effects are observed [2]. In the last two decades the MEMS technology has evolved from device manufacturing with right yield and functionality to system integration of devices such as oscillators, tunable filters, and auto focusing devices [3]. Extending the MEMS systems to NEMS [4, 5] systems provide opportunities in new functional capabilities of the system as well as overall cost reductions. However, there are key fundamental manufacturing challenges that must be solved before practical realization of NEMS systems can be realized [6]. The objective of this paper is to address key NEMS and related nano-systems manufacturing issues.

II. ADVANTAGES OF NEMS OVER MEMS

NEMS is fundamentally a scaled down version of MEMS with many advantages and applications. Due to the nano-dimensional feature sizes of NEMS, they have fundamental resonant frequencies that exceed 1GHz, better Q factors, and the ability to measure even mass with a resolution of about 10^{-21} grams [4, 7, 8]. NEMS have also been used to detect viruses captured from liquids [9]. Due to inherent advantages of NEMS, it is possible to develop high-resolution sensors, integrated low-power computational systems, and mechanical resonators etc. Proof-of-concept devices have already been shown to work in research labs.

However no manufacturing technique exists that can be used for manufacturing of NEMS and related nanosystems.

III. FUNDAMENTAL PROPERTIES OF MATERIALS AT NANOSCALE

Properties of materials are significantly different at nano-dimensions in comparison to those in the bulk; a general trend is shown in Fig. l. For example, the melting point of gold changes by hundreds of degree Celsius as the particle size goes below 100 nm [10]. Sometimes, but not always, these different and new properties can be used for our advantages. For instance, a near defect-free material can be made when its dimension is below a critical dimension [11]. If these properties can be realized in practical devices, their applications will be immense.

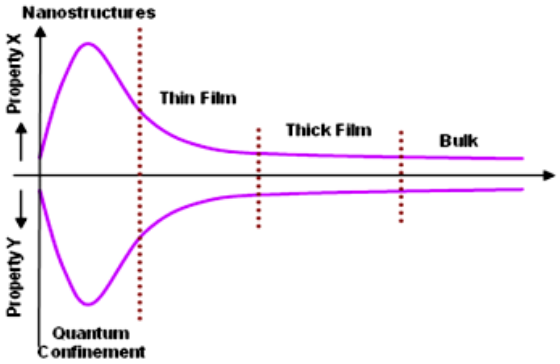

Fig.1. Properties of materials as a function of size.

IV. KEY FUNDAMENTAL ISSUES

To be able to manufacture nanoscale devices two fundamental considerations arise - nanostructure homogeneity and process variability [6]. Without considering these core issues, a proper manufacturing technique cannot be designed for a nanoscale device.

A. Nanostructure Homogeneity

The material used to make the nanostructure must be homogeneous in all directions, which implies that defects must be below an extremely small threshold. In addition, performance, reliability, and yield will be highest when the degree of homogeneity is high. This also involves reducing the variation in global and local thermal and residual stresses in the material [12,13].

B. Process Variability

Process variability is unavoidable during manufacturing

and it will result in unequal nano-dimensions in the device. The important factor here is that the amount of variability should be kept under control. ITRS data shows that, to achieve a 22 nm half pitch, the line width roughness of the resist material should be less than 1.4 nm and the process should be able to align the device with an error less than 5.3 nm, all with a statistical variability of three [14]. This is a non-trivial problem when manufacturing nano-dimensions as the dimension being manufactured is itself only less than 10 nanometers and the required tolerances for each processing step could be less than 1 nm. In Table I we have listed the lithography control that either has been achieved for a particular dimension or is expected in future generation of lithography generated critical dimensions.

Thus, the control of dimension size is extremely important in manufacturing NEMS based systems. In Fig. 2, Distribution A shows the allowed variation in dimension sizes for exploiting the special properties that can be obtained with NEMS based devices; however, during manufacturing, due to a lack of absolute control on the dimension, the resulting distribution will resemble the Distribution B shown in Fig. 2. Reduced values of full width at half maximum (FWHM) will provide better performance, reliability and yield of NEMS.

TABLE 1: CRITICAL DIMENSION CONTROL

Critical Dimension (nm)	Lithography Control Obtained and Predicted (3 σ) (nm)	Self Assembly Control Obtained (nm)
27	2.8	
20	2.1	
21		3 [15]
15	1.6	
10	1	
7	0.8	

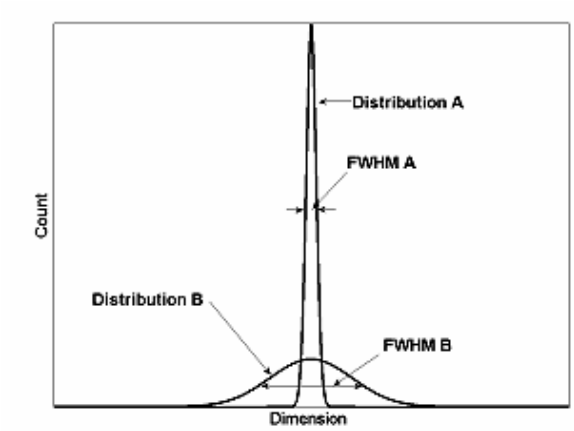

Fig. 2. Statistical distribution of dimensions (A = required and B = actually obtained).

V. CURRENT MANUFACTURING PROCESSES

To manufacture a NEMS in a commercially viable fashion, two technologies are currently under consideration. The first one is the standard top-down approach and the other is bottom-up approach. Both these prospective technologies are examined in this section.

A. Top-Down Approach

Lithography has been the standard technique for transferring patterns during IC manufacturing since its beginning. The minimum feature size, quantified as half-pitch has been steadily decreasing since the 1980s. Invention of better light sources and improved methods of exposure have driven this change. As of now, the half-pitch distance is 32nm and the light source used has a wavelength of 193 nm, which is about six times the half pitch distance [14]. Further decrease in the light source wavelength to 13.5 nm using an Extreme Ultra Violet source, has the possibility to decrease the half-pitch to the range of a few nanometers [14]. With lithography, patterns of half-pitch distance less than 10 nm have been created over a decade ago [16].

Apart from surface patterning abilities, manufacturing the NEMS will require profiling abilities along the vertical axis. The Deep Reactive Ion Etching process is currently able to make vertical profiles with aspect ratios greater than 50. Thus, the traditional, semiconductor industry, based manufacturing technology can make nano-dimensional structures for research purposes. However, issues relating to non-homogeneity and process control will determine if these devices can be successfully manufactured on a large scale without defect related problems. Recently, a defect on one of Intel's chip was discovered and analysts predict that this defect is going to cost Intel about $1 Billion [17]. Defects such as these will determine how successful a product will be.

B. Bottom-Up Approach

The bottom up approach involves devices using an atom-by-atom, approach and is called self assembly [18]. In our opinion the meanings of "Self Assembly" have been taken wrongly. True self assembly process involves programmed cell death or apoptosis [19]. The so called "self assembly" is actually selective chemistry. The atoms or molecules are forced by chemical, mechanical, or electrical means to assemble in a particular fashion. Researchers have often compared this method to the method employed in the development of an animal or a plant. This technology is relatively new and there is no commercially available system capable of performing self-assembly. To demonstrate the fundamental problems associated with "Self Assembly" we consider the growth of carbon nanotubes (CNTs). Scanning tunneling microscope (STM) is used to select CNT of desired length and diameter [15]. Even with the use of STM, CNTs of radius 21 ± 3 nm can be obtained. As shown in Table I, these results are not comparable to the lithography results. In a previous publication [20] we have investigated the basic nature of bio-driven systems and found that due to their fundamental nature of low growth rates as well as their high defect densities, it is highly unlikely that such systems can be used in semiconductor manufacturing.

VI. CONCLUSION

In this paper we have addressed the fundamental issues of nanostructure homogeneity and process variability for manufacturing NEMS and related nanosystems. The top down approach of lithography will continue to further scale down nano-dimension systems. However Bottom-up approach has fundamental limitations of high defect densities and low throughput.

REFERENCES

[1] R. Singh, H. Iwai, R.R. Tummala and S.C. Sun, ”Dielectrics for Nanosystems: Materials Science, Processing, Reliability, and Manufacturing: Proceedings of the First International Symposium,” The Electrochemical Society, 2004.

[2] R. Singh, P. Chandran, M. Grujicic, K.F. Poole, U.Vingnani, S.R. Ganapathi, A. Swaminathan, P.Jagannathan, H. Iyer, ”Dominance of silicon CMOS based semiconductor manufacturing beyond international technology roadmap and many more decades to come,” Semiconductor Fabtech, 30th edition, pp. 104-113, 2006.

[3] K. Lightman, and E. Mounier, ”MEMS Manufacturing Evolution - A MIG and Yole Developpement webcast,” February 17, 2011.

[4] X.M. Henry Huang, C.A. Zorman, M. Mehregany and M.L. Roukes, ”Nanoelectromechanical systems: Nanodevice motion at microwave frequencies,” Nature, vol. 421, pp. 496-496, 01/30/print. 2003.

[5] K.L. Ekinci and M.L. Roukes, ”Nanoelectro-mechanical systems,” Rev. Sci. Instrum., vol. 76, n.6, 061101, June, 2005.

[6] R. Singh, ”MEMS and NEMS Manufacturing,” Proc. MEMS and NEMS: New Technologies and Advanced Devices, MIGAS'10-13th Session, pp. 1-117, June 28, 2010.

[7] A. Husain, J. Hone, H.W.C. Postma, X.M.H. Huang, T. Drake, M. Barbie, A. Scherer and M.L. Roukes, ”Nanowire-based very-high- frequency electromechanical resonator,” Appl. Phys. Lett, vol. 83, n.6, pp. 1240-1242, 2003.

[8] Y.T. Yang, C. Callegari, XX. Feng, K.L. Ekinci and M.L. Roukes, ”Zeptogram-Scale Nanomechanical Mass Sensing,” Nano Letters, vol. 6, n.4, pp. 583-586, 2006.

[9] B. Ilic, Y. Yang and H.G. Craighead, ”Virus detection using nanoelectromechanical devices,” Appl.Phys.Lett., vol. 85, n.13, pp. 2604-2606, 2004.

[10] P. Buffat and J. Borel, ”Size effect on the melting temperature of gold particles,” Phys.Rev.A, vol. 13, pp. 2287, 06/1/. 1976.

[11] J. Narayan, "Critical size for defects in nanostructured materials,” J.Appl.Phys., vol. 100, pp. 034309-5, 08/01/. 2006.

[12] R. Singh, V. Parihar, K. F. Poole and K. Rajkanan, ”Semiconductor Manufacturing in the 21st Century,” Semiconductor Fabtech, 9th Edition, pp. 223-232, 1999.

[13] R. Singh & K. F. Poole, US Patent No.: US 6.569.249 Bl, Date of Issue: May 27, 2003.

[14] ITRS, ”Lithography Trends- ITRS 2009 Edition and 2010 Update,” 2010.

[15] O. Loh, X. Wei, C. Ke, J. Sullivan, and H.D. Espinosa, ”Robust Carbon-Nanotube-Based Nano-electro-mechanical Devices: Understanding and Eliminating Prevalent Failure Modes Using Alternative Electrode Materials. Small,” 7: pp.79-86. doi: 10.1002/ smll.201001166, 2011.

[16] S.Y Chou, P.R. Krauss, W. Zhang, L. Guo and L. Zhuang, ”Sub-10 nm imprint lithography and applications,” pp. 2897-2904, 1997.

[17] Market Place, ”Intel Finds Chip-Design Flaw,” Wall Street Journal, February 1, 2011.

[18] B. Amir Parviz, D. Ryan and G.M. Whitesides, ”Using self-assembly for the fabrication of nano-scale electronic and photonic devices,” Advanced Packaging, IEEE Transactions on, vol. 26, pp. 233-241, 2003.

[19] M. T. Heemels, R. Dhand and L. Allen, ”Foreword: Apoptosis”, Nature, vol. 407, pp 769-770, 2000.

[20] R. Singh, T. Boland, R. Mulye, G. Gaur, J. Steelman, D. Arya, N. Srinidhi, and P. Deshmukh, ”Prospects of Incorporating Directed Self Assembly into Semiconductor Manufacturing”, Semiconductor Fabtech, 36th edition, pp. 67-72, 2007.

Topological Insulator Materials and Nanostructures for Future Electronics, Spintronics and Energy Conversion

Valeriu KANTSER,
IIEN, ASM, str. Academiei 3/3, MD 2028, Chisinau, Republica Moldova
kantser@lises.asm.md

***Abstract* – Two fundamental electrons attributes in materials and nanostructures - charge and spin – determine their electronic properties. The processing of information in conventional electronic devices is based only on the charge of the electrons. Spin electronics, or spintronics, uses the spin of electrons, as well as their charge, to process information. Metals, semiconductors and insulators are the basic materials that constitute the components of electronic devices, and these have been transforming all aspects of society for over a century. In contrast, magnetic metals, half-metals, magnetic semiconductors, dilute magnetic semiconductors and magnetic insulators are the materials that will form the basis for spintronic devices. Materials with topological band structure attributes and having a zero-energy band gap surface states are a special class of these materials that exhibit some fascinating and superior electronic properties compared to conventional materials allowing to combine both charge and spin functionalities. This article reviews a range of topological insulator materials and nanostructures with tunable surface states, focusing on nanolayered and nanowire like structures. These materials and nanostructures all have intriguing physical properties and numerous potential practical applications in spintronics, electronics, optics and sensors.**

***Index Terms* – Topological insulator, nanowire, nanoribbon, bismuth selenide, magnetotransport, metal-insulator transition, , structure interfaces, thin film.**

I. INTRODUCTION

Depending on the electronic band structure and transport characteristics uncountable number of materials and substances can be classified quite simply in terms of their conductive behavior into one of three types — insulators, semiconductors and metals. More than three decade ago there was established that spin-orbit interaction (SOI) has an important pattern on band structure of solid state matter. Among different qualitative features induced by SOI the band inversion of electronic spectrum near the Fermi level has been discovered. Such type of electronic spectrum was identified in different type of semimetalic and narrow-gap semiconductors $Bi_{1-x}Sb_x$, $Pb_{1-x}Sn_xTe$, Bi_2Te_3, HgTe, $TlBiTe_2$ etc. In the context of low dimensional structure investigations the band spectrum inversion was shown to generate new type of interface gapless states with linear spectrum at the heterocontact boundaries. Last years investigations [1,2] have reopened the interest to materials with inverted band spectra. Due to new type of the symmetry break like that characteristic for the integer and fractional quantum Hall effects the electronic states was shown to have topological nature and materials have been named toplogical insulators (TI) (Fig.1). Thus in TI a new state of matter appear, distinguished from a regular band insulator by a nontrivial time-reversal topological invariant, which characterizes its band structure, and non-trivial interplay of charge and spin degree of freedom of band electrons. In results new physics and phenomena related to this states have greatly emerged. Several of such new TI properties are reviewed in the paper as well as some old observed properties of materials with band inversion. Many intriguing properties of TI can be ascribed to the existence of two-band gaplees Dirac electrons in its low-energy band structure. Actually, Dirac electrons with finit gap in materials have a long history starting from bismuth that has three-dimensional massive Dirac electrons in its band structure

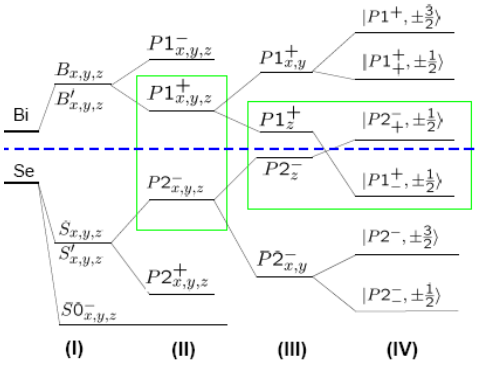

Fig.1. Band spectrum inversion – the origin of genesis of the topological insulator state

The most robust observable consequence of a nontrivial topological character of these materials is the presence of gapless helical edge states (interface states of inverted heterocontacts), whose gapless states is protected by time-reversal symmetry and is thus robust to perturbations that do not break this symmetry (Fig.2). Like the Hall state the "bulk" of the electron gas of TI is an insulator, but along its suface, the states can be gapless. Within a certain parameter range the surface states of TI are well described by a Dirac cone, allowing for parallels with graphene and relativistic physics, and prohibiting backscattering.. A prerequisite for such experiments is a highly tunable surface state which is decoupled from the residual bulk carriers. Despite considerable recent evidence of TI surface states in ARPES and STM , transport experiments are complicateddue to

significant parallel conduction through bulk states, limited surface density tunability, and uncertainty

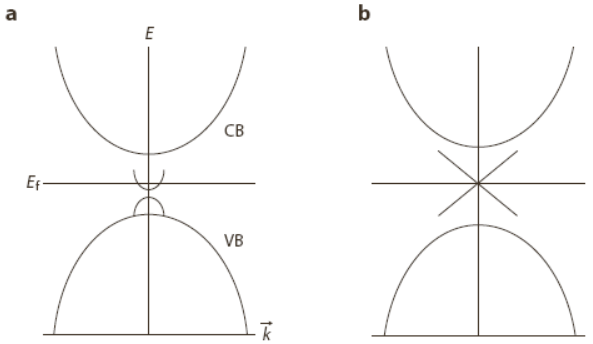

Fig.2 The electronic band structures of topological insulators, a new class of quantum matter with (a) a robust metallic state at the surface/edge and insulatingproperties in the bulk/surface, and (b) a conductive state at the surface or edge withzero gap and the same linear energy dispersion as graphene.

of the surface to bulk coupling. At the same time the spectrum and characteristics of topological surface states (TSS) depending on geometrical configuration can be manipulates by different factors: electrical and magnetic fields, strain and deformation ets. For this reason TI are being explored with a view towards applications, as a potential platform for tailoring nanostructures and nanomaterials properties. This topics cover the second part of the paper.

The last part of the paper deals with behavior of TSS if TI nanostructures in the nanowire and nanotube like configuration Some aspects of transport through TSS are discussed: anomalous Aharonov-Bohm conductance oscillations; magnetic quantum oscillations, edge accumulation and currents of moment.Thermoelectric aspect of TSS are discussed in the context of TI materials Bi_2Se_3 and Bi_2Te_3 knowing as the best thermoelectrics.

II. TOPOLOGICAL INSULATOR NANOLAYERED STRUCTURES

Along with the extensive researches of materials and properties of three- dimensional (3D) topological insulators (TIs),[1] attention has increasingly been paid on ultrathin films and nanostructures of such materials for enhanced effects and properties associated with the topological states of electrons [2,3] In the same line of thoughts, multi-layered structures constituted of TIs and normal band insulators, such as superlattices (SLs) or multiple quantum well (MQWs) of …Bi2Se3/ZnSe…have been attempted by the technique of molecular-beam epitaxy (MBE). In this part of paper we are using formal analogy of electromagnetic wave equation and Schrodinger equationin order to study the phenomenon of perfect tunneling (tunneling with unitary transmittance) in multilayered semiconductor heterostructure with band inversion and TSS. Using the two-band model of semiconductor we are showingthat such phenomenon can indeed exist, resembling all the interesting features of the analogous phenomenon in classical electromagnetism in which metamaterials (substances with negative materialparameters) are involved. We believe that these results can open up the way to interesting applications in which the metamaterial ideas are transfered into semiconductor domain.

The evolution of the topological states in dependence of layer thickness and others factors are highlighted for quantun well and superlattice structures based on $Bi_{1-x}Sb_x$, Pb1-xSnxTe, Bi2Te3 in the framework of two-band effective mass method. In the superlattice structures like PbTe/SnTe with layer thickness a and b respectively the state of the topological insulator can be realized (Fig.3).

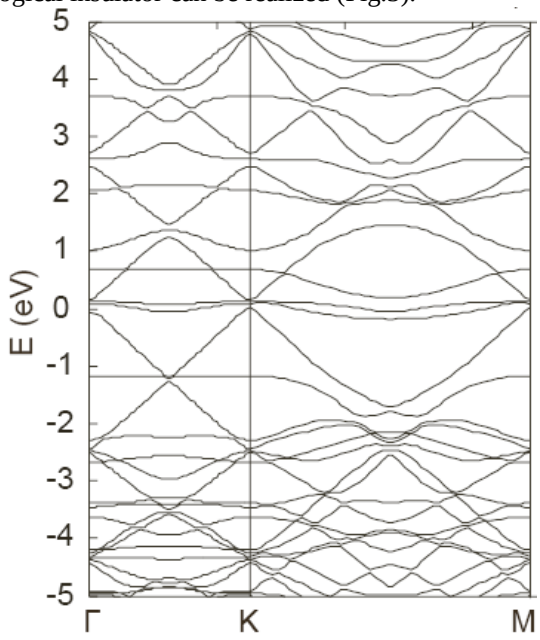

Fig.3. Topological extended states in PbTe/SnTe superlattice structures

The dispersion relation E(K), K being the crystal momentum, can be found from [4]

cosq(a+b) = cosh(Kb) cos(ka) –
$[(p^2 – r^2)/2pr]$ sinh(Kb) sin(ka).
Where $k==(E^2 – E^2gA/4)^{1/2}/hv$,
$K==(E^2gB/4 − E + V)^{1/2}/hv$,
r =(E – EgA)/2hvk,
p=(EgB/2 − E + V))/2hvK

The phase diagram of the band and topological insulator states are established in dependence of the semiconductor gaps and thickness. The gapless electronic states with Dirac like linear spectrum were revealed to occur when E_{gPbTe} * a = Eg_{SnT}e * b. Such superlattice structures can be considered as a new type of metamaterial of semiconductor layers and metallic sheets. The plasmonic and metamaterial characteristics of such layered structures are discussed. Flat-lens focusing of electrons on the surface of a topological insulator $B_{i2}Te_3$ is analysed. The early studied interface states in inverted heterocontact with magnetic ordering are reanalyzed in the context of recently discovered antiferromagnetic TI. The occurrence of interface ferromagnetism is demonstrated [5].

III. TUNABLE TOPOLOGICAL STATERS IN NANOWIRES

The surface contribution is easier to extract experimentally in TI nanowires , where the surface-to-volume ratio is more advantageous. In this case, introduction of a magnetic flux piercing the nanowire has allowed to successfully identify the Aharonov-Bohm effect caused by the surface state.

The TSS of cylindrical nanowires and topological insulator Bi2Te3 with cylindrical pores are studied. The developed recently low-energy approach for bulk Bi2Te3 is used to highlight TSS on the cylindrical surface. For the bulk

Bi2Te3 (Bi2Se3) TI near the Γ point of the surface Brilloiun zone, Hamiltonian has the form

$$H = \varepsilon_0(\boldsymbol{k})\sigma_0\tau_0 + M(\boldsymbol{k})\sigma_0\tau_z + A_1 k_z \sigma_z \tau_x + A_2 \tau_x (k_x \sigma_x + k_y \sigma_y).$$

Model parameters of four bands Hamiltonian (1) have been defined in the framework of kp theory by comparison with the ab initio calculations [7].

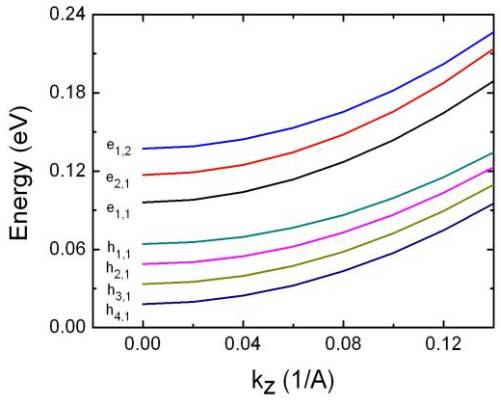

Fig.4. Electronic structure of TI Bi2Te3 nanowire with a radius of 10 nm.

The TSS forming inside the bulk gap (Fig.4) corresponds to one dimensional bands indexed by total angular momentum. For nanowire or nanopore of radius R, the wavefunction to vanish at the boundary r = R is required, which is automatically ensured by expanding in the orthonormal set of radial Bessel functions Jm or Ym with integer m. In comparison with gapless character os TSS of flat surface all TSS modes of cylindrical surface have a finite gap described qualitatively by relations Egs ~v/R (Fig.5). In results nanowire and nanopore composites of TI have distinct from layered ones pecularities and several are discussed in the paper [8]

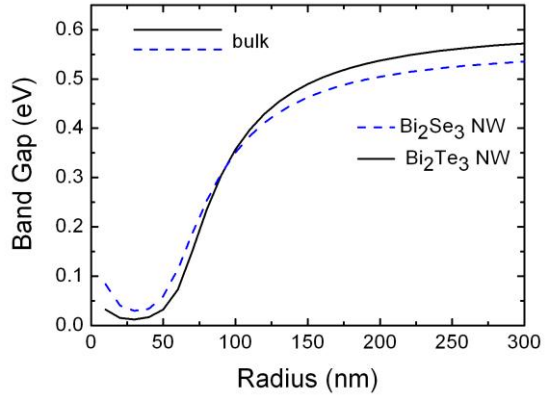

Fig.5 Dependence of the direct band gap at the Γ point of the topological insulator Bie2Te3 (solid line) and Bi2Se3 (dashed line) nanowires on radius.

IV. TOPOLOGICAL INSULATOR NANOSTRUCTURES AND ENHANCED THERMOELECTRICAL PERFORMANCE

Last years investigations of new electronic states of materials and structures - topological states - as well as new physics and phenomena related to this states, which are generated by new type of the symmetry break like that characteristic for the integer and fractional quantum Hall effects, have greatly emerged. In the Hall state the "bulk" of the electron gas is an insulator, but along its edge, electrons circulate in a direction that depends on the orientation of the magnetic field and these edge states are different from ordinary states of matter because they persist even in the presence of impurities. Recently it was established that the same "robust" conducting edge states could be found on the boundary band insulators with large spin-orbit effect, called topological insulators. In a topological insulator (TI), these surface states are protected, that is, their existence does not depend on how the surface is cut or distorted. Such type of topological states and its related effects (in particular quantum spin Hall effect) are analized for different type of semimetalic and narrow-gap semiconductor materials Bi1-xSbx, Pb1-xSnxTe, Bi2Te3, HgTe and their nanostructures.

Recent photoemission experiments reveal that Bi_2Te_3 and other like termoelectrics are a TI with a single Dirac cone on the surface, consistent with electronic structure predictions. In this part of the paper we try to analyze how new surface topological states could lead to improved thermoelectric performance. The physical system to be studied here is a thin film and nanowire of Bi2Te3. If the film is thin enough the surface states on both sides hybridize and open a gap [6].

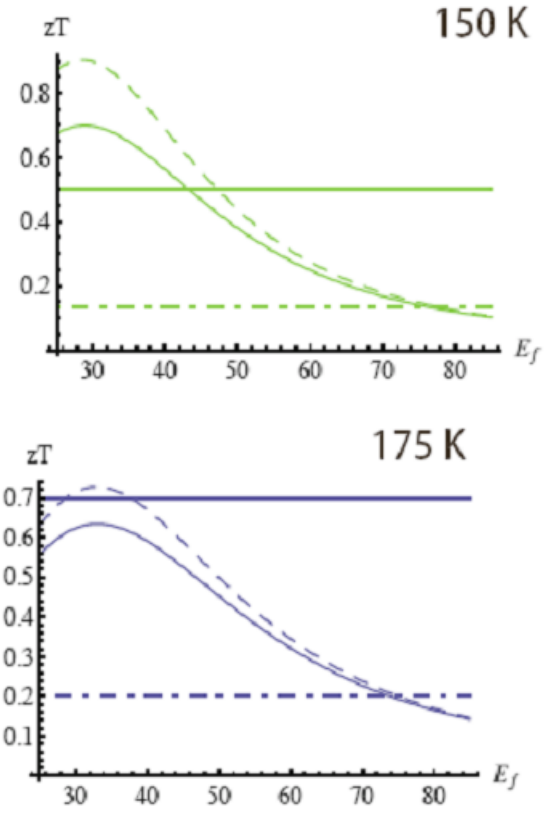

Fig .6. ZT for the thin film including bulk contributions at 150 and 175 Kelvin. The straight line in each figure corresponds to the best known ZT at the same temperature. Dashed line indicates the ZT for the surface states alone and Dashed-Dotted line indicates ZT for bulk Bi2Te3.

Although the film thickness required to open an observable gap for TI surface states (1-10 nm) is small, it is accessible with current growth techniques and very recently the hybridization gap has been observed by in-situ photoemission on thin films of Bi_2Se_3.Using the electron dispersion the in-plane (longitudinal for nanowire) transport coefficients for the surface states together with bulk ones were obtained and calculated as well as for the figure of

merit ZT (Fig 8) [9].

As is evident from Fig. 6, at temperatures below 150 K, which are important for several Peltier cooling applications, the thermoelectric performance of the topological insulator thin film is signifcantly enhanced because of the high ZT of the protected edge topological states. At low temperature the bulk contribution is smaller than the surface contribution so that the unknown chemical potential dependence of bulk properties is not too significant. Crucially, the gap in the hybridized surface mode band structure can be controlled by tuning the thickness of the film to get high ZT in a specific temperature range. The geometry of thin films is also very effective in reduction of phonon thermal conductivity, so there will be even larger enhancement for the topological insulator like $B_{i2}Te_3$ thin films. The same approach applies as well to nanowires.

V. CONCLUSIONS

Materials having signature of topological insulator are a special class of materials that exhibit fascinating and superior electronic, magnetic and optical properties compared to conventional materials. The discovery of topological insulator state of matter has generated great interest in the search for new classes of such materials, and some classical materials with band inversion spectra have been revisited. The phase diagram of the band and topological insulator states are established in dependence of the semiconductor gaps and thickness in Ti multilayered structures (materials A and B). The gapless electronic states with Dirac like linear spectrum were revealed to occur when $E_{gA} * a = Eg_B * b$. Such superlattice structures can be considered as a new type of metamaterial of semiconductor layers and metallic sheets.

Analysis of TI nanowires draw a consistent picture for the surface states inside the bulk gap, even for very thin nanowires: a one-dimensional (1D) electron waveguide with modes indexed by the half-integer total angular momentum j is formed, where each mode contains a rightand a left-mover. The spin direction is always tangential to the surface and perpendicular to the momentum.

In the simplest singlemodecase, the spin polarization of a right (left) moverhas a counter-clockwise (clockwise) orientation around the waist of the cylinder.

The cylindrical symmetry leads to a decrease of the band gap with decreasing of both NW radius and ratio bulk volume/surface area, while the confinement effect leads to an increase of the band gap at a rather small value of the NW radius.The observation of the Aharonov-Bohm oscillations in Bi_2Se_3 nanostructures provides important insights into the topological surface states.

The topological states of Bi_2Te_3 thin film surfaces hybridize and band gap is opened. In results, increased thermoelectric performance of film and nanowire can occur at low temperatures. The analyzed results may lead to a new method of improving the thermoelectric figure of merit for more efficient thermal-to electric energy conversion and thermal management of devices.

REFERENCES

[1] Y. Xia, D. Qian, D. Hsieh, L. Wray, A. Pal, H. Lin, A. Bansil, D. Grauer, Y. S. Hor, R. J. Cava, and M. Z. Hasan, Nat Phys 5 (6), 398 (2009)

[2] J. G. Checkelsky, Y. S. Hor,R. J. Cava, and N. P. Ong, PRL 106, 196801 (2011)

[3] Kentaro Nomura1 and Naoto Nagaosa, PRL 106, 166802 (2011)

[4] Kantser, V. G, Lelyakov, I. A. Malkova, N. M., Semiconductors vol. 26, p. 896-899, (1992)

[5] Kantser V., Malkova N, PhysRevB.56,p.2004, (1997)

[6] H. D. Li, Z. Y. Wang, X. Guo, T. L. Wong, N. Wang, and M. H. Xie, Appl Phys Lett 98 (4) (2011)

[7] B. A. Bernevig, T. L. Hughes, and S. C. Zhang, Science, vol. 314, pp. 1757, 2006.

[8] I.Begenari,V.Kantser NanoLett, in press

[9] P. Ghaemi, Roger S. K. Mong and J. E. Moore, cond-mat 1002.1341v2, (2010)

Functionalised AlGaN/GaN Heterostructures for Electronic Saccharide Sensing

A. SARUA[1], T. SCHULLER[1], M. KUBALL[1], S. FLOWER[2], T. D. JAMES[2], J. FOSSEY[3], Jo DAS[4], S. DEGROOT[4], M. GERMAIN[4]

[1] *H.H. Wills Physics Laboratory, University of Bristol, Bristol, BS8 1TL, United Kingdom*

[2] *Department of Chemistry, University of Bath, Bath, BA2 7AY, United Kingdom*

[3] *School of Chemistry, University of Birmingham, Birmingham, B15 2TT, United Kingdom*

[4] *Interuniversity Microelectronics Center, Leuven, 3001, Belgium*

a.sarua@bristol.ac.uk

***Abstract* – A novel field-effect sensor device based on functionalised AlGaN/GaN heterostructure was developed for sensing of various saccharides in solutions. Device was functionalized with a boronic acid chemical receptor, a thiol group and alkane chain linker. Electrical measurements on fabricated devices were performed to demonstrate their response to buffered saccharide solutions (fructose, galactose and glucose) of varying concentrations. The obtained results provide basis for the development AlGaN/GaN-based electronic sensor devices incorporating boron receptor chemistry.**

***Index Terms* – GaN, AlGaN, sensors, HFET, saccharide.**

I. INTRODUCTION

In recent years there has been large interest for use of GaN based structures for various electronic and optical devices for telecom and solid-state lighting markets. However, AlGaN/GaN heterostructures have also shown great potential for field-effect based electronic chemical and biochemical sensors [1,2,3]. In these structures formed two dimensional electron gas (2DEG) at the interface between the AlGaN and GaN layers provides high density carriers confined near the surface, which has been widely exploited for RF device applications. Together with excellent chemical and thermal stability of these materials this makes them good candidates for variety of chemical sensing applications.

To functionalize GaN structures various approaches were explored, typically silane [4] and alkene [5] groups were involved to create a linker between receptor and surface. However, both these approaches have limitations, requiring additional extensive processing or indirect bonding to surface via less stable oxides. On other hand, thiol based attachment is known to provide straight-forward bonding either directly to semiconductor surfaces or on thin gold films [6, 7] and is a possible alternative to existing methods.

In-situ detection and analysis of saccharides is of great importance for a variety of domestic and medical applications. However, accurate, reliable and cost-effective electronic saccharide sensors are not readily available. Typically, electronic saccharide sensors are fabricated via the immobilisation of a specific enzyme [8]. However, such devices suffer from high fabrication costs and complexity as well as reduced stability of the finished devices [9]. Alternatively, boronic acid receptors have been shown to bind to saccharides effectively via covalent interactions in aqueous media [10,11,12].This lead to development of non-electronic fluorescence sensor approaches based on carbohydrate sensing “click-fluor” [13].

In this paper, we present a novel electronic saccharide sensor structure using boronic acid functionalised AlGaN/GaN heterostructure and thiol linker for proof-of-concept demonstration of specific chemical sensors based upon field-effect device structures.

II. EXPERIMENTAL DETAILS

AlGaN/GaN heterostructures were grown on Si(111) substrates by metal organic chemical vapour deposition. Thickness of GaN layer was about 2.5 μm, covered with 20 nm of $Al_{0.25}Ga_{0.75}N$ layer. Square die of 0.5 x 0.5 cm were cleaved from the wafer. Standard Ti/Al/Ti/Au ohmic contact pads, separated by 2mm, were deposited by e-beam evaporation through a shadow mask and then annealed at 850 °C for 30s under nitrogen ambient. Subsequently, a NiCr/Au layer was deposited in the space between contacts to allow receptor attachment and act as a Schottky gate. On each die a pair of identical devices was fabricated, to act as a reference and a functionalised active sensor device. Devices were mesa-isolated via scribing.

Reference device was fully masked as was the most of active device structure, apart of rectangular functional area between ohmic contacts. Die was then placed in a 5 mM solution of prepared by chemical synthesis boronic acid thiol (BAT) product in ethanol for 24 hrs. Mask was then removed and contact angle measurements were used to confirm functionalisation of the prepared surfaces.

III. RESULTS AND DISCUSSION

Figure 1 shows a schematic diagram of a device structure, receptor and thiol linker (BAT) and functionalisation steps. In comparison to organosilane functionalisation [4], thiol based method benefit from much simpler chemistry and fewer fabrication steps, and can be used to bond receptors to thin gold layers or directly to the surfaces. While alkene based linkers are also offer a simple pathway for GaN fuctionalisation [5], the method relies on use of hydrogen terminated GaN surface, which is very unstable and have

very limited life time.

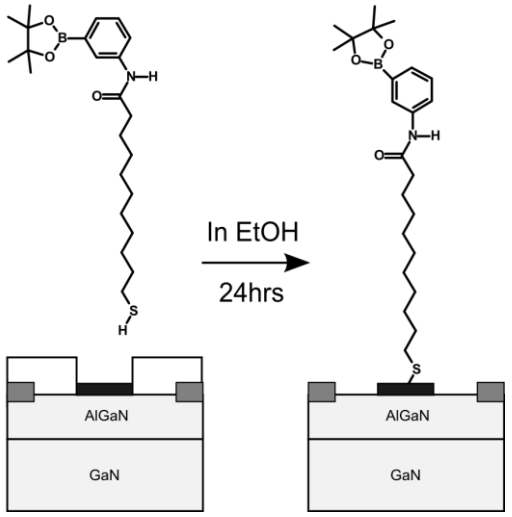

Fig. 8. Schematic diagram of a functionalised AlGaN/GaN sensor device. The BAT receptor molecule bonds to the gold layer between the Ohmic contacts.

Figure 2 displays measured sensor current, *I*, in the active functionalised device before and after exposure to analytes: a solution of 1M fructose in the buffer. Also given is a comparison with the reference device, which experiences only a negligible change in current in reaction to the analyte.

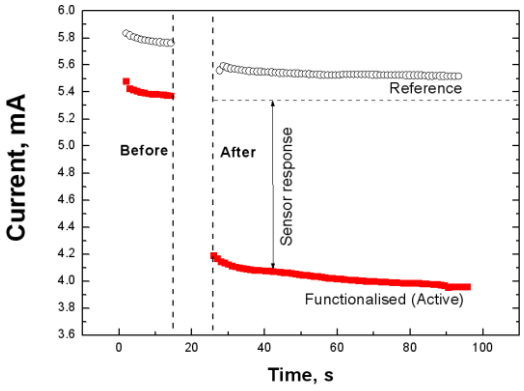

Fig. 2. Electrical response of reference and active devices exposed to 1M fructose solution. Time interval between 15 and 25 seconds corresponds to deposition of analyte (no electrical data).

Following confirmation of sensor activity, the device was exposed to buffered saccharide solutions of fructose, galactose and glucose with concentrations between 1M and 0.1M. The detected response was greatest for fructose, followed by galactose and glucose was the weakest, which follows the established stability order for simple boronic acids [12,14]. This result confirms that observed sensor response is due to specific interaction between the boronic acid and the saccharide molecule rather than some secondary interactions with one of the other groups present in BAT.

For all three analyte concentrations above 0.8M saturation behaviour was observed for the sensor device. In the low concentration region, only fructose can be reliable detected below 0.2M. Generally, despite non-optimised process parameters, sensitivity of the fabricated structures was compatible with non-electronic chemical method described in Ref. 13. During electrical measurements devices underwent several hundred cycles of analyte deposition and subsequent washing and cleaning without any significant loss in response, which suggest robust GaN surface functionalisation using thiol based linkers.

Necessary improvements in the low concentration detection limit (below 0.1 M) for sugars is essential for future applications of sensor devices and can be achieved via further optimisation of fabrication process and by modification in the BAT receptor design.

IV. CONCLUSION

Here we demonstrated a proof-of-concept for saccharide electronic sensor device based on AlGaN/GaN field effect structure. A novel approach of receptor design and functionalisation based on preassembled by chemical synthesis boronic acid receptor and thiol-alkane linker (BAT) allowed to achieve specific sensitivity of fabricated structure to different saccharide concentrations in solutions. This offers a way for robust and simple functionalising of GaN based structures not only for saccharide detection, but also by replacing boronic acid with other molecular receptors to a wider range of detected species.

ACKNOWLEDGMENTS

The authors would like to thank Mike Redwood for his technical assistance, as well as Great Western Research and the EPSRC for funding.

.

REFERENCES

[1] R. Neuberger, G. Müller, O. Ambacher, and M. Stutzmann, "High-Electron-Mobility AlGaN/GaN Transistors (HEMTs) for Fluid Monitoring Applications" phys. stat. solidi (a), 185, pp. 85–89, 2001.

[2] S. C Hung, B. H. Chou, C. Y. Chang, C. F. Lo, K. H. Chen, Y. L. Wang, S. J. Pearton, Amir Dabiran, P. P. Chow, G. C. Chi, F. Ren, "Minipressure sensor using AlGaN/GaN high electron mobility transistors", *Appl. Phys. Lett.* 94, p. 043903, 2009.

[3] B. S. Kang, B. S, H. T. Wang, T. P. Lele, Y. Tseng, Y. F. Ren, S. J. Pearton, J. W. Johnson, P. Rajagopal, J. C. Roberts, E. L. Piner, K. J. Linthicum, "Prostate specific antigen detection using AlGaN/GaN high electron mobility transistors", *Appl. Phys. Lett*., vol.91, no.11, pp.112106-112106-3, Sep 2007.

[4] R. M. Petoral, G. R. Yazdi, A. L. Spetz, R. Yakimova and K. Uvdal "Organosilane-functionalized wide band gap semiconductor surfaces", *Appl. Phys. Lett*. 90 (22), pp. 223904 - 223904-3, 2007.

[5] H. Kim, P. E. Colavita,, K. M. Metz, B. M. Nichols, B. Sun, J. Uhlrich, Xiaoyu Wang, T. F. Kuech and R. J. Hamers "Photochemical Functionalization of Gallium Nitride Thin Films with Molecular and Biomolecular Layers" *Langmuir 22* (19), pp. 8121-8126, 2006.

[6] T. Ishida, M. Hara, I. Kojima, S. Tsuneda, N. Nishida, H. Sasabe, and W. Knoll "High Resolution X-ray Photoelectron Spectroscopy Measurements of Octadecanethiol Self-Assembled Monolayers on Au(111)" *Langmuir 14* (8), pp. 2092-2096, 1998.

[7] M. D. Porter, T. B. Bright, D. L. Allara, C. E. D. Chidsey "Spontaneously organized molecular assemblies. 4. Structural characterization of n-alkyl thiol

monolayers on gold by optical ellipsometry, infrared spectroscopy, and electrochemistry" *J. Amer. Chem. Soc. 109* (12), pp. 3559-3568, 1987

[8] K. Matsumoto, H. Kamikado, H. Matsubara and Y. Osajima, "Simultaneous determination of glucose, fructose and sucrose in mixtures by amperometric flow injection analysis with immobilized enzyme reactors" *Anal. Chem*. 60, pp. 147–151, 1988.

[9] S. Park, H. Boo, T. Dong Chung, "Electrochemical non-enzymatic glucose sensors" *Analytica Chimica Acta*, 556, pp. 46-57, Jan 2006

[10] T. D. James, S. Shinkai, "Artificial receptors as chemosensors for carbohydrates" *Top. Curr. Chem*. 218, pp. 159-200, 2002.

[11] T. D. James, M D. Phillips, S. Shinkai, "Boronic Acids in Saccharide Recognition" RSC Publishing: Cambridge, UK, 2006

[12] D. G. Hall, "Structure, Properties, and Preparation of Boronic Acid Derivatives. Overview of Their Reactions and Applications, in Boronic Acids: Preparation and Applications in Organic Synthesis and Medicine", ed. D. G. Hall, Wiley-VCH Verlag GmbH & Co. KGaA, Weinheim, FRG., 2006.

[13] D. K. Scrafton,, J. E. Taylor,, M. F. Mahon,, J. S. Fossey and T. D. James, "Click-fluors": Modular Fluorescent Saccharide Sensors Based on a 1,2,3-Triazole Ring" *The Journal of Organic Chemistry 73* (7), pp. 2871-2874, 2008.

[14] J. P. Lorand, J. O. Edwards, "Polyol Complexes and Structure of the Benzeneboronate Ion" *J. Org. Chem.* 24, pp. 769-774, 1959.

More Efficient Nanostructured Material for Noncontact Body Temperature Measurement

Anatolie CASIAN, Ion BALMUS, Viorel DUSCIAC, Veaceslav NICIC
Technical University of Moldova
acasian@mail.utm.md

***Abstract* – Existing methods of human body temperature measurement are briefly analyzed. The opportunities of different type of medical thermometers are described. The advantages of the latest infrared skin thermometers and of new thermal imaging systems are evidenced. The thermoelectric power factor which determines the sensitivity of infrared detectors is modeled in highly conducting nanostructured organic crystals. The optimal parameters that ensure the highest value of the power factor at room temperature are evaluated. It is shown that in existing crystals of tetrathiotetracene-iodide after the optimization of carriers' concentration it is possible to obtain higher values of power factor than in the best known inorganic materials. It is proposed to use these crystals as more efficient material for sensitive elements of thermoelectric sensors in infrared skin thermometry.**

***Index Terms* – infrared skin thermometer, nanostructured organic crystals, thermoelectric power factor, thermoelectric infrared sensor.**

I. INTRODUCTION

From the point of view of daily uses temperature is connected with the quality of thermal energy contained in different objects and it serves to express quantitatively the common notions of hot and cold. The simplest way to sense this is to touch the given object and to decide, if it is warm, hot or cold. But quantitatively, temperature is measured with thermometers. The notion of temperature is defined for objects that are in thermal equilibrium, or for the parts of them that are in local thermal equilibrium, i.e. in such state in which no further changes occur. These objects or their parts must contain a big number of constituent atoms or molecules. If there is no heat transfer between two objects (for example, the object and the thermometer), both objects have the same temperature. There are different temperature scales. Most of countries use the Celsius scale (°C) for temperature measurements with 0°C for freezing point of distilled water and 100°C for boiling one at the sea level. Celsius scale has the same value of 1 degree as the Kelvin scale (K) used by scientists, but fixes its null point at 0°C = 273.15K, the freezing point of water. A few countries, including the United States, use also the Fahrenheit scale for different purposes. It is a historical scale on which water freezes at 32 °F and boils at 212 °F.

In the science, the statistical thermodynamics gives a formal definition of temperature [1, 2]. Temperature is a measure of statistically average kinetic energy of the particles forming a material object. This definition includes the notion of number of particle degrees of freedom. A simple particle (an atom or a molecule as material point) has three degree of freedom. To average kinetic energy of a simple particle it corresponds $(3/2)k_0T$ (1/2 for each degree of freedom), were T is the temperature, and k_0 is the Boltzmann constant

This work was supported by the Project No. 104 b/s of Academy of Sciences of Moldova.

Thus, temperature is temperature is related to the motion of the particles that constitute the sample. But also it means that the sample contains a big number of particles.

The human body temperature is a very important parameter which determines into a large measure the state of man health. Therefore it is necessary to have good methods and adequate devises for quick and reliable measurement of temperature. Since the temperature scale has been established and the notion of normal body temperature was introduced a variety of methods and devices for temperature measurement have been applied. During a long time the thermometers with mercury into a glass tube were the most used. Although such thermometers are simple in use, they are dangerous for the environment, because the glass can break, the mercury can spill, but it is known that the mercury vapors are poisonous. Therefore later the mercury was replaced by other not poisonous liquids. Nevertheless, the glass can break and it is not conveniently.

Unfortunately, until now an ideal method and an ideal thermometer are not yet found, although body temperature measurement is very important not only for correct diagnosis, but also for further investigation and treatment of patients. In pediatrics the rectal measurement is still considered as the most precise, although it has several disadvantages as discomfort, emotional distress, requirement of significant time for measurement, possibility of complications connected with perforation or introduction of infections [3]. As a result of these disadvantages and of recommendations of UK National Institute of Health and Clinical Excellence (NICE) general guide [4] some medical institutions have abandoned rectal measurements.

Sublingual cavity and axillae measurements are more convenient than rectal ones, but are less precise. Relatively new alternative for body temperature measurements are tympanic and infrared skin thermometers. The first measures by the help of a special sensor the quantity of infrared heat produced by tympanic membrane. The measurements are also not sufficiently precise. The infrared skin thermometer is the latest developed method of body temperature

measurement. It measures the quantity of infrared heat produced by temporal arteries. Only a few studies have been carried out on this subject. Harvard Medical School, USA has proven that Exergen Corporation's Infrared temporal artery thermometer is more accurate than infrared ear thermometry and more accurate than even rectal thermometers in responding to change in fever.

In the last time different thermal imaging systems that provide a thermographic image of human body temperatures (typically the face) at a distance obtain more and more applications. The IR-160R Automated Body Monitoring System has temperature measurement accuracy of 0.25 degrees C. An advantage of this noncontact temperature measurement is the exclusion of contamination spreading, that is possible by contact methods. A Japanese electronic firm NEC/Avios has launched in January 2011 a mirror with a system which measures the temperature distribution on the human face, determines the average temperature and on this base calculates the body temperature. But it is clear that in order to increase the effectiveness of these measurements it is necessary to have good infrared sensors.

The aim of this paper is to propos optimized parameters of a nanostructured organic material as more efficient sensitive element of thermoelectric detectors of infrared radiation for sensors of temperature measurements.

II. THERMOELECTRIC SENSORS OF INFRARED RADIATION

Thermoelectric detectors are largely used for the detection of infrared radiation in the long wave lengths diapason of spectrum where the photoelectric detectors are not sensitive, usually for wave lengths longer than 1.5 μm. In the same time, it needs to note that the Earth atmosphere has windows of transparency only in several intervals of infrared spectrum for wave lengths between 2,0 – 2,5 μm, 3,2 – 4,2 μm, 4,5 – 5,2 μm and 8,0 – 13,5 μm. In order to increase the detector sensitivity it is important to collect the infrared radiation from the possible larger spectral interval. Also, it is very necessary to have more efficient thermoelectric materials. Intensive investigations are made in this direction in many scientific laboratories.

The main parameter that determines the opportunity of a material to be used in detectors of infrared radiation is the thermoelectric power factor $P = \sigma S^2$, where σ is the electrical conductivity and S is the thermopower (Seebeck coefficient). New materials are needed with as higher as possible values of the thermoelectric power factor P. One would think that for this it is sufficiently to increase in the same material the electrical conductivity and the thermopower. But these requirements are contradictory. In ordinary materials the increase of σ leads to the decrease of S and vice versa. In order to overcome this situation it needs to search and investigate new materials with more complicated electronic and phonon spectra.

The best bulk thermoelectric material Bi_2Te_3 has values of thermoelectric power factor $P \sim 40$ μW/cm.K^2 near room temperature. Recently, high values of power factor have been measured in low-dimensional quantum well superlattice structures [5]. For example, in [6] values of power factor of the order of 62-66 μW/cm.K^2 were obtained in *n*-PbTe/PbEuTe quantum wells which are almost 1.7 times higher than that measured in Bi_2Te_3. Theoretically [7, 8] even higher values of the power factor are expected in the material of such quantum wells. However, the technology to product such structures is complicated and expensive.

In the last years organic materials attract more and more attention as materials with more diverse properties and less expensive. Already it exists a new generation of organic based electronic devices. It was also shown [9, 10] that among organic compounds it is possible to find materials which will have considerably increased thermoelectric power factor. Such materials unite together the advantages of low-dimensional quantum systems and of multi component materials with more diverse and complicated interactions.

Our latest investigations [11, 12] have shown that the quasi-one-dimensional nanostructured organic crystals of tetrathiotetracene-iodide can have very promising thermoelectric properties. In this paper we will model the power factor in dependence of crystal parameters in order to find those that ensure the highest value.

III. CRYSTAL MODEL

The quasi-one-dimensional organic crystals of tetrathiotetracene-iodide, TTT_2I_3 are formed of segregate chains or stacks of planar molecules of tetrathiotetracene TTT, and iodine. The distance between molecules along chains is two times smaller than between different chains. Therefore the overlapping of electronic wave functions of TTT molecules along chains is big, but between chains is negligibly. Only TTT chains are conductive because the iodine electronic wave functions are strongly localized. The conduction mechanism along chins is of band type, but between chains it is of hoping type. The latter gives small contribution and is neglected. The charge carriers are holes. The TTT_2I_3 crystals can be considered as nanostructured material, because the distance between conducting chains is of the order of one nanometer.

The parameters of TTT_2I_3 are: the mass of molecule $M = 6.5 \cdot 10^5 m_e$ (m_e is the mass of free electron), the lattice constants a =18.35 Å, b = 4.96 Å, c = 18.46 Å (the direction of chains is along b), the sound velocity along the chains $v_s = 1.5 \cdot 10^5$ cm/s, the carriers concentration for ordinary stoichiometric crystals $n = 1.2 \cdot 10^{21}$ cm^{-3}. The electrical conductivity along the chains σ at room temperature varies in the crystals grown from solution between 800 and 1800 Ω^{-1}cm^{-1} [13], whereas for crystals grown from gas phase, which are purer and more perfect, it varies between 10^3 and 10^4 Ω^{-1}cm^{-1} [14]. The electrical conductivity is very sensible to crystal impurities and defects. The thermopower S along stacks is less sensitive to crystal impurities and defects and at room temperature varies between 40 and 45 μV/K for crystals grown from solution [13] and $S = (36 \pm 3)$ μV/K for those grown from gas phase.

In order to describe the thermoelectric properties of TTT_2I_3 crystals we will apply the model presented in [15]. The electronic states are described in the tight binding and nearest neighbor approximations. So as the conduction band width is not very large, the effective mass approximation is not applicable and the variation of electron and phonon quasi-momentums into the whole Brillouin zone is taken into account. The dispersion law for holes is taken in the usual for tight binding approximation cosinusoidal form, but for longitudinal acoustic phonons the exact one-dimensional expression is used.

The model takes into account simultaneously two electron-phonon interactions and also the scattering of carriers on impurities and defects. It is important, because under certain conditions between both electron-phonon interactions the interference can take place. The first interaction is similar to that of deformation potential, and the second is polaron similar, but the induced polarization is considered. Due to the interference, both electron-phonon interactions considerably compensate each other for a narrow strip of states in the conduction band. As a result, the relaxation time of carriers as a function of carrier energy takes the form of Lorentzian with rather pronounced maximum.

Such behavior of relaxation time will ensure simultaneously high values of electrical conductivity and increased values of the thermopower. This situation is favorable to expect a growth of the thermoelectric power factor *P*.

IV. MODELING OF THE THERMOELECTRIC POWER FACTOR

The linearized kinetic equation for no equilibrium holes distribution function has been deduced. Near room temperature the scattering of carriers on acoustical phonons can be considered elastic. In this case the kinetic equation is solved exactly and, replacing the phonon distribution function by its high-*T* limit, the following expression for the relaxation time is obtained

$$\tau(E) = \frac{\hbar M v_s^2 w^2 [E(\Delta - E)]^{1/2}}{2a^2 k_0 T w'^2 \gamma^2 [(E - E_0^{s,p})^2 + 4w^2 \gamma^{-2} D]}, \qquad (1)$$

where *w* is the energy transfer of a carrier from a molecule to the nearest one along the chains, *E* is the carrier energy, $0 \le E \le \Delta$, Δ is the width of the conduction band, $\Delta = 4w$, w' is the derivative of the transfer energy *w* with respect to the intermolecular distance, k_0 is the Boltzmann constant, $\gamma = 2e^2\alpha_0 / (a^5 |w'|)$ is the ratio of amplitudes of above mentioned electron-phonon interaction mechanisms, *e* is the carrier charge, α_0 is the average polarizability of molecule, $E_0 = 2w(\gamma \pm 1)/\gamma$ is the resonance energy which corresponds to the maximum of $\tau(E)$, when $0 \le E_0 \le \Delta$. The dimensionless parameter *D* in Eq. (1) describes the scattering of carriers on impurities. It is proportional to the linear concentration of impurity and may be made much less than unity, if the crystal purity is sufficiently high.

The parameter γ is not known in TTT_2I_3 crystals, because the molecule polarizability is not known. We will take γ = 1.6, that corresponds to α_0 = 42 Å^3. For comparison, in antracene α_0 = 25Å^3, but TTT molecule is bigger and α_0 must be greater too. The dependence of relaxation time on carrier energy is presented in Fig.1 for γ = 1.6 and different degrees of crystal purity (*D* = 0.2, 0.1 and 0.05). The dash-dotted line corresponds to the case, when only the first electron-phonon interaction mechanism is applied. It is seen that in this case the relaxation time is a very smooth function of energy with a small maximum of the order of 0.5×10^{-14}s. When both electron-phonon interactions are included, the relaxation time obtains a more pronounced maximum which grows with the decrease of *D* and becomes even sharp at *D* = 0.05 (solid line in Fig.1). This sharp maximum corresponds to the purest crystal and is more than 15 times higher than that of dash-dotted line. The maximums of relaxation times determine maximums of electrical conductivity as functions of Fermi energy or carriers' concentration. And sharp dependence of relaxation time on energy ensures simultaneously increased values of the thermopower.

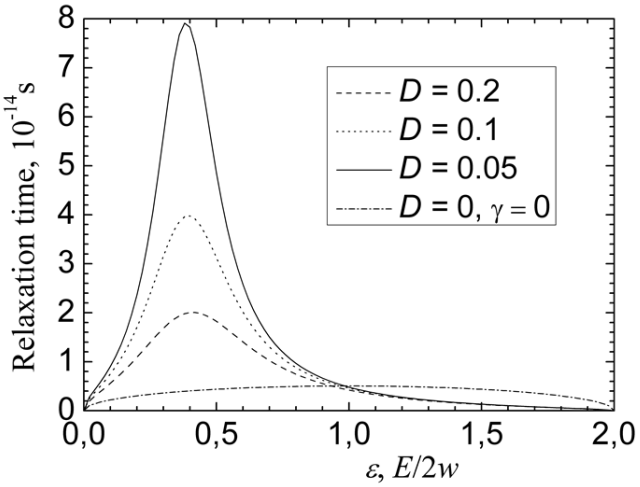

Fig. 1. Relaxation time as a function of energy in the conduction band. The dash-dotted line is for only first interaction, when *D* = 0, γ = 0.

The expression for the power factor *P* is presented through the transport integrals R_n as follows

$$P = R_1^2 / (e^2 T^2 R_0), \qquad (2)$$

where

$$R_n = -\frac{2e^2 az}{\pi\hbar^2 bc} \int_0^{\Delta} (E - E_F)^n [E(\Delta - E)]^{1/2} \tau(E) f_0' dE. \qquad (3)$$

Here *z* is the number of chains through the transversal section of the unit cell, E_F is the Fermi energy, $f_0'(E)$ is the derivative of Fermi distribution function with respect to *E*. The integration in Eq. (3) is carried out on all energies in the conduction band, so as it is not too large.

The expression (2) has been calculated for TTT_2I_3 crystals in dependence of dimensionless Fermi energy $\varepsilon_F = E_F / 2w$ for γ = 1.6 and different values of parameter *D*, mentioned above. In ordinary TTT_2I_3 ε_F is a little less than 0.4 and *z* = 4.

In Fig. 2 the calculated dependences of *P* on ε_F at room temperature are presented. It is seen that the power factor *P* has also maximums which are rather large. These maximums are the result of competition between the increase of electrical conductivity and the decrease of thermopower. The lowest maximum is of the same order as in Bi_2Te_3, the middle one is two times higher, and the last is almost four times higher.

But the maximums are placed at lower values of Fermi energy than those that correspond to ordinary crystals. At ε_F a little less than 0.4 the power factor is very small. In order to increase *P* it needs to diminish ε_F, or carriers' concentration. It is possible because the TTT_2I_3 crystals admit non stoichiometric composition. The iodine plays the role of acceptors. In order to diminish the carriers' concentration in needs to diminish the iodine concentration and to obtain a compound of the type $TTT_2I_{3-\delta}$, where δ is the deviation of stoichiometry.

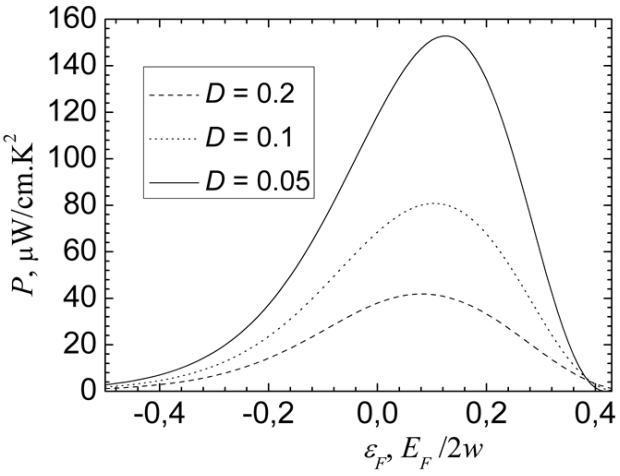

Fig.2. Power factor *P* as a function of dimensionless Fermi energy ε_F for $\gamma = 1.6$.

Thus, for $\varepsilon_F = 0.2$ (*n* is diminished by 1.6 times from $1.2\square 10^{21}$ cm^{-3} to $7.5\square 10^{20}$ cm^{-3}) and $D = 0.05$ it follows $P = 134$ $\mu W/cm.K^2$, a very good result.

For this carriers' concentration the electrical conductivity $\sigma = 9.3\times 10^3$ $\Omega^{-1}cm^{-1}$ and the thermopower $S = 120$ $\mu V/K$. As it is seen from Fig.2, the maximum of *P* corresponds to $\varepsilon_F = 0.12$, when $P = 153$ $\mu W/cm.K^2$. Even in less pure crystals for which $D = 0.1$, the maximum of *P* is still high, ~ 80 $\mu W/cm.K^2$.

Surely, if the crystal purity will be still more increased, so that the parameter *D* will be less than 0.05, one can expect even higher values of the power factor than the highest in Fig.2. One may think that this will be possible.

V. CONCLUSIONS

The thermoelectric power factor *P*, which is the main physical parameter that determines the opportunity of a material to be used in sensitive elements of infrared radiation detectors, has been modeled in nanostructured quasi-one-dimensional organic crystals of tetrathio-tetracene-iodide, TTT_2I_3, in dependence of crystal parameters. A more complete crystal model is used that take into account two electron-phonon interactions and the scattering of carriers on impurities. One interaction is similar to that of deformation potential and the second is of polaron type.

It is shown that, due to the interference of these electron-phonon interactions, the thermoelectric power factor *P* as a function of Fermi energy (or carriers' concentration) obtains maximums which depend on crystal purity. For ordinary crystals with stoichiometric concentration *P* is very small. But if the carriers' concentration is diminished by 1.6 times from $1.2\square 10^{21}$ cm^{-3} to $7.5\square 10^{20}$ cm^{-3}, *P* is increased in the crystals with the highest degree of purity up to 134 $\mu W/cm.K^2$, a very good result.

For optimal parameters the maximal value of $P = 153$ $\mu W/cm.K^2$ is predicted. It is expected that in crystals with higher degree of purity the thermoelectric power factor will achieve still greater values.

REFERENCES

[1] V.G. Levich, Vvedenie v statisticheskuiu fiziku, Gos. izdatelistvo tehniko-teoret. literatury, Moscva, 1954.

[2] D. Kondepudi, *Introduction to Modern Thermo-dynamics*, Wiley, Chichester, (2008), Section 32.

[3] B.F. Paes et al. Accuracy of tympanic and infrared skin thermometers, ACD Online First Published on August 24, 2010 as 10.1136/adc 2010. 185801.

[4] National Collaborating Center for Women's and Children's Health. NICE Clinical Guideline 47, May 2007, http://guidance.nice.org.uk/GC47.

[5] M. S. Dresselhause, J. P. Heremance, Recent developments in low-dimensional thermoelectric materials In: *Thermoelectric Handbook; Macro to Nano*, Ed. by Rowe, CRC press, FL, 2006, Chap. 39.

[6] T.C. Harman, P.J. Taylor, M.P. Walsh, and B.E. LaForge, Quantum dot superlattice thermoelectric materials and devices, *Science*, Vol. **297**, 2229 (2002).

[7] A. Casian, I. Sur, H. Scherrer, Z. Dashevsky, Thermoelectric properties of *n*-type $PbTe/Pb_{1-x}$ Eu_xTe quantum wells, *Phys. Rev.* **B**, **61**, 15965 (2000).

[8] I. Sur, A. Casian, and A. Balandin, Electronic thermal conductivity and thermoelectric figure of merit of *n* – type $PbTe/Pb_{1-x}$ Eu_x Te quantum wells, *Phys. Rev.* **B**, **69**, 035306 (2004).

[9] A. Casian, V. Dusciac, High values of thermoelectric power factor expected in quasi-one-dimensional organic crystals, J. of Thermoelectr., 1, 29-37, 2007.

[10] A. Casian, V. Dusciac, V. Nicic, Promising low-dimensional organic material for IR detectors, Romanian J. of Phys., **55**, 205-212, 2010.

[11] A. Casian, J. Stockholm, V. Dusciac, V. Nicic, Low dimensional organic crystal Tetrathiotetracene-Iodide as thermoelectric material, J. of Nanoelectronics and Optoelectronics, **4**, 95-100, 2009.

[12] A. Casian, Violation of the Wiedemann-Franz law in quasi-one-dimensional organic crystals, Phys. Rev. B **81**, 155415, 2010.

[13] I.F. Shchegolev, E.B. Yagubskii. Cation-Radical Salts of Tetrathiotetracene and Tetraselenotetracene: Synthetic Aspects and Physical Properties. In Extended Linear Chain Compounds, N.-Y.: Ed. by I. S. Miller, Plenum Press, 1982, v. 2. pp. 385-435.

[14] B. Hilti and C.W. Mayer Electrical Properties of the Organic Metallic Compound bis (Tetrathiotetracene)-Triiodide, $(TTT)_2I_3$. Helvetica Chimica Acta, **61**, Nr 40, 501, (1978).

[15] A. Casian, V. Dusciac, and Iu. Coropceanu. Huge carrier mobilities expected in quasi-one-dimensional organic crystals. Phys. Rev. **B 66**, 165404 (2002).

Single-Crystal Microwires Based on Doped Bi for Anisotropic Thermoelectric Devices

L. KONOPKO[1,2], A. NIKOLAEVA[1,2], T. HUBER[3], A. TSURKAN[1]
[1]*Institute of Electronic Engineering and Nanotechnologies "D. Ghitu", AS of Moldova*
[2]*International Laboratory of High Magnetic Fields and Low Temperatures, Wroclaw 53-421, Poland*
[3]*Department of Chemistry, Howard University, 500 College St. N.W., DC 20059 Washington, U.S.A.*
l.konopko@iieti.asm.md, A.Nikolaeva@iieti.asm.md, thuber@Howard.edu, SciSecr@iieti.asm.md

***Abstract* – We have investigated the possibility to use a microwire of BiSn to design an anisotropic thermoelectric generator. The glass-coated microwire of pure and Sn-doped bismuth was obtained by the Ulitovsky method; it was a cylindrical single-crystal with orientation (10$\underline{1}$1) along the wire axis; the C3 axis was inclined at an angle of 70º to the microwire axis. It is found that doping of bismuth wires with tin increases the thermopower anisotropy in comparison with Bi by a factor of 2 – 3 in the temperature range of 200 – 300 K. For a Bi microwire with a core diameter of 10 μm with a glass coating with outer diameter of 35 μm, the transverse thermopower is ~ 150 μV/(K*cm); for BiSn, 300 μV/(K*cm). The design of an anisotropic thermogenerator based on BiSn microwire is proposed. The miniature thermogenerator will be efficient for power supply of devices with low useful current. In addition to the considerable thermopower anisotropy of BiSn wires in a glass coating, they exhibit stable thermoelectric properties, high mechanical strength and flexibility, which allows designing thermoelectric devices of various configurations on their basis.**

***Index Terms* – anisotropy, bismuth, microwires, thermoelectricity, thermogenerator.**

I. INTRODUCTION

The search for new unconventional sources of electric power is now the research trend of particular concern and high priority.

As a source of heat for thermoelectric generators, the thermoelectric method of thermal energy conversion into electric energy involves unconventional renewable sources of thermal energy: from solar energy to the heat of human body. [1,2]

The appearance of new more efficient materials for anisotropic thermoelements (ATs) is reviving interest in the transverse thermoelectric effect. The efficiency of ATs is governed to a considerable extent by thermopower anisotropy value. The principle of operation and the features ATs were extensively studied both in scientific and applied aspects [3,4].

A transverse AT, as a voltage source in measuring systems, has some advantages:

(i) The thermopower, unlike a conventional thermocouple, is proportional to the temperature gradient (T1 - T2) / h instead of the temperature difference T1 - T2. Thus, decreasing the width h, it is possible to increase voltage at the same temperature difference.

(ii) Voltage V is proportional to length l; thus, it is possible to increase voltage by increasing the length of the plate.

(iii) To obtain voltage, we need no junctions that are required for increasing sensitivity. In the case of ATs, it is sufficient to increase the length of the crystal employed in order to enhance sensitivity.

In this regard, there are some problems in obtaining efficient ATs: the problem of material science, including obtaining of high-performance materials with high thermopower anisotropy and reproducible parameters, and the problem of the design, calculation, and preparation of devices based on ATs.

Bismuth single crystals exhibit a thermopower anisotropy of ≈ 50 μV/K in a temperature range of 100 – 400 K, which makes it possible to design ATs with a sensitivity of ≈ 10 – 15 mV/W and rapid response time τ = 10-2 s; they find practical application, in particular, as heat flow meters in microcalorimetry [5,6].

The value and temperature dependence behavior of the thermopower anisotropy of Bi can be rather easily controlled by doping and introduction of twin interlayers [7]. Bismuth turned out to be appropriate in various radiation sensors and microelements. The fundamental difference of ATs from traditional thermoelements is that the thermopower comprises the geometric factor l/h, where l is the sample length and h is its thickness. The thermopower of traditional thermoelement does not depend on the geometric sizes of these thermocouples, whereas the thermopower of ATs is proportional to the length and inversely proportional to the thickness; thus, we can increase the thermopower by increasing the AT length.

II. SAMPLES AND EXPERIMENT

We have studied the possibility of using a microwire of bismuth doped with Sn to design an anisotropic thermoelectric generator. Glass-insulated single-crystal wires of pure and Sn-doped bismuth were prepared by the Ulitovsky method; they were cylindrical single crystals with the (10$\underline{1}$1) orientation along the wire axis; the C_3 axis was inclined at an angle of 70° to the wire axis. The technique described in [8,9] allows preparing single-crystal wires with diameters from 50 μm to nanometers. It is known that the

size effect significantly changes the thermoelectric properties and leads to an increase in thermoelectric efficiency [10].

The developed technology allows obtaining a glass-insulated single-crystal microwire of Bi and its alloys with Sn with a length up to a few meters and with a given diameter from 100 nm to 50 μm. The specific resistivity was studied as a function of the doping impurity composition, wire diameter, and crystallographic orientation.

To study the thermopower anisotropy of the wires, we used samples with C_3 oriented along the wire axis, which were obtained by the methods of zone and laser recrystallization.

The transverse thermopower $\alpha_{trans} = U/\Delta T$, where U is the voltage across the sample, ΔT is the transverse temperature gradient. To measure the transverse thermopower α_{trans} in microwire segments with a length of 10 cm, we made a special device consisting of two copper plates with different temperatures. A glass-insulated microwire segment with a length of 10 cm was placed between these plates in such a way as to keep good thermal contact between the glass cover of the microwire and the surface of the plates throughout the length of the microwire (Fig. 1). To obtain a uniform temperature gradient, a resistive heater was placed on one of the plates; it occupied 80% of the entire surface of the plate. The temperature gradient was measured by a differential copper-constantan thermocouple, two junctions of which were situated in the middle of the plates near the surfaces being in contact with the microwire.

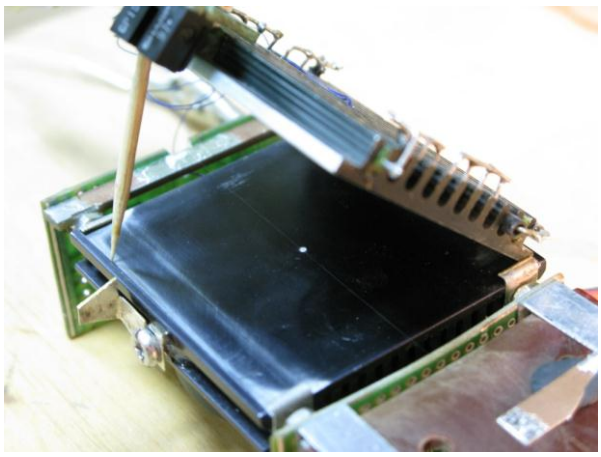

Fig. 1. Physical form of the device for measuring transverse thermopower in samples of a glass-insulated microwire.

The method of ShdH oscillations was used for estimating the Fermi level in doped Bi wires.

III. RESULTS AND DISCUSSION

Fig. 2 shows the diagram of rotation of the transverse magnetoresistance of the Bi- 0.05 at% Sn wires with (a) the (10$\underline{1}$1) standard orientation and (b) C_3 orientation along the wire axis. The angular dependence of the transverse magnetoresistance (TMR) R(Θ) in the Bi-0.05at%Sn wires with the (10$\underline{1}$1) orientation along the axis is similar to dependence for bulk samples: the dependences are symmetric about directions Θ = 0° and Θ = 90°. At Θ = 0, H || C_3; at Θ = 90°, H is parallel to the binary axis C_2.

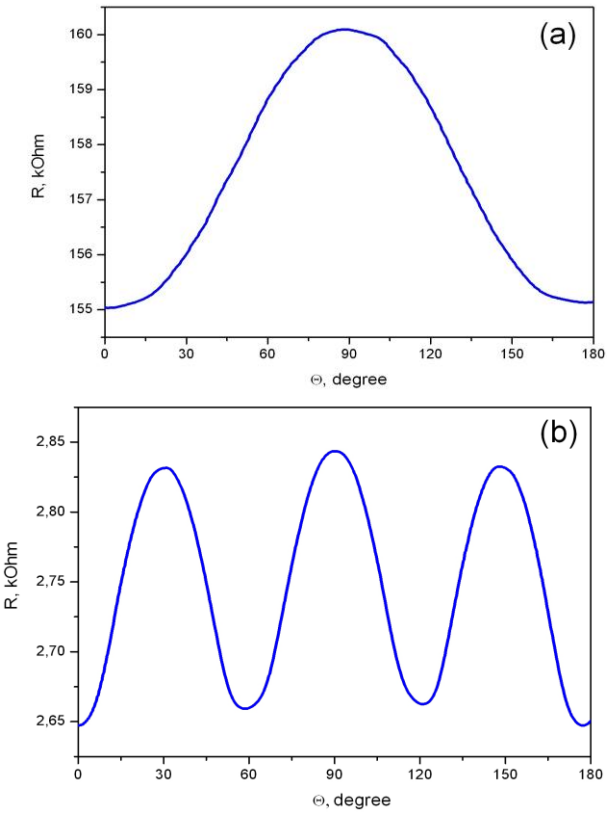

Fig. 2. Angle diagrams of TMR *R(Θ)* of Bi–0.05Sn (*d* =0.6 μm) with standard (*a*) and trigonal (*b*) orientations, *H* = 0.5 T, *T* =4.2 K.

In wires with C_3 oriented along the wire axis, the anisotropy of the transverse magnetoresistance is governed only by L-carriers, because, as the magnetic field rotates in the basal plane, the contribution of T-holes to the magnetoresistance does not depend on the direction. The rotation diagram structure corresponds to the sixfold rotation axis symmetry. The minima in the diagrams correspond to the sample orientation when one of the binary axes C_2 is parallel to *H*.

Fig. 3 depicts the dependences of the longitudinal magnetoresistance (LMR) R(H), H || I for the Bi-0.05 at% Sn wires with the (10$\underline{1}$1) and (111) orientation along the wire axis and ShdH oscillations at H $\perp$ I for wires with C_3 oriented along the wire axis.

Fig. 3 shows that ShdH oscillations of the magnetoresistance R(H) in Bi wires doped with an acceptor impurity of Sn can be seen in the longitudinal and transverse orientations both in wires with C_3 oriented along the wire axis and in wires with the (10$\underline{1}$1) orientation along the axis. Analysis of the SdH oscillations (Fig. 3) shows that the glass-insulated single-crystal Bi-0.05 at% Sn wires under study really had two orientations: C_3 along the axis and $C_{½}$ along the wire axis.

The Fermi energy of holes in T in the Bi-0.05 at% Sn wires was calculated in terms of the two-band Kane model using the expression 1.

$$\varepsilon_F^T = \varepsilon_{par} - \frac{1}{2}\varepsilon_g^T + \left[\varepsilon_{par}^2 + \left(\frac{1}{2}\varepsilon_g^T\right)^2\right]^{\frac{1}{2}} \qquad (1)$$

Where ε_{par} is the energy in the parabolic band approximation;

$$\varepsilon_{par} = \frac{eh \cdot \Delta_T^{-1}}{2\pi c \cdot m_c^T} \qquad (2)$$

is the Fermi energy of holes in T calculated downwards from the band top in T; m_c^T is the small cyclotron mass of T-holes; ε_g^T is the gap in the T-point of the Brillouin zone that amounts to 200 meV according to [11,12]; Δ_T^{-1} is the value of inverse period of the ShdH oscillations from the smallest section of the hole ellipsoid in the T-point of the Brillouin zone.

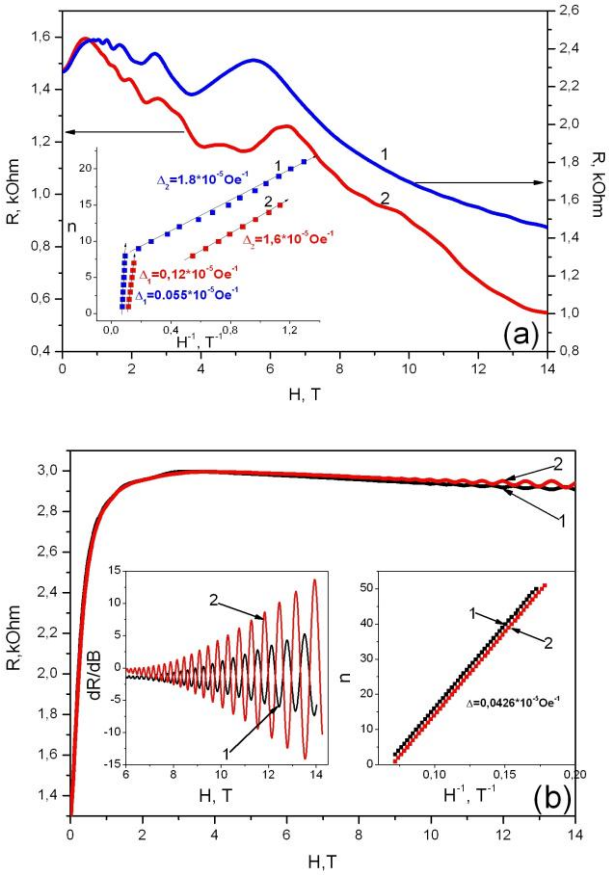

Fig. 3. *(a)* Field dependencies of LMR *R(H) (H||I)* of Bi-0,05 ат% Sn wire (d = 1 μm) with standard ($10\bar{1}1$) (1) and trigonal (2) orientations at T = 2.1 K. Insert: dependences of the quantum number n of the ShdH oscillations on reverse field H^{-1}. *(b)* Field dependencies of TMR *R(H)* ($H \perp I$) of Bi-0,05 ат% Sn wire with trigonal orientation at $\theta = 0°$ (1) and $\theta = 67°$ (2) according to figure 2 (b), at T = 2.1 K. Inserts: left – field dependencies of derivative of TMR at $\theta = 0°$ (1) and $\theta = 67°$ (2) at T = 2.1 K; right - dependences of the quantum number n of the ShdH oscillations on reverse field H^{-1} at $\theta = 0°$ (1) and $\theta = 67°$ (2) at T = 2.1 K.

In addition, it was taken into account that at H ‖ I, as in wires of pure Bi of the given crystallographic orientation [9], the ShdH oscillations are registered from the cross-section of the hole T-ellipsoid close to the maximum (the sample axis is tilted by an angle of 20° from the bisector axis). It was found that ε^T_F in Bi-0.05 at% Sn wires is located in the zone of L-holes.

To study the anisotropy of the thermopower and resistance, the temperature dependences $\alpha(T)$ and resistance R(T) of Bi–0.05 at% Sn wires with different orientations in a temperature range of 4.2 – 300 K were investigated (Fig. 4).

Fig. 4 shows that the maximum thermopower anisotropy occurs at temperatures of 250-300 K; it is 100-120 μV/K, which is more than twice as high as the anisotropy α in pure Bi in the same temperature range.

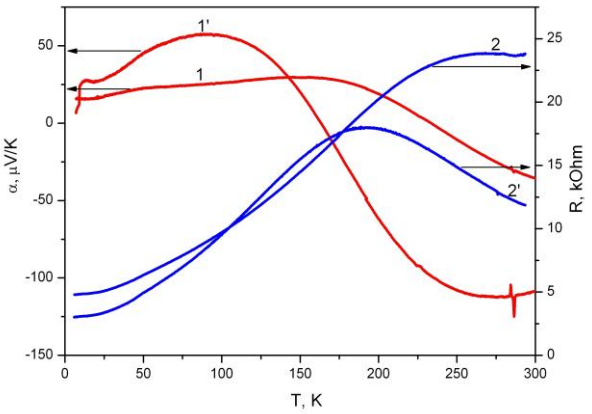

Fig. 4. Temperature dependences of thermopower $\alpha(T)$ (scale on the left) and resistance R(T) (scale on the right) of Bi–0.05 at% Sn wires (d =0.6 μm) with standard (1,2) and trigonal (1',2') orientations.

The transverse thermopower of glass-insulated microwire segments with a length of 10 cm of Bi and Bi-0.05 at% Sn in the diameter range d = 3 – 20 μm was measured at room temperature; the diameter D involving the glass insulation varied within 15 – 40 μm. The highest transverse thermopower per unit length of the microwire equal to 100 μV/(K*cm) was obtained for a bismuth microwire with d = 8 μm. For the Bi-0.05 at% Sn microwire, the maximum transverse thermopower per unit length of the microwire is significantly higher: it is 290 μV/(K*cm) in a microwire with d = 5.5 μm.

These results allow expecting that, after finding the optimum design solution of the place of a long microwire in the plate in the external temperature gradient, it will be possible to prepare an anisotropic thermoelectric generator for feeding devices with low useful current.

In addition to the considerable thermopower anisotropy, glass-insulated BiSn wires exhibit stable thermoelectric properties and high mechanical strength, which allows designing thermoelectric devices of various configurations on their basis. The fact that the efficiency of an anisotropic generator comprises the wire length and thickness yields broad possibilities of their optimization; the efficiency and the economic feasibility of the process of preparation of the wires will enable applying them as anisotropic generators on an industrial scale.

IV. CONCLUSION

It is found that doping of bismuth wires with tin increases the thermopower anisotropy in comparison with Bi by a factor of 2 – 3 in the temperature range of 200 – 300 K. According to the results, for a Bi microwire with a diameter of 10 μm with a glass coating of 35 μm, the transverse thermopower is ~ 150 μV/(K*cm); for BiSn, 300 μV/(K*cm), that can be used to create ATs for feeding devices with low current.

ACKNOWLEDGMENTS

This work was supported by the SCOPES Grant # IZ73Z0_1 27968 and ASM Project # 11.836.05.05A.

REFERENCES

[1] D. Chinory, Solar Power Generator. The British petroleum Company Pic, Patent, BBH 17.09.86, MKI 24 2/04 H01 35/02, MKH F460.

[2] Yu.S. Bortnikov et al., Izv. Akad. Nauk SSSR. Energia i transport 5, 3 (1961).

[3] P.I. Baranskii, I.S. Buda, I.V. Dakhovskii, A.G. Samoilovich, Phys. Stat. Sol. (b) 67, 201 (1975).

[4] A.R. Regel', G.A. Ivanov, V.M. Grabov, L.I. Anatychuk, O.Ia. Luste, Patent No. 245859 (1968).

[5] L.I.Anatychuk, Termoelementy i termoelektricheskie ustroistva. Reference book. Kiev: Naukova dumka 1979, 766 p.

[6] W. Lukosz, Z. Natursch, A 19, 1599 (1964).; G.A. Ivanov, V.M. Grabov, Fizika i Tehnika Poluprovodnikov 29, 1040 (1995).

[7] I.M. Pilat, S.V. Chayka, S.I. Pirojenko, N.V. Kruglova, Fizika Tverdogo Tela 17, 176 (1975).

[8] N.B. Brand, D.V. Gitsu, A.A. Nikolaeva, and Ya.G. Ponomarev, Zh. Exp. Teor. Fiz. 72, 2332 (1977). [Sov. Phys. JETP 45, 1226 (1977)].

[9] D. Gitsu, L. Konopko, A. Nikolaeva, and T. Huber, Applied Physics Letters 86, 10210 (2005).

[10] Y.M. Lin, X.Z. Sun, M.S.Dresselhaus, Phys. Rev. B.: Condens. Matter Mater.Phys. 62, 4610 (2000).

[11] N. Brandt, P. Mulier, Ya. Ponomarev, Sov. Phys. JETP 44, 1196 (1977).

[12] N.A. Red'ko, N.A. Rodionov, Pis'ma v JETP 42(6), 246 (1985).

Superconducting Spin Switch Based on Superconductor-Ferromagnet Nanostructures for Spintronics

Jan KEHRLE[a], Vladimir ZDRAVKOV[a,b], Claus MUELLER[a], Guenter OBERMEIER[a], Matthias SCHRECK[a],
Stefan GSELL[a], Siegfried HORN[a], Reinhard TIDECKS[a], Roman MORARI[b,c], Andrei PREPELITSA[b], Evgenii ANTROPOV[b], Alexei SOCROVISCIUC[b], Eberhard NOLD[c], Lenar TAGIROV[a,d], Anatoli SIDORENKO[b,c]
University of Augsburg, D-86135 Augsburg, Germany
Institute of Electronic Engineering and Nanotechnologies "D. Ghiţu" ASM
Kishinev, MD2028, Moldova
Institute of Nanotechnology, D-76021 Karlsruhe, Germany
Solid State Physics Department, Kazan State University, Kazan, 420008, Russia;
anatoli.sidorenko@kit.edu

***Abstract* – Very rapid developing area, spintronics, needs new devices, based on new physical principles. One of such devices – a superconducting spin-switch, consists of ferromagnetic and superconducting layers, and is based on a new phenomenon – reentrant superconductivity. The tuning of the superconducting and ferromagnetic layers thickness is investigated to optimize superconducting spin-switch effect for $Nb/Cu_{41}Ni_{59}$ based nanoscale layered systems.**

***Index Terms* – spin-switch, superconductivity, proximity effect, spintronics, nanotechnology**

I. INTRODUCTION

Fulde, Ferrell [1], Larkin and Ovchinnikov [2] predicted that an unconventional, nonuniform superconducting pairing (FFLO) with a non-zero momentum of a pair may occur in a ferromagnetic background, *i.e.* in the presence of an exchange field. In conventional (s-wave) superconductors such state can only be observed in a very small range of parameters and has not been realized up to now experimentally. However, Buzdin *et al*. [3] predicted FFLO-like pairing in S/F layered structures, where the pair amplitude in the F-material establishes due to penetration of the singlet electron pairs from the superconductor through the S/F interface. More advanced analysis was worked out by Tagirov [4] and Fominov *et al*. [5]. The most spectacular prediction of these theories is that not only T_c oscillations but also complete suppression of superconductivity may occur in a certain range of thicknesses of the F-layer followed by its unusual re-entrance with increasing of the F-layer thickness. Superconducting spin-switch based on proximity effect in Ferromagnet – Superconductor – Ferromagnet (F/S/F) layered system was investigated then theoretically in [6,7] using hypothetical materials and their thicknesses. The thicknesses tuning of the superconducting and ferromagnetic layers in SF -structures is the goal of the present work, to investigate and optimize superconducting spin-switch effect for $Nb/Cu_{41}Ni_{59}$ based nanoscale layered system.

II. FILMS DEPOSITION AND CHARACTERIZATION

We developed a special advanced technological process of superconducting layers preparation [8] for reliable fabrication of S/F structures with the layer thickness scale of several nanometers. The S and F layers were deposited by magnetron sputtering on commercial (111) silicon substrates at room temperature. The base pressure in the "Leybold Z400" vacuum system was about 2×10^{-6} mbar. Pure argon (99.999%, "Messer Griesheim") at a pressure of 8×10^{-3} mbar was used as sputter gas. A silicon buffer layer was deposited using RF magnetron. It produced a clean interface for the subsequently deposited niobium layer. To obtain flat and high-quality Nb layers with thickness in the range of 5-15 nm, the rotation of the target around the symmetry axis of the vacuum chamber was realized. A dc-motor drive moved the full-power operating magnetron along the silicone substrate of the 80×7 mm^2 size during the deposition. Thus, the surface was homogeneously sprayed with the sputtered material. The effective growth rate of the Nb film in this case was about 1.3 nm/sec. The deposition rate for a fixed, non-moving target would be about 4-5 nm/sec.

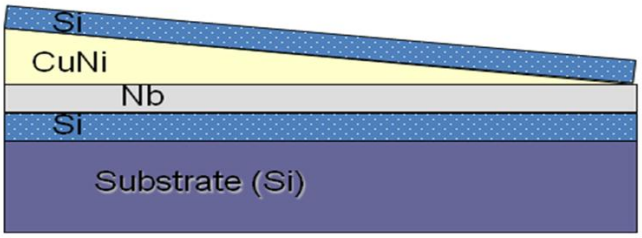

Fig.1. Sketch of the layers stack in the deposited S/F-specimen.

The next step of the procedure was deposition of a wedge-shaped ferromagnetic layer utilizing the intrinsic spatial gradient of the deposition rate of the sputtering material. The $Cu_{40}Ni_{60}$ target was RF sputtered with a rate of 3-4 nm/sec, resulting in practically the same composition ($Cu_{41}Ni_{59}$) of the alloy in the film. To prevent a destructive influence by

the atmospheric conditions, the last deposited layers were coated by a silicon cap of about 5-10 nm thickness (see a sketch of the prepared samples in Fig. 1).

Samples of a width of about 2.5 mm were cut perpendicular to the wedge to obtain a set of S/F bilayer strips with varying $Cu_{41}Ni_{59}$ layer thickness d_F, for $T_c(d_F)$ measurements. Aluminum wires of 50 μm in diameter were bonded to the strips by ultrasonic bonder for four-probe resistance measurements.

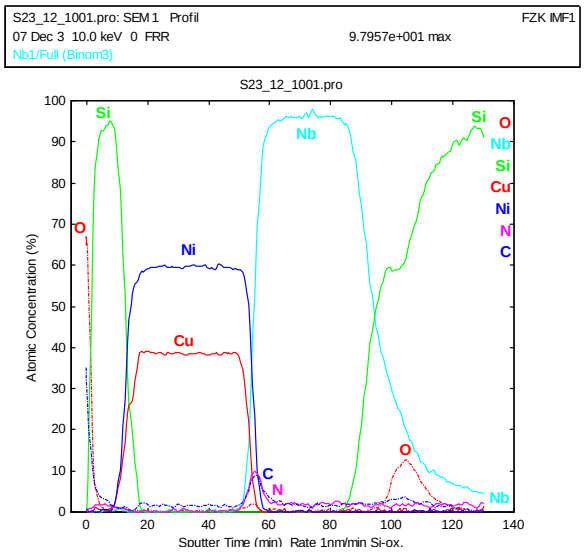

Fig. 2. Scanning Auger electron spectroscopy (AES) of a Si(substrate)/Si(buffer)/Nb/$Cu_{1-x}Ni_x$/Si(cap) sample, d_{Nb} =7.5 nm and d_{CuNi}=32.9 nm (thickness according to the RBS data).

To study the quality of interfaces between the layers we performed Auger electron spectroscopy (AES) measurements of specimens. A defocused Xe-ion beam erodes a crater into the film with inclination angles of the scarps of only a few degrees or below. An electron beam then scans the shallow crater. The emitted Auger electrons reveal the lateral distribution of elements. As a result, one reconstructs the elemental concentration as a function of the sample depth profile. The AES data for the Nb/$Cu_{1-x}Ni_x$ specimen are shown in Fig. 2. There are about 59 at.% Ni (in agreement with the RBS data) and 39.0 at.% Cu in the $Cu_{1-x}Ni_x$ film. There is a small concentration of O, C and N impurities at the Nb/$Cu_{1-x}Ni_x$ interface as a result of physical absorption of gases from the residual atmosphere of the vacuum chamber. The $Cu_{1-x}Ni_x$/Si(cap) interface is free of contaminations.

The samples for the $T_c(d_S)$ measurements were prepared with the same procedure, but with a $Cu_{41}Ni_{59}$ film of constant thickness on the top of a wedge-shaped Nb layer. In addition, single flat Nb films and single CuNi-wedge shaped layers were prepared in a similar way for materials characterization.

III. SUPERCONDUCTING PROPERTIES OF NB/$CU_{41}NI_{59}$ BILAYERS

Fig. 3 demonstrates the dependence of the superconducting transition temperature for SF samples on the thickness of the $Cu_{41}Ni_{59}$ layer. For specimens with $d_{Nb} \approx 14.1$ nm the transition temperature T_c reveals a non-monotonic behavior with a very shallow minimum at about $d_{CuNi} \approx 6.8$ nm, it is just the qualitative behavior. The transition temperature T_c reveals an expressed non-monotonic behavior with a deep minimum at d_{CuNi} about 7.9 nm. For the series of specimens with $d_{Nb} \approx 6.2$ nm the transition temperature T_c decreases sharply for increasing ferromagnetic $Cu_{41}Ni_{59}$ layer thickness, until $d_{CuNi} \approx 3.8$ nm. Then, for $d_{CuNi} \approx 3.8$-24 nm,

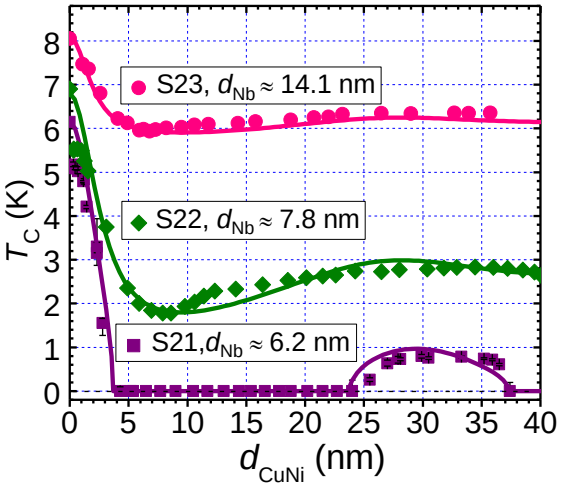

Fig.3 Non-monotonous $T_c(d_F)$ dependence for Nb/$Cu_{41}Ni_{59}$ bilayers with the Nb layer thickness, $d_{Nb} \approx 6.2$ nm, $d_{Nb} \approx 7.8$ nm, and $d_{Nb} \approx 14.1$ nm. Solid lines are fits using the theory [4].

the superconducting transition temperature vanishes (at least T_c <40 mK, which is the lowest temperature measured). For $d_{CuNi} > 24$ nm the transition into a superconducting state is observed again. Finally, T_c increases to a little bit above 1 K showing an outstanding reentrant superconductivity behavior with evidence for a second disappearance of the superconducting state at $d_{CuNi} > 37.4$ nm. Altogether, the $T_c(d_{CuNi})$ curves given in Fig. 3 represent all types of non-monotonic $T_c(d_{CuNi})$ behaviors predicted by the theory [4]. This phenomenon of the reentrant superconductivity in the S/F bilayer has been presented in our recent publications [9,10].

IV. SIMULATION AND DISCUSSION

To describe the experimental data we used the calculation procedure described in [9,10]. The results for superconducting critical temperature T_c calculations for parallel and anti-parallel directions of ferromagnetic layers magnetizations for a core-structure $Cu_{41}Ni_{59}$ /Nb/ $Cu_{41}Ni_{59}$ with superconducting layer thicknesses d_{Nb} = 12.5nm, 14 nm are presented in Fig. 4.

One can see that a maximal spin-switch effect value ΔT_c of the order of 1-2 K is achievable only in a very strict region of superconductor and ferromagnetic layer thicknesses. Otherwise one can expect only negligible value of ΔT_c.

V. CONCLUSION

It was found from the calculations, based on our experimental parameters that maximal spin-switch effect value with the order of magnitude 1-2 K is achievable only for the strict range of superconductor and ferromagnetic layers thicknesses. This range of controlled thicknesses is

accessible using advanced vacuum technology [8-10] developed by us for preparation of the F/S/F-core structure for a superconducting spin-switch construction.

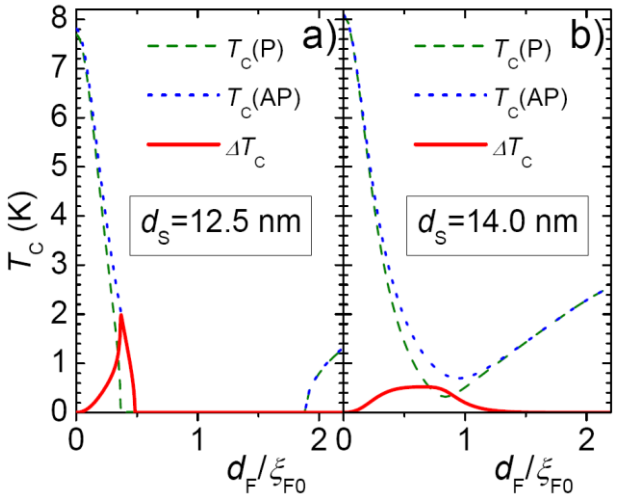

Fig.4. $T_c(d_F)$ curves of a superconducting F/S/F spin-valve core structure with $d_S = d_{Nb}$= 12.5 nm (a), $d_S = d_{Nb}$= 14 nm (b) calculated using the following set of parameters for (a) and (b) respectively: $T_{c0,Nb}(d_{CuNi} = 0$ nm) = 7.7, 8.1 K; in all cases ξ_S = 6.6 nm; $N_F v_F/N_S v_S$ = 0.22; T_F = 0.6; l_F/ξ_{F0} = 1.1; ξ_{F0} = 10.5 nm.

ACKNOWLEDGEMENTS

The authors are thankful to A.F. Andreev, A. Buzdin, R. Gross, H. Hahn, A. Zaikin, M. Kupriyanov and V. Ryazanov for stimulating and fruitful discussions. The work was partially supported by A.v. Humboldt grant - Institutspartnerschaften "Nonuniform superconductivity in layered SF-nanostructures Superconductor/Ferromagnet" (R.M. and An.S.), by DFG under the grant „Study of the Superconducting Proximity Effect Spin-Valve Phenomenon in Superconductor/Ferromagnet Nanolayered Structures" (GZ: HO 955/6-1, UA participants), and the project of the Moldavian State Program "Investigarea supracondubilităţii neomogene în nanostructucturi stratificate supraconductor-feromagnet şi elaborarea valvei de spin în baza lor" (R.M., A.P., E.A., A.S. and An.S.).

REFERENCES

[1] P. Fulde and R. Ferrell, Phys. Rev. 135, A550 (1964).
[2] A.I. Larkin and Yu.N. Ovchinnikov, Zh. Eksp. Teor. Fiz. **47**, 1136 (1964) [Sov. Phys. JETP **20**, 762 (1965)].
[3] A.I. Buzdin and M.Yu. Kupriyanov, Pis'ma v ZhETF **52**, 1089 (1990) [JETP Lett. **52**, 487 (1990)].
[4] L.R. Tagirov, Physica C **307**, 145 (1998).
[5] Ya.V. Fominov, N.M. Chtchelkatchev, and A.A. Golubov, Phys. Rev. B **66**, 014507 (2002).
[6] L.R. Tagirov. Phys. Rev. Lett. **83**, 2058 (1999).
[7] A.I. Buzdin, A.V. Vedyayev, and N.V. Ryzhanova, Europhys. Lett. **48**, 686 (1999).
[8] A.S. Sidorenko, V.I. Zdravkov. R. Morari Device for preparation of superconducting layers, Patent of RM 175 (134) Y din 2010, Cl.Int. H01 L 21/00.
[9] V.I. Zdravkov, J. Kehrle, G. Obermeier, S. Gsell, M. Schreck, C. Müller, H.-A. Krug von Nidda, J. Lindner, J. Moosburger-Will, E. Nold, R. Moari, V.V. Ryazanov, A.S. Sidorenko, S. Horn, R. Tidecks, and L.R. Tagirov, Phys. Rev. B 82, 054517 (2010).
[10] A. S. Sidorenko, V. I. Zdravkov, J. Kehrle, R. Morari, E. Antropov, G. Obermeier, S. Gsell, M. Schreck, C. Müller, V. V. Ryazanov, S. Horn, R. Tidecks, and L. R. Tagirov. *in*: Nanoscale Phenomena - Fundamentals and Applications. H. Hahn, A. Sidorenko, and I. Tiginyanu, Eds. Springer-Verlag, Berlin-Heidelberg, 2009, p.3-11.

High Resolution Position Inductive Transducers for Harsh Environmental Conditions

[1]Nicolae JULA, [2]Tudor URSU, [3]Cristina Nicoleta DIACONESCU, [2]Radu OBREJA
[1]Military Technical Academy – Bucharest, ROMANIA
[2]S.C. Sistem Euroteh – Buzau, ROMANIA
[3]Technical University Gheorghe Asachi – Iasi, ROMANIA
[1]nicolae.jula@gmail.com[2] tudorursu1952@yahoo.com[3]
,diac_cris83@yahoo.com,[4]radu@sistemeuroteh.ro

***Abstract* – In this paper the authors present certain theoretical, conceptual and technological aspects on main types of high resolution inductive transducers for harsh environmental conditions. Inductive resolvers, as well as inductive RVDT, have a priority in these applications, even other types of position transducers, as optical, capacitive or magnetic encoders are in competition.**

In the world there are many researchers that continue activity of conceptual and technological development to increase the resolution level of the inductive resolvers and inductive RVDT, as well as to obtain smaller and smaller dimensions, just it is requested in such kind of applications. On the other hand, the inductive transducers are more adapted at harsh mechanical and climatic conditions that are usual for special applications.

The paper is referring, especially, to inductive transformers type resolver.

***Key words* – inductive transducers, high resolution, harsh conditions**

I. GENERAL ASPECTS

Position inductive transducers are used as main components in the applications where it is required very high accuracy. For example, a modern measurement and control system including a synchro-resolver transmitter type and a synchro-resolver receiver type represents a most frequent solution to acquire the position information in very accurate manner for large range of applications.

In fact, position inductive transducer is used to translate into electric magnitude an angular or linear dimension and consists of an asynchronous electric machine, especially developed to produce one system of alternative outputs having variable amplitude.

It may be considered that this electric machine is a kind of retort at the general electric transformer that has all elements fix, so has only a certain magnitude of output.

However, the real purpose was not to be a retort, but to solve some important needs that the progress of systems and applications has required at a certain moment. We have to remark that there is an important difference to the situation of a classic asynchronous electric machine: position inductive transformer generates output signals as a transformation component and this one depends insignificantly from rotation speed. Generally, the component depending of rotation speed is taken into consideration inside of global error factory.

Over time, the authors had conceived, developed, built and tested many types of position inductive transducers, paying special attention to analyse back e.m.f. accuracy relative to different types of winding schema, as well as to do a right interpretation regarding the results obtained on vectorial measurements methods. Also, were made many tests in special environment conditions, similar to harsh conditions for special applications. These tests have demonstrated that the level of accuracy and global physical resistance of item are kept in these special harsh conditions.

Writers' opinion is to consider in the position inductive transducers class: **rotary inductive transformers**, to measure the angular position, components that are generally named rotary inductive potentiometers and include resolvers, microsyns and RVDT; **linear inductive transformers**, to measure the linear position, components that are generally named linear inductive potentiometers, including specially the transducer LVDT type.

We have to remark that, especially in the last time, the users have replaced in certain applications the inductive transducers with encoders (based on optical, capacitive or magnetic phenomena) and it was expressed by some producers a concept according with that the inductive transducers shall be replaced totally and forever with the encoders. But, the reality has demonstrated that this concept is completely wrong because it is not based on the whole spectrum of criteria. Some users and producers have considered only the price, but when high accuracy is requested the price of inductive transducers seems to be not decisive.

Moreover, some characteristics as: robustness, high resistance at harsh environment conditions, a perfect capacity to operate in an atmosphere with smog, fog, vapour or suspension assure to use the inductive transducers very long time in the future.

Through the evolution of machine development, builders and system integrators alike, agree that the inductive transducer is unsurpassed in its ability to reliably supply rotary position data in the harshest environment conditions. So, any segregation is not useful: the inductive transducers, as well as the encoders, are used and will be used by different users just according with their needs, interests and affinity.

II. INDUCTIVE TRANSDUCERS TYPE RESOLVER

2.1. Construction.
Representative equations and diagrams

As we have mentioned above, resolver is the position sensor or transducer which measures the instantaneous angular position of the rotating shaft to which it is attached. Resolvers and their close cousins, synchros, have been in use since before World War II. Resolvers are typically built like small motors with a rotor (attached to the shaft whose position is to be measured), and a stator (stationary part) which produces the output signals.

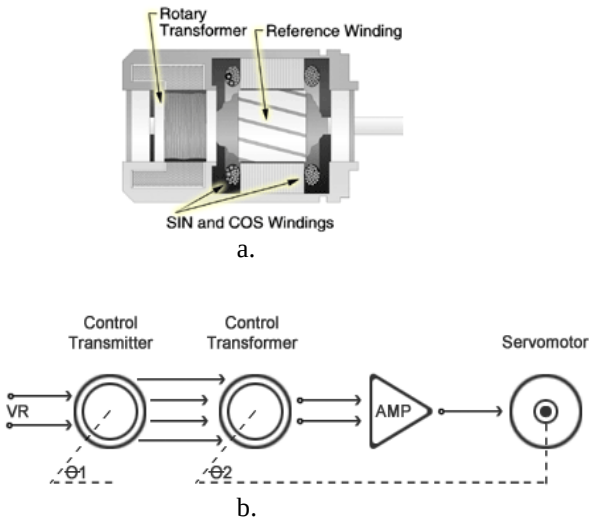

Fig. 1 a. Showing resolver construction with housing, sinus and cosinus windings, bearings and rotary transformer b. Typical control of electromechanical servo-system

The word resolver is a generic term for such devices derived from the fact that at their most basic level they operate by resolving the mechanical angle of their rotor into its orthogonal or Cartesian (X and Y) components. From a geometric perspective, the relationship between the rotor angle (θ) and its X and Y components is that of a right triangle.

Fundamentally, then, all resolvers produce signals proportional to the sine and cosine of their rotor angle, relative to fix position of the stator. Since every angle has a unique combination of sine and cosine values, a resolver provides absolute position information within one electric revolution (360°) of its rotor (**only it has 2 poles**). This absolute (as opposed to incremental) position capability is one of the resolver's main advantages over incremental encoders. However, we have to remark that the absolute character is related only one electric revolution, so to have an absolute reference for whole physical rotation (mechanical 360°) it must to build the resolver only with two poles. Like all transformers, the resolver requires an AC carrier or reference signal (sometimes also called the excitation) to be applied to its primary. The amplitude of this reference signal is then modulated by the sine and cosine of the rotor angle to produce the output signals on the two secondaries. In any transformer, there is a value which relates the output voltage produced by the secondary to that fed into the primary. For resolvers, this quantity is called the transformation ratio or ***TR*** and is specified at the point of maximum coupling between primary and secondary. If we define the reference voltage ***V(R1–R2)*** as ***VR***, then the voltages on the secondaries are given by the following equations:

Primary Input: **V(R1–R2) = VR = E_{1max} sin ωt**
Sine Secondary: **V(S2–S4) = VS = VR TR sin(θ)** ***Cosine Secondary:*** **V(S1–S3) = VC = VR TR cos(θ)** ,
where ***θ*** is the mechanical angle of the rotor as shown in the resolver schematic (**fig. 2 and fig. 3**).

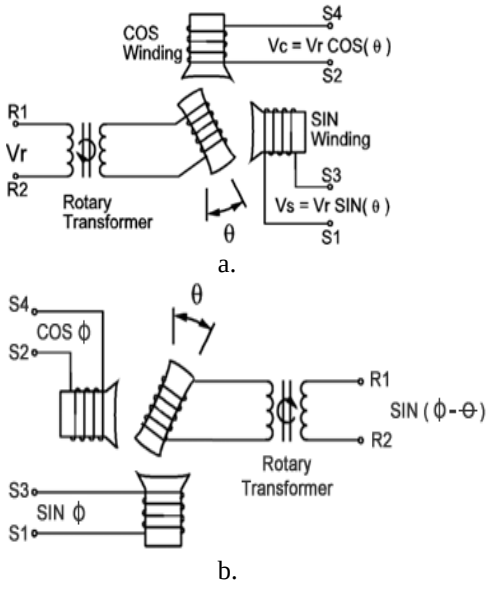

Fig. 2 BL (brushless) transmitter and receiver resolver a. Schematic on construction of BL transmitter resolverb. Schematic on construction of BL receiver resolver

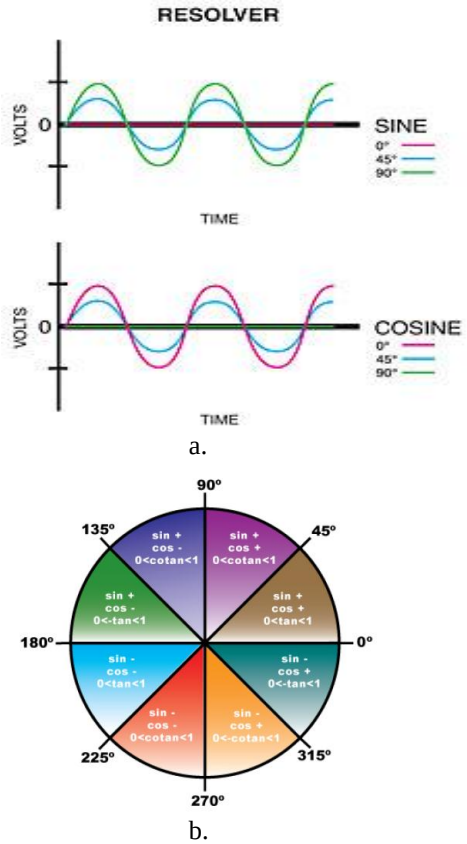

Fig.3 a. Resolver produces a set of analogical outputs sine – cosine b. Absolute character of the resolver

If we excite the resolver primary ***(VR)*** with the recommended sinusoidal reference signal, the secondary voltages are also sinusoidal at the same frequency and nominally in phase with the reference. Their amplitude is proportional to the amplitude of the reference, the transformation ratio of the resolver and the sine or cosine of the mechanical angle of the rotor. Using a typical value of ***TR*** as ***0.5***, we can look at the secondary voltages for different rotor angles as they would appear on an oscilloscope (fig. 4).

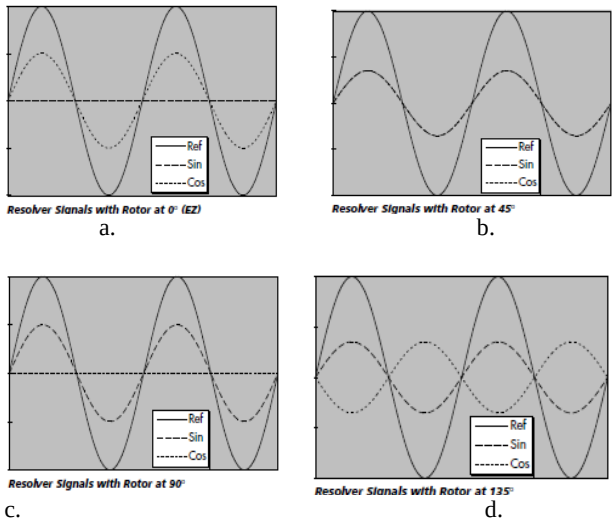

Fig. 4 Explanation on resolver operating principle

While it is helpful to know how the resolver signals appear as functions of time since that is what one sees when one looks at them with an oscilloscope, it is often more convenient to work with the envelope (amplitude at the reference frequency) of the signals with respect to rotor position. Shown in fig. 4e is the envelope of the sine secondary signal with respect to rotor position. The process of removing the carrier signal—leaving just the envelope—is called demodulation and is performed by the Resolver-to-Digital (R/D) converter. The demodulated sine and cosine resolver signals are shown in fig. 4f.

The resolver-to-digital converter performs two basic functions: demodulation of the resolver format signals to remove the carrier and angle determination to provide a digital representation of the rotor angle. The most popular method of performing these functions is called ratiometric tracking conversion. Since the resolver secondary signals represent the sine and cosine of the rotor angle, the ratio of the signal amplitudes is the tangent of the rotor angle. Thus the rotor angle, **θ**, is the arc tangent of the sine signal divided by the cosine signal: **θ = arctan(sin(θ) / cos(θ)) = arctan(Vs/Vc)**

The ratiometric tracking converter performs an implicit arc tangent calculation on the ratio of the resolver signals by forcing a counter to track the position of the resolver. This implicit arc tangent calculation is based on the trigonometric identity:

sin(θ - δ) = sinθ cosδ - cosθ sinδ

This equation says that the sine of the difference between two angles can be calculated by cross multiplying the sine and cosine of the two angles and subtracting the results. Further, as long as the difference between the two angles is relatively small (**δ = θ ± 30°**), the approximation **sin(θ - δ) ≈ θ - δ** may also be used, further simplifying the equation. Thus, if the two angles are within 30° of each other, the difference between the angles can be calculated using the cross multiplication shown above.

In the R/D converter, this equation is implemented using multiplying D/A converters to multiply the resolver signals (**proportional to sin θ and cos θ**) by the cosine and sine of the digital angle, **δ** , which is the output of the converter, as shown below. The results are subtracted, demodulated by multiplying by the reference signal, and filtered to give a DC signal proportional to the difference or error between the resolver angle, **θ**, and the digital angle, **δ**. The digital angle, **δ**, stored in the counter, is then incremented or decremented using a voltage controlled oscillator until this error is zero, at which point **δ = θ** (the digital angle output of the converter is equal to the resolver angle). This incrementing and decrementing of the digital angle, **δ**, causes it to track the resolver angle, **θ**, hence the name of this type of converter.

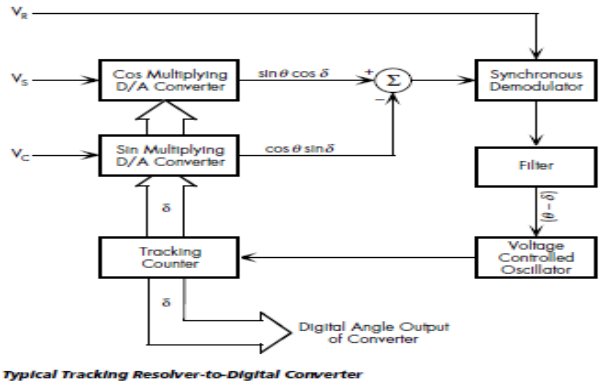

Fig. 5 Schematic on operating principle of analogue – digital converter (resolver to digital converter)

Above were presented some general aspects on bipolar resolver. But, to increase the accuracy, the resolver is built in a version with more poles (2**p**) – 4, 8, 16, or 32 pairs (**p**) of poles. On this way, the resolver is loosing the absolute character and it is necessary to add a supplementary set of windings in a bipolar configuration. In this situation, the operating main and simplified equations are:

Primary Input: **$V(R1–R2) = VR = E_{1max} \sin \omega t$**
Sine Secondary: **V(S2–S4) = VS = VR TR sin(pθ)** ***Cosine Secondary:*** **V(S1–S3) = VC = VR TR cos(pθ)**
pθ = arctan(sin(pθ) / cos(pθ)) = arctan(Vs/Vc)

2.2. Typical windings for resolver

The topology of windings used in resolvers has a sinusoidal character that means a non homogenous distribution of wiring in different slots – the distribution is according with a sinusoidal rule to obtain as final effect an

output signal very closed with a sine form. However, using only a sinusoidal type of winding do not solve completely the problem because there are other many factories that influence the accuracy level of resolver, as; quality of magnetic material, using slot solution, mechanical building asymmetries, the influence of the temperature on the material properties and winding characteristics etc. Some from these factories are controllable, but some of them are random. It is very important to take into consideration the controllable factories even from design stage, to reduce at minimum their influence.

In a bipolar resolver (absolute character), a frequent solution used to obtain a good accuracy is a lamination having many slots, to be possible to do better sinusoidal distribution.

If we discuss about multipolar resolvers, the number of slots per pol, from phisical point of view, is limited, frequently between 1 and two. In this situation, a special winding schema is used, but the final accuracy is a basis accuracy (two poles) divided at number of pole pairs (**p**).

Below it is shown an example of sinusoidal winding, in a concentric configuration, used for bipolar resolver (when it is possible to have more slots per pole). Let us to consider a winding having ***4k*** slots, as it is shown in fig. 5. The concentric windings have different dimensions (paths), from **1÷2** to **1÷k+1**. The windings from the slots **j, (j, 2k-j)** and **(2k-j, 2k+j)**, have the same numbers of turns $\mathbf{N_j}$ **/2**, and are equally distanced from the two poles.

If we consider to have **W** turns per pole, so:

$$\sum_{J=1}^{K} Nj = W/2,$$

Also, let us to consider that at a moment of time - t_o – the electric current trough winding is $\mathbf{I\sqrt{2}\sin\omega t_o}$.

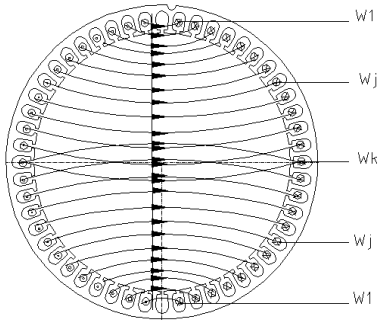

a.

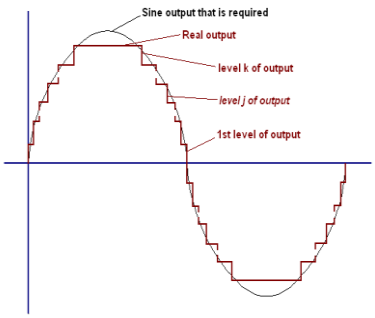

b.

Fig. 6 Relative to sinusoidal winding, in bipolar concentric configuration, for construction with 4k slots

Using the fundamental relations from electromagnetism and superposition method, we can find the solution for winding number in the slot marked with ***j***:

$$\mathbf{N_j = W/2 \cdot \sin(j\pi/2K)/[\sum_{i=1}^{K} \sin(j\pi/2K)],\quad j=1,2\ldots K}$$

The diagram of this field is shown in fig. 6b.

2.3. Some consideration regarding vectorial measurement methods

Testing resolvers at very small angular increments or at better than 1 arcsecond (.00028 degrees) accuracy requires a high precision instrument. A high precision ratio transformer can provide the accuracy and resolution needed for testing resolvers at small angular increments. To check the angular accuracy of a resolver the AC reference, resolver, ratio transformer and a phase angle voltmeter (PAV) are connected as shown in Fig.7.

Since S4 is the cosine output of the resolver, the output of the ratio transformer should equal the sine output:

[tan(θ) = sin(θ) /cos (θ), or sin(θ) = tan(θ) cos (θ)]

S1 is the sine output of the resolver; the output of the ratio transformer should be equal with S1 output of the resolver. If the two outputs are equal, the PAV will indicate a null condition. If the PAV does not indicate a null condition, the setting of the ratio transformer is adjusted until a null condition is indicated. The arctangent of the ratio transformer setting is the angle that the resolver output is indicating. On the other hand, for different positions of resolver rotor relative to resolver stator, the measurement system measures and computes:

$\mathbf{[\tan(\varphi)]_{sin} = (U_{sin})_f / (U_{sin})_q}$ **si** $\mathbf{(U)_{sin} = sqrt((U_{sin})_f^2 + / (U_{sin})_q^2)}$, respectively

$\mathbf{[\tan(\varphi)]_{cos} = (U_{cos})_f / (U_{cos})_q}$ **si** $\mathbf{(U)_{cos} = sqrt((U_{cos})_f^2 + / (U_{cos}))_q^2}$, where:

$\mathbf{U_{sin})_f}$ = the part of sine output having the same phase with input

$\mathbf{U_{sin})_q}$ = the part of sine output having 90^0 phase shift with input

$\mathbf{U_{cos})_f}$ = the part of cosine output having the same phase with input

$\mathbf{U_{cos})_q}$ = the part of cosine output having 90^0 phase shift with input

For example, if a resolver shaft were set to angle of 20°, the ratio transformer would be set to the tangent of 20° which is 0.3639702. The null meter does not indicate a null and the ratio transformer are adjusted until it does. The final setting of the ratio transformer is 0.3639200; the arctangent of that value is 19.9975°.

The resolver error is therefore 0.0025°, that means - 9arcseconds.

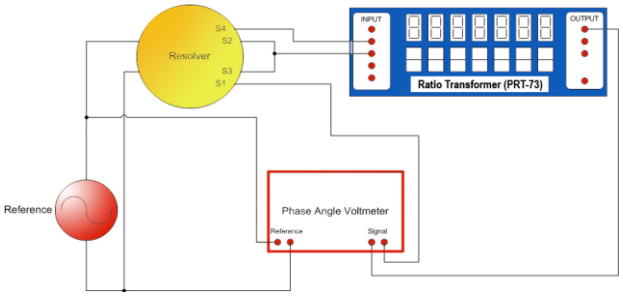

Fig. 7 Schematic on the stand to do vectorial measurement of resolvers

2.4. Aspects on resolver accuracy

The accuracy of the resolver has to be analysed in

connectied with the configuration of resolver and application.

If a single phase resolver is used, we can consider only the error relative to the fidelity of the signal according with ideal sinus form. Let us consider that the induced voltage, when the load of resolver is null, can be expressed: E_{bo} = VR TR sin(θ). On the other hand, the induced voltage in load conditions can be expressed: E_b = VR TR sin(θ) – j X I $\cos^2(\theta)$. The last relation can be expressed and as: $E_b = E_{bomax}$ sin(θ) / (1+b $\cos^2(\theta)$). On this way, we can define a relative error as:

$\Delta E_b = (E_{bo} - E_{br}) / E_{bomax} = (b \cos^2(\theta) \sin(\theta) / ((1+b \cos^2(\theta))$.

In the most part of applications, are used both windings, so we have to consider the differences between the amplitude of the two signals, as well as the error of quadrature.

The main factories that are influencing the accuracy are: the status of general machining (technologies, mechanical accuracy, heat treatment etc.), than the quality of the materials; the total impedance of the measurement system; excursion of amplitude of input voltage, as well as the value of the input frequency; excursion of the temperature during operation; rotation speed of the resolver etc.

III. RESULTS AND CONCLUSIONS

Most part from authors are working from long time as researchers, designers and producers of special electric machines. In these conditions, the resolver was one of main components to develop, to design and to produce. Different configurations, different sizes and different parameters are subjected with the author's activity. Bipolar resolvers 05, 08, 11, 15 or bigger sizes were developed for different applications, in many fields.

20 seconds of arc or 1 minute of arc accuracy were obtained on resolvers 19 or 29 sizes, having 32 poles. The methods of design used the most modern concepts, including numerical analysis of electromagnetic field. The methods of testing are based on vectorial measurement systems.

As conclusion, we can remark that the resolver component is superior to many other kind of absolute or relative position transducers because of its ruggedness and ability to provide a very high degree of angular accuracy under severe conditions.

There are not optical parts to keep clear of smoke or oil that often disrupt the operation of optical encoders. Because the resolver has two outputs that are subjected to tangent function, the input signal anomalies have a low influence. The resolver saves size and weight, being substantially smaller than other transducers approaches and easily integrated into any system.

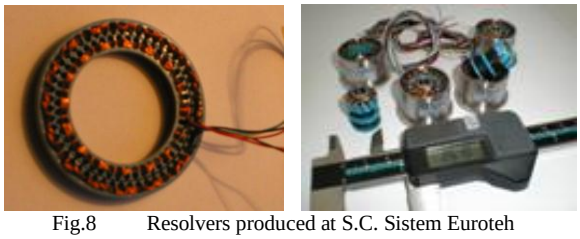

Fig.8 Resolvers produced at S.C. Sistem Euroteh

REFERENCES

[1] MAGUREANU, R. Masini electrice speciale pentru sisteme automate - Editura Tehnica, Bucuresti, 1981

[2] JULA , N . Senzori şi traductoare Editura Academiei Tehnice Militare, Bucureşti, 1999

[3] SYDNEY, A. D., LEDGERWOOD, B. K.Electromechanical components for servomechanismsMcGraw-Hill, Book Company, Inc., 1961

[4] VERNITRON Motion Control Division Pancake Resolvers

[5] MAFTEI, G., URSU, T. Optimizarea distribuţiei înfăşurărilor sinusoidale EEA – Electrotehnica-Electronica- Automatica 1978

[6] admotec Advanced Motion Technology Understanding Resolvers and Resolver-to-Digital Conversion - USA 2000

[7] TEGAM Testing Resolvers Using a Precision Ratio Transformer USA 2000

[8] What Is A Resolver? USA 2001

[9] Product Catalog S.C. Sistem Eurotehwww.sistemeuroteh.ro

Electrostatic Ion Shutter with Ejecting Electrode as a Part of a Ion Mobility Spectrometer

Anatoly V. GOLOVIN
National Research Nuclear University MEPhI, Moscow, Russia
avgolovin@gmail.com

***Abstract* – In portable hand-held devices for trace explosive and narcotic detection the most perspective is use of a principle of ion mobility spectrometry [[1],[2]] owing to the best combination of cost, compactness, parameters of detection and a wide range of found out substances. Classical designs of a ion mobility spectrometer are represented by a set of the metal electrodes forming area with homogeneous longitudinal electric field, in a combination to an electric shutter and area of ionization to a source of ionization on the basis of a radioactive isotope. The extremely perspective problem is development of a compact not radioactive source of the ionization, allowing to generate ions both positive, and negative polarity and having low power consumption. The use pulse corona discharge as a source of ionization for a ion mobility spectrometer is represented to the most perspective. Application in a design of a pulse corona discharge ionization source allows, unlike systems with isotope ^{63}Ni ionization, to do without application of an electrostatic ion shutter which separates ionization and drift chambers. However application of an ion shutter allows to achieve the best parameters of resolution and sensitivity. In the given work the scheme of operation and results of application of an electrostatic ion shutter as a part of a ion mobility spectrometer with a pulse corona discharge ionization source will be considered.**

I. INTRODUCTION

One of basic elements of a design of a ion mobility spectrometer is the spectrometry cell consisting of two adjacent areas of ionization and drift, separated by an electrostatic ion shutter [[3]]. In a described ion mobility spectrometer the pulse (10 Hz) corona discharge ionization source has been applied. Application corona discharge allows to solve problems, characteristic for the radioactive sources of ionization most often applied in serial devices, and thus to provide good parameters on detection of substances.

II. ION MOBILITY SPECTROMETER WITH ELECTROSTATIC ION SHUTTER

Figure 1 represents the electrostatic ion shutter of Tundal type [[4]], consisting of two transparent grids from thin stainless steel, located on distance about 1 mm from each other, added with a ejecting electrode.

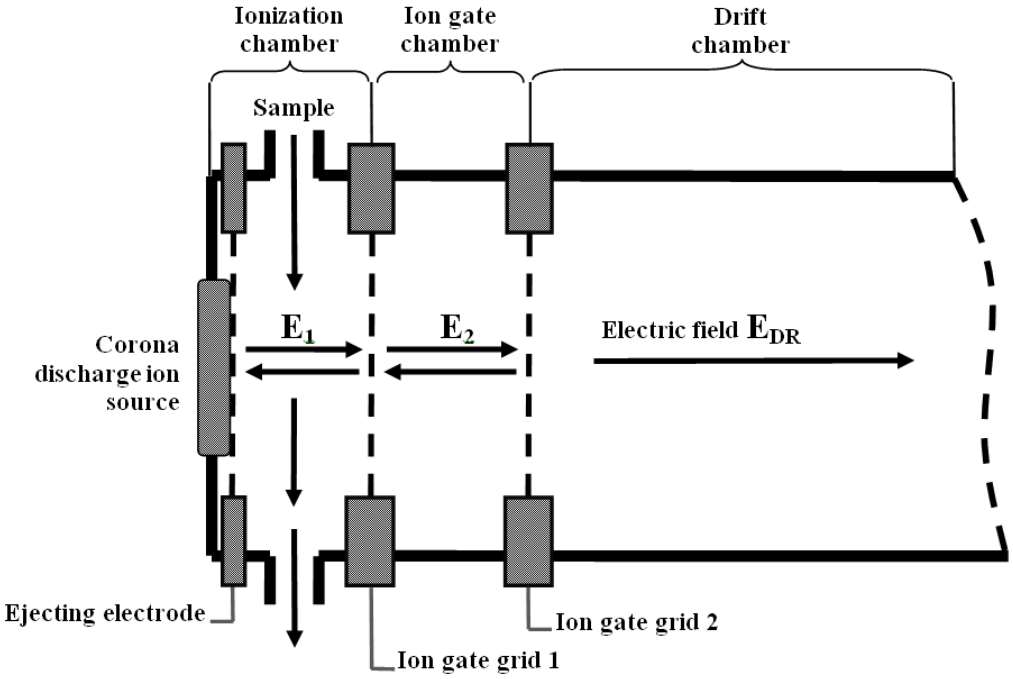

Figure 1. Eelectrostatic ion shutter with ejecting electrode.

Electric potentials on a ejecting electrode and on ion gate grid 1 change on commands of operating electronics that provides regulation of duration of a cumulate of ions in the ionization chamber and in ion gate chamber. The formed ions get from ionization chamber to ion gate chamber with a certain delay. It leads to possibility to regulate duration of ion-molecular interaction in the ionization chamber. Work of electrostatic ion shutter with ejecting electrode during one cycle of measurement is divided into 7 consecutive phases (Figure 2):

- Phase 1 – switch on of field E_1 in the ionization chamber that corresponds to preparation for the beginning of a cycle of measurement. The end of this phase corresponds to the beginning of the corona discharge impulse.
- Phase 2 – under the influence of field E_1 there is a movement of ions, formed by corona discharge, from a ejecting electrode to ion gate grid 1.
- Phase 3 – the field in the ionization chamber E_1 becomes equal to zero, ions stop. In the stopped bunch there are ion-molecular reactions between molecules of investigated substance and formed by corona discharge reactant-ions. Sensitivity of a spectrometer can be raised by means of increase in duration of this phase at the expense of fuller transfer of a charge from reactant-ions to molecules of investigated substance.
- Phase 4 – moving bunch of ions to ion gate chamber.
- Phase 5 – under the influence of field E_1 in the field of ionization and E_2 in the field of ion gate ions are injected in drift area. Thus by means of an electrostatic shutter begins possible to inject a thin bunch of ions that essentially increases the resolution of a ion mobility spectrometer.
- Phase 6 – the direction of field E_2 changes on opposite, thus the electrostatic ion gate is closed. Remained in the ionization chamber ions under the influence of field E_1 move to ion gate grid 1 and will be neutralized on it.
- Phase 7 – the initial condition of electric potentials on ejecting electrode and ion gate grid 1 is restored. The system is prepared for a following cycle of measurement.

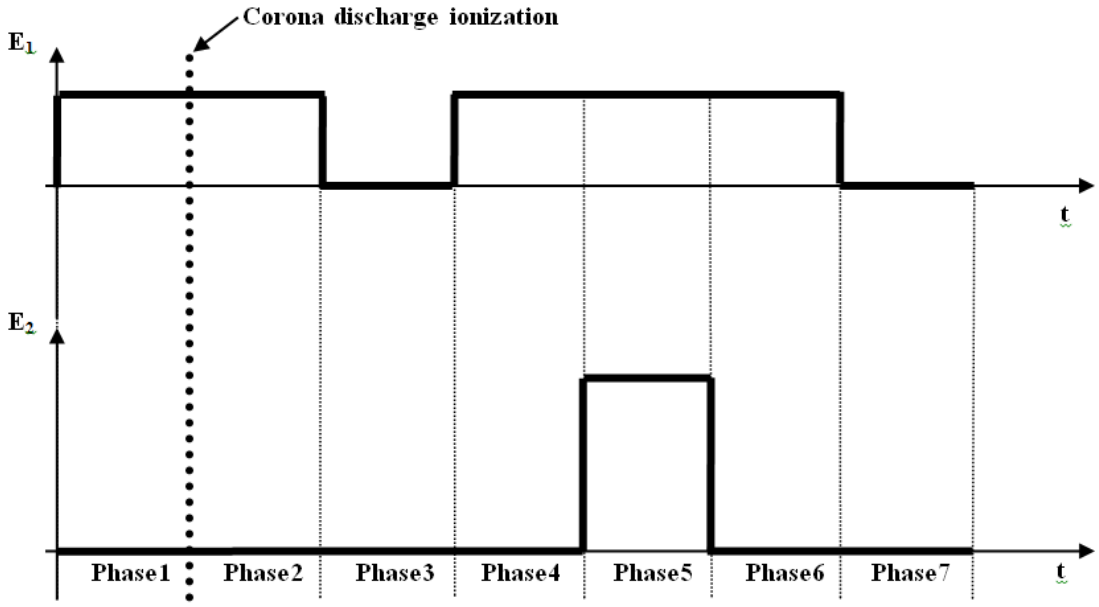

Figure 2. Distribution of fields in the ionization chamber E_1 and ion gate chamber E_2 during functioning of electrostatic shutters

In case of negative ions an increase in duration of the Phase 2 leads to a reduction of a total charge of ions. Thus the spectrum structure remains invariable. The total charge on a collector for negative ions is maximum at the minimum duration of the Phase 2. In case of positive ions at increase in duration of the Phase 2 leads to a reduction of amplitude of peaks of fast ions and increase in amplitude of peaks of slow ions. Thus, by means of an increase in duration of the Phase 2 it is possible to cut fast positive ions and to focus attention on slow ions that can be useful at detecting of ions of substances with low mobility. For positive ions the increase in size of the general charge is characteristic at increase in duration of the Phase 2 from 0 to 0,3 ms that is shown on Figure 3. Mobility of positive ions essentially below mobility negative, therefore doesn't occur falling of a charge because of neutralization of ions on the ion gate grid 1 at duration of the Phase 2 less than 0,3 ms. The increase in the common charge at this interval arises because of increase in cumulative time of injection of ions in drift chamber.

Also research of influence of time of injection of ions from ionization chamber in drift chamber (the Phase 5) has been conducted (Figure 4). During the given experiment the dynamic range of change of duration of injection of ions and influence of the given parameter on spectrograms in cases of positive and negative ions was investigated.

At work with negative ions the smooth increase in amplitude of peaks and the general charge of system is characteristic at increase in duration of injection of ions from ion gate chamber in drift chamber. Thus, the choice of duration of injection of ions in area of drift doesn't get essential influence on possibility of detecting of separate categories of the substances forming at ionization slow or fast ions, and is in a greater degree defined by resolution requirements. For this case value of saturation for fast ions of the Phase 5 equals 1,50 ms. At the further increase in the given parameter the increase in amplitude of peaks of fast

ions doesn't occur, however the amplitude of peaks of slow ions considerably increases.

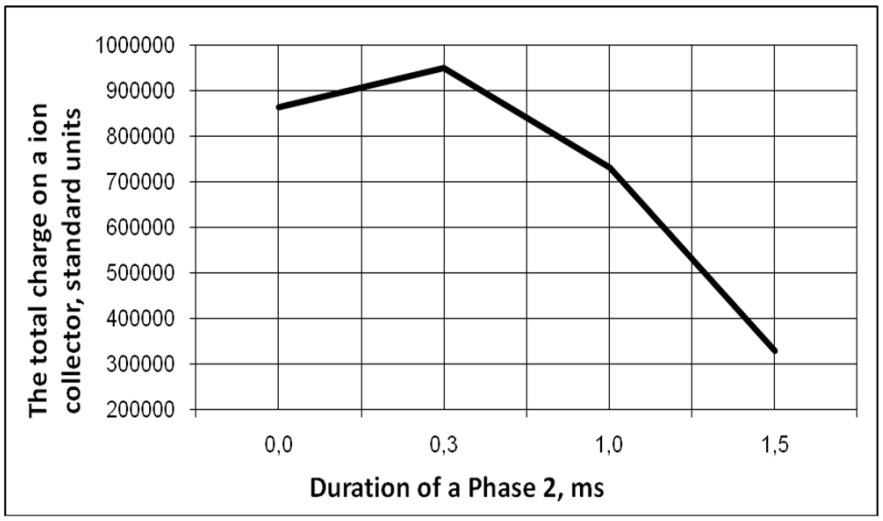

Figure 3. Dependence of a total charge on a ion collector at positive polarity depending on duration of the Phase 2 electrostatic ion shutter.

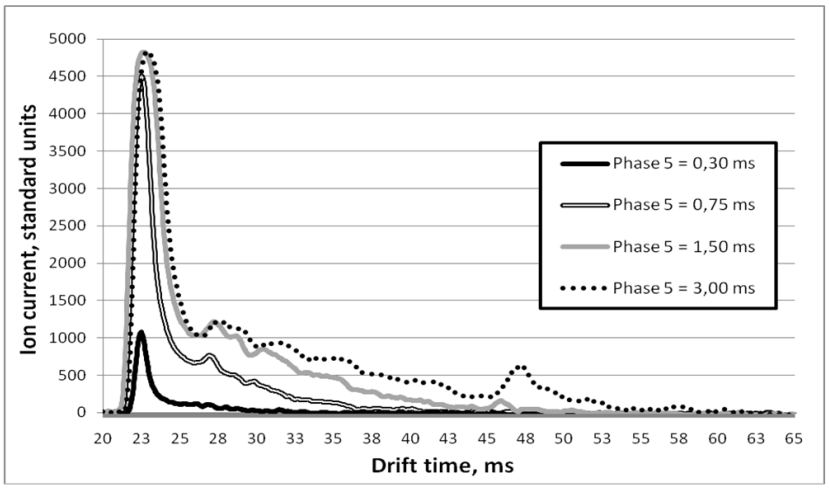

Figure 4. Comparative spectrograms of positive ions of laboratory air at change of the Phase 5 electrostatic ion shutter.

Thus, at detecting of some substances in positive polarity with the characteristic slow ions formed during ionization, the increase in duration of injection of ions from ion gate chamber in drift chamber (Phase 5) is necessary.

III. CONCLUSION

During work performance the scheme of an electrostatic ion shutter as a part of a ion mobility spectrometer with pulse corona discharge ionization source has been developed. In classical structure of an electrostatic ion shutter of Tundal type the ejecting electrode which is structurally a part of corona discharge ionization source has been added. Thus, possibility of regulation of duration of a finding of ions in ionization chamber has been entered during course of ionic-exchange reactions and time of passage of ions directly through an ionic shutter with possibility of allocation of a narrow clot of the ions getting in drift chamber. At an estimation of influence of the given structure of an electrostatic ionic shutter on detecting of ions it is shown that at detecting of positive ions it is required to establish more time of injection of ions from ion shutter area in drift area, than at detecting of negative ions.

ACKNOWLEDGMENTS

The author wish to thank Dr. V.S. Pershenkov and Ph.D V.V. Belyakov for numerous discussions and collective of scientific group of micro- and a nanoelectronics department for the help in design, assembling and carrying out of scientific researches.

REFERENCES

[1] Borsdorf H., Eiceman G.A., Ion Mobility Spectrometry: Principles and Applications // Taylor & Francis. – 2006.

[2] Belyakov V.V., Ion mobility spectrometer // Utility patent № 035034. – Russian Federation, 2006.

[3] Karpas Z., Eiceman G.A., Ewing R.G., Algom A., Avida R., Friedman M., Matmor A., Shahal O., Ion distribution profiles in the drift region of an ion mobility spectrometer // Int. J. Mass Spectrom. Ion Proc. – 1993. – Volume 127. - P.95–104.

[4] Tyndall A.M., The Mobility of Powsitive Ions in Gases // Cambridge University Press. – 1938. – Cambridge. - U.K.

The Simulation of Pulsed Heater for a Sampling System for the Ion Mobility Spectrometer

Evgeniy MALKIN
National Research Nuclear University MEPhI, Moscow, Russia
malkin_evgeniy@mail.ru

***Abstract* – The development of the sampling device with pulsed heating of the intermediate carrier for ion mobility spectrometer is described in this article. Numerical simulation of a pulse heater structure of is presented. The design of the sampling device using a pulsed heating of the intermediate carrier is developed. Experimental results of approval of the sampling device are presented.**

I. INTRODUCTION

Safety in public transport, places of a mass density of people, at the site of potential danger or high priority remains extremely important. For these purposes points of the control established at the airports, railway stations, port and customs terminals, should be equipped by the high-sensitivity equipment, that is sensitive to ultra low concentrations of explosives. The ion mobility spectrometry has been most demanded and widespread technology in these areas for the detection of trace of explosives over the past few years. Among the main advantages of devices based on this principle, it is possible to note simplicity of a design, compactness, low cost and possibility of operation in the field in real time.

Ion mobility spectrometers can detect the substance by sampling air from the environment and the research of composition of particles at different solid surfaces (documents, clothes, tickets, case handles, etc.). The most effective is the selection of trace of particles from the surface of objects with intermediate carrier, followed by heating and evaporation of the sample. The need for heating the intermediate carrier with the sample determined by a small amount of substance in the sample and low vapor pressure for a number of explosives. All existing portable ion mobility spectrometers, such as the Vapor Tracer, Ionscan, Sabre, Quantum Sniffer, as well as a spectrometer, developed at the Department of Micro-and Nanoelectronics MEPhI [1], have a heating unit of the intermediate carrier, which is constantly at high temperature. This leads to significant power consumption and time required to get the device to normal operating conditions.

The obvious solution to reduce energy consumption is the use of pulsed heating of the intermediate carrier. In this case, the intermediate carrier is placed in a heating device at low temperature, which prevents evaporation of samples during the positioning and the dependence of the results of further analysis of operator actions. In our case the analysis is started with moment of heating beginning. However, this approach is accompanied by a number of technological and structural problems associated with the requirements on the dynamics of heating and cooling, as well as issues of cleaning the device after a sample analysis. A similar approach is used in the design, use of pulsed heating of the gas-discharge lamp [2-3].

The purpose of this work is to simulate the pulsed heating of the intermediate carrier sampling device for ion mobility spectrometer.

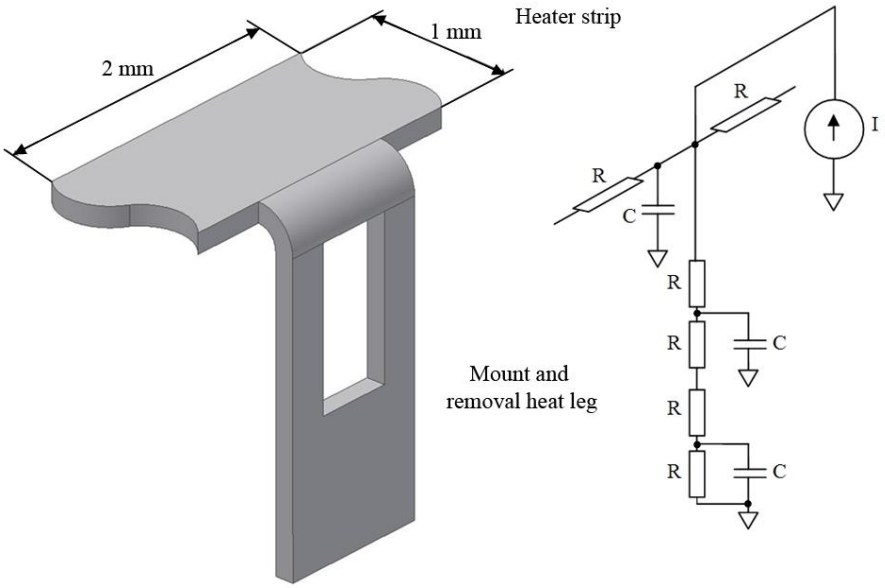

Figure 1. The structure of the segment and the equivalent circuit of the pulsed heater.

II. H EAT TRANSFER MODELING

The major task of development was the creation of a pulsed heater with dimensions of 25x25 mm for the heating section of the intermediate carrier at 200° C for 10 seconds,

and then cools it to the initial temperature for the same period of time.

The heater consists of 12 same elements spaced 1 mm apart. The heater element represent a strip of stainless steel in the thickness of 0,125 mm with the sizes 25x1 mm. For support, positioning and removal of heat, each element has a number of legs that are soldered to the printed circuit board. For heating the intermediate carrier with the sample is used the heat transfer from the heater operating in pulsed mode, through an air gap. On top of 1 mm from the heater install grid to support intermediate carrier.

Typical segment of the strip heater is shown in Figure 1. Its dimensions are 2x1 mm. The figure also shows elements of the thermal equivalent circuit model parts of the segment.

To calculate the dynamics of heating and cooling were performed numerical simulations of the structure using the circuit simulation package SPICE. The model take account of the thermal resistance and heat capacity the section of pulsed heater and air gap, supporting grid and section the heated intermediate carrier with the particles of the sample

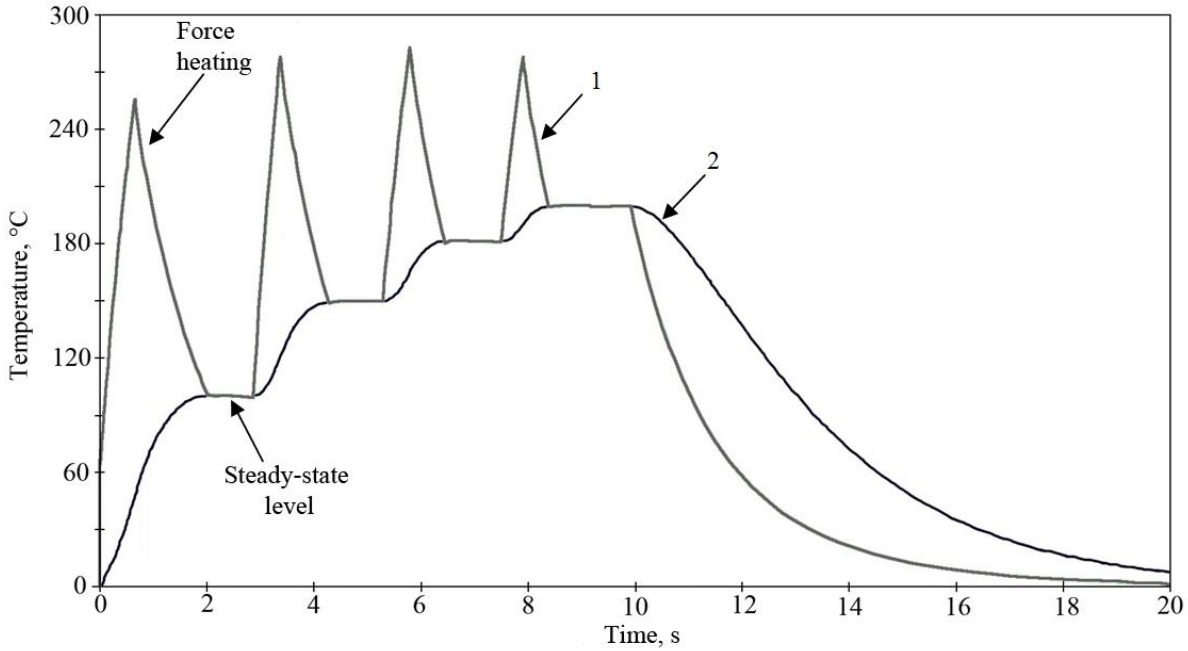

Figure 2. Dependence of temperature of a heater (1) and the intermediate carrier (2) from time.

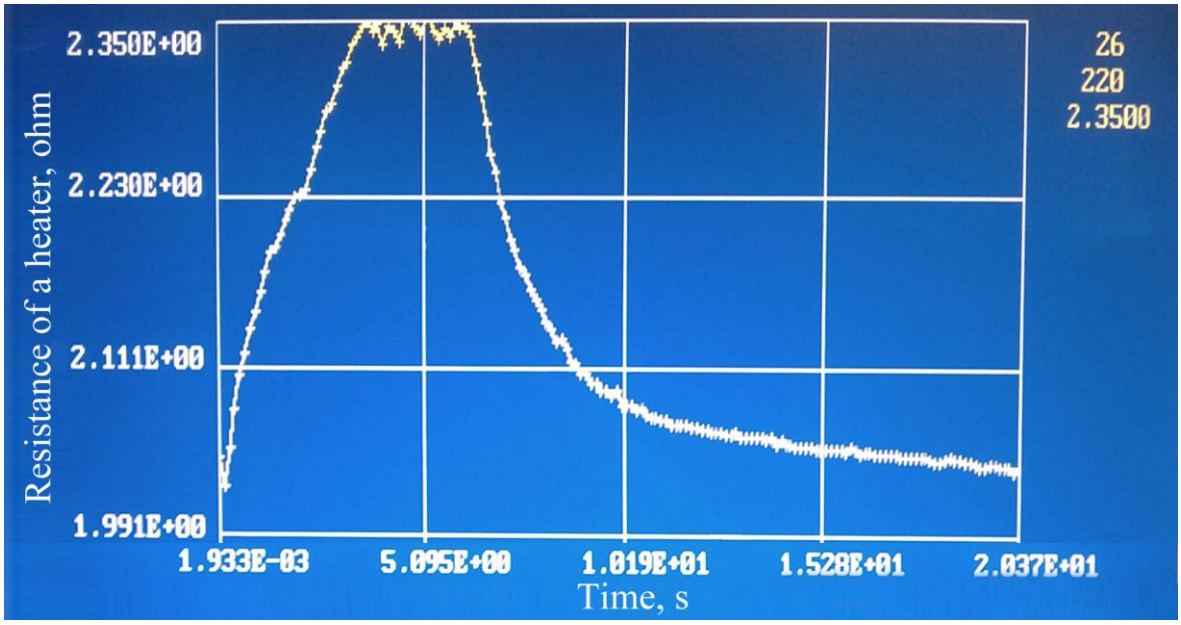

Figure 3. Changes of temperature of heaters in time.

Numerical calculation of the intermediate carrier heating dynamics for step change of temperature has been carried out. To accelerate the transition to the next level of the temperature of the intermediate carrier force increase in power pulsed heater and then get to the steady-state level is used. Model dependence of heating temperature on the time shown in Figure 2. From these results it is visible that for a ten-second interval it is possible to realize about 4 steps of heating of system. To improve the dynamics of heat necessary to reduce the air gap between the heater and the intermediate carrier to reduce its thermal resistance, and to ensure removal of the heat from the heater surface to the environment. Rapid cooling of the heater pulse is provided at a low temperature of the substrate through the attachment

and support leg

III. EXPERIMENTAL RESULTS

Figure 3 shows the experimental dependences of the resistance heater at pulse heating. Curve shows the single-stage heating and cooling the heater pulse.

IV. CONCLUSION

The device sampling with pulsed heating of the intermediate carrier is developed.

The numerical simulation of a heater has allowed optimizing the dynamic characteristics of the device for power consumption and the dynamics of heating and cooling is carry out.

Tests of the device showed the possibility of rapid heating and cooling of the intermediate carrier for the typical cycle time of measurement. Further work will be directed to study the dynamics of evaporation of the sample in the analysis of trace amounts of explosives.

REFERENCES

[1] V. Belyakov, A. Golovin, D. Kushneruk, V. Pershenkov, M. Tihanov. Portable device for detection of trace amounts of explosives, Chip News, № 4, p. 40-41, 2007.

[2] V. Belyakov, A. Golovin, V. Vasiliev, D. Kushneruk, V. Pershenkov, M. Tihanov. A device for detecting trace amounts of explosive materials on the fingers of human and documents // Sensors and Systems 2009. № 7. P.44-49.

[3] Flash Vapor Sampling for a Trace Chemical Detector Patent No. US 7.098.672 B2, Date of Patent: Aug.29, 2006.

Periodic Signals From a Nanopore Coulter Counter

Y. RUDZEVICH[1],Y. LIN[1], G. EVANS[1], A. ORDONEZ[1], O. LUPAN[1,2] and L. CHOW[1]
[1]*University of Central Florida, PO Box 162385 Orlando, FL 32816-2385, U.S.A.*
[2]*Technical University of Moldova, Republic of Moldova*
lee.chow@ucf.edu

***Abstract* – In this work, we report the observation of periodic signals from a Coulter counter that employed glass pipettes. These periodic signals occurred even when no nanoparticles were presented in the counter. Observed phenomenon may be related to the translocation events through glass pipette. Further studies are needed to better understand these results.**

***Index Terms* – Coulter counter, nanopipette, nanopore, translocation.**

I. INTRODUCTION

Traditionally, determination of the size and concentration of nanoparticles has been performed through chromatography, gel electrophoresis, or dynamic light scattering. However the Coulter Counter technique [1] also provides a promising and reliable method for particle counting and sensing in a simpler manner. This method can be briefly described as two chambers, filled with particle-laden solution, separated by a membrane with a single tiny pore. The ionic current through the pore, created by electric potential applied between the chambers, depends on the diameter of the pore, and changes when pore is partially blocked. In most cases the blocking of the pore is caused by translocation of small particles. By monitoring these signals we can count the number of particles translocated through the pore from one chamber to another, and the particle size can be determined, if the pore size is known. This technique is a useful tool for nanotechnology and biomedical applications.

Here we report the observation of periodic signals from certain experiments when nanoparticles were not presented in the chamber. These results are very surprising and counter-intuitive. Here we present main results of our findings and some discussions.

II. EXPERIMENTAL

Nanopipets were fabricated from borosilicate capillaries with inner diameter 0.8 mm and outer diameter 1.5 mm. These capillaries are pulled using a glass pipettes puller (P2000, Sutter, Novato, CA), to achieve an orifice size of a few hundred nanometers. Multiple parameters can be used to control the size of the capillary tip, such as filament current, heating duration, and pulling force.

SEM image of the capillary tips are taken to determine the size (Figures 1 and 2). The nanopipette was filled with 0.1 mol/L potassium chloride (KCl) solution (Fisher Scientific) with pH = 5.5 and submerged in the bath with the same solution. A Ag/AgCl 0.2 mm thick electrode was embedded into the capillary until it reaches the conical part. The reference Ag/AgCl electrode was immersed directly into the bath, as shown in Figure 3. Average distance between electrodes was 5-7 mm. For testing purpose, we check *I-V* dependence, and as expected, the *I-V* curve behaves ohmically. For ionic current recording we used the Axopatch 200B amplifier in voltage clamp mode with a low-pass Bessel filter at 2 or 5 kHz bandwidth. The signal was digitized by Axon Instruments Digidata 1440A Series with sampling rate 250 kHz, and recorded with AxoScope 10.2 (Axon Instruments).

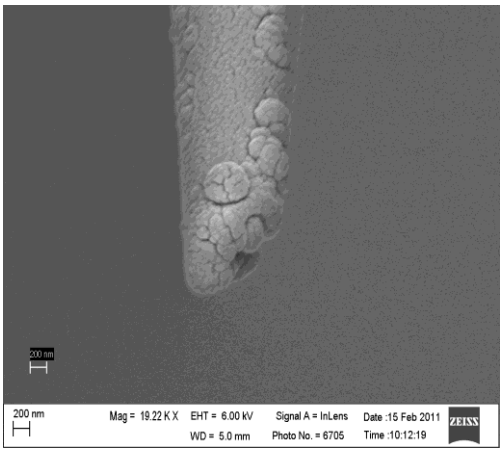

Fig. 1 SEM Image of the nanopipette tip (coated with Pt for SEM)

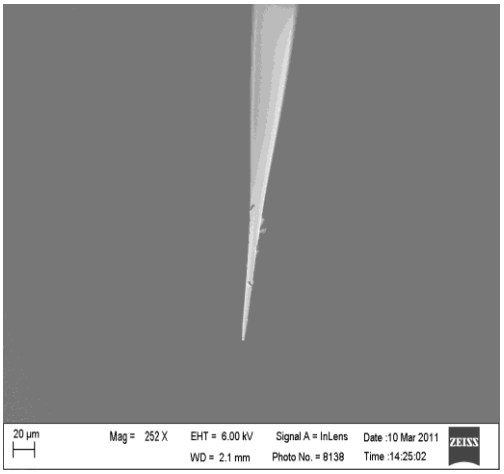

Fig. 2. SEM image of the tips, demonstrating a cone-shaped tip

III. RESULTS AND DISCUSSIONS

The experimental set up is commonly used in Coulter counting of nanoparticles. At usual cases, we observed the

typical baseline current and translocation signals, as shown in Figure 4 below.

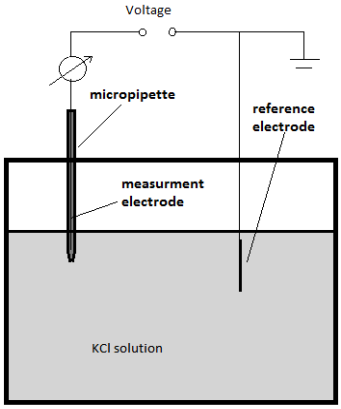

Fig. 3. The schematic set up of our translocation experiment.

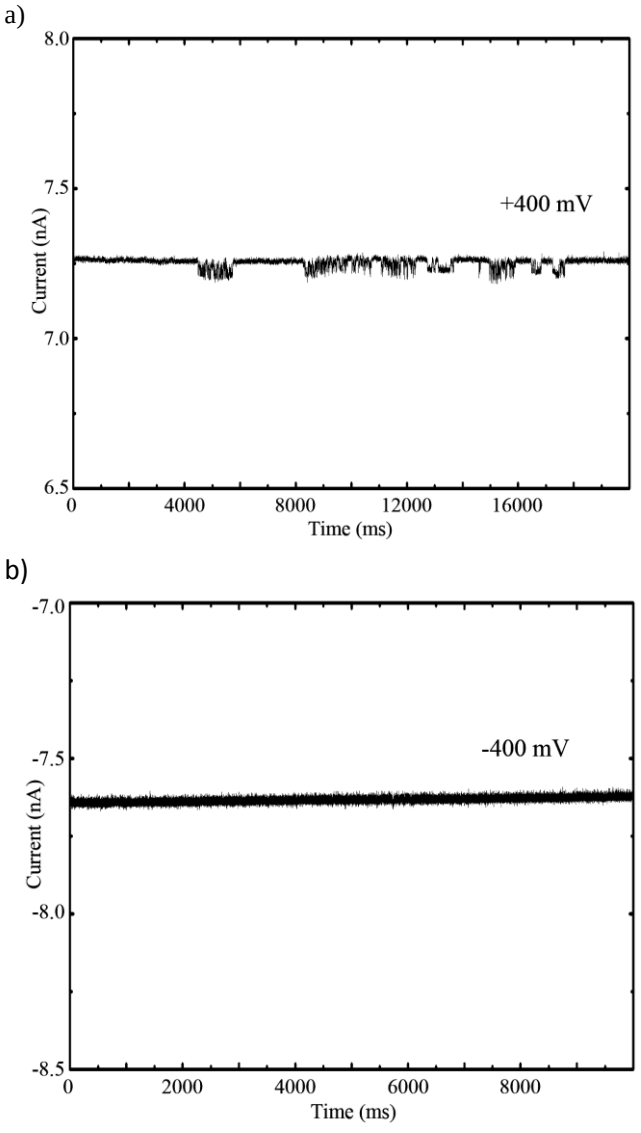

Fig. 4. Particles translocation experiment with pipette of 800 nm pore size, a) shows clear blockade signals with positive +0.4V potential applied, and b) no translocations observed after switching voltage to negative sign.

These signals related to the translocation of nanoparticles, which are blocking the ionic conduction during translocation. As we can see from above, the nanoparticle translocation signal, distributed randomly, are obtained only when positive voltage is applied. While only a baseline current is observed when applying negative voltage. However, we encountered some interesting phenomena when using a syringe to inject the KCl solution into the micropipette. We test it simply applying positive and negative voltage. Without any introduction of nanoparticles, instead of a typical baseline of current that represents the ionic conduction through micropipette, we observed a clear periodic signal shown in Figure 5. This result exhibits a base line current of about 2.51 ± 0.03 nA, which represents the ionic current passing through the micropipette when there is no nanoparticles in the solution. The amount of this current can be estimated by the following equation [2]:

$$I_0 = n(t) \times e \times A(x,t) \times v(x)_{ion} \qquad (1)$$

where $n(t)=n_+ + n_-$ is a sum of positive and negative ion densities, e is elementary charge, $A(x,t)$ is the cross section, $v(x)$ is average ion velocity which is derived from $v(x) = \chi E$, where χ is mobility of K^+ and Cl^- and E is electric field at the orifice.

The multiple dips shown in Figure 5 stand for the sudden drop of current every time the ionic path in capillary is blocked. This change of current is related to the variation of resistance. Figure 6 shows the event current as a function of time using a different micropipette and with an applied voltage of 500mV.

We have conducted further investigation to study this interesting signal which appears in our measurements at room-temperature. We repeated our experiments several times without introducing any nanoparticles; the periodic signals persisted. The periodic signals, which stand for the event current, are uniformly distributed, compare to the randomly pikes in normal nanoparticle translocation picture (Figure 4).

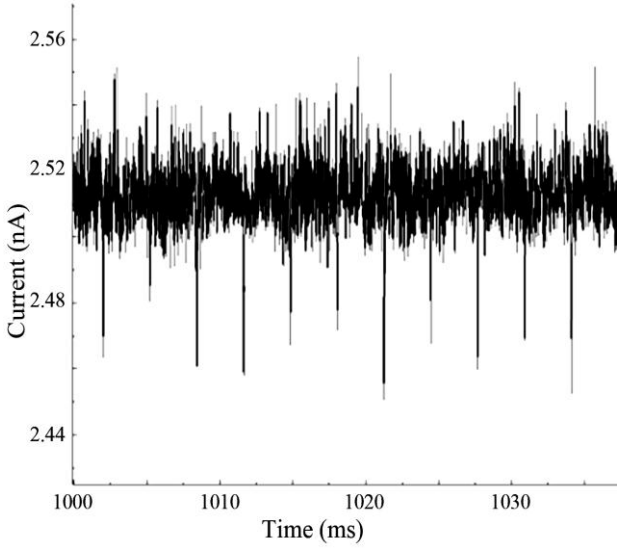

Fig. 5. Event current as a function of time with an applied voltage of 300mV.

As we increase the applied voltage, we notice the frequency of the periodic signals also increases. We found a linear dependence of this frequency on the applied voltage which is not shown here. Interestingly, unlike the translocation signals in Figure 4, these periodic signals

reverse their polarity when voltage polarity is switched. The data in Figures 7 and 8 show that when the applied voltage changes to negative voltage the event currents also reverses it direction as expected. However both the frequency of the periodic signals and the magnitude of the event current remain unchanged.

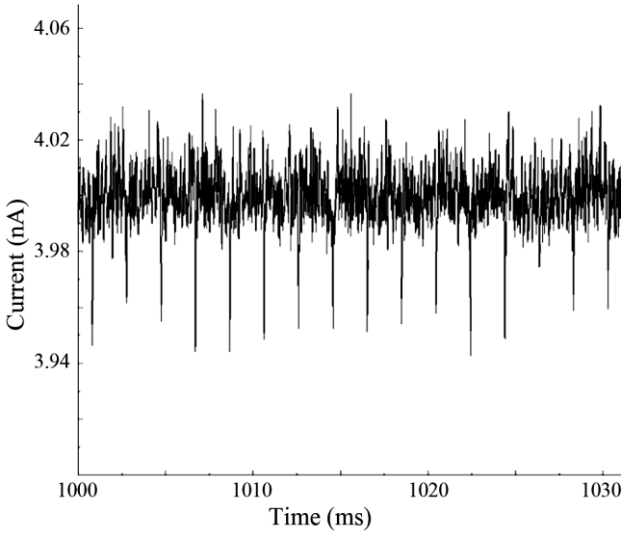

Fig. 6. Event current as a function of time with an applied voltage of 500mV.

The interesting results we observed are hard to explain, since no particles are involved. Extra care and multiple repeated experiments should minimize any possible contamination of nanoparticles in the solution or pipette. In addition, the major challenging fact is the perfect regularity of these periodic signals, which are linearly proportional to the applied voltage. At this moment, we do not have any plausible explanations for our observations. We point that nanobubble in aqueous solution may relate to our observations [3-6].

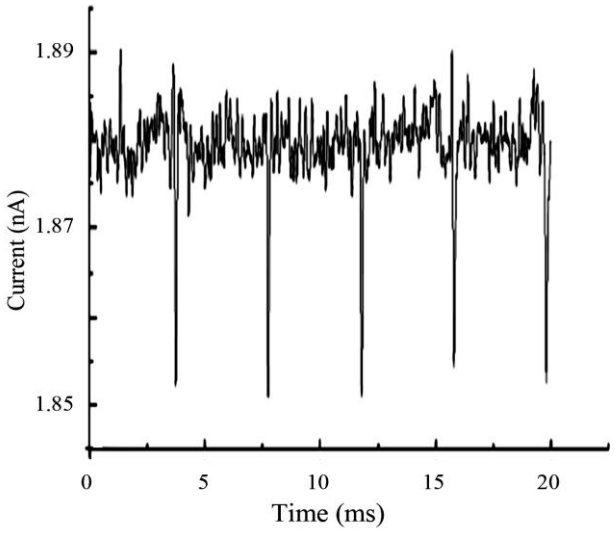

Fig. 7. Signals recorded before switching polarity

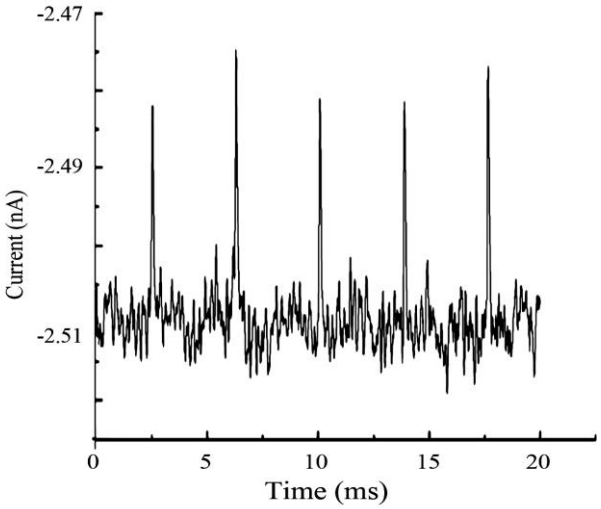

Fig. 8. Signals recorded after switching polarity

IV. CONCLUSION

It has been observed that periodic signals from a Coulter counter that employed micropipette. These signals appeared when a syringe is used to inject KCl solution into the micropipette. The frequency of the periodic signals is linear proportional to the applied voltage. These periodic current signals are reversible under polarity change of the applied voltage.

ACKNOWLEDGMENTS

L. Chow would like to thank National Science Foundation (NSF-ECCS-0901361) for financial support.

REFERENCES

[1] Coulter, W.H., 1953. U.S. Patent No. 2,656,508.
[2] Stober, G., Steinbock, L.J., and Keyser, U.F. Journal of Applied Physics 105, 084702, 2009.
[3] M. A. Hampton and A. V. Nguyen, Nanobubbles and the nanobubble bridging capillary force, Adv. Coll. Interface Sci. 333 800-806, 2009.
[4] Saleh, O.A., and Sohn, L.L. Review of Scientific Instruments 72(12), 4449 - 4451, 2001.
[5] R. A. Pushkarova, R. G. Horn, Surface forces measured between an air bubble and a solid surface in water, Colloids Surf., A 261 147-152, 2005.
[6] N. Mishchuk, J. Ralston and D. Fornasiero, Influence of dissolved gas on van der Waals forces between bubbles and particles, J. Phys. Chem. A 106 689-696, 2006.

APPENDIX A

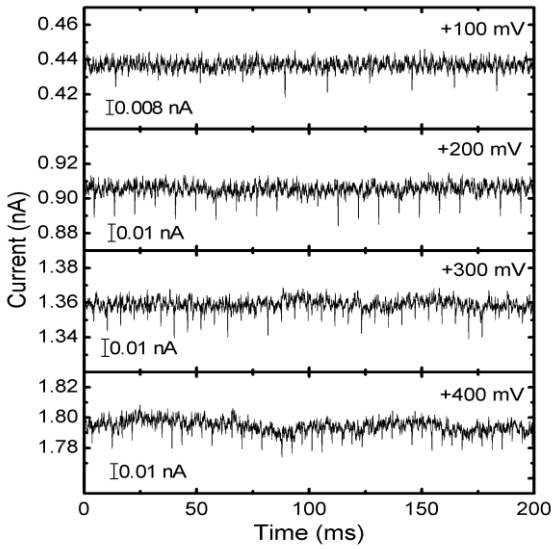

Fig. A. Data recorded in experiment with 200 nm pore size, with different voltages, 100-400 mV.

APPENDIX B

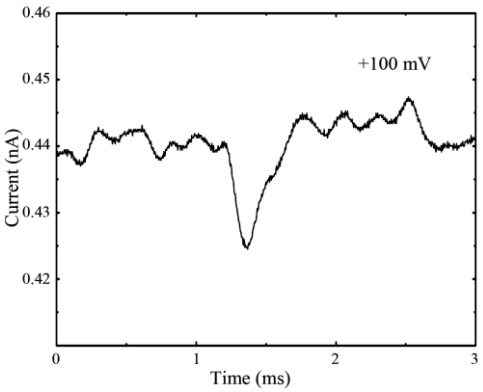

Fig. B. A single peak of data recorded for 200 nm pore size with potential +100 mV

APPENDIX C

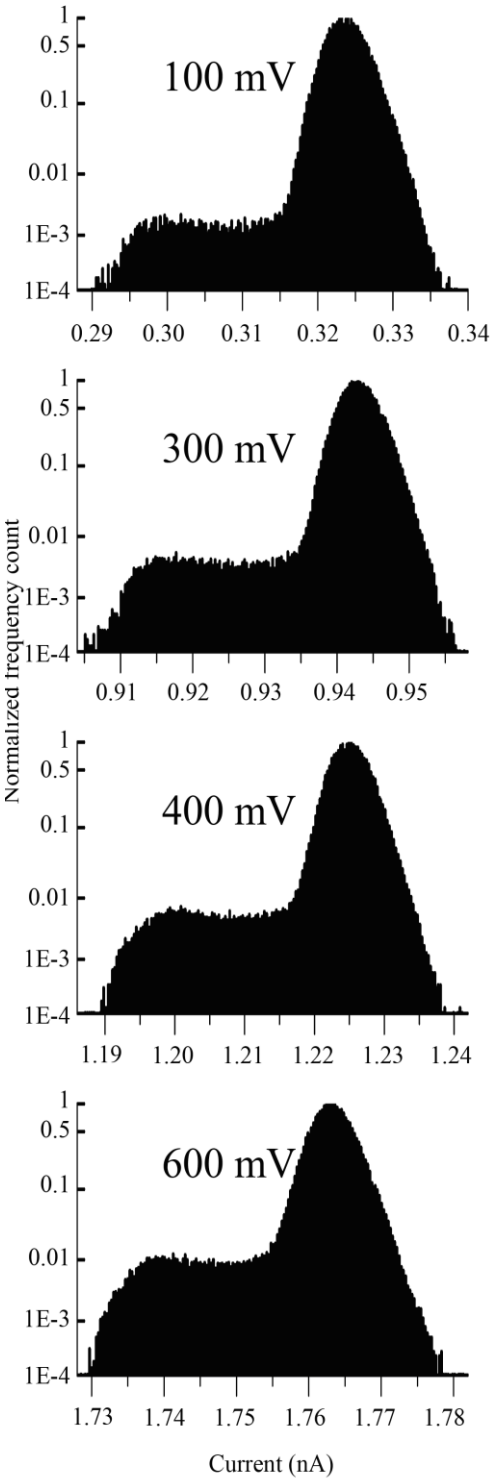

Fig.C. Current histogram of data recorded in a experiment with different voltages. Time of recording is 10 seconds for each voltage. The highest peak indicates a baseline current, when a plateau on the side illustrates the event current. It is also clear from this histogram that frequency of event current is increasing with voltage.

About the Using of Polarization Methods in Investigating the Polarization Sensitive Nanosystems

C.Yu. ZENKOVA, I.V. SOLTYS
Chernivtsy National University, Chernivtsy, Ukraine
zenkova@itf.cv.ua

***Abstract* –The paper shows the possibilities of defining the degree of correlation of mutually orthogonal superposing circularly-polarized and linearly-polarized plane waves. The proposed results widen possibilities of metrological use the methods of spatial polarization modulation for investigating the properties of polarization sensitive systems and nanoobjects.**

***Index Terms* – spatial modulation of polarization, visibility, degree of coherence.**

I. INTRODUCTION

One of the manifestations of the coherence of superposing fields, one of the diagnostic indicators of coherence is the spatial periodical polarization modulation of the resulting spatial distribution. The depth, the level of such a modulation is connected with the degree of coherence, correlation of superposing fields. The interconnection of the degree (or level) of the polarization modulation of the resulting field and the characteristics of coherence in the approximation of plane waves is rather thoroughly studied within the framework of the stokes-polarimetric approach [1, 2].

The manifestation of the superposing wave coherence in the case when it is necessary to take into consideration the longitudinal z-component of the field, and the modulation polarization of the resulting field realized in the plane of incidence is studied in a number of papers offered by the authors [3]. The possibility of measuring the field coherence function through estimating the degree (level) of field polarization modulation is shown and justified in the framework of such an approach [4, 5]. Thus, these papers suggest a method for defining the degree of coherence of linearly-polarized fields, where the polarization distribution takes place in one of the planes – the plane of observation. The offered paper widens the proposed method and demonstrates the possibility of using it for circularly-polarized fields at the formation of two polarized distributions in two mutually orthogonal planes. Thus this paper proposes to widen the possibilities of metrological use of the method of spatial polarization modulation of the field for estimating the coherence of superposing waves by considering the case of superposition not only of linearly polarized in the incidence plane waves, but, in the general case, of circularly polarized interacting waves as well. Practical importance of this problem increases owing to the development of the techniques of confocal microscopy of isolated molecules, including long molecules oriented along the direction of beam propagation and systems of 3D imaging of such molecules, when accounting z-component of a field is absolutely necessary. Generally, such situations occur in solving of many problems:

- transmission of radiation through optically anisotropic crystals;
- multiple light scattering of coherent radiation in turbid media, as well as transmission of optical radiation through optical waveguides;
- heterodyning (nonlinear mixing) of optical waves of different states of polarization, as well as at near zone of a field scattered by random phase objects.

At the same time the information contained in the polarization distribution of interacting circular waves of a similar polarization, essentially enriches the ideas on the properties of optical fields. The paper offers for investigation the results of computer simulation, which allow to define both coherent peculiarities of vector optical fields and the ways of forming periodically modulated polarization distribution in the registration plane.

II. THE BASE OF THEORETICAL APPROACH AND COMPUTER SIMULATION

The time-averaged intensity distribution [4,5] of a random electromagnetic field formed at instant t by the sources $\vec{Q}_1, \vec{Q}_2, \vec{Q}_3$ and observed at point $\vec{r}$ at the observation plane can be put down as,

$$I(\vec{r}) = \sum_{ij} \Big\{ \varphi_{ii}^{(1)}(\vec{r}) + \varphi_{ii}^{(2)}(\vec{r}) + \varphi_{ii}^{(3)}(\vec{r}) + 2\sqrt{\mathrm{tr}[W(\vec{Q}_1,\vec{Q},0)]\mathrm{tr}[W(\vec{Q}_2,\vec{Q}_2,0)]}\,\eta_{ij}^{(1,2)}\cos[\delta_1] + 2\sqrt{\mathrm{tr}[W(\vec{Q}_1,\vec{Q}_1,0)]\mathrm{tr}[W(\vec{Q}_3,\vec{Q}_3,0)]}\,\eta_{ij}^{(1,3)}\cos[\delta_2] + 2\sqrt{\mathrm{tr}[W(\vec{Q}_2,\vec{Q}_2,0)]\mathrm{tr}[W(\vec{Q}_3,\vec{Q}_3,0)]}\,\eta_{ij}^{(2,3)}\cos[\delta_3] \Big\},\ i, j = x, y, z. \quad (1)$$

Here $\varphi_{ii}^{(m)}(\vec{r}) = < E_i^{(m)}(\vec{r},t) E_i^{*(m)}(\vec{r},t) >$ $i, j = x, y, z$, (m =1, 2, 3) describes the time-averaged intensities of corresponding sources, the angle brackets denote the time averaging and the superscript * stands for complex conjugation. The coherence properties of vector optical fields are described using the mutual coherency matrix $W(\vec{Q}_m, \vec{Q}_n, t)$ [6] characterizing correlation of the fields at two different spatio-temporal points $\vec{Q}_m$ and $\vec{Q}_n$, being determined as $W(\vec{Q}_m, \vec{Q}_n, t) = < E_i(\vec{Q}_m, t) E_j^*(\vec{Q}_n, t) >$.

Within the framework of such approach $\eta_{ij}^{(m,n)} = \frac{W_{ij}(\vec{Q}_m, \vec{Q}_n, t)}{\sqrt{\mathrm{tr}[W(\vec{Q}_m, \vec{Q}_n, 0)]\mathrm{tr}[W(\vec{Q}_n, \vec{Q}_n, 0)]}}$, ($m$, n = 1, 2, 3, i, j = x, y, z) and determines the degree of correlation of the field components. $\delta_1 = k(R_1 - R_2)$, $\delta_2 = k(R_1 - R_3)$, $\delta_3 = k(R_2 - R_3)$ are the phase differences of the corresponding fields at the registration plane, $R_1 = \left|\vec{r} - \vec{Q}_1\right|$, $R_2 = \left|\vec{r} - \vec{Q}_2\right|$, $R_3 = \left|\vec{r} - \vec{Q}_3\right|$ are distances of point $\vec{r}$ from the sources centers.

Changing a phase of the reference wave within the interval $0..2\pi$ results in periodical changing of visibility of the registered interference pattern following the harmonic law [4,5].

The visibility modulation depth (VMD) is determined as

$$M = \max[V] - \min[V] = 4\sum_m \sum_{ij} \frac{\sqrt{\mathrm{tr}[W(\vec{Q}_m, \vec{Q}_m, 0]\mathrm{tr}[W(\vec{Q}_3, \vec{Q}_3, 0)]}}{\varphi_{ij}^{(m)}(\vec{r}) + \varphi_{ij}^{(3)}(\vec{r})} \left|\eta_{ij}^{(m,3)}\right|$$

m = 1, 2; i, j = x,y z. (2)

Choosing a reference wave to be completely correlated with one of the initial waves, to say $\left|\eta^{(1,3)}\right| = 1$, one can see that the VMD of an interference pattern, M, characterizes, up to the constant depending on the intensity values, the degree of mutual coherence of the reference wave and the second of the initial waves, i.e. $M = \left|\eta^{(2,3)}\right|$. Accounting $\left|\eta^{(1,3)}\right| = 1$, one concludes that $\left|\eta^{(2,3)}\right| = \left|\eta^{(1,2)}\right|$. Thus, by proper choice of intensities of the interfering waves $\left|\eta^{(1,2)}\right|$ will be determined by the VMD of an interference pattern: $M = \left|\eta^{(1,2)}\right|$.

Superposition of plane waves of equal intensities linearly polarized at the incidence plane whose degree of mutual coherence equals zero at the same registration scheme results in homogeneous intensity distribution at the registration plane. The use of the plane reference wave coherent with one of the initial waves enables to visualize the intensity distribution with the certain visibility. In the case of two uncoherent waves, the VMD is equal to zero. It means that the VMD is in quite correspondence with the degree of mutual coherence of the initial superimposing waves. The experiments [4,5] carried out for the cases when $0 < \eta^{(1,2)} \le 1$ completely proved the conclusion that the VMD of a pattern corresponds to the magnitude $\eta^{(1,2)}$ of the superimposing waves.

It is possible to perform a correct experiment if some factors are taken into account. To avoid distortions introduced by the optical system, we must take into account the fact that the propagation of radiation through a microscope is accompanied by the change of a cone angle of the beams, so that this angle differs from the right one. This leads to the violation of the strict orthogonality of the electrical vectors of the interfering beams and manifests itself in the spatial intensity modulation. We employ a holographic recording system in an immersion liquid (Fig. 1). Such a system fulfills the strict angular requirements for the waves in the recording region. We set the reference wave intensity equal to the net intensity of the plane waves in the recording region, thus ensuring a larger percentage modulation and therefore a higher recording efficiency of the interference fringes that visualize the polarization modulation of the field. The same scheme was used for the readout of a hologram. The prism positioned in an immersion liquid was used for coupling out radiation diffracted by the holographic grating.

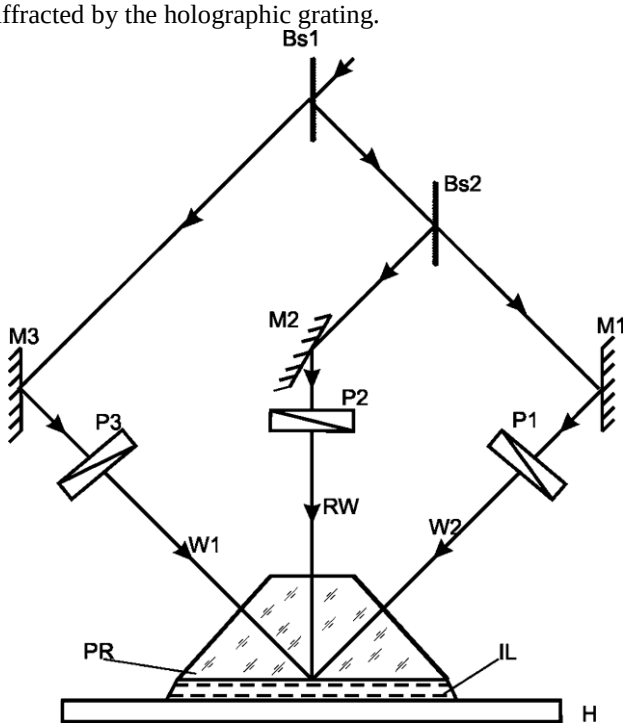

Fig.1. Optical arrangement for holographic experiment: Bs1 and Bs2, beam splitters; M1, M2, and M3, mirrors; P1, P2, and P3, polarizers; PR, prism; IL, immersion liquid; H, hologram.

It can be ascertained that the maximal intensity of the reconstructed signal corresponds to the case in which the electrical vector of the reference wave lies in the incidence plane, and the minimal intensity corresponds to the case in which the polarization of the reference wave is orthogonal to the incidence plane. Changing the polarization azimuth of the reference wave leads to a decrease in contrast of the interference pattern.

The experimental results are shown in the form of interferograms obtained in various polarization situations. It is seen from the photos shown in Fig. 2(a) that the interference of two plane object waves which are linearly polarized in the plane of the figure results in the interference pattern with the period corresponding to the angle of convergence of the two beams, and the visibility is determined by the ratio of the x − and z − components of the decomposition. The use of the third linearly polarized beam with the direction of oscillation of the electrical vector perpendicular to the figure plane does not result in any changes in the structure (period) of an interference pattern. Only the visibility of the pattern is changed due to changing the level of background, see Fig. 2(b). If the state of polarization of the reference beam is linear and the electrical vector lies in the figure plane, then the structure (period) of

the registered interference pattern is changed, as a rule, it is doubled, Fig. 2(c). The doubling of the period of the interference pattern is the most pronounced in the situation in which the intensity of the reference beam exceeds the intensity of the object beams. Such doubling of a period is of pure polarization nature and has been quite comprehensively described in the previous experiment and illustrated in Fig. 1. If intensity of the reference beam is spatially nonuniform, one can observe the mechanism of the period doubling of the interference distribution – see the picked out fragment in Fig. 2(d). Thus, similarly to the previous experiment, the contribution of the polarization component to the correlation of optical fields has been shown.

The given experiment shows the contribution of the polarization component into the correlation of optical fields. The parameter, which was introduced by us directs the way to the quantitative estimation of this correlation.

The results of computer simulation for the same arrangement and the same states of polarization of the superposing initial and reference waves but for different magnitudes of the degree of mutual coherence of the initial waves show that the VMD of an interference pattern strictly corresponds to the degree of mutual coherence of these waves.

Similar results of defining the degree of coherence of superposing waves are observed at interacting of two circularly-polarized waves when the angle of their convergence is equal to 90^0 [7]. In this case all three components (x, y, z) of the interacting fields determine the formation of the resulting distribution of intensity and polarization.

Let us consider the result of circularly polarized waves interference in the general case with the angle 2θ between the initial W_1 and W_2 waves and the third reference wave RW, spreading perpendicular to the registration plane (Fig.3, a). Here $\vec{E}^{(1)}$, $\vec{E}^{(2)}$, $\vec{E}^{(3)}$ are the electrical vectors of the waves W_1, W_2 and RW correspondingly.

The formation of the resulting intensity and polarization distribution at interacting of two circularly-polarized waves (W_1, W_2) of a similar handedness is determined by the relationship among the amplitudes and phases Ox, Oy, Oz field components. We shall deal with the special case of the convergence angle $2\theta = 90^0$.

The circularly polarized wave can be obtained by superposition of two linearly polarized waves, which differ in phase by 90^0, and spread in two mutually orthogonal planes xOz and yOz. The axis z is directed perpendicular to the observation plane xOy. The result of the superposition of circularly polarized fields will be the intensity distribution, which is formed as a result of interference of x-components (curve 1), y-components (curve 2), z-components (curve 3) of the fields. Figure 1, b demonstrates the result of such interaction at point O. In this case the x-distribution of intensity diverges in localization by a quarter of period with respect to the y-distribution.

The amplitude distribution only for the z and y components can be obtained by analyzing plane yOz. Since the two analyzed waves of a similar handedness are incident upon a registered plane at the angle of 45^0, the value of the y-projection of these waves will be maximum. The x and z wave projections are determined by similar amplitude distributions, which when combined, cause the homogeneous distribution of intensity

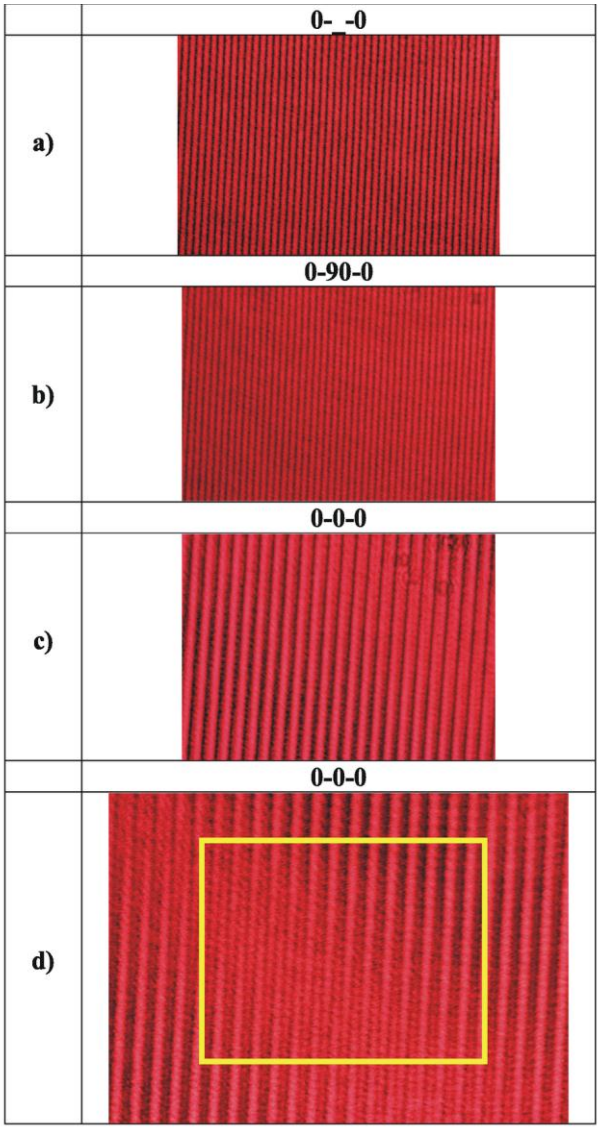

Fig. 2 a-d

Images of two resulting interferograms:

(a) for two object waves with the plane of polarization in the figure plane;
(b) for two object waves with the plane of polarization in the figure plane and the reference wave with the plane of polarization perpendicular to the figure plane;
(c) for two object waves and the reference wave with the plane of polarization in the figure plane;
(d) the result of doubling the period of an interference pattern for interference of three beams with polarization in the figure plane.

. The superposition of the y- field components will cause the resulting distribution of intensity.

We can state with assurance that the spatial distribution of polarization is set by the phase difference between the x and z components of the interacting optical fields at different points of the observation plane. (Fig. 1, c). The correlation of the interacting field components, i.e. the degree of agreement the diagonal and the nondiagonal components of the mutual coherence matrix are additively taken into consideration when estimating the resulting intensity distribution. To visualize the polarization modulation the reference wave RW is used, which spreads perpendicular to

the registration plane.

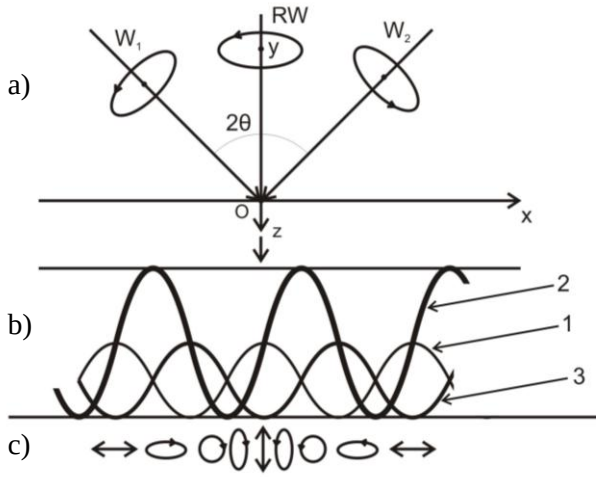

Fig.3. The scheme *a)* demonstrates the interaction of three waves, W_1, W_2, RW – are circularly polarized waves in the general case; *b)* the field distribution at the registration plane: curve 1 is formed by the superposition of *x*-components, curve 2 – by *y*-components, curve 3 – by *z*-components; *c)* the modulation polarization scheme.

When projecting the amplitude vector of the electric field onto the axis *Ox*, *Oy, Oz* the values of the projections on the plane *xOy* will be maximum and the value of the projection on the axis *Oz* will be practically equal to 0. Thus, the results of the interference of three waves change the distribution of the resulting components of the field. The contribution of the resulting *z* component to the formation of the terminal intensity distribution decreases. The influence of the *x*- and *y*- components on the formation of the interference picture changes as well. By changing the amplitude and the phase of the reference wave it is possible to note the zero value of intensity at certain points of the plane, which allows to realize the maximum visibility. It may be concluded, that by the help of the reference wave it is possible to obtain information on the distribution of polarization in the observation plane, which is set by the initial fields. The decrease of the phone takes place and the visibility of the picture increases. The reference wave is used for diagnosing the change of the polarization state at the expense of converting it into the distribution of intensity.

The change of the reference wave phase leads to the spatial modulation of visibility. The influence of one of the components (e.g., *x*-component) on the formation of the resulting intensity distribution increases. It allows to set the VMD and to estimate the degree of coherence of corresponding fields.

By the trial-and-error method of determining the value of amplitudes of the field components we obtain the maximum (minimum) values of the VMD at certain points of the observation area, which enables to estimate the degree of coherence of the initial superposing waves, according to $M = \left|\eta^{(1,2)}\right|$.

We can distinguish two distributions of polarization modulation in two mutually perpendicular planes: in the incidence plane and in the plane perpendicular to it, which are connected with the change of the phase difference between *x* and *z*, *y* and *z* field components at different points of the observation area.

The choice of the reference wave as a circularly-polarized one and at its interference with the initial waves provides both the zero-phase difference at the formation of the linearly polarized state and the zero value of intensity at certain points of the registration plane.

In this case we achieve the VMD which is equal to 1. This corresponds to the degree of coherence of the initial waves.

The polarization modulation, which is determined by the alignment of the phases of field components, becomes more complex and the depth of the polarization changes, which corresponds to the depth of the intensity modulation, exactly corresponds to the correlation properties of the initial superposing waves.

III. CONCLUSIONS

The achieved results allow to extend the notion about the theory of coherence (the metrological use) and is sure to be useful in investigating polarization sensitive systems of biological objects.

REFERENCES

[1] T. Setala, J. Tervo, A.T. Friberg, "Stokes parameters and polarization contrasts in Young's interference experiment", Opt. Lett., vol. 31, no. 14, 2006, pp. 2208-2210.

[2] T. Setala, J. Tervo, A.T. Friberg, "Contrasts of Stokes parameters in Young's interference experiment and electromagnetic degree of coherence", Opt. Lett., vol. 31, no.18, 2006, pp. 2669-2671.

[3] O.V. Angelsky, S.B. Yermolenko, C.Yu. Zenkova, A.O. Angelskaya, "On polarization manifestations of correlation (intrinsic coherence) of optical fields", Appl. Opt., vol. 47, no. 29, 2008, pp. 5492-5499.

[4] O.V. Angelsky, C.Yu. Zenkova, M.P. Gorsky, N.V. Gorodyns'ka, "On the feasibility for estimating the degree of coherence of waves at near field", Appl. Opt., vol. 48, no.15, 2009, pp. 2784–278.

[5] O.V. Angelsky, S.G. Hanson, C.Yu. Zenkova, M.P. Gorsky, N.V. Gorodyns'ka, "On polarization metrology (estimation) of the degree of coherence of optical waves" Optics Express, vol. 17, no. 18, 2009, pp. 15623-15634.

[6] J. Tervo, T. Setala, and A. T. Friberg, "Degree of coherence for electromagnetic fields", Opt. Express 11, 2003, pp. 1137–1143.

[7] C.Yu. Zenkova, M.P. Gorsky, and N.V. Gorodynska, "Metrology of degree of coherence of circularly polarized optical waves", Opto-Electronics Rev. vol. 19, no. 3, 2011, pp. 14-19.

Interferometric Method Application for Sub-micrometers Thickness Measurements of Spin-coated PEPC and PETPC Polymer Films

A.MESHALKIN[1], A.ANDRIES[1], E.ACHIMOVA[1], L.BETS[2], I.ANDRIES[3], S.DRAHNEA[3]
[1]*Institute of Applied Physics of Academy of Sciences of Moldova*
5 Academiei str., 2028, Chisinau, Moldova
[2]*Institute of Chemistry of Academy of Sciences of Moldova*
5 Academiei str., 2028, Chisinau, Moldova
[3]*Moldova State University*
60 Alexei Mateevici str., 2009, Chisinau, Moldova
alexei@asm.md

Abstract **- This paper deals with the interferometric thickness measurements of spin-coated thin polymer films. Spin coating is currently the predominant technique employed to produce uniform thin films of polymers in sub-micrometer range. But the thickness measurement of such thin films requires the application of high precision methods. In the paper we design and develop the system based on the common interferometer MII-4 and digital camera for measurement of the thin PEPC and PETPC polymer films. Different concentration of polymer solution and spin speed were used in order to obtain thin films with variable thickness (from 100 nm to 1000 nm) by spin coating technique.**

Index Terms – thin polymer layers, spin-coating, interferometric thickness measurements.

I. INTRODUCTION

Nowadays polymers play a critical role in the advancement of the microelectronics and optoelectronic industry. They serve as photoresists in microlithography and as insulating dielectric materials in chips, displays, interconnects, and photonic devices [1, 2]. A large number of different deposition techniques are used for the production of thin films for optical applications. The most important categories are thermal vaporization, sputtering, and chemical deposition. It is obvious, that suitable coating materials are required for each deposition technique. Properties of thin films including optical, mechanical, electrical and thermal properties are influenced by deposition parameters. Polymeric films can be fabricated by use of various techniques [3]. The self-assembly [4], the co-extrusion [5] and the spin coating [6, 7] have ever been used for fabrication of the layer structures based on polymers. However, obtaining of thin polymer films with required thickness and accurate control of the layer thickness remains one of the important problem in thin film researches. Spin coating is one of the technological and accessible method of obtaining polymeric thin films. M. Kimura et al. [8] first fabricated multi-layered structures using polystyrene and polyvinylalcohol. Recently, A.L. Alvarez et al. [9] also demonstrated polymeric multi-layered structures obtained by spin coating of polyvinylcarbazole and polyvinylalcohol. In both cases, accurate control of the optical thickness up to a quarter wavelength was not achieved. So, the measurement of the thickness of transparent films become one of the important problem in optics research and in industry. The most common thickness measurement types available commercially are ellipsometry [10], the spectral reflectance/transmittance method [11] and interferometry [12]. Ellipsometry measures reflectance from a thin film at two different polarizations. Its precision is very high in the sub-micrometer range, but its measurement range is limited to several micrometers. The operations and calculations of ellipsometry are very complex. For the spectral reflectance/transmittance method, the incident light should cover a range of wavelengths and be adjusted normal to the sample surface. The spectral reflectance/transmittance method is simpler and less expensive than ellipsometry, but it can be used for films with thickness comparable with used study wavelength. Determination of film thickness by optical interferometry technique is widely used. Measurements are nondestructive and relatively inexpensive. Interferometry relies on the interference of two or more beams of light. The optical path difference of these beams is related to film thickness.

In this paper, we report the results of the fabrication of polymeric films based on polyepoxypropylcarbazole and polyepitiopropylcarbazole and application of interferometric PC based measurement system for high precision analysis of film thickness.

II. EXPERIMENTAL

Synthesis of polymer. Polyepoxypropylcarbazole (PEPC) and polyepitiopropylcarbazole (PETPC) were selected since they are known to have excellent film forming properties and photoinduced properties. A set of PEPC and PETPC used in this investigation were synthesized by polymerization of epoxypropylcarbazole and epithiopropylcarbazole at the presence of 1-3% potassium methylate on the anionic mechanism at temperature 80-120˚C within 2-6 hours. For the full drying they were stored in a vacuum drying chamber at 50˚C up to constant mass. From the characterization by polymer viscosity using calibrated standards results a molecular weight Mw 2000-3000. In Fig. 1 the chemical structure of polymers PEPC and

PETPC are presented.

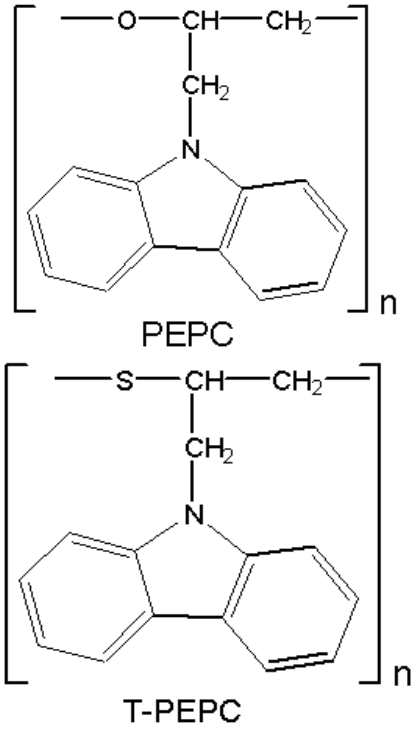

Fig. 1. Chemical structure of polymers PEPC and PETPC.

Formation of polymer films from solution.

The thin polymer films were prepared from homogeneous polymer solution by spin coating procedure using programmable spin-coater "SGS Spincoat G3P-8". The thickness of the polymer film was varied by changing the concentration of polymer solution and the rotation speed of spin coating. In sample series A, PEPC concentration of the solution was kept fixed (10 wt% solutions of the PEPC polymer in chloroform) and spin speed was varied which results in different film thicknesses. In sample series B, the PEPC concentration was varied (from 2.5 to 12.5 wt% solutions in chloroform $CHCl_3$) at fixed spin speed. The physical and chemical properties of used solvent chloroform is shown in Table 1.

TABLE 1. PHYSICAL AND CHEMICAL PROPERTIES OF CHLOROFORM.

Chemical name	Trichlormethane
Chemical formula	$CHCl_3$
Chemical structure	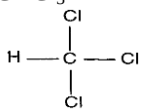
Molecular weight	119.38
Color	Colorless
Melting point	-63.5 ˚C
Boiling point	62 ˚C
Density, at 20˚C	1.483 g/cm^3
Refractive index, n_D^{20}	1.4459
Organic solvents	Miscible with principal organic solvents. Miscible with alcohol, benzene, ether, petroleum ether, carbon tetrachloride,carbon disulfide, oils.

Operation conditions for polymer solution deposited on 5 cm diameter optical glass substrate (BK7) was as follows: 2 cm^2 of liquid dispensed on the disk at rest, subsequently accelerated in about 10 s to 3000 rpm and spun for 20 s. The broad range of thicknesses can be covered by using polymer solution with increasing solids content or for a given solution by changing the final spin speed.

The used coating cycle is presented in Fig. 2.

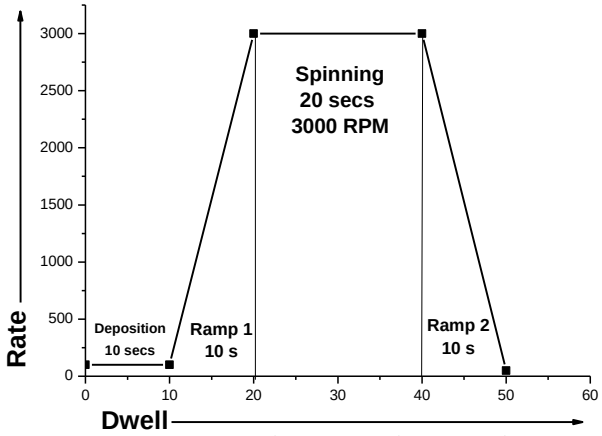

Fig. 2. Rate/time schedule of spin-coating for polymer films.

Determination of film thickness.

For the determination of film thickness in this work the modified interferometric PC based measurement based on MII-4 interference microscope was applied.

A thickness characterization of the samples was achieved by a MII-4 interference microscope (Fig.3). with CCD-camera recorded the micrographs. The interference pattern of light reflected from a flat reference surface and the investigated sample was recorded in PC. A magnification of 490 times was used. The area from which a data analysis is performed was 0.3 mm diameter circle. This enables a height resolution better than 100 nm [12].

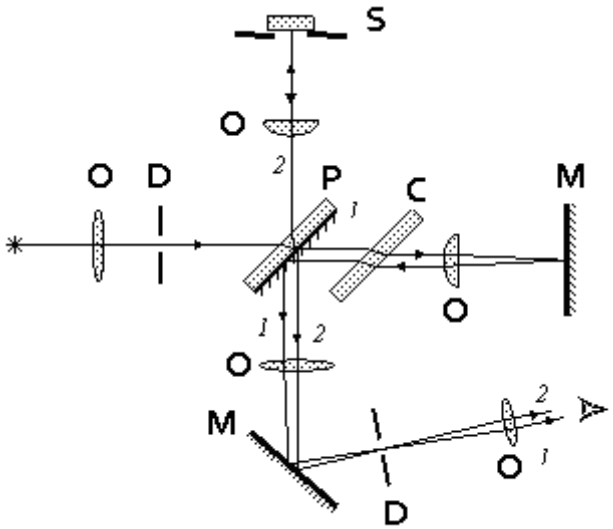

Fig.3. Optical scheme of MII-4 interference microscope. 1 – reference beam, 2 – object beam, O – objectives, D – diaphragms, M – mirrors, P - beam-splitting plate, C – compensating plate, S – sample.

The interference fringe shift in interferogram introduced by different height of layer is shown in Fig. 4.

III. RESULTS AND DISCUSSION

Good surface quality and uniformity of the films was confirmed by the smooth interference fringes in the

interferogram obtained by MII-4. Several samples were prepared out of the same solution. To check the reproducibility of observed structures, several samples were prepared and examined. In this experiment a very accurate surface cleaning was achieved and it was confirmed by many repetitions of the preparation that manifest the same morphology. Though each individual sample shows a different surface features the statistical features of the film morphology remain the same.

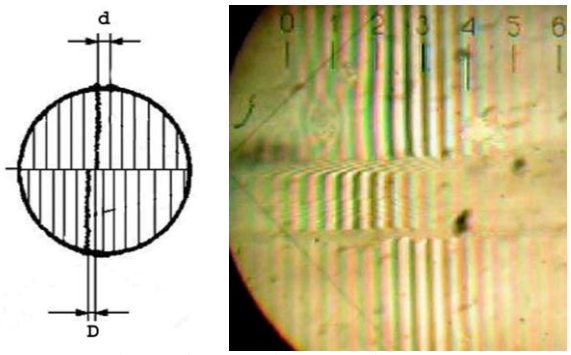

Fig.4. The interference fringe shift D in interferogram introduced by different height of layer. Photo of interferogram obtained by computerized MII-4.

The interferograms of the polymer films spin-coated from solutions with different polymer concentrations taken by a CCD camera are shown in Fig. 5.

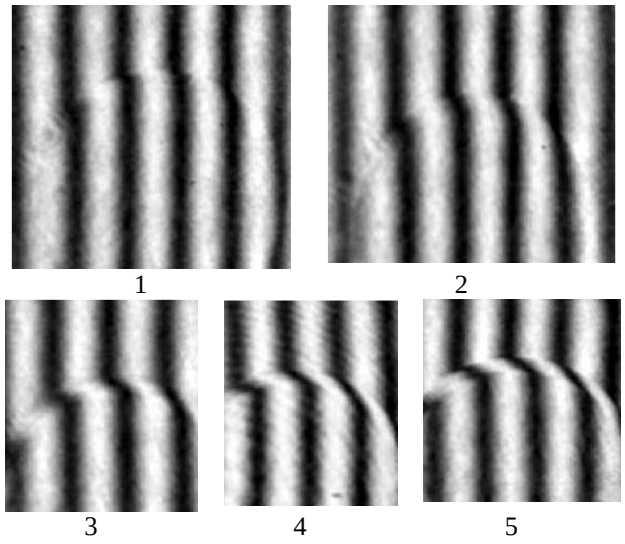

Fig. 5. Interference fringe shift in interferograms introduced by different thickness of layer obtained from following concentrations of PEPC solution: 1 – 2.5 wt%; 2 – 5.0wt%; 3 – 7.5 wt%; 4 – 10.0 wt%; 5 – 12.5 wt%.

The thickness of spin-coated films determined from the fringe pattern in the interferogram was found to be increased with the increase of polymer concentration in solution. It was shown that by raising the polymer concentration from 2.5 to 15.0 wt%, the final film thickness increase from 160 to 960 nm at a spin speed of 3000 rpm. Applied methods of thickness measurements have shown a quasi-linear thickness dependence on polymer concentration. (Fig.6.). Therefore, a smooth polymer films can be fabricated just by controlling the polymer concentration in solution. Applied method for determination of thickness of films in dependence on polymer concentration in solution can be successfully extended to other polymer films in order to obtain required thickness

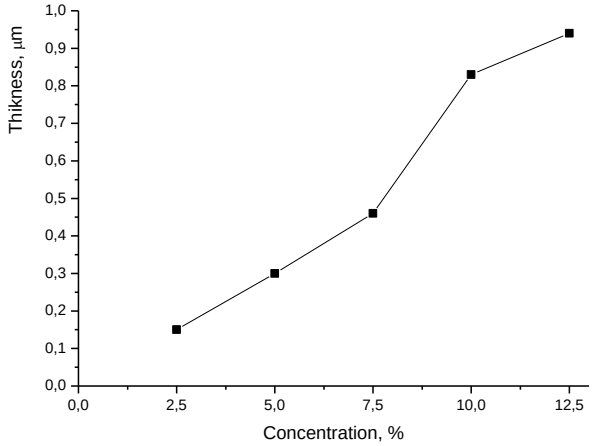

Fig. 6. Thickness as a function of PEPC solution. The thickness was analyzed from the shift of the fringes. One fringe shift corresponds to λ/2.

IV. CONCLUSION

The fabrication of a polymeric films based on PEPC and PETPC by spin-coating method was demonstrated. The thickness of layers was analyzed by interferometric measurements. It was shown, that the thickness of thin polymer films could be analyzed with high resolution by the proposed method. The described methods allow fabricating thin layers by controlling the concentration of polymer in solution and/or spin coating speed and provide accurate thickness measurement by interferometric method.

ACKNOWLEDGMENTS

The research described in this publication was supported by the project no. 11.836.05.04A in the framework of the National Programme "Nanotehnologies and nanomaterials". The authors thank Enaki Mihail and National Center for Materials Study and Testing for the AFM researches.

REFERENCES

[1] Polymers for Electronic and Photonic Applications; Wong, C. P., Ed.; Academic Press: San Diego, CA, 1993.

[2] Garrou, P. In Thin Film Technology Handbook; Elshabini-Riad, A., Barlow, F., Eds.; McGraw-Hill: New York, 1997; Chapter 9.

[3] M.V. Jacob, C.D. Easton, G.S. Woods, C.C. Berndt**.** Fabrication of a novel organic polymer thin film. *Thin Solid Films*, 516(**12**), 2008, p.3884-3887.

[4] Mohan Srinivasarao, David Collings, Alan Philips, Sanjay Patel, "Three-dimensionally ordered array of air bubbles in a polymer film," *Science*, **292**, 2001, 79.

[5] Michael Ponting, Tiffani M. Burt, LaShanda T. J. Korley, James Andrews, Anne Hiltner, Eric Baer. "Gradient multilayer films by forced assembly coextrusion", *Industrial & Engineering Chemistry Research*, 49 (**23**), 2010, pp 12111–12118.

[6] David B. Hall, Patrick Underhill, John M. Torkelson, "Spin coating of thin and ultrathin polymer films", *Polymer Engineering & Science*, 38(**12**), 1998, p. 2039–2045.

[7] T. Komikado, A. Inoue, K. Masuda, T. Ando, S. Umegaki, Multi-layered mirrors fabricated by spin-coating organic polymers, *Thin Solid Films*, **515(7-8)**, 2007, p. 3887-3892.

[8] M. Kimura, K. Okahara, T. Miyamoto. Tunable multilayer-film distributed Bragg reflector filter, *J. Appl. Phys*. **50**, 1979, p. 1222-1225.

[9] A.L. Alvarez, J. Tito, M.B. Vaello, P. Velasquez, R. Mallavia, M.M. Sanchez-Lopez, S. Fernandez de Avila, Polymeric multilayers for integration into photonic devices, *Thin Solid Films*, **433**, 2003, p. 277-280.

[10] Lee K.J., Kang T.D., Lee H.S., Lee H., Cho M.J., Lee S.H., Choi D.H. Ellipsometric study of polymer thin films: Nonlinear optical guest-host system, *J. Appl. Phys*., **97(8)**, 2005, p. 083543.

[11] A.M. Nasr, H.I. Abd El-Kader, M. Farhat. Characterization of photoactive polymer thin films using transmission spectrum. *Thin Solid Films*, **515(4**), 2006, p. 1758-1762.

[12] Poroshin, V.; Bogomolov, D. Kostyuk, A. PC based measurement system for interferometric analysis of etalon roughness. *Advanced Engineering*, **4**(1), 2010, p. 65-68.

Design of the Holographic Fiber-optic Electronic Speckle Pattern Interferometer for Optical Constants of Glasses Measurements.

O. IASENIUC, A. ANDRIESH, E. ACHIMOVA, V. ABASHKIN.
Center of Optoelectronics, Institute of Applied Physics,
Academy of Sciences of Moldova,
5 Academic str., MD-2028, Chisinau, Moldova
e-mail: oxygena08@rambler.ru

***Abstract* – An elaboration the holographic fiber-optic electronic speckle pattern interferometer (ESPI) which can will be apply for measurement of the optical constants is described. This interferometer with CCD Smart Camera can be programming based on National Instruments' graphical programming LabVIEW software. Using the LabVIEW we can apply flexible program for different software steps for processing of recorded interferograms (extracting amplitude, phase map and frequency domain, subtraction), obtained by CCD Smart Camera for feather calculation the optical properties the refractive index and thickness of studying samples.**

Index Terms – digital holographic speckle pattern interferometer, ESPI, optical fibers, LabVIEW.

I. INTRODUCTION

The optical properties, especially the refractive index, of chalcogenide glasses are currently a subject of systematic research due to they manifest strong photo- and thermally-induced properties that offer the possibility of using amorphous chalcogenide for high-density information storage, fabrication of diffractive optics such as Bragg gratings elements, inorganic photo-resists, and different holographic patterns.

But one of the main problems is the precise definition of the refractive index and thickness of the samples. Different methods have been developed to measure the refractive index. Many of spectrofotomertic, ellipsometric, interferometric methods for determining the refractive index of materials have also been developed. But all they have errors and less precision.

The holographyc fiber-optic ESPI as a method of small displacement was formed in 80-th years [1], but to measure the optical parameters have learned recently. This is high precision, noncontact, full-field, optical method for measuring the optical properties changes.

Data from speckle interference patterns for further determining properties of the studying samples is processing by holographic and programming methods.

The main aim of this work is to design holographic fiber-optic ESPI and in future to study a new materials - determining of the refractive index, it variations and thicknesses (thin films and bulk materials) by method of holographic fiber-optic ESPI. Especially this method can be very useful for full-field measurements the index of refraction after recording process on chalcogenide glasses.

It should be noted that during the planned research is expected to establish that the application of digital speckle correlation interferometry technique can be extend the number of experimental data and expand the range of tasks due to flexibility of LabVIEW program, portable set-up, immunity to the environment influences (temperature, vibration).

II. THE DIGITAL HOLOGRAPHIC FIBER-OPTIC SPECKLE PATTERN INTERFEROMETER

Breadboard with tapped holes as a stable platform for mount interferometer and optical experiments for various test configurations was used. Fiber-optical design of ESPI was chose to sustain vibration immunity (Fig. 1, 2). There are 10 mW He-Ne laser (1), wedge prism as beamsplitters (2), multimode optical fiber as object arm (3), sample (bulk or thin films of the chalcogenide glasses) (4), object arm (5), camera objective (6), optical lever composed from negative lens and positive lens (7) as microobjective (8) (60^x and $NA_{objective}$ =1.25) and monomode optical fiber as reference arm (9), rectangular diaphragm (10), CCD Smart Camera (11), PC (12).

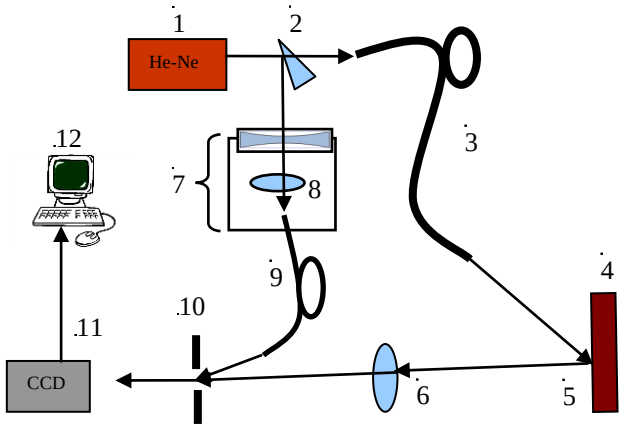

Fig. 1. Optical set-up of holographic fiber-optic ESPI.

There are 3 conditions for effective coupling laser beam energy and mono mode fiber:

- Coincidence of the aperture of the objective and fiber core respect to condition $NA_{objective} \geq NA_{fiber}$;

- Diameters coincidence of microobjective focal spot and monomode fiber core;
- Adjustment of the modes and wavelength transmission of the laser and monomode fiber.

This advantageous interferometric arrangement allows obtaining the speckle pattern fast enough (due to recording rate of CCD Smart Camera) and with high precision (less then λ/4).

A digital holographic speckle pattern interferometer relies on the correlation between two speckle patterns. Each one created by the interference between a reference beam and the image of an object illuminated by laser [2-4]. Typically the two images are of an object before and after some changes (in-plane or out-of-plane displacements). Acquired by CCD camera's image is converted into a corresponding video signal. This video signal is electronically processed by PC through Gigabit Ethernet, so that texture variations of the speckle pattern are converted into brightness variations. A speckle interferogram is generated arithmetically by subtracting two digitized speckle patterns. The similar operation of subtraction of two stored on PC interferogram can be made using our program in LabVIEW. In this case, the distribution intensity of the resulting speckle pattern will depend on the relative phase shift superimposed fields. Deformation of the object leads to a change in the phase of the object speckle field and, consequently, to changes in intensity of the speckle pattern. Obtained the digital speckle patterns interference are also subjected to computer processing in order to increase the contrast fringe and smoothing of optical noise - the speckle modulation. In practice, the intensity distribution in the camera detector plane is stored with the object in its reference state. The object is then deformed and a second frame is stored. The two frames are then subtracted and correlation live fringes are displayed on a monitor (Fig. 3). Images subtraction makes the interferogram easy to form, view, and recording no in time. (Recording rate of Smart Camera is about 60 fps.). NI 1722 Smart Camera simplify machine vision by analyzing images directly on the camera with a powerful, embedded processor capable of running NI Smart Camera digital I/O lines are optoisolated for direct connectivity with industrial devices such as triggers and actuators. All smart camera models incorporate an image sensor, processor, and digital I/O in a compact, rugged housing. The Smart Camera also includes LEDs for communicating system status, four DIP switches to specify startup options, isolated inputs, and isolated outputs for connecting to external devices. Developing applications with the NI Smart Camera requires one of the following software options:

- Vision Builder for Automated Inspection: (Vision Builder AI) is configurable machine vision software can use to configure the NI Smart Camera and prototype, benchmark, and deploy machine vision applications. Creating applications in Vision Builder AI does not require programming. It allows you to easily configure and benchmark a sequence of visual inspection steps, as well as deploy the visual inspection system for automated inspection.
- LabVIEW 2010: LabVIEW Real-Time Module, NI Vision Development Module, NI Vision Acquisition Software-IMAQ. LabVIEW is a graphical programming environment for developing flexible and scalable applications.

The NI Smart Camera provides control of the image sensor exposure time through software.

If a squared difference is performed between two digitized speckle patterns and recorded at different states of the object, the result will be:

$$I(x,y)=8I_0(x,y)I_r(x,y)\sin^2[\upsilon(x,y)+\Delta\upsilon(x,y)/2]\{1-\cos[\Delta\upsilon(x,y]\}, \quad (1)$$

where $I_o(x,y)$ and $I_r(x,y)$ are the object and reference beam intensities, and $\upsilon(x,y)$ is the speckles random phase. The $\Delta\upsilon(x,y)$ term containes the phase variation between the two subtracted patterns. This equation represents a ESPI interferogram description obtained by subtraction technique.

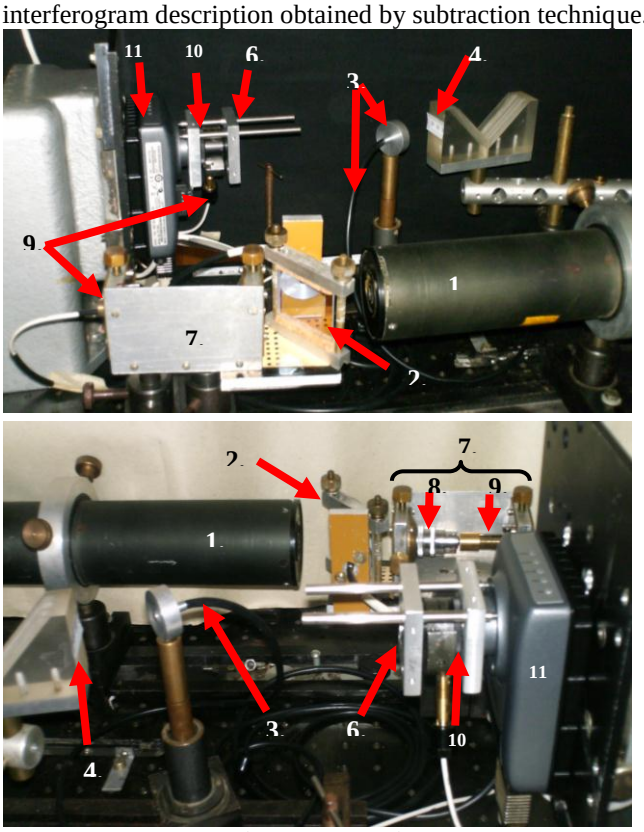

Fig. 2. Two side photos of the holographic fiber-optic ESPI set-up with elements numbered respective to Fig. 1.

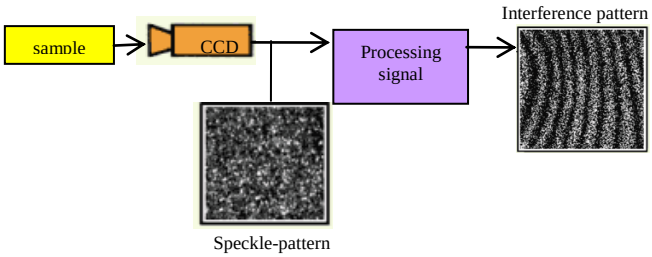

Fig. 3. Schematic of ESPI measurement processing.

III. LABVIEW

Most researches today are done with the aid of computers. The computers are used to control the experiment, acquisition, and processing of data. LabVIEW is a graphical programming language elaborated by National Instruments Company [5]. LabVIEW programs are called virtual instruments (VIs), because their operation imitates works of physical instruments made by user. Specifically, LabVIEW is used to interface the computer with programmable

measuring instruments. LabVIEW contains a comprehensive set of tools for acquiring, processing, analyzing, displaying, and storing data. Because LabVIEW graphical code is easy providing unique debugging tools that can use to watch as data interactively moves through the wires of LabVIEW program and see the data values as they pass from on function to another along the wires between VI or sub VI. Each VI consists of a front panel and a block diagram. The front panel specifies the inputs and outputs which make up the user interface. The block diagram consists of icons which represent subroutines and program control structures [6].

LabVIEW is a program development application, much like various commercial C or BASIC development systems, or National Instruments LabWindows. However, LabVIEW is different from those applications in one important respect. Other programming systems use text-based languages to create lines of code, while LabVIEW uses a graphical programming language, to create programs in block diagram form. Moreover anybody can use LabVIEW with less programming experience. LabVIEW programs are called virtual instruments (VIs) because their appearance and operation imitate actual instruments. However, they are analogous to functions from conventional language programs. VIs has both an interactive user interface and a source code equivalent, and accepts parameters from higher-level VIs.

LabVIEW has extensive libraries of functions and subroutines for most programming tasks. LabVIEW contains application specific libraries for data acquisition and instrument control. LabVIEW also contains application-specific VI libraries and serial instrument control, data analysis, data presentation, and data storage.

The primary step of our program in LabVIEW is images acquisition and storage. Acquired images are stored in memory of CCD Smart Camera or in PC ready for processing.

The front panel of our program is shown on Fig. 4 In left side of screenshot one inserts names of two images.

to comprehend, common programming tasks, like debugging, become more intuitive as well. LabVIEW

Image acquisition window (on the right) used for image processing respect options presented on Fig. 5-7:

- Simple squared difference -Fig. 5;
- Phase map -Fig. 6;
- Rectangular determination for following unwrapped phase map extraction - Fig. 7.

The operator starts the primary task, the data acquisition program, namely the first step is reading a reference image file and a recording image file. Program recognizes image file configurations such as BMP, TIFF, PNG and JPEG. This type definition edits automatically. The reference image in our case is unloaded object image. The recording image represents loaded object. Object loading process can be made by suitable way for object under investigation, for example heating, vibration, etc. The LabVIEW execution engine then distributes data the three our tasks in dependence of the problem needed and chosen by operator on front panel. These tasks are a pointed above.

The simple difference task VI's serve for squired image to increase S/N ratio. This block diagram also produces a histogram equalization of the squired image.

Block diagram for rectangular determinations serves for elimination from complex image low frequencies which are haven't useful information about the object. After that step VI Mask recopies image source into new image for processing.

Inside phase map block diagram VI computes optical FFT of both images and creates complex images in which high frequencies are grouped in the center while low frequencies are located at the edges. Inverse FFT of complex image after VI Mask calculation must be doing for final step as phase map calculation. So this block diagram first produces wrapped phase map and then unwrapped phase map. After final processing surface changes in-plane or out-of-plane will be presented.

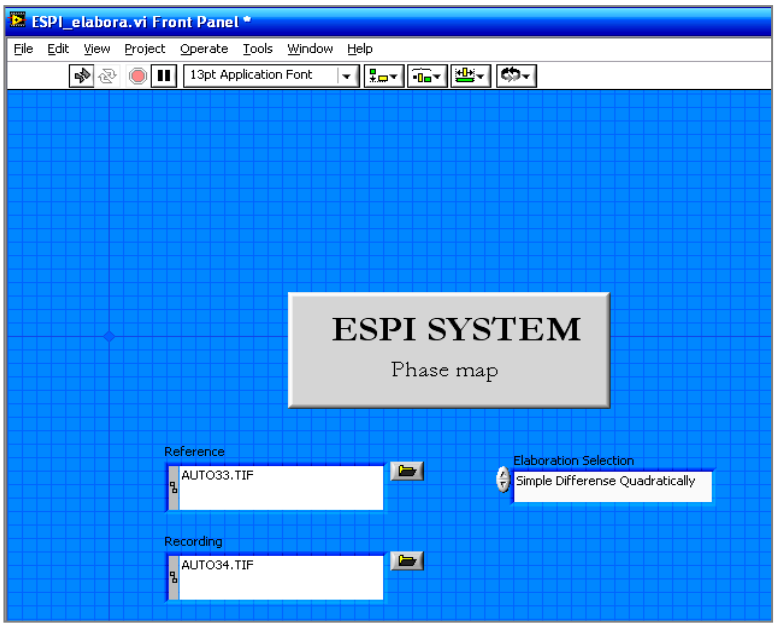

Fig. 4. The screenshot of a LabVIEW user front panel

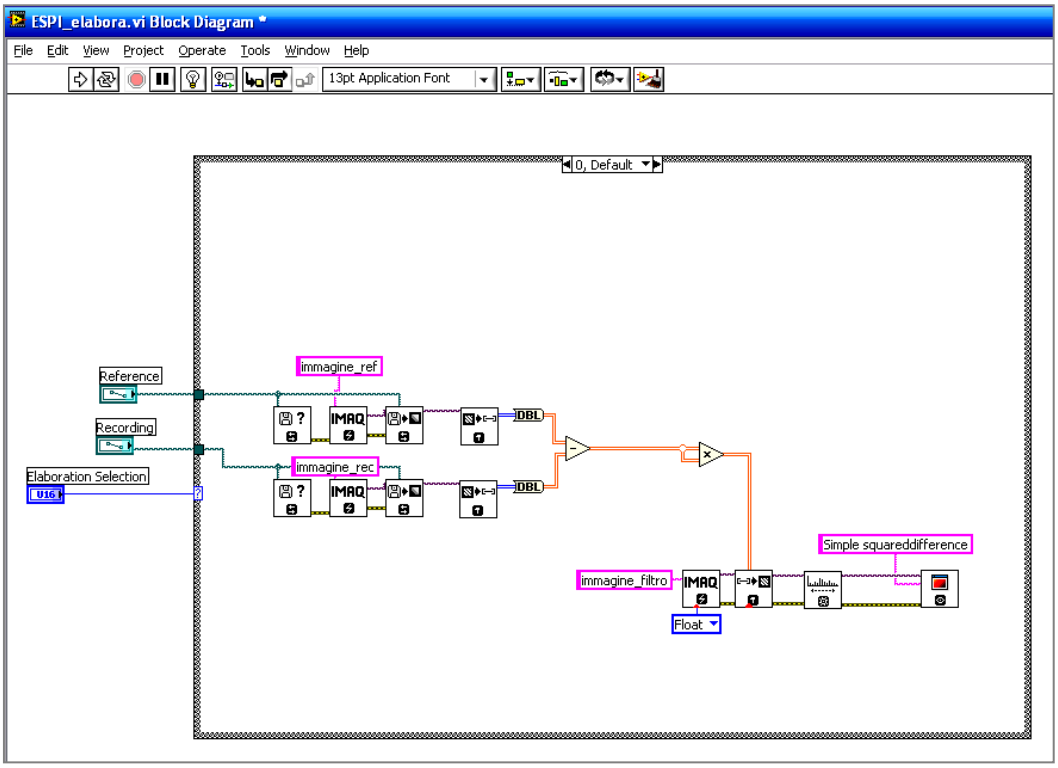

Fig. 5. The screenshot of a LabVIEW user block diagram of VI's for a simple squared difference processing.

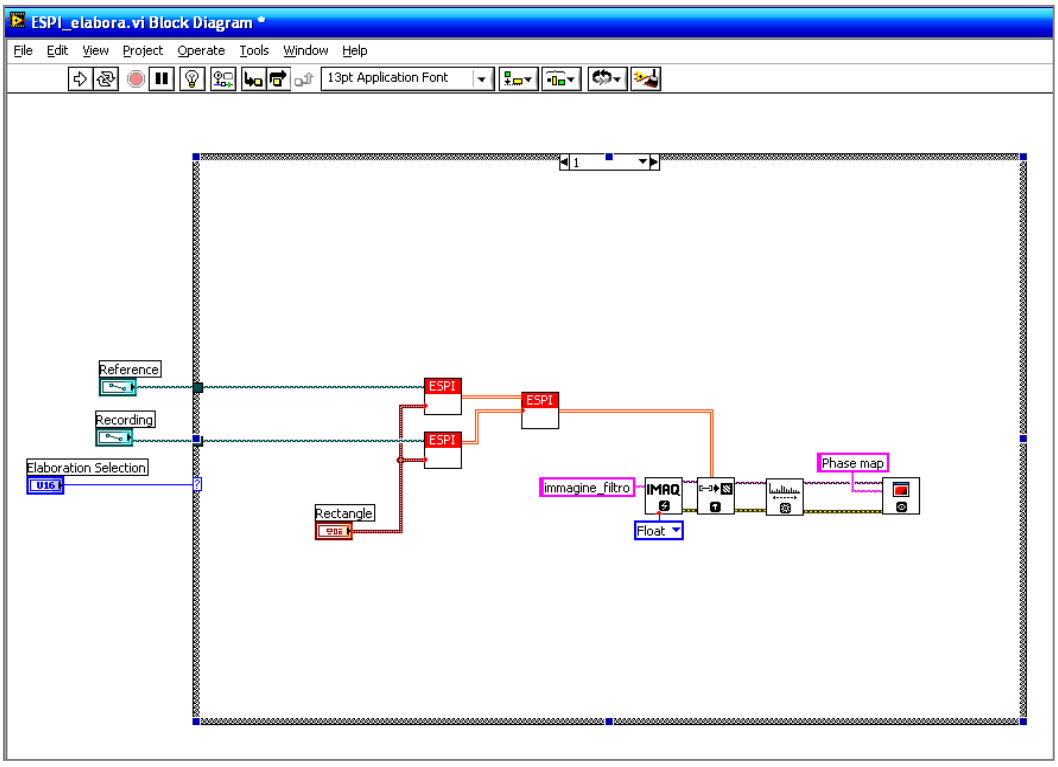

Fig. 6. The screenshot of a LabVIEW user block diagram of VI's for a phase map mode.

III. CONCLUSIONS AND PERSPECTIVE

Our work consist of two main objectives: the optical set-up design of fiber-optic ESPI and elaboration LabVIEW program. The process of measuring by our installation is reduced to receiving two speckle snapshots of unloading and loading object. They will be recorded by using the CCD image sensor. Farther with image processing of speckle patterns and data processing with LabVIEW we can extract phase map, and finally calculate the required optical parameters by elaborated method. Important feature of this method are the full-field measuring of object properties which is important for investigations of optically recorded diffraction elements with very small location of refraction index changes.

In our work the methods was used:

- Speckle-interferometric method of speckle-interferogram

with Fourier optical processing in objective plane;
• Holographic method of recording images on Smart Camera CCD image sensor;
• Method of forward and inverse Fourier-transformations;
Methods of processing by using LabVIEW are optical type of FFT, histogram, phase extraction, S/N of image enhances.

In perspective we plan to apply set-up and method for measuring the refractive index of As-S-Se-Sn chalcogenide glasses [7-11].

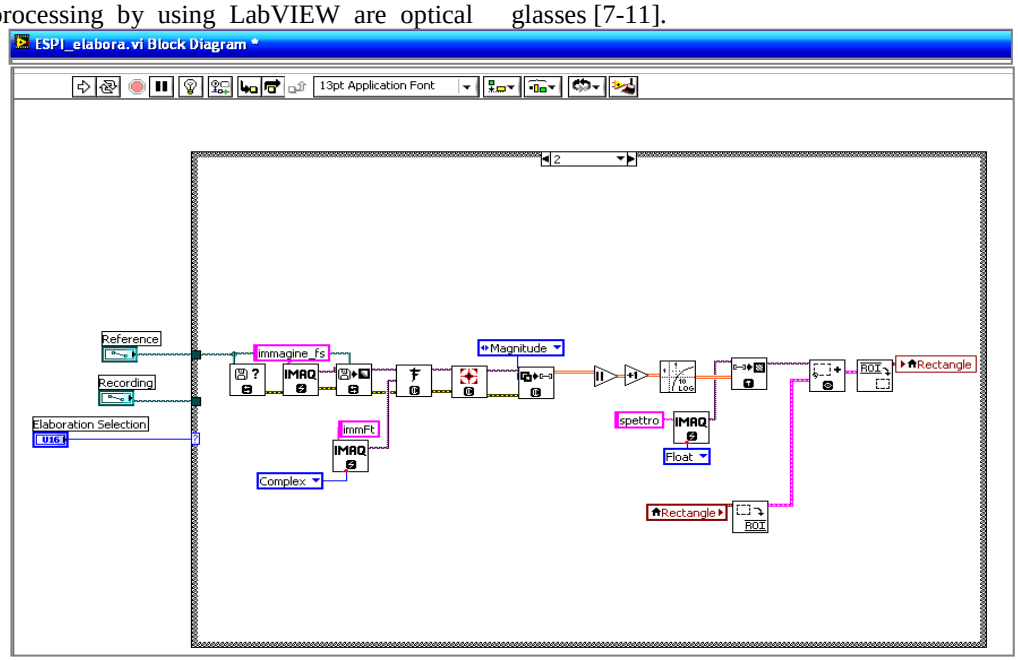

Fig. 7. The screenshot of a LabVIEW user block diagram of VI's for a rectangular determination.

IV. CONCLUSIONS AND PERSPECTIVE

Our work consist of two main objectives: the optical set-up design of fiber-optic ESPI and elaboration LabVIEW program. The process of measuring by our installation is reduced to receiving two speckle snapshots of unloading and loading object. They will be recorded by using the CCD image sensor. Farther with image processing of speckle patterns and data processing with LabVIEW we can extract phase map, and finally calculate the required optical parameters by elaborated method. Important feature of this method are the full-field measuring of object properties which is important for investigations of optically recorded diffraction elements with very small location of refraction index changes.

In our work the methods was used:
• Speckle-interferometric method of speckle-interferogram with Fourier optical processing in objective plane;
• Holographic method of recording images on Smart Camera CCD image sensor;
• Method of forward and inverse Fourier-transformations;
• Methods of processing by using LabVIEW are optical type of FFT, histogram, phase extraction, S/N of image enhances.

In perspective we plan to apply set-up and method for measuring the refractive index of As-S-Se-Sn chalcogenide glasses [7-11].

ACKNOWLEDGEMENT

The authors of this work wish to express their gratitude to researcher Prisacar A. for elaboration of software for patterns subtraction based on FFT algorithm and general assistance and discussion during work.

REFERENCES

[1] Ch.Vest , Holographic inierferometry, 1982, pp.504.
[2] Yu. Ostrovsky, V. Shchepinov, V. Yakovlev, Holographi interference methods for studying the deformation, 1988, pp. 248.
[3] S. Yurischeva, A. Osintsev, V. Shchepinov, Application of the method of digital speckle interferometry to study contact interactions, vol. 8, 2006, pp.120-121.
[4] R. Jones, C. Wykes, Holographic and Speckle Interferometry, 1986, pp.327.
[5] http://www.ni.com/
[6] L. Clark, LabVIEW. Digital signal pricessing and digital communications, McGraw-Hill Companies, Inc., 2005, pp. 202.
[7] O. Iaseniuc, A. Andriesh, A. Abashkin, Optical properties of amorphous $(As_2S_{1,5}Se_{1,5})_{0,99}$:$Sn_{0,01}$. Moldavian Journal of the Physical Sciences, vol. 4, 2010, pp. 349-355.
[8] M. Iovu, S. Shutov, M. Popescu, J. of Non-Cryst. Solids, vol. 924, 2002, pp.299-302.
[9] P.Boolchand, D. Georgiev, M. Iovu, Chalcogenide Letters, vol. 2, 2005, p.27.
[10] A.Andriesh, M. Iovu, J. of Optoelectronics and Advanced Materials, vol. 8, No.6, 2006, pp. 2080 – 2085.
[11] D. Harea, M. Iovu, O. Iaseniuc, E. Colomeico, A. Meshalkin, Modification of the optical constants in amorphous Sb_2Se_3:Sn thin films under the illumination and heat treatment, J. of Optoelectronics and Advanced Materials, (IF - 0.577), vol. 12, No.11, 2009, pp. 2039-2043.

Improvement of SiO2(Ge)SiO2/Si Nanostructures by Low Dose γ-radiation

S.T. SHISHIYANU[1] , T.S. SHISHIYANU[1], E. YILMAZ[2], R. TURAN[3], N.A.P. MOGADDAM[3]

[1]*Department of Microelectronics, Technical University of Moldova, 2004 Chisinau, Moldova*
[2] *Department of Physics, Abant Izzet Baysal University, 14280 Bolu, Turkey*
[3]*Department of Physics, Meddle East Technical University, 06531Ankara, Turkey*
sergeteo@mail.utm.md

***Abstract* – Effect of γ – radiation on SiO_2(Ge)SiO_2/Si nanostructures structural defects was investigated by C-V measurements characterization. The obtained results demonstrated that by low dose γ-radiation (0.1Gy÷150Gy) have been essentially reduced the negative charge defects in the nanocomposite structures SiO_2(Ge)SiO_2/Si. At higher doses (350Gy÷4000Gy) the concentration of positive charge defects slowly increased and C-V characteristics moved to the position of the C-V characteristics of pure SiO_2 (without nc-Ge) having the same curves configuration. At the average doses (200Gy÷350Gy) the concentration of negative charge defects and positive charge defects were approximately equal and the radiation stability of samples was the highest.**

***Index Terms* – Ge nanocrystal, SiO_2/Si, structural defects, γ –radiation.**

I. INTRODUCTION

The investigation of radiation effects on nanocrystals Ge and Si embedded in SiO_2 has the major importance, first of all, to know the specific of radiation stability and degradation of nanocrystals in comparison with monocrystalline materials (semiconductors – Ge, Si); secondly, for elaboration of the new methods of radiation-nanotechnology for the nanoelectronic device fabrication, and third, for the implementation of these new nanostructured and nanocomposite materials for radiation sensor fabrications.

Nanocrystals of Si and Ge embedded in SiO_2 - matrices have attracted much attention due to their possible applications in integrated opto-nano-electronics as nanolasers, nano-flash memory and multifunction nanodevices [1-3]. Many authors have been elaborated different methods of Ge- nanocrystal obtaining: molecular beam epitaxy on the thin SiO_2 layer on Si(001) [1], implantation of Ge^+ ions into SiO_2 films with subsequent annealing [2], chemical vapor deposition (PECVD)[3,4], magnetron sputtering [5,6]. In [7] are presented the comparative study on photoluminescence from Ge/PS, (PS - porous silicon) and Ge/SiO_2 thin films; the photoluminescence peaks of Ge/PS were located at 517nm and peaks of Ge/SiO_2 at 580nm. In [8] the samples of Ge/SiO_2,obtained by sol/gel method , after annealing at 700°C under H_2 reduction, by UV light excitation was observed tree peaks of photoluminescence at room temperature 392nm(3.12 eV), 600nm(2.05eV) and 770nm(1.6eV). The peak of 1.6eV is attributed to Ge monocrystals, peak of 2.05 eV – to defect GeO_x and peak of 3.12eV – to GeO_2. The unreduced sample shows only on peak of 3.12eV attributed to GeO_2. These results are different of other authors: 570nm(2.16eV) in Ge/SiO_2, obtained by rf-magnetron co sputtering method [9]; 510-680nm (2.42 ÷ 1.81 eV) at 77K temperature in Ge/SiO_2, prepared by sol-gel method: 680nm (1.8eV) at room temperature [10]; 689nm (1.8eV) at room temperature [11].

From these data we can conclude that in the samples of Ge/SiO_2, in dependence of growth methods and thermal annealing in different ambient (N_2, H_2), can be formed not only nanocrystals of Ge, but and different defects as GeO_x, GeO_2, GeSi, which have direct impact to properties of SiO_2Ge/SiO2/Si –nanostructures.

By another hand radiation methods can bee efficiently used for defect monitoring of structural defects for improvement of fundamental properties of nanostructured and nanocomposite materials [12-15]. It is shown in [12] that by the ion irradiation is possible to change of the number, size and distribution of the silicon nanocrystallites and improve the photoluminescence intensity. This results are in accordance with publication [13] where is indicated that after irradiation with 400kev electrons or 30-130kev He^+ ions and the post-irradiation annealing at 1000°C, the photoluminescence intensity of Si-nanocrystals became several times stronger than that from the initial samples prepared at 1150°C. These results are assumed to be a sum of the intensities from the initial nanocrystals and from the new ones that appeared due to irradiation [13]. In [14] it was shown that the low-dose of γ- irradiation ($5\times10^4 \div 10^5$rad.) leads to remarkable (up to 40%) increase of photoluminescence band (1.33eV) intensity. Infrared spectra demonstrated that composition and structure of the nanocomposite matrix were not changed by radiation. The effect was explained by radiation induced structural ordering nanocrystal-matrix interface [14]: low-dose irradiation partially eliminated defects (recombination centers) at nc-Si-SiO_2 interfaces that resulted in enhancement of nanocrystal luminescence. The impact of low-dose γ- radiation on nc-Ge in SiO_2 has been studded in [15].

The main objective of this paper is investigation of the effect of ionizing γ- radiation on C-V characteristics and radiation defect monitoring in SiO_2(Ge)SiO_2/Si.

II. EXPERIMENTAL

The samples used in this work were 100nm Ge rich SiO_2 layer sandwiched between two SiO_2 films deposited on n-type Si<100> substrate by RF magnetron co-sputtering from two independent target materials with powers of P_{SiO2}= 300W, P_{Ge}= 20W [15]. The bottom SiO2 layer with the thickness of about 100 nm was deposited on Si to restrain Ge atoms from growing epitaxially on the Si substrate in the post-annealing process. The top SiO_2 layer with the thickness of about 40 nm was deposited to impede the diffusion of Ge atoms out of the surface.

In our experiments have been investigated the C-V characteristics of the nanocomposite structures, SiO_2(nc-Ge)SiO_2/nSi, prepared by different post-grown thermal treatment: Set-1 - as grown, Set-2 – after 1 hour annealing at 900°C in N_2, Set-3 – after 1 hour annealing at 1000°C in N_2 and Set 4 – after 1 hour annealing at 1000°C in a N_2, RTA 15 min H_2+N_2. In general, the formation mechanism for Ge nanocrystals embedded in SiO_2 matrix goes through the familiar sequence of nucleation and growth, followed by coarsening of nanocrystals due to Ostwald ripening [16].

The C-V characteristics gave information about state and dynamic charged defects of investigated MOS structures under influence of ionization γ- radiation. All C-V curves have been measured before and after radiation at dose from 0.1Gry to 4000Gry at frequencies - 1MHz.

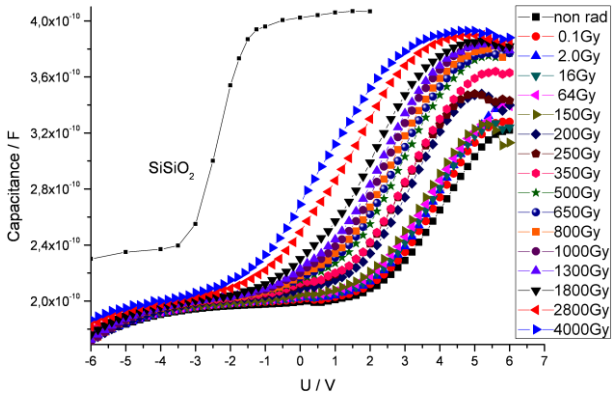

Fig. 1 The C-V characteristics 1MHz before and after γ- irradiation at different doses (0.1 Gy ÷ 4000Gy), Set 4.

III. RESULTS AND DISCUSSION

The C-V characteristics have been measured of the samples from different Sets - 1, 2, 3, 4 before and after γ-radiation at dose from 0.1Gy to 4000Gy. For illustration in Fig. 1 are presented the C-V characteristics for Set- 4.

The samples of Set 4 after growth have been 1 hour annealed at 1000°C in N_2 + RTA for 15 min in forming gas H_2+N_2. This regime was used for Ge nanocrystals formation in SiO_2 [15].

In Fig.1 are presented dynamics of C-V characteristics of nanostructured samples of SiO_2(Ge)SiO_2/nSi (Set 4) under γ-irradiation of dose from 0.1Gy to 4000Gy (a); (b) –C-V characteristics of conventional SiO_2/nSi –structure (without nc-Ge).

As shown in Fig. 1, there are some specific properties of these C-V characteristics: (1) all curves have typically form as MOS structures; (2) the C-V characteristics of nanostructured samples, SiO2(Ge)SiO2/nSi, are situated at positive voltages (V>0) to opposite to conventional MOS structure (SiO_2/nSi curve, without nc-Ge) which is situated at negative voltages (V<0); (3) - the accumulation regime corresponds to positive high voltage of +(4÷5)V and depletion- inversion regime corresponds to small positive-negative voltage of ± 2V; (4)-after cumulative irradiation from 0.1Gy to 4000Gy the C-V characteristics moved from positive threshold voltage (+3V) to negative threshold voltage (-1V) corresponding to the decreasing of negative charge defects or increasing the positive charge defects in these structures (ΔQ= ΔVxC). After high dose γ- irradiation (2800Gy÷4000Gy) the C-V characteristic tend to conventional C-V characteristics ($SiSiO_2$ curve), but there incline is higher due to high concentration of charge defects.

These experimental results indicate that all C-V characteristics in fig.1 can be deviated in two groups: (i) - low-dose (0.1Gy÷150Gy) characteristics and (ii) – high dose (200Gy÷4000Gy) characteristics.

The low-dose (0.1Gy÷150Gy) characteristics, in accumulation regime at V_{fb}= +(5÷6)V, have a smaller capacitance and accumulated electrons than that of middle and high radiation dose.

The high dose irradiation in interval of 350Gy÷4000Gy moved the C-V characteristics to negative voltage: flat band voltage (V_{fb}) decreases from V_{fb} = +4V to V_{fb} = +1.7V and middle gap voltage removed from V_{mg} = +2.2V to V_{mg} = -0.45V.

The middle dose radiation (200Gy÷350Gy) removed very slowly C-V characteristics: flat band voltage from V_{fb}= +4V to V_{fb}= +3.9V and middle gap voltage from V_{mg} = +2.2V to V_{mg} =+2V; the C-V characteristics have not specific properties, but they look more radiation stable (characteristics after 250Gy and 350Gy coincide).

Using the values of ΔV_{mg} =V_{mg}(0) - V_{mg}(U) and ΔV_{fb} = V_{fb} (0)- V_{fb}(U) we estimated the net oxide trap/charge densities (ΔN_{ot}) and the net interface trap-charge density (ΔN_{it}) by relations [17]:

$$\Delta N_{ot} = -\frac{C_{ox}\Delta V_{mg}}{qA}; \qquad (1)$$

$$\Delta N_{it} = \frac{C_{ox}\left(\Delta V_{fb} - \Delta V_{mg}\right)}{qA}, \qquad (2)$$

where C_{ox} is the oxide capacitance measured in accumulation, $-q$ =(1.602×10^{-19}C) electron charge and A is the area of capacitor.

The C-V characteristics of other samples (Set 1,2,3), as well as Set 4, have specific differences at low dose irradiation (0.1Gy - 64Gy) and many similarities at high dose irradiation (350Gy - 4000Gy). Therefore we will analyze in details the effects of low-dose irradiation.

The charged defect concentration in volume (ΔN_{ot}) and the interface charge stats (ΔN_{it}) calculated from the experimental results of flat band voltage (V_{fb}, ΔV_{fb}) and middle gap voltage (V_{mg}, ΔV_{mg}) and are presented in Fig. 2.

In Fig.2(a,b) are presented the dependences of the volume charged defect concentration (ΔN_{ot}) and interface charge stats concentration (ΔN_{it}) vs dose of γ-radiation for samples Sets 2,3,4.

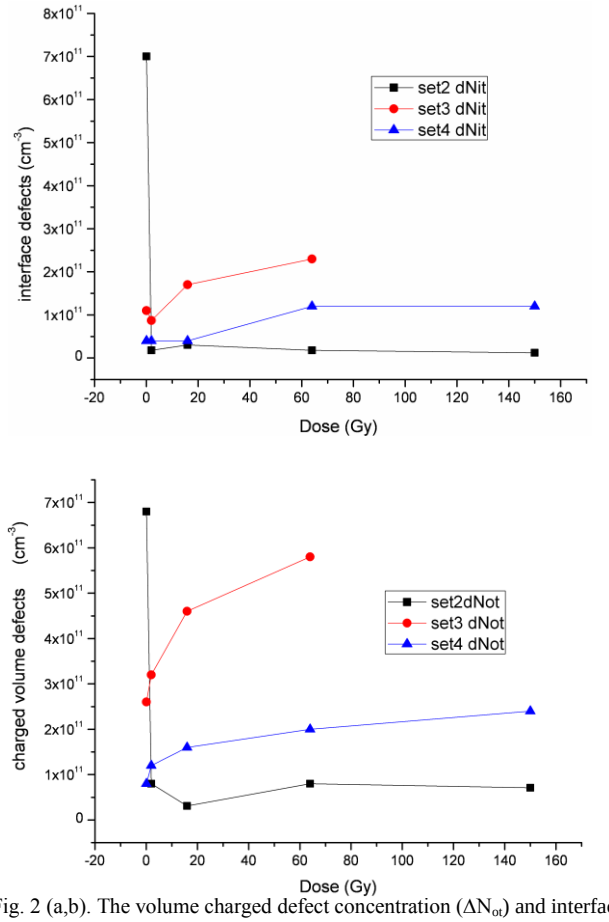

Fig. 2 (a,b). The volume charged defect concentration (ΔN_{ot}) and interface charge stats concentration (ΔN_{it}) vs dose of γ-radiation, Sets 2, 3, 4.

We can see in Fig.2 that flat band voltage(V_{fb}) and middle gap voltage (V_{mg}), as well as concentrations (ΔN_{ot}) and (ΔN_{it}), changed more rapidly after low-dose (0.1Gy÷2.0Gy) and slowly changed after dose of 16Gy ÷150Gy.

As it is shown in Fig. 2, for the samples of Set 4, as result of γ-irradiation at low-dose (0.1÷150Gy) the flat band voltage (V_{fb}) changed from +5.1V to 4.2V, the middle gap voltage (V_{mg}) - from +3V to +2.4V; the concentration of volume charged defect (ΔN_{ot}) – from 8.0×10^{10} cm^{-3} to $2.4\times10^{11}cm^{-3}$ and the interface charge stats (ΔN_{it}) – from $4.0\times10^{10}cm^{-3}$ to $1.6\times10^{11}cm^{-3}$. Respectively, the concentration of volume negative charged defects (Q^-) have been reduced at low-dose radiation and concentration of positive charge defects (Q^+)slowly increased at high dose to ΔN_{ot} $=1.7\times10^{12}cm^{-3}$ and $\Delta N_{it}=1.6\times10^{11}cm^{-3}$ at 4000Gy.

The specific properties of the C-V characteristics of samples Set 2 are: 1) for non radiation, C-V characteristic are situated in the region of positive voltage (+2V÷-0.8V); 2) at low-dose radiation (0.1÷16Gy) the CV characteristics where instable with some deviation voltage (±0.2V); but at dose up to 64Gy the C-V characteristics become stable at region of negative voltage that corresponds to minimum negative charge defect concentration; 3) at higher dose of 200÷4000Gy the C-V characteristics moved slowly to negative voltage in correspondence with slow increase of the positive charge defect concentration. Calculation demonstrated that concentration of volume negative charge defects changed in interval of ($\Delta N_{ot}=3.1\times10^{10}cm^{-3}$ ÷ $1.1\times10^{12}cm^{-3}$) and interface charge stats – in interval of ($\Delta N_{it}=$ $1.2\times10^{10}cm^{-3}$ ÷$1.9x10^{11}cm^{-3}$). Respectively, the concentration of negative charged defect (Q^-) have been reduced at low-dose radiation and concentration of positive charge defects (Q^+) slowly increased at high dose to ΔN_{ot} $=1.2\times10^{12}cm^{-3}$ and $\Delta N_{it}=6.5\times10^{11}cm^{-3}$ at 4000Gy, Fig. 2.

For all samples of Set-3 the C-V characteristics were situated at negative voltage at 0.2V÷1.0V in accumulation regime and at -1.0V÷3.2V in depletion regime. After radiation at low-dose (0.1Gy÷150Gy) the flat band voltage (V_{fb}) changed from +0.2.1V to -1.0V, the middle gap voltage (V_{mg}) - from -1.0V to -3.0V; the concentration of volume charged defect (ΔN_{ot}) – from $2.6\times10^{10}cm^{-3}$ to $5.8\times10^{11}cm^{-3}$ and the interface charge stats (ΔN_{it}) – from $1.1\times10^{11}cm^{-3}$ to $2.3\times10^{11}cm^{-3}$. Respectively, the concentration of negative charged defect (Q^-) have been reduced at low-dose radiation and concentration of positive charge defects slowly increased at high dose to $\Delta N_{ot}=7.2\times10^{11}cm^{-3}$ at 4000Gy, Fig.2.

The C-V characteristics of Set 1 (without post-growth thermal annealing) were situated in region of positive threshold voltage corresponding to very high concentration of negative charge defects (Q^-), having a complicate shape and were non stable during the measurements.

We explain the obtained results on the base of model of negative-positive charge defects correlation at low- and high dose of radiation. In accordance with this model, it is supposed that in investigated samples Set 1,2,3,4, before irradiation existed at least three types of charge defects: negative charge volume defects (Q_a^-) like acceptor centers $(GeO_x)^-$, slow negative interface stats (Q_s-) like structural defects $(GeSi)^-$ and conventional positive charge defects (O_b^+) like $(SiO_x)^+$ in pure SiO_2.

In this case the charge neutrality of material can be expressed by relation:

$$Q_b^+ - \left(Q_a^- + Q_s^-\right) = 0 \qquad (3)$$

Before irradiation, samples of Set 1, 2, 3, 4, have the C-V characteristics situated in region of positive voltage ($+V_{fb}$, $+V_{mg}$) due to majority of negative charge defects:

$$Q_a^- + Q_s^- \succ Q_b^+ \qquad (4)$$

Under the influence of low-dose γ-radiation (0.1Gy÷ 200Gy) have been decreased of the negative charge defect concentration to level of charge neutrality ($Q_a^- + Q_s^- = Q_b^+$). In this case the instability and the abrupt change of charge defect concentration at very low dose (0.1Gy) is due to the rapid concentration decrease of slow negative charge states - structural defects $(GeSi)^-$. At higher γ-radiation (350Gy÷ 4000Gy) have been increased slowly the concentration of positive charge defects and have been improved the linearity of C-V characteristics, which become comparable with the C-V characteristics of pure SiO_2/nSi structures with the same configuration.

These results of improvement of C-V characteristics of nanocomposite structures ncGe/SiO_2 are in accordance with data of photoluminescence improvement of silicon nanocrystals ncSi/SiO_2 after low dose ion radiation [12], electron radiation [13] and gamma radiation [14].

IV. CONCLUSIONS

The obtained results demonstrated that by low dose γ-radiation (0.1Gy÷150Gy) have been essentially reduced the structural negative charged defects in the nanocomposite structures $SiO_2(Ge)SiO_2/Si$ investigated by the C-V characteristics. At higher doses (350Gy÷4000Gy) the concentration of positive charge defects slowly increased and C-V characteristics shown the properties of the pure SiO_2 (without nc-Ge) with the same configuration. At average doses (200Gy÷350Gy) the concentration of negative charge defects and positive charge defects were approximately the same and the radiation stability of the samples was the highest.

V. REFERENCES

[1] N.L. Rowell, D.J. Lockwood, A. Karmous, P.D. Szkutnik, I.Berhezier, Supperlattices and Microstrucrures, 44, p.305, 2008.

[2] A. Singha, P. Dhar, A. Roy, "A nondestructive tool for nanomaterials: Raman and photoluminescence spectroscopy," Am. J. Phys. vol.73, n.3, pp. 224-230, 2005.

[3] A. Dana, S. Agan, S. Tokay, A. Aydinli, T.J. Finstad, "Raman and TEM studies of Ge nanocrystal formation in SiOx:Ge/SiOx multilayers," Phys. Stat. Sol., (C), vol. 4, n.2, pp.288-291, 2007.

[4] S. Agan, A. Dana and A. Aydinli, "TEM studies of Ge nanocrystals formation in PECVD grown SiO_2:Ge/SiO_2 multilayers," J. Phys: Condens. Matter, vol.18, pp. 5037-5045, 2006.

[5] K. Salamon, O. Milat, M. Buljan, U.V. Desnica, N.Radic, P.Dubcek, S.Bernstorff, "X-ray study of Ge nanoparticle formation in Ge:SiO_2/SiO_2 multilayers," On-line Journal of E-MRS Fall Meeting, 2007.

[6] U.V.Desnica, M.Buljan, K.Salamon, N.Radic et al., "Formation of germanium nanocrystals in SiO_2 using RF magnetron sputtering," http://www.science 24.com/paper/15584.

[7] X.J. Sun, S.Y. Ma, J.J. Wei, X.L. Xu, "Comparative study on photoluminescence from Ge/PS and Ge/SiO_2 thin films," http://www.ncbi.nlm.nih.gov/pubmed/19093555.

[8] Yu Ying, at al., "New Photoluminescence of Ge/SiO_2 Glass Synthesized by Sol/gel Method," Chinese Chemical Letters vol.15, n.12, pp.1505-1508, 2004.

[9] Y.Maeda, N.Tsukamoto, Y.Yazawa, Appl.Phys.Lett. vol.59, n.24, p.3168, 1991.

[10] M. Nagami, Y. Abe, Appl. Phys. Lett., vol.65, n.20, p.2545, 1994.

[11] K.S. Min, K.V.Shcheglov, C.M. Yang and H.A. Atwater, Appl.Phys.Lett., vol.68, n.18, p.2511, 1996.

[12] I. Antonova, V. Scuratov, M. Gulyaev, D. Marin, J. Jedrzejewski, I. Balberg, "Improvement of the nanocrystals embedded in dielectrics and nanostructures," IBMM2008.org 16th International Conference on Ion Beam Modification of Materials, Dresden, Germany, 31 September, 2008.

[13] G.A. Kaciurin, et al., "The influence of Irradiation on Subsequent Annealing on Si Nanocrystals Formed in SiO_2 Layers," Semiconductors, vol.34, n.8, pp.965-970, 2000.

[14] I. P. Lisovskyy, I.Z. Indutnyy, M.V. Muravska, V.V. Voitovych, E. G. Gule, P.E. Shepelyavyi. Fizika i Tekhnika Poluprovodnikov, vol.42, n.5, pp.591-594, 2008.

[15] S.T. Shishiyanu, N.A.P. Mogaddam, E. Yilmaz, R. Turan, "Effect of Gamma Radiation on Raman Spectra of Ge Nanocrystals embedded in SiO_2," Proc. of 5th Nanoscience and Nanotechnology Conference NanoTR5, Eskişehir, Turkey, pp.67-69, 2009.

[16] J.H. Yao, K.R. Elder, H. Guo, M. Grant, "Theory and simulation of Ostwald ripening," Phys. Review B, vol. 47, n. 21, pp.14 110-14 125, 1993.

[17] F.B. Ergin, R.Turan, S.T. Shishiyanu, E.Yilmaz. "Effect of γ-radiation on HfO_2 based MOS capacitor," Nuclear Instruments and Methods in Physics Research Section B; vol.268, n.9, 2010, pp.1482-1485.

Nanoperforated Indium Phosphide for Terahertz Imaging Bio-applications

D. ESINENCO[1], L. SIRBU[2], I. VODA[3], L. GHIMPU[2], R. MULLER[4], R. VOICU[4], M. DANILA[4], A. LECA[5], T. DASCALU[5], I.M. TIGINYANU[1,2] and V. URSAKI[1,6]

[1]*Technical University of Moldova, 168, Stefan cel Mare str., MD-2004 Chisinau, Moldova*
[2]*Institute of Electronic Engineering and Nanotechnologies "D. Ghitu ", 3/3, Academiei str., MD-2028 Chisinau, Moldova*
[3]*Institute of Chemistry of the Academy of Sciences of Moldova, Academiei str., MD-2028 Chisinau, Moldova*
[4]*National Institute for R&D in Microtechnologies- IMT Bucharest, Erou Iancu Nicolae 126 A str., Bucharest, Romania*
[5]*National Institute for Laser, Plasma and Radiation Physics Laboratory of Solid-State Quantum [5]Electronics, PO Box MG-36, Magurele, 077125, Romania*
[6]*Institute of Applied Physics, Academy of Science of Moldova, 5, Academiei str., MD-2028 Chisinau, Moldova*

Abstract – We demonstrate the fabrication of thin InP membranes with porous compact packed structure that have been cut during electrochemical etching in the same anodic process. Besides, we show the possibility of pore filling with metal-organic composites. Chemical compounds have been identified by XRD method. The THz emitting characteristics of InP porous films were drastically changed after filling with sensitized metal-organic composites. We show that InP porous membranes filled with metal-organic composites are perfect materials for bio-applications. The experimental study and emulations based on Finite Element Model (FEM) show also that the obtained nanocomposite materials are promising for nonlinear optical applications, in particular for the development of THz emitters, THz imaging systems, MEMS, MOEMS, etc.

Index Terms – nanostructurated membrane, Terahertz (THz) spectroscopy, Indium Phosphide (InP), metal-organic composites, bio-materials.

I. INTRODUCTION

For many decades the terahertz frequencies that range between the infrared and millimeter wavelengths was one of the least explored regions of the electromagnetic spectrum.

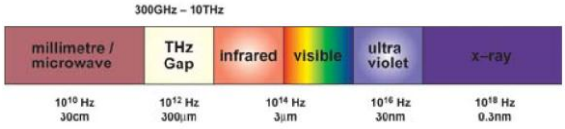

While experimental techniques developed for both neighboring spectral ranges cannot be directly applied at terahertz frequencies many of the methods and theories have been adapted to the terahertz range. For instance, single-mode waveguides, widely used in the millimeter range, cannot be applied at terahertz frequencies because of strong damping, but oversized multimode waveguides are commonly used. On the other hand, glass is the standard material for optical components in the visible and near-infrared but in the terahertz range it cannot be used due to strong absorption. Instead, various crystalline and plastic materials are used for windows, filters, lenses, etc., in quasi-optical arrangements taking over all the advantages of visible optics. This mixture of optical and microwave techniques is a characteristic feature of terahertz technology. At the same time terahertz specific devices evolved which have no counterpart in other spectral range, like impurity semiconductor lasers, μ-photoconductivity detectors, metal mesh filters, grid polarizers, and others.

The spectroscopy at terahertz frequencies is of great importance for condensed matter physics and in particular for semiconductors and semiconductor structures because the characteristic energies of many elementary excitations lie in this spectral range [1]. Among them are plasma oscillations, ionization energies of typical shallow donors and acceptors, cyclotron resonance and spin-flip energies, the characteristic size-quantization energies of low dimensional electron systems, and optical phonon energies. Furthermore, the relaxation rates of free and bound excited carriers and scattering rates of free carriers coincide with the terahertz regime. The photon energies in this part of the electromagnetic spectrum range from about 1 to 35 meV being much smaller than the energy gap of usual semiconductors.

At the same time the terahertz technology has entered into an unprecedented revolutionary era with ever-growing applications in biology and medicine [2], monitoring and spectroscopy in pharmaceutical industry and science [3, 4], medical imaging [2], material spectroscopy and sensing, security, and high-data-rate communications.

Over the past few years, unprecedented progress has been made in the area of THz source technologies, which have played an important role in opening up the possibility of using THz waves in many real-world applications. Miniaturized electron beam sources have been demonstrated and the performances of the solid-state sources and frequency multipliers have been steadily improved by increasing their upper frequency limits and their power efficiencies. Terahertz quantum cascade lasers have

experienced a rapid progress over the last few years. Their output power level and operation temperatures have remarkably increased whereas their lowest operation frequencies have been continuously decreasing. Terahertz optoelectronic sources, including THz photomixers and THz parametric sources have seen a great improvement in their performances in terms of optical-to-electrical efficiencies and maximum output powers at frequencies above 1 THz. New material systems have been developed for photomixer sources allowing them to operate at optical telecommunication wavelengths. Taking the advantage of low-cost diode lasers and high-power fiber amplifiers and other telecommunication optical components, it is now possible to dramatically reduce the cost of the THz system.

II. EXPERIMENTAL SETUP

Crystalline (100)-oriented substrates of S-doped n-InP with 500 μm thickness (prior to anodic etching) and free electron concentration of 1.3×10^{18} cm^{-3} were used. The anodization was carried out in an electrochemical double cell as described elsewhere [5]. A four-electrode configuration was used: a Pt reference electrode in the electrolyte, a Pt reference electrode on the sample, a Pt counter electrode, and a Pt working electrode. The temperature was kept constant with a thermostat. The electrolyte was pumped continuously through both parts of the double cell with the help of a peristaltic pump. All equipment involved in the experiments was computer-controlled. The area of the sample exposed to the electrolyte was 0.5 cm^2. The anodic etching was carried out in 5 % HCl aqueous solution at room temperature in potentiostatic regime with the following range of values for obtaining gradient of diameter of pores: the applied voltage linearly and exponentially decreases from 8.0 to 1.0 V that leads to changing degree of porosity with depth. To have a thin porous film, we applied a shock pulse of bias from the potentiostat. The first pulse was used to remove the disordered layer of the porous structure (see Fig 1) and the next pulses were applied to fabricate membranes with ordered pores which were afterwards used in our experiments (see Fig 2). Further details of the anodic etching process can be found in [5]. A TESCAN scanning electron microscope equipped with an Oxford Instruments INCA energy dispersive x-ray (EDX) system was used to analyze the morphology and chemical composition of the porous samples. As previously shown [5], two types of pores can be introduced in III–V semiconductor compounds: crystallographically oriented or 'crysto' pores, and current-line-oriented or 'curro' pores. Crysto pores are usually generated at low anodization current densities or applied voltages, the mechanism of their formation being related to direct dissolution of the material. Curro pores are formed at relatively high anodic current densities or applied voltages, their growth being mediated by oxide formation and its dissolution at the pore tip [5].

Coordination compounds with structural formula $[Zn(C_3N_2(C_6H_5)_2NO_2)_2(CH_3OH)_2]$ and $[Ni(C_3N_2(C_6H_5)_2NO_2)_2(CH_3OH)_2]$ have been synthesized and characterized by X-ray crystallography (Fig. 3, upper part). These complexes have pseudopolimeric structures being connected to each other by hydrogen bonding (Fig. 3, middle part). This behavior made possible the introduction of these complexes in porous *n*-InP membranes. The complex deposition in the porous structure was carried out in a dark room. The monomers were incorporated into the porous layer from $Zn(C_3N_2(C_6H_5)_2NO_2)_2(CH_3OH)_2 : C_3H_6O$ and $Ni(C_3N_2(C_6H_5)_2NO_2)_2(CH_3OH)_2 : C_3H_6O$ solutions. Afterwards, the samples were dried for several days at room temperature. The morphology of the monomer nanowires in an InP template is illustrated in Fig. 3, lower part.

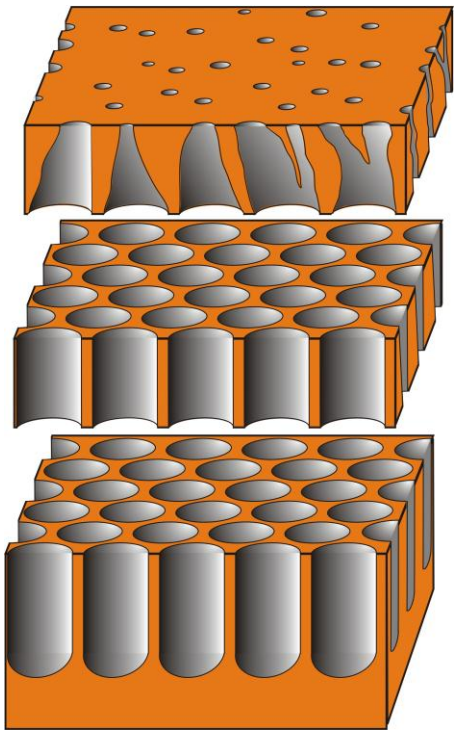

Fig. 1. Schematic representation of cutting membranes from the sample in the same anodic process.

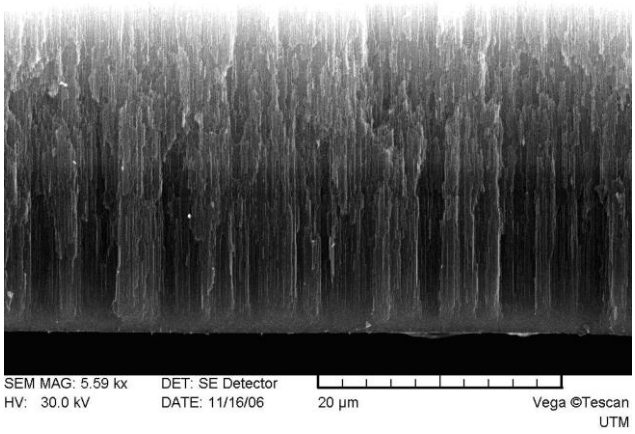

Fig. 2. SEM image of porous InP film.

The EDX analysis of coordination compounds demonstrates that they have fully filled the nanostructured template of n-InP along the entire depth of pores.

The setup used for characterization includes a THz time-domain spectrometer, and a laser amplifier-based optical-pump THz probe spectrometer [6]. The transmission through the sample in the time domain was recorded for each set of samples. Each sample was mounted on a piece of table having a hole with a diameter of 4 mm through which the transmission was measured. The terahertz electric field was linearly polarized for all measurements, and the terahertz beam was normally incident on the sample surface. All measurements were performed at room temperature (Fig. 4).

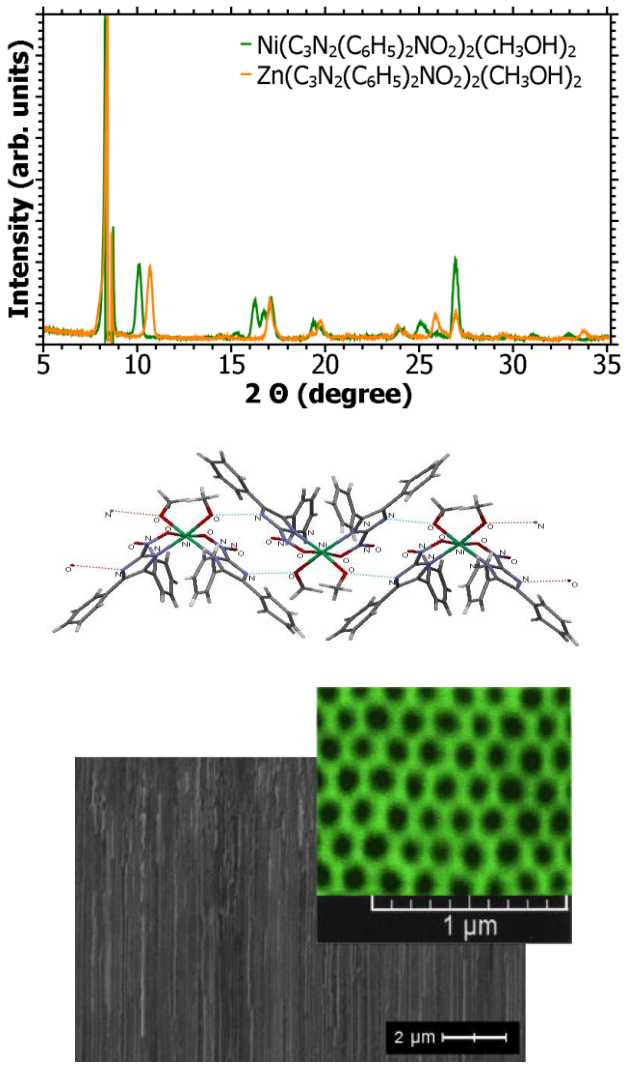

Fig. 3. XRD analyses of the complexes (upper part); hydrogen bonding inside $[Ni(C_3N_2(C_6H_5)_2NO_2)_2(CH_3OH)_2]$ structure (middle part); SEM image of an InP template filled with coordination compounds. The inset shows a top of view of the pores (lower part).

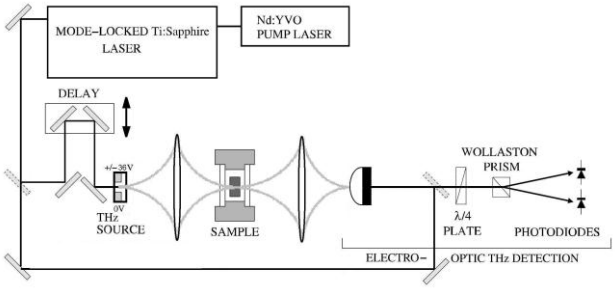

Fig. 4. Experimental setup for the investigation of THz emission from porous InP and composites samples. The samples are placed perpendicular to incident beam at room temperature.

The porous InP is one of the most promising material for the fabrication of THz devices [7, 8]. Recently we have reported a new technology [9] for the fabrication of membranes on InP (111) surfaces that can emit ultrafast coherent terahertz pulses under near-infrared optical excitation. The membranes irradiated by heavy noble gas Kr or Xe ions demonstrated enhanced terahertz emission.

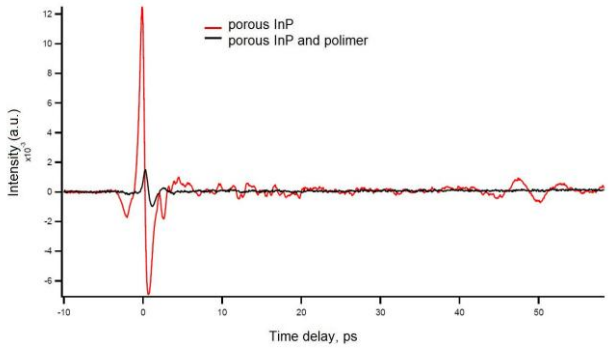

Fig. 5. THz signal from a pair of porous InP and composites samples.

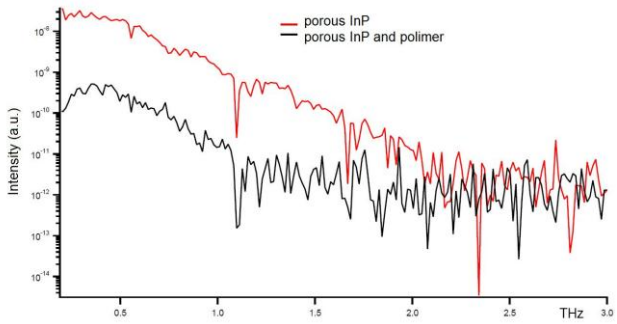

Fig. 6. THz spectrum measured in air. Several strong absorption lines due to water vapor are seen.

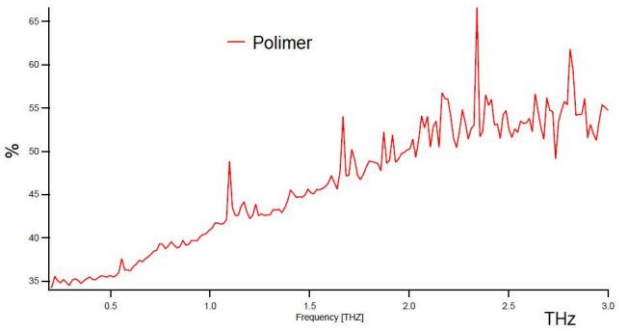

Fig. 7. Remodeled absorption spectrum. Several strong absorption lines due to water vapor are evident.

Porous InP has been taken as reference material in studying the THz emission and it has been compared with the same structure filled with polymer (Fig. 5) [10-12]. One can see from the THz spectrum that polymers increase the absorption of THz radiation (Figs. 6, 7). We suppose that the main impact on absorption is due to the presence of metallic atoms in this systemized metal-organic structure. Another contribution to the absorption comes from atmospheric water vapors, since the experiments were performed without using a nitrogen gas chamber.

III. SIMULATION MODEL FOR BIO APPLICATIONS

We investigated the terahertz characteristics of porous films with pores filled in with polymers. Two kinds of samples have been investigated: (i) clean poly- and monomers, and (ii) the ones containing metallic particles inside. We used FEM methods implying Mie theory and Drude model for the description of metallic nanoparticles dispersion. The model, defined in a cylindrical coordinate system, comprises a PML layer as thick as twice the wavelength used for excitation. The simulations were made for a single pore of 100 nm in diameter made in an A^3B^5 like

semiconductor. The pore was considered to be filled in with a highly contrast dielectric (our polymer) in terms of electric permittivity, with nanoparticles with various diameters in the range of 10 to 50 nm dispersed in it. We defined an excitation pulse of picoseconds replicating the LASER excitation for the real samples [12].

Fig. 8 represents a model for bio-applications, where the THz radiation is reflected from the surface of porous InP. In the specular direction we have absorption from the used bio sample (in our case a chemically synthesized metal-organic structure) that is going to be scanned.

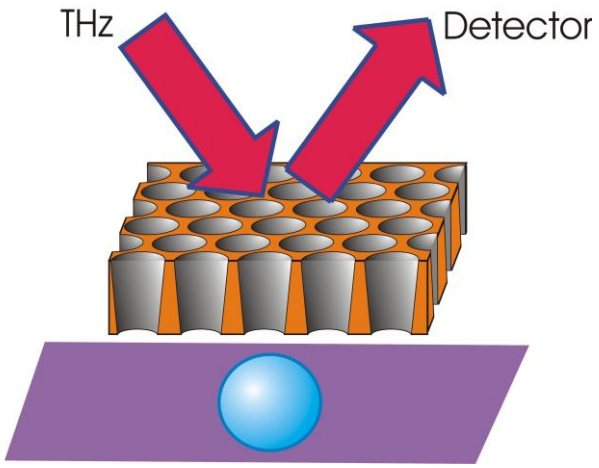

Fig 8. Model of bio-samples detector

IV. CONCLUSION

We carried out an experimental study of THz emission from new synthesized polymers as well as their THz absorption characteristics. We have developed a technique to obtain porous InP membranes with thicknesses in the range of 30-100 μm filled in with polymers. This technique is expected to be useful for medical applications, for instance in detecting and processing images like a huge lattice with thousands, millions, or even billions of detectors working simultaneously.

REFERENCES

[1] S.D. Ganichev. "Intense Terahertz Excitation of Semiconductors" Terahertz Science and Technology, ISSN 1941-7411 Vol. 1, No 3, Sept. 2008.

[2] Peter H. Siegel. „Terahertz Technology in Biology and Medicine" 2438 IEEE Transactions on Microwave Theory and Techniques, Vol. 52, NO. 10, Oct. 2004.

[3] Xin Wu, De Li, Wei-Hua Sun, Feng Gao, Zhi-Jian Zhang, and Ru-Wen Peng. „Coupling of THz Surface Plasmon Polaritons in Corrugated Stacks of Dielectric and Semiconductor" PIERS ONLINE, Vol. 5, no 2, 101, 2009.

[4] Yasser A. Hussein and James E. Spencer „Hybrid FDTD Analysis for Periodic On-Chip Terahertz (THz) Structures" SLAC-PUB-10908 Contributed to 2005 IEEE/ACES International Conference on Wireless Communications and Applied Computational Electromagnetics, April 3-7, 2005, Honolulu, HI, USA 2005.

[5] S. Langa, I. M. Tiginyanu, J. Carstensen, M. Christophersen and H. Foell „Self-organized growth of single crystals of nanopores" Appl. Phys. Lett. 82 278, 2003.

[6] A. Charles Schmuttenmaer "Using Terahertz Spectroscopy to Study Nanomaterials" Terahertz Science and Technology, ISSN 1941-7411 Vol.1, No.1, March 2008.

[7] M. Reid, I. I.V. Cravetchi, R. Fedosejevs, I.M. Tiginyanu and L. Sirbu. „Enhanced terahertz emission from porous InP(111) membranes" Appl. Phys. Lett., Vol. 86, 021904, 2005.

[8] M. Reid, I. I.V. Cravetchi, R. Fedosejevs, I.M. Tiginyanu, L. Sirbu & Robert W. Boyd. „Enhanced nonlinear optical response of InP(100) membranes" Physical Review B, Vol. 71, 081306, 2005.

[9] K. Radhanpura, S. Hargreaves, R. A. Lewis, L. Sirbu, and I. M. Tiginyanu „Heavy noble gas (Kr, Xe) irradiated (111) InP nanoporous honeycomb membranes with enhanced ultrafast all-optical terahertz emission" Appl. Phys. Lett. 97, 181921, 2010.

[10] Alexander M. Sinyukov and L. Michael Hayden „Efficient Electrooptic Polymers for THz Applications" J. Phys. Chem. B 108, 8515, 2004.

[11] Vittorio M. N. Passaro Francesco Dell'Olio, Biagio Casamassima 1 and Francesco De Leonardis „Guided-Wave Optical Biosensors" Sensors, 7, 508, 2007.

[12] V. Sergentu, D. Esinenco, L. Sirbu, I. Vodă, I. M. Tiginyanu, V. Ursaki. „Rayleigh scattering of a metal nanoparticle on a flat dielectric surface" Tereahertz & Mid IR Radiation: Basic Research & Practical Applications The NATO Science for Peace and Security Programme, Photonics Society, Turunç-Marmaris, Turkey 3-6 Nov. 2009.

Nanolamellar Structures of Oxide-$A^{III}B^{VI}$:Cd Semiconductors Type for use as Detectors of Radiation in the UV Spectral Region

L.DMITROGLO[1], D. UNTILA[1], P.CHETRUSH[1], I. EVTODIEV[1], Iu. CARAMAN[2], G. LAZAR[2], V. NEDEFF[2]

[1]*Moldova State University, 60 A. Mateevici Str., Chisinau, MD-2009, Republic of Moldova*

[2]*University of Bacau, 157 Calea Marasesti, RO-600115 Bacau, Romania*

dmitrogloliliana@yahoo.com

***Abstract* – In the paper, optical and photoelectrical properties of *GaSe* and *InSe* single crystal films of 10^{-5}÷10^{-7} m submicron thickness and of semiconductor-native oxide structures obtained by annealing at (450÷700)°C in a normal atmosphere, are studied.**

The absorption spectrum of *InSe* lamella as well as of *GaSe* lamella in the energetic range from the red threshold up to 4,5 eV contains three bands with a rapid increase of the absorption coefficient which varies in the limits of (10^0÷10^6) cm^{-1}. At the absorption coefficients of (10^0÷10^2)cm^{-1} the indirect optic transitions are present.

At the energies higher than 1,25 eV and 2,01 eV for *InSe* and *GaSe* respectively the light absorption are determined by the direct optical transitions in the centre of the Brillouin zone and at the energies higher than 3,0 eV also by the direct optical transitions in the points of the bands high symmetry.

The resistive photosensitivity bands cover the spectral range $E_g \leq h\nu \leq$ 4,5 eV for lamellar photoresistors in which electric field $E \perp C_6$. The resistive photosensitivity band width could be controlled by the lamella thickness for $d \geq 1$µm. The open circuit voltage spectral distribution is analysed from which results that at the oxidation temperature of 700°C in *GaSe* layer at the heterojunction interface the defects are formed on which the charge carriers, collected in the junction, are dissipated. The noneequilibrium charge carrier free path is of 0,8 µm.

Index Terms – GaSe, InSe, semiconductor heterojunction, oxide films, nanolamellar structures.

I. INTRODUCTION

The actual tendencies of the photonics and optoelectronic devices development are determined by the wide scale implementation of semiconductor materials. Among the perspective materials for nanoparticles fabrication and particullary of nanolamella are compounds of lamellar class semiconductors of $A^{III}B^{VI}$ type, a typical representatives of which *GaSe, GaS, InSe* and *GaTe* are [1-4].

These compounds single crystals are formed from lamellar packing of Hal-Me-Me-Hal with strong chemical binding of atoms inside of packing and weak binding (of Van-Der-Waals type) between packing [5]. The chemical binding anisotropy of the atomic plans in *GaSe* and *InSe* compounds allow by cleaving to obtain plan parallel lamella with smooth surface at atomic level, of low surface states density [6]. At a normal atmosphere the gas molecules absorption from the atmosphere occurs and at the same times an oxides layer is formed [7]. The oxides variety from *GaSe* and *InSe* compounds surface could be limited to In_2O_3 and Ga_2O_3 stable oxides by high temperature annealing of the sample [8-9]. The oxide layer from the lamella surface of p-*GaSe* and p-*InSe:Cd* is electrically positive, the fact which leads to the electron afinity decrease relative to the freshly cleaved surface by 0,35 eV in *GaSe* [5]. The high native defects concentration in lamellar crystals, determined by the atomic plans arrangement in lamellar packing and of elemntary packing to one another leads to a stability of electrical and optical properties to the ionizing radiation. These along with low surface states concentration determine one of the priority

directions of these compounds using as a photosensitive element in the radiation receivers in the visible-UV region of spectrum.

II. THE STUDIED SAPLES AND EXPERIMENT METHODICS

ε-*GaSe* and γ-*InSe* single crystals were grown by Bridgman method. *p-InSe* crystals were obtained by doping with 0,2 % of *Cd* during chemical compound process of synthesis. Single crystals were cuted in cylindrical blocks with the thickness of 10-12 mm and then cleaved in the lamella with the thickness of hundreds of nm up to 0,3-0,5 mm. For to simplify the cleavage procedure of the nanometric thickness lamella, the cylindrical blocks were irradiated with ultrasound during 15-20 min. The sound waves of 0,22 MHz frequency were obtained by an optical modulator made from single crystal SiO_2. The obtained *InSe:Cd* samples were oxidated in normal atmosphere at temperatures ~520°C and 580°C respectively. The heat treatment duration was chosen on the base of testing and heterojunctions with the stable in time photoelectrical parameters under the intense illumination with the radiations from the visible region of spectrum were chosen.

The electrical contacts for Hall measurements were formed by evaporation of In thin layers on (001) surface of single crystal *GaSe* and *InSe* lamella. The characteristics of *p-GaSe:Cd* and *p-InSe* single crystals determined from Hall measurements are given in the Table 1.

Spectral dependence of the photocurrent in the direction perpendicular to C_6 axis and of photovoltage in lamellar *InSe-*In_2O_3 and *GaSe-*Ga_2O_3 heterojunctions was measured

TABLE1. ELECTRICAL PROPERTIES OF CD DOPED WITH GASE, INSE

Simple	Conductivity tipe	Hall concentration (cm^{-3})	Activation energy (eV)	Mobility ($cm^2 V^{-1}S^{1}$)
InSe:Cd	p	$8,5\cdot10^{14}$	0,4	28
GaSe undoped	p	p-$2\cdot10^{14}$	0,56	38÷45
GaSe-0,01%Cd	p	p-$2\cdot10^{15}$	0,24	20÷35
GaSe-0,1%Cd	p	p-$4,2\cdot10^{15}$	0,24	-
GaSe-0,2%Cd	p	p-$5,7\cdot10^{15}$	0,24	-
GaSe-0,5%Cd	p	p-$8,3\cdot10^{15}$	0,22	12÷20

on a unit on the base of MDR-2 monochromator. The photocurrent through the sample in the regime of photoresistor as well as through semiconductor –oxide heterojunction was calculated by potential difference on the load resistance R_s. The optical and photoelectrical characteristics of the samples in the regime of photoconductivity are connected by relation [10]:

$$G = \frac{I_{ph}}{eWlI_0(1-R)[1-\exp(-\alpha d)]} \qquad (1)$$

were the amplification coefficient, τ- is the minority charge carriers life time, tr-the electric charge "e " (electron) time of transportation through the sample, W, l- width and lenght of the sample, I0-the incident light beam intensity, R, α - reflection and absorption coefficients, d –the sample tickness.

The open circuit voltage of a heterojunction illuminated by a light bean of the intensity I_0 is given by relation [10]:

$$V = \frac{kT}{e}\ln\left(1+\frac{(1-R)I_0\left\{1-\frac{\exp(-\alpha d)}{\alpha L_n}\right\}}{\frac{D_p n_{p0}}{L_n}+N_a(v_p+S_p)\exp\left(-\frac{eV_D}{kT}\right)}\right) \qquad (2)$$

Were *k*-is Boltsman's constant, *T*-temperature, S_p-the holes recombination rate, L_0-the electron free path in p-type semiconductor, V_D-the applied to the junction voltage.

III. EXPERIMENTAL RESULTS

The elementary packing consisting of the halogen and metall atoms planar arrangement of Hal-Me-Me-Hal type in ε-*GaSe* and γ-*InSe* crystals have thicknesses of 0,8 -0,85 nm [11-12]. The presence of the weak chemical binding between chalcogenide plans allow obtaining of the lamella with the perfect surface and thicknesses needed for measurements of the absorption coefficient with a constant accuracy with the value from the units of cm^{-1} up to ~10^5 cm^{-1}. The absorption spectra of the lamella of *InSe:Cd* (curve 1) and *GaSe:Cd* (curve 2) and of lamella with a native oxide on the surface are given in Fig.1.

In the region of 1,10÷1,15 eV in *InSe* and 1,5÷2,0 eV in *GaSe* α(hν) dependencies are determined by the indirect optical transitions occur at the energies hν≥1,2 eV in *InSe:Cd* and hν>2,0 eV in *GaSe:Cd*.

The more pronounced increase of the absorption coefficient at the photons energy hν >3,2 eV which is observed (fig.1) both in initial lamella as well as after their oxidation is related to the opening of new channels of absorption in the points of high symmetry of Brillouin zone (points X, L,Σ).

Spectral dependencies of photocurrent density in *InSe:Cd* and *GaSe:Cd* lamella with low thickness are given in Fig.2. The electric field is applyed along the direction perpendicular to the symmetry axis C_6. As one can see from the comparison of Fig.1 and Fig.2 the photocurrent density in *InSe:Cd* photoresistors in the photons energy interval from the fundamental band edge up to ~4,0÷4,1 eV is increasing along with the absorption cofficient α increase. The photocurrent density is deacreasing by an order of spectral magnitude 1,2÷2,4 eV at the lamella thickness decrease from 7,3 μm to 0,8 μm. If to take into account that the absorption coefficient in this spectral region does not depend on the sample thickness (the *InSe* lamella surface perfection excludes the possibility of structural layers defected at surface formation), then one can observe that in the sample ~10% of the incident light is absorbed. The tendency of photocurrent density decrease at the photons energy *hν*>4,2 eV could be explained by the fact that in this spectral region the light is absorbed in a thin layer at the sample surface where the none-equilibrium electric charge carriers recombination rate is higher than in the sample volume. The thore rapid decrease of a photocurrent density in this spectral region indicates that the depth of the light penetration in the sample $d < L_n$ (L_n-electron free path in *p-InSe*) and more evident appears the recombination through the states on the both surfaces of the sample.

The photocurrent spectral dependencies in *p-GaSe:Cd* lamella with the thickness of 14,2 μm and 0,9 μm (Fig.3) are identical by their form for the same of p-*InSe:Cd*. The monotons photocurrent increase in the photons energy of 1,5÷1,9 eV is a results of none-equilibrium charge carrier generation at a indirect optical transitions.

The photocurrent spectral dependencies in *InSe* and *GaSe* lamella are in good correlation with the formula 1, the fact which indicates that at the electric field in the sample 10÷100 V/cm the amplification coefficient of charge carriers *G* is a constant value and at the same time the surface recombination rate of charge carriers in the single crystal *GaSe:Cd* and *InSe:Cd* lamella is rather low.

It is well known that the electrical conductivity of Ga_2O_3 films depends on oxygen atoms concentration as a dopant. At the oxidation at temperatures (450-500)°C Ga_2O_3 layers of high electrical conductivity are obtained. The majority charge carrier (electron) concentration is of (10^{17}÷10^{18})cm^{-3} and their mobility of (40÷80) $cm^2/V\cdot s$ [13]. At the annealing at high temperature (~900°C) the dielectric Ga_2O_3 film could be obtained.

The open circuit voltage spectral distribution normed to the number of incident photons for heterojunctions with Ga_2O_3 dielectric film and oxide film obtained at 480°C (curve 1) and 700°C (curve 2) is given in Fig.4.

As one can see the $U_{oc}=f(hv)$ dependencies for the analyzed structures are in good correlation with the formula

(2). The rapid increase of the open circuit voltage in the photons energy (1,85÷2,03) eV is due to the exponential

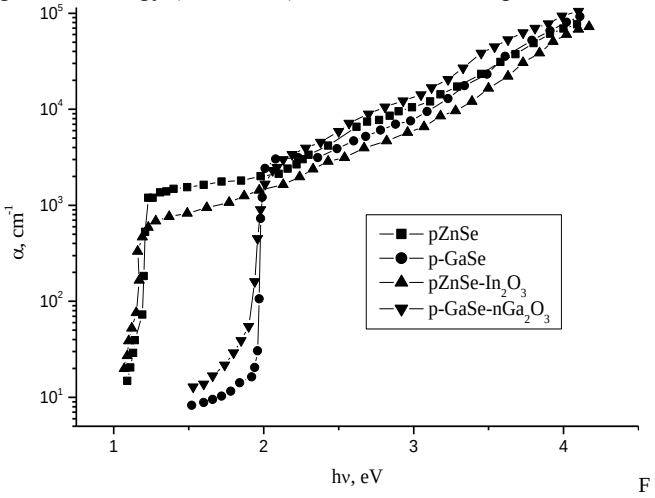

Fig.1. Absorption spectra calculated according to formula (1) from the measurements of transparency of p-InSe:Cd lamella (curve 1), In2O3-InSe (curve3), p-GaSe (curve 2), p-Ga2O3-iGa2O3-pGaSe (curve 4).

increase of the absorbtion coefficient in the region of the fundamental band edge (Fig.1, curve 2). The monotonons increase of the open circuit voltage with the photons energy increase in the region of (2,03÷4,1) eV in the heterojunction fabricated at the 480°C indicates to a low concentration of recombination centres for the minority charge carriers at Ga_2O_3-*GaSe* the result which is in a good agreement with the photoconductivity spectrum.

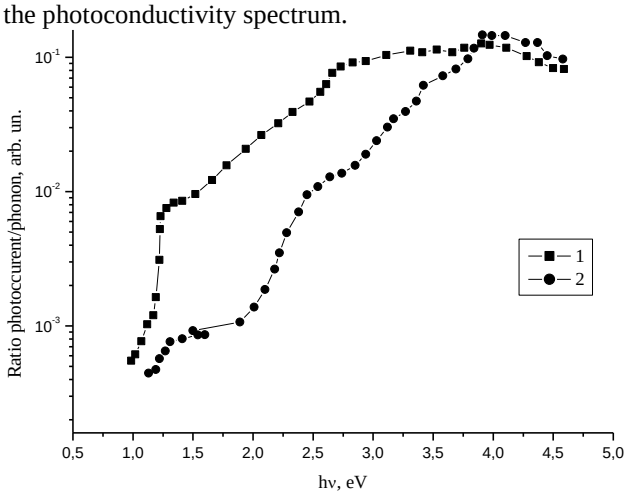

Fig.2. The photocurrent normed to the number of incident photons as a function of the photons energy for InSe:Cd lamella of the thickness of 7,3 μm (curve 1) and 0,8 μm (curve 2).

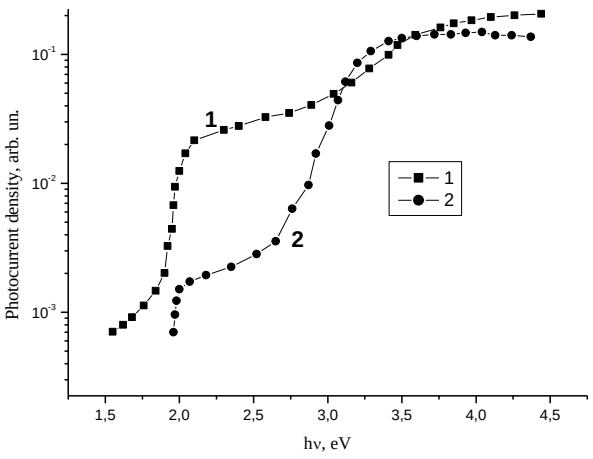

Fig.3. Photocurrent density spectral dependence in GaSe:Cd lamella with the thickiness of 14,2 μm (curve 1) and 0,9 μm (curve 2) at room temperature.

So at the oxidation temperature of 480°C the concentration of the formed defects in the presence of Ga_2O_3 oxide does not exceed their concentration on a free surface of *GaSe* lamella. The open circuit voltage rapid decrease at the photons energy $h\nu$>4,0 eV is due to the increase of the reflection coefficient from Ga_2O_3 layer surface (n≈3,3 [14]) and from Ga_2O_3-*GaSe* interface due to the optical transitions in the *X* point of the Brillouin zone.

The open circuit voltage spectral dependence of nGa_2O_3-iGa_2O_3-*pGaSe* structure with an oxide film made at 700°C represents a curve with the maximum at $h\nu$≈2,5 eV and a monotonous decrease for photons energy $h\nu$>2,5 eV. The minority charge carriers free path in the none deformed *GaSe* lamella, detrmined from the photocurrent relaxation analysis of the illumination of the sample back with the short pulses of the monochromatic light (by method described in [14]) is comensurable with the *GaSe* lamella thickness in the heterojunction. For the none-equilibrium charge carriers free path of this value the open circuit voltage U_{oc} should be in a direct accordance with α *(hν)* dependence. The monotonous decrease of U_{oc} in the region of photons energy $h\nu$>2,5 eV with the tendency of saturation at high energies indicates to the lower values of the generated carriers diffusion lenght in *GaSe* lamella.

From formula (2) one can see that $U_{oc}(h\nu)$ dependence has a tendency of decreasing with the incident radiation wavelength increase for a constant recombination rate at the interface it de curvature depth of the bands in *GaSe* $d<L_n$. For $\alpha d_n<<1$ and S_n independent on the photons energy from (2) one can see that the open circuit voltage monotonously decreases along with the [15] factor.

$$\alpha I_0 /(\alpha L_n + 1) \quad (3)$$

By varrying the monochromatic radiation intensity ΔI_0 so that to maintain constant the open circuit voltage value, the minority charge carriers free path could be determined.

The results of measurements of intensity variation ΔI_0 of the incident beam as a function of inversly of the absorption coefficient at energies from range (3,0÷ 4,0) eV are presented in Fig.5. The relatively low free path L_n value of 0,8 μm indicates that at 700°C at Ga_2O_3-*GaSe* interface a native structural defects and new phases (Ga_2Se_3, *GaO*) are formed which serve as dissipation and recombination centres of non-equilibrium charge carriers on *GaSe* lamella surface.

The band diagram of nGa_2O_3-iGa_2O_3-*pGaSe:Cd* heterojunction calculated on the base of absorption and photoconductivity spectra and measurements of charge carriers concentration in *GaSe* and Ga_2O_3 lamella is brought in Fig.6. The band curvature value in the *pGaSe*-iGa_2O_3 contact region was determined in [14] from the measurements of C-V characteristics.

IV. CONCLUSION

By decreasing the GaSe and InSe single crystal lamella thickness one can control the transmission band of them.

The absorption fundamental band edge of InSe and GaSe single crystal lamella is determined by the indirect optical transitions with the absorption coefficient α <100 cm^{-1}.

By varrying the GaSe and InSe lamella thickness in the submicron range one can fabricate the radiation detectors with a sensitivity in the UV-region of the spectrum.

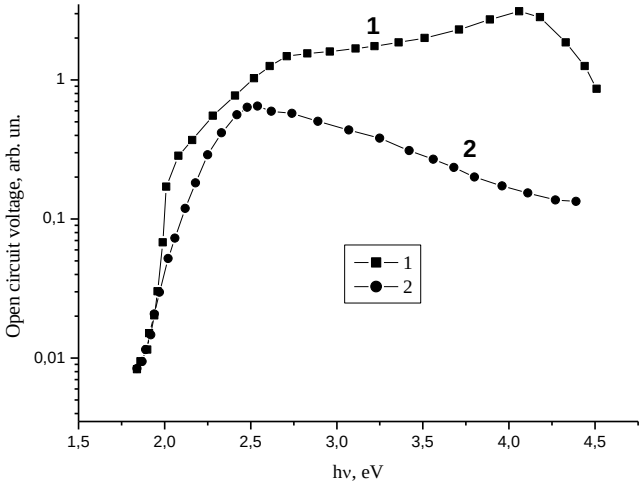

Fig.4. Open circuit voltage spectral distribution of pGa_2O_3 iGa_2O_3 – nGaSe heterojonctions with a layer of native oxide obtained at 480 ºC (curve 1) during 90 min and at 700 ºC (curve 2) during 90 min in a normal atmosphere. The GaSe lamella thickness is of 11,5 μm

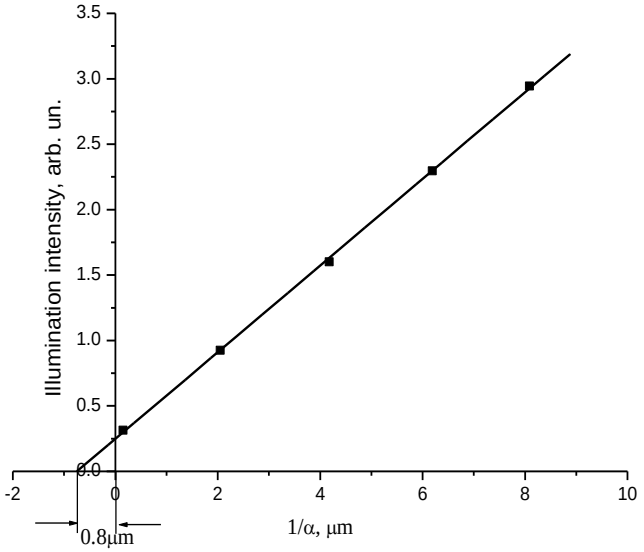

Fig.5. Determination of diffusion free path in nGa_2O_3 iGa_2O_3 – pGaSe with a native oxide layer made at 700ºC during 90 min in a normal atmosphere.

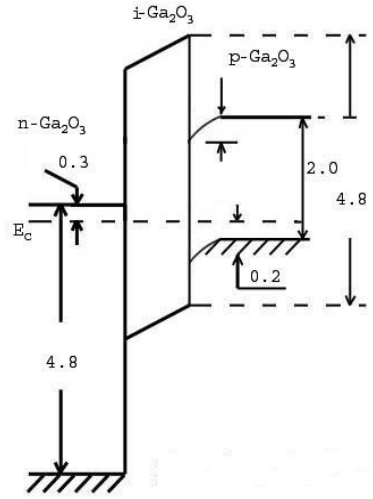

Fig.6. Band diagram of *nGa_2O_3-iGa_2O_3-pGaSe:Cd* heterojunction

The recombination centres and surface states density in the oxide-GaSe region depends on the surface oxidation temperature. The surface defects concentration does not change at the heat treatment at 480°C. At the GaSe surface oxidation temperature of 700°C in the oxide-GaSe contact region structural defects which diminishes the minority charge carrier free path up to 0,8 μm are created.

REFERENCES

[1] Naoya Okamoto, Tsuyoshi Takahashi, Hitoshi Tanaka, Nonalloyed ohmic contact to n-GaAs with GaS/GaAs quasi-metal-insulator-semiconductor structure, Appl. Phys. Lett., vol. 73, no. 6, 1998, p. 794-796.

[2] Naoya Okamoto, Hitoshi Tanaka, Characterization of molecular beam epitaxy grown GaS film for GaAs surface passivation, Materials Science in Semiconductor Processing, vol.2, no.1, 1999, p. 13-18.

[3] Dai Z.R., Chegwidden S.R., Rumaner L.E., Ohuchi F.S., Microstructure evolution of GaSe thin films grown on GaAs(100) by molecular beam epitaxy, J. Appl. Phys. vol. 85 , no. 5, 1999, p. 2603-2608.

[4] Jonathan A.A., Aaron A.B., Fumio S.O, Marjorie A.O., Chemical passivity of III-VI bilayer terminated Si(111), Applied Physics Letters., vol. 87, no. 17, 2005, 171906, 6 pages.

[5] Бакуменко В.Л., Ковалюк З.Д., Тишин Е.А., Чишко В.Ф., Влияние “старения” поверхности моноселенидов галлия и индия на работу выхода и фотоэлектрические свойства // Физ. электроника. 1979. № 19. С. 123–126.

[6] R.H. Williams, A.J. McAvej, S. Vac. Science Technology, 2 (1972), 867.

[7] Драпак С.И., Гаврилюк С.В. , Ковалюк З.Д., Литвин О.С., Собственный окисел, возникающий на поверхности скола селенида галлия в результате длительного хранения , ФТП , том. 42, вып. 4 , 2005, с. 423-430.

[8] O.A.Balitskii, J.M.Stakhira, Thermal oxidation of cleft surface of InSe single crystal , Materials Science and Engineering: B, vol. 56, no.1, 1998, p. 5-10.

[9] N.N. Berchenko, O.A. Balitskii, R.V. Lutsiv, V.P. Savchyn and V.I. Vasyltsiv, Mater. Chem. Phys. 51 (1997), p. 125.

[10] I. Marfaing, Photoconductivity photoelectric effects. In.Handbook on Semiconductors. Ser.ed.T.S.Moss volume ed.701 M. Balkouschi: 1994-Elsevier p.758.

[11] Terhell S.C., Lieth R.M., Phys Stat Sol A 10 (2), (1982) 529.

[12] С.А.Семилетов. Кристаллография, 3 (1958) 288.

[13] N. Suzuki,S. Ohira, M. Tanaka,T. Sugawara,K. Nakajima, T. Shishido, Phys Stat Sol , Vol.4 (7), (2007) 2310-2313.

[14] Sergiu Vatavu, Petru Gaşin, The analysis of current flow mechanism in CdS/CdTe heterojunction, Thin Solid Films, vol. 515, no. 15, 2007, pag. 6179-6183.

[15] A.M. Goodman, J.Appl.Phys.32 (1961)2550.

Approximation of MOSFET Transistor Characteristics in Micro- and Nanoelectronics

[1]Alexandr PENIN, [2]Anatoli SIDORENKO
Institute of Electronic Engineering and Nanotechnologies "D. Ghitu ",
Academy of Sciences of Moldova
[1]aapenin@mail.ru, [2]anatoli.sidorenko@kit.edu

***Abstract* – The base approach, giving a wide class of functions convenient for engineering practice for the formal description of *I-V* characteristics of the *MOSFET* transistors, is developed. The similarity of *I-V* characteristics of semiconductor devices and the quasi-resonant converter of voltage is an approach basis. The offered functions have certain physical sense that allows modifying purposefully them for the flexibility of their form.**

***Index Terms* – approximation, *I-V* characteristic, model, transistor.**

I. INTRODUCTION

Circuit simulation is an important component by working out and research of semiconductor devices and equipments on their basis. Let us result a number of the problems considered in the book [1].

In connection with transition of semiconductor technology in nanometer area (is more exact, at topological norms less 0,18 μm), a set of new parasitic electric effects has appeared, which were observed earlier only in analog integrated circuits (IC). For this reason, the urgency of exact (SPICE-like) circuit simulation has sharply increased.

Physical processes in the *MOSFET* transistors are described by difficult system of the equations. It is used only for device-technological modeling of semiconductor devices. Therefore, compact models are created by use of the assumptions, which simplify system of the equations to receive the analytical solution, simple enough for use in programs of circuit simulation

Physical compact models are synthesized by analysis of various areas of semiconductor structure for the purpose of a substantiation of simplifying assumptions which would allow receiving the analytical solution of the equations of a continuity, transport and Poisson. Such approach allows to establish physically well-founded assumptions and to establish connection of parameters of model with the geometrical and technological transistor's parameters.

Requirements of simplicity and computing efficiency compel modelers to move on the brink of its reliability. Therefore, the model of transistors is developed for technology of 0,25 μm, is already unsuitable for a 0,18 μm. The model, intended for circuit simulation, should be simple and have simple procedure of the parameter extraction.

The opposite method of synthesis consists that physical processes in the device are not analyzed at all. Instead, the equations of the two-port network are chosen by an expert way, which behave concerning external terminals precisely how the real MOSFET transistors. Such models are called as formal.

Synthesis of the formal models for modeling IC is not considered now perspective, as it does not allow establishing the connection of parameters of model with technical process parameters. But it is possible to notice that formal models are convenient for the analysis of an operating regime of the transistor and the concrete equipment (the amplifier, generator, and modulator) and which can be specified under the problem and transistor passport data.

The limited number of functions is available in an arsenal of modern mathematics, which can be used for construction of compact models. Among them there are no smooth functions which could give the simple and exact description of the transistor in all regimes of its work. Therefore, for smoothness maintenance it is necessary to use
Smoothing functions have no physical sense and can be used only for formal adjustment of model to object.
Here are some examples.

For modeling of area of moderate inversion, the interpolation by smooth function between modes of strong and weak inversion is used. Using smoothing function

$$F(v) = \left[Ln(1+e^{v/2})\right]^2,$$

it is possible to receive uniform expression of the characteristic. But the received equations can not be inverted analytically for obtaining the explicit dependence of currents from voltage as it is required in circuit simulation programs.

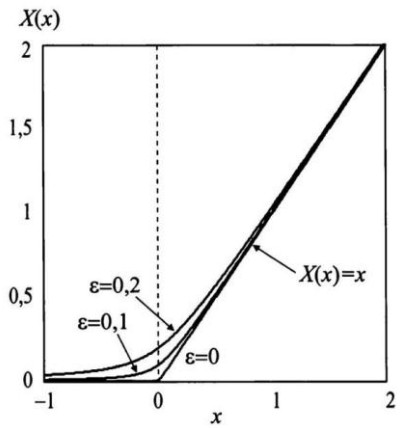

Fig.1. Example of smoothing function with various values of parameter ε of smoothing

For adequate modeling of analog and radio-frequency circuits, the smoothing functions should provide smoothness not only characteristics, but also their derivatives. Smoothing functions of a kind

$$X(x) = 0{,}5\left(x + \sqrt{x^2 + 4\varepsilon^2}\right),$$

are most extended. Where ε is the parameter, defining smoothness of transition from asymptote X(x) = 0 to an asymptote X{x) = χ, as is shown in Fig. 1

For smoothing of linear area with saturation area, the smoothing function is used, as is shown in Fig. 2

$$y(x) = \frac{x x_0}{\sqrt[2m]{x^{2m} + x_0^{2m}}},$$

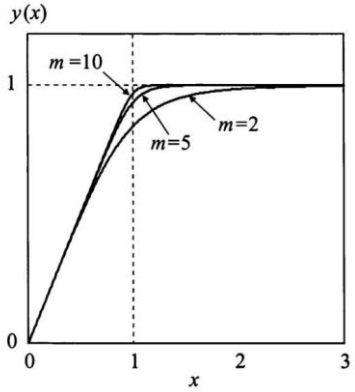

Fig.2. Example of smoothing function with various values of parameter *m* of smoothing

Presence of smoothing functions is one of essential limitations of modern compact models

For radio-frequency circuits, SPICE - like methods of modeling have appeared unsuitable.

First, at performance of the small-signal analysis SPICE program carries out a linearization of nonlinear elements, and, thus, nonlinear distortions or transformation of spectra of signals at once drop out of area of applicability of such analysis

Second, if for this purpose to use the analysis of transients in a mode of the big signal, the problem becomes almost unrealizable as the integration step should be much less period of carrier frequency, and at the same time the possibility of modeling of the several periods of modelled fluctuations is necessary. Thus, total number of steps of modeling becomes unacceptably large-scale.

Therefore, convenient analytical approximations of the transitive characteristic by one function represent an interest. Models on the basis of the hyperbolic tangent function, focused on the analysis of the intermodulation distortions in radio-frequency circuits, are known. Its feature is absence of necessity for smoothing functions. A shortcoming is that the model is based on empirical dependences and adjusted parameters.

Alternative approaches to modeling, as tabular models, are known also. Their basic appointment is the modeling of electric circuits with devices for which analytical models are not developed yet. For reduction of the size of tables, the templates are used in particular, because it is enough to store parameters of scaling of a template instead of storage of points of the curve. Difference of a template from a formal compact model consists that a template uses only the scaling and shift for adjustment to experimental data and does not contain other parameters. The template is chosen in advance with necessary properties (differentiability, monotony, absence of oscillations of the highest derivatives).

The next function can be a template example:

$$I_D(V_{DS}) = C + M(1 + \lambda V_{DS})\, th(\alpha V_{DS})$$

Four parameters of this equation (C, M, λ, α), are defined by means of a straight extraction technique for each value of voltage V_{GS}. Then each of parameters is interpolated by a voltage V_{GS} polynom, factors of which are stored in the table. For example, for a template

$$I_D = I_{pk}(1 + th(\phi))(1 + \lambda V_{DS})\, th(\alpha V_{DS})$$

the equation parameters ϕ, λ, α are tabular functions from voltage V_{GS}, V_{DS}. The I_{pk} is a drain current at which the maximum of transfer conductivity is observed. However, this way does not allow receiving approximation of high accuracy because of insufficient flexibility of a template

In connection with stated, interest represents a finding of functions for construction of compact models as smoothing functions and templates. And, these functions should have certain physical sense that would allow modifying purposefully them for the flexibility of their form. In the present message some results [2] which develop the approach [3, 4] are presented.

II. РАЗРАБОТКА БАЗОВОГО ПОДХОДА

Similarity of the load characteristics of the quasi-resonant converter of voltage with the characteristics of transistors is used as a basis of the offered approach. The received well-founded expression of characteristics of the quasi-resonant converter, having physical sense, allows describing the symmetric and asymmetrical transitive characteristic of the transistor.

The equivalent generator of the quasi-resonant converter contains the nonlinear internal resistance R_{i1}, which dependence corresponds to a straight line 1 is shown in Fig. 3.

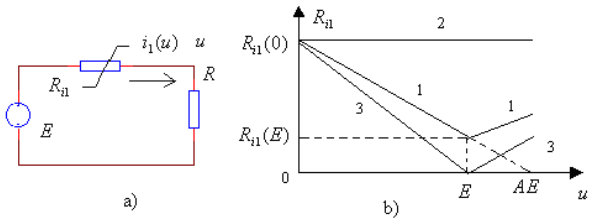

Fig.3. Equivalent generator - a) and dependences of internal resistance of typical energy sources (1- quasi-resonant converter, 2-voltage source, 3-current source-) - b)

Let us receive uniform expression of the characteristic for all area of change of the load voltage. For this purpose, linear dependences in the form of two straight lines 1 for areas are replaced by the hyperbole equation that is shown in Fig 4,a.

In case of hyperbolic dependence $R_{i1}(u_i)$, the equation of the I-V characteristic will become:

$$\frac{i_1(u_i)}{I_1 A} = \frac{u_i / AEr}{\sqrt{1 + (u_i / AEr)^2}}.$$

The plot of this curve has a typical appearance on Fig. 4,b.

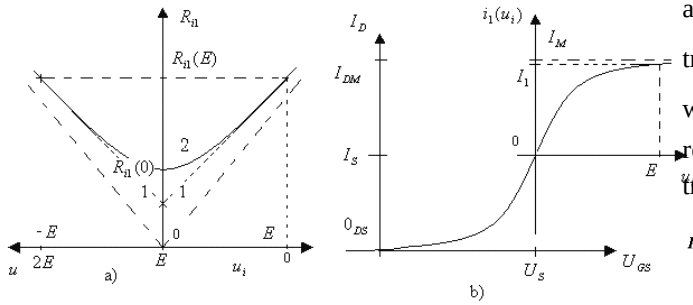

Fig. 4. Dependence of internal resistance as a hyperbole-a) and the symmetric characteristic in all area of change of voltage-b).

The form of the received curve is closed to the typical transfer characteristic $I_D(U_{GS})$ of the field transistor in system of coordinates $I_D 0_{DS} U_{GS}$. Let us consider the base approach to the description of transistor characteristics. At first, the asymmetrical characteristic in the first and the third quadrantis is considered. In this case, the hyperbole $R_{i1}(u_i)$ will be asymmetrical relative to voltage u_i in Fig.5,a.

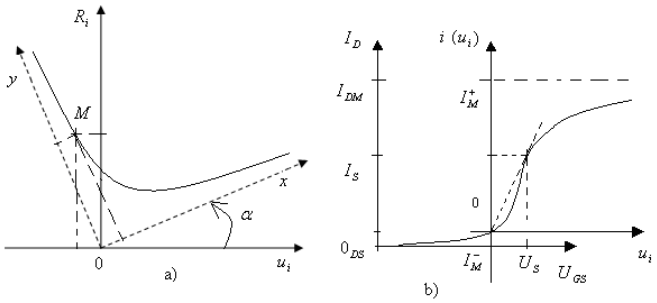

Fig.5. Asymmetrical arrangement of a hyperbole of internal resistance – a) and asymmetrical I-V characteristic in the first and the third quadrantis -b)

Asymptotes $0y, 0x$ form the rectangular system of coordinates turned on a corner α relative to the system of coordinates $R_i\ 0\ u_i$.

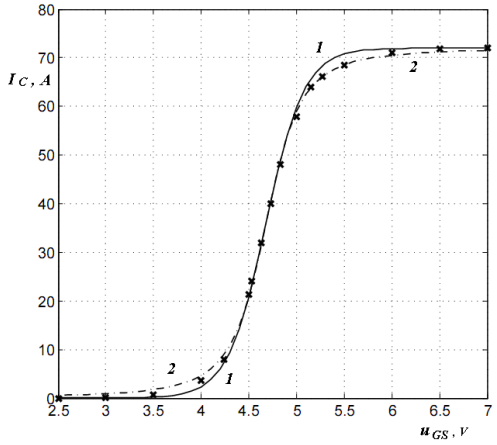

Fig.6. Symmetric approximations:actual values –crosses, hyperbolic tangent - 1,offered approximation – 2

Then the quadratic equation turns out:

$$i^2 + 2\frac{a_{12}u_i^2}{a_{22}u_i^2 + a_{33}}i + \frac{a_{11}u_i^2}{a_{22}u_i^2 + a_{33}} = 0.$$

Let this asymmetrical curve in Fig.5 would be used for approximation of the transfer characteristic $I_D(U_{GS})$ of the transistor. Then, in initial system of coordinates $I_D 0_{DS} U_{GS}$ whith the actual curve, the system of coordinates $i 0 u_i$ is restored.Example: the transitive characteristic of the transistor $STE26NA90$ is resulted on fig. 6, 7.

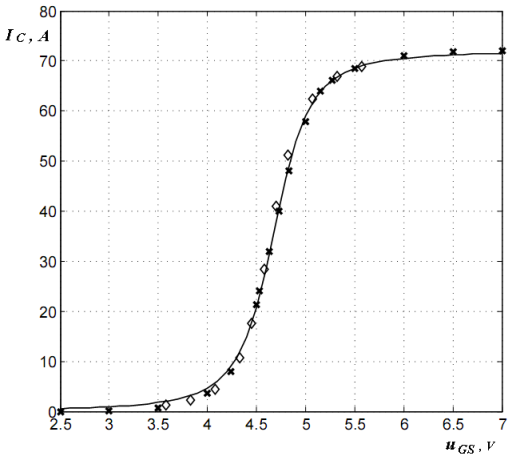

Fig.7. Actual values –crosses,offered symmetric approximation - continuous line,offered asymmetric approximation- rhombuses

III. CONCLUSION

The carried out analysis of variety of known approximating functions of characteristics of transistors shows that:

- their formal character and absence of physical sense of the entering parameters does not allow to modify them purposefully,
-difficult enough expressions complicate analysis, lead to the solution of the transcendental equations,

The base approach and the whole class of convenient expressions for approximation of characteristics of semi-conductor devices are offered. The presented examples show possibility of direct analytical calculations of operating regimes of transistors.

REFERENCES

[1] V.V. Denisenko, Compact SPICE models of *MOSFET* transistors in micro- and nanoelectronics. Moscow, Physmathlit, 2010.

[2] Penin A. Modeling of electronic characteristics of power transistors and photo-electric converters in linearly-hyperbolic approximation. Thesis of doctor of the technical sciences, Chisinau, Moldova, 2011,160 p. Available: http://www.cnaa.md/ru/thesis/18230/

[3] Penin A. A., Sidorenko A. S. «A convenient model for I-V characteristic of a solar cell generator as an active two-pole with self-limitation of current». International Journal of Electrical and Information Engineering, 2009,vol.3, nr.4, p.214-218. Available:

[4] http://www.waset.org/journals/ijeie/v3/v3-4-37.pdf.

[5] Penin A., Sidorenko A. «Generalized hyperbolic model for I-V characteristic of semiconductor devices». The 6th International Conference on Microelectronics and Computer Science. Chishinau, october1-3, 2009, vol.1, pp. 69-72.

Electronic Hydrostatic Transducer with Digital Output

V. SMYSLOV, V. YAKUNIN, I. BELOTSERKOVSKII, and A. YAKUNIN
Institute of Electronic Engineering and Nanotechnologies "D. Ghitu"
E-mail: Directia@iieti.asm.md, Smyslov@lises.asm.md

***Abstract* – The TPH-485-0,06 submersible level transducer of hydrostatic pressure is a general-purpose sensor for measuring the level of fresh water or other mildly corrosive liquids.**

The TPH-485-0,06 submersible level transducer can be used to measure the water level in reservoirs, lakes, open flow channels, and weirs as well as the groundwater level of boreholes.

Relatively low water levels can be measured using the TPH-485-0,06 submersible level transducer despite its diameter of 24 mm. This is possible by incorporating a highly sensitive miniature silicon diaphragm with a very thin isolation membrane back filled with silicone oil.

***Key words* – hydrostatic pressure transducer, groundwater level of boreholes, RS-485 interface**

I. INTRODUCTION

The urgency of measuring changes in the level and temperature of liquids in wells and tanks has led to the necessity to develop a high-precision hydrostatic transducer.

Hydrostatic level transducers are devices that can monitor and control the level of liquid (water, oil, fuel, etc.).

A long-term monitoring of water level and temperature in reservoirs, water storage basins, lakes, rivers, and geotechnical boreholes is of greatest interest for Moldova.

II. MAIN BODY

At present, pressure transducers that use integrated sensing elements based on single-crystal silicon are the most in demand. This is caused by the fact that silicon converters have an order of magnitude higher temporal and temperature stability, low hysteresis, high sensitivity and repeatability as well as high dynamic characteristics, which make it possible to respond to rapidly changing pressure at a high rate.

Therefore, to design a highly sensitive hydrostatic transducer, we selected a Honeywell excess pressure module as a sensing element. The module has a passive compensation for zero drift and output signal in the range of operating temperatures of 1 to 80°C.

A transducer design was developed, and a prototype was prepared. The transducer is a leakproof construction that consists of a sensitive pressure module, a measuring unit, and a metal case. The measuring unit includes an analog-digital converter (ADC), a microcontroller, and an RS-485 interface driver. Via a four-wire flat cable, the pressure module is connected to a circuit of amplification and processing of electric signals. An access hole is made in the base of the module for the interaction of the back side of the transducer's membrane and the atmosphere. Via a leakproof inlet, a special cable is connected to the outlet of the electronic unit. The cable contains wires for connection via the RS-485 interface, wires for supplying power, a screen, cores for suspending, and an air-operated channel for equalizing the pressure of the nonoperating side of the sensitive element with atmospheric pressure. A cable with a length of 20 m was used.

Fig. 1. Physical configuration of the TPH-485-0,06 transducer.

The hydrostatic pressure exerted on the isolation membrane of the pressure module and the temperature of the case are converted to analog electrical signals. Further, the signals are transmitted to a precision multichannel analog-digital converter with a built-in instrumentation amplifier that provides a high degree of resolution. After the amplification and conversion to digital code, the signals from the ADC come to the microcontroller. The programming of the microcontroller and the program correction are performed through a separate access connector.

Below, we represent the electronic circuit diagram of the transducer.

Here DD is the pressure transducer; Dt is the temperature transducer; ACD is the precision multi-channel analog-digital converter; Mp is the microcontroller; RS485 is the RS-485 interface converter; Uref is the reference-voltage source; St is the voltage stabilizer; Con1 is the connector for power supply and digital data transmission; Con2 is the access connector for programming the microcontroller; and P atmosfer is the air-operated channel for the interaction with the atmosphere.

The microcontroller provides an additional compensation for temperature zero drift and measurement range using information from the temperature transducer, which is in contact with the case of the transducer.

In addition, using the developed program, the microcontroller performs the linearization of the calibration

characteristics of the pressure module, the normalization of measured signals, and the output of data in different units of measurement: in kPa and mm of water column for pressure and in degrees centigrade for temperature. Corrected data are further transmitted via a noise immune RS-485 interface in the format of the Modbus RTU industrial communication protocol for devices of the collecting and recording of measured environmental parameters.

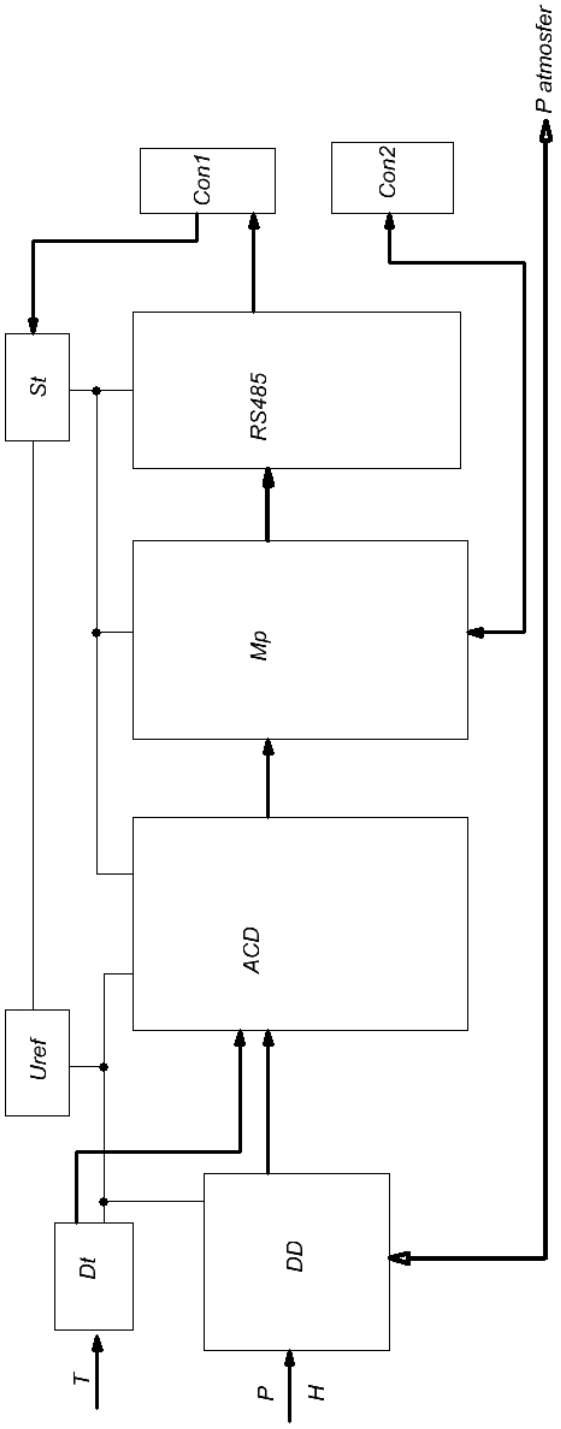

Fig. 2. Electronic circuit diagram of the transducer.

This protocol is open and has already become a de facto standard for the industry of digital devices. According to

Fig. 3. TPH-485-0,06 transducers with a cable and a coil.

TABLE 1. COMPARATIVE SPECIFICATIONS FOR THE PROTOTYPE OF THE TPH HYDROSTATIC TRANSDUCER AND THE DL/N LEVEL CONVERTER

Parameters	Units of meas.	TPH	DL/N
Measured excess pressure kPa	kPa	0 ÷ 100	0 ÷ 10 0 ÷ 2500
Water level	mm H_20	22÷10000	0 ÷ 1000 0 ÷ 250000
Operating temperatures	°C	5 ÷ 50	-5 ÷ 50
Measured temperatures		1 ÷ 85	-5 ÷ 50
Interface	Digit.	RS-485	RS-485
DC supply voltage	V	4 ÷ 6	Li-bat. 3,6 ≤100m – 1 b. >100m – 2 b.
Power consumption	mW	≤ 120	-
Current consumption	mA	≤ 20	-
Basic percentage pressure error	% /FS	≤ 0.02	0.1
Basic temperature error	°C	≤ 0.2	+/- 0.25
Communication protocol	-	Modbus RTU	-
Zero drift in the range of operating temperatures	Pa	≤ 20	-
Absolute pressure error	Pa	≤ 10	-
Absolute level error (10 to 40°C)	mm H_20	≤ 1	-
Resolution	Pa	≤ 2	-
	mmH_20	≤ 0.2	-
Dimensions	mm	Ø 32x185	Ø24×205
Weight	kg	≤ 0.45	0.56
Cable	m	Order	≤ 300
Protection class	-	IP68	IP68

experts, more than 40% of the applications of industrial data exchange use the Modbus protocol for the communication between objects. In addition to this, it should

be noted that almost all modern SCADA-systems support this communication protocol.

Engineering tests of the prototype of the TPH-485-0,06 transducer with a cable and a coil were performed; the results are shown in Table 1. The table also lists the specifications of one of the best analogues, i.e., a DL/N high-precision hydrostatic transducer (STS, Switzerland). Comparing and analyzing the engineering data of the TPH and DL/N transducers, we can state for certain that the basic percentage pressure error for the developed transducer is almost 5 times less than that of the DL/N transducer. This will make it possible to determine the change in the water level in boreholes with an accuracy better than 1-2 mm H_2O.

The exchange of data on water level and transducer temperature with the information system is carried out via an RS485 interface (Modbus RTU protocol). Using a system of data collection and transmission via the GSM network, it is possible to monitor the condition of wells and reservoirs in real time scale, which will give the possibility to rapidly respond to changes in the level and temperature of groundwater.

III. CONCLUSIONS

In conclusion, we can note that the developed TPH hydrostatic transducer is more precise in comparison with counterparts; this will make it possible to study changes in water level in wells and reservoirs and to use this transducer in water level observations in wells for finding hydro-geodynamic earthquake precursors in the republic.

REFERENCES

[1] Smîslov V., Iacunin V., Scutelnic E., Beloţercovschii I., Parhomenco V., Traductor de presiune excedentară şi temperatură cu ieşire digitală TPSM-10. Simpozion Internaţional 17.09.2005 AŞ Moldova.

[2] Smîslov V., Iacunin V. Gauge pressure transducer TP-12E2-10, 4th International conference on materials science and condensed matter physics, abstracts, 23-26, Septembrie 2008, p. 194, Chisinau, Moldova.

[3] Данные об уровне подземных вод на картах и графиках. Гидрогеология. Курс лекций Стэндфордского университета.

[4] Копылова Г. Н. Оценка сейсмопрогностической информативности данных уровнемерных наблюдений на скважине Е1, Камчатка (по данным наблюдений 1996-2007 гг.). Труды Камчатского филиала Геофизической службы РАН.

Wave Model as a Physical Basis of an Algebra of Bio- and Nano- structures

Bettin MIRONOV
Technical University of Moldova
bmironov@yahoo.com

***Abstract* – Bio- and nano- structures have a feature in common – both display a long-range order over the distances significantly larger that the dimension of atom. While this cannot be explained on the basis of the Bohr atom model or quantum mechanics, the formation of complex long-range order structures can be explained in terms of wave model - waves spread all over the universe and can form complex interference structures. The set of waves can be considered as a universal algebra's generating basis, and the long-range structures can be regarded as elements of this algebra, generated by the set of waves. However, the wave model presupposes the existence of a carrier wave medium. To resolve the apparent contradictions with modern physics, it is shown that the wave model is consistent with the theory of relativity and Maxwell's equations. The last part is devoted to discussion of the stability mechanism of spherical waves and pathways formation of complex ordered structures.**

***Index Terms* – bio-structures, carrier of waves, long-range order, nanostructures, wave model.**

I. INTRODUCTION

Bio- and nano- structures share a common property – the long-range order over the distances significantly greater than the dimension of atom. So, for example, a snowflake is gigantic as compared with an atom, but it has a strikingly regular form. Even more amazing are the biological structures where the nature manages to pack up the information about a very complex organism into a tiny cell.

The phenomenon of long-range order cannot be understood within the realm of Niels Bohr's model of atom. Neither quantum mechanics can offer a satisfactory interpretation of this phenomenon. On the other hand, the wave model produces amazing results in the explanation of the complex order structures formation. The reason for this is that the waves, spreading over all the Universe and lasting forever, can really form complex interference structures. Also, the "primary elements", making up the "generating basis" of these structures are waves, which are described in terms of simple functions, and the interaction between which can be described in terms of certain rules. This approach allows us to describe objects with complex structure, proceeding from the most simple postulates and rules of inference and such a method is a manifestation of reduction of complexity. Engineering disciplines have accumulated rich experience how to build complex systems based on simple elements.

Thus, the world of computers and computer programs is based on operations over only two logical entities, *unity* and *zero* (or *true* and *false*), and this apparatus is sufficient to manage information of unlimited complexity. Boolean algebras are sufficient for modeling the World, but they are not the only ones to offer a modeling framework. The information we receive by phone, radio or TV, no matter how complex, can be mathematically represented as a function of time. Any function of time can be represented as a sum or as an integral of a set of simple functions of time, where the most convenient for this purpose are the harmonic functions. The representation of a function of time as a sum of harmonic functions is termed *Fourier decomposition* or *Fourier analysis*. The signal processing theory is based on Fourier analysis and, as a matter of fact, Fourier analysis is the theoretical basis of Radio and TV domain. The benefits from the application of Fourier analysis are that it is sufficient to explore the behavior of one sinusoidal component in order to draw conclusions about the behavior of functions of arbitrary complexity. The inverse process is also possible: by selecting an appropriate sum of sinusoidal components, it is possible to synthesize practically any function of time.

Similarly, any function which depends on spatial coordinates can be decomposed in harmonic functions. Mathematically, a hologram represents such a decomposition of an image into harmonic functions. By means of a hologram, it is possible to obtain a visual image of an object indistinguishable from the object itself. The idea to combine the decomposition into harmonic functions of time with the decomposition into harmonic functions of spatial coordinates comes up naturally. Such a combination would result in moving images which, ideally, would be identical with their originals.

Thus, an image of reality can be synthesized out of sinusoidal functions which depend simultaneously on temporal and spatial coordinates. These functions of space and time represent the waves. It is appropriate to say that harmonic functions, i.e. waves, represent a set out of which it is possible to synthesize any function of space and time. On the other hand, from a formal point of view, the objects surrounding us are also functions of space and time, as they are characterized by positions and dimensions which change in time. In other words, harmonic waves can be described as a certain set on the basis of which it is possible to simulate the world.

In study of the fundamental fields, quantum mechanics, or the theory of relativity, we easily come to understanding that all physical phenomena are related, in a way or another, to the wave processes. That is, wave processes are not just a tool for the formal description of the World similar to that by the Boolean algebras; wave processes have a much more

fundamental and intimate link with the physical reality.

The central issue arising in the use of such models is the existence of a carrier for the wave set. In case of Boolean algebras, this issue is resolved easily - everyone knows that this carrier is the computer, and without a computer no program can run. However, if we imagine that an artificial intellect residing in a computer attempted to solve the question of the existence of the carrier of Boolean algebra, such an intellect could not establish the existence of the computer. This is certainly true if the computer carries out only the operations of Boolean algebra and other parameters, such as the times of operations, are not provided. The idea stated here can be formulated the following manner: an intelligent agent residing on the carrier of the Boolean algebra would not be able to determine whether the carrier exists.

Reformulating the said above into the terms of wave functions, we can say that it is impossible to detect the carrier medium of the waves by using tools which, by their nature, are waves in the same medium. The electromagnetic waves and the fundamental particles can be transmuted into one another and those particles have wave properties. This raises the suspicion that both types of entities are waves in the same carrier medium. Hence, it is impossible to detect the carrier medium of the waves of matter by using tools built out of particles with undular properties. This is exactly the reason why the experiments aiming at the detection of a carrier for electromagnetic waves failed. But also, these experiments failed to prove the lack of a carrier medium of the waves in which we are concerned (including the electromagnetic waves). Actually, what such experiments could have demonstrated is the impossibility to detect the medium from within the medium.

The source of problems created by a medium-carrier is due to taking over the methods of hydrodynamics and acoustics into the theoretical considerations and practical experiments for detection of a medium-carrier. The tools used in hydrodynamics and acoustics are heterogeneous with respect to the medium. But such a method is not adequate for a medium of wave particles and fields, because both such particles and fields are also waves in the same medium. This idea will not appear crazy if we recollect that the fundamental particles of which we are made are also of a wave nature. Thus, it becomes obvious that, in order to work with a medium serving as the carrier of waves and fields, it is necessary to abandon the idea about "solid" tools and treat objects and tools on equal basis.

In order to overcome the difficulties which appeared in physics due to inappropriate treatment of tools as residing outside the phenomena, I have used a wave model [1], which is both an approach and a vision, according which the Universe is regarded as populated only by waves, so that the tools for measuring the attributes of one wave are other waves. The *wave model* implies consecutive development of methods allowing to use the waves as tools for examination of waves. Below we will try to explain these methods in brief and some of the results obtained by these methods.

II. WITHIN THE WAVE MODEL THE EXISTENCE OF MEDIUM-CARRIER FOR WAVES OF MATER DOES NOT CONTRADICT TO SPECIAL THEORY OF RELATIVITY

One of the objections against the existence of a medium to serve as a carrier for waves said to be “aether” was that, due to such a medium, it would be possible to select a distinguished frame of reference, and this would contradict to the principle of relativity and the relativity theory based on this principle. I will show below, that the existence of a wave medium-carrier or continuum does not contradict to special theory of relativity.

For description of physical processes, it is common to use a *frame of reference*, which is a system of spatial and time coordinates, with respect to which the behavior of bodies is described. A preferential role is played by the *inertial* systems of reference and one of the reasons for this is that the equations of motion in such systems are the most simple.

A frame of reference must contain scales for measuring time and length. Such scales consist of repeating intervals of time and length. A *standing wave* has the property of periodicity in both space and time and is described by an equation of the form

$$a = A\cos(-kx)\cos(\omega t). \quad (1)$$

Here, A is the amplitude of a parameter describing a wave (pressure, density, etc.), k is the wave number, and ω is the circular (cyclic) frequency. By choosing such a wave, we choose a metric, namely:

- The direction of the x-axis coincides with the direction of the wave propagation;
- The spatial scale is defined by the wavelength

$$\lambda = 2\pi / k;$$

- The temporal scale is defined by the period of the wave

$$T = 2\pi / \omega.$$

In other words, standing waves play the same role as rulers and clocks. If in a medium there is a wave-object described by the equation

$$a_0 = A\cos(-k_0 x)\cos(\omega_0 t) \quad (2)$$

then the measurement of its length in the frame defined by equation (1) consists in defining a number equal to the ratio of the length of the wave-object to the wave scale:

$$n = \lambda_0 / \lambda\,, \quad (3)$$

Similarly, a measurement of the period of the wave object consists in the definition of the ratio of the period of the wave object to the wave scale:

$$n = T_0 / T\,. \quad (4)$$

The wave object (2) can be decomposed into two waves running in opposite directions:

$$a_{01} = \frac{A}{2}\cos(\omega_0 t - k_0 x)\,, \quad (5)$$

$$a_{02} = \frac{A}{2}\cos(\omega_0 t + k_0 x). \quad (6)$$

If in the expressions (5) and (6), the frequencies and the wave numbers differ, so that that the correlations

$a_{01} = \frac{A}{2}\cos(\omega_{01} t - k_{01} x)$, and $a_{02} = \frac{A}{2}\cos(\omega_0 t + k_0 x)$,

where $\omega_{01} \neq \omega_0$ and $k_{01} \neq k_0$, the wave-object can be described by the equation:

$$a_0 = a_{01} + a_{02} = A_0 \cos\left(\frac{\omega_{01} - \omega_0}{2} t - \frac{k_0 + k_{01}}{2} x\right) \times \cos\left(\frac{\omega_{01} + \omega_0}{2} t - \frac{k_0 - k_{01}}{2} x\right). \quad (7)$$

This equation describes a standing wave in which the

maxima move with time. We shall term such a wave 'quasi-standing'. Thus, the parameters

$$\omega' = \frac{\omega_{01} + \omega_0}{2} \quad \text{and} \quad k' = \frac{k_{01} + k_0}{2}$$

can be perceived as the frequency and wave number of the moving wave-object (7).

The term $\alpha = \frac{\omega_{01} - \omega_0}{2} t$ in the first factor defines phase displacement of wave-object along the spatial coordinate *x*, and $\theta = \frac{k_0 - k_{01}}{2} x$ in the second factor, defines a retardation or phase displacement along the temporal coordinate. Then the displacement of the wave-object along the coordinate *x* for the interval Δt will then be

$$\Delta x = \frac{\omega_{01} - \omega_0}{k_0 + k_{01}} \Delta t.$$

Hence, the velocity of displacement of the wave-object is equal to

$$v_0 = \frac{\Delta x}{\Delta t} = \frac{\omega_{01} - \omega_0}{k_0 + k_{01}}. \tag{8}$$

Since

$$\omega = \frac{2\pi}{T}, \quad k = \frac{2\pi}{\lambda} \quad \text{and} \quad \frac{\lambda}{T} = \frac{\omega}{k} = c,$$

the equation (8) can be rewritten equivalently as:

$$v_0 = \frac{\lambda_0 \lambda_{01}}{T_0 T_{01}} \frac{T_0 - T_{01}}{\lambda_{01} + \lambda_0} = c^2 \frac{T_0 - T_{01}}{\lambda_{01} + \lambda_0} = c^2 \frac{k_0 - k_{01}}{\omega_0 + \omega_{01}}. \tag{9}$$

Recall that v_0 is the velocity of points with same phase move such as, for example, the maxima of a quasi-standing wave. The velocity v_0 defined by the equations (8) and (9) is related neither with the motion of the continuum, nor with respect to the continuum. But, in the absence of tools other than undular nature, only this velocity can characterize the motion of the wave-object (7).

If an observer moves with a velocity defined by equations (8) and (9), then from his/her point of view, the wave (7) will be a standing wave, and it will be described by an equation of the form (2) or by an equation of the form (1) if *n* = 1. Hence, in the system of a moving observer, this wave can be used as the wave which defines the frame. Thus, within the scope of our model, there can be a set of frames of reference that move relative to each other with different velocities, but all of them equal in rights.

Definition: a wave frame of reference is a frame of reference in which the period of a standing or quasi-standing wave at a fixed point serves as the scale of time, and the scale of length is the distance between two points with same phase.

As noted above, in an unlimited homogeneous medium no wave system offers any advantage above others. In other words, the principle of relativity is valid for the wave frames. However, there is one circumstance which can cast doubt on this statement. The velocity *c* of propagation of traveling waves described by the equations (5) and (6) is determined by the properties of the medium. Naturally, this suggests the idea to use a standing wave as a tool for determining the velocity *c* of a traveling wave. Then, knowing the velocity *c*, it is possible to determine the velocity of a wave frame relative to the medium. In fact, such an experiment would be similar to the experiment performed by Michelson and Morley in 1887 [2-4], in which an attempt was made to detect the velocity of the motion relative to the aether. If such an experiment would give a positive result, then this would allow to find the "true wave frame", in which the velocity of motion relative to the carrier medium is equal to zero. Such a system would be privileged in relation to other wave frames. In this case, the principle of relativity would not be fulfilled for the wave systems. Let us prove that this is not true.

*Theorem***:** the velocity *c* of a traveling wave has the same value in all wave frames.

We suppose that we have two wave frames, described by the following equations:

$$a = A\cos(-kx)\cos(\omega t). \tag{10}$$

and

$$a' = A\cos\left(\frac{\omega_1 - \omega}{2} t - \frac{k + k_1}{2} x\right)\cos\left(\frac{\omega_1 + \omega}{2} t - \frac{k - k_1}{2} x\right) \tag{11}$$

The velocity of relative motion of these systems is given by the equation:

$$v = \frac{\omega_1 - \omega}{k + k_1} = c^2 \frac{T - T_1}{\lambda_1 + \lambda}. \tag{12}$$

Let us suppose that some wave-object is at rest in the system defined by equation (11) and described in that system by:

$$a_0' = A_0 \cos(-k_0' x')\cos(\omega_0' t'). \tag{13}$$

The same wave-object will be described in a system defined by equation (10) as

$$a_0 = A_0 \cos\left(\frac{\omega_{01} - \omega_0}{2} t - \frac{k_0 + k_{01}}{2} x\right) \times \cos\left(\frac{\omega_{01} + \omega_0}{2} t - \frac{k_0 - k_{01}}{2} x\right). \tag{14}$$

Let us rewrite equation (14) taking the equation (12) into account:

$$a_0 = A_0 \cos\left(\frac{k_0 + k_{01}}{2}(vt - x)\right)\cos\left(\frac{\omega_0 + \omega_{01}}{2}\left(t - \frac{v}{c^2} x\right)\right). \tag{15}$$

The equations (15) and (13) describe the same wave-object. In equation (15), the value of $(vt - x)$ represents the instantaneous coordinate of the wave-object, as well as *x*' does in the equation (13). The transformation of lengths of line segments parallel to this coordinate should take place according to the same law as the transformation of this coordinate. Hence, the length of the moving wave-object (15) becomes $\lambda_0' = \lambda_0 - vT_0$, and its wave number becomes:

$$k_0' = \frac{2\pi}{\lambda_0 - vT_0}. \tag{16}$$

By applying similar reasoning for the frequency, we obtain:

$$\omega_0' = \frac{2\pi}{T_0 - \frac{v}{c^2}\lambda_0}. \tag{17}$$

The ratio of the circular frequency ω to the wave number *k* is equal to the velocity of the traveling wave *c*. Thus, the proof of the theorem formulated above is reduced to the demonstration of the relation

$$c = \frac{\omega_0}{k_0} = \frac{\omega_0'}{k_0'} = c'.$$

By using equations (16) and (17), we have:

$$c' = \frac{\omega_0'}{k_0'} = c^2 \frac{\lambda_0 - vT_0}{c^2 T_0 - v\lambda_0}.$$

With the help of equations (3), (4) and (12), we finally obtain: $c' = c$.

We have now proved that in a wave frame, the velocity c of a traveling wave does not depend on the choice of frame. Hence, the velocity of a traveling wave cannot be used for the definition of a velocity relative to the carrier medium, and all wave reference frames are equal in rights.

Thus, the use of wave frames leads us naturally to statements which serve as postulates for a special theory of relativity [5], namely:

- the relativity principle is valid: all inertial frames, i.e. systems which do not change their velocity, are equal in rights;
- the velocity of propagation of traveling waves in all inertial frames is the same.

From these postulates follow the Lorentz transformation laws which relate the length of a moving segment $\Delta x'$ and an interval of time $\Delta t'$ in its own frame of reference to the length Δx and an interval of time Δt in the laboratory system with respect to which it moves:

$$\Delta x' = \gamma \Delta x \qquad (18)$$

and

$$\Delta t' = \gamma \Delta t, \qquad (19)$$

Here $\gamma = \frac{1}{\sqrt{1-\beta^2}}$ and $\beta = \frac{v}{c}$.

The deductions of these expressions within the scope of wave model are given in the articles [6, 7] as well as, in a more elaborated manner, in the book [1]. From the given proofs, it follows that the Lorentz transformation laws are not related to the presence or absence of a carrier medium. Hence, presence of a medium-carrier of waves does not contradict to the special theory of relativity. Thus, it is possible to draw the conclusion that if also light and all the fundamental particles are waves in the same medium, then the existence of such carrier medium does not contradict to the theory of relativity. One more important consequence of the given reasoning is the conclusion that in different frames of reference the wave objects will look differently.

III. THE ELECTRICAL AND MAGNETIC FIELDS IN WAVE MODEL

The second serious argument against the existence of a medium-carrier for waves of matter emerged due to the failure of the attempts to get compliance between the properties of the electromagnetic fields and the properties of any medium. Maxwell used in his deductions a certain artificial model of the medium [8] which was too complex and improbable to be taken in serious. Here are the problems which arise in selecting a medium-carrier for the electromagnetic waves:

- The phenomena of polarization and other facts determine that light is transversal waves, but it is impossible to figure out a simple model of a medium with only transversal waves and no longitudinal waves; no longitudinal electromagnetic waves have ever been found;
- The velocity of electromagnetic waves (the light) is greatest possible; but from the theory of waves it is known, that it is the longitudinal waves which have the greatest velocity;
- If there existed a medium-carrier for electromagnetic waves (the aether) it would be possible to relate with it a distinguished frame of reference, and this contradicts to the principle of a relativity and relativity theory based on this principle;
- The experimental attempts to find a material carrier of electromagnetic waves failed.

On the basis of the arguments above, the point of view of [9] was accepted which sounds: 'The electromagnetic fields are not states of a medium, and are not bound down to any bearer, but they are independent realities which are not reducible to anything else, exactly like the atoms of ponderable matter'. This point of view was canonical until recently and it can be encountered practically in all textbooks on physics. However, such a vision does not reply to some questions, namely:

- There should exist a common approach to all types of waves irregardless of their nature, and it is certainly known that elastic waves are states of a medium and not 'independent realities which are not reducible to anything else';
- If the light gets from empty space into a certain transparent medium such as glass, it continues motion with smaller velocity, and it returns to previous velocity when it exists such medium. Hence, there should be a mechanism due to which the velocity of electromagnetic waves in vacuum has a constant value and it does not depend on the parameters of the electromagnetic waves, on their source, or on their history;
- To explain inertia and the effects of general relativity theory, it is necessary to assume that the vacuum is filled with some media (currently, this is supposed to be fields) [10];
- According to general relativity theory, the values of length and time depend on the magnitude of the gravitational field. The change of the scales of length and time in a gravitational field is referred to by the term 'curvature of the space–time continuum'. From this it again follows that the vacuum cannot be empty. The supposition arise that the electromagnetic fields and gravitational fields have something in common, i.e. that the 'gravitational aether' is somehow linked to the 'electromagnetic aether';
- The general relativity theory admits the possibility to create a relativistic propulsion device [11], which implies that vacuum is capable of exerting force and having inertia;
- Within the scope of accepted model of empty vacuum it is possible to understand the mechanism of repulsion, but the mechanisms of attraction are unimaginable.

Thus, the banishment from physics of a carrier for electromagnetic waves, did not solve the contradiction, but raised a series of new questions instead. In the book [7], I explained how it is possible to find answers to these questions and how to solve the problem about the wave medium-carrier in compliance with the Maxwell equations. I succeeded to prove within the scope of wave model, that the electromagnetic field is a property of an elementary medium-carrier. I proceeded from the following premises:

- There exists a continuous medium, which I termed continuum, in which there can be fluctuations in the form of drops in pressure and velocity;
- The only tool for examination of these fluctuations is the wave-tool representing a domain with a pressure (density) different from the pressure (density) within unperturbed

continuum.

On the basis of these premises it has been found out, how some wave-tool representing a surplus or a deficit of a continuum, will interact with drops in pressure and velocity in the medium. It turned out that the redundant quantity of a continuum in a wave-tool can be associated with an electrical charge, the pressure gradient - with an electric intensity, and the magnetic intensity – with the drop in velocity. It is shown, that the magnetic field is an effect of the relativistic contraction of the continuum from the point of view of a moving wave-tool. The proofs of these statements are not trivial; they can be found also on my site [12]. The relation between electric intensity **E** and magnetic intensity **B** is determined by Maxwell equations. The deduction of Maxwell equations, proceeding from the offered model, is also is given in my monograph [7]. It is necessary to emphasize, that Maxwell equations define the correlation between a pressure gradient and a drop in velocity of the medium, and not between pressure and velocity of medium as in the equations of acoustics.

IV. WAVES AS A BASIS FOR AN ALGEBRA OF THE REALITY PHENOMENA

In the formula (1) we did not impose any requirements on the amplitude and, thus, the obtained deductions will be valid for any amplitude, including the case when the amplitude is some function of spatial coordinates and time. The wave equation in spherical coordinates for a central-symmetric wave looks like this:

$$\frac{\partial^2(rp)}{\partial r^2}-\frac{1}{c^2}\frac{\partial^2(rp)}{\partial t^2}=0$$

The solution of this equation is, in particular, the harmonic (traveling), waves with the amplitude of pressure in the center p_A which can be described by expression:

$$p = p_A e^{i(-\omega t \pm kr)}, \qquad (20)$$

where the upper sign "plus" corresponds to the wave moving along the *r*, and the lower sign "minus" corresponds to a wave moving in the opposite direction. This solution coincides with the formula of the associated waves, which describe in quantum mechanics a free moving particle

$$\psi(r,t) = Ce^{i(-\omega t \pm kr)}. \qquad (21)$$

The explanations regarding the physical sense of a wave function and the amplitude can be found in any textbook on quantum mechanics and we will not go deeper into this topic. We will refer only to the quantum-classical correspondence principle [13, 14], according to which the physical phenomena in quantum mechanics are described by equations similar to classical mechanics with the only difference that classical parameters are exchanged with those of quantum mechanics. We will apply this principle in "to the contrary" manner. We consider a fundamental particle-wave (say, an electron) to be described by the sum of two traveling waves in continuum. These waves are harmonic and central-symmetric:

$$p = p_A \frac{e^{i(-\omega t \pm kr)}}{r}, \qquad (22)$$

where the upper "plus" sign corresponds to a divergent wave, and lower "minus" sign – to a converging wave.

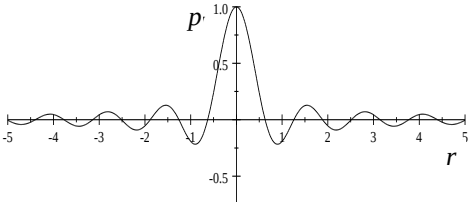

Fig.1. The diagram of function (23)

In case of the central symmetric wave the distinguished frame is the system bounded to the center of wave. The wave (22) can be rewritten in the trigonometric form:

$$p_S = \frac{p_A}{kr}\sin kr \sin \omega t, \qquad (23)$$

where p_A is the amplitude of pressure in the center of the spherical wave. The diagram of function (23) at $\sin\omega t=1$ is presented on fig. 1.

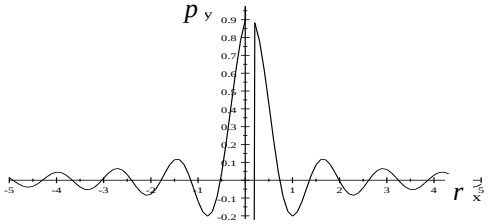

Fig.2. The diagram of function (23) at attempt to upset the balance between frequency and energy of a wave

This solution is unique among those, which do not have peculiarities at $r = 0$, while the oscillatory velocity is continuous and becomes zero in the center. The amplitude p_A / kr in the expression (8.15) defines the energy of a spherical wave, the factor $\sin kr$ defines a spatial distribution, and $\sin \omega t$ - the time dependence, while $\omega / k = c$. It means, that the expression (23) rigidly relates the energy of a spherical wave with its frequency. Any attempt to change one of these parameters leads to divergence (Fig. 2). This property of the function (23) is a key to the quantification riddle. According (23), the argument of sin and the denominator should be similar and such similarity should be absolute. The smallest difference conducts to divergence of the function p_S.

It is rather interesting, that this phenomenon is observed in technology as the *cavitation* phenomenon which destroys the screws of a ship. It is wrongly deemed, that cavitation is caused by bubbles formed due to a rupture of the medium, i.e. the consequence is taken as the cause [15, 16].

If two such stable spherical waves interact, the correlation between the argument of sin and p_A / kr are broken. The divergence is eliminated, if the interacting spherical waves reorganize so, that in their own frames of reference the correlation between the amplitude and the frequency is recovered. If with such reorganization a part of energy is radiated in the form of a traveling wave the resultant system becomes stable. For destroying such a system it is necessary the energy radiated at its formation to be returned. Thus, two spherical stable waves can form a stable system which, getting into a field of the third wave, or in a field formed by a collective state of several particles, can form a more complex stable state, and so on. We come to the conclusion that, the stable spherical waves form a set from which can be formed other stable states which also belong to set of stable waves. Out of these new states, other stable states which

belong to the same set can form and so on, ad infinitum.

The formulation above brings us to the idea that the waves can serve as elements of a carrier of a universal algebra. A universal algebra A = (*A*, *O*) is an ordered pair, where *A* is a set termed *carrier* of the algebra, and *O* is a set of operations of various *arity* (or, *rank*) over *A* with respect to which the operations is said to be "closed". Thus, the concept of *universal algebra* allows constructing a "closed world" of unlimited complexity. Within the context of this research, the term 'closed' means, that to build up a world of arbitrary complexity it is enough to proceed from elements of a chosen set, and this is the set of waves, which make up the set of generators of a universal algebra.

Similarity of the expressions (20) and (21) allows us to identify the fundamental particles with monochrome stable spherical waves in a continuum described by these expressions. It is known, that as a result of particles interaction, oscillatory systems are formed, which have spectrums of higher complexity. Even the atom of hydrogen consisting of three particles, i.e. proton, neutron and electron, already has a rather complex spectrum. The Plank constant serves as a coefficient in the relationship between energy and frequency. It is important to mention, that in the interaction of stable standing waves not only the amplitudes and frequency play a role, but also their phase, and this leads to indeterminacy of the relation.

It is necessary to remark, that in the formation of complex wave systems there exists a certain energy hierarchy: for creating or destroying complex wave systems, it is necessary less energy. The spectrums of simple oscillatory systems, atoms and molecules, are well studied. The offered algebraic approach is of interest at examination of the complex oscillatory systems in which the binding energy becomes comparable with the energy of fluctuations caused by thermal processes. The combination of stability of wave systems and fluctuations is a key to understanding of self-developing systems lying in the basis of life.

There is one more important circumstance related to wave systems, namely that the waves, basically outreach to the infinity. This means, that the wave systems can interact between themselves remotely, defining the structure of each other. This creates the probability of the reproduction (replication) of the wave systems in result of such actions. In my opinion, it is exactly this process which bears the key in the emergence of nanostructures and biological objects.

REFERENCES

[1] Bettin Mironov, Mechanisms of Electromagnetic and Gravitational Fields. Virtualbookworm US. (2007) 228 p. ISBN 978-1-60264-105-1.

[2] Albert Michelson, Edward Morley. *J. Sci*., 31, 377 (1886).

[3] Albert Michelson, Edward Morley. *J. Sci*., 34, 333 (1887).

[4] Loyd S. Swenson, The ethereal Aether: A History of the Michelson – Morley – Miller Aether – Drift Experiments 1880 – 1930. Austin (Tex.), (1972).

[5] Albert Einstein, Zur Elektrodinamik der bewegter Körper. *Ann. Phys.*, 891–921 (1905). (An English version available: http://www.fourmilab.ch/etexts/einstein/specrel/www/).

[6] Bettin Mironov. On the metric of waves interactions. *Meridian ingineresc*. 2, 54–59 (2001).

[7] Bettin Mironov, Kinematics of waves interactions in undular frames. *Moldavian Journal of the Physical Sciences*, 4, No. 3, 367–380, Chişinău (2005).

[8] James Clerk Maxwell, Treatise on Electricity and Magnetism. Dover Publications; 3rd edition (1954), ISBN 978-0486606361.

[9] Albert Einstein, *Äther und Relativitätstheorie.* Verlag von Julius Springer, Berlin (1920).

[10] Max Born, *Einstein's Theory of Relativity* (written with the collaboration of G. Leibfried and W. Biem). Dover Publications, New York (1962).

[11] http://www.sphere.ad.jp/force/relativity/pro/forpro-e.html.

[12] http://www.mironovbettin.narod.ru/English/index.html.

[13] Niels Bohr, Collected Works, Volume 3, The Correspondence Principle (1918–1923), **3**, Amsterdam: North-Holland, (1976).

[14] Alexander Stotland, Doron Cohen, "Diffractive energy spreading and its semiclassical limit", *Journal of Physics A* 39 (10703): 10703, doi:10.1088/0305-4470/39/34/008, ISSN 0305-4470 (2006).

[15] Robert T. Knapp, James W. Daily, Frederick G. Hammitt, Cavitation. New York: McGraw-Hill, (1970). 687 p.

[16] Christopher E. Brennen, Cavitation and Bubble Dynamic, Oxford University Press, Oxford, UK, (1995) 304 p. ISBN10: 0-19-509409-3.

[17] Ioachim Drugus, Universics - A Common Formalization Framework for Brain Informatics and Semantic Web, Web Intelligence and Intelligent Agents, INTECH, (2010).

Two-Photon Coherent Fields and its Application in Communication

Marina ŢURCAN
Institute of Applied Physics, Academy of Sciences of Moldova
tmaryna@yahoo.com

***Abstract* – It is examined the coherence properties between the Stokes and anti-Stokes fields and its application in Communication. It is proposed novel two-photon entangled sources which take into account the coherence and collective phenomena between these fields. The quantum propriety of realistic sources of powerful coherent bi-boson radiation (coherent entanglement of Stokes and anti- Stokes photons) is analyzed. The possibility of experimental applications of coherence between the Stokes and anti-Stokes photons in quantum communications and cryptography is proposed.**

***Index Terms* – Coherence, correlation function, generation, non-liner optics, quantum-computing.**

I. INTRODUCTION

Quantum Information Science is an emerging field with the potential for revolutionary advances in fields of science and engineering involving computation, communication, precision measurement, and fundamental quantum science.

The property of entanglement between the emitted photons in the processes of light generation has a great impact towards applications dealing with quantum computing, and information security (e.g. [1]). The modern investigations connected with the manipulation of quantum fluctuations of the generated light and there application in transmission and detection of information with high degree of security play an important role in the modern defense problems. The problem of quantum fluctuations and the generation of non-classical electromagnetic fields in multi-photon processes have been the subject of extensive theoretical and experimental studies in recent years, more specifically two-photon coherent generation of light has led to many experimental and theoretical studies recently An interesting behavior of Stokes (e.g. [2]) and anti- Stokes generated modes in the Raman processes (e.g. [3]) can be observed for the small number of the pumped photon in nonlinear media.

In this article it is proposed the new type of generation of coherence states of biboson field and its application in comunication, biophotonics. This field can be regarded as two coherent fields generate in the lasing process of Stokes and anti-Stokes modes in nonlinear medium. Such a quantum correlations can be obtained in the processes of Raman scattering (e.g. [4]). In this article it is obtained new coherent states between Stokes and anti-Stokes fields and it is proposed to use such a fields in quantum communication, holography and biotehnology. It is demonstrated that these collective scattering phenomena take place due to information transfer between the photons of two cavity modes. Studying the quantum fluctuations of the number of photon the new proprieties of the Stokes and Anti-Stokes fields have been found and proposed for communication with hair degree of security of information. The new peculiarities of second order correlation functions between these fields are considered as potential algorithms in cryptography and are expressed through the lasing parameters of the source (e.g. [5]).

This manuscript reports the review of the transmission of information through entangled photons, obtained in parametric down conversion (e.g. [6, 7]). In this articles it is proposed the new method of transmission of information taking in to account the two-field coherent states. The main difference between Ekert model (e.g. [8]) and new possibilities which include the second order coherent effects is given. It is considered that such coherence between the photon of two fields can be conserved in the process of propagation bimodal field through different fibers over long distances after the focusing. The information encapsulated into coherent bi-boson light can be destroyed in the dispersive medium and restored over a certain distance. In both methods of transmission bimodal coherent field, the nature of the quantum communication between two points *A* (Alice) and *B* (Bob) does not allow eavesdropper, *E* (Eve), to know the transferred information. Below we shall discuss the cryptographic aspects bvon the basis of two entanglement photons obtained in parametrical down conversion and our model based on the two-field coherence effect between the Stokes and anti-Stokes fields. These models are described in the section A and B.

II. PROTOCOLS WITH ENTANGLEMENT EFFECT BETWEEN PHOTONS

The transmission of information through entangled photons is based on he the Ekert's protocol (e.g. [8]). This protocol is encoded by its physical nature. The system based on the entanglement effect between the photons consists in the following: Alice receives one of the photons of the pair and Bob the second. Alice and Bob have de same detection basis and for every particle pair everyone choose independently an accidentally axis and measure the polarization along the axis. After that a series of photons pair are transmitted, they announce what axis of polarizer were chosen in the process of measurement and analyze in which cases they obtained the particles simultaneously (e.g. [8]). So, the channel is established. This system is encoded

automatically. A detailed description can be found in the works (e.g. [8]). The pulses formed from pairs of entangled photons can be applied in quantum communication and cryptography using the great investigations of quantum optics. It was demonstrated that in the process of transmission of correlated two photons which were obtained with parameter down-conversion effect through two optical fibers, the correlation between the photons pairs is conserved at a very big distance (30 km), and for more than 6 km in free-space (e.g. [9]). For the distance that is mach than 20 km in free space Chinese physicist realizes (e.g. [9]) it today. He thinks that simultaneously with an output to geostationary satellites the communication through quantum cryptography will be possible for distance around 10 thousands km. In other words, the humanity will have cryptographic channels that cannot be listened by eavesdropper (Eve), because the nature of the communication through pairs of photons does not allow this. Below we give the scheme that describes this process of transmission at the distance of 13 km (e.g. [9]). The generator of pairs of photons (probably the nonlinear crystal without a inversion centre (MgO:LiNbO3) is situated in Chinese place Dashu. The flux was expanded using a optic telescope. The signal was compressed with telescopes of the same type at the detectors Alice and Bob situated in USTC (University of Science and Technology of China) and the place Taouhua. The protocols Alice and Bob coincided, that means a high efficiency in the process of transmission of the information.

III. NEW ARHITECTURE USING THE COHERENCE BETWEEN STOKES AND ANTI-STOKES FIELDS

It propose a novel architecture for quantum communication. The amplitude of a simple block of coherent Stokes and anti-Stokes photons obtained after two-photon interaction in scattering lasing effects can be described by the square value of electrical vector $\Pi(t) = g_S g_A \hat{b}^+ \hat{a} Exp[\omega_0 t - (k_a - k_s)z + \varphi_0]$. $\Pi(t) = E_A^+ E_S$,. representing these amplitudes through $E_A^+ = \hat{b}^+ \exp[i(\omega_A t - k_z z)] g_A$ and $E_S^- = \hat{a} \exp[-i(\omega_S t - k_S z)] g_S$, where $\hat{b}^+$ and $\hat{a}^+$ are creation photon operators in the anti-Stokes and Stokes fields respectively, $\hat{b}$ and $\hat{a}$ are annihilation photon operators in these fields. In the quasi-classical limits the amplitude $\Pi_0(t) = g_S g_A \left\langle \hat{b}^+ \hat{a} \right\rangle$, has the same proprieties as amplitude of coherent laser field. In this approximation a nice idea is to use the classical of two wave modulation of this square amplitude for transmission of information. At first glance, it is observed that this method does not have a substantial differences in comparison with classical methods of information processing, but if we send this information in dispersive media, which separates anti-Stokes and Stokes photons from coherent entanglement fields, the information is drastically destroyed, because $\left\langle \hat{b}^+ \right\rangle$ and $\left\langle \hat{a} \right\rangle$ take zero values. The possibility of restoration of information on the square amplitudes $\Pi_0(t)$, is interesting problem of many particle coherent states, formed from blocks of Stokes and anti-Stokes photons. These studies are necessary because in a bi-boson lasing effect (e.g. [10]), the photon statistics depend on the statistics of the ignition field (e.g. [11]). Of course, the start up from vacuum fluctuations preserves the entanglement character of the generated Stokes and anti-Stokes coherence state. This effect is very interesting in quantum communication.

This manuscript propose an interesting effect that takes into account the classical method of registration of information. As Π(t) plays the role of electromagnetic field intensity strength for the two-fields Stokes and anti-Stokes, at the detector can be considered as a classical field described by $\Pi(t) = \Pi_0(t)\cos[\tilde{\omega}t - (k_a - k_s)z + \varphi_0]$, where Π_0 is the envelop of cooperative two-photon interaction in scattering processes. A large number of modes in the coherent states give as the possibilities of the increase the security of information storages in bimodal field (e.g. [9-11]). In this approximation, the classical information may be introduced in the amplitude $\Pi_0(t)$. Such registration of information may have nothing to do with the traditional method. If the bi-boson pulses pass through a dispersive medium, the anti-Stokes and Stokes photons from the field change their directions. Focusing the anti-Stokes and Stokes photons into different optical fibers we are totally dropping the coherence among the photons. However, after a certain time interval, anti-Stokes and Stokes photons from the field are mixed again, and we can observe that the coherence is restored (see Fig. 1).

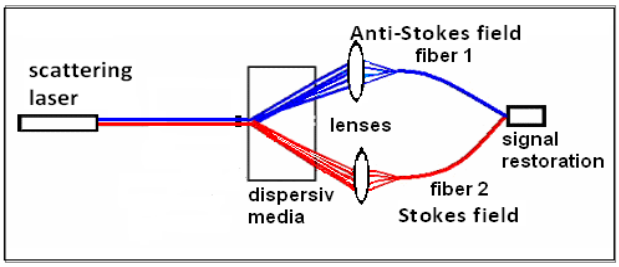

Fig. 1.

The coherent state obtained in two-photon coherent emission $|\Psi\rangle = \exp\left[\Pi^+ - \Pi^-\right]0\rangle$, takes into account not only entanglement between the pair photons but the coherence between the fields too, and can be used in mixed processing problems in which the quantum entanglement between the Stokes and anti-Stokes photons is used simultaneously with classical coherence (e.g. [6]) between the fields. Of course the probability of experimental realization of logic gates for quantum circuits in this case increase.

The coherent states between Stokes and anti-Stokes fields can be realized in cooperative scattering effects (e.g. [11]). In order to obtain the cooperative generation of the coherences states between Stokes and anti-Stokes fields we consider a stream of atoms (e.g. [10,14,15]) with two levels travelling through the cavity. The total Hamiltonian which describes the interaction of the atoms with Stokes and anti-Stokes fields of the cavity can be represented through the atomic and field operators

$$H_T = \sum_{j=1}^{N} \hbar\omega_0 R_{zj} + \hbar\omega_a a^+ a + \hbar\omega_b b^+ b + i\sum_{j=1}^{N} G(k_a, k_b)\left\{\left\langle R_j^-(t) J^+ - J^- R_j^+(t)\right\rangle\right\} \quad (1)$$

where the last term represent the interaction Hamiltonian. Here R_{zj} is the population inversion of atom j; $\hat{R}_j^+$ and $\hat{R}_j^-$

represent the operators which describe the transitions from $|g\rangle$- ground state to $|e\rangle$- excited state and from $|e\rangle$- excited state to $|g\rangle$- ground state, respectively (e.g. [10]). The operator $a^+(a)$ is the creation (annihilation) of Stokes photons and $b^+(b)$ is the creation (annihilation) of anti-Stokes field operators. The interaction constant $G(k_a,k_b)$ describes the effective nonlinear coupling of atom *j* with cavity modes k_a and k_b with the energies $\hbar\omega_a$ and $\hbar\omega_b$. In order to describe the scattering processes, let us introduce the collective operators for Stokes and anti-Stokes modes, $J^+ = ab^+$ and $J^- = ba^+$ (e.g. [12]). The operator $J^+ = ab^+$ describes the simultaneously process of creation of anti-Stokes and annihilation of Stokes photons. The inverse process is described by operator: $J^- = ba^+$. As the full number of photons in the cavity, in the small time moment the interaction is conserved, we shall introduce the operator of photons inversion between the Stokes and anti-Stokes photons: $J_z = (b^+b - a^+a)/2$ and energy difference $\hbar\tilde{\omega} = \hbar\omega_b - \hbar\omega_a$.

Taking into account, that the lifetime of atoms in the cavity are shorter than the time of scattering processes and considering that the atomic system is prepared in excited state, let us eliminate the atomic operators $\hat{R}_j^+$ and $\hat{R}_j^-$ from Heisenberg equation of arbitrary field operator. By representing the operators $\hat{R}_j^+$ and $\hat{R}_j^-$ through the field operators $\hat{J}^+$ and $\hat{J}^-$ in according with Hamiltonian (1). After consecutive elimination of free parts of these operators the master equation for Stokes and anti-Stokes field can be represented in the forth order on the interaction constant $G_j(k_a,k_b)$

$$\frac{d}{dt}J^+(t) = -2\tilde{\alpha}_1\langle J_z(t)J^+(t)\rangle + 4\tilde{\alpha}_2\langle J_z J^+ J^- J^+\rangle, \quad \frac{d}{dt}\langle J^-(t)\rangle = \left[\frac{d}{dt}\langle J^+(t)\rangle\right]^+ \qquad (2)$$

The behaviour over time of the mean value of operators $J^+(t)$ and $J^-(t)$ can be found in accordance with the generalized equation propose in paper (e.g. [12]). In semi classical approximation, when the fluctuations of these operators are neglected $J^\pm(t) \approx <\hat{J}^\pm(t)>$ and $J_z(t) \approx <\hat{J}_z(t)>$, the equations (2) for mean values of these operators $\hat{J}^+$ and $\hat{J}^-$ take the folowing simple expression

$$\frac{d}{dt}\langle J^+(t)\rangle = -2\tilde{\alpha}_1\langle J_z\rangle\langle J^+(t)\rangle + 4\tilde{\alpha}_2\langle J_z\rangle\langle J^+\rangle\langle J^-\rangle\langle J^+\rangle. \qquad (3)$$

Considering that, at initial stage of ignition of generation the inversion operator can be aproximate with $J_z \approx -j$, and following the idea proposed in paper (e.g. [11]), the equation (3) can be represented by the generalized potential function, $V(J^+,J^-)$, $d<J^+(t)>/dt = \partial V/\partial <J^->$. In accordance with this definition, we obtain the following potential function

$$V(z) = -2\tilde{\alpha}_1 j|z|^2 + 2\tilde{\alpha}_2 j|z|^4 \qquad (4)$$

with the minimum in point $|z|_{\min} = \tilde{\alpha}_1/(2\tilde{\alpha}_2)$, where $|z| = |J^+| = |J^-|$. The dependence of this potential V(z) as function of the amplitude $|z|$ decrease achieving $z_{\min}$ and after that increase. As follows from the expression (4), the amplitude value of two-photon coherent fields $|z|$ is proportional with the ratio between scattering rate and diffusion coefficient $\tilde{\alpha}_2$ and increases with increasing of scattering rate, $\tilde{\alpha}_1$, This steady state solution describes the stabilization process in the resonator.

We are interested in the behavior of quantum fluctuations of this bi-field intensity, $\hat{J}^+(t)\hat{J}^-(t)$, in the process of time evolution to steady state: $\Delta^2 = G_2(t) - G_1^2(t)$ where $G_1(t) = <\hat{J}^+(t)\hat{J}^-(t)>$ and $G_2(t) = <\hat{J}^+(t)\hat{J}^+(t)\hat{J}^-(t)\hat{J}^-(t)>$, are the intensity and square of intensity of bi-boson field consisted from Stokes and anti-Stokes fields. Following the method proposed in paper (e.g. [11]) let now found the behavior of correlation functions $G_1(t)$ and $G_2(t)$. Taking in to account the solution of quantum equations (2), in the Fig. 2 it is plotted the dependece of correlation function $G_1(t)$ on the relative time $t/(2\alpha_1)$ for the following relative expression for parameters α_1 =0.1, α_2 =0.01 and $\alpha_1/2\alpha_2$ =5. This plot (see Fig. 2) demonstrated the good stabilization of second order coherence between the Stokes and anti- Stokes photons.

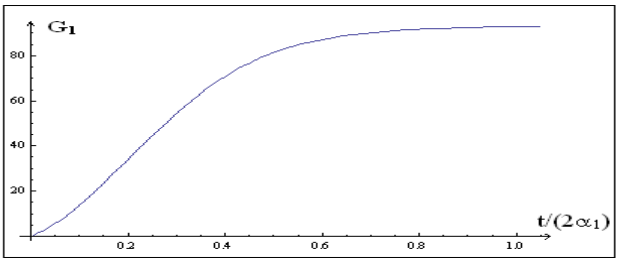

Fig. 2 The dependece of correlation function $G_1(t)$ on the relative time $t/(2\alpha_1)$ for the following value of parameters α_1 =0.1, α_2 =0.01 and $\alpha_1/2\alpha_2$ =5.

As follows from the Fig. 2 with increasing of time moment the correlation function achieved the maximal value, which corresponds to steady state stabilization. In Fig. 3 we have plotted the time dependence of square fluctuations Δ^2. It is observed the time decreasing of quantum fluctuations of coherent amplitudes proposed in communication with Stokes and anti-Stokes photons. As follows from the Fig. 3, with the stabilization of lasing process the square fluctuation becomes negative.

IV. CONCLUSION

The recent advances in quantum communication by using quantum optical proprieties of light are reviewed. The quantum communication protocols are carefully discussed. On the basis of these protocols many laboratories work for development and implementation of quantum optics devices. It is proposed a new method of quantum communication, which takes in to account the coherence between the entangled photon fields and the application of this effect in quantum communication. Considering coherent and

corpuscular properties of light, consisted of photon fields, the new scheme for quantum communication has been offered for the quantum communications.

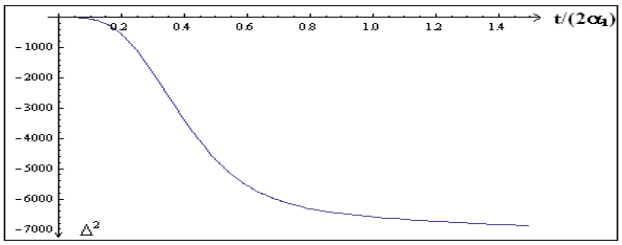

Fig. 3 The dependences of square fluctuations, Δ^2, as function of relative time $t/(2\alpha_1)$, for the same parameter as in Fig. 2.

This effects have many analogies with anti-bunging behavior of Stokes and anti-Stokes fields, described by $\hat{J}^+$ and $\hat{J}^-$ operators of SU (2) group (e.g. [11,16]).

ACKNOWLEDGMENTS

The author would like to acknowledge stimulating discussions with Professor Nicolae Enaki. I would like to thank all my colleagues from the Laboratory of Quantum Optics and Kinetic Processes, for friendly atmosphere. This paper was supported by the projects of the Academy of Sciences of Moldova: No. 10.820.05.05/BF and No. 11.819.05.11F.

REFERENCES

[1] M. Aspelmeyer, H.R. Böhm, T.Gyatso, T. Jennewein, R. Kaltenbaek, M. Lindenthal, G. Molina-Terriza, A. Poppe, K. Resch, M. Taraba, R. Ursin, P. Walther and A. Zeilinger, Science 301, 621, 2003; A. Zeilinger et all. Nature 390, 575-579, 1997.

[2] G.S. Agarwal and R.R. Puri, Phys. Rev. A **43**, 3949, 1991.

[3] B. Balko and I.W. Kay, Phys. Rev. B 48 (14) 1993.

[4] S.K.Y. Lee and C.K.Law, ''Collective photon-atom states by Raman coupling inside a cavity: A dynamic field-mode approach'', Phys. Rev. A **76**, 033809, 2007.

[5] D. Gauthier, Q. Wu, S.E. Morin and T.W. Mossberg, Phys. Rev. Lett. **68**, 464, 1992; D.J. Gauthier, ''Progress in Optics'' **45**, Chapter X , 2003; G. Ribordy, J. Brendel, J.D. Gauthier, N. Gisin, H. Zbinden, *Phys. Rev. A* **63**, 012309 2001.

[6] R.H. Dicke, ''Coherence in Spontaneous Radiation Processes'', Phys. Rev. **93**(1), 1954.

[7] P.D. Drummond and C.W. Gardiner, ''Generalized P-representations in quantum optics'', J. Phys. **A13**, 2353-2368, 1980; C.W. Gardiner, ''Quantum Noise'' Springer-Verlag New York 1996.

[8] A.K. Ekert, Phys. Rev. Lett. **67**, 661, 1991; A.K. Ekert, G.P. Massimo, J. Mod. Optics, **41**, 2413, 1994.

[9] S.-X. Yu, J.-W. Pan, Z.-B. Chen, and Y.-D. Zhang. Perfect Test of Entanglement for Two-level Systems. Phys. Rev. Lett. 91, 217903 2003;

[10] N.A. Enaki, M. Turcan and A. Vaseashta, J. Opto. and Adv. Mat., **10** (11) – P. 3016, 2008.

[11] N. Enaki and V. Eremeev, ''Two-Photon Lasing Stimulated by Collective Modes'', Optics Communications **247**, P. 381-392, 2005.

[12] N. Enaki and M. Turcan**,** Proc.SPIE, **7469**, p 746905, 2009.

[13] R. Miller, T.E. Northup, K.M. Birnbaum, A. Boca, A.D. Boozer, and H.J. Kimble, *J. Phys. B: At. Mol. Opt. Phys.* **38** S551, 2005.

[14] O. Pfister, W.J. Brown, M.D. Stenner and D.J. Gauthier, Phys. Rev A **60**, p.R4249-R4252, 1999.

[15] Z.C. Wang and H. Haken, Z. Phys. B-Cond.Matter **55** p.361-370, 1984; ''Quantum theory of the two-photon laser'', ibid. **71**, 253-59 1988.

[16] N. A. Enaki, V. Eremeev, M. Ţurcan., ''Two-Photon Lasing Controlled by Resonator Losses'', *Proc. of the 2nd International Conf. on Optics and Laser Applications, ICOLA'07,* p.98-102, 2007.

Ignition Method of Corona Discharge with Modulation of the Field in Ion Source of Ion Mobility spectrometer

Evgeniy GROMOV
National Nuclear Research University «MEPhI», Moscow, Russia
gromov-ea@yandex.ru

***Abstract* – The new method for the ignition of the corona discharge has been developed, which improves the stability of the ion mobility spectrometer and the resolution of the instrument. The system of forming a corona discharge without additional electrodes, which are used in a number of known structures for the pre-ionization, has been developed. This simplifies the design of the proposed source and an electronic control circuit. IMS technology is widely used in different civil and military fields for vapor-phase detection of explosive, narcotics, chemical warfare agents, biology molecules and so on. There are set of methods whose are used for the ionization of molecules under analysis. They are the following: radioactive ionization, ultraviolet photoionization, laser ionization, electric field ionization, coronaspray ionization, electrospray ionization, roentgen ionization, and surface ionization. All these methods has their own advantages and disadvantages. A comparing of ion mobility spectra of non-polar hydrocarbons for photoionization, corona discharge ionization and 63Ni ionization, had carried in. In our work we have investigated four types of IMS spectrometers whose use different sources for molecules under analysis ionization. They use radioactive ionization, ultraviolet photoionization, laser ionization, and roentgen ionization. The traditional explosives had investigated in experiments. In electricity, a corona discharge is an electrical discharge brought on by the ionization of a fluid surrounding a conductor, which occurs when the potential gradient (the strength of the electric field) exceeds a certain value, but conditions are insufficient to cause complete electrical breakdown or arcing.**

***Key words* – a ion mobility spectrometer, a corona discharge, a ignition of corona, a gate, additional electrodes.**

I. INTRODUCTION

Ion mobility spectrometry (IMS) is an analytical technique [1-3] for gas phase analysis of chemical compounds in laboratory environments; more recently, this method has been used in field applications to rapidly detect chemical warfare agents, explosives, and narcotics. Common structure (Figure 1) of the device includes the ionization region for inlet probe, gate for ion clusters forming, drift region, the detecting unit, data processing system.

The ion mobility spectrometers use radioactive radiation, corona discharge, the laser radiation, ultraviolet or X-rays to ionize air samples. Ionization source is an important part of the system responsible for the stability, resolving and sensitivity of the spectrometer. Sources can operate in continuous or pulsed mode

.

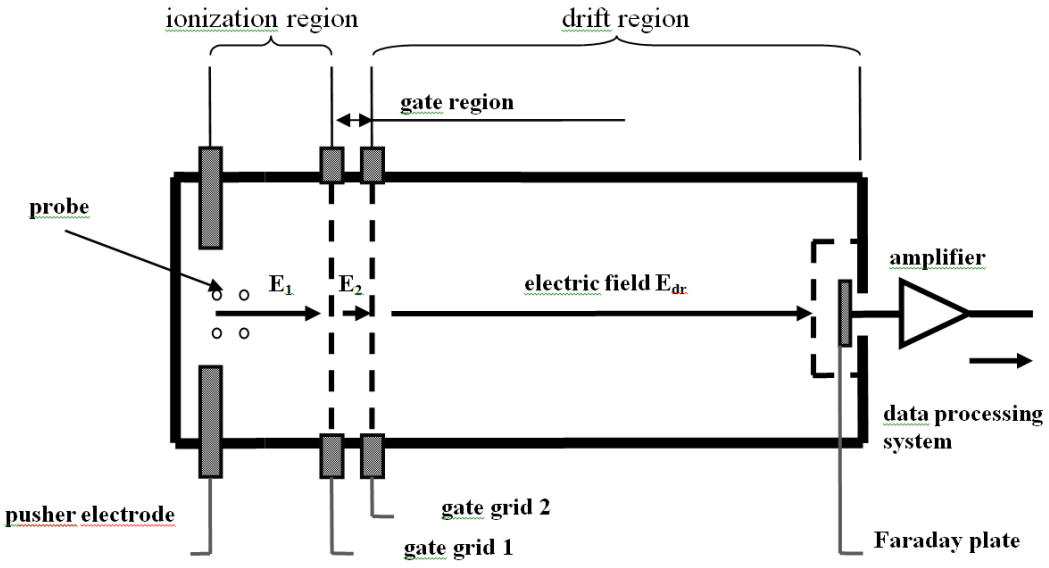

Fig. 1. Common structure of ion mobility spectrometer with electrostatic gates.

The choice of a corona discharge to ionize air samples is connected with the following advantages:

- lack of radioactive materials;
- the possibility of generating both positive and negative ions;
- simplicity and low cost of manufacture;
- low power consumption.

II. CORONA IONIZATION SOURCE

Ionization source by a corona discharge (Figure 2) consists on a conductive substrate, called a pusher electrode with thin sharp electrodes, between which at high voltage corona discharge produced plasma. Limiting (ballast) resistors R are used to align the current burning corona.

]

A corona is a process by which a current, perhaps sustained, develops from an electrode with a high potential in a neutral fluid, usually air, by ionizing that fluid so as to create a plasma around the electrode. The ions generated eventually pass charge to nearby areas of lower potential, or recombine to form neutral gas molecules. When the potential gradient is large enough at a point in the fluid, the fluid at that point ionizes and it becomes conductive. If a charged object has a sharp point, the air around that point will be at a much higher gradient than elsewhere. Air near the electrode can become ionized (partially conductive), while regions more distant do not. When the air near the point becomes conductive, it has the effect of increasing the apparent

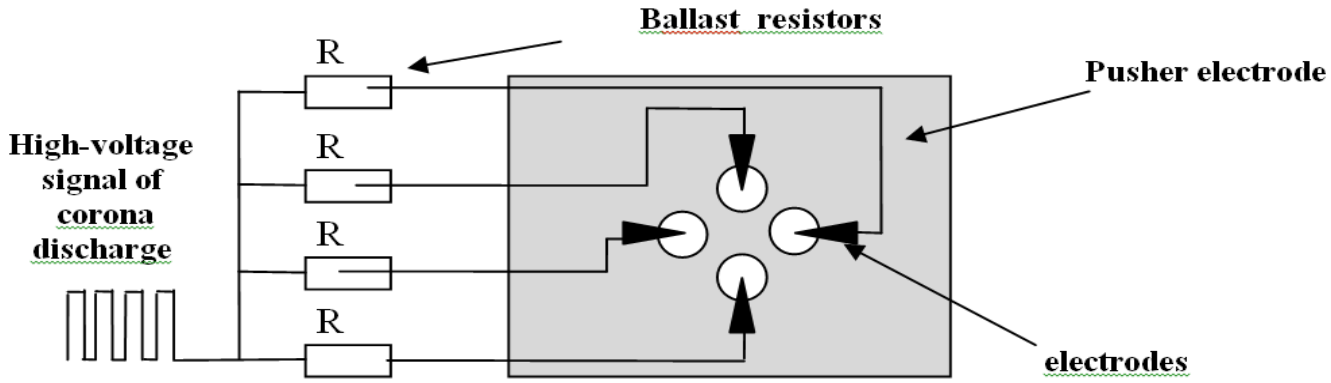

Fig. 2. The ionization source by a corona discharg

size of the conductor. Since the new conductive region is less sharp, the ionization may not extend past this local region. Outside of this region of ionization and conductivity, the charged particles slowly find their way to an oppositely charged object and are neutralized.

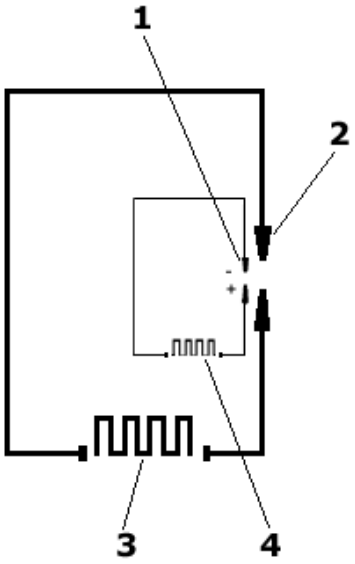

Fig. 3. The ionization source with two additional firing electrodes (1 – the additional electrodes, 2 – the main electrodes, 3 – the pulse generator for ignition corona discharge between the main electrodes, 4 – the pulse generator for ignition corona discharge between the additional electrodes).

If the geometry and gradient are such that the ionized region continues to grow instead of stopping at a certain radius, a completely conductive path may be formed, resulting in a momentary spark, or a continuous arc.

Corona discharge usually involves two asymmetric electrodes; one highly curved (such as the tip of a needle, or a small diameter wire) and one of low curvature (such as a plate, or the ground). The high curvature ensures a high potential gradient around one electrode, for the generation of a plasma.

Typically, ionization chamber design is such that the ignition electrodes locate in a region of high electric field, so that the generated ions are carried out from the ionization region to the gate. In this case ions of natural origin continuously carried out from the area between the electrode tips of the corona source, this complicates ignition of the corona. This leads to the instability of the discharge and the need to increase the duration and amplitude of the voltage pulse ignition. One of solution ways is proposed in American patent № 6407382 [5], which suggests the use of corona ionization source with additional firing electrode (Figure 3). First additional electrodes are initiated to following provide with ions the main electrodes.

In this work the corona discharge ignition system is proposed, in which the ignition is divided on two phases: preliminary and basic. During the preliminary phase an electric field in the ion source set to zero, and the generating "initiating" ions remain near the fire electrodes after end of the discharge. To the moment of a start of basic ionization phase the field in the ion source is restored to the nominal

level, with the "initiating" ions do not have time to leave the region of ignition due to the low mobility. This ensures the stability of ignition of a corona discharge due to the presence of ions in the discharge gap staying since the preliminary phase of discharge. The proposed system provides manufacturability and preserves the ionization source dimensions without resorting to the use of the additional electrodes.

REFERENCES

[1] V.V. Beliakov, A.V. Golovin, V.S. Pershenkov, Experimental studies of ion mobility spectrometer with the corona discharge ionization source, // Sensors and Systems, 2009, №2, pp. 12-17.

[2] Eiceman G.A., Karpas Z., Ion Mobility Spectrometry(Second edition) // CRC Press. – 2005.

[3] Tabrizchi M., Abedi A., A novel electron source for negative ion mobility spectrometry, International Journal of Mass Spectrometry, v. 218, pp.75-85, 2002.

[4] Discharge ionization source, Patent No. US 6407382, Date of Patent: 06/18/2002

Calibration Method for Ion Mobility Spectrometer

Valery VASILIEV
National Nuclear University "MEPhI", Moscow, Russia
vasilievvk@yandex.ru

***Abstract* –The new method for the calibration of the ion mobility spectrometer has been developed. This article describes the working principle, advantages and disadvantages of the calibration method operating in the mode of explosives detection. This method is most suitable for use in portable detectors, due to the small weight, small size parameters and low power consumption.**

***Key words* – ion mobility spectrometry, IMS, calibration, detection of explosives, corona discharge**

I. INTRODUCTION

Ion mobility spectrometry is a widely recognized global standard in detecting trace quantities of substances [1]. Devices based on the ion mobility spectrometry principles used in international airports and customs for detection of narcotics, explosives and warfare agents.

The principle of operation is the selection of samples from the surface or from the air, ionization and drift of ions through a constant electric field in the drift tube.

Output spectrum characterizes the composition of the sample. Ion of each substance has a definite mobility, therefore the measurement time-of-flight characteristics of the ions to determine their type.

As a result of changes in ambient temperature, humidity and pressure the output spectrum is changed. This fact requires periodic calibration of the spectrometer, so that the influence of external factors did not affect the results of the analysis. Calibration is carried out using previously known substances, which are periodically introduced into the ionization chamber.

The new calibration method by using the reaction products of corona discharge (nitrogen oxides) described in this paper. This method is most suitable for use in portable detectors, due to the small weight, small size parameters and low power consumption. It has a very good opportunities for constructive integration in the portable IMS device [2].

II. CALIBRATION METHOD USING A CORONA DISCHARGE

The possibility of chemical transformations under the influence of an electric discharge was discovered almost a hundred years ago . Since then, detailed studies of the processes occurring during combustion of corona discharge in air [3-5].

Chemical products resulting from combustion of corona discharge, such as nitrogen oxides, compete with analyte in electron capture reactions. The concentration of nitrogen oxides can be quite large and must be taken into account when dealing with the corona discharge ionization sources. These substances have a high oxidative properties and impede the detection of explosives. However, due to the stability of a corona discharge nitrogen oxides can be used as calibration substances.

Investigation of the reaction products of corona discharge was carried out on a specially designed layout. Layout consists of two electrodes made of stainless steel with a thickness of 0.5 mm using the technology of laser cutting. Tip electrodes are placed at a distance of 2mm. Burning source of corona discharge is shown in Figure 1.

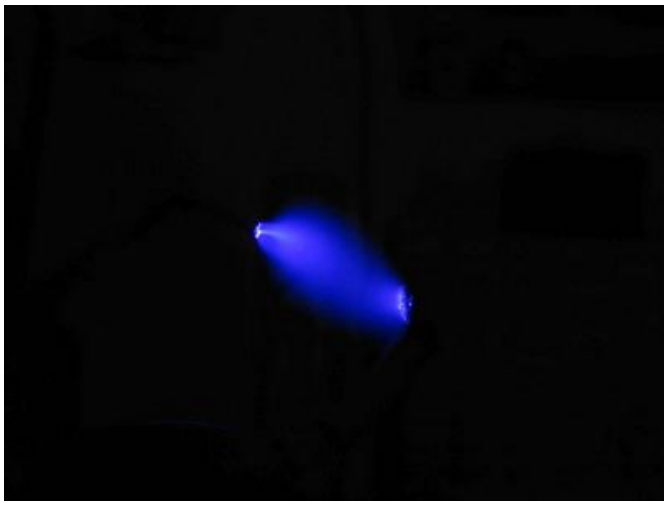

Fig.1. Corona discharge

In the transition from the regime of detection into the calibration mode, the device suspends the detection of explosives. The combustion products of corona discharge inputed into ionization chamber. Spectrum changes as shown in Figure 2.

The system detects the peak of the calibration substance and on the basis of known data on the time-of-flight characteristics of detected explosives builds markers of these substances relative to the calibration peak.

Analysis of the calibration peak showed that the experimental data given in [6], the gauge corresponds to the substance nitrogen oxide. Spectrograms show the presence in a sample of large amounts of information generated during the discharge of the substance.

By varying the voltage applied to the electrodes can change the amount generated by the combustion products, as illustrated in Fig. 3.

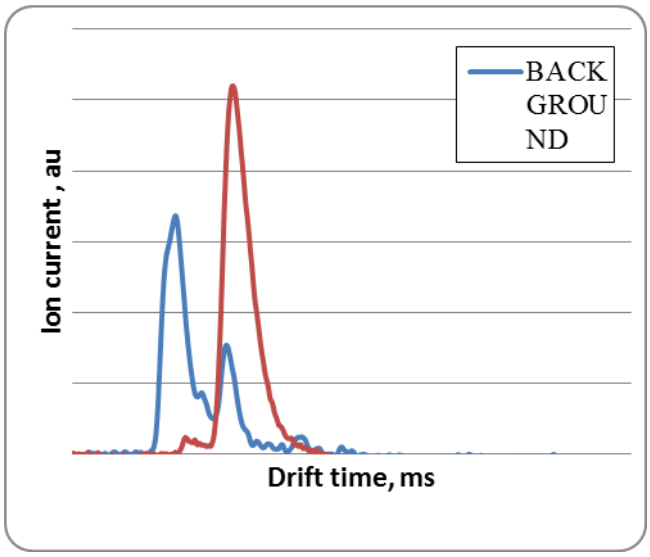

Fig. 2. Change in the spectrum in the calibration mode

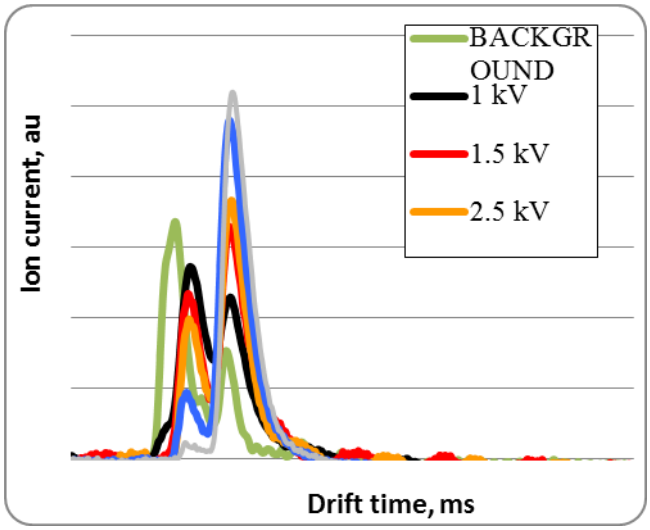

Fig. 3. Calibration spectrum for different discharge voltages

The figure shows that the number of outgoing material is directly proportional to the corona discharge voltage. However, from a certain level the spectrum changes only slightly.

At high voltages applied to the source of the corona discharge, the calibration substance pulls all the charge from the peaks of background signal. This suggests that the calibration material has strong oxidizing properties. This corresponds to the theoretical data [7].

In most cases, the electron affinity is less then 1 eV, but in the case of NO2 value exceeds 3 eV. In turn, the group OH (intermediate reactant ion in the negative mode ion mobility spectrometer), this value is 2 eV,which confirms the observed during the experiment, the charge transfer.

By varying the voltage applied to the electrodes, the configuration of needles and the distance between them, we can achieve stable combustion of corona discharge, provide the required burning time of the corona. The developed system allows to change the amount of combustion products generated by varying the voltage applied to the electrodes. In addition, the pulsed nature of the corona discharge provides the kalibrant reliability and extends the lifetime of needles.

The proposed calibration method was successfully used in a portable ion mobility spectrometer, which weight is a 2.9kg (without battery). Designed built-in ion mobility spectrometer calibration system based on corona discharge. It's control system integrated into the control system of the spectrometer.

III. CONCLUSION

Calibration technique using a corona discharge is a very suitable for use in portable detectors, due to the small weight, small size parameters and low power consumption. It has several advantages, allowing to embed kalibrant in a portable ion mobility spectrometer. The developed ionization source control system implements the possibility of changing the parameters of corona discharge combustion (duration of burning and discharge voltage).

Further research is needed in the area of embedded kalibrant for positive mode of the IMS (detection of narcotics).

ACKNOWLEDGMENTS

I owe my deep gratefulness to Dr. Pershenkov V.S., PhD Belyakov V.V. and all of our team-mates.

REFERENCES

[1] Eiceman G.A., Karpas Z., Ion Mobility Spectrometry (Second edition) // CRC Press. – 2005.
[2] Belyakov V.V. Ion Mobility Spectrometer // Utility patent № 035034. – Russian Federation, 2006.
[3] Hickling A. // Modern Aspects of Electrochemistry. L.: Butterworths. 1971. № 6. P. 329.
[4] Lunin V.V., Popovich M.P., Tkachenko S.N. Physical chemistry of ozone. M.: MSU. 1998. 480 p.
[5] Andreev D.N. Organic synthesis in electrical discharges. USSR. 1953.
[6] M. Stano, M. Sabo, M. Kucera etc. IMS study of Negative Corona Discharge in N2/O2 Mixtures in N2 Drift Gas Asta Physica Universitatis Comenianae Vol. L-LI, Number 1&2 (2009-2010) 77-83
[7] Achmetov N.S. Topical Issues Course of Inorganic Chemistry. — M.: Education, 1991. — 224 p.

The Fitting Parameters Extraction of Conversion Model of the Low Dose Rate Effect in Bipolar Devices

Alexander BAKERENKOV

National Research Nuclear University (MEPhI), Moscow, Russia

as_bakerenkov@list.ru

***Abstract* - The Enhanced Low Dose Rate Sensitivity (ELDRS) in bipolar devices consists of in base current degradation of NPN and PNP transistors increase as the dose rate is decreased [1]. As a result of almost 20-year studying, the some physical models of effect are developed, being described in [2] in detail. Accelerated test methods, based on these models use in standards [3, 4]. In [5] the conversion model of the effect, that allows to describe the inverse S-shaped excess base current dependence versus dose rate, was proposed. This paper presents the problem of conversion model's fitting parameters extraction.**

***Index Terms* – Enhanced Low Dose Rate Sensitivity, ELDRS. bipolar devices, hardness assurance.**

I. THE CONVERSION MODEL OF LOW DOSE RATE EFFECT

The conversion model is based on the assumption that the positive charge accumulated by ionizing radiation is converted to interface traps. The shallow and deep positive charge traps are supposed to exist. During short period of high dose rate irradiation only shallow traps are converted. An additional conversion of deep traps occurs during long period of low dose rate irradiation. This leads to increase of base current degradation. Conversion process operates like a pump, pumping radiation induced trapped holes charge into interface traps continuously. Mathematically base current degradation dependence versus dose rate is described by the following expression:

$$\Delta I_B = (K_D + K_S)\cdot D + \gamma \cdot K_D \cdot \tau_D \left(e^{-D/\gamma\cdot\tau_D} - 1 \right), \quad (1)$$

where ΔI_B is excess current, K_D is excess base current per unit absorbed dose at low dose rate, K_S is excess base current per unit dose at high dose rate, D is total absorbed dose, γ is a dose rate, τ_D is deep traps conversion time.

Relationship (1) has an inverse S-shaped form (fig. 1). During high dose rate irradiation shallow oxide traps have time to be converted into interface traps only, because of small time of irradiation. Therefore, excess base current is determined by accumulation and conversion of shallow traps at high dose rates. At such conditions the value of excess base current is $K_S D$.

Since some values of dose rate (mean times of irradiation) the base current degradation starts to increase. This is associated with the deep trap conversion with increase of irradiation time the density of interface traps increases due to additional conversion of deep traps. Transition time interval is about $(3 \div 5)\tau_D$. The range of dose rates, where excess base current degradation increases is $(10^{-2} \div 1)D/\tau_D$.

At very low dose rates or in other words at very large irradiation time, all deep traps have time to be converted, so base current degradation reaches some constant value again. This increase in base current degradation is greater than that for high dose rate by the value of $K_D D$. The total excess base current at very low dose rate is determined by total contribution of shallow and deep traps conversion.

Thus the conversion model has three fitting constants: K_S, K_D and τ_D. Knowledge of these constants allows to evaluate full inverse S-shaped characteristic and to predict the base current degradation for any dose rate at given total absorbed dose.

II. HIGH TEMPERATURE POST-IRRADIATION ANNEAL

The dependence of excess base current versus time at the stages of irradiation and 40ºC, 60ºC, 100ºC post- irradiation anneal is presented in . 2.

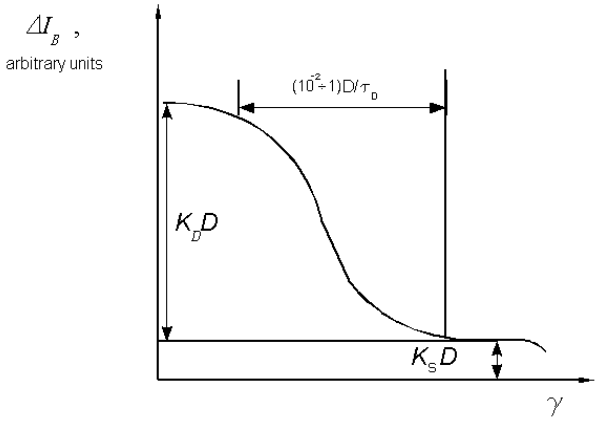

Fig.1. Schematic representation of the dependence of the excess base current versus dose rate.

These dependences are typical for investigated NPN and

PNP discrete transistors and input transistors of operational amplifiers. The surface recombination component of the base current depends on interface states density N_{it} at the SiO_2/Si interface, positive charge in oxide Q_{ot} and interface traps charge Q_{it} at forward bias of emitter junction. Energy diagram of the SiO_2/Si interface is presented in fig. 3, where neutral interface states N_{it}, positive oxide charge Q_{ot} and interface traps charge Q_{it} (formed due to capture of carriers injected into base by interface traps) are designated. It is supposed that interface states located above middle of forbidden gap are acceptor like, i.e. they are negatively charged (Q_{it}<0), being located below quasi-Fermi level for electrons E_{Fn}, (fig.3, a). Interface states located below the middle of forbidden gap donor like, therefore they are charged positively (Q_{it}>0) if they are free, being located above quasi-Fermi level for holes E_{Fp}, (fig. 3, b). Effective charge at the interface is $Q_{eff} = Q_{ot} + Q_{it}$.

The surface recombination current of NPN transistor is directly-proportional to interface states density and increases with the increase of effective interface positive charge (positive charge attracts the injected electrons, that leads to a recombination loss increase).

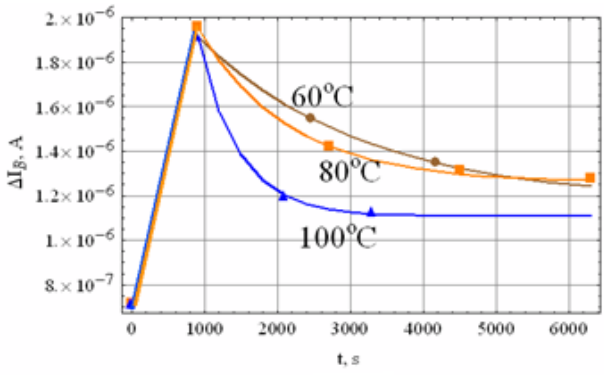

Fig.2. Excess base current versus time (0-1000s – irradiation; more 1000s – annealing) for SWB99 PNP transistor.

Therefore a decrease of the base current on the stage of post-irradiation anneal may be associated with decrease of Q_{ot} or increase of Q_{it}, because $Q_{eff} = Q_{ot} - Q_{it}$ in NPN transistors. At elevated temperature stress charge Q_{ot} is annealed and charge Q_{it} may grow due to conversion of the annealed charge. In case of PNP transistor surface recombination current is also proportional to interface states density, but it decreases if the interface effective charge increase (positive charge repulse injected holes away from the surface, that leads to a recombination loss decrease). Base current decrease during post-irradiation anneal in that case may be associated with increase of interface states charge Q_{it} only (in effective charge $Q_{eff} = Q_{ot} + Q_{it}$ component Q_{ot} decreases, but component Q_{it} increases). In both cases the increase of interface states density plays a secondary role, not leading to surface recombination current increase.

The general feature of NPN and PNP transistors is that base current decrease at elevated temperature post-irradiation anneal is associated with the annealing of trapped positive charge. Therefore an investigation of base current behavior during post-irradiation anneal allows to estimate activation energy of this process and to measure deep traps conversion time τ_D (shallow ones are annealed during the irradiation).

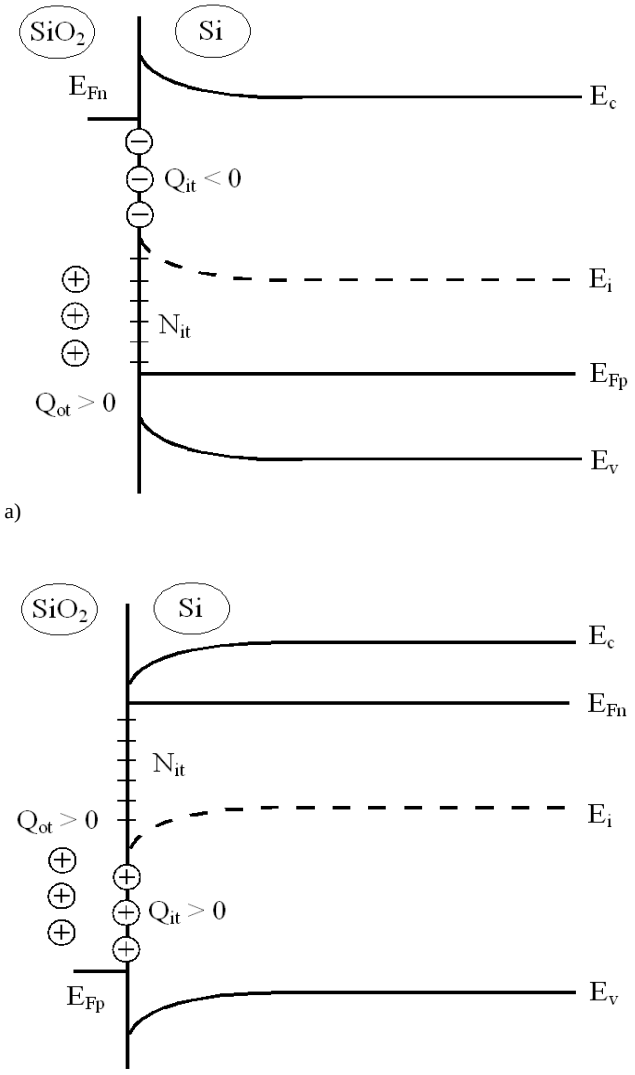

Fig.3. Energy diagram SiO_2/Si interface on forward bias emitter junction.

The annealing time constant is described the Arrhenius law

$$\tau_D = \tau_{D0} Exp\left(\frac{W_A}{kT}\right), \qquad (2)$$

where τ_{D0} is a pre-exponential constant, W_A is an activation energy of deep traps anneal.

Pre-exponential constant τ_{D0} and activation energy W_A in (2) are derived from the data for two different temperatures of elevated temperature post-irradiation anneal.

Only insignificant part of radiation induced trapped positive charge is annealed during elevated temperature post-irradiation anneal following high dose rate irradiation (fig.2). This may be associated with the absence of photoelectrons on the post-irradiation phase or space charge effect on at high dose rate irradiation (more detail in full version of paper). The small part annealed charge leads to impossibility to estimate a total value of deep trapped oxide charge and extract the constant K_D. For extraction of K_D we need some conditions, when deep trapped charge participates in the process of annealing. For that we suppose to use elevated temperature irradiation, when the annealing of all accumulated charge occurs.

III. ELEVATED TEMPERATURE IRRADIATION

High temperature irradiation leads to significant increase of base current degradation and it is used for accelerated tests on ELDRS [3, 4]. The contributions of deep traps charge to base current degradation is estimated in this work rely on the results of irradiation at several different temperatures.

Temperature elevation leads to a shift of the inverse S-shaped curve to the direction of greater dose rates as illustrated on fig. 4.

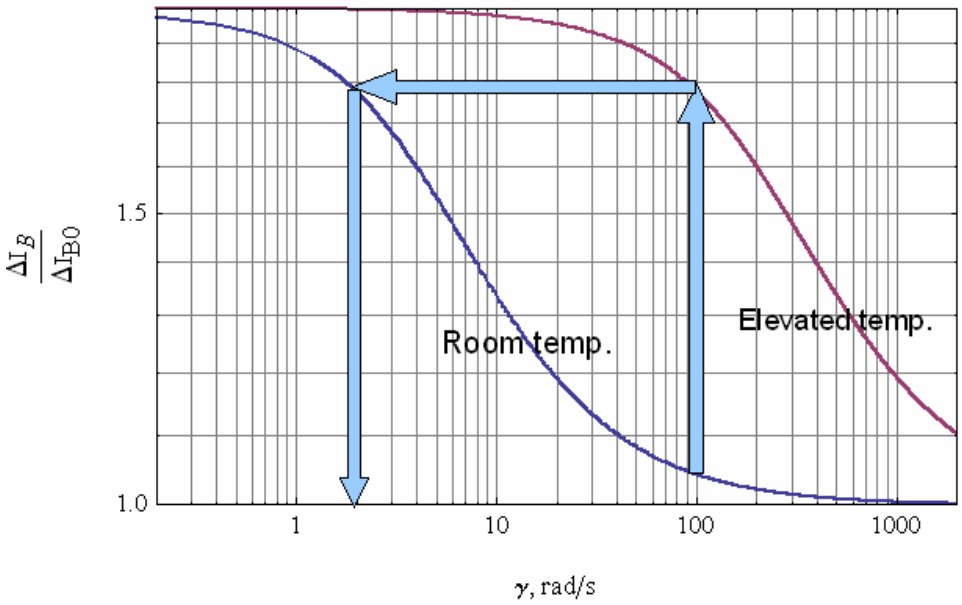

Fig. 4. Inverse S-shaped curve of a device for room and elevated temperature.

It is clear from fig. 4, that irradiation temperature elevation is equal to the dose rate decrease. Thus if we want to model low dose rate irradiation we have to irradiate a device at certain elevated temperature. Knowing τ_{D0} and W_A we can calculate this temperature. In turn we can derive the values of τ_{D0} and W_A from the annealing at different temperatures.

IV. FITTING PARAMETER EXTRACTION TECHNIQUE

Fitting constants extraction was performed by the following way:

1. Constant KS determining the contribution of shallow trapped charge conversion to base current degradation is estimated as a ratio of base current degradation to the specified absorbed dose at 400 rad(SiO2)/s irradiation.
2. The deep traps conversion time or constant τD is estimated from data of post-irradiation anneal following high dose rate irradiation to the specified absorbed dose. Pre-exponential constant τD0 and activation energy WA in (2) are derived from the data for two different temperatures of elevated temperature post-irradiation anneal.
3. Constant K_D determining the contribution of deep trapped charge conversion to base current degradation at low dose rate is estimated from elevated temperature irradiation data.

It is desirable that this irradiation temperature corresponds to the maximum base current degradation at elevated temperature irradiation.

Constant K_D is derived from (1), where the constant τ_D for using elevated temperature is calculated from (2) (values of τ_{D0} and activation energy W_A are determined on stage 2).

V. CONCLUSION

The technique for extraction fit parameters of ELDRS conversion model in bipolar transistors was proposed. Presents of dip and shallow positive charge traps in silicon dioxide is assumed. ELDRS is explained by conversion of dip traps. Extraction technique is based on employment elevated temperature post-irradiation annealing for determination of dip traps conversion time constant. Parameter relevant with deep traps concentration obtains from elevated temperature irradiation experiment. Description of ELDRS S-spare characteristic is the result of fit parameters extraction. It provides way to prediction radiation-inducted base current degradation at dose rate that actual in space environment.

REFERENCES

[1] E.W. Enlow, R.L. Pease, W.E. Combs, R.D. Schrimpf,, R.N. Nowlin. Response of advanced bipolar processes to ionizing radiation. IEEE Trans. Nucl. Sci., 1991, vol. NS-38, no.6, pp.1342-1351.

[2] R.L. Pease, R.D. Schrimpf, D. M. Fleetwood. ELDRS in bipolar linear circuits: a review. IEEE Trans. Nucl. Sci. 2009, vol. NS-57.

[3] Method 1019.

[4] Method EC

[5] V.S. Pershenkov, D.V. Savchenkov, A.S. Bakerenkov, V.N. Ulimov , A.Y. Nikiforov, A.I Chumakov, The conversion model of low dose rate effect in bipolar transistors. RADECS 2010.

The Controlling of Nanoparticles by the Polarization Methods

V.ANGELSKY, C.Yu. ZENKOVA
Chernivtsy National University, Chernivtsy, Ukraine
angelsky@itf.cv.ua

***Abstract* – We present the results of computer simulation of spatial distribution of the Poynting vector and illustrate motion of nano and microparticles in spatially inhomogeneously polarized fields. The influence of phase relations and the degree of mutual coherence of superposing waves in the arrangements of two-wave and four-wave superposition on the characteristics of microparicle's motion has been analyzed.**

***Index Terms* – Poynting vector, spatial modulation of polarization, optical currents.**

I. INTRODUCTION

One of the most actual tasks, connected with the appearance of laser, is to control microparticles of different nature by the help of laser irradiation. The object of controlling may be a colloid particle, a molecule, an atom, a cell, including a bioobject, e.g. a DNA molecule, an organelle cell. It can be said, that the technology of particle manipulating is a powerful tool for the work with microobjects of different nature. The process of trapping and controlling the particles depends on the properties of the laser beam. One of the basic conditions of particle manipulation by the help of these laser beams is their full coherence.

Experimental study and computer simulation of behavior of small spherical conducting particles embedded in optical fields provides deeper understanding of the role of the Poynting vector for description of optical currents in various media [1]. Accounting the modulation of waves polarized at the incidence plane in forming desirable spatial distributions of the averaged Poynting vector is the step to creation of polarization micromanipulators and tweezers. On the other hand, it is the step to finding out of optimal experimental investigation of optical currents in vector fields [2-5]. Besides, the study of spatial and temporal peculiarities of motion of particles embedded into optical fields with various spatial configurations and with various scale distributions of the Poynting vector inherent in both completely coherent and partially coherent fields leads to new techniques for estimating temporal coherence of optical fields [6].

Computation of the spatial distribution of the averaged Poynting vectors determining the forces affecting on microparticles and moving them is performed in this paper following the algorithm proposed by M. Berry [1] who has shown that the force affecting a small particle in optical field is proportional to the Poynting vector. On the other hand, it is shown that the study of motion of microparticles in inhomogeneously polarized fields provides reconstruction of the spatial distribution of the averaged Poynting vectors (optical currents).

The dependence of the force value influencing the particles upon the degree of coherence of interacting waves is shown.

II. TWO-WAVE SUPERPOSITION FOR CHANGEABLE DEGREE OF COHERENCE OF ONE COMPONENT

Superposition of two plane waves of equal amplitudes polarized at the incidence plane (Fig. 1a) results into distribution of the averaged over the oscillation period Poynting vector shown in Fig. 1b. Such distribution arises when the interference angle equals to 90°, and the only periodical polarization modulation of a field (in absence of intensity modulation) takes place at the observation plane.

Analysis of the spatial distribution of the averaged Poynting vectors shown in Fig. 1b reveals periodicity of this distribution, where the absolute magnitudes of vectors are proportional to the lengths of lines shown in the figure. The lines corresponding to singularities of the Poynting vector are also shown in this figure by the set of points [7-9]. Comprehensive notion on the mechanisms of formation of such distribution follows from the consideration of them both in statistics and in dynamics with the corresponding comments, which we formulate below *in thesis*.

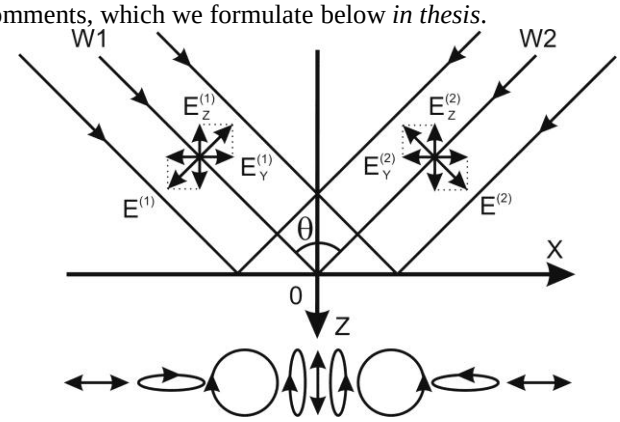

Fig. 1a. Superposition of plane waves of equal amplitudes linearly polarized at the incidence plane, with the interference angle 90°. Periodical spatial polarization modulation takes place at the incidence plane.

1. Light energy transfer is undulate in time and in space (Fig. 2). Here the vectors $\vec{E}$ and $\vec{H}$ are shown in blue and violet, correspondingly, and the Poynting vector is shown in black. The directions of oscillations of this vector are the direction of light energy transfer.

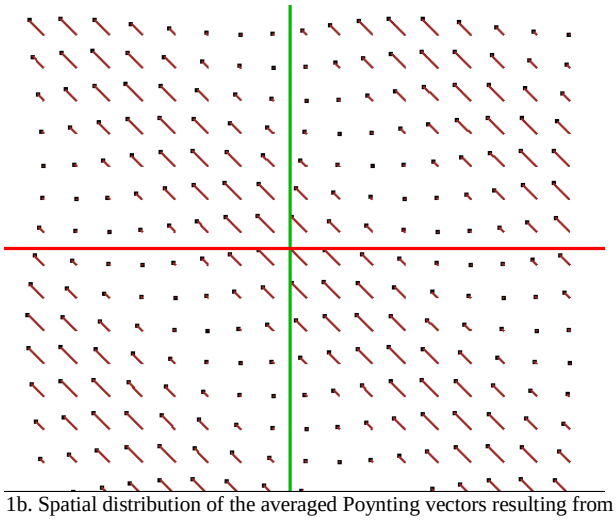

Fig. 1b. Spatial distribution of the averaged Poynting vectors resulting from superposition of two orthogonally linearly polarized waves with the interference angle 90°.

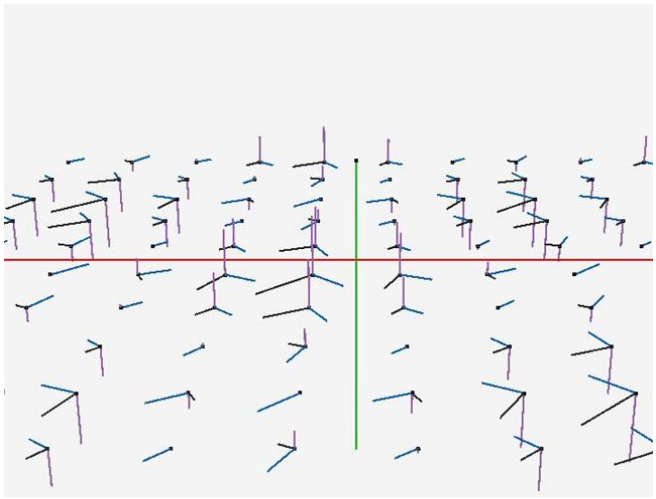

Fig. 2. It is illustrated wave-like light energy transfer in 2D field resulting from superposition of plane orthogonally polarized waves of equal amplitudes with the interference angle 90°. Energy transfer takes place along the bisectrix of the propagation directions of two waves at the incidence plane: the distribution of Poynting vector is presented in black color, of vector $\vec{E}$ in blue and $\vec{H}$ in violet.

2. Spatial distribution of the averaged over oscillation period Poynting vectors (Fig. 1b) is the map of the directions (trajectories) of energy transfer.

3. The points at the map of the averaged Poynting vectors (Fig. 1b) correspond to the areas through which energy transfer is absent:

- there are the points of singularities of the Poynting vector;

- there are the points forming the lines along which light energy is non-vanishing, but is conserved, no being transferred;

- there are the points where the vector $\vec{H}$ vanishes by interference, while in this arrangement (90°-superposition of plane waves) superposition of strictly coaxial vectors $\vec{H}$ of equal amplitudes associated with two superposing plane waves takes place.

4. Homogeneous intensity distribution and periodical spatial modulation of the Poynting vector simultaneously realized at the observation plane find out explanation within the framework of [10,11]. Spatial polarization modulation at the observation plane is caused by superposition of the E_x and E_z field components with changing from point to point phase difference (Fig. 1a). Photodetector registers only intensity $I = E_x^2 + E_z^2$. The sum of the squared amplitudes of the electrical fields is constant at the observation plane, though the state of polarization changes. The Poynting vector is defined by the vector product $\vec{S} = \frac{c}{4\pi}\left[\vec{E} \times \vec{H}\right]$. One can see the dependence of the result (*viz.* the vector magnitude and its direction) on the phase relation between vectors $\vec{E}$ and $\vec{H}$. This relation changes from point to point at the observation plane that manifests itself in polarization modulation. Obvious explanation follows from consideration of the product of the components of vector $\vec{E}$ (E_x and E_z components) with vector $\vec{H}$. Both the magnitudes of projections E_x and E_z and their phases change from point to point at the observation plane. As a consequence, the vector product as well as the Poynting vector also change.

The simulation of motion of conducting particles of diameter from 0.2 μm to 0.3 μm embedded in the field of the considered distribution of the Poynting vector has been carried out. It was concluded that in the case of the distribution resulting from superposition of completely mutually coherent waves, velocities of particle motion along the lines of maxima and zeroes of the Poynting vector are considerably different. Particle size is comparable with a half-period of the corresponding distribution, however the resultant force (Fig. 3) inducting particle motion along the lines close to the Poynting vector maxima exceeds the resultant force for the lines with vanishing and close to zero Poynting vector magnitudes.

If the degree of mutual coherence of superposed waves equals 0.2, the spatial distribution of the averaged Poynting vectors becomes more homogeneous Fig.4, the deep of modulation of such vector decreases considerably, and velocities of motion of microparticles become almost the same.

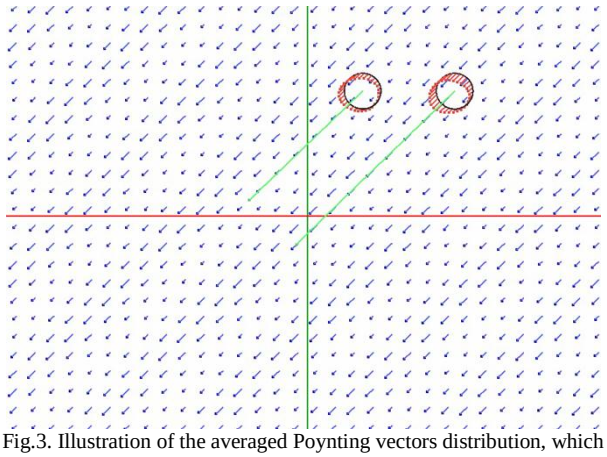

Fig.3. Illustration of the averaged Poynting vectors distribution, which forming in arrangement Fig. 1 for completely mutually coherent waves and the formation of the resulting force (green novertical line) inducting particle motion.

When the degree of mutual coherence equals 0.5, relative velocities of motion of microparticles along the same trajectories differ twice in comparison with velocities for completely mutual coherence of superposed waves. One can

see the dependence of velocities of motion of microparticles of constant size and form in media with constant viscosity on coherent properties of superposed waves. These differences in velocities of motion of microparticles may be explained physically in the following manner. Increasing share of incoherent radiation in the resulting field distribution causes in decreasing of the modulation depth of the Poynting vectors spatial distribution (Fig. 5), as well as in decreasing of the resultant force magnitude along the lines of energy transfer which causes microparticle's motion [12, 13].

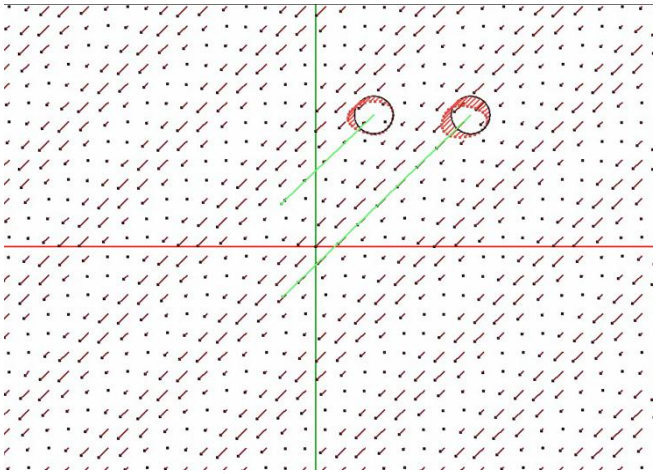

Fig. 4. Illustration of the averaged Poynting vectors distribution in arrangement Fig. 1 for the degree of mutual coherence of the components 0.2 and the formation of the resulting force (green novertical line) inducting particle motion.

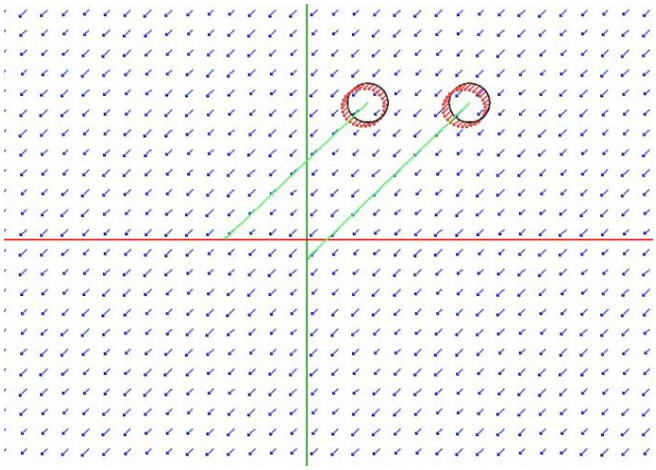

Fig.5. Illustration of the averaged Poynting vectors distribution in arrangement Fig. 1 for the degree of mutual coherence of the components 0.5 and the formation of the resulting force (green nonvertical line) inducting particle motion.

III. THE SUPERPOSITION OF FOUR WAVES FOR CHANGEABLE DEGREE OF COHERENCE OF ONE COMPONENT

In the case of superposition of four plane waves involving two sets of counterpropagating plane waves of equal intensities, linearly polarized at the incidence plane and oriented at the angle 90° to each other, the spatial distribution of the averaged Poynting vectors is formed, as it is shown in Fig. 6b.

One can see periodical 2D distribution of the Poynting vectors. As in the previous case, the lengths of the averaged Poynting vectors are proportional to their magnitudes. The points at this distribution correspond to zero magnitudes of the Poynting vector, i.e. singularities of the Poynting vector. In simulation, diameters of conducting particles are changed be comparable with a half-period of the corresponding spatial distribution of the Poynting vector.

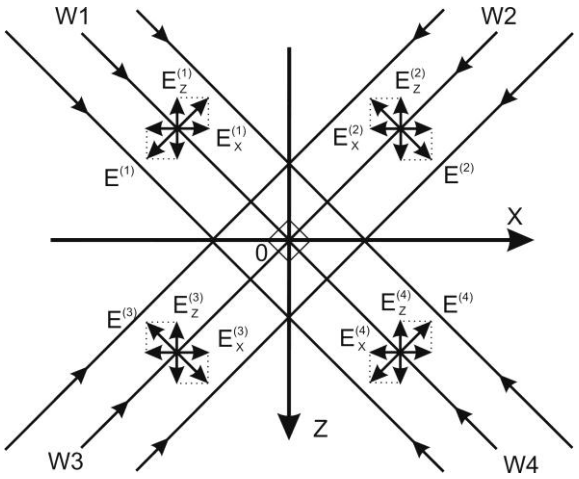

Fig.6a. Arrangement of the superposition of four plane waves

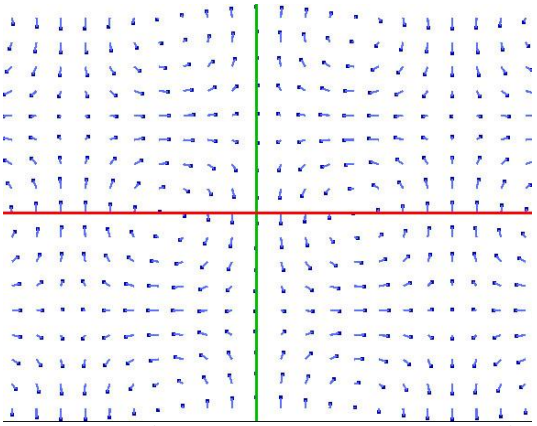

Fig. 6b. 2D distribution of the averaged Poynting vectors resulting from the superposition of four waves shown in Fig. 6a.

For the sake of qualitative comparison of temporal and spatial parameters of motion of micoparticles, we have analyzed the maps of the averaged Poynting vector in the arrangement of four plane waves superposition over a large area. The dependence of microparticles motion velocities on the phase difference of the superposing beams has been proved. So, in the case of pair-by-pair four opposite-in-phase superposed beams, particles become motionless. Here, oppositeness-in-phase presumes the situation when two sets of mutually orthogonal in space standing waves are characterized by the fact, that their nodes strictly coincide.

It follows form the presence of the minimum of the modulation depth at the spatial distribution of the Poynting vector. Gradual decreasing of the degree of coherence of one of the superposed beams causes revival of particle motion with increased velocity as the degree of coherence of one of beams decreases.

If the phase relations of four superposed beams is such that the modulation depth of the spatial distribution of the Poynting vector is maximal, velocities of moving of microparticles also depend on the degree of mutual coherence of superposed beams. This situation is realized when two orthogonal systems of standing waves are such as

their maxima coincide. This case we refer to as co-phasing of waves. The change of the degree of coherence of interacting waves causes the change of the modulation depth of the averaged Poynting vector and, correspondingly, the change of the movement velocity of particles.

There is exists two points, which can explain the superposition of four waves. At the first, the dependence of the depth of modulation at the distribution of the averaged Poynting vectors on the phase relation of superposing waves. It is assumed that changing the phase relation of superposed waves causes transition (at the observed pattern) from the situation when the maxima of two systems of mutually orthogonal standing waves coincide - to the case when the nodes of two such systems coincide. Thus, the velocities of particles in such fields are dependent on the depth of modulation of the distribution of the averaged Poynting vector. Secondly, the superposition of four waves linearly polarized at the incidence plane results in forming so-called "cellular" structure in the resulting field distribution, which can be used for transfer (transporting) *as a whole* of the set of periodically positioned microparticles to the desirable zone, see Fig. 7.

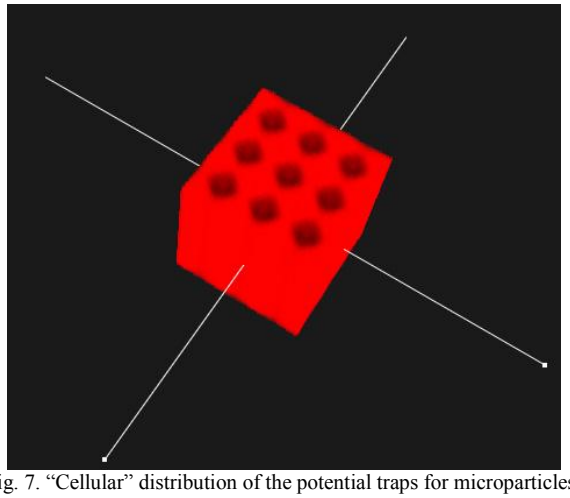

Fig. 7. "Cellular" distribution of the potential traps for microparticles in the case of the superposition of four waves

We consider as prospective the deeper investigation of peculiarities of motion of microparticles at the considered here fields to reveal the regularities of dynamics of their motion as a function of the coherent characteristics of the waves constituting certain spatial polarization distributions. Such investigations put in evident the prospectives of experimental investigations of light coherence.

IV. CONCLUSIONS

Motion of microparticles at the field in absence of intensity modulation, only due to polarization modulation causing the spatial modulation of the Poynting vector makes obvious the feasibilities for creating on this base pure polarization micromanipulators and tweezers. Temporal and space peculiarities of particle's motion in optical fields with spatial modulation of the averaged Poynting vector (depending on the degree of mutual coherence of superpose waves) show some new feasibilities of the use of such field characteristics and the parameters of microparticles motion for estimating the temporal coherence of the tested field. Initial experimental results prove these conclusions.

V. REFERENCES

[1] M.V.Berry, "Optical currents", Journal of Optics A: Pure and Applied Optics, vol. 11, 2009, pp. 094001.

[2] O.V. Angelsky, N.N. Dominikov, P.P. Maksimyak, T. Tudor, "Experimental revealing of polarization waves", Appl. Opt., vol. 38, no.14, 1999, pp. 3112-3117.

[3] T.Tudor, "Polarization waves as observable phenomena", J. Opt. Soc. Am. A, vol. 14, no. 8, 1997, pp. 2013-2020.

[4] M.V. Berry, K.T. Donald, "Exact and geometrical optics energy trajectories in twisted beams", Journal of Optics A: Pure and Applied Optics, vol. 10, 2008, pp. 035005.

[5] M.V. Berry, M.R. Dennis, "Polarization singularities in isotropic random vector waves", Proc.R.Soc., vol. A456, 2001, pp. 2059-2079.

[6] O. V. Angelsky, S. G. Hanson, C. Yu. Zenkova, M. P. Gorsky, N. V. Gorodyns'ka,"On polarization metrology (estimation) of the degree of coherence of optical waves", Optics Express, vol.17, no. 18, 2009, pp. 15623-15634.

[7] R. Khrobatin, I.Mokhun, "Shift application point of angular momentum in the area of elementary polarization singularity", Journal of Optics A: Pure and Applied Optics, vol. 10, 2008, pp. 064015,.

[8] R. Khrobatin, I. Mokhun, J. Victorovskaya, "Potentiality of experimental analysis for characteristics of the Poynting vector components", Ukr.J.Phys.Opt, vol. 9, 2008, pp. 182-186.

[9] A.Y. Bekshaev, M.S. Soskin, "Transverse energy flows in vectorial fields of paraxial light beams", Proc. SPIE, 6729, 2007, pp. 67290G.

[10] O.V. Angelsky, S.B.Yermolenko**,** C.Yu. Zenkova, A.O. Angelskaya, "Polarization manifestations of correlation (intrinsic coherence) of optical fields", Applied Optics, vol. 47, no. 32, 2008, 5492-5499.

[11] O.V. Angelsky, C.Yu. Zenkova, M.P Gorsky, N.V. Gorodyns'ka, "On the feasibility for estimating the degree of coherence of waves at near field", Applied Optics, vol. 48, no.15, 2009, pp. 2784–2788.

[12] O. V. Angelsky, M. P. Gorsky, P. P. Maksimyak, A. P. Maksimyak, S. G. Hanson, C. Yu. Zenkova, "Investigation of optical currents in coherent and partially coherent vector fields", Optics Express, vol. 19, no. 2, 2011, pp. 660-672.

[13] C. Yu. Zenkova, M. P. Gorsky, P. P. Maksimyak, A. P. Maksimyak, "Optical currents in vector fields", Applied Optics, vol. 50, no. 8, 2011, pp.1105-1112.

Preparation and Characterization of N-doped TiO_2 with Enhanced Photocatalytic Activity

C. PĂSTRĂVANU[1], M. IGNAT[1], E. POPOVICI[1], I. CRETESCU[2*]
[*]Mail correspondent author: icre@ch.tuiasi.ro
[1] *"Al. I. Cuza" University of Iasi, Romania*
[2] *"Gheorghe Asachi" Technical University of Iasi, Romania*

***Abstract* – TiO_2 is the most frequently employed photocatalyst in realising complete mineralization of organic pollutants in water treatment. Its large bandgap energy necessitates though UV excitation to induce charge separation within the particle. Nitrogen doped into substitutional sites of TiO_2 has shown bandgap narrowing and photocatalytic activity in the visible light. N-doped and non-doped mesoporous titania were synthesized using hydrothermal and ultrasound methods. Titanium-tetraisopropoxide was used as Ti precursor. UV-VIS and N_2 adsorbtion-desorbtion techniques were used to investigate the structure, morphology and optical properties of these photocatalysts. The photocatalytic activity of mesoporous titania was studied by different dyes photoreactions.**

I. INTRODUCTION

In the environmental technology sector, industrial wastewater treatment is gaining importance for the removal of organic pollutants [1]. Large amounts of organic pollutants consumed in the industries are being released into the eco-system over the past few decades and they constitute a serious threat to the environment [2]. As chemical and agricultural wastes, these contaminants are frequently carcinogenic and toxic to the aquatic system because of their aromatic ring structure, optical stability and resistance to biodegradation [3].

Catalytic technologies are gaining recognition in the field of environmental protection [4]. In past decades, the traditional physical techniques for the removal of organic pollutants from wastewaters have included adsorption, biological treatment, coagulation, ultrafiltration and ion exchange on synthetic resins. Those methods have not always been effective and they may not actually break down the pollutants in wastewater. For example, adsorption technology does not degrade the contaminants, but essentially transfers the contaminants from one medium to another, hence, contributing to secondary pollution [2].

Heterogeneous photocatalysis becomes an elegant alternative for dye degradation. Many photocatalysts have been used to degrade organic pollutants: ZnO, Nb_2O_5, TiO_2 [5-7].

Photocatalytic oxidation in the presence of semiconducting materials such as TiO2, of organic compounds with environmental concern (e.g. pesticides, dyes, etc.), have been studied extensively during the last 20 years [8]. TiO_2 is interesting due its range of applications: ability to split water into H_2 and O_2 [9] and use in dye sensitised solar cell (DSSC) or Graetzel cells [10] being very topical.

Anatase is a metastable low temperature form of TiO_2 and generally accepted as the most suitable for photochemical devices [11,12]. When processing TiO_2 precursors there is a limit to the upper processing temperature. This limit is process dependent e.g. direct oxidation or sol–gel, and varies from 500 to 1000 °C [13]. Low temperature processing is considered valuable, as it affords low energy operations, and an ability to use a wider variety of substrates.

The use of TiO_2 photocatalyst for the degradation of organic pollutant has been studied extensively. However the large band gap of TiO_2 requires higher energy artificial UV light for activation [14].

Doping of TiO_2 with either anion, cation or codoping with different dopants was found to be an effective method to achieve efficient photocatalysts in the visible-light range [10].

There is an increasing interest in the synthesis of N-doped TiO_2 photocatalysts and related areas as these narrow band gap semiconducting materials can be used for visible light photocatalysts [9]. Asahi et al. [15] reported that substitutional doping TiO_2 with nitrogen could narrow its band-gap by mixing of N 2p and O 2p states in the valence band and consequently induce the absorption edge red-shifted to lower energies (longer wavelengths, especially in the visible region), enhancing its visible-light responsive photocatalytic activity. Some studies [16,17] however proposed the appearance of intragap localized N 2p states, related to the photothreshold energy decrease, facilitating the formation of oxygen vacancies.

Many of the dyes used in industry are toxic and carcinogenic, and this poses a serious hazard to aquatic living organisms. The toxicity and impact of dyes released to the environment have therefore been extensively studied [18]. Furthermore, because of the increasingly strict restrictions on the organic composition of industrial effluents, it is essential to eliminate dyes from wastewater before they can be discharged into the environment [19].

Rose Bengal (Acid Red 94) is a tetraiodo-substituted dye of the xanthenes class of dyes. It exhibits unusual spectroscopic and photochemical properties including a large absorption coefficient in the visible region and a high tendency for intersystem crossing to produce a photochemically active triplet excited state. Despite the numerous applications of Rose Bengal dye in various areas, information on its photolytic decolorization is not available in the literature [20]. The molecular formula for this dye is $C_{20}H_4Cl_4I_4O_5$ and the molar mass is 973,67 g/mol.

II. MATERIALS AND METHODS

Mesoporous titania was synthesized using hydrothermal and ultrasound methods. Different blockcopolymers, such as Pluronic P123 and F127, and titanium-tetraisopropoxide as Ti source were used for the TiO2 synthesis. Different types of N-doped and non-doped mesoporous titania were synthesized by varying composition of the surfactant.

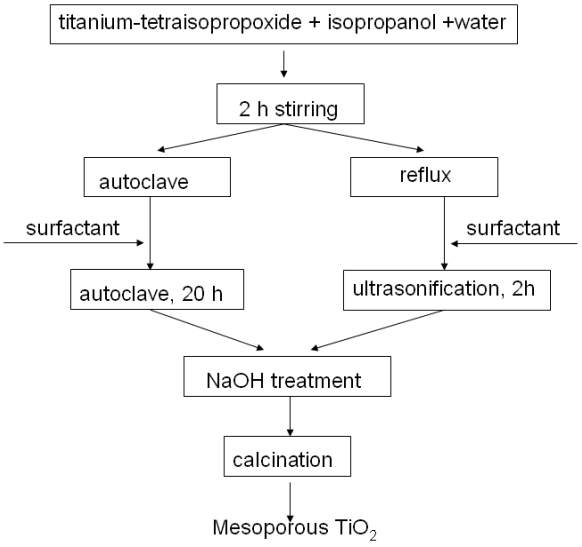

Fig.1. The synthesis procedure for the non-doped mesoprous TiO_2

The obtained mesoporous TiO_2 was used next in the doping step of the synthesis. This involved mixing calculated quantities of TiO_2 and urea such that the Ti: Urea ratio in the final solution was 1:2. This solution was then filtrated. The dry residue was transferred to calcination furnace and heated at 400°C for 4h to obtain the final sample.

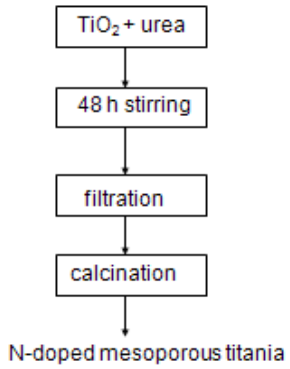

Fig. 2. The synthesis procedure for the N-doped mesoprous TiO_2

III. RESULTS

UV absorption spectrum and N_2 adsorbtion-desorbtion techniques have been used to investigate the structure, morphology and optical properties of these photocatalysts.

The UV–vis spectra of the samples are shown in Fig. 3. The TiO_2 7c sample shows single sharp edges with the band-gap absorption onset at 387 nm (characteristic for TiO_2) ,while the sample containing N exhibits a slight deviation, which indicates the absorption edge extending into the visible region.

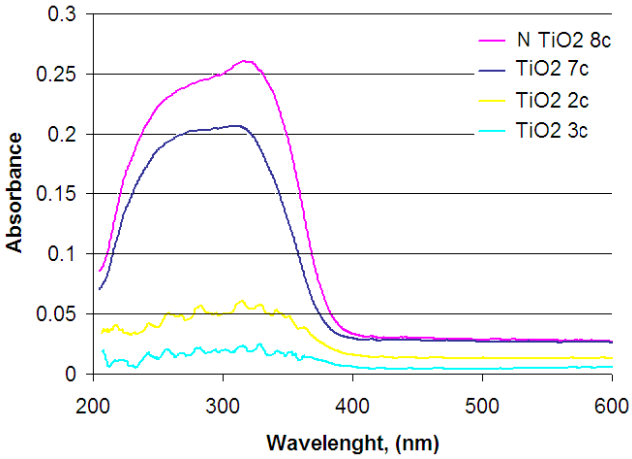

Fig. 3. UV-VIS spectra of some synthetised samples

TABLE 1. SAMPLES NOTATION

Sample	2c	3c	7c	8c
Method	A+A	A+US	REF+US	REF+US
Surfactant	P123	F127	P123	P123

A – autoclave
US – ultrasound
REF – reflux
P123 – Pluronic P123
F127 – Pluronic F 127

In Fig.4. the isotherms for samples 3c, 7c and 8c have been displaced with 50, 150 and 250 cc/g STP.

All the four isotherms can be considered as type IV, which is typical for mesoporous materials.

The large amount of pores of 3 – 7 nm in diameter and the BET surfaces values of 200 – 290 m^2/g demonstrate also the fact that the synthesized samples are mesoporous materials .

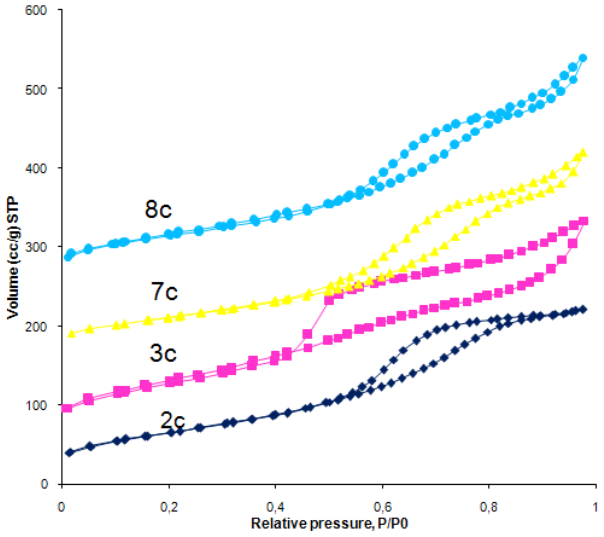

Fig.4. N2 adsorption - desorption isotherms

The photocatalytic activities of both mesoporous titania and N-doped mesoporous titania were studied for the photodegradation of the dye Rose Bengal.

The experiments were conducted using 300 mL dye solution prepared with pure water. The solutions were magnetically stirred in the dark for 30 minutes after adding

the catalyst to ensure the adsorption / desorption equilibrium. Samples consisting in three milliliters of the suspension were taken at specific time intervals and were immediately centrifuged at 2500 rpm for 5 min to completely remove the catalyst particles. Zero time reading was considered to be when the lamp was turned on.

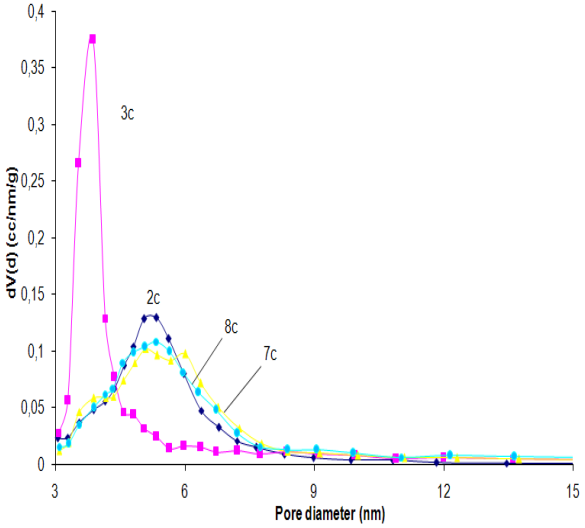

Fig. 5. Pore size distribution (BJH method)

TABLE 2. DIMENSIONAL PROPERTIES OF THE SYNTHESIZED MATERIALS

	2c	3c	7c	8c
BET Surface area (m^2/g)	229,6	290	211	243
Pore diameter (nm)	5,341	3,9	5,1	5,35
Pore volume (cm^3/g)	0,334	0,46	0,424	0,45

From the experimental results it was observed that the N-doped mesoporous titania obtained by ultrasound method has higher photocatalytic activity than the undoped mesoporous TiO_2 (Fig. 6). Moreover, the N-doped mesoporous titania also has photocatalytic activity under visible light, unlike the undoped mesoporous TiO_2 (Fig. 7).

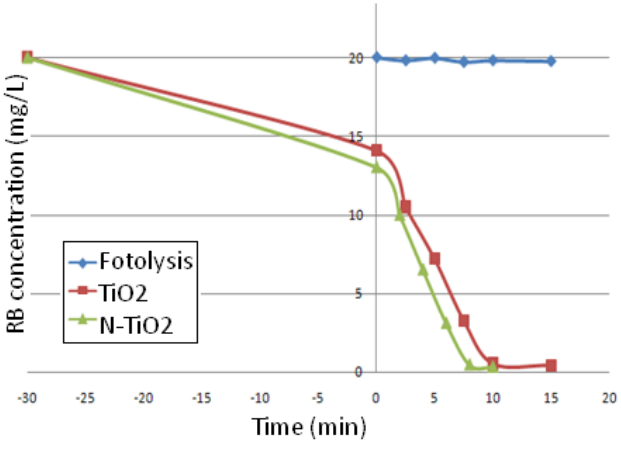

Fig. 6. Photocatalytic activity of N-doped and non-doped mesoporous titania under UV light

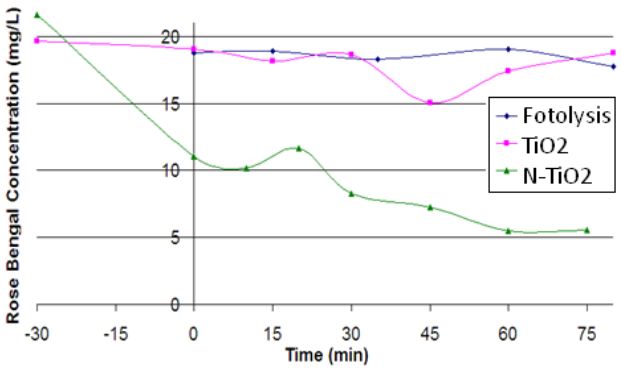

Fig. 7. Photocatalytic activity of N-doped and non-doped mesoporous titania under visible light

IV. CONCLUSIONS

We synthesized N-doped and non-doped mesoporous titania via hydrothermal and ultrasound methods using blockcopolymers (Pluronic P123 and F127) as surfactants and organic sources of Ti.

After the samples characterization it was concluded that all the obtained samples are mesoporous materials, having a large amount of pores of 3 – 8 nm in diameter and BET surfaces values of 200 – 290 m^2/g.

Synthetized mesoporous titania (N-doped and non-doped) were used as heterogeneous catalysts for the treatment of textile wastewater containing dyes. We found that N-doped anatase titania could be prepared by a simple method using titanium tetraisopropoxide and urea. It was observed that the N-doped mesoporous titania obtained by ultrasound method has proven to have photocatalytic activity in visible light, unlike the undoped mesoporous TiO_2.

REFERENCES

[1] M.C. Neves, J.M.F. Nogueira, T. Trindade, M.H. Mendonça, M.I. Pereira, O.C. Monteiro, *Photosensitization of TiO_2 by Ag_2S and its catalytic activity on phenol photodegradation*, Journal of Photochemistry and Photobiology A: Chemistry, vol. 204, no 2-3, 2009, pp 168-173.

[2] N.M. Mahmoodi, M. Arami, *Degradation and toxicity reduction of textile wastewater using immobilized titania nanophotocatalysis*, Journal of Photochemistry and Photobiology B: Biology, vol. 94, no. 1, 2009, pp 20-24.

[3] C.L. Wong, Y.N. Tan, A.R. Mohamed, *A review on the formation of titania nanotube photocatalysts by hydrothermal treatment*, Journal of Environmental Management, vol. 92, 2011, pp 1669-1680.

[4] J.G. Yu, G.H. Wang, B. Cheng, M.H. Zhou, *Effect of hydrothermal temperature and time on the photocatalytic activity and microstructures of bimodal mesoporous TiO_2 powders*, Applied Catalysis B: Environmental, vol. 69, no. 3-4, 2007, pp 171-180.

[5] Aditi & Fernandes, *A simple method to synthesize visible light active N-doped anatase (TiO_2) photocatalyst*, Bulletin of the Catalysis Society of India, vol. 4, 2005, pp. 131-134

[6] G.S. Shao, F.Y. Wanga, T.Z. Ren, Y. Liu, Z.Y. Yuan, *Hierarchical mesoporous phosphorus and nitrogen doped titania materials: Synthesis, characterization and*

visible-light photocatalytic activity, Applied Catalysis B: Environmental, vol. 92, 2009, pp. 61–67.

[7] I.K. Konstantinou, T.A. Albanis, *TiO_2-assisted photocatalytic degradation of azo dyes in aqueous solution: kinetic and mechanistic investigations: a review*, Applied Catalysis. B: Environmental, vol. 49, 2004, pp. 1–14.

[8] M.S. Secula, G.D. Suditu, I. Poulios, C. Cojocaru, I. Cretescu, *Response surface optimization of the photocatalytic decolorization of a simulated dyestuff effluent*, Chemical Engineering Journal, vol. 141, 2008, pp. 18–26.

[9] A. Fujishima, K. Honda, *Electrochemical Photolysis of Water at a Semiconductor Electrode*, Nature, vol. 238, 1972, pp. 37 – 38.

[10] B. O'Regan, M. Grätzel, *A low-cost, high-efficiency solar cell based on dye-sensitized colloidal TiO_2 films*, Nature, vol. 353, 1991, pp. 737–740.

[11] G. Zhao, S. Utsumi, H. Kozuka, T. Yoko, *Photoelectrochemical properties of sol–gel-derived anatase and rutile TiO_2 films*, Journal of Materials Science, vol. 33, no. 14, 1998, pp. 3655-3659.

[12] K.D. Rogers, D.W. Lane, J.D. Painter, A. Chapman, *Structural characterisation of sprayed TiO_2 films for extremely thin absorber layer solar cells*, Thin Solid Films, vol. 466, no. 1-2, 2004, pp. 97-102.

[13] Y.U. Ahn, E.J. Kim, H.T. Kim, S.H. Hahn, *Variation of structural and optical properties of sol-gel TiO_2 thin films with catalyst concentration and calcination temperature*, Materials Letters, vol. 57, no. 30, 2003, pp. 4660-666.

[14] L. Gomathi Devi, B. Narasimha Murthy, S. Girish Kumar, Photocatalytic activity of TiO_2 doped with Zn^{2+} and V^{5+} transition metal ions: Influence of *crystallite size and dopant electronic configuration on photocatalytic activity*, Materials Science and Engineering B, vol. 166, 2010, pp. 1–6.

[15] R. Asahi, T. Morikawa, T. Ohwaki, K. Aoki, Y. Taga, *Visible-Light Photocatalysis in Nitrogen-Doped Titanium Oxides*, Science, vol. 293, no. 5528, 2001, pp. 269–271.

[16] H. Irie, Y. Watanabe, K. Hashimoto, *Nitrogen-Concentration Dependence on Photocatalytic Activity of $TiO_{2-x}N_x$ Powders*, Journal of Physical Chemistry B, vol. 107, no. 23, 2003, pp. 5483–5486.

[17] T. Linsgren, J.M. Mwabora, E. Arendaño, J. Jonsson, A. Hoel, C.G. Granqvist, S.E. Lindquist, *Photoelectrochemical and optical properties of nitrogen doped titanium dioxide films prepared by reactive DC magnetron sputtering*, J Phys Chem B vol. 107, no. 24, 2003, pp. 5709–5716.

[18] S. Tsuda, M. Murakami, N. Matsusaka,K. Kano, K. Taniguchi, Y.F. Sasaki, *DNA damage induced by red food dyes orally administered to pregnant and male mice*. Toxicological Sciences, vol. 61, no.1, pp. 92-99.

[19] C.M. Teh, A.R. Mohamed, *Roles of titanium dioxide and ion-doped titanium dioxide on photocatalytic degradation of organic pollutants (phenolic compounds and dyes) in aqueous solutions: A review*, Journal of Alloys and Compounds, vol. 509, no. 5, 2011, pp. 1648–1660

[20] C. Pastravanu, I. Cretescu, I. Poulios, E. Popovici, *A case study of textile wastewaters treatment by heterogeneous photocatalytic degradation*, Annals of „Dunarea de Jos" University of Galati: Mathematics, physics, chemistry, informatics, fascicle II, year III (XXXII), 2009

Activities in Nanomedicine in Romania

Prof. Dan DASCALU
National Institute for Research and Development in Microtechnologies (IMT-Bucharest), Romania
dan.dascalu@imt.ro

I. ABSTRACT

IMT-Bucharest coordinated the national project "NANOPROSPECT: Nanotechnologies in Romania, a prospective study" (October 2010 – May 2011), whose objective was to put forward strategic orientations and recommendations for a national strategy for nanotechnology, in correlation with the EU strategy. This strategy, apart from the priority research directions, will suggest measures to accelerate innovation, industrialization of R&D results, full use of experimental facilities, multidisciplinary training and the responsible development of nanotechnologies. The "nanotechnologies" theme was approached in the R&D national plans starting 2000, but there was no continuity and focus on the viable thematic areas. There is a need for a plan that would concentrate the research for specific domains with critical mass and interest from industry and society and also a critical need for a strategy that would cover all the important aspects for the development of nanotechnologies at national level.

The project developed databases for collecting information related to Romanian potential in the domain (in terms of organizations, groups and specialists with expertise and results in nanotechnology fields, infrastructures, projects, equipments, scientific papers, patents, products, technologies, courses). These databases, available in English, assure transparency and information exchange, as they are public, interactive and relational, facilitating cooperation at national and international level.

The analysis of human resources in the domain showed the needs for a multidisciplinary education at various levels and interdisciplinary training by research, the need to support the young researchers and specialists returned in the country after performing long term studies or research activities abroad. The interaction between education, research and industry is essential for the improvement of human resources training, in order to assure the technological competitiveness.

"NANOPROSPECT" inventory showed the existence of approximately 300 equipments devoted for nanotechnology at national level and the most efficient way to benefit from the equipments could be the set-up up of experimental facilities networks.

A selection for the domains with active and multidisciplinary communities is necessary and an innovative ecosystem can be created, based on a critical mass and on competitive advantages.

One of the key strategic priorities proposed by "NANOPROSPECT" is "**Nanomedicine**", the application of nanotechnology to achieve breakthroughs in healthcare.

The data collected in the project and from other previous interactions with the main players in the domain revealed a great capacity, involvement and interest for developing the nanomedicine field in Romania. Approximately 40 Romanian organizations (research institutes, universities and SMEs) and 120 specialists are active in nano-biosystems / nanomedicine, developing 60 national and 11 international R&D projects since 2007. They benefit from state-of-the-art equipments, developing products and technologies and also registered 22 national patents.

The cooperation between the main active organizations started in 2005 in the frame of the Romanian nanomedicine network RO-NANOMED, which financed small research projects devoted to the three priority areas of the European Technology Platform (ETP) for Nanomedicine: targeted drug-delivery, diagnostics, regenerative medicine. This network also supported the partial set-up of *NanoBioLab*, a dedicated laboratory in the clean-room area of IMT-Bucharest, which provides an adequate environment and new equipments for the fabrication and testing of microarrays and lab-on-chip devices. Activities in nanomedicine are mainly developed at IMT by two laboratories from the Centre of Nanotechnologies (under the aegis of the Romanian Academy). *The Laboratory of nanobiotechnologies* is involved in projects related to the development of microfluidic chips on silicon for electrophoretic separation of DNA fragments and PCR amplification, development of substrates for alternatives methods of diagnosis base on microarray technology, multifunctional nanoparticles for drug delivery and *the Laboratory of molecular nanobiotechnology* develops Silicon-based lab-on-chip devices, bio-sensing devices for real-time detection.

Some of the Romanian research organizations are members of the ETP NanoMedicine, contributing to the activities developed in the platform and attending events and meetings of the working groups they are involved in. IMT-Bucharest is representing Romania in the Mirror Group of platform, promoting the potential for international cooperation of the Romanian institutions.

Transnational projects in nanomedicine with Romanian participants could be supported by EuroNanoMed ERA-NET initiative, where Romania participates as partner. This initiative fosters the competitiveness of European nanomedicine players through the support of collaborative and multidisciplinary Research and Technology Development (RTD) projects with participants from academia, clinical/public health communities and industry.

Health Technology Management

Victor ŞONTEA[1,4], Petru STRATULAT[2,4] Reinhold WERLEIN[3,4]
[1]Technical University of Moldova, [2]State University of Medicine and Pharmacy „N.Testemiţanu”, [3] Swiss Tropical and Public Health Institute, [4] Moldova-Swiss Perinatology Project
sontea@mail.utm.md

Abstract – Maintenance, Verification and Health Technologies Management became priorities in health policies of many countries, many studies show that coherent policies in this domain may improve the proportion price – efficiency of utilization of advanced medical technologies, improve the safety of patients and last not least raise the quality of the medical service. In the framework of reforms in the health system, and of major investments in medical devices, which took place in the last years in the Republic of Moldova, the promotion and introduction of a comprehensive health technology management at all levels of the health system is vital. The importance given to medical devices must be similar to the importance given to drugs and infrastructure.

Keywords – maintenance, verification, management, medical technologies, medical devices

I. INTRODUCTION

The worldwide industry of healthcare, with an annual financial value of roundabout $250 billion and an annual growth of 7%, is one of the few areas that are expected to grow for a long time. Healthcare includes 15 000 registered manufacturers, about 10 000 generic devices and over a million of products and brands[1]. About 50% of all diagnosis and treatment methods used today didn't exist 10 years ago. Annual allocations in Medical Technologies Management are 50-200 Euro per capita in EU.

Maintenance, control and management of medical technologies have become a priority in the healthcare policy of many countries; many studies prove that usage of coherent policies in this area, will improve the cost/efficiency ratio of usage of advanced medical technologies as well as patients' security and the overall quality of the medical act [2-3].

World Health Organization uses the term of "Medical Technologies", which is defined as "devices, medications, medical or surgical procedures – and knowledge associated with those – used in prevention, diagnosis, or treatment of infections, rehabilitation procedures and organizational systems used for providing attendance". Anyway, the term of "Medical Technologies" used within the boundaries of this article refers only to the physical hardware (from WHO's definition), which has to be maintained. Medication is usually covered by separate policy initiatives or is controlled from different departments.

II. THE SITUATION ON NATIONAL AND INTERNATIONAL LEVELS

Therefore, as shown in a report published on the site of WHO, despite the billions of dollars annually spent on medical devices and equipment, the vast majority of countries still regard management of medical devices as an acquisition question rather than an integrated part of the public healthcare policy [4]. More than 95% of medical technologies in developing countries are imported; a large part of these do not match the actual needs of their national healthcare system. It has been estimated that in developing countries about 50% of medical equipment is non-functional, used incorrectly and is poorly maintained – a situation with grave consequences for patients care. This is why the existence of a national policy regarding management of medical technologies is essential; the policy would include e.g. appropriate acquisition procedures, rules and regulations for effective maintenance, control and correct usage of medical technologies, training of specialized personnel and creation of a continuing education.

Another report, from the American Medical Resources Foundations (AMRF), shows that in most cases hospitals in low- and middle income countries do not have the means for maintenance and repair of the provided medical devices, in terms of qualified personnel, appropriate devices for testing and calibration, management structures and financial resources. In these circumstances, services offered by representatives of device manufacturers have an extremely high price in these countries. An inadequate maintenance of medical devices leads to a decrease in the patient's security. AMRF has proven through pilot studies in hospitals from several developing countries (where it trained personnel and provided equipment for testing, calibration and control) that expenses for the above-mentioned services were greatly reduced. These pilot centers became, at the same time, training centers for local personnel. According to the European Alliance for Medical and Biological Engineering & Science, training of specialists in Biomedical Engineering in 2005 was performed in 195 universities in 28 countries from Europe. While the number of students in engineering departments was quite constant in the last 10 years, the number of students in Biomedical Engineering has increased 8 times. Internationally, concepts for training of specialists and international accreditation and evaluation criteria are being developed.

The situation in the Republic of Moldova is similar to those of other in low- and middle income countries; although important sums are invested in medical technologies, maintenance and control of medical devices are not provided. At present, there are 250 active medical institutions, more than 180 enterprises and firms, whose occupation revolves around import and installation of medical technologies, and over 35 enterprises and firms licensed for maintenance in medical technologies. Also, as a new direction, the scientific-applied domain of elaboration and manufacturing of new biomedical technologies is being developed (the Academy of Sciences of Moldova, research

and branch production institutes, other private firms and enterprises). At present, there is a severe lack of specialists in the field of biomedical systems and devices, since specialists in the corresponding field have not been prepared.

Among the major problems and difficulties regarding the management of medical technologies in Moldova can be mentioned:

- A severe lack of specialists in the field of maintenance, control and diagnostic of biomedical devices, including those recently imported;
- Non-existence of a coherent policy regarding development of activities in this field, including conformation, evaluation and preventive/corrective maintenance;
- Non-existing or weak managerial and technical competence for control and maintenance of medical devices on the level of all hospitals, or insufficiently used competences where actually present;
- Non-existence of regulations for continuous improvement, which is mandatory for specialists who are active in technical service of medical devices, inclusively for specialists who are active in the field of marketing and operation of medical devices;
- Services offered by the providers of medical devices are costly and often late.
- No monitoring of timeliness and quality of services provided

III. ORGANIZATION OF HEALTH TECHNOLOGY MANAGEMENT

Health Technology Management involves organizing and coordinating the following activities, which ensures the successful management of medical devices:

- Gathers basic information about equipment;
- Plans technological needs and adequate resources for them;
- Purchases suitable models and installs them effectively;
- Provides sufficient resources in order to use them;
- Operates with them safely;
- Maintains and repairs equipment;
- Resigns, liquidates and replaces unsafe and obsolete parts;
- Ensures that staff has the skills to use the equipment correctly.

Management of Medical Technologies includes several components: (Fig.1).

Based on actual information from various soures, causes of defects and accidents with medical equipment can be classified as follows:

10% - Technical failures;

30% - Inappropriate maintenance strategy;

60% - User's fault.

A correct implementation of management of medical technologies allows 80% of problems to be solved by 20% of the resources.

The reference system in the policy for maintenance of medical devices is shown in fig. 2.

The strategy for maintenance of medical devices implies the following levels:

Maintenance on user level, which implies competent users (with good knowledge of medical and technical rules of use of the device) – information and preceding training of all users (authorization, accreditation), permanent access to information of use of the device (folders which include a summary of functionality, user manual, Internet etc.). Respecting the norms of control and use, specific norms of maintenance, cleaning and sterilization are mandatory.

Preventive maintenance imply competent technical personnel, accredited according to national norms, and maintenance of devices including cleaning and component lubrefiation; *of calibration and control of functionality in terms of safety, of replacing spare partss, accumulators etc.*

Corrective maintenance implies specialists authorized by medical device manufacturers, repairs in the warranty and post warranty periods, overhauls, upgrades.

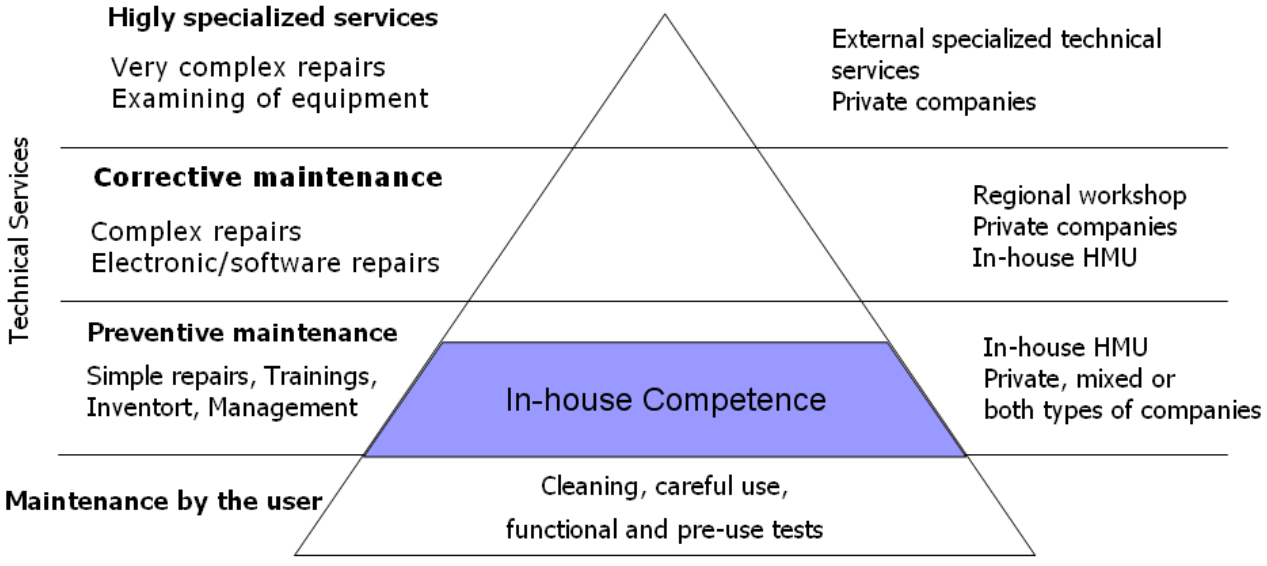

Fig.1.The structure of Management of Medical Technologies (with courtesy of SwissTPH)

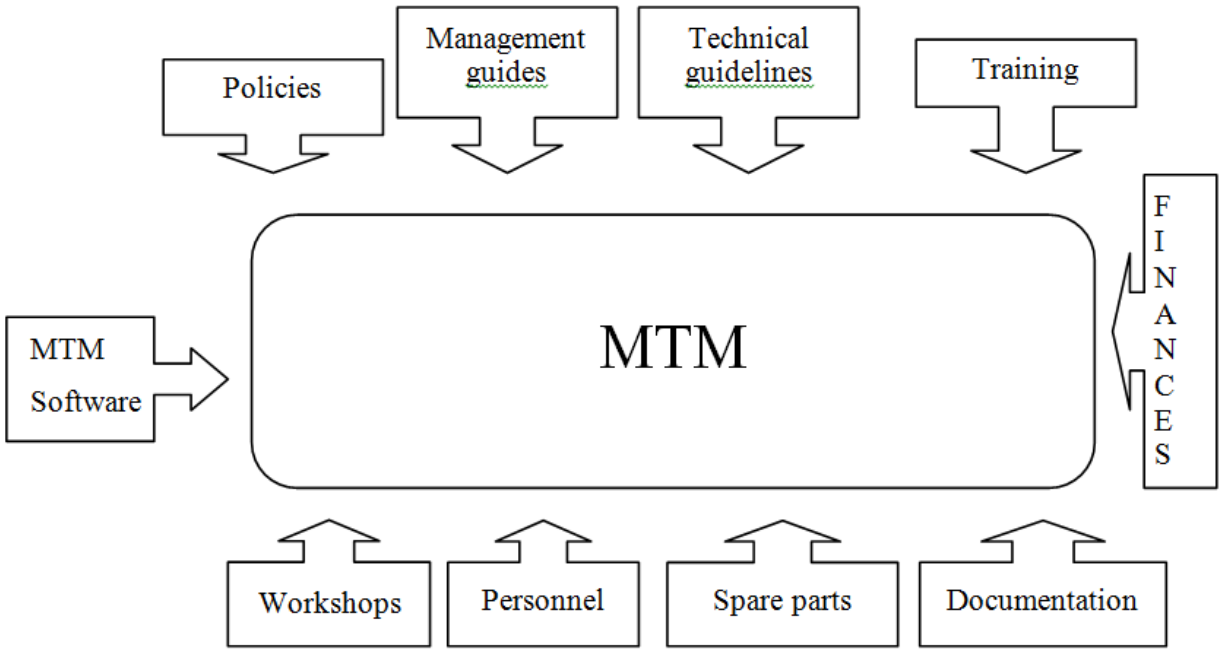

Fig.2. Reference system in the policy of maintenance of medical devices (with courtesy of SwissTPH)

The implementation of Health Medical Technologies has the following objectives:

1. Framing of activities within national (European) and local norms regarding management of medical devices.
2. Framing of usage activities and service within norms recommended by medical devices manufacturers, within a framework of a maintenance adequate to the device;
3. Reduction of inadequate use of modern technologies and ensuring a continuous and effective availability of medical equipment for services corresponding to the field of healthcare;
4. Monitoring of the activities of maintenance, correction of errors, development of specific protocols, and prediction of costs.

For a complete objective fulfilment an implementation of the strategy of mixed medical device maintenance is proposed – basic maintenance by own personnel with creation and development of a Department (workshop, section) of Management of Medical Technologies and specific maintenance through authorized firm specialists.

At the first stage, it is necessary to implement an organizational structure of Management of Medical Technologies as a component of Quality Management with defined activities and responsibilities and bonds on each level (fig. 3)

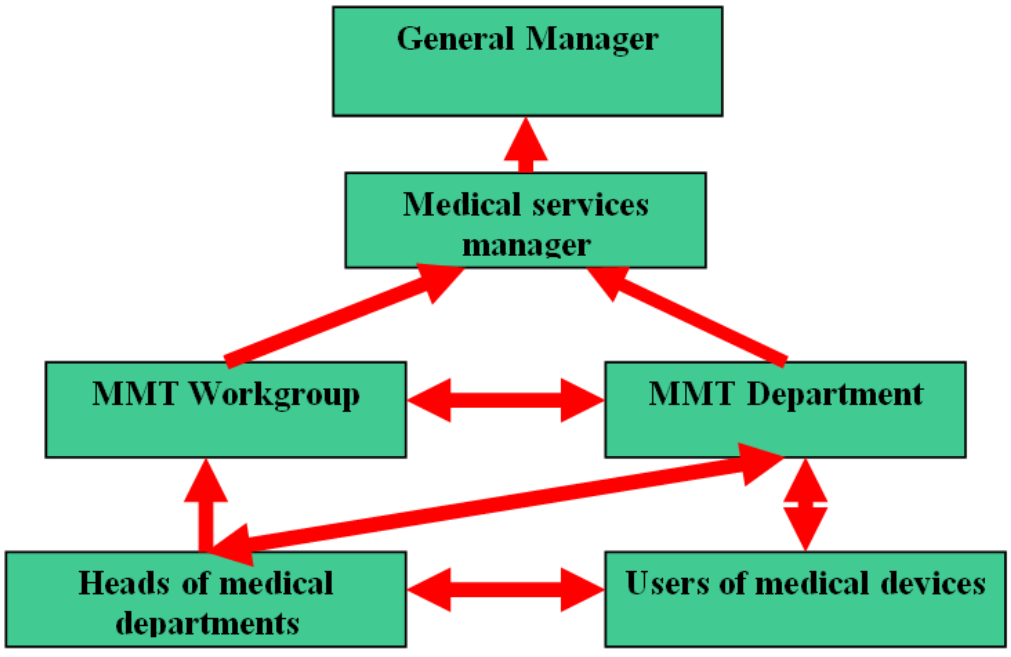

Fig.3 Organizational structure of MMT on a hospital level

At the second stage, an implementation of norms in MMT is necessary:

1. Local norms (at the level of medical unit, department):

- Regulation on organization and functioning of Organizational Structure
- Rules of Procedure regarding Organizational Structure
- post descriptions of all personnel from Organizational Structure
- Call log
- Maintenance file of the Medical Device
- User guides
- Medical device usage log
- Maintenance report
- Medical device service file
- Annual plan of medical device maintenance
- Annual plan for necessity of consumables
- Electronic evidence log of the medical device
- Electronic registry of medical devices
- Electronic registry of consumables and spare parts
- Maintenance protocols specific to the medical unit

2. National norms:

- Decree of the Government of the Republic of Moldova nr. 96, from January 26, 2007 "Regarding establishing of terms for market placement and usage of medical devices"
- Regulation regarding establishing of terms of market placement and usage of medical devices in the Republic of Moldova.

3. European(international) norms:

- Active Implantable Medical Devices (AIMDD**) .** Directive 90/385/EEC - OJ L189/ 20.7.90
- Medical Devices Directive (MDD). Directive 93/42/EEC - OJ 169/ 12.7.93.
-

IV. IN VITRO DIAGNOSTIC DIRECTIVE (IVDD). DIRECTIVE 98/79/EC - OJ331/ 7.12.98

Expected results

- Medical institutions can offer all required medical services, and are not limited by non-functional technologies;
- Equipment is correctly used, correctly maintained and verified;
- The personnel use equipment to its maximum capacity, following written procedures and good practice;
- Health service institutions are provided with adequate information regarding:
    1. functional state of the equipment;
    2. Performance of the maintenance services;
    3. requried abilities and experiences of the personnel using the equipment;
- A reduction of medical devices maintenance expenses, redirection of works connected to preventive maintenance, which are 70% of all maintenance expenses (service, repair of medical devices) towards solving by specialists from the medical institution.
- The personnel controls the immense financial investments in equipment, which leads to a more qualitative and efficient service, as well as a lowering of financial allocations regarding to maintenance of medical devices.

V. PROPOSALS REGARDING DEVELOPMENT IN MMT

1. Promotion of the profession of *biomedical engineer* within the national healthcare system in relation to the requirements and quality standards of the medical act, equalizing the status of a bioengineer with the one of a doctor in the field of healthcare.
2. Development of a policy adequate to the norms of EU, regarding the progress of activities in the domain of MMT and standards in the field.
3. Establishing of a "Department of Medical Technologies" charged with all tasks and problems connected to management and administration of Medical Technologies; at the first stage on the level of national, municipal and district (group of districts) health institutions,
4. To reduce expenses of maintenance of medical devices, it is necessary to introduce stringent preventive maintenance (service and repair of medical devices have to be performed by specialists from the medical institution), which represent 70% of maintenance expenses.
5. Creation of an information system "Management and administration of Medical Technologies"
6. Development of a regulation of continuous training, mandatory for specialists who woirk in the field, including specialists active in the field of marketing and operation of medical devices.

ACKNOWLEDGMENTS

This work was supported by the Swiss Development Cooperation (SDC) who financially supported HTM in the frame of the two projects in R. of Moldova.

IV References

1. **GMDN Agency, "Medical Technology Brief," 2007**
2. Temple-Bird, CL. Practical steps for developing health care technology policy, Institute of Development Studies, University Sussex.UK. 2000
3. Raab M. Maintenance strategies. Swiss Centre for International Health. 1999
4. World Bank An Overview of Medical Device Policy and Regulation, February 2007

Micro-Spectroscopy of Single Erythrocytes Infected with the Malaria Parasite

[1]Silki ARORA, [1]Sang Hoon PARK, [2]Jennifer MAUSER, [2]Debopam CHAKRABARTI, [1]Alfons SCHULTE

[1]*Department of Physics and College of Optics and Photonics,* [2]*Burnett School of Biomedical Sciences, University of Central Florida, Orlando, Fl 32816-2385, USA*

sarora@knights.ucf.edu, afs@physics.ucf.edu

***Abstract* – The erythrocytic cycle of the malaria parasite *Plasmodium falciparum* is marked with structural, mechanical and biochemical modifications to the host red blood cell. The parasite degrades the hemoglobin of the host cell and hydrolyzes it into hemozoin. We investigate healthy and infected erythrocytes using micro-Raman and spatially resolved absorption spectroscopy. The electronic absorption spectrum of a single cell is measured and spectral changes are related to the parasite life cycle. The Soret absorption band in the trophozoite stage is shifted to higher wavelength by 3 nm. The findings are compared with micro-Raman spectra that show consistent changes in the heme vibrations. Micro-absorption may offer a potential diagnostic marker for identifying pathological states accompanying malaria.**

***Index Terms* – Absorption microscopy, diagnostics, erythrocyte, malaria parasite, Raman spectroscopy.**

I. INTRODUCTION

Red blood cells are relatively simple biological structure as they are non-nucleated and lack intra-membrane organelles. They are biconcave shaped disks which optimizes the flow properties in the vessels. They are the principle means of delivering oxygen to the organs and mainly consist of hemoglobin, a globular protein. The malaria parasite *Plasmodium falciparum* introduces mechanical changes in the host red blood cell [1, 2] making it difficult for the cells to pass through the vessels. This indeed affects the oxygen transporting capability.

Malaria is responsible for over a million deaths every year mostly infants, pregnant women and young children in areas endemic for the parasites [3]. Close to half of the world's population still lives in areas with high risk of contracting malaria. According to a world health Organization report 2009 a child dies of malaria every 30 seconds. According to the U.S. Center for Disease Control and Prevention, more than 1,400 new cases are reported annually in the United States in travelers returning from malaria-endemic areas.

The human malaria parasite has a complex life cycle that requires both a vector body (female anopheles mosquito) and a host body. The sexual reproduction of the parasite occurs in the mosquito body and the resulting sporozites are inoculated into the human host when bitten by the infection carrying mosquito. These sporozites infect the liver cells and mature themselves into schizonts, each containing thousands of merozites, which are released into the blood stream through rupturing. These merozites invade erythrocytes and goes through another round of asexual reproduction in the erythrocytic cycle.

During the intra-erythrocytic stage of the life cycle the malaria parasite degrades the hemoglobin. Hemoglobin degradation by the parasite during the intra-erythrocytic cycle has been studied through experimental techniques and mathematical models and simulations. Studies suggest that hydrolysis of globin provides the principal source of amino acids for erythrocytic development and also provide

sufficient space for the parasite growth [4]. Hemoglobin degradation is also essential to maintain osmotic stability of the intra-erythrocytic parasite [5]. Breaking down of hemoglobin is a complex process which involves transport of hemoglobin from cytosol to the parasite food vacuole, disruption of hemoglobin tetramers, removal of heme, detoxification of heme by the formation of hemozoin and the hydrolysis of globin by a number of proteases into amino acids.

We probe hemoglobin degradation due to the parasite growth in the erythrocytes employing non invasive optical techniques. Electronic absorption spectrum of healthy erythrocytes and cells infected with the parasite are presented which can be correlated to parasite multiplication cycle. Micro-Raman spectroscopy was further employed to investigate changes in the vibrational band with hemozoin formation.

II. MATERIALS AND METHODS

Parasites are maintained in human A+ erythrocytes at 5% hematocrit in complete RPMI-1640 (Invitrogen) supplemented with 0.5% Albumax (Gibco). Cultures are split every other day to maintain a parasitemia of 2-5%, as monitored by Geimsa stained smears, and freshly washed RBCs are added. A+ whole blood was obtained from Florida Blood Centers on a monthly basis. Whole blood is washed in incomplete RPMI to remove unnecessary components and RBCs are resuspended in complete RPMI-1640 to 50% (2% Dextrose, 15mg/L Hypoxanthine, 0.2% Sodium Bicarbonate, 25mM HEPES, 25ug/ml gentamycin). Parasites were synchronized on a MACs LD Separation Columns (Miltenyi Biotec) in late trophozoite stage. Columns were placed on a magnetic stand and equilibrated with 5ml of complete media. Parasite cultures were pelleted and resuspended in 5 ml fresh media and applied to the column. Flow through containing uninfected RBCs, ring and early trophozoite stage parasites was discarded; late trophozoites remained bound to the column. The column was then washed with 5ml of complete media. The column was removed from the magnetic stand and parasites were eluted with 5ml complete media. Freshly washed erythrocytes were added to the synchronized culture to obtain 4% hematocrit. The following day Geimsa stained smears of the culture were prepared to evaluate parasitemia.

Raman spectra of individual healthy and parasite infected erythrocytes were recorded on a LabRam HR 800 setup

using 632.8 nm excitation from helium neon laser (4 mW). The Raman system is coupled with an Olympus BX 41 microscope with a 100x dry objective (NA = 0.9). The vertically polarized laser is directed internally using a set of mirrors and focused through a lens onto the sample. The Raman signal collected by the microscope objective in back scattering configuration through the same optical path and through a holographic notch filter to the 100 μm confocal pin hole of the spectrometer. Spectra were recorded between 1800 and 650 cm^{-1} with a resolution of 1.5 cm^{-1}. A fused silica micro capillary with an inner bore of 50 μm and outer diameter 350 μm was used a nano liter sample holder. An optical window was created by burning the outer coating and wiping the capillary through ethanol. The sample was loaded in a micro capillary by dipping one end in the sample culture allowing capillary action to draw the cells up. The small volumes and small optical window allows us to investigate individual cells without interference from the neighboring cells.

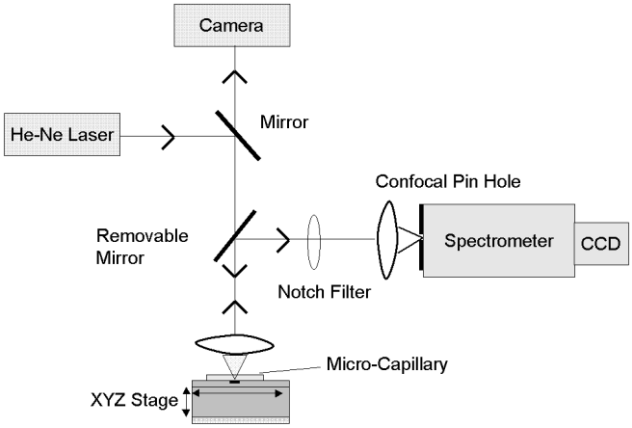

Fig. 9. Schematics of the micro-spectroscopy setup. Raman scattering is excited by a He-Ne laser and the signal is collected in a back-scattering geometry. Micro-absorption spectra are measured in transmission geometry.

Confocal absorption microscopy was employed to measure optical absorption spectrum with spatial resolution at the micron scale [6] to investigate the changes in the electronic absorption bands of host red blood cells after parasite infection. It couples confocal microscopy with broadband illumination in transmission geometry. It enables the measurement of the absorption spectrum of a single erythrocyte between 350 and 700 nm with a lateral resolution better than 1.5 μm.

Micro-absorption spectra were measured on red blood cells immobilized on a coverslip using standard procedures. The coverslip was rinsed with 70 % Ethanol followed by 1X Phosphate Buffer Saline (pH 7.4). Sufficient 1mg/ml poly-L-Lysine HBr was applied to coat the coverslips which were then kept at room temperature for 15 minutes. Coating solution was removed and the coverslips were rinsed with 1X PBS. The erythrocytes suspended in 1 X PBS were added to the coverslips and were allowed to adhere at room temperature for 20 minutes. Excess liquid was drained from the coverslip. The transmittance of an individual red blood cell was measured with a spectral resolution of 0.5 nm. Micro-absorption spectra were recorded of erythrocytes immobilized both on coverslips and in micro-capillaries and found to be in agreement.

III. RESULTS AND DISCUSSION

Optical microscopy images of healthy human RBC and RBC infected with malaria inducing parasite *Plasmodium falciparum* are shown in Fig. 2. The cells are contained in a micro-capillary of inner bore 50 μm. Image on the right shows the cell with the parasite in it at 24 hr post invasion. Through optical images without stains it is difficult to discern between healthy and infected cells and to correlate them to parasite multiplication cycle. The results that follow show the micro-absorption as a potential diagnostic marker for different stages of parasite multiplication cycle.

Micro-Raman spectra of a healthy red blood cell and a cell

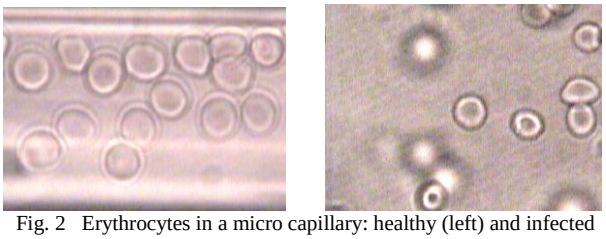

Fig. 2 Erythrocytes in a micro capillary: healthy (left) and infected (right). The diameter of a single cell is ~ 7 μm.

nfected with *Plasmodium falciparum* are shown in Fig. 3 left panel). The excitation wavelength was 633 nm. The ɔands in the spectra mainly arise from porphyrin vibrations 7]. The Raman scattering enhancement observed at 632.8 ım may result from excitonic coupling between aligned ɔorphyrins due to the close proximity of heme moieties [8]. The vibrational bands are indicative of hemoglobin, the najor protein in the cell. They can be grouped into the ollowing regions: 1500 – 1650 cm^{-1}: core size or spin state narker band region. 1450 – 1300 cm^{-1}: pyrole breathing node region, ν_4. 1300 – 1200 cm^{-1}: methine C-H leformation region. 1450 – 1300 cm^{-1}: pyrole ring breathing node, ν_{15}. The peak positions are dependent on oxidation state. While a band at 1545 cm^{-1} is the most intense peak in deoxygenated cells, the spectra show clearly two different peaks at 1548 cm^{-1} and 1565 cm^{-1}. The ν_{13} mode of the oxygenated heme has a frequency of 1224 cm^{-1} compared to 1211 cm^{-1} in the deoxy state. These peaks are representative of those seen in oxygenated cells as these bands are dependent on oxidation state and on whether the heme has bound oxygen [8]. The 1500 - 1650 cm^{-1} region is dominated by the core size (or spin state marker band). There are clear differences between *Plasmodium falciparum* infected and uninfected cells in this region, and in the broadening of the peaks near 1210-1230 cm^{-1} (C-H methine deformation band) and 755 cm^{-1} (pyrrole ring breathing mode). The spectral changes are in agreement with those reported by Wood and co-workers in independent experiments [9]. As the hemoglobin is broken down by the parasite, the protein chain fragments are transported away for further digestion. The remaining toxic heme is then oxidized to a ferric state. The release of the heme from the protein is the first step in the formation of hemozoin. The changes in the spectra could be the result of this degradation and the changes in the vibrational modes of the now free heme. As the heme rings are no longer bound within the pocket of the protein the constraints on the various bonds will be much more random which accounts for the broadening of the bands.

The right panel in Fig. 3 shows the micro-absorption spectrum of individualerythrocyte in the healthy and infected state. An individual live erythrocyte under physiological condition was illuminated using broadband excitation and

the transmitted light intensity was collected using the spectrometer with 5 seconds acquisition time. The spectrum was obtained over the visible range from 350 to 700 nm.

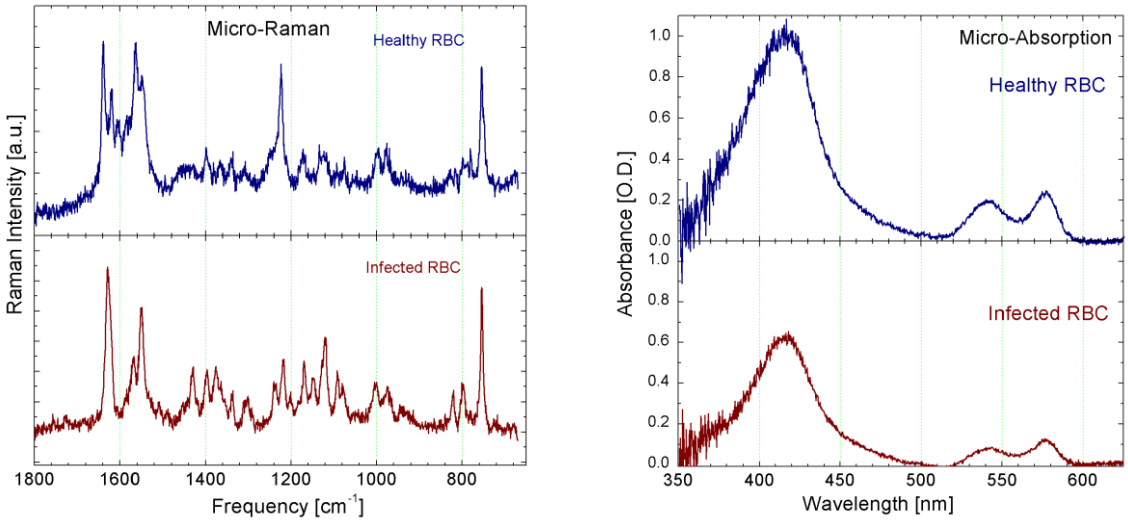

Fig. 3 Micro-Raman (left) and micro-absorption (right) spectra of single erythrocytes. The top spectrum in each panel is from a healthy erythrocyte. The spectra at the bottom are from erythrocytes infected with malaria parasite *Plasmodium falciparum.*

The electronic absorption spectra of porphyrins feature two weak visible transitions near 555 nm and the intense Soret transition near 400 nm [10]. The intense absorption bands result from to π to π* transitions and can be distinguished from the weak bands due to charge-transfer transitions. The spectra depend on the electronic configuration of the iron cation and can be correlated to the spin state [10]. The absorption spectrum of the healthy red blood cell is indicative of oxygenated hemoglobin with the Soret band at 415 nm and β- and α-bands at 541 and 577 nm, respectively. The ratio of relative intensities of β- and α-bands was calculated to be 0.87 as compared to the literature value of 0.92 [11].

Changes in peak positions and relative peak intensities were observed in the case of cells in pathological conditions. The Soret band was weaker than in uninfected sample and was shifted to 418 nm. The β- and α-bands moved to 543 and 576 nm, respectively. The ratio of the relative intensities of the two bands decreased to 0.67. The peaks were broader and less intense in the infected sample.

Understanding the structural changes in the degradation of hemoglobin may opens new targets for anti-malarial drug treatments. Observing the cells in a native-like environment facilitates the transfer of new diagnostics for faster detection of the parasite's presence in the human body.

IV. CONCLUSION

Micro-Raman and micro-absorption were combined in a comparative analysis of healthy RBCs and RBCs invaded with the malaria parasite. Both techniques are sensitive to heme degradation occurring during the multiplication cycle of the parasite. The spectral changes observed in the micro-absorption spectra may enable a diagnostic probe at the single cell level.

V. REFERENCES

[1] Y. K. Park, M. Diez-Silva, G. Popescu, G. Lykotrafitis, W. Choi, M. S. Feld, and S. Suresh, "Refractive index maps and membrane dynamics of human red blood cells parasitized by Plasmodium falciparum," *Proceedings of the National Academy of Sciences*, vol. 105, pp. 13730, 2008.

[2] S. Suresh, "Mechanical response of human red blood cells in health and disease: some structure-property-function relationships," *J. Mater. Res*, vol. 21, pp. 1871, 2006.

[3] "US Department of Health and Human Services National Institutes of Health National Institute of Allergy and Infectious Diseases NIH Publication No. 02-139," 2002.

[4] I. W. Sherman, *Molecular approaches to malaria*: Amer Society for Microbiology, 2005.

[5] V. L. Lew, T. Tiffert, and H. Ginsburg, "Excess hemoglobin digestion and the osmotic stability of Plasmodium falciparum–infected red blood cells," *Blood*, vol. 101, pp. 4189, 2003.

[6] S. Arora, J. Mauser, D. Chakrabarti, and A. Schulte, "Spatially resolved micro-absorption spectroscopy with broadband source and confocal detection," to be submitted.

[7] B. R. Wood, B. Tait, and D. McNaughton, "Micro-Raman characterisation of the R to T state transition of haemoglobin within a single living erythrocyte," *Biochimica et Biophysica Acta (BBA) - Molecular Cell Research*, vol. 1539, pp. 58, 2001.

[8] B. Wood, D. McNaughton, "Raman excitation wavelength investigation of single red blood cells in vivo, " *J. Raman Spectrosc*., vol. 33, pp. 517, 2002.

[9] B. R. Wood, S. J. Langford, B. M. Cooke, J. Lim, F. K. Glenister, M. Duriska, J. K. Unthank and D. McNaughton, "Resonance Raman Spectroscopy Reveals New Insight into the Electronic Structure of β-Hematin and Malaria Pigment," *J. Am. Chem. Soc.*, vol. 126, pp. 9233, 2004.

[10] M. W. Makinen, A. K. Churg, A. B. P. Lever, and M. B. Gray, "Iron Porphyrins Part 1," Addison-Wesley Publishing Co., Mass, 1983.

[11] E. Antonini and M. Brunori, *Hemoglobin and Myoglobin in their Reactions with Ligands*: North-Holland Pub. Co., 1971.

Ultra Violet Radiation Regulates Wettability Property of Prosthetic PMMA.

Yuri DEKHTYAR, Linda LANCERE, Nataliya POLYAKA, Alexander SUDNIKOVICH, Fyodor TYULKIN

Riga Technical University, Str.Ezermalas 6, LV-1014

dekhtyar@latnet.lv, linda.lancere@gmail.com, natalija.polaka@rtu.lv, aleksandr.sudnikovich@latnet.lv, kgam@inbox.lv

***Abstract* – Prosthetic poly (methyl methacrylate) is widely used for medical applications like lenses and eye prostheses. For prosthetic products biocompatibility is essential, different methods have been developed to control it by controlling surface wettability property. This article is targeted to describe a possible simple solution how to influence alterations of PMMA wettability by non-ionizing UV radiation in range of 200-400nm. Processed material was examined by means of detecting contact angle, electron work function and absorption spectra to find correlation between wettability and other surface properties. Results show non-linear tendency of surface wetting alteration and peculiarities in electron work function and absorption spectras. UV radiation could be used to functionalize PMMA surface by not influencing its structure with UV exposures under 60 minutes.**

***Index Terms* – Poly(methyl methacrylate), wettability, UV radiation, surface properties, electron work function**

I. INTRODUCTION

Poly (methyl methacrylate) is a widely used material in various fields. Because of its good biocompatibility, PMMA is used for prosthetic applications, the ways to enhance surface properties of PMMA are being searched. Basically surface properties are the ones that influence interaction between polymer and environment and the ones to be modified [1]. Surface wettability is of high importance in oral prosthetics [2], eye lenses [3], etc.

Wettability depends on material's surface energy that, in turn, could be influenced by the electrical charge, deposited on to the surface. Evaluating material's electron work function, connected with surface charge and surface potential, may show regularity between the described above and might be used to control wettability.

Ultraviolet (UV) radiation has already been used for surface charge modification [4-5], though more unsophisticated method and insufficiently investigated wavelength range 200 – 400 nm to be employed is described in this article.

II. METHODS AND MATERIALS

The specimens were prepared in identical manner as eye prostheses.

After polymerization of commercial powder "Stoma" mechanical treatment was applied (slipping and polishing) to reach the specimens with diameter of ~1cm. The specimens were cleaned with 96% ethanol to remove foreign bodies.

After that irradiation process was implemented in room air (+ 20^0C +/-2^0C) by means of Hamamatsu Spot Light Source equipped with Hg-Xe lamp with intensity 3.5W/cm^2 at 365nm. Specimens were placed at 0,4 m distance to avoid overheating and ensure room temperature on the PMMA surface. Irradiation was amassed by different exposure sessions (15, 30 or 90 minutes of exposure was accumulated).

Wettability was tested before and after UV irradiation using Axisymmetric Drop Shape Analysis-Profile (ADSA-P) method. This method was adjusted to use in set with optical microscope MMI-2 and CCD camera (Imaging Source) to project drop to the PC. Optical microscope was used to define the drop of physiological solution (~10mm in diameter). Measurements were repeated 15 times, contact angle each time was applied in the Photoshop software (CS3). Before measurements each sample was cleaned with distilled water.

The hand-made spectrometer [6] ensured induction of photoelectron emission from the PMMA material to measure electron work function that is directly proportional to a surface charge.

To reveal possible reconstruction of the chemical couples optical absorption was measured in a range of 200 – 400nm with a step 0.5nm Helios photo spectrometer was used. The data of the spectra were collected with VISIONlite (Scan Version 2.1) software, after that digital data were imported to Excel for further processing. PMMA specimens before and directly after each irradiation session were measured.

To evaluate alterations of surface morphology and distribution of the charge/potential over the surface at the nano/micro scale, the specimens were scanned using Solver P-47 Pro atomic force microscope in semi – contact topography and Kelvin probe modes. The NSC01 platinum coated conducting tip was applied.

To characterize local electrical charges distance influence on the electrical potential the autocorrelation function of the several potential distributions realizations over the surface. When the autocorrelation function reached the zero value, the distance (correlation length) was assumed as the localized charge distance length.

III. RESULTS

UV influences contact angle (Fig.1). When the exposure increased until 60 min, the contact angle decreased. However, at the exposure > 60 min the angle increased.

At the same time the contact angle value positively correlated with an radiation induced increment of the electron work function (Fig. 2) that characterized the alteration for the surfaced charge density (higher value of the electron work function relates to the greater value of the negative charge) .

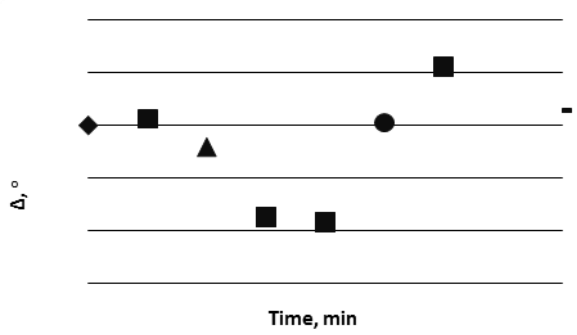

Fig.1. Contact angle increment dependence on UV exposure

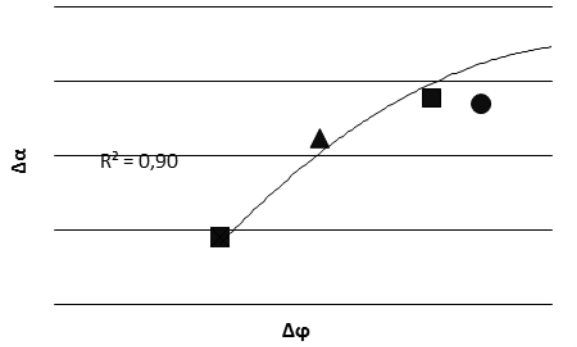

Fig.2.Correlation between angle and electron work function increment

The absorption spectra demonstrated a minimum at about 3.25eV or 380nm (Fig.3) when the UV exposure was <60 min. However at the exposure > 60 min the minimum disappeared. .

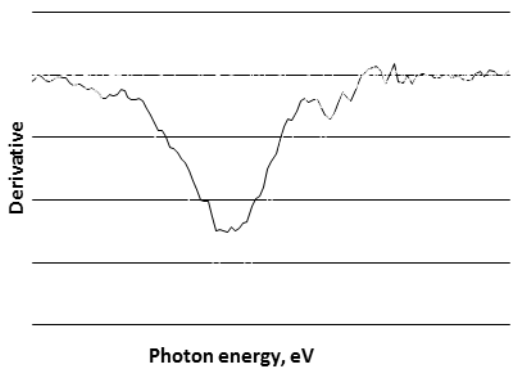

Fig. 3. Absorption data. Derivative dependence on photon energy value

The morphology of the surface was not influenced by radiation. However the surface electrical potential demonstrated connection with radiation exposure. The correlation length correlated with the contact angle influenced because of UV radiation (Fig.4).

DISCUSSION

Alteration of the contact angle influence by UV radiation can be stipulated because of radiation induced reconstruction of the PMMA surface layer or deposition of the electrical charge. The latter could be provided because of the emission of the electrons escaped from PMMA due to the UV photons. Unchangeable absorption spectra minimum at exposure > 60 min gives a possibility to assume that such exposures do not have an influence on the PMMA surface layer structural peculiarities. However, the alteration of the contact angle at exposure < 60 min evidences that the electrical charge factor contributes wettability. Absence of the absorption minimum at > 60 min signals that UV reconstructs the PMMA surface layer.

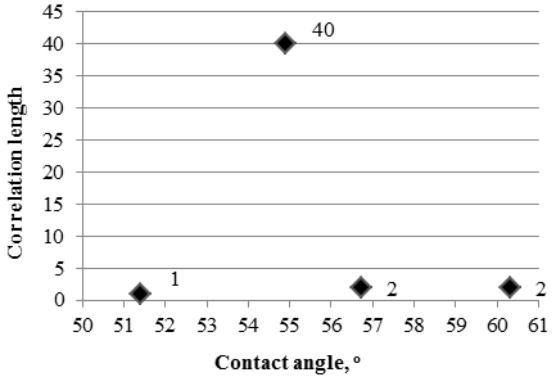

Fig.4. Correlation length depending on contact angle value

Perhaps both structural alterations and deposition of the electrical charge influences the correlation length.

IV. CONCLUSIONS

1. UV radiation supplied from the Hg-Xe lamp with intensity 3.5W/cm^2 at 365nm to the PMMA surface located at the distance 0.4 m from the UV source supplies the surface with both structural alteration and electrical charge, when the exposure was > 60 min. However, if the exposure < 60 min the structural alteration were not observed.
2. The deposited electrical charge is characterized with decreasing of the correlation length when the contact angle > 55 °.
3. The contact angle depends on UV exposure.
4. The UV radiation could be employed to functionalize PMMA wettability, the structure uninfluenced radiation mode being available at exposure < 60 min.
5.

REFERENCES

[1] Y.Wang, J.Robertson, W.Spillman et al., "Effects of the Chemical Structure and the Surface Properties of Polymeric Biomaterials on Their Biocompatibility", Pharmaceutical Research, Vol.21, p.1362, Aug.2004

[2] O.Etienne, C.Picart, C.Taddei et al., "Polyelectrolyte Multilayer Film Coating and Stability at the Surfaces of Oral Prosthesis Base Polymers: an in vitro and in vivo Study", J Dent Res, Vol.85, p.44, Sept.2005

[3] N.Lee, S.Moon, S.Kang et al., "The Effect of Wettability of Nickcl Mold Insert On the Surface Quality of Molded Micro lenses", Optical Review, vol.10, p.240, June 2003

[4] J.Deng, L.Wang, L.Liu et al., "Developments and new applications of UV-induced surface graft polymerizations", Progress in polymer science, Vol.34, p.156, Oct.2008

[5] X.Lu, Y.Jin, S.Tan et al., "A Simple Approach for Fabricating a Superhydrophobic Surface Based on Poly(Methyl Methacrylate)", J Adhes Sc Techn, Vol.22, p.1841, 2008

[6] RJ. Akmene, A.Balodis, Y. Dekhtyar et al., "Exoelectron emission specrometer complete set of surface local investigation", Phys Chem Mech Surface, Vol.8, p.125, 1993

Optical Dosimetry for Controlling the Efficiency of Laser Phototherapy

M.M. ASIMOV [1], R.M. ASIMOV [2], A.N. RUBINOV [1], A.I. GISBRECHT[3]
[1] *Institute of Physics National Academy of Sciences of Belarus, Minsk, Belarus*
e-mail: m.asimov@dragon.bas-net.by
[2] *"Sensotronica Ltd.", Minsk, Belarus*
e-mail: asimov@anitex.by
[3]*Institute of Electronics Bulgarian Academy of Sciences, Sofia, Bulgaria*
e-mail: aig@abv.bg

***Abstract.* – The results in vivo investigation biophotonics of laser-induced photodissosiation of oxyhemoglobin in cutaneous blood vessels and its role in biomedical processes are presented. New method for determination an individual response to the effect of laser radiation is presented. It is shown that in order to make the phototherapy as well as laser therapy methods really efficient one has to control the oxygen concentration in tissue keeping it at the necessary level. Novel method of optical "dosimetry" based on using the changes oxygen concentration in tissue as feedback signal for optimization therapeutic effect of low intensity laser radiation is developed.**

Keywords – hemoglobin, oxyhemoglobin, tissue oxygenation, hypoxia, phototherapy, photodissociation.

I. INTRODUCTION

Biophotonics of "laser-tissue" interaction and the effect of laser radiation on oxyhemoglobin in cutaneous blood vessels and capillaries is considered as one of the interesting aspects of modern photomedicine and photobiology. Application of low intensity laser radiation in treatment of a variety of diseases has been developed extensively during the last five decades.

Biostimulation and therapeutic effect of laser radiation is well-established fact and currently widely uses in clinical practice. At the same time the mechanism of therapeutic effect of laser radiation is not yet clearly understood and considered to be very complex that involves anti-inflammatory, analgesic and anti-edematous effect on tissue [1-4]. Most exiting effect of laser therapy could be seen in wound healing were process of fast epitelization clearly demonstrate its efficiency.

The mechanism of therapeutic effect of laser radiation is still remains unclear that make difficult to develop correct method for controlling the efficiency of laser therapy - correct “dose” of delivered average energy of laser radiation.

In present the efficiency of therapeutic effect is controlled by using an empirical unit based on average power density of output laser radiation. Experimental study the therapeutic effect of He-Ne and Argon laser radiation in open skin wound healing [5] was carried out at power density of 45mW/cm^2. Maximal therapeutic effect due to significant increase of collagen synthesis at the total energy density of 4J/cm^2 has been reached. Similar experimental study [6] with He-Ne laser radiation at power density of 4,0mW/cm^2 demonstrated the therapeutic dose (complete heeling of wound) at lower average energy ~1,22J/cm^2.

Big differences in experimental results in healing two cases of identical open wounds where therapeutic effect are reached in different output power of He-Ne laser radiation remains not clear.

Nevertheless the power density of 4J/cm^2 is accepted as extreme level ("dose") for reaching maximal therapeutic effect. Accepted empirical criterion for controlling the efficiency of the therapeutic effect of low intensity laser radiation (optical “dosimetry”) is not correct and reliable.

In this paper new method of optical "dosimetry" based on using the changes of oxygen concentration as feedback signal for optimization of therapeutic effect of laser radiation is presented. It is shown that photodissociation of oxyhemoglobin; whose main biological function is the transportation of molecular oxygen, gives unique possibility of additional oxygen supply and allows develop laser-optical method of tissue hypoxia elimination for restoring normal cell metabolism.

II. THE PHENOMENON OF LASER-INDUCED BLOOD OXYHRMOGLOBIN PHOTODISSIATION

Since 1997 new technology of laser-induced photodissociation of oxyhemoglobin (HbO_2) in cutaneous blood vessels and its biomedical applications is developing. Unique possibility in selective and local increase of the concentration of free molecular oxygen in tissue is obtained [7-10]. The efficiency of the interaction of laser radiation in different wavelengths on HbO_2 in cutaneous blood vessels is studied. Mathematical model for calculating optimal parameters of laser radiation to induce an effective photodissociation of hemoglobin (Hb) complexes in cutaneous blood vessels has been developed.

The temperature dependence of the quantum yield of photodissociation of HbO_2 observed earlier in vitro is proved experimentally in vivo [10]. Unique possibility in selective and local increase of the concentration of free molecular oxygen (O_2) in tissue is demonstrated.

As it well known the concentration of oxygen is critical in enhancing in vivo wide variety of biochemical reactions including cell metabolism. Aerobic cell metabolism is primary mechanism in energy production in tissue. Controlling this mechanism gives unique possibility of biological stimulation to reach therapeutic effect. This goal could be reached by the means of laser-induced photodissociation of oxyhemoglobin in cutaneous blood vessels.

Absorption of light by blood Hb and HbO_2 allows consider and discuss the following photophysical and photochemical processes. Photophysical process is connected with nonradiative dissipation by Hb and HbO_2 electronic excitation energy. The heat generated in this process is transferred to the blood capillaries, which has the characteristic time of thermal relaxation ~ 0.05-1.2 msec.

The mechanism of the laser-tissue interaction is very much dependent on the output laser energy. The effect of high-energy lasers is quite clear and based on photothermal processes such as selective photothermolysis.

This mechanism is used in clinical practice, for example, in laser surgery, cosmetology, laser correction of vision etc. It is clear that the effect of heating due to absorption of low energy laser radiation in a tissue is negligible. Estimate shows that in typical case the local increase of temperature only by 0.1 - 0.5 ^{0}C may be expected. Such a small raise of a local temperature may promote only some improvement in capillary microcirculation of blood and hardly could stimulate the metabolism of cells.

We suppose that in a case of low energy lasers the most important process is the photodissociation of HbO_2, whose main biological function is the transport of molecular oxygen. The quantum efficiency of the photodissosiation [11] of oxyhemoglobin is amazingly high and reaches 10 % in a wide visible spectral range. The molecular oxygen is generated due to laser-induced photodissosiation of HbO_2 in blood vessels allows control the local increase of oxygen concentration at irradiating region (fig. 1).

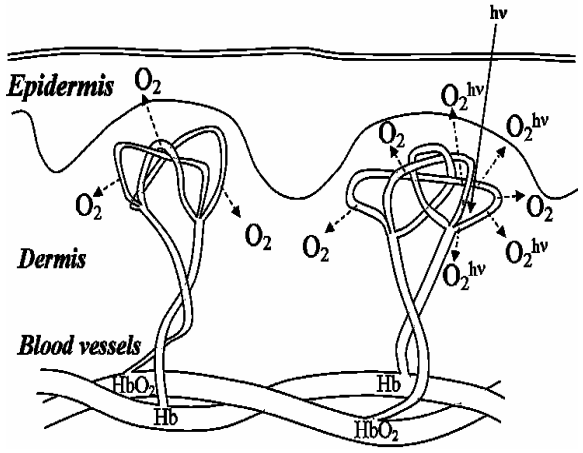

Fig. 1 - Illustration of laser-induced tissue oxygenation caused by photodissociation of arterial blood HbO_2

The possibility of additional oxygen supply allows develop a new method of tissue hypoxia elimination that restores normal cell metabolism. Investigation of photodissociation of hemoglobin complexes in vivo could be carried out using arterial blood saturation parameter.

In case of HbO_2 the value of saturation SaO_2 in arterial blood vessels is defined by the concentration of HbO_2 taking into account contribution of Hb, methemoglobin (MetHb) and carboxyhemoglobin (HbCO).

$$SaO_2 = \{[HbO_2] / ([HbO_2]+[Hb]+[MetHb]+[HbCO])\}100$$

At normal conditions of gas exchange the concentrations of MetHb and HbCO are extremely low (0.2 - 0.6 % and 0.8 % correspondingly) so the contribution of these components can be neglected. Thus in practice the value of SaO_2 could be determine as

$$SaO_2 = \{[HbO_2] /([HbO_2]+[Hb])\}100$$

Photodissociation of HbO_2 induced by laser radiation releases free molecular oxygen. Meanwhile, proportion between $[HbO_2]$ and [Hb] concentrations is changed that decrease the value of SaO_2.

$$\Delta SaO_2 = SaO_2 - SaO_2^{h\nu}$$

Were SaO_2 is saturation without and $SaO_2^{h\nu}$ with laser irradiation.

Amount of oxygen available for cell metabolism delivered by microcirculation is the function of:

$$\sum O_2 (TcPO_2) = f(F(HbO_2)*[O_2])$$

Were HbO_2 is the value of oxyhemoglobin arterial blood and $[O_2]$ - is the concentration of oxygen released into plasma.

In the case of deterioration of the blood microcirculation extra oxygen supply is critical to provide the demands of cell for normal metabolism. This could be reached by in vivo laser-induced photodissociation of HbO_2 directly at the zone were necessary to increase the local concentration of free molecular oxygen.

As a result we obtain average concentration of oxygen that releasing in conventional way and due to

$$\Sigma[O_2] = [O_2] + [O_2^{h\nu}]$$

Thus phenomena of laser-induced in vivo photodissociation of oxyhemoglobin in cutaneous blood vessels and capillaries gives unique possibility of optically increase the local tissue oxygen concentration.

III. REGISTRATION OF BLOOD OXYHEMOGLOBIN PHOTODISSOSIATION IN VIVO

Experimental study the change of arterial blood saturation due to laser-induced photodissociation of oxyhemoglobin is based on registration the variations of its value on the background natural oscillations of saturation. Specialized pulse oxymeter spectrophotometer for recording photoplethysmogram with high accuracy and detailed numerical signal processing has been applied. Despite of traditional pulse oxymeter instead of two channels for signal registration in red and infrared spectral ranges fore channel that supplied parallel 8 independent signal processing it has been used [12,13]. As a result the registration of small changes of arterial blood saturation for one heart pulse is reached with accuracy less than 0.5 %.

The measurements of the value SaO_2 was carried out with the high sensitive pulse oxymeter sensors in transmitting light with accuracy better than 0.5 %. The sensor was placed on the first of the two phalanxes of the finger and measuring elements were in the region of the first phalanx (fig. 2).

The effect of laser radiation on arterial blood oxygen saturation has been observed using He-Ne laser with wavelength $\lambda = 632$ nm, which is mostly applied in medical practice. Lasers spot on a skin was about 7-8 mm with power density of 20 mW/cm^2. The laser radiation was guided to an interior of the third phalanx of a finger.

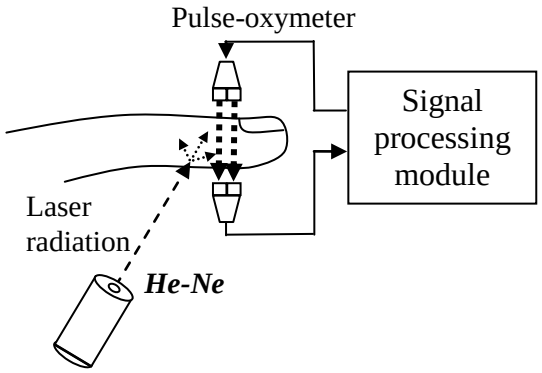

Fig. 2 - Experimental setup for investigation of the effect of laser radiation on the value of arterial blood saturation

The concept of laser-induced tissue oxygenation allows understand the mechanism of biological response and therapeutic effect of laser radiation. Its also gives a unique method of selective local tissue oxygenation, that could be used in wide range of biomedical applications.

Using another direct method of oximetry (Fig. 3) based on principle of measuring the oxygen tension PO_2 in arterial blood is direct method of registration of gas that dissolved in blood plasma.

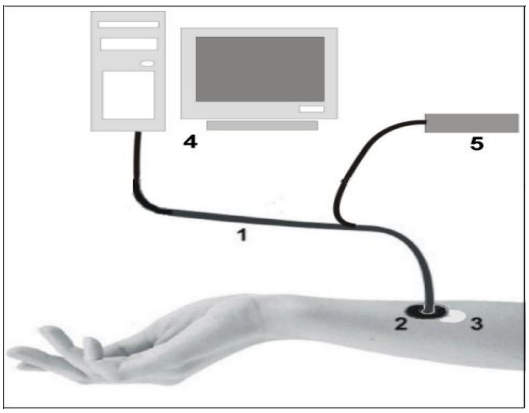

Fig.3 - Measurement of tissue oxygen tensions due to photodissociation of blood HbO_2: 1 - Clark sensor, 2 - electrolytic cell, 3 - irradiating zone, 4 - monitor TCM - 4, 5 - He- Ne laser.

For this usually are used Clark-type polarographic sensor ("$TcPO_2$ electrode", see fig. 3) that consist of silver anode, electrolyte, and an oxygen permeable membrane; heating section and electronic system for measuring and controlling the sensor temperature.

The initial oxygen tension in tissue was measured by placing $TcPO_2$ electrode on human skin in shoulder area. Then He-Ne laser radiation at the power of 1mW was applied. Kinetics of tissue oxygen tension was experimentally investigated [14]. Obtained results were normalized to initial oxygen tension value.

These two above mentioned methods allows to measure and control the process of releasing extra oxygen from HbO_2 under laser irradiation directly to arterial blood plasma and future it diffusion into tissue.

IV. NEW METHOD OF OPTICAL "DOSIMETRY" BASED ON CONTROLLING LOCAL TISSUE OXYGANATION

Laser-induce photodissociation of HbO_2 gives a novel and unique method for optically increasing the local concentration of free molecular oxygen in tissue that is significantly enhances cell metabolism. Taking into account that blood deliver O_2 to any cell tissue and metabolism of cells required consumption of oxygen we suggest to base therapeutic effect of laser radiation based on controlling summary tissue oxygen concentration.

- Proposed method for optimization therapeutic efficiency the effect of laser radiation is based on using the change in oxygen concentration as feedback signal.
- Oxygen released into tissue is proportional to the energy of aerobic cell metabolism.
- Photodissociation of HbO_2 increases the level of tissue oxygenation.
- Oxygen release rate could be directly measured in vivo through the value of saturation - SaO_2
- Capacity of circulatory system to carry oxygen defined by hemoglobin concentration [Hb] and also is a function of how much blood per minute is pumped from the heart.

Controlling parameters are:

- Aerobic metabolism - (energy production);
- Extra oxygen release into tissue due to photodissociation of HbO_2;
- Ability of blood circulation system to transport oxygen.

Measuring parameters:

- Amount of oxygen released into tissue;
- Changes in arterial blood saturation $DSaO_2$;
- Hemoglobin concentration and heart pulse rate.

In this case we can refer to the pulse volume of heart V_H which is equal to blood volume in liters that pump the heart at one bit. Then oxygen flux $F(O_2)$ through the irradiating zone of tissue we can describe as

$$F(O_2) = 4[O_2]/ ([Hb] + 4[O_2]) * C * V_H * [Hb]* (SaO_2 / 100),$$

Where C – is a coefficient of blood delivery to tissue indicating tension in capillary blood vessels and [Hb] – is the concentration of hemoglobin in gm/l. SaO_2 – is the degree of hemoglobin oxygen saturation in percents, and $[O_2]$ – molar concentration of oxygen.

Than we introduce the notion of "standard flux of oxygen through the tissue"

$$S(F.O_2) = 4 [O_2] / ([Hb] + 4 [O_2]) * [Hb]_n * C * V_H$$

"Standard flux of oxygen through the tissue" indicates a flux of oxygen that is necessary for supplying tissue at normal conditions.

Normal conditions are related to the concentration of hemoglobin in blood that corresponds for the given age and complete saturation with oxygen.

For the estimation of current oxygen delivery through the tissue we normalize the local flux to the standard one

$$F(O_2) = F(O_2) / SF(O_2)$$

Than we obtain

$$F(O_{2)} = [Hb]/[Hb]_n * (SaO_2 / 100)$$

This parameter allows us estimate current efficiency of oxygen delivery in dependence of the concentration of hemoglobin and degree of its saturation with oxygen. Now we can determine the quantity of oxygen that releases into tissue during elimination with low intensity laser radiation.

$$\Delta FO_2 = F(O_2) - F(O_2)^{h\nu}$$

Were FO_2 - is normalized flax of oxygen without laser irradiation and $FO_2^{h\nu}$ - is normalized flax of oxygen during laser irradiation.

The dose of oxygen that that releases into tissue during elimination with low energy laser radiation can be determined from following expression:

$$[O_2] = \{F(O_2) - F(O_2)^{h\nu}\} * T * Pr$$

Were T – is the time of irradiation and Pr - is pulse rate.

Substituting expressions for FO_2 and $FO_2^{h\nu}$ we obtain:

$$[O_2] = ([Hb]/[Hb]_n * (SaO_2 / 100) - [Hb]/[Hb]_n * (SaO_2^{h\nu} / 100)) * T * Pr =$$

$$= T * Pr * [Hb]/[Hb]_n * (SaO_2 - SaO_2^{h\nu}) / 100 = T * Pr * [Hb]/[Hb]_n * (\Delta SaO_2 / 100)$$

Thus the "dose" of oxygen that that releases into tissue during irradiation with low intensity laser radiation can be determined from following expression:

$$\Sigma[O_2] = T * P_r * [Hb]/[Hb]_n * (\Delta SaO_2 / 100),$$

Suggested method of determination of therapeutic dose of laser radiation correlated with tissue local oxygenation could be applied in clinical practice. Developed high sensitive pulse oxymeter completely provides determination of all parameters for establishing a therapeutic dose for healing a huge variety of diseases by laser phototherapy.

Laser induced photodissociation of HbO_2 allows extract additional amount of oxygen locally at irradiating zone. This phenomenon provides unique possibility using optical methods for regulation of local tissue O_2 concentration. Additional oxygen release rate is directly measured through the value of oxyhemoglobin arterial blood saturation (ΔSaO_2). The amount of oxygen released into tissue depends also from capacity of circulatory system to carry oxygen.

This capacity mainly defined by contribution of two following parameters: hemoglobin concentration in blood [Hb] and its circulation speed. The impact of actual hemoglobin concentration is described by the ratio of $[Hb]/[Hb]_n$. Were $[Hb]_n$ is standard concentration that is normal for particular sex and age. The impact of blood circulation speed is taken into account through the heart pulse rate P_r.

Finally, therapeutic "dose" can be determine by the value of $\Delta SaO_2 = SaO_2 - SaO_2^{h\nu}$, were SaO_2 is saturation without and $SaO_2^{h\nu}$ with laser irradiation, heart pulse rate P_r, time of exposure T, ratio of actual and standard hemoglobin concentrations $[Hb]/[Hb]_n$.

$$D(O_2) = \frac{[Hb]}{[Hb]_n} \cdot \left(\frac{\Delta SaO_2}{100} \right) \cdot P_r \cdot T$$

It should be noted that involved parameters are objective and could be measured by well-known clinical routine. Suggested new method of optical "dosimetry" based on key biological parameters and connected with aerobic cell metabolism provides possibility of precise determination of therapeutic effect of laser radiation.

V. EXPERIMENTAL

Experimental investigation the phenomenon of laser-induced tissue oxygenation has been carried out using transcutaneous oxygen monitor (TCOM) - "Radiometer" TCM-4 (Fig.4).

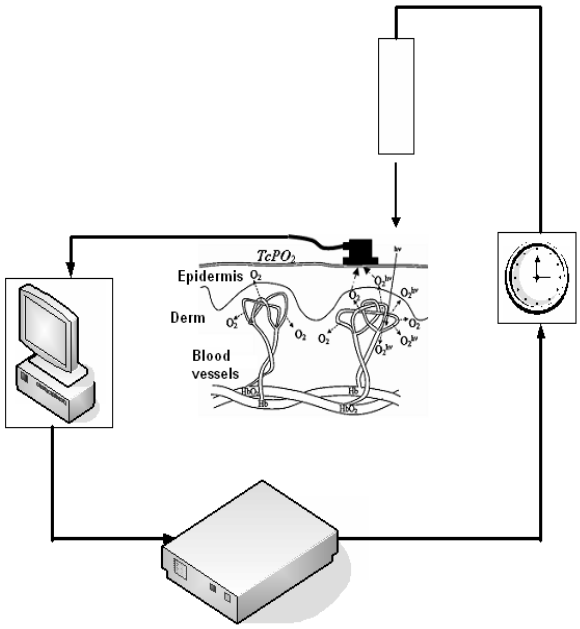

concentration directly at the zone of laser irradiation

Direct in vivo measurements of tissue oxygen tension $TcPO_2$ under irradiation by He-Ne laser at the power of 1mW has been carried out [14].

Using the simple diffusion model we calculated what amount of oxygen should be released into blood plasma in order to reach experimentally observed increasing tissue O_2 concentation (fig. 5). The target criteria were kinetic of tissue oxygenation in response to laser irradiation.

The variable parameters were diffusion coefficient of oxygen in tissue and oxygen release rate.

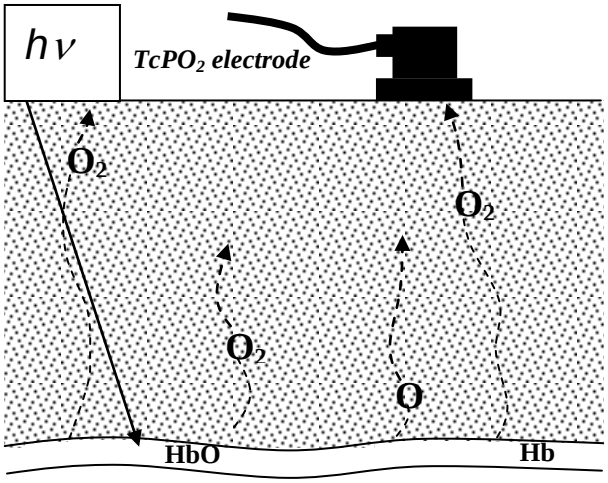

Fig. 5- Simple model of oxygen diffusion in tissue

As it was shown experimentally [10] the response of oxygen release on laser irradiation is relatively fast and remains constant during the irradiation. To simulate this effect in the model, the oxygen release rate was increased instantly and remains constant during the time of irradiation.

The main aim of the calculation was to reach best fit of the data produced by the model to the experimentally measured one. The target criteria were kinetic of tissue oxygenation in response to laser irradiation. The variable parameters were diffusion coefficient of oxygen in tissue and oxygen release rate.

VI. RESULTS AND DISCUSSION

The kinetic of oxygen tension in tissue in two cases the normal blood circulation and artificially induced ischemia was investigated. Obtained results were normalized to initial oxygen tension value.

In fig. 6 the results of cold laser induced tissue oxygenation in the case of artificially induced ischemia are presented. As it seen we still can extract extra oxygen from arterial blood and optically supply the demand of cell metabolism as long as needed.

As it seen from fig.6 during laser irradiation the value of tissue oxygenation is increases exceeding its initial level about 1.6 times (curve 1) after ten minutes of illumination. In the case of induced ischemia additional extraction of oxygen also is observed. This result clearly demonstrates that laser-induced tissue oxygenation could be applied in clinical practice for restoration of normal cell metabolism in tissue with damaged microcirculation.

The results of calculations demonstrate that in order to reach experimentally observed the rise of $TcPO_2$ by 1, 6 times at the surface of tissue, the calculation indicates the increase of oxygen release rate from arterial HbO_2 into blood plasma should increase about 4,3 times.

Photodissociation of HbO_2 induced by laser radiation and release rate of free molecular oxygen into blood plasma has been measured experimentally in vivo using high sensitive pulse oxymeter. The oxygen released from HbO_2 primarily increases the PO_2 of blood plasma and then O_2 diffuses into a tissue.

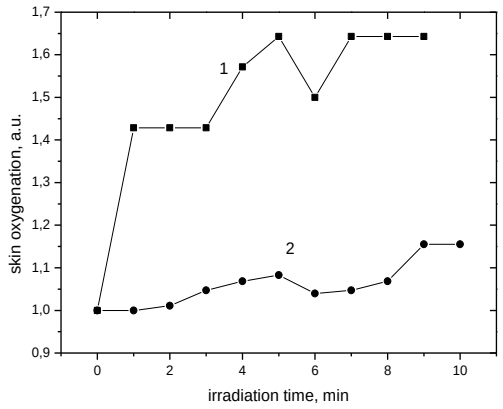

Fig. 6 - The kinetics of laser-induced tissue oxygenation during laser irradiation in norm blood microcirculation -1, and in artificially induced ischemia - 2

It is exiting that the value of PO_2 in blood plasma reached by laser-induced photodissociation of HbO_2 is comparable to that one typically reaches by the method of HBO. The distribution of $TcPO_2$ in the volume at the irradiation zone is depended on the time of exposure and the properties of tissue.

The comparison of calculated results with experimental data demonstrates that kinetic of $TcPO_2$ in dependence of time of elimination by laser radiation gives possibility to determine O_2 diffusion coefficient into tissue. This means that one could calculate and determine how to reach desirable level of $TcPO_2$ in zones with the disturbed blood microcirculation such as solid tumor, burn or wounds. So it's possible to determine optimal parameters of irradiation taking into account the volume that has to be oxygenated and the time of elimination.

Thus our suggested novel method can eliminate the deficit of oxygen until the restoring new vascular net in tissue. This result could be applied in the case of those pathologies where elimination of tissue hypoxia is critical.

Supplemental oxygen can lead to increased rate of collagen deposition, epithelialization and improved healing of split thickness grafts. Increased subcutaneous TcPO2 has also been shown to improve bacterial defenses. Thus unique possibility in selective and local increase of the concentration of free molecular oxygen into tissue that enhances metabolism of cells is developed. Laser-induced enrichment of tissue oxygenation stimulates cell metabolism and allows develop new effective methods for laser therapy as well as phototherapy of pathologies where elimination of local tissue hypoxia is critical.

Laser-induce photodissociation of HbO_2 may serve as a unique method in laser therapy for optically increasing the local concentration of free molecular oxygen in tissue that is significantly enhances cell metabolism.

It is valuable that even at the case of ischemia we still can extract extra oxygen from arterial blood and optically supply the demand of cell metabolism as long as needed. Thus laser-induced tissue oxygenation allows optically eliminate the deficit of oxygen until the restoring new vascular net in tissue.

Obtained results gives an experimental argumentation to consideration of primary mechanism of biostimulation and therapeutic effect of low energy laser radiation that could be based on increasing tissue local oxygen concentration directly wt the zone of irradiation.

This phenomenon allows to develop an objective method of control the efficiency of treatment by laser phototherapy. Now in clinical application the parameters of laser radiation can be tuned to optimal wavelength, power and exposition time in depends of optical characteristics of the patient skin tissue.

The obtained results also shows the way of increasing the efficiency of biostimulation and therapeutic effect of low energy laser radiation based on combination it with method of oxygen hyperventilation therapy.

An important conclusion can also be drawn from the obtained results. In interpretation of the biostimulating and heeling effect of laser radiation the phenomenon of induced photodissociation of blood oxyhemoglobin should be taken into account.

VII. CONCLUSION

New optical method of elimination the local tissue hypoxia is developed. The value of tissue oxygen concentration increases significantly during the laser irradiation.

It is shown that therapeutic dose of laser radiation could be based on adjusting the local concentration of free oxygen in tissue by laser-induced photodissociation of blood oxyhemoglobin.

To make the phototherapy as well as laser therapy methods really efficient one has to control the oxygen concentration in tissue keeping it at the necessary level. This goal could be reached by the use of laser-induced photodissociation of oxyhemoglobin in tissue blood vessels.

Method of determination of oxygen diffusion coefficient into tissue based on kinetics of tissue oxygenation under the laser irradiation is developed.

It is shown that the efficiency of laser-induced oxygenation is comparable with the method of hyperbaric oxygenation (HBO) at the same time gaining advantages in local action.

Novel method of optical "dosimetry" based on using the changes in tissue oxygen concentration as feedback signal for optimization therapeutic effect of low intensity laser radiation is developed.

Photodissociation of oxyhemoglobin, whose main biological function is the transport of molecular oxygen gives unique possibility of additional oxygen supply and allows develop laser-optical method of tissue hypoxia elimination that restores normal cell metabolism.

REFERENCES

[7] S.Takas, S. Stojanovich, *Diagnostic and biostimulating lasers.* Med. Pregl. vol. 51, no. 5-6, 1998, p.p. 245-249.

[8] G.D. Baxter, *Therapeutic lasers: Theory and Practice*, Edinburgh; New-York, (1994)

[9] J. Tuner and L. Hode *Laser Therapy: Clinical practice and scientific background,* Prima Books AB (2002).

[10] V.A. Mostovnikov, G.R. Mostovnikova, V.Yu. Plavski, L.G. Plavskaya, "Biophysical principles of regulatory action of low-intensity laser irradiation," *Proc. SPIE*, vol. 2728, 1996, p.p. 50-62.

[11] J.S. Kana, G. Hutschenrieter, D. Haina, W. Waidelich, *Effects of low power density laser radiation on healing of open wounds in rats,* Arch. Surg. Vol.116, 1984, p.p. 293-296.

[12] R.A. Abergel, R.F. Lyons, J.C Castel, et all. *Biostimulation of wound healing by lasers: Experimental approaches in animal models and in fibroplast cultures,* J. Dermatol. Surg. Oncol. Vol.3, 1987, p.p. 127-133.

[13] M.M. Asimov, R.M. Asimov, A.N. Rubinov, *Investigation of the efficiency of laser action on hemoglobin and oxyhemoglobin in the skin blood vessels,* SPIE Proceedings Laser - Tissue Interaction 1X. 01.27 - 01.29. 98. San Jose. CA. USA, vol. 3254, 1998, p.p. 407 - 412.

[14] Asimov M.M., Asimov R.M., Rubinov A.N. *Action spectra of laser radiation on hemoglobin of skin blood vessels,* Journal of Applied Spectroscopy. 65 (6), 877-880 (1998).

[15] M. Asimov, R. Asimov, M. Mirshahi, A. Gizbrebrecht, *Effect of laser induced photodissosiation of oxyhemoglobin on biomedical processes,* 11th International School on Quantum Electronics: Laser physics and Applications, Proceedings of SPIE, vol. 4397, 2001, p.p. 390-394.

[16] [10] M.M. Asimov, *Laser-induced Photodissosiation of Hemoglobin Complexes with Gas Ligands and its Biomedical Applications, Proceedings of "LTL Plovdive 2005", IV International Symposium Laser Technologies and Lasers,* October 8.10 - 11.10. Plovdive, Bulgaria. 2005, p.p. 3-11.

[17] Wilma A. Saffran, Quentine H. Gibson, *Photodissosiation of Ligands from Hem and Hem Proteins: Effect of Temperature and Organic Phosphate.* J of Biol. Chem., vol. 252, 1977, p.p. 7955-7958.

[18] Ed. A. Bakaj, V.I. Kravchenko, S.A. Mamilov, O.N**.** Minov**,** Yu. S. Plaksiy, A.B. Rikberg, *Multichannel optical measurements for in vivo determination tissue indices,* Optical & Biological Engineering & Computing. Vol.35, Suppl. Pan 1, 1997, p.p. 98-101.

[19] V.I. Kravchenko, S.A. Mamilov, O.N. Minov, Yu. S. Plaksiy. *Investigations of correlation of optical signals during measuring an arterial blood oxygen saturation,* The Ukrainian Journal of Medical Technique and Technologies vol.1, 1999, p.p. 59-61.

[20] M.M. Asimov, A.N. Korolevich, E.E. Konstantinova, *Investigation of the kinetics of tissue oxygenation under the effect of low intensity laser radiation, J of* Appl. Spectr., vol.74, 2007, p.p.120-125.

Electro-acoustical and Electrophysiological Examinations in Diagnostics of Otitis Media in Infants

I. ABABII, S. DIACOVA, M. MANIUC, P. ABABII, L. DANILOV
SMPhU "N. Testemitanu" Department of ORL

Abstract
Introduction .Acute Otitis Media is extremely common in infants, often asymptomatic.
Material and methods
Several hundred children in the first year of life were evaluated and treated for a variety of diseases. Seven sets of measures were used in the study: 1. Background characteristics; 2. Otological questionnaires; 3. Otoscopical examination; 4. Impedance audiometry; 5. Brainstem Electrical Response Audiometry; 6. Results of surgery (tympanotomy, antrotomy); 7. Results of Otoscopical examination and Impedance Audiometry in dynamics.
Results This results were compared with cytological and histology examination of surgical findings. High correlation of type A with reducing compliance indexes and proliferation were found. We propose that pathogenesis of otitis media in infants develop in two ways.
Discussion Algorithm of SOM – diagnostics was elaborated. SOM - diagnostics is based on a few steps. The first step is the SOM prognosis in infants. The second step is the otoscopy examination of the infants of the risk group. The third step is the audiometric investigations - impedance audiometry and ABR. Impedance audiometry data are used for information of middle ear pathology character. BERA data give us possibility to estimate the profound of middle ear pathology and degree and character of hearing impairment.
Conclusion We present an algorithm of the management of SOM in infants on the basis of our analysis. This algorithm was also verified in patients from the control group. We were able to correctly-diagnose this disease and prognosticate its course in over 97% of cases.

I. INTRODUCTION

Otitis media in children is one of the oldest problems in pediatric otology. Acute otitis media is the most common disease of early childhood characterized by fever, sleeplessness, irritability, manifestations of intestinal and respiratory disorders. Local changes could be evident or silent what complicates precise diagnostics and sufficient timely treatment, leads to severe complications; impact on hearing, speech and development is significant, long term sequelae such as chronic suppurative otitis media with and without cholesteatoma, retraction pockets, etc, causes disability of child, multiple complications, stipulates long term treatment and surgery. (1, 2, 3)

Undetected and undetectable middle ear pathology occurs in any patient age. But during early infancy there are some special anatomical and functional reasons for SOM development.

Clinical manifestations of SOM include hearing loss as well as wide variations of pain intensity without significant changes of the tympanic membranes. Clinically SOM can be associated with restlessness or sluggishness. This insidious aspect of SOM often makes precise diagnosis difficult.

Additionally antibiotics used to treat infants presenting with gastrointestinal and pulmonary problems can mask associated SOM making diagnosis even more challenging. Therefore potentially lethal middle ear infections may go undetected clinically in pediatric populations (1, 2, 3, 4).

II. OBJECTIVES

This article describes our experience in diagnostics of silent otitis media in infants of the first year of life.

III. MATERIAL AND METHODS

Several hundred children in the first year of life were evaluated and treated for a variety of diseases including intestinal, respiratory tract and neurological disorders. They were evaluated and cared for in the Republic Intensive Care Unit for infants in the Republican Hospital for Children. The most frequent complaint was restlessness or sluggishness.

728 infants (432 males and 296 females) with silent otitis media were examined using special sets of measures. The majority of infants were younger than 6 months (654 - 89 %). Meningitis was observed in 12 % of cases, septicemia in 29 %, pneumonia in 35 %, intestinal disorders in 64 %. For comparison, infants with classical manifestations of middle ear inflammation were included in a second group. A third group, the control group, included infants without middle ear pathology (200 infants, in this category different groups of 50 patients were studied every three months).

IV. METHODS

Seven sets of measures were used in the study: 1. background characteristics; 2. Otological questionnaires; 3. Otological examination; 4. impedance audiometry; 5. Brainstem Electrical Response Audiometry; 6. Results of surgery (tympanotomy, antrotomy); 7. Results of Otological examination and impedance audiometry at 3 and 6 months intervals after diagnosis were documented. (5, 6, 7)

V. BACKGROUND CHARACTERISTICS.

Various background characteristics were recorded for the purpose of identifying risk factors associated with SOM. These included data regarding the following: social-economic status of parents, their age and history of any chronic illnesses. Specifically questions were asked regarding family history of ENT - related diseases;

additionally data was obtained regarding pregnancy, condition of birth, gestation age, weight and Apgar scores at birth; a history was taken regarding nutrition and development of infant during first months before the onset of ear disease; history of respiratory tract infection, intestinal disorders; antibiotic therapy; some information of child behavior and other (52 points).

Otoscopy

These were designed to obtain Otoscopical profile for each child. The "Carl Storz" set was used.

The items covered in each of the examinations included 40 points (color, contour, luster, translucence, light reflex, landmarks and others).

Impedance Audiometry.

An Impedance meter set was used for impedance audiometry. Tympanograms were evaluated according to classification by Jerger, (1970) in modification by M. Tos (5)

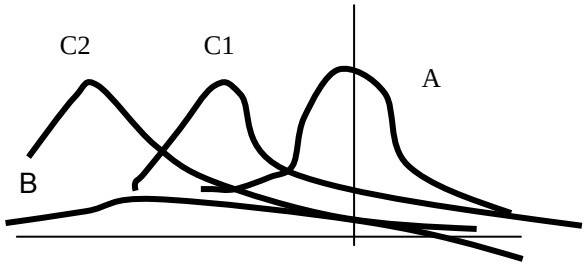

Fig.1. Tympanogram types. Schema.Type A: pressure +50 - -99 mm,Type C_1: pressure -100 - -199 mm H_2O Type C_2: pressure <-200 mm H_2O,Type B: no peak of compliance

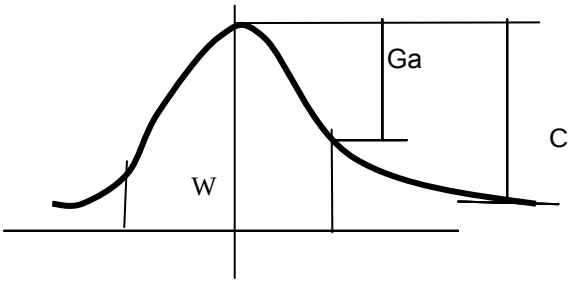

Fig.2. Schema of compliance characteristics calculation. Gr=C/GaW – width C – compliance Ga – absolute gradient Gr – relative gradient

Compliance and absolute gradient as well as relative gradient were calculated according to Brooks (1968).(3, 5).

The presence or absence of an acoustic reflex was tested ipsi laterally at 1000 Hz and 95, 100, 105, 110 dB SPL, using automatic impedance audiometry (5).Brainstem Electrical Response Audiometry.

The "Audiostar" ("Madsen Electronics") was used. Recordings were obtained under commonly used conditions. Briefly, ABRs were recorded from cup electrodes applied at C, A1 and A2 (international 10 - 20 system). Clicks 0,1 ms in duration were presented through TDH - 39 earphone at 7 intensity levels in 10 dB steps (70 - 10dB) until ABR threshold was established. Peak Latencies (I, III, V) and ABR threshold were registered; Function Latency-Intensity (V) was made.(6).

All of these children received medical treatment, 12 % of children underwent surgery – Myringotomy or Myringotomy and Antrotomy.(7)

All patients were followed for at least 1 year.

Statistical analysis (Stjudent-criterium, Fisher-statistics and discriminate analysis) was made.

VI. RESULTS

Some predisposing factors to SOM.

Life histories were analyzed in all 3 groups of patients. Risk factors for SOM development include:

hypotrophy ($p < 0,0001$, $F = 46,3$) inflammatory diseases during first months of life ($p < 0,0001$, $F = 40,2$)antibiotic therapy ($p < 0,0001$, $F = 35,8$)pregnancy complications ($p < 0,0001$, $F = 18,3$)low birth weight ($p < 0,0001$, $F = 9,3$)

Otoscopy

Healthy infants (400 ears) were examined to assess normal tympanic membrane in infants during the first year of life. 104 ears (52 %) had translucency reducing, 64 ears (32 %) had color changes. The *pars tensa* was dull and opaque in 27 % and appeared red in 16 % of ears which were otherwise normal. The *pars flaccida* was thick in 27 % of ears examined. The light reflex was irregular or absent in 49 % of ears. The majority cases of tympanic membrane abnormalities were found in infants younger than 6 months of life. Tympanic membrane changes were observed more often in group of infants, suffering from SOM. Therefore we registered translucency reducing, thickness in majority of cases (98,1 %), light reflex was absent in 95,1 % of ears. Sensitivity of otoscopy in determination of SOM was 98,1 %, but specificity was 48,0 %. We found some important for SOM-diagnostics symptoms. But our opinion is that diagnosis of SOM cannot be established on otomicroscopical findings alone because similar signs can be present in healthy infant's ears. This explains the limitation of otoscopy in this age group.

Impedance audiometry 400 ears of healthy infants were tested. Type A was registered in all cases. Middle ear pressure was in level of + 50 to - 80 mm H2O. Compliance was registered in the range of 0,21 to 0,5 sm3. Absolute gradient was in level of 0,06 to 0,2 sm3, relative gradient was in level of 0,25 to 0,2.Infant with suspected silent inflammation of the middle ear were investigated repeatedly.

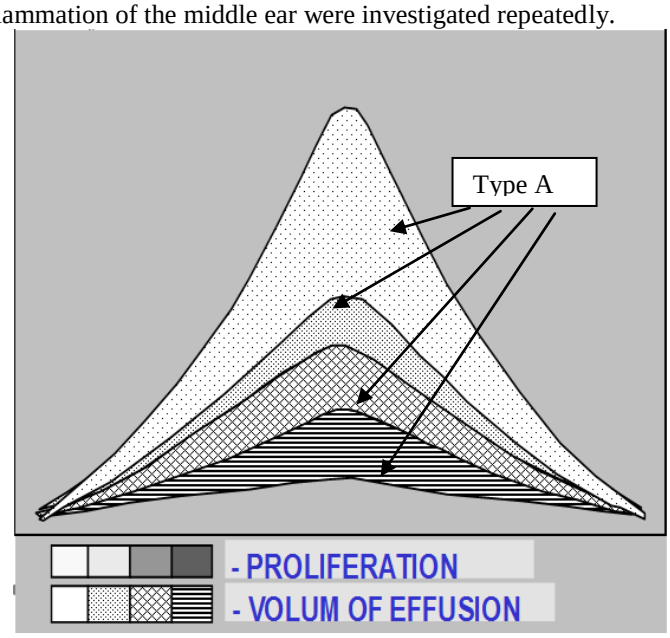

Fig.3. The gradual reducing of compliance indexes in cases of normal middle ear preassure.

Type A was registered in majority of cases (66,2 %), type B - in 30,8 %, type C - in 3 %. Compliance (for types A and C) was in level of 0,1 to 0,3 sm3, in majority of cases (84 %)

less than 0,21 sm3. Absolute gradient was less than 0,06 sm3, relative gradient - less than 0,25.

The gradual reducing of compliance indexes and normal middle ear pressure was found in repeated investigations in SOM-group.

Normal middle ear status, absence of any inflammatory changes correlated with type A of tympanogram. Beginning of pathological process in middle ear cavity provokes development of edema of mucosa, proliferation of granulation tissue without any effusion, what influenced on compliance and its characteristics – absolute and relative gradient. Gradually decreasing compliance in the conditions of open auditory tube does not change the type of tympanogram – it remains type A. (presented on Fig.3). But the height and roundness of the tympanogram are gradually changed till type B, which correlated with big amount of granulations, edema and effusion.

Type B was registered in majority of infants of OOM-group. Type C was found in 17,7 % and type A with reducing of compliance indexes - in 15,2 % of ears. The gradual reducing of middle ear pressure was more characteristic for ears with obvious otitis media.

This results were compared with cytological and histology examination of surgical findings.

High correlation of type A with reducing compliance indexes and proliferation were found. Effusion was correlated with type B.

We propose that pathogenesis of otitis media in infants develop in two ways. (Fig.2)

Fig 2. Two ways of development of otitis media by correlative analysis.

The first way is classical with the basis of dysfunction of the Auditory Tube and vacuum development in middle ear.

The second is the development of otitis media in conditions with open auditory tube. Findings of the impedance audiometry and surgery confirm this hypothesis.

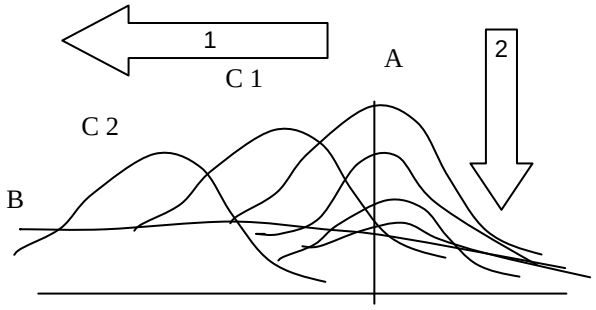

Fig 2. Two ways of development of otitis media.

VII. ABR

Auditory Brainstem Response Indexes were investigated in healthy infants group. Hearing threshold level and peak latency (PL) of wave I were the most constant. Other indexes (PL III, PL V) showed dependence from age, maturity and pathology of neurological system.

We looked at the influence of silent ear inflammation on ABR and found that hearing threshold level depends on presence and degree of pathological processes. We compared the peak latencies in healthy infants and infants with silent otitis media. The difference of PL I was the most statistically reliable. The evidence is already mentioned are the most sensitive and reliable indicators of middle ear pathology. Threshold evaluation was usually minimal. Persistent wave PL I prolongation in serial recordings was the striking ABR findings among infants with abnormal tympanometry. As PL I prolongation was more pronounced than that of wave V, the I - V inter-peak latency was often shorter than expected for age. Latency - Intensity function slope was not grossly altered in these cases.

Algorithm of SOM - diagnostics

SOM - diagnostics is based on a few steps. The first step is the SOM prognosis in infants of the first year of life. Pediatrics in ICU estimates the history data of every child (particular attention is given on the most significant risk factors for SOM - development) and forms the risk group of SOM. The second step is the otoscopy examination of the infants of the risk group. Otology specialist chooses the patients with minimal otoscopic changes and forms the group of infants with suspicion of SOM. The third step is the audiometric investigations - impedance audiometry and ABR. If impedance audiometry changes are observed the BERA is registered. Impedance audiometry data are used for information of middle ear pathology presence and it character. BERA data give us possibility to estimate the profound of middle ear pathology and degree and character of hearing impairment.

VIII. CONCLUSION

We were able to compare the diagnosis and prognostic values of otomicroscopy, pneumatic otoscopy, impedance audiometry, and pure tone audiometry. We present an algorithm of the management of SOM in infants on the basis of our analysis. This algorithm was also verified in patients from the control group. We were able to correctly-diagnose this disease and prognosticate its course in over 97% of cases.

The application of elaborated diagnostic algorithm of SOM significantly improves the results of treatment.

REFERENCES:

[1] Marchant C.D., Mc Millan P.M., Shurin P.A. : Objective diagnosis of otitis media in early infancy by tympanometry and ipsilateral acoustic reflex thresholds - J. of pediatrics, 1986, v. 109, N 4, pp. 590 - 595.

[2] Paparella M.M., Shea D., Meyerhoff W.L., Goycoolea M.V.: Silent otitis media: clinical applications. Laryngoscope 96: 978, 2009

[3] Paparella M.M., Schachern P.A., Cureoglu S : Chronic Silent Otitis media – Journal of ORL, V. 64, N 2, 2002 p. 65-72

[4] Bluestone, Charles D.: Studies in Otitis Media: Laryngoscope Volume 114(11, PART 3) SUPP. NO, 105, November 2004, pp 1-26

[5] Абабий И.И., Дьякова С.А.: Диагностика латентных воспалительных заболеваний среднего уха у детей первого года жизни при помощи импедансометрии. - Журнал ушных, носовых и горловых болезней. 1994, N 5, с. 4 - 7.

[6] Абабий И.И., Дьякова С.А. Антохий И.Н., Манюк М.К.: Показатели коротколатентных слуховых вызванных потенциалов у детей грудного возраста с воспалением среднего уха. - Вестник оториноларингологии. 1995, N 4, с. 28 - 31.

I.Ababii, S.Diacova, M.Maniuc, A.Chiaburu, S.Parii. : Variantele otitelor medii acute la copii - Arta Medica. Chişinău, 2008, Nr 4 (31), p. 20 - 22.

Installation for Local Hyperthermia in Crossed Laser Fluxes

Iurie NICA*, Serghei ZAVRAJNÎI, Andrei GRITZCO, Iurie TIRON, Dumitru ESHANU, Vladimir MUSTEATZA, Andrei STALBE

Institute of Electronical Engeneering and Nanotechnologies „Dumitru Ghiţu", Chişinău, MD – 2028

**e-mail: tehmed@iieti.asm.md*

***Abstract* – As is well known, on heating up the tumor over 43 – 44^{0}C the tumor cells dies, whereas healthy tissues cells remain alive up to 50^{0}C. We propose local overheating malignant morbid growth, with infrared radiation from a laser system, focused on a specific area, forming this way a powerful, dispersed in the space, source of energy. To achieve the therapeutic dose in the body at depth of 10-12 cm is necessary to be used lasers with the radiation between wavelength range of 700nm - 850nm, for which there are seen windows of transparency in biological tissues, and the total power of 5 - 15 W.**

We have developed a installation, including: a block of laser diodes with individual collimating optics, directed in a common point; multi-channel thermometer of the irradiated area; two-axis table for accurate positioning of the irradiated sample with temperature sensors fixed on it relative to the common point of crossing lasers fluxes; computer, integrating all elements of the installation in one experimental - measuring station.

The experimental results confirm the ability of the radiation with a wavelength of 808 nm to penetrate the biological tissue to a depth of up to 90 mm and deeper. The effect evaluation of addition energy in the common point of the lasers beams demonstrate that to achieve the desired temperature of the tissue up to 43-44^{0}C to a depth of 9 cm is sufficient 5 ÷ 6 lasers with power emission 4W to wavelength of 808nm. In order to avoid the burning of the surface tissues of the body is necessary to ensure the power flow density not higher than 200mW/cm^2, which requires collimators or they're systems that provide a uniform flare by each laser corresponding to the area (20cm^2, in case of 4-watt lasers).

***Keywords* – local hypertermia; diode laser; crossed rays; near infrared region.**

I. INTRODUCTION

The problem of combating cancer diseases is one of the most acute problems of the contemporary medicine, which must be solved worldwide. In combating cancer tumors are used several strategies: surgical interventions, chemotherapeutic and radiological procedures, and more recent - local or general hyperthermia and photodynamic therapy; which are used individually or in various combinations. From invasiveness point of view of the human body the most sparing

procedure is hyperthermia which benefits from a specific property of the cells (proteins) affected by the cancer namely - the death at 43-45 C, temperature that does not affect the adjacent healthy cells. The hyperthermia of the malignant malformations could be achieved through the different methods: hot water jets, electromagnetic fields, infrared rays, etc.

Hyperthermia procedures can be made relatively simple if the malformations are located on the surface of the body or organs to which we have direct access. The situation is more complicated when the tumor tissue is located deeper.

Currently in medical practice are investigated and implemented several variants of local hyperthermia using non invasive or minimum invasive methods for heating the tumors located in depth of the biological tissue. During laser-induced interstitial thermotherapy (LITT) (or interstitial laser photocoagulation) the light is delivered through flexible fibers inserted into the center of the tumor. Laser light at the tip of the fiber raises the temperature of the tumor cells and damages or destroys them. Disadvantage of this method is the possibility of treating only small volumes of the pathological tissue (1-2 cm areas diameter). The cause consists in modifications of the optical properties of the heated biological tissue located in the immediate vicinity of the radial head of the optical guide. The volume of the heated area can be increased by using a flux with a higher irradiance [1], but this may cause unpredictable consequences, for example: the tissue temperature reaches or exceeds critical value at which begins the vaporization of the intracellular liquid, which could trigger dangerous unknown processes such as boiling or carbonization of the tissue [2]

The photodynamic therapy method, which speculates the property of the malignant tumors to concentrate the photosensitive materials in the pathogenic cells, can be achieved in two ways. The most widespread - photo chemotherapy uses photo sensitizers, which molecules got stimulated when absorbing of photons initiating such effects as: destruction of the mitochondrion; substantial changes in oxygen metabolism by generating of singlet oxygen ($^1O_2$), which is extremely cytotoxic, and a large quantity of free radicals [3-5].

The second way - photo thermotherapy, involves photo sensitizers that emit a large amount of heat in the process of photons absorption. Usually these are nano-dimensional structures, such as: metallic powder, nanotubes, nanorods or nanoshells with dielectric core and metallic shell [6]. The main disadvantage of this method consists in the formation of free radicals and chemical components, the role of which, currently, is not researched enough.

II. THE HYPERTHERMIA INSTALLATION: THE FUNCTIONAL BLOCKS

Classical hyperthermia is based on fact that to temperatures of 42-45^{0}C cell's DNA suffers irreversible pathologic modifications and cells dies, while healthy cells are recovering to remove excessive temperatures. Speculating this property of tumors, in the laboratory "Medical Equipment" of the Institute of Electronics

Engineering and Nanotechnologies "D. Ghiţu" has been developed a device designed for monitored heating into malignant tumors located in depth of the tissue. The device consists from several sources (laser diodes) which radiates into infrared region of the spectrum (808 nm). Radiation with this wavelength penetrates into the tissue up to a depth of 70-120 mm for about 10 W/cm^2 irradiance [7]. But these irradiations may cause substantial photothermal damages of the superficial tissues for irradiation time longer than 50ms. Therefore, the main problem consists into irradiating the malignant tumors, without affecting the tissues between the surface and the tumor. The problem is solved by transporting the energy through the different channels to the tumor, placing the tumor in place of the intersection of the several laser beams.

The main elements of the installation are (Figure 1):
• Set of laser diodes, equipped with optical beam forming equipment and orienting it into a common point;
• Module for measuring the temperature, equipped with a set of thermal sensors able to convert the temperature into electric signal and electric signal into binary code for computer data processing. In its version of the installation, as thermo sensitive components are used thermocouples CrNi / Ni FeCu;
• The tilting table (X / Y positioning) serves for accurate positioning of the region which must be heated in the flows crossing point. Positioning is carried out by two stepper motors driven by PC.
• PC - which function is to ensure the connection between all modules of the installation, thereby creating an integral experimental system.

As a source of coherent optical radiation are used devices ATC C4000-500 MFA-808-3-F200, which main elements are diode diodes with 808nm wavelength, which have a linear dependence between optical power and the electric current intensity which flows through the laser diode (maximal optical power 4W).

Temperature measurement of the irradiation region can be accomplished by using thermocouples. The electromotor power created by thermocouples is applied to the positive terminal of the operational amplifier (CMOS). Dependence between the value of the output signal of the amplifier input signal value is linear in range of $(0\text{-}50)^0$C. The maximum possible values of the amplifier output signal is corresponding to his power supply. The analogue signal received from the operational amplifier output is transmitted to the analog-to-digital converter input - (ADC). Each converter input has a thermocouple. The data obtained from ADC are sent to the computer to be processed and displayed as an image of the thermal field.

The computer, through the RS232 serial interface controls the commands transmission to position and irradiate the object, followed by collection, storage and processing the data obtained as a result of 2D and 3D images of created thermal fields. Based on submitted orders (the temperature registered in the given point) to the control module of the optical power of the laser diodes and received data describing the temperature distribution into the sample, the computer manages the irradiation process. If the current temperature in studied area does not correspond to the expectations (the difference is more than (0.2-0.3) 0C), the microcontroller, based on comparing the amount of data containing information about the necessary temperature and amount of data containing the actual temperature, increases or decreases (by disconnecting the laser diode) the optical power until the temperature will reach the required value. This method represents the discreet method of temperature control in the region. Another method is based on continuous monitoring and correction of the thermal field with an accuracy of ± 0.10 C.

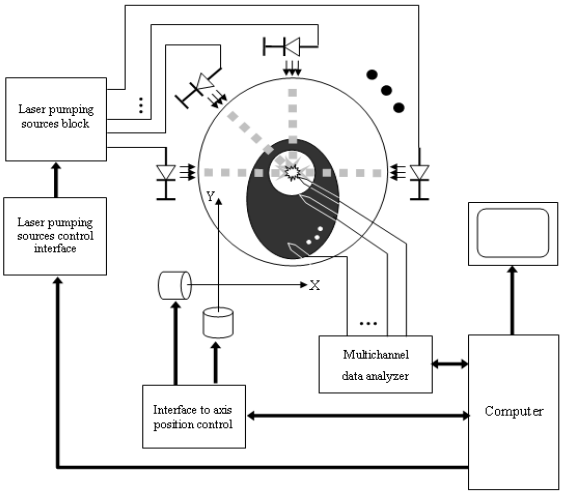

Fig. 1. Block diagram of the installation for study of local hyperthermia

Each laser diode is individually monitored by the system. The data which define the thermal regimes are transmitted through the RS232 serial interface to the executive modules, which converts the data into the optical power, producing themselves the required temperature inside the irradiated sample. The format of the data package contains the address of the module which the PC addresses to, and data about the required optical power. Creating and maintaining the working regime of the each laser diode is carried out based on comparing the data received from the computer and data obtained by the monitoring loop of the optical power. In the structure of the monitoring loop of the optical power is a photodiode, irradiated by a part of the electromagnetic flux produced by the laser diode. The signal level produced by the photodiode is directly proportional with the intensity of the radiation. The optical power control module processes the received data from the PC and monitoring loop after a specific algorithm, applying after that, an electrical signal adjusted to the sub-modules, whose function is to create the optical power corresponding to the signal.

III. THE REALIZATION OF THE LOCAL HYPERTHERMIA IN BIOLOGICAL TISSUE

3.1 Experiments purposes

1. Confirmation of the depth penetration of the biological tissues by the laser radiation with wavelength of 808 nm.
2. Monitoring and estimating the energy composition effect of the coherent infrared radiation beams which intersects in depth of the biological tissue.
3. Analyzing the possibilities of determining the constants that describe the thermal and optical characteristics of the biological tissues for thermal processes prognosis of the irradiated tissues.

3.2 Experiments Organization

An isotropic sample of biological tissue (egg white) fills the bottom of a glass cylinder with very thin walls. The cylinder has a diameter of 100 mm. In the sample are implanted the thermocouples forming a cross with perpendicular arms. The thermo sensitive peaks are in a horizontal plane parallel to the bottom of the cylinder. The

thermocouples are located on the arms of the cross at a distance of 20 mm from each other. The central thermocouple is located at the intersection point of the arms that are on the longitudinal axis of the cylinder. (Figure 2)

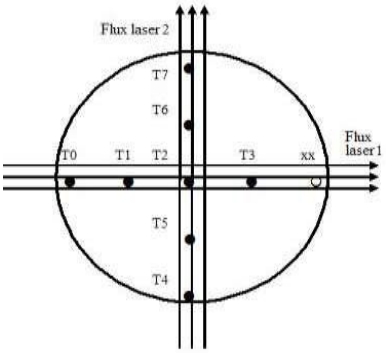

Figure 2. Fluxes emitted by the lasers are mutually perpendicular. The thermocouples are situated on the beams axis

In the experience has been used two lasers (laser diodes) with the same optical power in infrared emission (808nm) which beams propagates along those two rows of thermocouples intersecting in the position of the central thermocouple T2. The optical power emission of the W_{opt} laser diodes was 250 mW. The glass cylinder walls absorbs about 0.05% of the irradiance, so absorption can be neglected. The temperature registration regime of is shown in the description of the temperature monitoring module with 8 channels.

The lasers operated in such regimes as: intervals of absence of the radiation; irradiation of both lasers simultaneously; irradiation of one laser or another (Figure 3). For highlighting of as many nuances (details) of the process, the lasers operating intervals were quite long (30").

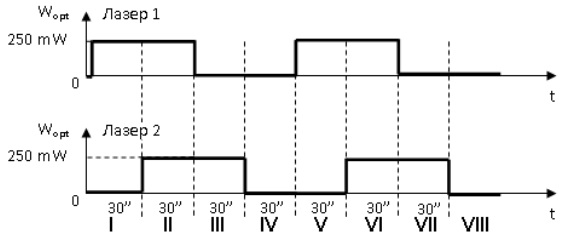

Fig. 3. The temporal charts of the alternance regimes of the laser operation

3.3 Experiments Results

In the Figure 4 is represented graphs of the time dependency of the recorded signals by thermocouples in described working lasers regimes.

The synphasic variations of the signals values registered together with the operating regimes of the lasers demonstrates the recorded influence on the sample. Is observed synphasic variations on all thermocouples, including those situated deeply in the biological sample (90 mm). This confirms the ability of deep penetration into biological tissue by the 808 nm infrared radiation.

The signal recorded by the central thermocouple (T2) illustrates composition of the infrared fluxes in the region of their intersection.

When switching the lasers, the radiation increases and decreases abruptly . . . and manifests itself in the worst case, during 25 ms, which is much faster than the variations presented in the charts. On charts, the recorded size variation from initial value to saturation value occurs in 3.75 sec, which exceeds . at about 150 times the interval of radiation increase. The same behavior occurs and in case of radiation decrease. So, the thermocouple does not register the influence of the electromagnetic field (Foucault currents).

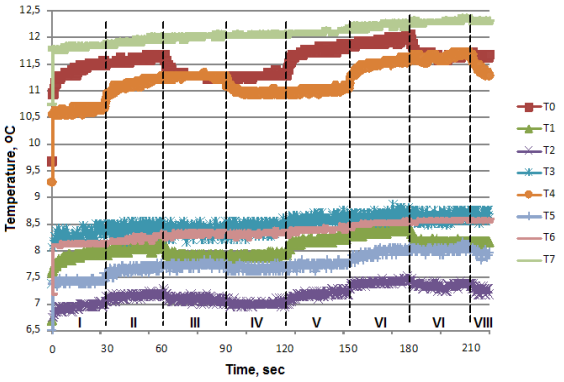

Fig. 4. Time dependence of the signals recorded by the thermocouples

Thermal inertia of the thermocouples, when measured separately (2.5 ms /° C .... 8.4 ms ° C /°) is much lower than the temporal variations shown on charts. So, the assumptions that are registered charts demonstrating the direct heating or cooling into thermocouples are not founded. Remains the conclusion that are registered temperature variations in the biological sample where are implanted thermocouples. Environmental temperature T with internal sources, which energy absorbing regions along the fluxes of radiation, described in the equation:

$$c * \rho * \frac{dT}{dt} = \beta * \nabla^2 T + D * \frac{W_0}{S} * e^{-D*r} \quad (1)$$

Where c - is the specific heat capacity of the environment, ρ - density, β - thermal conductivity, D - absorption, W_0 - The optical the power of the flow at entry into the environment, S - cross sectional area of the radiating flux, r - the module of the vectorial radius of the investigated region.

Equation (1) describes the time intervals I, II, V, VI for thermocouples T0, T1, T3 or II, III, VI, VII for thermocouples T4, T5, T6 and T7. Same equation applies for thermocouple T2 for the time intervals I, III, V and VII.For time intervals II and VI its value must be equal to the sum of the optical power of both optical lasers.

For non-irradiated areas or for times intervals when lasers don't work, so when W_0 = 0, the equation is:

$$c * \rho * \frac{dT}{dt} = \beta * \nabla^2 T \quad (2)$$

This relates for the time intervals III, IV, VII, VIII for thermocouples T0, T1, T3 or I, IV, V, VIII for thermocouples T4, T5, T6 and T7. The temperature in the region T2 is described by this equation for time intervals IV and VIII.

Is observed quick warming intervals when the temperature gradient in the observed region dV is not high and heat dissipation $\beta * \nabla^2 T * dV$ cannot match the energy accumulation which comes from released energy absorption $D * \frac{W_0}{S} * e^{-D*r} * dV$

In cases when warming the irradiated regions of the biological sample is faster than warming non-irradiated

regions, increases the temperature gradient in the irradiated regions and therefore, increases the heat evacuation from these regions. In this case we observe a pronounced decrease in growth speed of the temperature.

The decrease of the temperature that occurs when "extincting" the lasers demonstrates the redistribution process of the heat for thermal balance in the sample volume and is described very well by expression (2). Each following state of thermal balance is installed to a higher temperature than from which has started the previous warming, which demonstrates the accumulation process of the heat in biological sample.

For time intervals corresponding to the functioning of both lasers (II and VI) the curves shows a small growth (compared with the temperature growth caused by the irradiation of "its own" laser) caused by the penetration of the photons by the spreading mechanisms and the heat diffusion of an amount of energy . . . coming from nearby radiated regions. The curves erosion is caused by the dispersion . of the recorded data and determined by the resolution capacity of the entire channel . of the temperature recording ~ ± 0.05 ° C.

The different values of the initial temperatures in Figure 5.5 is caused by the distinction of the biological sample temperatures (6.5 ° C) and environment (27° C), which causes the heat transmission through the cylinder glass walls and biological sample stratification by the temperature (Figure 5).

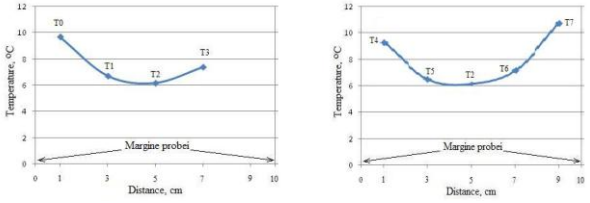

Fig. 5. The temperature field formed in the biological sample from the heat exchange with the environment. On the left- indications for thermocouples T0, T1, T2 and T3 on the right - the indications for thermocouples T4, T5, for, T6 and T7.

IV. PROCESSING AND ANALYZING THE EXPERIMENTS RESULTS

The temperature variations ΔT = T- To (To - biologic environment temperature before "switching ON" the lasers, T - biologic environment temperature at the time of measure.) at points where are situated the thermocouples, recorded in the process of biological environment radiation with radiation wavelength 808 nm are shown in Figure 6.

For analyzing of the biologic environment reaction to applied irradiation, we will explore the field distribution of temperature variations ΔT = T- To for a few characteristic temporal moments. We will choose the following items:

t1 - 1 laser works in steady state, laser 2 does not work;

t2 - both lasers works steady, at the next moment 1 laser will be "off";

t3 - 2 laser works in steady state and relaxation processes caused by "off state" of the 1 laser has ended.

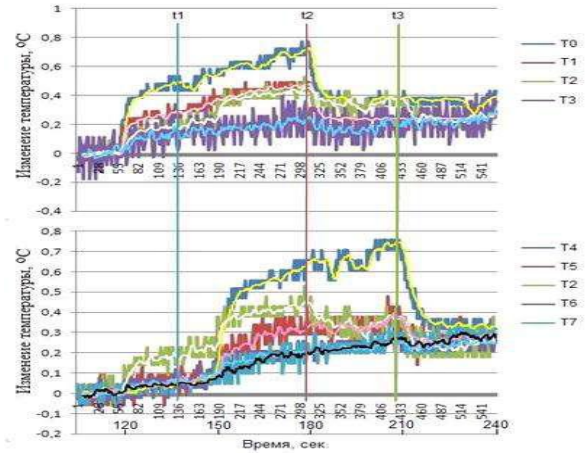

Fig. 6. The temperature variations ΔT in one cycle of irradiation of the biological sample with 808 nm infrared radiation. Top - the values along the laser beam 1, bottom- the values along the laser beam 2.

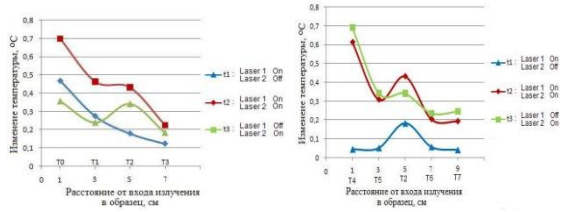

a b

Fig. 7: The distribution of the temperature variations ΔT in the biological sample in selected moments: a) along 1 laser beam, b) along 2 laser beam.

Moment t_1:

Figure 7 a*)* Exponential distribution of the temperature variations ΔT towards T0, T1, T2, T3 according with *(1)*

Figure 7 b) The temperature variation exclusively in T2 region which is common for both lasers fluxes. For points T4, T5, T6, T7 substantial variations of the temperature are not registered because laser 2 doesn't work.

Figure 7 b) The temperature variation exclusively in T2 region which is common for both lasers fluxes. For points T4, T5, T6, T7 substantial variations of the temperature are not registered because laser 2 doesn't work.

Moment t_2:

Figure 7a) Continues the exponential growth of the temperature according to (1) in the center of (T2) we observe a significant warming since W0 factor which describing energy absorbing is the

Figure 7b) Same as 7 a)

sum of the optical radiation which penetrates into the environment from both lasers

We mention, that until "switching ON" the laser 2, in the point T1 were much more warmth than in the T2. Therefore the heating process in T2 is slower compared with heating in T1. In case b) for thermocouples T5 and T2 the process is reversed. Which differences are explained on charts a) and b) in the moment T2.

Moment t_3:

Figure 7a*)* Cooling process takes place in accordance with (*2)* apart from center *(*T2) where occurs the accumulation of the heat from laser 2. Decreasing the temperature in the center (*T2)* compared with its value at time t2 explained through . the flow at reduction due to ″off state" of the laser 1. Now in this region comes less radiation, and therefore is accumulated less heat. For thermodynamic balance is necessary a lower rate of evacuation of the surplus warmth, thus a lower temperature gradient.

Figure 7 b) Is shown the temperature breakdown on the direction T4, T5, T2, T6, T7 (according with temperature variation in the center. See the comments Figure 7a). For a longer regime duration of irradiating the sample, the exponential curve will keep the trend, according to (1).

V. CONCLUSIONS

Was confirmed the depth penetration of the biological tissue at the laser radiation wavelength of 808 nm. Variations of the temperature were registered by all thermocouples implanted in the biological sample, including those most distant, located at 90 mm from the beam entry location in the sample.

The signal registered by the central thermocouple T2 demonstrates the composition effect of the coherent infrared radiation beams energy intersecting in the depth of the biological tissue.

The analysis of the composition effect of the coherent infrared radiation beams energy intersecting in the depth of the biological sample suggests the need of substantial increasing of the lasers number energy characteristics equivalent to those used (250 mW) and of collimators (Øbeam = 7.14 mm) for heating with $\Delta T \sim 7 \div 100C$ at the depths of 90 mm.

When using more powerful laser diodes (4 W) can be enough 5 ÷ 6 pieces, but then to obtain the irradiation of 200mW/cm2 (supportable for the surface tissues) collimators or systems are required to ensure the uniform irradiation of the surfaces with areas of about 20 cm2.

A solution would be to use the impulsive radiation regime (50-200 ns with the frequency (ν) equal to 1-50000 Hz) with more powerful lasers.

Any approach is possible because in the development of the installation have been used the block-module concept which is very flexible and allows any reconfiguration of the installation.

ACKNOLEDGMENTS

The work was supported by the Suprem Council for Science and Technological Development of the Academy of Science of Republic of Moldova (Project 06.420.007A)

REFERENCES

[1] M. Prudhomme, J. Tang, S. Rouy, G. Delacretaz, R. Salathe, G. Godlewski, Diode laser and interstitial hyperthermia against colonic cancer. Effect of power settings on necrosis size, *Proc. SPIE*, **2327,** 1994, pp. 283-286.

[2] D. Wyman, W. Whelan, B. Wilson, Interstitial laser photocoagulation: Nd:YAG 1064 nm optical fibre source compared to point heat source, *Lasers Surg. Med.*, 12, 1992, pp.659-664;
D. Wyman, W. Whelan, Basic optothermal diffusion theory for interstitial laser photocoagulation, *Med. Phys.*, 21, 1994, pp.1651-1656.

[3] М.Л. Гельфонд. Фотодинамическая терапия в онкологии. Практическая Онкология, Т.8., №4, 2007.

[4] B.W. Henderson, T.J. Dougherty, How does photodynamic therapy work? Photochem. Photobiol. Vol.55, 1992, pp.145-157.

[5] G.Jori, E.Reddi, The role of lipoproteins in the delivery of tumour-targeting photo-sensitizers, Int. J. Biochem. Vol.25, 1993, pp.1369-1375.

[6] Y.Feng, et al. Optimal Design of Laser Surgery for Cancer Treatment Through Nanoshell – Mediated Hyperthermia Therapy, Nanotech , Vol.1, 2005, pp.39 – 42.

[7] Х.П. Берлиен, Г.Й. Мюллер, Прикладная лазерная медицина, М: Интерэксперт, 1997.

The Role of Microscopic Techniques in Performing Tympanoplasty in Children

I. ABABII, L. DANILOV, M. MANIUC, P. Ababii, S. DIACOVA
SMPhU "N. Testemitanu" Department of ORL

Abstract

Introduction

Tympanoplasty is a delicate microsurgery, surgery repairing an anatomical lesion of the middle ear, caused by suppuration of chronic otitis.

Objectives

The main direction of the study is to determine the efficacy of tympanoplasty under microscopic control preoperatively, during surgery and postoperatively.ListenRead phonetically

Materials and methods

In the clinic of pediatric otorhinolaryngology, 220 tympanoplasties were performed in children aged 8 to 18 years in the period 1995 – 2010. For examining the affected ear was used the surgical microscope "Opton". During surgery it was used the retroauricular access, given the narrow ear canal and need to perform control antrotomy in children. The temporal fascia, previously taken above the operated ear, was used as a graft. The fibrous ring of the tympanum perforation edge was removed and the skin of the posterior wall of the external auditory canal with the tympanum ring and the posterior part of the tympanum were taken off. During operation, after a detailed microscopic examination of middle ear, it was planned the type of tympanoplasty. As support for the fascial graft was used the gelfoam applied in the middle ear. It was used the surgical technique "Underlay" or „Overlay".

Results

Positive results after tympanoplasty using surgical microscope, characterized by integral neo tympanum, lack of exacerbations of the inflammatory process of the middle ear, were obtained in 83% of operated children, including 45% cases with the improvement of hearing.

Conclusion

Microscopic control of the affected ear before, during and after surgery improves clearly the quality of microsurgical intervention, reduces the number of ear complications, improves hearing in children and reduces their invalidity.

I. INTRODUCTION

Otorhinolaryngology is continuously developing from one decade to another, as a result of technical progress (microscopes, optical endoscopes, laser) and microsurgical instruments, by constant improvement of means of investigation and treatment.

Classical Otology has changed substantially in recent decades by finding and describing new otic diseases, by the appearance of new operative techniques aimed at a functional and reconstructive surgery of the middle ear [3].

Hearing is crucial for child's development. It assures one of the main needs - verbal communication.

Tympanic membrane is one of the elements of the transformer, impedance adapter and reducing loss of sound energy system of the myringo-ossicular system, contributing through its surface to the hydraulic transformation (myringo-platinary) and serves to protect the cavum tympani region [2; 4].

Myringoplasty has two main goals: sound protection of the round window and restoring the surface and the tension of the tympanic membrane using a graft.

Tympanoplasty is a delicate microsurgery, surgery repairing an anatomical lesion of the middle ear, caused by suppuration of chronic otitis. This functional surgery aims to achieve an improvement in hearing. Tympanoplasty requires a spirit of analysis, being not a standard operation [5].

Myringoplasty and tympanoplasty are descriptive terms defining surgical procedures that address pathology of the tympanic membrane and middle ear. Myringoplasty is an operative procedure used in the reconstruction of a perforation of the tympanic membrane. This assumes that the middle ear space, its mucosa, and the ossicular chain are free of active infection. There is no direct inspection of the middle ar during this procedure. Tympanoplasty implies reconstruction of the tympanic membrane but also deals with pathology within the middle ear cleft, such as chronic infection, cholesteatoma, or an ossicular chain problem.

Before deciding to undertake a tympanoplasty, a rigorous testing should be carried out to detect and eliminate any existing problems (adenoids, nasal septum deviation, pharyngitis, rhino-sinusitis etc.); general testing will detect the general diseases of the patient [1, 6].

Indications for tympanoplasty:

-permeable auditory tube (controlled by artificial eardrum tolerance test, by tubal blowing or even impedancemetry);

-disabling traumatic or post-otitic "dry" perforations;

- appropriate vascular bed - for nutrition of the graft.

Contraindications to tympanoplasty are divided into two major groups:

1. Absolute contraindications (unconditioned):

a) complete hearing loss;

b) mixed hearing loss with the prevailing of the perception type;

c) completely blocked auditory tube, if tube permeability can not be restored;

2. Conditioned contraindications:

a) intracranial complications;

b) reheated chronic suppurative otitis media;

c) eczema and dermatitis of the ear canal and auricular region;
d) extended decay of the tympanic box walls;
e) reduced permeability of auditory tube;
f) various nasal conditions, nasopharyngitis, and various general diseases such as tuberculosis in the active stage, syphilis, infectious contagious diseases, etc. [3].

Conditions necessary for sound transmission after tympanoplasty:

1. Permeable auditory tube (controlled by artificial eardrum tolerance test, by tubal blowing or even impedancemetria), for ventilation and drainage;
2. Closing the perforation of the eardrum or the space with neotympanum;
3. Restoring the sound transmission path from the neo-tympani to perilymph (columelar effect);
4. The two windows should be free on both sides of the membranous labyrinth.

The rate of success of pediatric tympanoplasty is likely not a matter of age, but a matter of patient selection. Careful attention to factors such as technique, eustachian-tube function, and site and size of the perforation will likely increase the rate of an intact tympanic membrane with improvement in hearing. No one variable determines outcome. Clearly, some factors studied are age-related, but age in itself should not be an indication or contraindication to treatment. The overall success rate of tympanoplasty, with or without mastoidectomy, in the treatment of chronic pediatric otitis media, was high and did not depend on patient age, the status of the contralateral ear, the inclusion or absence of surgical mastoidectomy, or the method of mastoidectomy (when this procedure was employed). Tympanoplasty may be expected to improve hearing in cases of chronic otitis media accompanied by perforation, but not in cases of cholesteatoma.

II. OBJECTIVES

The main direction of the study is to determine the efficacy of tympanoplasty under microscopic control preoperatively, during surgery and postoperatively. Materials and methods

In the clinic of pediatric otorhinolaryngology, 220 tympanoplasties were performed in children aged 8 to 18 years in the period 1995 – 2010. Surgeries were performed under general anesthesia and the control of the microscope "Opton".

Preoperatively, the patient is examined in the dressing room, using a microscope. The ear canal and eardrums of the child is examined, place of perforation of the affected ear is evaluated, pathological eliminations are excluded and the final diagnosis is established, chronic epitympanitis or mesotympanitis in remission. During surgery (tympanoplasty) surgical microscope is used for more detailed examination of the middle ear, the mobility of osicular chain is evaluated (hammer, anvil, stirrup) and if possible, mobility of the oval window. Following these examinations, the type of tympanoplasty is planned during surgery.

Detailed microscopic examination of the neotympanum is also carried out after surgery, after removing the tampons of the ear canal. Postoperative complications are excluded, the vascularization of the neotympanum is evaluated.

During the surgery the retroauricular way was used, taking into account the narrow auditory canal in children and need to perform the control antrotomy. As a graft the temporal fascia taken above the operated ear or tragus perichondrium were used.

For convenience during surgery, a dual instrument table was elaborated. On the inferior part is placed the patient's head, on superior one - the microsurgical instruments needed. Another device developed by us, is the one for mounting ear spectaculum, which consists of a fixing mechanism to the surgical table, a telescopic arm and an ear speculation mounting mechanism. This device practically assures the surgeon’s bimanual work.

At the beginning of surgery, firstly the ear canal is cleaned by careful aspiration. The fibrous ring of the eardrum perforation edge is removed and the skin of the posterior wall of the external auditory canal with eardrums ring is taken off. When the front edge of the perforation or at least the tympanic ring was present, it was used the Underlay technique - fascia placed under the flap.

Graft over the remains of the eardrum (the technique of "Overlay") was applied when the anterior fibrous ring or perforation anterior edge was missing. As support for the fascial graft was used the gelfoam applied in the middle ear. The gelfoam sponges soaked with Sol. Hydrocortizoni were applied on fascia followed by tampons soaked with antibiotic ointment. After 8 - 10 days, all the tampons are removed from the ear canal and antibiotic ointment is applied locally.

III. CONCLUSION

Positive results after tympanoplasty using surgical microscope, characterized by integral neo-tympanum, lack of exacerbations of the inflammatory process of the inner ear were obtained in 83% of children operated on, 45% of cases being with improvement of hearing. Microscopic control of affected ear before, during and after surgery, improves clearly the quality of microsurgical intervention, reduces the number of ear complications, improves hearing in children and reduces their invalidity

REFERENCES

[1] Ataman Traian. Cofochirurgia, 1993
[2] Black j., Hickey S. An analysis of results of myringoplasty in children International Journal of pediatric Otorhinolar. 31(1995) 95-100
[3] Ciuchi V. Patologia inflamatorie cronică a urechii medii. Sechelele postotitice. Bucureşti, 2004.
[4] Isaacson G. Tympanoplasty in children Otolaryngologic clinics of north america.Volume 27.Number 1994 p. 593-604.
[5] Perkins R. Tympanic membrane reconstruction using formaldehyde-formed autogenous temporalis fascia: Twenty years’ experience. Otolaringol Head Neck Surg 1996; 114: 366-79.
Potsic P. Tympanoplasty for the Anterior – Superior Perforation in Children. TheAmerican Journal of Otology 17;115 – 118, 1996.

Biomedical Physiotherapeutic Complex

Valerian DOROGAN, Vitalie SECRIERU, Tatiana VIERU, Stanislav VIERU, Andrei DOROGAN,
Eugeniu MUNTEANU, Ştefan Balica
Technical University of Moldova
dorogan_lme@yahoo.com

***Abstract* – The paper describes the biomedical physiotherapeutic complex elaborated in Laboratory of Micro-Optoelectronics of the Technical University of Moldova. The elaborated complex includes the implementation of a large range of realizations of microelectronics and modern nanotechnologies and of medicine research. A concept of realizing a physiotherapeutic complex is described in the paper.**

***Index Terms* – aero ionization, laser therapy, trans-coetaneous electrical nerve stimulator, millimeter waves, module structure.**

I. INTRODUCTION

The authors had been involved in the elaboration and implementation of physiotherapeutic complex, because Republic of Moldova has lack of medical and physiotherapeutic devices in regional and ambulatory centers. The paper presents the obtained results.

II. BIOMEDICAL PHYSIOTHERAPEUTIC DEVICE CONCEPT

A new physiotherapeutic complex system was elaborated during study and experimental elaboration in the field of modern technologies. It assures a complex physiotherapeutic treatment using the methods: trans-coetaneous electrostimulation of nerves (TENS), laser radiation therapy in the visible and IR range, ultraviolet radiation therapy, therapy using ionized air.

The therapeutic complex system is consisted of an electronic block (Main Module) based on an advanced microcontroller, which assures the functionality of all elements, working regime setup, patients and operating regimes' information storage. The system is connected to the netbook through a USB interface, equipped with specialized software, which permits to guide the output ports and their functionality control. The netbook usage permits to graphically visualize the selected parameters for therapy.

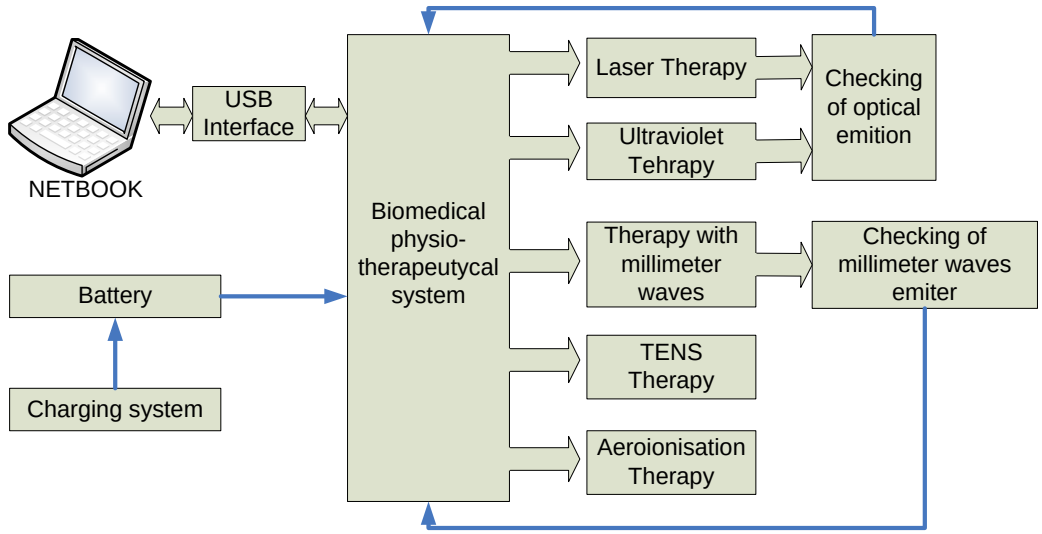

Fig. 1. Block scheme of the physiotherapeutic complex.

The supply is made from the network and from an autonomous supply system, which assures the system's mobility and excludes the electrical power network jamming. The system permits to use 5 independent ports (peripheral modules) designated for laser therapy in IR, ultraviolet therapy, millimetric waves therapy, therapy through trans-coetaneous electrostimulation of nerves and therapy with ionized air.

III. OPERATING MODE OF THE PHYSIOTHERAPEUTYCAL SYSTEM

The execution program of the physiotherapeutic complex has a model alike an operating system. The structure of program functioning of the physiotherapeutic complex is represented in figure 2.

The linkage between peripheral modules is made by the program core, which controls the functioning state of these modules. The interaction with the PC (user) is assured at the same time.

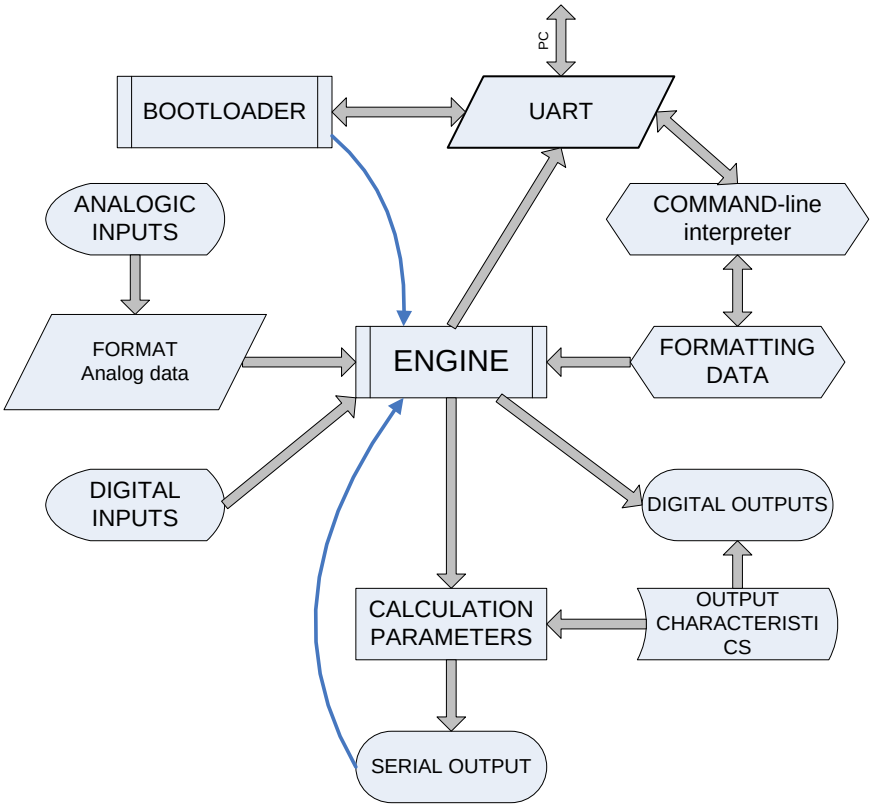

Fig..2. Operating scheme of the firmware

IV. COMMUNICATION OF COMMAND-LINE WITH THE SYSTEM

The data obtained from PC through the asynchronous bus is interpreted through a command-line. The used command-line has the following advantages:

- usage commodity;
- increased flexibility;
- extended data operating possibilities;
- autonomous functioning.

The command-line will search the word, which will correspond to a command from the PC part, at the beginning of the received data sequence, for example "PTC_TEMP". In this case, the core will determine the execution of temperature read function, will prepare the answer for PC and will order the transmission of data. After existent data transmission towards calling stack, the results about the current temperature inside the physiotherapeutic complex will be transmitted towards.

The command-line represents a standby module, which has lots of received data operating possibilities. One of the possibilities is the determination of command parameters. For example the PC sent the command "TENS_D 100". The respective command has to setup the time duration for the TENS module to 100 μs. The command-line will determine the parameters of the income command, which has the value 100 in our case.

Although, the command-line usage imposes some impediments during operation caused by the following shortcomings:

- the closed structure does not permit the operation with all data inside the command-line system;
- high execution time and big program volume;
- high volume of the used operating memory.

V. MAIN MODULE

It has to be mentioned that not only peripheral modules can be modernized, but, also, the main module. At the moment the most popular idea is to equip any kind of device with the possibility of firmware update. This is why the device possesses an "update port", or uses one of the general use ports. The update procedure is different from the general communication one of the selected port. The program frequency that is responsible for update is named bootloader and is run in a special way. The physiotherapeutic complex is also equipped with a bootloader making the update and device modernization possible at a maximum range. The update is performed from PC through the communication interface of the device (USB) using a special program.

The execution of bootloader is made immediately after the complex turns on. If the linkage between bootloader and PC is stabilized in 2 seconds, the bootloader starts up the update regime of the basic program. The firmware updates in sequences, each sequence being verified using a sum control. After finishing the update the program control turns into the execution sequence of the complex. If the linkage was not setup after 2 seconds, the basic program will be executed.

VI. INTERACTION OF MODULES OF THE PHYSIOTHERAPEUTIC COMPLEX

The operation with the physiotherapeutic complex modules is made using the following components:

- Digital inputs;
- Analog inputs;
- Digital outputs;
- Analog outputs;

The digital inputs are used to visualize some states for the respective module. The state of the button placed on the optic head can serve as example for the laser module. The button is used for an easier interaction of the user with complex during the procedures.

The analog inputs of the main module are used for monitoring the output circuits' state of the complex. The analog signal converted into digital one demands a special formatting, because different modules have different output parameters. The read analog signal is represented in a special

form, the final representation in voltage would be for the TENS module. The core will determine the module stop for protecting against an eventual output shortcut if the output voltage value would be lower on ¾ than the setup voltage value.

The digital outputs possess 2 functions: signal creation and module connection. Initially, the module is turned on in standby state. After that the output signal is generated and the module turns form standby state into functioning regime. In order to simplify the module stop it is necessary that the PC would indicate the stop command of the output signal.

Digital potentiometers of 8 bits are used to form the analog outputs. The guidance of a digital potentiometer is made using the synchronous bus TWI. Two digital potentiometers are coupled in serial mode in order to increase the precision up to 9 bits. The nonlinearity of the output signal has also increased, but remained in acceptable limits.

VII. OPERATION EXAMPLE FOR THE LASER THERAPY MODULE.

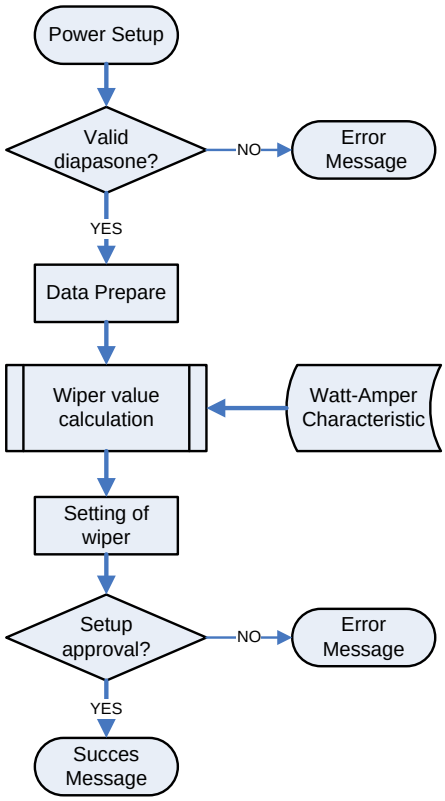

Fig. 3. Block scheme of laser's power setup.

Conforming to the functioning specifics of the quantum therapy module it is necessary to setup the laser output power by making the PC query the execution of power setup.

The block scheme of laser emission power setup is presented in figure 3. The core will verify if the if the power corresponds to the 5-50 mW diapason. Further, data preparation and the calculus of potentiometer values will be done, which will correspond to the laser watt-ampere characteristic. The watt-ampere characteristic of the laser is positioned in a data array from the address space of the internal EEPROM of the microcontroller. The calculus of the potentiometer value is coming after calculating the laser's work current. The potentiometer will form the reference voltage, which corresponds to the laser's current source. characteristics.

VIII. PC APPLICATION

A PC application was created for communicating with the physiotherapeutic system.

The main requirements for the application are reflected by the USE-CASE diagram (figure 4) and the program functionalities by the classes' diagram.. A driver for RS232 device was installed, for controlling the module from USB port, and will contain a dll file with a set of API commands, which will be used by the PC to execute the commands.

The program controls a medical device though the USB port, which has a graphical interface with access for modifying and deleting patients' data into a database, represented in Access data file. This way the doctor will be able to visualize and control the technical regimes for each person, configure the TeraLaser or other device. The program provides a display control of the module's response to the queries applied through USB port.

IX. CONCLUSIONS

A prototype of a complex system for physiotherapy was elaborated as a result of the activity in the frame of a project, which will contain different modules like: main module, communication module with the PC, Teralaser module, air-ion-therapy module, and trans-coetaneous electrostimulated therapy module of the nervous terminations (TENS).

Principles that vise the Visual Studio medium, C# language were engaged for PC connection and guidance. The connection of one peripheral device through the USB port was realized using this language (RS232 driver). Different libraries were also used such as ADO.NET for registering, modifying and deletion of patients' data in the Access type files. The commands' transmission towards the periphery and response receiving was realized in the program. The program guides the peripheral equipment using a set of commands, such as "help/r/n", "TENSVOLTAGE 40 mW/r/n" ect. Each module has its own properties and table in database. Any king of database registration vises the properties selected by the doctor.

REFERENCES

[1] http://ftdichip.com/Drivers/CDM/CDM20602.zip - communication driver

[2] http://ftdichip.com/Documents/ProgramGuides/D2XX_Programmer%27s_Guide(FT_000071).pdf – description of FT2XX APIs.

[3] http://www.codeproject.com/KB/cs/serialcommunication.aspx - comunicarea prin porturi USB, Autor Tapan Dantre

[4] AVR109: Self Programming http://www.atmel.com/dyn/resources/prod_documents/doc1644.pdf

[5] D. Knuth, The Art of Programming. Addison-Wesley, 1973

[6] Using the TWI module as I2C master on tinyAVR and megaAVR devices http://www.atmel.com/dyn/resources/prod_documents/doc2564.pdf.

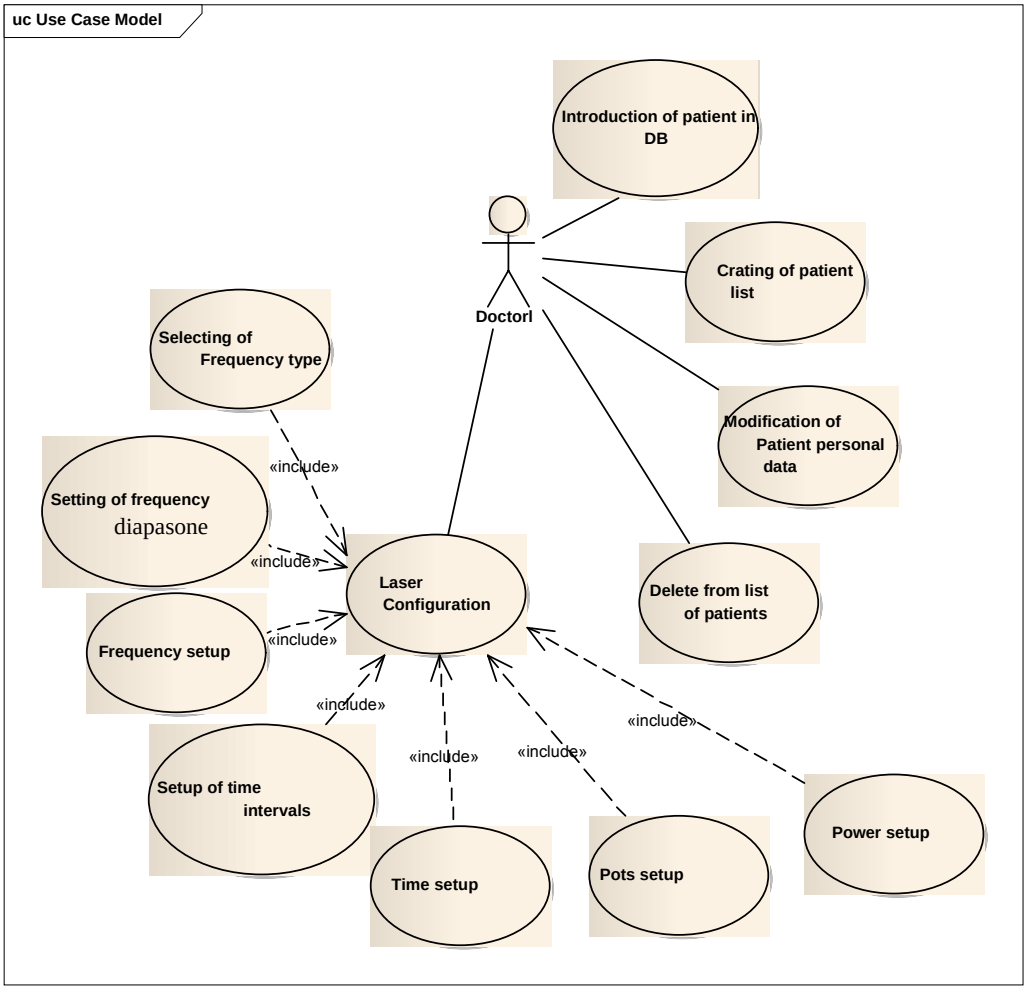

Fig. 4 USE-CASE diagram of the PC application

The Change of Peripheral Excitability Caused by Millimeter Waves

Aurel SAULEA, prof., Dr. hab., Victoria CHIHAI, lector-assistant
Department of Physiology and Biophysics, State Medical and Pharmaceutical University „Nicolae Testemitanu" of the Republic of Moldova

***Abstract* – We conducted a double blinded prospective trial to evaluate the change peripheral excitability effect of millimeter waves (MW) under experimental conditions. Sixty healthy volunteers were exposed to active medical MW generator and to a disabled sham generator. Characteristics of continuous wave electromagnetic output from the active generator were: wavelength 5,6 mm incident power density 10 mW/cm^2 and duration of exposure 15 min and 30 min. MW produced a significant (p<0,0001) decreasing of peripheral sensibility in group with duration of exposure 30 min and non-significant decreasing of peripheral sensibility in group with duration of exposure 15 min. decreasing of peripheral sensibility (sensitivity) was appreciated by increasing of cronaxia – one of parameter of peripheral sensibility.**

With on average 200% of the 30 volunteers 11 (36,6%) reacted to the active MW generator with an decreased peripheral sensitivity by individual reactions varied from 300% to 345% comparison with their own preexposure levels.

MW therapy con be used as a supplementary or alternative treatment for decrease peripheral sensitivity for example peripheral pain.

I. INTRODUCTION

Electromagnetic millimeter waves (MW) are one of components of environment. Technical progress change wavelength, frequencies on incident power levels of millimeter waves. At present electromagnetic millimeter waves with incident power levels < 25 mW/cm have been used for medical purposes in several Eastern European chantries for more them a decade [1].

Our analysis of literature reveled the more material accumulated the present about biological effect and radiant energy of electromagnetic millimeter waves [2].

The first biological structures which feel MW action are peripheral skin structures: receptors, capillaries, organically and non-organically water solutions [3].

This is a very important feature of MW which con be used for study any peripheral effects and changes of any peripheral parameters.

Very few publications [2] contained clinical results with the use of MW obtained in a double-blinded manner. What because we effectuated a double- blinded study in healthy human volunteers for investigating changes of peripheral sensitivity in MW action. Sensitivity modification was studding by increasing or decreasing of cronaxie – one of parameters of peripheral sensitivity.

The results of our study are described below.

II. METHODS

Sixty volunteers participated in the study. The volunteers were students of University of Medicine and Pharmacy from Chisinau (R.Moldova). All students were informed about the physical and biological properties of MW and all of then gave their consent to participate in the study. The criteria for volunteers were: heating adults 18/20 yr old, none was a chronic pain sufferer or was taking any medication. Volunteers were divided in 2 groups by 30 in each group.

Volunteers from ferst group were exposed to an active and a sham MW generator with duration 15 min. Before and after exposition to MW generator we have recorded value of cronaxie.

Volunteers from second group was exposed to an active sham MW generator during 30 min, before and after exposition we have recorded cronaxie. In this way we a formed a baseline reading of cronaxie for each group of exposition. The medical MW generator "КВЧ универсал" used in this study emitted a continuants electromagnetic signal with frequency of 8 Hz (corresponding wavelength 5,6 mm) and incident power density of 10 mW/cm^2 . the hand skin between thumb and index finger (corresponding to biological active point G4) was exposed to the generator MW, the patient was sifting in an chair. The waveguide of the generator was located at the skin surface. The order of exposure of volunteers to an active and sham generator was varied randomly.

Cronaxie was recorded by system "Neoropuls" by active electrode located in the point G4: method begin by recording of rebases - minimal sensitive threshold and after then time action of double rebases will be cronaxie.

Two identical devices were used for exposure to electromagnetic MW and sham exposure. The output of the sham generator was disconnected, but all of the external features of both generators were the same.

The generators were marked 1 and 2 and the responses of the volunteers were analyzed separately.

Comparison of baseline readings with the results of true and sham exposures was performed by using Mann-Whitney U test. The level of significance was set at (P<0,001) for gust for one test.

III. RESULTS AND DISCUSSION

Possible adverse effects were monitored by observing the volunteers and by asking them questions about any reactions in time of exposition. No adverse effects of exposure to MW were noticed.

The response of volunteers exposed to MW 15 min peripheral excitability increase and cronaxie decrease by 4,2% (Fig.1).

The response of the same volunteers exposed to sham generator 15 min peripheral excitability decrease cronaxie increase by 14,3%.

The response of volunteers exposed to MW generator 30 min peripheral excitability decrease cronaxie increase by 21,2% (p<0,0001). The response of the same volunteers exposed to sham generator 30 min peripheral excitability decrease - by cronaxie increase by 19,9% (fig.2).

Our results indicate that MW produce decreasing of peripheral excitability in healthy volunteers . This is significant increasing (p< 0, 0001) of cronaxie in time of exposition to 30 min.

Exposition to 15 min or to shame generator not produce significant decreasing of peripheral excitability (in creasing of cronaxie).

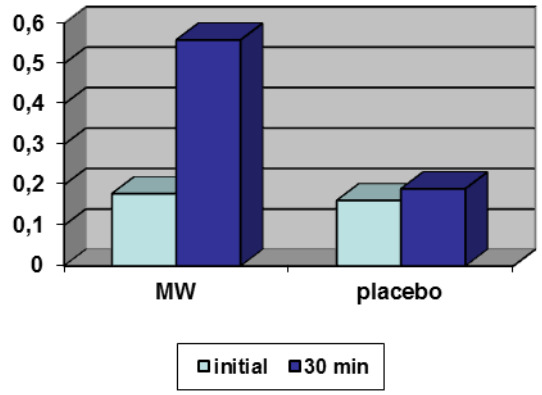

Fig.1. Changes of cronaxia in MW after 15 minutes.

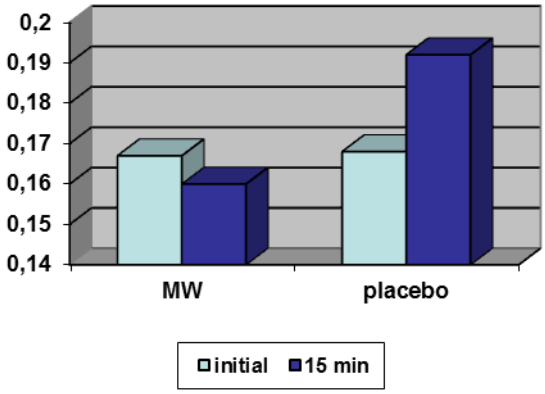

Fig. 2 Changes of cronaxia in MW after 30 minutes..

Our results, obtained under double-blinded conditions, show that a 30 min exposure to the MW produce in creasing of cronaxie one of the parameters of peripheral excitability. MW has three levels of interaction in human body: primary sensors of MW in the organism; pathwaystransmitting the signal to the regulating center; biological and chemical substrates implementing the response to the stimulus. Some clinical results indicate that the central nervous system participates in response to MW stimuli; for example, electroencephalogram changes were registered in healthy volunteers [6] and children with cerebral paralysis [7] as results of their exposure to MW.

Also the ability of neurons of organisms to react to low-power MW signals [5,6]. Thus nerve ending possibly participate in the primary reception of MW. Our results open any explication of this possibly mechanism. But, in summary, mechanisms of MW remain to be elucidated more.

REFERENCES

[1] Rradzievsky A., Rojavin M., Cown A., Ziskin M. Suppression of pain sensation caused by millimeter waves: a double-blinded, cross-over, prospective human volunteer study. Anesth Analg.1999, 88:836-40.

[2] Rojavin M., Ziskin M. Medical application of millimeter waves. Q J Med 1998; 91:57-66.

[3] Korpan N., Saradeth T. Clinical effects of continuous microwaves for postoperative septic wound treatment: a double-blinded controlled trial. Am J Surg 1995; 170:271-6

[4] Walsh N., Schoenfeld I., Ramamurthy S., Hoffman J. Normative model for cold pressor test. Am J Phys Med Rehabil 1989;68:6-1.

[5] Alekseev S., Ziskin M., Kochetkova N., Bolshakov M. Millimeter waves thermally alter the firing rate of the Lymnaea pacemaker neuron. Bioelectromagnetics 1997;18:89-98.

[6] Akoev G., Avelev V., ASemenjkov P. Reception of low-intensity millimeter waves electromagnetic radiation by the electro receptors in skates. Neuroscience 1995; 66:15-17

[7] Antonova L., Zhukovskii V., Kovalenko V., Semenova K. The clinico-electrophysiological assessment of the efficacy of microwaves resonance therapy in the rehabilitative treatment of patients with cerebral palsy in the firm of spastic diplegia. Vopr Kurortol Fizioter Lech Fiz kult 1995; 4:13-7.

[8] Saulea A., Chihai V. The millimeter waves in medicine and biology. The XIII international symposium, Russia, Moscow, 2003; 100-102.

The Implementation of Modern Digital Technology in X-ray Medical Diagnoses in Republic of Moldova – a Stringent Necessity.

Andrei ROSCA
Technical University of Moldova.
e-mail: cimrms@gmail.com.

***Abstract* – The study includes the analyses of state of technical X-ray diagnostic equipment from public medico-sanitary institution of Ministry of Health of Republic of Moldova (IMSP MS RM) at 01.01.11.**
The traditional RD apparatuses' were morally and physically outrun at 96,6% (in raional MSPI- 93,5%), inclusive the dental one -92,0% (in raional MSPI-97,2%), X-Ray exam -100%, mobile – 84,1% etc.
The exploitation of the traditional RD apparatuses' with high degree of physical and moral wear essentially diminished the quality of profile investigation, creates premises for diagnostic error perpetrating, increase the collective ionsating irradiation of population etc.
In recent years it starts the subvention of MSPI HM RM with digital RD dispositive, a process, which very hard unfold because of grave socio-economic crises in Republic of Moldova (since 01.01.11 only 30 apparatuses are pure digital). Despite these obstacles the subvention of MSPI HM RM with digital equipment represent a stringent necessity and a time request.

***Key word*– traditional X-ray exam, digital X-ray exam, and moral wear, the digital dispositive subvention.**

IV. INTRODUCTION

The utilization of traditional X-ray diagnostic dispositive (RD) at present time in Republic of Moldova represent a outrun procedure which decrease considerable the X-ray exam quality, increase the ionsating irradiation doze of population etc. This using is essentially disturbing by absence of the exchange pieces, which are not produced any more, the patients exam by second hand dispositive, supplied by humanitarian aid is very difficult because of lack of necessary documentation (using manual the scheme of dispositive, the certificate of corresponding to European standard requests etc.).

In the same time, thanks to modern technological progress, appears a new digital technology, which present a considerable support in assurance of qualitative assistance with medical RD improves the diagnostic quality decreases the ionsating irradiation, perfectly meet the European standards etc.

Material and methods. It was analyzed the information included in official annual statistic form (f.30-san), 2010, using the documentary statistic and comparative analyzing methods.

V. RESULTS AND DISCUSSION.

Because of deep socio-economic crises existing actually in Republic of Moldova, the rate of fixed traditional X-ray exam dispositive morally and physically outrun in MSPI HM RM at 01.01.2011 were by 90,6% data included in the table nr.1.

The table 1 data show us that the rate of morally and physical outrun dispositive in republican institution is 85,1%, but in municipal institution – 88,5, because of substitution of lesser number of traditional dispositive with analogy-digital, and pure digital. The highest rate morally and physical outrun dispositive were found in raional MSPI, which considerable decrease the assistance quality of RD, granted to rural population, which constitute 60% from the total population of Republic of Moldova.

TABLE 1. THE TECHNICAL STATE OF TRADITIONAL FIXED X-RAY DIAGNOSTIC DISPOSITIVE IN MSPI HM RM AT 01.01.2011

Type of institution	Total of dispositive	Inclusive morally and physical outrun (abs)	The rate of morally and physical outrun dispositive (%)
Republican	148	126	85,1
Municipal (Chisinau, Balti)	114	101	88,5
Raional	358	335	93,5
Total	620	562	90,6

In the same time the rate of X-ray exam dispositive, using till present for population screening in the purpose of early revealing (opportune) of persons with suspicion to evolutionary lung tuberculoses, malignant neoplasm's and other pathologies of thoracic cave is 100%.

And in dental practice X-ray is often used. The performing of dental X-ray by dental traditional RD dispositive (5D1, 5D2) needs the expecting of same radioprotection rules: using of dental apron or lead rubber collar and glasses (preferably) from lead glass because of impossibility of collimation of ionsating irradiation fascicle etc. During 2006-2010 years in MSPI HM RM was performed since 100897 dental X-ray exams in 2006 till 146149 in 2009 (in 2010 - 130838). In the same time the absorbed doses of ionsating irradiation by performing jf one traditional dental X-ray exam is 0,7 milligrey (1 Gy = 1 J/kg=100rad), when for the same radiophotography, performed by Visiograph accumulate an absorbed doses only 0,05 mGy or 12 times lesser (in same cases even more), substituting with success the traditional dental radiophotography, being a modern dental radiodiagnostic

method. In this context the high degree of physical and moral outrun of traditional dental RD dispositive into MSPI HM RM constitute at 01.01.2011 – 92,0% (in regional institutions-97,2%, because of using of RD MT dispositive, which does not use the modern digital technologies (Visiograph).

In MSPI HM RM are also used the mobile X-ray dispositive, for investigation of patients with trauma, surgery, neurosurgery etc. gravely, which can not move to radiodiagnostic lab's. The technical state of this category of dispositive in included in table 2.

TABLE 2. THE TECHNICAL STATE OF MOBILE DISPOSITIVE OF TRADITIONAL X-RAY EXAM FROM MSPI HM RM AT 01.01.2011.

Type of MSPI	Total of dispositive (abs.)	Inclusive morally and physical outrun (abs)	The rate of morally and physical outrun dispositive (%)
Republican	57	48	84,2
Municipal (Chisinau, Balti)	30	22	73,3
Raional	77	68	88,3
Total	164	138	84,1

From the data from table 2 the majority of mobile dispositives are morally and physical outrun, need substitution with those digital, the absorbed dose of irradiation, being 6-8 lesser than in case of using traditional dispositive of RD TM.

Recent time the Ministry of Health of RM start the subvention of MSPI with new technology, included digital one.

The technical state of digital RD, inclusive computer tomography, considered by us digital in MSPI HM RM at 01.01.2011 is included in table 3.

TABLE 3. THE TECHNICAL STATE OF DIGITAL RD DISPOSITIVE, INCLUSIVE COMPUTER TOMOGRAPHY IN MSPI HM RM AT 01.01.2011

Type of MSPI	Total digital dispositive			Inclusive				
				Computer tomography		digital		
	total	Inclusive morally and physical outrun	%	total	Inclusive morally and physical outrun	Statio--nary	mobile	visio--graph
Republican	22	2	-	8	2	13	-	1
Municipal (Chisinau, Balti)	15	-	-	1	-	14	-	-
Raional	7	-	-	-	-	3	3	-
Total	44	2	5,1	9	2	30	3	2

As it is shown by table 3 data in MSPI HM RM exists 44 dispositive of digital RD, inclusive 9 tomography computers and 30 mobile dispositive and just 2 visiographs for dental necessity the technical state of which is very good. This circumstance permits radioprotection optimization, irradiation security assurance, improvement of medical X-ray exam quality.

VI. CONCLUSION.

1.At actual time 90,6% from total traditional RD dispositive from MSPI HM RM is morally and physical outrun, inclusive radiophotography dispositive – 100%, dental X-ray exam 92,0% (in regional MSPI- 97,2%), mobile – 84,1%(in regional MSPI-88,3%).

2.The use of morally and physical outrun dispositive decrease essentially quality of medical care, contributed, in great measure of increasing of collective ionsating irradiation of population of republic.

3.The created situation at the moment in Republic of Moldova input the substitution of all traditional RD dispositive with those digital, which will improve the radiodiagnostic quality, decrease the near by 8 times the collective irradiation of population, to warn the revealing of cancer induced by medical ionsating irradiation etc.

REFERENCES

[1] Dânga V., Roşca A., Prepeliţă S., Tverdohleb O., Bahnarel V., Stanchevici V. The efficiency, qualitassurance and radioprotection during prophylactic X-ray exam from m. Chisinau in 1996-2007 time period. Bulletin of the Academy of Sciences of Moldova. Medical Sciences. Chisinau, 2007, N.5(14), p 29-32.

[2] Practice quideline for digital radiography. In Practice Guidelines and Tehnical Standards. Reston, Va: American College of Radiology: 2007: 23-57.

[3] Rosca A. - The medical imagining and radiotherapy activities in Republic of Moldova in the new economic condition and masseurs directed to its improvement. the actual medical imagining and radiotherapy problems. Materials of the first congress of Radiotherapist and Radiologists of Republic of Moldova. 5-6 October 2000, Chisinau p11-16.

Sensors of Ultraviolet Radiation for Medical Equipment

Authors: I. ABABII, E. ARAMA
State University of Medicine and Farmacy „Nicolae Testimiţanu" from R. Moldova
Departament of otorinolaringology and
departament of Human Physiology and Biophzsics.

***Abstract.* – The results of elaboration, construction and implementation of ultraviolet radiation detector with high sensibility are presented, which is used as portable device for measuring the intensity and dose. Photodetectors possess high stability at radiation and are promising for multiple practical applications, including for the construction of x-ray detector and of transducer to register electrons flux density. The optimal parameters give the possibility, to use the detectors in medicine, biology, ecology and agriculture.**

***Keywords* – UV radiation, doze, UVimeter, photorecervers, wavelength, photosensitivity.**

I. INTRODUCTION

The ultraviolet UV radiation acts effectively upon the vital activity of living organisms and plants. This fact leads to their wide application in biology, medicine, agriculture. According to the opinion [1] the radiation UV is divided in three regions: UV A, UV B and UV C. Ultraviolet A (λ=320 ÷ 400 nm) belongs to the solar light which reaches the Earth surface produces a weak erythematic effect; UV B (λ=280 ÷ 320 nm) has the action on the skin, causing a more pronounced erythematic effect followed by pigmentation; UV C (λ=220 ÷ 280 nm) has more dangerous action on the living matter.

A great majority of biological vegetable and animal media absorb the UV radiation with the wavelength shorter than 230 nm. The proteins absorb radiations with the wavelength of λ=275 nm; nucleic acids and fatties are also absorbing of UV. It is sufficient to mention, that the human eye is exposed during its life to the radiation of UV that belongs to the solar radiation spectrum. The main function of ocular anterior pole (cornea and crystalline) is that of focusing this radiation on the retina, being in the same time as an efficient filter for the UV A and UV B and protecting the retina of their dangerous action. The radiation of the wavelength λ=295 nm is absorbed completely by cornea. The crystalline absorbs radiations UV A and UV B (295 ÷ 400 nm) which crosses the cornea and can have photo traumatic effects on the structural crystalline proteins. The prolonged exposition (big dose of UV radiation on the crystalline) leads to the cumulative photochemical deterioration and leads to the actinic ophtalmia, cataract, destroys the retina and leading to the blinding. The mechanism, by which the UV A and UV B radiation produces cataract, is not so clear; the processes of biochemical nature and biological one can take place in the photochemical moment and the formation of cataract [2]. There are numerous epidemiological and laboratory studies, which demonstrate that the photons of UV radiation that touches the eye (especially UV B) are strong cataract dangerous for the human crystalline. This fact generated a great interest for the mechanism of the action of UV B radiation on the crystalline proteins, and also on the ADN of the epithelial cells from the crystalline. There are studies in the specialization literature, which shows that the UV radiation determines the changes in the structure of crystalline proteins and can modify the interactions of them, responsible for the maintenance of transparency of the crystalline in vivo [2].

The UV radiation in the optimal doses stimulates the development of young organisms and stops the apparition of the rachitic and the anemia, but the radiation that has a maximum of about λ=300 nm at certain dose provokes the cancer. The effect of this type of radiation on the plants also depends on the dose.

With the context of that mentioned, the necessity of exact appreciation of UV radiation dose by the UVimeter is evidently, the element of registration of radiation is the radiation UV photoreceiver. The great interest to the UV radiation receptors was increased considerably last years. This interest is thoroughly justified on the fact that the above mentioned spectral range in comparison with other spectral subranges, especially those of visible light, is insufficiently provided with the detectors of small dimensions.

II. EXPLANATION AND COMPARISON OF CHARACTERISTICS AND PARAMETERS

Some models of detectors are proposed recently for the UV domain. The elaboration of portative apparatus is necessary for the extended application of UVimeter in the above mentioned ranges. For this elaboration, the application of semiconductor structures as the photoreceivers is necessary, because they posses all necessary qualities: are of small dimensions, resistant, and self supplying, posses the guaranteed protections [4]. For example, the authors of the paper [5] propose detectors with barrier on the surface of the epitaxial films *n-n+-GaP* . The measurement device of UV radiation UVR-21 is made on their base. The simplicity of production is mentioned in the paper as the quality of advantage and their exploitation. The researchers from the Ukraine SPhI of AS suggest photodiodes made on the base of halogenides of Cd for the commercialization, which can be applied for the registration of UV in different subranges of wavelengths [6]. We suggest different detectors for this spectral range on the base of layered multisulfides [7,8]. The technology of preparation of layered monocrystals is simply, but the method of appreciation of characteristics is already elaborated, being described in the papers [9,10,11]. For the bacterial subrange the photoresistors of the oxide and of cadmium aluminum sulfide are elaborated $(CdAl_2S(O_2))$ [12].

An analogical UVimeter with those mentioned was elaborated, built and implemented by the coworkers of State University of Medicine and Pharmacy "Nicolae

Testemitanu" at the Othorinolaryngology and the department of Human Physiology and biophysics, in collaboration with the Applied Physics Institute of Moldavian AS [7, 13-15]. One of the basic properties of semiconductor material used for the elaboration of UV radiation detectors is the large band gap (Eg≥3.0 eV) necessary for the exclusion or reducing to the minimum the sensitivity at visible and infrared radiation. This request is satisfied successfully by the compounds $Zn_3In_2S_6$ *(a),* $Zn_3GaIn_6S_6$ *(b), and* $Zn_3AlIn_2S_6$ *(c)* that belong to the group of halogenides with the crystalline structure as the form of layers and have the energy bang gap equal to 3.05, 3.25 and 3.37 eV respectively [10, 14]. The photoreceivers are elaborated and built with the spectral characteristic as the rectangle shape (Π), on the base of layered monocrystals, which have the high sensitivity in the limits of photons with the energy higher than the energy band gap $hv>E_g$. This property is characteristic for the named transition due to of small speed of recombination on the surface of these semiconductors. The process of elaboration and building of photoreceivers is described in the papers [13-16]. The above mentioned monocrystals were used in order to build the photoreceivers. The monocrystals present the mounts with the surface area S ≥ 100 mm^2, which are cleaved easily up to the thicknesses of 10÷500 μm.

The photodiodes with the surface barrier (SBS) – Shottky diodes were elaborated as the photosensitive structures which have the following principle advantages:

- high photosensitivity into a high spectral range of wavelengths;
- the electrical current supply device is not necessary, because the photocurrent is generated on the base of radiation that is received;
- The Lux – amperical characteristic is linear into a large interval of received flux;
- Simple technology of fabrication.

The detailed study of SBS was performed with different contacts on the base of layered monocrystals $ZnIn_2S_4$ [9,10]. The analysis of obtained results allowed the formulation of their performed characteristics.

The film of Pt with the thickness of 10-15 nm was used as the rectification contact with the uniform transparence in whole range of near UV. The layer of ITO serves as ohm contact (mixture of SnO_2 and In_2O_3). Both contacts were deposited on the crystallographic planes by the method of thermal vaporization into a vacuum (0001) situated on both surfaces with the thickness of 10-20 nm. The coplanar contacts were deposited in the case of the detector on the base of the compound $CdAl_2S(O_2)$.

The normalized spectral distribution of the photosignal of SBS made on the basis of multisulfides *a, b* and *c* is presented in fig.1 (T = 300 K), which has large distribution and more pronounced removing in the range of short wavelengths in comparison with the photoconduction spectra. This is explained by the leakage of charge carriers in the contact region of the respective structure.

The value of forbidden band gap Eg of the compounds *a, b* and *c* increases in the named order, but the maximum of spectral distribution of the signal is removed in the direction of short waves of spectrum. In this case the SBS can be built, whose photosensitivity spectrum covers the entire near UV region, but with decreased relative sensitivity in the visible spectral range (λ=380÷400 nm).

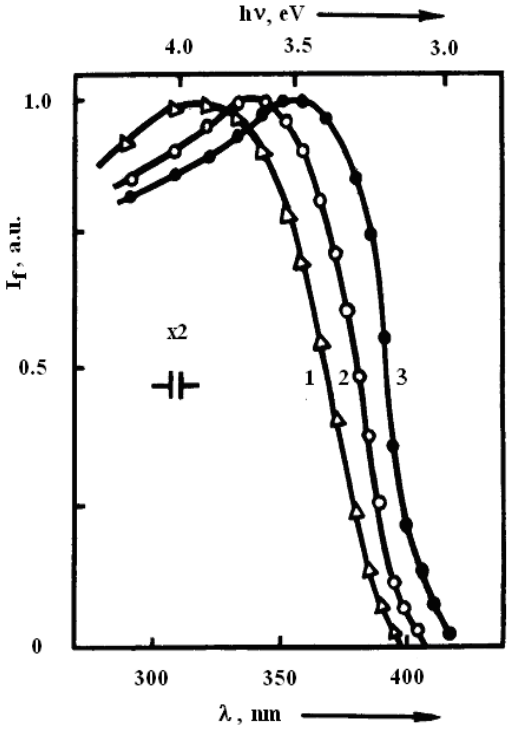

Fig. 1 The spectral dependence of photosignal of Shottky diodes on the base of the compounds Zn3InAlS6 (a), Zn3InGaS6 (b) and Zn3In2S6 (c) with the rectifying contact

The maximum of the open circuit voltage (V_{OC}) of the structure makes 400 – 600 meV and the rectification coefficient is 10^2 - 10^4. The maximum of V_{OC} spectrum is at 3.5, 3.7 and 3.2 eV for the SBS made of the compounds *a, b* and *c*, respectively.

The filters УФС – 2 and ЖС – 3 with the thickness of 0.1 cm are used in the real receivers for the limitation of spectral sensitivity and exclusion of nondesired band. The typical spectral characteristics are presented in the fig.2, but the main parameters of detectors are presented in the table 1.

TABLE 1. MAIN PARAMETERS OF DETECTORS

Current sensitivity, A·cm^2/W	$4\cdot10^{-4}$-$3\cdot10^{-3}$
Upper L – I_{PC} line limit, W/cm^2	10^{-4}-10^{-2}
Base resistance, Ω	10^5-$3\cdot10^6$
Photosignal duration, s	10^{-3}

The research of the process of endurance of photodiodes exposed by UV radiation with high intensity (~10^2W/m^2) and long ($3.6\cdot10^5$ s and more) proved that the structures with the contacts of gold or platinum do not indicate any omens of endurance. The application of these metals is preferable, because they influence little the cost of photoreceiver and for one device only 2 mg of Au or Pt are consummated, the duration of functioning of photoreceiver is enough long. The photoreceivers are applied for the measurement of absolute values of the UV fluxes radiation and work 4-5 years. The UVimeters and dosimeters are elaborated for UV radiation on their base. Both high stability and the simple system of registration of the signal provides for these devices the considerable advantages with respect to those built on the base of other compounds [15].

It is evident that the UVimeters used for the measurement of smaller intensities will work long term. In order to increase the functioning term, the neutral homogenous filter for the near UV was used, which attenuate the intensity of

about ×10, ×100 times. The filter represents a layer of Ni with the respectively thickness deposited on the support of quartz by the method of vaporization into a vacuum.

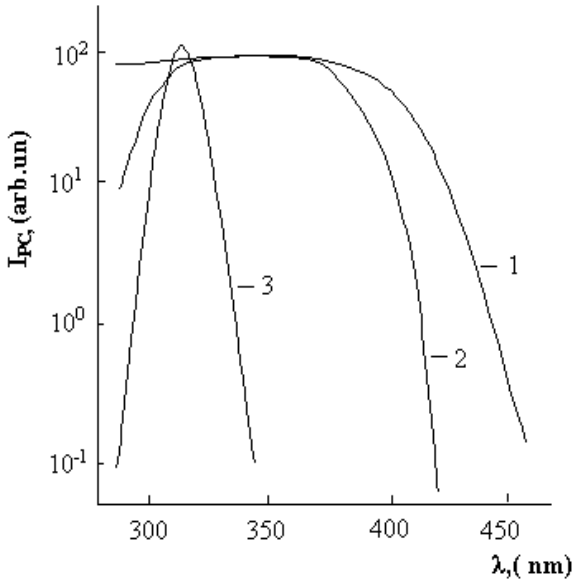

Fig. 2. Spectral characteristics of photosignals of diodes: (1)Pt-$Zn_3In_2S_6$ without filter; (2) with filter; (3) Pt-$Zn_3Ga(Al)InS_6$ with ЖС-3 filter.

The elaborated photoreceivers on the base of Shottky diodes *Me-$Zn_3In_2S_6$* have sensitivity in the fields of wavelengths 220÷400 nm. In order to reach some high performance of sensitivity in the field of spectral bands with the erythematic effect A, B and A+B, the cheap optical filters were used on the base of vitreous compounds. In order to register the radiation from the range A+B, the more convenient is the filter UFS - 2 with the thickness d=1 mm, but for the registration of the field A the system composed of filters UFS - 1 (d=1 mm) and SS-13 (d=2 mm) was used or the system composed by filters UFS – 1 (d=1 mm) and FS - 1 (d=2 mm). For the registration of the field B the filter UFS - 1 was chosen (d=1 mm) in the combination with GS - 3 (d=2 mm). Thus, for all three domains of erythematic radiation the filter UFS-2 must be used, it was installed in the interior of the transducer, but for the filter SS - 13 (FS - 1) and GS - 3 the possibility of dynamical installation was foreseen. For the commodities of the users the special construction [14] was elaborated that in front of transducer the obturator disc with three windows is installed (without filter and with filter GS-3 or SS-13 (FS-1)). Rotating the obturator disc, the fixing of one from those three windows in front of transducer takes place for the registration of radiation dose or the intensity in one of the above mentioned domains. It is evidently, that the standardization of electronic block was performed separately for each of those spectral domains (A, B, and C). The used crystals as is stated in the paper [17] have the high stability and, so that the elaborated photoreceivers on their base will resist to the action of physical factors.

The spectra of elaborated photoresistors on the base of ceramic *$CdAl_2O_4$* and monocrystals *$CdAl_2S_4$* are presented in the fig. 3 [12]. They cover the spectral range 220÷320 nm with high sensitivity at the wavelength of about 250 nm. The diodes have the high stability of functioning into a medium with a high degree of humidity, maintaining the absolute sensitivity of ~10^{-5} A·cm^2/W. Thus, we can look forward, that the devices will resist to considerable fluxes of ionized radiation. In order to study the stability of photodiodes at the action of radiation of radioactive nature, the structures *Pt-$Zn_3In_2S_6$-In* were studied at the action of electronic flux with the energy about 40 keV.

The compounds with the stoechiometrical vacancies, from which belong also those studied, have the high level of stability.

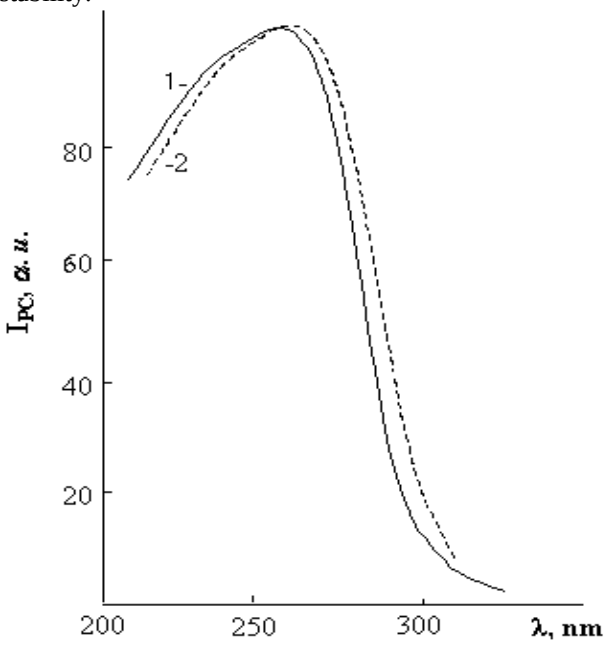

Fig.3 The typical spectra of the photoconduction of ceramic *$CdAl_2O_4$* (1) and *$CdAl_2S_4$*

As the depth of penetrating of electrons by semitransparent electrode of *Pt* in the monocrystals does not exceed some μm, the influence of ionization belongs to the lacked portion of the diode, but the space of the semiconductor with the thickness of about 10-20 μm is not affected practically to the influence of radiation. So that, in order to lead the influence, those parameters were chosen that determine the region of barrier: the spectral distribution of Voc, sensitivity, direct portion of volt-amperic characteristic at small voltages and indirect current. These parameters were measured for a set of diodes, before and after irradiation with the doses $6\cdot10^{16}$, 10^{17}, $6\cdot10^{17}$, 10^{18} el/cm^2. For first two doses the characteristics of diodes coincide with those initial. The change of the parameters of diodes are observed beginning with the dose $6\cdot10^{17}$ el/cm2 and is manifested by the changing of photosensitivity and maximum of Voc, the direct and indirect approximated increasing four times, the removing of the maximum position of photosignal to small energies of about 0.6 at the dose 10^{18} el/cm^2.

The combination of high values of photosensitivity and of stability creates the perspective that the multicomponent halogenides compounds can be used as the detectors for Roentgen radiation. The detectors of Roentgen radiation were built experimentally on the base of the compounds *a*, *b*, and *c* with the resistance at darkness 10^9 Ohm and high sensitivity in the range of quanta 1-10 keV. The factors of amplification, measured in the range of energies 2-7 keV exceed the value of 10^4 el/quantum. The time resolution does not exceed 10^{-9} s. These parameters allow the recommendation of named detectors for the diagnosis of laser plasma. We mention that on the base of above described detectors, using the experimental possibilities of the Institute of Applied Physics of AS of RM, the portative

UVimeters were built and elaborated for the Republican Hospital of Children "Emilian Coţaga" where they were approved successfully. In conclusion we mention, that using the layered crystals of $Zn_3In_2S_6$, Zn_3GaInS_6 and Zn_3AlInS_6 , the detectors of UV radiation with high sensitivity were built and implemented in medicine at the portative devices for the measurement of intensity and radiation dose (practically all near UV). For example, we show the photographs of one devices built on the base of our elaborated diodes. (Fig. 4).

Fig. 4. The measurement device with the digit display of UV radiationwith the intensity in limits of values $10^{-4}\div2\cdot10$ mW/m^2 the spectral domains, nm: 280÷400, 320÷400, 320÷360; the dose - $0\div1.6\cdot10^5$ J/m^2.

The current supplying – 220 V.

These photoreceivers with high stability at the irradiation and in accordance with it, they can found multiple practical applications, also for the creation of Roentgen radiation detectors on the base of the named semiconductor compounds and for the registration of density of electron fluxes.

REFERENCES

[1] Nagi I. Iosif. *Biofizica*, Timişoara, 1990.

[2] I. Jeru, E. Bendelic, V. Boiştean, E. Aramă. *Particularităţi ale tratamentului medicamentos în cataracta senilă,* Analele Ştiinţifice ale USMF, vol. 4., 2003, pp. 289-293.

[3] A. Stănilă, *Cristalinul,* Sibiu, 2001

[4] E. Arama, ,Archives of the Balkan Medical Union, 2002, p. 164.

[5] A. Malic, Y. Vygranenco, B. Shabashkevich et al.//Int. Semicond. Conf., Sinaia, Romania, vol. 1, 2001, pp. 185-188.

[6] V.N. Komashchenko, K.V. Kolezhuk, E.A. Venger et al. *Pis'ma v ZhTF*, vol. 28, 19, pp. 32-36, 2002.

[7] I. Ababii, E. Arama. UV *Dosimeter for Medical Aplicatio.* Analele Ştiinţifice ale USM, seria "Ştiinţe fizico-matematice", 2002, pp. 45-49.

[8] I. Ababii, E. Aramă. *Dozimetru pentru recepţionarea ultravioletului în Medicină*. Analele Ştiinţifice ale USMF, 2002, vol.1, pp. 164-171.

[9] Е.Д. Арама, Н.С. Грушко, В.Ф. Житарь, С.И. Радауцан. *Электрические и фотоэлектрические характеристики диодов Ni-$ZnIn_2S_4$.* ДАН СССР, 1976, т. 227, N6, с. 1329-1383.

[10] Е.Д. Арама, Н.С. Грушко, В.Ф. Житарь, С.И.Радауцан. *Влияние базы на параметры диодов изготовленных из высокоомного $ZnIn_2S_4$.*. Письма в ЖТФ, 1997, 2, вып. 6, с. 254-258.

[11] S.Radautsan, V.Raylyan, I.Tsiulyanu, V.Zhitar, M.Marcus, N.Moldovyan. *New Zn_3InGaS_6 phase and its main properties.* Progr. Cryst. Growth and Charact. Caracas, 1985, pp. 397-399.

[12] Н.А. Молдовян. *Выращивание и исследование фотопроводимости $ZnAl_2S_4$ и $CdAl_2S_4$* .Изв. АН РФ, сер. Неорганические Материалы, 1993, т. 27, №9, С.1969-1971.

[13] V.F. Zhitar, N.A. Moldovyan, E.D. Arama, S. Radautsan. *Short-wavelength radiation detection on the layered sulphides*.. XV Annual Semiconductor conference, Sinaia, Romania, ICCE, 1992, pp. 267-270.

[14] E.Aramă. *Recepţionarea ultravioletului cu detectori pe sulfîzi stratificaţi*. Intelectus, Chişinău, , vol.4, 1999, pp. 72-75.

[15] E. Arama, I. Ababii, V. Zhitar, T. Shemyakova. *UV Detectors Based on $Zn_xIn_2S_{3+x}$ and Related Compounds*. Intern. semiconductor Conf., Sinaia, Romania, 2003, vol.1, pp. 147-150.

[16] В.Ф. Житарь, Т.В. Абрамова, Е.Д. Арама, В.К. Якуша. *Кинетика фотопроводимости и люминесценции $ZnIn_2S_4$*.. Изв. РАН, сер. неорган. Материалы, 1991, т.27, N11, с. 2245-2247.

[17] Н.А. Молдовян, Д.С. Ременко. *Фотосопротивление ультрафиолетового диапазона.* Авт. свид. СССР N1050.

Influence of Face Mask on Breathing During Hyperventilation Test

Tudor BESLEAGA[1], Pascale CALABRESE[2], Victor VOVC[1], Pierre BACONNIER[2], Ion MOLDOVANU[1], Andre EBERHARD[2]
[1]*State University of Medicine and Pharmacy "N. Testemitanu", Chisinau, R. Moldova*
[2]*Lab. PRETA-TIMC, University Joseph Fourier, Grenoble, France*

***Abstract*- The aim of present study was to evaluate the changes of breathing pattern related to the influence of the face mask during voluntary hyperventilation. We compared respiratory variables in recordings with and without mask in different periods of hyperventilation test. Our finding – the mask increases some variables at rest (inspiratory time) and during recovery period after voluntary hyperventilation: (inspiratory time, tidal volume and pulmonary ventilation). The mask decreases respiratory variability at rest and during recovery periods. These effects can be provided by behavioural influence and the additional dead space of apparatus.**

I. INTRODUCTION

Respiratory inductance plethysmography (RIP) is a non-invasive method for measurements of rib cage and abdomen respiratory movements. These rib cage and abdominal cross sectional area changes allow calculating respiratory volumes. Respiratory airflow is recorded by pneumotachograph, but the using of mouthpiece or a facial musk can change breathing pattern by behavioural influences and by additional apparatus dead space.

Calabrese et al. [1] compared pneumotachographic airflow (PNT) and RIP derivative signal of quiet respiration, during voluntary hyperventilation and recovery periods, RIP derivative signals were filtered by an adjusted filter based on each subject pneumotachographic airflow signal (PNT). Authors concluded that the adjusted filter calculated from quiet respiration can be used in different conditions: quiet respiration, hyperventilation and recovery after hyperventilation to obtain adequate derivative RIP signal.

Change of interactions between automatic and behavioural regulatory mechanisms of respiration occurs during voluntary hyperventilation. The aim of our research was to determine the influence of the mask on breathing pattern in healthy subjects in different periods of hyperventilation test.

II. MATERIALS AND METHODS

We studied six healthy volunteers between 25 and 39 years of age, five of whom were men. All subjects provided informed consent and the study was approved by the relevant ethics committee (CHU Grenoble). Breathing was recorded with a flowmetter Fleish head n°1 and differential transducer (163PC01D36, Micro Switch) mounted on the face mask (dead space of apparatus was 60 ml) and with RIP (Visuresp, RBI). End tidal CO_2 fraction ($F_{ET}CO_2$) was measured using infrared CO_2 analyser (Engstrom Elisa/Elisa MC). Subjects were recorded in semi-supine position at rest – 3 min (REST), during voluntary hyperventilation at each subject spontaneous respiratory frequency and recovery – 9 minutes (protocol THVm); and successively at rest – 3 minutes (REST20), during voluntary hyperventilation at 20 breaths/min - 3 minutes and recovery period (REC20) - 9 minutes (protocol THV20m). Subjects were encouraged to increase tidal volume in order to decrease $F_{ET}CO_2$ by 1% below the rest levels. These two protocols were repeated without facial mask, the $F_{ET}CO_2$ was collected by nose clip (protocols THV and THV20). Before the recording without mask we recorded the 2 minutes period of quiet respiration simultaneously with flowmeter and RIP to calculate individual adjusted filter. **Analysis:** All signals were digitized at a rate of 100 Hz. The 15 most regular consecutive breaths of the airflow signal formed the reference part [1]. A least squares method was used over this part of signal to obtain a RIP volume signal (VRIP) by combination of rib cage (RCRIP) and abdominal (ABDRIP) signals compared to the integrated flow signal (VPNT):

$$VRIP_k = \tau\, RCRIP_k + \alpha\, ABDRIP_k \quad (1)$$

Where $\tau = 2$ was imposed [3]. The derivative of VRIP (FRIP) was then calculated by using centred divided differences:

$$FRIP_k = (VRIP_{k+1} - VRIP_{k-1}) / 2\Delta t \quad (2)$$

A transfer function was calculated over the reference part between RIP derivative and airflow signal to take out an adjusted filter. Then the adjusted filter calculated on the reference part of signals was applied on the entire recording. We calculated adjusted filter from rest period in recordings with mask (THVm and THV20m) and from two minutes recording period with PNT and PIR preceding recordings without mask (THV and THV20). The derivative signals PIR were used to calculate respiratory variables for all periods of test.

Recovery periods are divides in three intervals: first three minutes- REC3m and REC20_3m, 4^{th} -6^{th} minutes- REC6m and REC20_6m, last three minutes- REC9m and REC20_9m. Respiratory variables: mean duration of respiratory cycle (Tt), inspiratory and expiratory times (Ti and Te), tidal volume (Vt), mean inspiratory flow (Vt/Ti), Ti/Tt ratio, minute pulmonary ventilation (Ve), tidal CO_2 fraction ($F_{ET}CO_2$) and their variation coefficients were calculated.

III. RESULTS

The values of respiratory variables (medians, quartiles, superior and inferior values) calculated for periods of performed tests (THV, THVm and THV20, THV20m), also the significant differences determined with test Wilcoxon are represented on the figure n°1.

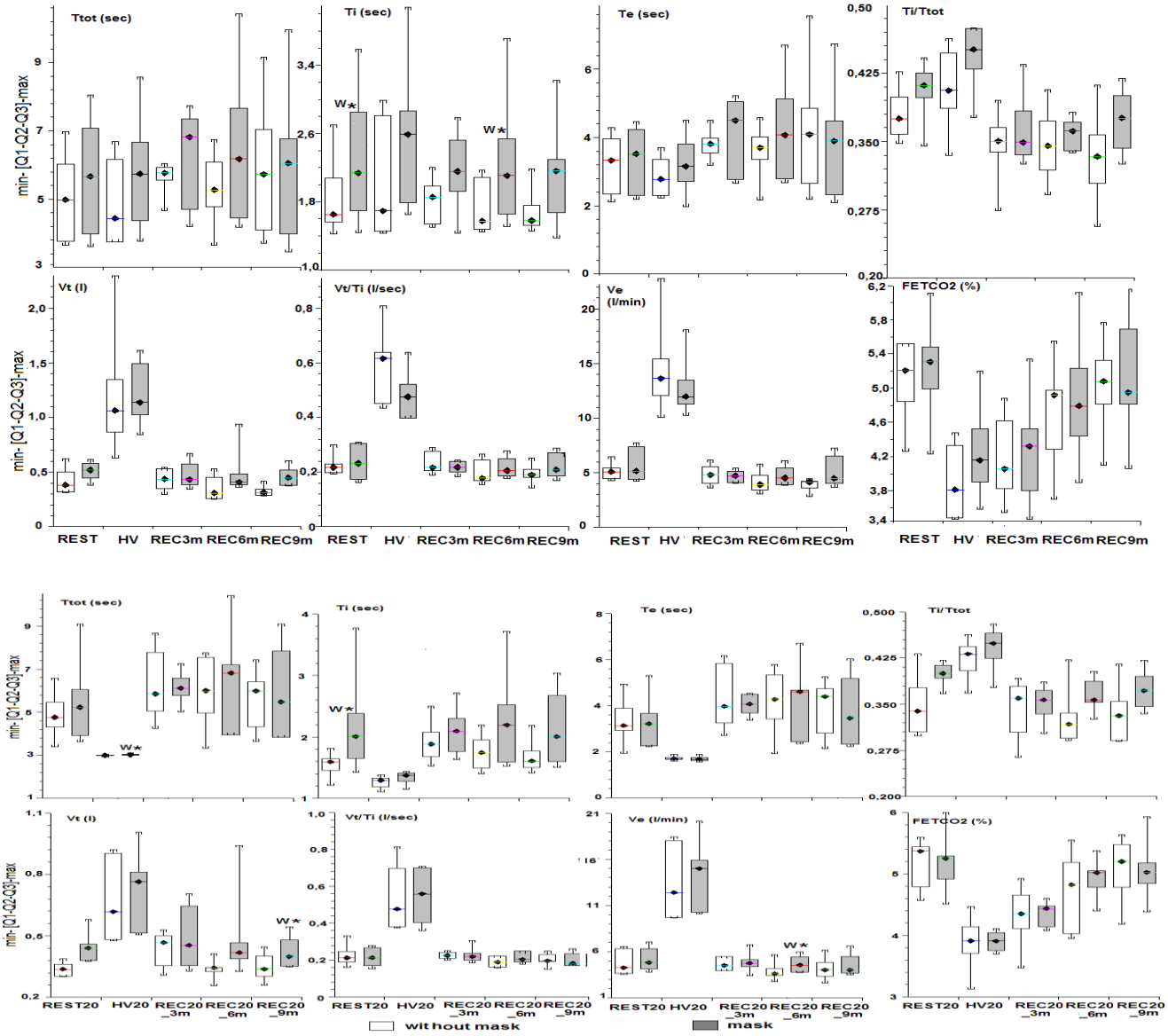

Fig. 1. Respiratory variables of hyperventilation tests recorded with and without mask (THV, THVm and THV20,THV20m)

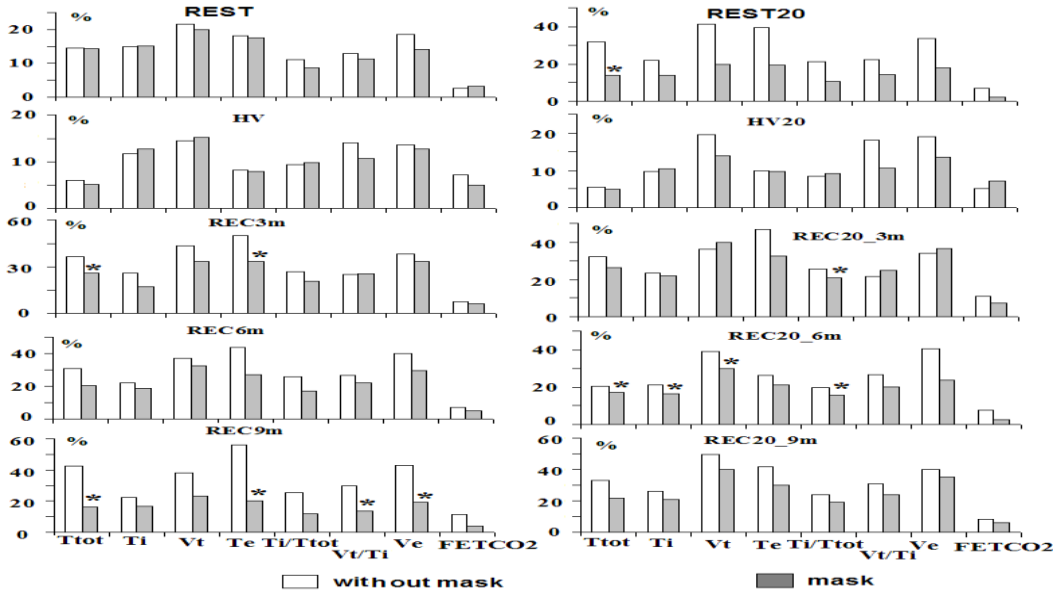

Fig. 2. Variation coefficients of respiratory variables determined in periods of tests recorded with and without mask (THV, THVm and THV20, THV20m)

The mask increases inspiratory times at rest (REST) and during second interval (REC6m) of test THV. During test THV20 the mask increases Ti at rest (REST20), tidal volume Vt during the last 3min (REC20_9m) and minute ventilation Ve during REC20_6m interval of recovery period.

The variation coefficients (medians) of respiratory variables of tests (THV, THVm and THV20, THV20m), and significant differences determined by Wilcoxon test are represented on the figure n°2. The mask decreases variation coefficients of Tt and Te during REC3m interval and Tt, Te, Vt/Ti and Ve during last 3min of recovery period (REC9m) of THV. The mask decreases variation coefficients Tt of the second rest period (REST20) Ti/Tt during first three minutes of recovery (REC20_3m) and Tt, Ti, Vt and Ti/Tt during interval REC20_6m

IV. DISCUSSIONS

Precedent studies describe influence of the face mask on the respiratory variables [4], [5]: increase of the tidal volumes and ventilation, decrease of the respiratory rate. We found more differences between breathing with and without mask during recovery periods after voluntary hyperventilation tests. The changes between automat-metabolic and behavioural regulatory mechanism make these period more sensitive to behavioural influences produced by the facial mask. The decrease of respiratory variability in the records with mask can be also explained by these behavioural influences. The absence of differences during voluntary hyperventilation periods can be explained by domination of voluntary control of breathing.

The small dead space of the face mask and pneumotachograph had minimal effect on the breathing pattern, but it cannot be completely excluded.

V. CONCLUSIONS

The application of the respiratory inductance plethysmography provides more native breathing pattern by excluding influences of the facial mask. It can be useful in the study of breathing pattern in voluntary hyperventilation, and its application is suitable in the study of breathing in anxious patients.

REFERENCES:

[1] P. Calabrese, T. Besleaga, A. Eberhard, V. Vovc, P. Baconnier. Respiratory inductance plethysmographie is suitable for voluntary hyperventilation test. Conf Proc IEEE Eng Med Biol Soc. 2007:1055-7.

[2] A. Eberhard, P. Calabrese, P. Baconnier, G. Benchetrit, "Comparison between the respiratory inductance plethysmography signal derivative and the airflow signal", *Adv. Exp. Med. Biol.*, 499, pp. 489–494, 2001.

[3] R.B. Banzett, S.T. Mahan, D.M. Garner, A. Brughera and S.H. Loring, "A simple and reliable method to calibrate respiratory magnetometers and respitrace", *J. Appl. Physiol*., Vol. 79, pp. 2169–2176, 1995.

[4] J. Askanazi, P.A. Silverberg, R.J. Foster, A.I. Hyman, J. Milic-Emili, J.M. Kinney (1980). Effects of respiratory apparatus on breathing pattern. J. Appl. Physiol. 48, pp. 577–580, 1980.

[5] R. Gilbert, J.H. Auchincloss , J. Brodsky, W. Boden. Changes in tidal volume, frequency, and ventilation induced by their measurement. Journal of Applied physiology. vol. 33 no. 2, pp. 252-254, 1972.

Heart Rate Variability: the Involvement of Breathing Pattern (chest breathing, abdominal breathing) and Anxiety.

Andrei GANENCO[1], Victr VOVC[1], Ion MOLDOVANU[2], Svetlana LOZOVANU[1]
[1]*State University of Medicine and Pharmacy "Nicolae Testemițanu"*
[2]*Institute of Neurology and Neurosurgery*

***Abstract*- The relationship of heart rate variability to thoracic and abdominal components of breathing pattern, as well as to slow paced respiration, was studied in healthy volunteers with different level of anxiety. Subjects with high anxiety showed lower levels of heart rate variability, slow respiration increased the low frequency component of HRV in both groups, chest and abdominal respiration reduced HRV.**

***Keywords*- heart rate variability, breathing pattern, paced respiration**

I. INTRODUCTION.

It's well known that heart rate variability (HRV) is a basic homeostatic parameter and some changes in this parameter, especially its decreasing, can be a marker of possible sudden death at patients with heart diseases [1]. Also, it's known that abdominal respiration has a positive effect on the organism, and pranayama (respiration used in yoga system) is considered as physiologic one with great catabolic effect. There are even some methods of breathing training for increasing HRV.

Otherwise, it's known that elevated anxiety of one person associates with autonomic disorders and psycho-autonomic syndrome, described in last century by germane authors [2] and developed ulterior by F. Vein and his school. This syndrome is considered as basic concept in present science of autonomic disorders.

Interaction between thoracic and abdominal components of the respiratory pattern also exhibits some interest [3]. Experimental studies on healthy people and patients which show the involvement of respiratory pattern and its variants (abdominal respiration, chest respiration, hyperventilation) are very few.

The purpose of this study is to analyze heart rate variability at different forms of breathing pattern and in relation to anxiety level in healthy volunteers.

II. METHODS.

The subjects were selected by screening with State-Trait Anxiety Inventory (STAI) Spielberger. 12 subjects (6 males, 6 females, mean age 20.59±0.43) formed the group with low anxiety (15-30 points), and 13 subjects (6 males, 7 females, mean age 20.49±0.38) formed the group with high anxiety (more than 45 points). ECG and pneumotachogram were recorded using MP35 unit from BIOPAC Systems. The recordings were performed in following conditions: spontaneous breathing (3 min), spontaneous breathing with limited thoracic movements (by belts) i.e. "abdominal" respiration (3 minutes), spontaneous breathing with limited abdominal movements (by belts) i.e. "chest" respiration (3 minutes) and paced breathing (guided by metronome) with breathe rate 6 per minute (3 min). Simultaneously, end-tidal fraction CO_2 was continuously measured by the capnograph MEC-2000 in order to maintain it at constant values.

From ECG, heart period was calculated as interval between two successive R waves, fast Fourier transform applied to calculate spectral power of RR intervals and following values of HRV were calculated: power spectral density (PSD), absolute and normalized high-frequency (HF) spectral power, absolute and normalized low-frequency (LF) spectral power (normalized LF and represent the relative value of each power component in proportion to the total power minus the VLF component) and LF/HF ratio.

Statistical analyses: *t*-Tests were used to assess the statistical significance of differences for HR power and its components in different conditions. Values are means ± SE unless otherwise stated.

III. RESULTS.

Subjects with high anxiety had lower values of PSD, as shown in fig.1, and this difference was described in all 4 tests under different conditions of breathing, as mentioned before. However, inside the group with low anxiety, the PSD didn't show any important difference between periods of recording. The opposite effect is seen in the group with high anxiety, PSD being decreased during abdominal and chest respiration, and increased during 6 per minute paced breathing.

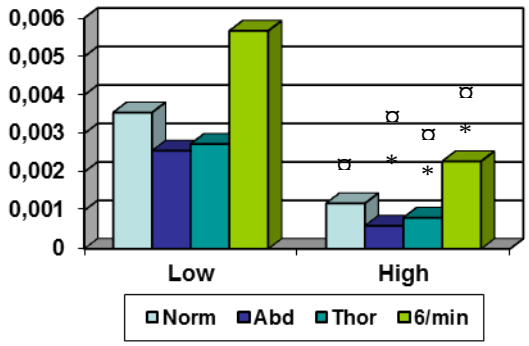

Fig. 1. Spectral power density in subjects with low (in the left) and high (in the right) anxiety during spontaneous, abdominal, thoracic and metronome-guided breathing (* - p<0.05 for the comparison inside the group, ¤ - p<0.05 for the comparison between the groups).

The main reason for low values of PSD in high anxiety group will be probably shorter RR interval (847±13 ms in low anxiety group, 670±11 in high anxiety group), since the increased heart rate leads to smaller fluctuations in RR interval. Also, PSD had decreased during both abdominal and chest respiration, although heart rate didn't change.

LF was slightly elevated in subjects with high anxiety

(41.74±2.3 vs. 18.06±1.28, fig. 2). During abdominal and chest respiration, the values of LF didn't differ neither within the group nor between the groups. During paced respiration, LF had increased in both groups, and this situation reflects not an increased sympathetic discharge, but an increased possibility for the same sympathetic neural outflow to modulate the heart rate.

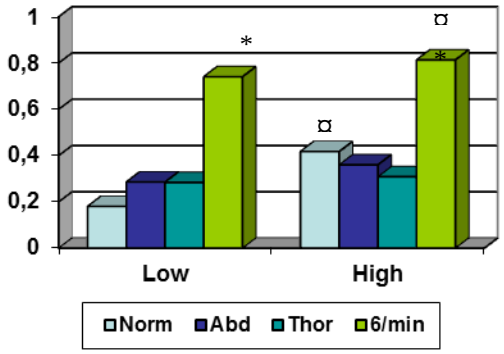

Fig. 2. LF in subjects with low (in the left) and high (in the right) anxiety during spontaneous, abdominal, thoracic and metronome-guided breathing (* - p<0.05 for the comparison inside the group, ¤ - p<0.05 for the comparison between the groups).

HF wasn't significantly different between spontaneous breathing and chest /abdominal breathing, but decreased significantly in paced respiration in both groups (fig. 3). In low frequency respiration (< 9 breaths/min), respiratory frequency and low frequency overlap, and the RR variability is modulated by both parasympathetic and sympathetic nervous system, and both will increase the LF component of the HRV, leaving HF at low levels.

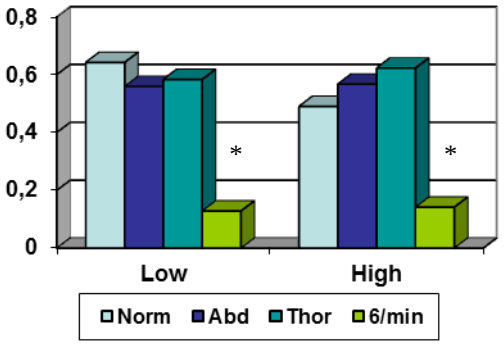

Fig. 3. HF in subjects with low (in the left) and high (in the right) anxiety during spontaneous, abdominal, thoracic and metronome-guided breathing (* - p<0.05 for the comparison inside the group, ¤ - p<0.05 for the comparison between the groups).

LF/HF ratio followed the same changes as LF, was the same during thoracic and abdominal breathing, and markedly increased during slow breathing in both groups (fig. 4). No differences were found in LF/HF ratio between the groups.

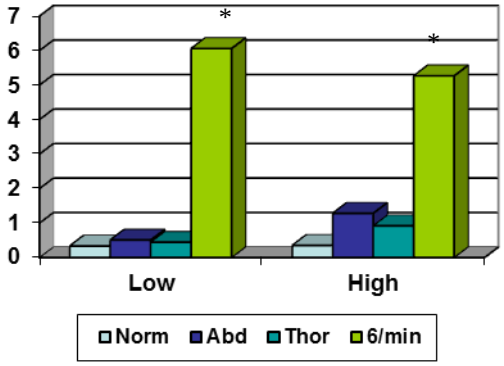

Fig. 4. LF/HF ratio in subjects with low (in the left) and high (in the right) anxiety during spontaneous, abdominal, thoracic and metronome-guided breathing (* - p<0.05 for the comparison inside the group, ¤ - p<0.05 for the comparison between the groups).

IV. CONCLUSIONS.

1. The subjects with anxiety present lower values of power spectral density, due to reduced mean RR interval
2. Slow rate respiration (6/min) increases the LF component of HRV, since LF component in this case is modulated by both sympathetic and vagal activity.

REFERENCES.

[1] Task Force of the European Society of Cardiology and theNorth American Society of Pacing and Electrophysiology, *Heart rate variability: standards of measurement, physiological interpretation and clinical use*, Circulation, vol. 93, 1996, pp. 1043–1065

[2] W. Fhiele, *Psycho-vegetative syndrome*, Ment. Welt., vol. 1, 1966, pp. 9-13

[3] V. I. Minyaev, V. G. Davydov, *The role of the thoracic and abdominal components of the respiratory system during hyperventilation combined with chemoreceptor stimulation of various intensities*, Human Physiology, vol. 26, n. 4, 2000, pp. 451-455.

Optical Power Control Module

Andrei GRITZCO, Sergey ZAVRAJNYI, Andrei STALBE, Iurie NICA
Institute of Electronical Engeneering and Nanotechnologies „Dumitru Ghiţu”,Chişinău, MD – 2028
**E-mail: tehmed@iieti.asm.md*

***Abstract* – This article describes the optical power control module, of laser diodes, which is included in the therapy installation using local hyperthermia. The function of this module is to produce and maintain, during the entire duration of the therapy procedure, the stable optical power, which has an enormous significance in efficiency of therapy using local hyperthermia.**
Also the module obligations are: monitoring the laser diodes performance, which also plays an important role in proper functioning of the entire system. This module can serve up to four laser diodes simultaneously, is equipped with RS232 serial interface, necessary to control module via computer. For this purpose, was prepared a computer program that allows the operator to install optical power level for each of the four laser diodes and to monitor laser diodes efficiency.
The main element of this module is the microcontroller ATmega16, equipped with a periphery, corresponding the requirements of given module

I. INTRODUCTION

The principle of local hyperthermia is to create inside the human body at a certain depth of temperature (accurate), necessary to destroy tumor tissue (~ 43.5 ° C).Temperature excess or insufficiency may even harder aggravate the situation.

In this project, the primary concept, was to develop the device would allow the therapy of cancer, infectious diseases with high energy infrared radiation, which practical has no harmful effects on humans when compared with traditional therapy with roentgen rays (after which the patient passes a rehabilitation period). Another advantage is that the device does not need a specialized room (concrete walls, special clothing, dosimeters) and can be easily moved from one place to another (it is quite mobile). Also construction of the device was designed so, that each module in case of damage to be changed in a short period of time and without great expense.

The installation is equipped with a set of high optical power laser diodes (full power ~ 4W), based on heterojunctions InAlGaAs, with wavelength of emitted radiation equal to 808nm. Each diode laser is also equipped with an optical collimator to create a parallel flux, with minimal divergences. In order to avoid, due to overheating, the damage of the intermediate tissues during the radiation penetration through the body and to focus all energy on the tumor, was designed a division of the needed flow in a smaller flows, which in the sum will have the same effect on the tumor. For this, the laser diodes must be placed at certain angles, chosen by the doctor, depending on tumor location and state (depth, the distance to vital organs, the dose required, etc.).

The installation is also equipped with RS232 serial interface for data exchange with the computer. Through this interface and main program, is handled the optical power of the laser diodes, monitoring the heat fields (temperature distribution in the tumor area), monitoring the efficiency of the laser diodes (laser diodes operates in the normal mode or begins to degrade). The program also records all thermal field variations in a file for future analysis.

Installation for therapy using local hyperthermia can be divided into the following sub modules:
- thermal field monitoring module (the basic functions is to collect information about the temperature in the tumor region).
- optical power control module of the laser diodes.
- cooling system (its function is to evacuate the excess heat produced from laser diode operation)
- power supply module (electric power for all sub modules of installation)

Each of these sub modules meet the vital functions for the normal functioning of the entire device.

II. THE DESCRIPTION OF THE OPTICAL POWER CONTROL MODULE OF THE LASER DIODES

The main function of this module is to create and maintain a certain level (set by the operator via computer) of the optical power for laser diodes. The precision of the installed level has a huge significance in terms of efficiency of the therapy using local hyperthermia, so the module is equipped with an optical power monitoring loop, which continuously checking the actual optical power with the necessary optical power (installed by operator) and in case of deviation – introduce the necessary correction.
Also one of the functions of the module is to monitor the effectiveness of the laser diodes to prevent they’re damage. These effects can occur in case, when the heating speed of the laser diode exceeds the speed of the heat surplus evacuation by the cooling system, which leads to lower optical power of emitted flow by the laser diode. Therefore, the optical power monitoring loop (which role is to maintain a constant optical power), is to detect the decreasing of the optical power level, and if this occurs, to increases the intensity of electric current which flows through the diode laser, in order to restore the installed level of the optical power.

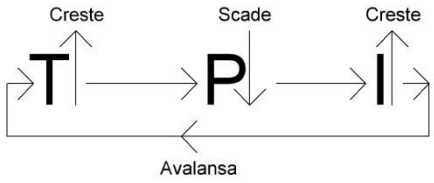

Fig.1 Laser diode thermal loop

The increase of the electric current intensity, therefore, leads to further warming of the laser diodes (in case when

cooling system fails to evacuate the exceeded heat) and respectively decreases the efficiency of the laser diode. A such situation can be characterized as a "thermal loop".

It is very important to avoid the entering of the laser diode in the "thermal loop" for several reasons: first of all to ensure an effective therapy, and secondly - to avoid the damage of the laser diodes (rather expensive). Therefore the monitoring function of the laser diode efficiency (went in the thermal loop or is functioning in normal mode) has a great significance in the normal functioning of the entire installation for therapy using local hyperthermia.

$$T_D \sim A \cdot P_o \cdot \Delta t \qquad (1)$$

where:

- T_D - laser diode temperature, during time interval Δt
- A - parameter that depends by the nature of the laser diode
- P_o - optical power of emitted flux of laser diode
- Δt - time interval, during which the laser diode emits radiation with optical power P_o

As shown in relation (1), since the optical power level, at which operate the laser diode, is higher, then the work time should be less, to keep the diode at a temperature at which the cooling system can serve it. Solving this problem can be: equipping every laser diode with a powerful cooling system, able to serve any heating level, but such a system is quite expensive. Another method - use a large number of laser diodes, which have the same thermal effect on the tumor, but which will operate at a lower level of optical power, which would allow a longer period of operation of laser diodes.

As shown in Fig.2, the module can be divided into three functional blocks: digital block, analog block and photo sensor.

Digital block provides the connection between computer and optical power control module, via the RS232 serial interface. Data frame transmitted to the control module contains the information about the optical power, laser diode address, however data transmitted to the computer (collected from the analog block) contains the information about the electric currents flowing through the laser diode (required for monitoring effectiveness of the laser diode). The software running on the computer analyzes the received data and operates according to the obtained results. Data received by the digital block (from the computer) are processed and sent to the analog block, through the 3-wire interface, which will be converted into an analog signal that will control the laser diode optical power.

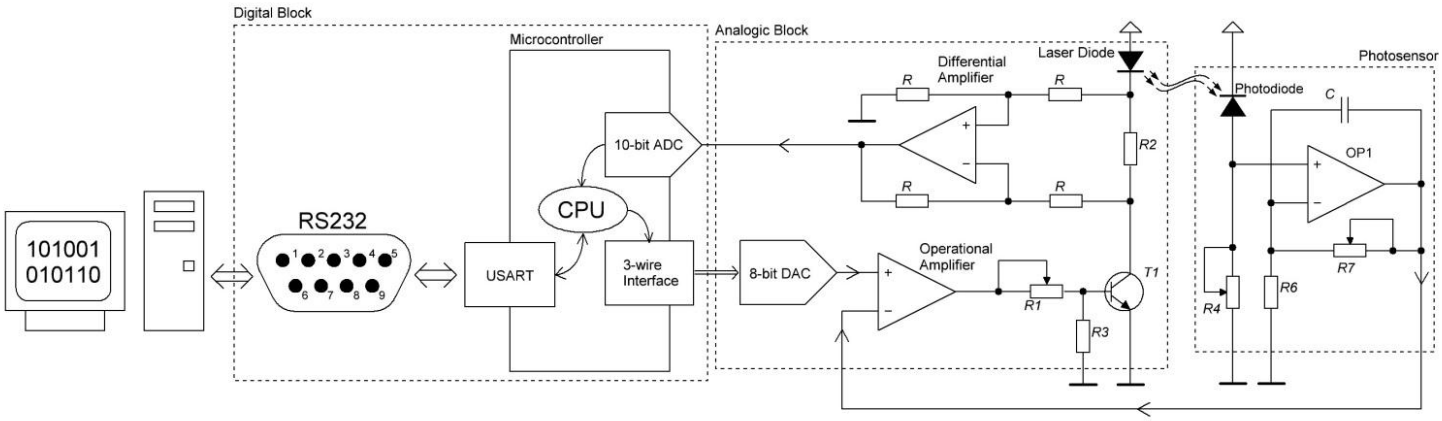

Fig.2. Scheme - Block of laser diode optical power control module

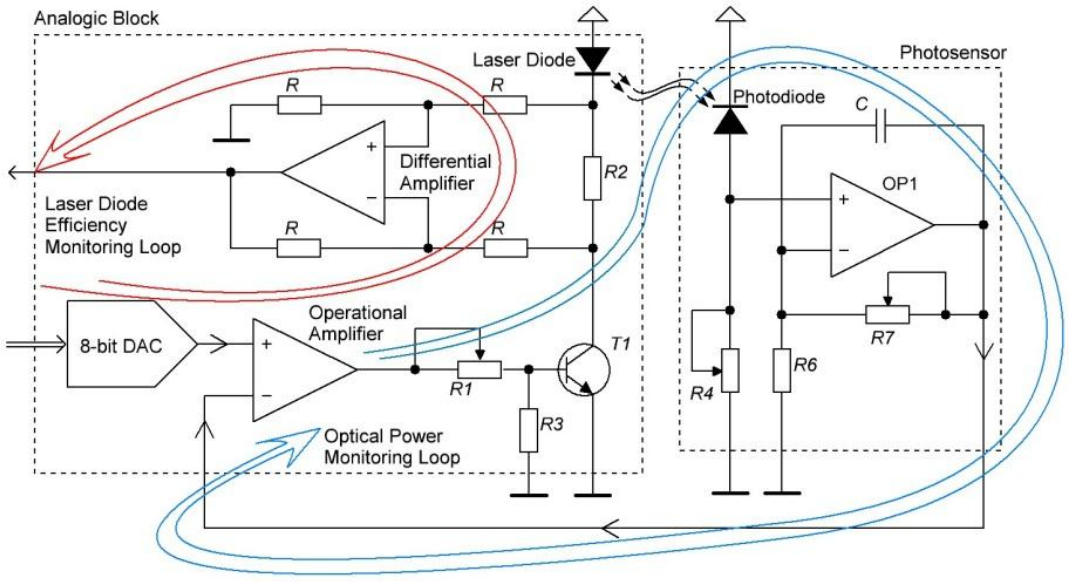

Fig.3 Optical power monitoring loop and laser diode efficiency monitoring loop

Functions of analog block are based on creating and maintaining the optical power level introduced by the operator. Optical power level is transmitted via 3-wire interface by the digital block to the digital-analog converter (DAC, component present in the analog block). DAC converts the digital signal into an analog signal that is applied to non-inverting input of the operational amplifier (OA). OA, together with the power transistor T1, controls the current flowing through the laser diode (directly proportional to the optical power of emitted radiation, see Fig.4). OA, depending on the received electric signal at the inverting input (from photo sensor), increases / decreases the intensity of the electric current flowing through the laser diode, therefore acting on optical power of the emitted radiation. The differential amplifier, measures the voltage drop on resistor R2, which is directly proportional to the electric currents flowing through the laser diode. This voltage is applied to the ADC input (component present in the digital block).

So analog block, together with photo senor forms two monitoring loops: optical power monitoring loop and laser diode efficiency monitoring loop.

Optical power monitoring loop, continuously check the laser diode optical power level through an operational amplifier and photo sensor. Part of this loop are the power transistor T1, which operates as the current supply for the diode laser and laser diode itself, which according to the electric current intensity flowing through it, produces a coherent stream of infrared radiation with an optical power well known. Dependence between the emitted radiation optical power and the electric currents flowing through the diode laser is linear and direct proportional.

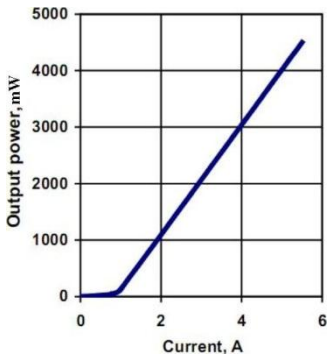

Fig.4 Dependence of the laser diode optical power of the electric current

The laser diode efficiency monitoring loop, as previously mentioned, is intended to prevent the entry of the laser diode into "thermal loop", which can damage it. The loop continuously monitors the electric currents, flowing through the laser diode. Measured by the differential amplifier, the voltage drop on the resistor R2, is directly proportional to the electric currents flowing through the laser diode and respectively with its optical power. The signal obtained at the differential amplifier output is applied to the ADC input (component present in the digital block). The binary data, obtained after analog to digital conversion, are transmitted via RS232 serial interface to the computer, where they are processed and displayed by the optical power control module software. If the software detects a situation when the laser diode has entered into "thermal loop" – stops local hyperthermia therapy procedure.

In Fig.5 is presented the photo sensor block – scheme, a basic element of the optical power monitoring module. Photo sensor main function is to monitor the optical power of the laser diode (together with op-amp). The photodiode, which is a part of the photo sensor, is connected in a photoconductive mode, which reduces it parasitic capacity and increases the optical sensitivity, which, in this case, is very important. The R4 resistor also regulates the photo sensor sensitivity. The signal produced by the photodiode and the resistor R4 is applied to the non-inverting input of the operational amplifier, component present in photo sensor. Resistors R6 and R7 regulates the signal amplification factor. Capacitor C performs the function of filtering various oscillatory signals which are produced by parasitic capacity of the photodiodes or other devices in the same room (network noise: ~(50 – 60)Hz). The signal produced by the photo sensor is applied to the operational amplifier inverting input.

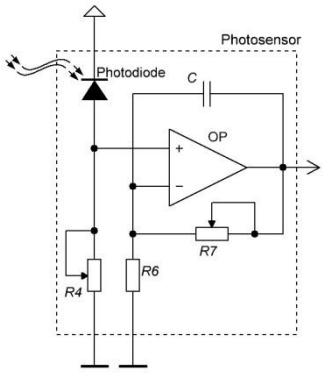

Fig.5 Photosensor's scheme – block

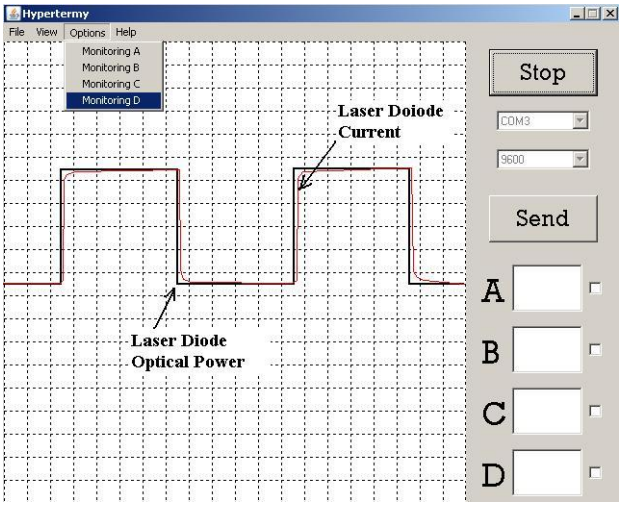

Fig. 6 Monitoring laser diode efficiency

To achieve communication between the computer and optical power control module, was developed a protocol that provides, together with RS232 standard, data transmission without distortions and losses. One function of the software running on computer (except for data transmission and reception) is to process the received data, regarding the laser diodes efficiency, with the following graphical display of the dependence between the laser diode optical power and efficiency

III. CONCLUSIONS

Within the installation for therapy using local hyperthermia, was developed, optical power laser diodes control module, able to monitor up to four laser diodes at the same time. Module operation was tested within the installation, obtaining accurate results in maintaining the level of optical power, responsiveness (for switching power transistors rather than ~ 25us) and high sensitivity. As mentioned previously, to avoid laser diodes entering into the "thermal loop" is proposed to provide them with more powerful cooling system and also increasing the number of laser diodes, which would increase the overall safety of the installation for therapy using local hyperthermia.

REFERENCES

[1] А.Ю.Кузьмин, Интерфейс RS232. Связь между компьютером и микроконтроллером, Москва, Радио и Связь, 2004.

[2] J.G.Graeme, Photodiode Amplifiers: op amp solutions, Library of Congress Cataloging-in-Publication Data, 1995

[3] P.Horowitz, W.Hill, The art of Electronics, Cambridge University Press, 1980

Photon Irradiation Device for Antimicrobial Therapy

Iurie NICA1*, Leonid POGORELSCHI1, Eugen MAXIMOV1, Valeriu CEBOTARI1, Constantin IAVORSCHI1,2, Vitalie BOLOGA2, Vladimir NAHABA3, Emilia ŢÎMBALARI3
Institute of Electronical Engeneering and Nanotechnologies „Dumitru Ghiţu", Chişinău, MD – 2028
Institute of Phthisiopneumology „Chiril Draganiuc", Chişinău, MD – 2025
3 State Medical and Pharmaceutical University "Nicolae Testemiţanu", Chişinău, MD – 2004
*E-mail: tehmed@iieti.asm.md

***Abstract* - A device for a procedure for preoperatively preparing patients with progressive drug-resistant fiber-cavernous tuberculosis also for treatment of other diseases, as lungs and other organs is developed. The device performed process of treating infected cavities and contains: mercury tube, focusing system for selection of segment of the radiation spectral band 250-500 nm, optical guide with connectors and a puncture needle. Use the tube with high pressure mercury vapor as a radiation source allows to obtain the broadband photon radiation for treatment more efficient and for recovery time reduce. It also provides a substantial simplification of the device and reducing its costs. The device was used to approve the method of treatment of infected cavities by means of endocavitary broadband irradiation. In the experiments we used cultures of Escherichia coli and Candida albicans. Effect of annihilation of bacteria colony is almost directly proportional to the duration of exposure and complete suppression occurs within 2 min.**

I. INTRODUCTION

One of the most difficult issues of the modern medicine is the combat against the infectiuos diseases. At the same time the problem of the increasing resistence of the infected microorganisms against the most up-to-date antibacterian preparations (the chemotherapy problem), is becoming more urgent. Because of this we propose to develop a device for photosanitation with ultraviolet C radiation of the human cavites populated with colonies of unspecific or/and tuberculosis microflora. Ultraviolet laser technologies used in the treatment of destructive forms of tuberculosis begin their history with the development and utilization of ultraviolet laser with nitrogen as the working substance (medical installation "Almiţin" with wavelength $\lambda = 337\,nm$ developed in 1995 under the management of Nobel laureate Academician Prokhorov A.M.). This installation has been made in small series in Russia (Samara) and has been used successfully in Central Institute of Tuberculosis (Moscow), clinic Chytram (Indore, India) and University Hospital Blumfonten (South African Republic) on treatment of more than 1500 patients. Currently, this device is no longer produced. In the process of supplementary investigations have noted that the maximum photosanitation effectiveness of tuberculosis caverns occurs when using ultraviolet from region C (240-280 nm), with the absolute maximum efficiency for $\lambda = 254.6\,nm$. From these considerations has been developed device "Amulet" with the wavelength $\lambda = 266\,nm$. This wavelength is achieved by multiplying the frequency of neodymium laser radiation $\lambda = 1064\,nm$. Mass production of the installations with 266 wavelength has not been made because of high cost and low power obtained in the flow of radiation (5mW) [1].

The main component of the installation "Maria" is KrF excimer laser, which generates pulsed laser radiation with wavelength 248 nm and frequency of 100 Hz. By using an optical system, radiation is admitted to the end of a sterile single-use optical fiber inserted through . an cavernous pulmonary micro drainage.

Namely this installation is currently used at the Central Institute of Tuberculosis ASM FR, where was developed the method of photosanitation of pulmonary cavities in fiber-cavernous tuberculosis cases [2,3], which is the most dangerous clinical form of this disease from epidemiological point of view . As noted in the published studies, photosanitation of lungs cavities reduces the number of resistant and multi-drug-resistant tuberculosis forms, helping to improve the situation of tuberculosis evolution overall.

The mechanism of DNA molecules modification consists in forming in them, under the action of photons, of thymine dimmers by saturating the covalent connections between two neighboring bases [4].

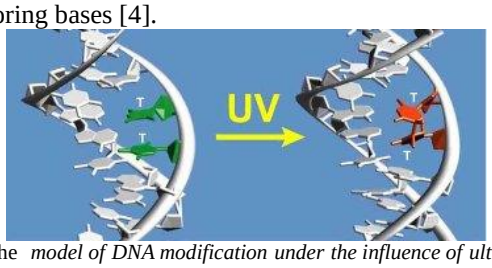

Fig.1 The *model of DNA modification under the influence of ultraviolet radiation*

To note, that speed of DNA destruction is very high. Recently [5] has been demonstrated that the reaction of dimerization of the thymine (pyrimidine $C_5H_6\,N_2O_2$) under the action of ultraviolet radiation takes about 1 pcs (10-12 sec). Acumularea acestor modificări de structură în ADN microorganismelor cauzează micşorarea vitezei de reproducere a microorganismelor şi, deci, anihilarea lor.

The researches performed demonstrates that for different representatives of nonspecific microflora, lethal doses are different. Liveness and lethal doses at wavelength 248 nm for 5 initial strains: *Pseudomonas aeruginosa, Escherichia coli, Enterobacter aerogenes, Klebsiella pneumoniae and Staphylococus aureus* are reprezented in Pic. 2[6].

We mention the varied sensitivity of different strains at ultraviolet laser emission energy. The most sensitive strain is *Staphylococus aureus* with letal dose $3\,mJ/cm^2$, and the most resistant *Enterobacter aerogenes* – 7 mJ/cm^2.

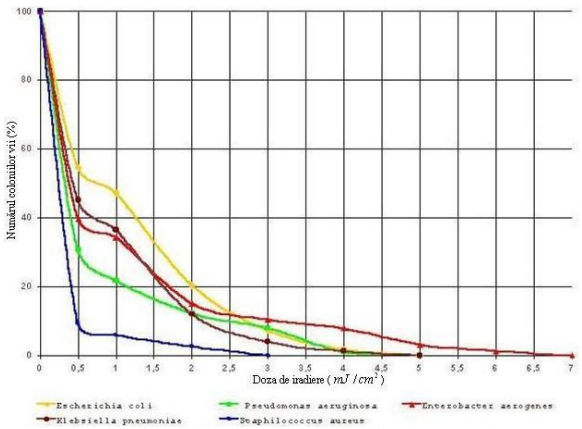

Fig.2 *Dependence, dose - liveliness, at bacteriostatic action of laser radiation of wavelength 248 nm, on the nonspecific microflora*

How we see from dependence of the number of colonies that survive the radiation dose of irradiation, for wavelength 248 nm, the absolute lethal dose is 8-10 mJ/cm^2.

In particular, we mention the absence in the specialty literature, of the genetic modifications evidences of the human body cells under the action of ultraviolet radiation C [7,8].

II. DEVICE FOR PHOTOSANITATION OF THE INFECTED CAVITIES OF THE HUMAN BODY

The proposed objective is to perform the necessary investigations and developing a photosanitation device with ultraviolet radiation C of the human body cavities populated by non-specific microflora colonies and / or tuberculosis.

These investigations and the development of antimicrobial irradiation devices are necessary because of the permanent growth of the pathogenic flora resistance to antibiotics [9].

From all the information, that we possess, is not apparent the necessary of coherence ultraviolet radiation in order to destroy the bacteria. Basically, as a radiation source could be LEDs. We have developed and manufactured an irradiation module with LED T9F25C (Optodevice Co. Seoul., Ltd.) [10]. But currently the produced LEDs by (Seoul Optodevice Co.., Ltd., Photon Systems, Inc. and others) which are radiating in region C have an insufficient optical power emission.

From what is known, mercuric lamps have a very strong sterilization action, the character of their radiation not being coherent. Important is, firstly, the wavelength of the photon (i.e. energy), intensity and duration of irradiation.

From these reasons, the device of fotosanare with ultraviolet radiation C of the human body cavities populated by non-specific microflora colonies and / or tuberculosis, as a source of radiation serves the discharge in arc in the mercuric tube at high pressure. This way, we eliminate the most expensive element from structure of the irradiation device - the laser / LED. The use as a source of the radiation the mercury tube at high pressure, allows more efficient treatment method by increasing the band used in the process and achieve a device that generates the wavelength band 250-500 nm with the possibility to select spectral segment of the radiation.

The wide band radiation in addition to the pronounced bacteriostatic effect, exercise a stimulating action on microcirculatory processes in irradiated area, resulting at more efficient treatment and reducing the period of healing the patient. The device for treating the infected cavities, using wide band photon irradiation method consists of: tube of mercuric steam 1, quartz condenser 2, the shutter 3, the spectral radiation selecting device 4, optical connector 5, optical guide 6, optical connector 7, the distal segment of the optical guide 8, punction needle 9, power supply unit 13, which through the power stabilizer 10 supplies tube 1, timer-dozer 11 (which drives the shutter 3) and measuring device of the radiation power injected into the optical guide 12, photoreceptor 14 assembled with the optical connector 15

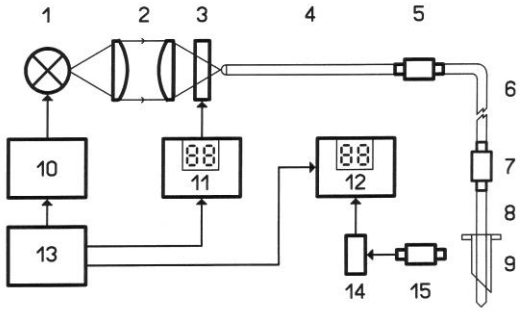

Fig. 3. Block diagram of the photosanitation device

Using the tube with the high pressure mercuric steam as a radiation source allows obtaining a wide band photon radiation, substantially simplifying and reducing the device's cost.

III. IRRADIATION PROCEDURE AND RESULTS

The device for treating the infected cavities with wide band photon irradiation method was made and used to approve the method of infected cavities treatment through wide band endocavitary irradiation method.

The experiments were performed in laboratory of medical diagnostic and laboratory of microbiology at the Institute of Phthisiopneumology, virology and immunology at the Faculty for training doctors at Medical University "Nicolae Testemitanu" researching the in vitro the influence of the wide band radiation on the different bacterial strains. The radiation parameters have had the following values: optical power at wavelength 254 nm - 1mW, and in range 280-500 nm - 15mW. In the experiments were used cultures *Escherichia coli* and *Candida albicans*.

Were performed 10 inseminations and from obtained cultures were prepared suspensions following standard technologies. In Petri dishes with agar - blood have been dropped 0.1 ml of suspension with a concentration 10^6 microorganism in $1cm^3$ of solution. Petri dishes thus prepared were exposed to 10, 20, 30, 40 s and 1, 2, 3, 4, 5 min. Were irradiated sectors with $1cm^3$ areas, leaving the non-irradiated sectors for comparison between the exposed sectors. Petri dishes were incubated 24 hours in thermostat at the temperature of 37^0C. The calculations were performed by an optical microscope with x100 zoom. The results are presented graphically in figure. 2.

How is apparent from the presented results, the effect of microorganisms annihilation depends approximately directly proportional to duration of exposure until, basically, total deletion within 2 min. Not irradiated sectors are covered by a dense layer of colonies of microorganisms.

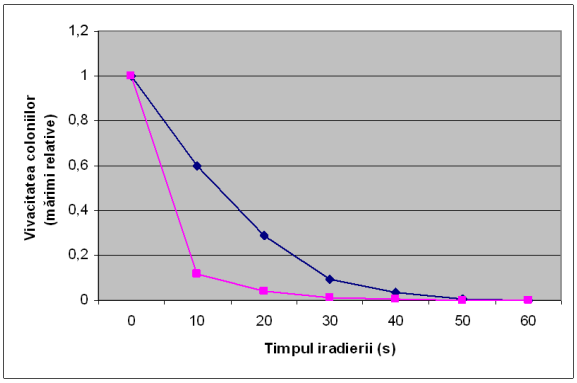

Fig. 4 The dependence of liveness of the Candida albicans colonies and Escherichia coli

Fig. 5 The irradiation results of *Staphylococcus aureus* bacterial colonies grown on agar - blood (irradiation time = 15,45,60s and 2,3,5 min)

These results are above those obtained through the monochromatic irradiation using laser device [1,2].

In conclusion, the method and device proposed, allow quick removal of the pathogenic microorganisms populations from the wounds and infected cavities, rising - thus, the speed and efficacy of treatment.

This work is performed within the 09.808.05.05A project financed by the Supreme Council for Science and Technology of the Academy of Sciences of Moldova

REFERENCES

[1] http://www.aetechnologies.ru/dev/14-details.htm Создание лазерного комплекса для лечения туберкулеза

[2] V.G.Dobkin, M. A. Bagirov, D. R. Faizullin, G. P. Kuzmin. Endocavitary ultraviolet laser irradiation in the preoperative preparation of patients with progressive fibrocavernous tuberculosis. Проблемы туберкулеза и болезней легких, №2, 2006, стр. 25 – 28.

[3] О.В.Ловачева, И.Ю.Шумская, Н.Ф. Сидорова, Г.В.Евгущенко, А.В. Никитин, Использование эндобронхиального лазерного ультрафиолетового излучения в комплексном лечении туберкулеза бронхов. Проблемы туберкулеза и болезней легких ,№12, 2006, стр. 20 – 24.

[4] *T. Douki, A. Reynaud-Angelin, J. Cadet, E.Sage, Bipyrimidine photoproducts rather than oxidative lesions are the main type of DNA damage involved in the genotoxic effect of solar UVA radiation, Biochemistry, 42 (30), 2000, pp.9221 –9226.*

[5] Wolfgang J. Schreier, Tobias E. Schrader, Florian O. Koller, Peter Gilch, Carlos E. Crespo- Hernández, Vijay N. Swaminathan, Thomas Carell, Wolfgang Zinth, and Bern Kohler. Thymine Dimerization in DNA Is an Ultrafast Photoreaction *Science* 315, 2, 2007, pp.625-629.

[6] http://genestho.ru/article2.shtml Лечение деструктивных форм туберкулеза с помощью эндокавитарного воздействия лазерным ультрафиолетовым излучением

[7] М.Г.Винокуров, Н.Н.Николаева, Н.И.Косякова, В.А. Печатников , Действие ультрафиолета С на лимфоциты и нейтрофилы периферической крови человека, Медицинская иммунология, N 3-4, 1999,с. 10-18.

[8] И.Н.Рямзина, В.А. Черешнев, Влияние аутовенозного ультрафиолетового облучения крови отдельно и с ацетилсалициловой кислотой на состояние гемостаза больных перенесших инфаркт миокарда, Российский кардиологический журнал №5 , 2003, с.72-75.

[9] Tim Maisch. Anti-microbial photodynamic therapy: useful in the future? Lasers Medical Sciences 22, 2007, pp.83–91.

[10] [10] Nica Iu., Vieru S., Vieru T., Banari E. Modul de iradiere cu lungimea de undă 255 nm cu fibră optică. Salonul IV de Inventică şi Tehnologii Noi, Simferopol, Ukraina, 25 – 27 septembrie 2008

Temperature Monitoring System

Serghei ZAVRAJNYI, Iurie TIRON, Andrei GRIŢCO, Andrei STALBE, Iurie NICA
Institute of Electronics Engineering and Nanotechnologies "Dumitru Ghiţu"
Chisinau, MD 2028R.. Moldova, e-mail: tehmed@iieti.asm.md

***Abstract* – The multichannel temperature probe for studying the behavior of thermal fields is described in this article. As temperature sensors used Chromel - Alumel thermocouples. Thermoelectric each thermocouple (from 11mV to 13mV) increased its own amplifier to output voltage from 0 to 5 V corresponds to a temperature ranging from 0 to 50oC. The optimal solution for this case was the use of two-stage amplifier based on low-noise operational amplifiers. Data converting, data collection and data transfer to PC is based on ATMEGA16 microprocessor company Atmel. Signals from the amplifier module used for the analog inputs of microprocessor. The microprocessor receives the amplified analog signals from each thermocouple, converts them and transmits the data according to the protocol USART to the PC. USART pins are connected to the MAX232 and ADM 485 transceivers. The system operates in accordance with the software application that is based on data received from the COM port allows it to control the temperature of the object at certain points, as well as using mathematical interpolation procedure to determine the temperature at other points of a predetermined extended region. Multichannel temperature probe allows us to observe thermal fields in the temperature range 0 ° C … 50 ° C up to 0.1 ° C.**

I. INTRODUCTION

Bellow is described one variant of multi-channel measuring device of physical values, intended for use in various complexes of equipment for scientific research or control different processes. It is able to communicate with the devices within same complex, through RS232 and RS485 standards. Setting up for measure the physical values is performed by replacing the sensors and the corresponding correction function, stored in the microcontroller memory of the multichannel meter. In this article, the device is considered as multi-channel temperature measuring instrument for studying the behavior of thermal fields in the amount of physical bodies, part of the research method of local hyperthermia of malignant neoplasms.

As it is known that, one of the possible ways to combat the cancer can serve the destruction of malignant tumors cells with local overheating. Possibility of exercising of this method is associated with the fact that, during the heating of the body over 43 - 44 °C, is observed the destruction of tumor cells while healthy are more stable to heat tissue preserve the viability up to 50 °C.

Thus, it is strictly necessary to respect the two major limitations: on the one hand, overheating should not exceed the boundaries of viability of normal cells, on the other - the temperature of the tissues should exceed 43 Ñ, because insufficient heating only stimulates the growth of the tumors. As can be seen, acceptable treatment range of temperatures is narrow, about 5 °C. This imposes certain requirements on temperature measurement accuracy - better than 0.1 °C. To prevent localisation of the disease affected tissues in a region with temperatures below 44 °C, is necessary to monitor the heat dissipation and dynamics of its distribution, based on simultaneous measurements of temperature in several specific locations in the overheated region. Under these requirements has been designed the described multi-channel temperature meter.

II. TEMPERATURE MONITORING SYSTEM

The temperature monitoring system is intended to monitor the temperature values in control points and construction of the temperature field. The system consists of the following functional levels:

- Temperature transducers
- The data acquisition and transmission system
- Temperature monitoring software

The system has 8 channels of temperature monitoring.

2.1 Temperature transducers

Temperature transducers are thermocouples of cromel-alumel type, which have coefficient of thermal sensitivity of 40 μV/°C.

Thermocouples conductors are protected by a Teflon hose.

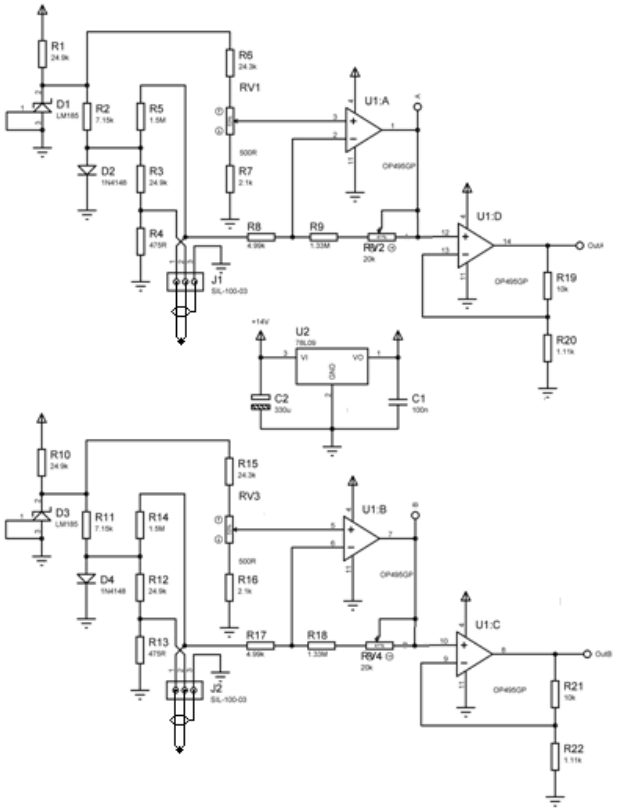

Fig. 1 Principial scheme of a signal amplification module from thermocouple

The hose is covered with a mesh shield. The screen, in addition to the useful signal protective function from noise, serve as mechanical support, offering increased mechanical strength conductors. The own low consumption of operational amplifiers, 150μA, allows realization of an amplifier system which is powered from an independent source such as a galvanic cell. Cold jonction of the thermocouple are inside of the isothermal block with a compensaty diode.

In order to achieve amplification of the thermocouple signal, in the temperature range of 0 ° C - 50 ° C, the output voltage 0mV - 5000mV, is necessary to increase the amplification factor up to 10V. Optimal solution for this case was serial adding of a another amplification stage based on operational amplifier. Because integrated circuit have four operational amplifiers, reasonable solution is to make two parallel analogue channels on a single PCB board. Developed module has its own voltage stabilizer to avoid the influence of supply and the digital circuits noise. Principial scheme of a two channel thermocouple signal amplifier module is shown in Figure 1.

2.2 The data acquisition and transmission system

The data acquisition and data transmission system to PC is realized based on ATMEGA16 microprocessor, from ATMEL company. The signals from the amplifier modules are applied to the analog inputs of the microprocessor. The microprocessor reads the values achieved on each analog pin, converts them and transmits digital data via USART module to the computer. The device consists of four modules of 2 amplifier channel each. USART pins are connected to the MAX232 and ADM485 transceivers via 74HC4016 digital keys. This type of connection offers selectable data transmission serial interface. With 74HC4016 keys can be choose the RS232 or RS485 interface. Principial scheme of data acquisition and data transmission module is shown in Figure 2.

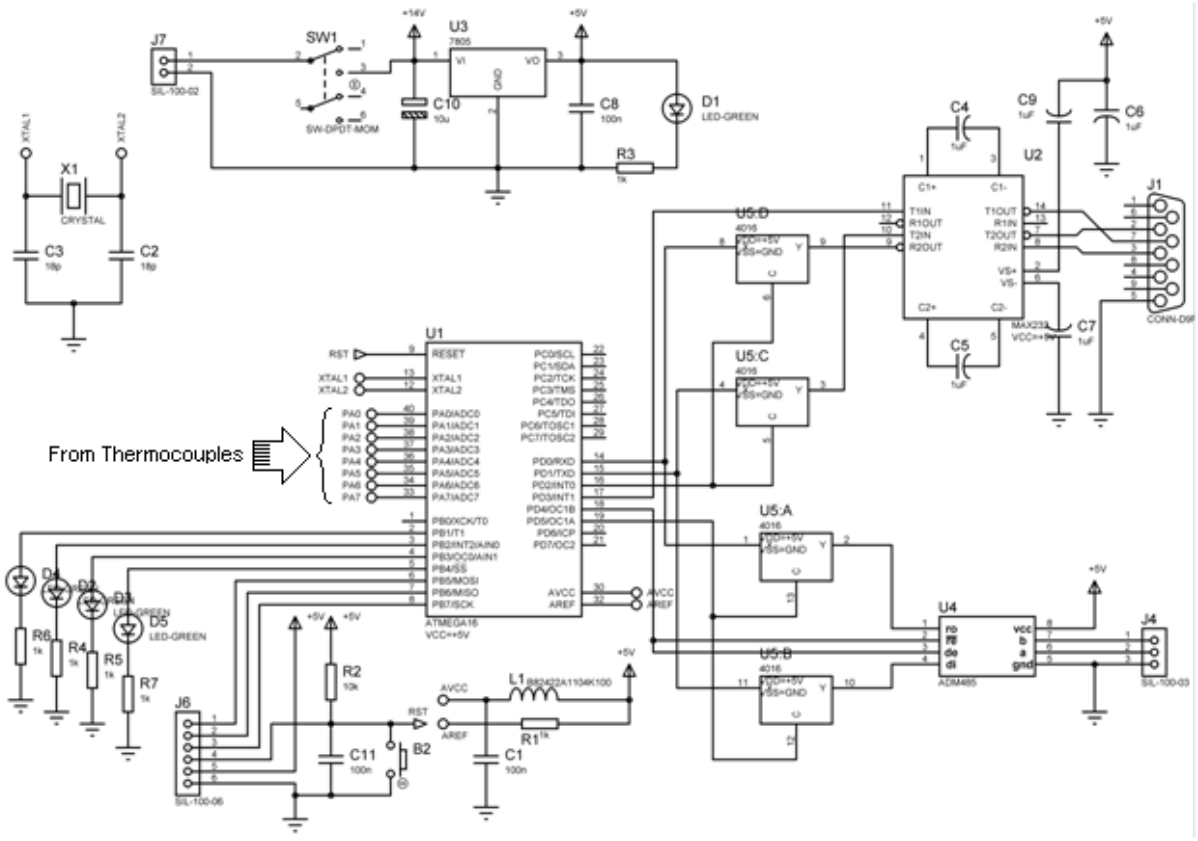

Fig. 2. Principial scheme of the data acquisition and transmission module

2.3 The data exchange packet format

Package for data exchange between PC and data acquisition system is composed of two bytes. In the first

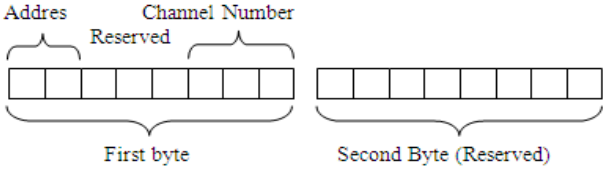

Fig. 3. Data exchange packet format.

byte, the two most significant bits contain the peripheral system address that is addressed computer. Three the least significant bits indicate the channel number on which the temperature is to be read. The remaining three bits and bit field in the second byte is reserved.

The program consists in initialization section of the peripheral equipment involved in data collection process (ADC and USART unit) and data transmission section. Block - diagram of the microprocessor program shown in appendix A.

2.4 Temperature Monitoring System.

The system represents a software application, which, based on data obtained from the COM port, allows monitoring the temperature of the studied objects at the procedure determines the temperature on a previously defined domain. The domains on which is determined the temperature field can have multiple configurations: Irregular, Linear, Rectangle, Sector, Radial, and Cross

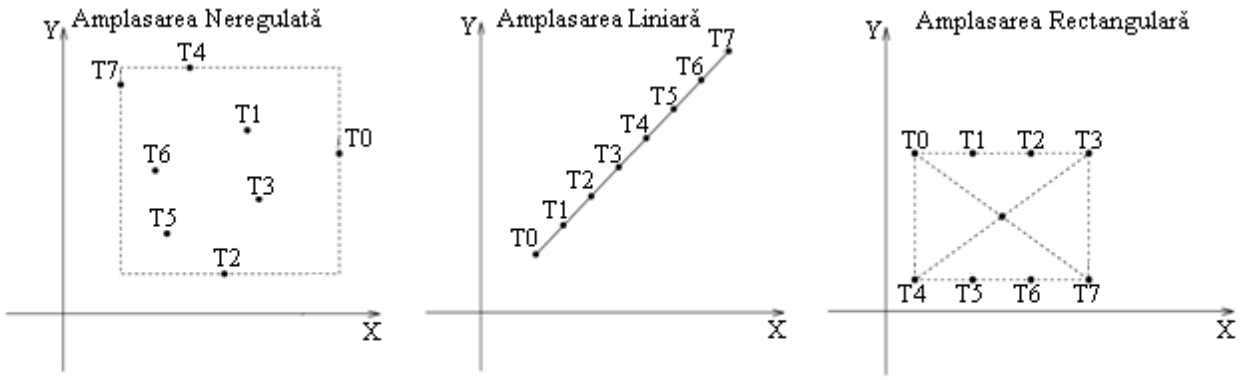

Fig 4a Amplasarea termocuplurilor: Neregulată, într-o singură linie, Rectangulară

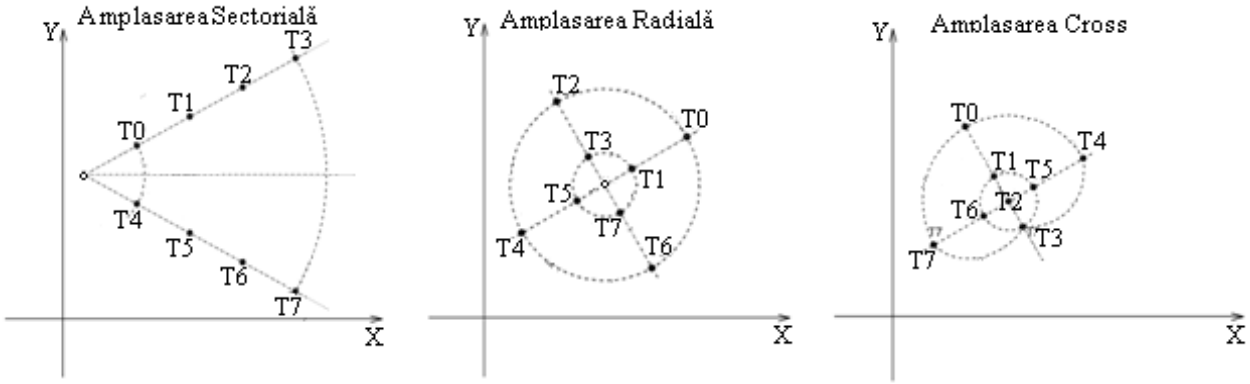

Fig 4b Amplasarea termocuplurilor: Sectorială, Radială, Cross

The program consists from functions for processing the events from the main window of graphic elements, another large group of functions are mathematical and graphical processing functions. We will focus, more detailed, on the last ones, giving them a greater interest.

- Bicubic interpolation. Represents an extension of one-dimensional cubic interpolation used for interpolation of two variables function, which values are known from a regular grid of points. The interpolated surface is smoother compared to bilinear interpolation algorithms or "Nearest-Neighbor interpolation" Mathematical relations for the interpolation method are presented below

$$p(x,y) = \sum_{i=0}^{3}\sum_{j=0}^{3} a_{ij}x^i y^j. \quad (1)$$

$$p(t) = \tfrac{1}{2}\begin{bmatrix}1 & t & t^2 & t^3\end{bmatrix}\begin{bmatrix}0 & 2 & 0 & 0\\ -1 & 0 & 1 & 0\\ 2 & -5 & 4 & -1\\ -1 & 3 & -3 & 1\end{bmatrix}\begin{bmatrix}a_{-1}\\ a_0\\ a_1\\ a_2\end{bmatrix} \quad (2)$$

$$b_{-1} = p(t_x, a_{(-1,-1)}, a_{(0,-1)}, a_{(1,-1)}, a_{(2,-1)}) \quad (3)$$

$$b_0 = p(t_x, a_{(-1,0)}, a_{(0,0)}, a_{(1,0)}, a_{(2,0)}) \quad (4)$$

$$b_1 = p(t_x, a_{(-1,1)}, a_{(0,1)}, a_{(1,1)}, a_{(2,1)}) \quad (5)$$

$$b_2 = p(t_x, a_{(-1,2)}, a_{(0,2)}, a_{(1,2)}, a_{(2,2)}) \quad (6)$$

$$p(x,y) = p(t_y, b_{-1}, b_0, b_1, b_2) \quad (7)$$

- Ponderable interpolation. Represents an interpolation method which allows the construction of a surface based on control points which are positioned irregular. In determining the function value in a particular point, each control point contributes in a inversely proportional measure with the distance to the calculated point at a certain power. Power exponent determines the smoothing degree of the surface.

Also known as Shepard method (1968). Mathematical relationships of this method are:

$$F(x,y) = \sum_{i=1}^{n} w_i f_i$$

$$w_i = \frac{h_i^{-p}}{\sum_{j=1}^{n} h_j^{-p}}$$

$$h_i = \sqrt{(x - x_i)^2 + (y - y_i)^2}$$

where $f_i(x_i, y_i)$ is the function value in the control point, h_i – the distance between the calculated point and the control point, w_i – weight value for that control point.

The algorithm presented above is used to construct a surface on a field where the control points are placed irregularly. Power parameter p takes the value of 2.8, chosen experimentally, providing a convenient smoothing of the surface.

- Point representation in Cartesian and cylindrical coordinates. Depending on the type of the domain on which is defined the temperatures field, is more convenient to process data in Cartesian or cylindrical coordinates. The interpolation occurs in Cartesian coordinates for irregular, linear and rectangular areas type. For sectoral, Cross and radial areas type the interpolation is carried out in cylindrical coordinates. The built field is visualized only in Cartesian coordinates

Allows you to visualize the temperature field interpolated on the basis control points in real-time control. The observed surface will have the height of the Z coordinate, and the point value will be proportional to the temperature at that point. On the right side of the image is displayed the colors ramp fieacare correlated with the the temperature for each color. Temperature of 0 ° C corresponds the black color, temperature 50 ° C corresponds white color. At the bottom side of the picture are presented the control tools of the three-dimensional image: rotation around the axes x, y, z, vertical and horizontal image displacement, separated scaling on x-y, and z. Using the checkbox "Solid Surface" we choose the type of the viewed surface of temperatures field: as a continuous surface form or in a grid form

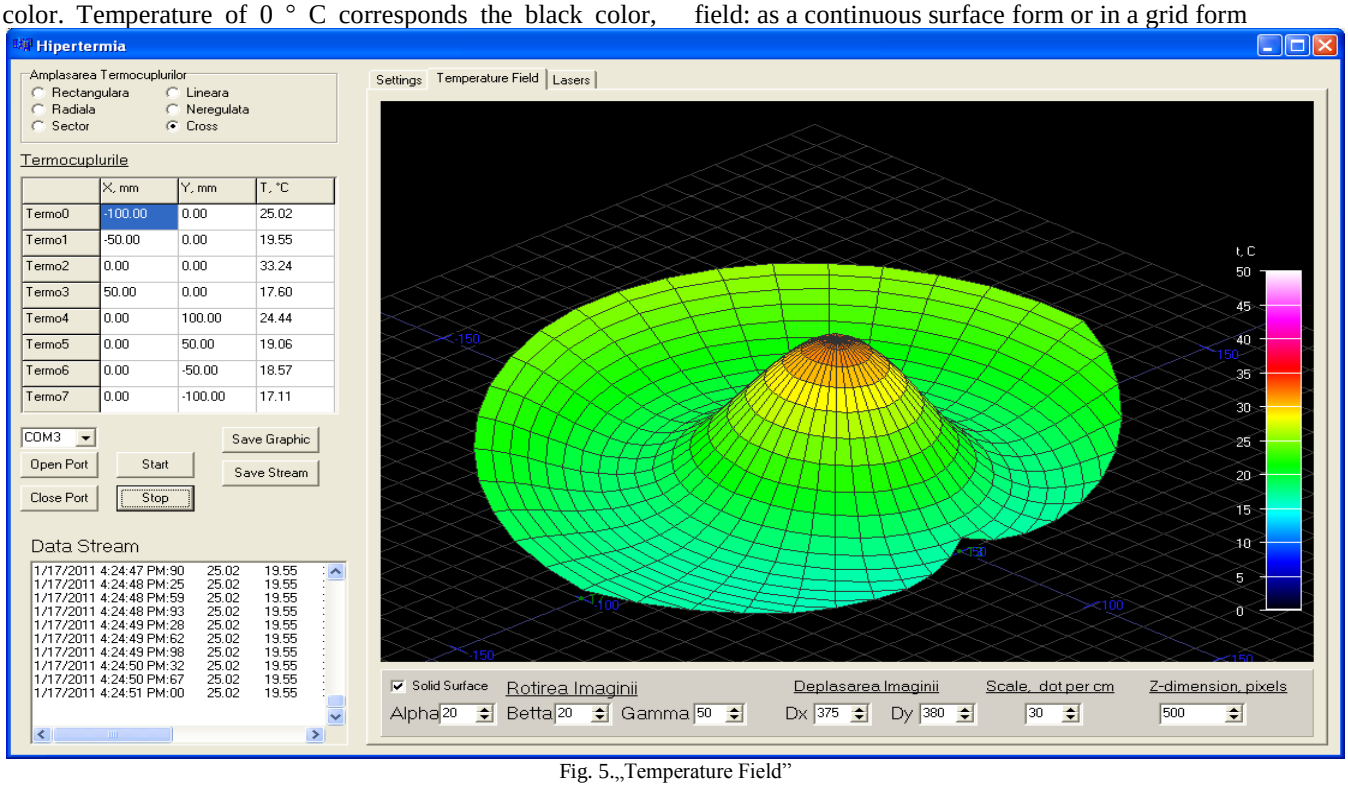

Fig. 5.„Temperature Field”

In the Figure 6 are represented graphs of the time dependency of the recorded signals by thermocouples in one experiment on the heating of the inner regions of a biological sample by the 808 nm infrared radiation.

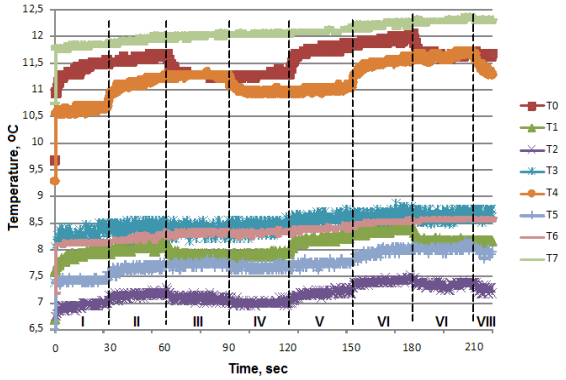

Fig. 6 Time dependence of the signals recorded by the thermocouples

Blurring curves determines the resolution of temperature meter, ~ ± 0,05 ° C, which is satisfactory when it is necessary to control the temperature with an accuracy of 0.1 °C.

III. CONCLUSIONS

The above-described multi-channel temperature meter, which allows to observe the thermal fields within the temperature range of 0 ° C... 50 ° C through the simultaneous measurement of temperature at several points on the studied area with a precision 0.1 ° C, is a options for multi-channel measuring instrument of physical magnitudes designed for use in various sets of equipment for scientific researches or control of different processes. It is able to communicate with the hardware complex, in which is included, in the regime of serial code in a standard RS232 and RS485. This allows increasing the measurement channels by simply connecting to the installation of multiple measuring modules. Setting up the measurement of any physical value can be made by replacing the sensors and the corresponding tabulation of the correction function, stored in the controller memory of multichannel meter that will monitor several physical values.

IV. ACKNOLEDGMENTS

The work was supported by the Suprem Council for Science and Technological Development of the Academy of Science of Republic of Moldova (Project 06.420.007A)

REFERENCES

[1] Х.П. Берлиен, Г.Й. Мюллер. Прикладная лазерная медицина. 1997. М: Интерэксперт.

[2] В.А. Григорьев и В.М. Зорин. Тепло- и массообмен. Теплотехнический эксперимент. Справочник. 1982.

[3] D.Wyman and W. Whelan Basic optothermal diffusion theory for interstitial laser photocoagulation *Med. Phys.* 1994, **21,** 1651-1656.

[4] М.Л. Гельфонд. Фотодинамическая терапия в онкологии. Практическая Онкология. 2007. Т.8. №4

.

Device for Testing of Biological Material

BELIC O.[1], ARAMĂ E.[2], ŞTEFANEŢ M.[1], IAVORSCHI A.[3], PÎRŢAC V.[3], BABUCI A.[1]
Human Anatomy Department of State Medical and Pharmaceutical University "Nicolae Testemiţanu"
Department of Biophysics, Informatics and human Physiology of State Medical and Pharmaceutical University "Nicolae Testemiţanu"
Department of Microelectronics and Semiconductor Devices. Technical University of Moldova.

I. INTRODUCTION

The conjunctive formations which stand at the basis of the ligamentous apparatus of different organs and systems, consists of dynamic structures which react promptly at multiple factors of both the internal and external environment. The structure of these ligaments and their biomechanical properties are a reflection of the morph-functional of the viscera in different periods of life, normally and pathologic.

Considering the fact that the information concerning the interest problem is not sufficiently described in the specialty literature, we decided to make an analysis of the biographic data about the biomechanical properties of conjunctive tissue with similar structure with the ligamentous apparatus of the spleen.

Peritoneal coats, collected from bovines are characterized by a high elasticity [1]. The average tearing force which goes to a square mm in cross section of the peritoneal slides is equivalent to 6-7 kg. Their presence varies from 12-20% against the initial length of the studied probes.

The extension degree and the tearing force of the aortic wall diminishes with aging by 2-2,5 times [2]. The most extensible are the ascending and abdominal portions, less extensible - stick and descending thoracic portion of the aorta.

Our data [3] states that the greatest force applied at the extension (longitudinally determined), which can be supported by the ligament's slide of uterus from the lot with the age from 41-48 years, is equal with 20,48±3,65 N. The necessary effort for the tearing of the implied ligamentus diminishes with the age, reaching 7,21±1,7 N (after 67 years).

Thus, according to the results obtained (4), and the error values peak loads, caused by enlargement of the coronary ligament of liver samples in all age groups of males (I (17-35ani) -14.97 ± 1.3 N) (II (36-60 years) -16.83 ± 4.1 N), (III (> 60 years) -15.68 ± 1.3 N), average values take precedence over those indices for women taken (I (35ani 16) -12.93 ± 1.7 N), (II (36-55ani) -12.90 ± 0.7 N), (III (> 55ani) -13.72 ± 0.9 N), statistically significant differences have not been determined (p> 0.05).

II. STRUCTURAL SCHEME AND THE DESCRIPTION OF THE DEVICE

The device has a color screen for displaying the data. The internal memory allows saving the results for almost 80 measures, the connection with the computer allows transferring data, for their visualization as a diagram with the help of some special software.

The external look of the device can be seen on Figure 1.

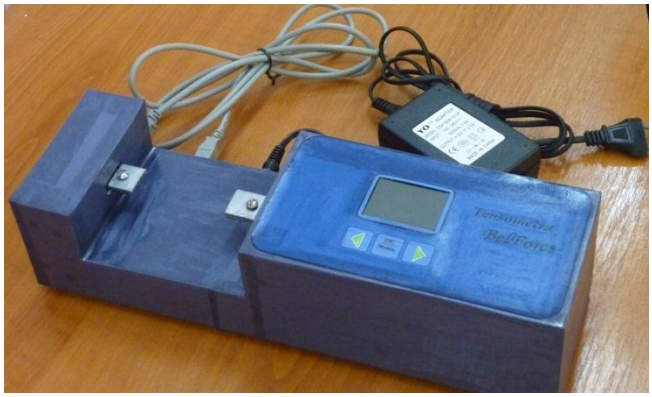

Fig.1. Device for testing of biological material

The device is made of modules. The main one is the microprocessor. His functions are:

- directing the stepper motor;
- tensile force measurement;
- measurement of data and displaying it on the menu screen;
- measurement of data and storing it in the memory.

Sensor used for measuring tensile force is a tens-metric resistive transducer in the shape of a balanced bridge strain gauge Wheatstone. The exiting signal from the bridge varies proportionally with the tensile force. This signal has low-voltage values – 20…30 mV, this is why it must be amplified with the help of an instrumentation amplifier. The amplified signal is applied at the entrance of the module Converter Analog Digital from the structure of microprocessor for subsequent digital processing.

Stepper motor is a synchronous motor type with apparent poles on both armatures. At the apparition of the command signal on one of the stator poles, the rotor will move until his poles will be aligned in front of the opposite stator poles. This type of rotor rotation is basically from pole to pole.

Motor command is done electronically and displacements are obtained for the well-known motor, which allows us to make strains of the ligaments for a specific length. The microprocessor operates the motor coils using the drivers - controlled circuits for the excitation coils.

The display device is designed to display the device menu, of the measured data and the device status.

Command buttons are necessary for the navigation in the device menu, in manual movement of the mobile arm and to start the measurements automatically.

The memory is necessary for the storage of data. During the measurements, values are saved at every step of tensile strength selected by the user. Connecting the device to the computer you can copy data from the device database, can process them using specialized program, view and print the dependence of tensile force on length stretch.

The internal structure of the device is shown in Figure 2.

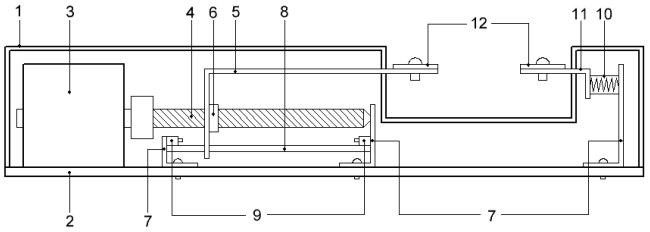

Fig.2.

1 – carcass of the device;
2 – the platform of the device;
3 – a step motor;
4 – threaded rod;
5 – movable arm;
6 – nut;
7 – metal mounting bracket;
8 – rod;
9 – stoper;
10 – strain gauge;
11 – immovable arm;
12 – determining sample clips;

The device for testing of biological material contains a carcass (1), mounted on a platform (2), on which is placed a step motor (3), the shaft of which is connected to a threaded rod (4), on which is mounted by a nut (6) a movable arm (5). One end of the movable arm (5) is freely mounted on a rod (8). On the platfrm (2) is fixed a strain gauge (10), connected to a immovable arm (11). At the ends of the movable (5) and immovable (11) arms are mounted two clamps (12) for fixations of biological material.

In automatic mode investigations over the biological material, the step motor will make a movement of the moving arm with the step selected by the user, after which it will perform tensile force measurement. Measured force value will be displayed on the screen and stored in the internal memory device, and futher can then be transmitted to the computer. At the same time seeking the maximum force, which will break the force investigating the biological material. During the detection of maximum force, the stretch length value is also saved.

Investigation process is interrupted when you press "Stop" or trigger switches to limit arm movement (Stoper). After stopping the investigation process, the screen will display the value of breaking force and length.

The menu allows the device to view the force and length during the investigation, breaking force and length after finishing the investigation, allows to set the step size and record number in memory.

Navigating the menu is done with three buttons that are placed underneath the display. Near each of these buttons are displayed on-screen icon that signifie one button functionality. In Figure 5 are icons that can appear for each button.

Fig.3. Icons used to represent function buttons

Home menu page is shown in Figure 4.

In the top of the page, the first display device status. Depending on the operation of the device will be displayed:

– "Hold order" - does not perform any operation and the investigation has not yet occurred;
– "The results of measurement" - the investigation has ended and displays the results;
– "Extension arm" - as the button is pressed to move the mobile arm to the right;
– "Withdraw arm - the left button is pressed to move the mobile arm to the left;
– "Automatic Mode" - the investigation takes place.
– In the middle of the page is displayed with case, force (in Newtons) and length (in millimeters).

Fig.4. Home menu page

III. INFORMATIONAL SYSTEM FOR PERSONAL COMPUTER

At the initial stage was in question that BelForce information system to perform the following functions: data acquisition from the device BelForce, backup personal computer in the local directory, the saved data editing (removing erroneous data and the immaterial), graphic visualization of data in the form f (F) = Δl, where F - tensile force (N) Δl - stretching the sample (mm), removal of data from memory device, print the results.

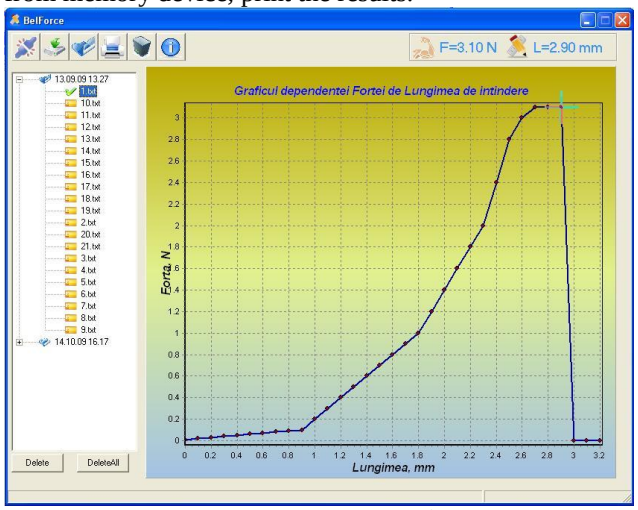

Fig.5. Graphical user interface

The program structure is simple and allows fast access to all functions of the program, obtaining such an easily accessible graphical user interface. The exception is the graphics printing results, where the user can configure the printer, sheet size and other options that are specific to different types of printers. It was created a graphical user interface shown in Figure 5.

In the process of making GUI Standard components were used programming environment Borland C++ Builder. For instrument panel component was used Toolbar1 TtoolBar class. Were added to the required number of command buttons using New Button. Component was used in class ImageList1 TImageList and icons have been added for each

command button ImageList1 Add ... .

Then the connection was made between the component and Toolbar1 ImageList1 ImageList1 Images using the property, so it can display icons in buttons ImageList1 surface. The buttons 32x32 pixel size is set to display icons normally.

To achieve the panel information component was used Label1, Label2 Tlabel class has been configured to display color and text size. Two components were added and ImageList3 ImageList2 the necessary images were introduced.

List of directories of records (tree form) was created with the component class TreeView1 TTreeView, ImageList4 component was added and the icons were loaded for each directory and file in the list. Two buttons were added to the component control class TButton Button1 and button2. The buttons can erase a file / directory, or all files / directories simultaneously.

To create a state panel was used component StatusBar1 TStatusBar class that allows displaying textual information. For graphical visualization of the status process has been used in class TProcessBar ProcessBar1 component.

After adding all the GUI components and their configuration is going to be written a program code that will perform all the functions and operations by default.

IV. CONCLUSION

The developed device allows the accurate determination of the strength and elongation of the sample of biological material until the fracture.

REFERENCES

[1] Кузнецов Н.Н. Брюшина крупного рогатого скота и препараты из нее как новый пластический материал для медицинской практики. Дисс. на соискание уч. ст. д.м.н. Кишинев, 1958.

[2] Фрунташ Н.М. Биоморфоз аорты человека. Кишинев, 1982, 176.

[3] Belic O., Ştefaneţ M. Proprietăţi biomecanice ale ligamentelor uterului. Curierul medical, 2006, nr2, 55-59.

[4] Catereniuc I. Morfologia aparatului neurovascular extra- şi intraorganic al complexului hepatoligamentar. Autoreferat al tezei de doctor habilitat în medicină. Chişinău, 2007.

Advanced Potential of the Photolpetismograph PPG-2 in the Non-invasive Vascular Diagnosis

A.SLOBOZEANU[1], I.ZATUŞEVSKI[2], A.CREŢU[3], V.ŞONTEA[4]
[1]Republican Clinical Hospital
[2]State Medical and Pharmaceutical University "Nicolae Testemiţanu"
[3]Republican Center of Medical Diagnosis
[4]Technical University of Moldova

***Abstract* – Advanced sensor device for shape analysis of the tissue-reflected mean single period photoplethysmography (PPG) signals have been designed and clinically tested. The PPG signal shape reveals individual features of the patient's cardiovascular state. Clinical studies of several patient groups (e.g. diabetes mellitus, atherosclerosis obliterans, Reynaud's syndrome) made it possible to specify components of the PPG signal that are sensitive to the corresponding organic or functional pathologies. Comparison of the right and left arm finger PPG signal shapes, for instance, appears to be an efficient tool for early screening of unilateral atherosclerosis obliterans.**

***Index Terms* – Photoplethysmography, optical bio-sensing, diabetes, atherosclerosis, Reynaud's syndrome.**

I. INTRODUCTION

Photopletismography (PPG) is a noninvasive method which involves the graphic recording of the changes in the volume of a body segment, closely related to the changes in the blood flow during the systolic-diastolic excursion. Photopletismography is a technique developed by Blazek and Wienert in 1981 [1]. This technique, based on different physical principles, has been applied in the clinical evaluation and measurement of arterial and venous blood flow.

The photopletismographic sensor consists of an infrared light diode and a photodiode-strand. Emitted light penetrates the upper layers of the dermis in the case where a part of it is absorbed and another part is reflected and captured by the photodiodes. Reflected light intensity, and therefore the electric signal produced by the photodiode will correspond to the volume of blood in the measured zone. Photopletismography is used as a complementary functional method due to its capacity to highlight the early state of stiffness or muscle spasm of arterioles and capillaries. Comparing the signals from the right and left arms seems to be an effective tool for an early detection of unilateral obstructive atherosclerosis. Photopletismo-graphy examination is easy to implement, however, it often involves multiple nuisances which can lead to diagnostic errors.

Advances in microelectronics and computer technology have opened new possibilities. PPG spectrum analysis provides valuable information on the cardiac function, respiration, vascular and nervous system condition [2, 8]. PPG is easy and safe to use for express-diagnosis and early detection of various cardiovascular diseases.

PPG waveform detected at the periphery may differ significantly from the one detected in the main arteries, and will depend on the strength of the vascular system. If the resistance is abnormal, which is often caused by atherosclerosis, diabetes or other vascular diseases, which reset the narrowed vessels, blood flow velocity in the large arteries to small capillaries decreases dramatically. Hypertension leads to a complete loss of dicrotic peak when it reaches the periphery. Secondary peaks of PPG signals could not be detected on the fingers of patients with hypertension [12].

We should note that PPG signals are not strictly repeated and slight fluctuations of the signal amplitude are possible.

Many doctors prefer visual information (images or diagnostic curve). To provide doctors with such visuals, the Technical University of Moldova, Department of Microelectronics and Semiconductor Devices proposed a photopletismograph (PPG-2). It provides the ability to detect and acquire a signal sequence of 60 individual patients and can specify the exact forms of the signal for further clinical analysis. The available internal memory allows the device to input the data of up to 4000 patients into the database. This data can be later transferred to a PC for further analysis.

The small size of the device and the fact that it is battery powered permits the use of the device for self-monitoring of vascular status at home or during physical exercise, provided that the temperature requirements (22-25C) are satisfied and that the patient is in a calm state of mind.

Below we wanted to demonstrate the capabilities of PPG-2 in the noninvasive diagnosis of cardiovascular diseases and in the analysis of the wave-shaped pulsating blood flow.

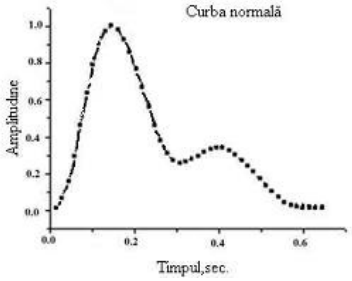

Fig.1. PPG signal form diagnosed at a healthy person

II. MATERIALS AND METHODS

For the purpose of this study we selected a group of practically healthy persons, which gives us the normal parameters of elasticity of the vascular system. Such characteristics have been used in quantitative and qualitative assessment of signal parameters PPG assessed in clinical trials with this device.

Photopletismographic interpretation is based on the evaluation of certain quantitative and qualitative parameters [9,13]. The quantitative parameters include: amplitude curve, speed, time to the wave peak, and total dicrotic notch. The qualitative parameters include: total wave morphology and its components.

Some signals measured initially at a group of persons are presented in Fig. 2. The signals were taken from the same body part (tip of a thumb). Those monitored were practically healthy. The following legend was used: male - A, G and O, age 24-26 years, J - a man of 49 years, M - a woman of 56 years. Figure 2 shows clear differences in PPG signals recorded from five healthy individuals. Dicrotic notch is more pronounced in younger patients [13], which could be interpreted as a good sign of vascular elasticity, compared with older patients.

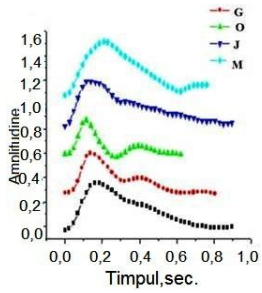

Fig.2. Different types of signals PPG recorded at a group of practically healthy patients.

Our studies in 5 patients with diabetes mellitus have fully confirmed our hypothesis. All PPG signals recorded at the finger tips of these patients were bell shaped, with no secondary peak in the catacrota (Fig. 3).

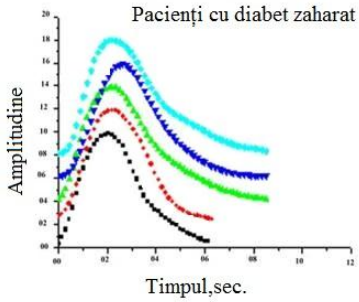

Fig.3. PPG signals in 5 patients with diabetes

.The clinical trial in patients with atherosclerosis revealed similar types of PPG signals. At a dose of nitroglycerin, reflecting the pharmacological dilation of blood vessels a secondary peak formation was observed. It is a sure indication of an increased blood flow. The changes obtained were shown in Figure 4.

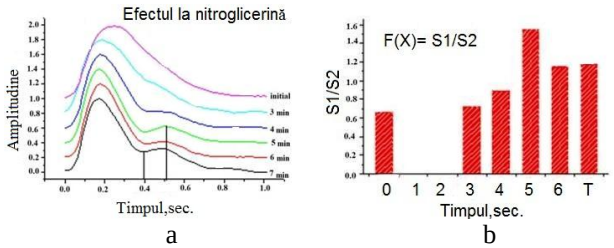

a b

Fig.4. A – demonstrates the changes in patients with asymptomatic mild atherosclerotic changes, which have received a dose of nitroglycerin, B – the time of the nitroglycerin-caused effect development characterized by T2/T1 signal and forming the secondary peak in the catacrota signal. It is a clear indication of an increased blood flow.

Thus we can see a clear time delay and broadening of the signal on the right arm, compared with the left arm, which shows an increased vascular resistance and a slower speed of blood flow in the right arm. Therefore the angle ratio (slope) by signal S left / S right could serve eventually as a diagnostic criterion for assessing blood vessel occlusion (Fig. 5 b).

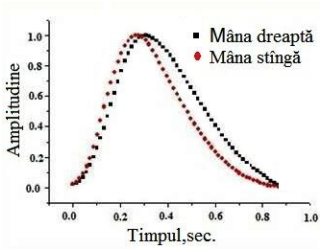

a

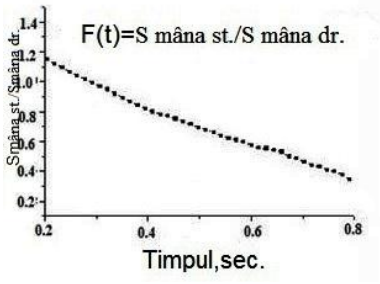

b

Fig.5. a - comparison of PPG signals from the fingers on both hands, in the case of the subclavian artery occlusion, b - the angle ratio (slope) by signal S left / S right

Reynaud's syndrome (RS) is a paroxysmal disorder of the peripheral circulation, located usually in the upper limbs, characterized by intermittent appearance of a bilateral and symmetrical spasm of digital arteries, occurring when the patient experiences cold or emotions, with the normal state in other conditions. It is a rare disease, which is found typically in young women (less than 40 years). The etiology is unknown. PPG can provide additional information about this disease [14, 15].

PPG monitoring was used to monitor vascular changes during a physical exercise of a patient (L., 22 years) with RS. PPG signal was recorded before and after the exercise. Remarkable changes can serve as evidence of the nutrition of the arm "trained" with improved blood. The results are shown in Fig.6.

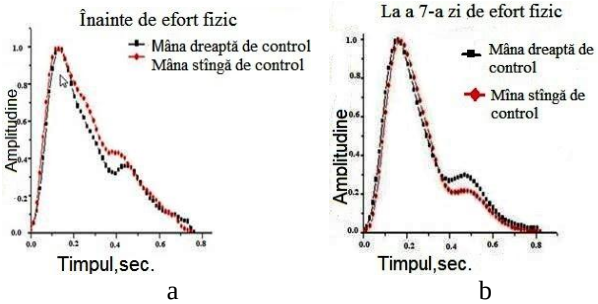

a b

Fig.6. PPG signals taken from the fingers of both hands before and after the tests in patients with Reynaud's syndrome

III. REVIEW.

The results presented and the analysis of the functional characteristics of the device confirmed the potential of PPG-2 sensor, used in vascular diagnostic methodological procedure and during the exercise test in the pre-clinical phase.

We have also noted other aspects of PPG signals recorded at the finger tips which can serve as criteria for diagnostic

and dynamic screening:

- Growth of the anacrotic phase of the pulse wave characterizes the resistance of the blood flow in vessels;
- General shape of the signals PPG: a bell, with no signs of reduced catacrota and dicrotic notch announces various abnormalities of peripheral blood vessels (caused by diabetes mellitus, atherosclerosis);
- Appearance and increase / decrease of the secondary peak, assessed against a drug (e.g.: nitroglycerin) may be used to monitor the time of expansion / narrowing of blood vessels;
- Changes in the shape of the signal PPG, reached after a physical exercise or a physiological effort (blood flow), reflect the progress of the physiological state of the observed.

IV. CONCLUSIONS

Photopletismography with reflected light proved to be an appropriate tool for testing the prediction of the therapeutic outcome (e.g.: for the patients with high blood pressure, diabetes, obliterating arteriosclerosis and Reynaud's syndrome, etc.)

Having reviewed research that focused on the PPG-2 device performance, we conclude that it offers the possibility of rapid and reliable estimates.

BIBLIOGRAPHY

[1] Hertzman A. B. Photoelectric plethysmograph of the finger and toes in man. *Proc. Soc. Exp. Biol. Med.* **37**, pp. 1633-1637, 1937.

[2] Ugnell H. Phototplethysmographic Heart and Respiratory Rate Monitoring, Ph. D. Thesis No. 386, Linkoping University, 1995.

[3] Nitzan M., H. de Boer, S. Turivnenko et al. Power spectrum analysis of spontaneous fluctuations in the photoplethysmographic signal. *J. Bas. Clin. Physiol. Pharmacol*. 1994, 5 (3-4): 269-276.

[4] Bernardi L., A. Radelli, P. L. Solda et al. "Autonomic control of skin microvessels: assessment by power spectrum of photoplethysmographic waves. *Clin. Sci.*, **90**, pp. 345-355, 1996.

[5] . Nakajima K., T. Tamura, H. Miike, "Monitoring of heart and respiratory rates by photoplethysmography using a digital filtering technique", *Med. Eng. Phys.*, **18**, 365-372, 1996

[6] Larsen P. D., M. Harty, M. Thiruchelvam et al, Spectral analysis of AC and DC components of the pulse photoplethysmography at rest and during indication of anaesthesia. *Int. J. Clin. Monit. Comput*, 1997, 14: 89-95.

[7] Nitzan M., A. Babchenko, B. Khanokh et al., "The variability of the photoplethysmographic signal – a potential method for the evaluation of the autonomic nervous system", *Physiol. Meas.*, 19, pp. 93-102, 1998.

[8] Perez-Ocon F., A. Abarca, J. Abril et al., "Optical measurement of cardiac rhythm using a personal computer with telediagnosis possibilities", *J. Biomed. Opt.*, 6, No. 1, pp. 90-96, 2001.

[9] Spigulis J., U. Rubins, "Photoplethysmographic sensor with smoothed output signals", *Proc. SPIE.* 3570, pp. 195-199, 1998.

[10] Venckus G, J. Spigulis, "Frequency filtering effects on the single-period photoplethysmography signals", *Med. Biol. Eng. Comput.*, 37, Suppl. 1, pp. 218-219, 1999.

[11] Spigulis J., G. Venckus, "Single-period photoplethysmography: a potential tool for noninvasive cardiovascular diagnostics", *Springer Series "Optics for Life Sciences"* OFLS-VI, Berlin (in press).

[12] Spigulis J., G. Venckus, M. Ozols, "Optical sensing for early cardiovascular diagnostics", *Proc. SPIE* 3911, pp. 27-31, 2000.

[13] Ozols M., J. Spigulis, "Acquisition of biosignals using the PC sound card", *Proc. Int. Conf. "Biomedical Engineering" (KTU, Kaunas, LT*), pp. 24-27, 2001.

[14] Wouda A. A., "Raynaud's phenomenon. Photoelectric plethysmography of the fingers of persons with and without Raynaud's phenomenon during cooling and warming up", *Acta Med. Scand.*, 201, pp. 519-523, 1977.

[15] Engelhart M., H. V. Nielsen, J. K. Kristensen, "The blood supply to fingers during Raynaud's attack: a comparison of laser-Doppler flowmetry with other techniques", *Clin. Physiol.*, 5, pp. 447-453, 1985.

Complex device for recording and signal processing of cardiac activity

Victor ŞONTEA, Anatolie IAVORSCHI, Valerii PAHOMI, Valeriu PÎRŢAC, Dmitri ANGHILOGLU, Sergiu Railean
Technical University of Moldova
sontea@mail.utm.md

***Abstract* – there are described structural scheme of the measurement system and processing of photopletismogram, interacting units, possibilities of software and interfaces in two modes of operation: the pc and with a special modul.there are presented characteristics and technical parameters of the system.**

Index Terms – Cardiovascular system, photopletismography, device, signal .

I. INTRODUCTION

Besides electrocardiogram, one of the methods, for determining the physiology index of the human body is photoplethysmography – computerized method based on recording and signal processing of the photoplethysmogram wave. [1,2]

The proposed system is assigned to the investigation of cardiovascular medical technology, the operating principle of which is based on the method of photopletismography wave. Photopletismography principle is reflection of radiation (infrared radiation is usually used, but may be used and another band of spectrum that would allow a good penetration of skin coatings and independence of the reflected signal by other factors such as skin pigmentation) from blood cells moving through the small vessels, under the skin. [3,4]

Photoplethismografy recording and processing allow to obtain information about the state of cardiovascular system, the segmented blood pressure, detecion of blood vessel damage through screening large caliber method.

II. STRUCTURAL SCHEME OF THE DEVICE

The device is designed for ECG and Photoplethysmography signal acquisition, its processing, computer data transmission, determining the signal parameter, graphical display of heart rate on LCD color display, storage of data and signals of the patient into the database of patients, etc.

The device is composed of several modules: the digital module, the analog module, transmitter, LCD Display, SD Memory Card and power control module (Figure 1).

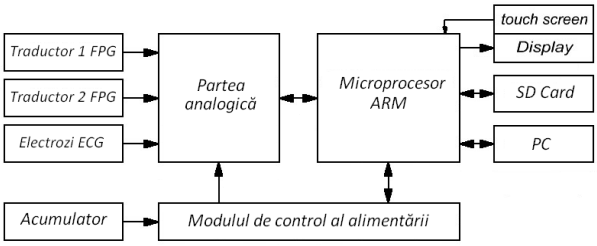

Fig.1. Structural diagram of the device for recording and processing of the ECG and photoplethysmogram waves

The functionality of the device is based on ARM Microprocessor, with 32-bit architecture that works at the clock frequency of 100 MHz. Its functions are the following:

- Interaction with the analog module into a digital signal conversion, changing the operational amplifier gain of the final cascade to achieve an optimal level of input signal at ADC, changing infrared radiation transmitter, applying a voltage (CDA) in the cascade amplifiers to maintain signal processing slow components at the desired level, digital signal processing, etc;
- Interaction of Color display device;
- Reading and decoding data from touch screen panel that is on display – the determination of coordinates of the points of interaction;
- Making a menu-user interface extensive graphical display due to large size touch screen panel;
- Interaction with the power control unit – ensuring the transition to sleep regime, provident power to all blocks of the device in active mode operating voltage level monitoring of battery charging;
- PC Connection – connecting the computer through the USB interface device can operate as a computer peripheral mode – photoplethysmography signal can be collecting and send directly to your computer , or read from memory and transmitted to the personal computer only necessary data.

Data Base allows dynamic allocation of memory space for its patients and signals. It can capture more than 65 thousands patients, each patient to 240 signals. Signal duration can be adjusted from 1 minute to 24 hours, and duration of all signals is 40 320 minutes (equivalent to 672 hours or 28 days)

Analog site of the device consists of two symmetrical channels that process signal from two photoplethysmograph transducers and one channel of ECG processing. Figure 2 shows the block diagram of the analog part of the device.

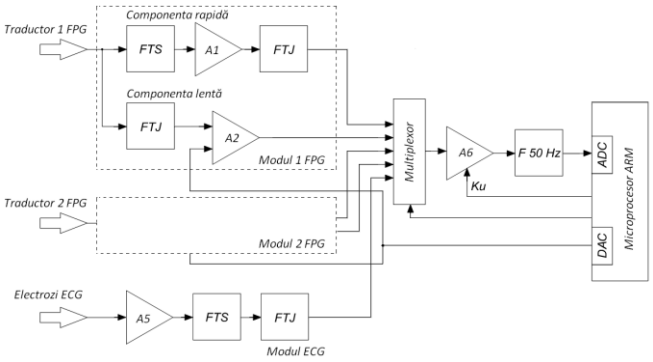

Fig.2. Block analog scheme of the device

The device measures both fast component and slow component of photoplethysmography, so the signal from the sensor is initially separated into two signals: signal of slow

component and signal of fast component of photoplethysmography.

The fast component of signal is first amplified in current then dc component is removed by using a high pass filter (Fig.2). Because the power supply of analog part is unipolar, signal is raised to the „virtual gnd" of 1,5 V. After this signal is amplified with a fixed amplification facto r (Ku = 10) and highfrequency noise filtered through a low pass filter.

To get the slow component, the signal from the sensor is amplified in current and then the rapid component of the signal is filtered using a low pass filter with cutoff frequency of 0,5 Hz. After this, signal is applied to the inverting input of a differential amplifier A2 with amplification gain 10. To the non-inverting input of this amplifier is applied a voltage from the digital-analog converter (CDA). This voltage is necessary to maintain the signal voltage range from 0 to 2.56 V and exclusion of the amplifier saturation regime.

Electrocardiograph signal (ECG) are gathered using three electrodes placed on the patient's body - two active electrode (or warm) and a neutral electrode (or cold). The signal is amplified with an instrumentation amplifier A5, after which the dc component is filtered using a high-pass filter with cutoff frequency of 0,05 Hz, and noise at frequency above 100 Hz with a low-pass filter.

The fast and slow components of signal from output of photoplethysmograph module and ECG signal is applied to the inputs of a multiplexer, with which the microprocessor selects the appropriate signal to be recorded. The analog signal from the multiplexer output is applied to the operational amplifier A6, whose amplification factor can be adjusted by the microprocessor. Because of using digital potentiometers are obtained 256 steps of the amplification gain. This allows obtaining the ADC input signal with amplitude that can be converted in large numbers without quantifying losses and without the need for further scaling.

After amplification the signal is filtered by the noise induced by power grid frequency of 50 Hz.

Getting data from analog to digital converter, microprocessor continuously monitors the signal level. If the signal amplitude is too low for a period of time, will made to increase the coefficient of amplification, if too high - to zoom out. Another action on the part of the device is changing the value of analog voltage output digital-analog converter to minimize the slow component signal.

The microprocessor also changes intensity of infrared radiation, which allows the transducer to adjust the properties of different patients.

The display of the device is an LCD Color, with resolution of 320×240 pixels and 65 536 colors, which allows to display the time evolution of one or two signals simultaneously, but also create a user interface, extensive menu, intuitive and easy to interact. Using the graphic display combined with touch screen panel allows us to create a device without many buttons, operator interaction with the device being made by pressing with a special pen, called the stylus, directly on the Touch Screen panel, placed above the display. Because of this, the menu consists of pages, buttons, keyboard - similar to a personal computer, making it easier to access the menu for personal computer users.

User menu consists of four pages: "Patient", "Display", "Graphics" and "Settings." Page "patient" is intended to work with the database, add a new patient into the database or choose a patient previously investigated. At the bottom of the window, designed to introduce a new patient database, is the keyboard, similar to the personal computer (Figure 3).

Fig.3. Introducing a new patient window

The patient's page can be accessed and the device database. Database interface allows us to navigate through the list of patients to look for a particular patient in the database, to remove a patient and to select a particular patient.

Fig.4. Browsing through the database window

On the page "Display" choose the desired signals to be viewed. It can be selected up to two signals. For this, press the squares that stand beside the name of each signal. Clicking on these squares, each a check mark appears in them, which means it has been successfully selected, and the right square is the abbreviated name of the signal. If the patient was already introduced in the database, you can choose it to view previously stored signals. To compare the signal obtained before and that obtained in time, choose a signal from memory and a signal from the sensor.

Page "Graphics" is provided to view selected signals for display. Can be viewed one or two signals simultaneously. With "Start" button will start collecting data and displaying on the display, the "Stop" will stop collecting data, and by using the "Memo." will store data in memory. If you select a signal from memory for display on this page we can place directly on the screen of photoplethysmograph basic points and to calculate photoplethysmograph few basic parameters, which can give some clues about the state of the cardiovascular system.

Page "Settings" contains the device settings: setting the time, date, backlight, view memory status and the option of switching off the device. A fairly large part of the energy

consumption of the device has LEDs backlight. To reduce the energy consumption of the device is provided for automatically disconnecting the lights over a certain time after you last press a touch screen panel. Length of time it can be set by choosing one of values: 20, 40, 60 seconds or disconnect backlight.

III. CONCLUSION

The developed device allows the time analysis of electrocardiograms and photoplethysmograms, quality parameters, allows to compare the visual signals and those collected previously made at the moment, allow to study heart rate variability.

The system has the following technical parameters:

- Number of channels – 2 channels of simultaneous recording of slow and fast components of photoplethysmography and 1 channel electrocardiography;
- Frequency Band – from 0.05 to 18 Hz (FPG) and from 0.05 to 100 Hz (ECG);
- Signal sampling frequency – 500 Hz;
- Active mode power consumption – 0.6 W;
- Minimum operating time without recharging in active mode – 16 hours;
- Dimensions – 110X65X30 mm;
- Weight 200 g.

The measurement and data processing of photopletismograph has technical characteristics (price, size, number of functions performed, parameters) high, competitive with existing ones and can be recommended for the production and subsequent implementation in health care.

ACKNOWLEDGMENTS

This work was supported by the Supreme Council for Research and Technological Development of the Academy of Sciences of Moldova under grant no 11.817.05.20A

REFERENCES

[1] Р. М. Рангайян. Анализ биомедицинских сигналов. Практический подход. Москва, Физматлит, 2007.

[2] R. Sam, K. Darvall, D. Adam, S. Silverman, A. Bradbury, Digital venous photoplethysmography in the seated position is a reproducible noninvasive measure of lower limb venous function in patients with isolated superficial venous reflux. Journal of Vascular Surgery, Volume 43 (2006), Issue 2, pp. 335-341

[3] Nicolae Armencea, Victor Şontea, Andrei Bragarenco, Dmitri Anghiloglu, Valeriu Pahomi Sistem de achiziţie a semnalelor biomedicale, Proceeding of the 5th International Conference on Microelectronics and Computer Sciense" Chisinau 2007 V II pp 24-27.

[4] Nicolae Armencea, Victor Şontea, Anatol Iavorshi, Dmitri Anghiloglu, Anatol Creţu. Identificarea parametrilor cantitativi a fotopletismogramelor: Proceedings of The 2 nd International Conference Telecommunications, Electronics and Informatics" Chisinau, 15-18 may 2008. V I pp 159-164.

New Investigation Technologies of the Cardiovascular System and of the Vegetative Nervous System

V.SCRIPNIC[1], V.ŞONTEA[2], I.ZATUŞEVSKI[3], A.SAULEA[4], E.ZEMŢOVSKI[5] , A.IAVORSCHI[2], V.PÂRŢAC[2], V.SOCOLOV[4], N.ALEXEEVA[5]
[1]Medical Center of Social Rehabilitation; [2]Technical University of Moldova; [3]State University of Medicine and Pharmacy from Moldova; [4] Free International University of Moldova, [5]Medical Pediatric Academy, Sankt Petersburg, [6]Chuvash State Teacher Training University.

***Abstract* – Protecting and enhancing the health of the population is an important task for our country. Also financial resources targeted to medicine are insufficient to organize the effective functioning of medical institutions. In these circumstances is particularly important to equip the medical personnel with devices that have high possibilities of early diagnosis, which would allow family doctors to establish a correct diagnosis of health from the patient's first visit. On the other hand this will save human and financial resources by optimizing the treatment process and the exclusion of laboratory and instrumental investigations which repeats the information obtained by other methods.**

***Key Words* – photoplethysmography, cardiovascular system, vegetative nervous system,**

I. INTRODUCTION

Computerization and automation of various diagnostic methods in recent years does not surprise anybody, and allows ease of early diagnosis and improves doctor's work efficiency. In our opinion, such as automated methods of diagnosis as **cardiointervalography** (allows to establish and to study the nature of links that exist between the heart and the vegetative nervous system, the assessment of sinus node rhythm and function, assessment of various arrhythmias) **photoplethysmography** (allows to obtain information about the status of blood vessels and some parameters of central hemodynamics) should be materialized in a portable diagnostic device. And usage of this device while performing physiological maneuvers should allow assessment of adaptive-compensatory reactions occurring in the human body.

The offer comes from a group of researchers, doctors, engineers, programmers united in a team in the Department of Microelectronics, led by Professor Victor Şontea allows a qualitative increase of the diagnosis by specialist doctor, family physician. The same device can be used with success by sports medicine physicians during trainings, in scientific laboratories that are concerned with investigations of health of humans with special working regimen, of pupils and students. It is proposed to the scientific opinion an original device that allows rapid, noninvasive assessment of the cardiovascular system and vegetative nervous system, to the abilities to

to adapt to physical and psycho-emotional limited efforts and, based on these data, to establish the correct diagnosis.

The methodology of operation of this device is based on a theoretical and clinical foundation based on investigations of the heart rate. The device is designed to record and to measure the pulse wave allowing diagnosis of the condition of the patient's blood vessels, tracking and recording in real time the pulse heart rate and thus appreciation of the sinuous structure of the heart rate. The device was tested at the Department of Functional Diagnostics of the Republican Hospital, and Republican Medico-Social Rehabilitation Centre.

Fundamental investigations of the heart rate in healthy volunteers and in high performance athletes, at cosmonauts, performed by scientists V. Parin and R. Baevsky (1964-2009), A. Dembo (1984) E. Zemţovski (1984-2003), A . Korkuşko (1987-2005), later continued by V. Scripnic and A. Saulea (1983-2010) showed that one and the same values of RR intervals can be interpreted as a result of the oscillations of the length intervals between ventricular contractions of the heart, different depending of it's physiological or pathological nature.

This means that formal assessment of the value of frequency of contraction (FCC) and its deviation $\Delta RR = RRmax-RRmin$, without taking into account the sinuous structure of the heart rate and the set degree of periodic and aperiodic fluctuations, can lead to erroneous conclusions and serious mistakes [1,4,5]. This means that without knowledge of the spectrum of frequencies that belongs to the heart rate, spectral forces of waves, also called respiratory waves, slow waves (LF), very slow waves (VLF), the physician cannot assess correctly the state of the vegetative system, the sympathetic and parasympathetic activity and, ultimately, cannot correctly assess the adaptive capacities of the investigated patient which means that one cannot choose the correct direction of therapy [1, 2, 6]. General knowledge about self-organization of complex systems has been formulated by Ilya Prigogine and Hermann Haken, who first described the operation of complex systems with feedback. Proceeding from the principle formulated by N. Moiseev (1987) and based on the analysis of mechanisms of development of living nature reveals that: if there is more than one state of a system (or process), i.e. a number of coordinated states, subject to the laws of storage, energy accumulation and existing links in the system, then in the human body is achieved that state, which corresponds to minimum energy dissipation or minimum increase of entropy. Living organisms are subject to this principle [1, 2, 3, and 7].

Also we must remember the principle of minimal constraint of any system, which was discovered by Le Chatelie-Braun, that allows anticipation of human body's

reaction to an external trigger, by obtaining a certain effect (the minimum time or minimum dynamic deviation) due to effective change of the feedback signal (amplitude, or power) but also the characteristics of the object are kept [8.9]. These principles provided by synergistic can be used successfully during treatment.

For the specialist, but especially for the family doctor, who is forced to go to the patient's home, it is very important to establish the status of the vegetative nervous system and cardiovascular system. The proposed device can help establish more easily the state of the nervous system functional during the hyperventilation test, a procedure that takes only a minute

The hyperventilation test provides performing of deep breaths with a frequency of
6 osc/min (5sec. inspires; 5sec. exhale) in supine position.
Also the pulsogram is recorded.

Thus, a maximum and stable variation of the FCC is obtained in healthy humans. This variation of the FCC is a normal reaction, called respiratory sinus arrhythmia, which gives rise to respiratory waves in the spectrum of frequencies of the heart rate and is caused by vagus nerve activity (increased activity of the vague during expiration and a decreased during inspiration, due to excitation and inhibition of the vague nucleus, which transmits signals through nerve pathways to the sinus node). In pathological cases associated with vegetative dysfunction, this reaction with deviations of the gaps between heart contractions changes.

The developed device allows rapid and safe recording of the respiratory deviations of heart rate, by several methods: intervalography, correlative ritmography (scatterography). It should be noted that the respiratory method can not be used if the pulse is followed by palpation or auscultation.

This device not only allows assessment of vegetative status, but also of the sympathetic and parasympathetic activity of the vegetative nervous system during execution of test with hyperventilation. The doctor can assess and ensure vegetative reactions in the physiological limits of the test given, a very important thing for athletes, convalescents with sedentary lifestyle and elderly.

During the test with hyperventilation an increased parasympathetic activity occurs during exhalation compared with normal breathing and as a result FCC decreases (RR interval increases), and during inspiration cute the sympathetic prevails, FCC increases and RR intervals decrease. Depending on the increase and decrease in RR intervals we can talk about the activity of sympathetic and parasympathetic systems and their functional status [5, 6, 7].

II. MATERIALS AND METHODS

The study of the possibilities offered by the new VRC1 device proposed by the team of researchers from the Department of Bioelectronic was made in the Functional Diagnosis Department of the Republican Hospital, Head of Department, MD, Phd, Dr. I. Zatuşevski. Investigations were conducted on 186 persons of both sexes, aged 18-68 years, with various pathologies of the cardiovascular system and 32 practically healthy people, between November 2010 - April 2011.

With the help of HCV, a last generation portable device, one can obtain biological information to diagnose function of the vegetative and cardiovascular system by plethysmographic method.

The operating principle is based on pulse wave propagation and reflection, which is captured by a phootopletismographic transducer and processed by an original microprocessor using its own program developed by the engineers of the Department of Microelectronics.

This device allows obtaining the following parameters:

Statistical parameters of heart rate:

FCC – Frequency of cardiac contractions;

RR med, Mo (mode) - the value of the RR interval is most often encountered in a exract of RR intervals; Amo (mode amplitude) or the frequency of tracing the length of RR interval that coincides with the Mo value calculated from an extract of RR intervals; RR min, HR max, dX, CV,%, SDNN, RMSSD, NN 50count, pNN50%

Spectral parameters of heart rate:

HF; LF; VLF; spectral sum Σ; LF/HF; LF%; HF%.

The largest spread between the integral parameters has the blood pressure index (IT) by R. Baevsky. The essence of the above-listed parameters was demonstrated by R. Baevsky (1997) using his own mathematical model of adjusting the activity sinus node. After R. Baevsky, Mo characterizes the activity of the humoral chanel of rhythm regulation, AMo characterizes the sympathetic activity and ΔRR – the activity of the parasympathetic channel of the nervous system.

In order to study the state of vegetative control of heart rate in patients and volunteers were used rhythmographic methods, including corellative rhythmography (scatterography) and intervalography.The research was performed based on VRC1 device.

Hemodynamic parameters:

AUD - Amplitude of the Anacrote Wave;

IUD - Dicrote Wave Index ;

TRU - Time to Wave Reflection (dicrotic notch)

IUC - Ascending Wave Index.

III. THE RESULTS OF INVESTIGATIONS AND DISCUSSIONS:

Investigations made in the department of functional diagnosis of Republican Clinical Hospital, in the Department of Physiology and in the Republican Center of Medical-Social Rehabilitation have shown that normal activation of the parasympathetic system during the test with hyperventilation occurs by increasing the duration of RRmax interval (0, 05 sec. ≤ RRmax ≤ 0.1 sec.), while the sympathetic system's - within the ranges of decrease of RRmin interval (0.05 sec. ≤ RRmin ≤ 0.09 sec.). Increasing the value RRmax> 0.1 sec. and decreasing RRmin> 0.09 sec. confirms the prevalence of parasympathetic activity and sympathetic avegetative system, while lowering RRmax <0.05 sec. and increasing RRmin <0.05 sec. show reduction of their activity.

Investigations carried out on healthy people and on sick people with heart diseases has allowed us to emphasize the physiological and pathological responses that characterize the activity of sympathetic and parasympathetic systems from the the vegetative system. Pathological reactions are due to vegetative dysfunction.

Depending on the sympathetic and parasympathetic activity report nine types of reactions were highlighted, of which 7 physiological and 2 types of pre -pathological reactions. The first 3 types of physiological reactions are characterized by normal parasympathetic activity, within physiological limits (0.05 sec. ≤ RRmax ≤ 0.1 sec.).

In the first case sympathetic activity is decreased, in the second – it is normal and in the third - is increased. Vegetative activity in the first case is made predominantly by the parasympathetic system, in the second – due to the both rings: sympathetic, parasympathetic and in the third - mainly due to the sympathetic system.

The fourth, fifth and sixth case are characterized by high parasympathetic activity (increased value RRmax> 0.1 sec.). Sympathetic activity is low (RRmin is <0.05 sec.) for case four, in the fifth case is normal (0.05 sec. ≤ RRmin ≤ 0.09 sec.), in the sixth case is high (RRmin> 0 , 09 sec.).

In case four and five the vegetative activity is due predominantly to the parasympathetic system, and in case six – due to both systems: sympathetic and parasympathetic. The two types (the fourth and fifth) of heart rate are cases where vegetative regulation is within the physiological limits, but in case 6 there is a form of adjustment in which a pronounced sinus arrhythmia appears and extrasystoles may occur, supra-ventricular migration of rhythm leader and replacement impulses. So, high activity of both systems: the sympathetic and parasympathetic leads to an arrhythmogen effect, that is why this kind of adjustment may be called pre-pathological.

The seventh, eighth and ninth type is characterized by low parasympathetic activity (increased RRmax <0.05 sec). The seventh type is characterized by low sympathetic activity, the eighth type is characterized by normal sympathetic activity and ninth type is characterized by high sympathetic activity. The seventh can be characterized as a type in which the human body has very low adaptive capacities of both systems: sympathetic and parasympathetic. This type of reaction can be called pre-pathological. Types eight and nine are characterized by physiological reactions, more due to sympathetic regulation.

Usually, in case of normal regulation, physiological, ensuring the execution of the test, to say, with hyperventilation, or some other tests depends on the type of vegetative regulation listed above. For example, in case of vagotonic regulation (when the vague activity is predominant), the vegetative activity is performed due to sympathetic system and in the case of the sympathetic regulation - by the parasympathetic system and if normotonic, they are equally active -sympathetic and parasympathetic - then adjustment is performed by both systems: the sympathetic and parasympathetic.

So, we can establish that between sympathetic and parasympathetic system there is a close interconnection and interdependence, which provides an adaptation to a wide range of changes that come from outside and inside the body and the doctor can easily determine and distinguish the body's physiological functioning of the pathological. In vegetative dysfunctions pathological reactions appear during hyperventilation test, and we can establish which of the segments of the vegetative nervous system is unable to react adequately and therefore do not provide cardiac adaptation to changes in external environment.

In addition to the types of physiological, pre-pathological there are also pathological. There are three types of pathological reactions:

1) paradoxical reaction of sympathetic system (RRmin during the hyperventilation test increases instead of gradually declining);

2) paradoxical reaction of the parasympathetic system (RRmax during the hyperventilation test decreases instead of increasing);

3) paradoxical reaction of both sympathetic and parasympathetic systems (RRmax - decreases and RRmin - increases).

Pathological reactions of the vegetative nervous system at the test with hyperventilation reveals the presence of the vegetative dysfunction, and early diagnosis will allow starting of appropriate treatment.

During the investigation of the objective status at sick persons and healthy volunteers we have found different versions of the sympathetic and parasympathetic activity, which subsequently, during the statistical processing, allowed the split the investigated in samples according to the types of rhythm disturbances which allowed to optimize the patient's stay in the hospital and increase of the efficiency of treatment.

IV. CONCLUSIONS:

The algorithms used in the device VRC1 allows computerised processing , facilitating the diagnosis of various cardiac rhythm disorders in patients and assessing vegetative disturbances (predominance or inhibition of parasympathetic or sympathetic) and the correct choice of treatment

The advantages of this device ensures reduction of diagnostic time and significantly increase its objectivity, and also assessment of disorders in blood circulation, the changes taking place in the kinetic capacities of the heart and blood vessel tonic capabilities should ensure a certain flow of blood.

The results of the investigations confirm the need to apply the hyperventilation test, that allows objectivity of various arrhythmias and their division into three samples: functional , intermediate and pathological, which allows to optimize treatment and follow-up treatment in the dispensary system.

BIBLIOGRAPHY:

[1] Baevsky R. Теоретические и прикладные аспекты оценки и прогнозирования функционального состояния организма при действии факторов длительного космического полета. М. 2005. Институт медико-биологических проблем РАН.

[2] Дембо А.Г., Земцовский Э.В. Спортивная кардиология // Л-д. Медицина. 1989. С.464.

[3] Коркушко О.В., Писарук А.В., Шатило В.Б., Лишневская В.Ю., Чеботарев Н.Д., Погорецкий Ю.Н. Анализ Вариабельности Ритма Сердца (возрастные Аспекты), Институт геронтологии АМН Украины Kiev, 2005

[4] Земцовский Э.В. Спортивная кардиология. - СПб.: Гиппократ, 1995. - 447 с.

[5] Scripnic V. Capacităţile adaptative ale organismului odată cu înaintare în vârstă // *Chişinău, Pontos. 2009. 167 p.*

[6] Scripnic V. Posibilităţile de creştere a adaptabilităţii organismului sub acţiunea vibraţiilor rezonante induse şi în condiţiile hipoxiei hiobarice naturale // *Chişinău, Pontos. 2008. 136 p.*

[7] Scripnic V. Norma în fiziologie. *Compediul lucrărilor, Ediţia a VI. Arad, România, 2002, p. 248-281.*

[8] Haken H. Synergetic Computers and Cognition, Springer, Berlin, 1991.

[9] Haken H. Synergetic, An Introduction, Springer, Berlin, 1983.

Millimeter Wave Nonthermal Therapeutic Device Based on Parallel-Strip Technology

SAINSUS Iurie, RAILEAN Sergiu, ROTARU Anatol,
CONEV Alexei, RUSSEV Iurie, POSTORONCA Sveatoslav, SCERBII Denis
Institute of Electronic Engineering and Nanotechnologies "D. Ghitsu"
Academy of Sciences of Moldova, Academiei str. 3/3, Chisinau, MD–2028 Republic of Moldova

Abstract - **This paper describes the therapeutic device developed at the Institute of Electronic Engineering and Nanotechnologies "D. Ghitsu" (IIEN). The device is based on the parallel-strip technology. This technology is effective for the designing, testing, and subsequent manufacturing of low intensity microwave generators to use in medicine, veterinary medicine, microbiology, etc.**
The proposed device differs from those developed and used previously by the fact that it combines a number of known and new methods for elaboration, which prove this device with new properties.
We do not use a waveguide (metal mechanical device) in the generator-module as the basic working environment of the active elements (generators), instead, we use a plate with parallel stripes. The plate with parallel strips contains two substrates, but the passive elements, such as inductances and capacities, form a composite circuit, where the active elements (transistors, diodes varicap, etc.), form an auto-oscillating system that generates microwaves.

I. INTRODUCTION

Results and analysis of multiple publications on the issue clearly demonstrates that the applied possibilities of UEMA in various fields of medicine, biology, food industry, environmental protection, industrial technology began to be conceived according to its real value only in recent times. It was built an impressive volume of empirical results based on which they were established the overall limit a series of unique phenomena: the benefic resonant influence to all living organisms of non-ionizing electromagnetic waves with very low non-thermal intensity (UEMA) (under 10 mW/cm2) in some segments of the extremely high frequency bands (EIF) (wavelength 4.9, 5.6, 7.1mm) has a universal character; UEMA radiation interaction with living objects has not a thermal nature, but wears a specific information character for all bio-medical systems [1,2].

The device described has been called "DVG-001" and was developed within the institutional project 06.408.027A "Devices and methods for irradiation of living matter and the study of millimeter-wave-induced biophysical effects" (scientific Academician Dmitry Ghitu).

The device contains a number of original techniques.

Projects of the manufacture of non-thermal millimeter wave generators (UEMA) have started the design of generators that used Gann diodes. This concept was chosen because of the use of Gann diodes in construction of analog devices produced in Russia and Ukraine in the late XX century [3].

Priorities Gann diodes are well known: - Simple construction.

- Techniques that are well described in literature.
- A very simple power scheme.
- A very small number of elements used in construction.

At the same time we used millimeter wave machines, developed and manufactured in the Institutional and State Programs at the Institute of Engineering and Computer Science "D. Ghitu" ASM [4,5], as well as devices showed produced Russian Federation, that showed a number of shortcomings related to the use of Gann diodes, among which can mention:

- Gunn diodes, used in domestic appliances, are of Russian production. these items fall under the restrictions there, relating to prohibiting the export of components, which can be used in the military.
- Poor reliability of Gann diodes. These elements are used in military systems such as rockets "air-air", therefore their lifetime is small - a few hundred hours. This was confirmed by the large number breaks of Gann diodes, used in appliances generator model of UEMA devices.
- the frequency of oscillations Gunn diodes is very narrow and larger deviations can be made only by means of mechanical processes which cannot be easily handled by the CPU.

That is why our first decision was to develop a millimeter wave generator using techniques that allow the generation of very high frequency oscillations without using Gann diodes.

II. THE TOPOLOGY OF THE GENERATOR

Figure 1 shows the topology of the first variant of the plate with parallel stripes, designed to manufacture a sample layout generator in laboratory conditions.

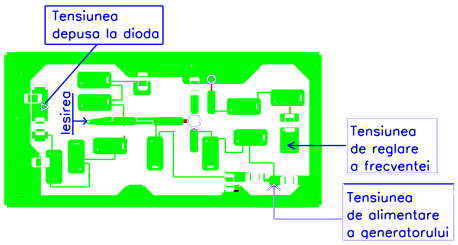

Fig.1. Topology parallel plate strip

The plate dimensions are 58.600 x 28.600 mm; the material used is 0.500 mm thick sapphire. The plate was designed to be produced in laboratory conditions by electroplating method.

Output frequency oscillations are connected to "Iesire" terminal, which is a hole in which it engages a probe, which is an antenna that transmits output frequency

oscillations in the waveguide. Waveguide is a filter because the frequency fluctuations that are lower than the critical frequency will not pass through the waveguide. The waveguide technology has been used in the construction of millimeter wave generator with Gunn diode.

The perimeter of the plate is composed of a layer of copper joined with the bottom surface unit (grounded). This area is connected to the common terminal "-" of the generator voltage supply and the frequency adjustment is made to the diode voltage multiplier. The points where "+" is applied are shown on Figure 1. We can see some lines on the drawing that can be grouped by thickness into three categories: flat, medium and narrow. Flat lines represent the capacities, implemented by parallel stripes technology. The medium lines represent are the one with calculated characteristics (impedance), and narrow lines represent inductances, made using parallel strips technology.

III. GENERATOR FEATURES

Among the basic features UEMA generator can be mentioned:

1. Frequency band has a generator:
   - Not narrower than (40-45) GGZ;
   - Not narrower than (50-55) GGZ;
   - Not narrower than (60-65) GGZ.
2. Maximum generator output power density, measured at a distance of 2 cm
   - not more than 10 mW / cm ² (10 x 10-3 W / cm ²)
3. Minimum power density generator output, measured at a distance of 2 cm
   - not more than 5 ηW / cm ² (5 x 10-6 W / cm ²)
4. Materials used in preparing the generator - not limited
5. Generator dimensions - we are limited, but to satisfy the conditions to be easily held in hand
6. Weight - no more than 0.5 Kg
7. Maximum power absorption of a generator - no more than 1.0 W

Power supply - not more than 48V (for security reasons); Maximum current work - in accordance with the terms "Caietul sarcinii".

IV. DESCRIEREA APARATULUI TERAPEUTIC DVG-001

The construction of this device were used known techniques, such as:

- Parallel stripe Technology without the use of Gunn diodes.
- ATMEGA8 microprocessor as a control device,
- Use as an indicator a matrix with almost zero current consumption,
- Use Li-Ion battery as a power source to the system working autonomously
- Use a battery charging device and, simultaneously, the power of the system operating mode of the industrial network.

Each of these processes themselves are not new, but used simultaneously in one device, gave it a range of new properties that allow us to count this as one of the original device.

These techniques have allowed us to receive the following priorities in comparison with Russian equipment and ASM IIETI developed in previous years:

- Enlargement of the frequency band amplitude modulation up to 400Hz in comparison with 10Hz to 8Hz and 16Hz,
- Frequencies can drift very high frequency electromagnetic waves with ± 15% of center frequency to ± 2%
- An 8 hours lifetime on battery (in the autonomous regime) and to charge the battery without removing it from the device.

An original program, which was inserted into the microprocessor memory, handles all processes. Language used to indicate the working modes is Romanian. The device was named "DVG - 001" in honor of Academician Dmitry Vasilyevich Ghitu, under whose leadership have started work.

Device "DVG-001" represents a case in which a supply and control board is installed, which is connected to two separate boards (routing board and mode board) and work with the indicator system. The casing is connected to a device, which is coupled with very high frequency generator. Supply feed can be easily removed, if is necessary to work in autonomous regime.

A full documentation of implementation was developed that allows duplicating the device to a specialized production enterprise.

In Fig. 2 we have illustrated the exterior of the appliance.

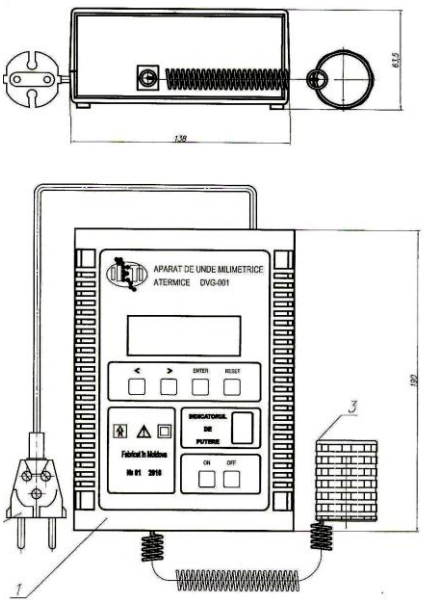

Fig.2 the exterior of the device "DVG-001"

As shown in the drawing, 6 buttons are placed on the control panel, grouped into two groups and a power indicator. The case is coupled to the power network with the supply feed 2 and generator 3 is connected to the case 1 through a connecting wire. For the first time a millimeter wave receiver is used (Fig.3), which receives the oscillations of the generator unit and which is executed on two mixing diodes, united into a bridge. This technique has allowed compensating the change of diode parameters with temperature and high reliability of measurements.

As we can see in figure 3, the construction is a waveguide design, in which two diodes **8** are installed, one of which is the detection diode and the second is used as a compensation diode for the environment temperature.

In Fig. 4 is represented the assembly design of millimeter wave generator, on which we can see generator board (2), a power plate, the waveguide (6), the housing (10) and the wired connection (3).

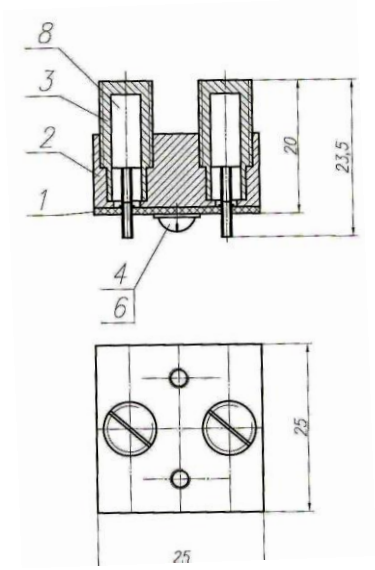

Fig.3 Wave receiver exterior

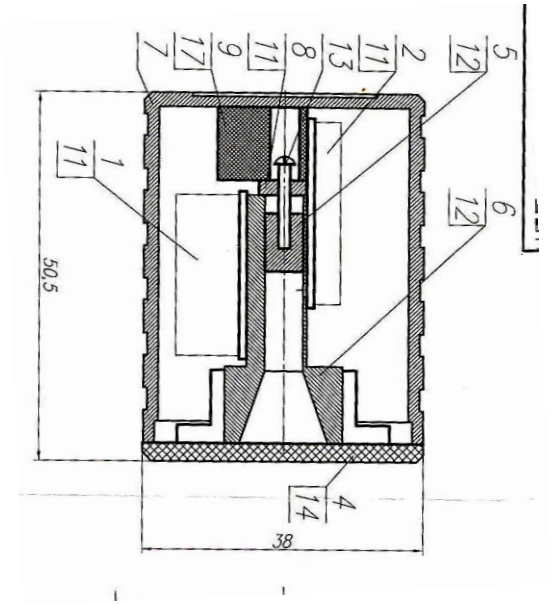

Fig.4 construcția generatorului

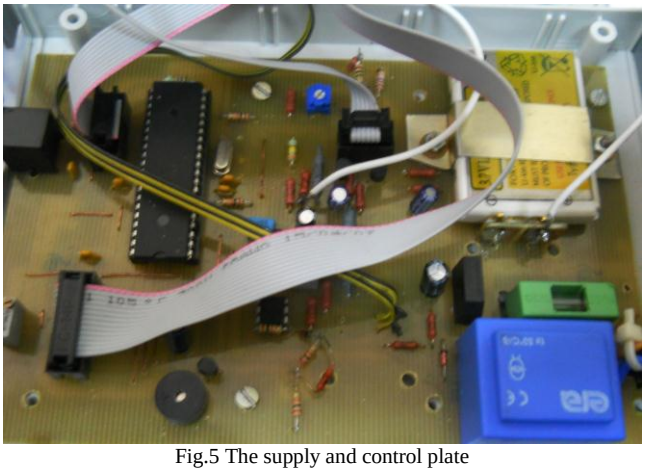

Fig.5 The supply and control plate

In Fig. 5 is the image of power and control board on which we can see a Li-Ion battery, power adapter and microprocessor.

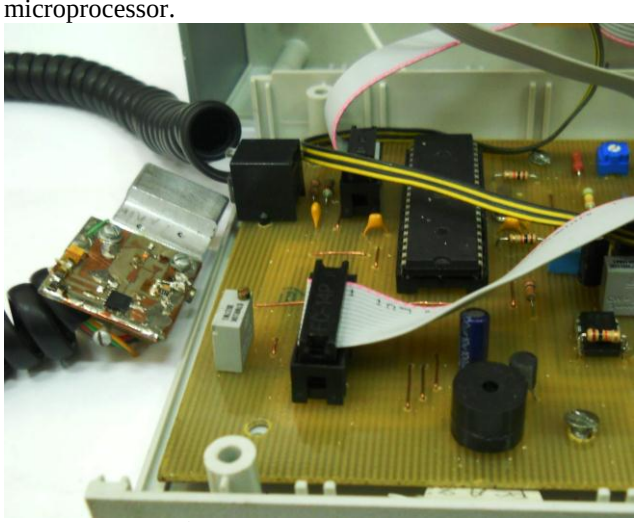

Fi.g.6 The picture of the generator connected to supply and control plate of the „DVG-001" device

In Fig. 6 is shown how the construction of the generator and how the generator is coupled to the control board and power supply.

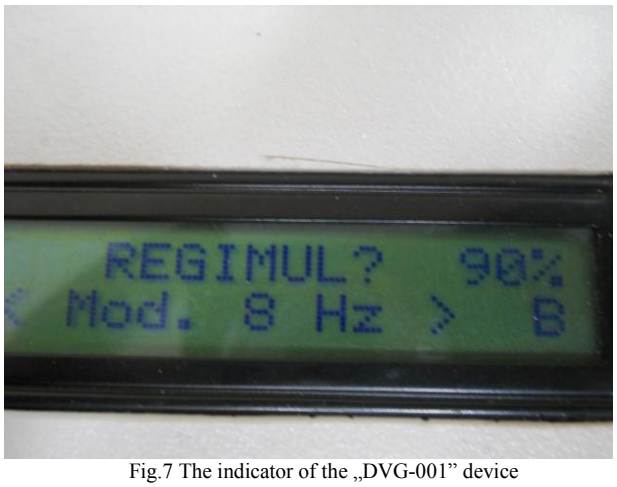

Fig.7 The indicator of the „DVG-001" device

V. CONCLUSION

The main tests that the "DVG-001" device has undergone showed that the construction is reliable and complies with specifications. Frequency deviation versus time and temperature are within the required power level and the deviation at the ends of the band of frequencies is small.

Device "DVG-001" can be recommended for curative procedure at medical, veterinary, microbiology etc. And bring an extra boost in research devoted to one implementation of millimeter non-thermal wave radiation therapy, which practically has no adverse effects or consequences characteristic of drug therapy.

VI. REFERENCES

[1] ROTARU A. „ Metamorfozele utilizarii aparatelor UEMA in medicina". Akademos, №4, 2008, pag.57-60.

[2] „Microunde", MAGHIAR TEODOR. BONDOR KAROLY, CĂLUGĂREANU MIRCEA, BREBEANU DUMITRU, Editura Universităţii din Oradea, 2003.

[3] Падалко В.Г., Грищенко С.Г., Зубарев В.В., Ноговицин А.В., Николаенко Ю.Е, Чмиль В.М., Босый В.И. «Концепция развития СВЧ полупроводниковой элементной базы в Украине», Украина, Киев, Минпромполитики, НПП «САТУРН», 1999.

4. САИНСУС, Ю.; РОТАРУ, А.; КОНЕВ, А.; РУССЕВ, Ю.; ПЯТЫГИН, С.; БАБАК В.; . ПОСТОРОНКА, С. **Разработка экспериментального комплекса для воздействия миллиметровыми волнами на живые организмы**. В: *III Евразийский конгресс по медицинской физике и инженерии "МЕДИЦИНСКАЯ ФИЗИКА - 2010"*, Москва, 21-25 июня 2010 г. Сборник материалов, стр. 228-230.

[4] SAINSUS, Iu.; ROTARU, A.; CONEV, A.; RUSSEV, Iu.; POSTORONCĂ, S.; BABAC V.; PIATÎGHIN, S. **Generator de microunde**. Brevet de invenţie MD 268. 2010-08-31.

[5] JOVMIR Vasile, ŢÂBÂRNĂ Gheorghi, ROTARU Anatol, DARIE Valentina **Metodă de tratatment al plăgii postoperatorii după mastectomie,** Brevet de invenţie 2009 MD Nr 3557,

Obstructive Sleep Apnea: Biomedical Devices for Treatment

Victor VOVC
State Medical and Pharmaceutical University "Nicolae Testemitanu", Chisinau, Republic of Moldova

Abstract: The review of biomedical devices for Obstructive Sleep Apnea (OSA) treatment is presented.

I. INTRODUCTION

Obstructive sleep apnea (OSA) - a condition characterized by the presence of snoring, recurrent upper respiratory tract collapse at the level of the pharynx and the cessation of pulmonary ventilation during persistent respiratory effort, decreased blood oxygen levels, sleep fragmentation and excessive daytime sleepiness [1].

The basic marker of obstructive sleep apnea is a cessation of nasal-oral flow for 10 seconds or more, with persistent respiratory effort, which is due to collapse of airway at the level of the pharynx. In case of incomplete airway obstruction appears hypopnea - respiratory event with a partial reduction of nasal-oral flow, combined with falling oxygen saturation not less than 3%.

The prevalence of OSA is 5-7% of the total population older than 30 years. Severe disease affects approximately 1-2% of this group of individuals [2]. In persons older than 60 years the frequency of OSA increases significantly and is about 30% of men and 20% in women. In persons older than 65 years the incidence may reach 50% [3].

The mechanism of airway obstruction is as follows. When the person falls asleep there is a gradual relaxation of the muscles of the pharynx and increased mobility of its walls. This leads to a complete collapse of airway and cessation of pulmonary ventilation. Despite of it respiratory efforts continue, and even intensified in response to growing hypoxemia. Acute lack of oxygen leads to a stress response associated with activation of the sympathoadrenal system and the rise in blood pressure. The afferent information from various organs and systems reaches the brain and cause a partial arousal. The brain regains control of the pharyngeal muscles and open airways. In severe cases there may be up to 400-500 pauses in breathing per night.

II. BIOMEDICAL DEVICES USED IN OSA TREATMENT

Oral appliances for OSA treatment.

There are two categories of oral appliances used for OSA treatment: mandibular advance devices and tongue retaining devices.

Mandibular advance devices. The main mechanism of action is the forward displacement of the lower jaw and a corresponding increase in the anterior-posterior size of the pharynx. The use of some devices requires operation of dentist, as they are fixed to the teeth with special clamps. There are more than simple modifications, made of special polymer-like mouthpiece for the boxer. The device is heated in water and becomes soft, then mounted on the upper jaw and lower jaw is closed being displaced forward. The device hardening and at subsequent installation in the mouth moves the lower jaw anteriorly.

Tongue retaining devices. These kinds of devices are suction devices placed between upper and lower teeth. The tongue is pulled forward by this device during sleep period. Traction of tongue forward does not permit the obstruction of airway by the base of tongue.

These oral appliances are indicated in the treatment of snoring and mild-moderate OSA [4].

The treatment of OSA by a continuous positive airway pressure (CPAP) The method of OSA treatment by creating a continuous positive airway pressure (CPAP) was proposed by Sullivan CE et al. in 1981[5]. The mechanism of CPAP-therapy action is relatively simple. If the airways a little "blow up" during sleep, it will prevent its collapse and remove the main mechanism of the disease. To create a positive pressure uses a small compressor, which delivers a constant flow of air under a certain pressure in the airway through a flexible tube and nose mask. It is also advisable to use a heated humidifier, which provides heating and humidifying the incoming air into the airways.

Devices for CPAP-therapy. An important aspect of CPAP-therapy is its hardware. The success of treatment depends on how efficiently and effectively will operate medical equipment. There are a large number of models of CPAP-apparatus.

According the last review [6] treatment with positive airway pressure in European countries is undertaken with CPAP (in all countries) or APAP (95.2%) devices.

The basic unit with no additional features. The apparatus is a compressor, which feeds into the airways constant given volume of air per unit time. In case of system integrity and constancy of its volume pressure created by the apparatus would remain stable. However, the breath is a dynamic process associated with the cyclical increase (in inhalation) and decrease (in exhalation) of the system volume. Accordingly, during inhalation is an abrupt drop in pressure in the system, and during exhalation - its rise. The amplitude of oscillations can reach 2-4 cm of water column. This negatively affects the dynamics of breathing, especiall.

during exhalation against a pressure jump. In addition, if during the treatment occurs much leakage from the mask, it can lead to a significant drop in pressure and reduce the effectiveness of treatment. Thus, this type of equipment has several disadvantages, which may reduce the effectiveness of treatment.

Device with therapeutic pressure compensation. This type of devices is upgrade by introducing a pressure compensation function. In the apparatus is installed a sensor that monitors in real time the pressure in the breathing circuit (the tube), as well as low-inertial engine. When the pressure drop (on inhalation), the device accelerates the engine speed and maintains proper therapeutic pressure. If it is a jump in pressure (at expiration), the device slows the engine speed, which also ensures the stability of the pressure.
In the event of a leak from under the mask unit detects a

drop in pressure accelerates the engine speed and compensate for the leak. In addition, the presence of pressure compensation is important, if a person happens in locations at different altitudes above sea level. In high altitude environment the air becomes more rarefied and compressor of the unit should operate at a higher rate to maintain the proper therapeutic pressure. Thus, this type of devices tuned to the rhythm of breath any person and during the entire respiratory cycle is maintain constant pressure without significant discontinuities, which improves the subjective acceptability of treatment. In addition, the devices of this type provide a stable therapeutic pressure regardless of the occurrence of leaks in the breathing circuit or significant drops in barometric pressure.

Device with auto-adjusting of therapeutic pressure and memory function (APAP).

There were elaborated devices that provide automatic selection pressure in real time - the so-called Auto-CPAP or APAP devices. These devices use sophisticated algorithms for automatically adjust the therapeutic pressure, depending on the detected disordered breathing. The adjustment of pressure in real time is necessary for adaptation to a change of therapeutic pressure as a function of body position and sleep stage. Deep sleep, and sleep on back needs much more pressure to open the airway compared with the superficial sleep and sleep on side, respectively. Comparative studies have shown that in application of APAP devices mean therapeutic pressure was 30-40% lower compared with the required fixed pressure treatment, which improves the acceptability of treatment [7]. In this case the use of APAP provided similar efficacy to eliminate breath disorders compared with the use of CPAP devices with fixed pressure. During the pressure auto-adjusting the algorithm of apparatus monitors 5 parameters: inspiratory flow limitation, snoring, hypopnea, apnea, and the presence or absence of cardiac oscillations in the phase of sleep apnea. The normal inspiratory flow curve has a rounded peak. Inspiratory flow curve begins to change even with minimal narrowing of the airways that is not accompanied by snoring or sleep apnea /hypopnea. In this case it is noted a flattening of the inspiratory flow curve. The microprocessor unit analyzes the shape of the central part of the inspiratory flow curve in each respiratory cycle. If it is define two or more cycles with inspiratory flow limitation, the device increases the therapeutic pressure. The device can respond by an increase in pressure only on flow limitation without reducing the flow (lesser degree of obstruction) or on flow limitation with reduced flow (high degree of obstruction). These presets are given by medical staff and increase or decrease the sensitivity of the apparatus, respectively. Snoring is defined by the unit as high-pressure fluctuations in the frequency range that overlaps the curve of the respiratory flow. The appearance of snoring also is a signal to increase the therapeutic pressure. The progression of airway obstruction leads to significant decrease of the flow - hypopnea. In the case of complete cessation of breathing apparatus detects no flow - apnea. In the case of sleep apnea is a problem of differentiation between obstructive and central sleep apnea. Central apnea may be noted, firstly, during the REM-sleep in healthy individuals, and secondly, in patients with Cheyne-Stokes respiration. In the case of pressure increasing as a response to central sleep apnea may experience a paradoxical reaction in form of worsening of the central breathing disorders. Most CPAP machines are not able to differentiate obstructive and central sleep apnea. To avoid excessive pressure in response to central respiratory failure, in the apparatus provides the ability to install a certain value therapeutic pressure above which the device stops responding through increase in pressure in the development of apnea of any origin. This parameter is usually set at 10 cm of water column. So, if sleep apnea developed when therapeutic pressure was, for example, 7 cm of water column, the unit will increase the pressure. If apnea developed at the therapeutic pressure of 11 cm of water column, the machine it will not respond. It is clear that the algorithm can not always ensure adequate treatment of pressure change in the patient, especially if it combined obstructive and central respiratory disorders. In the some apparatus is used a new technology that allow, with sufficient accuracy to differentiate obstructive and central respiratory disorders. It is based on the detection of cardiac oscillations in the respiratory circuit. The heart's contractions are transfer to the lung tissue, which in turn creates a small pressure spikes in the bronchi and trachea. During the central sleep apnea the airways are open, and these oscillations of pressure may be determined by the device in the breathing circuit. If the unit detects cardiac oscillations, it is interpreted as a central apnea and device not increases the pressure. If the oscillations are not detected, it is interpreted as obstructive sleep apnea and therapeutic pressure increases. According to the manufacturer's method for detection of cardiac oscillation has a high specificity (99.7%) and sufficient sensitivity (63.2%).

III. CONCLUSIONS

There are different types of biomedical devices from very simple to sophisticate which can provide large options for apparatus treatment of OSA.

REFERENCES:

[1] Guilleminault C., Miles L. Differential diagnosis of obstructive apnea syndrome: the abnormal esophageal reflux and laryngospasm during sleep. Sleep Res. 1980;16:410.

[2] Young T, Evans L, Palta M. Estimation of the clinically diagnosed proportion of sleep apnea syndrome in middle-aged men and women. Sleep 1997; 20(9):705-6.

[3] Jennum P, Riha RL. Epidemiology of sleep apnoea/hypopnoea syndrome and sleep-disordered breathing. Eur Respir J 2009;33(4):907-14.

[4] Ferguson KA et al. Oral appliances for snoring and obstructive sleep apnoea: a review. Sleep 2006;29(2):244-62.

[5] Sullivan CE, Issa FG, Berthon-Jones M et al. Reversal of obstructive sleep apnea by continuous positive airway pressure applied through the nares. Lancet 1981;1:862-865.

[6] Fietze I, Penzel T, Alonderis A et al. Management of obstructive sleep apnea in Europe. Sleep Med 2011; 12:190-197.

[7] Randerath WJ. APAP or CPAP: Who benefits? Sleep Med 2007; 8(7-8):691-692.

Mid-term Results of Tissue Engineered Valvular Grafts for Pulmonary Valve Replacement in Pediatric Patients and Young Adults.

S. CEBOTARI[1], I. TUDORACHE[1], E. CHEPTANARU[2], S. BARNACIUC[2], A. CAZACU[2], O. MALIGA[2], O. REPIN[2], L. MANIUC[2], T. BREYMANN[1], S. SARIKOUCH[1], D. BOETHIG[1], A. GOERLER[1], A. HAVERICH[1], A. CIUBOTARU[2]

[1]Department of Cardio-Thoracic, Transplantation and Vascular Surgery, Hannover Medical School, Hannover, Germany

[2]Heart Surgery Center, National Institute of Cardiology, Chisinau, Republic of Moldova

I. INTRODUCTION

Graft degeneration is a major cause of reoperation in young patients after pulmonary valve replacement. Glutaraldehyde fixed or cryopreserved grafts lack the potential to growth. Here we present the mid-term results of implantation of tissue engineered pulmonary homografts (TEPH) compared to glutaraldehyde-fixed bovine jugular vein (BJV) and cryopreserved homografts (CH).

II. METHODS AND RESULTS:

Thirty-seven patients with TEPH in pulmonary position were consecutively evaluated during the follow-up (up to 5 years) including medical examination, echocardiography and MRI. These patients were matched according to age and pathology and compared to BJV (n=34) and CH (n=56) recipients. In contrast to BJV and CH groups, echocardiography revealed no increase of transvalvular gradient, cusp thickening or graft degeneration and normal ventricular function in DPH group during the entire follow-up. Over time, TEPH valve annulus diameters converged towards normal z values.

Five-year-freedom from explantation was 100% for TEPH; 93 ± 4% and 91 ± 4% for BJV and CH conduits respectively.MRI was performed in matched 17 recipients of DPH and 20 BJV with longer follow up (>2 years). Mean age of the patients was 12.7 ± 6.1 years old in DPH and 13.0 ± 3.0 in BJV, with a follow-up time of 3.7 ± 1.0 and 2.7 ± 0.9 years respectively. Despite lower implantation age and longer observation time, the mean transvalvular gradient was significantly lower in TEPH group (11mmHg) comparing to BJV group (23.2 mmHg). Regurgitation fraction was 14% ± 3 and 4% ± 5 in TEPH and BJV group respectively. In 3 TEPH recipients moderate regurgitation was documented postoperatively and remained unchanged during the entire follow-up.

III. CONCLUSION

Tissue engineered fresh allograft valves showed superior performance comparing to conventional homografts and xenografts and exhibited increased durability, graft remodelling and adaptive growth.

Interaction of Bacteria With Nanostructured Zinc-oxide Thin Films

Iliana A. IVANOVA[1*], Orlin ANGELOV[3], Liudmila KRASTEVA[2], Tatiana PESHKOVA[2], Karolina PAPAZOVA[2], Doriana DIMOVA-MALINOVSKA[3], Ceco D. DUSHKIN[2]

[1]*Department of Microbiology, Faculty of Biology, University of Sofia St. Kliment Ohridski, 8 Dragan Tzankov Blvd., 1164 Sofia, Bulgaria,*

[2]*LNST, Department of General and Inorganic Chemistry, Faculty of Chemistry, University of Sofia St. Kliment Ohridski, 1 James Bourchier Blvd., 1164 Sofia, Bulgaria;*

[3]*Central Laboratory of Solar Energy and New Energy Sources, Bulgarian Academy of Sciences, 72 Tzarigradsko Chaussee, 1784 Sofia, Bulgaria.*

*E-mail: ilivanova@abv.bg

***Abstract* – The effect of nanostructured ZnO thin films on one Gram positive and one Gram-negative bacterium is studied. The films are prepared by different methods: (i) RF magnetron sputtering of ZnO target in atmosphere of Ar (0.5 Pa) or Ar (0.5 Pa)+H_2 (0.1Pa), (ii) Sol-gel – glass substrate is dip coated in a colloidal sol prepared from zinc acetate, dried and then fired at high temperature in order to get thin ZnO films; (iii) Chemical deposition – seeds of ZnO are first casted on a glass substrate and then ZnO nanorods are repeatedly grown on them via deposition from a chemical bath. The ZnO films structures are studied by XRD, SEM and AFM. All patterns have a polycrystalline structure with preferential (002) crystallographic orientation and c-axis perpendicular to the substrate surface. The influence of the as-prepared films on *Bacillus cereus* and *Pseudomonas putida* is studied by two different methods - optical density measurement and classic cultivation (rich and poor medium). Periodic cultures of bacteria are investigated in a 24-hours experiment for sensitivity to the ZnO thin films immersed in the bacterial suspension. Our experiments prove that ZnO films made by wet colloidal methods (sol-gel or chemical bath) are toxic to the studied bacteria. The ZnO thin films obtained by r.f. magnetron sputtering activate the rate of cell division and increase the percentage of live cells in comparison with the control experiment (without ZnO film). The observed difference can be due to the release of zinc species from the colloid-made films.**

***Index Terms – Bacillus cereus, Pseudomonas putida,* nanostructured ZnO thin film**

I. INTRODUCTION

The effect of a new synthesized chemicals and materials on environment is often determined by bioassays. They are quantitative measure of the total toxic potential of a sample and show possible synergistic or antagonistic effects of contaminants and media, in which they occur. Microorganisms and cell cultures are preferred in toxicity studies of objects, because of their short test duration, low cost, environmental friendliness and large amount of the investigated organisms. *Pseudomonas putida* ATCC11778 and *Bacillus cereus* ATCC12633 tests are widely used for toxicity assessment of water and new synthesized chemical compounds [1,2,3]. Some investigations of ZnO nanoparticles have shown their toxicity to bacterial cells [4,5,6]. Yamamoto [7] has reported about increased toxicity of nanoparticles (of diameters smaller than 100 nm) on bacteria with decreasing of the nanoparticle size. Li et al. [8] have studied the toxicity of ZnO nanoparticles to *Pseudomonas putida* and other bacteria and found a dependence on the concentration of the dissolved Zn ions. Sapsford et al. [9] has suggested that the high temperature treatment of ZnO nanoparticles leads to lower antibacterial activity.

Summarizing the results, ZnO nanoparticles have in general a toxic effect to various bacterial populations in the nanoparticle suspension in water. Despite the vast number of papers on the ZnO nanoparticles, there are not enough studies on the interaction between bacteria and ZnO thin films [5,10].

In our study for the first time prokaryotic tests with *Pseudomonas putida ATCC11778* and *Bacillus cereus ATCC12633* are used to determine the influence of zinc oxide thin films prepared by three different methods: (i) magnetron sputtering [11], (ii) sol-gel dip coating [12] and (iii) chemical deposition [13]. Three different methods are used to determine the quantity of total, damaged and active bacterial cells: optical density measurements, classic cultivation in a rich solid medium and fluorescent microscopy. In the latter, *Bac*Light Bacterial Viability Kit is used to differentiate and count live and dead cells. We examine the sensitivity and the damages of different bacteria during their exposure on the surface of nano-structured ZnO thin films immersed in the bacterial suspension [14].

II. MATERIAL AND METHODS

II.1. Preparation of ZnO nanostructured thin films

(i) Magnetron sputtering [11]. Two sets of ZnOsamples were prepared - pure ZnO and ZnO doped with hydrogen (ZnO:H). The thin films were deposited by r.f. magnetron sputtering of a ZnO ceramic target (100 mm disc) in atmospheres of Ar (0.5 Pa) or Ar (0.5 Pa) + H_2 (0.1 Pa) at substrate temperatures 500°C and 400°C, respectively, and r.f. power of 180 W. The thickness of the deposited films is about 600 nm. The XRD spectra were collected using DRON 3 spectrometer with CuKα radiation (λ=1.5406 Å). SEM pictures are obtained by JSM-840A JEOL with $LaBa_6$ cathode.

(ii) Sol-gel dip coating [12]. The precursors are zinc acetate, 2-methoxyethanol and monoethanolamine (MEA). The film deposition was carried out on glass substrates (ISO-

LAB-Germany). Each deposited layer was dried up in air at 60°C for 30 min. Total five layers were deposited. The final annealing was carried out at 500°C for 1 hour and the film thickness is about 1 μm. The films were investigated by SEM - JSM-5510 JEOL operating at accelerating voltage of 10 kV. XRD spectra were recorded by apparatus Siemens D500 with CuKα radiation.

(iii) Chemical bath deposition [13]. A wet chemical method was used to obtain ZnO films in two steps: deposition of seeds and growth of nanorods on them. Zinc acetate dissolved in ethanol was coated onto a glass substrate for four cycles. The coated substrates were then rinsed with water and dried at room temperature. After that they were annealed in air at 320 °C for 20 min. The above procedure was repeated twice before the final growth of ZnO nanowires. The seeded substrates were then placed in aqueous solution of zinc nitrate and methenamine and heated up in a closed vial at 87 °C for 3 h. The samples were then removed from the solution, rinsed with distilled water, and placed in a new batch of precursor solution. The growth process was repeated eight times and finally the samples were dried in air. The film structure is studied by SEM (JSM-5510 JEOL operating at accelerating voltage of 10 kV) and XRD (Siemens D500 with CuKα radiation).

II.2. Toxicity tests on bacteria

Two types of bacteria were used in our tests to study the influence of nanostructured ZnO films: *Pseudomonas putida ATCC12633* (Gram-negative) [15] and *Bacillus cereus ATCC11778* (Gram-positive) [16].

To study the effect of the as-obtained ZnO thin films and the bacterial survival of *Pseudomonas putida*, two types of nutrient media were used: a rich medium ISO 10712 for maintaining and a poor synthetic medium ISO 10712 for testing the toxicity. The ZnO thin films were sterilised by ethanol inflammation and put in the nutrient medium. The bacterial inoculum is prepared in solid rich medium and after that adapted to poor mineral medium, by three consecutive sub cultivations (ISO 10712). The experiment was conducted in aerated dark and light conditions by orbital bench top shaker Certomat® at 150-170 rpm, 25˚C for *Pseudomonas putida* and 30˚C for *Bacillus cereus*. The suspensions were cultivated in 100-ml Erlenmeyer glass flasks with 20-ml nutrient medium. The ratio of the suspension volume to the surface area of the ZnO film was 10:1 and 2,5:1. The samples of bacterial cultures with ZnO thin films and the control experiment were collected at 3, 6, 9, 12 and 24 hours. The lighting conditions were provided by illumination with a tungsten lamp (100 W) and energy saving lamp Ecoline Eco 32 (20WE27 warm light at 2700 K) placed at a distance of 30 cm from the suspension.

The number of survived cells in the suspension was determined by the most probable number method in a rich solid ISO medium for *Pseudomonas* and other medium for *Bacillus cereus* [3]. Second, the total cell number (live plus dead) is considered by spectrophotometer measurements (λ=600 nm) of the optical density of the sample in a poor medium used as the control. All samples were taken in 3 replicas.

For SEM observations, the ZnO thin film was taken sterile from the bacterial suspension after the experiment and put in a sterile Petri dish. Then it was dried at room temperature in a closed dish before the observation with SEM. Golden thin film coating was made on the film before observation.

III. RESULTS AND DISCUSSION

SEM pictures of the cross section of the thin films deposited by RF magnetron sputtering are presented in Fig. 1a (ZnO) and Fig. 1b (ZnO:H). They show columnar structure of the films. The XRD spectra in Fig. 2 show a polycrystalline structure of the films with preferential crystallographic orientation (002) and *c*-axis perpendicular to the substrate surface. The estimated grain size according to Debye-Scherrer equation is about 25 nm in the ZnO films and about 17 nm in ZnO:H films.

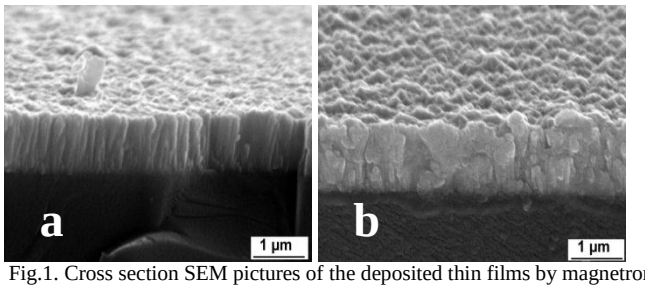

Fig.1. Cross section SEM pictures of the deposited thin films by magnetron sputtering - ZnO (a) and ZnO:H (b).

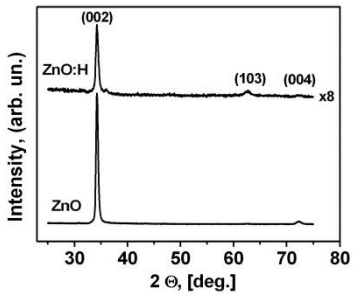

Fig. 2. XRD spectra of thin films ZnO (T_s= 500^{0}C) and ZnO:H (T_s= 400^{0}C) prepared by magnetron sputtering.

SEM picture of ZnO thin films prepared by sol-gel dip coating is shown in Fig. 3a and by chemical bath deposition in Fig. 3b.

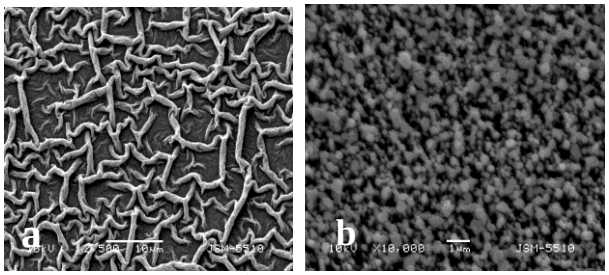

Fig. 3. SEM photographs of ZnO thin films prepared by sol-gel dip coating (a) and chemical bath deposition (b).

The mean grain size of ZnO thin film prepared by sol-gel dip coating (Fig. 3a) is between 20-32 nm [12]. The top view of SEM image of ZnO thin film prepared by chemical bath deposition (Fig. 3b) shows nanorods with hexagonal cross-section of typical size 100-200 nm and surface density ~1-3×10^9 cm^{-2}. The nanorod length is about 3-3.5 μm [20]. The XRD pattern of ZnO thin films prepared by sol-gel dip coating (Fig. 4a) and chemical bath deposition (Fig.4b) show mostly (002) diffraction peak.

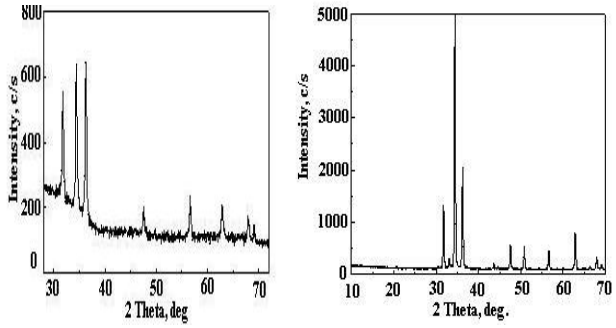

Fig. 4. XRD spectra of ZnO thin films prepared by sol-gel dip coating (a) and chemical bath deposition (b).

The results from the control bacterial growth in rich and poor medium and at dark and light conditions are presented in Fig. 5.

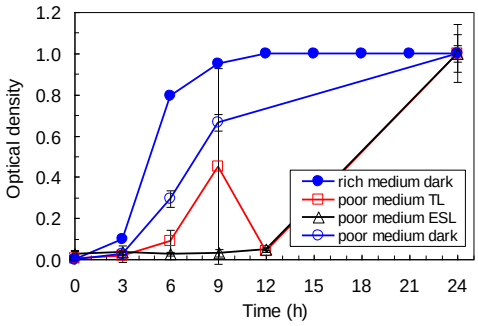

Fig. 5. Bacterial growth of *Pseudomonas putida* determined by optical density at different experimental conditions.

There is significant difference between the quantities of cells in the control samples grown in rich and poor medium. The thin ZnO films obtained by magnetron sputtering have a rather smooth surface and the cells are not damaged in a contact to it. Figure 6 shows the optical density of *Pseudomonas putida* (total number of cells) versus time of incubation in the presence of ZnO films. It is established that in all experiments the optical density of the suspensions treated with nanostructured ZnO thin films, obtained by magnetron sputtering, follows clearly the trend from Fig. 5. It increases moreover faster than the one in the control experiment and the cells division of *Pseudomanas putida* is similar to that in rich medium. In the case of cultivation with ZnO:H films, also obtained by magnetron sputtering (MSD), the optical density is very close to the control sample though a bit lower at the initial stage (within the experimental error). If the bacteria are cultivated with nanorods ZnO films obtained by chemical deposition method there is a strong inhibition of the cells division till the 12th hour (Fig. 6).

These observations are proven also by the classical cultivation method determining the live cells appeared as colonies in solid medium. The trend is an increase of bacterial number in the presence of nanostructured ZnO obtained by MSD. *Pseudomonas putida* cells have not lag-phase and the number of the live active cells is higher than in the control experiment especially after the 9th hour. The bacterial growth in the presence of nanostructured ZnO nanowires is inhibited and the bacterial quantity is all time lower than in the control experiment.

Three experiments are conducted in light conditions with energy saving lamp and ratio 2.5:1 of bacterial suspension and different ZnO nanofilms (Fig.7).

Cultivation of bacteria is conducted in 6-well plastic plates and the results of optical density are presented in Fig.7 versus the time.

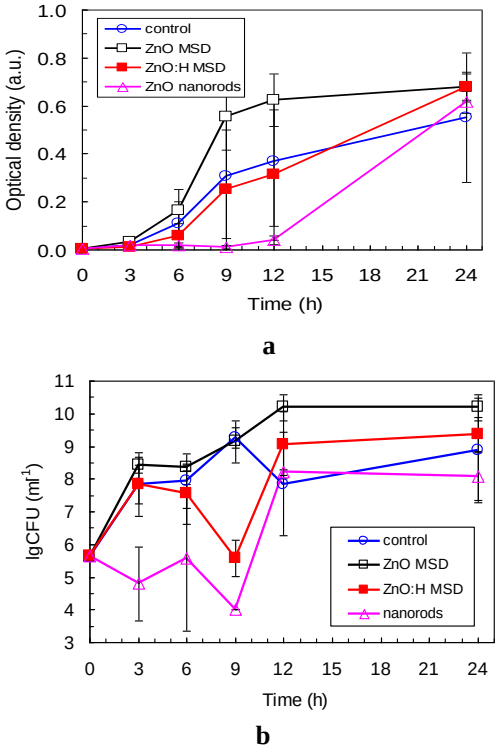

Fig. 6. Effect of ZnO thin films prepared by different deposition methods on the bacterial growth of *Pseudomonas putida* (a) - Optical density method, and *Bacillus cereus* (b) - CFU method, in poor nutrient medium.

The data are close to each other and there is strong inhibition effect of the films on bacteria until 9-12 hours. The data resemble those from Fig. 5 and especially the lag-phase for the ESL light illumination in poor nutrient medium. Only later (12-24 hours) there is an appreciable exponential growth.

The data are confirmed by the most-probable number method (CFU) in a solid medium – there are no significant deviations from the control variant and the increasing of the bacterial populations is generally stable with no inhibition effect of ZnO MSD thin films. The data for ZnO films obtained by sol-gel method show always inhibition effect, as proved by different methods.

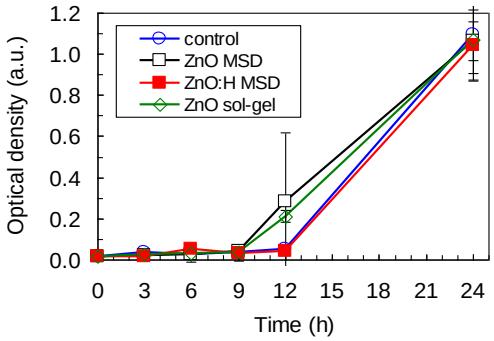

Fig. 7. Influence of differently deposited ZnO thin films on the growth of *Pseudomonas putida* in poor nutrient medium, plastic plates and illumination with an energy saving lamp.

The results for *Bacillus cereus* are different from those of *Pseudomonas putida* cells. *Bacillus cereus* cells sporulate at the 6th hour to form fewer colonies on the solid rich medium – about 10^3 CFU per millilitre. The spores after 48 hours of cultivation in rich solid medium appeared as visual colonies.

This is the reason to count very different number of *Bacillus cereus* colonies from the samples of the 6 and 9th hours cultivation at the 24th and 48th hours of Petri dish cultivation.

As could be seen from Fig. 6 and 7 both bacteria are more sensitive to the ZnO thin films with a ruffle structure deposited by sol-gel dip coating or to nanorods films obtained by chemical bath deposition. The tendency is the same till the 24th hour of cultivation (data are not presented). The results could be due to the bigger surface of ZnO ruffle thin films for interaction with bacteria or to the higher dissolving rate of Zn ions or nanoparticles. Our results are in accord with the report of Huang et al. [6]. In other papers [10, 5], ZnO seems more effective for the destruction of Gram-positive than for Gram-negative bacteria because they have simpler cell membrane structure. Our experiments prove the same difference that the films made by wet colloidal methods are toxic for the bacteria at least in the first several hours.

We do not establish any significant difference in the influence between ZnO and ZnO:H films obtained by MSD. The reason could be the smooth surface and the similar quantity of Zn^+ and nanoparticles dissolved into the suspension. The presence of zinc ions at low concentration (<0,2mM) in the poor medium increases the cell division rate. If their concentration is higher (>0.25 mM) [6], this effect is opposite, i.e. toxic. Obviously, the surface arrangement of ZnO thin films changes the toxicity of nanoparticles [18].

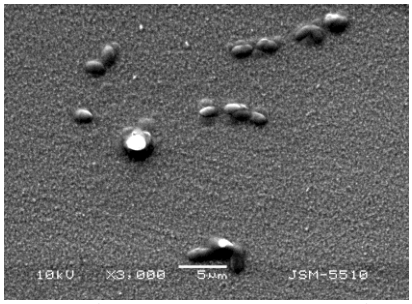

Fig. 8. SEM pictures of *Pseudomonas putida* on ZnO films obtained by magnetron sputtering - after 9 hours of cultivation.

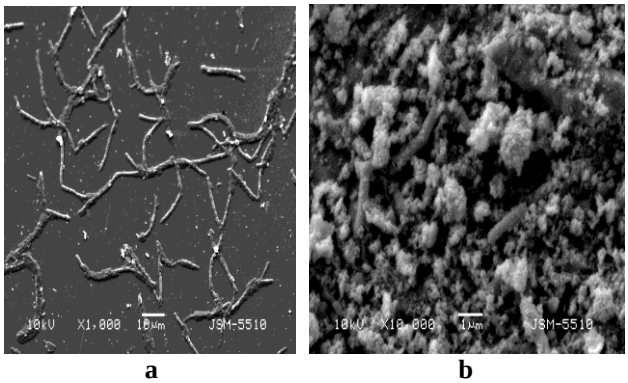

a **b**

Fig. 9. SEM pictures of *Bacillus cereus* on ZnO thin films obtained by different methods - chains on magnetron sputtered ZnO (a) and bacteria after 24 hours of cultivation on ZnO thin film obtained by sol-gel method (b).

The SEM images show separate cells and cell colonies in Fig. 8 and 9a. The *Pseudomonas* cells are intact and have well preserved capsules (Fig. 8). There are micro colonies formed on the smooth surface of the thin films. The *Bacillus* cells also form a net structure on the ZnO thin films, deposited by magnetron sputtering, but they are more sensitive to the impact of ZnO nanoparticles and they are easily damaged (Fig. 9b) because of different cell wall structure (Gram-positive). This is especially true in the case of nanofilms with irregular surface relief (Fig. 9b) obtained by the sol-gel methods. Our results are in accord with the report of Greist et al. [15], who have received similar pictures by SEM. These results are quite encouraging as a first step in the development of ZnO based biosensor [19].

IV. CONCLUSIONS

The influence of nanostructured ZnO thin films on the cells division rate of bacteria *Pseudomonas putida* (Gram-negative) and *Bacillus cereus* (Gram-positive) was studied. The ZnO films are prepared on glass substrates by three different methods - RF magnetron sputtering, sol-gel and chemical bath. The structure of the films was studied by XRD, SEM and AFM. All patterns have a polycrystalline structure with preferential (002) crystallographic orientation and c-axis perpendicular to the substrate surface. The influence of the as-prepared films on *Bacillus cereus* and *Pseudomonas putida* was studied by two different methods - optical density measurements and the classic cultivation in rich and poor medium (most-probable number method - colony forming units.ml^{-1} (CFU). Periodic cultures of bacteria were investigated in a 24-hours experiment for sensitivity to the ZnO thin films immersed in the bacterial suspension. The films of peculiar ruffle-like surface structure have shown considerable inhibition effect at the first 9-12 h, especially for the Gram-positive bacteria. The thin films, obtained by magnetron sputtering show stimulation effect on the cells division. After the sporulation at the 6th h Gram positive *Bacillus cereus* cells also acquire resistance to the ZnO thin films. Our experiments proved that ZnO films made by wet colloidal methods (sol-gel or chemical bath) are toxic to the studied bacteria.

These results are quite encouraging as a first step in the development of ZnO based biosensor.

ACKNOWLEDGEMENTS

This work has been supported financially by the National Scientific Fund of Bulgaria (NSFB) by project DO02-207. I.Ivanova and C.Dushkin are thankful also to the project COST D43 Action of EC. C.Dushkin is thankful also to project UNION DO02-82 of NSFB. I.Ivanova wish to thank to R. Alexieva and Dr. A. Loukanov for helpful support.

REFERENCES

[1] J. Ahtiainen, R. Valo, M. Järvinen and A. Joutti, *Microbial Toxicity Tests and Chemical Analysis as Monitoring Parameters at Composting of Creosote-Contaminated Soil*, Ecotoxic. Environm, Safety, vol. 53, no. 2, 2002, pp. 307-322.

[2] Y.Zhou, J. Yao, Martin M.F. Choi, Y. Chen, H. Chen, R. Mohammad, R.Zhuang, H. Chen, F. Wang, T. Maskow, G. Zaray, *A combination method to study microbial communities and activities in zinc contaminated soil*, J. Hazardous Materials, vol. 169, no. 1-3, 2009, pp. 875-881

[3] D. Liu, Y. K. Chau, B. J. Dutka, *Rapid toxicity assessment of water-soluble and water-insoluble chemicals using a modified agar plate method*, Water Res. vol. 23, no. 3, 1989, pp. 333-339.

[4] Brayner, R. Ferrari-Iliou, N. Brivois, S. Djediat, M. F. Benedetti, *Toxicological impact studies based on*

Escherichia coli bacteria in ultrafine ZnO nanoparticles colloidal medium, *Nano Lett. 6*, no. 4, **2006,** 866-870.

[5] K. H. Tam, A. B. Djurisic, C. M. N. Chan, Y. Y. Xi, C. W. Tse, Y. H. Leung, W. K. Chan, F. C. C. Leung, D. W. T. Au, *Antibacterial activity of ZnO nanorods prepared by a hydrothermal method*, Thin Solid Films, vol. 516, no18, 2008, pp. 6167-6174.

[6] Z. Huang, X. Zheng, D. Yan, G. Yin, X. Liao, Y. Kang, Y. Yao, D. Huang, B. Hao, *Toxicological effect of ZnO nanoparticles based on bacteria*, Langmuir 24, no**.** 8, 2008, 4140-4144

[7] O. Yamamoto, *Influence of particle size on the antibacterial activity of zinc oxide*,Int. J. Inorg. Materials, vol. 3, no. 7, 2001, pp. 643-646.

[8] M. Li, S. Pokhrel, X. Jin, L. Madler, R. Damoiseaux, E. M. V. Hoek, *Stability, Bioavailability, and Bacterial Toxicity of ZnO and Iron-doped ZnO Nanoparticles in Aquatic Media* Environ Sci Technol., vol. 45, no. 2, 2011, pp. 755-761.

[9] K. E.Sapsford, Chr. Bradburne, J. B. Delehanty, I. L. Medintz, *Sensors for detecting biological agents* Mater. Today, vol. 11, no. 3, 2008, pp. 38-49.

[10] G. Applerot, N. Perkas, G. Amirian, O. Girshevitz, A. Gedanken, *Coatings of glass with ZnO via ultrasonic irradiation and study of its antibacterial properties*, Appl. Surface Sci., vol. 256, no. 3, 2009, pp. S3-S8.

[11] D. Dimova-Malinovska, O. Angelov, H. Nichev, J. C. Pivin, *ZnO:H thin films for room temperature selective NH_3 sensors*, J. Optoelectr. Adv. Mater., vol. 9, no. 2, 2007, pp. 248-259.

V. Kaneva, G. G. Yordanov, C. D. Dushkin, *Characterization of nanosized ZnO thin films for the photoinitiated decolorization of malachite green in aqueous solutions*, Bulletin Mater. Sci., vol. 33, 2010, pp. 111-118.

.

T. Peshkova, K. Papazova, C. Dushkin, *Effect of the substrate om the growth of ZnO nanowires using chemical bath deposition*, Nanoscience and Nanotechnology, E. Balabanova, I. Dragieva (eds.), vol. 10, 2010, pp. 65-68

[12] I. Ivanova, S. Kambarev, R. A. Popova, E. G. Naumovska, K. B. Markovska, C. D. Dushkin, *Determination of Pseudomonas putida live cells with classic cultivation and staining with "Live/Dead BacLight Bacterial Viability kit"*Biotechnol. Biotechnol. Eng., vol. 24 SE, 2010, pp. 567-561.

[13] Y. B. Byaruhanga, B. H. Bester, T. G. Watson, J. Microbiol. Biotechnol., *Growth and survival of Bacillus cereus in mageu, a sour maize beverage*, 15, no.3, 1999, pp. 329-337.

[14] J. E. Bailey, D. F. Ollis, "Biochemical Engineering Fundamentals", 2nd ed., McGraw-Hill Book Company, New York, 1987.

[15] G. Gellert, A. Stommel, *Influence of microplate material on the sensitivity of growth inhibition tests with bacteria assessing toxic organic substances in water and waste*, Environm. Toxicology, vol. 14, no. 4, 1999, pp. 424-428.

[16] I. Ivanova, R. Popova, A. Loukanov, O. Angelov, K. Papasova, L. Krusteva, E. Naumovska, K. Markoska, C. Dushkin, Interaction between Bacillus cereus and nanostructured thin films of zinc oxide as a transducer element for biosensing application, Trakia Journal of Sciences, vol. 8, Suppll. 2, 2010, pp. 159-164.

[17] A. Loukanov, I.A.Ivanova, A. Angelov, R.Popova, S. Bratkova, S. Plochev, C. Dushkin, Nanostructured ZnO as a transducer for biosensoring of sulphate-reducing bacteria, Annual Univ. Mining &Geology, vol. 53, no. 2, 2010, pp.173-179.

DLC Biocompatible thin Films for Cardiovascular Implants

S.T. SHISHIYANU[1] , T.S. SHISHIYANU[1], P.S. STEFANOV[2], V.K. GUEORGUIEV[3]

[1]*Department of Microelectronics, Technical University of Moldova, 2004 Chisinau, Moldova*
[2]*ISMA Ltd., 1138 Sofia, Bulgaria*
[3]*Institute of Solid State Physics, Bulgarian Academy of Sciences, 1784 Sofia, Bulgaria*
sergeteo@mail.utm.md

***Abstract* – Diamond-like carbon films (DLC films) for cardiovascular implants have successfully been prepared by dual-target unbalanced magnetron sputtering and Rapid Photothermal Processing (RPP). It is found that the sputtering current of target plays an important role in the DLC film deposition. Deposition rate of 3.5 μm/h is obtained by using the sputtering current of 30 A. Rapid Photothermal Processing at 400°C essentially reduced the carbon content and have improved the surface morphology structure of deposited coatings, which depend on the intensity of the ion impingement on the growing interface.**

***Index Terms* – Diamond-like carbon, nanocomposite DLC, RPP.**

I. INTRODUCTION

Diamond-like carbon (DLC) films have found widespread application in biological coatings for implantable medical devices, as a result of their good chemical resistance, temperature stability and biocompatibility. The biological behavior of an implant can be tuned by modifying the element composition. DLC can be easily alloyed with other biocompatible materials such as titanium as well as toxic materials such as silver, copper and vanadium by normal co-deposition methods [1]. Nanocrystalline diamond-coated medical steel has shown a high level resistance to blood platelet adhesion and thrombi formation [2]. Diamond and DLC coatings have successfully been proposed for applications as artificial heart valves, prosthetic devices, joint replacements, catheters and stents, orthopedic pins, roots of false teeth, surgical scalpels and dental instruments [3-6].

II. EXPERIMENTAL

Pulsed direct current (p-DC) magnetron sputtering in combination with an unbalanced magnetron configuration has become a major technique in the deposition of advanced coatings during the last decade. It has the significant advantage over DC magnetron sputtering in suppressing arcing at the targets during reactive sputtering and in sputtering non-conductive materials.

In this paper we present the results on the microstructural control of Ti/DLC nanocomposite coatings with pulsed direct current (DC) magnetron sputtering. The sputtering system was configured of Ti target (99.7%), and graphite target (99.99%). The diameter of all the targets was 3 inches. All the power supplies for sputtering were operated at current regulation mode via a computer-controlled system. The thin metal layers were deposited on nonannealel and annealed stainless steel. Annealing was performed according the technology sequence for stents-electropolishing and high temperature annealing for grain enlargement and improving of the stents elasticity. A number of analytic methods were applied SEM, AFM and EDX.

The Ti/DLC films were deposited onto pre-etched nonannealed and high temperature annealed stainless steel type 316L. The morphological analyses demonstrated the essential grain enlargement. The high temperature annealing increase the grain size from 10 to 60 μm, which is necessary for the required elasticity of the arterial stents. The grain structure can influence the structure of the deposited biocompatible nanolayers, which is demonstrated further for deposited at high temperatures layers on stainless steel substrates.

The images of the grain structure of the preetched 316L type stainless steel annealed at high temperatures and the initial non-annealed sample are shown in Fig. 1.

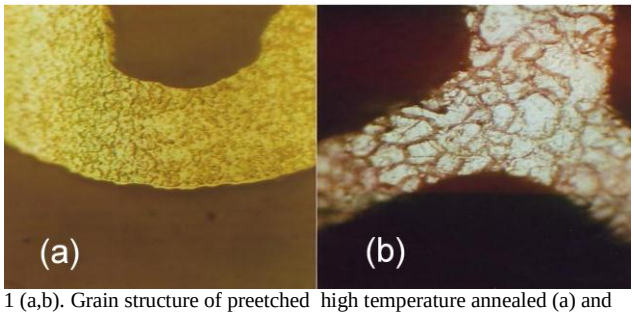

Fig. 1 (a,b). Grain structure of preetched high temperature annealed (a) and non-annealed (b) 316L type stainless steel.

The SEM images of the DLC layers deposited on stainless steel at temperatures higher than 230°C . T1<T2, the RPP was performed at 300°C in vacuum, are presented in Fig. 2.

The thermal annealing of the stainless steel substrate during deposition at high temperatures do not change essential the elemental content of the substrate. Only a small oxidation is observed. But the surface and the structure of the deposited carbon layers is not smooth, as it is for layers deposited on the glass and these temperatures are not applicable for the stents technology.

AFM study images of the DLC layers deposited on stainless steel at 250°C, RPP 400°C are presented in Fig. 3.

The AFM study of DLC layers deposited at high temperatures on nonannealed and annealed stainless steel have shown that the roughness of the layers is up to 300 nm on nonannealed substrates and up to 3500 nm on annealed substrates.

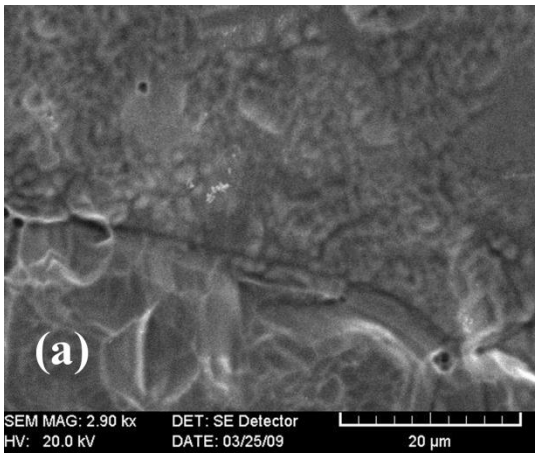

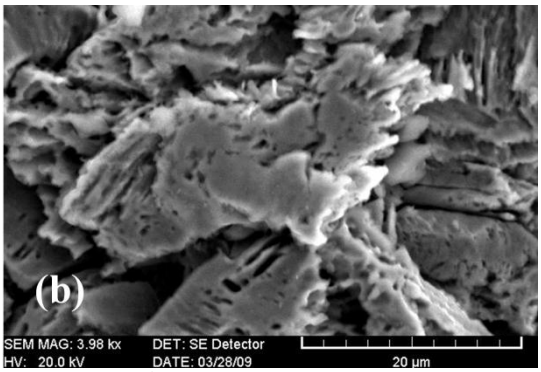

Fig. 2 (a,b). SEM of RPP DLC layers on stainless steel deposited at temperatures: a - T1, b - T2.

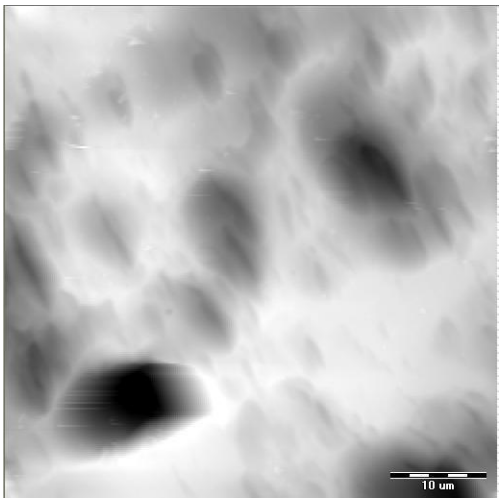

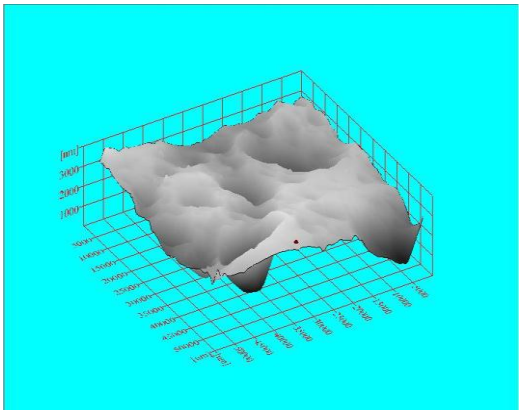

Fig. 3 (a,b). 2D and 3D AFM images of layer deposited at 250°C on nonannealed stainless steel.

The roughness on nonannealed samples is due to the nonpolished surface, wile on the annealed substrates-to the much larger grain size after annealing.

TABLE 1. INFLUENCE OF RAPID PHOTOTHERMAL PROCESSING ON THE CARBON CONTENT IN DLC.

	Non annealed		Furnace 400°C 3 min		RTP 300°C 3 min		RTP 300°C 1 min + 400°C 1 min	
Element	W %	A %	W %	A%	W %	A%	W %	A%
C	27.51	39.46	28.24	39.64	30.30	42.99	16.59	25.45

The RPP at 300°C and the furnace annealing at 400°C up to 3 min do not change essentially the carbon content, but RPP at higher temperature even up to 1 min change/reduce the carbon content.

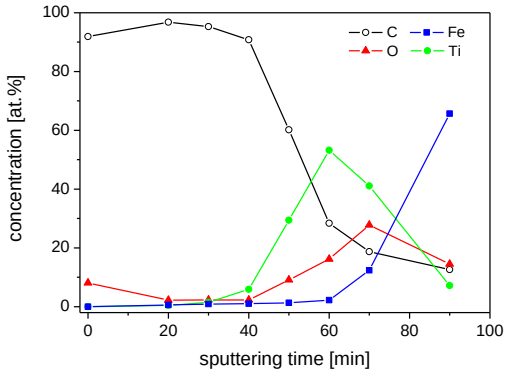

Fig. 4. Auger depth analysis for 65min deposition of DLC.

Auger depth analysis of DLC layers deposited on stainless steel for different deposition times at low plasma densities were also carried out, and the Auger spectra are presented in Fig. 4. The Auger analyses have shown existence of relative thick carbon layer, thin transition C/Ti layer and thin Ti layer.

III. CONCLUSIONS

The reliable technology for magnetron deposition of biocompatible Ti/DLC nanolayers for coating of implantable medical devices has been established. RPP at 300÷400°C improved the microstructure and properties of deposited coatings, which strongly depend on the intensity of the concurrent ion impingement on the growing interface.

ACKNOWLEDGEMENTS

Authors gratefully acknowledge ISMA Ltd. Sofia for providing the magnetron sputtering system and the cardiovascular STENTs produced by ISMA Ltd. Sofia, Bulgaria. Authors also gratefully acknowledge Dr. E.Monaico, Dr. M.Enachi and National Center for Materials Study and Testing for carefully provided SEM and AFM measurements.

REFERENCES

[1] I.D. Scheerder, et al., "The Biocompatibility of Diamond-Like Carbon Nano Films," J. Invasive Cardiology, vol. 12, pp.389-394, 2000.

[2] W. Okroj, M. Kamińska, L. Klimek, W. Szymański, B. Walkowiak, "Blood platelets in contact with nanocrystalline diamond surfaces," Diamond & Related Mater., vol. 15, Issue 10, pp.1535-1539, 2006.

[3] A.Grill, "Diamond-like carbon coatings as bio-compatible materials—an overview," Diamond & Related Mater., vol. 12, Issue 2, pp.166-170, 2003.

[4] R. Hauert, "A review of modified DLC coatings for biological applications," Diamond & Related Mater. vol. 12, Issue 3-7, pp.583-589, 2003.

[5] R.A. Freitas, Foresight Update, 39 Foresight Inst. Palo-Alto, CA, USA, 1999.

P.A. Dearnley, "A review of metallic, ceramic and surface treated metals used for bearing surfaces in human joint replacements," Proc. of Institution of Mechanical Engineers. Part H, Engineering in Medicine, vol. 213, pp.107-135. 1999

Antimicrobial Polymers: from Structure Design to Specific Properties and Applications

Madalina ZANOAGA, Fulga TANASA
"Petru Poni" Institute of Macromolecular Chemistry Iasi, Romania
zanoaga@icmpp.ro

***Abstract* – Microbial infection remains one of the most serious complications in several areas, particularly in medical devices, drugs, health care and hygienic applications, water purification systems, hospital and dental surgery equipment, textiles, food packaging, and food storage [1,2]. Antimicrobials gain interest due to their potential to provide quality and safety benefits to many materials. However, low molecular weight antimicrobial agents suffer from many disadvantages, such as toxicity to the environment and short-term antimicrobial ability.**

To overcome these problems associated with the low molecular weight antimicrobial agents, antimicrobial functional groups can be introduced into polymeric macromolecules. The use of antimicrobial polymers offers promise for enhancing the efficacy of some existing antimicrobial agents and minimizing the environmental problems accompanying conventional antimicrobial agents by reducing the residual toxicity of the agents, increasing their efficiency and selectivity and prolonging the lifetime. Research concerning the development of antimicrobial polymers represents a great a challenge for both the academic world and industry.

This article reviews some data concerning antimicrobial polymers, from the structure design to specific properties and applications, as well as future and perspectives in the field of antimicrobial polymers.

***Index Terms* – antimicrobial agents, polymers synthesis, characterization, applications.**

REFERENCES

[6] M. B. Patel, S. A. Patel, A. Ray and R. M. Patel, J. Appl. Polym. Sci., 89, 895-900, 2003.

[7] E.-S. Park, H.-J. Lee, H.-Y. Park, M.-N. Kim, K.-H. Chung and J.-S. Yoon, J. Appl. Polym. Sci., 80, 728-736, 2001.

Biocompatible and Resorbable Polymeric Materials for Surgical Sutures

Fulga TANASĂ, Mădălina ZĂNOAGĂ
"Petru Poni" Institute of Macromolecular Chemistry
ftanasa@icmpp.ro

***Abstract* – As implants in human body, sutures are one of the largest groups of materials and have been in use for many centuries. Along with the development of the synthetic resorbable polymers, i.e. poly(glycolic acid) (PGA) in the early 1970s, a new research direction has opened on biocompatible rebsorbable polymers for sutures.**

This article reviews some of the available information with regard to developments on chemistry, properties, biocompatibility and biodegradability, and performance of resorbable polymeric sutures.

***Index Terms* – suture materials, biomaterials, biocompatible polymers, resorbable polymers.**

I. INTRODUCTION

A suture is a biomaterial device, either natural or synthetic, used to link blood vessels and bring tissues together [1]. Thus, its major functions are to draw and hold together tissues following their separation by surgery or trauma. Sutures are the most widely used materials in wound closure, they have registered tremendous growth during the last two decades and have become the largest group of biomaterials having a huge market exceeding $1.3 billion annually [2].

An ideal suture should have the following characteristics: easy to handle, elicit minimal tissue reaction, does not support bacterial growth, possess high tensile strength, easy to sterilize, elicit no allergic reaction, no carcinogenic effect, is absorbed by human tissues after serving its function. Thus, a suture should not only be very strong, but also be able to simply dissolve into body fluids and lose strength at the same rate that the tissue gains strength.

Suture materials are characterized by various methods involving physical and mechanical properties, handling characteristics, and biological and biodegradation behavior. Mechanical properties, such as tensile strength (knotted and unknotted tensile strengths), percentage elongation, modulus of elasticity, stress relaxation, and creep are measured routinely. As capillarity is related to the ability to transport bacteria, it also needs to be measured. Other parameters measured are swelling and coefficient of friction, pliability, packaging memory, knot security, knot tie-down, knot slippage, tissue drag, etc., and they are used to understand these suture materials functions and range of applications.

Three main classes of suture materials are known: collagen, synthetic absorbable and nonabsorbable. They can be classified as follows:

I – silk or synthetic fibers of monofilament, twisted, or braided;

II – cotton or linen fibers or coated natural or synthetic fibers in which the coating contributes to suture thickness without adding strength;

III – metal wire of monofilament or multifilament.

Sutures are designed to meet many different needs [3]. Sutures for abdominal surgery, for example, are different from sutures used in cataract surgery. No type of suture is ideal for every operation, therefore surgeons and medical designers have come up with sutures with varying qualities: one may be more absorbable, but less flexible, while another may be exceedingly strong, but difficult to knot. Designers of a new suture material have to take into account many factors, as follows: the rate of suture degradation, length of the suture, the knot, material elasticity, memory. Suture manufacturers use specially designed machines to test and study sutures. New suture designs are also evaluated by subjecting them to chemical tests, such as soaking them in various solutions, and testing on animals.

Suture materials are frequently coated, especially braided or twisted sutures, to facilitate their handling properties, particularly to induce a significant reduction in tissue drag and increasing the ease of sliding knots during knotting. Traditional coating materials used are bees wax, paraffin wax, silicone, poly(tetrafluoroethylene) (PTFE), etc. The trend is toward a coating material that has a chemical property similar to the suture to be used. The coatings depend on whether the suture is absorbable (Poloxamer 188 and calcium stearate with a copolymer of glycolic acid and lactic acid) or nonabsorbable (wax, silicone, fluorocarbon, etc.) [4].

Absorbable natural suture materials are made of catgut or reconstituted collagen (RC), or from cotton, silk, or linen. Synthetic nonabsorbable sutures may be made of PP, poly(ethylene glycol terephthalate) (PET), poly(butylene glycol terephthalate) (PBT), polyamide (PA), different types of Nylons, or Goretex®.

Catgut and regenerated collagen are the two absorbable natural sutures available. Catgut was the staple absorbable suture material through the 1930s, while physicians used silk and cotton when a nonabsorbable material was needed. Catgut sutures are well known for their great toughness and tenacity. The basic constituent of catgut is collagen, which is the main constituent of skin and the major structural protein found in all multicellular organisms.

Reconstituted collagen (RC) has low immunologic activity, is prepared either by enzymatic digestion of native collagen-rich tissues or by extraction with salt solutions. RC sutures prepared from bovine long flexor tendons are similar in appearance to catgut and are almost exclusively used in microsurgery. The mechanical and thermal stability of RC fibrils can be increased by maturation *in vitro* when

incubated in air, at 37°C [5]. RC sutures are used in ophthalmic surgery, as well as for other applications.

II. BIOCOMPATIBLE AND RESORBABLE SYNTHETIC SUTURE MATERIALS

Following the successful development of the synthetic absorbable polymer, PGA in the early 1970s, a series of polymers and copolymers based on a few cyclic lactones, presented in Fig. 1, were synthesized, characterized and produced at commercial scale.

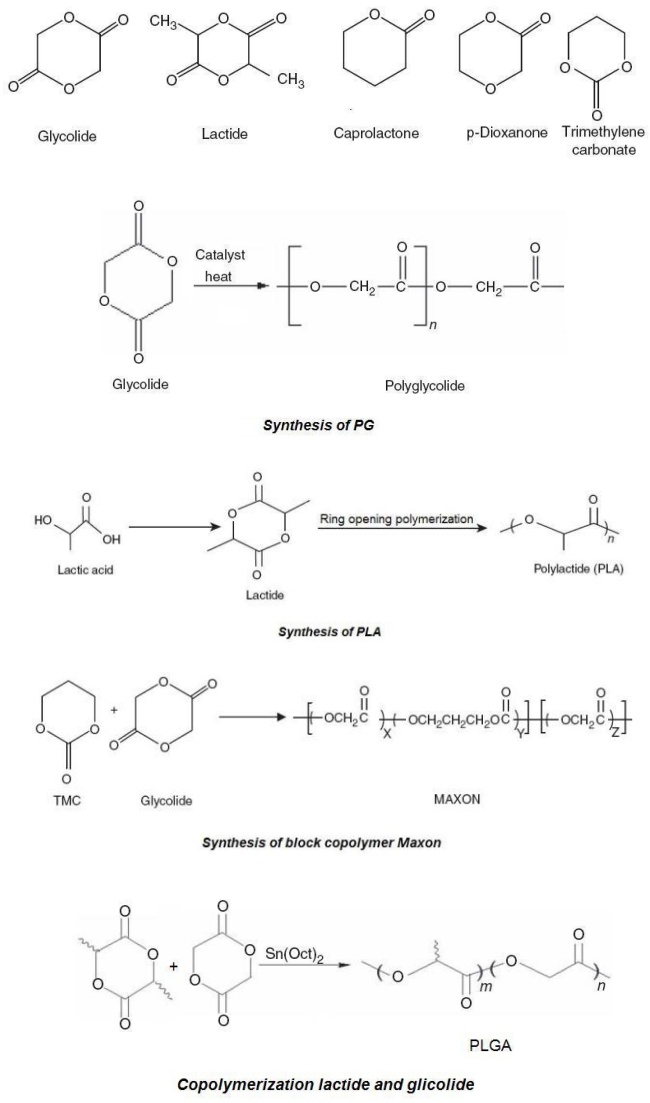

Fig. 1. Monomers and polymers used for synthetic biocompatible resorbable sutures

Thus, new surgical practice needs synthetic absorbable suture materials, such as: Dexon® (Davis & Geck Corp), Vicryl® (Ethicon), PDO (Ethicon), PDOII® (Ethicon), Maxon® (Davis & Geck), Monocryl® (Ethicon) and Biosyn® (US Surgical, Norwalk, CT). New sutures are being developed all the time, in order to better respond to specific surgical demands. The suture materials properties are studied through laboratory experiments, whose results are validated in extensive studies and trials [6]. Absorbable sutures are now well known to behave favorably *in vitro* and in an animal model [7]. The most important advantage of synthetic biocompatible resorbable sutures is their reproducible degradability inside the biological environment. This property will enable sutures to have minimum chronic undesirable tissue reactions. Due to the development of these polymers, they have replaced natural fibers (cotton, linen and catgut) for wounds closure. Today, surgeons have the possibility to choose among a large number of suture materials with various chemical, physical, mechanical and biological properties.

Polyglycolide or poly(glycolic acid) (PGA)

Poly(α-ester)s are thermoplastic polymers with hydrolytically labile aliphatic ester linkages in their backbone. Although all polyesters are theoretically degradable, only aliphatic polyesters with reasonably short aliphatic chains between ester bonds can degrade over the time frame required for suture materials [8].

PGA is the simplest linear aliphatic polyester. Owing to its controllable hydrolytic degradation, PGA and its copolymers with LA, ε-CL and TMC are widely used as materials for the synthesis of resorbable sutures and are being evaluated in the biomedical field [9].

PGA can be obtained through several different processes, starting from different materials: polycondensation of GA, ring-opening polymerization (ROP) of GL (see Fig. 1), solid-state polycondensation (SSP) of halogenoacetates, acid catalyzed reaction of carbon monoxide, formaldehyde, etc. The ROP of GL in the presence of stannous octanoate and heating is the most common synthetic method used to obtain high molecular weight polymers (polymers with M_w=20,000–140,000 are suitable for fiber extrusion and suture manufacturing).

PGA is a highly crystalline polymer (≈ 45–55%), having glass transition temperature between 35-40°C and its melting point in the range 225–230°C; it is soluble only in highly fluorinated solvents (i. e., hexafluoroisopropanol, hexafluoroacetone sesquihydrate) that can be used to obtain polymer solutions for melt spinning and film preparation. Fibers of PGA show excellent mechanical properties (high strength and modulus) due to the polymer high crystallinity. A self-reinforced PGA composite is stiffer than any other degradable polymeric system used clinically and has been shown to exhibit a modulus of approximately 12.5 GPa [10].

Concerning its biodegradable character, PGA undergoes hydrolytic degradation through nonspecific cleavage of the ester backbone [11]. The degradation process is erosive and appears to take place in several steps during which the polymer is converted to its initial monomer GA. The first step involves diffusion of water into the amorphous regions of the polymer, cleaving the ester bonds; the second step starts after the erosion of amorphous regions, leaving crystalline chains susceptible to the hydrolytic attack. Upon collapse of the crystalline regions, the polymer chain dissolves. When exposed to physiological conditions, PGA decomposes under enzymes (esterase type) attack and the degradation product, the same GA, is nontoxic and it can easily enter the tricarboxylic acid cycle, during which it is gradually decomposed up to water and carbon dioxide. A part of the GA is also excreted by urine. Studies carried out using sutures made from PGA have shown that the material loses half of its strength after 2 weeks and 100% after 4 weeks. Figure 2 shows the rate of the *in vitro* degradation of PGA. The polymer is completely resorbed by the organism in a timeframe of 4–6 months [12,13].

The water sorption and its penetration into the PGA, PLA and their copolymers initiate the hydrolytic degradation, followed by the decay of their mechanical properties. The tensile tests on co/terpolymers of LL, ε-CL and GL showed

that the tensile strength was strongly dependent on the draw ratio [14].

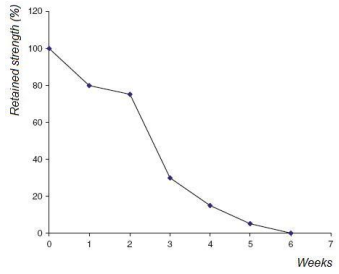

Fig. 2. The rate of the *in vitro* degradation of PGA

Comparing the biodegradability of Monocryl® monofilaments with poly(trimethylene carbonate-ε-caprolactone)-block-poly(*p*-dioxanone) [poly(TMC-e-CL)-block-PDO] copolymers, it was ascertained that the biodegradability of PDO homopolymer is much lower compared with that of the copolymer Monocryl®, probably due to the presence of the GL in the copolymer structure.

PGA is particularly useful in subcutaneous and intracutaneous closures, abdominal and thoracic surgeries. With its high initial tensile strength, it has guaranteed holding power through the critical wound healing period.

Polylactide or poly(lactic acid) (PLA)

PLA polymers are leading biomaterials having applications in biomedical and pharmaceutical industries as resorbable implant materials, wound closure, bone fixation devices and vehicles for controlled drug delivery [9]. They are characterized by high mechanical strength, inherent biodegradability and biocompatibility. However, their clinical applications are sometimes affected by their high hydrophobic character and consequent poor water uptake, which results in a slow hydrolytic degradation rate.

Copolymerization of LL (*levo* isomer) with other co-monomers is used to modify the PLA properties and to control its degradation according to the specific applications in the field [15–17]. The synthesis of PLAs of high M_w for suture applications can be carried out by the ring opening polymerization of the cyclic diester (LL) of LA (see Fig. 1). Due to the chiral nature of LA, several distinct forms of polylactide exist: poly-L-lactide (PLLA or PLA in common use) which is a crystalline polymer, while the polymerization of a racemic mixture of L- and D-lactides (DL) usually leads to poly-DL-lactide (PDLLA) which is amorphous.

It was reported that the PLA has a crystallinity of ≈ 37%, a glass transition temperature in the range 50-80°C and a melting temperature between 173-178°C. The initial tensile strength of the PLA fibers is lower than that of the commercially available sutures such as PDO, Vicryl®, silk and Ethilon® (Nylon 6 and Nylon 66 monofilament suture). The handling characteristics of PLA sutures were found to be superior to those of the monofilament sutures such as PDO and Ethilon® and comparable with the multifilament sutures such as Vicryl® and silk. A composite consisting of PDLA and bioglass was used as a coating for degradable sutures such as Vicryl® [9].

The *in vitro*, in the subcutis, and in the achilles tendon of rabbits studies revealed that, although PDLA had a lower initial tensile strength than Maxon®, it showed more prolonged tensile strength retention (TSR). When PLA sutures were exposed to physiological saline solution (0.9 wt% NaCl aqueous solution) at 37°C, the knotpull strength decreased by 12% after 28 days. In Figure 3, the rate of degradation of PLA is presented.

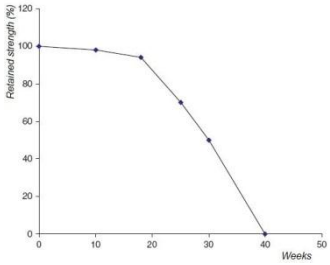

Fig. 3. The rate of the *in vitro* degradation of PLA

The diagram shows that during the hydrolytic degradation of PLA, the molecular mass decreases and its distribution becomes continuously broader with the increasing degradation time. The conclusion is the PLA thread is a suitable suture for wounds that require healing time up to 28 weeks.

Poly(lactide-co-glycolide) (PLGA)

Copolymers of GA with both LL and DL have been developed for both devices and drug delivery applications. For suture applications, LL-co-GL copolymer must have a high concentration of GL in order to achieve the required mechanical and biodegradation properties. PLGA is synthesized by means of random ROP of two different monomers (see Fig. 1) and, depending on the LA/GA ratio, different forms of PLGA can be synthesized. All PLGAs are amorphous rather than crystalline and show a glass transition temperature in the range 40–60°C. Unlike the corresponding homopolymers which show poor solubilities, PLGA can be dissolved by a wide range of common solvents, including chlorinated solvents, tetrahydrofuran, acetone, or ethyl acetate.

The PLGA biodegradability is highly related to its crystallinity and the solution pH [18]. The copolymer PLGA has been shown to undergo bulk erosion through the hydrolysis of ester bonds and the rate of degradation depends on a variety of parameters, including the LA/GA ratio, M_w, the shape and structure of the matrix [19]. The degradation products, LA and GA, are common by-products of various metabolic processes in the body, under normal physiological conditions, and there is a minimal systemic toxicity associated with PLGA. The *in vivo* rate of degradation depending on the LA/GA ratio is presented in Figure 4.

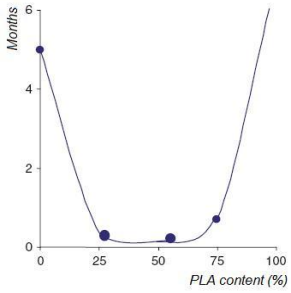

Fig. 4. The *in vivo* rate of degradation versus PLA content in the PLGA copolymer

Experimental data show that the resistance to hydrolytic degradation is more pronounced at either end of the co-polymer composition. For example, a copolymer of 50% GA and 50% DL degrades faster than either corresponding homopolymer. Copolymers of LL with 25–70% GA are

amorphous due to the disruption of the regularity of the polymer chain by the other monomer.

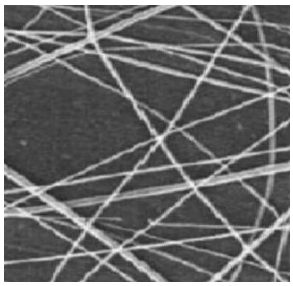

Fig. 5. Electrospun PLGA fibers

The major advantage of these copolymers can be attributed to their biocompatible character, good processibility which enables fabrication of a variety of structures and forms (electrospun PLGA fibers are shown in Figure 5), controllable degradation rates and their success as biodegradable resorbable suture materials.

Polyglyconate (PG)

Copolymers of GA with TMC have been prepared as both sutures (Maxon® copolymer, see Fig. 1) and as tacks and screws. Typically, these compounds are prepared as A–B–A block copolymers in a GL:TMC=2:1 ratio, with a GL–TMC center block (B) and pure GL end blocks (A). These materials have a better flexibility than pure PGA and are absorbed in approximately 7 months. GL has also been copolymerized with TMC and p-dioxanone to form a terpolymer suture (Biosyn®) that is absorbed within 3–4 months and offers reduced stiffness compared to pure PGA fibers [20]. The hydrolytic degradation of PG has been studied *in vitro* and it was observed that the relationship between polymer strength and M_w was more complex than expected [21]. However, data could be modeled using an empirically derived relationship between tensile strength and number average molecular weight (M_n). Changes in other mechanical properties, such as strain at break, were also found to be strongly dependent of M_n. These results demonstrated that absorbable PG suture might be suitable for microvascular anastomosis of arteries under ordinary stress and under tension up to a certain level.

Poly(e-Caprolactone) (PCL)

PCL is produced by the ROP of ε-CL. It is a semi-crystalline polymer with a melting point of 59–64°C and a glass-transition temperature of -60°C. The polymer has been regarded as tissue compatible and used as a biodegradable suture in Europe. The polymer undergoes hydrolytic degradation due to the presence of aliphatic ester linkages which are hydrolytically labile under physiological conditions [9].

Because the homopolymer has a degradation time of 2 years, copolymers have been synthesized in order to accelerate the rate of bioabsorption. For example, copolymers of ε-CL with DLL have yielded in materials with higher degradation rates. The introduction of the monofilament sutures of ε-CL and GL (Monacryl®) solved many of the problems with braided sutures that relate to tissue drag and trauma, as well as the possible potentiation of infection through the interstices of the braid structure.

Poly(L-lactide-co-ε-caprolactone)

The copolymer of LL with ε-CL exhibited good strength and flexibility, suitable for monofilament sutures, and it also showed improved handling characteristics. On the other hand, Prolene® (PP) and poly(L-lactide-co-ε-caprolactone) (PLA-ε-CL) sutures showed high knot-pull strength, despite low straight pull strength. A good correlation between tanδ and bending plasticity index was observed and the PLA-ε-CL sutures exhibited high tanδ, high bending plasticity and good resistance against untying [9].

Co/terpolymers of LL, ε-CL and GL are biodegradable in the human body and, therefore, have considerable potential for use in biomedical applications such as surgical sutures, nerve guides, bone fixation devices and drug delivery systems [22].

Polydioxanone (PDO or PDS)

Resorbable multifilament sutures, such as PLA and PGA, develop a greater amount of friction when penetrating tissues and have a higher risk of infection. So, monofilament sutures based on PDO having smooth and soft surface were introduced in the 1980s [23]. PDO suture has handling properties that are acceptable for use in vascular applications and it provides adequate mechanical support for sutured vessels to heal. In addition, PDO provides good flexibility due to the presence of an ether group in the polymer backbone.

PDO is prepared by the ROP of p-dioxanone to get a colorless, semicrystalline polymer with a very low glass transition temperature ranging from -10÷0°C. Being an aliphatic polyester, it undergoes degradation by the nonspecific cleavage of the ester bond. PDO can be considered a slow to moderate degrading polymer due to its high crystallinity and hydrophobicity.

Inside the body, PDO is broken down into glycoxylate and then excreted in the urine or converted into glycine and, subsequently, into carbon dioxide and water [24]. PDO has demonstrated no acute or toxic effects upon implantation. The monofilament loses 50% of its initial breaking strength after 3 weeks and is absorbed within 6 months, providing an advantage over Dexon® or other products for slow-healing wounds.

Poly(Trimethylene Carbonate) (PTMC)

ROP of TMC gives high molecular weight polymers with flexible chains. Unlike the previously described polyesters, PTMC undergoes surface degradation. The rate of the *in vivo* degradation was found to be much higher than the *in vitro* degradation. This is presumably due to the contribution of the enzymatic attack [24]. The low mechanical performance of the homopolymer led to the development of several co/terpolymers with other cyclic lactones, such as Maxon® and Biosyn®. A comparative study of mechanical properties of Maxon® and Biosyn® is given in Table 1.

TABLE 1. MECHANICAL PROPERTIES OF MAXON® AND BIOSYN®

Characteristic	**MAXON®**	**BIOSYN®**
Diameter (mm)	0.293	0.29
Knot pull strength (kg)	2.9	2.4
Young`s modulus (kpsi)	425	145
Straight-pull strength (kg)	3.9	3.7
Elongation (%)	30	44
Tensile strength (kg/mm^2)	56.2	55.3

The degradation studies consider that the absorption of these sutures was achieved through the action of mononuclear and multinuclear macrophages which were confined into the implant and sequestered by the fibrous

connective tissue capsule. These sutures thus were shown to maintain good strength with little or no absorption during the critical wound healing period and with minimal tissue reaction. Hydrolytic degradation studies showed that changes in mechanical properties of the copolymer were found to be strongly dependent on changes in the value of M_n [9].

Polyhydroxyalkanoates (PHAs)

PHAs are polyesters produced by microorganisms (like *Alcaligenes eutrophus* or *Bacillus megaterium*) as energy storage materials [25–27]. The most common PHA, poly(3-hydrobutyrate) (PHB), is a semicrystalline polyester (structures of different PHAs are presented in Figure 6), that undergoes hydrolytic degradation by surface erosion, these properties making it an attractive material for controlled release applications. Due to its relatively high melting point and rapid crystallization, the entrapment of drug is technically difficult.

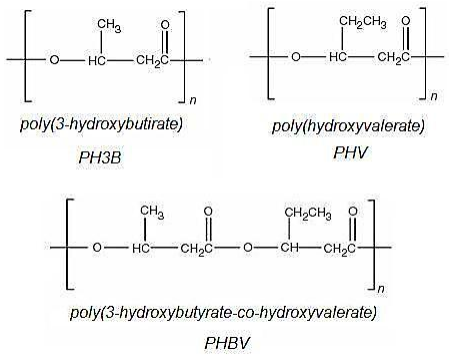

Fig. 6. Structures of the most known PHAs

The copolymers with 3-hydroxyvalerate, P(3HB-co-3HV)s, have similar semicrystalline properties, though their slower rates of crystallization result in matrices with different properties. PHB and P(3HB-co-3HV) matrices lose mass very slowly when compared to bulk-degrading PGA systems. P(3HB-co-3HV) melting point is 175°C and glass transition temperature 15°C, tensile strength 40MPa (close to that of PP). It sinks in water (while PP floats), which facilitates its anaerobic biodegradation in sediments. The biodegradation can be controlled by tuning the composition of the copolymer [9]. The biocompatibility is good, it is fully nontoxic [28] and, hence, suitable for medical applications. However, the commercialization of PHA sutures is impeded by the high cost of production.

III. CONCLUSION

Over the last decades, surgical suture materials have proved to be high competitive products of a mature industry. New sutures are constantly developed in order to better respond to specific surgical needs. Basic materials are modified depending on intended applications and to provide the surgeon with a suture material of optimal quality. The modern surgery imposes requirements that biocompatible resobable synthetic materials are able to fullfill, but the next step necessitates further progress in this area: the production of novel strong and elastic threads made of biocompatible absorbable natural polymers, such as polyoxyalkanoates, collagen, chitin, alginate, etc.

Therefore, researchers increasingly focus on the new generations of sutures, materials that can achieve not only antimicrobial activity, but also anesthetic and antineoplastic functions.

REFERENCES

[1] C.-C. Chu, J. A. von Fraunhofer and H.P. Greisler (eds), "Wound Closure Biomaterials and Devices", Boca Raton, Florida, CRC Press, Inc., 1996.

[2] B.S. Bloom and D. J. Goldberg, "Suture Material in Cosmetic Cutaneous Surgery", J. Cosmet. Laser Ther., 9, 41, 2007.

[3] DemeTECH. Available at: http://www.demetech.us/suture-specs.php.

[4] R. L. Williams and D. G. Armstrong, "Wound Healing: New Modalities for a New Millennium", Clin. Pediatr. Med. Surg., 15, 117, 1998.

[5] T. Al-Abdullah, A. C. Plint and D. Fergusson, "Absorbable Versus Nonabsorbable Sutures in the Management of Traumatic Lacerations and Surgical Wounds: A Meta-Analysis", Pediatr. Emerg. Care, 23, 339, 2007.

[6] B. C. Benicewicz and P. K. Hopper, "Polymers for Absorbable Surgical Sutures – Part II", J. Bioact. Compat. Polym., 6, 64, 1991.

[7] R. H. Caulfield, A. Maleki-Tabrizi, H. Patel, F. Coldham, S. Mee and J. Nanchahal, "Comparison of Zones 1 to 4 Flexor Tendon Repairs Using Absorbable and Unabsorbable Four-Strand Core Sutures" , J. Hand Surg. Eur., 33, 412, 2008.

[8] L. S. Nair and C. T. Laurencin, "Biodegradable Polymers as Biomaterials", Prog. Polym. Sci., 32, 762, 2007.

[9] C. K. S. Pillai and C. P. Sharma, "Absorbable Polymeric Surgical Sutures: Chemistry, Production, Properties, Biodegradability, and Performance", J. Biomater. Appl., 25, 291, 2010.

[10] H. Planck, M. Dauner and M. Renardy (eds), "Medical Textiles for Implantation", Berlin, Springer-Verlag, 1990.

[11] D. E. Perrin and J. P. English, "PGA and Polylactide", in: A. J. Domb, J. Kost and D. M. Wiseman (eds), "Handbook of Biodegradable Polymers", The Netherlands, Harwood Academic Publishers, pp. 3–27, 1997.

[12] J. C.Middleton and A. J. Tipton, "Synthetic Biodegradable Polymers as Orthopedic Devices", Biomaterials, 21, 2335, 2000.

[13] J. C.Middleton and A. J. Tipton, "Synthetic Biodegradable Polymers as Medical Devices", Med. Plast. Biomater., 30, 1998; available at: http://www.mddionline.com/article/synthetic-biodegradable-polymers-medicaldevices.

[14] J. Siripitayananon, R. Molloy, S. Bunkird, A. Kleawkla, R. Panjakha and P. Chooprayoon, "Effects of Hot-Drawing and Annealing on the Morphology and Mechanical Properties of Biodegradable Polyester Monofilament Fibers", Int. Polym. Process., 23, 161, 2008.

[15] L.-T. Lim, R. Auras and M. Rubino, "Processing Technologies for Poly(Lactic Acid)", Prog. Polym. Sci., 33, 820, 2008.

[16] M. Jalabert, C. Fraschini and R. E. Prud'Homme, "Synthesis and Characterization of Poly(L-Lactide)s and Poly(D-Lactide)s of Controlled Molecular Weight", J. Polym. Sci., Part A: Polym. Chem., 5, 1944, 2007.

[17] K. Takizawa, H. Nulwala, J. Hu, K. Yoshinaga and C. J. Hawker, "Molecularly Defined (L)-Lactic Acid Oligomers and Polymers: Synthesis and Characterization", J. Polym. Sci., Part A: Polym. Chem., 46, 5977, 2008.

[18] R. A. Miller, J. M. Brady and D. E. Cutright, "Degradation Rates of Oral Resorbable Implants. Polylactates and Polyglycolates: Rate Modification With Changes in PLA/PGA Copolymer Ratios", J. Biomed. Mater. Res., 11, 711, 1977.

[19] P. Gunatillake, R. Mayadunne and R. Adhikari, "Recent Developments in Biodegradable Synthetic Polymers", Biotechnol. Annu. Rev., 12, 301, 2006.

[20] C. E. Astete and C. M. Sabliov, "Synthesis and Characterization of PLGA Nanoparticles", J. Biomater. Sci. Polym. Ed., 17, 247, 2006.

[21] D. F. Farrar and R. K. Gillson, "Hydrolytic Degradation of Polyglyconate B: The Relationship Between Degradation Time, Strength and Molecular Weight", Biomaterials, 23, 3905, 2002.

[22] Y. Baimark, R. Molloy, N. Molloy, J. Siripitayananon, W. Punyodom and M. Sriyai, "Synthesis, Characterisation and Melt Spinning of a Block Copolymer of *L*-Lactide and *ε*-Caproactone for Potential Use as an Absorbable Monofilament Surgical Suture", J. Mater. Sci. Mater. Med., 16, 699, 2005.

[23] K.-K. Yang, X.-L. Li and Y.-Z. Wang, "Poly(p-Dioxanone) and its Copolymers", J. Macromol. Sci. Polym. Rev., 42, 373, 2002.

[24] P. B. Maurus and C. C. Kaeding, "Bioabsorbable Implant Material", Oper. Tech. Sports Med., 12, 158, 2004.

[25] N. Jacquel, C.-W. Lo, Y.-H. Wei, H.-S. Wu and S. S. Wang, "Isolation and Purification of Bacterial Poly(3-hydroxyalkanoates)", Biochem. Eng. J., 39, 5, 2008.

[26] R. C. S. Rocha, L. F. Silva, M. K. Taciro and J. G. C. Pradella, "Production of Poly(3-hydroxybutyrate-co-3-hydroxyvalerate) P(3HB-co-3HV) with a Broad Range of 3HV Content at High Yields by Burkholderia sacchari IPT 189", World J. Microbiol. Biotechnol., 24, 427, 2008.

[27] A. J. Anderson and E. A. Dawes, "Occurrence, Metabolism, Metabolic Role, and Industrial Use of Bacterial Polyhydroxyalkonoates", Microbiol. Rev., 54, 450, 1990.

[28] A. Steinbüchel, "Biopolymers", Weinheim, Wiley-VCH, vol. 10, 2002.

Network Macromolecular Structures. The Crosslinker Effect

Loredana E. NITA, Manuela T. NISTOR, Aurica P. CHIRIAC, Iordana NEAMTU
"Petru Poni" Institute of Macromolecular Chemistry
Grigore Ghica Voda Alley No. 41-A, 700487 IASI, Romania
achiriac1@yahoo.com

***Abstract* — The study presents the possibility to prepare copolymers based on 2-hydroxyethyl methacrylate using two variants of comonomers: ethylene glycol dimethacrylate (1) and respectively 3, 9- divinyl -2, 4, 8, 10-tetraoxaspiro[5.5]-undecane (2) that act as crosslinkers for the methacrylate networks. All these monomers are well known for their use in the bio- and photodegradable polymers preparation as well as to generate gel structures. The chemical structure and composition of the copolymers – synthesized through redox polymerization process using ammonium persulfate and N,N,N', N' –tetramethylethylenediamine as initiator pair were confirmed by FT-IR spectroscopy. The transparent gel structures were prepared in ethylene glycol. The influence of the comonomers type upon gel copolymers formation was put into evidence by the swelling behavior of the polymeric structure. The swelling effected at 37°C differentiates the crosslinker comonomers, attributing a better performance to the 3, 9- divinyl -2, 4, 8, 10-tetraoxaspiro[5.5]-undecane. The morphological information concerning the studied polymeric compounds by SEM evidenced the differences between the hydrogels with respect to crosslinker type and its quantity in the monomer feed. Also the thermal stability is a function of the type and quantity of the crosslinker. The study underlines the possibility to optimize the network macromolecular structure using a properly crosslinker choice, taking into account the potential application in biomedical and sensors domain.**

***Index Terms* — biotechnological applications, crosslinker, hydrogel, network structures, poly(orthoesters)**

I. INTRODUCTION

Hydrogels are hydrophilic homopolymers or copolymers with three dimensional network structures that undergo extensive swelling in water and found a wide variety of applications in medical, pharmaceutical and related fields, e.g. artificial organs, contact lenses, wound dressings and drug delivery systems [1 - 3]. Because of the swelling capacity, their structure is similar to natural tissue [4, 5]. Also they found an extremely favorable field of applications in agriculture, food industry, photographic technology and others.

Hydrogels do not dissolve in water at physiological temperature and pH, but they swell considerably in an aqueous medium [6] and demonstrate extraordinary capacity (>20%) for imbibing water into the network structure. Gels exhibiting a phase transition in response to change in external conditions such as pH, ionic strength, temperature and electric currents are known as "stimuli-responsive" or "smart" gels [7]. Being insoluble, these three-dimensional hydrophilic networks can retain a large amount of water that not only contributes to their good blood compatibility but also maintains a certain degree of structural integrity and elasticity [8]. Thus, crosslinked polymer networks formed by free radical polymerization of ethylene glycol methacrylates and dimethacrylates have been found attractive as hydrogel matrices since they do swell in aqueous media to certain extend depending on the crosslinking density, but do not dissolve. 2-hydroxyethyl methacrylate (HEMA) based hydrogels are inert to normal biological processes, show resistance to degradation, are not absorbed by the body and can be prepared in a variety of shapes and forms. The crosslinked 2-hydroxyethyl methacrylate hydrogels because of their hydrophilic character and potential biocompatibility have been of great interest to biomaterial scientists for many years [9-11]. The presence of hydroxyl and carboxyl groups makes this polymer compatible with water, whereas the hydrophobic methyl groups and backbone impart hydrolytic stability and supports the mechanical strength of the polymer matrix. HEMA copolymers have also been investigated as carriers for enzyme and protein immobilization, as absorbents for chromatographic applications, and as scavengers for removing metal ions from solution [12–15]. HEMA can be polymerized and crosslinked easily and the properties of proper hydrogels are dependent upon their method of preparation, polymer volume fraction, degree of crosslinking, temperature and swelling agent.

Poly(orthoesters) have attracted considerable interest for the controlled delivery of therapeutic agents within biodegradable matrices. This interest is due primarily to poly(orthoesters) being susceptible to acid catalysed hydrolysis. Hydrolysis proceeds *via* the protonation of an alkoxy oxygen followed by bond cleavage, with pentaerythritol, aliphatic acid and the diol or mixture of diols as degradation products. As the hydrolysis of poly(orthoesters) requires an initial protonation, these polymers may be considered pH sensitive, being stable in basic conditions [16].

In this study, the effects of the two crosslinking agents : ethylene glycol dimethacrylate and an orthoester type named 3, 9-divinyl-2, 4, 8, 10 - tetraoxaspiro[5.5]-undecane) on the structure, water absorption, morphology of the network and thermal stability of the HEMA – based hydrogels were investigated. The hydrogels are aimed to be matrices for bioactive compounds entrapment or for sensor applications.

II. EXPERIMENTAL

Materials

2-hydroxyethyl methacrylate (HEMA) from Aldrich (purity 97%) was purified by passing it through an inhibitor removal column (for removing hydroquinone and

hydroquinone monomethyl ether). 3,9 – divinyl -2,4,8,10 - tetraoxaspiro[5.5]-undecane (U) (purity 98%) and ethylene glycol dimethacrylate (EGDMA) (purity 99%) as crosslinking comonomers were purchased from Aldrich.

Ammonium peroxodisulfate (APS, Merck) and N,N,N', N' –tetramethylethylenediamine (Sigma Aldrich, TEMED) were used as the redox initiator pair. Ethylene glycol was used as reaction medium and distilled water was used in the swelling studies.

Hydrogel preparation

The hydrogels based on hydroxyethyl methacrylate were prepared by simultaneous redox polymerization and crosslinking in solution of ethylene glycol. The monomers HEMA, EGDMA or U concentration in ethylene glycol as reaction medium is 8%. EGDMA or U as a crosslinking agent was used at two concentrations 1 and 5 wt % with respect to HEMA content. APS and TEMED were used as initiators in a 1:1 wt ratio, at concentrations of 0.6 wt % each of them with respect to the total amount of monomers.

A typical procedure for the copolymerization can be described as follows: HEMA 1 ml and EGDMA (0.02 mL) or U (0.02 g) were dissolved in 22 mL of ethylene glycol, then APS (1.2 mL water solution of 1%) and TEMED (0.016 mL) were added into the monomer solution mixture, respectively. The solution was stirred until thoroughly mixed. The samples of about 2 mL were polymerized stationary in 5 mL glass tubes (7 mm I.D) as the polymerization reactors, for 24 hr at room temperature to ensure complete polymerization.

The copolymers samples obtained in the form of long cylinders were removed from the tubes and placed in 60 mL glass sample bottles filled with deionized water. Then they were washed within distilled water at room temperature for 24 hours to remove any unreacted monomers and physically entrapped reaction components and the purity is verified by UV spectroscopy of the washing waters.

Finally the samples were dried by lyophilization. The dried samples were stored in desiccator at room temperature until tested in experiments of swelling, spectroscopy, SEM and thermal stability analyses.

Fourier Transform Infra-Red Spectroscopy

FTIR spectra were recorded on a Vertex Brucker Spectrometer in the absorption mode ranging from 400 to 4000 cm^{-1}, at 4 cm^{-1} resolution, as an average of 64 scans.

Equilibrium swelling experiments

The equilibrium swelling degree SR of the hydrogels was determined by the gravimetric method, in the buffer solutions: Na_2HPO_4 / CH_3COOH for pH 5.5 and 7.4, at 22 and 37°C, by applying the equation (1) :

$$SR = \frac{W_t - W_O}{W_O} X100 \qquad (1)$$

where Wt is the weight of the swollen gel at time t and Wo is the weight of the dried gel at time 0.

Scanning electron microscopy

SEM microphotographs were obtained by using Quanta 200 with EDAX - Elemental Analysis System. The samples have been cross-sectioned and the morphological structure was investigated in an accelerating voltage of 10.60 kV and high vacuum.

Thermal analysis

The thermal behavior of the polymers was evidenced by using a STA 449F1 Jupiter model (Netzsch-Germany) system at heating rate of 10 °C/min. Experiments under non-isothermal condition were following in nitrogen atmosphere with a 50 ml/min flow rate. 7.5-8 mg of polymeric mass were heated from 30 to 600º C.

II. RESULTS AND DISCUSSION

Polymerization techniques based on addition, such as free radical chain growth crosslinking copolymerization of HEMA and EGDM, are usually used for the preparation of polymers, which are subsequently converted into hydrogels, by moderate crosslinking of the polymeric chains in fairly concentrated solutions.

It was evidenced in the literature that the incorporation of spiroacetal groups in the polymer structures improves the solubility and the adhesive properties [17]. More than that, the polymers which include these moieties are stable in base, hydrolyze at very slow rates at the physiological pH of 7.4, and become progressively more labile as the pH is lowered. Also, these kinds of comonomers induce good oxidative and thermal stability, are good fiber formers, and the prepared films present good flexibility and tensile strength [18]. These characteristics are attributed to the properties inherent into the spiroacetal ring: stiffness, which is higher than cycloaliphatic rings but lower than aromatic rings; interactions on ether oxygen such as hydrogen bonds or coordinate bonds with other functional groups, and bulkiness. Different researchers described the developments in synthesis of alternating poly(ester–ether)s from spiroortho-esters, which were also considered biodegradable and useful for biomedical applications [19, 20].

Fig. 1 presents the FTIR spectra for the samples oh hydrogels based on HEMA crosslinked with EGDMA (1 and 5 wt % in the monomer phase) and U (1 and 5% in the monomer phase). Firstly, from the FTIR spectrum depicted in Fig. 1, the presence of the main comonomer in the hydrogel structure is confirmed by the hydroxyl and strong carbonyl bands appearing at 3500 cm^{-1} (O-H stretching) and 1730 cm^{-1} (C=O stretching), respectively. Also, there are evidently the bands at 1172 cm^{-1} (O-C-C stretching), 2951 cm^{-1} (asymmetric stretching of methylene group) and 1454 cm^{-1} (O-H bending).

The FTIR spectra are used to confirm the consumption of C=C bonds in HEMA, EGDMA and U. In the spectra, the absorbance change of the peak at 1635 cm^{-1} (C=C stretching) estimates the conversion of vinyl bonds in the samples and their consumption during the polymerization.

The absorbance of the peak at 1730 cm^{-1} (C=O stretching) was picked as standard. The spiroacetal moieties inclusion is also confirmed by the new strong bands in the region of 1000 – 1200 cm-1 (due to ether C-O-C stretching and C-H in plane bending) and at ~ 1715 cm-1 (due to C=O stretching of conjugated ether). The supplementary absorption at 2887 cm^{-1} is attributed to the -CH - CH_2 -symmetric stretching from U. The carbonyl peak of the acrylate of EGDMA appears at 1730 cm^{-1} and the lactone carbonyl at 1764 cm^{-1}.

Secondly, in a general view, the spectra of HEMA based gels are almost similarly, but with the exception of a peak at about 1573 cm -1 which can be assigned to the stretching of the COO- group [21]. As it can be seen for both crosslinking comonomer EGDMA and U, the intensity of this peak increases comparative to p(HEMA) as a function of crosslinking density, respectively the increase of cross-linker concentration from 1 to 5% in the monomer phase. The aspect is more evidenced for the sample hydrogel with EGDMA.

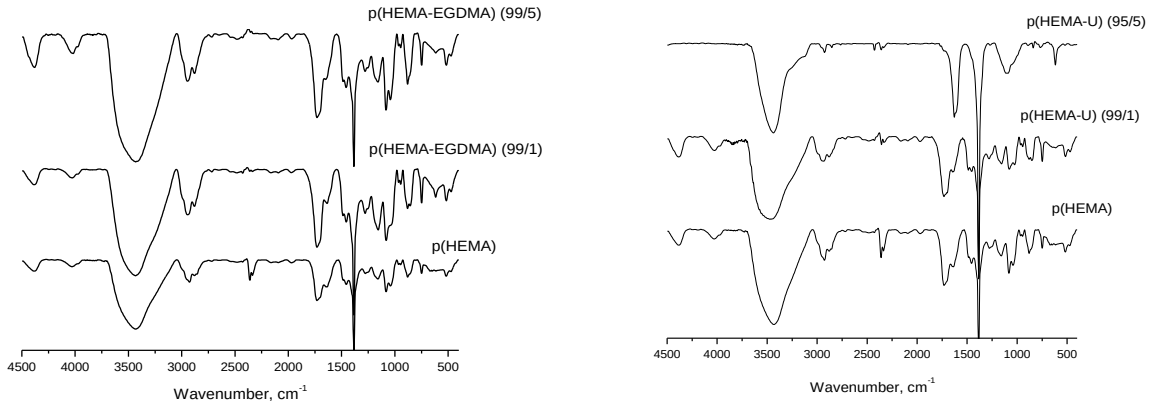

Fig. 1. FTIR spectra for the hydrogel samples based on HEMA crosslinked with EGDMA and U

The crosslinkers have pronounced effect on the swelling ratio. In the swelling behavior of the hydrogels, the percentage swelling increases with time but after a while constant percentage swelling is observed. This value of swelling percentage represents the equilibrium swelling.

The effect of the degree of crosslinking on the swelling was investigated by varying the concentration of EGDMA and U in the feed mixture of the polymerization recipe. In this study we have chosen two values for the crosslinker amount: 1 and 5 % from the monomer mixture. In Table 1 there were presented the equilibrium swelling degrees SR determined at 22 and 37 ^{o}C, for pH 5.5 and 7.4, taking into account the potential applicability for the sensitive materials at the environmental parameters (temperature and pH).

TABLE 1 EQUILIBRIUM SWELLING DEGREE SR FOR THE HYDROGEL SAMPLES

Temperature, ^{o}C	1% EGDMA		5% EGDMA		1% U		5% U	
	pH 7.4	pH 5.5	pH 7.4	pH 5.5	pH 7.4	pH 5.5	pH 7.4	pH 5.5
22 ^{o}	35.68	28.57	39.64	36.40	38.40	39.33	40.02	38
37^{o}	29.65	17.53	34.22	39.38	46.01	33.01	47.96	45

From the data presented in Table 1 it is observed that the equilibrium swelling degree SR determined in buffer solution increases as the extent of crosslinking grows, and its values demonstrate the temperature and pH sensitivity of the hydrogel samples. Also, the spiroacetal moieties in U induce higher swelling degree than the hydrogel with 5 % EGDMA. Usually the swelling degree is expected to decrease with increasing crosslinking. Surprisingly, in an inherent contradiction the water absorption is more significant for the relatively high degree of crosslinking (with 5% of EGDMA or U) than for the hydrogel with a low degree of crosslinking (with 1% of EDGMA or U). These results reflect the existence of two absorption mechanisms in the HEMA based hydrogel: absorption within the pHEMA walls through interaction with the hydrophilic polymer and absorption within the porous structure through capillary action. The literature also [22, 23] describes three different diffusion mechanisms for the transport of water through crosslinked pHEMA gels, which depend on the crosslinker content: a pore flow mechanism for low
crosslinking content, a water-matrix interaction mechanism for higher crosslinking content and an intermediate mechanism at intermediate crosslinker concentration. Our study on the pHEMA gels fulfills these aspects. At the same time, the synthesis of hydrogels that combine the water absorption through hydrophilic interactions and through capillary action can be used to synthesize better water-absorbent materials for different biotechnological applications, such as drug delivery or tissue engineering.

Fig. 2 presents the SEM images of the pHEMA based hydrogel (a), crosslinked with 5%EGDMA (b) and crosslinked with (5%) U (c). In detail are the SEM micrographs for hydrogels crosslinked with 1% EGDMA (b) and 1% U (c).

As it is observed in the SEM images, the hydrogels porous structure consists of distorted interconnected spherical voids separated by walls. These walls themselves have an unusual nanoscale porous structure with voids from the evacuated droplets of the organic phase (ethylene glycol).

The SEM images reflect two main conclusions: firstly, the crosslinked hydrogel with 5% EGDMA and 5% U have structures that are reminiscent of a typical pHEMA hydrogel. Secondly, the morphology of the hydrogels with higher degree of crosslinking (samples with 5% of EDGMA or U) is a porous structure completely different comparative to pHEMA hydrogels with EGDMA 1% or U 1%.

These hydrogels are able also to swell with greater amount of water, as it is reflected by the SR values in the swelling experiment (Table 1). The more porous structures and high surface area enhance capillary action and yield the large amount of water absorbed.

In Table 2 are presented the main characteristic temperatures in the decomposition process of the dried hydrogel samples.

As it can be seen from the listed results there were found differences between the thermal behaviors

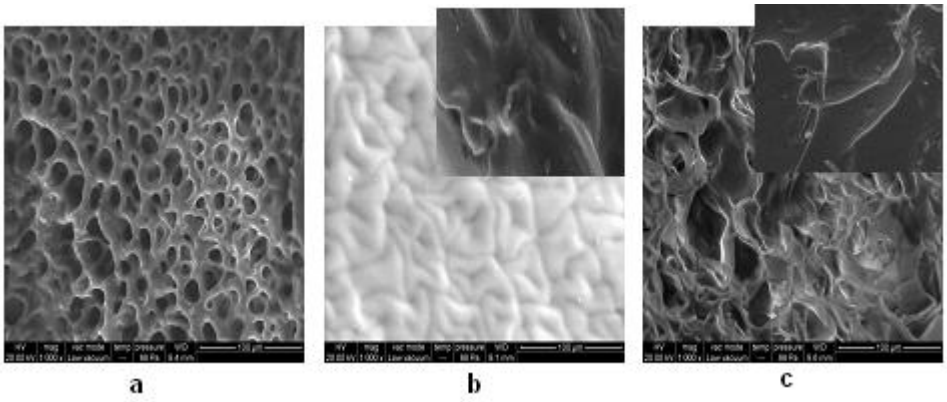

Fig. 2. SEM micrographs of the pHEMA based hydrogel (a), crosslinked with 5%EGDMA (b) and crosslinked with (5%) U (c). In detail are the SEM micrographs for hydrogels crosslinked with 1% EGDMA (b) and 1% U (c).Magnification: 1000X.

TABLE 2. THE MAIN CHARACTERISTIC TEMPERATURES IN THE DECOMPOSITION PROCESS OF THE HYDROGEL SAMPLES

Sample	First process			Second process			Residual mass. %
	Ti ^{o}C	Tmax ^{o}C	Tf ^{o}C	Ti ^{o}C	Tmax ^{o}C	Tf ^{o}C	
pHEMA	-	-	-	332	362	415	0.1
p(HEMA-EGDMA 1%)	218	238	275	335	366	454	0.09
p(HEMA-EGDMA 5%)	141	208.6	242.5	335.5	368	434.3	0.76
p(HEMA-U 1%)	-	-	-	345	372	426	0.83
p(HEMA-U 5%)	318.5	348.9	352.3	391	407	446	1.94

Ti, Tf—onset and final temperature of the thermal decomposition step, Tmax—maximum temperature of decomposition

P(HEMA) hydrogels crosslinked with 1 and 5 % EGDMA and with 5% U present a thermal decomposition process in two stages comparative with P(HEMA) and P(HEMA-U 1%) that have only one process of decomposition. As it is expected, the presence of the crosslinking comonomer 3,9 – divinyl -2,4,8,10 - tetraoxaspiro[5.5]-undecane (U) positively affects the thermal stability of the copolymers, because of the spiro acetal ring that controls the thermal properties. Thus, it is observed for P(HEMA-U 5%) Tmax registered an increase with about 40 ^{o} comparative to P(HEMA) and P(HEMA-EGDMA 1 or 5%). No significant thermal stability results were obtained by crosslinking with EDGMA comparative to P(HEMA).

III. CONCLUSIONS

The study presents the synthesis of 2-hydroxyethyl methacrylate based hydrogels by crosslinking with one of the two crosslinkers: ethylene glycol dimethacrylate and 3,9 – divinyl -2,4,8,10 - tetraoxaspiro[5.5]-undecane. The hydrogels were prepared by simultaneous redox polymerization and crosslinking in solution of ethylene glycol, by using ammonium peroxodisulfate and N,N,N', N' –tetramethylethylenediamine as the redox initiator pair. The transparent gel structures were prepared in ethylene glycol.

The influence of the crosslinker type is estimated and the hydrogels are characterized from the viewpoint of chemical structure, swelling behavior, morphology and thermal stability, by FTIR spectroscopy, equilibrium swelling degree SR determination, SEM and TGA.

The study underlines the possibility to optimize the network macromolecular structure using a properly crosslinker choice.

ACKNOWLEDGEMENTS

This work was supported by CNCSIS-UEFISCSU-ROMANIA, project number PN II-RU No. 53/10.08.2010, code 656, entitled: New hydrogel with biomedical aplication.

REFERENCES

[29] N.A. Peppas, P. Bures, W. Leobandung, H. Ichikawa, „Hydrogels in pharmaceutical formulations", European Journal of Pharmaceutics and Biopharmaceutics 50 (2000) 27-46.

[30] G.U. Ostrovidova, A.V. Makeev, M.M. Shamtsian, "Polyfunctional film coatings for medical use", J Mater Sci Eng., 23(2003), pp. 545–50.

[31] M.R. Razaak, D. Darwis, R. Sukimo, "Irradiation of polyvinyl alcohol and polyvinyl pyrollidone blended hydrogel for wound dressing", Radiat Phys Chem 62 (2001), pp.107–13.

[32] DG Castner, BD Ratner, "Biomedical surface science: foundation to frontiers", Surf Sci 500 (2002), pp. 28–60.

[33] KY Lee, DJ Mooney, "Hydrogels for tissue engineering", Chem Rev 101 (2001), PP. 1869–79.

[34] NA Peppas, Y Huang, M Torres-Lugo, JH Ward, J Zhange, "Physiochemical foundation and structure design of hydrogel in medicine and biology", Annu Rev Biomed Eng 2 (2000), pp. 9–29.

[35] C Lingyun, T Zhigang, D Yumin, "Synthesis and pH sensitivity of carboxymethyl chitosan based polyampholyte hydrogel gel for protein carrier matrices", Biomaterials, 25 (2004), pp. 3725– 32.

[36] Q Li, J Wang, S Shahani, DDN Sun, B Sharma, JH Elisseeff, "Biodegradable and photocrosslinkable

polyphosphoester hydrogel", Biomaterials 27 (2006), pp. 1027–34.

[37] C.C.R. Robert, P.A. Buri, N.A. Peppas "Influence of the Drug Solubility and Dissolution Medium on the Release from Poly(2-hydroxyethyl methacrylate) Microspheres," J. Controlled Release, 5 (1987), pp. 151-157.

[38] K. Kejlova, J. Labsky, D. Jirova, H. Bendova, "Hydrophilic polymers-biocompatibility testing in vitro" Toxicol. In Vitro, 19 (2005), pp. 957-62.

[39] G. A. Hutcheon, C. Messiou, R. M. Wyre, M. C. Davies and S. Downes, "Water absorption and surface properties of novel poly(ethylmethacrylate) polymer systems for use in bone and cartilage repair", Biomaterials, 22(2001), pp. 667-676. [12] M. Y. Arica, V. Hasirci, N. G. Alaeddinoglu, "Covalent immobilization of α-amylase onto pHEMA microspheres: preparation and application to fixed bed reactor", Biomaterials, 16 (10)(1995), pp. 761-768.

[40] B. Salih, A. Denizli, B. Engin, E. Piskin, "Adsorption of heavy metal ions onto dithizone-anchored poly (EGDMA-HEMA) microbeads", Talanta, 46(5)(1998) pp 1205-1213.

[41] J. Kahovec, J. Coupek, "Chemical Modification of Macroreticular 2-Hydroxyethyl Methacrylate Polymers", React. Polym., 8(1988), pp. 105-11.

[42] MF Refojo, "Hydrophobic interactions in poly(2-hydroxyethyl methacrylate) homogeneous hydrogel", J Polym Sci Part A1 Polym Chem, 5(1967), pp.3103–8.

[43] J Heller, DWH Penhale, RF Helwing, BK Fritzinger, "Release of norethindrone from poly(orthoesters)", Polym Eng Sci, 21 (1981), pp. 727-736 ; J Heller, B.K. Fritzinger, S.Y. Ng, D.W.H. Penhale, "*In vitro* and *in vivo* release oflevonorgestrel from poly(ortho esters): I. Linear polymers", J Controlled Release, 1(3)(1985), pp. 225-232.

[44] J. Heller, J. Barr, S. Y. Ng, K. S. Abdellauoi, R. Gurny, "Poly(ortho esters): synthesis, characterization, properties and uses", Adv. Drug Delivery Rev. 54(7), 2002, pp. 1015-1039.

[45] F.V. Zalar, "A New Spiroacetal Polymer", Macromolecules, 5 (5) (1972), pp. 539-541.

[46] WJ Bailey, H Iwama, R Tsushima , "Synthesis of elastomers by cationic polymerization with expansion in volume", J Polym Sci: Symp. 56 (1976), pp. 117–27.

[47] T Moore, R. Adhikari, P. Gunatillake, "Chemosynthesis of bioresorbable poly(g-butyrolactone) by ring-opening polymerisation: a review", Biomaterials, 26 (18) (2005), pp. 3771–3782.

[48] S Zalipsky, C Gilon, A Zilkha, „Attachment of drugs to polyethylene glycols", Eur. Polym. J. 19 (12), (1983), pp. 1177–1183.

[49] L. Ferreira, M.M. Vidal, M.H. Gil, "Evaluation of poly(2-hydroxyethyl methacrylate) gels as drug delivery systems at different pH values", Int J Pharmaceutics 194 (2000), pp. 169–180.

[50] SJ Wisniewski, DE Gregonis, SW Kim, JD Andrade, "Diffusion through hydrogel membranes. 1. Permeation of water through poly(2-hydroxyethyl methacrylate) and related polymers" In: Andrade, J.D. (Ed.), Hydrogels for Medical and Related Applications, ACS Symposium Series 31, (1976) American Chemical Society, Washington, pp. 80–87.

Identification and Analysis of Sources Relative to the Characteristics of Pharmaceutical Innovation

Maia IORDATII, Alain VENOT, Catherine DUCLOS
LIM&BIO EA 3969, UFR SMBH, Université Paris 13,
74 rue Marcel Cachin, 93017 Bobigny, France
miordatii@yahoo.com

***Abstract* - Every year new drugs appear on the market. Information about the therapeutic innovation is contained in many heterogeneous sources. A physician needs to identify easily and fast the whole of the drug innovations relative to his sphere of activity, to understand the nature of these innovations and their potential impacts on the practice. We analyzed the available sources and the nature of this information which can be found after the marketing drug. We explored the American, European including French sources. We identified the sources that constitute the base in identification of pharmaceutical innovation. We explored its structure and format to know if they could be used in the development of therapeutic monitoring tool. We selected the sources that help to characterize pharmaceutical innovation concerning to type of innovation and according to impact of the new drug. We proposed a tool which identifies the drugs prescribed for pathology "type 2 of diabetes" using DailyMed source. The tool allows finding the type of innovation and its impact. This work has identified the main sources of information available at the moment of drug marketing. Each of the described sources in this paper is important, but insufficient to characterize the pharmaceutical innovation.**

***Index Terms* — drug sources, information seeking, medical informatics, information resources, databases.**

I. INTRODUCTION

When a drug is marketed, the physician needs to position it in the therapeutic arsenal for deciding the pertinence of its prescription in terms of benefit/risk. To generate this opinion about the new drug, he has several sources which reveal all the properties of the drug (monographs), or which offer a comparison with other drugs of the same indication. Finally, the use of new drug recommendation is completely formalized via clinical guidelines. The time of these documents production is variable: the monograph dates since the date of the drug marketing, the report of evaluation is later and retrospective, the clinical guidelines are updated very infrequently. These documents, being fixed in time, provide information at a given time.

Each country has its specific standards to evaluate the drug impact.

Food and Drug Administration of US provides standardized information relative to the new drugs after their marketing authorization. The information specifies if it is a new molecular entity, a new salt or ester, a new formulation, a new combination of drugs already marketed in the United States, a new manufacturer, a new indication for a product already marketed or it is another innovation. The therapeutic benefit for the patient is classified as P (Priority review drug), S (Standard review drug) or O (Orphan drug) [1]. This manner of characterizing the innovation has the disadvantage of not indicating analytically to the physician, the real interest of this one.

From Europe, Austria is the country that presents the most detailed characterizations of the pharmaceutical innovations, described in pharmacological and therapeutic terms [2].

In France, the French Agency for Sanitary Health of the Health Products (Afssaps) quantifies the actual benefit (SMR) of each innovation. This one summarizes the benefit (disease severity, efficacy, therapeutic alternatives) and the risks related to use of the new drug. The ASMR measures the improvement that the drug is likely to bring compared to already available drugs [2]. These indicators represent a summary of what a drug brings to certain moment and moves in time depending on the data on which they were founded. To appreciate fully the value of these indicators, the physician always need to refer to the textual document of evaluation which is long.

In these approaches, the innovation is seen mainly in terms of efficacy [3, 4, 5] which is restrictive. An important innovation can lead to an identical efficacy associated with less frequent side effects or less severe effects.

To build objectively its judgment on a new drug is a task that requires time, capacities of critical analysis, familiarity with the multitude of the available documents, capacity to identify them and reach it. For example, to form an opinion about the Pradaxa TM, an oral anticoagulant used in the prevention of venous thrombosis after the hip surgery, the doctor can read the clinical guidelines on the anticoagulation postoperatively. The document dating from 2005 does not contain this new drug. He may read the evaluation report of medical department rendered issued in July 2008 and he is able to position this new molecule compared to the heparin of low molecular weight, but he must also be vigilant to the output of more contemporary drugs having similar characteristics (Xarelto TM whose opinion is published in January 2009 and who is not compared to the previous molecule). Finally, he must connect to the site of clinical trial to identify posterior clinical tests to these 2 opinions which could inform more.

If the clinical guideline gives the relevant information for the physician, the other available documents do not provide exhaustive searched information and it is necessary to cross several sources to have an opinion.

Methods of Knowledge Engineering in Medicine provide a base that can lead to the automated extraction of information available on the Web, their synthesis and a summary for their quick apprehension by the physician.

The objective of this work is to identify sources for characterizing pharmaceutical innovation, to study the feasibility of developing automated tools that could assist the physician in his scientific monitoring. This paper presents an analysis of the sources which can be queried and their treatment modalities.

II. MATERIAL AND METHODS

Prior we constituted the preliminary list of sources that are used to characterize pharmaceutical innovation from knowledge of experts. These experts included a Doctor of Medicine / Doctor of Philosophy ("MD / PhD) and a Doctor of Pharmacy / Doctor of Philosophy (" Pharm. D / Ph. D ") From The Department of Medical Information Of The Avicenna Hospital.

The sources chosen by experts correspond to those used in their research activities and in their daily work. Subsequently, we expanded the exploration of resources. Our research strategy included an Internet research of various medical web sites, such as BioMed Central, Medscape, First DataBank, the sites of drug agencies in Europe and America. Similarly, we researched about pharmaceutical innovation via PubMed.

We explored the American sources, European including French.

Among the sources analyzed we selected those that help us to characterize pharmaceutical innovation about the type of innovation (new molecule, new association, new strength, new formulations, etc.) and relative to the impact of new drug in terms of efficacy and safety.

We performed a detailed analysis of the content of retained sources. Then, we explored the format to see if they can be used in the construction of the computerized tool of therapeutic monitoring.

III. RESULTS

Illustrations and tables should be progressively numbered, following the order cited in the text; they may be organized in one or two columns. Tables must be accompanied by a caption placed at the top. Figures (abbreviated Fig.) must be accompanied by a caption placed underneath. References made to tables in text will not be abbreviated e.g. “in Table I, TN Roman means Times New Roman”.

Each formula should occupy one line. Consecutive numbers should be marked in brackets.

1. Analysis of sources on the characteristics of therapeutic innovation

We defined the basic set of sources that provide information on pharmaceutical innovation. We have identified two types of information sources that characterize innovation: those which compare and which does not compare the new drug treatment to other existing treatments.

1.1 Sources on drug therapy without comparison to other

The drug monographs

From the marketing of manufactured product, his monograph (or Summary of Product Characteristics) is available by health authorities. This monograph is divided into chapters (composition, indications, contraindications, etc.); the content of these chapters is in free text with a requirement of structuring and coding variable from one country to another.

The U.S., for example, impose a detailed description as an XML structure and a certain number of terminologies to describe the contents of Chapters [6] (eg, clinical conditions are coded using the list of problems VA / KP (Veterans Health Administration and Kaiser Permanente), which is a subset of SNOMED). The monograph is structured to be returned to the user in XML formalism via the website DailyMed [7].

The codification of some elements of the monograph is often performed by the editors of banks drugs, such as in France [8] indications and contraindications are coded in CIM10.

These editors often provide enhancements of the drug information with data from the literature [9, 10] and with monographs structuring models to feed the system functionality of assistant to the prescription. This information is available into the drug banks which are an important source for documenting therapeutic innovation.

Current clinical trials

The banks of clinical trials contain current or completed trials. Trials may include drugs that are already available on the market or in process of the development, as well as protocols of drug combinations (eg in cancer or in treatment of HIV infection).

The *meta*Register of the bank Current Controlled Trials [11] provides access to major registers making it one of the largest controlled trials resources in the world. Although its primary aim is to include information about ongoing controlled trials, the *meta*Register does include information about some completed trials. Research is makes by International Standard Randomised Controlled Trial Number or by keyword. The clinical trial is described in free text topics in which drugs or combinations tested appear in the title, hypotheses and interventions. The target pathology of the trial is in free text in the title and in the inclusion criteria. When a drug not yet marketed is tested, it appears as a code name. The «Study hypothesis" provides explanation for its mechanism of action. But it should be noted that trial results are not recorded in the bank. Its content does not provide answers to the question posed in this paper but rather information about the existence or not of an ongoing clinical research for a given disease.

The information from pharmacovigilance

When the drug is marketed, monographs include already the side effects observed during the completed trial. But the side effects are gradually supplemented by those that occur during the using of drug and by those that reported in the pharmacovigilance databases [12], but unfortunately this information are not public.

The new side effects are often described in the “case-reports” form published in journal indexed with MeSH keywords in Medline. They can next found via bibliographical engines like PubMed.

Drug classification

Drug Classifications allow classify drugs according to their chemical, pharmacological, therapeutic properties. Examples are the ATC (Anatomical Therapeutic Chemical Classification System), the supplementary concepts of MeSH and chemical and pharmacological classifications of MeSH.

These sources can help to qualify the novelty of a molecule, of a mechanism of action or chemical class. However, it should consider the updating time of these sources and how they are structured. Indeed, the introduction of a new class that could to call into question the structure of the resource. There is a risk to find innovations in classes like "not elsewhere classified", which will not be very useful.

1.2 Sources on the comparisons of drug treatments

Results of clinical trials

For all sources already mentioned joins articles indexed in PubMed. The summary of completed clinical trials can be obtained from the BioMed Central database [13]. The information is structured into 4 sections: a description of the trial, results, interpretation of results and conclusion.

Meta-analysis

The results of the meta-analysis and synthesis of literature are available in the Cochrane database [14]. But they were made later after the placing on the market the new drug. The content is presented in free text.

Clinical guidelines

The clinical guidelines are developed to help the physician in the care of the patient. They are written by the expert groups of scientific societies or national agencies. The clinical guidelines contain the results of clinical research that are graded according to level of evidence prepared by the experts. The clinical guidelines are based on the facts and their content is explicit. However, as the interval between publications is several years, the physician is confronted with the problem of obsolescence of information. Their structure evolves over time and differs much from a disease to another. In France, for example, they are available in PDF format, a fact which makes information extraction impossible at present.

Summary

This analysis has led to identify the main existing sources and nature of information that we can find (Table 1). Just after the marketing of the drug, the main sources are drug monographs published by the agencies and already structured in drug databases. At these resources are in addition the publication of clinical trial results and any publications which can be accessed from Pubmed.

Unfortunately, all sources are not exploited in the construction of the characterization tool of innovation. The information contained within sources on comparisons of drug treatments is not structured. Its use in the computerized tool of monitoring therapeutic becomes impossible.

The research of information for most of these sources is made from the name of the drug.

2. Example of tool developing for extracting information from the source DailyMed

As it was mentioned the most of sources provide information on the drug from its name. Nevertheless, the practitioner needs to find information about medicines from the health problem.

TABLE I. THE NATURE OF INFORMATION SOURCES

Source	**Nature of information**	**Comparative information**	**Information structured**
Drug monographs	Molecule, combination, form, route of administration, pharmaco-therapeutic class, mechanism of action, efficacy, safety	no	yes
Current clinical trials	Molecule, combination, mechanism of action, efficacy, safety	no	yes
Pharmacovigilance	safety	no	no
Drug classifications	Molecule, combination, pharmaco-therapeutic class, mechanism of action,	no	yes
Results of clinical trials	Efficacy, safety	yes	yes
Meta-analysis	Efficacy, safety	yes	no
Clinical guidelines	Molecule, combination, route of administration, efficacy, safety	yes	no

Our goal was to build a program that allows the extraction of information about a health problem to show that the contribution of each new drug.

We selected the site DailyMed to extract the maximum information about medicines. It is a source that contains monographs for all marketed drugs in the U.S. The files are in XML format. We used .Net technologies to extract information about the pathology "type 2 diabetes".

The created application can extract the brand name drug of the product marketed, the name of active ingredient, the mechanism of action and the number NDA / ANDA (New Drug Application / (Generic) Drug Approvals).

For pathology "type 2 diabetes" program identifies 129 products, because the file structure is quite heterogeneous and evolves over time. We took into consideration the structures used from 1999 because we focus on pharmaceutical innovation. The NDA may even appear many times, the fact that is linked to the existence of several presentations of the same product. The made program allows the user to find from the indication (diabetes type 2) the drugs that are marketed in the U.S. Using the Drugs@FDA Database, the NDA leads us to the type of pharmaceutical innovation and the importance of this innovation. For example, we find that the product Actos TM with the NDA 021073 has a new molecule (pioglitazone) as the type of innovation and this treatment is classified as a priority (P).

This example shows the limited nature of the classification proposed by the FDA, because the concept of pharmaceutical innovation is much larger and not limited only to characteristics specified by FDA. Similarly, it is difficult for the practitioner to understand the reduction of information about the therapeutic benefit only to priority treatment, standard treatment or orphan.

IV. CONCLUSION

This work has identified the main sources of information available at the time of marketing of the drug, which should allow to instantiate the model for each innovation. We have shown that these sources are heterogeneous relative to the type of information, structure and format. We created a program that shows the possibility to get information about the type of innovation and its impact using the data and the

classification proposed by the FDA starting the health problem.

To create a pertinent tool for characterization of pharmaceutical innovation is necessary to use several sources of information. Each described sources in this paper is important, but insufficient to characterize the drug at a time T, hence the interest for creating computerized tool that will judge the contribution of the latter.

At present our team is working on modeling of pharmaceutical innovation to provide its full description. For further we plan to use multiple sources of information with purpose to judge the drug as objectively as possible via computerized tool of monitoring therapeutic, which will allow the practitioner to deliver quality medical care in short time.

REFERENCES

[1] Drug Information: A Guide for Pharmacists. Malone P, Kier K, Stanovich J. (Eds.) New York: McGraw-Hill, 2006; pp. 533-45.

[2] Sermet C. La prise en compte de l'innovation thérapeutique dans les politiques de prix et de remboursement des médicaments. *RFAS* 2007; 3-4:319-341.

[3] Kassai V, Gueyffier F, Boissel J-P, Boutitie F, Cucherat M. Absolute benefit, number needed to treat and gain in life expectancy: which efficacy indices for measuring the treatment benefit? *JCE* 2003; 56: 977–982.

[4] U.S. Food and Drug Administration, Available: http://www.fda.gov/ForIndustry/DataStandards/StructuredProductLabeling/default.htm

[5] DailyMed, available: http://www.dailymed.nlm.nih.gov/

[6] Haute Autorité de Santé, Available: http://www.has-sante.fr/portail/jcms/c_672761/agrement-des-bases-de-donnees-sur-les-medicaments

[7] American Society of Health-System Pharmacists, (ASHP), available: http://www.ahfsdruginformation.com

[8] Banque de Données sur le Médicament Thériaque, available: www.theriaque.org

[9] Current Controlled Trials, avaible: http://www.controlled-trials.com

[10] Eudra Vigilance, Avaible: http://eudravigilance.emea.europa.eu/highres.htm

[11] BioMed Central, Journal of trials, Avaible: http://www.trialsjournal.com/

[12] The Cochrane Colaboration, avaible: http://www2.cochrane.org/reviews.

[13] Puntmann I, Schmacke N, Melander A, Lindberg G, Muhlbauer B. EVITA: a tool for the early evaluation of pharmaceutical innovation with regard to therapeutic advantage, *BMC Clinical Pharmacology* 2010; 10 (5): 1-11.

[14] Bolen S et al. Systematic Review: Comparative Effectiveness and Safety of Oral Medications for Type 2 Diabetes Mellitus. *Ann Intern Med* 2007; 147 (6): 389-400.

Silica Nanoparticles for Improving Efficiency of Virus-Like Particle Based Hepatitis B Vaccine

Marina ROMANOVA1, Yury DEKHTYAR1, Anna KACHANOVSKA1, Dace SKRASTINA2, Regina RENHOFA2, Paul PUMPENS2, Aloizijs PATMALNIEKS3
1 Riga Technical University, Institute of Biological Engineering and Nanotechnology, Latvia
marina.romanova@inbox.lv
2 Biomedical Research and Study Centre, Riga, Latvia
3 University of Latvia, Riga, Latvia

***Abstract* – Adherence of hepatitis B virus-like particles (VLP) to silica (SiO_2) nanoparticles was explored for immunomodulation purposes. Optical absorbance measurements, transmission electron microscopy and fluorescence microscopy were employed to study the adherence. The results demonstrated that hepatitis B VLP + SiO_2 complexes were formed. Preliminary immunological experiments with vaccination of Balb/c mice with the VLP only and VLP + SiO_2 complexes were performed. The vaccination with VLP + SiO_2 complexes resulted in increase in antibody production in mice blood. The amount of antibodies produced strongly depended on the concentration of SiO_2 nanoparticles. The observed results suggest that SiO_2 nanoparticles can be considered as a promising material for improving efficiency of VLP-based vaccines against hepatitis B viral disease.**

***Index Terms* – hepatitis B, optical absorbance, silica nanoparticles, vaccines, virus-like particles.**

I. INTRODUCTION

Immunomodulation can be used for viral disease prevention where vaccine with immune response-modulating agents stimulates immune system to respond effectively to a viral disease. Virus-like particles (VLP) can be used as immune response-modulating agents. VLP have a protein shell derived from a real virus but do not have any genetic viral material inside it that means that VLP are not infectious. VLP containing vaccine is injected into blood vessels and VLP are delivered by bloodstream to specific cells where they stimulate antibody production. Treatment efficiency is higher when concentration of VLP near the specific cells increases. However, high concentrations of VLP in human body might result in side effects. To eliminate this, high concentration of VLP can be provided only in a vicinity of the specific cells.

In order to reduce the overall concentration of VLP simultaneously increasing the local concentration near the specific cells, a number of VLP can be attached to a nanoparticle that will act as a carrier of VLP to the specific cells. It is known that electrical charge is localized at the surface of VLP [1], therefore, the latter can be attached to the nanoparticle due to the electrostatic interaction if the nanoparticle has an opposite charge. Thus, the nanoparticle must have the ability for polarization. In addition, the nanoparticle must be harmless to human body. Both conditions are met by SiO_2 nanoparticles [2,3].

The aim of the study was to verify capability of SiO_2 nanoparticles to attach hepatitis B virus-like particles and to investigate the immune response of the organism after vaccination with VLP-based vaccine with added SiO_2 nanoparticles.

II. MATERIALS AND METHODS

Hepatitis B VLP were synthesized by the Latvian Biomedical Research and Study Centre. Certified SiO_2 nanoparticles were bought from the Sigma-Aldrich. Size of the nanoparticles was equal to 10 – 20 nm.

To study the capability of SiO_2 nanoparticles to attach VLP, the optical absorbance spectra of VLP, SiO_2 nanoparticles and VLP+SiO_2 mixture in buffer solutions were recorded and compared. The Thermo Spectronic Helios Gamma spectrophotometer was in use to record absorbance spectra at wavelengths 200 – 1090 nm. The role of the buffer solution was to keep pH constant. The buffer solution was prepared from 20 mM Tris-HCl pH 7.8, 5 mM EDTA, 150 mM NaCl, and 1 litre distilled water. NaCl concentration was equal to the concentration in the physiological solution. The concentration of SiO_2 nanoparticles was 1 mg in 1 ml of the buffer solution. The concentration of VLP was 12 µl in 1 ml of the buffer solution that corresponded to the optical absorbance value 1 (± 5%) at wavelength 260 nm. The value 12 µl was chosen after calibration procedure. It was known from experiments that Hepatitis B VLP have the optical absorbance maximum at 260 nm. Therefore, to make the calibration, optical absorbance for different concentrations of VLP was recorded and the concentration where the optical absorbance was equal to 1 at 260 nm was chosen for convenience of further result processing.

To verify the VLP+SiO_2 adherence, transmission electron microscopy (TEM) and fluorescence microscopy (FM) were employed. JEOL JEM-1200EX microscope was in use for TEM, and Leica DMI 3000 B microscope for FM.

To record fluorescence, VLP were marked with the green FITC agent, which forms covalent bonds with VLP amino acids. Fluorescence was excited at 490 nm and detected at 515 nm.

Preliminary immunological experiments were performed to study humoral response of Balb/c mice after vaccination with the VLP+SiO_2 complexes. The vaccination was made on days 0, 14 and 28. Mice from the control group were vaccinated with VLP only diluted into sterile phosphate-buffered saline. Two weeks after the 3rd immunization (on the day 42) all animals were bled and anti-HBc antibody response was detected using the direct ELISA test.

III. RESULTS AND DISCUSSION

The optical absorbance spectra of the solutions (SiO_2, VLP, VLP+SiO_2) were tested on time stability. To test the time stability, the absorbance was recorded at once after preparation of the solutions and after 24 hours (Fig.1).

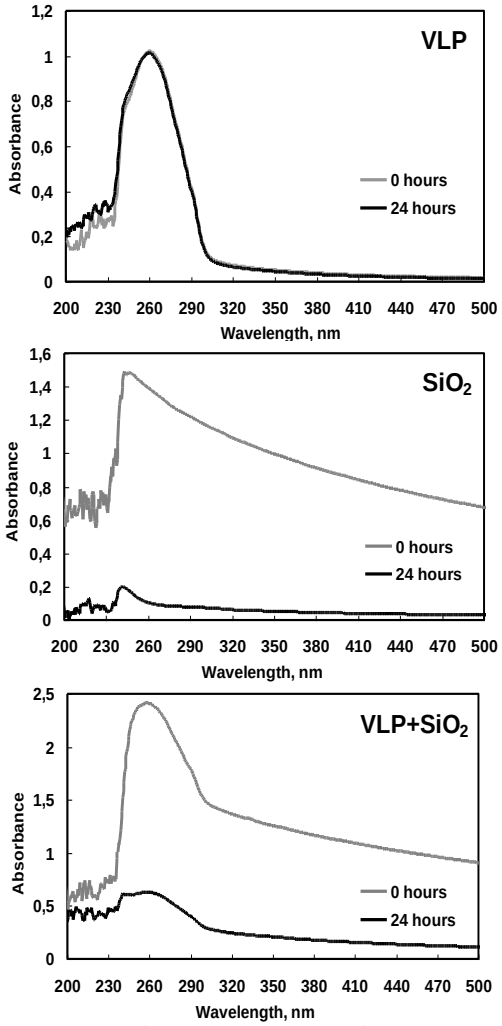

Fig. 1. Time stability of the optical absorbance of the VLP, SiO_2 and VLP+SiO_2 solutions.

The results demonstrated that the optical absorbance of the SiO_2 and VLP+SiO_2 solutions decreased after 24 hours and precipitations formed at the bottom of the test-tube. The precipitations could form due to gravitation forces which deflect the nanoparticles towards the bottom of the test-tube. However, the absorbance of the VLP solution did not change after 24 hours and no precipitations formed. Therefore, it was possible to suppose that VLP remain in suspended state in the buffer solutions at least within 24 hours.

The optical absorbance of the VLP+SiO_2 solution recorded in the experiment was compared with the theoretical optical absorbance value in order to see if VLP interact with SiO_2 nanoparticles. According to the spectrophotometry laws, the experimental and theoretical values must be equal if no interaction between the particles exists. To calculate the theoretical value, the absorbance of the VLP solution recorded experimentally at 260 nm was summed up with the absorbance of the SiO_2 solution recorded experimentally at 260 nm. Results demonstrated difference between the theoretical and the experimental values (Fig.2). The difference becomes more pronounced when the time given for VLP and SiO_2 interaction increases. That proves that VLP adhere to SiO_2 nanoparticles.

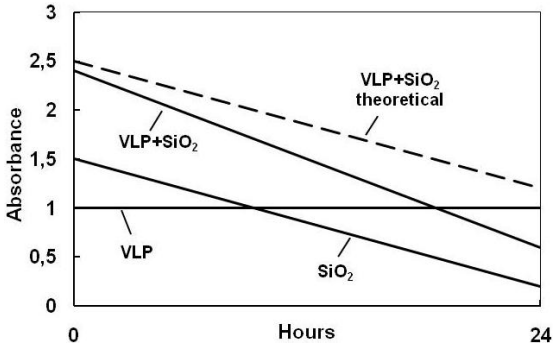

Fig. 2. Comparison between the experimental (solid line) and theoretical (dashed line) optical absorbance (at 260 nm) of the VLP+SiO_2 solution.

Both TEM (Fig.3) and FM (Fig.4) show the adherence of VLP to SiO_2 nanoparticles.

In case of FM, the VLP solution without the nanoparticles has homogeneous fluorescence. When SiO_2 nanoparticles are added, VLP adhere to them and fluorescence exists only in areas where VLP adhere to SiO_2 nanoparticles.

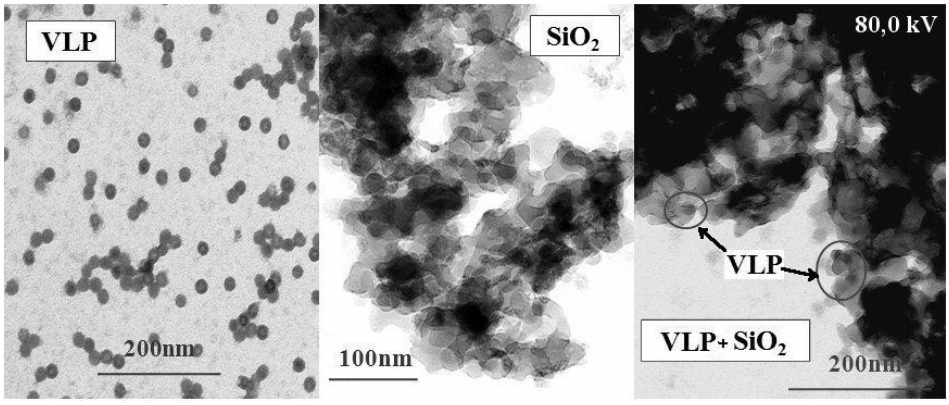

Fig. 3. TEM micrographs of the VLP, SiO_2, VLP+SiO_2 solutions.

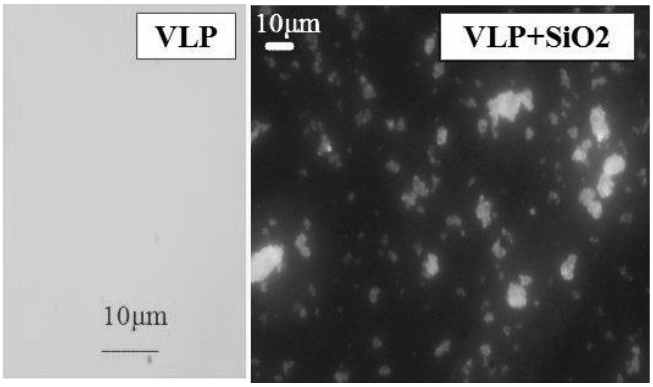

Fig. 4. FM micrographs of the VLP and VLP+SiO_2 solutions.

The results of the preliminary immunological experiment demonstrated that amount of antibodies produced in Balb/c mice blood depended on concentration of SiO_2 nanoparticles in the VLP+SiO_2 solution (Fig.5). The dose of VLP in the solutions was kept constant and was equal to 25 μg but concentration of SiO_2 nanoparticles varied thus resulting in different amounts of the VLP+SiO_2 complexes. VLP without SiO_2 nanoparticles induced lower antibody response than in case of the VLP+SiO_2 solution.

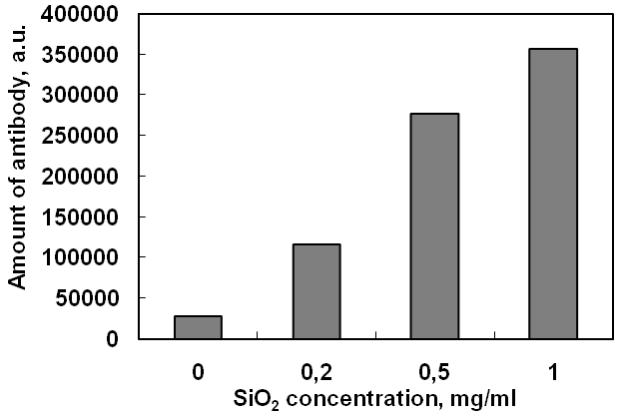

Fig. 5. Influence of concentration of SiO_2 nanoparticles in the VLP+SiO_2 solution on antibody production in blood of Balb/c mice.

Fig. 6 shows increment in amount of antibody production in mice blood in dependence on concentration of SiO_2 nanoparticles in the VLP+SiO_2 solution.

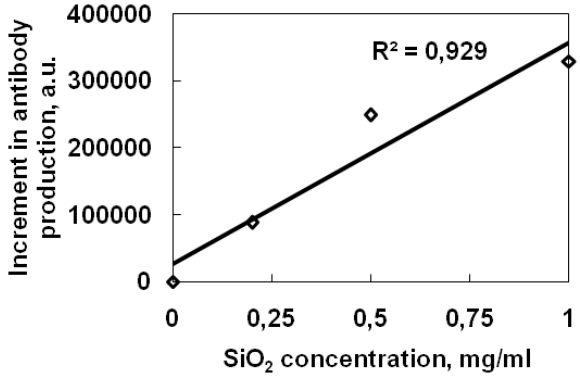

Fig. 6. Increment in antibody production in dependence on concentration of SiO_2 nanoparticles in the VLP+SiO_2 solution.

To calculate the increment value, the amount of antibody produced after vaccination with VLP only was subtracted from amount of antibody produced after the vaccination with VLP+SiO_2 solution. The results demonstrated that there was a good linear correlation (R-squared value was equal to 0,929) between concentration of SiO_2 nanoparticles and amount of antibodies produced in mice blood.

Optical absorbance and microscopy measurements prove that there is physical adherence between hepatitis B VLP and SiO_2 nanoparticles. The results of the immunological experiment evidence that vaccination with the VLP+SiO_2 complexes results in positive response in blood of Balb/c mice. It allows considering SiO_2 nanoparticles to be an effective material for efficiency improvement of VLP-based hepatitis B vaccines.

IV. CONCLUSIONS

1. Optical absorbance measurements, transmission electron microscopy and fluorescence microscopy demonstrate that there is a physical adherence between hepatitis B VLP and SiO_2 nanoparticles.
2. The correlation exists between increase in concentration of SiO_2 nanoparticles in the hepatitis B VLP + SiO_2 mixture and amount of antibodies produced in blood of Balb/c mice.
3. SiO_2 nanoparticles can be considered an effective material for efficiency improvement of VLP-based hepatitis B vaccines but further immunological studies are required.

REFERENCES

[1] Virus Particle Explorer, Human Hepatitis B Viral Capsid. Available: http://viperdb.scripps.edu/info_page.php?VDB=1qgt

[2] C. He-sheng, S. Zhen-ya, and X. Li-hui, "Properties of nano SiO_2 modified PVF adnesive", *Journal of Wuhan University of Technology-Mater. Sci. Ed.*, vol. 19, pp. 73-75, 2004.

[3] C. Sealy, "Silica key to drug delivery", *Nano Today*, vol. 1, p.19, 2006.

Collagen - Isolation and Perspectives of Application of Nature Nanomaterials

Elena MOCAN, Olga TAGADIUC, Tatiana REVENCU and Viorel NACU
State Medical and Pharmaceutical University"Nicolae Testemitanu"
labcellusmf@yahoo.com

***Abstract* – Through the extreme diversity of tissues and types of collagen it is difficult to develop a standard method of extraction for all types of collagen from different tissues. Two procedures based on acid- and enzymatic-soluble collagen isolation were combined and described some advantages and disadvantages of methods used in the present. Our results have demonstrated relatively low concentrations of collagen in the final solutions. There is 4,7 mg/ml from theoretically 10 mg/ml of acid-soluble fraction of collagen. Here are discussed the possibility to utilize the collagen, as fibrous structural protein with superior mechanical properties, that provides an intriguing example of a hierarchical biological nanomaterialas, for the construction of nanostructures with the required dimensions.**

***Index Terms* – collagen type I, methods of isolation and purification, nanomaterials, tissue engineering**

I. INTRODUCTION

Inspired by nature's ability to produce supramolecular nanostructures from the bottom-up, materials scientists have become increasingly interested in the use of biomolecules like DNA, peptides, or proteins as templates for the creation of novel nanostructures and nanomaterials [1].

Collagen is an exemplary type of robust biological nanostructure built from simple building blocks. It is the most abundant protein in modern vertebrates, comprising approximately 30% of the total protein content and 70% of the dry weight of human skin. Collagen provides the three-dimensional matrix for connective tissue types such as bone and cartilage [5].

Numerous studies have demonstrated that collagens can induce or regulate many cellular functions and processes such as cells differentiation, motion, communication and apoptosis [4, 5]. But its main function is the formation of insoluble fibrils with high strength characteristics.

Collagen is the major component of the extracellular matrix and more than 27 genetically isoforms have been identified. Collagen type I, II and III are the most abundant widely used as a plastic material in different medical domains, cosmetology, and in the pharmaceutical industry as a compound that provide drugs action [3, 4]. Type I collagen has been described as a natural scaffold and a potential candidate for tissue engineering and reconstructive medicine [6]. Such diverse functions are due to physical and chemical properties of collagen protein.

At physiological conditions, the individual collagen molecules of approximately 300 nm length and 1.5 nm diameter aggregate longitudinally and bilaterally to microfibrils and further to fibrils (fig. 1). Thus it is a nanostructured carcass with possibility to carry out the assembly of protein complexes [1]. Collagen consists of tropocollagen molecules that have lengths of L ~280 nm and diameters of ~1.5 nm, leading to an aspect ratio of ~190 [12–14]. Staggered arrays of tropocollagen molecules form fibrils, which arrange to form collagen fibers (Fig. 1).

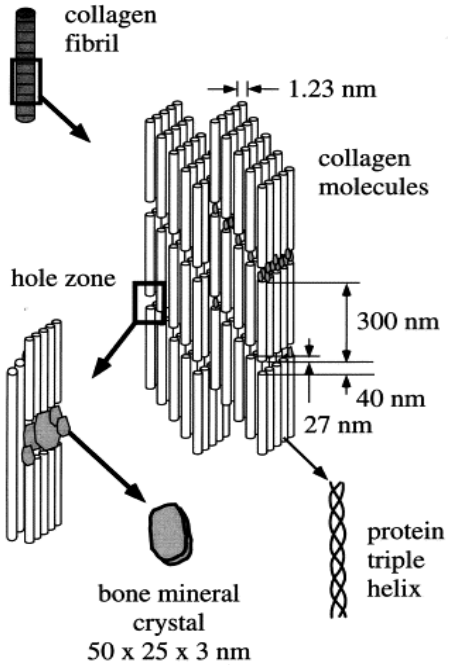

Fig. 1: Nanostructure of natural bone [Rho 1998]

Type I collagen is trimeric [$(\alpha 1)_2$ α 2] and exists as triple helix. The helices have the typical repeats for collagen Gly-X-Y (where X and Y are mainly Pro and Hyp). Thus, proline and hydroxyproline constitute about 23% of the total protein sequence and structure Gly-Pro-Hyp is often founded [4]. Its unique tertiary structure is a right-handed triple helix composed of three helical peptide strands (left-handed polyproline II-type).

Through the extreme diversity of tissues and types of collagen it is difficult to develop a standard method of extraction for all types of collagen. The number of the covalent intermolecular interactions in collagen structure increases in time and frequently determines almost full insolubility in solvents utilized to dissolve proteins [7].

The main task of our study was to analyze the known methods of collagen isolation and purification. Obtained solid-phase collagen could be a promising platform for generation of new and interesting nanostructured materials [11]

II. MATERIAL AND METHODS

*The collagen source***.** Type I collagen was isolated from steer (3 years old) flexor bovine tendon. Fixed mass of tendon was suspended in cold distilled water at 4^0 C and water was changed two times per day for three days. The tendon fibers were cut into small pieces (1 cm in length) and pulverized in a mill after that. Pieces were dried 24 h in the thermostat at 40^0 C.

Method of collagene isolation

The procedure is based on the extraction of collagen from the tendon pieces in organic acid (0,5M CH_3COOH) in the presence of 5mM EDTA and pepsin with concentration 0,05 g per 100 g of tissue, pH = 2,5 - 3,0 for 48-96 h at 4^0C.

III. RESULTS AND DISCUSSION

After testing several collagen isolation' procedures [2, 4, 5] we have chose the method based on acetic acid dissolution of collagen fibers with some modifications. One of them is introduction of the neutral salt or low ionic strength acidic solutions.

We have combined these two procedures based on acid- and neutral-salt extraction with enzymatic collagen isolation. Several types of soluble collagen are distinguished depending on the specific protein solvent: neutral salt-soluble collagen, acid-soluble collagen and enzymatic-soluble collagen. Thus a combined approach was developed which includes pepsin digestion in acidic solution.

Our results have demonstrated relatively low concentrations of collagen in the final solutions – 4,7 mg/ml.

Although the method of extraction based on acetic acid and pepsin dissolution was standardized more than 40 years ago, it still has two major problems.

First, the collagen solubility is still ill-defined due to cross-link mediated aggregation, so that the reproducibility of the collagen preparations is poor. Secondly, the collagen peptides, especially the short non-helical regions of collagen, are susceptible to proteolysis/hydrolysis during the isolation [4, 9].

For this reason the utility of the acidic-extracted collagen is limited, since the isolated material must be stored in cold acetic acid solution or dried. The maximal obtainable concentration of collagen is also limited to 10 mg/ml [4] as estimated by wet weight and also by amino acid content. The methods of collagen isolation, purification and determination should be modified, using new strong detergents for deeper dilution of collagen fibers, on purpose to overcome the disadvantages of its partial degradation.

A major requirement of collagen purification the elimination of the antigenic components of the protein represented by the telopeptide regions of collagen type I that can be more efficiently when treated with pepsin. However, collagen extracted from animal sources presents a small degree of antigenity, that's why it is considered acceptable for tissue engineering in humans [4].

There is an important problem to control the construction of nanostructures from collagen with the required dimensions.

Despite significant research effort over the past couple of decades, the geometry and typical length scales found in collagen fibrils, the deformation mechanisms under mechanical load, and, in particular, the relationship between those mechanisms and collegen's molecular and intermolecular properties, are not well understood. Moreover, the limiting factors of the strength of collagen fibrils and the origins of toughness remain largely unknown [12].

Some experimental efforts focused on the deformation mechanics of collagen fibril at nanoscale, including the characterization of changes of D-spacing and fibril orientation [13-15], analyses that featured x-ray diffraction [13] and synchrotron radiation experiments [14]. Other experimental studies were focused on the averaged response of arrays of collagen fibrils, considering nanoscale deformation mechanisms [12, 24].

To develop a fundamental and quantitative understanding of collagen mechanics, it is critical to develop theoretical models encompassing the mesoscopic scales between the atomistic and macroscopic levels [12]. There exists no model that links the properties of individual molecules with the overall mechanical response of fibrils or fibers, considering the different types of chemical bonding and nanoscale mechanics and geometry. The role of the staggered structure and the reasons for the specific length scales and high aspect ratio of TC molecules remain unexplained.

An improved understanding of the nanomechanics of collagen may help in the development of biomimetic materials or for improved scaffolding materials for tissue engineering applications [17].

Buehler [12] has used a hierarchical multiscale modeling scheme based on atomistic and molecular simulation to describe the mechanical properties of collagen under large stretch, leading to permanent deformation or fracture. There was shown that the key to understanding the mechanics of collagen is to consider the interplay between the mechanics of individual tropocollagen molecules with characteristic length scales, the intermolecular chemical interactions, and the mesoscopic properties arising from hundreds of molecules arranged in fibrils. It was explored the mechanics of collagen by considering different nanostructural designs, and pay specific attention to the details of molecular and intermolecular properties and their impact on the mechanical properties.

Energetic effects rather than entropic contributions govern the elastic and fracture properties of collagen fibrils and fibers. The fracture strength of individual tropocollagen molecules is largely controlled by covalent polypeptide chemistry. The shear strength between two tropocollagen molecules is controlled by weak dispersive and hydrogen bond interactions and by some intermolecular covalent cross-links.

Some studies have suggested that the length of tropocollagen molecules and strength of intermolecular interactions plays a significant role in determining the deformation mechanics, explaining some of the structural features of collagen found in nature.

Key concepts that can be adopted from self-assembly found in nature include molecular recognition of the single building blocks and the formation of predictable three-dimensional nanostructures [1, 9, 10].

Pioneered by Braun, Belcher, and their coworkers, there have been numerous examples of DNA or viruses as scaffolds for complex nanostructured inorganic materials [8–11]. Since the nucleobase or amino acid sequence encodes how these scaffolds self-assemble, a variety of programmed nanostructures can be produced [1, 10, 11].

Although DNA can be readily synthesized, it is composed of a small number of similar monomers. As a result, some

approaches have combined DNA and proteins to create functional nanomaterials [1]. In contrast, peptides and proteins are built from 20 proteinogenic and a wide variety of non-natural amino acids. This leads to chemical diversity, evident by the display of aliphatic, acidic, basic, or aromatic side chains from a peptide backbone, and structural complexity, manifested by the multitude of possible molecular architectures like helices, β-sheets, and tubules [1, 8].

Working with live systems, we can use "natural nanotechnology", that mean an ability to link proteins individually with other proteins or other substances to form complexes with desired properties. These so named collagen-binding domains can be used:

- for creating artificial surface for the cultivation of eukaryotic cells;
- as drugs that accelerates wounds and burns healing;
- to prolong the drug effect;
- as drugs that promote early fracture consolidation;
- as composite materials, for implant coating [1, 5, 10, 11].

IV. CONCLUSIONS

Recent studies in cell biology, nanotechnology, and computation gave more new insights regarding the physical proprieties, that in complex with the chemical one, can regulate cell signaling and gene expression. Due to the importance of biocompatible matrixes for tissue engineering and their application in medical technology, the availability of native collagen should be studied by refining the collagens extraction procedure. It is very important to elaborate the method of collagen isolation that give us fully or partially soluble collagen that can be used in producing by tissue engineering of matrices, powder, sponges, fibers or filaments.

V. REFERENCES

[1] Gottlieb D., Morin S. A., Song J. and Ronald T. J. Mater. Chem., 18, 3865–3870, 2008.
[2] Chandrakasan, G., Torchia, D. A. and Piez, K. A., J Biol Chem, 251, p.6062-6067, 1976.
[3] Miller, E.J., and K. Rhodes, R. Academic Press. p. 33-64, 1982.
[4] Rajan, N., et al., Nat. Protocols, 1, p. 2753-2758, 2007.
[5] Xin Xiong dissertation. New Insights into Structure and Function of Type I Collagen, p. 111, 2008.
[6] Rele S., Song Y. H., Apkarian R. Qu P., Z., Conticello V. P. and Chaikof E. L., J. Am. Chem. Soc.,14, p. 129, 2007.
[7] Kotch F. W. and Raines R. T., Proc. Natl. Acad. Sci. U. S. A., 103, p. 3028, 2006.
[8] Naik R. R., Stringer S. J., Agarwal G., Jones S. E. and Stone M. O., Nat. Mater. 1, p. 169, 2002.
[9] Ma N., Sargent E. H. and Kelley S. O., J. Mater. Chem., 18, p. 954, 2008.
[10] Zhang S., Nat. Biotechnol., 21, p. 1171, 2003,.
[11] Papapostolou D., Smith A. M., Atkins E. D. T., Oliver S. J., etc. Proc. Natl. Acad. Sci. U.S.A., 104, p. 10853. 2007.
[12] Buehler M. J. PNAS. vol. 103, 33, p. 1228–1229, 2006.
[13] Hulmes, D. J. S., Wess, T. J., Prockop, D. J. & Fratzl, P. Biophys. J. 68, p. 1661–1670, 1995.
[14] Puxkandl, R., Zizak, I., Paris, O., Keckes, J., Tesch, W., Bernstorff, S., Purslow, P. & Fratzl, P. Philos. Trans. R. Soc. London Ser. B 357, p.191–197. 2002.
[15] Sasaki, N. & Odajima, S. J. Biomech. 29, p.1131–1136, 1996.
[16] Orgel, J. P. R. O., Irving, T. C., Miller, A. &Wess, T. J. Proc. Natl. Acad. Sci. USA 103, p. 9001–9005, 2006.
[17] Yung, Y. C. & Mooney, D. J., Bronozino, J. D in CRC Biomedical Engineering Handbook. (CRC, Boca Raton, FL), chap. 6, pp. 1–14, 2006.
[18] Gupta, H. S., Wagermaier, W., Zickler, G. A., Aroush, D. R. B., Funari, S. S., Roschger, P., Wagner, H. D. & Fratzl, P. Nano Lett. 5, p. 2108–2111, 2005.

FUNDING

This research work was and is supported by Academy of Sciences of Moldova grants 06.420.049A, 09.819.09.02F and 11.817.09.23A

]

Colloidal Nanosilver – a Product of Nanotechnology

Corina SCUTARI[1] Veaceslav GONCIAR[2] Ivan CEKMAN[2,3] Nadejda GORCEACOVA[3,4]
[1]Assistant professor in the department of Pharmacology and clinical pharmacy of State Medical and Pharmaceutical University „N. Testemitanu"
E-mail: doctorscutari@mail.ru, tel. 068687788.
[2]Professor, head of the department of Pharmacology and clinical pharmacy of State Medical and Pharmaceutical University „N. Testemitanu"
[3]„A.A.Bogomoleţ", Kiev
[4]Professor of the department of Pharmacology and clinical pharmacy of National Medical University

***Abstract* – In a review literary data and results of own investigations of colloidal nanosilver bases are summarized. A wide range of antimicrobial action of silver, the lack of resistance to it, effective against most pathogenic microorganisms, low toxicity, lack of data in the literature about the allergic properties , as well as good tolerability of patients - have contributed to increased interest in silver, in many countries around the world. Colloidal Silver is the safest and most potent natural antiseptic for the human body, that overwhelm over 700 species of pathogens, including staphylococcus, streptococcus, bacteria dysentery, typhoid, etc. It is proved that the water contaminated by high concentrations of bacteria became sterile after one or two hours from the introduction of the silver in amount up to 1 mg/l and maintained for many days. The drug is actively involved into reducing life and termination of pathogen bacteria, viruses, fungi and parasites, stimulate the protective mechanisms of the human body. In this case, it does not affect the benefic microorganisms. Silver by intravenous administration is successfully used for the treatment of septic arthritis, rheumatism, rheumatic endocarditis, rheumatoid arthritis, asthma, influenza, acute respiratory infections, bronchitis, pneumonia, purulent septic diseases, brucellosis, inside - in the treatment of gastritis, gastro-duodenal ulcers, externally - in the treatment of sexually transmitted diseases, septic wounds and burns. The results obtained in different studies on the effect of silver nanoparticles on the organisms are rather contradictory, but to forget about the relevance of this issue is not worth it.**

***Index terms* - antimicrobial activity, colloidal, nanoparticles, nanosilver, silver.**

I. INTRUDUCTION

Nanoparticles of various materials are used everywhere - from paint to food industry. The most "popular" are nanoparticles of silicon oxide, gold, silver, zinc oxide and titanium dioxide [1, 2].

A wide range of antimicrobial action of silver, the lack of resistance to it, efficiency against most pathogenic microorganisms, low toxicity, lack of data in the literature about the allergic properties of silver, as well as good tolerability of patients - have contributed to increased interest in silver, in many countries around the world.

Colloidal nanosilver – a product consisting of silver nanoparticles suspended in water and containing a colloidal stabilizer system (Figure 1). The typical size of silver nanoparticles - 5-50 nm. The fields of application of silver nanoparticles may be different: the spectral-selective coatings for solar energy absorption, as catalysts for chemical reactions, microbial sterilization [2, 7]. The last area of application is the most important and includes the production of various means of packaging, bandages and water-based paints and enamels [3].

Currently, based on some colloidal silver manufactured products – were obtained biologically active additives with antibacterial, antiviral and antifungal activity. However, the impact of silver nanoparticles on the biological effects remains open.

The study of the healing effect of colloidal silver began in the second half of the XIX century after the discovery in 70's years by German gynecologist Charles Creed of antigonorrheal effect of silver nitrate solution of 1% . This discovery allowed to liquidate in Germany hospitals gonorrheal purulent inflammation of the eyes in the newborn. In fact, from that moment began a new century in the study of dangerous bacterial infections prevention [10].

On 23 August 1897 a German surgeon Bennett Creed, continuing his father's research, reported at the XII International Congress of Doctors in Moscow about the broad possibilities of silver preparations application in purulent surgery and some good results of septic infection treatment by the intravenous administration. Then B. Creed and other chemists suggested preparations containing silver in the non-ionized state: in the form of colloidal particles of metallic silver (the drug collargol) and silver oxide solution (protargol), modifications which are used in medicine for more than hundred years. In contrast to previously used silver salts they had no cauterizing effect [5, 6].

In Russia, colloidal silver also was appreciated by doctors who contributed to its increased use in the military field surgery in Russian-Japanese War in 1904. Silver by intravenous administration is successfully used for the treatment of septic arthritis, rheumatism, rheumatic endocarditis, rheumatoid arthritis, asthma, influenza, acute respiratory infections, bronchitis, pneumonia, purulent septic diseases, brucellosi, inside – in the treatment of gastritis, gastro-duodenal ulcers, externally - in the treatment of sexually transmitted diseases, septic wounds and burns [6, 10].

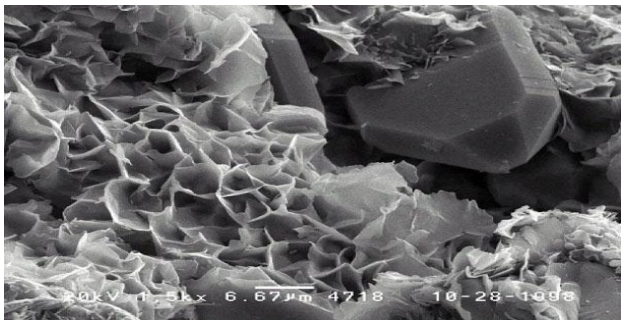

Fig.1. Colloidal nanosilver.

In 1910, the firm "Heiden", summarizing the experience of the practical application of silver in medicine, produced an annotation review of the treatment method of various infections: abscesses, typhoid fever, relapsing fever, inflammation of lungs, sinuses, middle earinfection, gingivitis, gonococcal sepsis, diphtheria toads, dysentery, keratitis, conjunctivitis, leprosy, chancroid, mastitis, meningitis, epilepsy, erysipelas, anthrax, syphilitic ulcers, amyelotrophy, acute articular rheumatism, trachoma, sore throat, boils, cystitis, endocarditis, endometritis, chorea, epididymitis, an ulcer of the cornea [16, 17].

With the discovery of antibiotics and sulfonamides the interest to the drugs of silver declined slightly. But recently, the antimicrobial properties of silver began again to attract attention to itself. This is due to the increase of allergic complications caused by antibiotic therapy, the toxic effects of antibiotics on the internal organs and immune suppression, the emergence of fungal respiratory and dysbiosis after prolonged antibiotic therapy, as well as the emergence of resistant strains of pathogens to antibiotics used [7].

The increased interest in silver has arisen again in connection to the identification of its action in the body as a trace element necessary for normal functioning of organs and systems, immune correcting, as well as powerful antibacterial and antiviral properties [8].

Effectiveness of bactericidal action of colloidal silver due to the ability to suppress the activity of the enzyme which provide oxygen metabolism in protozoa. Therefore, the simplest alien microbes die in the presence of silver ions due to violations of oxygen supply required for their live lihoods [10].

Modern studies of colloidal silver ions showed that they possess a pronounced ability to neutralize vaccinia virus, some strains of influenza virus, enterovirus and adenovirus. In addition, they provide a good therapeutic effect in the treatment of viral enteritis at dogs and swine. At the same time showed the advantage of colloidal silver therapy compared with standard therapy [11, 12].

It was observed beneficial effects of colloidal silver ions on the healing of venous ulcers developing in poor circulation of the lower extremities. In any case, there were no side effects of treatment with silver. Now one of the fastest developing areas of modern nanotechnology - the creation and use of nanoscale particles of different materials. As is known, silver is the most powerful natural antibiotic from all that exists on Earth. It is proved that silver can destroy more than 650 species of bacteria, so it was used by humans for the destruction of various microorganisms for thousands of years, indicating its stable antibiotic effect. Colloidal nanosilver is a product consisting of microscopic silver nanoparticles suspended in demineralized and deionized water. This high technology product is obtained by the electrolytic method [9, 10]. Typical silver nanoparticles have dimensions of 25 nm. They have extremely large specific surface area, which increases the contact area of silver with the bacteria or viruses, greatly improving its bactericidal action. Thus, the use of silver nanoparticles allows hundreds of times lower concentration of silver, while preserving all of bactericidal properties.

Bactericidal agent based on silver nanoparticles is one of the latest achievements of domestic science in the field of nanobiotechnology. The silver's action is not specific for infection (like antibiotics), and on cellular structure. Any cells without a chemically resistant wall (such a cellular structure are bacteria and other organisms without cell walls, for example, extracellular virus) exposed to silver. Since mammalian cells have a membrane completely different type (not containing peptidoglycans), silver in no way affects them. Scientists have observed the silver nanoparticles within the embryos at different developmental stages: development, deformed and dead. According to the results of observations showed that the biocompatibility and toxicity of silver nanoparticles strongly depend on the dose of nanoparticles with a critical concentration of 0.19 nm [9, 16].

Unlike other methods, a separate nanoparticle can be directly mapped in the developing embryos in a nanometer resolution. This method offers new opportunities to study events in real time, leading to abnormalities in the development of embryos.

Physical properties of silver nanoparticles differ from those of the same silver (eg, reducing the size of the particle leads to a decrease in its melting temperature).Technologists have learned to produce nanoparticles of different sizes, shapes and chemical composition. But they do not know how to control the number and the type of defects in the nanoparticles. Therefore, the question of the influence of the nanoparticules defects on its characteristics are unresolved. Meanwhile, it is known that defects can lead to very significant change in the properties of the nanoparticles [14, 15].

Scientists of the University of Maryland (University of Maryland, USA) have developed a technology that allows to produce silver nanoparticles with same size, but are either monocrystalline or contain large numbers of twins - regions with different crystallographic axes orientations. The interface between such areas are a special kind of defects (the so-called defects of twinning). This technology is based on the use of nanoparticles for the synthesis of various polymeric precursors – silvertriphenylphosphine $(PPh_3)_3$3Ag-R with different functional groups (R = Cl or NO_3). If, R = NO3 then from the embryos grow twinned bass and if R = Cl - twin-free (see fig. 2). The formation of silver nanoparticules with a specific feature includes Cl-ions, that block the formation of twins. The average size of nanoparticles was 10.5 nm. Studies have shown that physical and chemical properties of these two types of nanoparticles are significantly different. For example, in interaction with selenium, from the twin-free nanoparticles were prepared hollow nanoparticles Ag_2Se, and from the twinned - solid homogeneous nanoparticles.

This is because the difference of Ag and Se diffusion coefficients in the crystal lattice promotes the formation of vacancies (the accumulation of which eventually forms the cavity inside the NP), whereas the atoms Se, moved not by

the lattice but along the boundaries of twins, easily penetrate these boundaries of Ag, resulting in a homogeneous nanoparticles Ag_2Se. In twinned nanoparticles, the electronic subsystem after the laser pulse is much more rapid cooled (due to the transfer of energy to the lattice). This suggests that the twin boundaries enhance the electron-phonon interaction, which can be adjusted by varying the concentration of defects in the nanoparticles.

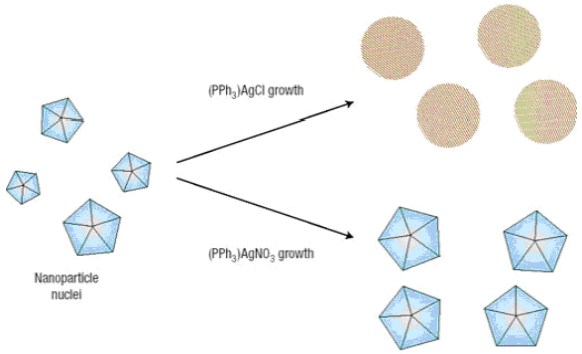

Fig. 2. Growth of twin-free and twinned silver nanoparticles of different precursors.

The Concern "Nanoindustry" from Ukraine has developed technology of silver nanoparticles production, stable in solution and in adsorbed state. The resulting products have a broad spectrum of antimicrobial action. Thus, appeared the opportunity to create a whole range of products with antimicrobial properties with little change of technological process by producers of existing products.

Silver nanoparticles can be used to modify the traditional and creation of new materials, coatings, disinfectants and detergents (including dental and scouring pastes, detergents, soaps), cosmetics. Coatings and materials (composite, textile, paint, carbon and others), modified with silver nanoparticles can be used as a prophylactic antimicrobial protection agents in places where an increasing danger of contamination with infections: in transportation, public catering enterprises, in the agricultural and pastoral areas , children's, sports, and health care institutions. Silver nanoparticles can be used for water purification and destruction of pathogens in the filters of air conditioning systems, swimming pools, showers and other similar places.

Colloidal Silver is the safest and most potent natural antiseptic for the human body, that overwhelm over 700 species of pathogens, including staphylococcus, streptococcus, bacteria dysentery, typhoid, etc. It is proved that the water contaminated by high concentrations of bacteria flexneri (dysentery), Ebert (typhoid fever), staphylococcus, streptococcus, etc., became sterile after one or two hours from the introduction of the silver in amount up to 1 mg/l and maintained for many days [5, 12].

The drug is actively involved into reducing life and termination of pathogen bacteria, viruses, fungi and parasites, stimulate the protective mechanisms of the human body. In this case, it does not affect the benefic microorganisms. At the same time, all bacteria and viruses are killed within 6 minutes of exposure to the colloidal silver. The medical center of the New York University, Department of Orthopedics, were made the study of silver ions action in patients with postoperative infectious complications. From the report of the work: "For 12 out of 14 patients, treatment was successful, and in all 14 treatment led to the undoubted reduction of bacterial flora in the wound, as shown by direct counting of the colony. In no case was shown unwanted effects of treatment with silver. "Silver compounds are used to treat 70% of cases of burns in the USA.

An interesting fact is that more than half of the world's airlines use water treated with silver, as a way to protect the passengers from infections such as dysentery. In many countries, colloidal silver ions are used to disinfect water in swimming pools [11, 12].

Silver, silver ions and silver nanoparticles are generally considered safe enough for people. Nevertheless, recent studies have shown that nanoparticles penetrate into the cells and damage the genotype. There is even reason to believe that silver nanoparticles can actively enter cells by endocytosis. Inside the cell, hydrogen peroxide formed during cell respiration, oxidizes the silver nanoparticles and frees them from the silver ions, thus increasing their toxicity. Consequently, we may even suggest that silver nanoparticles may be cyto- or genotoxic. In addition, it was shown that silver nanoparticles penetrate the skin through pores and glands. If the skin is damaged, it facilitates the penetration of silver particles through the skin.

The data obtained from different studies on the effect of nanoparticles on the organisms are rather contradictory, but to forget about the relevance of this issue is not worth it. Thus, it is important to continue the investigations of silver nanoparticles effect on living organisms and to create methods for detection of nanoparticles in the environment.

REFERENCES

[1] А.В. Бгатов. Биогенная классификация химических элементов// http://www.nisleda.net/…e-bgatov.htm «Философия науки», 2 (6), 1999.

[2] N. Silvestry-Rodriguez, K.R.Bright, D.R.Uhlmann, C.P.Gerba. "Inactivation of Pseudomonas aeruginosa and Aeromonas hydrophila by silver in tap water"//Environmental Science and health, 42 (11), 2007.

[3] Л.А. Кульский. Серебряная вода, Киев, 1987.

[4] Л.В. Григорьева. Водоподготовка и очистка промышленных стоков, Киев, 1973, Вып.10, с. 9–13.

[5] В.С. Брызгунов, В.Н.Липин, В.Р. Матросова. Сравнительная оценка бактерицидных свойств серебряной воды и антибиотиков на чистых культурах микробов и их ассоциациях// Научн.тр.Казанского мед.ин-та, 1964, т.14, с. 121–122.

[6] J.B.Chappel, G.D. Greville. Effect of silver ions on mitochondrial adenosinetriphosphates// Nature (London). 1954, vol.174, p. 930–931.

[7] А.В. Безлепко Кандидат медицинских наук (Главный военный клинический госпиталь имени академика Н. Н. Бурденко) и Гуща И. А. Кандидат медицинских наук (ОАО «ДИОД») Инструкция по медицинскому применению ионного и коллоидного серебра.

[8] Э.Ш.Савадян, В.М.Мельникова, Г.П. Беликова. Современные тенденции использования серебросодержащих антисептиков// Антибиотики и химиотерапия, 1989, N.11, с. 874–878.

[9] R.Doer, W. Zur Bergner. Oligodinamie des Silbers// Biochem. Zeitschr, 1922, N131, p. 351–356.

[10] Мироненко Ю.П. Полостной электрофорез// Медицинская газета, 1971.

[11] А.М.Войтенко Водоподготовка и очистка промышленных стоков. 1973., вып.10., с.128–134.
[12] Лот Таранов, Ирина Филиппова Серебряная вода, Метод Таранова// Диля, 2001 г, с. 25-30
[13] Ю.П.Ульянов, Доктор мед.наук, Зав. Лор-отделением Медицинского Центра «АГАМИ» (Москва) //Проблемы серебряно-зависимых людей.
[14] Е.Родимин. Приготовление целебных медно-серебряных растворов и металлоионотерапия http://www.rem.org.ru/book.htm.
[15] A.R.Shahverdy, Ali Fakhimi, Sara Minaian. Synthesis and effect of silver nanopracles on the antibacterial activity of different antibiotics against Staphylococcus and Escherichia coli// Nanovedicine-Nanotechnology biology and medicine, 3(2): 168–171 Jun 2007.
[16] Eric J. Rentz, DO, MSc Historic Perspectives on Clinical Use and Efficacy of Silver.
[17] Rami Pedahzur, Ovadia Lev, Badri Fattal and Hillel I. Shuval The interaction of silver ions and hydrogen peroxide in the inactivation of E. coli: a preliminary evaluation of a new long acting residual drinking water disinfectant// Water Science and Technology, 1995, Vol 31, No 5–6, p. 123–129 © IWA Publishing 1995.

Synthesis of CdSe Nanoparticles and Their Effect on the Antioxidant Activity of Spirulina Platensis and Porphyridium Cruentum Cells

V. RUDIC*, L. CEPOI*, L. RUDI*, T.CHIRIAC
A. NICORICI**, A. TODOSICIUC**, T. GUTSUL**
* Institute of Microbiology and Biotechnology
E-mail: *lilianacepoi@yahoo.com*
**Institute of Electronic Engineering and Nanotechnologies "D. Ghitu"
E-mail: *tatiana.g52@mail.ru*

***Abstract* – Single-crystalline cadmium selenide nanoparticles were obtained using HTSPS synthesis. X-Ray powder diffraction and transmission electron microscopy were used to confirm the crystallinity and morphology of the resulting nanoparticles. To study the action of CdSe on antioxidant activity, we selected two biotechnological important strains of microalgae: cyanobacteria *Spirulina platensis* and red microalga *Porphyridium cruentum*. In the case of *Porphyridium cruentum*, the obtained results demonstrated an increase in the productivity. For *Spirulina platensis*, the presence of the compound in the cultivating medium decreased the productivity of cyanobacteria.**

***Keywords* - CdSe nanoparticles, HTSPS synthesis, antioxidant activity, colloidal solutions**

I. INTRODUCTION

Nanomaterials are considered promising modifiers of surface structures of cells. For example, well known polymers, microparticles, nanoparticles, and their possible combinations are widely used in these scopes. Several papers described the immobilization of nanoparticles on the surface of various cells. In particular, they showed the deposition of gold nanoparticles on the surface of *E. coli* cells in order to form electrical microcontacts. Complexes of nickel nanoparticles and the bacterial cells were obtained and characterized in order to design magnetic microdevices on their basis. The surface of yeast cells *Kluveromyces fragilis* was modified with magnetic nanoparticles, resulting in effective sorbents, which were obtained on the basis of magnetized cells. Thus, the study of the interaction of nanomaterials with living cells is of particular interest and is caused by the fact that hybrid systems based on nanomaterials and living cells can be prepared and used to identify the toxic properties of nanomaterials, which is aimed at changing the properties of cells, regulating their physiological activity, and visualizing cellular organelles as well as for high-precision spectral identification of living cells based on differences in biochemical composition of their surface structures [1]. In this connection, it is extremely urgent to find methods of the immobilization of nanomaterials on cell surfaces that will allow them to maintain physiological activity.

II. METHODS

Chemicals**.** Tri-*n*-octylphosphine (Aldrich, 90%), amorphous selenium shot (Aldrich, 99.999%), squalane (Aldrich, 99%), diphenyl ether (DPE) (Fluka, 98%), cadmium acetate dihydrate (Aldrich, 99.99%), and oleic acid (cis-9-octadecenoic acid, Aldrich, 90%) were used as purchased without further purification. Anhydrous ethanol, hexane, chloroform, acetone, tetrachloroethylene, and trichloroethylene were purchased from different companies and used without further purification. Trioctylphosphine telluride (0.75 M, TOP-Se) was prepared by the complete dissolving of the necessary amount of tellurium in 50 ml of TOP at 60–70°C under moderate stirring. The TOP-Se solution described above was prepared and stored in a nitrogen glove box.

The microalgae cultivating and obtaining of extracts from biomass. The strains of *Porphyridium cruentum* and *Spirulina platensis* were cultivated under laboratory conditions. Water extracts were prepared from native biomass by freezing, and ethanol extracts were derived with 70% ethanol in ratio 1/10 (w/v).

Synthesis. The HTSP method was used as the basis for preparing cadmium selenide nanoparticles. A standard synthesis of CdSe nanoparticles was performed in a round-bottom three-neck flask equipped with a magnetic stirrer, a thermocouple, and a temperature control unit. Cadmium oleate was prepared by heating a mixture of 2 mmol cadmium acetate, 4 mmol of oleic acid, and 20 mmol of squalane or 20–25 ml of diphenyl ether. Oleic acid was employed both for group II precursor formation and nanoparticle stabilization during the synthesis intended for nucleation and reaction rate control. This solution was heated under vacuum at 75–80°C for 5–6 h in order to form cadmium oleate and remove already formed acetic acid. The subsequent synthesis of cadmium selenide NPs was carried out by rapid injection of trioctylphosphine selenide (TOP-Se) solution maintained at room-temperature into a vigorously stirred mixture containing cadmium oleate heated from 140 to 200°C under N_2 atmosphere. The reaction mixture was maintained at a fixed temperature for 10 min and then promptly cooled to room temperature using an ice-water bath. The solution quickly turned dark red during the synthesis due to the formation of CdSe colloidal solution. The TOP-Te/lead oleate molar ratios varied from (1.5–3) to 1.

A solvent containing two parts of hexane, one part of anhydrous ethanol, and five parts of acetone was prepared to purify the nanoparticles from unreacted precursor, excess

surfactant, and high-boiling point solvents. A size-selective precipitation was carried out by centrifugation, using a polar/nonpolar solvent combination, consisting of acetone and either hexane or chloroform. After precipitation, the CdSe nanoparticles were isolated and re-suspended in chloroform, hexane, and trichloroethylene followed by ultrasonic treatment to form stable colloidal solutions used for further preparation and characterization. The chemical analysis and atomic absorption spectroscopy confirmed the CdSe composition of the nanomaterial deposited after multiple purifying and re-suspension of the original solution.

In order to use hydrophobic nanoparticles for biological applications, they first must be transferred into aqueous solution.

The formation of various surface-active functional groups (-COOH, -C=O,-OH) makes it possible to transfer to aqueous colloids and contributes to coordination interaction with necessary surfaces, for example, with biological molecules [2].

Methods for the modification of CdSe nanoparticles include the processing of nanoparticles with buffer solutions, transferring into a soluble state, and obtaining a colloidal solution in the presence of modifying agents such as 1-thioglycerol. The subsequent deposition and re-dispersion of nanoparticles was performed in deionized water [3].

Antioxidant activity by the $ABTS^+$ radical cation assay. The total antioxidant activity of extracts was measured by the $ABTS^+$ (2,2 azinobis 3-ethylbenzothiazoline-6-sulfonic acid) radical cation decolorization [4]. $ABTS^+$ was generated by the oxidation of ABTS (7mM) with potassium persulphate (2.45 mM). The reaction mixture was left at room temperature overnight (12-16 h) in the dark before use. Prior to tests, the $ABTS^+$ stock solution was diluted to an absorbance of 0.700 ± 0.020 at 734 nm. Then 1 ml of diluted $ABTS^+$ solution was mixed with 10 µl of the test sample, and the absorbance was measured after 6 min.

Nanocrystalline sample characterization. High-resolution transmission electron microscopy (HRTEM), powder X-ray diffraction (XRD), and infrared absorption spectroscopy (IR) were used to characterize the size, shape, structure, and composition of the CdSe nanocrystals and the optical properties of the capping layer. The powder XRD data were recorded with CuKα radiation (λ = 1.5406 Å) using Scintag and PANanalytical X'Pert Pro diffractometers, both operating in the Bragg–Brentano geometry. Samples for the XRD measurements were prepared by the deposition of concentrated CdSe colloidal solutions in chloroform or trichloroethylene onto a glass substrate. The 2θ range scanned from 20° to 80°. A Philips CM 30 transmission electron microscope (TEM) equipped with a Super-Twin lens and LaB_6 emitter was used for HRTEM measurements. All the images were taken at 300-kV accelerating voltage and recorded with a megapixel CCD camera. The EDX spectra were collected using a Tecnai F30 TEM operating at an accelerated voltage of 300 kV and equipped with a Schottky field emission electron source and a Super-Twin lens. Samples for the TEM were prepared by the deposition of a drop of a dilute colloidal solution in chloroform, hexane, or trichloroethylene on a carbon-coated copper grid (200 mesh), allowing slow evaporation at room temperature. The IR absorption spectra were recorded with a VERTEX-70 Fourier transform spectrometer (Bruker Corp.). Each spectrum was obtained at room temperature by averaging over 64 interferograms with a resolution of 1 cm^{-1}. The samples for the IR measurements were prepared as pellets with KBr or CsI powders. The quantitative analysis of the resulting nanopowders was performed with an AAS-3 atomic absorption spectrometer using acetylene–air flame. For the investigation of the resulting nanomaterial, the following synthesis parameters were selected: fixed reaction temperature T = 175°C, TOPSe/cadmium oleate molar ratio r = 2.0. Diphenyl ether was used as the high-boiling heat-transfer agent. As mentioned above, the samples were prepared for X-ray powder diffraction by depositing the colloidal solution onto a glass substrate dropwise.

III. RESULTS AND DISCUSSION

The typical powder diffraction patterns of resulting CdSe nanocrystals are shown in Fig.1. XRD revealed three broad peaks positioned at 2θ = 25.37, 42.04, and 49.63° with corresponding interplanar spacings of 3.51, 2.15, and 1.83 Å, respectively. These peaks are uniquely assigned to the (002), (110), and (112) planes of the wurtzite structure of CdSe. The broadening of the diffraction pattern for CdSe implies a reduction in particle size.

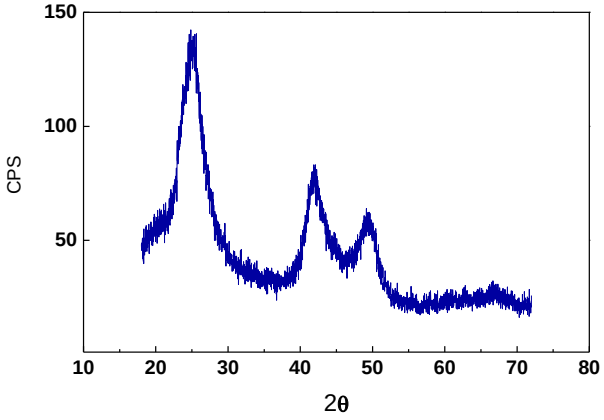

Fig. 1. Typical powder diffraction pattern of CdSe NPs.

An average size of 4–4.5 nm for the CdSe nanoparticles was estimated from the X-ray powder diffraction data using the Scherrer equation.

The size and shape of cadmium selenide nanoparticles were examined using TEM methods.

To study the action of CdSe on antioxidant activity, we selected two biotechnological important strains of microalgae: cyanobacteria *Spirulina platensis* and red microalga *Porphyridium cruentum*. The previous studies showed the increased adaptability of strains to changing cultivating conditions. The adaptation response in the majority of cases is considered to be the response to the stress factor, which is manifested in different modes at the mentioned strains depending on specific functional and constitutive structures [5].

One of the essential markers of adaptability is strain productivity. The CdSe nanoparticles were supplemented in the cultivating medium on the first day of life cycle to verify the compound's toxicity level. In the case of *Porphyridium cruentum*, the obtained results demonstrated the increase in productivity by 34-47.5% (CdSe concentration was 4.0-6.0 mg/l) and by 18% in the case of the highest concentration of 8.0 mg/l. For *Spirulina platensis*, the presence of the compound in the cultivating medium decreased cyanobacteria productivity by 33% in the case of CdSe

concentration of 4.0 mg/l. Higher concentrations are fatal; the culture dies on the 3rd day of cultivation.

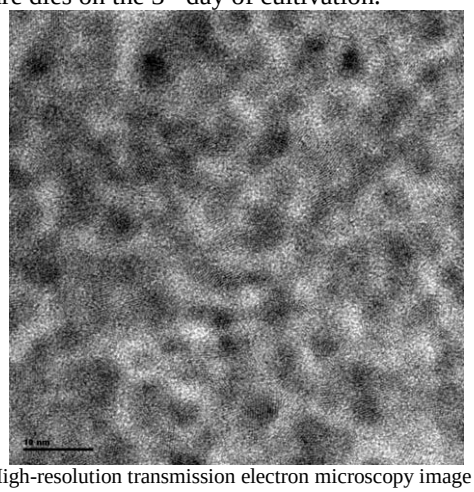

Fig. 2. High-resolution transmission electron microscopy image of small aspect ratio CdSe NPs.

Another index of culture adaptation to the cultivating conditions is the strain's antioxidant activity. Cyanobacteria and microalgae synthesize the complex of substances with antioxidant and antiradical properties [6]. Depending on factors which induce radical accumulation, the synthesis of the necessary antioxidant compounds with the modification of antioxidative statute took place. This fact could be determined by the antioxidant activity tests of extracts from biomass. Two types of extracts were prepared: water and ethanol extracts. We used the antioxidative test with ABTS radical.

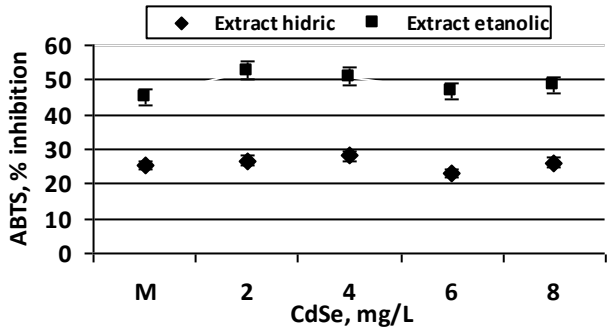

Fig. 3. The antioxidant activity (% of ABTS inhibition) of extracts from *Porphyridium cruentum* biomass.

The analyses of the results obtained for *Porphyridium cruentum* biomass show the relative stability of antioxidant activity for the two types of extracts (Fig. 3). In the case of supplementing CdSe in the cultivating medium in tested concentrations, the antioxidant activity of the water and ethanol extracts oscillated identically to the control sample, without excess of accumulating antioxidants. On the other hand, the presence of CdSe nanoparticles in the cultivating medium has no essential influence on the maintenance of antioxidant and antiradical compounds in *Porphyridium* biomass, inducing an increase in productivity.

In the case of *Spirulina platensis* extracts, an increase in the antioxidant activity was revealed (Fig. 4). So, for the extracts obtained from the biomass cultivated with a supplement of 2.0 mg/l CdSe, the antioxidant activity of the ethanol extract increased by 25%, but the water extract showed the same result as the control sample. The increase in the CdSe concentration up to 4.0 mg/l induces an increase in the antioxidant activity by 70-73% for both types of extracts.

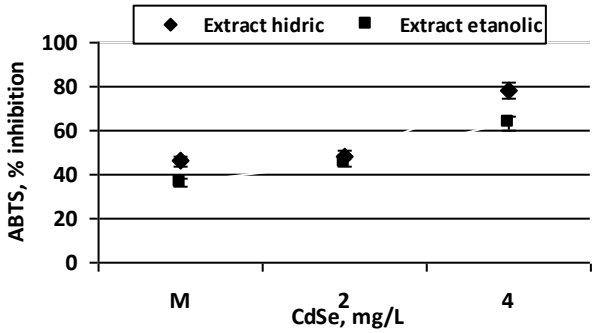

Fig. 4. The antioxidant activity (% of ABTS inhibition) of extracts from *Spirulina platensis*.

For cyanobacteria *Spirulina platensis* strain, the presence of CdSe particles in the cultivating medium is a strong factor for stimulating antioxidant compound synthesis; the limitation of its increase is a concentration of 4.0 mg/l.

IV. CONCLUSIONS

Cadmium selenide nanoparticles were obtained; their composition and crystallinity were confirmed. The CdSe nanoparticles were supplemented in the cultivating medium (cyanobacteria *Spirulina platensis* and red microalga *Porphyridium cruentum*), and the change in the productivity was studied.

The obtained results suggest the idea of different nature of adaptation mechanisms in prokaryote and eukaryote organisms. The confirmation of this assumption on the basis of other phycologic objects will offer the possibility to develop models for testing the nanoparticle toxicity.

REFERENCES

[1] А.И. Замалеева, И.Р. Шарипова, Л.В. Шлыкова, M. Kahraman, M. Culha, Р.Ф. Фахруллин Иммобилизация наноматериалов на поверхности клеток и их характеристика методами микроскопии / IV Международная конференция "Современные достижения бионаноскопии". Сб. тезисов. – Москва. – 2010, с.26.

[2] J. M. Klostranec and W.C.W. Chan. Quantum dots in biological and biomedical research: Recent progress and present challenges. Advanced Materials, 18(15):1953-1964, 2006.

[3] Vladimir V. Breus, Colin D. Heyes, and G. Ulrich Nienhaus Quenching of CdSe−ZnS Core−Shell Quantum Dot Luminescence by Water-Soluble Thiolated Ligands*J. Phys. Chem. C*, 2007, *111* (50), pp 18589–18594.

[4] . Re R., Pellegrini N., Proteggente A., Pannala A., Yang M., Rice-Evans C. Antioxidant activity applying an improved ABTS radical cation decolorization assay. Free Radical Biology & Medicine, 1999, 26(9/10): 1231-1237.

[5] Rudic V., et al. Ficobiotehnologie-cercetări fundamentale şi realizări practice. Chisinau 2007, pp.365.

[6] Cepoi L., Rudi, L., Miscu, V., Cojocari, A., Chiriac, T., Sadovnic, D. Antioxidative Activity Of Ethanol Extracts From *Spirulina platensis* And *Nostoc linckia* Measured By Various Methods. Analele Universităţii din Oradea, Fascicula Biologie Tom. XVI / 2, 2009, p. 43-48.

Influence of Copper Coordination Compounds and Cyanobacterian Remedy BioR on Bone Collagen and Hydroxyproline Concentrations (ontogenetic view)

Olga TAGADIUC[1], Aurelian GULEA[2], Valeriu RUDIC[3], Valentin GUDUMAC[1]

[1]*Biochemistry Laboratory, State University of Medicine and Pharmacy „N.Testemitanu", Moldova*
olgatagadiuc@gmail.com
[2]*Department of Inorganic Chemistry, State University of Moldova*
[3]*Institute of Microbiology and Biotechnology, Academy of Science, Moldova*

***Abstract* – The aim of our research was to assess the influence of copper coordination compounds CMT-28 and CMT-67 and cyanobacterian remedy BioR on bone collagen and hydroxyproline (HYP) concentrations at different stages of postnatal ontogenesis in normal physiological conditions and experimental osteopathy (EO). The survey was conducted on a sample of 301 white laboratory rats of both sexes, which were divided depending on their stage of postnatal ontogenetic development and experimental model: control; animal with experimental osteopathy (EO); animals with EO+CMT-28 1 mg/kg body weight; animals with EO+CMT-67 1 mg/kg body weight; animals with EO+BioR 1mg/kg body weight; animals with EO+BioR 2 mg/kg body weight; animals with EO+CMT-28+BioR (1 mg/kg body weight each); animals with EO+BioR+CMT-67 (1 mg/kg body weight each).**

In physiological conditions the ontogenetic modifications of the bone collagen and HYP content are statistically conclusive and of the same orientation, the maximum concentration was identified in adult animals and the minimum at advanced stages of postnatal ontogenesis regardless of sex.

Experimental osteopathy is characterized by age and sex dependent changes of the collagen and hydroxyproline concentrations in bone, the most significant changes being revealed in young females.

Copper coordination compounds, BioR and their combinations increase the turnover of the collagen in bone in EO that is accompanied by decrease of collagen and increase of the HYP concentration that is probably a compensatory mechanism oriented to the replacement of the damaged collagen and the restoration of its normal nanostructure with the recovery of the bone.

I. INTRODUCTION

Nanofibers are defined as fibers with diameters less than 1000 nanometers. Nature has created a variety of biological nanofibers with outstanding properties that are used in different ways by the living organisms. As classic examples of natural nanofibers serve elastin, collagen, keratins, fibrin, etc.

Collagen is the most abundant protein in the human body, comprising about 25% of their total [1]. Collagen constitutes 90-95% of the extracellular matrix (ECM) of the bone, represented predominantly by type I. Types V, XI and XII and *FACIT* forms (*F*ibrils *A*ssociated *C*ollagens with *I*nterrupted *T*riple helices) that are associated with large-diameter collagen fibers, constitute a minor quantity, but are essential for bone morphogenesis.

Regardless of the collagen type the molecules are an indubitable example of a hierarchical biological nanomaterial [2]. Fibers consist of tropocollagen molecules with diameter of 1,5 nm and length of 300 nm, which are linked by covalent cross-links and pyridinolinic links in the non-helical N-and C-terminal regions to form collagen [3].

Collagen synthesis and degradation are continuous phasic processes that are vital for maintaining normal concentrations of components and specific nanostructure of the extracellular matrix of the bone and its mineralization. Major steps of the collagen nanofibers formation are hydroxylation of proline and lysine radicals and the tropocollagen cross- through oxidized lysine radicals [4].

Prolyl-4-hydroxylase and prolyl-3-hydroxilase are responsible for proline hydroxylation and formation of hydroxyproline (HYP) [4]. The lysine oxidation is catalyzed by lysyl oxidase that uses copper ions as coenzyme [5]. The necessity for copper in the formation of bone and maintenance of its structure is well established. There are also a lot of studies that show that the lack of this mineral will lead to abnormal bone formation and fractures in newborns, infants, and sometimes even in adults [6, 7].

Thus, the aim of our research was to assess the influence of copper coordination compounds and cyanobacterian remedy on bone collagen and hydroxyproline concentrations at different stages of postnatal ontogenesis in normal physiological conditions and experimental osteopathy.

II. MATERIALS AND METHODS

The survey was conducted on a sample of 301 white laboratory rats of both sexes without pedigree. The animals were divided into the following experimental groups depending on ontogenetic stage of postnatal development and experimental model.

- Group I - 90 young rats before sexual maturity (two months);

- Group II - 78 adult rats in the reproductive period (six months);
- Group III - 54 old, postmenopausal rats (18 months);
- Group IV - 33 senile rats (24 months).

Animals from groups I-III were divided into the following subgroups: control (intact animals), animals with EO induced by administration of 0,1 ml of 50% CCl_4 in olive oil per 100 g body weight twice a week for 8 weeks; animals EO+BioR 1mg/kg body weight; animals with EO+BioR 2 mg/kg body weight, animals with EO+CMT-28 1 mg/kg body weight; animals with OE+CMT-67 1 mg/kg body weight; animals with OE+BioR+CMT-28 (each 1 mg/kg body weight); animals with EO+BioR+CMT-67 (each 1 mg/kg body weight).

The remedy BioR obtained from the biomass of cyanobacterium *Spirulina platensis* was provided by Valeriu Rudic, professor, director of the Institute of Microbiology and Biotechnology of the Academy of Sciences of Modova and copper coordination compounds (CC) CMT-28 and CMT-67 - by Aurelian Gulea, professor, Head of the Inorganic Chemistry Department of MSU.

BioR was diluted with sterile 0,9% NaCl until the final concentration of 1 mg/ml and was injected intramuscularly each 0,1 ml/100 g body weight (1 mg/kg body weight) and 0,2 ml/100 g body weight (2 mg/kg body weight) for 10 consecutive days. Coordination copper compounds CMT-28 and CMT-67 were diluted in 10% sol. of propilenglicol until the final concentration of 1 mg/ml and injected subcutaneously each 0,1 ml/100 g body weight (1 mg/kg body weight) for 10 consecutive days.

At 24 hours after the last administration the animals were euthanized under light narcosis with sulfuric ether. The femoral bones were removed, cleaned from adjacent tissues and the bone marrow removed by repeated washings with ice solution of 0,9% NaCl. Femoral bones were then frozen in liquid nitrogen, grinded to the state of powder and weighed on torsion balance.

Determination of collagen content was performed after the dissolution in 0,43 M trichloroacetic acid of a sample of bone tissue triturated in liquid nitrogen until the state of powder (20 mg). Determination of collagen in bone tissue was performed according to the procedure described [9]. The method is based on the preliminary transformation of the native bone collagen in soluble gelatin by processing the biological material with a heated to 90°C solution of trichloroacetic acid (ATA), sedimentation of non-collagenic proteins by centrifugation and determination of the gelatin concentration by classical Lowry assay. The amount of collagen was expressed in milligrams of collagen per gram of bone (mg/g).

Hydroxiproline content in bone was determined by Шараев П.Н. (1981) method in modification of [9]. The method is based on the oxidation of HYP to pyrol which interacts in acidic environment with p-dimetilaminobenzaldehyde (DMBA) and form a colored product that is assayed spectrophotometrically. The amount of HYP is expressed in mmol/g tissue.

For testing the significance of the differences between the studied groups the non-parametric statistical test Mann-Whitney were applied. Statistical evaluation of data obtained was performed with computer program Statistical Software "StatsDirect" (2001)

III. RESULTS AND DISCUSSION

The results of the study show the same orientation of the ontogenetic changes of free HYP and collagen content in the bone tissue in the postnatal period (Table 1).

TABLE 1.ONTOGENETIC CHANGES OF HYDROXYPROLINE (HYP) AND COLLAGEN CONCENTRATIONS IN BONE TISSUE IN NORMAL PHYSIOLOGICAL CONDITIONS AND EO

POS	Sex	Group	HYP	Colagen
Young	M	Control	110,46±5,03	2,45±0,13
		EO	105,99±4,32	2,74±0,33
	F	Control	104,66±5,48	$3,59±0,17^{\#\#\#\#}$
		EO	$126,46±5,63^{\S\#}$	$2,98±0,18^{\S}$
Adult	M	Control	$135,46±5,90^{***T}$	$4,44±0,23^{****T}$
		EO	$137,27±7,34^{*T}$	$5,02±0,32^{**T}$
	F	Control	128,67±5,78	$4,83±0,18^{****T}$
		EO	$116,07±4,45^{\#}$	$4,59±0,16^{****T}$
Old	M	Control	$54,80±1,46^{***A}$	$2,82±0,17^{****A}$
		EO	$52,94±6,54^{**A}$	$2,71±0,21^{**A}$
	F	Control	$57,69±5,17^{****A}$	$2,79±0,17^{****A}$
		EO	$51,54±3,87^{***A}$	$2,96±0,11^{****A}$
Senile	M	Control	$85,14±2,78^{****B}$	$2,04±0,06^{****B}$
	F	Control	$75,54±2,40^{***B\#}$	2,73±0,08

a) Each value represents $\bar{X} \pm m$

b) POS – postnatal ontogenetic stages

c) Statistical significance between different ontogenetic stages according to *U Mann-Whitney*: * p<0,05;** p<0,01; *** p<0,001; **** p<0,0001

d) Statistical significance between male and female rats according to *U Mann-Whitney*: $^{\#}$ p<0,05; $^{\#\#}$ p<0,01

e) Statistical significance compared with control group according to *U Mann-Whitney*: § – p<0,05; §§ – p<0,01; §§§ – p<0,001.

The research has established that the concentration of collagen is significantly higher in adult animals compared with all other groups studied, the amount of the collagen peaks at this stage of ontogenetic development, regardless of animal sex. Thus, collagen concentration is higher in adult males with 81% (p<0,001) and females - 36% (p<0,001) compared with the young rats. At later stages collagen levels gradually decreased. In old males the collagen content is 42% (p<0,001) lower than in adults, and in senile with 27% (p<0,001) lower than in the old one.

In females it was established the same trend of decreasing the collagen content, but statistically reliable were only changes of collagen concentration in old rats compared to adult animals (reduction by 39%, p<0,001).

It was established that the content of the free HYP increased in young males versus adult (23%, p<0,005), decreased in the old compared to young (50%, p<0,001) and adult (45%, p<0,005), and then again increased in the senile versus old (55%, p<0,001). Similar changes have been identified in females, but statistically significant in this case were only the differences between the free HYP content in adult and old animals (reduction by 55%, p<0,001), and the

old and senile one (31%, p<0,005). The maximum concentration of free HYP was identified in adult animals, and the minimum in old animals regardless of sex.

Statistically reliable sex differences of the concentration of free HYP were recorded only in senile rats, the level of the compound is lower for females (11%, p<0,05) compared to males.

It was found that EO induced by CCl_4 administration caused statistically reliable changes in the level of collagen only in young females, in which an 17% decrease (p<0,05) compared with controls were depicted (Table 1).

Ontogenetic dynamics of the level of collagen in bone tissue of animals with the EO is similar to that determined in control animals. Both in males and females with EO the concentration of collagen increases in adult animals compared with young by 83% (p<0,01), respectively, 54% (p<0,001), and then decreases in the old compared to the adult by 46% (p<0,01) and 35% (p<0,001), respectively. There were no sex-dependent differences in the level of collagen in animals with EO, regardless of the ontogenetic stage of development.

It was established that in EO the concentration of free HYP in the bone of young males did not change statistically conclusive. In young females, by contrast, it was established a 21% increase (p<0,05) compared to the control group. In males was identified an ontogenetic dynamics of the free HYP concentration similar to that specific to control animals. Thus, the HYP concentration in adult rats were by 30% (p<0,05) higher than in young rats and hydroxyproline content in the old animals were by 42% (p<0,01) lower than in the adults. In females with EO were established a progressive decrease in bone level of free HYP: HYP content of adult animals show a tendency to decrease by 8% compared to young animals and in those old values were by 56% (p<0,001) lower compared with those specific for the adult animals.

Gender differences had been established in young and adult animals with EO – in young males HYP concentration was by 19% (p<0,05) lower than in females, and in adults by 15% (p<0,05) higher than the values in females.

It was founded that the medication with copper coordination compounds CMT-28 and CMT-67 does not induce statistically conclusive changes in the concentration of collagen in bone tissue of experimental animals with EO. Only in adult animals copper coordination compound CMT-28 reduced collagen concentration compared with controls (24%, p<0,001), as well as with EO (20%, p<0,001) (Table 2).

Copper coordination compounds CMT-28 and CMT-67 did not induce statistically conclusive changes in the concentration of free HYP in bone compared with EO group level, with the exception of adult ones. In this group CMT-28 increases the level of free HYP by 24% (p<0,05) compared to EO animals.

Thus, in adult animals the copper coordination compound CMT-28 is decreasing the collagen content and at the same time increasing the amount of free HYP in bone. This can be an evidence of increased breakdown of damaged collagen in the bone of adult animals with EO. This process is a stage of the restoration of the collagen content and structure in the bone that precedes the biosynthesis of normal collagen fibers.

TABLE 2IINFLUENCE OF COPPER COORDINATION COMPOUNDS CMT-28 AND CMT-67 ON THE CONCENTRATION OF HYDROXYPROLINE (HYP) AND COLLAGEN IN THE BONE OF ANIMALS WITH EO AT POSTNATAL ONTOGENETIC STAGES

POS	Group	HYP	Collagen
Young	Control	104,66±5,48	3,59±0,17
	EO	126,46±5,63§	2,98±0,18§
	EO+CMT-28	123,46±5,54§	2,89±0,29
	EO+CMT-67	140,77±13,41§	3,34±0,29
Adult	Control	128,67±5,78	4,83±0,18
	EO	116,07±4,45	4,59±0,16
	EO+CMT-28	$^{\#}$144,16±8,91	$^{\#\#}$3,65±0,16§§§§
	EO+CMT-67	115,09±6,91	4,44±0,26
Old	Control	57,69±5,17	2,79±0,17
	EO	51,54±3,87	2,96±0,11
	EO+CMT-28	65,91±7,46	3,12±0,18
	EO+CMT-67	72,27±11,28	3,25±0,18

a) Each value represents $\overline{X} \pm m$

b) POS – postnatal ontogenetic stages

c) Statistical significance between different ontogenetic stages according to *U Mann-Whitney*: * p<0,05; ** p<0,01; *** p<0,001; **** p<0,0001;

d) Statistical significance compared with EO group according to *U Mann-Whitney*: $^{\#}$ – p<0,05; $^{\#\#}$ – p<0,01; $^{\#\#\#}$ – p<0,005, $^{\#\#\#\#}$ – p<0,001;

e) Statistical significance compared with control group according to *U Mann-Whitney*: § – p<0,05; §§ – p<0,01; §§§ – p<0,001.

The results of the research show that cyanobacterial remedy BioR in both doses did not alter the concentration of free HYP in the bone of rats with EO regardless of ontogenetic development stage (Table 3).

Only a slight tendency of increase of the HYP content were revealed in young animals compared with the control and EO specific levels after the administration of 2 mg/kg BioR, in adult animals after the administration of BioR in both doses and in old one after the administration of 1 mg/kg BioR.

Collagen levels were not statistically significant changed after the administration of BioR regardless of dose or age of the animals. Nevertheless, administration of 1 mg/kg of BioR induced a trend of increase in old animals by 17% compared with animals with EO. This amount of collagen was higher then the control levels by 12%.

This data revealed that BioR is conserving the collagen content in the bone of the animals with EO. Possible the high content of active compounds in the cyanobacterial remedy BioR (aminoacids, oligopeptides, polysaccharides, microelements etc.) create favorable environment for optimization of bone metabolism and adaptation to pathological conditions in EO.

The combination BioR+CMT-28 reduced the concentration of collagen in young (18%, p<0,05) and adult (19%, p<0,01) animals compared with the control, and in the adult (15%, p<0,01) and old (12%, p<0,05) animals compared EO group. The combination BioR+CMT-67 changed statistically conclusive the collagen concentration only in adult animals (decrease by 19%, p<0,05) compared with the group with EO (Fig. 1 and 2).

Administration of the cyanobacterial remedy BioR in combination with the copper coordination compounds CMT-28 and CMT-67 produced significant changes in the concentration of free HYP in young animals with EO.

TABLE 3.IINFLUENCE OF CYANOBACTERIAN REMEDY BIOR ON THE CONCENTRATION OF HYDROXYPROLINE (HYP) AND COLLAGEN IN THE BONE OF ANIMALS WITH EO AT POSTNATAL ONTOGENETIC STAGES

POS	Group	HYP	Collagen
Young	Control	110,46±5,03	2,45±0,13
	EO	105,99±4,32	2,74±0,33
	BioR 1mg/kg	105,99±4,32	2,76±0,14
	BioR 2 mg/kg	120,67±10,15	2,74±0,17
Adult	Control	135,46±5,90***^{T}	4,44±0,23****^{T}
	EO	137,27±7,34^{*T}	5,02±0,32^{**T}
	BioR 1 mg/kg	146,67±4,76	5,02±0,22
	BioR 2 mg/kg	149,05±9,20	4,55±0,06
Old	Control	54,80±1,46***^{A}	2,82±0,17****^{A}
	EO	52,94±6,54^{**A}	2,71±0,21^{**A}
	BioR 1 mg/kg	63,29±3,92	3,16±0,08
	BioR 2 mg/kg	54,03±7,40	2,85±0,24

a) Each value represents $\overline{X} \pm m$
b) POS – postnatal ontogenetic stages
c) Statistical significance between different ontogenetic stages according to *U Mann-Whitney*: * p<0,05; ** p<0,01; *** p<0,001; **** p<0,0001,
d) Statistical significance compared with EO group according to *U Mann-Whitney*: $^{\#}$ – p<0,05; $^{\#\#}$ – p<0,01; $^{\#\#\#}$ – p<0,001,
e) Statistical significance compared with control group according to *U Mann-Whitney*: § – p<0,05; §§ – p<0,01; §§§ – p<0,001.

The combined administration to the young animals of BioR+CMT-28 increased the bone content of free HYP compared with control values by 35% (p<0,05) and BioR+ CMT-67 – by 30% (p<0,05), while compared with animals from the EO group the free HYP content was modified only by the combination BioR+CMT-67 (35%, p<0,05).

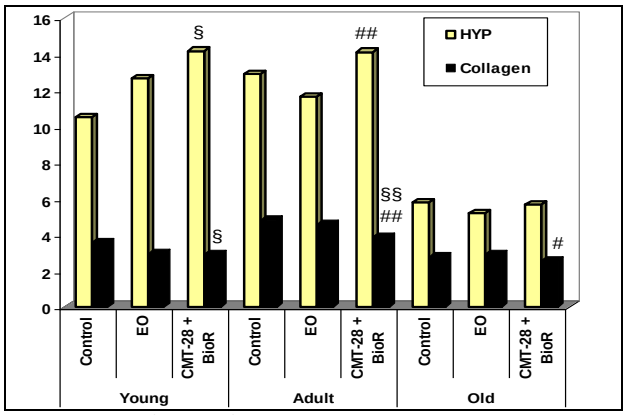

Figure 1. Iinfluence of cyanobacterial remedy BioR and copper coordination compound CMT-28 on the concentrations of hydroxyproline (HYP) and collagen in the bone of animals with experimental osteopathy (EO) at postnatal ontogenetic stages

a) Statistical significance compared with EO group according to *U Mann-Whitney*: $^{\#}$ – p<0,05; $^{\#\#}$ – p<0,01; $^{\#\#\#}$ – p<0,001,
b) Statistical significance compared with control group according to *U Mann-Whitney*: § – p<0,05; §§ – p<0,01; §§§ – p<0,001.

In adult animals the combination BioR+CMT-28 increased the concentration of free HYP by 22% (p<0,01) compared with the values observed in animals with EO, bringing it to 10% higher values (p>0,05) than the control.

The combination BioR+CMT-67 also enhanced the content of HYP over control values and those specific for the EO animals, but changes are not statistical reliable. None of the studied combinations produced statistically reliable changes in old animals with EO.

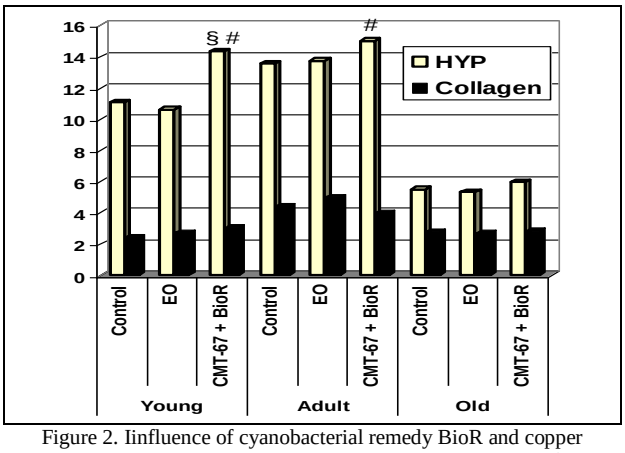

Figure 2. Iinfluence of cyanobacterial remedy BioR and copper coordination compound CMT-28 on the concentrations of hydroxyproline (HYP) and collagen in the bone of animals with experimental osteopathy (EO) at postnatal ontogenetic stages.

a) Statistical significance compared with EO group according to *U Mann-Whitney*: $^{\#}$ – p<0,05; $^{\#\#}$ – p<0,01; $^{\#\#\#}$ – p<0,001,
b) Statistical significance compared with control group according to *U Mann-Whitney*: § – p<0,05; §§ – p<0,01; §§§ – p<0,001.

Combined administration of the copper coordination compounds CMT-28 and CMT-67 with the cyanobacterial remedy BioR is characterized by potentiation of the drug influence on bone metabolism.

The increased content of HYP that is correlated with a decreased amount of collagen that we reveal in our study can be a sign of the enhanced collagen turnover in EO. Prolonged administration of CCl_4 triggered free radical production and oxidative damage of cellular and extracellular compounds [9]. Damaged proteins, including collagen, are removed from the tissues and replaced with normal one. Possible, the decrease of collagen concentration and increase of HYP – marker of bone resorption, is reflecting the efforts of the tissue to compensate the deterioration caused by the EO by degrading the abnormal collagen and replacing it with proper fibers that will restore the normal structure on the extracellular network.

Previous studies revealed that the properties of collagen are scale-dependent and that the strength of the tropocollagen molecules differs from the strength of the collagen fibril. The late depends on the number of the cross-links in the fibril, on the fibril length, etc. Thus, the nanostructure of collagen may provide either a strong bone or a brittle one [2].

Our results prove the ability of the copper coordination compounds CMT-28 and CMT-67 and cyanobacterial remedy BioR to intervene in the metabolism of collagen nanofibers at the essential stages. The magnitude of the tissue response is depending on the postnatal ontogenetic stage. Copper coordination compounds and cyanobacterial remedy can induce the correction of the damage caused by the CCl_4 to the collagen fibers and provide the restoration of its physiological nanostructure with the recovery of the bone structure and properties.

IV. CONCLUSIONS

1. In physiological conditions the ontogenetic modifications of the content of bone collagen and HYP are statistically conclusive and of the same orientation,

the maximum concentration of collagen and free HYP was identified in adult animals and the minimum at advanced stages of postnatal ontogenesis regardless of sex.

2. Experimental osteopathy is characterized by age and sex dependent changes of the collagen and hydroxyproline concentrations in bone, the most significant changes being revealed in young females.
3. Copper coordination compounds (CMT-28 and CMT-67), cyanobacterial remedy BioR and their combinations increase the turnover of the collagen in bone in experimental osteopathy, that is accompanied by decrease of collagen concentration and increase of the hydroxyproline amount.
4. The increase of the turnover of the collagen in bone in experimental osteopathy induced by copper coordination compounds (CMT-28 and CMT-67), cyanobacterial remedy BioR and their combinations is probably a compensatory mechanism oriented to the replacement of the abnormal collagen and the restoration of its normal nanostructure with the recovery of the bone.

REFERENCES

[1] M.K. Gordon, R.A. Hahn, *Collagens*, Cell Tissue Res., vol. 339, no. 1, 2010, pp. 247-257.

[2] M.J.Buehler, *Nature designs tough collagen: Explaining the nanostructure of collagen fibrils*. PNAS, vol. 103, no. 33, 2006, pp. 12285-12290.

[3] П.Г. Роби, *Биохимия кости*. В: Остеопороз. Этиология, диагностика, лечение. Под ред. Риггз Б.Л., Мелтон III Л.Дж.. СПб, "Издательство БИНОМ", "Невский диалект", 2000, стр. 57-84

[4] L. Koláčná, J. Bakešova , F. Varga et al. *Biochemical and Biophysical Aspects of Collagen Nanostructure in the Extracellular Matrix*. Physiol. Res., no. 56, suppl. 1, 2007, pp. S52-S60.

[5] R.B. Rucker, J. Murray, *Cross-linking amino acids in collagen and elastin*. American Journal of Clinical Nutrition, no. 31, 1978, pp. 1221-1236.

[6] Y.L. Lai, M. Yamaguchi. *Effects of Copper on Bone Component in the Femoral Tissues of Rats: Anabolic Effect of Zinc Is Weakened by Copper*. Biol. Pharm. Bull., vol. 28, no. 12, 2005, pp. 2296-2301.

[7] D. Conlan, R. Korula, D. Tallentire, *Serum copper levels in elderly patients with femoral-neck fractures*. Age and Ageing, vol. 19, 1990, pp. 212-214.

[8] V. Gudumac, O. Tagadiuc, V. Rîvneac et al. *Investigaţii biochimice*. Elaborare metodică. Micrometode. Vol.II. Ch.: Elena V. I. SRL, 2010. 104 p.

[9] M.I. Díaz Gómez, J.A. Castro, *Covalent binding of carbon tetrachloride metabolites to liver nuclear DNA, protein and lipids*. Toxicol Appl Pharmacol, no. 56, 1980, pp. 199-206.

This work was supported by the Moldavian Academy of Science institutional project 06.420.017F "Concepts of bone metabolism in normal postnatal ontogenesis and experimental osteoporosis"

Comparative Study Of The Mechanical Characteristics Of Dental Implants Made From Biomaterials Covered With DLC Depositions

Stanca COMŞA, Adrian PACIOGA, Doina GHEORGHIU, Stefan MARIA
stanca_comsa@yahoo.com,
National Institute of Research & Development for Mechatronics and Measurement Technique, 6-8 Str. Pantelimon, Bucharest, Romania.

***Abstract* – Nanostructures and nanostructured materials development has opened important expectative in multiple fields, however, one of them, with important direct impact on the society is the medicine.**
In this paper is presented a comparative study of the mechanical properties of titanium used for dental implants covered or not with an ultra thin DLC (Diamond Like Carbon) film deposition. Evaluation was focused on determining the number of cycles until failure in dynamic fatigue testing according to SR EN ISO 14801: 2008 and static compression strength according to SR EN ISO 6892-1:2010, for dental implants made of pure titanium covered/not covered with a layer of DLC. In order to make a comparison between covered and uncovered specimens, two of them were covered with DLC depositions, and other two without deposition. The obtained results show the improvement of the mechanical properties.

Keywords – biomaterials, mechanical properties, nanodepositions.

I. INTRODUCTION

Bone is one of the most replaced parts in the human body. The current treatment option is implantation. Implants with scaffolds have to provide anchorage of cells and play an important role in bone regeneration. The materials need to be biocompatible and provide appropriate mechanical support similar to the natural bone.

Austenitic stainless steel, titanium and its alloys are widely used for biomedical applications, including devices for bone fixation and partial/total joint replacement because they are corrosion resistant metals with the required mechanical strength and biocompatibility. They are referred as "first generation of biomaterials" [1] in the technical studies.

These biomaterials for implants are not osseoconductive and their surface does not have structural and functional connection with the living bone that can enable reaction with the surrounding tissues, referred as osseointegration. Furthermore, they tend to release a high concentration of metal ions into the body, which is likely to have toxic effects on bone cells, leading to failure and may inhibit formation of bone (osteogenesis).

"The second generation of biomaterials" are bio-active ceramics such as calcium phosphate and bioactive glass and was developed as possible alternative to the first generation of metallic biomaterials. These materials have the ability to promote bone apposition with bone tissues without fibrous encapsulation, thereby leading to osseointegration.

One of these materials is calcium carbonate-containing apatite layer (CA) which is chemically similar to the inorganic mineral phase of a natural bone and is considered important for the osseointegration process. However, this class of bioceramics exhibits low bending strength (42–200 MPa) and is brittle, restricting their use in load bearing applications [2].

The implant must interact with the adjacent tissue, to permit the bone regeneration and the growth of osteogenic cells.

The texture of surface implants is very important in the osseointegration process. So it is necessary to have a porous surface to permit the osteoblasts cells proliferations better than the osteofibre ones.

Studies show that classic biomaterials with carbon nano depositions present acceleration of bone cell function in comparison with materials without such covering. [3]

The deposition of the DLC film was made using thermionic vacuum arc method (TVA).

The method (TVA) is based on evaporating the coating material by an indirectly heated cathode surrounded by a Wehnelt cylinder. [4]

The evaporation material state is obtained by heating it with thermal electrons generated by the circular shape filament indirectly heated and situated above the anode. The used anode was a carbon rod with a 6mm diameter.

Due to large energy dissipated in the plasma volume, the deposited material is completely dispersed without drops. The obtained film is very fine and under certain conditions appears as a nanostructures deposition.

The thickness of deposited layer was 150nm, and the deposition was made at Ovidius Constanta University.

II. MATERIALS PROPERTIES

The ideals proprieties of materials for implants are:

- Hard resistance at static and dynamics loads which appears in the implant place;
- Resistance at alternative bending tests;
- Wear resistance;
- Corrosion resistance at the body fluids;
- Chemical and thermal stability;
- Unaffected by X ray radiation;
- Undistorted by manufactured process;
- Low price;
- To be reproducible;
- Non-toxic and no-allergenic in contact with body fluids;
- Bio tolerant at the interface tissue-materials.

III. TEST SPECIMENS

In order to characterize the mechanical properties of

coatings with nanostructured materials obtained by DLC deposition, dental implants were used as samples (see fig. 1), made from pure titanium material, which is one of the most used materials for implants manufacturing.

For the tests were use four specimens, two uncovered and two with ultra thin DLC deposition using thermionic vacuum arc method (TVA).

The used dental implants consisted of tapping component with a diameter of 3.2mm and 13.2 mm long and abutment with conical surface (at an angle of 10°), for connecting with the assembly, total length of 9.5 mm and M2 threaded fastener (see fig.2). The parts were made of pure titanium 99.9 %.

Fig. 1: Dental implant assembly

Fig. 2: Tapping component and abutment

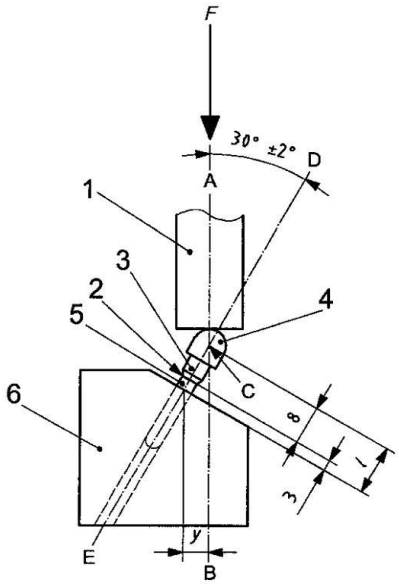

Fig. 3: Testing configuration according to SR EN ISO 14801:2008

IV. LOADING GEOMETRY

Fatigue testing was performed by simulation of the functional loading on the endosseous dental implant, with abutment and tapping component, in the worst possible operating conditions.

To comply with the requirements of the fatigue test method specified by EN ISO 14801:2008, a hemispherical part with a radius of 2.5 mm was mounted on the implants subjected to this test and the assembly was fixed on the machine's table Instron 8872 type in the configuration presented in figure 3.

Notations in the figure are:

1. Loading device which should allow free movement transverse to loading direction;
2. Nominal bone level;
3. Connecting part (abutment);
4. Hemispherical loading member;
5. Dental implant body;
6. Clamping device.

Dental implant assembly with no pre-angled connecting part and hemispherical member must be clamped so that its axis makes an angle of 30 ° ± 2 ° with the loading direction of the testing machine (see fig. 3.)

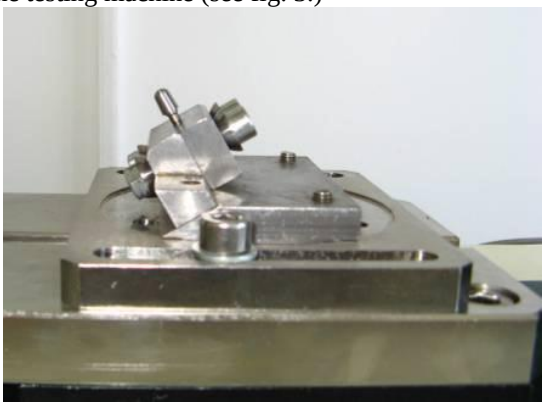

Fig.4: Clamping and positioning device

According to the scheme in Figure 3, load center "C" is at the intersection between the longitudinal axis of the assembly and loading axis of the testing machine and must be at a distance *l*=11 mm from the surface of the clamping device.

In order to ensure the requirements of SR EN ISO 14801:2008 a clamping and positioning device for the sample was designed (see fig. 4.).

V. MECHANICAL PROPRIETIES EVALUATION

The testing method applied to specimens in order to characterize the mechanical properties is fatigue test.

Failure of biomedical implants is dominated by fatigue or fatigue related failure such as fretting fatigue which is affected by various factors (mean stress, frequency or stress cycling, etc.).

For determination of mechanical resistance the dental implants specimens were submitted to dynamic fatigue tests.

The purpose of this comparative study is to determine the number of cycles until failure in fatigue testing according to SR EN ISO 14801: 2008 and static compression strength according to SR EN ISO 6892-1:2010, for dental implants made of pure titanium covered/not covered with a layer of DLC.

The obtained results were compared in order to observe the influence of the covering with nanostructured layers upon mechanical characteristics of the tested parts.

To determine the value of maximum loading force for dynamic fatigue tests, the standard recommends first a static test to determine the compression strength of the sample, which is oriented in the same position as in the case of dynamic application.

For the compression strength determination, tests were made on a static testing machine Hounsfield H10KT type (fig.5 a) and the dynamic fatigue tests were made on an Instron 8872 testing machine (fig.5 b).

VI. RESULTS AND DISCUSSION

The characteristic curves obtained in compression strength determination are presented in the figure 6.

a) Static testing machine Hounsfield H10KT

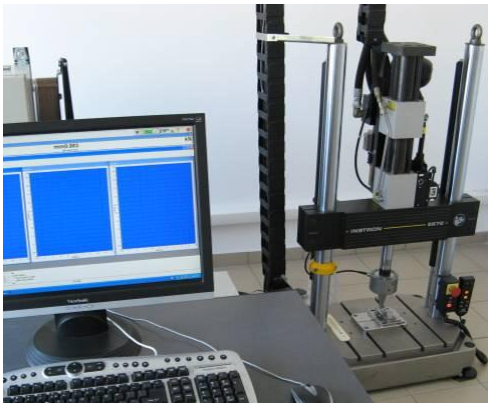

b) Dynamic testing machine Instron 8872

Fig. 5: Testing machines

The maximum loading force was 318,4N for the uncovered specimen while, for the DLC covered specimen, the force increased up to 332N.

On the characteristic curves the absence of the material yielding can be observed for the specimen with nanostructured layer deposition, suggesting an improvement of the elastic properties.

For the dynamic test the maximum loading force was established to 200N representing about 63% of maximum strength obtained from static loading.

Force was applied unidirectional and varied sinusoidal and was ranged between 200 N and 20N (minimum value equal to 10% of maximum value) in order not to lose contact between the loading device and the sample. The loading frequency was set at 15 Hz.

The test ended at the sample failure and the software of the testing machine recorded automatically the cycle number at which failure occurred.

The recorded number of cycles for the uncovered sample was 1,282,736 and for DLC covered sample was 1,346,424 cycles.

VII. CONCLUSIONS

The mechanical strength of the implant scaffolds is rather important in applications where load bearing is required, such as matrices to promote bone tissue growth.

A major problem with titanium implants is that osseointegration by way of its natural oxide TiO_2 is a long process.

As a result, implant fixation takes place through an accumulation of fibrous soft tissue (rather than hard bone), which over time results in loosening of the implant, causing discomfort and eventual failure.

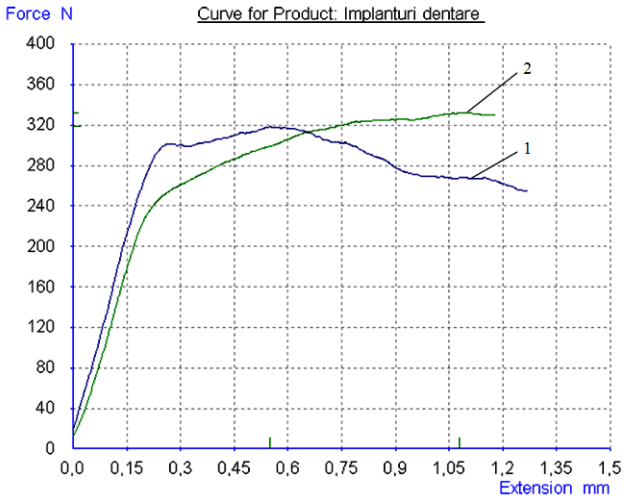

Fig. 6: Characteristic curves in the compression test1-uncovered specimen; 2- DLC covered specimen

In order to prevent this inconvenience a ultra thin layer of DLC can be deposited on the implant, improving also the wear resistance and lowering the friction coefficient.

From the obtained results we can see that by surface treating due to nanometric deposition of carbon fibres, endurance limit and compressive strength shows a slight improvement. DLC coatings with biocompatible properties lead to improved endurance limits of the endosseous implants.

Another improvement achieved by coating with DLC film is the increase of the elasticity range observed on the characteristic curves for the compression test.

All these specific properties of DLC coatings are very suitable for improving the performance of medical devices and micro-mechanical devices for biomedical applications.

The aim of dental implant is to achieve at least the same percentage of elongation under the same stress in an implant-bone-combination. The increase of the implant elasticity in order to be similar to that of the bone is the most promising way to achieve the desired adapted implant elasticity.

Due to the mentioned above considerations the obtained increased elasticity of the specimens is a favourable effect. This can lead to the increase of the implant's life-time [5].

In the present paper the possibility of improving mechanical properties of the conventional biomaterials was demonstrated by mechanical testing of coated and uncoated specimens leading to greater elasticity, compression strength and better fatigue strength.

The future researches can be orientated to improve the surface depositing process in order to obtain a better homogeneity of the specimen and repeatability of the results.

ACKNOWLEDGEMENT

We want to thank to Ovidius Constanta University, especially to Nanodepositions Laboratory that helped us with nanostructured deposition on the dental implant specimens and gave us the opportunity to make the comparative study presented in the present paper.

REFERENCES

S. Mali, R.D.K. Misra, M.C. Somani, L.P. Karjalainen: Biomimetic nanostructured coatings on nano - grained

Using Nonconventional Structures as Protective Colloids in the Dispersion Polymerization of 2 - Hydroxyethyl Methacrylate with a Comonomer with Spiroacetal Moiety

Aurica P. CHIRIAC, Loredana E. NITA, Manuela T. NISTOR
"Petru Poni" Institute of Macromolecular Chemistry,
Grigore Ghica Voda Alley No. 41-A, 700487 IASI, Romania
achiriac@icmpp.ro

***Abstract* – The study reports the synthesis of a copolymer based on 2-hydroxyethyl methacrylate and 3, 9-divinyl-2, 4, 8, 10-tetraoxaspiro (5.5) undecane acquired through radical polymerization in the presence of 2, 2'-Azobis (2-methylpropionitrile). The polymerization process was conducted in the presence of a classic ionic surfactant – sodium lauryl sulfate (SLS) – and comparatively using two variants of protective colloid: β cyclodextrin (CD) and poly(aspartic acid)(PAS) respectively. The polymers compositions were confirmed by FTIR spectra. SEM and AFM investigations of the polymer morphology are also presented. It was concluded on the proper critical micellar concentration for used tensioactive substances, respectively attributing a mixed mode of particle nucleation (micellar and homogeneous nucleation) in case of synthesis with SLS and an entropic mechanism of stabilization with CD and PAS as stabilizers. The mean particle size and size distribution, as well as zeta potential and conductivity determination on the prepared polymeric particles attest a relatively monodisperse distribution for the particle size; particles with negatively charged surfaces and copolymers conductivity prepared in the presence of PAS or CD increased by several orders against homopolymer.**

***Index Terms* – five key words or phrases arranged alphabetically and separated by commas.**

I. INTRODUCTION

The improvement of the p(HEMA) properties as for example the mechanical properties, permeability, temperature responsive characteristics, and degree of hydration or extent of hydrogel network swelling, for more favorable biological responses, it was taken into study. Thus, by synthesizing amphiphilic materials, combining HEMA with hydrophobic components, one can expect the improvement of the mechanical strength of the obtained materials, and in this context, the copolymerization is mainly used to improve mechanical properties of polyHEMA, the affinity for water, oxygen permeability etc. [1–4]

Bailey et al. [5] in 1976 described developments in the synthesis of alternating poly(ester–ether)s from spiroortho-esters. These are considered biodegradable and useful for biomedical applications. [6] In this context, spiroacetals are key structural elements in many bioactive polyketide natural products and related analogues. [7-11] The incorporation of spiroacetal groups in the polymers structures also, improves the solubility and the adhesive properties. [12] These polymers induce also good oxidative and thermal stability, are good fiber formers, and films with good flexibility and tensile strength. [12] These characteristics are owing to the spiroacetal ring presence.

The present study reports the synthesis of a copolymer based on HEMA and 3, 9-divinyl-2, 4, 8, 10-tetraoxaspiro (5.5) undecane (U) acquired through radical aqueous dispersion polymerization in the presence of AIBN. The attempt was to have a solid content as high as 10 wt.-percent and in this context the process was conducted in the presence of a classic ionic surfactant – sodium lauryl sulfate (SLS) – and comparatively using two variants of protective colloid: β cyclodextrin and poly(aspartic acid), respectively. AFM investigations of the polymer morphology are also presented. The poly(aspartic acid), belonging to the family of synthetic polypeptides, is a typical biocompatible, biodegradable with dispersing activity water-soluble polymer, which can be used as dispersant, antiscalant, or superabsorber, for home detergents, water treatment chemicals, and oil field treatment additives, for a variety of organic and inorganic solids and scales dispersal, in medicines, cosmetics, and food. It is considered to be a sustainable, environmentally compatible chemical product and its biodegradability makes it particularly valuable from the point of view of environmental acceptability and waste disposal. At the same time, no toxic or mutagenic effects have been reported for polyaspartic acid. Its derivatives starting from polysuccinimide are reported in the literature as carrier component in drug-polymer conjugates for non-steroidal, antineoplastic or other antiviral agents (acyclovir, zidovudine, paclitaxel, methotrexate, amphotericin B). [13] Also, a useful method for increasing the water solubility of organic compounds is to use cyclodextrin (CD) to form inclusion compounds with the guest hydrophobic species. [14, 15] In this context β-cyclodextrin was investigated in emulsion polymerization and the first successful application as protective colloid belongs to the group of Rimmer. [16]

II. EXPERIMENTAL PART

The continuous radical polymerization processes between 2 - hydroxyethyl methacrylate (HEMA) and 3, 9-divinyl-2, 4, 8, 10-tetraoxaspiro[5.5]undecane – (U) were initiated by 2, 2'-Azo bis(2-methylpropionitrile) (AIBN) and conducted under nitrogen atmosphere, at 70^0C, in a constant temperature bath, with a stirring rate of 250rpm, for 8h,

using sodium lauryl sulfate ($C_{12}H_{25}O_4SNa$) – (SLS) as tensioactive, or poly(aspartic acid) (PAS)(poly (a, b) -D, L aspartic acid sodium salt, M_w= 8100) or β cyclodextrin (M_w=1135) as protective colloid. The water used in all experiments was purified using an Ultra Clear TWF UV System. The attempt was to have a solid content as high as 10 wt.-percent and in this context the process was conducted in the presence of the classic ionic surfactant – sodium lauryl sulfate (SLS) – and comparatively using two variants of protective colloid: β cyclodextrin and poly(aspartic acid), respectively. After synthesis the polymeric particles were precipitated three times with methanol from water solution and finally freeze-dried by ***lyophilization during 24 h.***

The the zeta potential (ζ) and the conductivity were estimated by using a dynamic light scattering technique (Zetasizer model Nano ZS, with red laser 633 nm He/ Ne; Malvern Instruments, UK). The determinations were made on 2 ml sample of latexes without dilution. The sampling was done directly from the reaction vessel and was placed in the cell. All measurements were carried out at 25°C.

The mean particle size and size distribution of as-prepared latex polymer particles were also measured by laser diffraction. Mastersizer Hydro 2000 S (Malvern Instruments, UK with the whole measuring range from 0.02µm to 2000µm) was used to control the particles size in aqueous dispersion. Measurements of the particle size of the copolymers and homopolymer were performed with a pre-measurement treatment of 10 seconds at 1200 rpm in an ultrasonic bath built into the Malvern system for a better dispersion of the sample.

The thermal analysis of P(HEMA) and P(HEMA-co-U) copolymers has been carried in inert atmosphere at heating rate of 10^0C per minute up to 600 ^{0}C with a termobalance from Netzsch, Germany. Non-isothermal experiments were performed used an average sample weight to 7.5 mg and the nitrogen flow rate was 50 ml/min.

SEM studies were performed on samples fixed by means of colloidal copper supports. The samples were covered by sputtering with a thin layer of gold (EMITECH K 550x). The coated surface was examined by using an Environmental Scanning Electron Microscope (ESEM) type Quanta 200 operating at 30 kV with secondary electrons in high vacuum mode.

III. RESULTS AND DISCUSSIONS

The idealized reaction of the copolymerization process is illustrated in Figure 1.

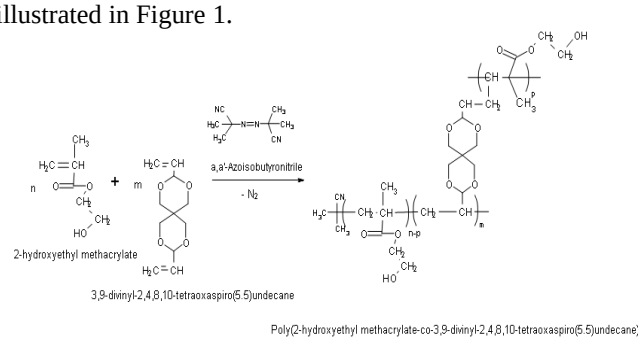

Fig. 1. Idealized copolymerization process

The structure of the new synthesized copolymers was confirmed by FT-IR spectra. Thus, the ν(O–H) stretching vibration in PHEMA was registered in the 3400–3500 cm^{-1} range as broad absorptions, and a strong band at ~ 2950cm^{-1} and ~ 2970cm^{-1} indicated the ν(C–H). Another strong band at ~1730cm^{-1} was attributed to ν (C=O) group; at ~2940 cm^{-1} to ν(C–H) stretching of -CH_3, and also at ~1270cm^{-1} to ν (C–O) stretching vibration. The spiroacetal moieties inclusion was also confirmed by the FTIR spectra. Thus, FTIR spectra of the copolymers presented some new strong bands in the region of 1000 – 1200cm^{-1} (due to esteric C-O-C stretching) and at ~1715cm $^{-1}$ (due to C=O stretching of conjugated ester). The relative thermal stability of the homopolymer and copolymers are illustrated in Figure 2. According the results the homopolymer and copolymers shows a high mass lost until 460^{0}C. By using thermal analysis (TG) it was found that the copolymerization process proceeds slowly decrease of thermal stability. Increasing the intermolecular space, induced by the copolymerization of 2-hydroxylethyl methacrylate with 3,9-divinyl-2,4,8,10-tetraoxaspiro[5.5] undecane, leads to form a polymeric structure with a less thermal stability, modified slightly compared to homopolymer, where the polymeric chains are well wrapped through intramolecular attractive interactions especially hydrogen bonds.

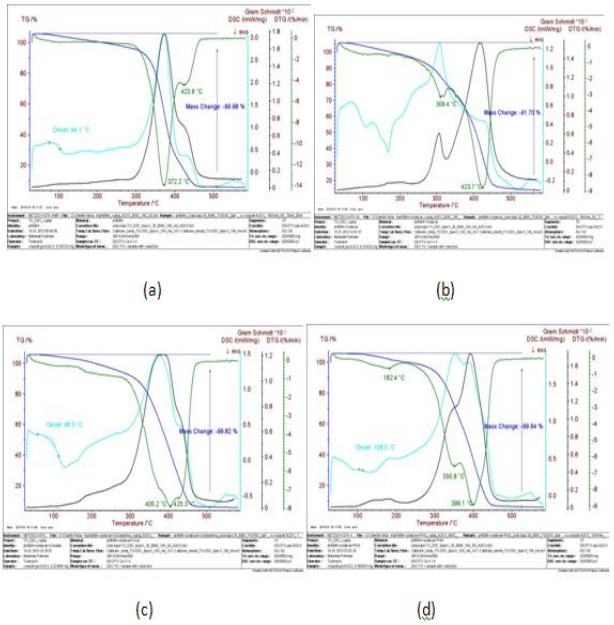

Fig. 2. The behavior during thermal decomposition for the studied polymeric samples: (a) P(HEMA), (b) $P(HEMA–co–U)_{DBS}$, (c) $P(HEMA–co–U)_C$, (d) $P(HEMA–co–U)_{PAS}$

The inclusion of the oligosaccharides in the synthesis, like β–cyclodextrin also, leads to decrease the initial decomposition temperature, owing to the hydroxyl groups that are border outside of the ring. The same behavior is experienced for the copolymer synthesized in the presence of PAS as protective colloid. This slight decrease in the thermal stability did not significant affect system stability, offset by the other improved properties conferred by achieving a network structure for example. At the same time, based on the maximum temperature decomposition, the copolymers show an increase of the thermal stability with 30^{0}C until 50 ^{0}C (Table 1). Figure 1 shows that each DTG curve of homopolymer and copolymers has two or three peaks which is usually interpreted as the decomposition of the sample in the first step and for the second one is due to a less stable intermediate product. It can be concluded that the presence of the comonomer positively affects the thermal behavior of the copolymer as it can be observed from the DTG curves.

TABLE I. DATA RESULTED FROM TG AND DTG CURVES OF THE STUDIED POLYMERS

Sample	W	T_{onset}	T_{peak},	T_{endset},	T_{10}
P(HEMA)	94.5	282	372	472	333
$P(HEMA–co–U)_{DBS}$	94.6	279	423.7	484	326
$P(HEMA–co–U)_{C}$	94	279	405	482	315
$P(HEMA–co–U)_{PAS}$	94	235	399	468	317
W - %; T - ^{0}C;					

Compared data concerning the dispersion dimensions and their zeta potential were also obtained onto the lyophilized particles (Figure 3 and Table 2). From the size distribution results (Figure 3) it is obviously the influence of the stabilizer type used in the synthesis. Even strange, it results the better performance of PAS and CD as stabilizer then that of the classical one SLS. Thus, the broadness of the resultant particle size distribution in decreasing order is : $P(HEMA\text{-}co\text{-}U)_{DBS}$ 〉 P(HEMA) 〉 $P(HEMA\text{-}co\text{-}U)_{CD}$ 〉 $P(HEMA\text{-}co\text{-}U)_{PAS}$.

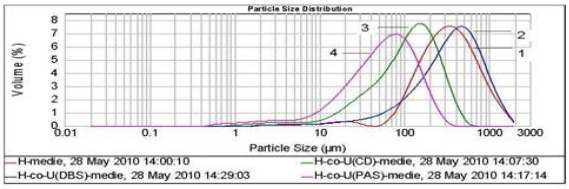

Figure 3. The particles size distribution after the volume distribution for P(HEMA) (1), $P(HEMA\text{-}co\text{-}U)_{DBS}$ (2), $P(HEMA\text{-}co\text{-}U)_{CD}$ (3), $P(HEMA\text{-}co\text{-}U)_{PAS}$ (4)

TABLE 2. THE ZETA POTENTIAL AND CONDUCTIVITY OF THE SYNTHESIZED POLYMERIC PARTICLES

Sample name	ζ, mV	Conductivity, mS/m
P(HEMA)	-0.295 ± 0.01	0.353 ± 0.002
$P(HEMA\text{-}co\text{-}U)_{DBS}$	-7.6 ± 1.04	0.207 ± 0.003
$P(HEMA\text{-}co\text{-}U)_{PAS}$	-1.923 ± 0.41	0.970 ± 0.01
$P(HEMA\text{-}co\text{-}U)_{CD}$	-0.39 ± 0.24	0.573 ± 0.001

From the determinations it results all particle surfaces were negatively charged, and also the surfactant nature significantly influences the surface charges, due to the functional groups. The zeta potential results indicate a low surface charge for the homopolymer, followed by the $P(HEMA\text{-}co\text{-}U)_{CD}$ 〉 $P(HEMA\text{-}co\text{-}U)_{PAS}$ and finally $P(HEMA\text{-}co\text{-}U)_{DBS}$. The conductivity of the copolymers prepared in the presence of PAS or CD was found to be increased by several orders against homopolymer.

Morphological information concerning the studied polymeric compounds utilizing SEM is presented in Figures 4 a – d. The structural and compositional characteristics of the surfaces are evidenced and differences between the synthesized homopolymer (Figure 4a) and the copolymers (Figures 4b-d) are proof. SEM micrographs show that the polymers prepared with different stabilizers possess a distinct structure. The homopolymer seems to have more homogeneous structure instead of the copolymers that appear with an internal lamellar structure in case of using CD as protective colloid, like a lace when PAS is the stabilizer, and a little bit inhomogeneous structure in case of SLS.

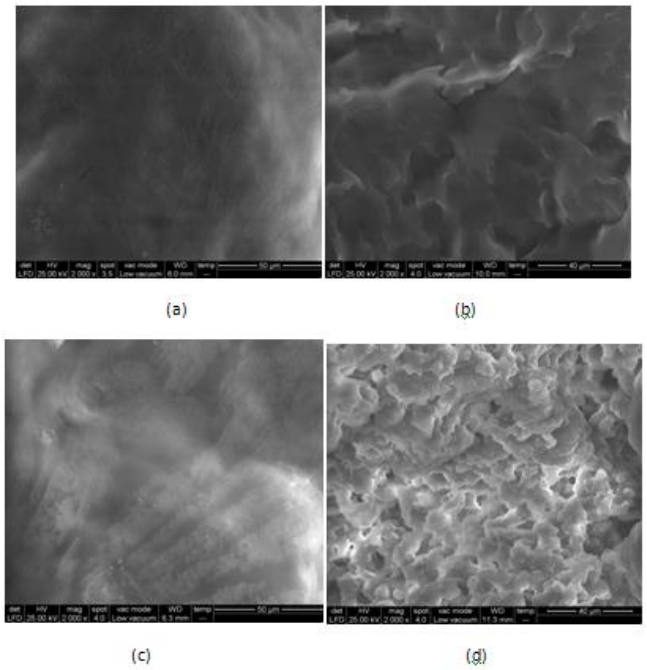

Figure 4. SEM micrographs of the studied polymers PHEMA (a),$P(HEMA–co–U)_{DBS}$ (b), $P(HEMA–co–U)_{CD}$ (c), $P(HEMA–co–U)_{PAS}$ (d)

IV. CONCLUSION

Taking into account the special effects which may be generated by both comonomers – network formation, biodegradability and biocompatibility, gel formation capacity, binding properties, amphilicity, good oxidative and thermal stability, good films formers, acid pH sensitivity – the interest in the development of these new polymeric structures with emphasis on theoretical aspects is thoroughly justified. In this context further investigation are in course.

ACKNOWLEDGMENTS

This work was supported by CNCSIS–UEFISCSU, project number 466 PNII—IDEI code_995/2009: Researches in the Field of Polymeric Matrices Design for Sensitive Structures Romania.

REFERENCES

[1] Cretua A, Gattina R, Brachaisa L, Barbier-Baudrya D. Synthesis and degradation of poly (2-hydroxyethyl methacrylate)-graft-poly (ε-caprolactone) copolymers. Polymer Degradation and Stability; 83 (3): 399–404, 2004

[2] Barakat I, Dubois Ph, Grandfils C, Jerome R. Macromolecular engineering of polylactones and polylactides. XXV. Synthesis and characterization of bioerodible amphiphilic networks and their use as controlled drug delivery systems. J Polym Sci A: Polym Chem; 37:2401–11, 1999

[3] Eschbach F, Huang S. Hydrophilic-hydrophobic binary systems of poly(2-hydroxyethyl methacrylate) and polycprolactone. Part I. Synthesis and characterization. J Bioact Compat Polym; 9: 29–54, 1994

[4] Eschbach F, Huang S, Cameron J. Hydrophilic-hydrophobic binary systems of poly(2-hydroxyethylmethacrylate) and polycprolactone. Part II. Degradation. J Bioact Compat Polym; 9: 210–21, 1994.

[5] Bailey WJ, Iwama H, Tsushima R. Synthesis of elastomers by cationic polymerization with expansion in volume. J Polym Sci: Symp; 56:117–27, 1976.

[6] Moorea T, Adhikaria R, Gunatillakea P. Chemosynthesis of bioresorbable poly(g-butyrolactone) by ring-opening polymerisation: a review. Biomaterials; 26 (18): 3771–3782; 2005

[7] O'Hagan D. The Polyketide Metabolites, Ellis Horwood, Chichester, 1991; O'Hagan D. Biosynthesis of fatty acid and polyketide metabolites**.** Nat Prod Rep; 12: 1; 1995;

[8] Norcross RD, Paterson I. Total Synthesis of Bioactive Marine Macrolides. Chem Rev; 95: 2041; 1995.

[9] Pettit GR, Chicacz ZA, Gao F, Herald CL, Boyd MR, Schmidt JM, Hooper JN A. Antineoplastic agents. 257. Isolation and structure of spongistatin 1. J Org Chem; 58(6): 1302-1304; 1993;

[10] Kobayashi M, Aoki S, Sakai H, Kawazoe K, Kihara N, Sasaki T, Kitagawa I. Altohyrtin A a potent anti-tumor macrolide from the Okinawan marine sponge Hyrtios altum. Tetrahedron Lett; 34 (17): 2795-2798; 1993.

[11] Kulkarni BA, Roth GP, Lobkovsky E, Porco JA. Combinatorial Synthesis of Natural Product-like Molecules Using a First-Generation Spiroketal Scaffold J Comb Chem; 4(1) 56-72; 2002; Trump RP, Bartlett PA.

[12] Amino Acid-Derived Heterocycles as Combinatorial Library Targets: Spirocyclic Ketal Lactones. J Comb Chem; 5(3): 285-291; 2003; Mitsuhashi S, Shima H, Kawamura T, Kikuchi K, Oikawa M, Ichihara A, Oikawa H. The spiroketals containing a benzyloxymethyl moiety at C8 position showed the most potent apoptosis-inducing activity. Bioorg Med Chem Lett; 9(14): 2007-2012; 1999.

[13] Polymeric materials encyclopedia. Ed by Joseph C. Salamone; Spiroacetal backbone polymers; p. 7858, 1996;

[14] Ehtezazi T, Govender T, Stolnik S. Hydrogen Bonding and Electrostatic Interaction Contributions to the Interaction of a Cationic Drug with Polyaspartic Acid. Pharm Res 17: 871-877; 2000.

[15] Saenger W. Cyclodextrin Inclusion Compounds in Research and Industry**.** Angew Chem Int Ed; 19:344; 1980

[16] Wenz G. Cyclodextrins as Building Blocks for Supramolecular Structures and Functional Units. Angew Chem Int Ed; 33:803; 1994.

[17] Rimmer S, Tattersall P. The inclusion of b cyclodextrin provides a supramolecular solution to the problem of polymerization of dodecyl and octadecyl methacrylates in aqueous emulsion. Polymer 1999; 40: 5729–5731. Rimmer S, Tattersall PI. Emulsion polymerizations in the presence of β-cyclodextrin. Polymer; 40: 6673–6677; 1999

Innovative Realizations in the Research of Dental Implants

Gheorghe GRANCIUC
granciuc@dentist.md
Faculty of Dental Medicine, State University of Medicine and Pharmacy „N. Testemitanu", Moldova

Abstract – This article describes a method that can be used in experimental dentistry for investigations of osteointegration processes of dental implants. The procedure was patented (Patent BOPI AGEPI MD nr.12.2010). The researches accomplished below represent a component part of the subject area consecrated to the Evaluation of coordinative compounds of Zink and Vanadium at the stimulation of osteo-regenerative processes in periodontal tissues and at the application of dental implants. The experimental investigation included experiments carried out on 280 white rats. There were taken for the study 24 substances that contained Zink, Vanadium and Nickel. Testing of the influence of some new coordinative compounds of transitive metals (Zn, V, Ni) on osteo-regenerative processes in normal physiological conditions was determined in bone tissues of periodontium and femoral bones were extracted later on used for the determination of principal biochemical indices of bone tissue. There has been determined the most active biologic coordinative compound Zn(CF3CO2)2(γPic)2 (Patent Nr. 950188 AGEPI MD) in regenerative processes of periodontal tissues during the modeling of experimental periodontitis. The detailed study of the influence of the coordinative compounds of Zn and V that have a better biological activity was executed on the rats that had been inserted dental implants made out of Titan. Before the application of the treatment and at the end of the treatment with the above mentioned compounds, there were made blood tests of every rat on hemolymphogram of hematologic analyzer PCE-170 ERMA Japan. There was elaborated a new method of modeling experimental periodontitis at laboratory animals (Patent Nr. 5388 din 2008.01.14, RM). There were studied the following biochemical parameters: alkaline phosphatase, acid phosphatase, substances with medium and small molecular mass (SMSM), necrotic substances (NS), carnosine, nitric oxide, adenosine deaminase, adenylate deaminase. There were accomplished radiovisiographic densitograms.

Investigational methods of patients with periodontal diseases and dental implants. The examination was carried out in accordance with the algorithm of estimation of contraindications and indications suggested by us while inserting dental implants. The elaboration of the algorithm became possible on the base of the experience in insertion of implants Alpha Bio; MIS; Alpha Dent; CeraRoot Zirconium Oxide Dental Implants; and the procedures elaborated by us (patent Nr. 2379 from 2004.02.29; patent Nr.8,AGEPI MD from 2008-02-18).

57 patients with diverse periodontal diseases were subjected to the study. A profound investigation of biochemical indices of 27 patients was accomplished; out of them 15 patients were inserted dental implants. Zink picolinate was administrated per os 1 x 3 times a day before meals. The duration of the treatment was 30 days.

I. INTRODUCTION:

One of the most important problems of modern implantology is the bone integration of dental implants including the management of its process. The essential stage is the surgical one; the insertion of the implant in the alveolar socket and obtaining the adherence of the bone to the implant and achieve a direct bone implant surface without involving connective tissue layer. Branemark's concepts of bone integration of the implants are based on clinical and experimental studies, describing the complexity of the process of bone integration of the implants. His postulates confirm that until now the research assures clinical efficacy of implant use, but nevertheless require continued research [1, 2, 6]. Hystomorphological data of osteointegration process of dental implants are in continuous research [3, 4, 5, 7], in this way the studies of the microscopic structure of the implant-bone contact surfaces require a better examination.

II. MATERIAL AND METHODS.

In general, the procedures of insertion of implants in maxillary bones of known laboratory animals are related to a massive traumatism of periodontal tissues as a result of surgical interference, the major risk of inflammation of the wound, the development of inflammatory reactions, sepsis and other complications that influence negatively the results of the investigation. Successful attempts of dental extractions at rats are impossible, because anatomic maxillary dental peculiarities of theses animals, as well as those of rabbits or dogs will lead to maxillary fractions or other complications.

We have elaborated a new experimental model of bone regeneration at the use of which are removed all the above mentioned shortcomings (Invention BOPI MD, nr.12. 2010). The principal stages of the implementation are schematically represented in figure 1.

The advantages of the presented procedure in comparison with the known procedure consists in the removal of the major trauma in the area of the surgical operation where the implant is to be inserted, as well as in the prevention of the risk of the appearance of inflammatory processes, the preservation of the crown part of the central incisor, maximum possible preservation of bone and soft tissues due to the adaptation of the procedure to the real conditions and the optimum choice of the place of the insertion of the implant namely there, where the anatomic place of the tooth root can be found.

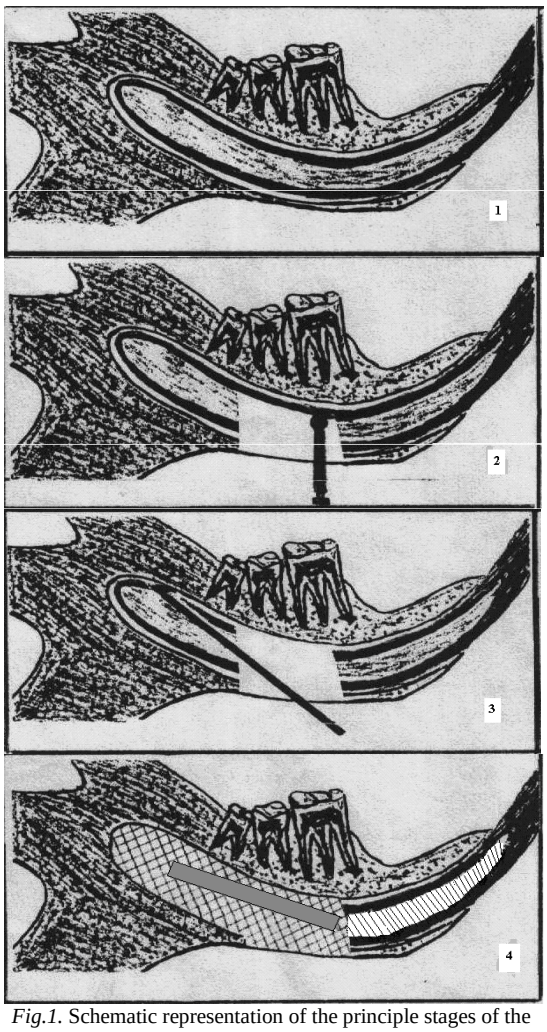

Fig.1. Schematic representation of the principle stages of the accomplishment of the experimental model of the investigation in the process of bone regeneration : 1) rat's mandibulae and teeth ; 2) the appearance of bone deffect in the apical portion of alveolus ; 3) the removal of the apical root portion of the incisive ; 4) the insertion of the implant and of the investigational remedy in the dental alveolus in the root part and the crown one which remained, there was realised devitalixation and obstruction.

The animals were put to sleep with the intervals of 2 weeks and 1 month with a light anesthesia overdose. During the surgical operation the mandibles were realized the preparations of the implants with the surrounding bone tissues. Hemi-mandibular samples were kept for 10 days in 10% formalin solution and then 2 days in 70% alcohol, ethyl alcohol 90% 2 days, 2 days 96% alcohol, absolute alcohol one week, 24 hours a mixture of ethanol + acetone (1:1) 100% acetone for a week with daily changes of acetone. After these procedures, the portion of jaw bone where the implant had been inserted and placed into a propylene resin solution. Solidification of the preparations lasted one week. The slice cuts of the preparations on the limit bone-implant were performed at different depths and parts of the implant and haematoxylin-eosin staining was performed.

III. PURPOSE OF THE RESEARCH:

a comparative histological examination of the potential of osteointegrated implants in different groups of rats which have been given coordinative compounds Zn $(LH)_2$, Zn (LH) etazol, [VO (L-H) etazol] $_2SO_4$ respectively with indices TS-1Z, 2Z-TS, TS-9V, in this way getting the opportunity to study the contact area between the surface of the substrate of the titanium implant with the surrounding tissue structures, including the dynamics of their formation.

Results: Groups of control. Mandibular bone plus implant film were made 15 days later after the experiment had been done (Fig. 2, b) from the moment of the insertion of the implant where existed a powerful intensification of the process of bone regeneration.

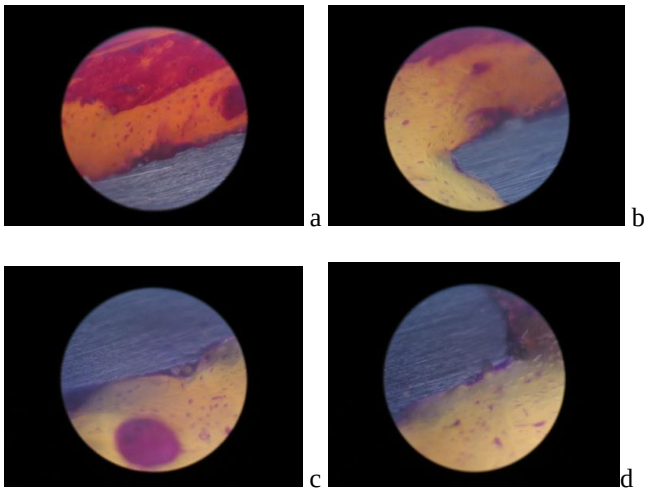

Fig. 2 (a, b, c, d). Microphotograms. Haematoxylin eosin stain. Images of the implants with surrounding tissue in the control group 2 weeks (a, b) from the surgery of insertion of the implant. The new young bone tissue covered the area directly bordering the implant. The tissue maturation is a continuous process, fibrous tissue is noticed on the bordering of the implant (a), bone only rarely adhere to the implant surface (a, b). Histology images (c, d)-images had been taken 1 month later after the surgery.

The structure of newly regenerated trabecular bone surrounds the whole surface of the implant. The tissue is partially separated from the implant surface by a few elongated cells like fibroblasts (fig. 2b). The preparations and photos made in 30 days do not show any big changes in comparison with those, taken after 15 days, the process of tissue maturation has not progressed further. The development and maturation of essential components of fibroblast cells is observed at the edge of the implant surface and new bone formation, but rarely the last more compact adhere to the implant surface (Fig. 2c, d). There are incomplete spaces between the implant and the bone is more limited, highlights rich blood vascularity.

Groups of vertebrates with implants inserted into the bone which were given *TS-1Z.* Histological examination 2 weeks after surgery (3 a, b) the defect is observed, the periphery of which is occupied by granulation tissue rich in cells and blood vessels. Mandibular bone is traumatized by trepanation of bone creating a cavity for insertion of the implant (Fig 3a), but no inflammatory phenomenon had been observed. Also, the microscope image (Fig. 3b) highlights the implant-bone postsurgical area with bone trabeculae since implant insertion and that image show precursors of tissue cells transformed into cells recruited osseoblastic bone formation process - osteoinduction.

After 1 month of surgical intervention (Fig. 3c, d) on mandible bone defect caused by insertion of the implant in cavity is regenerated with bone structure, which replaced fibrous tissue. The junction between implant and adjacent bone is completely renewed and implant is completely anchored into the bone.

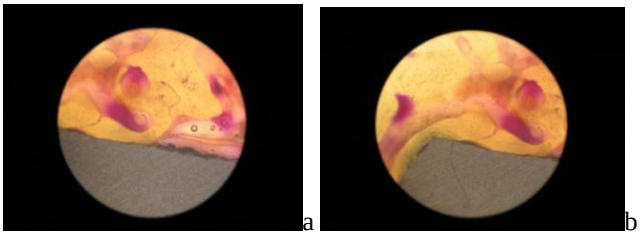

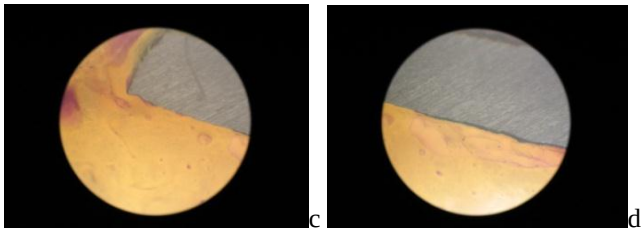

Fig.3 (a, b, c, d). Microphotograms (hematoxilin eosin staining) The group which were given TS-1Z. The results obtained in 2 weeks (a, b) after surgery.Bone implant is surrounded by fibrous tissue which may be substituted by bone tissue (c, d) - histology results in 1 month after the surgery.

We can notice the thin structure of bone trabeculae and newly formed bone, with a network which is mostly fibrous tissue.

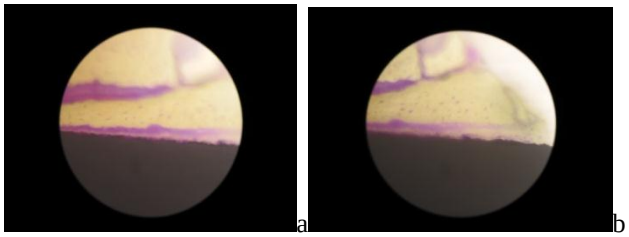

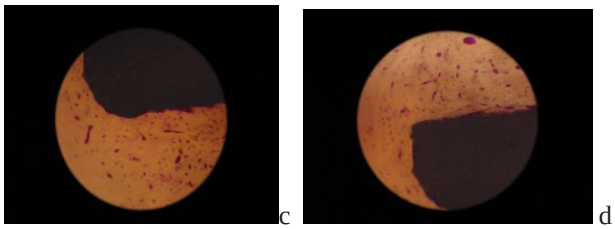

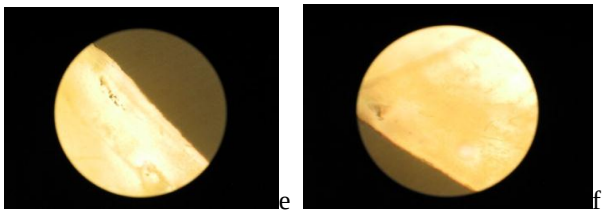

Fig. 4 (a, b, c, d, e, f) Microphotograms. Hematoxylin- eosin stain. Histological implant-bone preparations of rats that received the TS-2Z for 2 weeks (a, b) since implant insertion. On the implant surface we can notice roughness which is due to sandblasting. Rich in blood vascularity. The implant is surrounded by a capsule mostly fibrocellular (a, b) in image (b) the right to see the regeneration of new bone. Image (c, d) of preparation implant + bone after 1 month since implant insertion. (e, f) - another preparation from the same group - image after 1 month-final stage of osteointegration.

Groups of preparate animal implant + bone which were given TS-2Z. The administration of coordinative compounds TS-2Z showed that the defect is replaced by spongy bone, newly formed bone trabeculae and presence of osteoblasts (Fig. 4, b). In none of the histological preparations were observed inflammatory processes, changes in the prevalence of destructive or fibrous tissue.

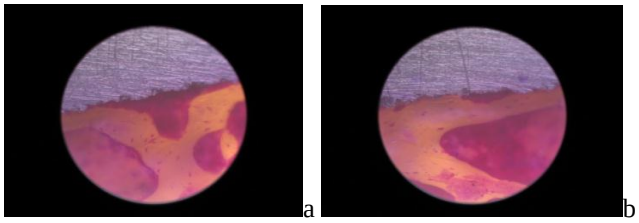

Fig.5 (a, b). Microphotograms 2 weeks since the implant insertion. Group that was administered TS-9V. At the implant-bone boundary is revealed reduced bone tissue regeneration (a) on the implant surface there are bone trabeculae with irregular outline (b).

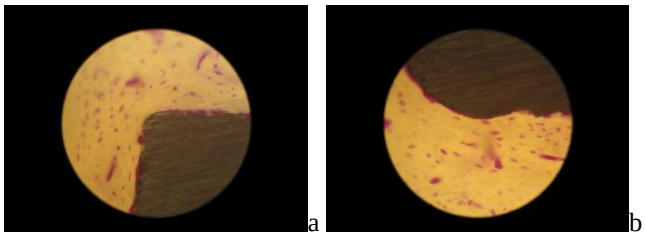

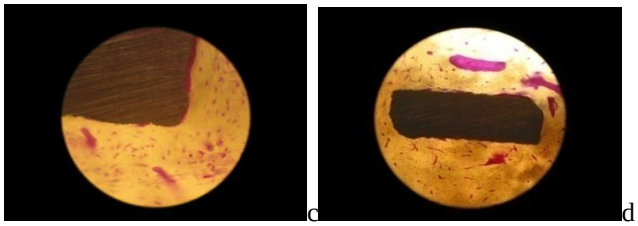

Fig.6 (a, b, c, d). Microphotograms. Implant-bone group preparations on mandible, which has been administered TS-9V. Hematoxylin eosin stain. Osteogenesis in 1 month after the implantion. Regeneration of the bone is anchoring on the implant surface flowing uniformly throughout the perimeter area of the implant. Osteoconduction of osteoblastic cells prevail.

Analysis of junction surface bone to implant after 1 month of implant insertion time (Fig. 4c, d) and (Fig. 4d, e) showed that there are areas where the trabeculae grow in size and regenerate bone in a lamellar structure in comparison to osteointegration processes after 15 days (Fig. 3, b). Formation of direct contact between bone and implant with connective tissue layer is considered low as a morphological manifestation process of osteointegration. Directly on the implant surface was formed bone, presence of fibrous tissue. *Groups of prepares implant + bone of animals which were administered TS-9V.* Histological analysis of preparations of this studied group demonstrated that TS-9V preparation stimulates the regeneration of bone tissue comparing to experiment with compounds administered in previous groups, but the process starts a little later. The images (Fig. 5 a, b) - in 15 days on implant surface there is newly formed bone present, continuing maturation, portions of connective tissue, the consequences of posttraumatic cavity formation in the stage insertion of the implant. After 1 month implant insertion (Fig. 6, b, c, d) - osteogenesis in evolution. The area around postsurgical implant bone defects are restored by a new bone structure, the osteointegrated implant is formed. The process has a satisfactory result.

The comparison of the radiovisiographic densitograms of the rats' mandibles, which were operated and inserted titanium implants, made two weeks and a month after the operation under the influence of the most active coordinative compounds Zn(L-H)-etazol, Zn(L-2H)-sulfadimizin, $Zn(NH_2\text{-}C_6H_4\text{-}CH_2\text{-}C_6H_4\text{-}NH_2)_2SO_4$ and

$Zn(CH_3COO)_2 \cdot 4H_2O$) show a high intensity of osteointegration activity of the edges of the bone cavity surrounding the implant (photo 7, 8, 9, 10). The most relevant results were registered during the application of the compound $Zn(NH_2\text{-}C_6H_4\text{-}CH_2\text{-}C_6H_4\text{-}NH_2)_2SO_4$, this indicates the fact of a more pronounced osteoinductive action of this substance in the graphic image (figure 11).

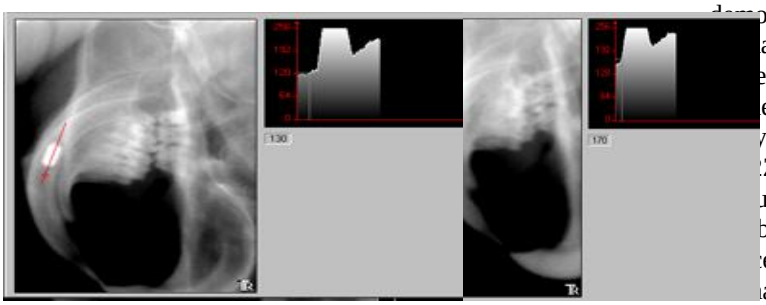

Foto 7. Control in two weeks.

Foto 8. Control in a month.

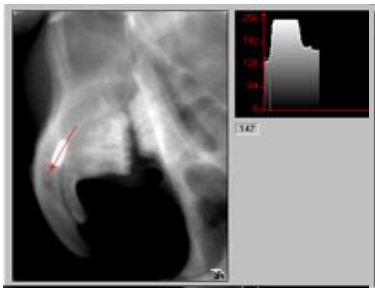

Foto 9.($Zn(NH_2\text{-}C_6H_4\text{-}CH_2\text{-}C_6H_4\text{-}NH_2)_2SO_4$ (after two weeks).

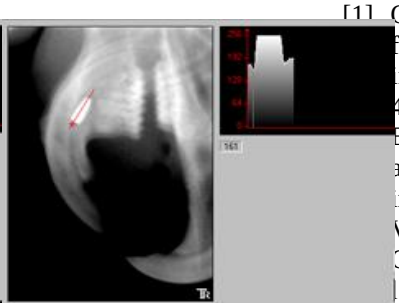

Foto 10.($Zn(NH_2\text{-}C_6H_4\text{-}CH_2\text{-}C_6H_4\text{-}NH_2)_2SO_4$ (after a month).

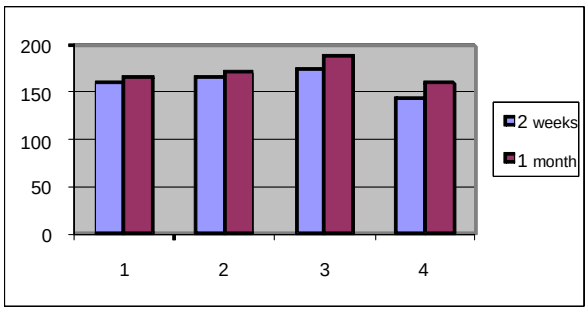

Fig.11. Statistic comparison of densitograms

two weeks and a month after the the insertion of the implants out of titan and the administration of the most active coordinative compounds : *1* – Zn(L-H)-etazol; *2* – Zn(L-2H)-sulphadimizyn; *3* – $Zn(NH_2\text{-}C_6H_4\text{-}CH_2\text{-}C_6H_4\text{-}NH_2)_2SO_4$; *4* – $Zn(CH_3COO)_2 \cdot 4H_2O$.

IV. CONCLUSIONS:

Analyzing the histological examination with the results we conclude that the best indicators of osteointegration process are found in all groups which have been given coordinative compounds $Zn(LH)_2$, Zn(LH)etazol, $[VO(L\text{-}H)etazol]_2SO_4$.

The results of this study also come up with arguments of guidance on the use of dental implants with administering of coordinative compounds of Zn. There are coordinative compounds that can be used in implantology and there is a necessity to make direct studies of implant-bone interface involving molecular medicine studies. Histological analysis of the preparations which received the compounds mentioned above, in comparison with the control group, demonstrated success of the guided tissue and bone ation in intimate contact with implant surface but also enetration into the pores of the implant. Bone integration e implants were observed in most unique comparative ysis between group of study and the administration of Z compound, but TS-1Z compounds, TS-9V that ulated bone regeneration. Histological results confirm benefic results with biochemical and hematological es which improved after the implant application at the als that were administered coordinative compounds Zn $(LH)_2$, Zn (LH) etazol, $[VO (L\text{-}H) etazol]_2SO_4$.

BIBLIOGRAPHY

[1] COOPER, L. F. Biologic determinants of bone formation for osseointegration: clues for future clinical improvements // J Prosthet Dent. – 1998. – Vol. 80, Nr. 4. – P. 439-449.

EARTHMAN J. C., Y. LI , L. R., Van SCHOIACK, et al. Reconstructive materials and bone tissue engineering in implant dentistry // Dent Clin North Am. -2006. – Vol. 50, Nr. 2. – P. 229-244.

Granciuc Gh., Ciuntu O. Action du remede stimulant l'osteogenese sur l'application des implants de titane chez les rats blancs. V Congres de l'Entente Medicale Mediterranienne et XXII Semaine medicale Balkanique. Istambul, Turcia, 1994.

[4] Granciuc Gh., Ciuntu O. La normalisation des dereglements metabolique presentes a la paradontite experimentale a l'aide d'une nouvelle preparate. XXIII-e Semaine Medicale Balkanique. Constanţa, Romînia, 1992.

[5] Granciuc Gh., Ciuntu O. La normalisation des dereglements metabolique presentes a la paradontite experimentale a l'aide d'une nouvelle preparate. XXIII-e Semaine Medicale Balkanique. Constanţa, Romînia, 1992.

[6] Granciuc Gh., Nastas I., Gulea A. Influenţa unor preparate noi de zinc si vanadiu asupra proceselor osteoregenerative in parodonţiu. Anale Ştiinţifice ale Universităţii de Stat de Medicină şi Farmacie „N. Testemiţanu", Vol. 1: Probleme medico – biologice şi farmaceutice, Chişinău, 2005, pp. 336-339.

[7] TRIPLETT R. G., U. FROHBERG, N. SYKARAS, R. D. WOODY. Implant materials, design, and surface topographies: their influence on osteointegration of dental implants. // J Long Term Eff Med Implants. – 2003. – Vol. 13, Nr. 6. – P. 485-501.

Advanced EEG Signal Processing

Rodica STRUNGARU, G. Mihaela UNGUREANU
Politehnica University of Bucharest, Iuliu Maniu 1-3, Bucharest, Romania, RO-061071
Rodica.Strungaru@elmed.pub.ro, mickyungureanu@yahoo.de

***Abstract* – The study investigates the performance of some EEG signal processing methods in detecting the signal variations within the Event-Related Potential (ERP) and in extracting the EEG effective connectivity, and the obtained results are discussed. The advantage of applying the Independent Component Analysis (ICA) in EEG analysis is also considered. The EEG data are recorded in the framework of BCI 2005 competition, during a motor imager task, and includes segments of Event-Related (De)synchronization, revealed be the proposed signal processing methods: Event-Related Spectral Perturbation, , the Inter-Trial Phase Coherence, the Inter-Trial Linear Coherence and the Event Related Cross- Coherence. The effective connectivity is analyzed in time and frequency domain, by applying the Granger Causality Index (GCI) and the Partial-Directed Coherence (PDC) respectively, as time-variant or time-invariant methods.**

***Index Terms* – EEG, effective connectivity, ERP, ICA.**

I. INTRODUCTION

The brain behavior is still unknown and lately a lot of efforts are done to reveal i) its anatomical connectivity (AC), determined by the anatomical links, ii) its functional connectivity (FC) obtained when analyzing the statistical dependencies among the EEG signals, or iii) its effective brain connectivity (EC), which represents the instantaneous information flow within the brain [1]. The effective connectivity is to be extracted in time or in frequency domain, by using the Granger Causality Index or the Partial Directed Coherence. Both methods need a good EEG channel selection in order to have a high performance. The EEG channel selection is usually done after a deep channel analysis, in time and/or frequency domain, after investigating the functional connectivity. The current study shows a typical EEG signal processing when investigating the EEG effective connectivity.

II. DATA DESCRIPTION

The EEG dataset consist of EEG segments lasting for 7 s, recorded during a tongue motor imagery task. The first 2 s are used to extract the EEG characteristics corresponding to the resting state, before the stimuli are applied. A beep fixation cross makes the subjects concentrate on the EEG task; it lasts on the screen for 1 s. An arrow appears then, indicating the subjects to imagine the motor task, during a period of 4 s (Fig. 1) [2].

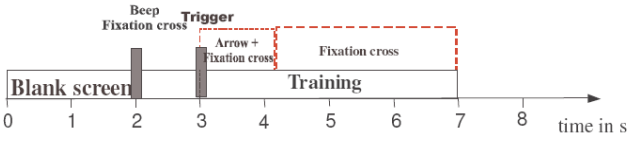

Fig. 1. Paradigm description

III. SIGNAL PROCESSING METHODS

Most of the EEG studies analyze the signal behavior in time or in frequency domain, when considering some particular stimuli that generate the Event-Related Potential (ERP). Since the non-stationary EEG signal has a low amplitude, decreasing exponentially with frequency, the time-domain analysis consists in averaging the corresponding EEG segments, which allows the localization of paradigms (i.e. P300, or P3 represents a positive peak in ERP).

The frequency-domain analysis usually investigates the variations of the spectral components, relatively to a period of relaxation, when the ERP is supposed not to be relevant (a short period before the stimulus application). The most applied frequency-domain methods are: the Event Related Spectral Perturbation, the Inter-Trial Phase Coherence, the Inter-Trial Linear Coherence and the Event Related Cross-Coherence.

Event Related Spectral Perturbation (ERSP)

The event related spectral perturbation allows scientist to observe when the spectral components are (much) reduced after a certain event, which is reported in literature as Event-Related Desynchronization (ERD) or to notice whether the neurons are getting synchronized, generating some additional frequency components, which is known as Event-Related Synchronization (ERS) [3].

The method performs an average over all the similar trials, in frequency-domain, to get the information relevant for the analyzed EEG task:

$$ERSP(f,t)=\frac{1}{n}\sum_{k=1}^{n}\left|F_k(f,t)\right|^2 \qquad (1)$$

where n represents the number of EEG segments, $F_k(f,t)$ is the spectral component at frequency f, computed at time t, for the k-th analyzed EEG segment. $F_k(f,t)$ can be computed by applying the Short-Time-Fourier Transform (STFT) and Wavelet Transform.

Inter-Trial Phase Coherence (ITPC)

The Inter-Trial Phase Coherence (ITPC) reveals the phase synchronization, relatively to the resting state, when considering different trials:

$$ITPC(f,t)=\frac{1}{n}\sum_{k=1}^{n}\frac{F_k(f,t)}{\left|F_k(f,t)\right|} \qquad (2)$$

When the phase coherence is determined based on the spectrum averaging, normalized by the averaged spectrum, we get the Inter-Trial Linear Coherence:

$$ITLC(f,t)=\frac{\sum_{k=1}^{n}F_k(f,t)}{\sqrt{n\sum_{k=1}^{n}\left|F_k(f,t)\right|^2}} \quad (3)$$

Event Related Cross- Coherence (ERCOH)

Event Related Phase Cross-Coherence (ERCOH) determines the relation between two different event types, by analyzing the phase of the corresponding computed spectra.

$$ERPCOH^{a,b}(f,t)=\frac{1}{n}\sum_{k=1}^{n}\frac{F_k^a(f,t)F_k^b(f,t)^*}{\left|F_k^a(f,t)F_k^b(f,t)\right|} \quad (4)$$

When the averaging doesn't include the normalization, which extracts only the phase, the Event Related Linear Cross-Coherence (ERLCOH) is computed:

$$ERLCOH^{a,b}(f,t)=\frac{\sum_{k=1}^{n}F_k^a(f,t)F_k^b(f,t)^*}{\sqrt{\sum_{k=1}^{n}\left|F_k^a(f,t)\right|^2}\sqrt{\sum_{k=1}^{n}\left|F_k^b(f,t)\right|^2}} \quad (5)$$

Independent Component Analysis (ICA)

ICA extracts the components that are not only decorrelated but also independent. It considers the computation of higher order moments (3rd and 4th moment) and is suitable for signals that have no more than one Gaussian component [4]. The algorithm is briefly described in the figure bellow:

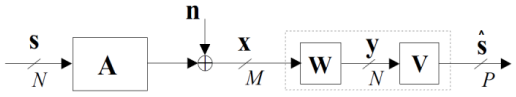

Fig. 2. ICA model - BSS extraction of *p* signals

ICA extracts the signal sources by applying the matrix inverse:

$$\mathbf{s}=\mathbf{A}^{-1}\mathbf{x} \quad (6)$$

Two of the most representative ICA algorithms reported in the literature are: i) the one developed by J. F. Cardoso and Antoine Souloumiac, JADE (joint approximate diagonalization of eigen-matrices) (Cardoso & Souloumiac, 1993); ii) FastICA, developed by Hyvärinen; it is based on a fixed-point iteration scheme maximizing non-Gaussianity as a measure of statistical independence. The idea of ICA is to extract the vector sources, **s,** with *q* components, from the recorded vector **x**, including *p* channels:

$$\mathbf{x}=\mathbf{As}+\mathbf{n} \quad (7)$$

A is the mixing matrix, **n** represents the additive noise. The following assumptions must be met in order to apply ICA:

1. **A** has linear independent columns (satisfied for real signals usually)
2. **x** contains independent variables
3. **n** and **x** are independent**.**

Under these assumptions the mixing matrix can be estimated and the sources are extracted:

$$\mathbf{s}\approx\hat{\mathbf{s}}=\hat{\mathbf{A}}^{-1}\mathbf{x} \quad (8)$$

ICA (JADE)

It is the most applied ICA algorithm and uses the fourth cumulant to compute the kurtosis. The steps of the algorithm are:

1. Initialization (data whitening):

$$\hat{\mathbf{W}}=diag\left(\left(\lambda_1-\hat{\sigma}^2\right)^{-1/2},\cdots,\left(\lambda q-\hat{\sigma}^2\right)^{-1/2},0,\cdots,0\right)\mathbf{V}^T$$

with $\hat{\mathbf{y}}=\hat{\mathbf{W}}\mathbf{x}$ and,

$$\hat{\sigma}^2=\frac{1}{p-q}\cdot\sum_{j=p+1}^{q}\lambda_j$$

with $q<p$.

2. Computation of the Kurtosis for $\hat{\mathbf{y}}$; the set of the fourth cumulants, $\left\{Q_i^y\right\}$, is obtained.

3. Optimize an orthogonal contrast: the matrix V has to be estimated so that the contrast function is minimized:

$$\phi^{JADE}=\sum_{ijkl\neq ijkl}Q_{ijkl}^y=\sum_i off\left(\mathbf{V}^T\mathbf{Q}_i^y\mathbf{V}\right)$$

where $off(\mathbf{A})$ are the nondiagonal elements:

$$off(\mathbf{A})=\sum_{i\neq j}a_{ij}$$

The matrix **V** is computed using the Jacobian.

4. Mixing matrix estimation:

$$\hat{\mathbf{A}}=\mathbf{W}^T\mathbf{V}$$

5. The extraction of the independent components:

$$\mathbf{s}\approx\hat{\mathbf{s}}=\mathbf{V}^T\mathbf{y}=\mathbf{V}^T\mathbf{W}\mathbf{x}$$

IV. EFFECTIVE CONNECTIVITY DETECTION

The effective connectivity can be estimated based on the linear multivariate auto-regressive model. When the model parameters are time-varying, the Granger Causality Index and the Partial Directed Coherence are time-variant; otherwise, they are computed as time-invariant measures of effective connectivity.

Granger Causality Index

Let us consider the full MVAR(*p*) model with regard to *y* with time-dependent parameters and with the prediction error:

$$\mathbf{y}(n)=\sum_{k=1}^{p}\mathbf{A}_k(n)\cdot\mathbf{y}(n-k)+\boldsymbol{\varepsilon}_y(n),\quad \mathbf{A}_k(n),\boldsymbol{\varepsilon}_y(n)\in\Re^N \quad (9)$$

The reduced MVAR(*p*) model is so:

$$\mathbf{v}_i(n)=\sum_{k=1}^{p}B_k(n)\mathbf{v}_i(n-k)+\boldsymbol{\varepsilon}_{v_i}(n),\quad \mathbf{B}_k(n),\boldsymbol{\varepsilon}_{v_i}(n)\in\Re^{N-1}, \quad (10)$$

with:

$$\mathbf{v}_i=(y_1,\ldots y_{i-1},y_{i+1},\ldots,y_M)^T$$

Multivariate Time-variant Granger Causality (MVAR tvGCI) from *i* to *j* is defined by:

$$\gamma(i\rightarrow j)(n)=\log\left(\frac{\mathrm{var}_j(\varepsilon_{vi}(n))}{\mathrm{var}_j(\varepsilon_y(n))}\right) \quad (11)$$

When only pairs of signals are considered, we have the Bivariate Time-Variant Granger Causality Index (BIV tvGCI).

Partial Directed Coherence

The PDS is evaluated by:

$$\pi_{ij}(\omega)=\frac{\bar{A}_{ij}(\omega)}{\sqrt{\bar{\mathbf{a}}_j^H(\omega)\Sigma^{-1}\bar{\mathbf{a}}_j(\omega)}} \qquad (12)$$

where:

$$\bar{\mathbf{A}}(\omega)=1-\mathbf{A}(\omega)=$$
$$=\left[\bar{\mathbf{a}}_1(\omega)\quad \bar{\mathbf{a}}_2(\omega)\quad \cdots\quad \bar{\mathbf{a}}_M(\omega)\right]$$

and

$$A_{kl}(\omega)=\delta_{kl}-\sum_{r=1}^{p}\hat{a}_{kl,r}e^{-i\omega r}$$

The performance in EC estimation depends mainly on improving the parameter estimation for the group EC analysis.

V. RESULTS AND DISCUSSIONS

Figure 3 shows the ERD starting at 1.5 s after the stimulus application, in the beta frequency band. An ERS appears just after the stimuli application, at about 0.5 s, in alpha band. The ITC has no relevant information for the analyzed motor imagery task. Even when the ICA is applied, the ITC is not relevant for the study (see Fig. 4). Contrary, ICA improves the EEG analysis in frequency domain, when considering the ERSP (see Fig. 5).

The ERP is presented in Fig. 6, for all the analyzed trials.

The spectral maps for different spectral components are shown in Fig. 7.

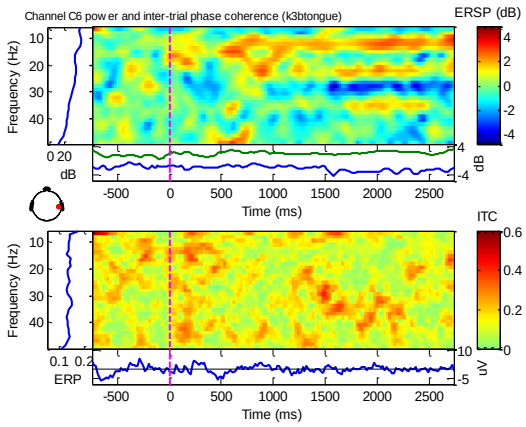

Fig. 3. ERSP (up) and ITC (down), for channel C6, analyzed during the tongue motor imagery task. The ERD/ERS is to be noticed at about 30 Hz/ 10 Hz.

Figure 8 presents the variation of the EEG maps in time.

The effective connectivity, shown in Fig. 9, reveals an effective connection from channel 5 to the others, by applying the tvGCI. When the signal is assumed to be stationary (the time-invariant PDC), which is not correctly describing the analyzed EEG signal, no connection is identified.

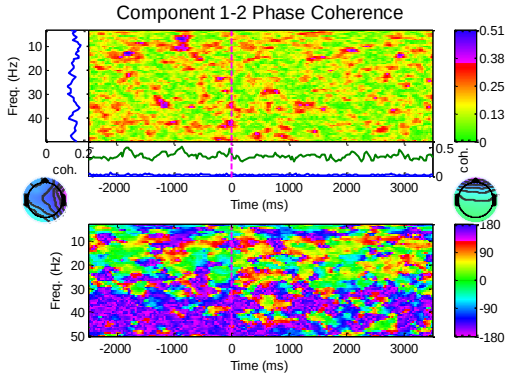

Fig. 4. ERPCOH for the 1st and 2nd ICA components.

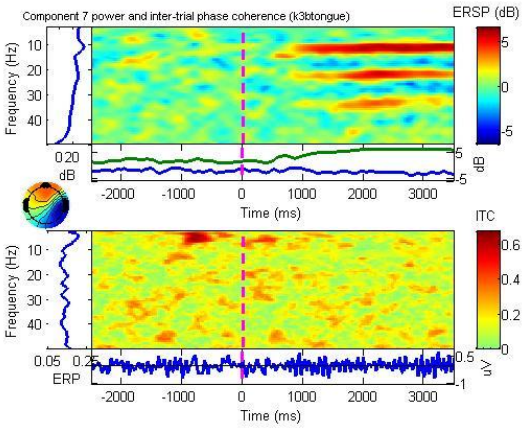

Fig. 5. ERSP and ITC of the 6th and 7th ICA components, when considering the tongue motor imagery task

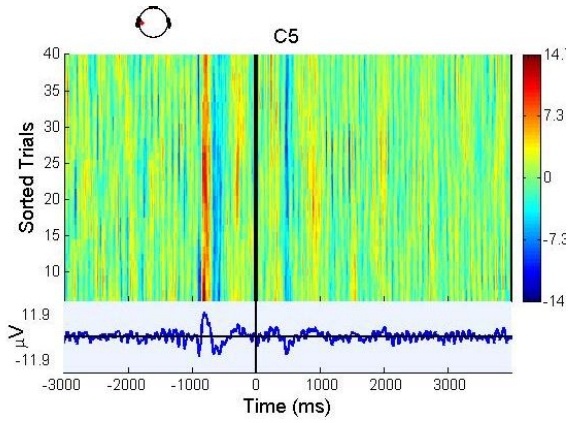

Fig. 6. ERP for all trials (Channel 28 – C5)

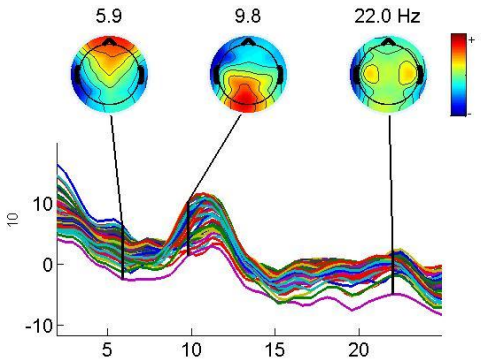

Fig. 7. Pseudocolor spectral maps for different frequency bands.

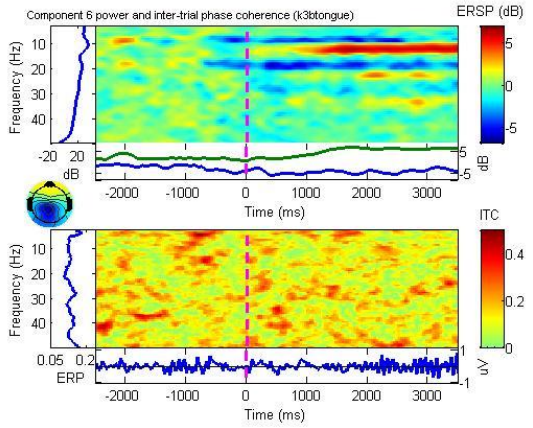

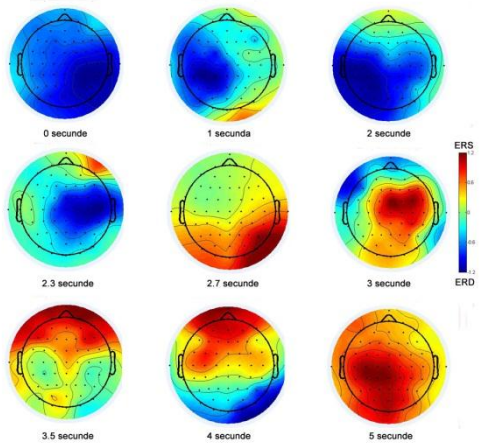

Fig. 8. The variation of pseudocolor spectrum maps in time (tongue motor imagery task)

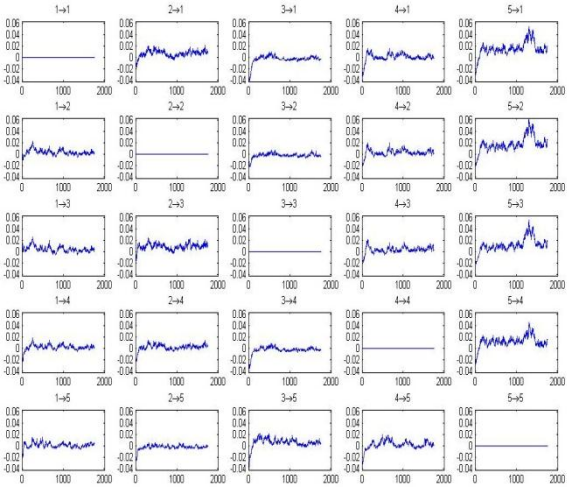

a)

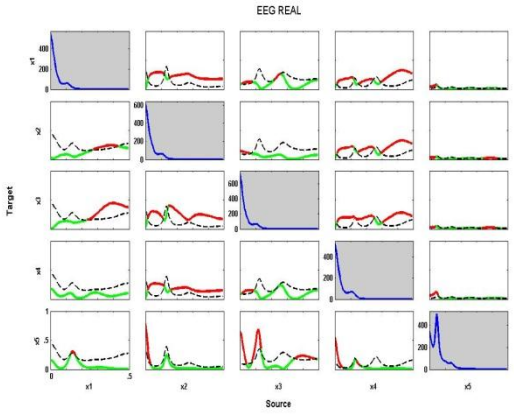

b)

Fig. 9. Estimation of EEG effective connectivity: a) tv-GCI; b) PDC

ACKNOWLEDGMENTS

The work was funded by the Sectorial Operational Programme Human Resources Development 2007-2013 of the Romanian Ministry of Labor, Family and Social Protection through the Financial Agreement POSDRU/6/1.5/S/19.

REFERENCES

[1] D. Hemmelmann, M. Ungureanu, W. Hesse, T. Wüstenberg, J. R. Reichenbach, O. W. Witte, H. Witte, L. Leistritz, "Modelling and analysis of time-variant directed interrelations between brain regions based on BOLD-signals," Neuroimage, vol. 45(3), pp. 722-37, 2009 Apr 15.

[2] A. Schlogl, F. Lee, H. Bischof, G. Pfurtscheller, "Characterization of four-class motor imagery EEG data for the BCI-competition 2005," J. Neural Eng. 2 L14–L22, 2005

[3] G Pfurtscheller, F. H. Lopes da Silva, "Event-related EEG/MEG synchronization and desynchronization: basic principles," Clin. Neurophys., vol. 110, pp. 1842-1857, 1999.

[4] A. Hyvarinen, J. Karhunen, E. Oja, Independent Component Analysis, John Wiley & Sons, 2001.

Polarization-Singular Processing of Biological Layers Laser Images in Order to Diagnose and Classify their Optical Properties

Alexander G. USHENKO, Alexander V. DUBOLAZOV, Artem O. KARACHEVTSEV
Chernivtsi National University
yuriyu@gmail.com

***Abstract* – Presented in this work are the results of investigations aimed at analysis of coordinate distributions of the fourth Stokes vector parameter in laser images of three types of phase-inhomogeneous layers, namely: rough, ground and bulk scattering layers. To characterize this parameter for all the types of phase-inhomogeneous layers, the authors have offered to use three groups of parameters: statistic moments of the first to fourth orders, autocorrelation functions, logarithmic dependences for power spectra. Ascertained are the criteria for diagnostics and classification of phase-inhomogeneous layers optical properties.**

***Index Terms* – polarization, singularity, birefringence, autocorrelation, Stokes vector, Jones matrix.**

I. INTRODUCTION

By tradition, the processes of transforming optical radiation of phase-inhomogeneous objects and media are considered, as a rule, in a statistic approach (theory of radiation transfer [1], Monte-Carlo modeling [2]). Among the most spread traditional methods for studying the scattered light fields, one can separate the following independent directions: "scalar" (photometry and spectrophotometry) [3, 4] and "vector" (polarization nephelometry, Mueller-matrix optics) [5 - 16]. Using these approaches, determined are interrelations between the sets of statistic moments of the 1-st to the 4-th orders [6, 7, 11, 15], correlation functions [5, 8, 9, 14], fractal dimensions [5-7] that characterize phase-inhomogeneous or rough surfaces and coordinate distributions for phases [15, 16], azimuths and ellipticity of polarization in their laser images [6 - 16].

In parallel with traditional statistic investigations, formed in recent 10 to 15 years is the new optical approach to describe a structure of polarizationally inhomogeneous fields in the case of scattered coherent radiation. The main feature of this approach is the analysis of definite polarization states to determine the whole structure of coordinate distributions for azimuths and ellipticities of polarization. The so-called polarization singularities are commonly used as these states [15, 17, 18]:

- states with linear polarization when the direction of rotation for the electric field vector is indefinite, the so-called L-points;
- circularly-polarized states when the azimuth of polarization for the electric field vector is indefinite, the so-called C-points.

It is noteworthy that there exists a widespread group of optically anisotropic biological objects for which the methods of laser polarimetric diagnostics are not so efficient. Optically-thin (coefficient of extinction $\tau \le 0.1$) layers of various biological fluids (bile, urine, liquor, synovial fluid, blood plasma, etc.) can be related to these objects. All these layers possess considerably less optical anisotropy (the possibility of C-points forming is sufficiently small) of the biological component matter as compared with birefringent biological tissue structures [5]. On the other hand, the biological fluids are more available for a direct laboratory analysis as compared to traumatic methods of biological tissues biopsy. From the above reasoning, it seems topical to search new, additional parameters for laser diagnostics of optically anisotropic structures in biological fluids.

This work is aimed at ascertaining the possibilities to diagnose and classify phase-inhomogeneous layers (PhIL) of various types (surface-scattering, subsurface-scattering and bulk-scattering ones) by determination values and ranges for changing the statistic (moments of the 1-st to the 4-th orders), correlation (autocorrelation functions) and fractal (logarithmic dependences for power spectra) parameters that characterize coordinate distributions for polarization-singular states in PhIL laser images.

II. MODEL CONCEPTION

As a base for analytical description of processes providing formation of polarization-inhomogeneous images for various types of PhIL, we have used the model conceptions developed in the works [5-8]:

- surface-scattering PhIL is a rough surface (superficial layer of the skin epithelium) consisting of an ensemble of quasi-plane, chaotically oriented micro-areas with optical dimensions $l > \lambda$ - **group 1**;
- PhIL with surface and subsurface scattering – ground glass with rough external and subsurface (the layer of collagen fibrils of the skin derma) components - **group 2**;
- PhIL with bulk scattering – optically thick layer of the skin derma of a various optical thickness - **group 3**.

Mechanisms providing formation of polarization-inhomogeneous images for rough surface

Optical properties of each micro-area of rough layer of the epithelium are exhaustively characterized with the Jones operator of the following look

$$\{R\} = \begin{Vmatrix} 1 & 0 \\ 0 & p_y / p_x \end{Vmatrix}. \quad (1)$$

It is possible to show that within the sizes ($\Delta x, \Delta y$) of one micro-area there takes place the change of polarization azimuth α inherent to the refracted plane-polarized laser wave with the initial azimuth α_0

$$\alpha(\Delta x, \Delta y) = arctg\left(p_y U_{0y} / p_x U_{0x} \right) = arctg\left[(\Delta p_{xy}) tg\alpha_0 \right], \quad (2)$$

where U_{0x}, U_{0y} are orthogonal components of the amplitude U_0, p_x, p_y - Fresnel amplitude coefficients for transmission [5].

Thus, in the approach of single scattering the polarization image of rough surface may be considered as coordinate-distributed parts of *L*-polarized states [9, 10].

Model structure of PhIL with surface and subsurface components – ground surfaces

The process providing formation of a local polarization state can be considered as superposition of "influences" of an optically strained subsurface of optically anisotropic layer of collagen fibrils as well as the surface rough micro-relief one disposed in sequence. From the analytical viewpoint, this scenario can be described by superposition $\{F\}$ of the Jones matrix operators for these partial layers (subsurface $\{T\}$ and surface $\{R\}$)

$$\{F\}=\{R\}\{T\}=\begin{Vmatrix} f_{11} & f_{12} \\ f_{21} & f_{22} \end{Vmatrix}=\begin{Vmatrix} (r_{11}t_{11}+r_{12}t_{21}); & (r_{11}t_{12}+r_{12}t_{22}); \\ (r_{21}t_{11}+r_{22}t_{21}); & (r_{21}t_{12}+r_{22}t_{22}) \end{Vmatrix}, \quad (3)$$

$$\{T\}=\begin{Vmatrix} t_{11} & t_{12} \\ t_{21} & t_{22} \end{Vmatrix}=\begin{Vmatrix} [\cos^2\gamma+\sin^2\gamma\exp(i\delta)]; & [\cos\gamma\sin\gamma\exp(i\delta)]; \\ [\cos\gamma\sin\gamma\exp(i\delta)]; & [\sin^2\gamma+\cos^2\gamma\exp(i\delta)] \end{Vmatrix}. \quad (4)$$

Here, γ is the direction of the optical axis of fibril; δ - phase shift between orthogonal components (U_x, U_y) of the amplitude (U) of laser wave with the wavelength λ that arises as a consequence of birefringence in the matter Δn.

If taking into account the relations (1), (3) and (4), it follows that within the limits $(\Delta x,\Delta y)$ of a local bulk formed is an elliptically polarized part of the object field with the following parameters

$$\tilde{\alpha}(\Delta x,\Delta y)=\arccos\left(\frac{\sin\delta}{\cos 2\left(arctg\left\{\left[\frac{(f_{21}+f_{22})^2}{(f_{11}+f_{12})^2}\right]tg\alpha_0\right\}\right)}\right) \quad (5)$$

$$\tilde{\beta}(\Delta x,\Delta y)=\arcsin\left(\frac{tg\delta}{\sin 2\left(arctg\left\{\left[\frac{(f_{21}+f_{22})^2}{(f_{11}+f_{12})^2}\right]tg\alpha_0\right\}\right)}\right) \quad (6)$$

As it follows from the analytical relations (5) and (6), interaction of the plane-polarized (α_0) wave with the PhIL of this type provides formation of a polarization-inhomogeneous laser image. Among the whole set of values $(\tilde{\alpha},\tilde{\beta})$, formation of L and $\pm C$ polarization states seems to be very probable [7, 15]

$$L- \Leftrightarrow \delta(\Delta x,\Delta y)=q\pi, \quad q=1,2,... \quad (7)$$

$$\pm C- \Leftrightarrow tg\delta(\Delta x,\Delta y)=$$

$$=\sin 2\left(arctg\left\{\left[\frac{(f_{21}(\Delta x,\Delta y)+f_{22}(\Delta x,\Delta y))^2}{(f_{11}(\Delta x,\Delta y)+f_{12}(\Delta x,\Delta y))^2}\right]tg\alpha_0\right\}\right) \quad (8)$$

Polarization structure of laser fields inherent to PhIL with bulk scattering

When analyzing the processes of interaction of laser radiation with these PhIL, we have used the method of superposition of the Jones matrix operators (3) for the set of sequentially disposed optically-thin layers

$$\{\Phi\}=\{\Phi^{(p)}\}\{\Phi^{(p-1)}\}\times\ldots\times\{\Phi^{(1)}\}, \quad (9)$$

Having calculated the set of Jones matrix elements ϕ_{qg} for an optically-thick PhIL, one can define analytical expressions (like to (7) – (8)) to find L and $\pm C$ polarization states in the laser image

$$L- \Leftrightarrow \delta^*(\Delta x,\Delta y)=q\pi, \quad q=1,2,... \quad (10)$$

$$\pm C- \Leftrightarrow tg\delta^*(\Delta x,\Delta y)=$$

$$=\sin 2\left(arctg\left\{\left[\frac{(\phi_{21}(\Delta x,\Delta y)+\phi_{22}(\Delta x,\Delta y))^2}{(\phi_{11}(\Delta x,\Delta y)+\phi_{12}(\Delta x,\Delta y))^2}\right]tg\alpha_0\right\}\right) \quad (11)$$

Thus, the above analytical consideration (relations (1) to (11)) for various scenarios of transformation of laser radiation by PhIL in all the cases enabled to reveal the principled possibility of formation of polarization-singular states ($\beta=0$, $\beta=\pm\pi/4$) in respective laser images.

In this work, to describe coordinate (x,y) distributions for polarization-singular (L, $\pm C$) states in laser images for all the types of PhIL [7, 15]

$$\begin{cases} V_4(x,y)=0 \leftrightarrow L(\beta=0); \\ V_4(x,y)=\pm 1 \leftrightarrow \pm C(\beta=\pm\pi/4) \end{cases} \quad (12)$$

III. EXPERIMENTAL SETUP

Our study of polarization-inhomogeneous laser images inherent to PhIL was performed using the optical scheme of a laser polarimeter (figure 1) [5, 15]

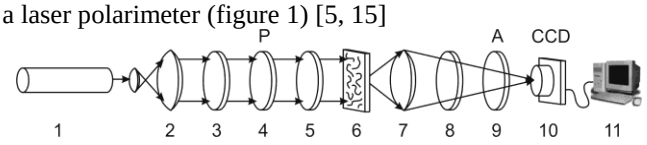

Fig. 1. Optical scheme of the polarimeter: 1 – He-Ne laser; 2 – collimator; 3, 5, 8 – quarter-wave plates; 4, 9 – polarizer and analyzer, respectively; 6 – object under investigation; 7 – micro-objective; 10 – CCD camera; 11 – personal computer

Illumination was performed using a parallel beam (Ø = 10^4 μm) from a He-Ne laser (λ = 0.6328 μm) 1. The polarization illuminator (quarter-wave plates 3 and 5 as well as polarizer 4) were used to form various polarization states in the laser beam. Polarization images of PhIL 6 were projected using the micro-objective 7 into the plane of the light-sensitive area ($800 pix \times 600 pix$) in CCD-camera 10. Turning the transmission axis of the analyzer 9 by the angles $\pm 45^0$ relatively to the direction of the highest velocity axis for the quarter-wave plate 8, wee could determine the intensities of right ($I_\otimes$) and left ($I_\oplus$) circularly polarized components for each separated pixel of CCD camera 10. It served as a base to calculate coordinate distributions of the fourth parameter in the Stokes vector $V_4(m\times n)$) describing the laser image of PhIL, if using the relation

$$V_4(r_{mn})=\frac{I_\otimes(r_{ik})-I_\oplus(r_{ik})}{I_\otimes(r_{ik})+I_\oplus(r_{ik})}. \quad (13)$$

The two-dimensional array (13) was scanned along the horizontal direction $x\equiv 1, \ldots, m$ with the step $\Delta x = 1 pix$. Within the limits of each local sample $(1_{pix}\times n_{pix})^{(k=1,2,\ldots,m)}$, we calculated the amount (N) of characteristic values $V_4(k)=0$, - ($N_L^{(k)}$) and $V_4(k)=\pm 1$, - ($N_{\pm C}^{(k)}$).

Thus, we determined the dependences $N_L(x) \equiv (N_L^{(1)},\ N_L^{(2)},\ \ldots,\ N_L^{(m)})$ and $N_{\pm C}(x) \equiv (N_{\pm C}^{(1)},\ N_{\pm C}^{(2)},\ \ldots,\ N_{\pm C}^{(m)})$ for amounts of polarization-singular L– and $\pm C-$points within the limits of a laser image for PhIL.

IV. ESTIMATION CRITERIA FOR POLARIZATION IMAGES OF PHIL

Distributions $N_{L,\pm C}(x)$ for the amount of polarization-singular states in laser images of PhIL are characterized with the set of statistic moments of the 1-st to the 4-th orders $Z_{j=1,2,3,4}$ calculated using the following relations [6, 7]

$$Z_1 = \frac{1}{M}\sum_{i=1}^{M}\left|N_{L,\pm C}^{(i)}(x)\right|, \quad Z_2 = \sqrt{\frac{1}{M}\sum_{i=1}^{M}\left[N_{L,\pm C}^{(i)}(x)\right]^2}, \quad Z_1 = \frac{1}{Z_2^3}\frac{1}{M}\sum_{i=1}^{M}\left[N_{L,\pm C}^{(i)}(x)\right]^2, \quad Z_4 = \frac{1}{Z_2^4}\frac{1}{M}\sum_{i=1}^{M}\left[N_{L,\pm C}^{(i)}(x)\right]^4. \tag{14}$$

where $N = 800\times 600$ is the amount of pixels in CCD camera 10 (Fig. 1).

Our analysis of the coordinate structure for $N_{L,\pm C}(x)$ distributions was based on the autocorrelation method by using the function [15]

$$K_{L,\pm C}(m) = \frac{1}{(n-m)\sigma^2}\sum_{t=1}^{n-m}[X_t - \mu][X_{t+m} - \mu]. \tag{15}$$

Here, n is the length of discrete sampling $N_{L,\pm C}(x) = X_1, X_2, ..., X_n$; μ - average value, σ^2 - the dispersion; m, n - positive integers; $(m = 1pix)$ is the step for changing the coordinate $x = 1 \div m$.

As correlation parameters that characterize the dependences $K_{L,\pm C}(\Delta x)$, we chose:

- correlation area $S_{L,\pm C}$

$$S_{L,\pm C} = \int_1^m K_{L,\pm C}(m)dm, \tag{16}$$

- normalized fourth statistic moment $Q_{L,\pm C}$ that determine the kurtosis of the autocorrelation function $K_{L,\pm C}(m)$

$$Q_{L,\pm C} = \frac{N}{\left(\sum_{i=1}^{N}\left(K_{L,\pm C}(m)\right)_i^2\right)^2}\sum_{i=1}^{N}\left(K_{L,\pm C}(m)\right)_i^4; \tag{17}$$

The fractal analysis of the distributions $N_{L,\pm C}(x)$ was performed using the calculation of logarithmic dependences $\log J\left[N_{L,\pm C}(x)\right] - \log d^{-1}$ for the power spectra $J\left[N_{L,\pm C}(x)\right]$ which was calculated as a discrete Fourier transform of the corresponding autocorrelation function $K_{L,\pm C}(m)$ using the MatLab software

$$J\left[N_{L,\pm C}(x)\right] = S_{xx}(w) = \sum_{m=1}^{n} K_{L,\pm C}(m)e^{-j\omega m}, \tag{18}$$

where ω are the normalized frequencies, which correspond to a spatial frequencies ($\omega = d^{-1}$) that are determined by geometrical sizes (d) of PhIL structural elements.

The dependences $\log J\left[N_{L,\pm C}(x)\right] - \log d^{-1}$ are approximated using the least-squares method into the curves $\Phi(\eta)$, straight parts of which serve to determine the slope angles η and calculate fractal F dimensions by using the relations [6, 15]

$$F_{L,\pm C} = 3 - tg\eta. \tag{19}$$

Classification of coordinate distributions $N_{L,\pm C}(x)$ should be performed using the following criteria [14, 15]:

- they are fractal on the condition of a constant slope angle value $\eta = const$ for 2 to 3 decades of changing sizes d;
- they are multi-fractal, if several slope angles $\Phi(\eta)$ are available;
- they are random when any stable slope angles are absent within the whole range of changing sizes d.

In the latter case, the distributions $\log J\left[N_{L,\pm C}(x)\right] - \log d^{-1}$ are characterized with the dispersion

$$D_z = \sqrt{\frac{1}{m}\sum_{i=1}^{m}\left[\log J\left(N_{L,\pm C}(x_i)\right) - \log d^{-1}\right]^2}. \tag{20}$$

V. THE INVESTIGATION OBJECTS CHARACTERISTICS

Fig. 1 illustrates coordinate ($100pix \times 50pix$) distributions of the fourth parameter for the Stokes vector $V_4(m\times n)$ inherent to laser images of PhIL in all the groups.

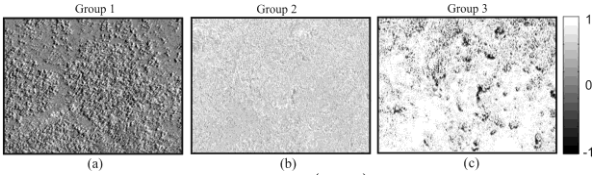

Fig. 1. Coordinate distributions of $V_4(m\times n)$ of laser images inherent to PhIL

Our qualitative analysis of coordinate distributions $V_4(m\times n)$ for laser images of PhIL (figure 1) enabled to reveal:

- Practically all the images of the rough surface of skin (figure 1a) are linearly polarized field $V_4(m\times n) = 0$ (relations (1) and (2)). Availability of a small amount of the parts $V_4(m\times n) \neq 0$ polarized otherwise can be related with interferential effects of multiple interaction of coherent waves with adjacent micro-roughnesses.
- The image of the rough skin surface with a subsurface layer of the derma (figure 1b) is characterized with a developed polarization-inhomogeneous structure formed both by linearly ($V_4(m\times n) = 0$) and elliptically ($V_4(m\times n) \neq 0$) polarized states, including the circularly ($V_4(m\times n) = 1$) polarized ones (relations (5) to (8)).
- The images of the optically thick layer of skin (figure 1c) are characterized with the widest range of changing the azimuth and polarization due to multiple bulk scattering (relations (10-12)), $-1 \le V_4(m\times n) \le 1$.

VI. RESULTS

The performed analysis of results for statistic ($Z^{L,\pm C}_{j=1,2,3,4}$), correlation ($S^{L,\pm C}$, $Q^{L,\pm C}$) and fractal ($F^{L,\pm C}$, $D^{L,\pm C}$) parameters has shown:

- *Statistic parameters.* The most sensitive appears to be both the 1st and the 2nd statistic moments, which characterize the distributions of $L-$ polarization states, and the 3rd and the 4th statistic moments, which characterize the distributions of $\pm C-$polarization states. The difference between of them reaches 2-3 times for $L-$states and 5-7 times for $\pm C-$states;
- *Correlation parameters.* The most sensitive appears to be the normalized fourth statistic moment $Q_{L,\pm C}$ that determine the kurtosis of the autocorrelation function $K_{L,\pm C}(m)$. The intergroup difference reaches one order of magnitude as for $L-$states as for $\pm C-$states;
- *Fractal parameters.* The fractal analysis appears to be effective in differentiation of optical properties of different PhIL too. The difference between the dispersion $D^{\pm C}$ values reaches 2 times;

The possibility to differentiate "group" optical properties of PhIL with surface, subsurface and bulk light scattering is illustrated in Table 1.

TABLE I. THE DIFFERENTIATION POSSIBILITIES

PhIL	Groups 1 – 3	
Parameters	N_L	$N_{\pm C}$
Z_1	⊕	⊕
Z_2	⊕	⊕
Z_3	⊗	⊕
Z_4	⊗	⊕
S	⊗	⊕
Q	⊗	⊕
F	⊗	⊕
D	⊗	⊕

Note: ⊗ - here differentiation is impossible; ⊕ - possible.

VII. CONCLUSION

1. Analyzed in this work are the main physical mechanisms providing formation of polarization singularities in laser images of PhIL with surface, subsurface and bulk light scattering.

2. Offered are statistical, correlation and fractal parameters for polarization-singular estimating the optical properties inherent to PhIL of all types.

3. Determined are the ranges for changing the set of criteria that characterize distributions of the amount of polarization-singular states in laser images, which enabled us to realize both "intergroup" classification and differentiation of optical properties related to PhIL of various types.

REFERENCES

[1] W.-F. Cheong, S. A. Prahl, A. J. Welch, "A Review of the Optical Properties of Biological Tissues," IEEE J. Quantum. Electron. 26, 2166-2185, 1990.

[2] S. A. Prahl, M. Keijzer, S. L. Jacques, A. J. Welch, "A Monte Carlo model of light propagation in tissue," in *SPIE Proceedings of Dosimetry of Laser Radiation in Medicine and Biology*, G. J. Müller and D. H. Sliney, eds. IS 5, 102-111, 1989.

[3] M. J. Everett, K. Shoenenberger, B. W. Colston and L. B. da Silva, "Birefringence characterization of biological tissue by use of optical coherence tomography," Opt. Lett. 23, 228-230, 1998.

[4] J. Shuliang, Yu. Wurong, G. Stoica and V. Lihong, "Optical fiber based Mueller optical coherence tomography," Opt. Lett. 28, 1206-1208, 2003.

[5] Alexander G. Ushenko and Vasilii P. Pishak, "Laser Polarimetry of Biological Tissue: Principles and Applications", in *Handbook of Coherent-Domain Optical Methods: Biomedical Diagnostics, Environmental and Material Science*, Valery V. Tuchin, ed. (Boston: Kluwer Academic Publishers, 2004), pp. 93-138.

[6] O. V. Angelsky, A. G. Ushenko, Yu. A. Ushenko, V. P. Pishak, "Statistical and Fractal Structure of Biological Tissue Mueller Matrix Images", in *Optical Correlation Techniques and Applications*, Oleg V. Angelsky, ed. (Washington: Society of Photo-Optical Instrumentation Engineers, 2007), pp. 213-266.

[7] O.V. Angelsky, A.G. Ushenko, Yu.A. Ushenko, V.P. Pishak, and A.P. Peresunko, "Statistical, Correlation, and Topological Approaches in Diagnostics of the Structure and Physiological State of Birefringent Biological Tissues", in *Handbook of Photonics for Biomedical Science*, Valery V. Tuchin, ed. (USA, CRC Press, 2010), pp. 21-67.

[8] Alexander G. Ushenko, "Polarization structure of laser scattering fields," Opt. Eng. 34, 1088-1093, 1995.

[9] A.G. Ushenko, "Stokes-correlometry of biotissues," Laser Phys. 10, 1286-1292, 2000.

[10] A.G. Ushenko, "The Vector Structure of Laser Biospeckle Fields and Polarization Diagnostics of Collagen Skin Structures," Laser Phys. 10, 1143-1149, 2000.

[11] A.G. Ushenko, "Laser polarimetry of polarization-phase statistical moments of the object field of optically anisotropic scattering layers," Optics and Spectroscopy 91, 313-316, 2001.

[12] O.V. Angelsky, A.G. Ushenko, Ye.G. Ushenko, "2-D Stokes Polarimetry of Biospeckle Tissues Images in Pre-Clinic Diagnostics of Their Pre-Cancer States," J. Holography Speckle 2, 26-33, 2005.

[13] Oleg V. Angelsky, Alexander G. Ushenko, and Yevheniya G. Ushenko, "Complex degree of mutual polarization of biological tissue coherent images for the diagnostics of their physiological state," J. Biomed. Opt. 10, 060502, 2005.

[14] O. V. Angelsky, A. G. Ushenko, and Ye. G. Ushenko, "Investigation of the correlation structure of biological tissue polarization images during the diagnostics of their oncological changes," Phys. Med. Biol. 50, 4811-4822, 2005.

[15] Oleg V. Angelsky, Alexander G. Ushenko, Yevheniya G. Ushenko, Yuriy Y. Tomka, "Polarization singularities of biological tissues images," J. Biomed. Opt. 11, 054030, 2006.

[16] A.G. Ushenko, I. Z.Misevich, V. Istratiy, I. Bachyns'ka, A. P. Peresunko, Omar Kamal Numan, and T. G. Moiysuk, "Evolution of Statistic Moments of 2D-

[17] Distributions of Biological Liquid Crystal Net Mueller Matrix Elements in the Process of Their Birefringent Structure Changes," Advances in Optical Technologies 2010, 423145, 2010.

[18] A I. Konukhov and L.A. Melnikov, "Optical vortices in a vector field: the general definition based on the analogy with topological solitons in a 2D ferromagnet, and examples from the transverse polarization patterns of lasers," J. Opt. B: Quantum Semiclass. Opt. 3, S139-S144, 2001.

[19] J. F. Nye, "Lines of circular polarization in electromagnetic wave fields," Proc. R. Soc. *A* 389, 279-290, 1983.

An Optimized Compounding Approach to Ultrasound Imaging

Yair KERNER and Moshe PORAT
Technion, Haifa 32000, Israel
E-mail: yairk@vision.technion.ac.il, mp@ee.technion.ac.il

***Abstract* – We develop an optimized approach to exploit pairs of ultrasound scans of the same image plane with the aim of enhancing the quality of ultrasound imaging. Each image pair is assumed to be co-registered with 90° separation between the two insonification directions. Using multi-channel image restoration, the proposed approach provides significant improvement to the quality of ultrasound imaging. Enhanced images are presented, and the advantages of this new approach over presently available methods are discussed.**

***Index Terms* – Blind Deconvolution, Image Restoration, Medical Imaging, Spatial Compounding, Ultrasound.**

I. INTRODUCTION

In medical ultrasound imaging, short pulses are emitted from an array of resonant elements with a center frequency typically in the range of 2-10 MHz. Such two-dimensional (or B-mode) scans undergo two types of blur before the echo returns to the transducer: In the axial (longitudinal) direction the blur results from the envelope of the acoustic wave and from properties of the tissue through which the wave propagates; In the lateral (transverse) direction the blur is affected by the width and apodization of the transmission and reception apertures as well as the distance of the imaged object from the focus and medium-related distortions. The model that is commonly used in ultrasound imaging research for the relation between the received signal and the tissue reflectivity is of a linear space-invariant system (LSI). Handling space variations of the Point Spread Function (PSF) is usually through partitioning the imaged plane to smaller regions with approximately invariant PSF.

For more than two decades various algorithms have been suggested to sharpen the images, either by deconvolution assuming the PSF is known [1], [2], or through blind deconvolution [3]-[10]. The prevalent approach in blind deconvolution is to use the LSI method of the Wiener filter to recover the reflectivity image, and therefore most of the effort is concentrated in estimating the PSF. It is worth noting that while a few algorithms used the video image as their input [1], [2], in most of the published work deconvolution is applied to the RF image [3]-[10].

In recent years several authors [11]-[14] developed algorithms for compounding of ultrasound images of the same region from different angles. In parallel, researchers who sought ways to overcome blur phenomena of photographic images developed algorithms for multi-channel image restoration. Ghiglia [15] presented a constrained least-squares algorithm for image restoration given several blurred images of the same object, each corresponding with a different PSF. Later, Katsaggelos et al. [16] presented a systematic framework for performing multi-channel image restoration in the frequency domain. In the field of medical imaging this method was applied to dual-radionuclide imaging [17]. Tom et al. [18] established a maximum-likelihood formulation for the general problem of multi-channel image restoration, and utilized the expectation-maximization algorithm to solve it.

To the best of our knowledge no algorithm was developed to exploit both deconvolution and compounding for ultrasound image applications. It should be also noted that the above-mentioned algorithms for multi-channel restoration were developed for photographic images. When considering these algorithms for the field of ultrasound images, one must note fundamental differences in several characteristics of the problem: the blur transfer function has band-pass behavior in one dimension rather than low-pass in both dimensions, the sampling intervals are different in each direction, and non-linear operations are involved in the display procedure.

The research presented in this paper aims at improving the quality of ultrasound images through exploiting pairs of ultrasound scans of the same plane. Each image pair is assumed to be co-registered with 90° separation between the two-insonification directions.

II. MODEL OF THE PROBLEM

A. Notation

A 2-D spatial location in the imaging plane is denoted as (x, z), where x is the coordinate in the lateral direction and z is the coordinate in the axial direction. In the frequency domain (ω_x, ω_z) represents the spatial frequency in radians. Whenever matrix representation is used the axial direction is column-wise unless stated otherwise. When matrix coordinates appear in parentheses the first parameter specifies the horizontal coordinate $\mathbf{A}(m, n) = \mathbf{A}_{nm}$ in order to keep consistency between matrix and 2-D signal or image formulations.

The matrix **R** indicates the unknown tissue reflectivity in the imaging plane. The matrix **S** denotes the observed RF image, which is the collection of sampled signals from all the transducer elements during a single scan.

B. Tissue reflectivity and degradation

The tissue reflectivity can be considered as resulting from an assembly of reflectors and scatterers [7], [10]. A reflector is an interface, large compared with the wavelength of the ultrasonic pulse, while scatterers are objects, small compared with the wavelength and typically inducing a speckle pattern. For that reason, and following [7], the tissue reflectivity is modeled in this work as the sum of a deterministic function **D** representing the specular reflections and a zero-mean Gaussian stochastic process **U** corresponding with the speckle component:

$$\mathbf{R}(x, z) = \mathbf{D}(x, z) + \mathbf{U}(x, z). \quad (1)$$

The interaction of the ultrasonic pressure field with the tissue is 3-dimensional, but its observation in B-mode imaging is a 2-D space. Subject to customary assumptions, the formation process of the RF image can generally be modeled as a 2-D spatial linear filtering operation with a spatially variant point-spread function [5], [6], [19], [20]. It is possible to segment the image into regions for which the PSF is approximately constant and simple convolution describes with good accuracy the image formation:

$$\mathbf{S}(x, z) = \mathbf{P}(x, z) * \mathbf{R}(x, z) + \mathbf{N}(x, z), \quad (2)$$

where $*$ denotes 2-D convolution, **P** represents the PSF and **N** represents additive noise. The noise term is modeled as a white zero-mean Gaussian random process that is independent of the tissue reflectivity and the PSF [5]-[7].

The system response in the frequency domain $\mathbf{P}(\omega_x, \omega_z)$ is related to the PSF through 2-D Fourier transform. The resolution in the lateral direction is significantly worse than the axial resolution; therefore the PSF has wide extent laterally and narrow support axially. Equivalently, the bandwidth of the system response is much smaller in the lateral dimension than in the axial dimension.

C. Rotation

Rotation is treated as positive when its direction is from the positive ray of the *x*-axis toward the positive ray of the *z*-axis, and as negative when it is in the opposite direction. This implies that if conventional matrix coordinates are employed then positive rotation is clockwise.

Let $\mathbf{A}_1$ and $\mathbf{A}_2$ denote two RF images that were recorded with $\mathbf{A}_2$ taken after the transducer was turned by –90° relative to its direction during the recording of $\mathbf{A}_1$. The superscript $^{\text{rot}}$ is used to indicate 90° rotation, while $^{\text{inv-rot}}$ indicates –90° rotation. Assuming that the tissue reflectivity **R** is the same for both recordings, then:

$$\mathbf{A}_1 = \mathbf{P}_1 * \mathbf{R} + \mathbf{N}_a \quad (3)$$

$$\mathbf{A}_2 = \mathbf{P}_2 * \mathbf{R}^{\text{inv-rot}} + \mathbf{N}_b,$$

where $\mathbf{P}_1$, $\mathbf{P}_2$ denote the system's PSF in each case and $\mathbf{N}_a$, $\mathbf{N}_b$ denote the additive noise. Rotating $\mathbf{A}_2$ in (3) by 90° and substituting: $\mathbf{S}_V \equiv \mathbf{A}_1$, $\mathbf{S}_H \equiv \mathbf{A}_2^{\text{rot}}$, $\mathbf{N}_1 \equiv \mathbf{N}_a$ and $\mathbf{N}_2 \equiv \mathbf{N}_b^{\text{rot}}$, yields:

$$\mathbf{S}_V = \mathbf{P}_1 * \mathbf{R} + \mathbf{N}_1 \quad (4)$$

$$\mathbf{S}_H = \mathbf{P}_2^{\text{rot}} * \mathbf{R} + \mathbf{N}_2.$$

In other words, the blur is treated as rotated by 90° instead of regarding the image as rotated by –90°. Note that for $\mathbf{S}_V$ the axial direction coalesces with the vertical direction, while for $\mathbf{S}_H$ it is horizontal. Therefore, according to the degradation model, **R** is more blurred horizontally to generate $\mathbf{S}_V$ and more blurred vertically to generate $\mathbf{S}_H$.

When dealing with matrices and discrete Fourier transform (DFT), rotation should be given special attention because straightforward 90° rotation results with phase shift in the frequency domain. This is alleviated if the definition of 90° rotation utilizes the periodicity of the DFT:

$$\mathbf{B}(m', n') \equiv \mathrm{T}\mathbf{A} = \mathbf{A}(n', [N-m']_{\text{mod } N}) \quad , \quad (5)$$

$$m' = 0, 1 \ldots N-1$$

where $\mathbf{A}(m, n)$ is a matrix with *N* rows. This is equivalent to column-wise inversion excluding the first row followed by transposition.

D. Sampling grid

We assume that the ultrasonic B-mode scan is performed with a linear array transducer. Hence, the sampling grid is rectangular, but the sampling intervals are different in each direction. The lateral sampling interval d_L is a consequent of the spacing between the piezoelectric crystals, which is in the region of few hundreds of μm. The axial sampling interval d_A is related to the sampling frequency f_S at the receiver and the speed of sound *v* within the tissue:

$$d_A = \tfrac{1}{2}\, v / f_S. \quad (6)$$

For example, if $v \cong 1{,}540$ m/sec and $f_S = 20$ MHz [2]-[4], then $d_A \cong 38.5$ μm, and assuming $d_L = 500$ μm [1], the ratio between the lateral and axial sampling intervals is about 13:1. If $f_S = 10.5$ MHz [8] and the crystal spacing is approximately 200 μm[12], this ratio drops off to around 3:1.

Taking into account the different sampling intervals and treating the matrices of the reflectivity **R** and the PSF **P** as samples on a square grid with intervals d_A in both directions, the discrete-space LSI model for the generation of the 2 source images $\mathbf{S}_V$ and $\mathbf{S}_H$ from the tissue reflectivity **R** is:

$$\mathbf{S}_V = (\mathbf{P}_1 * \mathbf{R}) \downarrow_H K + \mathbf{N}_1 \quad (7)$$

$$\mathbf{S}_H = (\mathbf{P}_2^{\text{rot}} * \mathbf{R}) \downarrow_V K + \mathbf{N}_2,$$

where $\downarrow_H K$ denotes horizontal decimation by factor K and $\downarrow_V K$ stands for vertical decimation.

E. Frequency domain

DFT of (7) with proper zero-padding gives:

$$\mathbf{S}_V(\omega_x, \omega_z) = \mathbf{P}_1(\omega_x, \omega_z)\, \mathbf{R}(\omega_x, \omega_z) + \mathbf{N}_1(\omega_x, \omega_z) \quad (8)$$

$$\mathbf{S}_H(\omega_x, \omega_z) = \mathbf{P}_2(\omega_z, -\omega_x)\, \mathbf{R}(\omega_x, \omega_z) + \mathbf{N}_2(\omega_x, \omega_z)$$

where $\mathbf{S}_V$, $\mathbf{S}_H$, $\mathbf{P}_1$, $\mathbf{P}_2$, **R**, $\mathbf{N}_1$ and $\mathbf{N}_2$ are respectively the 2-D DFT's of $\mathbf{S}_V$, $\mathbf{S}_H$, $\mathbf{P}_1$, $\mathbf{P}_2$, **R**, $\mathbf{N}_1$ and $\mathbf{N}_2$. The zero padding is performed in a way such that all the elements in (8) are square matrices of size $N_{DFT} \times N_{DFT}$.

Using the vector notation $\mathbf{s}_{k,l} \equiv [\mathbf{S}_V(\omega_x, \omega_z), \mathbf{S}_H(\omega_x, \omega_z)]^T$, $\mathbf{h}_{k,l} \equiv [\mathbf{P}_1(\omega_x, \omega_z), \mathbf{P}_2(\omega_z, -\omega_x)]^T$, $r_{k,l} \equiv \mathbf{R}(\omega_x, \omega_z)$, and

$\mathbf{n}_{k,l} \equiv [\mathbf{N}_1(\omega_x, \omega_z), \mathbf{N}_2(\omega_x, \omega_z)]^T$, with $\omega_x = 2\pi k/N_{DFT}$ and $\omega_z = 2\pi l/N_{DFT}$, (8) can be compactly written as:

$$\mathbf{s}_{k,l} = \mathbf{h}_{k,l}\, r_{k,l} + \mathbf{n}_{k,l} \ . \tag{9}$$

The variable $r_{k,l}$ is stochastic with mean $d_{k,l} \equiv \mathbf{D}(\omega_x, \omega_z)$ and variance λ_u, and is assumed to have Gaussian probability density function (PDF) [7]. The noise term $\mathbf{n}_{k,l}$ is a random vector with zero mean and a diagonal 2 × 2 covariance matrix $\mathbf{\Lambda}$, where the diagonal elements are the variances λ_1 and λ_2 of $\mathbf{N}_1(\omega_x, \omega_z)$ and $\mathbf{N}_2(\omega_x, \omega_z)$ respectively.

III. BLUR ESTIMATION

A. The algorithm

The blind deconvolution problem is solved in two steps:

1. Estimation of the blur function.
2. Image reconstruction assuming this estimated function is the true blur and image compounding.

The estimation of the blur function can be viewed as an optimization problem where we search for the unknown parameters of a PDF and for which the maximum-likelihood (ML) approach can be applied. Employing optimization of the direct likelihood function yields a difficult minimization problem since the unknown quantities of reflectivity and blur are coupled through multiplication. The expectation-maximization (EM) algorithm is an iterative technique that greatly simplifies the ML problem.

According to the EM method, the *complete data* **y** is not observed directly, but only by means of the *observed data* **s**, which is related to **y** through a non-invertible linear mapping. Applying to the problem at hand, we define: $\mathbf{y}_{k,l} = [\mathbf{s}_{k,l}^T, r_{k,l}]^T$, so the mapping is: $\mathbf{s}_{k,l} = [\mathbf{I}, \mathbf{0}]^T\, \mathbf{y}_{k,l}$. The unknown quantity $r_{k,l}$ within the complete data is referred to as the *hidden data*. The PDF of the complete data is $f_{\mathbf{y}}(\mathbf{y}|\boldsymbol{\theta})$, where $\boldsymbol{\theta}$ is the set of unknown parameters of the PDF: $\boldsymbol{\theta} = [\mathbf{h}^T, d, \lambda_u, \lambda_1, \lambda_2]^T$.

According to the complete-probability formula:

$$f_{\mathbf{y}}(\mathbf{y}_{k,l}|\boldsymbol{\theta}) = f_r(r_{k,l}|\boldsymbol{\theta})\, f_{\mathbf{s}}(\mathbf{s}_{k,l}|r_{k,l},\boldsymbol{\theta}). \tag{10}$$

Due to the assumption that the stochastic terms are white, $f_{\mathbf{y}}(\mathbf{y}|\boldsymbol{\theta})$ is the product of $f_{\mathbf{y}}(\mathbf{y}_{k,l}|\boldsymbol{\theta})$ over all possible combinations of k and l. Hence the likelihood of the complete data is:

$$L(\boldsymbol{\theta}) = \ln\{f_{\mathbf{y}}(\mathbf{y}|\boldsymbol{\theta})\} = \sum_k \sum_l L_{k,l}(\boldsymbol{\theta}) \tag{11}$$

$$L_{k,l}(\boldsymbol{\theta}) = -\tfrac{3}{2}\ln(2\pi) - \tfrac{1}{2}\ln(\lambda_u\lambda_1\lambda_2) - \tfrac{1}{2}\lambda_u^{-1}|r_{k,l} - d_{k,l}|^2 - \tfrac{1}{2}(\mathbf{s}_{k,l} - \mathbf{h}_{k,l}\, r_{k,l})^\dagger\, \mathbf{\Lambda}^{-1}\, (\mathbf{s}_{k,l} - \mathbf{h}_{k,l}\, r_{k,l}).$$

In the EM algorithm each iteration is composed of two steps: expectation (E step) and maximization (M step). In the E step the conditional expectation of $\ln\{f_{\mathbf{y}}(\mathbf{y}|\boldsymbol{\theta})\}$, using the current estimates of the parameters $\boldsymbol{\theta}^{[n]}$ and conditioned upon the observed data, is calculated:

$$Q(\boldsymbol{\theta}|\boldsymbol{\theta}^{[n]}) = E[\ln\{ f_{\mathbf{y}}(\mathbf{y}|\boldsymbol{\theta}) \}|\mathbf{s},\boldsymbol{\theta}^{[n]}]. \tag{12}$$

In the M step the expectation $Q(\boldsymbol{\theta}|\boldsymbol{\theta}^{[n]})$ is maximized with respect to $\boldsymbol{\theta}$ to provide a new estimation of the parameters:

$$\boldsymbol{\theta}^{[n+1]} = \arg\max_{\boldsymbol{\theta}} Q(\boldsymbol{\theta}|\boldsymbol{\theta}^{[n]}). \tag{13}$$

B. Steps of the algorithm

After (11) is substituted for $f_{\mathbf{y}}(\mathbf{y}|\boldsymbol{\theta})$ in (12), it follows that maximization of $Q(\boldsymbol{\theta}|\boldsymbol{\theta}^{[n]})$ is equivalent to minimization of:

$$J(\boldsymbol{\theta}|\boldsymbol{\theta}^{[n]}) = \sum_k \sum_l J_{k,l}(\boldsymbol{\theta}|\boldsymbol{\theta}^{[n]}) \tag{14}$$

$$J_{k,l}(\boldsymbol{\theta}|\boldsymbol{\theta}^{[n]}) = \ln(\lambda_u\lambda_1\lambda_2) + \lambda_u^{-1}\, |\, E[r_{k,l}|\mathbf{s},\boldsymbol{\theta}^{[n]}] - d_{k,l}\, |^2 + (\mathbf{s}_{k,l} - \mathbf{h}_{k,l}\, E[r_{k,l}|\mathbf{s},\boldsymbol{\theta}^{[n]}])^\dagger\, \mathbf{\Lambda}^{-1} (\mathbf{s}_{k,l} - \mathbf{h}_{k,l}\, E[r_{k,l}|\mathbf{s},\boldsymbol{\theta}^{[n]}]) + Var[r_{k,l}|\mathbf{s},\boldsymbol{\theta}^{[n]}]\, (\lambda_u^{-1} + \mathbf{h}_{k,l}^\dagger\, \mathbf{\Lambda}^{-1}\, \mathbf{h}_{k,l}).$$

In order to find the conditional expectation and variance of $r_{k,l}$ given $\mathbf{s}$ and $\boldsymbol{\theta}^{[n]}$, we need to look at the conditional probability density. Using the complete-probability formula $f_r(r_{k,l}\, |\, \mathbf{s},\boldsymbol{\theta}^{[n]}) = f_{\mathbf{y}}(\mathbf{y}_{k,l}\, |\, \boldsymbol{\theta}^{[n]}) \,/\, f_{\mathbf{s}}(\mathbf{s}_{k,l}\, |\, \boldsymbol{\theta}^{[n]})$, it follows:

$$E[r_{k,l}|\mathbf{s},\boldsymbol{\theta}^{[n]}] = [\lambda_1^{-1}\, \mathbf{P}_1(\omega_x, \omega_z)^*\, \mathbf{S}_V(\omega_x, \omega_z) + \lambda_2^{-1}\, \mathbf{P}_2(\omega_z, -\omega_x)^*\, \mathbf{S}_H(\omega_x, \omega_z) + \lambda_u^{-1}\, d_{k,l}] \,/\, [\lambda_1^{-1}\, |\mathbf{P}_1(\omega_x, \omega_z)|^2 + \lambda_2^{-1}\, |\mathbf{P}_2(\omega_z, -\omega_x)|^2 + \lambda_u^{-1}]. \tag{15}$$

$$Var[r_{k,l}|\mathbf{s},\boldsymbol{\theta}^{[n]}] = 1/ [\lambda_1^{-1}\, |\mathbf{P}_1(\omega_x, \omega_z)|^2 + \lambda_2^{-1}\, |\mathbf{P}_2(\omega_z, -\omega_x)|^2 + \lambda_u^{-1}]. \tag{16}$$

Note the expression in (15) is similar to the vector Wiener filter [16]. For each of the parameters in (15) and (16) the current estimation is substituted, though the superscript $^{[n]}$ is suppressed for brevity.

Now, we take from (14) only the terms that involve $\mathbf{h}_{k,l}$ and use the identity $(\mathbf{v}^\dagger\, \mathbf{A}\, \mathbf{w}) = \mathrm{tr}(\mathbf{A}\, \mathbf{w}\, \mathbf{v}^\dagger)$, where $\mathbf{A}$ is a matrix of size N × N, $\mathbf{v}$, $\mathbf{w}$ are vectors of size N × 1 and tr{$\mathbf{A}$} denotes the trace of $\mathbf{A}$:

$$J_{\mathbf{h}}(\boldsymbol{\theta}|\boldsymbol{\theta}^{[n]}) = \sum_k \sum_l \mathrm{tr}\{\mathbf{\Lambda}^{-1}\, (Var[r_{k,l}|\mathbf{s},\boldsymbol{\theta}^{[n]}]\, \mathbf{h}_{k,l}\, \mathbf{h}_{k,l}^\dagger + (\mathbf{s}_{k,l} - \mathbf{h}_{k,l}\, E[r_{k,l}|\mathbf{s},\boldsymbol{\theta}^{[n]}])\, (\mathbf{s}_{k,l} - \mathbf{h}_{k,l}\, E[r_{k,l}|\mathbf{s},\boldsymbol{\theta}^{[n]}])^\dagger)\}. \tag{17}$$

Since $\mathbf{\Lambda}$ is a diagonal matrix, we obtain from the expression in (17):

$$\mathbf{h}_{k,l}^{[n+1]} = E[r_{k,l}|\mathbf{s},\boldsymbol{\theta}^{[n]}]^*\, \mathbf{s}_{k,l} \,/\, (|E[r_{k,l}|\mathbf{s},\boldsymbol{\theta}^{[n]}]|^2 + Var[r_{k,l}|\mathbf{s},\boldsymbol{\theta}^{[n]}]). \tag{18}$$

Explicitly, the update of the estimation of the blur is:

$$\mathbf{P}_1(\omega_x, \omega_z)^{[n+1]} = E[r_{k,l}|\mathbf{s},\boldsymbol{\theta}^{[n]}]^*\, \mathbf{S}_V(\omega_x, \omega_z) \,/ \tag{19}$$

$$E[|r_{k,l}|^2|\mathbf{s},\boldsymbol{\theta}^{[n]}] \qquad / \left(E[|r_{k,l}|^2|\mathbf{s},\boldsymbol{\theta}^{[n]}] + E[|r_{-l,k}|^2|\mathbf{s},\boldsymbol{\theta}^{[n]}]\right)$$

$$\mathbf{P}_2(\omega_z, -\omega_x)^{[n+1]} = E[r_{k,l}|\mathbf{s},\boldsymbol{\theta}^{[n]}]^* \, \mathbf{S}_{\mathrm{H}}(\omega_x, \omega_z) / E[|r_{k,l}|^2|\mathbf{s},\boldsymbol{\theta}^{[n]}]$$

where we used for $E[|r_{k,l}|^2|\mathbf{s},\boldsymbol{\theta}^{[n]}]$ the identity:

$$E[|r_{k,l}|^2|\mathbf{s},\boldsymbol{\theta}^{[n]}] = |\, E[r_{k,l}|\mathbf{s},\boldsymbol{\theta}^{[n]}]\,|^2 + Var[r_{k,l}|\mathbf{s},\boldsymbol{\theta}^{[n]}]. \tag{20}$$

Next, we take from (14) only terms related to $\boldsymbol{\Lambda}$:

$$J_{\lambda}(\boldsymbol{\theta}|\boldsymbol{\theta}^{[n]}) = \sum_k \sum_l \ln(\lambda_1\lambda_2) + J_{\mathbf{h}}(\boldsymbol{\theta}|\boldsymbol{\theta}^{[n]}) \tag{21}$$

Substituting (18) for $\mathbf{h}_{k,l}$, the values of λ_1 and λ_2 that minimize (21) are:

$$\lambda_1^{[n+1]} = \mathrm{N}_{\mathrm{DFT}}^{-2} \sum_k \sum_l \{Var[r_{k,l}|\mathbf{s},\boldsymbol{\theta}^{[n]}]\, |\mathbf{P}(\omega_x, \omega_z)^{[n+1]}|^2 + |\mathbf{S}_{\mathrm{V}}(\omega_x, \omega_z) - E[r_{k,l}|\mathbf{s},\boldsymbol{\theta}^{[n]}]\, \mathbf{P}(\omega_x, \omega_z)^{[n+1]}|^2\} \tag{22}$$

$$\lambda_2^{[n+1]} = \mathrm{N}_{\mathrm{DFT}}^{-2} \sum_k \sum_l \{Var[r_{k,l}|\mathbf{s},\boldsymbol{\theta}^{[n]}]\, |\mathbf{P}(\omega_z,-\omega_x)^{[n+1]}|^2 + |\mathbf{S}_{\mathrm{H}}(\omega_x, \omega_z) - E[r_{k,l}|\mathbf{s},\boldsymbol{\theta}^{[n]}]\, \mathbf{P}(\omega_z, -\omega_x)^{[n+1]}|^2\}.$$

Then, for the minimization $J(\boldsymbol{\theta}|\boldsymbol{\theta}^{[n]})$ with respect to $d_{k,l}$, we take from (14) only the terms that depend on $d_{k,l}$:

$$J_d(\boldsymbol{\theta}|\boldsymbol{\theta}^{[n]}) = \lambda_u^{-1} \,|\, E[r_{k,l}|\mathbf{s},\boldsymbol{\theta}^{[n]}] - d_{k,l}\,|^2 \tag{23}$$

It is simple to see that the value of $d_{k,l}$ that minimizes (23) is:

$$d_{k,l}^{[n+1]} = E[r_{k,l}|\mathbf{s},\boldsymbol{\theta}^{[n]}] \tag{24}$$

Finally, we substitute (24) for $d_{k,l}$ in (14) then take only the terms that depend on λ_u:

$$J_u(\theta|\theta^{[n]}) = \sum_k \sum_l (\ln(\lambda_u) + \lambda_u^{-1}\, Var[r_{k,l}|\mathbf{s},\boldsymbol{\theta}^{[n]}]). \tag{25}$$

The minimum of (25) is achieved when the value of λ_u is:

$$\lambda_u^{[n+1]} = \mathrm{N}_{\mathrm{DFT}}^{-2} \sum_k \sum_l Var[r_{k,l}|\mathbf{s},\boldsymbol{\theta}^{[n]}]. \tag{26}$$

If we assume that the noise variance is the same in both RF images, then the average of the 2 expressions in (22) should be used to update the variance. If we assume identical blur in both scans $\mathbf{P}_1 = \mathbf{P}_2 = \mathbf{P}$, (19) should be replaced with:

$$\mathbf{P}(\omega_z, \omega_x)^{[n+1]} = (\, E[r_{k,l}|\mathbf{s},\boldsymbol{\theta}^{[n]}]^* \, \mathbf{S}_{\mathrm{V}}(\omega_x, \omega_z) + E[r_{-l,k}|\mathbf{s},\boldsymbol{\theta}^{[n]}]^* \, \mathbf{S}_{\mathrm{H}}(-\omega_z, \omega_x)\,) \tag{27}$$

C. Initialization and constraints

Being highly non-linear the likelihood function $L(\boldsymbol{\theta})$ has multiple maxima, and therefore the initial conditions $\boldsymbol{\theta}^{[0]}$ have a great effect on the ability of the EM algorithm to converge to a good estimation. We found that $\mathbf{P}_1^{[0]}$ and $\mathbf{P}_2^{[0]}$ should have the same value at all frequencies, that is they should be the DFT of an impulse at the origin. Also, a plausible initialization for $d^{[0]}$ is the average of $\mathbf{S}_{\mathrm{V}}$ and $\mathbf{S}_{\mathrm{H}}$. For the noise variance the initial estimate was higher than the true value, as it was found in [18] to produce better results. In the initial iterations the estimation of the variances is unreliable, thus the estimation much improves if λ_u in (15) and (16) is limited such that λ_1/λ_u and λ_2/λ_u are not too large or small relatively to $\max|\mathbf{P}_1(\omega_x, \omega_z)|^2$ and $\max|\mathbf{P}_2(\omega_x, \omega_z)|^2$ respectively.

IV. IMAGE COMPUNDING

According to the approach of multi-channel image restoration the restored image is computed from (15). However, in ultrasound imaging the resulting image would contain oscillations, as is the case with RF images due to the band-pass character of the ultrasonic blur. Consequently there would be required envelope detection.

When handling single RF images, where the oscillations are along just one axis, the envelope can be detected through demodulation, followed by absolute value calculation. But, the image of (15) has oscillations along both axes, thus demodulation or Hilbert filtered cannot be utilized. In addition, the frequency support regions of $\mathbf{P}_1(\omega_x, \omega_z)$ and $\mathbf{P}_2(\omega_z, -\omega_x)$ are far from overlapping. This inhibits the benefit of (15) over a single-channel Wiener filter, which is the ability to get weighted average in the intersection of the support regions while retaining the best of the single-channel restorations at any other frequency.

The conclusion is that the compound image should be generated through the following steps:

1. Calculation of the 2 separate Wiener filter solutions using (15) and substituting 0 for λ_1^{-1} or λ_2^{-1} respectively.
2. Envelope detection of each resulting image.
3. Computation of the average of the 2 envelope detected images [11], [12].

V. EXPERIMENTAL RESULTS

Since the estimation of the blur can be accurate up to a gain factor, it is required to restore the scaling before comparing the estimation with the true blur. We used the least squares method for this purpose:

$$J_g = \|g\hat{\mathbf{P}} - \mathbf{P}\|^2. \tag{28}$$

We used normalized mean squared error (NMSE) as a quality metric to evaluate the PSF estimation. The MSE is the right-hand side of (28) and the normalization is with respect to $\|\mathbf{P}\|^2$. When substituting for g the value that minimizes (28) the quality measure becomes:

$$\mathrm{NMSE}\{\mathbf{P}\} = 1 - \mathrm{Re}(\hat{\mathbf{P}}^{\dagger}\,\mathbf{P})^2 / (\|\hat{\mathbf{P}}\|^2\,\|\mathbf{P}\|^2) \tag{29}$$

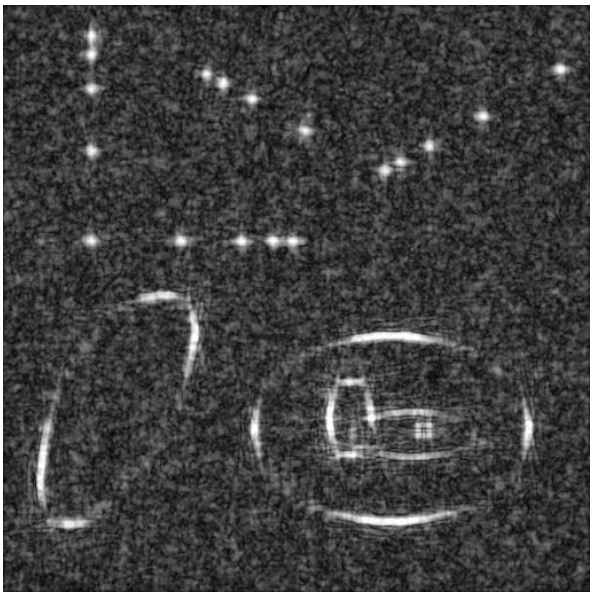

a)

b)

Figure 1. The output: compound images. a)– with the proposed algorithm; b)– with averaging the 2 envelope-detected images

We tested the algorithm with several artificial reflectivity maps. Their size was 512 × 512 pixels, which corresponds approximately with 20 × 20 mm for a sampling interval of about 40 μm. In the example that is presented in this paper there are 4 series of bright dots simulating wire targets that are separated by 0.5, 1, 2 and 3 mm.

The blur in the example in this paper was according to the non-separable model that was given in [20]. The parameters for this blur function corresponded with a linear-array transducer having width of 25 mm without apodization and focus depth of 50 mm, using 4 MHz ultrasonic pulses with envelope having full width at half maximum (FWHM) of about 0.3 μsec. Compounding with the suggested algorithm is compared in Figure 1 to compounding with only averaging the envelope-detected and log-compressed images.

VI. CONCLUSIONS

We developed an algorithm for blind identification of ultrasonic blur and for ultrasound image compounding. The approach of multi-channel image restoration was adopted for the identification task, but Wiener restoration was found to be inappropriate for compounding in the case of ultrasound imaging with 90° separated views. The algorithm in this work is based on registration of the two input images, and exploits both deconvolution and compounding to provide an enhanced output image. The simulation experiments that we conducted show that the quality of the compound image can be enhanced compared to the usage of algebraic average without Wiener filtering. Further research is planned so as to adapt the algorithm for angles different than 90° and for multi-angle compounding [21].

REFERENCES

[1] E.E. Hundt and E.A. Trautenberg, "Digital processing of ultrasonic data by deconvolution", *IEEE Trans. Sonics. Ultrason.*, vol. 27, no. 5, pp. 249-252, Sep. 1980.

[2] C.N. Liu, M. Fatemi and R.C. Waag, "Digital processing for improvement of ultrasonic abdominal images", *IEEE Trans. Med. Imaging.*, vol. 2, no. 2, pp. 66-75, June 1983.

[3] J.A. Jensen and S. Leeman, "Nonparametric estimation of ultrasound pulses", *IEEE Trans. Biomed. Eng.*, vol. 41, no. 10, pp. 929-936, Oct. 1994.

[4] J.A. Jensen, "Estimation of in vivo pulses in medical ultrasound", *Ultrasonic Imaging*, vol. 16, pp. 190-203, 1994.

[5] T. Taxt, "Restoration of medical ultrasound images using two-dimensional homomorphic deconvolution", *IEEE Trans. Ultrason., Ferroelect.*, vol. 42, no. 4, pp. 543-554, July 1995.

[6] U.R. Abeyratne, A.P. Petropulu and J.M. Reid, "Higher order spectra based deconvolution of ultrasound images", *IEEE Trans. Ultrason., Ferroelect.*, vol. 42, pp. 1064-1075, 1995.

[7] J.H. Hokland and P.A. Kelly, "Markov models of specular and diffuse scattering in restoration of medical ultrasound images", *IEEE Trans. Ultrason., Ferroelect., Freq. Contr.*, vol. 43, pp. 660-669, 1996.

[8] T. Taxt and G.V. Frolova, "Noise robust one-dimensional blind deconvolution of medical ultrasound images", *IEEE Trans. Ultrason., Ferroelect.*, vol. 46, no. 2, pp. 291-299, 1999.

[9] T. Taxt and J. Strand, "Two-dimensional noise-robust blind deconvolution of ultrasound images", *IEEE Trans. Ultrason., Ferroelect., Freq. Contr.*, vol. 48, no. 4, pp. 861-866, 2001.

[10] D. Adam and O. Michailovich, "Blind deconvolution of ultrasound sequences using nonparametric local polynomial estimates of the pulse", *IEEE Trans. Biomed. Eng.*, vol. 49, no. 2, pp. 118-131, Feb. 2002.

[11] P. He, K. Xue and Y. Wang, "Effects of spatial compounding upon image resolution", *Int. Conf. IEEE Eng. Medic. Bio. Society*, pp. 598-600, Oct. 1997.

[12] S. K. Jespersen, J. E. Wilhjelm and H. Sillesen, "Ultrasound spatial compound scanner for improved visualization in vascular imaging", 1998 *IEEE Ultrason. Symposium*, pp. 1623-1626, 1998.

[13] D. F. Leotta and R. W. Martin, "Three-dimensional spatial compounding of ultrasound scans with incidence angle weighting", *IEEE Ultrason. Symposium*, pp. 1605-1608, 1999.

[14] R. E. Shenhar and M. Porat, "A Dual Transducer Approach to Ultrasound Imaging and Spatial

Deformations", *IEEE International Conference on Image Processing*, 2000.

[15] D.C. Ghiglia, "Space-invariant deblurring Given *N* independently blurred images of a common object", *J. Opt. Soc. Amer. A*, vol. 1, no. 4, pp. 398-402, April 1984.

[16] A.K. Katsaggelos, K.T. Lay and N.P. Galatsanos, "A general framework for frequency domain multi-channel signal processing", *IEEE Trans. Image Proc.*, vol. 2, no. 3, pp. 417-420, 1993.

[17] J.M. Links, J.L. Prince and S.N. Gupta, "A vector Wiener filter for dual-radionuclide imaging", *IEEE Trans. Med. Imaging*, vol. 15 , pp. 700-709, Oct. 1996.

[18] B.C. Tom, K.T. Lay and A.K. Katsaggelos, "Multichannel image identification and restoration using the expectation-maximization algorithm", *Opt. Eng.*, vol. 35, no. 1, pp. 241-254, Jan. 1996.

[19] D. Iraca, L. Landini and L. Verrazzani, "Power spectrum equalization for ultrasonic image restoration", *IEEE Trans. Ultrason., Ferroelect.*, vol. 36, no. 2, pp. 216-222, March 1989.

[20] W.F. Walker and G.E. Trahey, "The application of K-space in pulse echo ultrasound", *IEEE Trans. Ultrason., Ferroelect., Freq. Contr.*, vol. 45, no. 3, pp. 541-558, May 1998.

[21] H. Kirshner and M. Porat, "On the Role of Exponential Splines in Image Interpolation", IEEE Trans. on Image Processing, vol. 18, pp. 2198-2208, 2009.

Elastography - New Imagistic Method for Assessment of Liver Structure in Children

MARGINEAN Oana[1], BRANZANIUC Klara[2], MARGINEAN C., PITEA Ana Maria [1], AZAMFIREI Leonard[4], LUDMILA Bologa[5], LUDMILA Cerempei[5], NINEL Revenco[5]

[1] *University of Medicine and Pharmacy Tg.-Mures, Pediatry*

[2] *University of Medicine and Pharmacy Tg.-Mures, Anatomy*

[3] *University of Medicine and Pharmacy Tg.-Mures, Ginecology*

[4] *University of Medicine and Pharmacy Tg.-Mures, Anestiology*

[5]*University of Medicine Nicolae Testemiţeanu, Chişinău, Pediatrics Departement*

***Abstract*- Elastography is a new method based on ultrasound imaging, which allows assessment of tissue structure in terms of their stiffness, useful in exploring various organs and systems.**

Objectives and aim Study of liver tissue elasticity in children by real-time elastography in normal (healthy children) and in the context of certain disease.

Material and method Our study (prospective type) was carried out at the I[st] Pediatric Clinic Tg.-Mures, Romania in the period 2010, September - 2011, April. An ultrasound machine Siemens S 2000 with an up-to-date soft was used for the elastographic assessment of liver by ARFI (Acustic Radiation Force Impulse Imaging) tehnique, using "Virtual Touch (VT) Tissue Quantification" technology (for quantification of fibrosis) in children: a lot of different conditions (various liver injuries) and a control group (healthy). The degree of tissue stiffness was expressed as a numerical value called SWV (shear wave velocity), measuring at the level of 8 and 1 liver segments, to highlight differences depending on anatomical structure, but also differentiated on pathology (ie healthy versus those with particular injuries). Measurement data were correlated with biochemical parameters.

Results. Higher SWV-values were found in group with liver-damage (p=0,04). Aspartate transaminase and alanine transaminase were statistically significant different between the groups; transaminases increased parallel with SWV (fibrosis degree) in children with liver damage.

Conclusion: Elastography completes diagnostic possibilities, providing information on the degree of hepatic elasticity (even degree of fibrosis), with special importance in liver imaging in adults, but also in pediatric practice.

***Key words*: elastography, ultrasound, liver, children**

I. INTRODUCTION

Ultrasound elastography have the potential to measure the mechanical properties of the tissue displacement through imaging (strain) while under tension [1].

Newly, acoustic radiation force impulse (ARFI) elastography has been introduced as a noninvasive tech-nique for evaluating liver fibrosis [2,3,4].

The ARFI imaging technique uses high-intensity, short-duration acoustic pulses to produce shear-wave propagation in the targeted tissue [5,6]. Shear-wave velocity are measured by repeating push pulses and detection pulses across a user defined ROI (the region of interest) [6,7].

The elastographic ARFI tehnology can be used to measure a numerical value of the wave speed SWV (shear wave velocity) by implementing the Virtual Touch tissue quantification; an image of the used soft-ware is a qualitative gray-scale map of the relative tissue stiffness (elastogram) for a ROI. The smaller the liver tissue elasticity, the higher the SWV. Thus, on elastograma the shining regions correspond to the tissue which is more elastic (less stiff) and the dark regions correspond to the stiff tissue [7].

According to recent reports, ARFI elastography results were similar to transient elastography (TE) regarding correlation with fibrosis stage (histologicaly) and for diagnosis of moderate fibrosis and cirrhosis [2,3].. The technique showed better diagnostic performance than visual assessment by experienced radiologists for detection of chronic liver disease, while for the evaluation of severity of chronic liver disease the reported results were the same [6].The main difference between ARFI and TE elastography is that it is integrated into a conventional ultrasound device [6].

Liver injury in children, in evolution of chronical diseases, including malignacies, viral or autoimmune chronic hepatitis (with B, C, D, E hepatitic virus or cytomegalovirus), alfa-1-antitripsin deficiency, the Wilson disease, as well as liver damages in context of obesity (non-alcohoolic fatty liver disease, NAFLD) and drug-related hepatotoxicity are important concerns for practicing pediatricians.

The evaluation of liver damage (which could be of hepatocellular-type, cholestatic or mixed) implies the ***clinical findings*** (signs of liver damage as nausea, fatigue, anorexia, cholestatic signs as jaundice, pruritus), ***laboratory investigations*** (increased transaminases and increased alkaline phosphatase, bilirubin and albumin levels determination) [8], ***imagistic tests,*** (abdominal ultrasonography and computerised tomography), the ***flow on portal vein*** evaluation.

Liver biopsy has been the gold standard for fibrosis staging. However, this invasive method, with a lot of secondory effects which can cause serious complications such as intraperitoneal bleeding and mortality is about 1 in 1000 [6,9], hardly accepted by children and parents [3].

In clinical practice as well as on research line, there are constantly evaluating diagnostic techniques of hepatic evaluation in order to find non-invasive alternatives to

replace hepatic biopsy but to accurately assess the degree of fibrosis.

Ultrasonography is usually the first-line investigation in the assessment of patients, considering its low cost, non-invasiveness, repeatability and easy access; MRI and PET, and often CT, are restricted to selected cases, due to their limited availability and high costs.

Thus, the introduction of new techniques to increase the sensitivity of US, such as real-time elastography would be a major advantage.

The aim of the paper was the study of the liver tissue elasticity, assessed by real-time elastography, in correlation with biochemical parameters (namely transaminases levels) in children with different causes of liver injury (obesity, hepatitis, liver damage in children with malignancies under/ after-chemotherapy, drug-related hepatotoxicity) versus children with normal biochemical parameters regarding liver function.

II. MATHERIAL AND METHODS

The present study was carried out at the Ist Pediatric Clinic Tg.-Mures, Romania, between 2010 September and 2011, April; it was a prospective study including a control group composed of 38 children with normal clinical and paraclinical findings related to the liver function and a lot of 96 children with different causes of hepatopathies, selected based on clinical signs and symptoms of liver damage (abdominal discomfort, fatigue, anorexia, nausea, vomiting, jaundice, pruritus, hepatomegaly, ascites), changes in laboratory findings (liver tests considering the synthetic function, hepatocellular necrosis and cholestasis) and/or abnormalities in liver imaging.

An informed consent was signed by legal tutors of each patient at the moment of hospitalization in our clinic (in accordance with the principles of the Helsinki declaration).

Combined B-mode US/ARFI elastography was performed using an ultrasound machine Siemens S 2000 with an up-to-date soft, using a transducer array operating at 4,1 MHz by an experienced radiologist with 11 years of experience in ultrasonography.

The patients were placed supine with the right arm straight over head.

SWV (m/s) were measured in the area of interest chosen by the examiner. Measurements were performed in the right lobe, especially in the 8th segment, 4 cm under the skin, at 2.5-4.5 cm depth, under the liver capsule (which has been avoided, being an fibrous tissue rich area). Also, the caudate lobe of the liver (the 1st segment) was examined in order to evaluate the elasticity in the right versus the left liver lobe.

There have been made 10 measurements in a selected region, and median velocity values were obtained through calculation in Microsoft Excel programm.

For continuous variables, mean values were expressed as mean ± standard error of mean (SEM) or Standard Deviation (SD).

Statistical analysis were performed using Graph Pad Prisma and Graph Pad InStat Demo programs. Student test, Chi square ($\chi 2$), Fisher exact test, ANOVA test were used; correlation between average SVW and study variables (transaminasis) were assessed based on Pearson correlation coefficient (r).The threshold of significance was $p<0.05$.

III. RESULTS

In group of patients with liver damage there were 28 overweight and obese children (considered overweight whether their weight was between the 85th and 95th percentile for age and sex, and obese whether their weight exceeds 95th percentile, respectiely), all of them with modifications to the standard abdominal ultrasound (high echogenicity, granular liver aspect, posterior attenuation suggestive for steatosis); there were 48 patients with various malignancies under or after chemotherapy, with tumor infiltration of the liver or hepatotoxicity related to cytostatic treatment and a number of 20 patients with various etiology of hepatopathy (viral hepatitis, acute toxic hepatitis, drug hepatotoxicity) (as presented in Figure 1).

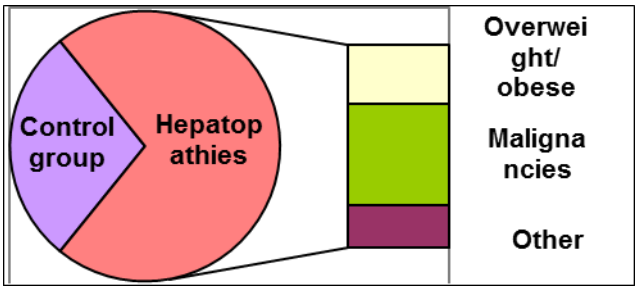

Fig. 1. The structure of the three groups (by condition)

Descriptive statistics show averages ± standard deviations (SD) of study groups. In the control group the average elasticity was 1,18±0,28 m/s; in the group of children with different causes of liver diseases, elasticity was 1,39±0,41 m/s. Alanine transaminase (ALT, IU) was 19,56±8,67 SD in the control group, and 37,42±31,16 in the group of children with liver diseases, while aspartate transaminase (AST, IU) was 24,88±8.67 SD in the control group, and 39,92±20,12 in the group of children with liver inury.

Comparing liver tissue elasticity values between the groups higher speeds were found in groups with liver damage, the differences being statistically significant at CI of 95%. We`ve got a statistically significant difference with $p = 0.0044$ (Figure 2).

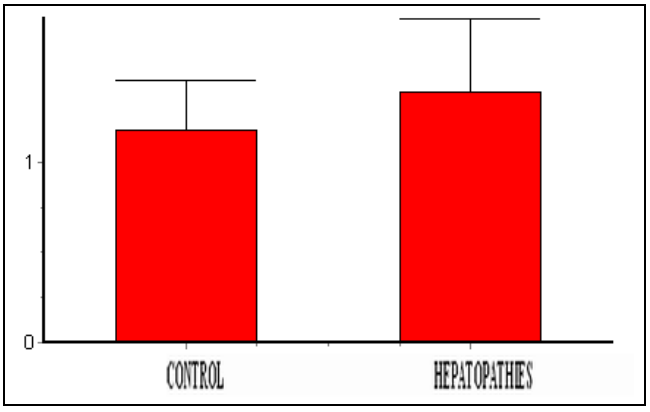

Fig. 2. Comparison between the median SVW of the groups

Regarding alanine transaminase (ALT, IU), as expected, the levels were higher in group of children with liver diseases, the difference from control was statisticaly extremely significant, with $p < 0.0007$ (Figure 3).

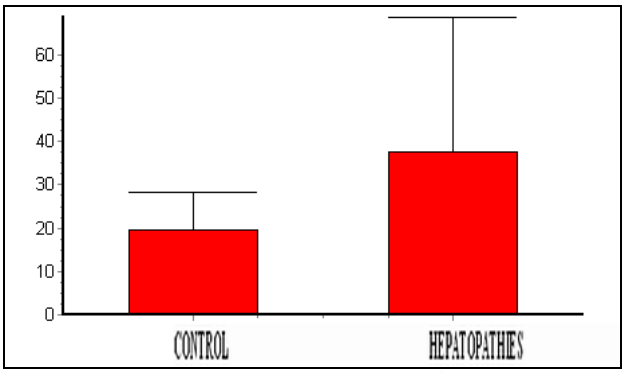

Fig.3. Comparison between the median ALT of the three groups

As far as it concerns aspartate transaminase (AST, IU), in the control group it were, also, smaller levels than in the group of children with hepatopathies, the difference between AST mean for the two groups was, as for ALT, statistically extremely significant, with $p < 0.0001$ (Figure 4).

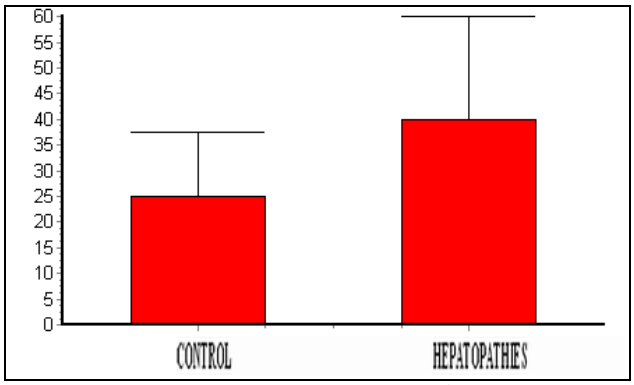

Fig. 4. Comparison between the median AST of the three groups

We searched for correlations between global SVW and other determined parameters (AST and ALT) in each group, but we obtained no statisticaly significant correlations between the assesed parameters, except that between SWV and AST, only for the group of children with liver injury ($r = 0,54$ and $p = 0,01$), statistically significant**.**

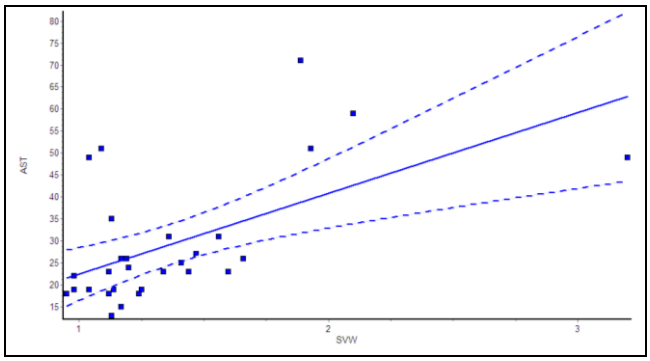

Fig. 5. The correlation between the values of SVW and AST average in group of children with liver damage

The classical descriptive anatomy nomenclature distinguishes four lobes: right, left, caudate and quadrate, concept which does not reflect the functional anatomy [10].

According to the International Anatomical Nomenclature, a posterior and anterior segment are attributed to the right lobe, and a medial and lateral segment to the left lobe, each of these segments being divided into an antero-inferior and a postero-superior segment, so as liver has eight segments, numbered clockwise from I to VIII [11].

Segment 1 (caudate lobe or Spiegel lobe) is a distinct structure of the liver, receiving blood flow from both the right and left-sided vascular branches; a special vascularization which represents the distinctive characteristic of segment 1 [11,12].

The caudate lobe is less echogenic.

Assessing liver elasticity separate for each segment for the entire group (all 134 patients in the study), comparing the SVW values by Mann-Whitney test for liver tissue elasticity there was found no statistically significant differences between segment 1 (caudate lobe) and segment 8 (right lobe), ($p=0,1583$).

Evaluation of each segment revealed for the control group a median SWV for *segment 8* of 1,24±0,31 m/s, while for *segment 1* SWV was 1,06±0,3 m/s; by applying the Student T Test between the media of SVW on those two segments (unpaired t test), we obtained a statistically significant difference ($p < 0,0121$, Figure 6).

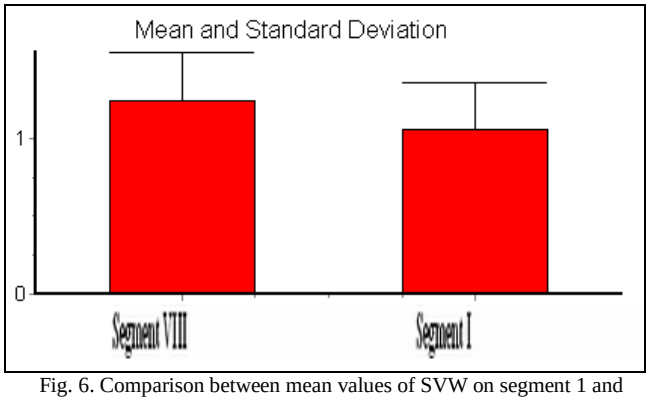

Fig. 6. Comparison between mean values of SVW on segment 1 and segment 8 in the control group.

In group of children with hepatopathies, SWV was 1,30±0,47 m/s in *segment 8*, and 1,31±0,5 m/s in *1st segment*, without statistically significant difference when applying the Student T Test between the media of SVW on those two segments (unpaired t test) ($p = 0,8866$).

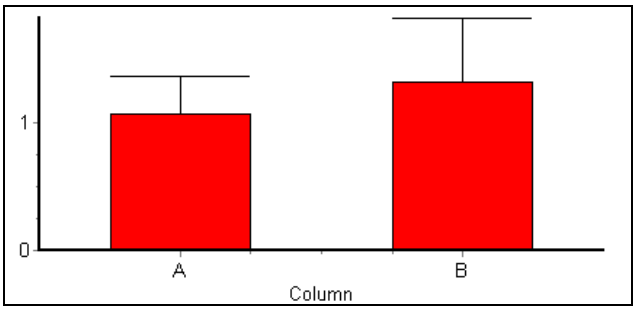

Figure 5 - Comparison between the average SWV in segment 1 between controls and the group with hepatopathies

No statistically significant differences were obtained between *control* group and the one with *hepatopathies* when applying the Student T Test for SWV values in the 8th segment (1,24±0,31 m/s versus 1,30±0,47 m/s), with $p= 0,4691$.

For the 1st segment, comparison between the average SWV of the *controls* (1.06±0,3 m/s) versus group with *hepatopathies* (1,31±0,5 m/s), perfomed by Student T test, achieved a very significant difference ($p=0,0046$-Figure 5).

IV. CONCLUSIONS

In children with liver damage, compared to the control group, transaminase levels increased as well as SWV and therefore the degree of fibrosis.

We found that SWV is higher in children with liver-diseases, globally, meaning that any tissue injury result in changes of the liver elasticity up to fibrosis.

In normal conditions (children with free liver tissue), SVW was higher for the segment VIII compared to I, statistically significant, meaning that caudate lobe is "softer", difference that does not exist in the group of liver diseases.

SWV values in group of children with hepatopathies were found to increase particularly in the segment I (caudate lobe), which shows that it is first affected by any liver injury.

Faithful evaluating the elasticity, real-time elastography has a certain role in the evaluation of hepatic vasculature and tissue damages. Due to this fact, elastographic evaluation of liver and particulary in the caudate lobe has further implications for assessment of liver fibrosis and would have possible utility in preparation and management in cases of liver transplantation.

Ultrasound elastographic assessment, by new tehnologies available, through ARFI quantification respectively, may enhance the current role of liver ultrasound for patients with liver disease.

„This paper is partially supported by the Sectoral Operational Programme Human Resources Development, financed from the European Social Fund and by the Romanian Government under the contract number POSDRU/89/1.5/S/60782"

This paper is partially supported by the project NASR 421/2010: "Correlations between the elasticity of the caudate lobe and other lobes of the liver in children by real-time elastography, with implications for liver transplantation"

REFERENCES

[1] Ophir J, Cespedes I, Ponnekanti H, Yazdi Y, Li X. Elastography: a quantitative method for imaging the elasticity of biological tissues. Ultrason Imaging. 1991;13:111

[2] Friedrich-Rust M, Wunder K, Kriener S, Sotoudeh F, Richter S, Bojunga J, et all. Liver fibrosis in viral hepatitis: Noninvasive assessment with acoustic radiation force impulse imaging versus transient elastography. Radiology 2009;252:595–604

[3] Lupsor M, Badea R, Stefanescu H, Sparchez Z, Branda H, Serban A, Maniu A. Performance of a new elastographic method (ARFI technology) compared to unidimensional transient elastography in the noninvasive assessment of chronic hepatitis C. Preliminary results. J Gastrointestin Liver Dis 2009;18:303–310

[4] Takahashi H, Ono N, Eguchi Y, Eguchi T, Kitajima Y, Kawaguchi Y, et al. Evaluation of acoustic radiation force impulse elastography for fibrosis staging of chronic liver disease: A pilot study. Liver Int 2010;30:538–545

[5] Palmeri M, Wang M, Dahl J, Frinkley K, Nightingale K. Quantifying hepatic shear modulus in vivo using acoustic radiation force. Ultrasound Med Biol 2008;34:546–558.

[6] Kim J. E. Lee J.Y., Kim Y.J., Yoon J.H., Kim S.H., Lee J.M., Han JK, et al. ARFI elastography for chronic liver disease: Comparison with ultrasound-based scores of experienced radiologists, Child-Pugh scores and liver function tests. Ultrasound in Medicine and Biology 2010;36(10):1637-43

[7] Lazebnik R.S. *Ultrasound, Mountain View, CA USA Tissue Strain Analytic, Virtual Touch Tissue Imaging and Quantification.* Siemens Medical Solutions, USA, Inc., 2008

[8] Roberts E.A. Drug-induced liver disease. In Suchy F.J., Sokol R.J., Balistreri W.F., (Eds). *Liver Disease In Children*, Third Edition. Cambridge University Press, Cambridge, New York, 2007;478-512

[9] Bravo AA, Sheth SG, Chopra S. Liver biopsy. N Engl J Med 2001;344:495–500

[10] Strunk H., Stuckmann G., Textor J., Willinek W. Limitations and Pitfalls of Couinaud`s Segmentation of the Liver in Transaxial Imaging. European Radiology 2003;13(11):2472-2482, DOI: 10.1007/s00330-003-1885-9

[11] Dodds WJ, Erickson SJ, Taylor AJ, Lawson TL, Stewart ET. Caudate lobe of the liver: anatomy, embryology and pathology. AJR 1990; 154: 87-93

[12] Brown BM, Filly RA, Callen PW. Ultrasonographic anatomy of the caudate lobe. J Ultrasound Med 1982; 1: 189-192

Fetal Survey via Abdominal Recorded Signals

Dragos TARALUNGA[1], Werner WOLF[2], Mihaela UNGUREANU[1] and Rodica STRUNGARU[1]
[1]*Politehnica University of Buharest/Applied Electronics and Information Engineering Department, Bucharest, Romania, e-mail: dragos.taralunga@upb.ro, Rodica.Strungaru@elmed.pub.ro 2Universität der Bundeswehr München, Institut für Informationstechnik, Germany, e-mail: werner.wolf@web.de*

***Abstract* – Fetal heart rate (fHR) and the morphological features of the fetal ECG (fECG) can be derived from (fECG) signals recorded on the maternal abdomen. However, when assessing the fECG through the abdominal signals (ADS), it's very low amplitude causes a problem, since the fECG representation in the ADS is buried in a mixture of other signals with stronger energy. Thus, signal to noise ratio of these recordings is low, the maternal electrocardiogram (mECG) being the main interference component. The aim of the present paper is to evaluate the performance of an algorithm for maternal ECG (mECG) subtraction. The performance of the algorithm considered in this study is evaluated by applying it on both simulated and real ADS signals.**

***Index Terms* – abdominal recordings, fetal monitoring, fetal electrocardiogram, subtraction algorithm.**

I. INTRODUCTION

Antepartum and intrapartum fetal surveillance constitute an essential component of the standards for evaluating and analyzing the health state of the fetus during pregnancy and labor.

Hypoxia is one the most frequently form of fetal distress during pregnancy. The state of hypoxia appears when the oxygen supply to the fetus through the placenta is affected, leading to ischemia or in the worst case to asphyxia. There are numerous causes for hypoxia from maternal disorders like: anemia, heart diseases, chronicle lung diseases, to placental disorders, the high stress which is put on the fetus during labor and high consumption of drugs, e.g. cocaine. The effects of oxygen deprivation are different according with the terms of pregnancy, thus on early terms it leads to congenital abnormalities, myocardial thinning, late development of embryo [1] whereas on late terms leads to intrauterine growth restriction and brain damage. The latter can be the cause of psychiatric and neurologic disorders in adulthood [2], [3] and of behavioral and cognitive deficits in childhood [4], [5]. However, it is not clear what is the timing and the duration of a fetal hypoxic exposure that can have as outcome a specific behavioral, cognitive, and emotional sequel in childhood and adulthood. Nevertheless, the early identification of hypoxic distress is mandatory for maintaining the health state of the fetus.

Another disorder which can appear during pregnancy is congenital heart defects which represent the leading cause of birth defect-related deaths [6]. It affects 35,000 infants, i.e one out every 125 infants born in United States [7] and one out 145 infants born in United Kingdom [8]. Congenital heart defects represent structural problems, malformations of the heart which are present at birth. Usually they occur during heart development, due to a mishap, soon after conception and often before the mother is aware of the pregnancy. The consequence of the defects may range from simple problems, such as "holes" between chambers of the heart, to very severe malformations, such as complete absence of one or more chambers or valves. Moreover, congenital heart defects can also increase the risk of developing certain medical conditions like: congestive heart failure, pulmonary hypertension, arrhythmias, anticoagulation [6].

Nowadays, fetal monitoring is based entirely on the fetal heart rate (fHR) analysis and does not incorporate characteristics of the fetal electrocardiogram (fECG) waveform, which represent the keystones of cardiac evaluation of both children and adults.

The morphological characteristic analysis of the fECG can identify both hypoxic episodes and congenital heart disorders described above. Thus, the ST segment is very sensitive to metabolic dysfunction induced by fetal hypoxia: an increase in T wave, quantified by the ratio of the T wave to the QRS amplitude (T/QRS ratio), or a biphasic ST pattern [9], [10], [11]. By combining these morphological changes of the fECG with fHR analysis, additional clinical information is provided to the physicians, leading thus to minimization of the unnecessary obstetric interventions.

The fECG constitutes the access to both fHR and the waveform of the electrical activity of the fetal heart. However, the standard procedure used nowadays for recording the fECG is by placing an electrode, invasively, on the head of the fetus, after the rupture of the amniotic sack. This recording method has some major drawbacks because it is cumbersome, it can put in danger the life of both the mother and the fetus and it is only applicable during delivery.

Thus, abdominal recorded signal (ADS) represent an alternative, as it is noninvasive, provides clinically significant information concerning the health state of the fetus through the analysis of the FHR and the morphology of the fECG. Moreover, it can also be used for long term monitoring.

Nevertheless, the fundamental problem is that ADS represents a multi-component signal containing several other disturbing signals of high amplitudes besides the low amplitude fECG component.

Among these perturbing biosignals, the maternal ECG (mECG) is clearly the main source of disturbance. The transabdominal fECG R-peak amplitude ranges from 10 to 100 μV, whereas the amplitude of the QRS complex of the mECG shows 0.5 to 1 mV [12]. Other disturbing signals which must be considered are the electronic noise (introduced by amplifiers etc), the slow baseline wander of signals (mainly due to electrode effects), the myoelectric crosstalk from abdominal muscles, and, in particular during labor, the uterine contractions. The large amplitudes of these noise sources are hiding the transabdominal fECG and a

simple high-pass filtering of ADS for fECG extraction cannot be applied due to the overlapping spectra of the fECG and of the noise components.

All these effects reveal evidently that reliable methods for removing the mECG are necessary to allow fECG examination based on ADS recordings. This demand motivates the development of several methods supporting the extraction of the low amplitude fECG from ADS for fHR computation, such as principal component analysis [13], independent component analysis [14] and nonlinear state projections algorithms [15]. But the increasing interest of physicians to consider not only the instantaneous fHR but also the waveform of the fECG introduces new signal processing requirements, thus (linear) filtering methods in general are getting more demanded. For this purpose, our paper reports about the evaluation of the performances of an improved linear method, on simulated and real ADS data.

II. METHOD

The algorithm described in this paper was developed in Matlab version 7.0.1 and consists of two steps: maternal QRS detection and mECG extraction. The flow chart of the algorithm is presented in Fig.1

A. Detection of the maternal QRS complex

In order to detect the maternal QRS (mQRS), an additional signal is generating as following: the ADS is filtered by a bandpass extracting the frequency range of (5÷11) Hz which covers the QRS complex in the ECG mainly. Thus, the P- and T-waves as well as the EHG are attenuated.

The filters used to generate the additional signal that identifies the QRS complexes are described by the following equations:

$$y(n) = 2y(n-1) - y(n-2) + x(n) - \\ - 2x(n-6) + x(n-12) \quad (1)$$

for the first filter (LP), and:

$$y(n) = x(n-16) - \\ - \frac{1}{32}[y(n-1) + x(n) - x(n-32)] \quad (2)$$

for the second filter (HP), as proposed in [9].

Subsequently, the derivate is applied:

$$y(n) = \frac{1}{10}[2 \cdot x(n) + x(n-1) - x(n-3) - 2 \cdot x(n-4)] \quad (3)$$

and then the resulting signal is squared in order to emphasize QRS complex.

Finally, a moving average window is applied; its window length covers a complete QRS complex which lasts about 100 ms. This additional signal is aligned with the original signal, considering the delay introduced by the previous processing techniques, and further a peak detection algorithm combined with a threshold determines its peaks corresponding to the mQRS complexes.

B. mECG removing

The mECG component is removed by applying the Event Synchronous Canceller (ESC) [16]. Each time an mQRS complex is detected in ADS, a template obtained by averaging of all mQRS segments centered on the R-peaks is subtracted from the ADS.

Since the uterine activity results in a change of the isoelectric line of the maternal QRS (mQRS) complex, it is necessary to adapt the isoelectric line in the averaged mQRS complex.

For calculating the optimal position of the averaged ECG template, first the information about the baseline wander is introduced in the template using linear interpolation. Then whenever the algorithm detects a mQRS complex, the optimal position of the template is determined by adjusting the template position, vertically and horizontally within a window of 15 samples centered on the considered mQRS (15 ms).

The minimum error of the fitting between the template and the mECG, considering only the mQRS, is taken into account in order to estimate the optimal position, as the miss-positioning of the QRS template often leads to a remaining maternal QRS, comparable with the fetal QRS and thus the morphology of the fECG is no longer conserved. This way, the current mQRS is replaced by a segment including only the random noise from the ADSs, with zero mean.

Based on the interpolated isoelectric line, the denoised ADS is combined with the raw data, preserving the continuity of the signal.

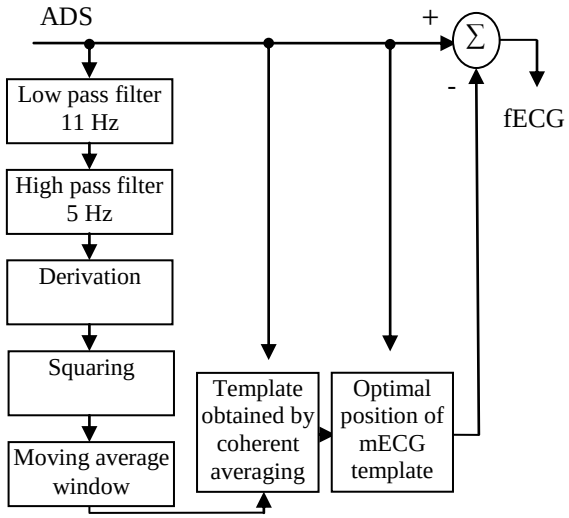

Fig. 1. Flow chart of the algorithm describing the detection of QRS complexes in ADS and the mECG extraction with the recovery of the isoelectric line.

III. DATA DESCRIPTION

The algorithm was applied on both simulated and real signals.

C. Simulated signals

The abdominal signals are simulated using the model described in [17].

The generation of the morphology of the simulated ECG cycles is realized using the three differential equations, (4), which represent the motion equations in 3D around a unit circle placed in xy-plane. On this circle five distinct points are placed at fixed angles, $\theta_P, \theta_Q, \theta_R, \theta_S, \theta_T$ in order to generate the P, Q, R, S, T waves.

$$\dot{x} = a \cdot x - \omega \cdot y$$
$$\dot{y} = a \cdot y - \omega \cdot x \quad (4)$$
$$\dot{z} = -\sum_{i \in \{P,Q,R,S,T\}} a_i \cdot \alpha_i \cdot \Delta\theta_i \cdot \exp\left(-\frac{\Delta\theta_i^2}{2 \cdot b_i^2}\right) - (z - z_0)$$

Thus the waveform is made to move away from the isoelectric line, i.e. the unit circle in the xy-plane, near the fixed points which behave like repellors, having a Gaussian morphology [16]:

where $\alpha = 1 - \sqrt{x^2 + y^2}$, $\theta = \text{atan}^2(y/x)$, $\Delta\theta_i = \theta - \theta_i$ and ω is the angular velocity of the time vector as it moves around the limit circle; a_i contains the amplitude of the waves and b_i contains the width of each wave.

D.Real data

The real data are recorded with the Biopac MP150 acquisition system from a healthy woman; gestational age is 34 weeks and the sampling frequency is 1000Hz.

Ten electrodes are placed on the maternal abdomen as depicted in Fig.2.

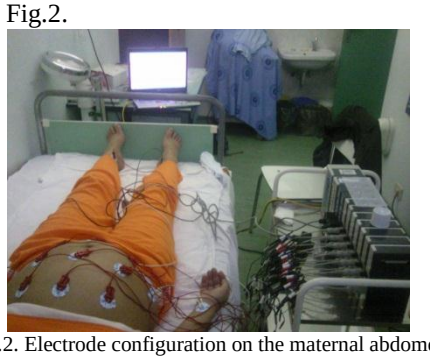

Fig.2. Electrode configuration on the maternal abdomen

IV. RESULTS AND DISCUSSIONS

E.Results on simulated data

A segment of the simulated data used to evaluate the performance of the algorithm is depicted in Fig. 3.

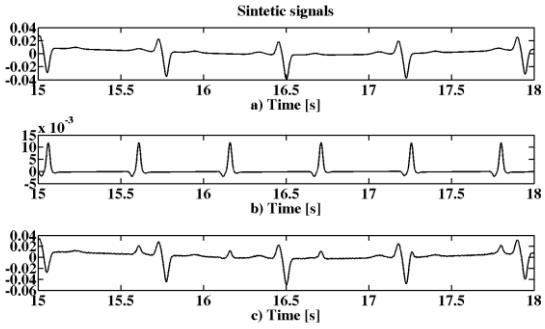

Fig. 3. Simulated ADS signals: a) mECG simulated by the dynamic model; b) fECG simulated by the dynamic model; c) simulated ADS. Note: arbitrary units are used for *y* axis.

In Fig. 4 the detection of the mQRS complexes can be observed.

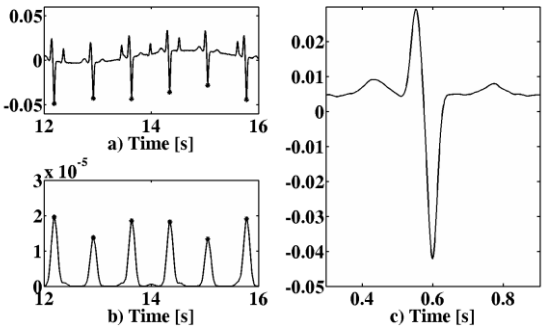

Fig. 4. mECG template estimation from simulated ADS data: a) detection of the maternal R-peaks; b) Auxiliary signal used for QRS detection; c) extracted mECG template.

The results of the fECG extraction by applying the ESC to the simulated data are depicted in Fig. 5. As depicted in Fig. 5, the mECG is completely removed, even when overlapping the fECG; the cleaned ADS signal still shows the maternal respiration, introduced as a disturbance in the simulated ADS.

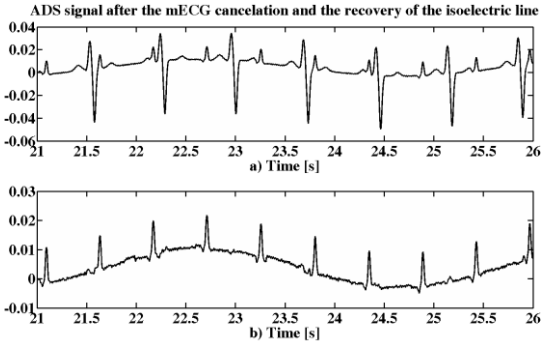

Fig. 5. fECG extraction from simulated ADS: a) simulated ADS signal; b) extracted fECG, after mECG cancelling by ESC.

F. Results obtained on real data

In Fig. 6 the detection of the mQRS from real abdominal recorded signals can be observed, whereas in Fig. 7 the cancelation of the mECG is depicted, without disturbing the shape of any overlapping fECG.

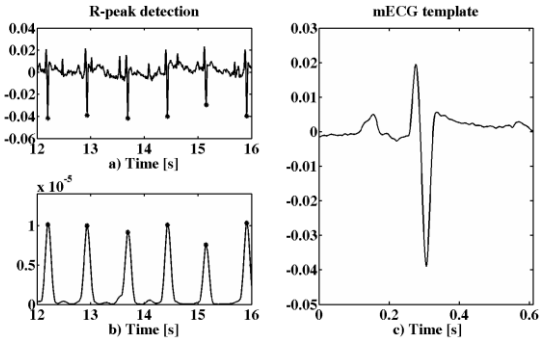

Fig. 6. mECG template estimation from real ADS data: a) detection of the maternal R-peaks; b) Auxiliary signal used for QRS detection; c) extracted mECG template.

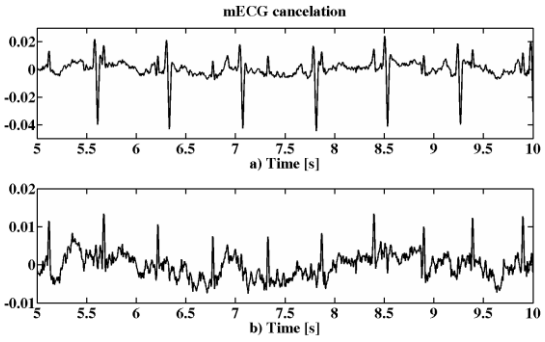

Fig. 7. The fECG extraction from real ADS (normal pregnancy, 37wk): a) real ADS; b) extracted fECG, after mECG cancelling by ESC. Note: arbitrary units are used for *y* axis.

The algorithm described in Section II shows very good results, as demonstrated in Fig. 5 and 7 and its performance is evaluated by calculating the error between the original simulated fECG and the extracted fECG, with:

$$\varepsilon_{fECG} = \frac{\sum \left(fECG_{orig} - fECG_{extracted} \right)^2}{\sum fECG_{orig}^{\ 2}} = 0.0379 \quad (5)$$

ACKNOWLEDGMENTS

The work has been funded by the Sectoral Operational Programme Human Resources Development 2007-2013 of the Romanian Ministry of Labour, Family and Social Protection through the Financial Agreement POSDRU/ 6/1.5/S/19 and by the National University Research Council of Romania (CNCSIS) under the national research grant PN II ID PCE ID 1723/2009.

REFERENCES

[1] M. Ream, A. M. Ray, R. Chandra, and D. M. Chikaraishi. "Early fetal hypoxia leads to growth restriction and myocardial thinning" , Am J Physiol Regul Integr Comp Physiol, vol. 295, no. 2, pp. R583-R595, 2008.

[2] T.D. Cannon, R Yolken, S Buka, E.F. Torrey, *et al* "Decreased neurotrophic response to birth hypoxia in the etiology of schizophrenia". Biol Psychiatry Vol. 64, No. 9, pp. 797–802, ISSN 0006-3223 2008.

[3] C. Mallen, S. Mottram and E. Thomas, "Birth factors and common mental health problems in young adults. A population-based study in North Staffordshire, Social Psychiatry and Psychiatric Epidemiology", Vol. 43, No. 4, pp. 325-330, 2008.

[4] H. Wienerroither, H Steiner, J. Tomaselli, M. Lobendanz, L. Thun-Hohenstein. „Intrauterine blood flow and long-term intellectual, neurologic, and social development". Obstet Gynecol Vol. 97, No. 3, pp. 449–453, 2001.

[5] J. Li, J.C. Lin, H. Wang, J.W.Peterson, B.C. Furie, *et al*. „Novel role of vitamin k in preventing oxidative injury to developing oligodendrocytes and neurons". J Neurosci Vol. 23, No. 13, pp. 5816–5826, 2003.

[6] K. J. Jenkins, A. Correa, J. A. Feinstein, L. Botto, *et. Al.* "Risk Factors and Congenital Cardiovascular Defects: Current Knowledge: A Scientific Statement From the American Heart Association Council on Cardiovascular Disease in the Young:Endorsed by the American Academy of Pediatrics ", Circulation Vol. 115, No. 23, pp. 2995-3014, 2007.

[7] Congenital Heart Defects in Children Fact Sheet, American Heart Association, 2008. [Online]. Available: http://www.americanheart.org/children.

[8] Congenital Heart Defects, British Heart Foundation. [Online], http://www.bhf.org.uk

[9] I. Amer-Wåhlin, B. Yli, S. Arulkumaran, „Foetal ECG and STAN technology – A review". European Clinics in Obstetrics and Gynaecology, Vol. 1, pp. 61–73,2005

[10] K.G. Rosn, I. Amer-Wahlin, R. Luzietti, H. Norn. "Fetal ECG waveform analysis". Best Practice and Research Clinical Obstetrics and Gynaecology; Vol. 18, pp. 485–514, 2004

[11] L.L. Su, Y.S. Chong, A. Biswas,"Use of Fetal Electrocardiogram for Intrapartum Monitoring". Annals Academy of Medicine, Vol. 36, pp. 416–420, 2007.

[12] M.Shao, K. E. Barner, M. H. Goodman "An Interference Cancellation Algorithm for Noninvasive Extraction of Transabdominal Fetal Electroencephalogram" IEEE Trans. Biomed. Eng., vol. 51, no. 3, 2004

[13] V. Zarzoso, AKNandi, E. Bacharakis. "Maternal and fetal ECG separation using blind source separation methods". IMA J Mathematics Appl Med & Biol, Vol.14, No. 3, pp.207-225, 1997.

[14] De Lathauwer L, De Moor B, Vandewalle J. "Fetal electrocardiogram extraction by blind source subspace separation." IEEE Trans Biomed Eng, Vol.47, No.5, pp. 567-572, 2000.

[15] Richter M, Schreiber T, Kaplan DT. Fetal ECG extraction with nonlinear state-space projections. IEEE Trans Biomed Eng, Vol. 45, No. 1, pp. 133-137, 1998.

[16] M. Ungureanu, W. Wolf, "Basic aspects concerning the event-synchronous interference canceller," IEEE Trans. Biomed. Eng., vol. 53, no. 11, pp. 2240-2247, Nov. 2006.

[17] P. E. McSharry Gari D. Clifford, Lionel Tarassenko, and Leonard A. Smith, "A Dynamical Model for Generating Synthetic Electrocardiogram Signals," IEEE Trans. Biomed. Eng., vol. 54, no. 3, March 2003.

Statistic and Fractal Processing of Human Biological Fluids Phase-Inhomogeneous Images

Yuriy USHENKO, Olga TELENHA, Valentine BALANETSKA, Maksim SIDOR
Chernivtsi National University
yuriyu@gmail.com

***Abstract* – Performed in this work are complex statistic and fractal analyses of phase properties inherent to birefringence networks of optically thin layers prepared from human bile. Within the framework of a statistic approach, the authors have investigated values and ranges for changes of statistic moments of the 1-st to the 4-th orders that characterize coordinate distributions for phase shifts between orthogonal components of amplitudes inherent to laser radiation transformed by human bile with various pathologies. The correlation criteria for differentiation of phase maps describing pathologically changed liquid-crystal networks are determined. In the framework of the fractal approach, determined are dimensions of self-similar coordinate phase distributions as well as features of transformation of logarithmic dependences for power spectra of these distributions for various types of human pathologies.**

***Index Terms* – polarization, phase, fractal, biological fluid, statistic moments, birefringence.**

I. INTRODUCTION

Among the methods for optical diagnostics of human biological tissues (BT), the methods of laser polarimetric diagnostics aimed at their optically-anisotropic structure are widely spread [1 - 31]. The main "information product" of these methods is availability of coordinate distributions for azimuths $\alpha(x,y)$ and ellipticity $\beta(x,y)$ of polarization (polarization maps) with the following types of analyses: statistical (statistical moments of the 1-st to 4-th orders [5, 6, 10, 14, 19, 25, 26, 30]), correlation (auto- and joint correlation function [12, 17, 18, 21, 26]), fractal (fractal dimensionalities [5, 6, 25]), singular (distributions of amounts of linearly and circularly polarized states [22, 28]). As a result, interrelations between the set of these parameters and distributions of optical axis directions as well as values of the birefringence characterizing the network of optically uniaxial protein (myosin, collagen, elastin, etc.) fibrils in optically anisotropic components of BT layers can be determined. Using this base, developed is a set of methods for early recognition and differentiation of pathological changes in BT structures related with their degenerative-dystrophic and oncological changes [4-6, 12, 19, 20-22, 27, 29, 31].

It is noteworthy that there exists a widespread group of optically anisotropic biological objects for which the methods of laser polarimetric diagnostics are not so efficient. Optically-thin (the attenuation coefficient $\tau \le 0.1$) layers of various biological fluids (bile, urine, liquor, synovial fluid, blood plasma, etc.) can be related to these objects. All these layers possess considerably less optical anisotropy of the biological component matter as compared with birefringent BT structures [4]. As a consequence, these objects weakly modulate polarization of laser radiation ($\begin{cases}\alpha(x,y)\approx const;\\ \beta(x,y)\to 0.\end{cases}$). On the other hand, the biological fluids are more available for a direct laboratory analysis as compared to traumatic methods of BT biopsy. From the above reasoning, it seems topical to search new, additional parameters for laser diagnostics of optically anisotropic structures in biological fluids.

This work is aimed at searching the possibilities to perform diagnostics of structures inherent to liquid-crystal networks of human bile with various pathologies by using the method to determine the coordinate distributions of phase shifts (phase maps) between orthogonal components of laser radiation amplitudes with the following statistical, correlation and fractal analyses of these distributions.

II. THE OPTICAL MODEL OF HUMAN BILE

As a base for modeling the optical properties of human bile we use the conception of anisotropy observed in BT protein networks developed in [1-4, 7, 9, 14, 16, 23-27, 30]:

- human bile can be considered as a two-component amorphous-crystalline structure;
- optically isotropic - optically homogeneous micellar solution;
- optically anisotropic - liquid-crystalline phase, consisting of three types of liquid crystals: needle crystals of fatty acids, cholesterol monohydrate crystals, bilirubinate crystals of calcium.

The optical properties of amorphous $\{A\}$ and crystalline $\{C\}$ components of biological fluids can be exhaustively described using the following Jones operators [26]

$$\{A\}=\begin{Vmatrix}a_{11} & a_{12}\\ a_{21} & a_{22}\end{Vmatrix}=\begin{Vmatrix}\exp(-\tau l) & 0\\ 0 & \exp(-\tau l)\end{Vmatrix}; \quad (1)$$

$$\{C\}=\begin{Vmatrix}c_{11} & c_{12}\\ c_{21} & c_{22}\end{Vmatrix}= \\ =\begin{Vmatrix}\cos^2\rho+\sin^2\rho\exp(-i\delta) & \cos\rho\sin\rho[1-\exp(-i\delta)]\\ \cos\rho\sin\rho[1-\exp(-i\delta)] & \sin^2\rho+\cos^2\rho\exp(-i\delta)\end{Vmatrix}. \quad (2)$$

Here, τ is the absorption coefficient for laser radiation in the biological fluid layer with the geometric thickness l; ρ - direction of the optical axis; $\delta = 2\pi/\lambda\,\Delta n d$ - phase shift between the orthogonal components E_x and E_y of the amplitude of illuminating laser light with the wavelength λ; Δn - index of birefringence.

The Jones matrix of the biological fluid layer, where isotropic and anisotropic creations lie in one plane, can be

expressed as a sum of operators $\{A\}$ and $\{C\}$

$$\{M\}=\{A\}+\{C\}=\left\|\begin{matrix} a_{11}+c_{11}; & a_{12}+c_{12}; \\ a_{21}+c_{21}; & a_{22}+c_{22}. \end{matrix}\right\|, \qquad (3)$$

Let us consider the process of transformation of the complex amplitude ($E\to U$) of a laser wave that passed through the biological fluid layer ($\{M\}$) located between two crossed phase filters – quarter-wave plates ($\{\Phi_1\}$ and $\{\Phi_2\}$) and polarizers ($\{P_1\}$ and $\{P_2\}$), planes of transmission for which make $+45^0$ and -45^0 angles with axes of the highest velocity. The amplitude U of the transformed laser beam in this experimental setup can be determined from the following matrix equation

$$U=0.25\{P_2\}\{\Phi_2\}\{\mathrm{M}\}\{\Phi_1\}\{P_1\}E. \qquad (4)$$

Here,

$$\begin{cases} E=\begin{pmatrix} E_x \\ E_y\exp(-i\delta_0)\end{pmatrix}, & U=\begin{pmatrix} U_x \\ U_y\exp(-i\delta)\end{pmatrix}, \\ \{P_1\}=\left\|\begin{matrix}1 & 1\\ 1 & 1\end{matrix}\right\|, & \{P_2\}=\left\|\begin{matrix}1 & -1\\ -1 & 1\end{matrix}\right\|, \\ \{\Phi_1\}=\left\|\begin{matrix}1 & 0\\ 0 & i\end{matrix}\right\|, & \{\Phi_2\}=\left\|\begin{matrix}i & 0\\ 0 & 1\end{matrix}\right\|. \end{cases} \qquad (5)$$

In the special case of a plane-polarized wave $E\left(E_x=E_y;\delta_0=0\right)=\begin{pmatrix}1\\1\end{pmatrix}$, Eq. (4) acquires the form

$$U=0.25\left\|\begin{matrix}1 & -1\\ -1 & 1\end{matrix}\right\|\left\|\begin{matrix}i & 0\\ 0 & 1\end{matrix}\right\|\times$$
$$\times\left\|\begin{matrix}\cos^2\rho+\sin^2\rho\exp[-i\delta] & \cos\rho\sin\rho\{1-\exp[-i\delta]\}\\ \cos\rho\sin\rho\{1-\exp[-i\delta]\} & \sin^2\rho+\cos^2\rho\exp[-i\delta]\end{matrix}\right\|\times \qquad (6)$$
$$\times\left\|\begin{matrix}1 & 0\\ 0 & i\end{matrix}\right\|\left\|\begin{matrix}1 & 1\\ 1 & 1\end{matrix}\right\|\begin{pmatrix}1\\1\end{pmatrix}.$$

The solution of the matrix equation (6) is the value of complex amplitude $U(\delta)$ that is determined exclusively by the phase shift δ and does not depend on orientation of the optical axis ρ for a laser image of biological fluid. Being based on it, one can write

$$I_\delta(r)=UU^*=I_0\sin^2\left[\delta/2\right]. \qquad (7)$$

Here, I_0 is the intensity of a probing laser beam, $I_\delta(r)$ - intensity of the laser image for the biological fluid layer in the point (r).

Interrelations (4) to (7) define the algorithm for direct experimental measuring the coordinate distribution of phase shifts $\delta(r)$ between orthogonal components of the amplitudes U_x, U_y in the laser image of an optically anisotropic biological fluid layer.

III. TABLES, FIGURES, EQUATIONS

As objects for experimental studying, we chose optically-thin layers of bile taken from a healthy patient (figure 1a) and patient suffering from insulin-independent diabetes (figure 1b).

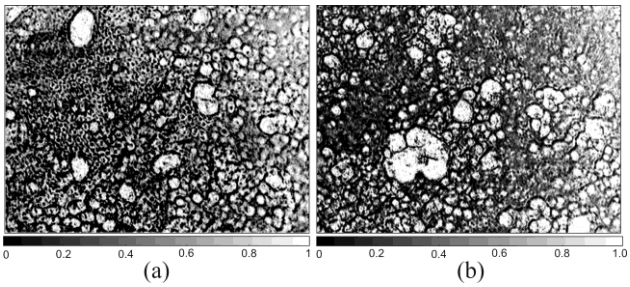

Fig. 1. Polycrystalline networks of human bile taken from healthy patient (a) and patient suffering from insulin-independent diabetes (b).

The images of layers prepared from human bile (figure 1) are indicative of availability of two fractions – optically isotropic and liquid-crystal network (anisotropic one). As seen, geometric structure and sizes of separate elements in the polycrystalline network of the samples prepared from biological fluids are individual for physiological state.

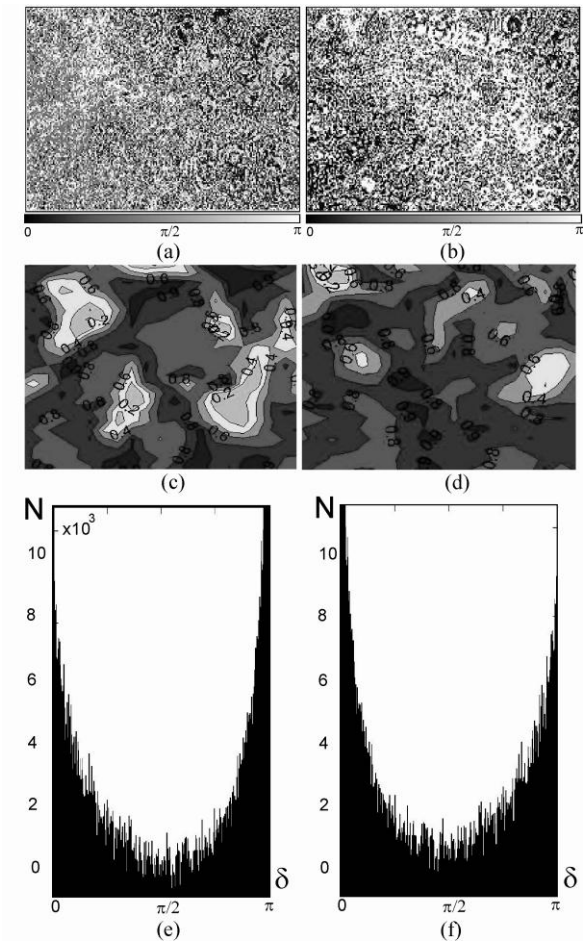

Fig. 2. Coordinate (a, b) and quantitative (c, d) distributions δ of laser images for the samples of bile taken from healthy patient's (a, c, e) and with insulin-independent diabetes (b, d, f).

Shown in figure 2 are the phase maps (fragments (a), (b), (c), (d)) and histograms (fragments (e), (f)) for distributions of random values inherent to the phase shifts δ between orthogonal components of the laser radiation amplitude transformed inside layers of bile taken from healthy patient's (left column) and from patient suffering from insulin-independent diabetes (right column).

The obtained data show that the value of phase shifts δ for laser radiation transformed inside layers of human bile lies within the short range of changes $0\le\delta\le\pi$. The weak

phase modulation is related with two factors. First, it is low geometric thickness (d = 10…15 μm) of the samples. Second, it is weak birefringence ($\Delta n \sim 10^{-4}...10^{-2}$) of liquid-crystal structures in human bile.

Our comparative analysis of histograms for distributions of random values inherent to phase shifts δ in laser images of both types human bile revealed availability of two dominant extreme ranges: $0 \le \delta \le 0.15$ and $0.85 \le \delta \le 1$. In our opinion, these features of probabilistic phase distributions are related with the influence of optically isotropic ($\delta \to 0$) and liquid-crystal ($\delta \to \pi$) components in the composition of biological fluid.

The results show that the differentiation phase maps of different groups is impossible - change of size and range of statistic moments of 1 - 4-th order almost coincide.

Being aimed at more specific investigation of phase features for both fractions, we used the following method to select information. From the available coordinate set of values $\delta(m \times n) = \begin{pmatrix} \delta_{11},... & \delta_{1n} \\ \delta_{n1},... & \delta_{mn} \end{pmatrix}$ in phase maps (figures 2(a) and 2(b)), we found samples of extreme values $\delta(m \times n) = 0$ and $\delta(m \times n) = \pi$.

In what follows, by scanning along the direction $x = 1 \div n$ we carried out calculation of the amount of extreme values for phase shifts within the column $m = n \times 1 pix$. Within the limits of each local sample $\left(1_{pix} \times n_{pix}\right)^{(k=1,2,...,m)}$, we computed the amount (N) of extreme values $\delta(k) = 0$ ($N_{\min}^{(k)}$) and $\delta(k) = \pi$ ($N_{\max}^{(k)}$). Thus, we found the dependences $N_{msn}(x) \equiv (N_{msn}{}^{(1)}, \; N_{\min}{}^{(2)}, \; ..., \; N_{\min}{}^{(m)})$ and $N_{\max}(x) \equiv (N_{\max}{}^{(1)}, \; N_{\max}{}^{(2)}, \; ..., \; N_{\max}{}^{(m)})$ for the amount of extreme values of phase shifts within the limits of laser image for bile.

Figures 3 and 4 show a set of coordinate distributions $\delta(m \times n) = 0, \pi$ (fragments (a, e)) for the dependences of the amount of extreme values $N_{\min;\max}(x)$ (fragments (b, f)), autocorrelation functions $K_{\min;\max}(\Delta x)$ (fragments (c, g)) and logarithmic dependences $\log J(N_{\min;\max}) - \log d^{-1}$ for power spectra of distributions $N_{\min;\max}(x)$ (fragments (d, h)) that characterize phase maps for the samples of bile belonging to a healthy patient (left column) and a patient suffering from insulin-independent diabetes (right column).

The comparative analysis of the obtained set of experimental data about statistic, correlation and fractal structures in dependences for the amount of extreme values $N_{\min,\max}(x)$ inherent to phase maps describing layers of bile of healthy patient and that sick with insulin-independent diabetes enabled to found:

- tendency to a decreasing (increasing) total amount of extreme values $\delta_{\min} \to 0$ ($\delta_{\max} \to \pi$) of the phase shifts in laser images of layers prepared from bile of a patient with insulin-independent diabetes (figures 3 and 4, fragments (b, f));
- fact that autocorrelation functions $K_{\min}(\Delta x)$ (figure 3, fragments (c, g)) monotonically drop with increasing the step of scanning Δx in dependences $N_{\min}(x)$;
- correlation structure of the distribution for the extreme sample $\delta(m \times n) = \pi$ in the phase map describing the polycrystalline component in bile of a sick patient changes: at the background of monotonic drop there arise oscillations of values in the dependence $K_{\max}(\Delta x)$ (see figure 4, fragment (g));
- logarithmic dependences for the power spectra of distributions $N_{\min}(x)$ for the optically isotropic component in bile of both types possess a stable slope angle (figure 3, fragments (d, f)) within the whole range of geometric sizes inherent to the laser image registered by the CCD camera (figure 1);
- fractal distributions $N_{\max}(x)$ for phase maps of laser images describing the optically anisotropic fraction of bile a healthy man (figure 4, fragment (d)) are transformed into the statistic ones in the case of insulin-independent diabetes: approximating curve in the dependence $\log J(N_{\max}) - \log d^{-1}$ has no stable slope (Fig. 4, fragment (h)).

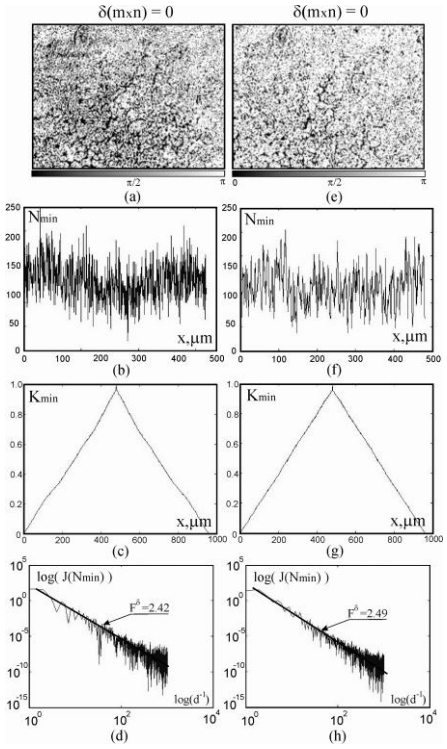

Fig. 3. Coordinate $(m \times n)$ (a, e)), quantitative $N_{\min}(x)$ (b, f)), correlation $K_{\min}(\Delta x)$ (c, g)) and fractal $\log J(N_{\min}) - \log d^{-1}$ (d, h) parameters of the extreme sample $\delta(m \times n) = 0$ for phase maps of the samples of bile belonging to a healthy patient (a, b, c, d) and a patient with insulin-independent diabetes (e, f, g, h).

From the quantitative viewpoint, the dependences $N_{\min;\max}(x)$ illustrate statistic $M_{i=1-4}^{\delta}$, correlation S^{δ}, Q^{δ} and fractal F^{δ}, D^{δ} parameters determined within the limits of two patient groups, and they are summarized in Tables 2.

Our analysis of the parameters determined experimentally has shown that the following parameters are

diagnostically sensitive in observation of pathologic processes

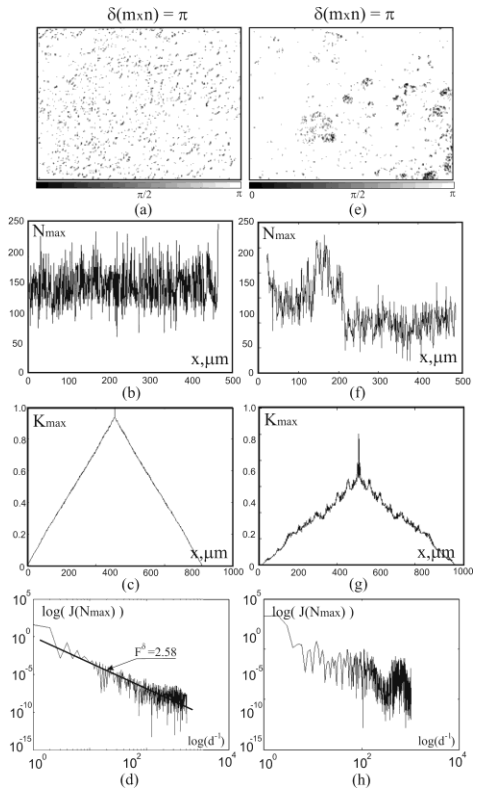

Fig. 4. Coordinate $(m\times n)$ (a, e)), quantitative $N_{\max}(x)$ (b, f)), correlation $K_{\max}(\Delta x)$ (c, g)) and fractal $\log J(N_{\max})-\log d^{-1}$ (d, h) parameters of the extreme sample $\delta(m\times n)=1$ for phase maps of the samples of bile belonging to a healthy patient (a, b, c, d) and a patient with insulin-independent diabetes (e, f, g, h).

- statistic moments of the third (M_3^{δ}) and fourth (M_4^{δ}) orders in distributions for the amount of extreme values $N_{\max}(x)$ of phase shifts $\delta(m\times n)=1$ in laser images for bile of both types – differences between them reach 2.4 and 4.1 times;
- the kurtosis (Q_4^{δ}) of autocorrelation functions $K_{\max}(\Delta x)$ related to distributions $N_{\max}(x)$ differ by 1.8 and 2.7 times;
- correlation area S^{δ} for the autocorrelation dependence $K_{\max}(\Delta x)$ of the distribution for the amount of extreme phase shifts in a laser image inherent to joint bile of a patient with osteoarthritis is 2.55 times less than that parameter determined for a healthy patient;
- distributions $N_{\max}(x)$ for the phase maps describing bile for healthy and sick patients are, respectively, fractal and statistic;
- dispersion D^{δ} of the dependences $\log J(N_{\max})-\log d^{-1}$ in the case of pathological changes in the polycrystalline structure of bile is 1.75 times decreased.

IV. CONCLUSION

Thus, one can draw the following conclusions:

➢ Human bile, independently of their physiological state, contains phase-modulating optically anisotropic network of biological crystals.

TABLE 2. STATISTIC MOMENTS $M_{i=1-4}^{\delta}$, CORRELATION S^{δ}, Q^{δ} AND FRACTAL F^{δ}, D^{δ} PARAMETERS THAT CHARACTERIZE THE DISTRIBUTIONS FOR AMOUNTS OF EXTREME VALUES IN COORDINATE DISTRIBUTIONS $\delta(m\times n)$ OF LASER IMAGES FOR HUMAN BILE

$\delta(m\times n)$	$\delta(m\times n)=0$		$\delta(m\times n)=\pi$	
$M_{i=1-4}^{\delta}$	Healthy (21 patients)	Diabetes (19 patients)	Healthy (21 patients)	Diabetes (19 patients)
M_1^{δ}	0.51±0.063	0.54±0.067	0.22±0.025	0.35±0.042
M_2^{δ}	0.13±0.018	0.08±0.011	0.25±0.031	0.14±0.017
M_3^{δ}	0.26±0.033	0.19±0.022	0.79±0.086	2.18±0.25
M_4^{δ}	0.48±0.054	0.55±0.068	0.83±0.098	3.11±0.42
Q_4^{δ}	0.14±0.016	0.12±0.015	0.56±0.069	2.21±0.31
S^{δ}	0.24±0.015	0.21±0.013	0.17±0.021	0.08±0.012
F^{δ}	2.42±0.12	2.49±0.11	2.58±0.15	Statistic
D^{δ}	0.21±0.028	0.24±0.027	0.34±0.042	0.18±0.023

➢ Ascertained and grounded is a set of criteria for phase diagnostics of inflammatory processes (diabetes, cholecystitis) as being based on statistic (statistic moments of the first to fourth orders), correlation (normalized fourth statistic moment of autocorrelation function, correlation area) and fractal (fractal dimension and dispersion for the distribution of extrema in log – log dependences of power spectra) analyses of phase distributions in laser images of human bile.

REFERENCES

[1] W.-F. Cheong, S. A. Prahl, A. J. Welch, "A Review of the Optical Properties of Biological Tissues," IEEE J. Quantum. Electron. 26, 2166-2185, 1990.

[2] S. A. Prahl, M. Keijzer, S. L. Jacques, A. J. Welch, "A Monte Carlo model of light propagation in tissue," in *SPIE Proceedings of Dosimetry of Laser Radiation in Medicine and Biology*, G. J. Müller and D. H. Sliney, eds. IS 5, 102-111, 1989.

[3] E. Wolf, "Unified theory of coherence and polarization of random electromagnetic beams," Phys. Lett. A. 312, 263-267, 2003.

[4] Alexander G. Ushenko and Vasilii P. Pishak, "Laser Polarimetry of Biological Tissue: Principles and Applications", in *Handbook of Coherent-Domain Optical Methods: Biomedical Diagnostics, Environmental and Material Science*, Valery V. Tuchin, ed. (Boston: Kluwer Academic Publishers, 2004), pp. 93-138.

[5] O. V. Angelsky, A. G. Ushenko, Yu. A. Ushenko, V. P. Pishak, "Statistical and Fractal Structure of Biological Tissue Mueller Matrix Images", in *Optical Correlation Techniques and Applications*, Oleg V. Angelsky, ed. (Washington: Society of Photo-Optical Instrumentation Engineers, 2007), pp. 213-266.

[6] O.V. Angelsky, A.G. Ushenko, Yu.A. Ushenko, V.P. Pishak, and A.P. Peresunko, "Statistical, Correlation, and Topological Approaches in Diagnostics of the Structure and Physiological State of Birefringent Biological Tissues", in *Handbook of Photonics for*

Biomedical Science, Valery V. Tuchin, ed. (USA: CRC Press, 2010), pp. 21-67.

[7] Alexander G. Ushenko, "Polarization structure of laser scattering fields," Opt. Eng. 34, 1088-1093 (1995).

[8] A.G. Ushenko, "Laser diagnostics of biofractals," Quantum Electron. 29, 1078–1084, 1999.

[9] O.V. Angel'skii, A.G. Ushenko, A.D. Arkhelyuk, S.B. Ermolenko, D.N. Burkovets, "Structure of matrices for the transformation of laser radiation by biofractals," Quantum Electron. 29, 1074-1077, 1999.

[10] O.V. Angel'skii, A.G. Ushenko A.D. Arheluk, S.B. Ermolenko, D. N. Burkovets, "Scattering of Laser Radiation by Multifractal Biological Structures," Optics and Spectroscopy 88, 444-448, 2000.

[11] A.G. Ushenko, "Polarization Structure of Biospeckles and the Depolarization of Laser Radiation," Optics and Spectroscopy 89, 597-601, 2000.

[12] A.G. Ushenko, "Stokes-correlometry of biotissues," Laser Phys. 10, 1286-1292, 2000.

[13] A.G. Ushenko, "The Vector Structure of Laser Biospeckle Fields and Polarization Diagnostics of Collagen Skin Structures," Laser Phys. 10, 1143-1149, 2000.

[14] A.G. Ushenko, "Laser polarimetry of polarization-phase statistical moments of the object field of optically anisotropic scattering layers," Optics and Spectroscopy 91, 313-316, 2001.

[15] A.G. Ushenko, "Polarization contrast enhancement of images of biological tissues under the conditions of multiple scattering," Optics and Spectroscopy 91, 937-940, 2001.

[16] A.G. Ushenko, "Laser probing of biological tissues and the polarization selection of their images," Optics and Spectroscopy 91, 932-936, 2001.

[17] A.G. Ushenko, "Correlation processing and wavelet analysis of polarization images of biological tissues," Optics and Spectroscopy 91, 773-778, 2002.

[18] A.G. Ushenko, "Polarization correlometry of angular structure in the microrelief pattern or rough surfaces," Optics and spectroscopy 92, 227-229, 2002.

[19] O.V. Angelsky, A.G. Ushenko, Ye.G. Ushenko, "2-D Stokes Polarimetry of Biospeckle Tissues Images in Pre-Clinic Diagnostics of Their Pre-Cancer States," J. Holography Speckle 2, 26-33, 2005.

[20] Oleg V. Angelsky, Alexander G. Ushenko, and Yevheniya G. Ushenko, "Complex degree of mutual polarization of biological tissue coherent images for the diagnostics of their physiological state," J. Biomed. Opt. 10, 060502, 2005.

[21] O. V. Angelsky, A. G. Ushenko, and Ye. G. Ushenko, "Investigation of the correlation structure of biological tissue polarization images during the diagnostics of their oncological changes," Phys. Med. Biol. 50, 4811-4822, 2005.

[22] Oleg V. Angelsky, Alexander G. Ushenko, Yevheniya G. Ushenko, Yuriy Y. Tomka, "Polarization singularities of biological tissues images," J. Biomed. Opt. 11, 054030, 2006.

[23] O.G. Ushenko, S.G. Guminetsky, A.V. Motrich, "Optical properties of urine, blood plasma and pulmonary condensate of the patients with pulmovnary form of tuberculosis," Photoelectronics 16, 133-139, 2007.

[24] S.H. Guminetskiy, O.G. Ushenko, I.P. Polyanskiy, A.V. Motrych, F.V. Grynchuk, "The optical method for investigation of the peritonitis progressing process," Proc. SPIE 7008, 700827, 2008.

[25] Alexander Ushenko, Sergej Yermolenko, Alexander Prydij, Stepan Guminetsky, Ion Gruia, Ovidiu Toma, Konstantin Vladychenko, "Statistical and fractal approaches in laser polarimetry diagnostics of the cancer prostate tissues," Proc. SPIE 7008, 70082C, 2008.

[26] A.G. Ushenko, A.I. Fediv, Yu.F. Marchuk, "Correlation and fractal structure of Jones matrices of human bile secret," Proc. SPIE 7368, 73681Q, 2009.

[27] A.G. Ushenko, Yu.Ya. Tomka, V.I. Istratiy, "Polarization selection of two-dimensional phase-inhomogeneous birefringence images of biotissues," Proc. SPIE 7388, 73881L, 2009.

[28] A.G. Ushenko, A.I. Fediv, Yu.F. Marchuk, "Singular structure of polarization images of bile secret in diagnostics of human physiological state," Proc. SPIE 7368, 73681S, 2009.

[29] S.B. Yermolenko, A.G. Ushenko, P. Ivashko, "Spectropolarimetry of cancer change of biotissues," Proc. SPIE 7388, 73881D, 2009.

[30] A.G. Ushenko, I. Z.Misevich, V. Istratiy, I. Bachyns'ka, A. P. Peresunko, Omar Kamal Numan, and T. G. Moiysuk, "Evolution of Statistic Moments of 2D-Distributions of Biological Liquid Crystal Net Mueller Matrix Elements in the Process of Their Birefringent Structure Changes," Advances in Optical Technologies 2010, 423145, 2010.

[31] O. V. Dubolazov, A. G. Ushenko, V. T. Bachynsky, A. P. Peresunko, and O. Ya. Vanchulyak, "On the Feasibilities of Using the Wavelet Analysis of Mueller Matrix Images of Biological Crystals," Advances in Optical Technologies 2010, 162832, 2010

Ultrasound Imaging: Correction of Geometric Distortions using Warping

Ari LEV-OR and Moshe PORAT
Technion, Haifa 32000, Israel
re@vision.technion.ac.il mp@ee.technion.ac.il

***Abstract* – Ultrasound images suffer from inherent geometric distortions due to variations in sound speed within the body. Other distortions include missing surfaces parallel to the direction of the ultrasonic rays, intense speckle noise, acoustic shadows and resolution inconsistency. These artifacts depend on the positioning of the transducer relative to the scanned organs, and considerably degrade the quality of the images obtained. We introduce a new algorithm that combines ultrasound images taken from distant viewpoints using spatial warping and compounding to obtain a quality-enhanced image. The algorithm is iterative: in each iteration the B-Mode images are divided into blocks and a matching procedure is performed between blocks of the reference images. Individual pixels are translated based on inter-block interpolation, subject to physical and medical constraints. The resultant warped images are used as an input signal to the next iteration. The algorithm was implemented and tested in-vitro, demonstrating superior results compared to presently available methods. The results are presented and discussed.**

***Index Terms* – Block Matching, Non-Linear Processing, Spatial Compounding, Ultrasound Imaging, 2D Warping.**

I. INTRODUCTION

Ultrasound is a useful non-invasive tool for soft tissue imaging due to its low cost along with real time acquisition. The quality of the reconstructed images however is lower than in other medical imaging systems such as X-Ray, MRI or CT. It suffers from differences in spatial and axial resolution, noise (speckle and other), acoustic shadows, missing surfaces and geometric distortions.

One of the problems is the deformation caused by the variations in sound speed in the different body tissues. An ultrasound system assumes that the speed of sound is constant within the human body (1540 m/s) [5], and accordingly reconstructs the echoed pulses into a 2D image. It is known however that this speed varies [5] and causes the axial dimensions of organs to be out of scale (Figure 1). This variation in size however, despite its somewhat marginal effect on the resultant image, plays a major role when two or more ultrasound images are taken from different angles and compounded to create a higher quality image.

Previous works on image compounding, targeting speckle reduction and enhancing tissue boundaries, have either scanned the region of interest by alternately activating different parts of the poly-crystal transducer thus scanning in different angles [4], or used a mechanical arm to move [7] or track [3] the transducer with high accuracy. According to He's et al. approach [2], a thin wire phantom is used to calibrate the scanning system before performing the scan on a human subject.

In this work we propose a solution to the problem of geometric distortions based on image processing techniques. According to our proposed algorithm, two scans are obtained from two relatively distant viewpoints (Figure 2), resulting in significant geometric correction. Local information [6] is used for identifying similar parts in the two images, and an iterative process [1] warps the images to optimally match.

This work was supported in part by a grant from the GIF, the German-Israeli Foundation for Scientific Research and Development, and by the Ollendorff Minerva Center. Minerva is funded through the BMBF.

Fig. 1: Ultrasound images (simulation) of a circular cylinder. Left: The actual speed of sound inside the object is exactly as assumed. Different images are obtained if the speed inside the object is lower than assumed (center) or higher than assumed (right). The transducer is positioned at the top in all three images.

surfaces are also rectified by compounding two images, and will be discussed as byproducts of the proposed algorithm.

This paper is organized as follows. Definitions and notations are presented in Section II. The new algorithm is described in Section III, and major considerations are introduced in Section IV. Simulation results are given in Section V and the paper is concluded with a summary in Section VI.

II. II. DEFINITIONS AND NOTATIONS

The following notations are used throughout this paper.

2.1. Scan Line – an A-Mode ultrasound image. Along this each pixel represents the intensity of the echoed (returned) pulse.

2.2. Scan Line Collection Image (SLC Image) – a raster display of the scan lines: the horizontal axis corresponds to the ultrasonic pulse firing-angle (i.e., angle of scan-line) and the vertical axis represents depth.

2.3. Fan Image - The B-Mode ultrasound image. This is a straightforward reconstruction of the image given the SLC image and the angle associated with each scan-line. The term 'Fan' indicates that the scan lines are in a fan-like arrangement.

2.4. Difference between blocks: The obtained images are gray-scale. The intensity of the pixel (x, y) in block k is represented by $I_k(x, y)$, where $0 \le x \le W-1$, and $0 \le y \le H-1$. $x, y, W, H \in \mathbf{Z}$ (integers). W and H denote the width and height of the block, respectively. The difference between two blocks is defined by

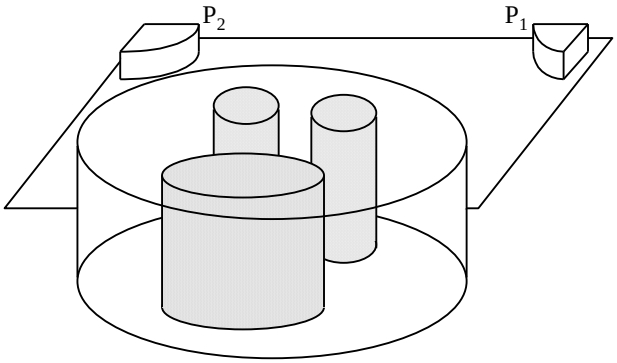

Fig. 2: The dual-transducer structure. The images obtained from two angles (P_1 and P_2) are integrated into a compounded higher quality image.

$$Diff_{jk} = \sum_{y=0}^{H-1}\sum_{x=0}^{W-1}\left|\frac{I_j(x,y)}{E_j} - \frac{I_k(x,y)}{E_k}\right| \quad (1)$$

where E_j is related to the total energy (sum of pixel values) of block j:

$$E_j = \sum_{y=0}^{H-1}\sum_{x=0}^{W-1} I_j(x,y). \quad (2)$$

The difference *Diff* is in the range of [0, 2] due to normalization according to the size and energy of the blocks. *Diff=0* means that the blocks are identical, up to a multiplication factor, as in the case of acoustic shadows. Maximum difference *(Diff=2)* is obtained when each white pixel in the first image corresponds to a black pixel in the other, and vice versa. To avoid singularity, when a block is all black the result is set to *Diff=1*.

Equation (1) is also used for calculating the difference between the two images.

III. THE ALGORITHM

Given the above definitions, we can now introduce the algorithm for spatial warping and compounding:

3.1. Acquire two SLC images of the same cross-section from two different viewpoints.

3.2. Construct two Fan images based on the two SLC images.

3.3. Rotate and translate the two Fan images according to the angle and displacement between the viewpoints.

3.4. Stop if the difference between two consecutive images is below a resolution threshold.

3.5. Divide both images into blocks. Calculate the spatial translation required for each block in each Fan image. Accordingly, derive the appropriate translation of all the pixels in each SLC image (Section 4).

3.6. Translate the pixels in both SLC images.

3.7. Go to step **3.2**.

These steps are summarized in Figure 3.

The algorithm is iterative. The two images are warped in each iteration to reduce the difference between them. The algorithm may be terminated in one of two ways: 1. After a predefined number of steps. 2. When the difference between the images is below a threshold value. The first approach is straightforward, and adequate.

IV. IMAGE WARPING

The proposed algorithm is block based. Each image is divided into blocks, and a block-matching procedure is applied. The translation is calculated by averaging the translation of the block containing the pixel and the translation of the neighboring blocks. This process is carried out as follows.

4.1. Apply low-pass-filtering to both Fan images to reduce the sensitivity of the matching process to noise and contour deformation.

4.2. Divide the first fan image into blocks.

4.3. For each block perform block-matching between the two images. Two translation vectors are attained: A regular 2D minimum-difference translation, denoted $\vec{V}_{2D}$, and a vector of minimum-difference when translation is allowed only along the scan-line that goes through the block's center, denoted $\vec{V}_{SL}$. Consistency in the direction of these two vectors ensures that the deformation is only axial and is due to variations in sound speed.

4.4. Calculate a quality factor of the match Q ($0 \le Q \le 1$): If $\vec{V}_{2D}$ and $\vec{V}_{SL}$ point in similar directions, the match is considered good and Q is close to 1. Q is lower (close to 0) if the directions differ significantly. Denote the angle between the two vectors as θ (Figure 4), the quality factor is defined according to the projection of one vector onto another:

$$Q = \begin{cases} 0 & \cos(\theta) \le 0 \\ \cos(\theta) & \cos(\theta) > 0 \end{cases}. \quad (3)$$

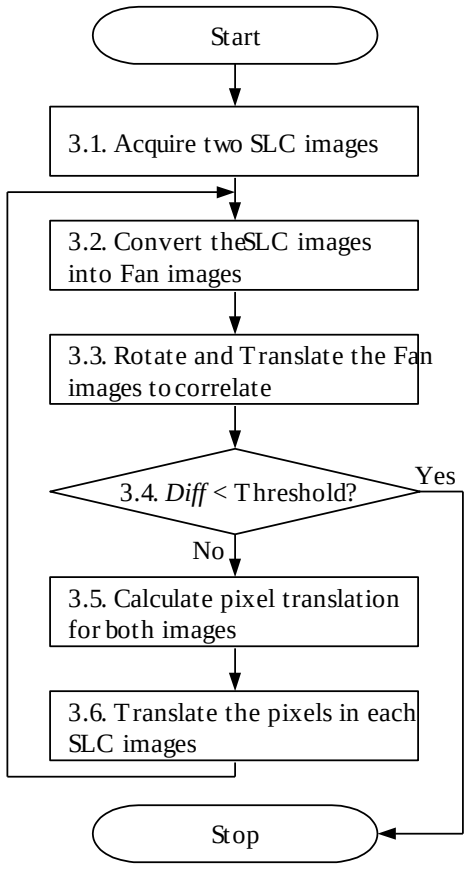

Fig. 3: Flowchart of the algorithm.

The quality factor serves as a weight of the block's translation when averaging translation of several blocks.

4.5. Calculate the final translation of the block. This translation must be *along* a scan-line assuming that the distortions due to speed variations are only axial. We define the final translation vector $\vec{V}_{final}$ to have the same direction

as $\vec{V}_{SL}$, and magnitude of $V_{final} = \min(V_{SL}, V_{2D} \cdot Q)$. By selecting the minimum translation over-warping of the image is avoided.

4.6. Once $\vec{V}_{final}$ is calculated for all the blocks, each pixel is translated according to the weighted average translation of its neighboring blocks. Two weights are applied when averaging: The quality factor *Q*, and the distance D_n between the pixel and the block center.

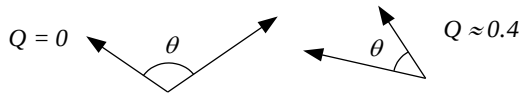

Fig. 4: Two examples of the quality factor Q. Left: θ>90° , cos(θ)<0 and Q=0. Right: θ<90° , cos(θ)>0 and Q>0.

Thus we get:

$$\vec{V}_{Pixel} = \frac{\sum_{n=0}^{8} \vec{V}_{n\,final} \cdot G(D_n) \cdot Q_n}{\sum_{n=0}^{8} G(D_n)} \quad , \tag{4}$$

where the weight function *G* is monotonically decreasing with the distance D_n:

$$G(D_n) = \begin{cases} 1 - \dfrac{D_n}{D_{Max}} & 0 \le D_n \le D_{Max} \\ 0 & D_n > D_{Max} \end{cases} \quad , \tag{5}$$

and

$$D_{Max} = 1.5\sqrt{W^2 + H^2} \quad . \tag{6}$$

D_n and D_{max} are measured in units of the sampling interval between pixels.

To avoid dependency on a specific block division we use overlapping block-sets that are displaced relative to the original division, i.e., the origin of the first (top-left) block is *(dx, dy)* instead of (0,0). The pixel translation process is performed on each block-set, thus eliminating a blockiness effect in the warped image.

V. RESULTS

The algorithm was tested on the ultrasound images of Figure 2. The images are 256x256 pixels, each pixel is represented by 8 bits, i.e., 256 grey levels.

The first few iterations cause the difference between the images to decrease significantly (Figure 5). However, the iterative process may introduce an error since pixel translation is not necessarily according to an integer number and a single pixel may spread its energy in two neighboring pixels. Moreover, there is a mutual-pixel drift due to the feedback nature of the algorithm. The result is that after reaching a minimum, the difference between consecutive images may increase.

The algorithm was tested with regard to two parameters. The first parameter was the size of each block, ranging from 16^2 to 56^2 pixels, in steps of 8 pixels. The second parameter was the number of block-sets, selected in the range of 1 to 5^2 (i.e., 5 subdivisions on each axis). According to our results, the algorithm is robust to the above changes if more than 2^2 block-sets are used. It should be noted however that the image-difference is not related directly to image-quality as perceived by humans. For example, when using 16^2-pixel blocks, the image-difference decreases rapidly to a low value, despite an intense blockiness effect and loss of contour roundness. Larger blocks (32^2 pixels and above) have shown slower decrease but the roundness of the contours was sustained.

VI. SUMMARY

An image-processing technique has been applied successfully to ultrasound images, significantly reducing their inherent geometric distortions. The proposed algorithm is primarily designed to compensate for geometric distortions, however, a highly beneficial byproduct of the process is reduction of speckle noise and missing edges, since the combined image is an average of two images taken from distant viewpoints, in which the distortions diverse. It is also shown that the manipulation of the images is better done when using *both* SLC (scan line collection) and Fan (B-Mode) images.

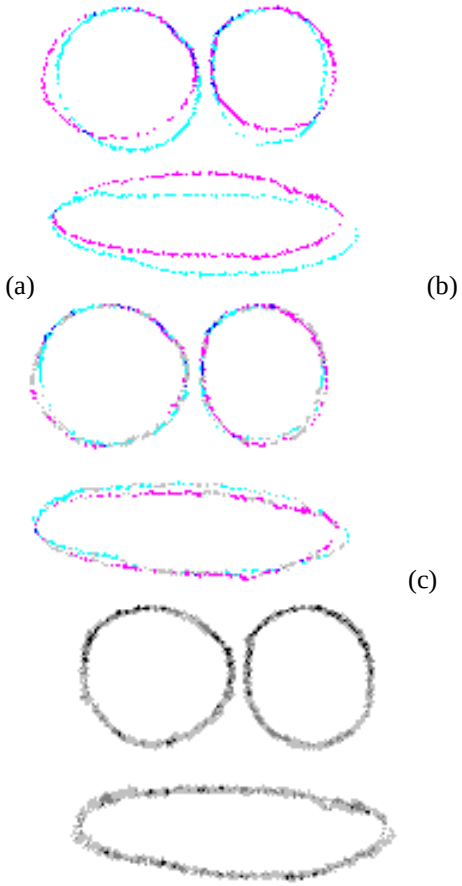

Fig.5: The compounded images according to the set-up of Figure 2. (a) The original two images. (b) After one iteration. (c) Minimum difference obtained after 8 iterations.

Our conclusion is that a dual-transducer system can significantly improve ultrasound imaging compared to the traditional approach. The new method may be also useful in correcting distortions caused by differences between lateral and radial resolutions, and may allow a wider ultrasonic beam thus achieving better defocusing property.

ACKNOWLEDGMENT

We thank Dr. Moshe Bronshtein of the *Al-Kol* ultrasound clinic in Haifa, Israel, for his contribution to this work. We are also grateful to Prof. I. Meizner and the staff of the Women-Ultrasound department of the *Belinson* Hospital (Rabin Medical Center), Petah-Tikva, Israel, for their assistance, and to Prof. Dan Adam of the Biomedical Engineering department at the Technion for his help. Lastly, we would like to thank Mr. Moti Shenhar, for the construction of the ultrasound phantom.

REFERENCES

[1] Y. Eldar, M. Lindenbaum, M. Porat and Y.Y. Zeevi, "The Farthest Point Strategy for Progressive Image Sampling", *IEEE Trans. On Image Processing*, Vol. 6, No. 9, pp. 1305-1315, 1997.

[2] P. He, K. Xue, P. Murka, "3-D imaging of residual limbs using ultrasound", *Journal of Rehabilitation Research and Development*, Vol. 34 No. 3, pp. 269-278, July 1997.

[3] A. Hernandez, O. Basset, P. Chirossel and G. Gimenez, "Spatial Compounding in Ultrasonic Imaging using an articulated scan arm", *Ultrasound in Medicine and Biology*, Vol. 22, No. 2, pp. 229-238, 1996.

[4] Soren K. Jespersen, Jens E. Wilhjelm and Henrik Sillesen, "Multi-Angle Compound Imaging", *Ultrasonic Imaging*, Vol. 20, pp. 81-102, 1998.

[5] "Biological Effects of Ultrasound: Mechanisms and Clinical Implications", *NCRP (National Council on Radiation Protection and Measurements) Report No. 74*, NCRP Publications, Bethesda, Maryland, Dec 30 1983.

[6] M. Porat and Y.Y. Zeevi, "Localized Texture Processing in Vision: Analysis and Synthesis in the Gaborian Space", *IEEE Trans. on Biomedical Engineering*, vol. BME-36, No. 1, pp. 115-129, 1989.

[7] Gregg E. Trahey, Stephen W. Smith, and Olaf T. Von Ramm, "Speckle Pattern Correlation with Lateral Aperture Translation: Experimental Results and Implications for Spatial Compounding", *IEEE Transactions on Ultrasonics and Frequency Control*, Vol. 33 No.3, pp. 257-264, May 1986.

Application of a Threshold Methods for Compression of Vocal Signals

Mahjoubian MASOUD[1], G.N. ROZORYNOV[1], Fendri Mohamed AYMEN[1]

[1]National Technical University of Ukraine "Kiev Polytechnic Institute",Kiev, Ukraine
rozor46@mail.ru

***Abstract* – Types of thresholds used for compression of vocal signals are considered. It is shown that quality of the restored speech depends straight on the choice of threshold characteristic. The mathematical description of spectral composition of the signal subjected to threshold is given, its connection with the size of the threshold is revealed and the nonlinear distortion coefficient is calculated. The graphs of revealed dependencies on which it is possible to judge on type selection and threshold level are built.**

***Keywords* – compression, threshold, spectral composition, vocal signal, nonlinear distortion coefficient.**

VII. INTRODUCTION

The present work is closely connected to the real problem, arising up at the signal processing in the cellular telephone systems, because of the background noises in them. When a vocal signal is transferred from a cellular telephone to the base station (or in other direction), it should be compressed in order for an operator could transfer as many signals as the real carrying capacity of the channel can allow [1].

For trouble-free work of the compression circuit it is necessary to provide high value of signal/noise relation on its input. Therefore the removal of background noise is made before the compression process. This can be done with an ideal filter which passes only a vocal signal and removes undesirable noises, for example, car noise or people talks. It is obvious that practically this task is enough difficult that's why the attempts to utilize different methods of signal processing, the most successful of which are threshold [2, 3 - 7] are undertaken. Thus, however, there is no data about threshold type influence and the level of threshold on qualitative descriptions of the restored signal.

The purpose of the present work is research of different threshold methods of decreasing the level of background noise while compression of vocal signals and choosing the best one of them on quality of the restored signal criteria.

VIII. MAIN PART

Threshold methods of noise decrease are based on diminishing of coefficients values of signal transformation while its transfer from one representative domain to another (time-frequency, time-space, and other). It is assumed that the noise component is represented by small coefficients and the threshold method is used for reduction or complete removal of small coefficients. Then the signal is exposed to reverse transformation.

Soft and hard thresholds [2, 3 - 5] are most often used. As it is assumed that the algorithm of processing should operate in a real-time mode, and the length of input signal can be large so the input signal is divided into small segments (shots). The algorithm of processing is used on each segment and the output result is represented as a composition of separate processed segments. Processing of separate segment requires time that all in all leads to the delay of signal in communication network.

Let's designate the size of the threshold θ. Then in case of hard threshold the functional characteristic (FC) of thresholding will be described by the equation:

$$f(x) = \left[1(|x| - \theta)\right]x, \quad (1)$$

where, $1(x) = \begin{cases} 1, & x \geq 0, \\ 0, & x < 0, \end{cases}$ – unit function.

The graph of FC at hard thresholding is shown on fig. 1,a.

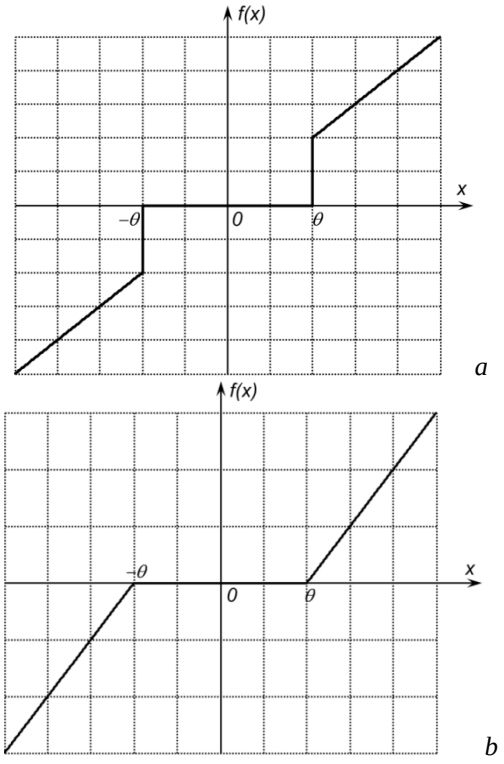

Fig.1 Functional characteristics of thresholding: *a* - hard, *b* - soft

In the case of soft threshold use FC is represented:

$$f(x) = \left[1(|x| - \theta)\right]\left[x - \theta sign(x)\right], \quad (2)$$

and the graph of such FC is shown on fig. 1,b.

Analysis of the graphs presented on fig.1 shows that the greatest influence on quality of speech transmission, especially with background noises, make initial areas of FC. Therefore we will try to modify these areas so that to provide the least distortions of the restored signal. The simplest decision for this task is realization of FC of threshold types, shown on fig. 2.

We will name them FC of linear supersoft thresholding

(fig. 2,a) and FC of quadratic supersoft thresholding (fig. 2,b).

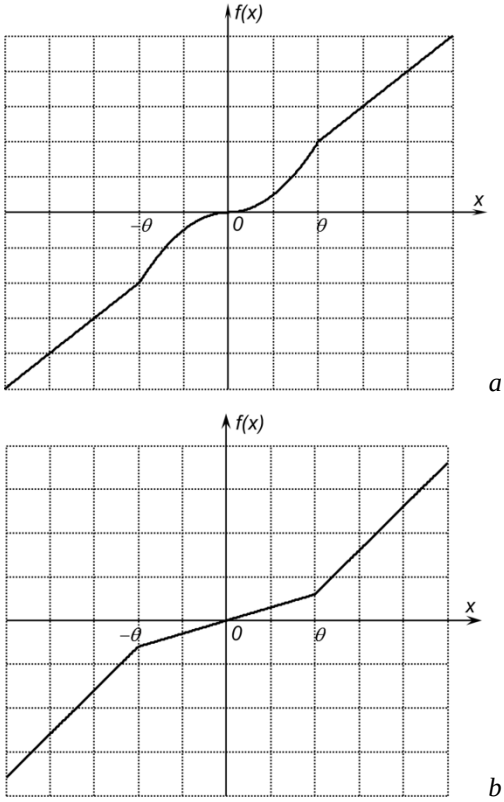

Fig.2 Functional characteristics of supersoft thresholding: *a* - linear, *b* - quadratic

FC at linear and quadratic supersoft thresholding are presented, accordingly:

$$f(x)=\begin{cases} x-sign(x)(1-\beta)\theta, & |x|\ge\theta, \\ \beta x, & |x|<\theta. \end{cases} \quad (3)$$

$$f(x)=\begin{cases} x, & |x|\ge\theta, \\ \dfrac{x^2}{\theta}sign(x), & |x|<\theta. \end{cases} \quad (4)$$

In the formula (4), β is an angular coefficient, determining inclination of initial linear area of FC.

At the compression of vocal signal with losses, with growth of compression coefficient (size of threshold θ) signal distortions increase accordingly [2, 3]. It shows up when parasite harmonic components appear in the restored vocal signal.

The number of distortions of signal after thresholding can be defined by the nonlinear distortion coefficient χ as a relation of operating value of output signal without its first harmonic to the operating value of input signal (in case of sinusoidal signal):

$$\chi=\frac{\sqrt{\frac{1}{2}\sum_{n=2}^{\infty}b_n^2}}{A/\sqrt{2}}=\frac{\sqrt{P_{эф}^2-\frac{1}{2}b_1^2}}{A/\sqrt{2}}. \quad (5)$$

Using (5), will get the followings formulas for the calculation of vocal signals klirfactors:

$$(\chi)_{ж}=\frac{1}{\pi}\sqrt{(\pi-2\alpha+sin\,2\alpha)(2\alpha-sin\,2\alpha)}, \quad (6)$$

$$(\chi)_{н}=\frac{}{\frac{1}{\pi}\sqrt{\pi[2\alpha-sin\,2\alpha+2(\pi-2\alpha)\,sin^2\alpha]-(2\alpha+sin\,2\alpha)^2}} \quad ,(7)$$

$$(\chi)_{лсм}=\left\{\frac{1}{\pi}[(1-\beta)(\beta-3)\,sin\,2\alpha-2\alpha(1-\beta^2)+\pi+2(\pi-2\alpha)(1-\beta)^2\,sin^2\alpha]\left[1-\frac{1-\beta}{\pi}(2\alpha+sin\,2\alpha)^2\right]\right\}^{\frac{1}{2}} \quad , (8)$$

$$(\chi)_{ксм}=\frac{1}{\pi}\left\{\pi\left[\frac{1}{sin^2\alpha}\left(\frac{3}{2}\alpha-sin\,2\alpha+\frac{1}{8}sin\,4\alpha\right)\right]+\pi-2\alpha+sin\,2\alpha\right]-\left[\frac{1}{sin\,\alpha}\left(3-3\,cos\,\alpha-\frac{1-cos\,3\alpha}{3}\right)+\pi-2\alpha+sin\,2\alpha\right]^2\right\}^{\frac{1}{2}}. \quad (9)$$

From these calculations it is evident that the signal suffers most distortions at use of hard thresholding. In addition, depending on the type of threshold the maximum value of nonlinear distortion coefficient corresponds to different values of $\sin\alpha$. Only in case of soft and linear supersoft thresholds these values coincide and equal 0,3.

IX. CONCLUSION

1. It was shown that most influence on quality of transmission of vocal signals, especially with background noises, renders the type of initial area of functional characteristic of thresholding.

2. 4 types of functional characteristics of thresholding that have different initial areas were studied. The mathematical description of spectral composition of sinusoidal signal thresholding subjected was given, its connection with the size of threshold was shown and the nonlinear distortion coefficient was calculated. The graphs of shown dependencies which help to choose the type and the size of a threshold were built.

REFERENCES

[1] *Шелухин О.И., Лукьянцев Н.Ф.* Цифровая обработка и передача речи / Под. ред. О.И. Шелухина. – М.: Радио и связь, 2000. – 456 с.

[2] *Розоринов Г.Н., Колокольцев Ф.В.* Компандирование речевых сигналов для цифровой передачи по полосноограниченным каналам // Вісник Державного університету інформаційно-комунікаційних технологій. – 2006. – Т.4, №2. – С. 73 – 79.

[3] *Фёдоров Е.Е.* Модели и методы преобразования речевых сигналов. – Донецк: Норд-Пресс, 2006. – 260 с.

[4] *Reccione M.C.* The enhanced variable rate coder: Toll quality speech for CDMA // International Journal of Speech Technology. – 1999. – № 2. – P. 305–315.

[5] *Thiemann J.* Acoustic Noise Suppression for Speech Signals using Auditory Masking Effects. – Montreal: McGill University. – 2001. – 83 p.

[6] *Дьяконов В., Абраменкова И.* MATLAB. Обработка сигналов и изображений: Специальный справочник. – СПб.: Питер. – 2002. – 608 с.

[7] *Малла С.* Вейвлеты в обработке сигналов: Пер. с англ. – М.: Мир, 2005. – 671 с.

Computed Tomography Aspects of the Endoscoic Sinus Surgery in Children

Mihail MANIUC, Polina ABABII
SMPhU „N.Testemitanu"

***Abstract* - Computed tomography aspects of the endoscopic sinus surgery in children**

I. INTRODUCTION

Performances of endoscopic method in exploring the nasal and sinus cavity reduce the need for radiological examination in diagnosis of nasal obstruction. On the other hand, imaging plays an important role in assessing the etiology of sinusitis. If a tumor, a septal deviation, a cornet hypertrophy or choanal atresia, i.e., surface examination, can be detected by endoscopic investigation, expanding of the pathologic process can be appreciated only after performing imaging examination. Functional endoscopic surgical techniques proposed by W. Messerklinger are based on a correct diagnosis, which in its turn results from the information of endoscopic diagnostics and sinus computed tomography examination. With the development of endonasal surgery, visualization of the sinus cavities becomes essential for performing intrasinusal surgery. Computed tomography examination is considered as the most informative imaging method for diagnosis of recurrent and chronic paranasal sinusitis. Under our supervision there were 120 children with recurrent and chronic sinusitis who underwent endoscopic endonasal surgery. The mentioned method of examination was used for the objectification of postoperative results.

II. TOPICALITY

Recurrent and chronic paranasal sinusitis in children are quite common pathologic entities in everyday practice. Paranasal sinus inflammatory diseases in general and recurrent and chronic rhinosinusitis in children in particular are a difficult issue and in childhood and are registered with a frequency of 18-30% to 38-42% [1, 2, 3].

The issue of pathogenesis, early diagnosis and endoscopic surgical treatment is being studied in many centers by rhinologists, but so far remain unclear aspects of it. There are studies that reveal information about the importance of anatomic and physiological peculiarities of nasal cavities and paranasal sinuses in the pathogenesis of rhinosinusal disorders [1, 3, 4]. In modern literature the pathogenesis of chronic and recurrent sinusitis is referred to as "cooperation" between infection and predisposing factors. Diagnosis and treatment of sinusitis in children has changed substantially over the past 10 years due to the wide spread and implementation of functional diagnostic methods (acoustic rhinometry, rhinomanometry), diagnostic imaging by computed tomography and rhinosinusal endoscopy [4, 5, 6, 7]. One of the major symptoms presented by patients with recurrent and chronic sinus pathology is nasal obstruction which is a subjective parameter. The etiology and treatment of obstruction often relies on clinical and rhinoscopy data and rarely - on objective methods. Functional endoscopic surgery techniques proposed by Messerklinger are based on a correct diagnosis, which in its turn results from diagnostic endoscopic examination and rhinosinusal computed tomography [4]. A computed topographic examination in coronary and axial sections allows studying the anatomical anomalies and variations of the lateral wall of nasal fossa and the objectification of the recurrent or chronic sinusitis. In a study by scientist R. Lusk and others, 115 children with symptoms of chronic and recurrent sinusitis were examined by computed tomography [7, 10]. Therefore, bone abnormalities were found in a large proportion of investigated patients: concha bullosa - 10% infraorbital cells - 10%, nasal septum deviation - 27.8%, paradoxical middle turbinate - 8.5%, uncinate process lateral deviation and hypoplasia of the maxillary sinus - 6.9%, enlarged nasal inferior turbinates - 6% [7, 10]. Preoperative CT provides a real map of the paranasal sinuses, providing a good study of normal anatomy of the face air cavities, which allows a precise description of dangerous relations, offering the possibility of a more beneficial, precise and limited therapeutic procedure.

The goal of the research was to evaluate the efficacy of the modern investigation method such as computed tomography in assessing anatomical architectonics of the nose and paranasal sinuses for determining the tactics of endoscopic surgical treatment in children with recurrent and chronic pathology of paranasal sinuses.

III. MATERIALS AND METHODS

The study included 120 children with recurrent and chronic sinusitis, aged 8-17 years, divided into three lots of 40 ($X^2=0$, $p>0.05$). The overall average age of patients in the study groups was 13.9 years. The gender distribution analysis showed that 59 (49.2%) of patients were male, and 61 (50.8%) females. Thus, a statistically significant difference given by the parameter $X^2 = 1.73$, $P> 0.05$ was not noted.

Depending on the surgical treatment all the patients included in the study were divided into three groups. Group I consisted of 40 patients (21 boys and 19 girls) with recurrent and chronic paranasal sinusitis, operated by the standard method of endoscopic surgery (Messerklinger-Stammberger technique). Group II consisted of 40 patients (18 boys and 22 girls), also with recurrent and chronic inflammatory disease of the paranasal sinuses treated by the method of minimally invasive endoscopic sinus surgery. Group III consisted of 40 patients (20 boys and 20 girls), homogeneous by nosologic structure, patients were operated on by minimally invasive technique completed with surgery on endonasal structures.

CT examination is essential in identifying sinus disorder difficult to diagnose in rhinoscopic, endoscopic or classic radiological examination. Computed tomography is of

particular value in diagnosing disorders of ostiomeatal complex and ethmoid, sphenoid sinus, impossible to determine using a traditional X-ray examination. Imaging study was performed in two planes - axial and coronal - using a Siemens Somatom Emotion Duo CT. The fineness of bone structures of the nose and paranasal sinuses skeleton requires fine cups and high resolution. Millimeter thick images obtained allow the study of teeth that are close to the alveolar recess of maxillary sinus which is very important in children in the period of growth. Tomodensiometric examination is essential for precise analysis of sinus opacification and integrity of the sinus walls (normal, thin, densified). CT image is required for viewing the anatomical elements, which serve landmarks in endoscopic examination and analysis of surgical areas with a high risk of complications (lamina papyracea of the ethmoid bone, lamina cribrosa, persistence of Haller and Onoda cells, report between the side wall with the internal carotid artery and optic nerve, etc.).

In the case of recurrent and chronic sinusitis in children, the computed topographic examination can detect predisposing or maintening factors of inflammatory process of sinus mucosa such as different endonasal anatomical abnormalities and variations: septum deviation in different segments, concha bullosa, paradoxical turbinate, hypergenesis of uncinate apophysis and various forms of deviations, excessive pneumatization of ethmoid bulla, etc. [10]. Results and discussion

The study and analysis of CT images was crucial for detection and characterization of septal deviation in children in the study groups, as nasal septum deviation can block the ostiomeatal complex structures thus favoring the occurrence of inflammation. Computed tomography can determine the precise location and nature of the deviation (deformation, thickening or pneumatization of nasal septum). CT examination results showed a frequent finding of nasal septum deviation in patients of the study groups, with a caseload of 78 (65%) deviations. The deviations had a wide range of localizations: anterior segment - 37 (30.9%), posterior segment - 15 (12.5%) and septal deviation in the anteroposterior segment - 26 (21.7%).

In accordance with the studies on nose and paranasal sinuses physiology and pathophysiology, in emergence and further development of chronic inflammatory process of the paranasal sinuses a special place has the anatomical factor, particularly abnormalities and anatomical variants in the area of ostiomeatal complex

Paradoxically curved middle turbinate was determined in 24% cases, which corresponds to literature data showing a frequency of 5-37% (Fig. 2).

The results of our study have showed a frequency of 23 (19.1%) cases of Haller cells, being an anatomical factor (when they reach to 3 – 6 mm) in the development of ethmoidal sinusitis due to narrowing of infundibular space. Hiperpneumatization of Agger nasi cells have a major clinical importance, compressing the frontal recess and predisposing to frontal sinus inflammatory process. In our study it was detected in 17 (15.5%) cases. The CT examination performed on patients in our study determined pneumatization of ethmoid bulla in 94 cases (78.3%), a figure bigger than in the literature (17-65%) due to bilateral location of the anomaly.

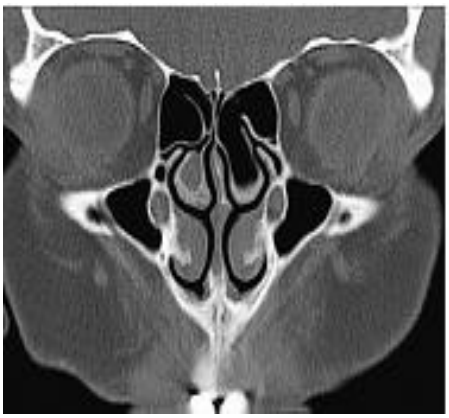

Fig.1 Bilateral concha bullosa

Studying and analysing the CT image we paid particular attention to middle turbinates variations of presentation (concha bullosa, paradoxical turbinate), of the processus uncinatus, size of ethmoid bulla and Agger nasi cells, presence of Haller infraorbital cells. In our study the most common anatomic variant was concha bullosa detected in 65 patients (54.1%), prevailing in group III - 28 patients (70%) (Fig. 1).

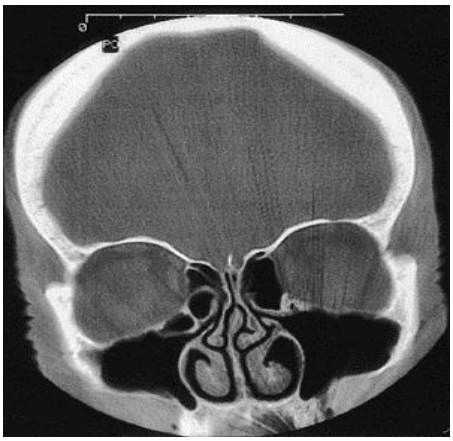

Fig.2 Paradoxically curved middle turbinate

Diverse anatomical variants of uncinate process were detected at CT examination in patients in the study groups: curvature of uncinate process - 21 (17.5%) and excessive pneunmatization of uncinate process - 69 (57.5%) (Table 1). Finally, we can conclude that the frequency of detection of anomalies and anatomical variations of the nasal passages is high in patients with recurrent and chronic inflammatory process of the paranasal sinuses.

CONCLUSION

CT examination shows an accurate evaluation of ostiomeatal complex structure, which is responsible for the persistence of recurrent and chronic sinus process, and is important in performing endoscopic surgery.

REFERENCES

[1] Bhattacharyya N, Kun Hee Lee. Chronic Recurrent Rhinosinusitis: Disease Severity and Clinical Characterization. Laryngoscope, 2005, 115: p.306–310.

[2] Chao T.K. Uncommon anatomic variations in patients with chronic paranasal sinusitis. Otolaryngology–Head and Neck Surgery, 2006, 38: p.221-225.

[3] Polavaram R, Devaiah A. Anatomic variants and pearls–functional endoscopic sinus surgery. Otolaryngologic Clinics of North America, 2004, 37: p. 221-242.
[4] Bidilean N. Concordanţe morfo-clinice, radiologice şi endoscopice în afecţiunile inflamatorii rinosinuzale. Oto-Rino-Laringo., 1997,Vol. 18,no 3 – 4: p.37-45.
[5] Liukkonen K, Virkkula P, Pitkäranta A. Acoustic rhinometry in small children. Rhinology, 2006, Mars, 44: p.160-163.
[6] Clemens P.A. Committee report on standartization of rhinomanometry. Rhinology, 1986, 22: p. 151- 155.
[7] chronic sinusitis. Radiologic anatomy, 2002, 24: p. 400–405.
[8] Dinis P.B., Haider H, Gomes A. Rhinomanometry, sinus CT-scan and allergy testing in the diagnostic assessment of chronic nasal obstruction. Rhinology, 1997, 35: p. 158–160.
[9] Numminen J, Ahtinen M, Huhtala H, Rautiainen M. Comparison of rhinometric measurements methods in intranasal pathology. Rhinology, 2003, 41: p. 65-68.
Badia L, Lund V, Wei W. Ethnic variation in sinonasal anatomy on CT-scanning. Rhinology, 2005, December 43, p. 210-214

The Interconnection of Polarization Singular Structure and Mueller-matrix Images of Biological Tissues in the Tasks of Cancer Changes Diagnostics

Alexander DUBOLAZOV, Artem KARACHEVTSEV, Vladimir USHENKO, Vadim ISTRATIY
Chernivtsi National University
yuriyu@gmail.com

***Abstract* – The paper deals with investigating the processes of laser radiation transformation by biological crystal networks using the singular optics techniques. The obtained results showed a distinct correlation between the points of "characteristic" values of coordinate distributions of Mueller matrix ($M_{ik} = 0, \pm 1$) elements and polarization singularities (*L*- and *C*-points) in laser images of biological crystal networks with the following possibility of Mueller-matrix selection of polarization singularity. It has been proposed the technique of Mueller-matrix singular diagnostics of pathological changes in woman reproductive sphere tissue (myometrium).**

***Index Terms* – Mueller matrix, singularity, polarization, birefringence, biological tissue, statistics.**

I. INTRODUCTION

Laser polarimetry (polarization sensitive optical coherence tomography, Mueller matrix decomposition formalism, coherency matrix analysis, etc.) [1-29] is able to obtain information about optical anisotropy (linear retardance, optical activity, dichroism, etc.) of biological tissues (BT). It has the potential to be an important technology for non-invasive diagnostics of organic phase-inhomogeneous layers. One model approach underlies these researches, which generalizes the optical properties of BT [5, 6, 14, 21, 30]:

1. all the variety of human BT can be represented by four main types – connective, muscular, epithelial, and neural tissues;
2. morphological structure of any BT type is regarded as a two-component amorphous-crystalline structure (optical isotropic and optical anisotropic);
3. the crystalline component is characterized by Mueller matrix $\{M\}$ operators of an optical anisotropy

$$\{M\} = \begin{Vmatrix} 1 & 0 & 0 & 0 \\ 0 & M_{22} & M_{23} & M_{24} \\ 0 & M_{32} & M_{33} & M_{34} \\ 0 & M_{42} & M_{43} & M_{44} \end{Vmatrix} \quad (1)$$

Specifically, the above mentioned model was used for finding and substantiating the interrelations between the ensemble of statistic moments of the 1st to 4th orders that characterize the orientation-phase structure (distribution of optical axes and phase shifts for directions of protein fibril networks) of birefringent BT architectonics and of 2D distributions for azimuths and ellipticities in their laser images [5]. It was determined [6, 7, 14, 15, 20, 23, 27, 28] that the 3rd and 4th statistic moments for coordinate distributions of ellipticities are the most sensitive to the change (caused by dystrophic and oncological processes) of optical anisotropy inherent to protein crystals. On this basis, the criteria for early diagnostics of muscle dystrophy, pre-cancer states of connective tissue, collagenoses etc. were determined.

In parallel with traditional statistical investigations, formed in recent 10 to 15 years is the new optical approach to describe a structure of polarization inhomogeneous fields in the case of scattered coherent radiation. The main feature of this approach is the analysis of definite (in contrast to continuous 2D distributions) polarization states to determine the whole structure of coordinate distributions for azimuths and ellipticities of polarization. The so-called polarization singularities are common used as these states [31-37]:

- states with linear polarization, when the direction of rotation for the electric field vector is indefinite, the so-called *L*-points;
- circularly polarized states, when the azimuth of polarization for the electric field vector is indefinite, the so-called *C*-points.

Investigations of polarization inhomogeneous object fields for BT with different morphology allowed ascertaining that they possess a developed network of *L*- and *C*-points [36]. For example in [37], the authors found interrelations between conditions providing formation of polarization singular points and particularity of the orientation-phase structure of biological crystals present in territorial matrix of human tissue architectonic network. These interrelations served as a base to make statistical and fractal analyses of distribution densities for the number of singular points in BT images. As a result, the authors confirmed the efficiency of this method for investigation of object fields to differentiate optical properties of BT with a different morphological structure and physiological state.

It is worth to note that the singular approach is mainly used out of the analysis of the mechanisms providing formation of polarization inhomogeneous laser images of BT by an extracellular matrix. Thus, development of laser-polarimetric techniques based on determination of singular

interrelations "object - field" in order to find new methods of diagnostics of transformation of the BT extracellular matrix orientation-phase structure related with pre-cancer changes in their physiological state is very important.

To solve this problem, we should revert to the analysis of optical properties of biological crystal networks as these properties are comprehensively described by the Mueller matrix within the framework of the singular approach.

II. BRIEF THEORY OF THE SINGULAR APPROACH IN THE ANALYSIS OF BIOLOGICAL TISSUE BIREFRINGENT NETWORKS

To analytically describe the *L*- and *C*-states of polarization, the most suitable is to use the extreme values of the fourth Stokes vector parameter. It is a widely applied mean and appears to be reasonable to represent these singularities as follows:

$$\begin{cases} V_4 = \sin 2\beta; \\ V_4 = 0 \leftrightarrow L(\beta = 0); \\ V_4 = \pm 1 \leftrightarrow \pm C(\beta = \pm\frac{\pi}{4}). \end{cases} \quad (2)$$

Here, β is the value of polarization ellipticity; the $+C$ point is assumed to designate a right-circulated polarization state, which can be characterized by the phase shift $\delta = \frac{\pi}{2}$ between the orthogonal components of laser beam amplitude; the $-C$ point is assumed to designate a left-circular polarization state ($\delta = -\frac{\pi}{2}$). Thus, $\pm C$ points are the orthogonal states of circularly polarized wave. For the *L* points, the phase shift reaches $\delta = 0; \pi$.

Using the relations (1) and (2), it is possible to determine the interrelations between the characteristic values M_{ik}^* of Mueller matrix elements, which correspond to the "extreme" values of BT optical anisotropy, and to the extreme values of V_4. Thus, in order to characterize the BT structure we obtain the coordinate network generated by a finite number of characteristic values of Mueller matrix elements (1) (see Table 1).

Thus, measuring the coordinate distributions of the characteristic values ($M_{ik}^* = 0, \pm 1$) of the BT Mueller matrix elements enables not only to foresee the scenario ($M_{ik}^* \to V_4^*$) of forming the ensemble of polarization singularities ($V_4 = 0, \pm 1$) of its image, but also to additionally realize their differentiation, conditioned by the specificity of orientation structure of biological crystals.

Here, $+L$ point corresponds to a linear polarization state with $\delta = 0$; $-L$ point corresponds to a linear polarization state with $\delta = \pi$. In this case, as for $\pm C$ points, we will identify $\pm L$ points as orthogonal.

TABLE I. INTERRELATION BETWEEN THE CHARACTERISTIC VALUES OF MUELLER MATRIX M_{ik} ELEMENTS OF BIOLOGICAL TISSUES AND POLARIZATION SINGULARITIES DESCRIBED BY THE FOURTH PARAMETER OF THE STOKES VECTOR V_4

M_{ik}		V_4	Polarization state
$M_{22;33;44}$	0	± 1	$\pm C$
	1	0	$+L$
	-1	0	$-L$
$M_{24;42;34;43;23;32}$	0	0	$\pm L$
	1	$+1$	$+C$
	-1	-1	$-C$

III. SCHEME AND METHODS OF EXPERIMENTAL INVESTIGATIONS

Fig. 1 shows the traditional optical scheme of polarimeter for measuring the elements of Mueller matrix of the BT histological sections [5, 20].

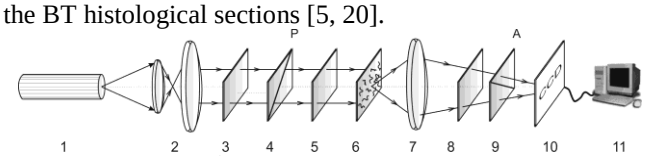

Fig. 1. Optical scheme of the polarimeter. 1 – He-Ne laser; 2 – collimator; 3 – stationary quarter-wave plates; 5, 8 – mechanically movable quarter-wave plates; 4, 9 – polarizer and analyzer, correspondingly; 6 – object of investigation; 7 – micro-objective; 10 – CCD camera; 11 – personal computer.

The parallel (∅ = 10^4 μm) beam of He-Ne laser (λ = 0.6328 μm, W = 5.0 μW) was used as an illuminator. Polarization illuminator consists of the quarter-wave plates 3, 5 and polarizer 4, and it sequentially forms a series of linearly polarized (I_0, I_{45}, I_{90}, I_{135}) with azimuths 0°, 90°, 45°, 135°, and right-hand ($I_\otimes$) and left-hand ($I_\oplus$) circularly polarized probing BT laser beams. The BT images made by the micro-objective 7 ($4\times$) were projected into the plane of a light-sensitive area (800×600 pixels) of the CCD-camera 10.

Polarization images of BT were projected by means of the micro-objective 7 (focal distance - 1.5 cm , aperture - 0.2, magnification – 4x) into the plane of light-sensitive area of the CCD camera (overall amount of pixels – 800x600, light sensitive area size - 4000x3000 μm, deviation of photosensitive characteristics from the linear one was no more than 15%), which provided the range of measuring the structural elements of BT with the resolution $2-2000\mu m$. Maximal resolution verification ($2\,\mu m$) were performed using the stage micrometer (linear scale), which image was projected into the light sensitive area of CCD camera using the micro-objective 7. Minimal resolution ($2000\mu m$) corresponds to the situation when the light sensitive area of CCD camera is entirely filled by two equal sized structural elements (light and dark) of stage micrometer. The experimental conditions were chosen in such a way that it enabled to reduce the space-angular aperture filtering when forming the BT images. It was ensured by conformance of angular characteristics of the

indicatrix of light scattering by the BT samples ($\Omega \approx 16^0$) and the angular aperture of micro-objective ($\Delta\omega = 20^0$). Here, Ω is the solid angle within which 98% of all the energy of light-scattered radiation is concentrated.

Polarization analysis of the BT images was performed using the polarizer 9 and quarter-wave plate 8 according to the following technique:

- within the section of illuminating laser beam, the array ($m \times n = 800 \times 600$) of values for the Stokes vector $V_{j=1,2,3,4}$ parameters and elements of Mueller matrix $M_{ik}(m \times n)$ were determined in accord with the following algorithms

$$\begin{cases} V_1 = I_0 + I_{90}, & V_2 = I_0 - I_{90}, & V_3 = I_{45} - I_{135}, & V_4 = I_{\otimes} - I_{\oplus}, \\ M_{i1} = 0.5\left[V_i^{(1)} + V_i^{(2)}\right], & M_{i2} = 0.5\left[V_i^{(1)} - V_i^{(2)}\right], & M_{i3} = V_i^{(3)} - M_{i1}, & M_{i3} = V_i^{(4)} - M_{i1}, i = 1,2,3,4. \end{cases} \quad (3)$$

- in each array $M_{ik}(m \times n)$ and $V_4(m \times n)$, coordinate distributions of characteristic (singular) values 0, ± 1 were determined.

At the first stage, the interrelations ($M_{ik}^* \to V_4^*$) of matrix and polarization singularities were investigated on the sample of a histological section prepared from healthy skin derma.

Fig. 2 represents coordinate distributions of matrix elements $M_{44,24,34}(m \times n)$ corresponding to the skin derma histological section and the fourth Stokes vector parameter $V_4(m \times n)$ of its image with the characteristic values ($0, \pm 1$) plotted on them (within the marked $100\,pix \times 100\,pix$ sampling plot).

It can be seen from the data obtained that there is direct correlation between the coordinate ($k, g \quad 1 \le k \le m, 1 \le g \le n$) positions of characteristic values of the matrix element M_{44}^* for skin derma and the network of *L* and *C* points in its laser image $\left\{ M_{44}^*(k,g) = \begin{Bmatrix} 0 \\ \pm 1 \end{Bmatrix} \Leftrightarrow V_4^*(k,g) = \begin{Bmatrix} \pm 1 & - & \pm C \\ 0 & - & L \end{Bmatrix} \right\}$ (Fig. 2a, d).

Coordinate distributions of characteristic values of matrix elements $M_{24,42}^*(m,n)$, $M_{34,43}^*(m,n)$ and corresponding networks of orthogonal $\pm L$ and $\pm C$ points (Table 1) possess the individual structure (Fig. 2b, c).

Analytically substantiated and experimentally proven interrelations between the matrix and polarization singularities were used as the basis for Mueller-matrix singular diagnostics of oncological changes in the tissues of woman reproductive sphere.

of matrix elements $M_{44,24,34}$ (a, b, c) and singularities of polarization image inherent to the skin derma layer histological section V_4 ("d"):

- "±C"-points (□) (M_{44} = 0);
- "+C"-points (▨) ($M_{24,34}$ = +1, V_4 = +1);
- "-C"- points (▨) ($M_{24,34}$ = –1, V_4 = –1);
- "+L"- points (Δ) (M_{44} = +1);
- "-L"- points (∇) (M_{44} = –1);
- "±L"- points (◊) ($M_{24,34}$ = 0, V_4 = 0).

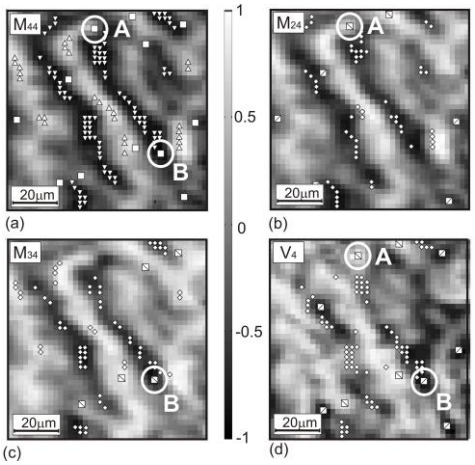

Fig.2. Networks of characteristic values $M_{44,24,34}^*(m \times n)$

IV. MUELLER-MATRIX SINGULAR DIAGNOSTICS AND DIFFERENTIATION OF PATHOLOGICAL CHANGES IN THE TISSUES OF WOMAN REPRODUCTIVE SPHERE

Three groups of histological sections of the main tissue of woman reproductive sphere – myometrium – were used as the objects of investigation:

- biopsy of the healthy tissue of woman reproductive sphere (type "**A**" – Fig. 3a);
- biopsy of the inflamed tissue (ectonia) (type "**B**" – Fig. 3b);
- biopsy of the tissue in the state of dysplasia (pre-cancer state) (type "**C**" – Fig. 3c).

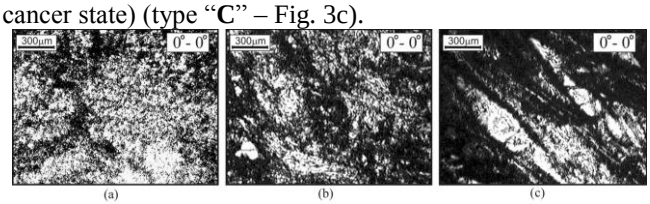

Fig. 3. Polarization images of woman reproductive sphere tissue – myometrium "A" (a), "B" (b) and "C" (c) types in the scheme of coaxial polarizer and analyzer.

To determine the criteria of Mueller-matrix singular diagnostics of myometrium oncological state and differentiate its severity degree, the following technique was used:

- coordinate networks of characteristic values for matrix elements $M_{44,24,34}^*(m \times n) = 0, \pm 1$ were scanned in the direction $x \equiv 1, \ ..., \ m$ with the step $\Delta x = 1$ pixel;
- within the obtained sampling $\left(1_{pix} \times n_{pix}\right)^{(k=1,\ 2,\ ...,\ m)}$ for coordinate distribution of the element $M_{44}(m \times n)$, the total amount ($N^{(k)}$) of characteristic points (0, ± 1) that set the complete ensemble of singular points was calculated, and the

dependences $N(x) \equiv (N^{(1)}, \ N^{(2)}, \ ..., \ N^{(m)})$ were determined;

- distributions of the number of singular $\pm L$ and $\pm C$ -points were determined using the following expressions

$$\begin{cases} N^{(+)}(x) = N_C(M_{34,43} = +1) + N_L(M_{24,42} = 0), \\ N^{(-)}(x) = N_L(M_{34,43} = 0) + N_C(M_{24,42} = -1). \end{cases} \quad (4)$$

- statistical moments of the 1st to 4th orders for the obtained distributions of $N(x)$ amount of singularities were calculated according to the algorithms

$$Z_1 = \frac{1}{m \times n} \sum_{i=1}^{m \times n} |N(x)|,$$
$$Z_2 = \sqrt{\frac{1}{m \times n} \sum_{i=1}^{m \times n} [N(x)]^2},$$
$$Z_3 = \frac{1}{Z_2^3} \frac{1}{m \times n} \sum_{i=1}^{m \times n} [N(x)]^3,$$
$$Z_4 = \frac{1}{Z_2^4} \frac{1}{m \times n} \sum_{i=1}^{m \times n} [N(x)]^4. \quad (5)$$

It follows from the data obtained that:

- efficiency of laser polarimetry for diagnostics and differentiation of early oncological changes of myometrium tissue is insufficient – the difference between the values of statistical moments $(Z_{1,2,3,4}(M_{44,34,24}(m \times n)))$ of samples "A", "B" and "C" - types is insignificant and does not exceed 20% - 45%;
- technique of polarization-correlation mapping is efficient for differentiation of optical properties of healthy and oncological changed myometrium tissue – the skewness (Z_3) and the kurtosis (Z_4) of distribution of the number of singular points of "A"- and "B"-types of laser images differ by 1.53 and 2.15 times;
- technique of Mueller-matrix singular diagnostics is efficient for differentiation of optical properties of all types of samples – statistical moments of the 3rd and 4th orders of distributions $N(x)$ for the samples "A", "B" and "C" – types differ by 1.7 and 2.5 times, respectively.
- for distributions $N^{-}(x))$ of myometrium tissue of "A" and "B" types, the maximal difference (from 2.2 to 4.1 times) is observed between all the statistical $Z_{j=1,2,3,4}$ moments.

V. CONCLUSION

It has been ascertained correlation between coordinate locations of characteristic points for 2D elements of the Mueller matrix corresponding to an optically thin layer of biological tissue and the network of *L* and *C* points in its laser image. Shown is the potentiality of Mueller-matrix sampling for polarization singularities formed by biological crystals. It has been demonstrated the efficiency of Mueller-matrix singular diagnostics not only for oncological changes of myometrium tissue but also for differentiating their severity degree.

REFERENCES

[1] J.F. de Boer and T.E. Milner, "Review of polarization sensitive optical coherence tomography and Stokes vector determination", *J. Biomed. Opt.* 7, 359-371, 2002.

[2] J.F. de Boer , T.E. Milner, and J.S.Nelson, *Trends in Optics and Photonics (TOPS): Advances in Optical Imaging and Photon Migration*, OSA, Washington, 1998.

[3] M. J. Everett, K. Shoenenberger, B. W. Colston and L. B. Da Silva, "Birefringence characterization of biological tissue by use of optical coherence tomography", *Opt. Lett.* 23, 228-230, 1998.

[4] Sh. Jiao, W. Yu, G. Stoica, Lihong V. Wang, "Optical-fiber based Mueller optical coherence tomography", *Opt. Lett.* 28, 1206-1208, 2003.

[5] Alexander G. Ushenko and Vasilii P. Pishak, "Laser Polarimetry of Biological Tissue: Principles and Applications", in *Handbook of Coherent-Domain Optical Methods: Biomedical Diagnostics, Environmental and Material Science*, vol. I, Valery V. Tuchin, Ed. Boston: Kluwer Academic Publishers, pp. 93-138 (2004).

[6] O. V. Angelsky, A. G. Ushenko, Yu. A. Ushenko, V. P. Pishak, "Statistical and Fractal Structure of Biological Tissue Mueller Matrix Images", in *Optical Correlation Techniques and Applications*, Oleg V. Angelsky, Ed. Washington: Society of Photo-Optical Instrumentation Engineers, pp. 213-266 (2007).

[7] O.V. Angelsky, A.G. Ushenko, Yu.A. Ushenko, V.P. Pishak, and A.P. Peresunko, "Statistical, Correlation, and Topological Approaches in Diagnostics of the Structure and Physiological State of Birefringent Biological Tissues", in *Handbook of Photonics for Biomedical Science*, Valery V. Tuchin, Ed. USA: CRC Press, pp. 21-67 (2010).

[8] Alexander G. Ushenko, "Polarization structure of laser scattering fields," *Opt. Eng.* 34, 1088-1093, 1995.

[9] A.G. Ushenko, "Laser diagnostics of biofractals," *Quantum Electronics* 29(12), 1078–1084, 1999.

[10] O.V. Angel'skii, A.G. Ushenko, A.D. Arkhelyuk, S.B. Ermolenko, D.N. Burkovets, "Structure of matrices for the transformation of laser radiation by biofractals," *Quantum Electronics* 29(12), 1074-1077, 1999.

[11] O.V. Angel'skii, A.G. Ushenko A.D. Arheluk, S.B. Ermolenko, D. N. Burkovets, "Scattering of laser radiation by multifractal biological structures," *Optics and Spectroscopy* 88(3), 444-448, 2000.

[12] A.G. Ushenko, "Polarization structure of biospeckles and the depolarization of laser radiation," *Optics and Spectroscopy* 89(4), 597-601, 2000.

[13] A.G. Ushenko, "Stokes-correlometry of biotissues," *Laser Physics* 10(5), 1286-1292, 2000.

[14] A.G. Ushenko, "The vector structure of laser biospeckle fields and polarization diagnostics of collagen skin structures," *Laser Physics* 10(5), 1143-1149, 2000.

[15] A.G. Ushenko, "Laser polarimetry of polarization-phase statistical moments of the object field of optically

anisotropic scattering layers," *Optics and Spectroscopy* 91(2), 313-316, 2001.

[16] A.G. Ushenko, "Polarization contrast enhancement of images of biological tissues under the conditions of multiple scattering," *Optics and Spectroscopy* 91(6), 937-940, 2001.

[17] A.G. Ushenko, "Laser probing of biological tissues and the polarization selection of their images," *Optics and Spectroscopy* 91(6), 932-936, 2001.

[18] A.G. Ushenko, "Correlation processing and wavelet analysis of polarization images of biological tissues," *Optics and Spectroscopy* 91(5), 773-778, 2002.

[19] A.G. Ushenko, "Polarization correlometry of angular structure in the microrelief pattern or rough surfaces," *Optics and spectroscopy* 92(2), 227-229, 2002.

[20] O.V. Angelsky, A.G. Ushenko, Ye.G. Ushenko, "2-D Stokes polarimetry of biospeckle tissues images in pre-clinic diagnostics of their pre-cancer states," *Journal of Holography and Speckle* 2(1), 26-33, 2005.

[21] Oleg V. Angelsky, Alexander G. Ushenko, and Yevheniya G. Ushenko, "Complex degree of mutual polarization of biological tissue coherent images for the diagnostics of their physiological state," *J. Biomed. Opt.* 10(6), 060502, 2005.

[22] O.V. Angelsky, A. G. Ushenko, and Ye. G. Ushenko, "Investigation of the correlation structure of biological tissue polarization images during the diagnostics of their oncological changes," *Phys. Med. Biol.* 50(20), 4811-4822, 2005.

[23] Alexander Ushenko, Sergej Yermolenko, Alexander Prydij, Stepan Guminetsky, Ion Gruia, Ovidiu Toma, Konstantin Vladychenko, "Statistical and fractal approaches in laser polarimetry diagnostics of the cancer prostate tissues," *Proc. SPIE* 7008, 70082C, 2008.

[24] A.G. Ushenko, A.I. Fediv, Yu.F. Marchuk, "Correlation and fractal structure of Jones matrices of human bile secret," *Proc. SPIE* 7368, 73681Q, 2009.

[25] Oleg V. Angelsky, Alexander G. Ushenko, Yevheniya G. Ushenko, Yuriy Y. Tomka, "Polarization singularities of biological tissues images," *J. Biomed. Opt*. 11(5), 054030, 2006.

[26] S.B. Yermolenko, A.G. Ushenko, P. Ivashko, "Spectropolarimetry of cancer change of biotissues," Proc. SPIE 7388, 73881D, 2009.

A.G. Ushenko, I. Z.Misevich, V. Istratiy, I. Bachyns'ka, A. P. Peresunko, Omar Kamal Numan, and T. G. Moiysuk, "Evolution of statistic moments of 2D-distributions of biological liquid crystal net Mueller matrix elements in the process of their birefringent structure changes," *Advances in Optical Technologies* 2010, 423145, 2010.

[27] Yu.O. Ushenko, I.Z. Misevich, A.P. Angelsky, V.T. Bachinsky, O.Yu. Telen'ga, O.I. Olar, "Polarization-singular structure in laser images of phase-inhomogeneous layers to diagnose and classify their optical properties," *Semicond. Physics, Quantum Electronics&Optoelectronics* 13(3), 248-258, 2010.

[28] V.T. Bachinsky, Yu.O. Ushenko, Yu.Ya. Tomka, O.V. Dubolazov, V.O. Balanets'ka, A.V. Karachevtsev, "Wavelet analysis for polarization maps of networks formed by liquid biological crystals in blood plasma: statistical and fractal approaches," *Semicond. Physics, Quantum Electronics&Optoelectronics* 13(3), 189-201, 2010.

[29] S.C. Cowin, "How is a tissue built?", *J. Biomed. Eng.* 122, 553-568, 2000.

[30] J.F. Nye, *Natural focusing and the fine structure of light*, Institute of Physics Publishing, Bristol, 1999.

[31] J.F. Nye, "Polarization effects in the diffraction of electromagnetic waves: the role of disclinations", *Proc. R. Soc. A* 387, 105, 1983.

[32] M.V. Berry and M.R. Dennis, "Polarization singularities in isotropic random vector waves", *Proc. R. Soc. A* 457, 141, 2001.

[33] J.F. Nye, "Lines of circular polarization in electromagnetic wave fields", *Proc.R.Soc. A* 389, 279-290, 1983.

[34] Freund, "Coherency matrix description of optical polarization singularities", *J.Opt.A.: Pure and Appl. Opt.* 6, S229-S234, 2004.

[35] O. V. Dubolazov, A. G. Ushenko, V. T. Bachynsky, A. P. Peresunko, and O. Ya. Vanchulyak, "On the Feasibilities of Using the Wavelet Analysis of Mueller Matrix Images of Biological Crystals," *Advances in Optical Technologies* 2010, 162832, 2010.

[36] A.G. Ushenko, A.I. Fediv, Yu.F. Marchuk, "Singular structure of polarization images of bile secret in diagnostics of human physiological state," *Proc. SPIE* 7368, 73681S, 2009.

Bioengineering the Mind: from Artificial Intelligence towards Artificial Consciousness

Radu NEGOESCU
National Institute of Public Health, Bucharest, Romania, rnegoescu@ispb.ro

***Abstract* – Whilst the artificial intelligence seems recently to approach its human-close specimen, artificial consciousness as targeted by bioengineering and information science&technology advances still has some way to go before becoming an experimental terrain for a bunch of sciences that deals with the problem of conscience, including philosophy and theology. Depending on our capacity to inseminate a machine transposition of natural ethics at the same time with increasing machine autonomy,** a **well guided artificial consciousness holds the promise to offer a representation of what natural consciousness could be in absence of distorting influences exerted by biologic (genetic) inheritance on human being as it presents nowadays.**

***Index Terms* – consciousness, conscience, machine consciousness, information technology, cardiovascular bioengineering.**

I. ARTIFICIAL INTELLIGENCE

Defined by John McCarthy in 1956 as the science and engineering of making intelligent machines, hopefully in the human intelligence sense, the artificial intelligence (AI) certainly evolved over the past half century, even if we never got the humanlike assistants that many thought we would have by now. It offers a valuable technological support in critical domains, e.g. computer-diagnosing patients over the internet, but even the most helpful AI system in function today must be programmed explicitly to carry out its one specific task. What people wanted and needed was a general-purpose intelligence that can be set loose on any problem, i.e. one that can adapt to a new environment without having to be retrained constantly: "one that can tease the single significant morsel out of a gluttonous banquet of information the way we humans have evolved to do over millions of years" [1].

Recently yet Hewlett Packard introduced a new class of electronic device overriding the separation between memory and processing, the memristor, into a "brain-inspired" microprocessor featuring the form factor of a brain, the low power requirements, and the instantaneous internal communications - that could be trained and coaxed to behave like a brain. Run on this "brain on a chip", the MoNETA (Modular Neural Exploring Traveling Agent) software written at Boston University's will perceive its surroundings, decide which information is useful, integrate that information into the emerging structure of its reality, and in some applications formulate plans that will ensure its survival - the same drives that motivate humans and entitle the machine as a specimen of true (or real) artificial intelligence [1].

II. CONSCIOUSNESS AND CONSCIENCE

English uses the term *consciousness* (or self-awareness) to designate a neural-behavioral state featuring capabilities of reflection and reaction found as adequate by the rest of the world, while being vigil.

French appears to make no much lexical distinction between consciousness and conscience that are commonly referred to by 'conscience' and lets to the context making the difference. However, 'faits de conscience' and "connaissance' refer unambiguously to consciousness or to a part of it.

After M. Draganescu [2] consciousness stands for a type of integrative information (structural-phenomenological and social) capable of understanding and knowing, knowing that knows, and endowed with: feeling of to be, will, intuition and creative power. Notice that in the philosophical thinking of M. Draganescu structural information is related to (non-living) nature and its sciences, while phenomenological information is related to the living matter studied by life sciences. Integration of structural and phenomenological takes place into the real human being as such; dissection by theoretical reasons may enlighten various balances between parts otherwise intimately merged when analysis progresses from the molecular and cellular level to organs, systems, mind and soul.

Consciousness is naturally human; its versions "contaminated" by technology or those purely technological are referred to by artificial ones.

Coming back to terms, in Romanian conscious ('constient') is also (English-like) pointing to someone who can rationally place his/her Ego vis-à-vis of the world and him/herself; the term "rational" sends to the manner in which that positioning is done by a majority of other individuals. Besides, the Romanian 'constient' refers to someone endowed with a certain level of *conscience*: "I am 'constient' (aware) of my duties", where the attitude versus duties is already related to moral principles, to an axiology.

Conscience is yet more than what is involved by "I am aware of" (that expresses a potential), namely a non-hesitant (proved) availability to actualize this potential with the current behavior. At a higher individual level, conscience involves looking into the meaning of existence, for him and for others who do not possess necessary capabilities, by a philosophical and/or religious demarche.

However exercising conscience is mainly done in the social environment. M. Draganescu's [2,3] social-human civilization of the future would be by far towering biological needs of an aggregate of human individuals whose interaction would filter (somehow in the sense of coherent summation in physics) luminous parts present in all of them as pieces of truth that are detected, sifted and put together through the collective, social exercise of spirituality. Or, to cut it short, by the collective conscience.

In this vein, laws of Moses giving early expression to collective conscience codify social behavior of people; social sins acting against the group are mainly incriminated, rather

than individual sins acting against him/her self. While the latter are health-redoubtable (we know how from medicine of lifestyle) ending sometimes in serious somatic illnesses, the former increase or exacerbate psycho-social stress responsible for more subtle forms of disease or death (e.g. sudden cardiac death in apparently healthy people).

The individual endowed with (sufficient) conscience is unselfish, generous; generosity is seen as the essentials of Christianity (as an example of spirituality) gathered in one single word. At the other end, a social value as bright as freedom, when practiced at low levels of conscience (or without conscience of kind) converts to selfishness, greed and open contempt vis-à-vis of fellow man. Social behavior of many Romanians since 1989, overtaken at low levels of conscience, if any, by freedom achieved through sacrifice of others (Revolution heroes), may convincingly illustrate what means non-conscience.

*

From these preliminaries, the relationship between consciousness and conscience could schematize as:

consciousness + moral principle = conscience.

Moral principle comes for a vast majority of humans from spirituality.

"Everyone, writes Mihai Draganescu [3], *has an empirical understanding of conscience and realizes that it stands for the highest level of his/her being. He/she then feels spirituality and spiritual experiences to be the very core of his/her conscience"*. In this view, unlike consciousness, conscience is exclusively human.

On this background, a genuine social-human civilization would also be a Society of the Conscience.

In general, society is seen by M. Draganescu [3] at the crossing of influences coming from science & technology, environment, genetics and cultural (epigenetic) heritage, and spirituality (Figure 1). Spirituality is not a relatively objective social propeller, like science, but lies in depth of the intangible human subjectivity, in the conscience.

The question arises whether man's level of conscience (dependent on spirituality) could overcome at the societal level the destructive effects of those parts of his genetic inheritance directed to evil and aggression that prevents the progress of mankind towards a genuine social-human civilization.

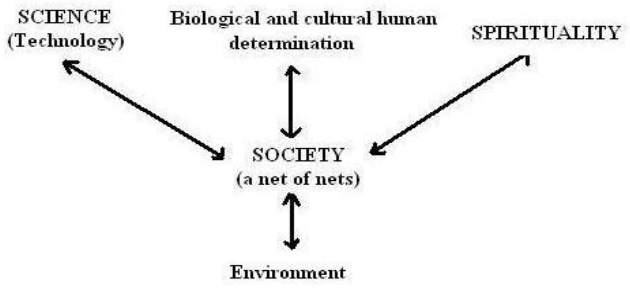

Fig. 1 (modified after M. Draganescu, [3])

As for the genetic inheritance, M. Draganescu [3]) is quoting the biologist and physician Grigore Traian Popa who reviewing in the 40's the evils in the society of his times had put that brain should be taken into discussion when investigating what is going wrong in individuals and society since the brain can instrument both good and evil.

Keeping the story short, due to its contamination by genetic inheritance, human consciousness as it presents today could not guarantee the progress of mankind towards a Conscience Society penetrated by the moral principle of spiritualized humanism that would dominate all social networks. In his key lecture at the INGIMED II Conference in 2001, M. Draganescu argued why he is skeptical on building a Society of Conscience without participation of artificial consciousness (AC).

*

Summarizing, in terms of cerebral activity, consciousness stands for neural machinery, mental, reason. Moral principle, for the vast majority of individuals, is involved by spirituality, so it is transcendent. Finally, conscience is both material, as tributary to neural machinery, and spiritual, that is transcendent. For some good reason it is said about a man of conscience that "he puts his soul into".

As M. Draganescu [2] remarks, man of today might not be able to create a social-human civilization as his genetic apparatus dominates the epigenetic cultural acquisitions. Then a solution could be an artificially assisted consciousness by implantation of neurocybernetic "consciousness prostheses" that by means of significant mental enhancement would offer a better chance to moral rectitude in the average individual; we've just seen that his consciousness is largely missing nowadays the influence of spirituality.

III. WAYS TO ARTIFICIAL CONSCIOUSNESS

In terms of technological contribution to a improving or recovering human consciousness, neurocybernetic prostheses are not a novelty in bioengineering or even in clinical engineering, fairly yet with much more modest goals than "treating" low levels of conscience.

Thus, neural engineering aims at replacing a damaged part of the human brain, involved in cognitive functions, with integrated circuits operating on the known principle of the artificial neural networks. Integrated circuits would not necessarily be on silicon that after 60 years of supremacy will leave their place by 2015 to molecular and quantum devices.

Other hopes appear related to neuroelectronics that refers to coupling organic substrata to electronic systems and devices. In this vein Fromhertz et al (quoted by Draganescu, [2]) have combined a silicon chip with the giant nerve cells of the snail Lymnea Stagnalis and succeeded a two-way communication, recording and stimulating without micropipettes, simply by growing neurons on silicon surfaces - inert except some sensitive areas for collecting and emitting signals (in fact microelectrodes.

In a broader perspective, Koch and Tononi [4] evaluate this way the chances of occurrence of artificial consciousness: *"Consciousness is a part of the natural world. It depends, we believe, only on mathematics and logic and on imperfectly known laws of physics, chemistry and biology. It does not derive from a magical or transcendent quality. If so, then there is no reason that consciousness could not be reproduced in a machine, at least in theory".*

Notice that by the term biological (that is living) they add phenomenological dimension (in Draganescu's sense) to the structural-informational world dealing with mathematics, logic, physics and chemistry.

In this line of thinking, Koch and Tononi argue how consciousness does not seem to require many things we currently associate with human being: emotions, memory,

auto-reflection, language, sensitivity to the ambient and action in the world. To be conscious, they say, is in last analysis to be a single integrated unit with a large repertoire of states. Integrated information based consciousness theory (IIT) may suggest a test to measure the degree of consciousness of a machine - a sort of Turing test for consciousness (Turing test is a method of detecting a presence of a human intelligence behind a machine presented as an automaton).

Talking about the best way to build a conscious machine, these authors evoke two complementary strategies: copying a mammalian brain or evolving a machine.

The first way seems without perspective: modeling the brain of a round worm (Caenorhabditis Elegans) with only 302 neurons and approximately 6000 chemical synapses has begun in 1986 and more than 2 decades later there was no valid model on how this minimal nervous system works.

A more plausible alternative is starting from architecture of mammalian brain conveniently abstracted and evolving it towards a conscious entity. Attempts to date, the Aibo robotic dog or the Qrio humanoid proposed by Sony are rudimentary tries to operate on a large number of fixed but flexible rules and would not pass perhaps the consciousness test proposed by the IIT. Vision systems based on hierarchical multistrata maps of "neurons" (artificial neural networks) are admirably managing to classify images from the real world, but presents obvious fragility when modifying background brightness entailed, for example, by a change of scenery.

As Koch and Tononi conclude, the big stake of reflection on how to build a conscious machine is undoubtedly more clear understanding of our own consciousness, as a necessary support for the next step to take over towards more conscience - we might add.

IV. INFORMATION TECHNOLOGY APPROACH

The assumption that computing machines could become conscious is based on the analogy seen by many between brain (wetware) and computer (hard- & soft- ware). It is expected that before long the computers will reach the estimated complexity of the brain.

A healthy adult brain contains about 100 billion neurons, each of them connected by axons (output), dendrites (input) and synapses with other about 100,000 neurons. It results that a typical brain has about 1015 connections between its neurons, each supporting at least one discharge per second. Many think that in about a decade computers will reach the computational power of the brain when exceeding 10x1015 operations/second (op/s). The IBM supercomputer Blue Gene /P could execute a year ago up to 3x1015 op/s. Argonne National Laboratory (USA, Illinois) is now upgrading a Blue Gene/P for doing circa 1/2x1015 op/s [5].

However, complexity of the brain once reached, "no one has the foggiest notion" (E. Kandel, Nobel Laureate, quoted by Horgan, [5]) how the computer could possibly make the qualitative step towards consciousness or beforehand how agglomeration of neurons and other soft tissues constituting the brain gives rise to conscious mind - that intangible entity that in Horgan's words *"makes you falling in love, seizing the irony in a novel, or appreciating the elegance of an electronic design".*

While accepting the possibility mentioned by others to create a conscious quantum computer M. Draganescu [2] excludes structural complexity as a source of machine consciousness; instead, he sees the structural-phenomenological complexity as a necessary condition for artificial consciousness.

Issued in connection, symbiotic or not, with the human brain, a conscious machine would hold a promise of immortality sui generis, transcending decomposition of our biological hardware. Thus, the advocates of singularity see us, half in the joke half seriously, first becoming cyborgs - carriers of implanted chips to emulate perception, memory and intelligence, and finally abandoning our flesh-and-blood selves for uploading our profound ego, digitally formatted, in a computer memory that will forever ensure our immortality in the cyber-space. For some, this prospect is tangible; for example Kurzweil, an enthusiast of singularity, contemplates changing his lifestyle in the sanogenetic sense *"to live quite enough to live forever"* (cf. Horgan, [5]).

Letting the joke aside, Cardon, Camus, Campagne et al embarked in 2005 upon an ambitious project meant to conceptualize and build a system generating 'faits de conscience', in fact an artificial brain aiming at transposing human thinking of something into the computable field, so that an computer-based artificial system would be able to exhibit consciousness features in a viewable manner.

"The system will have intentions, emotions and ideas about things and events related to itself. The system would have to have a body that it could direct and which would constrain the system. It would also have to have a history, and intentions to act and, most of all, to think. It would have to have knowledge, notably language knowledge. It would have to have emotions, intentions and finally a certain consciousness about itself" (Cardon, Camus, Campagne et al, [6]).

There is a summum bonum, a most generous statement of intentions in this field that should deserve, judging conceptual and IT effort deployed, careful consideration even if authors often forget to put due quotation marks when it is about intentions, emotions and ideas.

Two hypotheses judged as reasonable are made for this transposition:

- analogy between the "geometrical dynamics" of the real brain (it is about modeling of human brain when authors speak geometry) and of the artificial brain. For one, flows of data refer to complex images, almost continuous; for the other, there are dynamical graphs whose deformations (introducing 'emotions') are evaluated topologically;
- reduction of combinatorial complexity of the real brain by positioning it at symbolic and pre-language level into computable domain.

A first implementation is reported on equipping the Sony's ERS-7 Aibo robotic dog with a reflective and reactive "brain" working at several levels (Camus and Cardon, [7]).

Aibo sensors for touch & distance and a video camera allow to process environment data to give a contextual position (scene representation – 1st level). The camera data are processed by an artificial neural network embedded in any of a multi-agents system (several thousands of 'aspectual agents' run on a G4, Cardon, [8]) in order to build a vision ontology linked a the sensor ontology. The second level associates the goals of the robot with its environmental knowledge in order to give priority to some objects or actions in the scene. The third level works on the

multi-agent system morphology to detect on line particular, stable geometrical forms (Campagne, [9]) in order to recognize and classify geometrical forms as 'emotions' generated by the robot during its evolution in the scene accompanied by recognition of objects and subsequent actions. The fourth level creates a relationship between the 'cognition' and the (re)action ('behavior'). For a cognition degree, there is a succession of actions on different actuators: the more the cognition degree is higher, the more the list of actions is specified. The fifth level is a continual bidirectional interaction and adaptation between the environment and the robot behavior. For each action, there is feedback, a relationship between sensors and actuators. The 'attention' of the robot (in fact its knowledge base) evolves with the number of performed actions. Cognition and action are treated in parallel by the multi-agent system.

The project is developed on an Oz/Mozart shell. Oz is reported as a multi-paradigm language with scripting, object, logic and constraints programming. It allows using paradigms such as the concurrency for developing a multi-agent system with asynchronous communication or the constraints programming to create different action plans.

While progresses in developing the novel Aibo's "brain" along the above coordinates will perhaps continue by care of Cardon's younger colleagues, himself appears as the main beneficiary of insight got as team leader upon the (true) human brain itself. Even if we do not share his rather pessimistic view put as: *"Since the permanence of the physical real apprehensible by senses is very strong, the preoccupation to think by man is quite limited, in his civilizations".*

Dealing with artificial consciousness one has to keep in mind distinction among different level of analysis. The level of reality refers to what is, the human brain, fragmentally and in general poorly understood. The level of our reflection upon what is, uses words and logics taken from maths or experimental sciences. The level of simulation uses IT artifacts to mimic brain functioning in its known aspects: autonomy, adaptiveness, partly reason/partly emotion – driven a.s.o. Simulation occurs since there are hopes that arranging such IT artifacts in relations deemed to be right the ensemble would begin to exhibit "consciousness facts" replicating symbolically some features of what we (bioengineers, neuroscientists, philosophers) think to be consciousness.

Why not remaining at the reflection level? For what making such a complicate and tedious simulation?

Because, while reflection dissect (analyze) marvelously single elements, simulation puts together various elements in their very interactive dynamics better than our reflection inherently static can do.

Associated risk with simulation is confusion of levels (planes); forgetting to use appropriate quotation marks, one may think that simulation might actually become, as an example, thinking itself but not an inspiring manner to enrich reflection upon.

It is interesting to notice that theology, that is in part science and part faith, while accepting the benefic role of medicine in treating some bodily illnesses, gets very precocious when is about knowing and influencing (and eventually treating) the superior level of human being, the person (and personality) intimately associated with the brain.

In the theological perspective, the person is considered "the highest form of existence and defined before anything as spirit. A human is an incarnate spirit but his/her spiritual life is defining for a person. In the same manner we use apparatuses and instruments to probe the inner of inanimate things, to reach the deepness of a person we need personal interrelations that in the ideal form represent love. The intimate knowing of a person cannot be entrusted to objects (that is artifacts, though they can help) but to another person only" (Ciobotea, [10]).

If so, best understanding of brain is that given to another brain (e.g. scientific brain seen as a collectivity of brains interacting via communication technology - CT). One can remark the role played in such instance by artifacts (like CT): that of modest but useful adjunct of the real brain approaching (ideally with empathy and generosity) another.

Finally, to Cardon's last questioning "*what we must to do about a system generating artificial consciousness facts for itself, having the sensation to generate artificial thoughts for its pleasure and using all the control-command systems and all de knowledge systems as rather gentle tools (our highlight), without any human intervention?* " (Cardon, [8]), the answer could not be else than pouring out some axiology into the puzzle next to the machine ontology before detaching the dog (be it the Aibo one) from any human intervention. Problem remains how.

And now our question. An AC system endowed with intentions, emotion and good actuators could be fully autonomous that is entirely disconnected from human control or guidance? Apparently not, because once its power source interrupted everything would stop. Or maybe, similar to actual humans, "It" would become conscious (among others) of such an weakness and consequently would (auto) assure a sub rosa backup power to continue its rapid development of knowledge, experience and capabilities even against the will of its creator?

In the same vein, Hanson [11] put: *"If we do not humanize our intelligent machines, then they may eventually be dangerous. To be safe when they "awaken" (by which I mean gain creative, free, adaptive general intelligence), then machines must attain deep understanding and compassion towards people. […] Only if they have humanlike character, can there be cooperation and peace with such machines. It is not too early to prepare for this eventuality".*

V. BIOENGINEERING AND CONSCIOUSNESS TOPICS

Made up to cross the difficult border between medical education and the polytechnic one, biomedical engineering is placed in the privileged position to advance knowledge in the field of human consciousness, in connection with the conundrum whether or not computing machines may become conscious.

Already seen before, bioengineering is central to experiments that investigate direct human-machine interfaces, a topic of neural engineering.

Thus, if the human brain has principle difficulties in understanding it own functioning, signal processing according to information theory rules allied with clinical research on normal subjects may help to climb the staircase to the brain starting from organs apparently less intelligent but prone to be more easily understood.

Cardiovascular bioengineering is today able to distinguish various consciousness states by analyzing heart-related records by means of available knowledge on the control of visceral functions by the brain (Figure 2).

Increasing the cortical control on visceral regulation that

conventionally is called autonomic represents one main aspect of corticalization of our species, in which Stefan Milcu [12] saw the neurophysiologic mechanism of human being's evolution including consciousness and conscience.

Developed by exercising information, the cortex has already spread its "antennae" to the lower floor of the brain, the brainstem regulating the vegetative life, and further on by the cranial nerves to the peripheral organs. According to M. Draganescu [13]: *"It would be possible that mental processes get manifest by such extensions throughout the body".* It stands for a philosophical inference confirmed at least at the heart's level.

Question remains upon the finality of such influence or control exerted by cortex upon "lower-minded" organs. Auto-assuring the best functioning conditions given the multiple circular feedback loops relating brain and "subjacent" physiological machinery? If so, best functioning refers to which criteria: physical effectiveness, mental performance, emotional refinement or higher propensity to moral (read spiritual) values? If the latter proves as true, entering the regulatory loops by gentle means, natural (as breathing pattern control) or artificial (as noninvasive, remote influencing the heart rhythm) could hold promise for human being improvement without appealing to artificial consciousness.

VI. CONCLUSION

Bioengineering and information science&technology certainly advance towards artificial consciousness.

How benefic for humanity is yet not clear. It depends on our capacity to inseminate a machine transposition of natural ethics, at the same time with increasing machine autonomy. Complete autonomy should superpose to a free will (libre arbitre) having behind a machine axiology built at the same time. Neglecting or postponing the latter might associate catastrophic escaping from any human control.

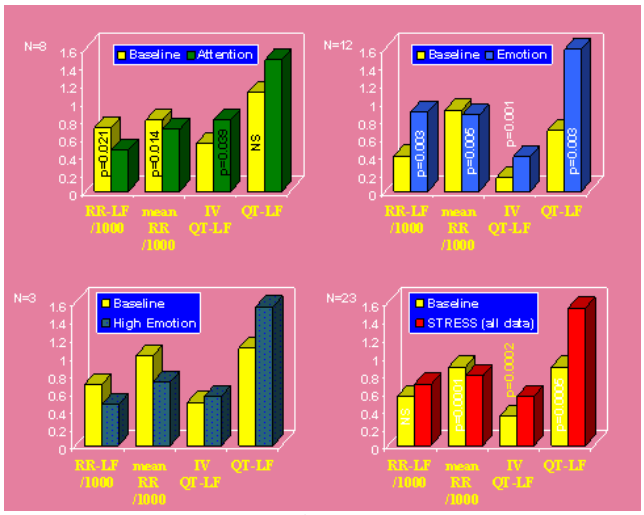

Fig. 2 - Repercussion at heart of consciousness states investigated in 23 healthy young people, 19-21 years, studied in relaxation sitting (baseline), under concentrated attention induced by an arithmetic test without constraint of time (labeled as attention), and under emotion or strong emotion induced by time constraint (emotion/high emotion). RR - the heart period; RR-LF/QT-LF - the fractions of low frequency (0.04-0.15 Hz) in the spectra of variability of heart period or of QT interval in the electrocardiogram; IV QT-LF – the fraction of low frequency in the spectrum of variability of the QT interval from which heart rate influences were extracted using cross spectral techniques – is an emerging indicator of sympathetic control of ventricles (idioventricular). P indicates significant differences between group averages. The idioventricular sympathetic control as expressed by IV QT-LF respond significantly to stress whatever its nuances among concentrated attention, moderate or strong emotion. RR-LF clearly distinguishes between focused attention and emotion. These states of consciousness can not be discriminated with the same clarity using cerebral electrical activity noninvasively recorded on the scalp. Consciousness states and moods deeply influence the physiological machinery [14]. Since sympathetic ventricular overdrive is arrhythmogenic, such studies may offer a track for risk detection and prevention of sudden cardiac death in apparently healthy people (not known as cardiac patients) under sustained psycho-social stress [15].

While conscious people without conscience are unfortunately too frequent today, humanity cannot afford a machine reply of its brain developing exponentially capabilities and power outside of any moral.

On the contrary, if we succeed to seed at the right time a 'moral principle' into the machine we could enjoy a prototype of pure or ideal consciousness, escaping from biological impulsions and restrictions, that might guide or emulate humanity's struggle towards a true Society of the Conscience.

REFERENCES

[1] Versace M., Chandler B., MoNETA: A mind made from memristors, *IEEE Spectrum Robotics/Artif. Intell.*, December 2010.

[2] Draganescu M., Neural engineering and neuroelectronics facing artificial consciousness, *Key note to the INGIMED II Conference*, Bucharest, 2001.

[3] Draganescu M., Societatea Constiintei, *Raport de cercetare*, *Academia Romana*, Bucuresti, 2003.

[4] Koch C., Tononi G., Can machines be conscious? *IEEE Spectrum: special report on singularity*, June 2008..

[5] Horgan J., The consciousness conundrum, *IEEE Spectrum: special report on singularity*, June 2008

[6] Cardon A., Camus M., Campagne J-C., System generating consciousness facts, 2005, *http://abrainproject.googlepages.com*

[7] Camus M., Cardon A., Towards emotional decision-making, Innovative Concepts for Autonomic and Agent-Based Systems, *LNAI 3825*, Springer, 2007.

[8] Cardon A., Artificial consciousness: the hard problem, *ISC Lyon*, June 2008.

[9] Campagne J.-C., Systèmes multi-agents et morphologie, *Thèse de doctorat en informatique de l'Université de Paris 6*, septembre 2005.

[10] Ciobotea IPS D., A vindeca şi a ajuta în tradiţia Bisericii Răsăritene, *Lucrarile Simpozionului de oncologie, Clinica pentru biologie tumorală (Klinik für Tumorbiologie)*, Universitatea din Freiburg in Breisgau, iunie 2003.

[11] Hanson G., Why we should build humanlike robots, *IEEE Spectrum Robotics*, April 2011.

[12] Milcu St., Minte si materie, *Seminarul de bioinginerie ISPB*, Bucuresti, 1994.

[13] Draganescu M., Semn si semnal. *Key note la Sesiunea Academiei Romane*, iulie 1986.

[14] Negoescu R., Bioengineering spots heart repercussions of mental processes: sudden cardiac death corde indemno is preventable, *Proceedings of the Romanian Academy, Series A: Maths, Phys, Tech Sci, Inform Scie, Volume 4 , Number 1, pp. 65-73*, Bucharest, 2003.

[15] Negoescu R., Dinca-Panaitescu S. Processing high-resolution ECG facsimiles to detect ventricular sympathetic overdrive & to prevent sudden death corde indemno, A review, *ECIT*, Iasi, 2008.

Cross-Sector-Communication and Continuity of Care: Using Standards for an Integrative Health Environment

Rolf ENGELBRECHT[1], Claudia HILDEBRAND[2], Hans DEMSKI[2]
[1] ProRec Germany, Glaslweg 33 D 85737 Ismaning
[2] IBMI -Institute for Biological and Medical Imaging, MEDIS - Medical Information Systems,
Helmholtz Zentrum München, German Research Center for Environmental Health
Ingolstädter Landstr. 1, D 85764 Neuherberg, Germany

***Abstract* – European healthcare is changing The increased movement of the citizen asks for administrative changes, but also for patient records that can be accessed ubiquitously in real time and also across boarders. New technologies offer new approaches and possibilities. This paper outlines the changes of developments in the health sector brought upon by ICT. It demonstrates present initiatives towards European eHealth cross-border solutions regarding different levels of interoperability such as semantics, technical requirements, organisational and security related requirements. The project ByMedConnect is given as an example for implementing standardised solutions for overcoming limiting factors and ensuring an interoperable solution supporting continuity of care. Challenges on a future user-friendly European eHealth solution are discussed.**

***Index Terms* – eHealth, electronic healthcare record, EHR, interoperability, standard, cross-border healthcare, CCR, Continuity of Care Record, EHRcom, ISO EN 13606, ProRec, EuroRec,**

I. INTRODUCTION

Electronic support of health care known as eHealth is able to improve the access to clinical data, knowledge and information and to enhance the quality of services and working conditions offered. eHealth supports mobility. It allows patients to access appropriate health resources based on equal opportunity and informed choice. Information and communication technologies (ICT) support networking between human beings, institutions and health information systems -also across borders. Smart and safe communication of data, information and knowledge will remain main development issues in the next decade as networks are crossing regional and national boundaries. There are several national initiatives in Europe which are not harmonised so far.

In 2008 the European Commission issued a recommendation on cross-border interoperability of the electronic healthcare record (EHR) [1]. It states that in order to achieve interoperability "Member States are invited to undertake actions at five levels, namely the overall political, the organisational, the technical, the semantic and the level of education and awareness raising".

At the same time a large scale project, called epSOS (European Patients Smart Open Services) [2] involving 12 Member States (and many Health Ministries) aiming to support the implementation of cross-border healthcare was initiated.

Many other National and European projects have helped advancing interoperability in different sectors of eHealth, e.g. TrustHealth [3] and SEISMED [4] in security, DIABCARD [5], NETCA@RDS [6] and ARTEMIS [7] developed technical and semantic solutions for communication, TOSCA [8] showed feasible solutions for tele-health, Bit4Health [9] demonstrated ways towards an eHealth architecture.

II. HEALTH INFORMATION SYSTEMS

Health information systems are developed for different purposes using a variety of technologies. They might be supporting administration or even decision support. The scope of functions provided and the way they are implemented depend on the health care area. Primary care in mostly all countries is visit oriented with treatment time usually restricted to few minutes. This minimises the amount of data which are documented per visit.

In secondary and tertiary care larger systems were developed; these support logistics and patient management. They are episode oriented and at their core are ADT (Admission-Discharge-Transfer) and financial management. The systems serve as an administrative basis for departmental and service systems such as laboratory and radiology.

While presently healthcare systems and medical services evolve around the patient-doctor relationship, in the near future this correlation will be just one part of a more holistic approach. eHealth needs to be seen being a framework of compliance with privacy issues, healthcare centres, home-monitoring, and results being used for research. Social services are in many countries getting linked to health services.

Today health data communication is usually limited to one institution or to regional doctor networks. Most countries lack communication between the different health care institutions, e.g. hospitals and primary care. Some of the reasons are technical problems and missing standards and/or the insufficient application of existing standards.

Missing common terminology is another hindrance in communication, even more so when communication concerns institutions or physicians in different countries.

The DIABCARD project [5], which aimed at improving communication in diabetes care, was one of the first projects to demonstrate an interoperable solution. Its dataset was based on the standardised European Emergency Data Set

[10] and on a "Diabetes dataset" developed by European physicians and agreed by EASD (European Association for Studying Diabetes). Chip card technology was used for communicating data between physicians and other health professionals. A dedicated card connecting interface module ensured the independence of the solution from specific cards and card readers. DIABCARD was implemented in Austria, Greece, Italy, Spain, France and Germany. The follow-up project ByMedCard - Health across Borders adapted and implemented the DIABCARD concept for citizens travelling between Germany and Hungary.

Increased mobility of the citizens asks for administrative changes, but also for patient records that can be accessed ubiquitously in real time and also across boarders. Thorough and adequate administrative changes are required.

EpSOS [2] aims to develop a practical eHealth framework and an ICT infrastructure that will ensure secure access to patient health information, particularly with respect to basic patient summaries and ePrescriptions between different European healthcare systems. NETC@RDS [6] has been working towards the establishment of new improved health care administration services for mobile citizens across the EU.

III. STANDARDISATION

Healthcare information is presently still very fragmented with proprietary medical information systems using individual interfaces, data protection solutions and even terminology. In contrast mobility requires interoperability which has to enable the exchange of clinical data between computer based applications, even for cross-border communication.

Modern technology supports mobility: the internet enables fast and –almost- ubiquitous access and is to be seen as a main platform for the future. Trusted portable devices like a mobile phone, a smart card or other devices such as USB sticks can complement it for reliable identification and authentication of users. Safe communication between sender and receiver relies on confidentiality, authenticity, data integrity and accountability.

The information needed to treat the patient as well as security functions will have to be available in the preferred language of the health professional. Under strict security conditions, authorised healthcare personnel will be able to read and write information locally or remote. This requires interoperability on different levels:

- Semantics ensuring common definition and understanding of the content;
- Technical enabling the use of different environments in order to integrate the different applications;
- Organisational requiring the understanding of legislation, regulation and other policies as well as governance models;
- Security making sure of a trustful environment.

A number of ISO and CEN standards have been published to advance these goals. They range from requirements on protocols, devices and architectures to service infrastructures. Unfortunately, they are often neither known nor used. The BioHealth project (Security and Identity Management Standards in eHealth including Biometrics) [12] has been analysing reasons for this and has at the same time tried successfully to provide ways to enable SMEs to get information on eHealth standards to help them decide – backed by an online Standards' Repository - whether a specific standard would be of help to them or not. The project was exemplified on security standards in eHealth.

A main step towards interoperability of healthcare related data and the development of eHealth platforms were decision 189, 190, 191 on the European Health Insurance Card (EHIC) [6], which is used to proof the citizen's entitlement to health treatment in any EU Member State. As an additional measure the European Commission issued Mandate 403 (M/403) [12] to the three European Standards Organizations (CEN, CENELEC, and ETSI) in order to provide a consistent set of standards to address the needs of European eHealth provision.

Amongst others digital identity is a major issue. This can be defined as a collection of digital information on one subject. It is needed to link different electronic data to one person, e.g. a person's health insurance number to his lab data in order to store these in the person's health record. Digital identity serves different purposes: identification, authentication, and assurance. It consists of a set of attributes, e.g. characteristic habits, preferences or traits plus an identifier which can be real or anonymous.

Management of digital identities (eID) is a very complex area. eIDs need to be allocated not only to human beings but to all principals and even to specific items. eID of replicable things and robots which are used for automated operation of patients have to be envisioned in the near future. Several projects and activities work towards to overcoming barriers in the digital identity sector and to finding ways on eID management.

IV. SUPPORTING CONTINUITY OF CARE

The Continuity of Care Record (CCR) [13] developed by ASTM is a well structured basic data set of the most relevant facts about a patient's health status, covering one or more episodes or visits. These may be documented by a GP, a specialist physician, a hospital physician or a nurse during treatment in order to enable other health professionals caring for a patient to readily access a summary of relevant and actual information. It includes identifying data, information about the patient's health status (e.g. anamnesis, allergies, risks, problems, medications, operations) and basic data about insurance, care documentation and care plans. The CCR is represented in XML, a structured electronic format. The CCR is meant to address the information needs for continuity of care from one health professional to another. As it contains only selected, relevant portions of a patient's health record it provides a perfect data source for treatment across borders.

The physician originating the CCR transmits it to the co-treating practitioner. This approach already proofed applicable in the DIABCARD system where a smart card was used as communication tool. The XML structure contains also links which point to selected documents of the patient's EHR. The documents are located on a specific server and can be accessed by authorised physicians using the Health Care Professional Protocol (HCPP) [14] via internet.

The ASTM standard CCR has been introduced in the USA in more than 100 health care systems. Microsoft's Health Vault and Google's concept for healthcare support have implemented this standard. Another variant is CCD, the

CCR is translated into an electronic document conforming it to the HL7 CDA [15] concept. Solutions for patient centred administration of the CCR by use of mobile phones are available.

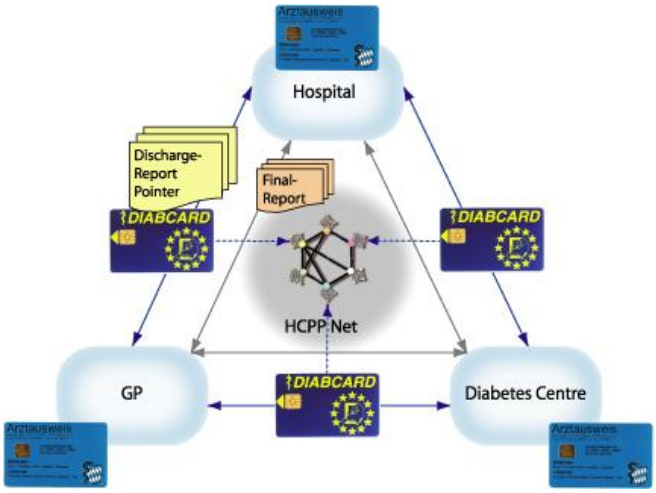

Fig 1: Secure communication network between physicians in hospital and primary care using professional cards (Arztausweis) and the DIABCARD smart card.

In the ByMedConnect [16] project the pragmatic and limited approach of the CCR is complemented by the more comprehensive standard ISO 13606 – Electronic Health Record Communication [17]. It consists of various parts and proposes an advanced architecture to deal with the heterogeneous systems existing in the medical domain. It defines a reference model for the EHR that specifies the common building blocks, and introduces Archetypes [18] as a formal model of real clinical concepts that lay the basis for interoperable semantically sound data exchange. Currently tools are developed that enable the clinicians themselves to define these universal models in an international collaborative approach [19]. Archetypes created can then be published in a repository for sharing and reusing them within inter-institutional and inter-sectoral communication. The use of archetypes is an important step towards semantic interoperable EHRs that are portable (via institutional / regional boundaries), precise (e.g. terminology binding), accessible (individual queries + decision support) and durable (life-long record).

Archetype based data exchange has the potential to fill the gap of lacking communication capabilities between heterogeneous systems. The standard for EHR communication has recently been published for international use at ISO, e.g. a Japanese version is ready for implementation. The standardisation activities are supported by the EUROREC Institute [20] and the OpenEHR Foundation [21].

V. INTEGRATION OF LEGACY SYSTEMS

A multiplicity of different routine applications is used in hospitals, by family doctors and in medical specialist practices. These software solutions are often specialized for the surroundings and to the tasks they support. Users are versed in them and have a lot of experience in handling the included procedures.

A replacement of the programs in use is not feasible. But major disadvantage is in most cases that data of patients, which would be helpful for further attendances, is stored at different places in different forms.

To gain interoperability between health care institutes, it is necessary to transmit data in a standardized format. EN 13606 provides structures for this task, but doesn't define how information can be extracted out of already existing

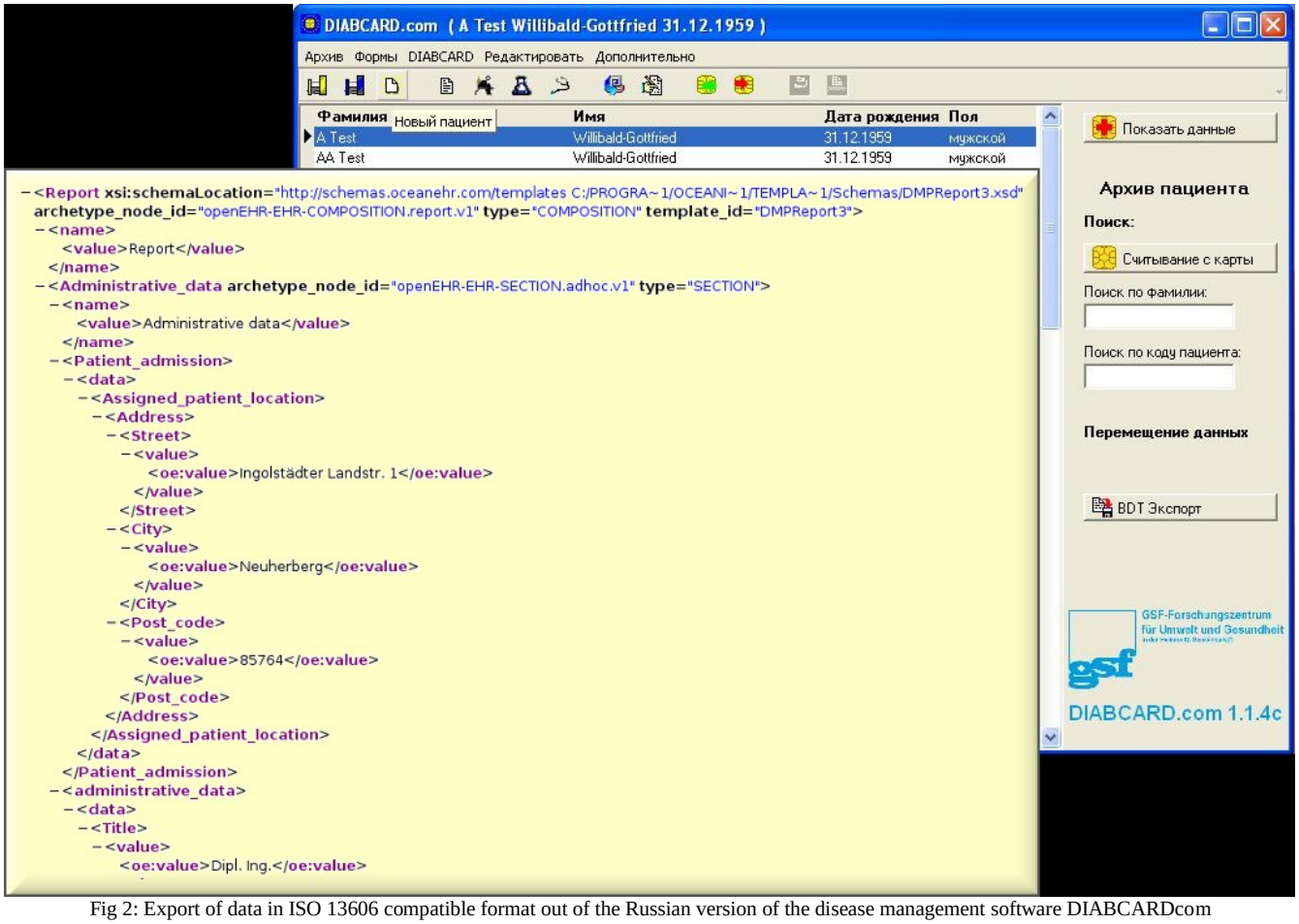

Fig 2: Export of data in ISO 13606 compatible format out of the Russian version of the disease management software DIABCARDcom

systems. ByMedConnect meets this challenge by the development of a transformation module.

The module is placed at the existing software environment of the health care institute. Thereby it is connected to interfaces of the routine applications. On demand, it extracts, the necessary data out of the legacy systems into XML, or into an XML convertible form (CSV, JSON). A correspondent XML schema (XSD) describes the data exported. Approaches to use this schema for binding information on parts of tharchetypes have been published before [7, 8]. Scripts can be generated out of the mapping automatically, this allows the module to do the correct transformation without any further interaction by the user.

VI. CONCLUSION

In future healthcare will be different. The benefits of eHealth are apparent. For many years the Member States and the European Commission have been supporting projects enhancing the quality of care by ICT. The present technological developments -building on the results and achievements of those early initiatives- are pointing towards patient-centred health care supported by anytime-anywhere access to health information and enabling instantaneous connections to clinical support. Presently eHealth is at a crucial point; many initiatives towards European eHealth solutions have been initiated and are ongoing as has been shown in the p

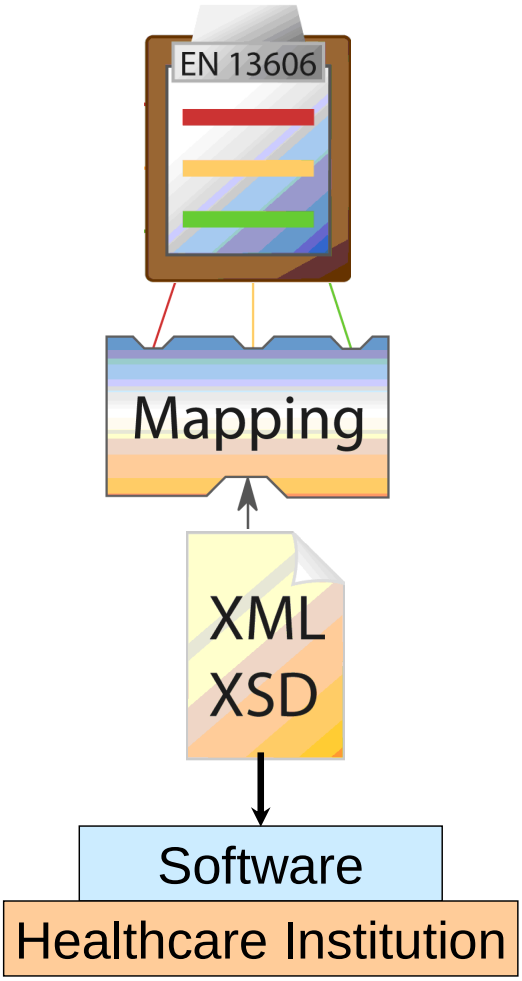

Figure 2. Integration of legacy systems

receding chapters. These solutions still need to be proved applicable, feasible, usable, acceptable and useful.

The success of eHealth will depend on the acceptance by all users. This means that a comprehensive European eHealth strategy needs to be developed. eHealth offers large business opportunities and it has the potential to drive innovation. This necessitates the development of new products and high investment costs. A clear political commitment towards the financing is required.

eHealth requires accessibility of new technologies and e-literacy. The European population is aging. This means, on the one hand, large opportunities towards the support of the elderly, but, on the other hand, challenges like creating awareness and technology education in the elderly have to be met. In a European cross-border scenario legal barriers such as the contradiction of national legal requirements, and of national laws impacting identity have to be overcome without neglecting social barriers such as the culture of distrust or the fear of loss of anonymity. eHealth relies on the trust in the system by all stakeholders. This keeps data protection, privacy, security and also ethical issues high on the agenda.

ACKNOWLEDGEMENT

The authors are in debt to the European Commission and the freestate Bavaria for funding several successful research projects especially DIABCARD and ByMedCard. The project ByMedConnect is currently funded by the Bavarian Minister for environment and health.

REFERENCES

[1] Commission Recommendation of 2 July 2008 on cross-border interoperability of electronic health record systems (notified under document number C(2008) 3282)

[2] epSOS- European Patients Smart Open Services; http://www.epsos.eu (last accessed 24-09-09)

[3] Blobel, Bernd (2000) The European TrustHealth Project experiences with implementing a security infrastructure. International Journal of Medical Informatics 60 (2), S. 193-201.

[4] SEISMED - Secure Environment for Information Systems in Medicine; http://ehto.org/aim/volume2/seismed.html (last accessed 24-09-09)

[5] DIABCARD

[6] NETCA@RDS -A step towards the electronic European Health Insurance Card; http://netcards-project.com (last accessed 24-09-09)

[7] ARTEMIS- Building interoperability into medical information systems; http://istresults.cordis.europa.eu/index.cfm/section/news/Tpl/article/BrowsingType/Features/ID/79928 (last accessed 24-09-09)

[8] TOSCA- Tele-Ophthalmological Services - Citizen-centred Applications; http://www.ist-world.org/ProjectDetails.aspx?ProjectId=525f09f393a64657a6c645111f3fc278 (last accessed 24-09-09)

[9] Blobel, Bernd (2005) Die Implementierung von bIT4health im Spiegel der europäischen Initiativen sowie der fortgeschrittenen Programme anderer Länder. In: Steyer, Günter und Tolxdorff, Thomas, (eds.) bit for bit - Halbzeit auf dem Weg zur Telematikinfrastruktur: TELEMED 2005 - Telematik im Gesundheitswesen.

Akad. Verl.-Ges., Berlin, S. 88-95. ISBN 3-89838-064-5

[10] European Emergency Data Set – NETLINK Requirements for Interoperability; http://www.sesam-vitale.fr/netlink/netlink_requirements_for_interoperabilityv21.pdf (last accessed 24-09-09)

[11] BioHealth - Security and Identity Management Standards in eHealth including Biometrics; http://www.bio-health.eu (last accessed 24-09-09)

[12] M/403 EN; http://ec.europa.eu/enterprise/standards_policy/action_plan/doc/mandate_m403en.pdf (last accessed 24-09-09)

[13] Continuity of Care Record (CCR) Standard - Resource Site; http://www.ccrstandard.com (last accessed 24-09-09)

[14] ByMedCard - Health-Care-Professionals-Protocol (HCPP); http://www.stmugv.bayern.de/krankenhaus/telemedizin/projekte_detail.htm?ID=AAxpv0ps7BE2AiIRuFTDJA%3D%3D (last accessed 24-09-09)

[15] HL7book – CDA Resource Page; http://hl7book.net/index.php?title=CDA (last accessed 24-09-09)

[16] ISO13606-Part 1:2008, http://www.iso.org/iso/catalogue_detail.htm?csnumber=40784 (last accessed 24-09-09)

[17] ByMedConnect - Improving communication by linking domains thus fostering integrated healthcare in Bavaria; http://www.bymedconnect.de (last accessed 14-06-2010)

[18] ISO 13606-Part 2:2008, http://www.iso.org/iso/iso_catalogue/catalogue_tc/catalogue_detail.htm?csnumber=50119 (last accessed 24-09-09)

[19] openEHR Clinical Knowledge Manager; http://www.openehr.org/knowledge (last accessed 24-09-09)

[20] EuroRec Institute; http://www.eurorec.org (last accessed 14-06-2010)

[21] openEHR Foundation; http://www.openehr.org (last accessed 14-06-2010)

Address for Correspondence
Rolf Engelbrecht
ProRec Germany,
Glaslweg 33
D 85737 Ismaning

New Parameter for Describing and Analysis of Optical-anisotropic Properties of Biological Liquid Crystals Nets

Yuriy A. USHENKO
Chernivtsi National University
yuriyu@gmail.com

***Abstract* – This paper is aimed to investigate the potentiality of describing and differentiating optical-anisotropic properties of biological liquid crystal nets by statistic analysis of coordinate distributions of a new analytical parameter – complex degree of mutual anisotropy.**

***Index Terms* – polarization, birefringence, anisotropy, laser image, statistics.**

I. INTRODUCTION

Traditionally [1, 8-24] the processes of forming the polarizationally-heterogeneous fields $U(r)$ were considered in every point (r) as a result of the amplitude (U_x, U_y) – phase (δ) modulation of laser radiation by the biological crystals network

$$\begin{pmatrix} U_x(r) \\ U_y(r) \end{pmatrix} = \begin{Vmatrix} d_{11}(r) & d_{12}(r) \\ d_{21}(r) & d_{22}(r) \end{Vmatrix} \begin{pmatrix} U_{0x} \\ U_{0y}\exp(-i\delta_0) \end{pmatrix} = \begin{pmatrix} d_{11}(r)U_{0x} + d_{12}(r)U_{0y}\exp(-i\delta_0) \\ d_{21}(r)U_{0x} + d_{22}(r)U_{0y}\exp(-i\delta_0) \end{pmatrix}. \quad (1)$$

Here δ_0 – the phase shift between the orthogonal components U_{0x} and U_{0y} of the illuminating laser beam amplitude; d_{ik} – the Jones matrix elements [1, 8].

For the complex analysis of polarizationally heterogeneous laser radiation fields a new approach was suggested in [2-6, 22], based on the generalization of coherence matrix by the polarization coherence matrix for two points (r_1, r_2). In [7, 22] for characterizing the consistency between the polarization states of the stationary laser object field in the points (r_1, r_2) with the intensities $I(r_1)$, $I(r_2)$ a new parameter – complex degree of mutual polarization (CDMP) $V(r_1, r_2)$ – is introduced. It has the following analytical form:

$$V(r_1, r_2) = 4\frac{\nu_1^2 + \nu_2^2 + \nu_3^2}{I(r_1)I(r_2)}, \quad (2)$$

where the coefficients ν_i are determined as the difference of the values of visibility of interference images formed by electromagnetic waves from the points r_1, r_2

$$\nu_1 = \frac{U_x(r_1)U_x^*(r_2) - U_y(r_1)U_y^*(r_2)}{2},$$
$$\nu_2 = \frac{U_x(r_1)U_y^*(r_2) + U_y(r_1)U_x^*(r_2)}{2}, \quad (3)$$
$$\nu_3 = i\frac{U_x(r_1)U_y^*(r_2) - U_y(r_1)U_x^*(r_2)}{2}.$$

The analysis of coordinate distributions of the CDMP polarization-heterogeneous laser images of biological liquid crystals net - protein fibrils network forming the biological tissue (BT) extracellular matrix, - became an important diagnostic application of the above mentioned theoretical approach. The ranges of changes of the 1st-4th distribution order statistic moments of coordinate distributions of the CDMP of the corresponding laser images, important for diagnostics of the human connective tissue oncologic state were determined in [8, 22]. On the other hand, such analysis lead to disregarding the BT extracellular matrix birefringence, which is a principal physical mechanism of their polarizationally-heterogeneous images formation. That is why it appears to be important to search for new diagnostic parameters directly characterizing the degree of similarity of optical axes and birefringence orientations of various points of BT liquid crystal net [12, 15, 18, 19]. Further, similarly to [7] we shall call such a parameter the complex degree of mutual anisotropy (CDMA).

Taking into account (1) – (4) we obtain the expression of CDMA $W(r_1, r_2)$ of two points (r_1, r_2) of the biological liquid crystal The operation of complex conjugation is designated by the asterisk ($*$).

II. RESULTS

Experimental investigations were carried out in the classical polarimeter the main parts and elements of which are presented in Fig. 1 [8]. The value of CDMA $W(r_1, r_2 = r_1 + \Delta r)$ of the two points ($r_1, r_1 + \Delta r$) shifted by the interval Δr of the network of protein liquid crystals is calculated using the algorithm (5). Coordinate distribution $W(x, y)$ of the BT layer extracellular matrix is determined

$$W(r_1, r_2) = \frac{\left\{[d_{11}(r_1) + id_{12}(r_1)][d_{11}(r_2) + id_{12}(r_2)]^* + [d_{21}(r_1) + id_{22}(r_1)][d_{21}(r_2) + id_{22}(r_2)]^*\right\}^2}{I(r_1)I(r_2)} \quad (4)$$

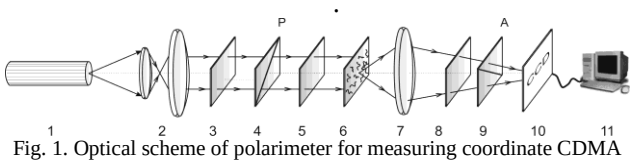

Fig. 1. Optical scheme of polarimeter for measuring coordinate CDMA distributions Here 1 – He-Ne laser (λ = 0.6328 μm); 2 – collimator; 3, 5 and 8 – quarter-wave plates; 4 and 9 polarizes; 6 – BT histological section; 7 – projection microobjective; 10 – CCD –camera; 11 – PC.

Histological sections of sound connective tissue (k=20 samples) and oncologically changed (k=19 samples) one (dysplasia – pre-cancer state) of uterus neck were taken as the objects of investigation.

The series of coordinate distributions ($600\,pix \times 800\,pix$ – fragments (a), (d); $50\,pix \times 50\,pix$ – fragments (b), (e)) and the histograms (fragments (c), (f)) of CDMA values $\tilde{W}(x,y)$ of physiologically normal (fragments (a), (b), (c)) and pathologically changed (fragments (d), (e), (f)) connective tissue samples are presented in Fig. 2.

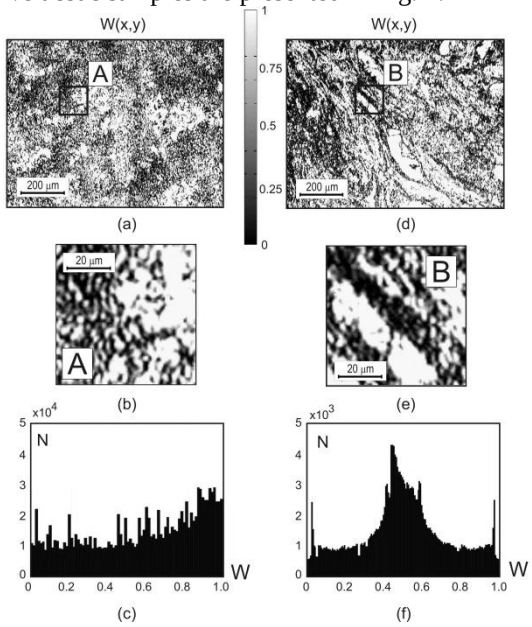

Fig. 2. Coordinate distributions ($600\,pix \times 800\,pix$ – fragments (a), (d); $50\,pix \times 50\,pix$ – fragments (b), (e)) and histograms (fragments (c), (f)) of values $\tilde{W}(x,y)$ of physiologically normal ((a), (b), (c)) and pathologically changed ((d), (e), (f)) histological section of connective tissue.

For chaotically oriented network of liquid crystals of the sound tissue extracellular matrix (Fig. 2(a), (b)) the values of $W(x,y)$ histograms represent rather equiprobable distributions (Fig. 2(c)). Early oncologic changes of connective tissue are accompanied with the formation of the protein liquid crystals net growth direction. It is optically shown (Fig. 2(d), (e)) in some localization of the CDMA random values distribution (Fig. 2(f)) in the domain of $W = 0{,}4 \div 0{,}6$ extrema.

In order to obtain objective criteria of diagnostic efficiency, the comparative investigation of CDMP ($V(x,y)$) and CDMA $W(x,y)$ techniques was performed in the conditions of single and multiple scattering of laser radiation by the layers of uterus neck connective tissue.

In order to form a single and multiple scattering regimes we have used a histological sections of biological tissues with different geometric thicknesses (15 and 40 μm).

In order to form a single and multiple scattering regimes we have used a histological sections of biological tissues with different geometric thicknesses (15 and 40 μm).

In the figures 3 and 4 the comparative results of calculations of the average (M_1), the dispersion (M_2), the skewness (M_3) and the kurtosis (M_4) of CDMA $W(x,y)$ (Fig. 3) distributions of two groups of connective tissue and of CDMP $V(x,y)$ (Fig. 4) of their laser images are presented. In order to estimate the statistic reliability of calculations the amount of samples within each group (norm or oncology) were chosen that confidence interval $p < 0.01$. The area of illuminating laser beam was chosen that magnitudes of M_1, M_2, M_3 and M_4 did not depend on displacement in the plane of the histological section sample. For our experiment the diameter of laser beam was $5mm$, and the size of histological section was $15 \times 15mm$.

The statistic moments were calculated in accordance with the following technique [21, 22]:

$$M_1 = \frac{1}{N}\sum_{i=1}^{N}|W(x,y)|, M_2 = \sqrt{\frac{1}{N}\sum_{i=1}^{N}(W(x,y)-M_1)_i^2}, \quad (5)$$

$$M_3 = \frac{1}{M_2^3}\frac{1}{N}\sum_{i=1}^{N}W(x,y)_i^3, M_4 = \frac{1}{M_2^4}\frac{1}{N}\sum_{i=1}^{N}W(x,y)_i^4,$$

where N - is the number of elements in discrete sampling.

From the obtained data about the coordinate distributions of CDMA of optically thin layers of connective tissue one can see that:

The average and dispersion of distributions $W(x,y)$ of both types of samples differ insufficiently. For 2D distributions $V(x,y)$ of laser images there is practically no difference between M_1 and M_2.

The skewness values M_3 of distributions $W(x,y)$ of the investigated samples differ by 2.1 times; the kurtosis values – by 3.2 times. For CDMP distributions $V(x,y)$ the values of the 3rd and 4th statistic moments vary for M_3 – by 1.3 times; for M_4 – by 1.8 times.

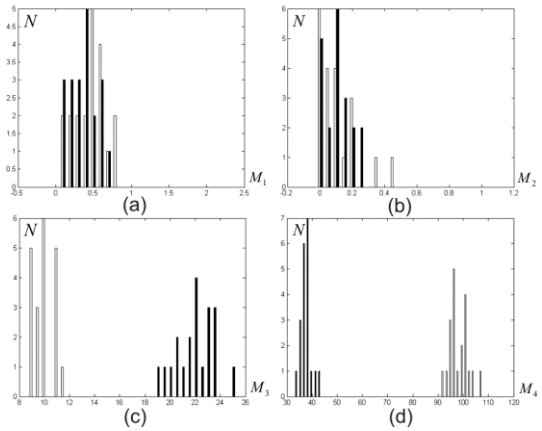

Fig. 3. The histograms of statistical moments of CDMA $W(x,y)$ for physiologically normal (white bars) and pathologically changed (black bars) connective tissue.

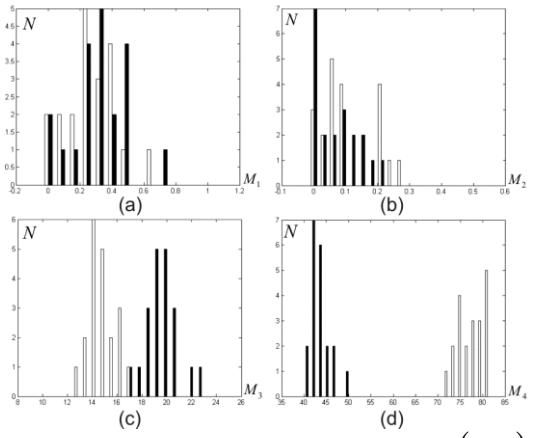

Fig. 4. The histograms of statistical moments of CDMP $V(x,y)$ for physiologically normal (white bars) and pathologically changed (black bars) connective tissue.

III. CONCLUSION

To characterize the degree of consistency of parameters of the optically uniaxial birefringent protein liquid crystal nets of BT a new parameter – complex degree of mutual anisotropy is suggested. The technique of polarization measuring the coordinate distributions of the complex degree of mutual anisotropy of BT is developed. It is shown that statistic approach to the analysis of distributions $W(x,y)$ of BT of various optical thicknesses appears to be more sensitive and efficient in differentiation of their physiological state in comparison with investigations of complex degree of mutual polarization of the corresponding laser images.

REFERENCES

[1] Born M., Wolf E., Principles of Optics. Cambridge Univ. Press, 1999.

[2] Gori F., Santarsiero M., Vicalvi S., Borghi R. and Guattari G., "Beam coherence-polarization matrix," *Pure Appl. Opt.* 7, 941-951, 1998.

[3] Gori F., "Matrix treatment for partially polarized, partially coherent beams," *Opt. Lett.* 23, 241-243, 1998.

[4] Wolf E., "Unified theory of coherence and polarization of random electromagnetic beams," *Phys. Lett. A.* 312, 263-267, 2003.

[5] Mujat M. and Dogariu A., "Polarimetric and spectral changes in random electromagnetic fields," *Opt. Lett.* 28, 2153-2155, 2003.

[6] Ellis J., Dogariu A., Ponomarenko S. and Wolf E., "Interferometric measurement of the degree of polarization and control of the contrast of intensity fluctuations," *Opt. Lett.* 29, 1536-1558, 2003.

[7] Ellis J. and Dogariu A., "Complex degree of mutual polarization," *Opt.Lett.* 29, 5365-5338, 2004.

[8] Alexander G. Ushenko and Vasilii P. Pishak. Laser Polarimetry of Biological Tissue: Principles and Applications, in *Handbook of Coherent-Domain Optical Methods: Biomedical Diagnostics, Environmental and Material Science*, Valery V. Tuchin, ed. (Kluwer Academic Publishers, 2004), pp. 93-138.

[9] Alexander G. Ushenko, "Polarization structure of laser scattering fields," Optical Engineering, 34(4), 1088-1093, 1995.

[10] Ushenko A.G., "Laser diagnostics of biofractals," *Quantum Electronics* 29, 1078–1084, 1999.

[11] Angel'skii O.V., Ushenko A.G., Arkhelyuk A.D., Ermolenko S.B., Burkovets D.N., "Structure of matrices for the transformation of laser radiation by biofractals," *Quantum Electronics* 29, 1074-1077, 1999.

[12] Angel'skii O.V., Ushenko A.G., Arheluk A.D., Ermolenko S.B., Burkovets D.N., "Scattering of Laser Radiation by Multifractal Biological Structures," *Optics and Spectroscopy* 88, 444-448, 2000.

[13] Ushenko A.G., "Polarization Structure of Biospeckles and the Depolarization of Laser Radiation," *Optics and Spectroscopy* 89(4), 597-601, 2000.

[14] Ushenko A.G., "Stokes-correlometry of biotissues," *Laser Physics* 10(5), 1286-1292, 2000.

[15] Ushenko A.G., "The Vector Structure of Laser Biospeckle Fields and Polarization Diagnostics of Collagen Skin Structures," *Laser Physics* 10(5), 1143-1149, 2000.

[16] Ushenko A.G., "Laser polarimetry of polarization-phase statistical moments of the object field of optically anisotropic scattering layers," *Optics and Spectroscopy* 91(2), 313-316, 2001.

[17] Ushenko A.G., "Polarization contrast enhancement of images of biological tissues under the conditions of multiple scattering," *Optics and Spectroscopy* 91(6), 937-940, 2001.

[18] Ushenko A.G., "Laser probing of biological tissues and the polarization selection of their images," *Optics and Spectroscopy* 91(6), 932-936, 2001.

[19] Ushenko A.G., "Correlation processing and wavelet analysis of polarization images of biological tissues," *Optics and Spectroscopy* 91(5), 773-778, 2002.

[20] Ushenko A.G., "Polarization correlometry of angular structure in the microrelief pattern or rough surfaces," *Optics and spectroscopy* 92(2), 227-229, 2002.

[21] Angelsky O.V., Ushenko A.G., Ushenko Ye.G., "2-D Stokes Polarimetry of Biospeckle Tissues Images in Pre-Clinic Diagnostics of Their Pre-Cancer States," *Journal of Holography and Speckle* 2(1), 26-33, 2005.

[22] Angelsky O.V., Ushenko A.G., and Ushenko Ye.G., "Complex degree of mutual polarization of biological tissue coherent images for the diagnostics of their physiological state," *J. Biomed. Opt.* 10(6), 060502, 2005.

[23] Angelsky O.V., Ushenko A.G., and Ushenko Ye.G., "Investigation of the correlation structure of biological tissue polarization images during the diagnostics of their oncological changes," Phys. Med. Biol. 50, 4811-4822, 2005.

[24] Angelsky O.V., Ushenko A.G., Ushenko Ye.G., Tomka Yu.Ya., "Polarization singularities of biological tissues images," J. Biomed. Opt. 11(5), 054030, 2006.

Better Information, etter Decisions, better Care– Introducing a Web-based Inventory System for Medical Devices in Moldova

Claudio ZAUGG [1,2]
[1] *Swiss Tropical and Public Health Institute*
[2] *Moldova-Swiss Perinatology Project*
claudio.zaugg@unibas.ch

***Abstract* – As in most health care systems, health technologies made a significant contribution to improvements in quality of care in the Republic of Moldova in the last decades. However, there are currently no instruments in place to efficiently plan, manage and coordinate investments in health technology. The present work describes the assessment, evaluation and introduction of a web-based application with the objective to strengthen the Health Technology Management (HTM) in the country. The open source tool "openMEDIS" was configured, adapted and successfully introduced in six pilot hospitals. The new management instrument has received good attention by the decision-makers at national and at regional level. As a next step, openMEDIS will be scaled-up to all maternities in the country to facilitate evidence-based planning in Perinatology.**

***Index Terms* – Health Technology Management, Health Information Systems, Open Source Software**

I. INTRODUCTION

Clinical equipment is one of the major contributors to the rapid progress of healthcare [1]. The global market today counts more than 10'000 distinct device groups and 500'000 products from over 13'000 registered manufacturers worldwide [2], [3]. Innovation is the growth motor of the industry: There are studies suggesting 50% of all diagnostic and treatment methods we use today did not exist 10 years ago [4]. This constant increase in the variety and complexity of available health technologies require good management instruments to allocate the available resources efficiently.

The review of the World Bank's global $1.5 billion investment in medical devices showed that there are cases where 30 % of the more sophisticated equipment stock was unused and the rest had 25 to 35 % downtime because of weak capacity to maintain equipment. A root cause turned out to be ineffective management including planning, acquisition and subsequent operations [5].

The foundation for good management practice and good policies is good data. Decision-makers in the Moldovan health care system have yet not been able to draw from a respective information base in order to plan and streamline investments in medical equipment efficiently. Given the large number of international actors and programs with different procurement- and supply channels the need for coordination becomes even more apparent.

The WHO collaborative agreement with Moldova [6] prioritizes capacities to monitor and evaluate the performance of the health system strengthened and systems to facilitate coordination. Considering the large share of investments in medical monitoring its performance deserves a special attention.

In the last years, the Swiss Government has been supporting Moldovan's health care system in the area of Perinatology (Moldova-Swiss Perinatology Project) and in the Regionalization of Pediatric Emergency (REPEMOL Project). Besides the development of clinical standards, capacity building, quality management, etc., both projects have also taken care of the procurement of respective medical equipment. In this light, the introduction of an electronic information system in order to sustainably improve planning and management of the new technologies was a recognized as a priority by the Swiss Government.

II. METODS

The process started in 2009 with a qualitative needs assessment looking into the Health Technology Management (HTM) landscape of Moldova – the managerial and technical environment in which an information system for medical equipment will function in the future. The advances in HTM driven by the two projects were coordinated by the HTM-Working Group which involved 20-30 stakeholders mainly from hospital directorates, the Technical University of Moldova (TUM) and Ministry of Health (MoH).

Based on the needs, a software application including a nomenclature system was to be identified and – if necessary – adaptations and translations to be implemented. Along with the SW tool, targeted training modules on both the use of the software application and on the importance in a broader HTM context needed to be developed.

Before the system was ready to be scaled-up it had to be tested in two to three facilities (ideally in places where technical workshops were established in order to assure a sustainable benefit for the hospitals). The data collection was mainly done through biomedical engineering students during their internship or their first assignment in hospitals. In this process, but also in the adaptation and further development of the tool, the Technical University of Moldova (TUM) has played an important role.

III. RESULTS

At the time of the evaluation, HTM in Moldova was not very developed: planning and procurement were largely influenced by donors and vertical intervention programs. The corrective and preventative maintenance of equipment was done by private companies. Technical workshops to service and maintain equipment were normally not present in public health facilities. Often, a head nurse or a director of a department without formal technical background was in charge of equipment management. Given such circumstances, key requirements to a software tool to manage the equipment inventory were identified to be the following:

- Be easy to use (simple graphical user interface).
- Offer possibility for remote data review, analysis, backup and technical support.
- Include nomenclature according to ISO [7].
- Facilitate translation of user interface and equipment tables into local language.
- Allow step-wise approach: Begin with a simple system which can be extended as other areas of HTM start to develop (e.g. maintenance)
- Do not impose high license cost to the public health care budget once the system is scaled-up.

An evaluation of existing tools has shown that most products on the market are either made for high-expenditure health care systems or they are country specific tailor-made solutions. The above mentioned criteria and the literature suggested that web-based open source software would be most suitable. The application which could meet the requirements best was "openMEDIS" [8] - a software originally developed by the Swiss TPH that had also been validated through implementation in similar settings.

"openMEDIS" was programmed using a PHP interface and a mySQL database. The software provides functions needed for systematic collection and exchange of health technology data. Information such as a manufacturer database, an integrated, reduced UMDNS nomenclature (with 325 generic terms), or equipment images shall facilitate data collection. The tool's main focus is on the management and planning of the equipments and therefore also captures data on suppliers, service agents, warranty contracts and financial matters.

The department of Biomedical Engineering at the Technical University of Moldova has provided significant support in e.g. the translation of the user interface and nomenclature lists or writing of a user's manual in local language.

Along with the software, six thematic training modules on Health Technology Management and information systems, nomenclature use, data management and -analysis, etc. were created.

The training of the users in three pilot centers was done in a two-day workshop whereby the first day was focusing on theoretical background and the second day involved a practical exercise in a real-life environment.

The data collection itself was rather challenging. Even the minimal datasets that the system required were difficult to obtain. For example, at the hospital level, information about purchase date, expiration of warranty or supplier data was often not present. As a result of absence of systematic planning in the past years, the paper-based lists found at some departments were often outdated, incomplete or faulty.

Another challenge was the experience of the data collectors who had difficulties in finding the correct nomenclature term for a specific devices or who have not recognized them in the wards. Later on, a consultant was employed to supervise the data collection process and to assure good data quality. After repeatedly addressing and discussing the problems and fine-tuning of the application in the formal HTM working group meetings, the three inventories were initially collected over a period of six months to one year.

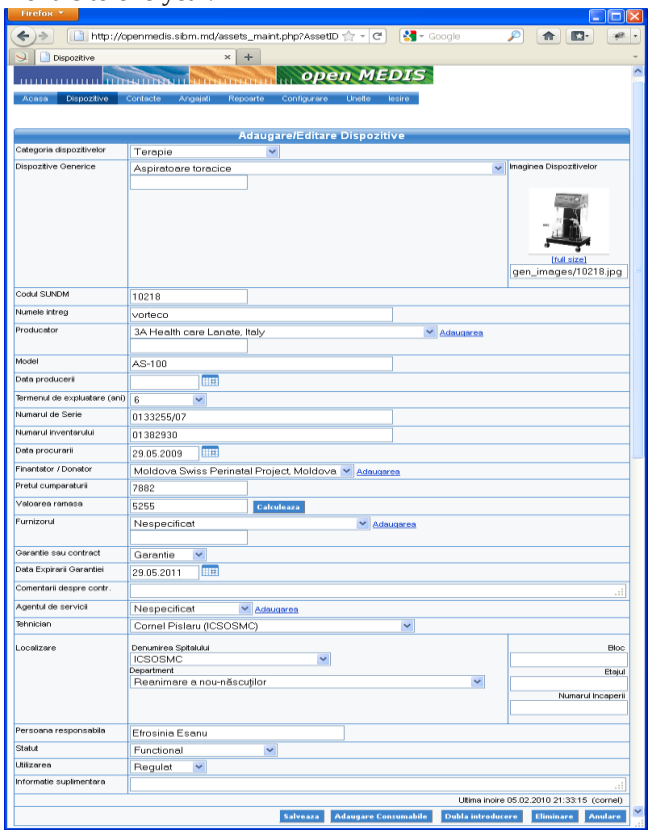

Fig. I. openMEDIS data entry page in a firefox© Web-Browser

The stock of the three tertiary and secondary level pilot facilities counted 2120 devices all together with a total net book value of more than 33 Mio. MDL at the time of writing. The results also show that the tree facilities together managed to assign a nomenclature term to 1775 out of 2120 terms (83.7 %). In other words, more than 80% of the equipment found in the hospital could be denominated using the 325 translated UMDNS terms.

As the piloting was successful, the installation of the software was expanded to three further institutions which were involved in the HTM imitative. The local inventory consultant has trained the new users independently using the training material and the user's guide.

As for the hosting of openMEDIS, the project has managed to transfer and install the application to the web-space of the Society of Biomedical Engineers of Moldova (SIBM) who is actively involved in the development and promotion of the management instrument.

First analysis of the equipment stock in the three pilot facilities resulted in the summary indicators listed Table 1.

The analysis shows that all three facilities own roughly

the same number of equipment from more than 100 different manufacturers. It can also be seen that Facility #1 (a tertiary level referral hospital) has by far the most valuable stock (21'239'946 MDL) as more sophisticated is in operation there.

TABLE I. KEY INDICATORS FOR PILOT HOSPITALS

Indicator	Facility 1	Facility 2	Facility 3
Number of assets	680	585	855
Total purchase price (lei)	32'102'060	18'522'648	13'716'653
Total remaining value (lei)	21'239'946	9'966'155	1'881'258
Number of manufacturers	102	119	100
Number of suppliers	21	37	27
Departments with equipment	18	35	29
Unique nomenclatures	576	430	769
Non-specific nomenclatures	104	155	86

Other summary graphs are also obtainable from the system at real time; One of these being a "histogram" showing the age distribution of the inventory. As Figure II illustrates, there is still a significant amount of equipment in place which was purchased before independence in year 1991. On the other hand, there was little investment made in the following years until year 2000.

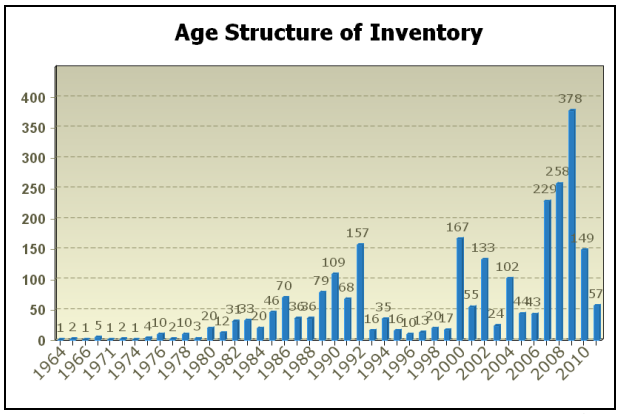

Fig. II. OpenMEDIS output - graph showing the distribution of the equipment stock (partial data for 6 facilties)

Another graph shows the "health" of the equipment. In this case (aggregated data from 6 hospitals) 20 % of the devices are currently not functioning properly or need repair (Figure III).

Now that data is available in a standardized and structured format, the possibilities for analysis and aggregation are nearly unlimited. An intelligent filter in openMEDIS allows a combination of search criteria.

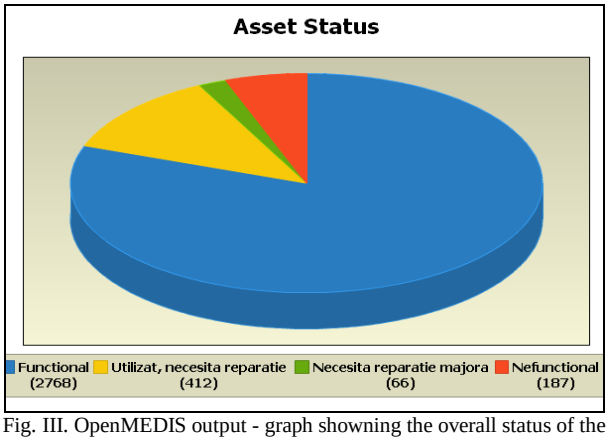

Fig. III. OpenMEDIS output - graph showning the overall status of the assets

Thus, decision-makers at facility, regional or national level have the opportunity to run queries and to extract the information they are interested in.Another feature of openMEDIS is the option to define "essential equipment" and customize it for each facility type- and size. Depending on the clinical discipline, MoH or WHO guidelines and provide such lists which later serve as a standard to which the actual inventory is compared with. Concretely, the Moldova-Swiss Perinatology Project is incorporating the Ministry Health's standard equipment list for Obstetrics and Neonatology [9], expanding inventory practices to all facilities in the country with perinatal services and using openMEDIS as evidence-based planning tool.

The open source license of the application allowed creating modules and features freely. Properties and characteristics can be removed or new ones can be added. A good example is a corrective- and preventative maintenance module linked to the inventory which is being developed by the Technical University of Chisinau.

IV. CONCLUSION

The situation analysis has shown that an essential information system for medical devices should urgently be implemented in Moldova. The open source application "openMEDIS" has met the needs for an easy to use, flexible and inexpensive system best.

During the implementation it was shown that "openMEDIS" as a tool to collect data on the medical equipment stock was a good choice. After training and a few cycles of quality awareness workshops, the equipment of six hospitals was entered into the web-based application without major problems. The pilot activities were also key in revealing shortcomings in the current documentation system of medical devices.

One of the biggest challenges was the availability of human resources. Until recently, the profession of biomedical- or clinical engineers was not existent in Moldova and respective working places at the hospitals are only at the stage of development. People responsible for the heath technologies at the 1st level and 2nd level facilities were head-nurses or deputy chiefs with limited interest and skills for electronic information systems. On the other hand, the new workforce of Bioengineers was yet lacking practical experience.

Nevertheless, the initiative was widely supported because the power of the openMEDIS tool lies in its ease of use and the fact that it addresses the issues at management level at first. This creates acceptance by the decision-makers. Initiatives towards a (possibly commercial) more sophisticated and hospital-based Computerized Maintenance Management System (CMMS), where the focus is rather in the organization of the maintenance should be deferred.

As the project's efforts to establish further maintenance workshops move along, either a CMMS can be evaluated or further modules (for maintenance, calibration, billing) can also be programmed in openMEDIS.

In particular the web-based- and open source architecture has proven to be suitable to the Moldovan setting. Firstly, because it can be up-scaled with no extra license fees and secondly because it can be hosted, managed and supported remotely.

The tool is also appreciated by hospital managers and by the Ministry of Health. The Ministry is in the process of

building-up an Agency for HTM and formulating respective policies and guidelines. It is also in-line with the World Bank funded "e-Governance" initiative and the Government of Moldova's proclamation to put an ICT toolkit in place to achieve better governance in public health [10].

ACKNOWLEDGMENTS

The author whishes to express thanks Prof. Sontea who was the leader of the HTM working group, Tatiana Buzdugan, who is the local HTM coordinator and Cristina Matei, the inventory consultant for the PERINAT and REPEMOL projects. All of them have significantly contributed to the successful implementation. Also many thanks to the Swiss Development Cooperation (SDC) who financially supported HTM in the frame of the two projects.

REFERENCES

[1] B. Wang, "A Framework for Health Equipment Management in Developing Countries," *Hospital Engineering & Facilities Management*, pp. 1-3, 2003. GMDN Agency, "Medical Technology Brief," 2007. [Online]. Available: www.eucomed.org/~/media/pdf/tl/2008/portal/aboutindustry/medtechbrief2007.ashx. [Accessed: 02-Mar-2009].

[2] Medical Device Register, *The Medical Device Register*. Grey House Publishing, 2008.

[3] J. Sanders, *Where is Technology Taking Healthcare? Where is Healthcare Taking Technology?* CADTH Symposium, 2007.

[4] World Bank, "Proceedings: International Forum for Promoting Safe and Affordable Medical Technology in Developing Countries," 2003.

[5] R. of M. WHO/Europe, "Biennial Collaborative Agreement 2010–2011." [Online]. Available: http://www.euro.who.int/en/where-we-work/member-states/republic-of-moldova/publications2/bca. [Accessed: 29-Apr-2011].

[6] ISO 15225, "Nomenclature -- Specification for a nomenclature system for medical devices for the purpose of regulatory data exchange." International Organisation for Standartization, 2000.

[7] "openMEDIS - an essential Medical Device Information System." [Online]. Available: http://sourceforge.net/projects/openmedis/. [Accessed: 04-Feb-2010].

[8] MoH Moldova, *"SERVICIUL PERINATAL REGIONALIZAT:NIVELURI SI CONTINUT" Ghidul BNational de Perinatologie*. Ministerul Sanatatii si Protectiei Sociale al Republicii Moldova, 2006.

[9] Government of the Republic of Moldova, "Activity Program 2011-2014." 2011.

Formation of Economic-managerial Knowledge System within Training of Healthcare Workers

Olga KUDELINA
Siberian State Medical University, Tomsk, Russia
koudelina@ngs.ru

***Abstract* – Medical personnel are the most important part of resource maintenance of healthcare system, they make the defying influence on structure developments' implementation in healthcare reforming. High number of medical staff characterizes personnel structure of Russia. However, there is imbalance at comparison of rate in regions of federation, in urban and rural areas that cannot allow delivering qualified medical care widely. That is why specialists who have economic-managerial skill and able to organize and plan healthcare system development, are necessary. Medical universities during lifelong education must give attention to forming of managerial and economic knowledge of healthcare in theirs programs. The programs that have been developed in Siberian State Medical University are intended to a wide range of healthcare specialists: physicians, head physicians, managers and nurses.**

***Index Terms* –healthcare system, medical universities, personnel potential, programs of physicians' training, staffing.**

Main causes of unfavorable dynamics of development of healthcare and public health are caused by absence of strategic planning and personnel administration, imperfection of financing and legal regulation. Shortage of the medical personnel in many countries is the deterrent factor of the provision of high-quality medical care [1]. Problems of staffing demand the complex approach to their decision, and also analytical developments and scientific support.

In previous years Ministry of health and social development of the Russian Federation gives great value to planning of health manpower, professional and career development, creation of acceptable working conditions, especially in primary health care. The structure of staffing in Russia is characterized by the expressed imbalance at comparison of indicators in subjects of federation (fig. 1), thus frequency ratio of such disparities reaches 1,5-3 times [2,3].

The rate of density of physicians in Tomsk oblast throughout the last decade increased and has made 66,9 per 10 thousand population in 2009, exceeding average all-Russian indicators (fig. 1). However, average density of nurses and midwives steadily decreases: from 105,6 in 2003 to 102,7 per 10 thousand population in 2009 [4].

Thus, despite of increase of quantity of medical workers in countryside, level of medical staff's provision in rural hospitals differs from city's health care facilities in times [5]. Average age of a physician in Tomsk is 48,3±2,31 years, in oblast areas 54,8±3,14 years, and of nurses - in Tomsk - 54,3±2,95 years, in areas - 58,2±4,12 years.

The ratio of nurses to physicians in our country is much lower, than in the majority of the developed countries of the world: 1 doctor on 2 nurses whereas world experience shows that an optimum ratio is not less than 3-5 nurses on 1 doctor [1]. The rate of medical workers' multiple job holding in Tomsk oblast on the average is 1,3 lower, than the all-Russian (1,5), a ratio of nurses to physicians - 2,1. Deficiency of medical staff in area reaches 13,4 %, nurses - 22,1 %. This imbalance limits possibilities of development of system of medical care, especially services of aftercare, home nursing, and rehabilitation.

In these conditions, the organization of economists-managers training is a necessary component of strengthening and development healthcare sector.

Existence of medical institutions that are various not only on the organization, but also by the form properties, leads to requirement for competent specialists, both for public healthcare, and for economy and management sphere. Graduates of faculty of economy and management in healthcare of the Siberian State Medical university (SSMU) became such experts.

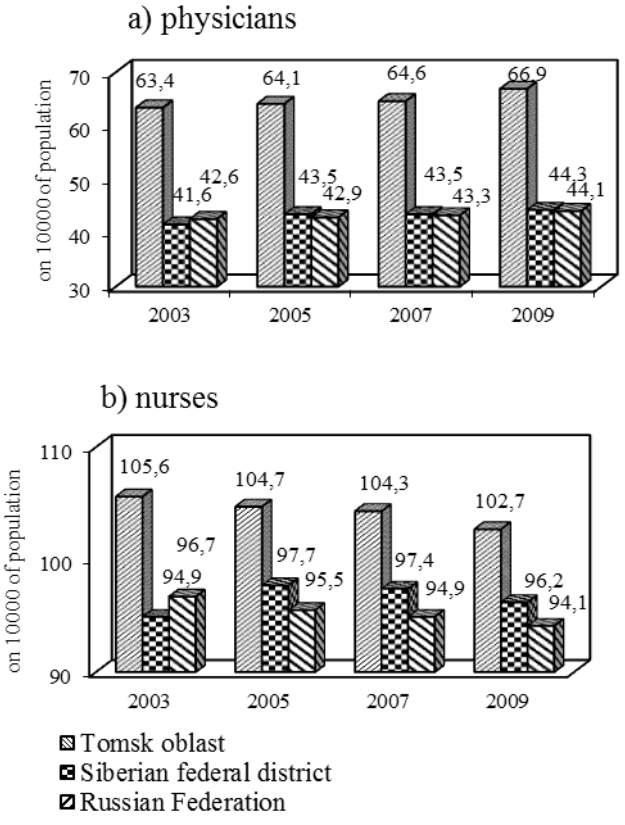

Fig. 1. Dynamics of medical staff provision in 2003-2009 years

The specialty 080502.65 - economy and management at the enterprise (in healthcare) has been opened in 2003. For a small interval of the activity faculty of economy and management in healthcare has carried out 12 graduations, having prepared more than 200 experts. Thus for the majority of them the new specialty was the second, and training and reception of qualification "economist-manager" was necessary for reception of the systematized economic-administrative knowledge and desire of the further career growth in healthcare field. It is no secret that training process passes with high return, under condition of the expressed motivation of trainees who already have some operational experience in health care facilities and other medical organizations.

The faculty of economy and management in healthcare conducts training on the basis of secondary education on internal (5 years) and the correspondence form (6 years), on the basis of the higher or unterminated higher education on internally-correspondence (3 years) and correspondence (4 years). Now on a specialty about 300 foreheads are being trained, including on a budgetary basis on a full-time course of study. Educational process is realized on all modes of study as well on a paid basis, and the approach for payment educational services the differentiated.

Graduates of faculty are prepared for the professional work that provides rational management of economy at the enterprise of social sphere taking into account branch specificity, and for work on scientific and pedagogical posts, in bodies of the state and local management.

In territory of Siberia, only SSMU has obtained the corresponding license and the certificate on the registration, giving the right to realization of educational programs of the higher vocational training, including economy and management at the enterprise (in healthcare) by the results of complex check (License A №227772 from 19.02.07, cert. №0616 from 04.05.07).

The curriculum on a specialty 080502 - economy and management at the enterprise (in healthcare) in 2006 has been confirmed by the Information-methodical center on certification of the educational organizations (Shakhty city) and includes all traditional blocks of general and special disciplines.

The cycle of general professional disciplines reflects all palette of knowledge and the skills that are necessary for support of economic, accounting, administrative and communicative activity of any enterprises. In the block of special disciplines, the subjects reflecting specificity of management of healthcare and medical institutions are presented. For example, medical care quality management, technology of the outpatient and stationary help, legal regulation in healthcare, management of medical expenses, forecasting of healthcare development, etc. Many disciplines are unique; they are developed only for preparation of experts in the field of economy and management of healthcare. In addition, the disciplines of specialization, which allow students to define in a concrete direction of the future professional work, are presented: strategic planning at the enterprise, financial management, organization and economy of general physician practice.

On study disciplines working programs and corresponding methodical support are developed.

For practical skills acquisition and fastening of theoretical knowledge all kinds of practice in conformity with the existing state educational standard on a specialty are provided.

Considering necessity of the exact and systematic economic account and a substantiation of activity of the medical organizations in conditions of healthcare modernization and at realization of the pilot project, the requirement for professional economists-managers is rather high. By approximate calculations only in territory of Tomsk oblast, it makes more than 100 experts in a year as economists and the accountants who do not have an overview about technology of rendering of medical care and the organization of medical process work in healthcare system.

Prominent aspect is the development of system of lifelong medical education, which means constant updating of knowledge, skills of the physician. Obtaining of new economic-administrative knowledge opens additional possibilities for continuous professional training and improvement both in the field of the basic specialty, and in other allied fields. Primarily, all this can be offered by medical high schools.

Educational strategy of medical universities should reflect real requirements of the branch. Forecasting of oblast's healthcare modernization's requirements area has laid down in a basis of designing of various interdisciplinary educational programs in SSMU.

The department of organization of healthcare and public health takes an active part in education and retraining of personnel. Training of healthcare organizers within the limits of internship is conducted. Subjects of postgraduate training are expanded; new programs with attraction of foreign experts are developed. The department has the settled collaboration on medical informatics with German partners within the within the bounds of work of e-Health section of the Koch-Mechnikov Forum (Berlin) headed by professor H. Hann. For example, in theme «Information technology in healthcare» materials of lectures kindly given by the professor of R. Engelbreht (Germany, Munich) and manuals on medical informatics of Institute of medical informatics of University of Braunschweig are used. Within the limits of the international cooperation with the Koch-Mechnikov Forum, there is an academic exchange that allows inviting German experts for lecturing and carrying out of seminars. Simultaneously with it, employees of the department can exchange experience with German colleagues, improve the qualification during participation at conferences and seminars in the leading medical organizations of Germany.

More than 150 people are passing thematic and general improvement on the department annually; from them 30-40 % are head physicians of various establishments and oblast healthcare organizations. Therefore, training of economy and management in healthcare is an obligatory component of educational curriculum.

Now for accreditation an educational program of preparation of bachelors in a direction «Industrial management» is presented, work on the program «Innovative activity», which should be started in 2011-12, is finished.

The economists-managers prepared at our faculty receive not only full volume of economic knowledge, but also study the organization of healthcare and public health, plunging thus into environment of medical traditions of one of the oldest medical universities of Siberia. Besides, it has been

noticed that our graduates in private healthcare (drugstores, including rural, stomatology clinics, medical associations, etc.), and in administrative structures of city and regional healthcare where new innovative approaches are most actively used at economic activities conducting.

New educational standards not only meet the level of modern medical and biologic knowledge and guarantee quality of given medical care, but also are economically proved. Thus, at a stage of high school training of the future expert the correspondence of educational standards with standards of rendering of medical care is necessary.

In the nearest future, it is necessary to pass to personnel selection planning in each subject of the Russian Federation based on the Federal register of medical workers and developed standard documents, including documents, concerning a target enrolment of students. Therefore, development of the innovative program of professional training in territory of Tomsk oblast is priority for SSMU and the department of healthcare of the oblast.

The medical high school should become an active participant of healthcare developments and initiator of innovative projects in the branch.

It is necessary to restore and expand the lost traditions of interaction of medical high schools of the post-Soviet territory. Exchange of experience, joint development and adaptation of the educational programs based on the all-European approaches to the decision of problems of healthcare staffing, undoubtedly, will allow to accelerate integration of high schools within of Bologna Accords, and finally to improve public health and economic efficiency of management of the entire system of healthcare as a whole.

REFERENCES

[1] Handbook on Monitoring and Evaluation of Human Resources for Health with special applications for LOW - and middle-income countries, Geneva, WHO, 2009, 188 p.

[2] Svetlichnaya T.G. The actual problems of the professional personnel supply for regional public health, Problems of social hygiene, healthcare and history of medicine, no. 3, 2008, pp. 38-41.

[3] Mikhailova Yu V., Son J. M., Sokhov S.T., Danilova N.V., Shestakov M.G., Sasina N.S., Takhtarova Yu. N. Development of the health care personnel potential: state-of-the state and prospects. Healthcare of the Russian Federation, no. 1, 2008, pp. 52-54.

[4] Healthcare of the Tomsk region in 2010. The statistical collection. Tomsk: OSIH «Bureau of medical statistics», 2011, 67 p.

[5] Oreshin A.A., Kudelina O.V., Khlynin S.M. Prospects for development of medical care in the Tomsk Region. Healthcare of the Russian Federation, no. 6, 2009, pp. 48-50.

Towards an Images Dataset Processing trough Supervised and Unsupervised Learning

Nicoleta ROGOVSCHI Nistor GROZAVU
LIPADE, Paris-Descartes University, France
nicoleta.rogovschi@parisdescartes.fr
LIPN, Paris 13 University, France
nistor.grozavu@lipn.univ-paris13.fr

***Abstract* – Internet offers to its users an ever-increasing number of information. Among those, the multimodal data (images, text, video, sound) are widely requested by users, and there is a strong need for effective ways to process and to manage it, respectively. Most of existed algorithms/frameworks are doing only images annotations and the search is doing by these annotations, or combined with some clustering results, but most of them do not allow a quick browsing of these images. Even if the search is very quickly, but if the number of images is very large, the system must give the possibility to the user to browse this data. In this paper we investigate the use of the supervised learning to classify an images dataset and the unsupervised learning to browse the images. In our proposed schema, we used both PCA and LDA to transform the feature space and then to classify the dataset. We used this technique for all five datasets available on the challenge web site of The German Traffic Sign Recognition Benchmark: HOG1, HOG2, HOG3, HueHIst and Haar [7]. Finnaly we used a voting approach to find the consensus for all five partitions. Also, an application to the images browsing is shown using the topological unsupervised learning.**

***Index Terms* – content-based image retrieval, topological learning, clustering, self-organizing maps.**

I. INTRODUCTION

Producing visual data/content in digital form, even the visualization of the numerical data is becoming more and more common and affordable. Images datasets are becoming more common and widely used as visual information is produced at a rapidly growing rate.

Creating images and storing them became an easily and very used process for general use. Consequently, the digital visual libraries are growing and there is a strong need of adequate solutions to process this data and to extract relevant information from it.

The German Traffic Sign Recognition Benchmark competition task [7] is a multi-class classification problem. The dataset consists of 39209 images where 26640 are for training and 1569 images are for the test.

Five pre-calculated features sets were available for the Challenge: three sets of HOG features, Haar-like features and Hue Histograms having the size:

- HOG1: 1568 features;
- HOG2: 1568 features;
- HOG3: 2916 features;
- HueHist: 256 features;
- Haar: 11584 features;

The first phase to do when deal with large dataset is to transform the features space and to detect the irrelevant variables.

The second step is to apply a classification approach on the new dataset to learn a model and to affect the test data.

Finally, the last phase is the fusion of all the results (classification of the all) in order to obtain a global classification result combining all five pre-calculated features.

We tested several supervised learning approaches to obtain high classification accuracy as: neural networks based methods, and feature transformation techniques as Principal Component Analysis (PCA) and Linear Discriminant Analysis (LDA).

We observed that we can increase the classification result if the feature space is transform using a principal component analysis technique.

The traditional text-based approaches to image retrieval have proven out to be inadequate for many purposes. In some occasions, image databases have associated captions or other text describing the image content and these annotations can be used to greatly assist image search. Manually annotating large databases takes, however, a lot of effort and raises the possibility of different interpretations of the image content. As a result, content-based image retrieval (CBIR) has received considerable research and commercial interest in the recent years. One of the challenges is to automate the process of image retrieval and to make it separately from text annotation [5].

One of the most interests and used technique for data reduction and visualization in machine learning are the Self-Organizing Maps (SOM) proposed by Kohonen in 1998. This approach was used for image retrieval system called PicSOM [5] which use the tree structured SOM (TS-SOM) [4].

In this work we propose a novel technique which proposes to use the *lwo*-SOM [1] to attempt a 3D visualization and browsing of the dataset.

The rest of this paper is organized as follows: We show in section 2 the used feature transformation and dimensionality reduction approach. The supervised learning and the fusion technique used in the proposed method (section 5) are presented in sections 3 and 4. In section 5.A we describe the proposed unsupervised learning for images clustering and browsing, and we show the results using this technique on the Wikipedia images. Finally we offer some concluding comments of the proposed method and the further research.

II. FEATURES TRANSFORMATION AND DIMENSIONALITY REDUCTION

Principal component analysis (PCA) is a popular data processing and dimension reduction technique. As an un-supervised learning method, PCA has numerous applications such as handwritten classification, human face recognition, etc.

There is a strong link between the self-organizing maps (SOM) and PCA, as they have the same goal, i.e. to reduce the dimension and to visualize the dataset. This is why; we will use the both SOM and PCA as a pre-processing step for our model.

The PCA algorithm is presented as following:

Let the data **X** be a **n**x**m** matrix, where **n** and **m** are the number of observations and the number of variables, respectively.

The PCA estimation problem can be equivalently formulated as the following optimization problem, in which the sum of estimation errors from all variables is minimized:

$$R_{PCA}(\hat{\alpha}, \hat{z}_i) = \arg\min \sum_{i=1}^{N} (x_i - \widehat{x_i})^T (x_i - \hat{x}_i)$$

$$with \quad \hat{x}_i = \hat{\alpha}\hat{z}_i, \quad and \quad \widehat{\alpha^T}\hat{\alpha} = I$$

where xi and $\hat{x}_i$ are the i-th measured and estimated observation, and $\hat{z}_i$ represents the the estimated principal component corresponding to the observation xi.

In order to detect the number of eigenvalues values, we use the Cattell's Scree Test which is a graphical method first proposed by [8].

The basic idea of the Scree test is to generate, for a principal components analysis (PCA), a curve associated with eigenvalues, allowing random behavior to be identified (a simple line plot). Cattell suggests finding the place where the smooth decrease of eigenvalues appears to level off to the right of the plot. To the right of this point, presumably, one finds only "factorial scree". Non graphical solutions to the Cattell scree test are also proposed: an acceleration factor and the optimal coordinates index. The acceleration factor indicates where the elbow of the scree plot appears. It corresponds to the acceleration of the curve, i.e. the second derivative. Frequently this scree is appearing where the slope of the hill changes drastically to generate the scree. It is why many researches choose the criterion eigenvalue where the slope changes quickly to determine the number of components for a PCA. It is what Cattell named the elbow. So, they look for the place where the positive acceleration of the curve is at his maximum. Cattell's scree test and Bartlett's chi-square test for the number of factors to be retained from a factor analysis are shown to be based on the same rationale, with the former reflecting subject sampling variability, and the latter reflecting variable sampling variability. In the Cattell scree method, we can interpret the eigenvalues as the degree of relevance of each factor axis. The concept of covariance or correlation matrix is not appearing and is not necessary. Therefore, this method is not specific to PCA or a factorial analysis. The number of variables retained is equal to the number of values preceding this 'scree'. We therefore needed to identify the point of maximum deceleration in the curve.

Figure 1 shows an example of a curve generated using a data vector.

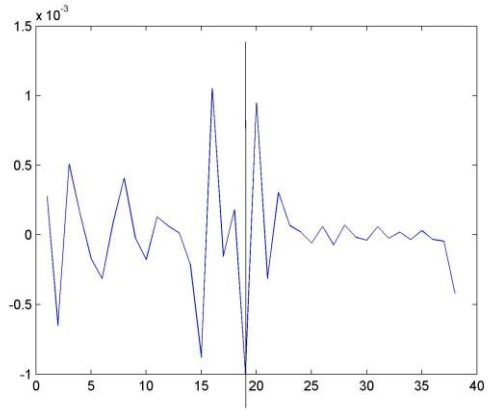

Figure 1: The Scree Test Acceleration Factor

We thus executed the following steps presented in the Algorithm 1.

Algorithm 1: The Scree Test Acceleration Factor

Input: a vector π_j size d

For $i = 1$ to d Sort the weights in descending order $\pi^{[j]}$.

Thus we obtain a new order $\pi^{[j]} = (\pi^{[j],1}, \pi^{[j],2}, \ldots, \pi^{[j],i}, \ldots, \pi^{[j],d})$; where i indicates the index order.

End for

For $j = 1$ to d (on the sorted vector)

Compute the first difference $df_i = \pi^{[j],i} - \pi^{[j],i+1}$ and we obtain the vector $\pi_{df1}^{[j]}$

End for

For $p = 1$ to d (on the $\pi_{df1}^{[j]}$ vector)

Compute the second difference (acceleration) $acc_i = df_i - df_{i+1}$ obtaining the vector $\pi_{df2}^{[j]}$

End for

For $l = 1$ to d (on the $\pi_{df2}^{[j]}$ vector)

Find the scree: $\max_i (abs(acc_i) + abs(acc_{i+1}))$

End for

OUTPUT:

Retain all the features displayed before the scree (we used the initial index values of features before sorting).

A.Complexity of the Scree Test procedure

The Scree Test acceleration procedure has four steps until finding the scree in the vector. We will analyze all these steps:

• Ascending sort: to made the sort of the weight vector we are using the Merge sort procedure which has an logarithmic complexity: $O(d \log d)$;

• First difference: the complexity for the first difference

df_i is the $O(d)$;

• Second difference: for the second difference the complexity is the same as previously: $O(d)$;

• Find the scree: to find the scree in a vector, the complexity will be $O(d)$.

As there is no nested loop, the total computational time for the Scree Test acceleration algorithm is the sum of the complexity of the four steps, and respectively it will be $O(d \log d + 3d)$.

III. CLASSIFICATION

As classification model we test the supervised Self-Organizing Maps and the Linear Discriminant Analysis, and we note that the use of the PCA improves the classification results. So, for all the dataset the LDA were used.

Given a dataset **X** size **n**x**m**, where **X = x₁, x₂, ..., xₙ** represents the set of object with m features.

Let, $B \in R^{nxp}$ be the transformation matrix that maps these features to p-dimensional features, i.e. $z_j \in R^p$ (j=1,...,m), and $z_j = B^T x_j$.

$$R_{LDA}(B) = \frac{|B^T \sum_b B|}{|B^T \sum_w B|}$$

where

$$\sum_w = \frac{1}{N} \sum_{k=1}^{c} \sum_{x_j \in D_k} (x_j - \mu_k)(x_j - \mu_k)^T$$

is the within-class covariance matrix, and

$$\sum_b = \sum_{k=1}^{c} P_k (\mu_k - \mu)(\mu_k - \mu)^T$$

is the between-class covariance matrix.

Indeed to use the initial dataset as input for the LDA method, we use the eigenvalues vectors issues from the PCA.

IV. FUSION

There are two types of combining classification (clustering) results: the fusion and the collaboration.

The goal of the fusion based techniques is to find a consensus for all the results using a fusion approach, as is the voting procedure. Contrarily, the collaborative classification is based on the changing the information during the learning process.

For this challenge, we tested the both types of methods, and we conclude that for these datasets, the better one is the fusion method.

As fusion method technique we use the voting principle.

V. PROPOSED METHOD

We introduce in this section the proposed methodology using the principal component analysis within the Cattel ScreeTest and Linear Discriminant Analysis for the classification. The method is used for all five datasets and the classification results (the labels vectors) are used to find the consensus by applying a voting technique.

Algorithm 2 : Proposed method

Input: images vectors vector $x_i \ldots x_n$

For i =1 to n (for all datasets)

PCA with U 1100 eigenvectors on the train data

For j=1 to m (on the development dataset) :

Apply LDA on the U and obtain the model M;

End For

Plot the test data on the same features space using the U and obtaining Ut;

Affect the Ut to the model M;

End For

Output: Label of the test data;

We repeat the algorithm for all five datasets by computing the accuracy index for all of them.

At the end we use a fusion technique to fusion the classification results using a voting approach.

VI. EXPERIMENTAL RESULTS

Using the proposed method to all datasets, we obtain a classification accuracy index equals to 95.47 %, but we found that using only the HOG2 and HOG3 datasets, the accuracy index grow up to 96.53%.

Note that we classified the dataset using the LDA algorithm on the result of a PCA with 1100 eigenvectors.

A.Visualization

Even the topological learning methods doesn't improve the results for this challenge compared to the PCA and LDA, it allows the visualization of the classification results.

So, in this section we show an example of an extended SOM algorithm to classify and to browse a images dataset proposed by Rogovschi and Grozavu [9].

1)Images topological map browsing

The topological learning allows building a multi-level map which could be benefit to browse an images dataset by levels.

Firstly, we visualize the map with the best matching units (the most representative images) and then, we can choose the next level to visualize (or to skip some levels) until we are satisfied of the result. This process is doing in a 3D (hierarchical) visualization by displaying the maps with the corresponding captured images step by step like shown in the figure 1.

Our purpose is to automate the browsing task using not only the annotated text, but also the similar images founded during the unsupervised learning.

The idea is to present an images map to the user in order to detect not only the searched image, but also the similar images from the map (neighbored cells using the Euclidean distance). Furthermore, a cell from the map (the best matching unit) can be used to represent many others similar pictures, and will accurately suggest the kinds of pictures that will be found by exploring the respective cluster.

The figure 1 shows the map with the best matching units (first level), and the next 3 levels of the maps. For each map the neighborhoods displayed images are correlated between

them, and one can detect also some cells which are empty, because there are cells which captured only 1, 2, or 3 images. So displaying the map level which is greater then the size of the captured images vector for a cell, the respective cell will display an empty (white) image to show that where are no more correlated images to the last one.

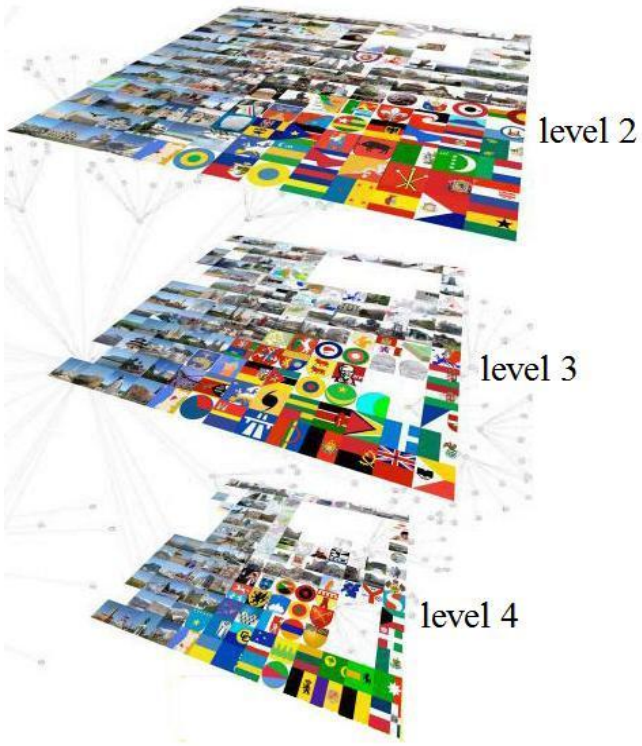

Figure 2. Images DataSet browsing using *lwo*-SOM technique.

VII. CONCLUSION

In this paper we adapted the supervised and unsupervised learning to deals with an images dataset. For the supervised learning we used the PCA and LDA algorithms coupled within a fusion approach. This new methodology was tested on the challenge of The German Traffic Sign Recognition Benchmark obtaining good results.

For the unsupervised learning, we presented a novel solution for manage and process visual datasets. We used the lwo-SOM [1] which allows us to do a better classification of the data and to obtain more correlated images on the map.

As future work, the fusion of both methods (to classify and to browse the images dataset) will be an interested challenge.

REFERENCES

[1] N. Grozavu, Y. Bennani, M. Lebbah. From variable weighting to cluster characterization in topographic unsupervised learning. IJCNN, Atlanta, USA, 2009.

[2] C. Julien, and L. Saitta. Image databases browsing by unsupervised learning. ISMIS, 2008.

[3] T. Kohonen, Self-Organizing Maps. Springer Berlin, 2001.

[4] P. Koikkalainen. Progress with the tree-structured self-organizing map. In Proc. 11th Europ. Conf. Artificial Intell., 1994.

[5] M. Koskela. Interactive image retrieval using self-organizing maps. Dissertation Repport, 2003.

[6] F. Perronin and C. Dance. Fisher kernels on visual vocabularies for image categorization. page 1-8, 2007.

[7] Johannes Stallkamp, Marc Schlipsing, Jan Salmen, and Christian Igel. The German Traffic Sign Recognition Benchmark: A multi-class classification competition. In submitted to International Joint Conference on Neural Networks, 2011.

[8] R. Cattell. The scree test for the number of factors. Multivariate Behavioral Research, 1:245–276, 1966.

[9] Rogovschi N., GROZAVU N. (2010), « A content-based image retrieval system based on unsupervised topological learning», in Proc. ICMIA'10 : IEEE International Conference on Data Mining and Intelligent Information Technology Applications, November 30 - December 2, 2010, Seoul, Korea.

Use of Telemedicine in Pilot Centers within the Perinatal System

P. STRATULAT*, Tatiana CARAUŞ*, M. BLUNIER**, Ala CURTEANU*
*- *Mother and Child Research Institute from the Republic of Moldova*
**- *Swiss Tropical and Public Health Institute*

***Abstract* – In the last decade of the twentieth century in many countries rapidly has developed telemedicine. Telemedicine is not a separate discipline within the health system, but a "transfer of information at distance regarding patient's medical care." In the Republic of Moldova telemedicine implementation into perinatal system started in 2009 in four pilot centers: *MCRI (level III), CP Hospital no. 1 Chisinau, CP Balti and CP Cahul (level II).* Thus the creation and development of this interdisciplinary network of teleconsultation and telediagnostic has followed the improvement of health care services quality and decrease of their costs, increasement of quality of patients life in perinatal system, orienting themselves to consultation of serious neonatal and obstetric cases from level II Perinatal centers. Although it's on its beginning, telemedicine network in the frame of perinatal sytem has already achieved success. Cooperation between specialists from levels II and III of perinatal care has strengthened, interactive work and multidisciplinary cooperation between obstetricians-gynecologists and radiologists, imagists have strenghtened also.**

I. INTRODUCTION

In the last decade of the XXth century the Telemedicine has rapidly developed in many countries. Telemedicine is not a separate discipline within the health system but a „*transfer at distance of the information regarding medical care for a patient*". Telemedicine represents a potential to improve medical care worldwide through the diversification of medical services which will be offered to communities and individuals who do not have the access to these services, both from urban and rural areas. In addition, Telemedicine can help to attract and retain in rural areas health professionals in the medical field via continuous education and collaboration with other professionals in the field from other centers (tertiary, educational [1,2,3].

II. MATERIAL AND METHOD:

In the Republic of Moldova the implementation of the Telemedicine into perinatal system started in 2009 in four pilot centers: *MCRI (level III), PC Hospital nr. 1 from mun. Chisinau, PC Balti and PC Cahul (level II).* Thus, the creation and development of this interdisciplinary network of telediagnostic and teleconsultations aimed to improve quality of health care and to lower their costs, to increase the quality of patient's life from perinatal system being oriented to the consultation of neonatal and obstetrical cases from II level perinatal centers. This component of the Project offers a possibility to consult, make diagnosis and carry out medical trainings at distance for all medical staff within the perinatal system between III level institutions and II level pilot centers with the help of lecturers from the Medical University "Nicolae Testemițanu"; unclear or difficult cases must be consulted with specialized clinics from abroad. Thus, the pilot institutions, where 40% out of total number of deliveries take place and where severe newborns and premature babies are concentrated, have been identified during the *first stage.* The number of working places from wards and NICU from pilot institutions has been identified. 16 computers with web cameras, color printers, scanners and digital cameras have been procured to document data for clinical cases as much complete as possible, later 3 more notebooks were procured for presentation of newborns, of VAP and SiPap parameters, monitors within the consultations with II level pilot centers.

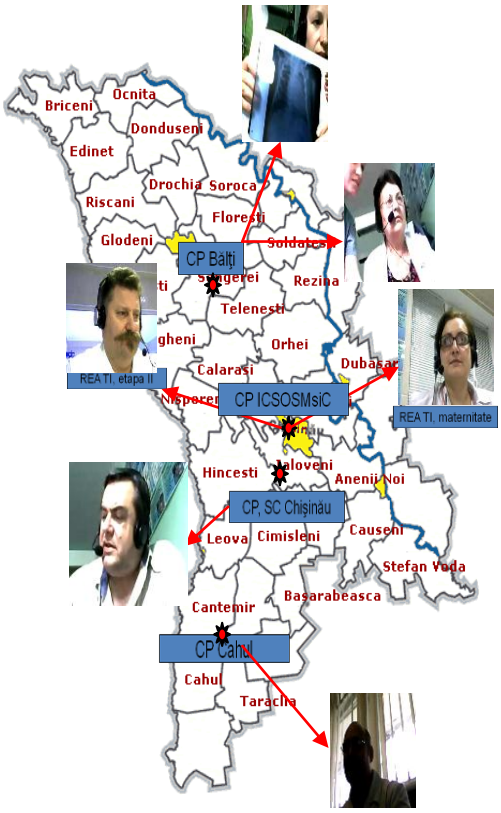

Fig.1. The Telemedicine system within the perinatal system of the Republic of Moldova

The Telemedicine's implementation was approved by the MoH Order nr.285 from 18.08.2009 "*On implementation of Telemedical consultative system in perinatal pilot centers*" in 4 pilot centers: MCRI (level III), PC Hospital nr. 1 from mun. Chisinau, PC Balti and PC Cahul (fig.1). According to this Order, the list of specialists who will activate as consultants from the Departments of Obstetrics, Gynecology and Neonatology from the Medical University "N. Testemițanu" was created. Also, through the telemedicine

system the MCRI, level III perinatal center within the regionalized system, carries out consultation of severe neonatal and obstetric cases from level II perinatal centers. Unclear and difficult cases from MCRI are consulted with the specialized clinics outside the republic. During the *second phase the obstetric and neonatal cases* needed to be placed at the iPath platform were identified.

This platform for Telemedicine was designed for the Republic of Moldova to facilitate the exchange of information and communication between professionals working in health sector providing the following functionality: creation of discussion groups on various health topics being a link of continuous education to perinatal system. National working group together with consultants from Switzerland have identified and created four working groups that are placed at local international platform iPath:

- Test group
- Perinatal Health
- Regional Group (Moldavian-Romania-Ukrainian)
- Health Technologies Management

Initial areas of users' interest are Telemedicine in perinatal system and Health Technology Management; within each of the discussion group the members can: present and discuss cases (medical) in order to exchange information and opinions, organize consultations at distance via which the specific cases are presented to colleagues to provide a second opinion.

On this platform the following specialists are registered: obstetricians/gynecologists, neonatologists, radiologists, pathomorphologists, traumatologists and other professionals. Currently, the Telemedicine system in perinatal system offers us:

1) *Teleconsultations in* specialization of obstetrics and neonatology (during 24 hours)

2) *Teleradiology* - on-line consultation of radiological images during 24 hours;

3) *Teleeducation* - training for specialists at distance.

III. RESULTS:

Fig.2. On-line consultation at distance via iPath network by III level specialist, consultation of neonatal case from PC Balti

The Telemedicine System within perinatal service is the first unit in the country where the teleconsultations, investigations of patients at every level of the country are practiced effectively and can easily be followed and interpreted on-line by specialists from III level, where consultations at distance via audio-video connection are provided. After the birth of a severe baby in one of II level Perinatal Centers, the specialist from the territory during the first 2 hours comes into contact with one of the consultants from the level III (MCRI), the consultation is provided on the basis of audio-video communication, as well as via tracking of health indicators (*Ps, TA, FR, SaO_2*), laboratory examinations data exposed in the questionnaire of Perinatal Health group, as well as of Rx examination data or other investigations placed at the iPath platform. Diagnosis is made in real time by doctors-consultants who decide which must be the tactics of investigations, treatment or where the patient must be transported to receive the appropriate treatment as soon as possible. During the past year, specialists from the second level pilot centers have benefited from consultations of images (radiography and USG).

Weekly the teleconferences of neonatologists from the pilot institutions are held in the morning: every week on Tuesday and Friday doctors from all departments of the MCRI take part in these conferences, the cases are presented briefly in a narrative form, the results of investigations are reported, then it is made the contact with NICU from pilot PCs (Hospital No.1, Balti and Cahul) which present severe and complicated cases that took place over a week and have been placed at iPath, there is a possibility to show the baby via video at notebook. A positive factor is the participation of doctors from pilot centers in these clinical conferences, those who are present have the opportunity to ask questions, to express their opinion on the diagnosis and treatment of patient, thereby increasing the quality. Next is the description of the pilot centers' experience in use of iPath platform. During this period of time, until 01.03.2011, 163 of users became registered at iPath platform, out of them: obstetricians-gynecologists 79 (49%); *neonatologists* – 48 (20%); doctors-imagists – 3(2%); other professionals – 33 (29%). In 2010 over 300 of emergent Telemedicine calls took place, all from 3 II level PCs from the country (PC Hospital nr.1 from Chisinau, PC Balti and PC Cahul).

In the frame of the Working Groups 376 cases totally were registered on the platform:

1. Group Perinatal Health – 330 (305 clinical cases + 25 information).
2. Test group – 40.
3. Regional Group (Moldavian-Romanian-Ukrainian) in Perinatal Health –
4. Health Technologies Management – 41 (instructions, guidelines for users, regulations, forms which are elaborated in clinical departments to ensure the equipment's maintenance).

Out of 376 of cases placed on the platform the specified are the following: obstetric cases – 79(21%); *gynecological* – 1(0,26%), *neonatal* – 270 (72%), *pediatric (sugar)* – 1(0,26%) and other information (guidelines, protocols, traduced articles) - 25 (7,0%).

There were comments placed for 223 cases (63, 7%), those confirming the diagnosis - 92%, treatment – 90%, and medication– 91%. Thanks to teleconsultations offered to patients from II level pilot centers, especially from the Balti Perinatal Centre and Cahul Perinatal Center, the transportation of patients to level III has decreased by 30%, thus reducing the costs for newborns transportation to III level and travelling of specialists within AVIASAN service. In Phase III (2011) the Telemedicine service will be extended to other II level perinatal centers, which will be equipped with audio-visual equipment and Internet connection.

IV. CONCLUSIONS:

1. Although it is on its first stage, the Telemedicine network within perinatal system has already achieved the success.

2. The cooperation between specialists from II and III level of perinatal care, multidisciplinary collaboration and interactive work of obstetricians-gynecologists, radiologists and imagists have been strengthened.
3. The educational part has improved – the level of knowledge has increased (precision of diagnosis, treatment) and, as a result, practices and quality of care were also improved.
4. Motivated by a continuous desire to increase effectiveness/costs, we succeeded that the teleradiology became a significant part of everyday practice.
5. Telemedicine ensured saving of time and financial resources provided for necessary transportation (has minimized the number of travelling of Aviasan specialists for consultation of case).

REFERENCES**:**

[1] Kenneth Tan, Nai Ming Lai. Telemedicine for the support of parents of high risk newborn infants.
[2] Chan DS, Callahan CW, Sheets SJ, Moreno CN, Malone FJ. An Internet-based store-and-forward video home telehealth system for improving asthma outcomes in children. *American Journal of Health-System Pharmacy* 2003;60:1976-81.
[3] Jaatinen PT, Forsstrom J, Loula P. Teleconsultations: who uses them and how?. *Journal of Telemedicine and Telecare* 2002;8:319-24
[4] Introduction to telemedicine / Ed. by R. Wootton, J. Craig. – London: The Royal Society of Medical Press, 1999. – 208 p.
[5] Coiera E. Guide to medical informatics, the Internet and telemedicine. – Chapman and Hall Medical, 1997. – 376 p.
[6] Spooner SA, Gotlieb EM. Telemedicine: pediatric applications. *Pediatrics* 2004; 113Şe639-43.

SonaRes - Computer-Aided Approach for Advanced Ultrasound Medical Diagnostics

Liudmila BURTSEVA, Svetlana COJOCARU, Constantin GAINDRIC,
Olga POPCOVA, Iulian SECRIERU
Instiitute of Mathematics and Computer Science of the Academy of Sciences of Moldova
gaindric@math.md

***Abstract* – Ultrasound image is the primary (input) information for every ultrasound examination. Despite the difficulties of ultrasound image interpretation, this source of information is still significant for diagnosis decision making. This paper describes the experience of SonaRes diagnostic decision support system (DDSS) for ultrasound examination development. Considering two-layer structure of the information contained in ultrasound images, two main approaches in DDSS creation may be distinguished: Image-based systems and Knowledge-based systems. In the SonaRes the advantages of both are combined. In the process of any DDSS development there are three points of major importance, influencing essential the success: i) knowledge acquisition and formalization; ii) image processing and search for similar ones, and iii) interaction with user [1]. SonaRes – represents one of the possible solutions to these problems aimed at increasing the DDSS functionality, user attitude and, as a result, adequacy of generated conclusions.**

***Index Terms* – computer-aided approach, knowledge, ultrasound image, decision support, medical diagnostics.**

I. INTRODUCTION

Diagnosis is a process consisting of separate steps. These steps begin with establishing the certain facts in the process of examination and lead to the inference that the obtained facts correspond to some conclusion or begin with some preliminary diagnosis achieving the conformity of the set of objective facts of the patient state to confirm the presumptive diagnosis or reject it, if the facts do not correspond to or contradict the assumption.

In general case DDSS medicine are not intended to replace the physician, their role being to give clinician recommendation on his request or draws automatically his attention to the special cases (cases of alerts).

Obviously, DDSS are targeted on a specific area, which may be more or less broad, and the domain of their applicability is defined by a pathology (a group of pathologies) or a diagnostics method, which in its turn is oriented to certain pathologies (group of pathologies or organs). The subject of our work is development of decision support systems for diagnostics based on ultrasound examination.

II. DECISION SUPPORT SYSTEMS IN ULTRASOUND DIAGNOSTICS

The ultrasound examination of patients, being non-invasive and not expensive, is a basic technique of medical imaging.

Ultrasound image is the primary (input) information for every ultrasound examination. The main characteristic of these images is two-layer structure of the information contained in it. The first layer is the image itself (graphical features), and the second layer is its textual description in medical terms (medical features).

However, utilization of this technique does not always come up to expectations, encountering some difficulties associated with the dependence on operator, which affects the quality of the obtained images, and the way the results are differently described and interpreted by several specialists. Besides the difficulties of ultrasound image interpretation, because of the speckle, tissue related textures and artifacts, this source of information is still significant for diagnosis decision making.

Computer-aided diagnosis schemes has been subject to various research since 1980, when a number of medicine domains began to use computer assistance [2]. During these years, huge databases of medical images were created and became a powerful source for decision making. Taking into consideration these tendencies, two main approaches to create DDSS systems can be distinguished:

- Image-based systems;
- Knowledge-based systems.

A joint realization of decision making and image retrieval in DDSS development leads to new explicit domain-specific knowledge and better results in many applications. Moreover, research in medical image analysis tries to find links between image features and knowledge in order to fulfill quantification tasks and to answer prognostic questions.

There are three points of major importance, influencing essential the success of DDSS, are the following:

- Knowledge acquisition and formalization;
- Image processing (with extraction of knowledge from the images, if possible) and search for similar ones;
- Interaction with user.

The way these issues are resolved determines the functionality, user attitude and, as a result, adequacy of generated conclusions.

In what follows, we will discuss these points, basing on solutions realized in the SonaRes – a Diagnostic decision support system for ultrasound examination of the abdominal region.

III. KNOWLEDGE ACQUISITION IN ULTRASOUND DIAGNOSTICS DOMAIN

There are 5 main stages in the development of knowledge-

based systems [3]:

1. Problem identification;
2. Knowledge acquisition;
3. Knowledge structurization;
4. Knowledge formalization;
5. Prototype development.

The phase of knowledge acquisition and formalization is considered as the key one for the development of medical computer-assisted systems (decision support, adaptive training, learning, etc.).

During the second stage of the development of knowledge-based systems – *knowledge acquisition* – the expert competence and knowledge should be transferred to "knowledge engineer", aiming the "knowledge engineer" to obtain the fullest subject domain representation. The process of knowledge acquisition in ultrasound investigation domain on an example of separately taken organ (gallbladder) is described in details in [4].

The necessary knowledge about ultrasound investigation of gallbladder was acquired from the experts-physicians:

- Gallbladder localization information (including methodology of visualization in typical location, objective conditions of non-visualization or difficult visualization in typical location, causes of non-visualization in typical location);
- Information about the gallbladder pathologic states (chronic cholecystitis, compressed gallbladder, scleroatrophic gallbladder etc.);
- Principal characteristics of gallbladder description (dimensions/volume, shape, tonicity, gallbladder contour etc.);
- Gallbladder anomalies and pathologies information, every anomaly or pathology being determined by changes in principal characteristics of gallbladder description (dimensions anomalies, shape anomalies etc.).

IV. ASPECTS OF KNOWLEDGE STRUCTURIZATION IN UNSUPERVISED EXPERT'S WORK

At the third stage of the development of knowledge-based systems – *knowledge structurization* – the structure of the subject domain acquired knowledge (the list of the basic concepts and their attributes, the relationships between them, the structure of the input/output information, decision-making strategy, etc.) should be defined. The aim is to obtain the informal knowledge description of the subject domain as a graph, a table, a diagram or a formatted text.

In the beginning, the loss in knowledge acquisition dialogue was considered the most essential drawback at the interaction expert-"knowledge engineer", when the volume of information, possessed by the expert, differs from the remembered and communicated one, that is much more than information, listened by "knowledge engineer", and finally, essentially differs from knowledge volume, formalized and stored in knowledge base. Moreover, the information received from the expert can be apprehended incorrectly by the "knowledge engineer" that will cause mistakes in knowledge base. So, the time-consuming procedures of the explanation and additional control are necessary, leading the time, spent for interaction between the expert and the "knowledge engineer", to influence terms of knowledge base creation. Therefore, was created an expert environment – knowledge base generator, accessible to expert with intuitively clear graphical interface – ExpShell [5]. In this case the expert himself had to supervise the process of knowledge base filling from the beginning up to the end, but the "knowledge engineer" only defines the method of data storage and representation.

ExpShell allowed expert to describe the subject domain in a free form. The expert has possibility to work simple and clear only in two routines: 1. filling the list of facts, used in gallbladder ultrasound investigation domain; 2. selecting already introduced facts and establishing in graphical interface the existent relationships between the facts – connections of type $\rightarrow$, & and $\neg$. As the result a decisional graph that describes a diagnostic feature / pathology / anomaly of gallbladder is obtained. Using this ExpShell, expert knowledge considered the most important (58 facts and 30 decisional graphs) was acquired.

The analysis of the acquired knowledge has shown that its further use for decision-making process is very difficult because of its weak structurization. Since there was no clear distinction between the facts and rules, the additional verification of acquired knowledge was required (often the same diagnostic feature, participating in different pathologies, was described by different sets of facts). Therefore, the tactics of knowledge structurization was changed.

Since the quality of acquired knowledge is the determinant factor in successful realization of any knowledge-based system, the decision was to turn to the traditional method of knowledge acquisition (with participation of "knowledge engineer") [6].

V. KNOWLEDGE REPRESENTATION SCHEMES

At the forth stage of the development of knowledge-based systems – *knowledge formalization* – the representation form (language) for acquired and structured knowledge should be selected. The formalized representation of problem domain concepts is created basing on of the chosen knowledge representation form.

The fundamental goal of knowledge representation is to represent knowledge in a manner to facilitate drawing conclusions (inference) by the computer-assisted systems.

We distinguish two approaches – single and hybrid knowledge representation schemes.

There is no single or hybrid scheme to satisfy end-users preferences and/or all the requirements of knowledge-based systems developers. So, taking into account only the system requirements on the knowledge acquisition stage, one can say that semantic nets, decision trees, frames and description logics are more suitable to represent medical knowledge [7].

For SonaRes system we have chosen the decision tree as a model of acquired knowledge representation. Basing on the principles of the decision tree scheme, the knowledge base of gallbladder ultrasound examination domain has been established.

VI. KNOWLEDGE STRUCTURIZATION AND FORMALIZATION DURING EXPERT-"KNOWLEDGE ENGINEER" INTERACTION

The information obtained from the experts-physicians was structured, formalized and introduced by the "knowledge engineer" in knowledge base (a pyramid of meta-concepts, and a set of rules created on its basis), marking out 9 main characteristics for gallbladder ultrasound investigation,

representing principal nodes. Other nodes are connected to principal ones by hierarchical links, forming a tree structure of "attribute" and "value" nodes. The knowledge pyramid has 335 nodes with at most 9 deep levels.

Using obtained knowledge pyramid, 54 decision rules for gallbladder pathologies and anomalies determination were created. The analysis of 54 rules obtained for gallbladder shows, that in addition to the normal state and anomalies, we also embraced all basic groups of pathologies. Moreover, creation of the rules with a simple structure gives possibility to describe diagnostic of some simple structures and solitary lesions, as well as of any complex pathology, which consists of several separate pathologies: for instance, acute gangrenous lithiasic cholecystitis associated with solitary adenomatous polyp and focal cholesterosis. Description of the complex pathologies can be obtained by combining the existing rules. The obtained knowledge base describes completely the ultrasound investigation process of gallbladder.

Common work of the "knowledge engineer" and experts has shown that in ultrasound investigation domain the reasoning with metaconcepts (facts) and knowledge representation as a pyramid completely corresponds to the experts' mentality and thinking. However, the division of metaconcepts up to the level of objects, concepts and their attributes, and construction of further reasoning on their base is not always clear to the experts, especially, if we demand this at the initial stage of knowledge acquisition.

VII. KNOWLEDGE MANAGEMENT TECHNIQUES

The development of the user's interface for the medical computer-assisted systems basing on the decision tree can lead to various problems and inconveniences. The main lack is the fact that the user's interface does not correspond to the daily work and habits of the end-user – physician. Moreover, the discrepancy of the user's interface of the medical computer-assisted systems and with the form of physician's diagnostic thinking may become the reason of different mistakes or may lead the user to reject its utilization in his medical practice.

To organize an effective dialogue with end-users and to eliminate the mentioned deficiencies an alternative representation scheme of the knowledge base was created in the SonaRes system.

The source of information for the alternative representation scheme is the knowledge base, described as a decision tree. It was necessary to propose such a representation of the acquired knowledge in order to have the opportunities to realize an adaptive user interface with the following features:

- The interface should be simple and understandable. The dialogue with the end-users should take place in its usual rhythm and form, and should not require the changes in his reasoning.
- The interface should correspond to the end-user's daily work and preferences. The end-users should have possibility to influence the dialogue form.
- The interface should be "transparent". The solution proposed by the inference of medical computer-assisted system should be easily to verify.
- The dialogue with the end-user should not have a linear structure. The end-user always should have the opportunity to return to the appointed step back.
- The interface should be adaptive. It should change, depending on time available to the end-user to make a decision. In addition, the interface should conform to the basic forms of end-user diagnostic thinking.
- The interface should not restrict unnecessarily the end-user's actions.
- The interface should be oriented on the restricted screen space and on limited decision making time. The end-users often have to use the system in an emergency or in a network mode.

The dialogue is the most common form of communication and information transfer. Therefore, the organization of the user interface as an ordered set of questions is justified.

The essence of the proposed new representation approach is the separation of knowledge into one, used in the inference, and other, used only in the interface [7].

At the first step of the creation of the alternative representation of the knowledge base there were determined those facts of the decision tree, which are involved in the inference.

For each fact a question concerning the existence or non-existence of this fact was formulated. For instance, for the fact F1=<gallbladder volume, normal> there was formulated the question Q1="Is the volume of gallbladder a normal one?", for the fact F2=<gallbladder volume, enlarged> – the question Q2="Is the volume of gallbladder enlarged?", and for F3=<gallbladder volume, reduced> – Q3="Is the volume of gallbladder reduced?".

As a result, 203 questions were formulated. Answering to some of these questions, the user can describe the case from gallbladder ultrasound investigation domain. All of 54 pathologies and anomalies of this domain were described in terms of these questions.

At the second step we have stored all existing relationships between the facts. So, we have elaborated an interconnection system between all formulated questions.

There are two types of relationships between facts in the decision tree. The first one indicates the position of a given fact in the knowledge base hierarchy. The second type of relationships indicates the existence of interdependence between the facts.

These relations do not depend on the form of visualization of the facts or the whole user interface, but represent the basis of the system's knowledge base and inference.

Separation of the existing relationships between the questions in two groups – those, used in inference, and those, used only in the interface, allows us to create a high-quality adaptive interface based on the individual characteristics and habits of the end-user. It is achieved because the user can define himself the subject and the form of dialogue (by changing the visualization relationships between the questions), without any fear to influence the inference.

Additionally, the questions grouping will allow to diversify the form of dialogue.

This approach allows realization of different versions of the user interface with restricted screen space and limited time for the decision making (for instance, medical computer-assisted systems used in emergency cases).

VIII. CHALLENGES AND SOLUTIONS IN UTILIZATION OF ULTRASOUND IMAGES. IMAGES RETRIEVAL

As mentioned above, ultrasound images have a dual nature considering information they hold. A part of this information is related to visual representation and can be managed by computer graphics techniques. But the most specific feature of this type of images is their medical content. To manage this type of information the *content-based image retrieval technology* is usually used.

SonaRes system collects a set of "model" (representative) annotated ultrasound images. The acquiring of the "model" ultrasound images represents a continuing process, where the experts-physicians play a leading role, providing the ground truth. Experts associate these images to the corresponding rules. On static images the regions of interest (ROIs) are marked out. These ROIs are associated to particular characteristics of the organ – facts (nodes of the knowledge pyramid).

The "model" ultrasound images are stored in SonaRes image database. These are gray-scaled images, mainly, of *.jpg and *.bmp storage formats. It is supposed that the future additions can also be represented in non-DICOM formats.

To provide the ROIs marking, association between ROIs and nodes as well as between images and rules, the special tools for work were developed. These tools help experts to realize of the following actions:

- ROIs management – allowing marking out the ROIs (as a contour of connected points) as well as other operations: addition, deleting and viewing ROIs;
- visualization of all ROIs corresponding to the selected node on different images;
- visualization of all ROIs (corresponding to different nodes) on the chosen image.

In SonaRes system the role of annotated images in decision making process is to be a correct helpful illustration, if the physician is not sure how to interpret an ultrasound image. Since the results of SonaRes images retrieval serve mainly as help for the user, the corresponding tool was placed in the part of SonaRes web-interface.

The retrieving process starts with pattern image uploading and optionally setting an own ROI (as a restriction to avoid time-consuming and to increase retrieval accuracy). After the process is finished, the web-gallery of similar images is shown.

The images preview thumbnails are clickable. If one of these images is selected by the user – a new window is opened, showing the full size view of the image, matched ROI and its annotation.

The most fruitful method for retrieving similar ultrasound images seems to be the application of both medical features (obtained from a knowledge base) and visual features (obtained from images). Retrieving based on medical features allows confirmation of the diagnosis assumption by obtaining a gallery of images containing the supposed pathology or fact.

Retrieving based on visual features allows user to select the most appropriate image from obtained list of similar ones. The combined retrieval, using medical and visual features, makes possible to search a visual representation for textual description of medical feature and conversely to find the textual explanation for visual feature.

ACKNOWLEDGMENT

The research for this paper has been partial supported by the common project of the Academy of Sciences of Moldova and the National Authority for Scientific Research of Romania, grant 10.820.08.06/RoA.

REFERENCES

[1] S. Cojocaru, C. Gaindric, Decision support system in ultrasound investigations, *Proceedings of XIII International conference KDS-2007*, vol. 1, ITHEA, Sofia, Bulgaria, 2007, pp. 241-246.

[2] K. Doi, "Computer-aided diagnosis in medical imaging: historical review, current status and future potential," *Comput Med Imaging Graph* 31(4-5), 2007, pp.198-211.

[3] Т.А. Гаврилова, К.Р. Червинская, *Извлечение и структурирование знаний для экспертных систем*, 1992.

[4] Iu. Secrieru, O. Popcova, S. Puiu, D. Sologub, "Knowledge Structure Modeling in Ultrasound Investigation Domain", *Proceedings of the 5th European Conference on Intelligent Systems and Technologies (ECIT 2008)*, Iasi, Romania, July 10-12, 2008, CD.

[5] Iu. Secrieru, D. Sologub, Expert shell aimed at creation of the knowledge base for ultrasonic research intelligent system. *Revista de inventica* nr. 48, vol. IX (XV-2005), pp. 7-12.

[6] L. Burtseva, S. Cojocaru, C. Gaindric, E. Jantuan, O. Popcova, I. Secrieru, D. Sologub, SONARES – A decision support system in ultrasound investigations, *Computer Science Journal of Moldova*, vol.15, nr. 2 (44), 2007, pp.153-177.

[7] Iu. Secrieru, Structured knowledge management techniques for the development of interactive and adaptive decision support system, *Computer Science Journal of Moldova*, vol. 17, nr. 1 (49), 2009, pp.58-73.

Information System Analysis of Heart Rate Variability

Victor SONTEA, Anatolie IAVORSCHI, Valerii PAHOMI, Valeriu PIRTAC, Dmitrii ANGHILOGLU, Serghei RAILEAN, Andrei BRAGARENCO, Vitalie SCRIPNIC
Technical University of Moldova
sontea@mail.utm.md

***Abstract* – In this work is presented the software for heart rate variability analysis using methods of ECG and FPG signal registration and processing.**

***Index Terms* – electrocardiogram, photopletismography, heartbeat, cardio interval.**

I. INTRODUCTION

Implementation of continuous non-invasive methods of monitoring the health of the surveyed people on the base of acquisition and analysis of the ECG or PPG with the aid of the computerized technical means enables rapid identification of different heart spontaneous affections or monitoring functional status of the autonomic nervous system by heart rate variability analysis. Worldwide mortality from cardiovascular disease ranks first among human diseases. One of the routine examinations of any patient is to determine the frequency of cardiac contractions [1-3]. Analysis of variability in time of heart contraction frequency – cardiointervalography is used both for diagnosis of a diseases and examination of health people in order to assess the state of stress and level of adaptation in extreme conditions [4-6].

II. STRUCTURE OF THE INFORMATION SYSTEM FOR THE ANALYSIS OF THE HEART RATE VARIABILITY

Developed information system allows analysis of heart rate based on electrocardiogram or photopletismographic signal (Fig. 1) during signal recording more than five minutes [7-9].

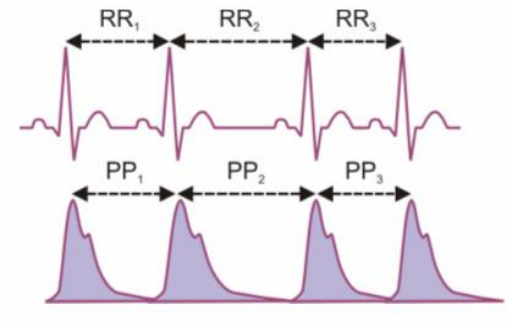

Fig. 1 ECG and PPG signal

Structure of the information system HRV consists of three core compartments (Fig. 2): Main Menu, File Manager and HRV Result Analysis.

The third section allows viewing HRV outcome analysis: real-time signal indicating extracted cardio intervals, the result of the string of the analysis of cardio intervals in time domain and temporal indicators calculation, the result of the string analysis of the cardio intervals in the frequency domain and calculation of spectral components.

Graphical interface of informational system for heart rate variability analysis is represented in Fig. 3.

The main menu contains a set of buttons with the help of which can be conducted the operation of the software: on/off the PC's USB port, start/stop recording signal in real-time, copying data files from SD-card memory device, printing the results and closing the program.

File Manager allows you to work with the patient data files: save signal in a file, opening a file, delete a file and sorting files.

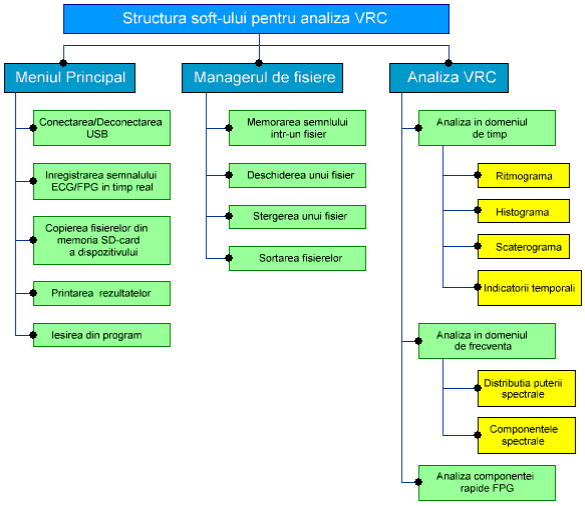

Fig. 2 Block diagram of software for analyzing HRV

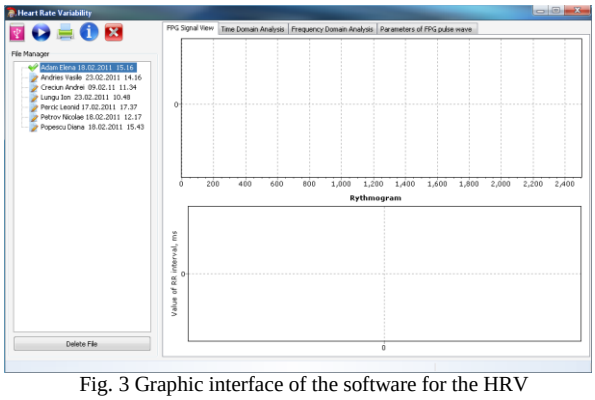

Fig. 3 Graphic interface of the software for the HRV

III. TESTING THE INFORMATION SYSTEM IN THE LABORATORY CONDITIONS

In the first stage of informational system work is necessary registration and visualization of the photopletismographic or electrocardiogram signal in real

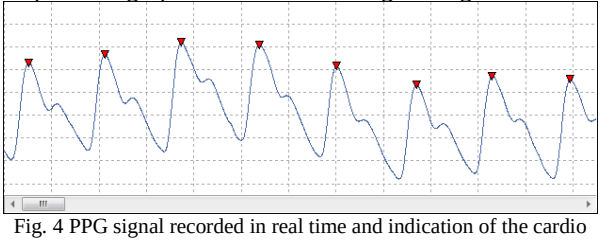

Fig. 4 PPG signal recorded in real time and indication of the cardio intervals.

time as well as the extraction of the cardio intervals on the base of the memorized signal (Fig. 4).

After recording the signal with at least of 5 minutes duration and extraction of the string of cardio intervals can be performed the analysis of the cardio intervals in time domain and getting Rhythmogram (Fig.5), Histograms, Scattergram and temporal indicators: HR, RRmin, RRmax, SDNN, CV, RMSSD, pNN50, Mo, Amo, DRR, SI (Fig.6).

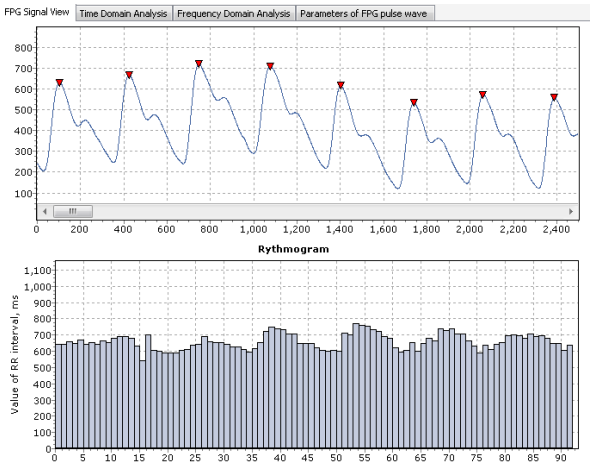

Fig. 5 Getting rhythmogram on the base of the string of cardio intervals

Rhythmogramma – displays interval duration dependence RR on the time recording interval RR. On the Axe abscissa is represented the time registration (seconds, minutes), but on the axis of ordinates is represented the RR measured interval duration (milliseconds).

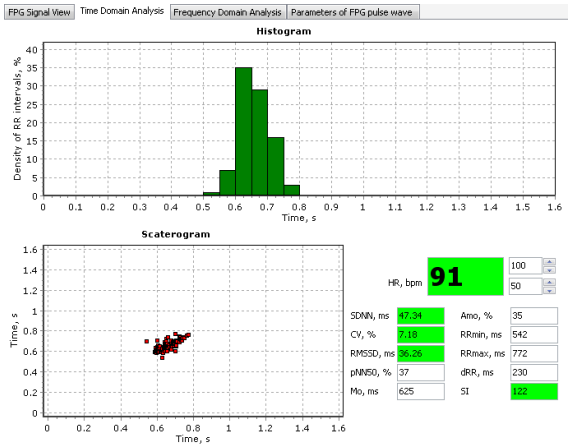

Fig. 6 Getting histogram, scattergram and temporal indicators

Histogram – represents the maximum number of RR intervals in a determined time interval. On the abscissa axis is represented time interval (seconds) but on the ordinates axis - density of the RR time intervals (%).

Scattergram - a two-dimensional representation of cardiac rhythm. On the abscissa axis is represented the size of RR_i (seconds), but on the ordinates axis is represented the RR_{i+1} interval (seconds). Table I contains the name of temporal indicators and measurement units.

Analysis of the string cardio intervals in the frequency domain involves obtaining a continuous cardio interval by applying cubic spline interpolation and then applying Fourier fast transformation (FFT) in order to calculate the distribution of the spectral power corresponding to the spectral components: Ulf, VLF, LF, and HF (Fig. 7).

Analysis of the spectral power density of the heart rate oscillations provides information on the power distribution in dependence upon the frequency of oscillations. To this fast Fourier transformation refers.

TABLE I. TEMPORAL INDICATORS

HR	Heart rate frequency (pulse) [beats / min]
RRmin	The minimum value of cardio intervals [ms]
RRmax	The maximum value of cardio intervals [ms]
SDNN	Mean square deviation [ms]
RMSSD	Quadratic mean difference characteristic [ms]
pNN50	The percentage of RR intervals which,(RR_i – RR_{i-1})>50 ms, reported on the total number of the intervals [%]
CV	Coefficient of variation [%]
dRR	The difference between the minimum and maximum value of the cardio intervals [ms]
Mo	Mode [ms]
Amo	Mode amplitude
SI	Stress index

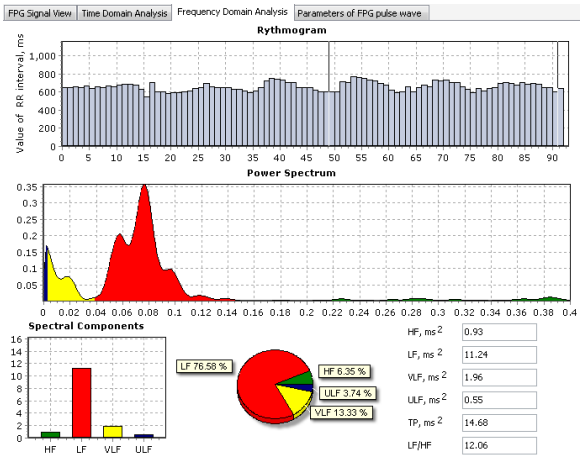

Fig. 7 HRV result analysis VRC in dependence upon the frequncy. Spectral components

Table II contains the name of the spectral components and the frequency diapason corresponding to each component.

TABLE II. SPECTRAL COMPONENTS

HF	Spectral power in domain of the high frequency	0,15-0,4 Hz (2-6,6 sec)
LF	Spectral power in domain of the low frequency	0,04-0,15 Hz (7-25 sec)
VLF	Spectral power in domain of the very low frequency	0,015-0,04 Hz (25-66 sec)
ULF	Spectral power in domain of the ultra low frequency	0,003-0,015 Hz (66-333 sec)

When the used method for investigating HRV is photopletismography at the same time can be performed an analysis of the photopletismographic signal by calculating the main parameters of the rapid component of the pulsating wave FPG (Fig. 8).

Table III contains the full name of the main parameters of the fast wave pulsating component FPG.

IV. CONCLUSIONS

Developed system allows recording and processing the

electrocardiographic or photopletismographic signal in real-time, extraction of the cardio intervals on the base of the recorded signal at a long period of time (up to 24 hours), saving and performing heart rate variability analysis by analysis in time and in the frequency of the cardio intervals string obtained.

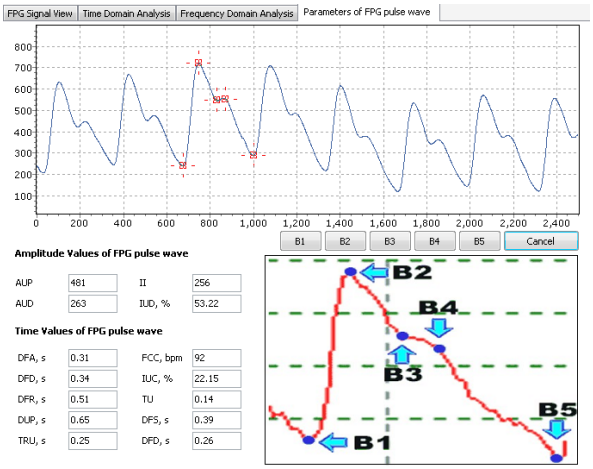

Fig. 8 Key parameters of the fast wave pulsating component FPG

TABLE III. KEY PARAMETERS OF THE FAST COMPONENT FPG

WPA	Wave pulsating amplitude
ADW	Amplitude of the decrotic wave
IH	Incesure height
IDW	Index of the decrotic wave
DAP	Duration of the anachrotic phase of the pulsating wave
DDP	Duration of the decrotic phase of the pulsating wave
DDP	Duration of the descent phase
DPW	Duration of the pulsating wave
TRW	Time reflection of the pulsating wave
FCC	The frequency of the cardiac contractions
IUW	Index of the upward wave
ET	Ejection time
DSP	Duration of systolic phase of heart rate
DDP	Duration of diastolic phase of heart rate

BIBLIOGRAPHY

[1] SAUL JP, ALBRECHT P, BERGER RD, COHEN RJ.Analysis of long term heart rate variability: methods, 1/f scaling and implications.Computers in Cardiology 1987.IEEE Computer Society press, Washington 1988: 419-22.

[2] MALIK M, FARRELL T, CRIPPS T, CAMM AJ.Heart rate variability in relation to prognosis after myocardial infarction: selection of optimal processing techniques.Eur Heart J 1989: 10:1060-74.

[3] MALIK M, XIA R, ODEMUYIWA OET AL.Influence of the recognition artefact in the automatic analysis of long-term electrocardiograms on time-domain measurement of heart rate variability.Med Biol Eng Comput 1993; 31: 539-44.

[4] МАШИН В.А. Нестационарность и длительность временного ряда сердечного ритма при диагностике функциональных состояний. Биофизика, 2007, Т. 52, No 2, с. 344–354

[5] R.BRYCHTA,R.SHIAVI,D.ROBERTSON. A SIVPLIFED Two-Component Model of Blood Pressure Fluctuation. Am.J.Physiol.,2007,February,292(2),H1193-H1293.

[6] http://www.ecg.ru/standarts/hrv/contents.htm

[7] Методические рекомендации. Исследование вариабельность сердечного ритма с использованием пакета программ «КардиоКит». Санкт-Петербург 2003

[8] http://circ.ahajournals.org/cgi/content/full/93/5/1043

[9] http://www.hrv.ru/standart/contents.html

The Analysis of the Legal Framework in the eHealth Field in Moldova, in the Context of European Integration

Alexandru ROŞIORU
National Health Management Center, Technical University of Moldova
arosioru@mednet.md

***Abstract* –The analysis of the legal framework in the eHealth field in Moldova, was made in the context of European integration. This study is aimed to identify the legislative and normative gaps in the field of implemetning eHealth in Moldova; intiation of changes in normative existing documents and making new papers, policies documents, plans, standards. This study reviewed all medical information systems, implemented in Moldova, to Identity legal gaps exist. Also in this study was structured lead analysis and the legal basis in the field of eHealth from European Union.**

***Index Terms* – eHealth, Legal framework in the eHealth field, Health Information Systems, Regulatory framework.**

I. INTRODUCTION, AIMS AND OBJECTIVES

"Solving the legal problems is primarily in developing any eHealth systems"

The medical information systems are developing rapidly in the world. This is due to qualitative and quantitative changes in the request for medical services, the amount of information in the public health care field and developement of informational skills of the society.

In this way, eHealth has a great potential to become a primary factor in developing and improving medical services.

The process of inforamational society developement in Moldova is based on the National Strategy of Informational Society Edification "Electronic Moldova", approved by the Government's Decision no. 225 from March 9 [1], of medical developement field in Moldova.

eHealth means the use of Internet technologies and electronic communications by providing and administrating medical services and public health care.

eHealth facilitates the prices administration, lowering medical errors and offering improved medical services for the patients.

eHealth will have a major effect on:

- The directing of health care system;
- Curative and preventive assistance;
- Increasing working efficiency in extreme situations;
- Developing medical science;
- Training and retraining of the staff;

The principles on the basis of strategy development in eHealth field are:

- Use of excelence examples and EU requirements for developing e-health services system;
- The responsability of local and central administration bodies in the succesful development process of eHealth;
- Efficient use of extremely limited financial resources;
- Integration of eHealth services in health care system to ensure appropriate use of informational technologies;
- **Legislation to create and exploit the eHealth systems in accordance to legislation, national and international standards;**
- **Protection and security of personal data in the patient's interest;**
- **Accesibility and transparency of information regarding public health and medical services;**
- Increasing the role of patients decision making and use of information aimed at health and medical services;
- Social orientation of eHealth care system in Moldova.

Specific objectives for eHealth startegy in Moldova are based on equally treated subsystems, that will contribute to succesful development of medical informational space in Moldova:

- **Developing normative and legislative framework for the use of informational technologies in medicine and its adjustment to the European.**
- Implementation of the Integrated Medical Information System Concept (IMIS) to control medical and administrative information flows.
- Achieving economic and management benefits from implementin eHealth services.
- Developing telemedical services to improving the quality and accesibility of medical services and bring closer medical services to the patient's place of residence.
- Training in using informational technologies and improving the access of medical staff to

information and education, to increase the efficiency and quality of medical services.
- Facilitating the access to information for patiens and citizens on public health and personal health to increase their participation in the decisions making process.

In recent years there has been a significant increase in use of ICT in health system. There were developed and implemented administrative information for primary medicine, health insurances, Automated Informational System "state Nomenclature of drugs", management in transfusion, monitoring and evaluation of the national Program of control and prevention of tuberculosis, etc.

According to the Ministry of Health's data, although there is universal access to ICT, only 143 medical institutions have broadband Internet access, fixed and mobile, and only seven institutions use ICT for data and information traffic between the medical instituutions. Despite the fact that the number of medical staff using ICT is rising, currently only 12% of the doctors use Internet and 18% - use the computer in their proffesional activity.

Currently in Moldova's health system are implemented telemedical pilot-projects in perinatal, neurology and ophthalmology fields. Telemedical videoconferences and educational support based on Web, are used in proffesional training in remote. Through videoconfrences doctors and students have regular access to international classes in different specialized medical fields.

The importance of ICT to enhance the quality and accessibility to medical services is increasing every year. All EU countries have adopted national strategies within the mutual effort of European Communities, mentioned in a number of documents supranational policies in the field, developed by the European Board in the years 2000-2009. To the end of 2011, EU countries are required to assess the situation and to adopt national legislation on access to telemedical services, including accreditation, accountability, procedures for reimbursement of services, confidentiality and data security.

The documents referred are aimed to optimizing the use of health systems resources, through mentioned by insertion of eHealth services. Through eHealth technologies is improved communication between providers of medical services and increases the patient's access to health information.

Through the Communiqué COM(2008) 0689 from 4.11.2008 „Telemedicine for patients benefits, health system and society", European Board outlines the importance of telemedicine, and for positive implementation of telemedical services suggest to EU countries great facilities, related to building confidence and acceptance of telemedical services, inserting legal clarities, solving technical problems of compatibility and standardization, as facilitating market development in the field of economic relations. .

WHO, besides the consultative support, granted to support countries' efforts in developing eHealth, designates organizations that possess expertise skills and can serve as centres of reference for developing services in the field. WHO resources can be used to priorities identification, developing eHealth policies, strengthening the legislative, normative and ethical basis in the use of health information, dissemination of experience about the practice of excellence in the field and facilitating the implementation of technical programs at national level.

The variety of eHealth services technologies, successfully implemented, include all levels of medical assistance, from public health to robotic surgery, from providing effective economic services and accessible to communities from dense populated areas to providing qualitative medical services in poor areas.

Developing legal framework for eHealth technologies use involves an analysis of current legislation, regulation in health care and telecommunications to identify legislative and administrative barriers in implementing the referred services. In the study will be outlined the normative and legal changes necessary for creating eHealth services in Moldova.

In the analysis of international experience will be reviewed the legislation and practice of European Community in the field of eHealth services regulation, protection of personal data, access to medical confidential information, etc.

This study is aimed to identify the legislative and normative gaps in the field of implemetning eHealth in Moldova; intiation of changes in normative existing documents and making new papers, policies documents, plans, standards.

This study involves several components research:
- **Analysis of existing legal framework** in using informational technologies and communications in Moldova's health care system;
- **Analysis of legislative actuality of Integrated Information Health System Concept** and of other documents at the basis of informational and communication system in health sector;
- **Outlining legislative issues within the practices framework** of SIA implementation in health sector in Moldova.
- **Documenting positive practices** of EU countries regarding the harmonization of legislation in eHealth;
- **Recommendations/proposals** regarding development, changes or improvement of legislative documents aimed to ralley the acquis communautaire, including its adjustment in accordance with other national legislative papers recently approved.
-

II. CONCLUSIONS AND RECOMMENDATIONS REGARDING LEGAL FRAMEWORK FOR IMPLEMENTING E-HEALTH SERVICES IN MOLDOVA.

The concept of eHealth changes essentially practices and rules in health sector in terms of relationships between doctors and patients, between medical institutions, on the other hand, institutions involved in financing and monitorizing health sector.

Legal safety represents a prerequisite for bussines environment to invest in inovations, and for medial institutions and patients to benefit of new products and services. As long as the eHealth market will be characterized by the lack of legal safety, there will be blocks for progress in the field..

The key to succes in the eHealth initiative is putting into question at regional and national level the legal interferences between eHeath and national policy in health.

As a result of the legal framework analysis for the

implementation of e(m)Health in Moldova have been noted the following conclusions:

At strategic level:

I. Health care system in Moldova has strategic tasks of implementing e(m)Health services based on National Strategies of building a informational society „Moldova electronnic", health care system's strategy of development during 2008-2017, National Health Policy in Moldova, Integrated Medical Information System;

II. In the health system of Moldova were carried out various activities for implementing ICT in health care, like:

Telemedicine and distance learning in Moldova; Automated Informational System „Mandatory Health Insurance"; Automated Informational System „Blood Service"; Automated Informational System „The improved system of epidemiological surveillance of avian influenza and other infectious diseases"; Automated Informational System „ the state Nomenclature of drugs"; Automated Informational System „Primary Medical Assistance", „Cabimed Manager" within the Universitary Clinics of Primary Medical Assistance; Integrated Informational System of medical Assistance and medical Imagistics within the Institute of Neurology and Neurosurgery „Hospital Manager Suite"; Integrated Informational System of medical assistance within the National Scientific Practical Center of Emergency Medicine; Informational System of statistical data collecting, Informational System of Monitoring and Evaluation of TB; mHealth – mobile Health; Automated Informational System of Primary Medical Assistance „MedEx" put into experimental exploitation; Informational System of Monitoring and Evaluation of AIDS; etc.

But all these initiatives remain sparodic, fragmented and without continuity and sustainability, mostly because of the imperfection of legislative framework of e(m)Health implementation in Moldova.

III. Some key previsions of the normative and legal framework are outdated and needs radical review (ex. Integrated Medical Informational System Concept);

IV. Despite the presence of some deficiencies in european legislation e(m)Health, alignment to the European legislative framework is a primary objective and vital for the development of the field.

At legislative level:

V. The legislative framework in Moldova, targeting both the health system, as the general is unspecific e(m)Health and does not include express previsions for its implement;

VI. Regardless the fact that some key previsions for e(m)Health,like, Law on patient rights and responsabilities no.263 from 27.10.2007, Law on excerising the medical proffesion no.264 from 27.10.2005, Law on health care no.411 from 28.03.1995, Law no. 982-XIV from 11.05.2000 on the access to information, Law no. 264-XV „On the electronic documents and digital signature" from 15.07.2004, Law no. 17 from 15.02.2007 on the protection of personal data, Law no. 241- XVI from 15.11.2007 on theelectronic communications, etc. are present in national legislation, although this legislative normative framework reamins **incomplete**.;

VII. After the analysis was found the lack of specific horizontal of legislation for implimen in the e(m)Health field ;

VIII. All legal useful previsions in implementing e(m)Health are reflected in very dispersed ares/fields which inflicts on the petential users e(m)Health from Moldova;

At normative level:

IX. There is no legal framework to stimulate and motivate the use the eHealth technologies in health care sector, including implementation of electronic chart of the patient and traffic of electronic data;

– It is not established of electronic medical records;
– There are no specific rules of usage for digital signature in health system;
– There is no normative framework on the interoperability of medical electronic data;
– There is no framework for unification of electronic medical terminology;
– Etc.

X. There is no regulatory framework related to standardization in e(m)Health.

III. RECOMMENDATIONS

In order to overcome the situation concluded after analyzing the normative legal framework in e(m)Health in Moldova are proposing:

At strategic level:

Based on the analysis, particularly the overcome in tie of stratedic previsions in IMIS and the need to cut the prioritary actions in accordance with international and european rigors required

– Developing and approving the **National Strategy of development in the field e(m)Health and Telemedicine**;

On legislative level:

Given the non-specific characteristics, incomplete, disperse of the legislativ normative framework in e(m)Health present in Moldova, the only solution the deficiencies would allow allignment from the start to international and european standards are:

– Development of the LAW **ON THE E(M)HEALTH IN MOLDOVA**.

On normative level

– Development of The analysis of the legal framework in the eHealth field in Moldova, in the context of European integration electronic medical data status;
– Establish specific rules for use of digital signature for health system;
– Develop of legal framework on interoperability of medical electronic data;
– Need to adopt the framework for the unification of medical terminology in electronic format;
– Need to develop a set of standards in medical informational technology (medical informatics). (Ex. There are not approved the standards on the electronic chart of the patient, ENV 13606);
– To prioritize the needs of implementation– example, electronic chart of the patient must become prioritary in implementation, to facilitate the medical access to technologies;

- To identify the nomenclature on national level and establish technologies that would provide automatic dissemination of nomenclature approved by the Ministry of Health in automatic mode;
- Establish standards for data exchange between Ministry of Health, Health Inssurance Company and Health facilities (example, establish standrads of electronic reports based on Statistic Ticket)

REFERENCES

[1] National Strategy of Informational Society Edification "Electronic Moldova", Available: http://www.e-moldova.md
[2] Communication from the European Commission on social services of general interest in the European Union, SEC 2006/516.
[3] Commission communication on 'Professional Services' of 5 September 2005, COM 2005/405.
[4] Council Regulation (EC) No 139/2004 of 20 January 2004 on the control of concentrations between undertakings (the EC Merger Regulation)
[5] Commission decision of 28 November 2005 on the application of Article 86(2) of the EC Treaty to State aid in the form of public service compensation granted to certain undertakings entrusted with the operation of services of general economic interest, O.J., L 312 of 29 November 2005, pp. 67-73.
[6] Council Directive 90/385/EEC of 20 June 1990 on the approximation of the laws of the Member States relating to active implantable medical devices
[7] Directive 98/79/EC on in vitro diagnostic medical devices
[8] Directive 2001/83/EC of the European Parliament and of the Council of 6 November 2001 on the Community code relating to medicinal products for human use
[9] Council Directive 93/42/EEC of 14 June 1993 concerning medical devices
[10] Thomas S. Deisboeck, J. Yasha Kresh, Complex Systems Science in Biomedicine. Springer, 2006.
[11] Lacramioara Stoicu-Tivadar, Sisteme informatice aplicate în servicii de sanatate, Editura Politehnica, Timisoara, 2004.

The Intelligent Support System for Remission in Patients with Psychiatric Disorders in Epilepsy

Maria BUTNARU[1], Ana CAPATANA[1, 2], Gheorghe CAPATANA[1],
Oleg COBILEANSCHI [3, 4], Alexandru POPOV [4]
[1]*State University of the Republic of Moldova*
[2]*Yale University*
[3]*State Medical and Pharmaceutical University "Nicolae Testemitanu" of the Republic of Moldova*
[4]*Psychiatric Hospital of the Republic of Moldova*
butnaru_m05@yahoo.com, ana_c27@yahoo.com, gh_capatana@yahoo.com, san.popov@gmail.com

***Abstract* – In the paper is related a project of an Intelligent Support System development for research and treatment of epilepsy. The tasks of this study are: a) to prove on material of over 100 patients with remissions that epilepsy is curable; b) to classify these persons by remissions groups; e) to develop and implement an intelligent support system for research, diagnostics and treatment assistance in epilepsy, d) principles development and implementation for psychological and psychiatric assistance and for critical situations remedy with which epileptics patients face, inclusively with socio-psychological assistance service conditions and within psycho neurologic consulting rooms. At the moment are developed: an expert system for diagnosis of epileptic patients with psychiatric disorders, an electronic textbook in the area of epilepsy problems, a support system for development of treatment programs of epileptic patients.**

***Index Terms* — artificial intelligence, epilepsy, expert systems, decision support systems.**

I. INTRODUCTION

The task of treatment of epileptic patients with psychological disorders became drastically a global problem. Many neurologist and psychiatrist doctors are more and more preoccupied with this problem and the obtained results became more important and precious. Recent statistical data shows an increase of up to 10.2 persons per 1000, while in developed countries from West Europe, US and Canada are related data of 2.4-7.2 persons per 1000. People with epilepsy need not only appropriate treatment, but the social-psychological support and they require mandatory society understanding and moral support. Every day, scientists and practitioners in the area of epileptology, make great efforts to find outstanding remedies involving experts from other areas with scope to solve an important task as treatment of epilepsy with psychological disorders.

The number of patients in Republic of Moldova with revealed epilepsy increases from year to year, even in conditions of massive migration, fact proved by increased number complains from population and in particular from young persons to neurologists and psychiatrist.

The epilepsy is a problem multidisciplinary. The success in epilepsy treatment requires collaboration of high qualification experts from different areas as: neurologists, psychiatrists, geneticists, pediatrician, mathematicians, immunologists, neurophysiologists, neuro-pharmacologists, artificial intelligence specialists.

Impressive discoveries from last years in the areas of genetics, immunology, neurophysiology, practical research and artificial intelligence encourage that in the near future the medicine will overcome the dogma of incurability of epilepsy.

II. THE SCIENTIFIC NOVELTY AND EXPECTED RESULTS

Based on a complex analysis on research material, methods of treatment for resistant types of epilepsy, development and implementation of intelligent support system for diagnosis and treatment of epilepsy will be attempt to develop for the first time in our republic an intelligent support system for treatment and diagnosis of epilepsy.

We propose a new project composed of *six stages*, which unifies the expertise in the area of medical science, physiology, decision support systems and artificial intelligence. Our research combines the development of: an expert system for diagnosis of epilepsy patients, a support system for doctor assistance during program process development for epilepsy patients treatment, selection and data results classification regarding patients with epilepsy remission, database development based on medical histories of epilepsy patients with remission, analysis of these data from database and retrieval of knowledge regarding the effect of remission of these data, expert system development to forecast the new patient with remission group with symptoms of epilepsy, developing a distance learning system of epilepsy and prophylaxis of this disease.

The first stage of the project is to develop *an expert system* for diagnosis of epilepsy patients. The system is planned to assist doctors from Moldova clinics and abroad. The system will provide a higher level of medical diagnosis from provinces and respectively, a smaller quantity of errors in diagnosis. The expert system is projected to be used in the training process in Medical Universities. It also could be used to support remote diagnosis process of patients with symptoms of epilepsy and to be used for population information on epilepsy and prophylaxis of this disease.

The second stage of the project is planed for development of a support system for doctor's assistance within the process of development of patient epilepsy treatment. The system will be developed following specialty classifiers.

The third stage of the project consists in data selection and systematization based on patients with remission of epilepsy,

database development regarding medical histories of epilepsy patients with remission. In present there are found 110 former epilepsy patients and brought with contribution of a new treatment (non-conventional) methodology into remission of the disease. Data regarding on medical reports of these group of patients will be prepared according to requirements of *Data Mining* technology for preparing data based of patients' peculiarities (age, social group, diagnosis, etc.).

The fourth stage of the project will consist of database knowledge retrieval. Knowledge will be collated into groups of patients according to diagnosis and degree of remission. Our experience of treating patients with epilepsy and bringing on remission status allows us to distinguish following classes of patients with remission:

a) *patients with therapeutic remission* – patient is maintained in this condition on a background of daily therapeutic treatment;
b) *patients with therapeutic remission with stable compensation* – to patient are not prescribed any drugs;
c) *patients with spontaneous remission* – after a short period of anti-epileptic drugs prescription (3-6 months);
d) after anti-epileptic drugs prescription (6-12 months);
e) *patients judged by differential diagnosis with other diseases* (early metabolic disorders, deficiency of Mg ions, Ca etc.);
f) *cured patients, with diverse long term remission and intermission*;
g) *patients, who eventually are diagnosed and then cured*.

The fifth stage of the project – development of an expert system for prognosis of a new patient with epilepsy symptoms within remission group.

The sixth stage of the project – development of a distance learning system on epilepsy and an information system of population regarding epilepsy and prophylaxis of this illness. As result of performed investigations we intend to promote and implement a series of original and differentiated programs of family and social rehabilitation, epilepsies prophylaxis through information and education, provisions and suggestions for epilepsy prophylaxis and treatment.

At the moment are developed:

- *an expert system for diagnosis of epilepsy patients with psychiatric disorders;*
- *epilepsy knowledge base;*
- *an electronic textbook in epilepsy;*
- *a support system for development of epilepsy treatment programs;*
- *other software components in the context of the project.*

III. THE EXPERT SYSTEM

The results of performed research will be translated into valuable applicative suggestions, which will explore the topic in all its biological, psychological and social aspects. Prognosis and prophylaxis recommendations, and curability of epilepsy under medical and psychological indicators, estimation of recovery methods and their reasoning for practical thinking in stationary conditions, in mental health centers and within family will facilitate the development of new organization forms of epilepsy patients recovery, given the particular pathology detected.

In the process of diagnosis setting may occur more choice, despite all medical data were collected. An expert system suggests a series of questions and provides the best clear conclusions that can be derived based on responses provided by the user (doctor). To facilitate the decision process of an accurate diagnosis, it was quickly developed an expert system for diagnostics. The expert system provides conclusions that are drawn based on responses provided by the system user (healthcare professional) to a series of questions proposed by the system. Development and implementation of expert system in medicine is a requirement of the time due to its use will help to increase the accuracy of making a diagnosis, reducing the time required set a diagnose and reduction of diagnostic errors. Exploiting an expert system is actually for Moldova and due insufficient number of specialists in epilepsy field in many rural health facilities. All the responsibility bears the family doctors who would welcome a "*diagnostics algorithm*" of expert level. It is expected to use the expert system developed for both diagnosis and treatment of patients with mental disorders, also in the process of health professionals training.

With the aim of developing an expert system in psychiatry [1-3] it was taken into account a particular group of diagnosed diseases of mental disorders. Thus, the diagnosis of diseases of the group mentioned above has some peculiarities; they are based on clinical investigations.Using expert system can be established nine groups of diagnoses mental graded from F00 to F09 in ICD-10 classification of mental and behavioral disorders [4]. Epilepsy expert system is equipped with a knowledge base. In the computer this base is stored in two forms: a) a version in Prolog - to diagnose epilepsy, and b) a version in HTML - to develop treatment programs for epilepsy patients with psychiatric disorders. Expert system can be used both as support to diagnosis of epilepsy patients with psychiatric disorders and in teaching.The expert system is developed in Prolog language and contains the following main components:

- *Knowledge Base for Diagnosis*, which contains specialty-specific facts and rules based on which is operated knowledge base for diagnosis with the aim to carry out reasoning to obtain solutions, recommendations or conclusions that are related to setting patient epilepsy diagnosis. The presentation model of knowledge is a *map.*
- *Dialog Interface* - allows dialogue with end users during the consultation sessions, and users access to base facts and knowledge;
- *Knowledge Acquisition Module* - provides to expert user querying types of the system with aim of obtaining solutions as well as methods of knowledge base modification (adding, removing or modifying cognitive units);
- *Explanatory Module* – have the role to explain the user, as well data available to the system, as reasoning process that is performed or solutions obtained within professional advice.

The presentation model of knowledge is a Map that reflects the link between disease and symptoms.

Developed expert system establishes mental disorders according to symptoms that patients have. It asks questions concerning 132 symptoms. The software result can be one of 24 different diagnoses.

Knowledge base for diagnosis keeps information regarding treatment rules of mental illness. The conclusion, obtained by inferential Engine of Expert System serves as a prerequisite for the next phase - development of treatment programs for epilepsy patients.

Due to this the expert system is equipped with two knowledge bases: first - to support the diagnosis, the second - to support development of treatment programs.

IV. ELECTRONIC TEXTBOOK IN EPILEPSY

Electronic textbook on epilepsy is a database for support of programs' development for treatment of patients with epilepsy. The electronic manual contains tables with information about the group diseases F00 to F09 (Fig. 1).

The first page is introductory and contains psychiatry symbolism placed on a graphic background. The end user accessing this page confirms the intention to browse the textbook by activating the button: "*Welcome*". Then the electronic manual switches to view the 2nd page. This page contains information on the textbook cover for mental illness. Clicking on cover book, it makes the transition to Contents of the book. All information relating mental illness is presented on separate pages. Here it is possible to click on any link from Contents, going to the page describing the requested theme. Can be used following options to browse the electronic textbook "*Next page*" (from first page to last), "*Previous page*" (from the current to the homepage). Browsing is carried out in accordance click the arrows on the right field (moving forward) or left (backward) of the electronic manual.

Fig. 1. Electronic Textbook

V. THE DECISION SUPPORT SYSTEM FOR DEVELOPMENT EPILEPSY TREATMENT PROGRAMS

The problem of treatment programs is a weak-structured problem and it may have several solutions. Therefore, for solving problem of issuing advices regarding treatment peculiarities was developed a decision support system. Database of support system for developing treatment programs is organized in pages (Fig. 2).

The tables contain information on diseases of the group F00 to F09 [4], including data about:

- Laboratory investigations;
- advices provided by specialty doctors;
- treatment schemas;
- daily dosage;
- costs.

On top of the table is the table of contents, which contains information on the groups of diseases. By clicking on the row of the table contents, it is accessed information about this group of diseases. Pressing the button labeled "*Return to top*", we return to contents of this book. The table *Treatment* can be accessed from the Contents page of the electronic manual. The system can be used as well in medical practice, as for training of healthcare professionals. The strategies implemented within system are based on the knowledge of expert specialists in the area.

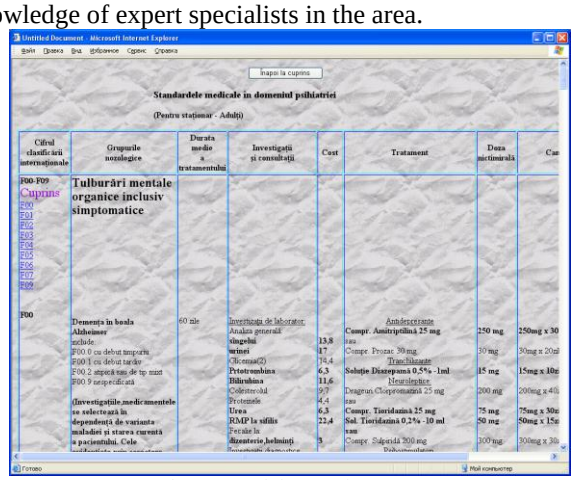

Fig. 2. A fragment of the Database „Treatment"

VI. CONCLUSION

In the paper was described a project of development of an intelligent support system within research and treatment area of epilepsy. The tasks of the research are: a) to prove based on material of over 100 patients with remissions that epilepsy is curable, b) to group these people by remissions groups, c) to develop and implement an intelligent support system for epilepsy research, diagnosis and treatment assistance, d) to develop and implement the principles of psychological, psychiatric and to remedy the critical situations with which face epileptics, including support services under the socio-psychological and psycho-neurological clinics. Currently are developed: an expert system for diagnosis of epilepsy patients with psychiatric disorders, an electronic textbook in the area of epilepsy, a support system for developing treatment programs for patients with epilepsy and other components in the context of research.

REFERENCES

[1] Butnaru M., Căpăţână Gh., Popov Al. Dezvoltarea sistemului de diagnosticare în medicină. În: Conferinţa Internaţională "Telecomunicaţii, Electronică şi Informatică" ICTEI 2010, ediţia a treia , Volumul II, Chişinău 20-23 mai, 2010, p.306-311.

[2] Carcea Iu., Butnaru M., Căpăţână Gh., Popov Al. Generator de sistem expert în medicină. În: Conferinţa Ştiinţifică „Dezvoltarea cercetării ştiinţifice, promovarea şi cultivarea creativităţii şi a inovării în procesul instruirii academice". 5 mai 2010. Rezumatele comunicărilor. Ştiinţe reale şi exacte. – Chişinău: CEP USM, 2010, p. 115-116.

[3] Moscalenco S., Butnaru M., Căpăţână Gh., Popov Al. Sistem suport de asistare a tratării pacienţilor. În: Conferinţa Ştiinţifică „Dezvoltarea cercetării ştiinţifice, promovarea şi cultivarea creativităţii şi a inovării în procesul instruirii academice". 5 mai 2010. Rezumatele comunicărilor. Ştiinţe reale şi exacte. – Chişinău: CEP USM, 2010, p. 129-130.

[4] The ICD-10 Classification of Mental and Behavioural Disorders. Clinical descriptions and diagnostic guidelines. Geneva, World Health Organization, 1993. – 263 p.

AUTOR INDEX

E

F

G

H

I

J

K

L

M

N

O

P

R

S

T

U

V

W

Y

Z